Rishi Gupta · Min Sun · Svetlana Brzev ·
M. Shahria Alam · Kelvin Tsun Wai Ng ·
Jianbing Li · Ashraf El Damatty ·
Clark Lim   *Editors*

# Proceedings of the Canadian Society of Civil Engineering Annual Conference 2022

## Volume 3

Springer

# Lecture Notes in Civil Engineering

Volume 359

**Lecture Notes in Civil Engineering** (LNCE) publishes the latest developments in Civil Engineering—quickly, informally and in top quality. Though original research reported in proceedings and post-proceedings represents the core of LNCE, edited volumes of exceptionally high quality and interest may also be considered for publication. Volumes published in LNCE embrace all aspects and subfields of, as well as new challenges in, Civil Engineering. Topics in the series include:

- Construction and Structural Mechanics
- Building Materials
- Concrete, Steel and Timber Structures
- Geotechnical Engineering
- Earthquake Engineering
- Coastal Engineering
- Ocean and Offshore Engineering; Ships and Floating Structures
- Hydraulics, Hydrology and Water Resources Engineering
- Environmental Engineering and Sustainability
- Structural Health and Monitoring
- Surveying and Geographical Information Systems
- Indoor Environments
- Transportation and Traffic
- Risk Analysis
- Safety and Security

To submit a proposal or request further information, please contact the appropriate Springer Editor:

- Pierpaolo Riva at pierpaolo.riva@springer.com (Europe and Americas);
- Swati Meherishi at swati.meherishi@springer.com (Asia—except China, Australia, and New Zealand);
- Wayne Hu at wayne.hu@springer.com (China).

**All books in the series now indexed by Scopus and EI Compendex database!**

Rishi Gupta · Min Sun · Svetlana Brzev ·
M. Shahria Alam · Kelvin Tsun Wai Ng ·
Jianbing Li · Ashraf El Damatty · Clark Lim
Editors

# Proceedings of the Canadian Society of Civil Engineering Annual Conference 2022

Volume 3

Springer

*Editors*
Rishi Gupta
Department of Civil Engineering
University of Victoria
Victoria, BC, Canada

Min Sun
Department of Civil Engineering
University of Victoria
Victoria, BC, Canada

Svetlana Brzev
Department of Earthquake Engineering
The University of British Columbia
Vancouver, BC, Canada

M. Shahria Alam
The University of British Columbia,
Okanagan Campus
Kelowna, BC, Canada

Kelvin Tsun Wai Ng
University of Regina
Regina, SK, Canada

Jianbing Li
Environmental Engineering Program
University of Northern British Columbia
Prince George, BC, Canada

Ashraf El Damatty
The University of Western Ontario
London, ON, Canada

Clark Lim
Department of Civil Engineering
The University of British Columbia
Vancouver, BC, Canada

# Conference Committee Members

## Volume 1

Dr. Rishi Gupta (Chair)
Dr. Svetlana Brzev (Technical Co-chair)
Dr. Min Sun (Technical Co-chair)
Dr. Jianbing Li (Cold Regions Specialty Chair)
Dr. Kelvin Tsun Wai Ng (Environmental Specialty Chair)

## Volume 2

Dr. Rishi Gupta (Chair)
Dr. Svetlana Brzev (Technical Co-chair)
Dr. Min Sun (Technical Co-chair)
Dr. Ashraf El Damatty
Dr. Ahmed Elshaer

## Volume 3

Dr. Rishi Gupta (Chair)
Dr. Svetlana Brzev (Technical Co-chair)
Dr. Min Sun (Technical Co-chair)
Dr. Ashraf El Damatty (Structural Specialty Co-chair)
Dr. Ahmed Elshaer (Structural Specialty Co-chair)
Dr. Shahria Alam (Material Specialty Chair)
Dr. Clark Lim (Transportation Specialty Chair)

## Volume 4

Dr. Rishi Gupta (Chair)
Dr. Svetlana Brzev (Technical Co-chair)
Dr. Min Sun (Technical Co-chair)
Dr. Ashraf El Damatty (Structural Specialty Co-chair)
Dr. Ahmed Elshaer (Structural Specialty Co-chair)
Dr. Shahria Alam (Material Specialty Chair)
Dr. Jianbing Li (Cold Regions Specialty Chair)
Dr. Kelvin Tsun Wai Ng (Environmental Specialty Chair)

# Contents

**Structural Specialty: Durability of Structures**

**Structural Specialty: Analysis and Design of Bridges**

## Materials Specialty: Advanced Composite Materials and Technology

**Materials Specialty: Innovatinve and Emerging Materials**

**Materials Specialty: Cement and Concrete**

# About the Editors

**Dr. Rishi Gupta** is a Professor in the Department of Civil Engineering at the University of Victoria. He leads the Facility for Innovative Materials and Infrastructure Monitoring (FIMIM) at UVic. He received both a masters and a Ph.D. in Civil Engineering from the University of British Columbia. His current research is focused on studying smart self healing cement-based composites containing supplementary cementitious materials and fiber reinforcement. His areas of interest include development of sustainable construction technologies, structural health monitoring, and non-destructive evaluation of infrastructure. He has more than 20 years of combined academic and industry experience. His industry experience includes working as the Director of Research of Octaform Systems Inc in Vancouver.

Rishi is a Fellow of Engineers Canada, the Canadian Society of Senior Engineers, and a past chair of the EGBC's Burnaby/New West branch. He is the past Chair of the international affairs committee of the Canadian Society of Civil Engineering (CSCE). He is a long standing member of the American Concrete Institute and is also a voting member of several subcommittees of ASTM C 09.

**Dr. Min Sun** is an Associate Professor and the Director of Undergraduate Program in the Civil Engineering Department at the University of Victoria (UVic). His research interests lie primarily in the field of structural engineering. His past research activity has included the development of design rules for hollow structural section connections and fillet welds, which have been incorporated into Canadian and American national steel design standards. From 2018 to 2020, he was the Western Region VP of the Canadian Society for Civil Engineering (CSCE). In 2019, he received the Faculty Award for Excellence in Teaching at UVic. Before joining UVic, he worked as a structural designer at Read Jones Christoffersen.

**Dr. Svetlana Brzev** is currently an Adjunct Professor at the Department of Civil Engineering, University of British Columbia. She has more than 35 years of consulting and research experience related to structural and seismic design and retrofitting of masonry structures in Canada and several other countries. Her research has been focused on seismic behaviour and practical design and construction issues related

to masonry structures. She has served as a member of the Technical Committee responsible for developing current Canadian masonry design standard CSA S304 since 2009 and is a member of the Technical Committee 250/SC8/WG1 responsible for developing Eurocode 8 provisions for seismic design of masonry buildings. She has been actively involved in several international initiatives related to promoting safe housing in seismically active regions, such as the EERI-sponsored World Housing Encyclopedia and Confined Masonry Network. Dr. Brzev served as a Director and Vice-President of EERI, a Director of the Masonry Society, and is currently a Director of the International Association for Earthquake Engineering. Dr. Brzev has co-authored two books related to design of masonry structures and a textbook on design of reinforced concrete structures and numerous papers and publications.

**Dr. M. Shahria Alam** is a Professor of Civil Engineering and the Tier 1 Principal's Research Chair in Resilient and Green Infrastructure in the School of Engineering at The University of British Columbia (UBC)'s Okanagan campus. He is serving as the founding Director of the Green Construction Research and Training Center (GCRTC) at UBC. Dr. Alam is the Vice President (Technical Program) of the Canadian Society for Civil Engineering (CSCE) and Chair of the Engineering Mechanics and Materials Division of CSCE. He received his Ph.D. in Civil/Structural Engineering from Western University in 2008. His research interests include smart and recycled materials and their structural engineering applications. He has published more than 350 peer-reviewed articles in these areas. He is the recipient of more than forty national and international awards including three best paper awards. Currently, Dr. Alam is serving as an Associate Editor of *ASCE's Journal of Bridge Engineering* and *Journal of Materials in Civil Engineering.*

**Dr. Kelvin Tsun Wai Ng** major fields of interest are in sustainable waste management system, disposal facility design, and data-driven waste policy. Kelvin has over 120 publications, and his projects have been supported by NSERC, Mitacs, CFI, Innovation Saskatchewan, Ministry of Environment, and other national and provincial sponsors. Kelvin has received both research and teaching awards, including six RCE Education for Sustainability Recognition Awards (2018–2022), Elsevier's Top Reviewer Award—Waste Management (2021), Saskatchewan Innovation Challenge (2019), McMaster Engineering Top 150 Alumni for Canada's Sesquicentennial (2017), and the University of Regina President's Award for Teaching Excellence (2017). Provincially, he has been appointed by the Ministry of Environment in Saskatchewan to serve on the Solid Waste Management Advisory Committee. Kelvin has been serving on the Association of Professional Engineers and Geoscientists of Saskatchewan (APEGS) Award Committee since 2017. Currently, he is chairing the APEGS Awards Committee. Kelvin is the Environmental Division Chair for Canadian Society for Civil Engineering and has organized and chaired/co-chaired a number of conferences, including the CSCE General Conference in 2015, and four CSCE Environmental Specialty Conferences in 2019, 2020, 2021, 2022. Currently, he is organizing the 2023 CSCE Environmental Specialty Conference at Moncton.

**Dr. Jianbing Li** is a professor and professional engineer in the Environmental Engineering program at the University of Northern British Columbia (UNBC). He received his Ph.D. degree in environmental systems engineering from the University of Regina. He has research interests in environmental pollution control, petroleum waste management, contaminated soil and groundwater remediation, environmental modelling and decision analysis, environmental risk assessment, and oil spill response. He has produced more than 300 publications in international journals and conferences, including over 200 refereed journal publications, with an h-index of 45 (Google Scholar). His research has been supported by various organizations, including Natural Science and Engineering Research Council of Canada (NSERC), Fisheries and Oceans Canada (DFO), Natural Resources Canada (NRCan), BC Ministry of Forests, and Geoscience BC. He obtained the 2013 Northern BC Business and Technology Award (Collaborative Research Award with Husky Energy), the 2010, 2014 and 2019 UNBC Research Excellence Award, and the 2013 UNBC Achievement Award in Professional Practice and Mentorship. Dr. Li was nominated for the 2022 and 2023 CUFA BC Ehor Boyanowsky Academic of the Year Award. He served as a member of NSERC's Research Tool and Instruments Selection Committee for Civil, Industrial and Systems Engineering in 2016–2021, and the Committee Chair for the 2021 competition. He is also a member of NSERC's Discovery Grant Evaluation Group for Civil, Industrial and Systems Engineering (EG1509) (2022–2025). He has been a member of the Academic Examiners Subcommittee with Engineers and Geoscientists BC since 2017. He has served as the co-director of the UNBC/UBC environmental engineering program for 4 years (2013–2017). He served as a guest editor for seven international journals, and is currently an Associate Editor or Editorial Board member of seven journals. He is the inaugural Chair of the Northern British Columbia Section of Canadian Society for Civil Engineering (CSCE). Dr. Li was named a CSCE Fellow in 2022.

**Dr. Ashraf El Damatty,** Professor and Chair of the Department of Civil and Environmental Engineering, Western University. He is a Fellow of the Canadian Academy of Engineering, the Engineering Institute of Canada, and the Canadian Society of Civil Engineering (CSCE). He is a Research Director at the WindEEE Research Institute and Editor-in-Chief of the *Journal of Wind and Structures*. He holds honorary Professorship titles at four international universities. He obtained B.Sc. and M.Sc. from Cairo University, Egypt, Ph.D. from McMaster University, and MBA from University College London, UK. He is the founder of the CSCE Steel Structures Committee and served for five years as the Chair of the CSCE Structures Division. He has written more than 250 publications, supervised more than 60 graduate students and has been invited as keynote speaker in 14 countries. He received several awards including the Alan Yorkdale Award by ASTM, Best Paper Award at the Canadian Conference on Effective Design, Honourable Mention in 2014 Casimir Gzowski Medal, 2015 CSCE Whitman Wright Award, 2016 CSCE Horst Leipholz Medal, Western University Faculty Scholar Award, 2018 Professional Engineers of Ontario Medal of Research and Development, 2021 Pratley Award for Best Paper on Bridges, and the 2021 Western Engineering Award for Excellence in Research,

Western University. He is an international leader in the interdisciplinary field of Wind and Structural Engineering. His research has influenced the international codes and the Engineering practice worldwide. It resulted in the first specifications in the world for downburst and tornado loading on transmission line structures that was recently incorporated into the guidelines of the ASCE.

**Clark Lim** has over three decades of experience in public, private, and academic sectors, specializing in analytical methods and information systems for transportation applications. As a consultant, he advises senior officials on policy, technology, and governance matters, where he utilizes an evidence-based and technically progressive approach to establish sound policy frameworks. In the mid-1990's, he was part of the team that established TransLink, the Greater Vancouver Transportation Authority, where he was also the Project Manager of the Evergreen Rapid Transit Line planning and consultation process. At UBC Clark is currently an Adjunct Professor in the Department of Civil Engineering where he has taught transportation engineering and planning to senior undergraduate and graduate students since 2006. His previous research at UBC focused on intelligent transportation systems for freight, and the impact quantification of the 2010 Winter Olympic Games. Currently he is researching the effects of hybrid working on transportation policies, the impacts of ride-hailing trips through big data methods, and developing tools to measure sustainability and diversity-equity-inclusion indices for corporate boards.

# Structural Specialty: Timber Structures

# Experimental Evaluation on Nail-Laminated Timber (NLT)—Steel Fiber-Reinforced Concrete Composite Beams with Notch Connections

**Hamidreza Chaboki, Lei Zhang, Jianhui Zhou, and Thomas Tannert**

**Abstract** In North America, timber–concrete composite (TCC) floor system is gaining increasing interest in recent years thanks to their superior structural performance and low self-weight. Notched connections are a feasible and economical shear connecting solution for panel-type TCC floors. However, the concrete layer is prone to cracking under bending due to stress concentration around notches, which could lead to a brittle failure pattern and a decrease in the load-carrying capacity of the TCC floors. To address this issue, in this study, five groups of nail-laminated timber (NLT)–concrete composite beams were fabricated with varying notch depth, number and locations of notches, and ratios of thickness. The concrete layer was reinforced with steel fibers as a potential solution to mitigate the formation of cracks in the notches. Three-point bending tests were conducted to examine their bending performance. The results showed that the bending capacity of specimens is highly related to the ratio of the thickness and the number of notches so that the load-bearing capacity and stiffness of group 5 with the thickness ratio of 1:1 increased 34.6% and 49.4%, respectively, in comparison to reference group.

**Keywords** Nail laminated timber · Composite floor · Notch connections · Flexure performance

## 1 Introduction

Timber–concrete composite (TCC) floors, as an alternative to pure timber slab systems, have been used in multi-story timber buildings in recent decades to improve the bending stiffness and load-bearing capacity of the timber floors [1]. The use of

H. Chaboki · J. Zhou (✉) · T. Tannert
School of Engineering, University of Northern British Columbia, Prince George, Canada
e-mail: jianhui.zhou@unbc.ca

L. Zhang
Department of Civil and Environmental Engineering, University of Alberta, Edmonton, Canada

3

concrete in the upper section of the floor, which is the compression zone, and timber in the bottom section, which is the tensile zone, results in an efficient utilization of the mechanical properties of both materials [2]. Undoubtedly, the structural performance of TCC floors is dependent on the efficiency of the connections that are responsible for restricting the relative slip between two layers. For a TCC system under bending, the longitudinal shear forces between concrete and timber are developed by the connection system in resisting the relative slips. Various types of connectors for TCC floors have been developed and tested in the past decades. Most connectors typically consist of metal fasteners that are often expensive in terms of constructability, quality control, and labor intensity. Moreover, the notched connections can be prefabricated at low cost before the beams or panels are sent to the construction site [2–5].

Notched connections are typically cut by a computer numerical control (CNC) machine that provides precise, fast, and low-cost production [6]. These connections can be made by cut-outs or drillings in the timber members or by gluing blocks to the structural timber members. In addition to the advantages of these connections, such as a great balance between simplicity and mechanical performance, some disadvantages, such as low axial load-carrying capacity and brittle failure, still exist [7]. The high rigidity of notched connections can cause a low magnitude of slip within the interlayer between the top and bottom layers. Therefore, the notches are generally located at a noticeable distance along the beam. Because of this, when timber and concrete are connected with interlocking notched connections, the concrete layer is prone to cracking under bending due to stress concentration. The cracking of concrete notches without any reinforcement can lead to a brittle failure pattern and a decrease in the load-carrying capacity of the TCC floors.

It is possible to strengthen the concrete layer with steel fibers to decrease the formation of cracks and to control the crack propagation and growth [8]. In addition to the capability of post-crack bridging, fibers can decrease the width of the crack and the restrained area of the concrete [9]. Through the hardening of the concrete, the fibers bond and bridge the cracks, delaying their growth at any load level. The presence of a high-volume fraction of fibers may result in an increment in the matrix tensile strength of concrete [8]. As the concrete reaches its tensile capacity, fibers continue to restrain the growth and opening of cracks, based on their length and bonding characteristics, effectively bridging macro-cracks. The post-peak macro-crack bridging capability is the main reinforcement mechanism in fiber-reinforced concrete (FRC) composites, the benefits of which are strain-hardening response before localization, increased tensile strength, and enhanced toughness beyond crack localization. The presence of the fibers in an element results in flexural performance improvement and, at the same time, causes delays in the extension of cracks [10].

In this study, the structural efficiency of notched connections and steel fibers in concrete was evaluated in nail-laminated timber (NLT)–concrete composite beams. For this purpose, five groups of TCC beams with various notch depths, numbers, and locations were prefabricated and tested. The concrete layer was reinforced with steel fibers to mitigate the formation of cracks in the notches and to ensure that the load-carrying capacity is governed by timber bending failure. The specimens were tested under three-point bending, in which failure modes, ductility, bending stiffness,

and peak loads were evaluated to investigate the effect of notches on the bending properties and the effectiveness of the fibers in preventing or delaying the brittle failure of notched connections.

## 2 Methodology and Materials

### 2.1 Specimen Design

As shown in Fig. 1, five groups of TCC specimens with a dimension of 190 mm (width) × 150 mm (thickness) × 3006 mm (length) were fabricated in this study. Each group had three replicates. The rectangular notched connections were symmetrically spaced about the mid-span, but the number and depth of the notches varied between specimens. The shear length of timber in front of notches in all specimens was 400 mm. The width and depth of these notches, as well as their positions, are depicted in Fig. 1. In each specimen, three 100 mm self-tapping screws were utilized vertically at the mid-span and two ends to prevent gap opening, as illustrated in Fig. 3. Screw embedment lengths in both wood and concrete were 50 mm (60 mm into wood in SP7 due to the thicker timber layer).
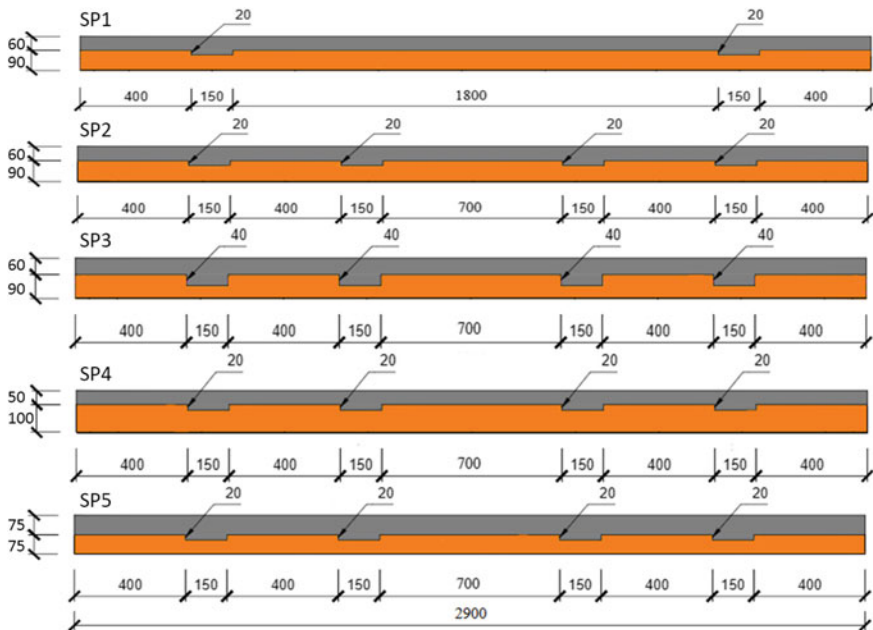


**Fig. 1** Composite floor specimen configurations (dimensions in mm)

SP2 was considered as the reference group, which had four notches with a depth of 20 mm and a length of 150 mm, and a concrete and timber thicknesses of 60 mm and 90 mm, respectively. SP1 included two 20 mm deep notches that were 1800 mm apart. The number of notches in SP2 was doubled to investigate the effect of notch number on stiffness and strength. The notched connections in SP3 had the same locations and length as in SP2, but the depth was 40 mm to examine the influence of notch depth. SP4 and 5 had the same geometry and locations of notches as the reference specimen but had different timber-to-concrete thickness ratios.

## 2.2 Materials

The NLT beams were made up of five 38-mm thick lumber planks that were nailed together to form a 190-mm wide beam. Spruce/pine dimension lumber of No. 2 or better grade was used. The lumber had a density of 444 kg/m$^3$ and a moisture content of 13% as measured right before the bending tests. The notches were cut using a router, as shown in Fig. 3.

The concrete was supplied by a local concrete company. To avoid the formation of voids around the corners of notches, the nominal maximum coarse-aggregate size was 10 mm. HE-4550 steel fibers with a 50 mm length and two bend ends were introduced specifically for reinforcing at 0.5% in terms of volume (see Fig. 2). All of the specimens were made from the same batch of concrete. Three cylinders with a nominal diameter of 100 mm and a height of 200 mm were cast at the same time and subjected to ASTM C39/C39M-20 testing after 28 days [11]. The average compressive strength of concrete cylinders was 39.3 MPa, with a coefficient of variation of 0.96%. Concrete cylinders had a density of 2325 kg/m$^3$. According to Eq. (1), the Young's modulus of concrete was determined to be 28,027 MPa based on the 28-day compressive strength ($f_c'$) and density ($\gamma_c$) [12].

$$E_c = \left(3300\sqrt{f_c'} + 6900\right)\left(\frac{\gamma_c}{2300}\right)^{1.5}. \tag{1}$$

## 2.3 Test Setup

The TCC beam specimens were subjected to three-point bending tests based on ASTEM 198-15, as illustrated in Fig. 4. The supports were made 100 mm wide to avoid indentation of the timber at the supports. Two string potentiometer sensors were employed to measure the mid-span deflection, and four LVDTs were installed at the two ends of each beam on each side to measure the relative slip between timber and concrete. The load was applied by an actuator, conveyed to the composite floors by a steel plate, and then distributed to the specimens by the plywood layer. The steel plate

**Fig. 2** Steel fibers (type HE-4550)

and plywood were both 200 mm wide. To avoid any short-term creep, displacement from the actuator was applied monotonically at a loading rate of 2–3 mm/min to ensure that specimens would fail in roughly 20 min.

The theoretical bending stiffness of a non-composite floor can be calculated using Eq. (2), where $E_c$ and $E_t$ are the concrete and timber moduli of elasticity, and $I_c$ and $I_t$ are the concrete and timber second moments of area, respectively [13].

$$\text{EI}_{\text{no}} = E_C I_C + E_t I_t. \tag{2}$$

The bending stiffness for the theoretical full composite floor is determined according to Eq. (3)

$$\text{EI}_{\text{full}} = E_C I_C + E_t I_t + \left( \left( \frac{h_c + h_t}{2} \right)^2 \Big/ \frac{1}{E_C A_C} + \frac{1}{E_t A_t} \right), \tag{3}$$

where $A_c$ and $A_t$ are the cross-section areas of concrete and timber, respectively, and $h_c$ and $h_t$ are the concrete and timber depths. Equation (4) was used to determine the ultimate bending moment in each group and then was normalized to 1-m width as provided in Table 1.

$$M_{\text{max}} = \frac{P_{\text{max}} L}{4}, \tag{4}$$

where $L$ is span and $P_{\text{max}}$ is the peak load. The deflection and load were recorded for calculating the bending stiffness values and moment capacities. The serviceability bending stiffness (referred to as bending stiffness herein) of the floors was determined
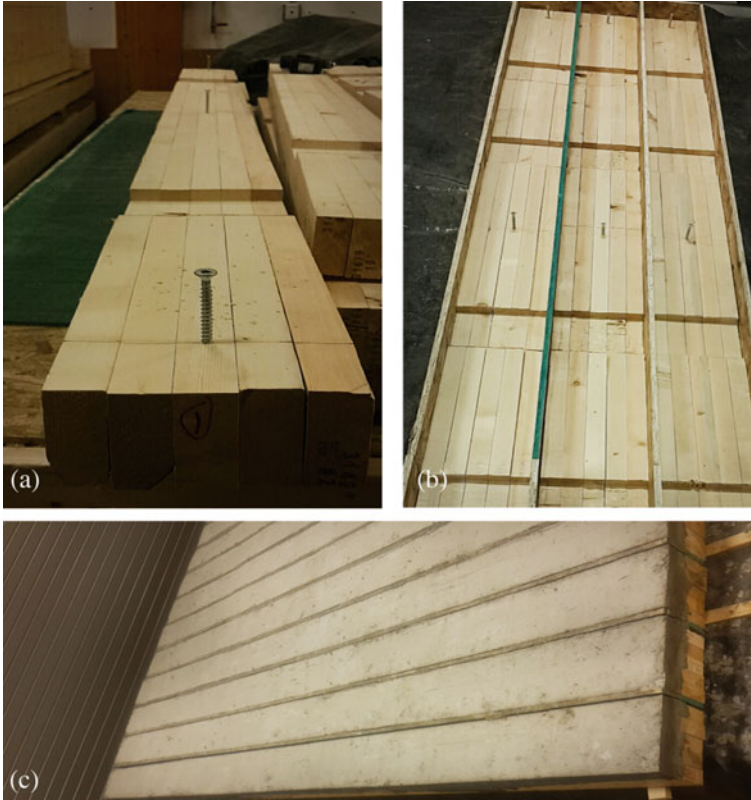
**Fig. 3** Preparation process of the specimens: **a** specimen with notches cut and self-tapping screw, **b** specimens ready for casting of concrete, **c** final specimens after curing of the concrete
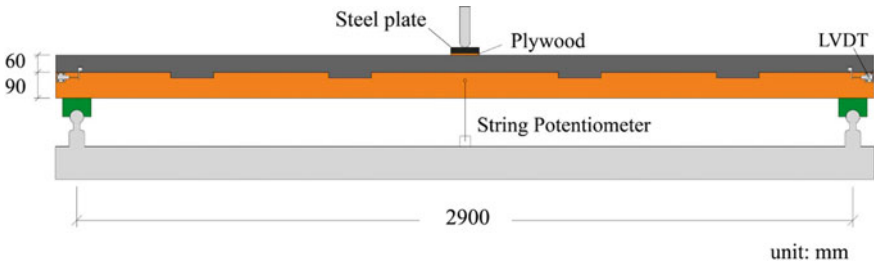


**Fig. 4** Schematic of the bending test setup

from Eq. (5) [14]

$$\text{EI} = \frac{PL^3}{48\Delta},$$ (5)

where $L$ is span and $P/\Delta$ is the slope of the load–deflection curve between 10 and 40% of peak load, which is regarded as the load level at serviceability limit states [15]. Equation (6) was used to determine the ultimate bending stiffness of the floors:

$$\text{EI}_{\text{ult}} = \frac{L^3}{48} \frac{0.8 P_{\text{max}}}{\Delta_{0.8}},$$ (6)

where $\Delta_{0.8}$ indicates the mid-span deflection at 80% of peak load [15]. Stiffness drop from the serviceability stage to the ultimate state for each specimen is shown in Table 1. The composite efficiency of the tested floors [16] is calculated using Eq. (7), which ranges from zero (non-composite) to one (fully composite).

$$\lambda_1 = \frac{\text{EI} - \text{EI}_{\text{no}}}{\text{EI}_{\text{full}} - \text{EI}_{\text{no}}}.$$ (7)

A deflection-based definition of composite efficiency [17] is shown in Eq. (8).

$$\lambda_2 = \frac{\Delta_{\text{no}} - \Delta}{\Delta_{\text{no}} - \Delta_{\text{ful}}} = \frac{\frac{1}{\text{EI}_{\text{no}}} - \frac{1}{\text{EI}}}{\frac{1}{\text{EI}_{\text{no}}} - \frac{1}{\text{EI}_{\text{full}}}},$$ (8)

where $\Delta_{\text{no}}$, $\Delta_{\text{ful}}$, and $\Delta$ are the deflections of the non-composite floor, full composite floor, and tested floor under the same load (10–40% of peak load). Table 1 shows the deflection-based composite efficiency from Eq. (8), which had higher values than the stiffness-based composite efficiency.

**Table 1** Test results of the specimens

| Specimen group | $P_{\text{max}}$ (kN) | $M_{\text{max}}$ (kN m) | EI (kN m$^2$) | EI$_{\text{ult}}$ (kN m$^2$) | Reduction of stiffness (%) | $\lambda_1$ (%) | $\lambda_2$ (%) |
|---|---|---|---|---|---|---|---|
| SP1 | 19.0 | 72.4 | 439.4 | 431.7 | 1.4 | 53.0 | 77.0 |
| SP2 | 23.7 | 89.5 | 458.0 | 342.7 | 26.1 | 55.0 | 82.0 |
| SP3 | 23.4 | 89.3 | 438.4 | 383.2 | 12.6 | 48.0 | 78.0 |
| SP4 | 33.4 | 127.3 | 578.4 | 532.5 | 8.0 | 71.0 | 90.0 |
| SP5 | 31.9 | 121.9 | 684.4 | 581.3 | 15.2 | 74.0 | 90.0 |

# 3 Results and Discussion

## 3.1 Load Deflection Behavior and Bending Properties

Figure 5 shows the typical load–displacement curves for the specimens, with the mid-span deflection calculated as the average of the deflections measured on both sides of each specimen. The load–displacement curves in Fig. 5 show how the strength, ductility, and rigidity differ between SP2 and other specimens. The peak load and stiffness of all the groups are listed in Table 1, while Table 2 shows the failure modes for all the specimens. The peak load of the beams was taken during the test as $P_{\max}$ for each group. Figure 5 and Table 1 clearly showed that SP4 and SP5 had the highest strength of 33.4 kN and 31.9 kN, respectively, while SP1 experienced the lowest load-bearing capacity with 19 kN.
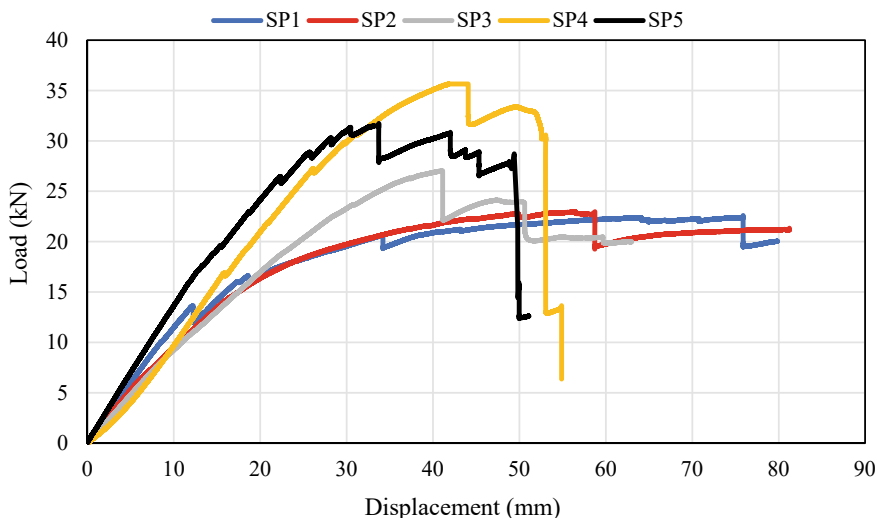


**Fig. 5** Load–displacement curves

**Table 2** Failure modes of the specimens

| Specimen group | Failure mode |
| --- | --- |
| SP1 | Timber tensile failure in one lumber plank |
| SP2 | Timber tensile failure in two lumber planks with shear failure in concrete |
| SP3 | Timber tensile failure in two lumber planks with notch shear failure in concrete |
| SP4 | Timber tensile failure in two lumber planks with notch shear failure in concrete and concrete buckling |
| SP5 | Timber tensile failure in three lumber planks with shear failure in concrete layer |

As shown in Table 1 and Fig. 5, SP4 and SP5 exhibited significantly higher bending stiffness than SP2 with 26.3% and 49.4% improvement, respectively. The effectiveness of SP3 was the lowest among the other specimens with 12% decrease in comparison to the reference one. Moreover, the stiffness of the reference specimen dropped the most with the 26.1%.

Although bending stiffness was lower in SP3 than in SP2, its ultimate load-carrying capability was higher which means that the stiffness reduction of SP3 was almost half of reference one. However, they used the same number of connections (four), but deeper notch depth in SP3 improved the bending stiffness. The results also revealed that SP4's ultimate load-carrying capability was much higher than the reference specimen. The SP5 had equal concrete and timber thickness (75 mm), and the concrete thickness was increased, while the timber thickness was decreased from the reference specimen. This adjustment resulted in an 4.5% reduction in strength and a 18% increase in stiffness in comparison to SP4. The bending stiffness of specimens 1 and 3 was low, although their failure pattern was ductile.

## 3.2 Failure Modes

The major failure patterns of the tested TCC beams are shown in Fig. 6 and listed in Table 2. Different connection designs and relative thicknesses of timber and concrete in TCC beams resulted in various failure patterns. When the floor was under bending, the notched connectors resisted shear forces. Almost all specimens with notches had diagonal concrete cracking at the notched corners (shear cracks), as seen in Fig. 6b.

It can be argued that the failure happened in the timber part in almost all specimens. Concrete shear cracks started from notches around the load-transfer area under the shear load between timber and concrete. These cracks originated from the notched corners in a diagonal or almost vertical orientation, then spread more or less horizontally. With increasing load, a gap between the timber and concrete layers can be seen. Under the shear forces, the notched connections finally sheared off, starting with one external notch (near the support) and then the internal notch on the same side. The failure of the notches resulted in an abrupt gap between the two components. As a result, the concrete component that was under compression failed due to buckling. The sudden and brittle failure was avoided in all specimens thanks to the use of steel fibers. In SP5, after failure in the timber portion, buckling occurred in the concrete with increased load, although it is worth noting that steel fibers supplied ductility in the concrete part by regulating the crack width.

The timber component of SP1 failed due to combined bending and tensile forces. There was no evident damage to the concrete, but a flexure crack was discovered at the bottom of the concrete at mid-span. Shear failure was not seen in the notches of SP1; however, a gap was formed between the two layers. All of the remaining examples showed the same overall failure mode.

The failure mode of SP5 is shown in Fig. 6e. This specimen's bending stiffness and load-carrying capability were significantly higher than the reference specimen. The
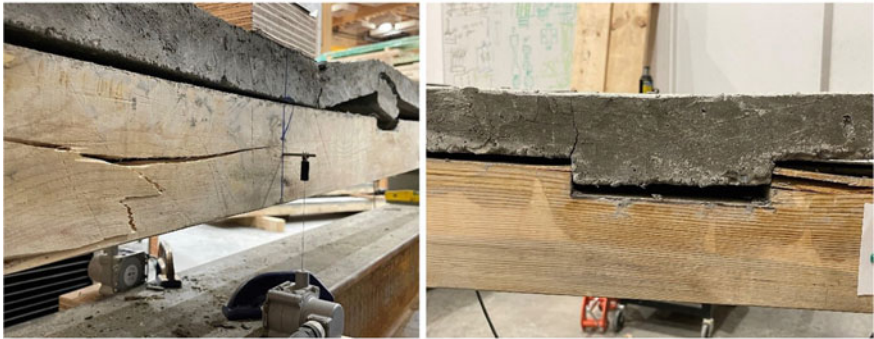
**Fig. 6** **a** Failure of SP1. **b** The failure of SP2. **c** The failure of SP3. **d** The failure of SP4. **e** The failure of SP5

(e)

**Fig. 6** (continued)

bearing capacity of the concrete layer is raised when the concrete part is reinforced with steel fibers, and steel fibers can effectively reduce the development of crack width, which resulted in the failure of the timber layer in virtually all of the specimens.

Minor cracks at the corners of the notches in concrete appeared in all specimens quickly after the test began and spread slowly, but the failure of almost all groups was governed in the timber part at the peak load. The benefit of using NLT along with steel fibers in concrete can be seen in SP4. When the load increased, three individual lumbers in the NLT of SP4 failed, but it was able to take a higher load, and the steel fibers were able to curb and regulate the crack breadth in concrete, resulting in maximum strength and stiffness, and eventually buckling failure of the concrete.

## 4 Conclusion

The bending properties of five NLT–concrete composite floors with varied notched connection patterns are investigated experimentally in this work. The following conclusions can be derived from the tests:

- As the number of the notches doubled, the load-bearing capacity and bending stiffness improved. Having deeper notch depth had no significant impact on the bending capacity of the specimens.
- When the concrete-to-timber ratio is 1:1 and 1:2, the load-carrying capacity of the NLT–concrete composite flooring was improved significantly with 34.6% and 41%, respectively, in comparison to reference group.
- Steel fibers could help to strengthen the concrete section by reducing the width of cracks and stopping them from spreading. As a result, the failure in notch connection was delayed and all the beams experienced failure in the timber part at the peak load.
- Because the notched connection of the composite floors was semi-rigid, only partial composite action was found in the specimen.

# References

1. Aicher S, Klock W, Dill-Langer G, Radovic B (2003) Nails and nailplates as shear connectors for timber-concrete composite constructions. Otto-Graf-Journal 14:189
2. Zhang L, Chui YH, Douglas T (2020) Tomlinson, experimental investigation on the shear properties of notched connections in mass timber panel-concrete composite floors. Constr Build Mater 234:117375
3. Negrão J, Oliveira F, Oliveira CA, Cachim PB (2010) Glued composite timber-concrete beams. II: Analysis and tests of beam specimens. J Struct Eng 136(10):1246–1254
4. Yeoh D, Fragiacomo MD, Franceschi M, Heng Boon K (2011) State of the art on timber-concrete composite structures: literature review. J Struct Eng 137(10):1085–1095
5. Boccadoro L, Frangi A (2014) Experimental analysis of the structural behavior of timber-concrete composite slabs made of beech-laminated veneer lumber. J Perform Constr Facil 28(6):A4014006
6. Jiang Y, Crocetti R (2019) CLT—concrete composite floors with notched shear connectors. Constr Build Mater 195:127–139
7. Dias A, Schanzlin J, Dietsch P (2018) Design of timber–concrete composite structures: a state-of-the-art report by COST action. Report No. FP1402/WG
8. Weiss WJ, Shah SP (1997) Recent trends to reduce shrinkage cracking in concrete pavements. Presented at the Proceedings of the 1997 Airfield Pavement Conference
9. Zaetang Y, Sata V, Wongsa A, Chindaprasirt P (2016) Properties of pervious concrete containing recycled concrete block aggregate and recycled concrete aggregate. Constr Build Mater 111:15–21
10. Banthia N, Gupta R, Mindess S (2004) Developing crack resistant FRC overlay materials for repair applications. Presented at the NSF Conference, Bergamo, Italy
11. ASTM (2020) Standard test method for compressive strength of cylindrical concrete specimens. ASTM C39/C39M-20, ASTM, West Conshohocken, PA
12. CSA (Canadian Standards Association) (2019) Design of concrete structures. CSA A23.3-19, CSA, Mississauga, ON, Canada
13. Mai KQ, Park A, Nguyen KT, Lee K (2018) Full-scale static and dynamic experiments of hybrid CLT–concrete composite floor. Constr Build Mater 170:55–65
14. ASTM (2015) Standard test methods of static tests of lumber in structural sizes. ASTM D198-15, ASTM, West Conshohocken, PA
15. CEN (1991) European Committee for Standardization. Timber structures—joints made with mechanical fasteners—general principles for the determination of strength and deformation characteristics. EN 26891, CEN, Brussels, Belgium
16. Zhang L, Zhang S, Chui YH (2021) Analytical evaluation to the timber-concrete composite beam connected with notched connections. Eng Struct 227:111466
17. Gutkowski R, Brown K, Shigidi A, Natterer J (2008) Laboratory tests of composite wood–concrete beams. Constr Build Mater 22(6):1059–1066

# Assessment of the Lateral Bearing Capacity of Traditional Walls Made of Timber Planks

**Mohamed Hassen Kraiem, Amar Khaled, and Marie-José Nollet**

**Abstract** Evaluation of the structural capacity of existing buildings is a key component in the seismic risk assessment process to estimate damage and socioeconomic losses due to earthquakes. In Eastern Canada, a large number of traditional residential buildings were built between 1860 and 1915 using a mixed structural system of unreinforced masonry «URM» and wood. The lateral stability and resistance of several of those traditional buildings rely on the behaviour of the peripheral walls made of timber planks covered by a brick veneer. These traditional walls, called "carrés de madriers", are composed of timber planks, stacked horizontally between two wood posts delimiting panels between the wall openings. The lateral resistance is provided by the interaction and friction mechanisms between the horizontal timber planks and their interaction with the vertical wood posts. The main objective of this paper is to present: (1) a structural and mechanical characterization of a typical wall and (2) an evaluation of the lateral capacity using an analytical model and a finite element (FE) model. The analytical model is derived from the literature and used to estimate the maximum lateral displacement/resistance for this type of walls when subjected to in-plane lateral forces. In addition, major outcomes of a FE numerical investigation carried out on a single wood panel with the software ABAQUS© are discussed for different loading conditions (i.e. in-plane lateral and vertical compressive loads). Recommendations are given to improve the FE model especially the modelling of the connections between the horizontal and vertical elements.

**Keywords** Structural capacity · Seismic risk · Mixes structural · Timber planks · Carrés de madriers · Finite element (FE) · ABAQUS

M. H. Kraiem (✉) · A. Khaled · M.-J. Nollet
Department of Construction Engineering, École de Technologie Supérieure, Montreal, QC, Canada
e-mail: mohamed-hassen.kraiem.1@ens.etsmtl.ca

# 1 Introduction

Recent researches have identified the potential for severe damage due to earthquakes in Eastern Canada, particularly in large urban centres like Montreal, where density of the buildings and population increase the seismic risk [3]. In large urban centres such as Montreal, Ottawa and Quebec City, residential buildings constitute most of the built environment and are thereby exposed to seismic risk (95% in Montreal and Ottawa, 85% in centre Quebec City) [15]. A recent study on seismic risk to residential buildings in Montreal Island showed that more than 79% of 284 646 residential buildings are wood light frame construction type (WLF) and 18% are unreinforced masonry (URM). For a scenario of magnitude 5 with an epicentre 5 km from the centre of the island, 27% of WLF buildings and 67% of URM buildings would be subject to damage ranging from moderate to complete [8, 16, 19, 20]. Among the most vulnerable buildings, many traditional residential constructions were built between 1860 and 1915 using a mixed structural system of unreinforced masonry and traditional walls made of timber planks. The typical wood wall system, designated as «*carrés de madriers*», consists of a series of timber planks, stacked horizontally between two wood posts delimiting panels. In the centre of the city of Montreal, these mixed structures represent about 46% of 70,000 residential buildings. No studies carried out to date has considered the specific lateral behaviour of those mixed construction systems and how the lateral response of such buildings may differ from a typical URM or WLF structure, nor specific capacity or fragility data are available [2]. Damage assessment is thereby carried out using capacity and fragility data for URM or WLF constructions, which could lead to an inadequate evaluation of damage.

The estimation of the lateral resistance of traditional buildings is therefore the key in improving damage assessment in seismic risk studies. This paper investigates the seismic response of traditional walls made of timber planks. The in-plane lateral response of wood panels, made of timber planks stacked horizontally between two wood posts, is investigated through analytical and numerical models using finite elements (FE). The finite element numerical investigation on the capacity of a wood panel was carried out with ABAQUS©.

# 2 Methodology

Visual inspections of typical houses undergoing renovation or rehabilitation work, as well as a literature assessment on the history of residential constructions and architecture in Montreal, were used to characterize residential buildings build with a mixed structural system of unreinforced masonry «URM» and traditional walls made of timber planks. These buildings are identified as URM-W. Building materials, composition and dimensions of the roof, walls, floors and foundations, as well as connection details between elements and between the wood and masonry systems, are
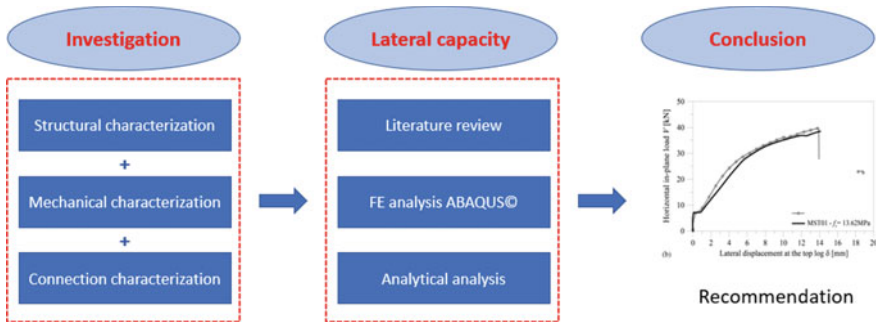
**Fig. 1** Assessment of the lateral capacity of a wood panel

considered in the structural characterization. In most inspected buildings, the floors are supported by the facade walls made of stacked timber planks with openings for doors and windows.

Following the structural characterization, the next step is to create a prototype that could be used to analyse the timber plank walls. The approach used to model and analyse the timber plank walls is similar to the one used for traditional URM walls [14]. The wall is considered as a combination of wood "panels" and openings of different dimensions. The prototype wood panel is defined using the geometry and structural features information obtained in the previous step. Material properties were taken from previous experimental tests collected from the literature review.

Two approaches are used to study the lateral behaviour of a wood panel. In the first approach, an analytical model proposed in the literature for wooden walls in log constructions is adapted to consider the particularity of the timber plank walls. This modified analytical model allows to estimate the lateral in-plane capacity a timber plank panel considering the static friction between the planks and the flexural rigidity of the vertical posts to which the planks are connected. In the second approach, a numerical model of the wood panel is developed, and a static nonlinear analysis based on the finite element method (Pushover Analysis) is carried out using the software ABAQUS©. The analysis provides for the simulation of possible deformations and failures. Figure 1 summarizes the different steps to estimate the lateral capacity of traditional wood wall.

## 3 Characterization of Timber Plank Wall

The most common URM-W building (Fig. 2a) is a single-family house of two or three storeys, part of a row of buildings with individual units separated by a common unreinforced brick firewall. The storey height varies between 6 and 7 m. The URM walls are composed of one to two rows of brick masonry bonded by lime or cement-lime mortar, with thickness decreasing at higher floor levels. In the majority of
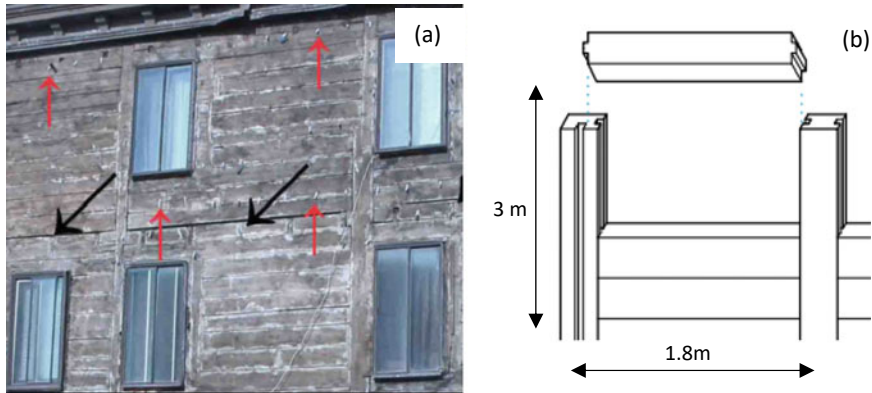
**Fig. 2** Typical timber plank wall: **a** facade wall and **b** typical tongue and groove joint [10, 18]

URM-W buildings, the wood framing of the floor and roof is supported by traditional timber plank walls. These walls were made with 3 in. thick wood planks, 12–16 in. long, stacked horizontally between two vertical posts. The connections between the vertical and horizontal wood elements are made by tongue and groove joints, used for fitting panels of wood together by their edges. This is done by joining the two pieces with a groove and a tongue (Fig. 2b) [18]. The façade wood walls are covered by a brick veneer in order to protect it from the humidity and weather. 4-inch nails are used as connection between the planks and the brick veneer. The sill horizontal plank is joined at the foundation level. The foundation is made of stones and is 24 in. thick. The peripheral walls, URM or timber planks, ensure the lateral stability of the building in both directions [1].

## 4 Lateral Capacity of Typical Timber Plank Panel

### 4.1 Analytical Model

The analytical model used in this study was adapted from a model proposed for log-house walls by Sciomenta et al. [17]. In this type of structure, the shear wall is constructed by the superposition of *n* logs in contact along their top–bottom surfaces and a sill log attached at the foundation, as shown in Fig. 3a. The longitudinal logs connect with the orthogonal elements via corner joints. The distribution load (*p*) represents the vertical load on the wall, and the lateral load F at the top of the wall is the lateral capacity. To simplify the analytical model, Sciomenta et al. [17] assume that the corner joints are represented by linear elastic spring with rigidity $K_{el,i}$. In addition, the static friction behaviour is accounted for by Coulomb forces. Figure 3b represents the simplified analytical model.
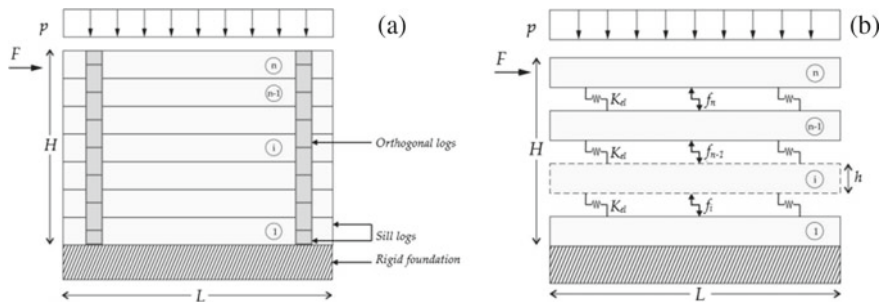
**Fig. 3** Log-house shear wall: **a** global view of shear wall and **b** analytical model [17]

The static friction contribution at the contact of two logs, according to Fig. 3b, is traditionally defined as

$$f_i = \mu\{[(n-1)+1]mg + pL\},\tag{1}$$

where $\mu$ is the static friction coefficient defined in Sect. 4.2, $p$ is the in-plane uniform distributed load (kN/m), *m is the masse of a timber log (kg),* $g$ is the gravitational acceleration (m/s$^2$), and $n$ is the number of logs. The lateral resistance of the panel, $F$ (kN), is therefore defined by the summation of the friction contribution and the stiffness of the orthogonal logs as

$$F = \sum_{i=2}^{n} f_i + 2K_{\text{el},i}\delta_i.\tag{2}$$

In the case of a timber plank panel, the planks are stacked horizontally between two wood posts, as represented in Fig. 4a. The distribution load ($p$) represents the vertical load on the wall, and the lateral load F at the top of the wall is the lateral capacity. The lateral resistance $F$ of the timber plank panel is provided by the contribution of the static friction contribution at the contact of between the timber planks, $f_i$, and the flexural resistance of the vertical posts shown in Fig. 4b, as expressed in Eq. 3:

$$F = \sum_{i=2}^{n} f_i + 2K_{\text{el,column}}\delta_{\text{top}},\tag{3}$$

where $K_{\text{el,post}}$ is the flexural stiffness and $\delta_{\text{top}}$ is the lateral top post displacement.
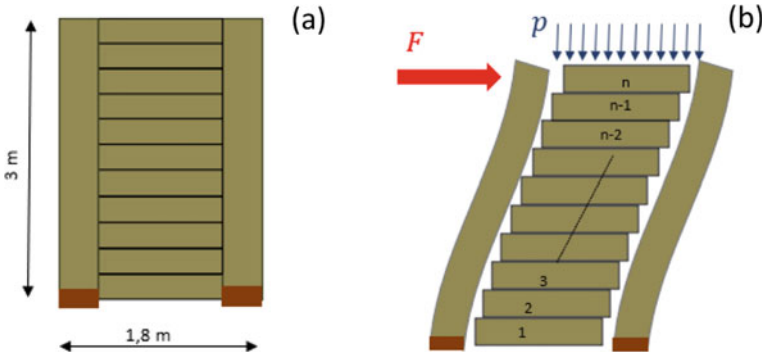
**Fig. 4** Traditional wood panel made of timber planks: **a** global view of panel and **b** deformation assumption

## 4.2 Finite Element Numerical Model

The software ABAQUS© was used to investigate the lateral capacity of the timber plank panel using FE modelling. The global model of the timber plank panel is composed of ten horizontal timber planks between two vertical posts (Fig. 5a). Figure 5b and c represents, respectively, the vertical post and horizontal plank with a specific geometry defined according to Fig. 4a. The mesh pattern and size were chosen to enhance the computational efficiency of FE models while maintaining prediction accuracy, particularly in the contact regions between the timber planks.

The timber planks and posts are pine wood defined as an ideal, orthotropic, linear elastic behaviour of the material. The input mechanical properties were derived from experimental data from literature finding on small-scale log-house components [6]. The average wood mechanical properties presented in Table 1 are used for the analysis.
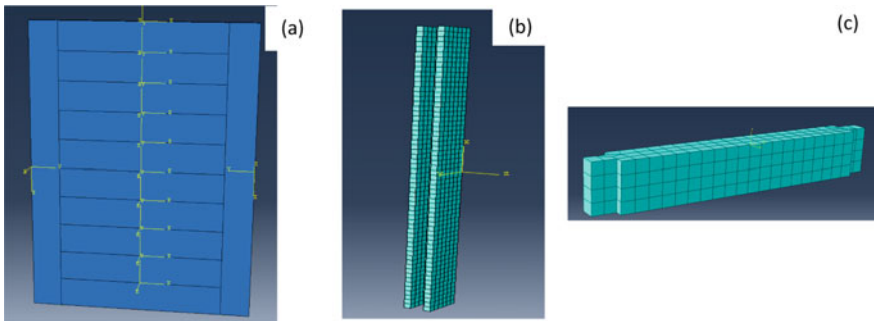


**Fig. 5** Numerical model with ABAQUS: **a** global numerical model of traditional timber plank panel and **b** vertical post and **c** horizontal plank

**Table 1** Wood material properties

| | Parameter | Value |
|---|---|---|
| $E_{11}$ | Modulus of elasticity | 14,788 MPa |
| $E_{22}$ | | 1848 MPa |
| $E_{33}$ | | 1087 MPa |
| $G_{11}$ | Shear modulus | 1220 MPa |
| $G_{22}$ | | 971 MPa |
| $G_{33}$ | | 366 MPa |
| $f_{c,90}$ | | 0.39 MPa |
| $f_{c,0}$ | | 0.46 MPa |
| $f_v$ | | 0.67 MPa |
| $W$ | Density | 3.5E−07 |
| $\mu$ | Coefficient of friction | 0.28 |

The definition of the mechanical interaction between wood planks contact surfaces has an important role for the lateral behaviour modelling. Surface-to-surface interactions are automatically recognized between overlapping planks, along their whole length, and between planks extremities, along groove and tongue, and vertical posts based on the geometry of adopted joints, using a formulation provided in the ABAQUS library. Appropriate mechanical behaviours were provided for all contact interactions (a total of 4378) to accurately simulate relative sliding between two adjacent surfaces (tangential behaviour) or interactions caused by loads perpendicular to surfaces in contact. For the tangential behaviour, the static friction coefficient is the fundamental input parameter. In accordance with Eurocode 5 [9], friction is not considered a resistant mechanism in wood panel shear walls. Branco and Araùjo [7] evaluated the intensity of friction created along two notched contact surfaces subjected to in-plane lateral loads. They used a simple plank specimen with cross section geometry like a plank in wood shear wall (Fig. 6). The static friction coefficient used in this study, $\mu = 0.28$, was proposed by Hirai et al. [13] for timber log walls. For the behaviour in the vertical direction, the equivalent stiffness of standard joint, $K_{el,joint}$, is the main input parameter. It is determined by applying different vertical loading configurations and extracted from the load/displacement response curve of standard joints, obtained experimentally [11, 12]. The value of the equivalent stiffness, $K_{el,joint}$, used in this study was taken equal to 15 kN/mm, as suggested by Sciomenta et al. [17].

A uniformly distributed constant vertical load of 20 kN/m is applied to the upper surface of the top plank to represent the load of the upper storeys. The weight of the wood panel is automatically computed by ABAQUS©. A pushover analysis is carried out using a displacement control method.

**Fig. 6** Experimental set-up
for static frictional tests
performed on simple planks
[5]
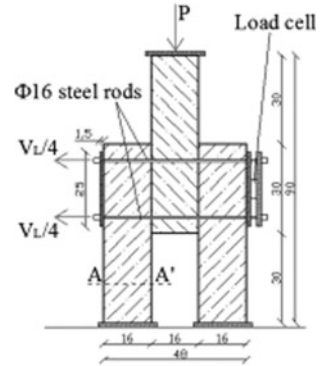


## 4.3  Results and Analysis

In order to use the analytical model, the stiffness of the two vertical elements was
determined by modelling with ABAQUS© a simple structure consisting of two
vertical posts joined by a rigid beam at the top. A stiffness of 712.5 N/mm is deter-
mined from the load/displacement curve. The lateral resistance computed using Eq. 3
is equal to 42 kN.

The results of the nonlinear static pushover analysis are shown in Fig. 7. Figure 7a
shows symmetric distribution of principal stress on the two edges of the wall panel.
The stress is the highest at the bottom corners of the vertical posts and decreases
going up. This can cause a failure by bending at the base of the vertical element. In
the horizontal timber planks, stress is very low or null since the horizontal elements
slide in the direction of the wall movement, and no damage is expected. In the joint
between the horizontal planks and the vertical posts, compressive stress is observed
mostly at the base of the panel. Figure 7b represents the capacity curve of the timber
plank panel resulting from the pushover analysis of the prototype. The capacity
curve can be idealized by a bilinear curve that represents a perfectly elasto-plastic
behaviour. The capacity and the stiffness of the wall panel are respectively 57 kN
and 828 N/mm. Bedon et al. [4] studied the lateral behaviour of a log wall with
similar dimension and material. The lateral resistance of the latter was estimated at
47 kN. The difference between these results is mainly related to the contribution of
the flexural rigidity of the vertical posts. The difference between the lateral resistance
determined by the analytical model and the numerical method is about 26%.

(a)



(b)
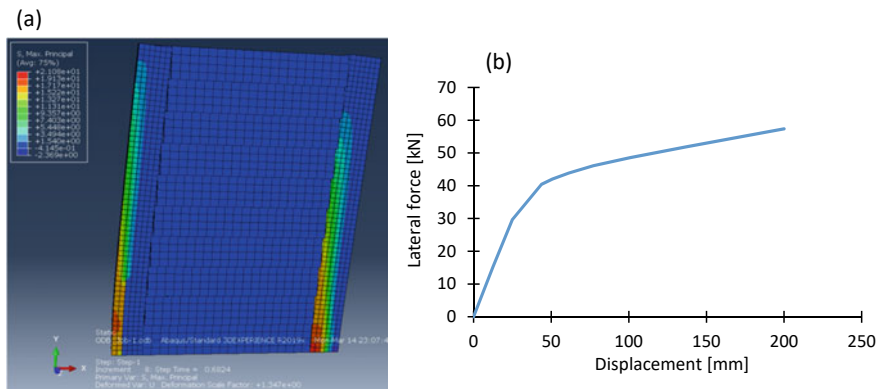
Fig. 7 Pushover analysis **a** stress distribution and **b** capacity curve of traditional wood wall in one direction

## 5   Conclusion

In this paper, the in-plane seismic performance of traditional walls made of timber plank elements found in mixed structural systems in residential buildings in Montreal has been investigated using an analytical and a finite element numerical model. The structural characterization of a typical building built with timber plank walls and unreinforced masonry walls was carried out. The characterization showed that the timber plank walls are often the bearing load system and the only lateral in-plane resisting system. An analytical model was developed to evaluate the lateral capacity of a wood timber plank panel. The analytical model is based on previous research work on log houses. Mechanical properties were taken from collected data in the literature and used to develop a numerical model for a timber plank panel. The surface-surface interaction at joints, between the timber planks, was investigated in this paper. The parameters were extracted from the literature. Nonlinear pushover analysis, using the software ABAQUS©, was conducted to derive the capacity curves of traditional timber plank panel. Results of the pushover analysis show that the lateral capacity of the wood panel is in the order of 57 kN (Fig. 7b). The results show also that the failure of the wood panel could occur at the base, where the stresses reach their maximum, due to the failure in bending of the vertical posts.

The lateral capacity of the panel computed using the developed analytical model (Eq. 3) is in the order of 42 kN. This result show that the lateral capacity of the wood panel is underestimated by 26% compared to the lateral capacity computed by ABAQUS©. This underestimation could be attributed mainly to the characterization of the material and the joints between planks and the calibration of the analytical model using ABAQUS©. An experimental programme is underway to better characterize the material and the joints between the planks to improve the analytical model and calibrate the numerical model. The result of one panel wood will be generalized and used to estimate the total lateral capacity of traditional wood wall.

# References

1. Abo El Ezz A (2013) Probabilistic seismic vulnerability and risk assessment of stone masonry structures. Ph.D. Thesis, École de technologie supérieure, Montreal, QC, Canada
2. Abo El Ezz A, Nollet M-J, Nastev M (2015) Assessment of earthquake-induced damage in Québec City, Canada. Int J Disaster Risk Reduct 12:16–24
3. Adams J, Halchuck S (2004) A review of NBCC 2005 seismic hazard results for Canada—the interface to the ground and prognosis for urban risk mitigation. In: Proceedings of the 57th Canadian geotechnical conference, pp 1–9
4. Bedon C, Rinaldin G, Fragiacomo M (2015) Non-linear modelling of the in-plane seismic behaviour of timber Blockhaus log-walls. Eng Struct 91:112–124
5. Bedon C, Fragiacomo M (2019) Experimental and numerical analysis of in-plane compressed unprotected log-haus timber walls in fire conditions. J Fire Saf J 107:89–103
6. Bodig J, Jayne BA (1982) Mechanics of wood and wood composites. Van Nostrand Reinhold, New York, NY, USA
7. Branco J, Araújo JP (2010) Lateral resistance of log timber walls subjected to horizontal loads. In: Proceedings of WCTE 2010 (CD-ROM)
8. Chouinard L, Rosset P, Nollet MJ, Youance S (2017) Analyse du risque sismique résidentiel à Montréal: Évaluation des dommages et conséquences. Rapport émis pour la Direction de la prévention et de la planification, Ministère de la Sécurité publique, QC, Canada, 13 p
9. Eurocode 8 (2009) Design of Structures for Earthquake Resistance. Part 1: General Rules, Seismic Actions and Rules for Buildings, EN 1998-1:2004. European Committee for Standardization (CEN), Brussels, Belgium
10. Gendron A (2018) Caractérisation structurale des bâtiments en bois et en maçonnerie non-armée (MNA) en vue de leur évaluation sismique. École de technologie supérieure, Montréal
11. Giovannini T, Grossi P, Sartori T, Tomasi R (2014) Blockhaus system: experimental characterization of corner joints and shear walls. In: Proceedings of the world conference on timber engineering—WCTE2014, Quebec City, QC, Canada, 10–14
12. Grossi P, Sartori T, Giongo I, Tomasi R (2016) Analysis of timber log-house construction systems via experimental testing and analytical modelling. Constr Build Mater 102:1127–1144
13. Hirai T, Kimura T, Yanaga K, Sasaki Y, Koizumi A (2004) Lateral resistance of log constructions. In: Proceedings of WCTE 2004 (CD-ROM), vol 1
14. Lestuzzi P, Badoux M (2013) Evaluation parasismique des constructions existantes: Bâtiments en maçonnerie et en béton arme. PPUR Presses polytechniques
15. Ploeger SK, Nollet MJ, Sawada M, Abo El Ezz A (2018) Inventory models for regional scale natural hazard risk assessment. Open File 8402, Natural Resources Canada, p 43
16. Rosset Ph, Kert M, Youance S, Nollet M-J, Chouinard L (2019) The use of HazCan to assess the earthquake risk of residential buildings in Montreal, Canada. Extended abstract for the Conference of the Canadian Society of Civil Engineering, Laval, Canada, 12–15 June, 4 p
17. Sciomenta M, Bedon C, Fragiacomo M, Luongo A (2018) Shear performance assessment of timber log-house walls under in-plane lateral loads via numerical and analytical modelling. J Build 8(8):99

18. Varin F (2017) Comprendre les techniques d'assemblage. J Contin 152:42–44
19. Youance S, Nollet M-J (2017) Inventaire du bâti résidentiel sur l'île de Montréal: Étude des typologies structurales. Rapport émis pour la Direction de la prévention et de la planification, Ministère de la Sécurité Publique, QC, Canada, 61 p
20. Yu K, Rosset Ph, Chouinard LE (2016) Seismic vulnerability assessment for Montreal. Georisk 10(2):164–178

# Validation of Proposed Analytical Model and Design Procedures for Multi-panel CLT Shearwalls Through Experimental Investigation

**Mohammad Masroor, Ghasan Doudak, and Daniele Casagrande**

**Abstract** Multi-panel CLT shearwalls are expected to provide more flexibility and energy dissipation than single-panel walls, mainly due to the contribution of the vertical joints between panels. Despite several analytical models and design approaches being proposed in the literature, timber design standards provide limited guidelines on the lateral and capacity-based design approaches for CLT shearwalls. This shortcoming is mainly due to inadequate experimental results on multi-panel CLT shearwalls to help validate the developed equations and substantiate the proposed kinematic modes and shearwall behaviour. This study investigates the lateral behaviour of CLT shearwalls by carrying out two full-scale testing on shearwalls consisting of three panels and subjected to monotonic lateral load. The experimental results were used to validate results obtained from proposed analytical expressions and numerical models. Connection-level monotonic tests were also carried out on hold-down and panel-to-panel joints to be used as the input for the analytical expressions and numerical models. Preliminary results from two shearwalls tests are presented in this paper, and comparisons to the numerical models show a reasonable match.

**Keywords** Structural capacity · Seismic risk · Mixes structural · Timber planks · Carrés de madriers · Finite element (FE) · ABAQUS

M. Masroor (✉) · G. Doudak
Department of Civil Engineering, University of Ottawa, Ottawa, Canada
e-mail: mmas100@uottawa.ca

D. Casagrande
Institute of Bioeconomy—National Research Council of Italy (CNR-IBE), Trento, Italy

27

# 1 Introduction

Cross-laminated timber (CLT) shearwalls have been increasingly used in timber constructions, primarily due to the high in-plane strength and stiffness of the CLT panels, as well as the wall's ability to dissipate energy through controlled failure mechanisms in the connections. These primarily include energy-dissipative joints between individual panels and capacity-protected connections between wall panels and supporting floors or foundations. These capabilities make CLT shearwalls a suitable alternative for mid- to high-rise buildings to those composed of steel and concrete.

CLT shearwalls can be composed of a single or multiple panels, which can have significant impact on their mechanical performance. When using commonly available joints, multi-panel CLT shearwalls are expected to provide more flexibility and energy dissipation, which is particularly suitable for high seismic regions. The majority of the energy dissipation is expected to be achieved in the joints attaching adjacent panels, since they typically consist of small diameter fasteners, such as nails or screws.

Several studies have been conducted with the aim to develop analytical models and design procedures for CLT multi-panel shearwalls. Gavric et al. [13] and Flatscher et al. [12] developed analytical expressions for single and two-panel walls and conducted experimental tests to validate the proposed models. Casagrande et al. [5] and Nolet et al. [16] developed analytical equations considering the elastic and elastic-perfectly plastic behaviour of the connections, assuming that only hold-down and panel-to-panel connections (i.e. vertical joints) contribute to the rocking behaviour, whereas angle brackets only behave in shear to prevent sliding. Masroor et al. [14] extended the applicability of the equations to include the bidirectional (i.e. combined uplift and shear) contribution of the angle brackets and hold-down.

Casagrande et al. [6] proposed a capacity-based design (CD) approach for light-frame and single- and multi-panel CLT shearwalls, based on the analytical expressions proposed by Casagrande et al. [5] and Nolet et al. [16]. It was reported that the seismic energy dissipation occurs primarily in panel-to-panel connections, whereas non-dissipative elements, such as CLT panels, were required to remain elastic. The proposal was extended by Masroor et al. [15] to also include the bidirectional contribution of the angle brackets. Casagrande et al. [4] summarized the developed CD approaches and proposed design provisions based on the Canadian and European wood design standards [7, 8].

Despite several analytical models and design approaches being proposed in the literature, timber design standards (e.g. [8]) only provide limited guidelines on the lateral capacity and stiffness of multi-panel CLT shearwalls. The lack of analytical and design expressions has resulted in designers lacking the needed resources and adequate knowledge to design such structures. This shortcoming might be attributed to inadequate experimental testing on multi-panel CLT shearwalls, especially with walls containing more than two panels, in order to validate the developed equations and substantiate the proposed kinematic behaviour. The research includes a comprehensive experimental study with the aim to develop a database of full-scale
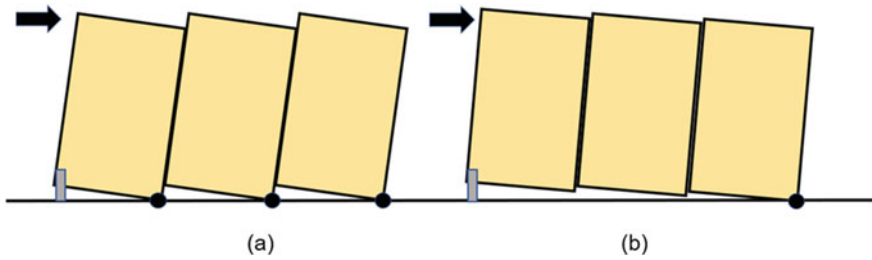
**Fig. 1** **a** CP kinematic mode **b** SW kinematic mode

test results for CLT shearwalls undergoing various kinematic behaviours and failure modes. The paper provides updates on the ongoing testing programme and presents some preliminary results from the connection and full-scale testing campaign.

## 2  Objective

The current research has been established with the aim to carry out full-scale experimental tests on shearwalls containing three panels and subjected to monotonic lateral loading. The main goal of the current study is to validate the analytical expressions and numerical models available in the literature (e.g. [5, 16]). The study is limited in scope to shearwalls where the contribution of the angle brackets to the rocking behaviour is omitted. Two examples from the experimental campaign, related to the most common kinematic behaviour, namely coupled panel (CP) and single wall (SW) (Fig. 1), are presented and discussed. The results obtained from the analytical, numerical, and experimental tests are compared in terms of kinematic modes, displacements, and strength capacity. Connection-level monotonic tests were also carried out on hold-downs subjected to uplift and panel-to-panel connections subjected to shear loads, with the aim to be utilized as input in the analytical and numerical models.

## 3  Experimental Tests on Connections

The connection-level tests were conducted for hold-downs and panel–panel joints subjected to uplift and shear forces, respectively. Two repeat specimens were considered for each connection. The displacement rate used during the testing was 3 mm/min for the hold-down and 4.5 mm/min for the panel-to-panel connections, in order to achieve failure within 10 min. The WHT620 hold-down connection [10] consisted of a 3-mm-thick steel bracket with 55 (fully nailed) and 22 (partially nailed) LBA $4 \times 60$ mm threaded annular ring nails, 20-mm-thick washer, and 20-mm bolt, as

illustrated in Fig. 2a. The panel-to-panel connection was composed of HBS 6 × 70 mm screws, as shown in Fig. 2b [11].

Figure 3 presents the test set-up for the hold-down under monotonic uplift load. The CLT panel consisted of three layers, E1 grade, in accordance with ANSI/APA [1]. The total thickness of the panel was 105 mm (i.e. layer thickness of 35 mm), and the width of the individual boards was 89 mm.
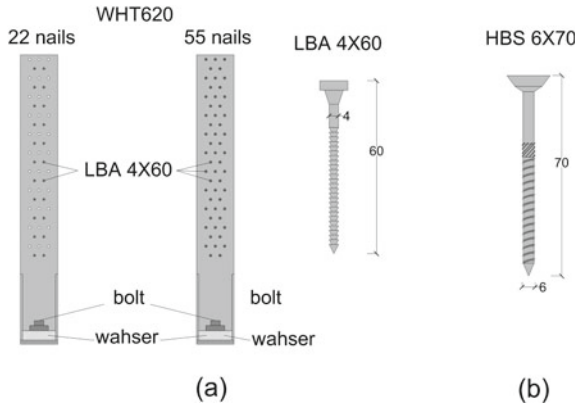


**Fig. 2** **a** Hold-down connection WHT620. **b** Panel-to-panel screw connection HBS 6 × 60 mm
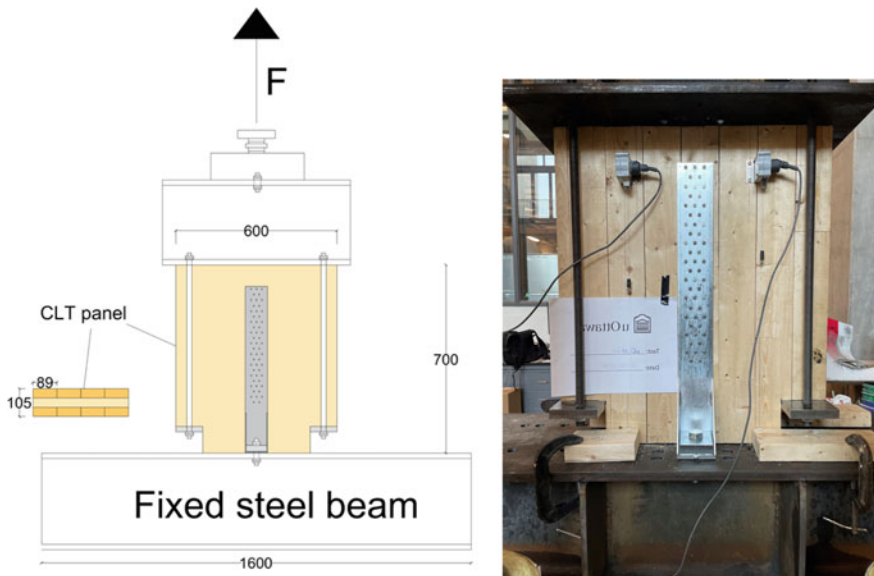


**Fig. 3** Test set-up of hold-down connection
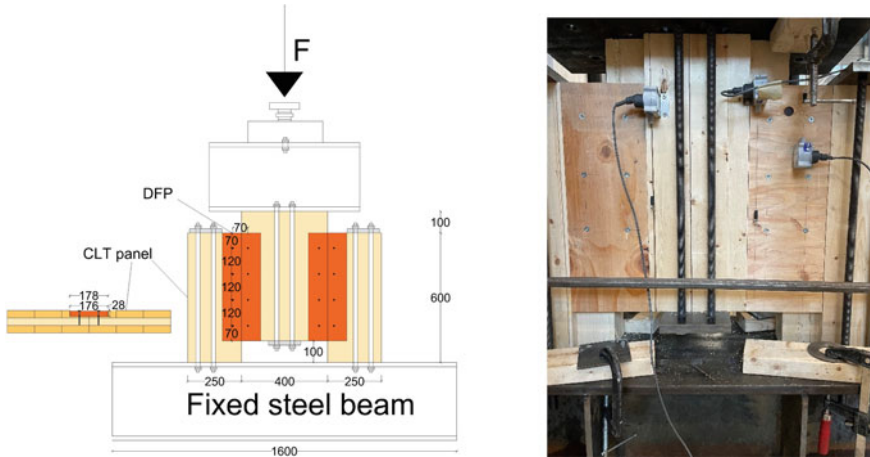
**Fig. 4** Test set-up of panel-to-panel connection

The panel-to-panel connection specimen consisted of three CLT panels joined together with HBS $6 \times 70$ mm screws, as shown in Fig. 4. The connection represented a half-lap joint, using D-Fir plywood (DFP) with thickness of 25.5 mm and width of 176 mm. Fastener spacing of 120 mm was used to meet the minimum requirements in the CSA O86-19 [8] standard and to limit splitting in the wood.

Figure 5 presents the force–displacement curves for two repetitions for each of the fully nailed hold-down (HD-F-1 and HD-F-2), partially nailed hold-down (HD-P-1 and HD-P-2), and vertical joint (VJ-1 and VJ-2) tests. The graphs represent the behaviour of a single hold-down and a pair of panel-to-panel screw joint (i.e. two screws connecting the plywood side plate to two CLT wall panels). Table 1 summarizes the maximum applied loads from the tests, $F_{max}$, and its respective displacement, $v_{max}$, and presents the mechanical properties obtained from the curves using the equivalent energy elasto-plastic (EEEP) bilinear simulation, in accordance with ASTM E2126 [2]. This idealization of the connection behaviour is intended to be used in the analytical expressions. $r_y$ and $d_y$ are the yield strength and displacement, respectively, $k$ represents the elastic stiffness, $d_u$ is the ultimate displacement, and $D_{EEEP}$ is for the ductility, obtained as the ratio between the ultimate and yield displacements.

The failure mechanisms observed from the experimental testing on hold-downs consisted of tensile tension failure in the vertical steel plate near the first row of nails for the fully nailed, as shown in Fig. 6a, and failure in the nails due to the cap breakage combined with nail withdrawal and bending for the partially nailed, as shown in Fig. 6b. The panel-to-panel connection failure was represented by a ductile failure mode, in which embedment crushing failure in the plywood and CLT combined with yielding in the fasteners was observed, as shown in Fig. 6c.
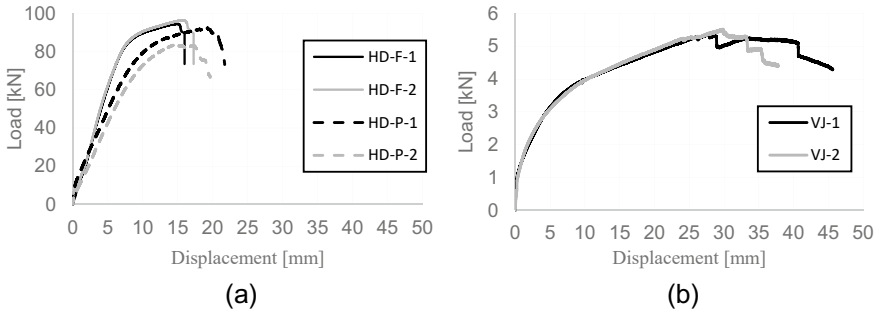
**Fig. 5** Connections force–displacement curve for **a** hold-down and **b** panel-to-panel connection

**Table 1** Mechanical properties of connections obtained from experimental tests

| Connection | Test | | EEEP simulation | | | | |
|---|---|---|---|---|---|---|---|
| | $F_{max}$ (kN) | $v_{max}$ (mm) | $r_y$ (mm) | $d_y$ (mm) | $k$ (kN/mm) | $d_u$ (mm) | $D_{EEEP}$ (−) |
| HD-F-1 | 94.5 | 14.9 | 89.8 | 7.43 | 12.1 | 16.0 | 2.15 |
| HD-F-2 | 96.4 | 15.7 | 91.8 | 7.17 | 10.5 | 17.3 | 2.24 |
| HD-P-1 | 92.31 | 19.29 | 85.82 | 9.16 | 9.36 | 21.71 | 2.37 |
| HD-P-2 | 83.92 | 14.91 | 78.0 | 9.44 | 8.26 | 19.63 | 2.08 |
| VJ-1 | 5.37 | 27.80 | 4.69 | 5.82 | 0.71 | 45.6 | 7.83 |
| VJ-2 | 5.52 | 29.86 | 4.62 | 5.10 | 0.83 | 37.7 | 7.39 |
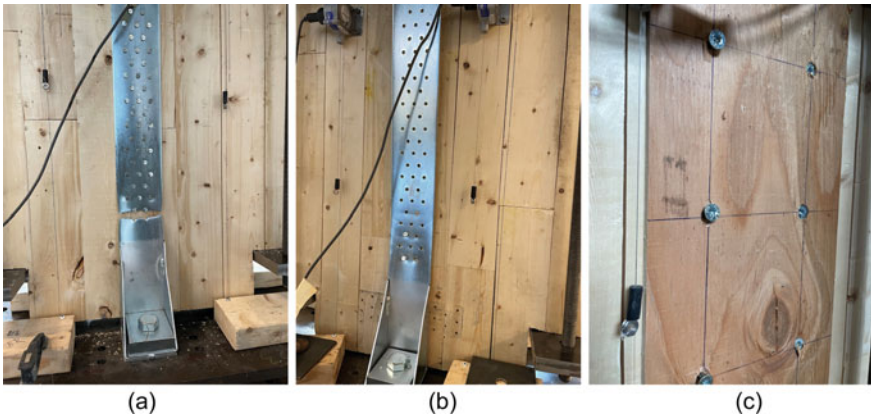


**Fig. 6** Failure in: **a** fully nailed hold-down, **b** partially nailed hold-down, and **c** panel-to-panel joints

## 4  Investigation on Multi-panel CLT Shearwalls

Two CLT shearwalls with the configurations showed in Fig. 7 were investigated by conducting experimental tests. The height and total length of the shearwall were equal to 2438 mm and 3657 mm, respectively. Hold-down and panel-to-panel connections, consistent with those tested in the joint-level tests (i.e. WHT620 and HBS 6 × 70), were utilized to anchor the wall to the steel base. The same type of CLT panels that was used in the connection-level tests was also used in the full-scale shearwall tests. Table 2 presents the connection types and configurations and provides the anticipated kinematic modes. The number of panel-to-panel joints and the stiffness and yield strength of the hold-down and vertical joint connections were selected based on preliminary numerical runs to ensure that CP and SW behaviour are obtained in Test #1 and #2, respectively. No gravity load was considered in these tests; however, the weight of the panels and various test set-up attachments were estimated to be equal to 1.45 kN/m and considered in numerical and analytical models.
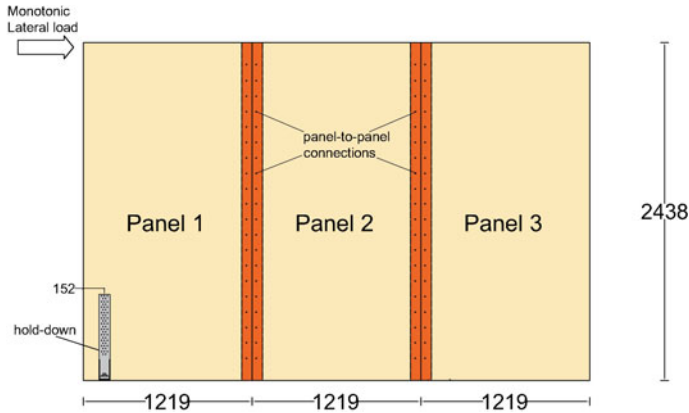


**Fig. 7** Three panels CLT shearwall used for numerical and analytical models and experimental tests

**Table 2** Number of connections and kinematic mode

| Test | Number of hold-downs | Number of panel-to-panel connections | Nailing of the hold-down | Expected kinematic mode |
|------|------|------|------|------|
| #1 | 2 | 9 | Fully nailed (55 nails) | CP |
| #2 | 1 | 35 | Partially nailed (22 nails) | SW |

## 4.1 Numerical and Analytical Investigations

Figure 8 presents the numerical model developed using the SAP2000 software [9]. The connections were modelled using multi-linear link elements representative of the real curves obtained from the connection tests. A concentrated lateral load is applied at the top of the wall, consistent with the loading actuator position in the experimental tests. A uniformly distributed gravity load, $q$, of 1.45 kN/m was applied on top of the wall to account for the weight of the panels and test set-up attachments. Sliding was prevented in the model by restraining horizontal movement at the centre of rotation of each panel, and gap elements, which are only active in compression, were assigned a high stiffness equal to $10^8$ MPa to simulate the contact between the panels and the base. Diaphragm constraints were considered at the top and bottom of the panels.

The CLT panels were modelled with orthotropic material properties. The values of $E_0$, $E_{90}$, and $G_0$ were obtained from Canadian wood design standard [8] for E1 CLT grade and were equal to 11,700, 300, and 731 MPa, respectively. The effective moduli, utilized to define the orthotropic material properties, $E_{\mathrm{eff},1}$ (along the horizontal direction) $E_{\mathrm{eff},2}$ (along the vertical direction), and $G_{\mathrm{eff}}$, are obtained using Eqs. 1–4, based on work by Brandner et al. [3].

$$E_{\mathrm{eff},1} = \frac{E_0 \cdot t_{90} + E_{90} \cdot t_0}{t_{\mathrm{CLT}}} = \frac{11700 \cdot 35 + 300 \cdot 70}{105} = 4100\,\mathrm{MPa} \qquad (1)$$

$$E_{\mathrm{eff},2} = \frac{E_0 \cdot t_0 + E_{90} \cdot t_{90}}{t_{\mathrm{CLT}}} = \frac{11700 \cdot 70 + 300 \cdot 35}{105} = 7900\,\mathrm{MPa} \qquad (2)$$

$$\alpha = 0.53 \cdot \left(\frac{t_{\mathrm{mean}}}{w}\right)^{-0.79} = 0.53 \cdot \left(\frac{35}{89}\right)^{-0.79} = 1.11 \qquad (3)$$
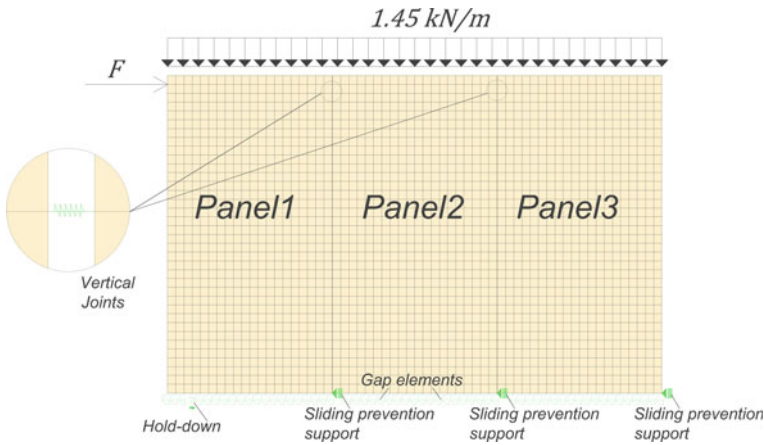


**Fig. 8** Numerical model of a three-panel CLT shearwall in SAP2000

$$G_{\text{eff}} = \frac{G_0}{1 + 6 \cdot \alpha \cdot \left(\frac{t_{\text{mean}}}{w}\right)^2} = \frac{731}{1 + 6 \cdot 1.11 \cdot \left(\frac{35}{89}\right)^2} = 361.1 \, \text{MPa}, \qquad (4)$$

where $t_0$ and $t_{90}$ are the total thicknesses of the longitudinal (vertical) and transverse (horizontal) layers, $t_{\text{CLT}}$ is the total thickness of the panel, and $w$ is the width of laminations.

Nolet et al. [16] presented analytical procedures to obtain the rocking behaviour of three-panel CLT shearwalls for CP and SW kinematic modes, as illustrated in Fig. 9. Table 3 summarizes the expressions required in the analytical procedures and the respective values defining the shearwall behaviour from Fig. 9. The expressions for CP were updated by factors $\gamma_1$ and $\gamma_2$ to account for the real position of the hold-down and the loading actuator in experimental tests. These variables represent the ratio of the distance between the centre of rotation of the first panel and the hold-down to the length of each panel ($b$) and the ratio of the distance between the bottom of the wall and the position of the lateral load to the height of the wall. The analytical equations are calculated using the mechanical properties for connections obtained from the EEEP curves (Table 1) for hold-down and vertical joints. Additional subscripts associated with each connection are included in each parameter, such as $h$ for the hold-down and $c$ for panel-to-panel connection. As such, $n_c$ represents the number of joints between adjacent panels.

**Table 3** Analytical expressions developed by Nolet et al. [16] and their respective values

| Point | Expression | | Values | |
|---|---|---|---|---|
| | $F$ | $\Delta_r$ | $F$ (kN) | $\Delta_r$ (mm) |
| CP,1 | $\frac{q \cdot m \cdot b^2}{2 \cdot h \cdot \gamma_2}$ | – | 1.32 | 0 |
| CP,2 | $\frac{[\gamma_1^2 \cdot k_h + (m-1) \cdot n_c \cdot k_c] b}{k_c \cdot \gamma_2} + \frac{q \cdot m \cdot b^2}{2 \cdot h \cdot \gamma_2}$ | $d_{y,c} \cdot \frac{h}{b}$ | 90.84 | 9.34 |
| CP,3 | $\frac{b}{h \cdot \gamma_2} \cdot \left[\gamma_1 \cdot r_h + r_c \cdot (m-1) \cdot n_c + \frac{q \cdot m \cdot b}{2}\right]$ | $\frac{d_{y,h}}{\gamma_1} \cdot \frac{h}{b}$ | 134.32 | 17.74 |
| CP,4 | $\frac{b}{h \cdot \gamma_2} \cdot \left[\gamma_1 \cdot r_h + r_c \cdot (m-1) \cdot n_c + \frac{q \cdot m \cdot b}{2}\right]$ | $\min\left(d_{u,c}, \frac{d_{u,h}}{\gamma_1}\right) \cdot \frac{h}{b}$ | 134.32 | 39.72 |
| SW,1 | $\frac{q \cdot m \cdot b^2}{2 \cdot h}$ | – | 1.32 | 0 |
| SW,2 | Equation (5) | Equation (6) | 3.93 | 0.14 |
| SW,3 | Equation (7) | Equation (8) | 6.50 | 0.30 |
| SW,4 | $\frac{1}{h} \cdot \left[r_h \cdot m \cdot b + \frac{q \cdot m^2 \cdot b^2}{2}\right]$ | Equation (9) | 120.98 | 9.25 |
| SW,5 | $\frac{1}{h} \cdot \left[r_h \cdot m \cdot b + \frac{q \cdot m^2 \cdot b^2}{2}\right]$ | $\Delta_{r,\text{SW},4} + \left[\frac{h}{m \cdot b} \cdot (d_{u,h} - d_{y,h})\right]$ | 120.98 | 15.97 |
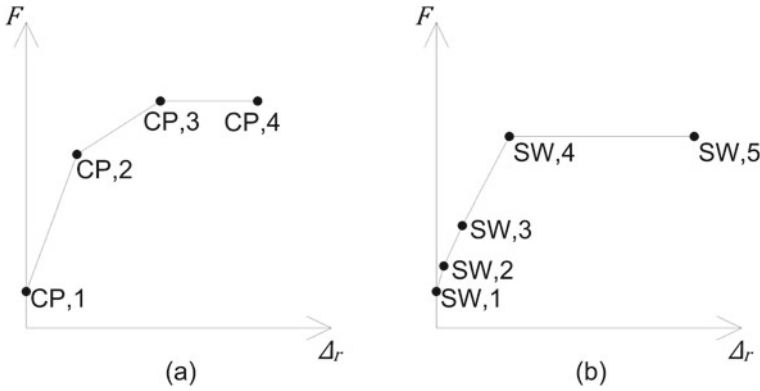
**Fig. 9** Analytical curves developed by Nolet et al. [16]: **a** for CP; **b** for SW

$$F_{\text{SW},2} = \frac{q \cdot m^2 \cdot b^2}{2 \cdot h} \cdot \frac{k_h \cdot \left(\frac{3 \cdot m - 2}{m^2}\right) + \left(\frac{2 - m}{m^2}\right)}{n_c \cdot k_c - k_h} \tag{5}$$

$$\Delta_{r,\text{SW},2} = \left(F_{\text{SW},2} - \frac{q \cdot m \cdot b^2}{2 \cdot h}\right) \frac{h^2}{b^2 \cdot [k_h + (m - 1) \cdot n_c \cdot k_c]} \tag{6}$$

$$F_{\text{SW},3} = \frac{q \cdot m^2 \cdot b^2}{2 \cdot h} \cdot \frac{k_h \cdot \left(\frac{m + 6}{m^2}\right) + \left(\frac{5 \cdot m - 6}{m^2}\right)}{n_c \cdot k_c - k_h} \tag{7}$$

$$\Delta_{r,\text{SW},3} = \left(F_{\text{SW},3} - \frac{q \cdot m \cdot b^2}{2 \cdot h}\right) \frac{h^2 \cdot [k_h + n_c \cdot k_c]}{b^2 \cdot [(m + 2) \cdot k_h + (m - 2) \cdot n_c \cdot k_c] \cdot n_c \cdot k_c} \tag{8}$$

$$\Delta_{r,\text{SW},4} = \left\{ \frac{F_{\text{SW},4} \cdot h^2}{b^2} - \left[ \frac{\left(\frac{1}{k_h} + \frac{m - 1}{n_c \cdot k_c}\right)^{-1}}{k_h} \cdot \frac{q \cdot m^2}{2 \cdot h} \right] \right\} \cdot \frac{1}{m^2 \cdot \left(\frac{1}{k_h} + \frac{m - 1}{n_c \cdot k_c}\right)^{-1}}, \tag{9}$$

where $F_{\text{SW},i}$ is the lateral load at point SW, $i$ for $i = 2{:}4$.

Since the analytical expressions were developed assuming rigid behaviour of the CLT panels, bending and shear deformations of panels are added to account for the flexibility in the panels. These are calculated using Eqs. (10) and (11) for bending and shear deformations, respectively.

$$\Delta_b = \frac{F \cdot h^3}{3 \cdot \text{EI}_{\text{eff}}} \tag{10}$$

$$\Delta_{\text{sh}} = \frac{F \cdot h}{G_{\text{eff}} \cdot t_{\text{CLT}} \cdot m \cdot b}, \tag{11}$$

where $F$ is the lateral load and $G_{eff}$ is obtained from Eq. (4).

The value for $EI_{eff}$ for CP and SW can be calculated using Eqs. (12) and (13), respectively.

$$EI_{eff,CP} = m \cdot \left( E_0 \cdot t_0 \cdot \frac{b^3}{12} + E_{90} \cdot t_{90} \cdot \frac{b^3}{12} \right) = 3.76 \times 10^{14}\,\text{N mm}^2 \qquad (12)$$

$$EI_{eff,SW} = E_0 \cdot t_0 \cdot \frac{(b \cdot m)^3}{12} + E_{90} \cdot t_{90} \cdot \frac{(b \cdot m)^3}{12} = 3.38 \times 10^{15}\,\text{N mm}^2. \qquad (13)$$

## *4.2　Experimental Tests on Shearwalls*

The experimental test configuration is illustrated in Fig. 10. Horizontal support mechanisms were designed and implemented at the base of each panel in order to prevent sliding, while allowing free rotation. In an actual CLT wall, construction sliding would be limited by angle brackets, which as mentioned earlier would contribute to the shear and uplift of the wall panels. Future testing will investigate the effect of angle brackets on the shearwall behaviour. The displacement rate at the top of the walls was selected to 6 mm/min in order to achieve consistent displacement rates between the connection-level and full-scale level tests.

Figure 11 presents the force–displacement curves obtained from the two tests. Comparisons between the two curves show that more ductility can be observed in test #1 since the wall behaviour is dominated by the engagement of the panel-to-panel connections. Wall test #2 exhibited higher stiffness but significantly lower ductility due to rigid connections between the panels, resulting in the wall behaving almost like a single-panel wall. The ductility of the wall is primarily driven by the behaviour of the hold-down connection which is less ductile than the panel-to-panel joints (refer to Fig. 5).

Figures 12 and 13 present the failure mechanism obtained at the end of test #1 and #2, respectively, and highlight that the failure in the connections at the shearwall level was consistent with those obtained at the connection-level tests. It is important to note that the walls achieved the anticipated kinematic modes, as indicated in Table 2, where wall test #1 exhibited CP kinematic mode while wall test #2 attained SW kinematic mode, as shown in Figs. 12 and 13, respectively. Table 4 summarizes the results obtained from the tests and includes the parameters obtained from the idealized EEEP curve.
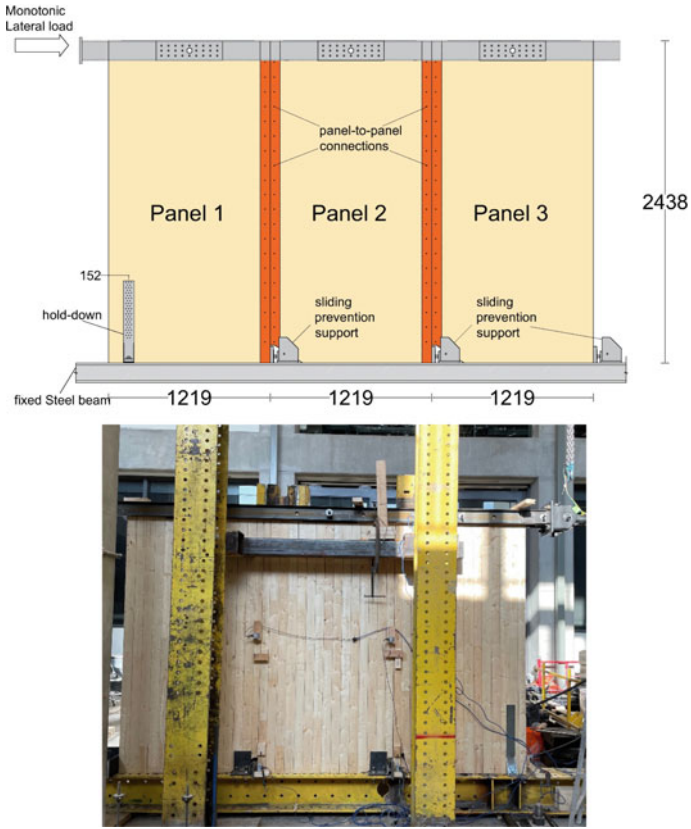
**Fig. 10** Set-up of CLT shearwall test



**Fig. 11** Force–displacement curve for shearwalls experimental tests
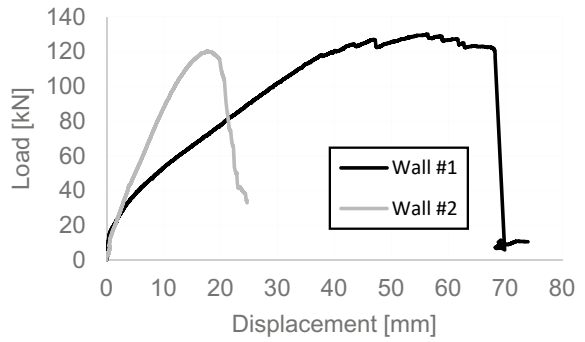
**Fig. 12** Lateral behaviour and failure of CLT shearwall experimental test #1
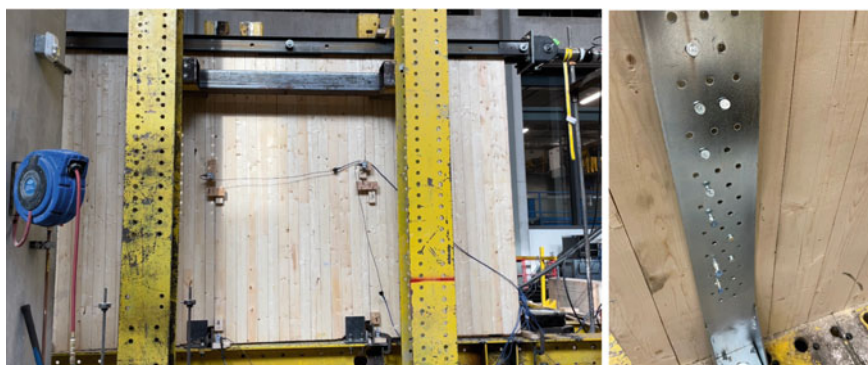


**Fig. 13** Lateral behaviour and failure of CLT shearwall experimental test #2

**Table 4** Results of experimental tests on CLT shearwalls

| Test | $F_{max}$(kN) | $v_{max}$(mm) | $F_{y,EEEP}$(mm) | $v_{y,EEEP}$(mm) | $k_{EEEP}$(kN/mm) | $v_{u,EEEP}$(mm) | $D_{EEEP}$(−) |
|------|------|-------|--------|-------|------|-------|------|
| #1 | 130.0 | 56.39 | 114.96 | 24.55 | 4.68 | 68.2 | 2.78 |
| #2 | 120.3 | 17.70 | 109.49 | 11.76 | 9.31 | 20.84 | 1.77 |
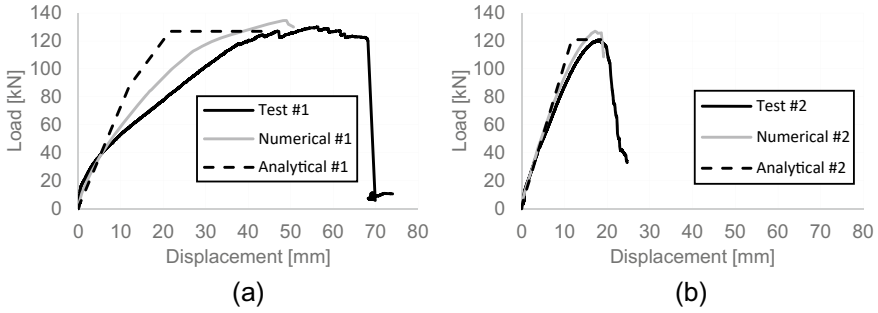
**Fig. 14** Experimental, numerical, and analytical curves of the shearwalls: **a** wall #1; **b** wall #2

## *4.3  Discussion*

Figure 14 presents the three curves obtained from the experimental results, numerical and analytical models for wall #1 and wall #2. As can be observed, reasonable match can be found in terms of the general behaviour and the shape of the curves for both walls. In particular, the match between the models and test results for the wall dominated by SW behaviour is close due to the fact that the behaviour is generally dominated by the hold-down mechanical properties. Wall #1 involves a more complex behaviour where both the hold-down and the vertical joints participate in the performance of the wall.

Table 5 summarizes the key parameters obtained from each method, including the percentage difference between experimental test and numerical model results, denoted as $\xi_{T/N}$, and between experimental test and analytical model results, denoted as $\xi_{T/A}$. The results show that the maximum force, $F_{max}$, and yield force, $F_{y,\text{EEEP}}$ match reasonably well with maximum difference of 6% and 10%, respectively. Maximum displacement, $v_{max}$, and yield displacement, $v_{y,\text{EEEP}}$, present more deviation between the results for wall #1, with difference around 18% for the numerical model and 14% for analytical model, whereas for wall #2 the maximum difference was 8%. For the elastic stiffness, $k_{\text{EEEP}}$, and ultimate displacement, $v_{u,\text{EEEP}}$, significant differences were observed especially for wall #1, with 21% and 35% for the numerical model and 54% and 63% for the analytical model, respectively. The stiffness is notoriously difficult to estimate due to the nonlinear nature of the behaviour of wood shearwalls even at low displacement levels. The ultimate displacement is also particularly difficult to predict since the behaviour of post yield and peak loads is erratic and depends on multiple failure mechanisms. The significant discrepancy observed in the analytical model, especially for wall #1, could be attributed to using the EEEP idealization curve for the panel-to-panel connections. It can be observed that significantly better fit is obtained for wall #1 in numerical model owing to using the real connection curve obtained from the joint-level tests.

**Table 5** Results obtained from experimental tests and numerical and analytical models

| Wall | Content | $F_{max}$(kN) | $v_{max}$(mm) | $F_{y,EEEP}$(mm) | $v_{y,EEEP}$(mm) | $k_{EEEP}$(kN/mm) | $v_{u,EEEP}$(mm) | $D_{EEEP}$(−) |
|---|---|---|---|---|---|---|---|---|
| #1 | Test | 130.07 | 56.39 | 114.96 | 24.55 | 4.68 | 68.21 | 2.78 |
| | Numerical | 134.64 | 48.98 | 117.59 | 20.75 | 5.68 | 50.62 | 2.44 |
| | Analytical | 126.93 | – | 126.93 | 21.49 | 7.23 | 41.91 | 1.69 |
| | $\xi_{T/N}$ | 4% | 15% | 2% | 18% | 21% | 35% | 14% |
| | $\xi_{T/A}$ | 2% | – | 10% | 14% | 54% | 63% | 64% |
| #2 | Test | 120.25 | 17.70 | 109.49 | 11.76 | 9.31 | 20.84 | 1.77 |
| | Numerical | 126.98 | 17.18 | 114.21 | 10.91 | 10.47 | 19.14 | 1.75 |
| | Analytical | 120.98 | – | 120.98 | 11.73 | 10.13 | 18.51 | 1.58 |
| | $\xi_{T/N}$ | 6% | 3% | 4% | 8% | 12% | 9% | 1% |
| | $\xi_{T/A}$ | 1% | – | 10% | 0% | 9% | 13% | 12% |

## 5   Conclusion

The lateral behaviour of CLT shearwalls was studied by carrying out two wall-level experimental tests on three-panel walls under monotonic lateral load. The results were compared with numerical and analytical models. The key findings of this research can be summarized as follows:

- The connection-level tests showed that the failure mechanisms observed in the hold-downs were of tension failure in the vertical steel plate near the first row of nails for the fully nailed, while failure in partially nailed hold-downs was in cap breakage combined with nail withdrawal and bending. The panel-to-panel connections were represented by a ductile failure mode, in which embedment crushing failure in the plywood and CLT combined with yielding in the fasteners was observed.
- Two experimental tests on CLT shearwalls were carried out, using the same type of CLT panels and connections used in the joint-level tests. Force–displacement curves and respective properties of each wall were presented. The wall with SW behaviour exhibited higher stiffness but significantly lower ductility due to the rigid connections between adjacent panels.
- Numerical and analytical models were evaluated, and results were compared with those obtained through the experimental tests. Reasonable match was observed in terms of the general behaviour and the shape of the curves in both walls. The values for maximum and yield forces showed reasonable match for both walls, while differences were found in the elastic stiffness and ultimate displacement, especially for the wall that exhibited CP behaviour.

## References

1. ANSI/APA (2020) ANSI/APA PRG 320:2019 standard for performance-rated cross-laminated timber. APA—The Engineered Wood Association
2. ASTM E2126 (2019) Standard test methods for cyclic (reversed) load test for shear resistance of vertical elements of the lateral force resisting systems for buildings
3. Brandner R, Dietsch P, Dröscher J, Schulte-Wrede M, Kreuzinger H, Sieder M (2017) Cross laminated timber (CLT) diaphragms under shear: test configuration, properties and design. Constr Build Mater 147:312–327. https://doi.org/10.1016/j.conbuildmat.2017.04.153
4. Casagrande D, Doudak G, Masroor M (2021) A proposal for capacity-based design of multi-storey CLT buildings. In: INTER—international network on timber engineering research
5. Casagrande D, Doudak G, Mauro L, Polastri A (2018) analytical approach to establishing the elastic behavior of multipanel CLT shear walls subjected to lateral loads. J Struct Eng 144(2):04017193. https://doi.org/10.1061/(ASCE)ST.1943-541X.0001948

6. Casagrande D, Doudak G, Polastri A (2019) A proposal for the capacity-design at wall- and building-level in light-frame and cross-laminated timber buildings. Bull Earthq Eng 17(6):3139–3167. https://doi.org/10.1007/s10518-019-00578-4
7. CEN (2004) European Standard EN 1995: Eurocode 5: Design of timber structures. European Committee for Standardization
8. CSA O86-19 (2019) Engineering design in wood. CSAO86:19. CSA Group
9. CSI (2018) SAP2000 integrated software for structural analysis and design (No. 18). Computers and Structures Inc.
10. European Technical Approval ETA-11/0086 (2018) European Organization for Technical approval
11. European Technical Assessment ETA-11/0030 (2019) European Organization for Technical approval.
12. Flatscher G, Bratulic K, Schickhofer G (2015) Experimental tests on cross-laminated timber joints and walls. Proc Inst Civ Eng Struct Build 168(11):868–877. https://doi.org/10.1680/stbu.13.00085
13. Gavric I, Fragiacomo M, Ceccotti A (2015) Cyclic behavior of CLT wall systems: experimental tests and analytical prediction models. J Struct Eng 141(11):04015034. https://doi.org/10.1061/(ASCE)ST.1943-541X.0001246
14. Masroor M, Doudak G, Casagrande D (2020) The effect of bi-axial behaviour of mechanical anchors on the lateral response of multi-panel CLT shearwalls. Eng Struct 224. https://doi.org/10.1016/j.engstruct.2020.111202
15. Masroor M, Doudak G, Casagrande D (2022) Design of multipanel CLT shear walls with bidirectional mechanical anchors following capacity-based design principle. J Perform Constr Fac 36(1). https://doi.org/10.1061/(ASCE)CF.1943-5509.0001693
16. Nolet V, Casagrande D, Doudak G (2019) Multipanel CLT shearwalls: an analytical method- ology to predict the elastic-plastic behaviour. Eng Struct 179:640–654. https://doi.org/10.1016/j.engstruct.2018.11.017

# Structural Specialty: Steel Structures

# Parametric Study of Slender Shear Walls Reinforced with Shape Memory Alloy Bars

**Deepak Saud, Lisa Tobber, and M. Shahria Alam**

**Abstract** In mid-rise and high-rise buildings, reinforced concrete (RC) shear walls are frequently used to resist seismic forces in earthquake-prone countries. The post-earthquake repair and retrofitting of these walls are very expensive or uneconomical, as observed in the 2010 Chile and 2011 Christchurch earthquakes. This paper explores the use of shape memory alloy (SMA) bars in the plastic hinge region of slender reinforced concrete (RC) shear walls. A comprehensive numerical parametric study was performed to understand the effects of various parameters on the hysteretic (force–deformation) response. Several models were developed with different aspect ratios, axial load ratios, reinforcement ratios, and types of SMA. The walls were then subjected to axial and reverse cyclic lateral loading, and the responses were assessed. Based on the responses, new trends were identified between design parameters and response outputs such as stiffness, residual deformation, force–deformation, and critical damage states (i.e. cracking, yielding, and crushing of SMA RC walls). These new relationships can be used to inform the design of low damage SMA RC walls for high seismic regions in Canada and worldwide.

**Keywords** Parametric study · Shear wall · Shape memory alloy · Axial and cyclic loading · Numerical modelling

## 1 Background and Introduction

One of the most common lateral force resisting systems in mid-rise and high-rise buildings is reinforced concrete shear walls (referred to herein as *shear walls*). In addition to resisting earthquake and wind loads, shear walls also support gravitational loads. Under strong earthquake shaking, these shear walls are designed for life safety, where the building can endure heavy damage. Past earthquakes have shown that buildings designed to this criterion underwent severe damage, particularly in

D. Saud (✉) · L. Tobber · M. S. Alam
The University of British Columbia, Kelowna, Canada
e-mail: dsaud@student.ubc.ca

many mid-rise and high-rise reinforced concrete buildings [8, 9]. The post-earthquake repair and retrofit of these buildings are expensive or uneconomical. Therefore, shear walls should be designed to minimize damage to these structural elements, resulting in low or no permanent deformation in the buildings. One alternative is to use supere-lastic shape memory alloy (SMA) bars at the critical locations (plastic hinge regions) of the shear walls in lieu of typical steel reinforcing [14].

SMA is an innovative material that has a superelastic property. This material can return to its initial shape and position after removing the loading on the structure [3]. The SMA demonstrates superelasticity behaviour when it is in the austenite state. In addition to the superelasticity property, SMA has a very low or negligible residual strain after unloading. Moreover, SMA can dissipate substantial energy during repeated load cycles. Therefore, SMA material has significant potential for civil engineering applications to make structures seismic-resistant in earthquake-prone areas.

Figure 1 shows the stress–strain behaviour of SMA under reversed cyclic lateral loading at a constant temperature. When stress is applied to SMA, the material changes its form from austenite to a martensite state. The transformation can be represented by four parameters, namely austenite-to-martensite starting stress ($f_y$), austenite-to-martensite finishing stress ($f_{P1}$), martensite-to-austenite starting stress ($f_{T1}$), and martensite-to-austenite finishing stress ($f_{T2}$).

The self-centring system developed with SMA in shear walls can reduce perma-nent deformations and damages. This reduction in damage could avoid the demolition and reconstruction of structures in high seismic areas. Therefore, although the SMA bars are expensive compared to the steel reinforcement, they are economical in the long term when used at the plastic hinge regions of the shear walls.

The superelastic SMA is connected with steel rebars by mechanical couplers. SMA rebars were successfully implemented in the plastic hinge regions of SMA RC elements by various researchers [11, 12, 17]. However, only a few studies have been

**Fig. 1** 1D superelastic model of SMA incorporated in FE packages (adapted from Auricchio et al. [5])
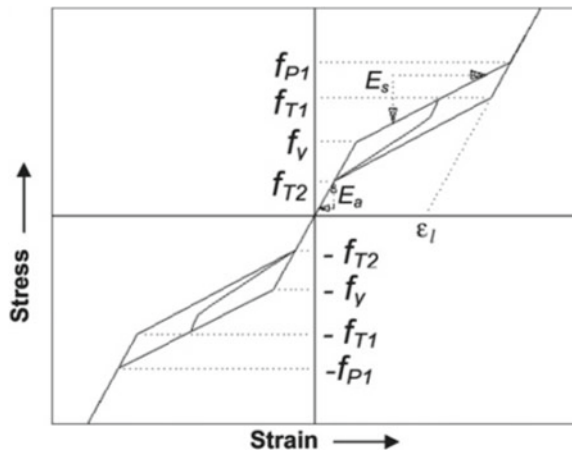
conducted on SMA bars as potential reinforcements in the plastic hinge regions of shear walls [1, 4, 7, 15].

In previous experimental tests conducted on SMA RC walls, the specimens were limited to axial load forces less than 4% $f_c' A_g$ and aspect ratios (length to height ratio of a shear wall) between 1 and 2.2 because of the laboratory size and equipment availability. Most of these tests were only tested under quasi-static lateral loading, except the test done by Almeida et al. [4], in which the walls were tested under both axial and quasi-static loading. Further, most experimental tests showed overturning due to axial load less than 3%, except the test done by Almeida et al. [4], which had 81%. Table 1 provides the detail of experimental tests conducted in recent years on shear walls connected with SMA bars.

In Table 1, the aspect ratio is the ratio of the height of the wall ($h_w$) to the length of the wall ($l_w$), $P$ is the axial load including self-weight of the wall, $f_c'$ is the concrete cylinder compression strength, $A_g$ is the cross section of the wall, and $V$ is the peak force observed during the test.

Due to the lack of literature on the experimental testing of SMA RC shear walls, there is a significant knowledge gap in understanding the behaviour of shear walls with SMA in their plastic hinge regions. Most shear walls have an axial load ratio between 5 and 10% in real buildings. Therefore, it is critical to determine the behaviour of SMA RC walls made of higher aspect ratios under varying axial loading (5 and 10%).

The present study explores the potential use of SMA bars in slender reinforced concrete (RC) shear walls. A comprehensive numerical parametric analysis was performed to understand various parameters' effects on the hysteretic (force–deformation) response. The critical parameters analysed were aspect ratio, axial load ratio, types of rebars, and vertical reinforcement ratio. Several finite element models were developed using these parameters. The walls were then subjected to axial and reverse cyclic lateral loading for assessing the response. Finally, the results obtained from this numerical study will lead to an experimental testing programme for slender SMA RC shear walls.

**Table 1** List of experimental tests conducted on SMA RC shear wall

| Experimental tests | Aspect ratio ($h_w / l_w$) | Axial load ratio ($P/f_c' A_g$) (%) | $V/A_g / f_c'$ (%) | $Pl_w / 2Vh_w$ (%) |
|---|---|---|---|---|
| Almeida et al. [4] | 1.7 | 3.83 | 1.43 | 80.52 |
| Kian et al. [15] | 2 | 0.08 | 1.84 | 1.05 |
| Abdulridha et al. [1] | 2.2 | 0.17 | 2.81 | 1.35 |
| [7] | 2.2 | 0.07 | 1.13 | 1.31 |
| Cortés-Puentes [7] | 1 | 0.19 | 4.31 | 2.25 |
| | 1 | 0.18 | 7.75 | 1.13 |

## 2 Parametric Analysis

A parametric analysis was performed to understand the cyclic response of SMA bars compared to steel rebar. The most appropriate type of SMA observed for structural applications is NiTi due to its ability to recover considerable strain, superelasticity, and excellent corrosion resistance [3]. FeMnAlNi alloy developed by Omori et al. [10] exhibits superelasticity in the range of NiTi, but at a low austenite finish temperature. This enables FeMnAlNi to function in the superelastic range even at a low temperature [6]. The SMA properties shown in Table 2 were referenced from the studies of [3, 10].

The parametric study considered three aspect ratios, three different rebar types (steel, NiTi, FeMnAlNi), two axial load ratios ($P/f_c'A_g$), and three different vertical reinforcing ratios ($\rho_v$). A total of 54 walls were analysed ($3 \times 3 \times 3 \times 2 = 54$ models) under cyclic loading. A constant cross section of 150 mm thick and 1200 mm long was considered for all shear wall models. This cross section was selected as per the capacity at the structure's laboratory at the University of British Columbia, Okanagan Campus. Three different types of rebars—steel ASTM A706 Grade 60, NiTi and FeMnAlNi, of size #3, #5 and #7 were varied in the concentrated zones of the shear wall. In this study, the vertical reinforcement ratio ($\rho_v$) was taken as the longitudinal reinforcement ratio of only one portion of the concentrated zone, shown in Eq. 1.

$$\rho_v = \frac{4(\text{Area of rebar})}{150\,\text{mm} \times 210\,\text{mm}} \times 100\%. \tag{1}$$

The #3 steel rebars were provided as longitudinal and transverse rebars in the wall web for all models. Figure 2 shows the cross section of the shear wall and reinforcement detailing. Table 3 shows the parameters studied.

**Table 2** Properties of SMA

| Properties | NiTi | FeMnAlNi |
| --- | --- | --- |
| Modulus of elasticity ($E$) | 62.5 GPa | 68 GPa |
| Austenite-to-martensite starting stress ($f_y$) | 401 MPa | 435 MPa |
| Austenite-to-martensite finishing stress ($f_{P1}$) | 510 MPa | 535 MPa |
| Martensite-to-austenite starting stress ($f_{T1}$) | 370 MPa | 335 MPa |
| Martensite-to-austenite finishing stress ($f_{T2}$) | 130 MPa | 170 MPa |
| Superelastic plateau strain length ($\varepsilon_1$) | 6% | 8% |
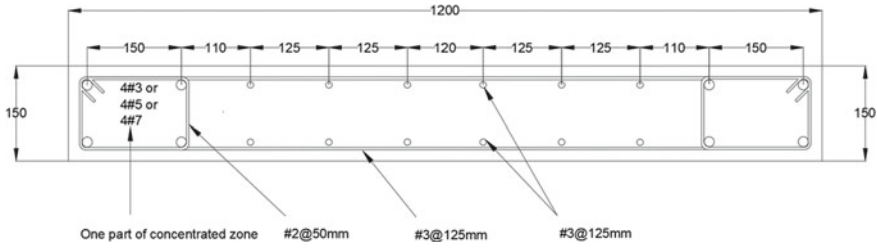
**Fig. 2** Cross section of wall model

**Table 3** Parameters to study

| Parameters | | Value | | |
|---|---|---|---|---|
| a | Aspect ratio ($h_w/l_w$) | 2 | 3 | 4 |
| b | Axial load ratio ($P/f'_c A_g$) | 5% | | 10% |
| c | Types of rebars | Steel ASTM A706 Grade 60 | NiTi | FeMnAlNi |
| d | Vertical reinforcement ratio ($\rho_v$) | 0.89% | 2.48% | 4.86% |

## 3  Numerical Modelling

Two-dimensional finite element models of the shear walls were developed using Seismostruct software [13]. The inelastic displacement-based frame element type was selected to model the walls. The nonlinear behaviour of concrete and steel was modelled by the Mander model (1988) and Menegotto and Pinto model (1973). The SMA material was modelled with the available Auricchio and Sacco model (1997) in Seismostruct. Static time-history analysis was performed to simulate the quasi-static behaviour of shear walls under axial load and cyclic loading. The compressive strength of concrete and the yield strength of steel was taken as 56 MPa and 470 MPa, respectively [16].

The height of the various models was raised as per the aspect ratios of 2, 3, and 4. The bottom of the wall was fixed. The reverse cyclic lateral loading which incrementally increases the drift amplitude was used as shown in Fig. 3. The loading protocol was referenced from the study of [4]. Further, the loading protocol was also selected as per the capacity of horizontal and vertical actuators available in the laboratory. A vertical load of $0.05A_g f'_c$ or $0.1A_g f'_c$ was applied at the top with the reversed cyclic lateral loading in the shear wall models as shown in Fig. 4.

**Fig. 3** Applied loading
protocol
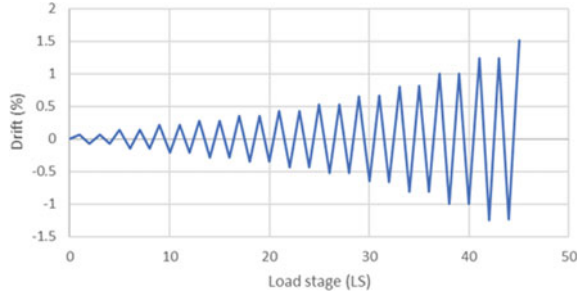


**Fig. 4** Numerical model



## 4 Result

A model was developed for each of the 54 combinations, and each model was anal-
ysed under cyclic loading. The combination was named *R#A#P#*, where *R* = rebar
size, *A* = aspect ratio, and *P* = axial load ratio. For instance, *R3A3P5* represents
rebar size #3, aspect ratio 3, and axial load ratio 5%.

### 4.1 Hysteretic Response and Trends

While assessing the various hysteretic responses for steel, NiTi and FeMnAlNi,
interesting trends were observed. These trends are shown in Figs. 5, 6, and 7. From
the hysteretic plots, it can be observed that there is a significant difference in the
hysteretic shapes of steel and SMA (NiTi and FeMnAlNi) shear walls. Generally, the
shear walls with only steel reinforcing showed larger hysteresis "loops" and, for the
majority of models, had residual deformations. Contrastingly, the SMA models had
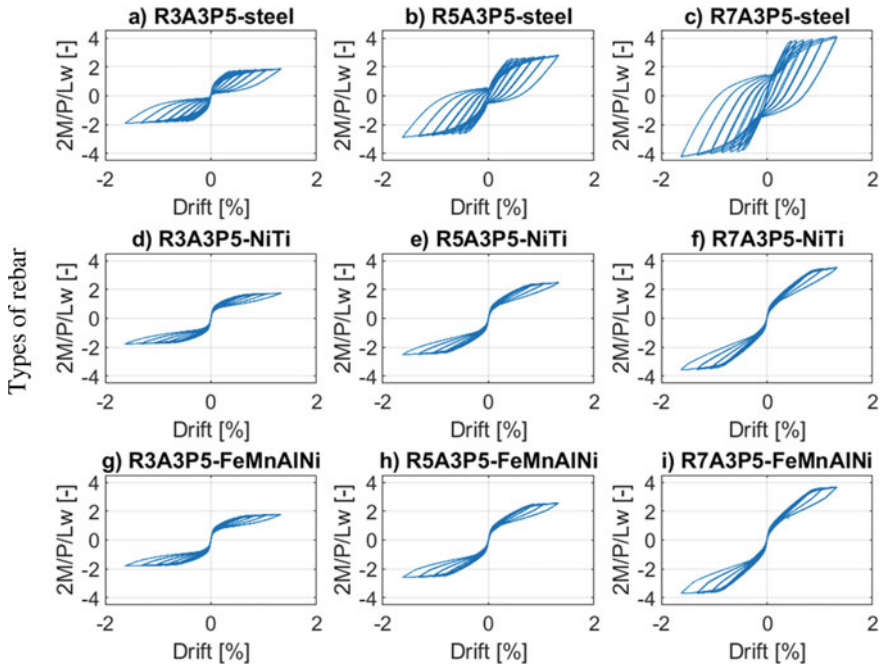
**Fig. 5** Hysteresis trend for same aspect ratio and axial load ratio with varying rebar size ($R =$ rebar size; $A =$ aspect ratio; $P =$ axial load ratio)

limited energy dissipation but showed minimal residual displacements, showcasing the SMA's excellent self-centring capabilities.

Figure 5 shows the different hysteresis for different vertical reinforcement ratios, a constant aspect ratio ($A = 3$), and a constant axial load ratio ($P/A_g/f_c' = 5\%$). In all cases, an increase in vertical reinforcement resulted in an increase in an overturning moment. In the steel models, a higher reinforcing ratio resulted in higher residual drifts. On the other hand, the SMA walls had low residual drift for all reinforcing ratios.

Figure 6 shows the different hysteresis for different aspect ratios, a constant reinforcing ratio of 2.48% (for rebar size #5), and axial load ratio ($P/A_g/f_c' = 5\%$). In all cases, a higher aspect ratio results in lower stiffness. Increasing the aspect ratio does not increase the capacity. Generally, a lower aspect ratio resulted in more energy dissipation (larger hysteretic loops) than a high aspect ratio.

Figure 7 shows the different hysteresis for different axial load ratio ($P/A_g/f_c' = 5\%$ and 10%), a constant reinforcing ratio of 2.48% (for rebar size #5), and aspect ratio ($A = 3$). Generally, increasing axial load resulted in a more pinched hysteresis (i.e. more prominent self-centring capability). However, a higher axial load led to earlier degradation of strength compared with a low axial ratio.
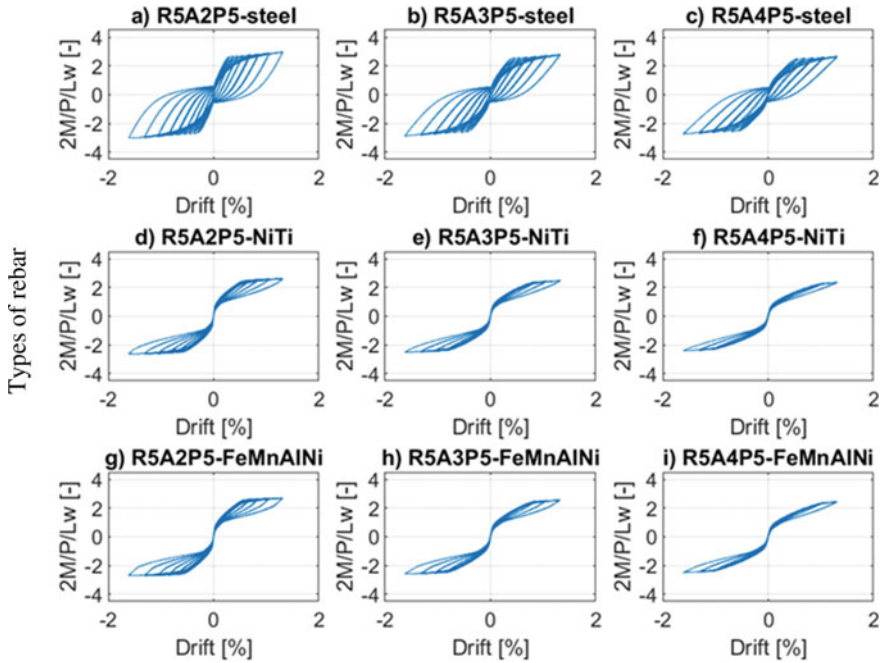
**Fig. 6** Hysteresis trend for same rebar size and axial load ratio with varying aspect ratio ($R$ = rebar size; $A$ = aspect ratio; $P$ = axial load ratio)

## 4.2 General Response

The residual drift is vital to determine the severity of damage to buildings after an earthquake. For this study, residual drift is taken as the ratio of permanent deformation over the height of the wall. Figure 8 shows the relationship between residual drift and vertical reinforcement ratio for steel, NiTi and FeMnAlNi at 5 and 10% axial load ratios.

As shown in Figs. 8a and d, residual drift was observed for all steel shear walls except for specimens with a reinforcing ratio of 0.89% ($R3$) and axial load ratio of 5%, where no residual drift was observed. Generally, an axial ratio of 10% had higher residual drifts than the axial ratio of 5%. The trend for the axial ratio of 5% walls showed that high vertical reinforcing ratios resulted in high residual drift. On the other hand, at an axial ratio of 10% walls with high vertical reinforcing ratios resulted in lower residual drift, except for $R5A4P10$, where the residual drift was low. In both axial ratios of 5% and the axial ratio of 10%, walls with a higher aspect ratio had lower residual drifts.

The SMA materials for an axial ratio of 5% showed no residual drift (i.e. Fig. 8b and c). On the other hand, the axial load ratio of 10% showed small residual drifts at the lower reinforcing ratios (i.e. Fig. 8e and f). The highest residual drift for SMA
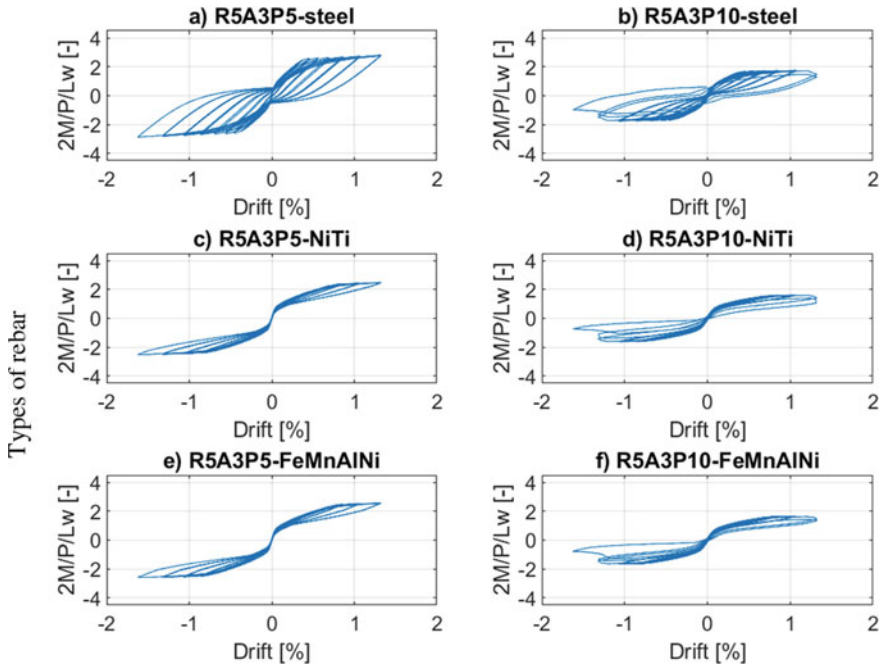
**Fig. 7** Hysteresis trend for same rebar size and aspect load ratio with varying axial load ($R$ = rebar size; $A$ = aspect ratio; $P$ = axial load ratio)
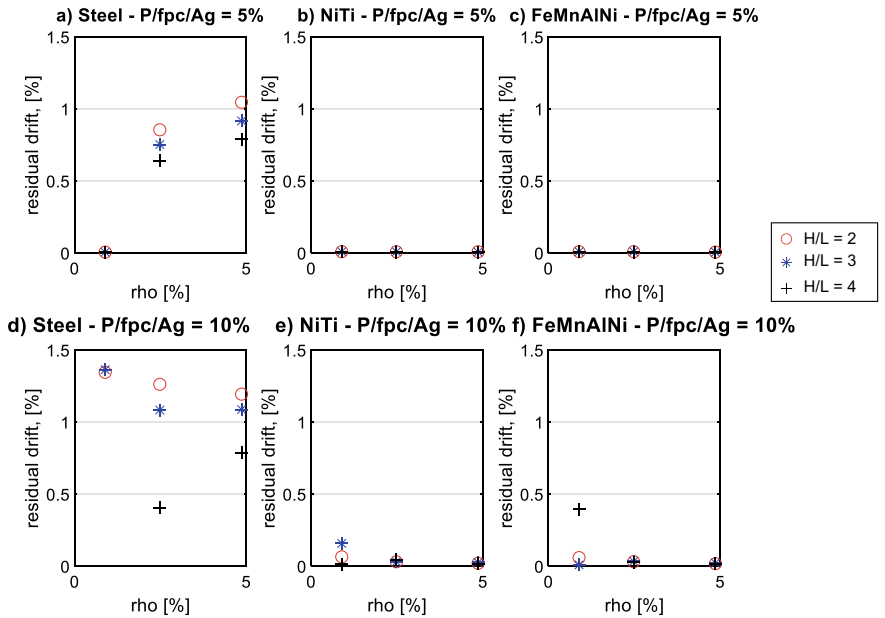


**Fig. 8** Residual drift versus vertical reinforcement ratio

walls was about 0.2% for aspect ratio 3 specimen at a 0.89% reinforcement ratio. On the other hand, the highest residual drift for steel walls was observed at around 1.4% for all three varying aspect ratios specimens.

Energy is the accumulation of hysteretic energy (i.e. inelastic force–deformation response) over all the cycles, which is normalized by the maximum shear force ($V_{max}$) and the maximum displacement ($\Delta_{max}$). The normalized energy (Energy/$V_{max}$/$\Delta_{max}$) was used to show energy dissipation capacity.

Figure 9 shows that the normalized dissipated energy for steel is higher than the NiTi and FeMnAlNi at 5 and 10% axial load ratios. For steel, energy dissipation was increased with the high reinforcement ratio. In contrast, there was low energy dissipation for shear walls with a high aspect ratio.

Shear walls with NiTi and FeMnAlNi bars showed low energy dissipation for high reinforcement ratios, as shown in Fig. 9b, c, e, and f. The energy dissipation capacity of NiTi was slightly lower than the FeMnAlNi. Overall, the NiTi and FeMnAlNi showed less than half of the energy dissipation than steel.

The cyclic degradation rotation ($\theta_{80\%}$) is the drift when the shear force is degraded to 80% of the maximum shear force. The value of $\theta_{80\%}$ is important as it represents the system ductility, which is a critical design parameter. For a 5% axial load ratio, no strength loss was observed in all three types of rebars. However, strength loss was observed for a 10% axial load ratio. Figure 10 shows the drift when the force degraded to 80% of the peak force. For a 10% axial load ratio, a higher reinforcing
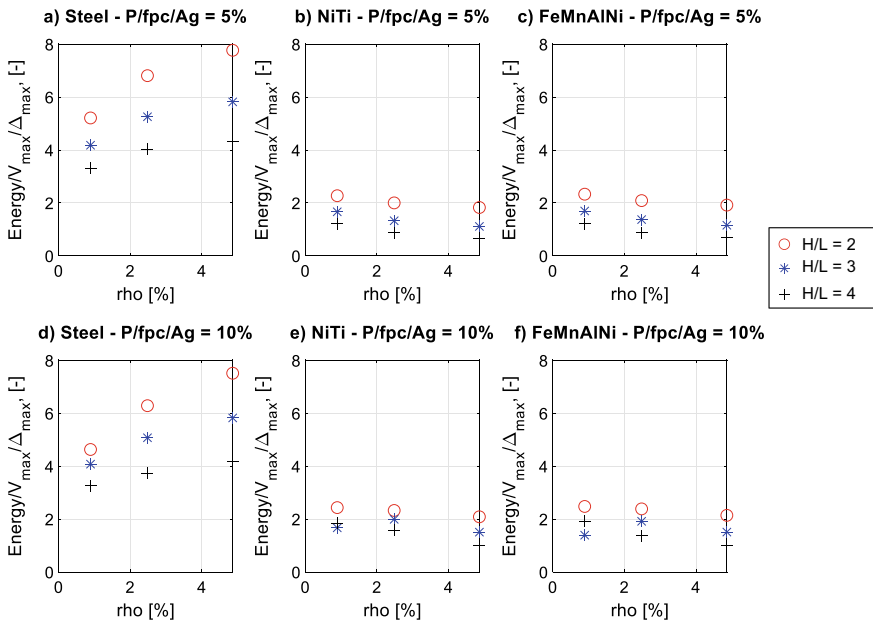


**Fig. 9**  Normalized energy dissipation versus vertical reinforcement ratio
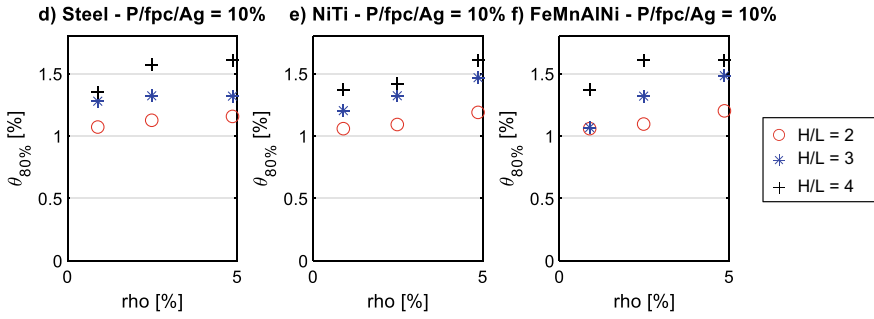
**Fig. 10** Drift at strength loss ($\theta_{80\%}$) versus vertical reinforcement ratio

ratio resulted in a higher $\theta_{80\%}$. Furthermore, higher rotation values were observed for the higher aspect ratios.

The critical damage states (cracking, spalling, yielding, crushing) were analysed and shown in Fig. 11 with the help of boxplots. This was performed by the rotation distribution to four performance limit states to see the effect of various parameters. For NiTi and FeMnAlNi, the spalling of the concrete cover was observed before yielding the SE SMA rebars. This behaviour is because the SMA rebars effectively resist the forces after cracking. A similar observation was also observed in a previous study conducted by Billah and Alam [6] and Ahmad and Shahria Alam [2]. The median rotation value of yielding for NiTi and FeMnAlNi was more than twice the value of steel. Similarly, the median rotation value of crushing was observed at 1.2 for NiTi and FeMnAlNi, while it was observed at 0.98 for steel.
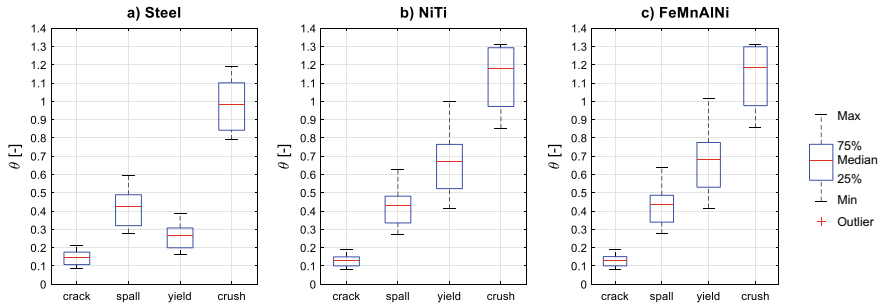


**Fig. 11** Boxplot for critical damage states

## 5 Summary and Conclusion

A detailed parametric study was performed with the force–deformation response and strain obtained from 54 models. The major conclusions drawn from the study are as follows:

- There is a lack of availability of experimental data due to the limited test on SMA RC shear walls.
- The NiTi and FeMnAlNi reinforced shear walls showed minimal residual displacements, demonstrating SMA's excellent self-centring capabilities.
- Significant residual drift was observed for steel shear walls except at a reinforcement ratio of 0.89% and axial load ratio of 5%. In contrast, it was observed very low to none in NiTi and FeMnAlNi.
- The NiTi and FeMnAlNi showed less energy dissipation than steel-reinforced shear walls at 5 and 10% axial load ratios.
- No strength loss was observed at 5% axial load ratio for all three rebar types. However, strength loss was observed for a 10% axial load ratio.
- The spalling of the concrete cover was observed before yielding in NiTi and FeMnAlNi because of SMA's excellent capacity to resist the forces after cracking.

## 6 Future Work

A comprehensive literature review showed little experimental data is available on slender shear walls connected with SMA rebars. This study showed the excellent self-centring capacity of NiTi and FeMnAlNi shear walls. Further, very low residual drift was observed for NiTi and FeMnAlNi. However, experimental work is needed to further explore the appropriate detailing methods for SMA shear wall. Therefore, for future research, an experimental study of slender shear walls connected with shape memory alloy bars can be conducted based on this parametric study.

## References

1. Abdulridha A, Palermo D (2017) Behaviour and modelling of hybrid SMA-steel reinforced concrete slender shear wall. Eng Struct 147:77–89
2. Ahmad N, Shahria Alam M (2015) Damage states for concrete wall pier reinforced with shape memory alloy rebar. In: The 11th Canadian conference on earthquake engineering
3. Alam MS, Youssef MA, Nehdi M (2008) Analytical prediction of the seismic behaviour of superelastic shape memory alloy reinforced concrete elements. Eng Struct 30(12):3399–3411
4. Almeida JP, Steinmetz M, Rigot F, de Cock S (2020) Shape-memory NiTi alloy rebars in flexural-controlled large-scale reinforced concrete walls: experimental investigation on self-centring and damage limitation. Eng Struct 220:110865
5. Auricchio F, Taylor RL, Lubliner J (1997) Shape-memory alloys: macromodelling and numerical simulations of the superelastic behaviour. Comput Methods Appl Mech Eng 146(3–4):281–312

6. Billah AHMM, Alam MS (2016) Performance-based seismic design of shape memory alloy–reinforced concrete bridge piers. I: development of performance-based damage states. J Struct Eng 142(12). American Society of Civil Engineers (ASCE)

7. Cortés-Puentes L, Zaidi M, Palermo D, Dragomirescu E (2018) Cyclic loading testing of repaired SMA and steel reinforced concrete shear walls. Eng Struct 168:128–141

8. Elwood KJ (2013) Performance of concrete buildings in the 22 February 2011 Christchurch earthquake and implications for Canadian codes. Can J Civ Eng 40(8):759–776

9. Jünemann R, de la Llera JC, Hube MA, Vásquez JA, Chacón MF (2016) Study of the damage of reinforced concrete shear walls during the 2010 Chile earthquake. Earthq Eng Struct Dyn 45(10):1621–1641

10. Omori T, Ando K, Okano M, Xu X, Tanaka Y, Ohnuma I, Kainuma R, Ishida K (2011) Superelastic effect in polycrystalline ferrous alloys. Science 333(6038):68–71

11. Saiidi MS, Wang HY (2006) Exploratory study of seismic response of concrete columns with shape memory alloys reinforcement. ACI Struct J 103:436–443

12. Saiidi MS, Sadrossadat-Zadeh M, Ayoub C, Itani A (2007).Pilot study of behavior of concrete beams reinforced with shape memory alloys. J Mater Civ Eng 19(6):454–461

13. Seismosoft (2022) SeismoStruct 2022—a computer program for static and dynamic nonlinear analysis of framed structures. Available from https://seismosoft.com/

14. Shahnewaz M, Alam MS (2015) Seismic performance of reinforced concrete wall with superelastic shape memory alloy rebar. In: Structures congress 2015, pp 2230–2240

15. Tolou Kian MJ, Cruz-Noguez C (2018) Reinforced concrete shear walls detailed with innovative materials: seismic performance. J Compos Constr 22(6):04018052

16. Tran TA, Wallace JW (2012) Experimental study of nonlinear flexural and shear deformations of reinforced concrete structural walls. In: Proceedings of the 15th world conference on earthquake engineering, Lisbon, Portugal

17. Youssef MA, Alam MS, Nehdi M (2008) Experimental investigation on the seismic behavior of beam-column joints reinforced with superelastic shape memory alloys. J Earthq Eng 12:1205–1222

# Effect of Low-Cycle Fatigue on the Seismic Vulnerability of Aluminium and Steel Domes

**Akossiwa Constance Efio-Akolly and Charles-Darwin Annan**

**Abstract** The low-cycle fatigue resistance of a material can influence the seismic vulnerability of a structure. Aluminium alloys are generally more susceptible to failure under low-cycle fatigue compared to steel. However, aluminium is an effective solution for domes exposed to aggressive environments such as chemical storage facilities, domes covering large spaces such as stadiums and domes with structural members connected efficiently (e.g. Mero) using extruded aluminium profiles. This is due to the durability, the high strength-to-weight ratio and the extrudability of aluminium alloys. The vulnerability of aluminium domes under earthquake ground motions may be influenced by its cyclic mechanical properties, including low-cycle fatigue. The rupture of a member under low-cycle fatigue can be captured by considering the earthquake-induced plastic strain cycle in the member. In the present study, the seismic vulnerability of aluminium and steel domes under the same gravity load are compared by developing fragility functions based on incremental dynamic analyses. The results showed that the low-cycle fatigue resistance of the material has a significant influence on the seismic performance of the domes. The aluminium dome and the steel dome were able to sustain seismic loads with spectral accelerations at the fundamental period up to 2 g and 2.5 g, respectively. It was observed that the aluminium dome showed a good seismic resistance for practical intensities representative of the design spectrum of Vancouver, BC, Canada.

**Keywords** Aluminium alloys · Carbon steel · Low cycle fatigue · Incremental dynamic analyses · Lattice dome · Fragility analysis · Seismic vulnerability

A. C. Efio-Akolly (✉) · C.-D. Annan
Department of Civil and Water Engineering, Laval University, Quebec City, QC, Canada
e-mail: akossiwa-constance.efio-akolly.1@ulaval.ca

# 1 Introduction

Lattice domes are structural systems with a spherical surface spanning large circular open spaces. They are widely used for buildings that accommodate many people, such as airport terminals, exhibition halls, auditoriums and stadiums. Lattice domes are built by assembling profile members arranged in a triangulated lattice and held together with bolted or welded connections. Steel lattice domes have exhibited a superior seismic performance than conventional buildings. For example, several structures collapsed during the 1995 Kobe earthquake of magnitude 7.2 in Japan, but no total collapse was reported for domes. Damage to the steel domes was limited to the non-load-bearing elements and the roofs [13]. The same observation was made during the 2008 Wenchuan earthquake of magnitude 8 in China. Numerical research results on the seismic performance of domes also confirmed this observation [10, 21, 22]. These conclusions on the seismic vulnerability of domes from research results and historic reports were associated with steel domes. However, aluminium has become an effective alternative to steel for the construction of domes. The preference for aluminium is justified by its advantageous physical and mechanical properties, namely its high strength-to-weight ratio, high corrosion resistance, durability and aesthetic appearance [14]. Little is known about the seismic vulnerability of aluminium domes, although experimental research data is available on the cyclic mechanical properties of aluminium alloys. When subjected to cyclic inelastic loadings, aluminium alloys and steel experience combined kinematic and isotropic hardening and low-cycle fatigue [1, 5]. However, aluminium alloys are more prone to fatigue failure than steel since they have a lower fatigue strength than structural steel [4, 15].

# 2 Research Objectives and Scope

Since aluminium and steel have different cyclic mechanical properties, it is necessary to study the influence of the material on the seismic vulnerability of domes subjected to strong earthquakes. Of great importance in the present study is the low-cycle fatigue behaviour of the materials. Yang et al. [20] demonstrated that low-cycle fatigue properties could reduce the superior seismic performance associated with domes under severe earthquake loading. Therefore, this study seeks to examine the vulnerability of aluminium domes and steel domes, considering the low-cycle fatigue resistance of the materials.

This study is focused on medium-rise single-layer diamatic lattice domes. The diamatic and the geodesic configurations are the most common configuration. In addition, the diamatic and geodesic domes have very similar dynamic behaviour, as demonstrated in the works of [12]. Therefore, this study will be limited to diamatic domes. A medium-rise shape was considered since it is the most common shape for lattice domes directly supported on foundations. Moreover, several parametric studies on the seismic behaviour of domes conducted by Hosseinizad [12] and Takeuchi et al.

[18] show that medium-rise domes are less resistant to seismic loads than shallow domes. The materials considered are 350WT steel [1, 9] and 6082-T6 aluminium alloy [2, 4]. The alloy 6082 T6 was selected for its excellent corrosion resistance and acceptable cyclic mechanical properties.

## 3    Seismic Hazard and Selected Ground Motion Records

Seismic fragility analysis is commonly used to describe the probability of collapse of a structure with respect to the earthquake intensity. One common approach for defining a fragility function is the incremental dynamic analysis proposed by Vamvatsikos and Allin Cornell [19]. The methodology is such that several nonlinear time history analyses are carried out for a suite of ground motions records, and each ground motion record is scaled up until the frame collapses. Therefore, a suite of ground motions is needed for the incremental dynamic analyses. Our interest is in earthquake-prone areas, such as western Canada.

To propose a methodology to evaluate the inelastic seismic demands of building systems using Incremental Dynamic analyses, FEMA P695 [11] recommended a set of 22 ground motions records representative of the west of North America for the far-field analysis. These records were selected to be representative of the seismicity of the west coast of North America, where very strong earthquakes are expected. Therefore, this set of ground motions is applicable to our study. The FEMA set of ground motions was considered an initial set. From this set, we selected the first 11 ground motions with the least mean squared error to Vancouver design spectrum using PEER NGA [17]. This selection was made considering a range of periods from 0.1 to 1 s since the natural periods of single-layer medium-rise steel domes usually fall between 0.3 and 0.5 s. Figure 1 shows the acceptable match obtained between the mean spectra of the eleven ground motions and the target spectrum of Vancouver for matching periods. The description of the selected eleven ground motions is listed in Table 1.

## 4    Finite Element Analysis Model

The pilot dome considered in this study is shown in Fig. 2. The dome consists of eight main radial ribs and eleven latitudinal circles. The diameter of the dome is 40 m, and the height to span ratio equals 1/3. The dome is assumed to be directly connected to a firm foundation. The boundary conditions of the dome are modelled as three-way pinned supports. Connections between members are assumed to be rigid. The domes were designed for a dead load of 0.5 kN/m$^2$, a snow load of 1.82 kN/m$^2$, and a roof load of 1 kN/m$^2$. The tensile and compressive members of the domes were designed for the ultimate limit states considering second-order effects, using the Canadian standards [6–8]. Moreover, a nonlinear buckling analysis was conducted

**Fig. 1** Mean spectra of the set of ground motions
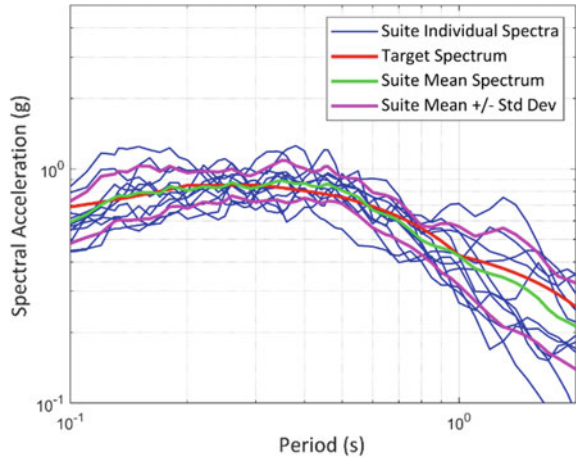


**Table 1** Description of the set of ground motions

| PEER record sequence number | Earthquake name | Year | Station name | Magnitude |
|---|---|---|---|---|
| 125 | "Friuli_Italy-01" | 1976 | "Tolmezzo" | 6.5 |
| 169 | "Imperial Valley-06" | 1979 | "Delta" | 6.53 |
| 721 | "Superstition Hills-02" | 1987 | "El Centro Imp. Co. Cent" | 6.54 |
| 725 | "Superstition Hills-02" | 1987 | "Poe Road (temp)" | 6.54 |
| 848 | "Landers" | 1992 | "Coolwater" | 7.28 |
| 900 | "Landers" | 1992 | "Yermo Fire Station" | 7.28 |
| 960 | "Northridge-01" | 1994 | "Canyon Country - W Lost Cany" | 6.69 |
| 1158 | "Kocaeli_Turkey" | 1999 | "Duzce" | 7.51 |
| 1602 | "Duzce_Turkey" | 1999 | "Bolu" | 7.14 |
| 1633 | "Manjil_Iran" | 1990 | "Abbar" | 7.37 |
| 3746 | "Cape Mendocino" | 1992 | "Centerville Beach_ Naval Fac" | 7.01 |

to ensure that the ratio of the buckling load to the design load is greater than 2.5 as recommended in the works of [11, 12]. At the end of the design process, the selected tubular profiles were 4.00 in. OD × 0.125 in. WALL, with an outside diameter of 101.6 mm and a wall thickness of 3.2 mm for the aluminium dome members, and HSS73 × 3.2, with an outside diameter of 73 mm and a wall thickness of 3.2 mm for the steel dome members.

The designed domes were modelled in Opensees [16]. Each dome member was discretized into four elements. The elements were arranged in the shape of the first member buckling mode shape of the member scaled to 1/300 of the span of the

**Fig. 2** Pilot dome model
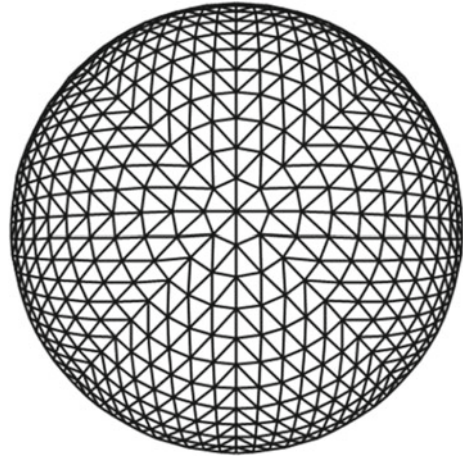


dome. Moreover, a P-Delta coordinate transformation object was assigned to the dome model to account for the second-order effects. The elements were modelled as fibre-based beam-column elements. This element model uses the fibre-based frame elements approach, which divides the cross-section of the element into fibres to capture local axial stresses and strains. The uniaxial cyclic stress–strain behaviour was simulated by defining a uniaxial material object that included the calibrated material properties of the Chaboche combined hardening model and the Coffin Manson low-cycle fatigue model. The defined material object was then assigned to each fibre to account for material nonlinearities. The calibrated material model properties input in the uniaxial material objects for the 6082T6 alloy and the low carbon steel 350WT were obtained from [1, 2, 4, 9]. The strength properties and Coffin Manson low-cycle fatigue model parameters of 6082T6 alloy and low carbon steel 350WT are shown in Table 2. For the dynamic analyses, damping was applied in the model using the Rayleigh damping formulation with a damping ratio of 2%.

The aluminium and steel domes were subjected to a modal pushover analysis and an incremental dynamic analysis. For the modal pushover analyses, the lateral loads were gradually applied at each joint in a pattern proportional to a selected mode shape. The first three modes having the most significant mass participation ratio in the horizontal direction were considered to determine the lateral load in

**Table 2** Low-cycle fatigue properties of 350WT and 6082T6

| Material name | Modulus of elasticity, $E$ (MPa) | Yield strength, $F_y$ (MPa) | Ultimate strength, $F_u$ (MPa) | Coffin Mason fatigue ductility coefficient, $\varepsilon_f$ | Coffin Mason fatigue ductility exponent, $c$ |
|---|---|---|---|---|---|
| 350 WT | 211,180 | 364 | 503 | 0.33 | − 0.54 |
| 6082T6 | 66,500 | 307 | 330 | 0.209 | − 0.593 |

each modal pushover analysis. The recorded demand measure was the maximum nodal displacement of the dome. The total response was obtained by combining the individual response of each of the three modal pushover analyses using the Complete Quadratic Combination (CQC) method.

Nonlinear time history analyses were conducted on the domes for each ground motion in the selected suite to assess the seismic vulnerability of the domes. The seismic intensity measure was taken as the 2% damped spectral acceleration at the fundamental period of the structure since this intensity measure refers to the degree of seismic excitation of the ground motion and the expected dynamic characteristics of the structure. For each increment of seismic intensity, the normalized yield element ratio, the maximum nodal displacement and the fatigue life of the domes were determined. The normalized yield element indicates the spread of plasticity throughout the dome by measuring the ratio of fully yielded elements. The fatigue damage was calculated using the Coffin Mason equation, the Palmgren–Miner rule and the rainflow cycle counting algorithm. The incremental dynamic analysis results were statistically processed to construct seismic fragility curves and establish the seismic vulnerability of the single-layer reticulated domes.

## 5    Seismic Performance and Vulnerability of the Domes

This section presents the results of the incremental dynamic analyses and the fragility analysis. For ease of reference, the aluminium dome and the steel dome are referred to as AD40f3 and SD40f3, respectively.

### 5.1    Seismic Performance of the Aluminium and Steel Domes

This section describes the seismic behaviour of the aluminium and steel domes subjected to the suite of ground motions. The incremental dynamic curves of the steel dome and aluminium dome, with the maximum nodal displacement as the demand measure, are presented in Fig. 3. This figure shows that greater displacements occur in the aluminium domes as compared to the steel domes, with a ratio of about two for all the ground motions considered.

To better understand the seismic performance of the domes, incremental dynamic curves were plotted, considering the yield element ratio and the fatigue life as engineering demand parameters. These graphs are shown in Figs. 4 and 5, respectively. It is observed that there is a higher percentage of yielded members in the aluminium dome than in the steel dome. Moreover, there was no fully yielded member for spectral accelerations lesser than 3.5 g in the steel dome and 2 g in the aluminium domes. These results show an overall good performance for both domes for seismic intensities lesser than 2 g. At seismic intensities greater than 2 g, the number of yielded elements rapidly increased in the aluminium dome compared to the steel
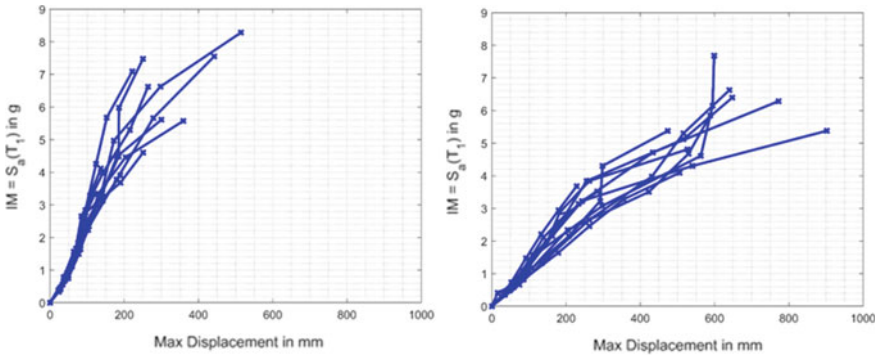
**Fig. 3** Incremental dynamic analysis curves for the steel dome (left) and the aluminium dome (right), considering the maximum nodal displacement

dome. No dynamic buckling occurred except for the domes subjected to the Duzce_ Turkey (RSN 1602) earthquake. Therefore, the results obtained with the Duzce_ Turkey were excluded in the processing of the incremental dynamic analyses results.

The influence of the fatigue resistance on the seismic performance of the domes is shown in Fig. 5. The fatigue life was calculated as the reciprocal of the maximum fatigue damage in the elements and expressed in units of repeats. When the maximum fatigue damage in an element is less than one, no fatigue occurs. In this case, the fatigue life in units of repeats would be greater than one repeat. For simplicity, whenever the calculated fatigue life was greater than one repeat, the low-cycle fatigue life value shown in Fig. 5 was 1. This was done to group all cases where no fatigue failure was observed to highlight those cases where low-cycle fatigue failure was recorded. It can be observed that the low-cycle fatigue properties of the material have a significant influence on the overall performance of the domes. In other words, the aluminium dome was more prone to fatigue failure than the steel dome. This is
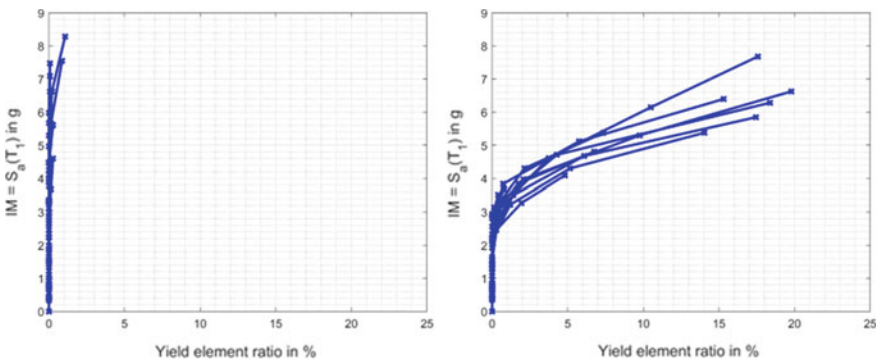


**Fig. 4** Incremental dynamic analysis curves for the steel dome (left) and the aluminium dome (right), considering the normalized yield element ratio
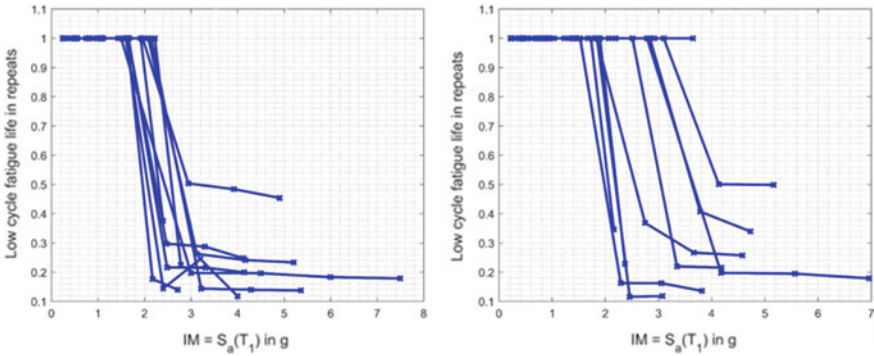
**Fig. 5** Incremental dynamic analysis curves for the steel dome (left) and the aluminium dome (right), considering the fatigue life

shown by the density of points in the lower part of both curves. In addition, it is observed that there is less risk of fatigue failure for spectral accelerations lesser than 3 g in steel domes and 2 g in aluminium domes.

## 5.2 Seismic Vulnerability of the Aluminium and Steel Domes

A modal pushover analysis was carried out to determine the threshold values for the collapse limit state. The threshold values were determined as the maximum nodal displacement when the domes exhibit a post-yield stiffness nearly equal to zero. Since the threshold values were determined when the domes had little residual stiffness and large permanent deformations, these threshold values can be considered to represent the collapse prevention structural performance levels as described in [3]. The measured values are 130 mm for the steel dome and 210 mm for the aluminium dome.

To further investigate the seismic performance of the domes under severe earthquakes, the fragility curves for both domes were constructed from the incremental dynamic analysis results and the threshold values. These fragility curves describe the seismic risk associated with each dome. For comparison, the fragility curves of the aluminium dome and the steel dome are plotted in Fig. 6. It is observed that, for seismic intensities representatives of very strong earthquakes, the steel dome has a lesser probability of collapse than the aluminium dome. However, the seismic risk associated with both domes is the same for seismic intensities representative of our study area (western Canada), where the design spectral accelerations are between 0.4 and 1.3 g.
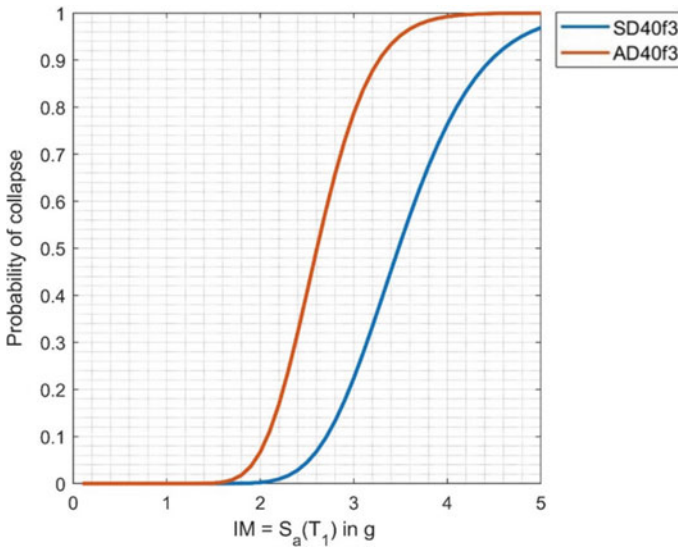
**Fig. 6** Fragility curves of the steel dome and the aluminium dome

## 6 Conclusion

This paper has examined the influence of the low-cycle fatigue resistance of the material on the seismic vulnerability of steel and aluminium lattice domes. The seismic vulnerability of the domes was determined from the incremental dynamic analyses results. The steel dome and the aluminium dome exhibited a good performance under all the unscaled ground motions considered. This was evident because there was no fatigue failure or fully yielded members in the aluminium or steel domes subjected to the set of unscaled ground motions. The steel dome showcased a good seismic performance when subjected to severe earthquakes with spectral accelerations up to 3 g. For all seismic intensities considered, the nodal displacements and the spread of plasticity were always more significant in the aluminium dome than in the steel dome. Moreover, this study demonstrated that low-cycle fatigue significantly influences the seismic performance of aluminium domes. Fatigue failure is expected in aluminium domes that are subjected to severe earthquakes, with a spectral acceleration greater than 1.5 g. However, the aluminium dome showcased an overall good performance when subjected to seismic intensities representatives of the seismicity of western Canada. Finally, the seismic risk associated with both domes was the same for seismic intensities representatives of the seismicity of western Canada.

# References

1. Annan CD, Beaumont E (2020) Low-cycle fatigue of stainless steel plates under large plastic strain demands. J Build Eng 29:101160. https://doi.org/10.1016/j.jobe.2019.101160
2. Arslan E, Zigo M, Kepplinger G (2020) A novel approach for determination of hardening parameters of an aluminum alloy under cyclic loading with high amplitudes. IOP Conf Ser: Mater Sci Eng 947(1):6–11. https://doi.org/10.1088/1757-899X/947/1/012009
3. ASCE (2017) Seismic evaluation and retrofit of existing buildings (Issue June)
4. Borrego LP, Abreu LM, Costa JM, Ferreira JM (2004) Analysis of low cycle fatigue in AlMgSi aluminium alloys. Eng Fail Anal 11(5):715–725. https://doi.org/10.1016/j.engfailanal.2003.09.003
5. Brammer AT, Jordon JB, Allison PG, Barkey ME (2013) Strain-controlled low-cycle fatigue properties of extruded 6061–T6 aluminum alloy. J Mater Eng Perform 22(5):1348–1350. https://doi.org/10.1007/s11665-012-0411-0
6. CNRC (2015) Code national du bâtiment: Canada: 2015, vol 1
7. CSA Group (2017) Strength design in aluminum/Commentary on CSA S157-17, strength design in aluminum
8. CSA Group (2019) Design of steel structures (Issue December)
9. Dehghani M, Tremblay R, Leclerc M (2017) Fatigue failure of 350WT steel under largestrain seimic loading at room and subfreezing temperatures. Constr Build Mater 145:602–618. https://doi.org/10.1016/j.conbuildmat.2017.03.183
10. Fan F, Shen SZ, Parke GAR (2005) Study of the dynamic strength of reticulated domes under severe earthquake loading. Int J Space Struct 20(4):235–244. https://doi.org/10.1260/026635105775870251
11. FEMA (2009) Quantification of building seismic performance factors. In: Fema P695 (Issue June)
12. Hosseinizad (2018) Seismic response of lattice domes, p 47. https://doi.org/10.1503/cmaj.180710
13. Ishikawa K, Kawaguchi K, Tagawa K, Sakai T (1997) Report on gymnasium and spatial structures damaged by hyogoken-nanbu earthquake. AIJ J Technol Des 3(5):96–101. https://doi.org/10.3130/aijt.3.96
14. Mazzolani FM (2006) New challenges for aluminium structures: an introduction structural applications of aluminium in civil engineering fields of application. Struct Eng Int 4:1–4
15. Nečemer B, Zupanič F, Gabriel D, Tarquino EA, Šraml M, Glodež S (2021) Low cycle fatigue behaviour of ductile aluminium alloys using the inelastic energy approach. Mater Sci Eng A 800. https://doi.org/10.1016/j.msea.2020.140385
16. OpenSees (2006) Open System for Earthquake Engineering Simulation—Home Page. https://opensees.berkeley.edu/
17. Pacific Earthquake Engineering Research Center (2013) PEER Ground Motion Database—PEER Center. https://ngawest2.berkeley.edu/
18. Takeuchi T, Okada K, Ogawa T (2016) Seismic response evaluation of freeform lattice shell roofs with supporting substructures. J Struct Constr Eng 81(727):1467–1477. https://doi.org/10.3130/aijs.81.1467
19. Vamvatsikos D, Allin Cornell C (2002) Incremental dynamic analysis. Earthq Eng Struct Dynam 31(3):491–514. https://doi.org/10.1002/eqe.141
20. Yang D, Yun C, Wu J, Yao Y (2018) Seismic response and failure mechanism of single-layer latticed domes with steel columns and braces as substructures. Thin-Walled Struct 124:458–467. https://doi.org/10.1016/j.tws.2017.12.038
21. Zhang Y, Zhi X, Fan F (2020) Fragility analysis of reticulated domes subjected to multiple earthquakes. Eng Struct 211. https://doi.org/10.1016/j.engstruct.2020.110450
22. Zhi XD, Nie GB, Fan F, Shen SZ (2012) Vulnerability and risk assessment of single-layer reticulated domes subjected to earthquakes. J Struct Eng 138(12):1505–1514. https://doi.org/10.1061/(asce)st.1943-541x.0000589

# Detection of Local Buckling in Thin-Walled Hollow Structural Steel Sections Using Fibre Optic Cables

**John Kabanda, Andre Brault, and Colin MacDougall**

**Abstract** Fibre optic cable-based techniques have recently been introduced in the steel construction industry. This is due to their high sensitivity, ability to resist electromagnetic interference, be lightweight and efficiently multiplex. However, fibre optic cable sensors are still limited due to their initial high cost and unfamiliarity to the users. This paper compares fibre optic cable sensors to traditional strain gauge sensors via an experimental program comprising four-point bending and three-point bending tests. The sensors were used to detect the location and initiation of local buckling in thin-walled polygonal hollow section (PHS) and rectangular hollow section (RHS) beams. The results showed that for these deep thin-walled beams with similar cross-sectional dimensions, the PHS beams were able to reach their yield moment capacities, while the RHS beams failed due to local buckling at about 40% below their yield moment capacities. In addition, unlike the strain gauges, the fibre optic cable sensors were able to detect the location and initiation of local buckling along the length of the tested beams.

**Keywords** Buckling · Fibre optic cable · Thin-walled sections

## 1 Introduction

As their quality continues to improve, fibre optic cable sensors have the potential to replace traditional strain gauge sensors in steel structures. This is because of their higher sensitivity, ability to resist electromagnetic interference, be lightweight and efficiently multiplex. However, fibre optic cable sensors are still limited due to their initial high cost and unfamiliarity to potential users [10]. Nevertheless, the ability to measure along a given length gives fibre optic cables a critical advantage and is the main criterion that differentiates them from traditional strain gauge sensors, Fig. 1. This paper compares fibre optic cable sensors with strain gauge sensors via

J. Kabanda (✉) · A. Brault · C. MacDougall
Department of Civil Engineering, Queen's University, Kingston K7L 3N6, Canada
e-mail: 14jsk3@queensu.ca

an experimental program, comprising four-point bending and three-point bending tests. The sensors are used to detect the location and initiation of local buckling in thin-walled polygonal hollow section (PHS) and rectangular hollow section (RHS) beams.

Thin-walled rectangular hollow sections (RHS) have very high torsional rigidity, and thus make a very economic choice for applications which are susceptible to lateral torsional buckling (e.g., long unbraced cantilever beams). However, as the depth of a thin-walled RHS increases to ensure adequate bending stiffness, it may fail due to local buckling of its compression flange, resulting in a reduced capacity. In contrast, a recently proposed polygonal hollow section (PHS) has the potential to minimize the local buckling failure mechanism [8]. The PHS starts as a basic RHS but includes discrete bends in its web and flange, Fig. 2, which are easier to fabricate than a continuous curvature.
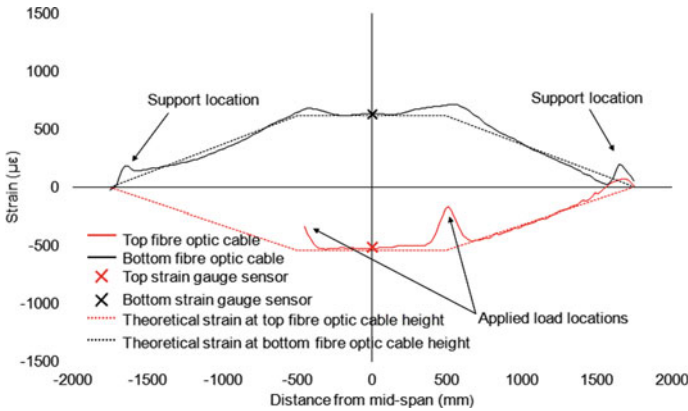


**Fig. 1** Measurement of strain along a beam using fibre optic cable and strain gauge sensors
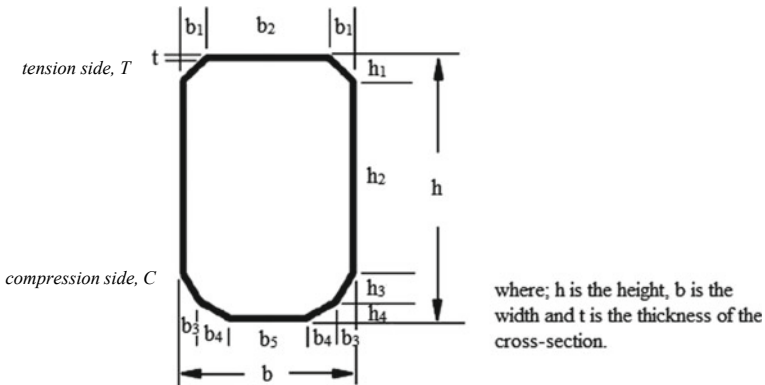


**Fig. 2** Illustration of the proposed PHS [8]

Local buckling failure is a major consideration in the design of cold-formed steel sections [1]. The Canadian steel design standard [4], for example, provides design equations to calculate resistance of wide flanges under concentrated loads. For loads that exceed this resistance, welded web stiffeners may be provided. There is no similar guidance, however, for hollow structural sections. Elliptical hollow sections (EHS) have been proposed as a solution to minimize local buckling failure in hollow structural sections [6]. However, the cross-section of an EHS requires highly specialized design expertise in comparison with a PHS. In addition, the bends of the PHS increase its bending strength and rotational capacity, and thus minimize web crippling in the beam's cross-section [9]. Previous research on PHS has also been very limited; Yamashita et al. [13] and Song et al. [12] only considered the axial crush behavior of short polygonal stub columns.

In this paper, PHS beams are compared with RHS beams of similar cross-sectional dimensions via an experimental program consisting of four-point and three-point bending tests. The objective of these tests is to compare the behavior of PHS and RHS beams under concentrated loads, with either distributed fibre optic cable sensors installed along each beam's length or strain gauges sensors installed at discrete locations along each beam. Unlike conventional strain gauges which are typically placed at a predefined location, distributed fibre optic sensors can detect localized deformation and buckling without prior knowledge of the location of the critical areas [7].

## 2 Experimental Investigation

A total of 10 specimens (4 stub columns and 6 beams), which comprised 5 PHS and 5 RHS of varying lengths, were fabricated. The nominal dimensions of the 4 cross-sections used to construct the PHS and RHS specimens tested herein are given in Tables 1 and 2. The RHS were fabricated with a single seam weld on the web of the cross-section, while the PHS had seam welds on the top and bottom flanges of the cross-section. The specimens were all cold-formed members with ASTM A500 (Grade C) steel. The RHS were Class 3 or 4 as per the Canadian steel design standard [4] while there is currently no similar classification for the PHS.

Prior to the bending tests, the dimensions and material properties of the four cross-sections listed in Table 1 were examined via experimental investigations consisting of

**Table 1** Nominal dimensions of the cross-sections of the RHS and PHS specimens

| Cross-section | $h$ (mm) | $b$ (mm) | $t$ (mm) | $I$ ($\times 10^6$ mm$^4$) | b/t | $\omega_o$ (mm) |
|---|---|---|---|---|---|---|
| RHS305 | 305 | 203 | 6.4 | 76 | 31.7 (class 3) | 0.71 |
| RHS356 | 356 | 254 | 6.4 | 129 | 39.7 (class 4) | 0.97 |
| PHS305 | 305 | 203 | 6.4 | 65 | N/A | 0.91 |
| PHS356 | 356 | 254 | 6.4 | 109 | N/A | 1.01 |

**Table 2** Dimensions of the cross-section of the PHS specimens

| Dimension (Fig. 2) | PHS 305 (mm) | PHS 356 (mm) |
|---|---|---|
| $b$ | 203 | 254 |
| $b_1$ | 49.5 | 62 |
| $b_2$ | 104 | 130 |
| $b_3$ | 33.5 | 42 |
| $b_4$ | 42 | 53 |
| $b_5$ | 52 | 64 |
| $h$ | 305 | 356 |
| $h_1$ | 57 | 66 |
| $h_2$ | 191 | 223 |
| $h_3$ | 39.6 | 46 |
| $h_4$ | 17.4 | 21 |
| $t$ | 6.4 | 6.4 |

geometric imperfection measurements, tensile coupon tests, residual stress analyses and stub column tests.

## 2.1 Geometric Imperfections

For each cross-section tested herein, the imperfection measurements were completed using an edge ScanArm and the details are provided in [9]. The measured data points were used to determine the highest imperfection amplitude $\omega_o$ (Table 1), which is the difference between the measured and nominal dimensions and was within the permitted limits of the ASTM A500 standard [3].

## 2.2 Tensile Coupon Tests

The tensile stress–strain properties of the PHS and RHS specimens herein were obtained through tensile coupon tests. The tensile coupons, cut from the same length of tubes as the test specimens, were quasi-statically tested in accordance with the ASTM A370 standard [2]. The key results from the tensile coupon tests and the corresponding nominal (mill certificate) properties of the investigated specimens are listed in Table 3; where $f_y$, and $f_u$ are the yield and ultimate strengths of the materials respectively, and $E$ denotes Young's modulus. The yield stresses were determined using the 0.2% offset method.

**Table 3** Nominal (nom) and experimental (exp) tensile material properties of the PHS and RHS

| Cross-section | $f_{y,nom}$ (MPa) | $f_{u,nom}$ (MPa) | $f_{y,exp}$ (MPa) | $f_{u,exp}$ (MPa) | $E_{,exp}$ (MPa) |
|---|---|---|---|---|---|
| RHS305 | 423 | 478 | 398 | 425 | 202,547 |
| RHS356 | 486 | 523 | 448 | 494 | 206,384 |
| PHS305 | 517 | 564 | 513 | 541 | 205,610 |
| PHS356 | 573 | 521 | 515 | 547 | 209,789 |

**Table 4** Key results from the PHS and RHS stub column and residual stress analyses

| Cross-section | $L$ (mm) | $A$ (mm$^2$) | $E$ (MPa) | $f_p$ (MPa) | $f_u$ (MPa) | $(\sigma_{rs}/\sigma_y)_{stub-column}$ | $(\sigma_{rs}/\sigma_y)_{residual-stress}$ |
|---|---|---|---|---|---|---|---|
| RHS305 | 964 | 5877 | 217,209 | 138 | 301 | 0.49 | 0.54 |
| RHS356 | 977 | 7040 | 208,495 | 129 | 256 | 0.44 | 0.47 |
| PHS305 | 1088 | 5724 | 207,731 | 159 | 431 | 0.61 | 0.67 |
| PHS356 | 1103 | 6880 | 215,087 | 164 | 410 | 0.58 | 0.61 |

## 2.3 Residual Stress Analyses

During preparation of the tensile coupons, a few of the extracted coupons were observed to curve away from their initial geometry. This is due to the presence of through-thickness bending residual stresses. The residual stresses were measured using the sectioning method [11]. The stresses were then used to derive the maximum longitudinal residual stress ratio $(\sigma_{rs}/\sigma_y)_{residual-stress}$ using the Davison and Birkemoe [5] relationship. For each section, the computed maximum longitudinal residual stress ratio $(\sigma_{rs}/\sigma_y)_{residual-stress}$ is given in Table 4. The PHS specimens contain about 19% more residual stress than the RHS specimens and this is due to extra bends of the former.

## 2.4 Stub-Column Tests

The purpose of the stub-column tests was to determine the overall compressive yield strength of the PHS and RHS specimens. A total of four stub columns were tested under pure axial compression and the details of the test frame are provided in [9]. The tests were completed in accordance with the procedure described by Ziemian [15].

Typical normalized stress–strain curves and the key results from the stub-column tests are shown in Fig. 3 and Table 4, respectively. For each stub column, the compressive stresses $f$, including the proportional stress limit $f_p$ and ultimate load stress $f_u$ were obtained by dividing the corresponding compression load by the cross-sectional area A. The average compressive strain over the cross-section was obtained
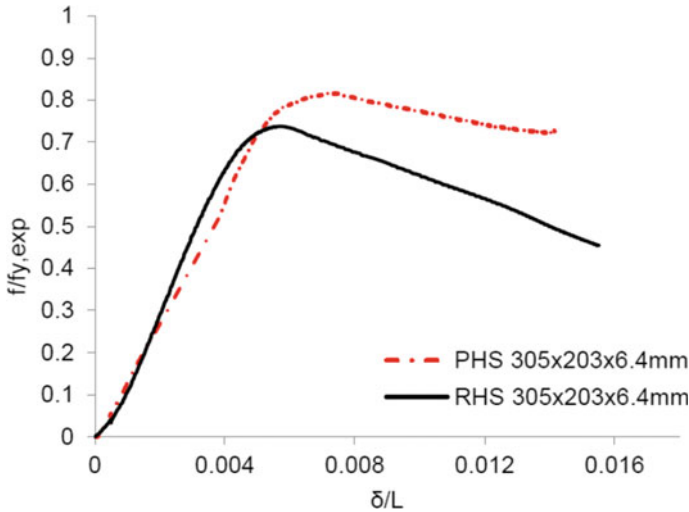
**Fig. 3** Typical normalized stress–strain curves for the PHS and RHS stub columns

by dividing the end-shortening $\delta$ by the initial stub-column length $L$. For the stub-column tests, the maximum longitudinal compressive residual stress values ($\sigma_{rs}/\sigma_y$)$_{\text{stub-column}}$ were computed as $(1 - f_p/f_y)_{\text{stub-column}}$.

## 2.5 Bending Tests

Four-point and three-point bending tests were conducted on PHS and RHS beams, to compare their buckling strength and to detect the location and initiation of local buckling under concentrated loads.

The four-point bending tests consisted of two beams fabricated from the PHS356 and RHS356 cross-sections, Table 1. The PHS beam was labeled as PHS356A and the RHS beam was labeled as RHS356A. The length L of all the beams was fixed at 3500 mm. Figure 4 shows an illustration of the four-point bending schematic and the test setup is described in [9].

Each beam was fitted with steel end caps and the simple support conditions were achieved by means of a steel roller between the beam and a profiled stiffening plate at each end support. Steel rollers were also placed between the spreader beam (1000 mm long) and a profiled stiffening plate at each loading point, Fig. 4. The tests were displacement controlled at a rate of 2 mm/min and were completed using a 1200 kN Riehle testing machine, Fig. 5.

Fibre optic cables were installed along the top and bottom of the web of each beam, Fig. 4. Electrical strain gauges were also attached to the web and flange of
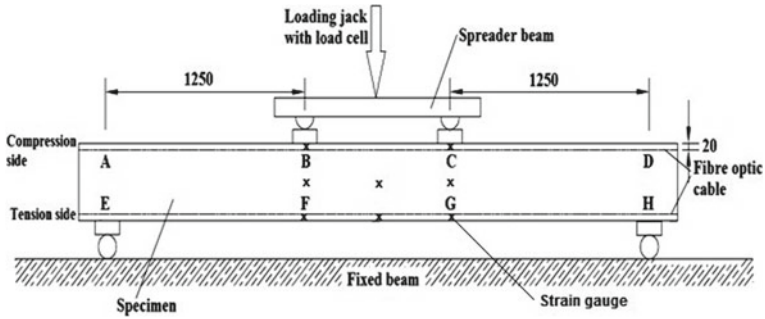
**Fig. 4** Illustration of the four-point bending test schematic



**Fig. 5** General view of the four-point bending test setup

each beam. This was done at the center and at 500 mm from either side of the loading point of each beam, Fig. 4.

Figure 6 shows the general view of the fibre optic cable installed along the length of a beam relative to strain gauges placed at specific locations. A strain gauge can offer high strain resolutions of the order of 1 microstrain; however, it only enables measurements to be taken at a discrete location which makes detecting localized issues difficult without prior knowledge [7]. Distributed fibre optic sensors, on the other hand, enable strain measurements to be taken along the full length of a given

**Fig. 6** General view of a fibre optic cable relative to strain gauges

specimen. In other words, there are potentially thousands of sensors along the specimen allowing for distributed measurements, which is ideal for localized damage detection applications where the location of critical areas is not known prior to testing [7].

Figure 7 shows the normalized moment-strain curves from the four-point beam bending tests. The normalized mid-span moments are plotted against strains which are recorded using a strain gauge located at the center of the bottom flange of each beam. Furthermore, in Fig. 7, the yield moment capacity $M_y$ was calculated by multiplying the measured yield stress from the tensile coupon tests and the corresponding section modulus.

The results in Fig. 7 show that the RHS356A beam failed at about 21% below its yield moment capacity. Contrariwise, the PHS356A beam was able to reach its yield moment capacity. The RHS356A beam is a Class 4 section and was thus expected to prematurely buckle before the onset of yielding [4]. On the other hand, the PHS356A beam, through the provision of bends in its flanges, was able to avoid the premature local buckling failure. The beam was able to attain its full cross-sectional capacity, and failure occurred only after yielding.

Figures 8, 9, 10, 11, 12 and 13 show the strain measurements along the length of the PHS356A and RHS356A beams recorded using the fibre optic cable sensors. The strains were measured along the web of each beam on the compression side and tension side. For each PHS356A and RHS356A beam, two different load stages are presented to capture the strain development with the increase in loading; 100 kN (20% of $M_y$) and 300 kN (59% of $M_y$). For the PHS356A beam only, two additional load stages are shown; 500 kN (99% of $M_y$) and 600 kN (119% of $M_y$). The PHS356A beam was able to reach its yield moment capacity, and the purpose of the additional load stages is to show the strain distributions at yield and just after yielding.
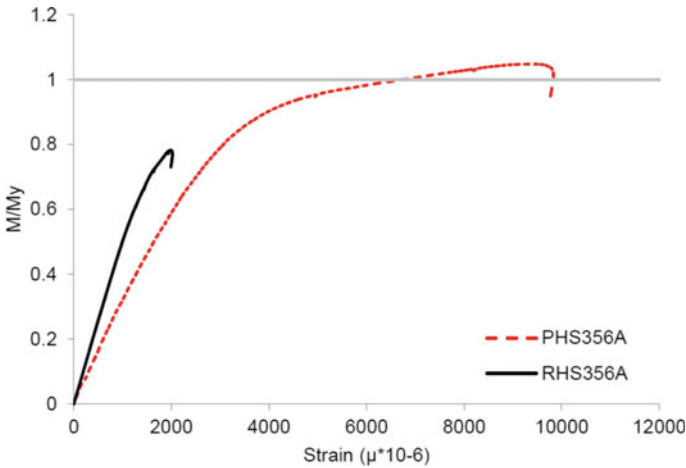
**Fig. 7** Normalized moment-strain curves at the mid-spans of the PHS356A and RHS356A beams

In Fig. 8a, strains measured using from the fibre optic cable sensors are compared with those recorded using strain gauge sensors at the top and bottom center of the PHS356A beam. The strains are in good agreement which shows that measurements from fibre optic cable sensors are comparable with existing measurement techniques.

Figures 8b and 9 show the strain measurements along the length of the PHS356A and RHS356A beams at 100 kN—within the linear range of each beam. The strain measurements of both beams are in good agreement with the theoretical strains, with the tensile strains in the central bending region of the beams more or less uniform, typical of steel in the linear range before yielding. Furthermore, for both beams, the fibre optic cable sensors reasonably capture the strain profile along the length of each beam and show the sudden increase in strain at the support and loading points due to the concentrated compressive loads at those locations. This is not possible with strain gauge sensors, as indicated by Fig. 7. The strain gauge sensor can only capture strain at a discrete location.

Figures 10 and 11 show the strain measurements along the length of the PHS356A and RHS356A beams at 300 kN. The strain measurements of both beams are still in good agreement with the theoretical strains. However, on the compression side at the loading and on the tension side at the support points, the difference between the measured strains and theoretical strains for the RHS356A beam (Fig. 11) is greatly higher than that of the PHS356A beam (Fig. 10). For example, at the loading points, the theoretical and recorded strains differ by 50% for the PHS356A beam, while they differ by 81% for the RHS356A beam. This is because the high concentrated loads at the loading points cause the web of the of the RHS356A beam to buckle outward, creating a region of high tension and low compression, which is captured by the fibre optic cable sensors, Fig. 11. For the PHS356A beam, the bends in its flanges are able to minimize the premature local buckling failure and as such the strain differences at the loading and support locations are not as high, Fig. 10. As such, the initiation
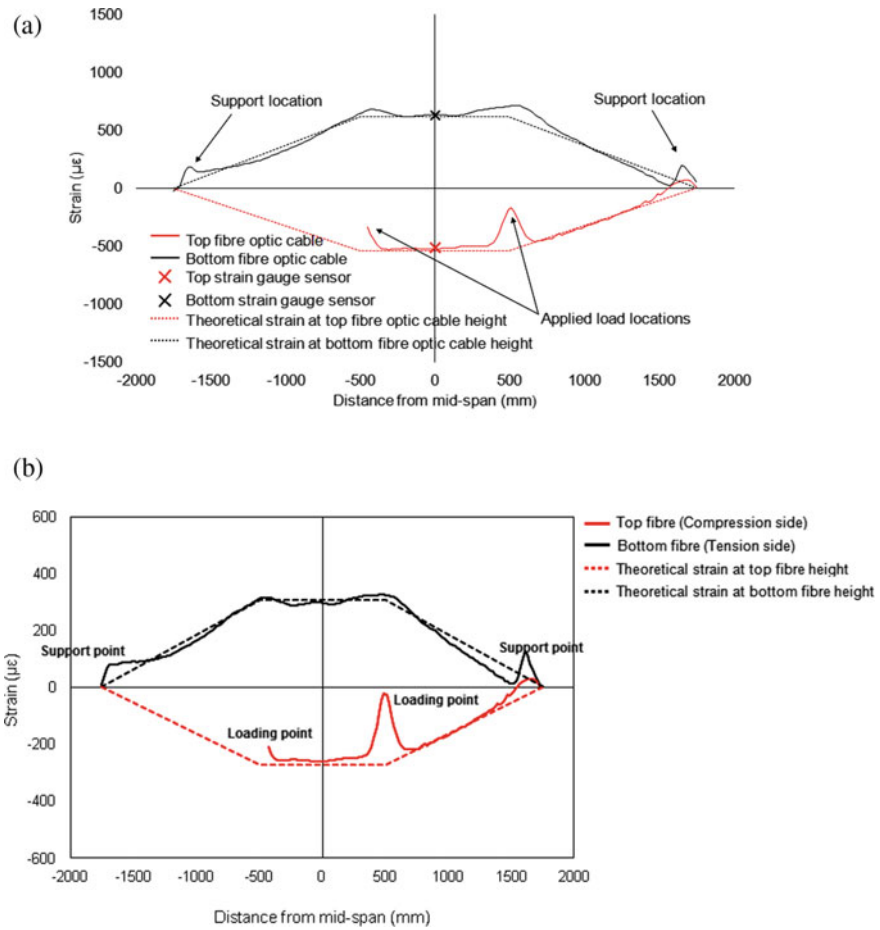
**Fig. 8 a** Measurement of strain along a beam using fibre optic cable and strain gauge sensors. **b** Strain measurements along the length of the PHS356A beam at 100 kN

of local buckling at the loading and support points happens sooner in the RHS356A beam than the PHS356A beam.

Figures 12 and 13 further show that at the loading and support points for the PHS356A beam, even at higher loads of 500 and 600 kN, the measured strains are not drastically higher than the theoretical strains. As previously mentioned, this is because the bends in the compression flange of the PHS356A beam help minimize web crippling and ovalization in the beam's cross-section [14]. This reduces the potential of local buckling at the loading and support points before yielding, and the PHS356A beam is thus able to minimize the increase in compressive strains unlike the RHS356A beam. This fibre optic cable observation offers an explanation as to why, in comparison with RHS beams, the PHS beams are able to attain their full cross-section capacity and reach their expected moment yield capacity. This observation would
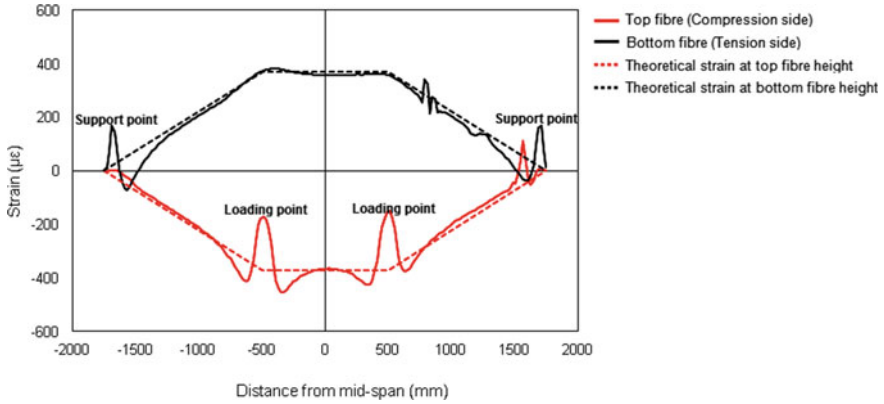
**Fig. 9** Strain measurements along the length of the RHS356A beam at 100 kN
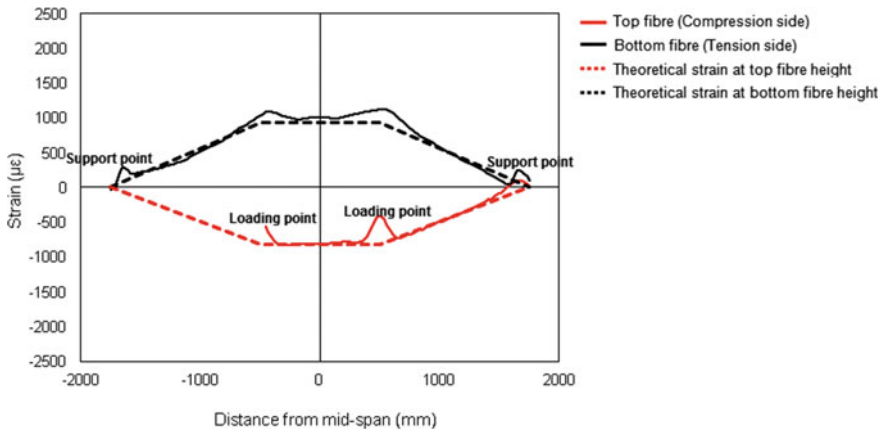


**Fig. 10** Strain measurements along the length of the PHS356A beam at 300 kN

not have been possible with only strain gauges sensors installed on the PHS and RHS beams. In Fig. 12, the bottom fibre strain readings show a significant difference in the measured strains compared with the theoretical strains. This difference is caused by nonlinear effects as at about 500 kN, though local buckling has not occurred yet, the PHS356 beam starts to yield in bending.

Following completion of the four-point bending tests, additional PHS and RHS beams were tested in a three-point bending scenario. For these tests, a total of four beams with short span ($L$) to depth ($h$) ratios ($L/h \leq 3$), in order to induce high concentrated loads at failure, were tested. The beams were fabricated from the PHS305, PHS356, RHS305 and RHS356 sections, Table 1. The PHS beams were labeled as PHS305B ($L = 1230$ mm) and PHS356B ($L = 1140$ mm). The RHS beams were labeled as RHS305B ($L = 1230$ mm) and RHS356B ($L = 1140$ mm).
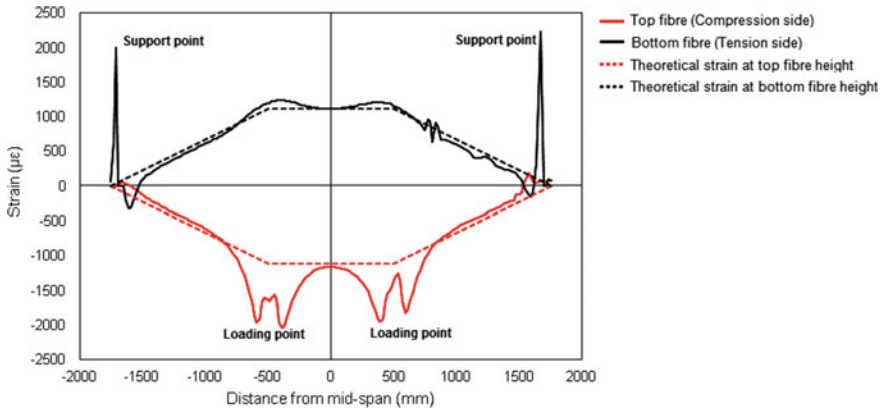
**Fig. 11** Strain measurements along the length of the RHS356A beam at 300 kN
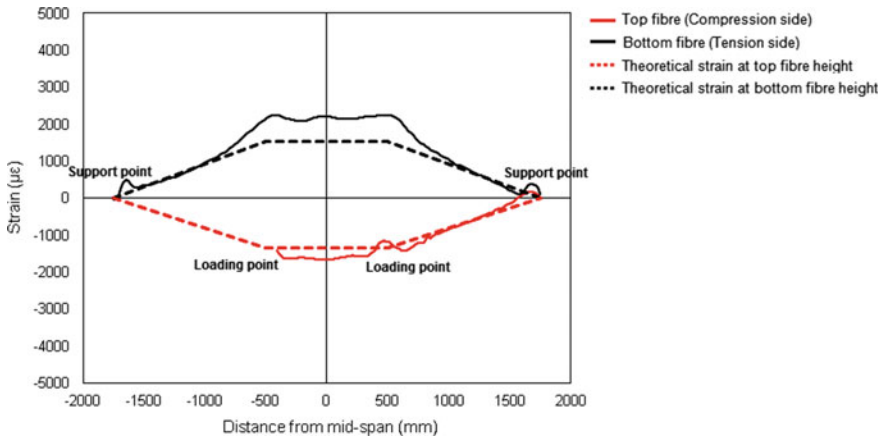


**Fig. 12** Strain measurements along the length of the PHS356A beam at 500 kN

The general view of the symmetrical, simply supported three-point bending tests is shown in Fig. 15 and the test setup is described in [9]. Each beam was fitted with steel end caps and the simple support conditions were achieved by means of a steel roller between the beam and a profiled stiffening plate at each end support, Fig. 14. Electrical strain gauges were attached to the web and flange of each beam to measure the change in strain. This was done at the center and at 100 mm from either side of the loading point of each beam, Fig. 14. The tests were displacement controlled at a rate of 1.0 mm/min and were completed using a 300 ton hydraulic jack cylinder.

Figure 16 shows the normalized moment-strain curves from the three-point beam bending tests. The normalized mid-span moments are plotted against strains which are recorded using a strain gauge at the center of the bottom flange of each beam,
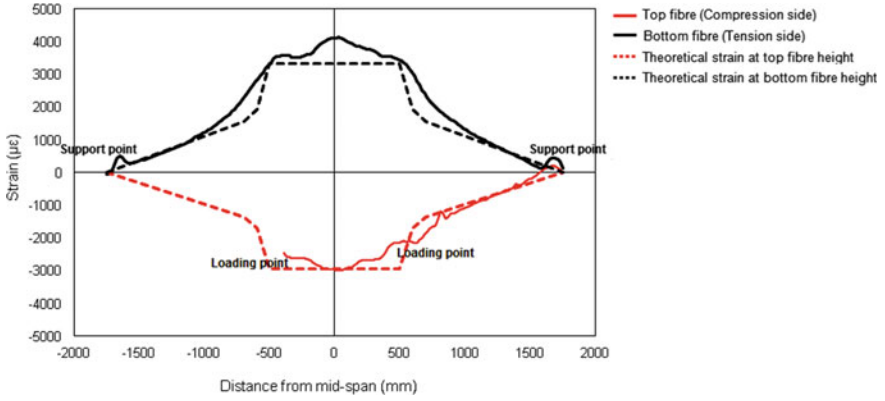
**Fig. 13** Strain measurements along the length of the PHS356A beam at 600 kN
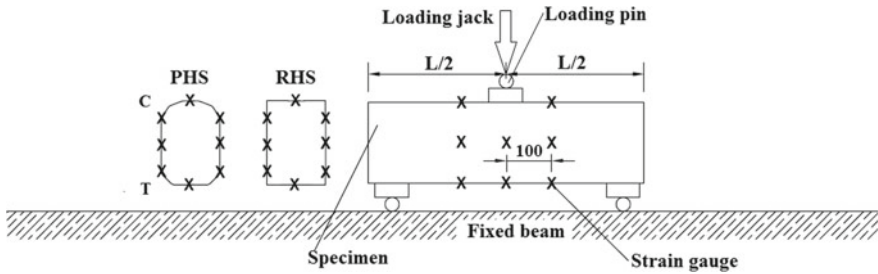


**Fig. 14** Illustration of the three-point bending test schematic



**Fig. 15** General view of the three-point bending test setup

**Fig. 16** Normalized moment-strain curves at the mid-spans of the PHS and RHS beams
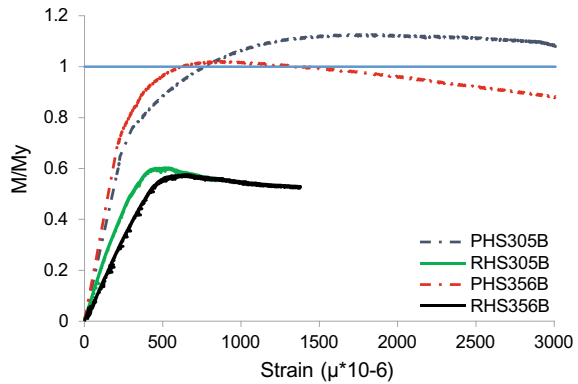


Fig. 14. For each section, the yield moment capacity $M_y$ was calculated by multiplying the measured yield stress from the tensile coupon tests and the corresponding section modulus.

In Fig. 16, the RHS305B and RHS356B beams failed at 42.5% and 40% below their yield moment capacities, respectively. Contrariwise, the PHS305B and PHS356B beams were able to reach their yield moment capacities.

Similar to the four-point bending tests, the RHS356B beam herein is a Class 4 section, and was thus expected to prematurely buckle before the onset of yielding [4]. On the contrary, the RHS305B beam is a Class 3 section and was therefore expected to buckle once its outer most fibres had yielded [4]. However, in the three-point bending test setup, the beam spans ($L$) were short compared with the depth ($h$) of the beams (i.e., $L/h \leq 3$), and as such had short moment arms. The short moment arms induced high concentrated loads at the loading points. These high concentrated loads caused local buckling of the slender compression flange and webs of the RHS sections, Fig. 17, and the premature failure before yielding.

In contrast, the PHS305B and PHS356B beams were able to avoid the premature local buckling failure, Fig. 18. The beams were able to attain their full cross-sectional capacity, despite the high concentrated loads. Failure occurred only after yielding. As previously mentioned, this is most likely due to the provision of bends in their flanges which minimize web crippling and ovalization in the beam's cross-section.

The three-point bending tests were conducted without the fibre optic cable sensors. Though the strain gauge data was able to give an indication that premature local buckling occurred in the RHS beams and did not occur in the PHS beams; the data does not provide any more information beyond that. On the other hand, fibre optic cable sensors would have been able to record the strain profile along the length of the beams. This strain profile, similar to the four-point bending tests, would have been able to provide more information at the loading and support points. With this information, a more definite conclusion regarding the premature local buckling of the beams can be made.

**Fig. 17** Deformed shape of the RHS 356 × 254 × 6.4 beam



**Fig. 18** Deformed shape of the PHS 356 × 254 × 6.4 beam

## 3  Conclusion

A series of four-point and three-point bending tests have been conducted on polygonal hollow section (PHS) and rectangular hollow section (RHS) beams to compare fibre optic cable sensors with strain gauge sensors. The sensors are used to detect the location and initiation of local buckling during the tests. In addition, the tests were used to compare the buckling strength and failure shapes of the PHS and RHS beams under concentrated loads. For the three-point bending tests, only strain gauges were

used to record the strain measurements, while for the four-point bending tests, both strain gauge and distributed fibre optic cable sensors were used.

The data showed that unlike strain gauge sensors, fibre optic cable sensors are able to capture the strain profile and varying strains along the length of a beam at different load stages. The recorded strain profiles were also in good agreement with the theoretical strain data. Additionally, the data showed that the fibre optic cables have the capability to detect the location and initiation of local buckling without prior knowledge of the area of interest. This is the criterion that differentiates fibre optic cable sensors from strain gauge sensors and the main reason why fibre optic cable sensors should be more widely used in monitoring and measuring strain in steel structures, especially now that costs are less.

The results also showed that for four-point bending tests, the RHS beams failed prematurely below their moment yield capacity. This can be attributed to local buckling of the compression flange initiated by the large applied concentrated loads at the loading points. In contrast, the PHS beams reached their yield moment capacity before local buckling and final failure occurred. This was further evidenced by the three-point bending tests which showed that at the loading points, unlike the RHS beams which experienced an increase in the compressive strains, the PHS beams were able to minimize this increase. Though more tests are required for a definite conclusion, this is most likely because the bends of the PHS beam help prevent web crippling and ovalization of the beam's cross-section.

# References

1. AISI S100-2007—North American specification for the design of cold-formed steel structural members 2007 edition
2. ASTM (2009) Standard test methods and definitions for mechanical testing of steel products, ASTM A370-09a. American Society for Testing and Materials, West Conshohocken, PA, USA
3. ASTM (2013) Standard specification for cold-formed welded and seamless carbon steel structural tubing in rounds and shapes, ASTM A500/A500M-13. American Society for Testing and Materials, West Conshohocken, PA, USA
4. CSA C (2019) CSA-S16-19. Design of steel structures. Canadian Standards Association, Toronto, ON, Canada
5. Davison TA, Birkemoe PC (1983) Column behaviour of cold-formed hollow structural steel shapes. Can J Civ Eng 10(1):125–141
6. Gardner L, Ministro A (2004) Testing and numerical modelling of structural steel elliptical and oval hollow sections. Department of Civil and Environmental Engineering, Imperial College of London, 04-002-ST

7. Hoult NA, Ekim O, Regier R (2014) Damage/deterioration detection for steel structures using distributed fiber optic strain sensors. J Eng Mech 140:04014097
8. Kabanda JS, MacDougall C (2016) STR-959: optimization of a polygonal hollow structural steel section in the elastic region
9. Kabanda JS, MacDougall C (2017) Comparison of the moment rotation capacities of rectangular and polygonal hollow sections. J Constr Steel Res 137:66–76
10. Kersey AD (1996) A review of recent developments in fiber optic sensor technology. Opt Fiber Technol 2(3):291–317
11. Key PW, Hasan SW, Hancock GJ (1988) Column behavior of cold-formed hollow sections. J Struct Eng 114(2):390–407
12. Song J, Chen Y, Lu G (2012) Axial crushing of thin-walled structures with origami patterns. Thin-Walled Struct 54:65–71
13. Yamashita M, Gotoh M, Sawairi Y (2003) Axial crush of hollow cylindrical structures with various polygonal cross-sections: numerical simulation and experiment. J Mater Process Technol 140(1):59–64
14. Young B (2005) Local buckling and shift of effective centroid of cold-formed steel columns. Steel Compos Struct 5(2–3):235–246
15. Ziemian RD (ed) (2010) Guide to stability design criteria for metal structures. Wiley

# Structural Specialty: Concrete Structures

# Image-Based Microstructural Finite Element Model of Concrete Subjected to Freeze–Thaw Cycles

**Mustafa Alhusain and Adil Al-Mayah**

**Abstract** Sample-specific image-based three-dimensional (3D) microstructural finite element (FE) models of the freeze–thaw damage of cylindrical concrete samples were developed. Each model consists of image-based aggregates, cement mortar, and air voids that were constructed using high-resolution micro-computed tomography (μCT) images. The voids were later filled with water that was subjected to freezing temperatures. The applied material properties and contact conditions were adopted from the literature, and the two modeled concrete elements were subjected to 40 freeze–thaw cycles under temperatures of 0 and $-22$ °C. The frost-induced stress distribution, volume loss, and damage propagation were analyzed to investigate the severity and mechanisms of the freeze–thaw damage. The volume loss and damage progression were compared well with the experimental results.

**Keywords** Concrete · Finite element model · Freeze–thaw · Micro-computed tomography

## 1 Introduction

Concrete structures frequently exposed to sub-zero temperatures are susceptible to frost damage, mostly because of the freezing and expansion of the water entrained within the concrete capillaries [5, 7]. Also, the significant fluctuation between the cold (e.g., $-20$ °C) and warm (e.g., 20 °C) temperatures can induce thermal stress

M. Alhusain (✉) · A. Al-Mayah
Mechanical and Mechatronics Engineering, University of Waterloo, Waterloo, Canada
e-mail: malhusain@kfu.edu.sa; malhusain@uwaterloo.ca

A. Al-Mayah
Civil and Environmental Engineering, University of Waterloo, Waterloo, Canada

M. Alhusain
Mechanical Engineering, College of Engineering, King Faisal University, Al-Hofuf, Al-Ahsa, Saudi Arabia

within the mortar-aggregate interfacial zone due to the varying thermal expansion coefficients of the two materials [12].

The frost damage occurs when the tensile stress induced by the expanding ice exceeds the tensile strength of concrete [24]. The freeze–thaw damage typically initiates at the concrete's external surface due to its direct exposure to the cold environment and lack of confinement, resulting in layer-by-layer scaling damage propagating inward [10], as illustrated in Fig. 1. The frost-induced cracks tend to extend along the interfacial zone between the mortar and aggregates due to its low strength, making it more vulnerable to stress concentration [17]. In addition to causing mass loss and strength reduction, the frost damage of concrete considerably increases its permeability, degrading its resistance to all forms of environmental damage. Thus, the rate of frost damage increases exponentially as concrete is subjected to more freeze–thaw cycles [13].
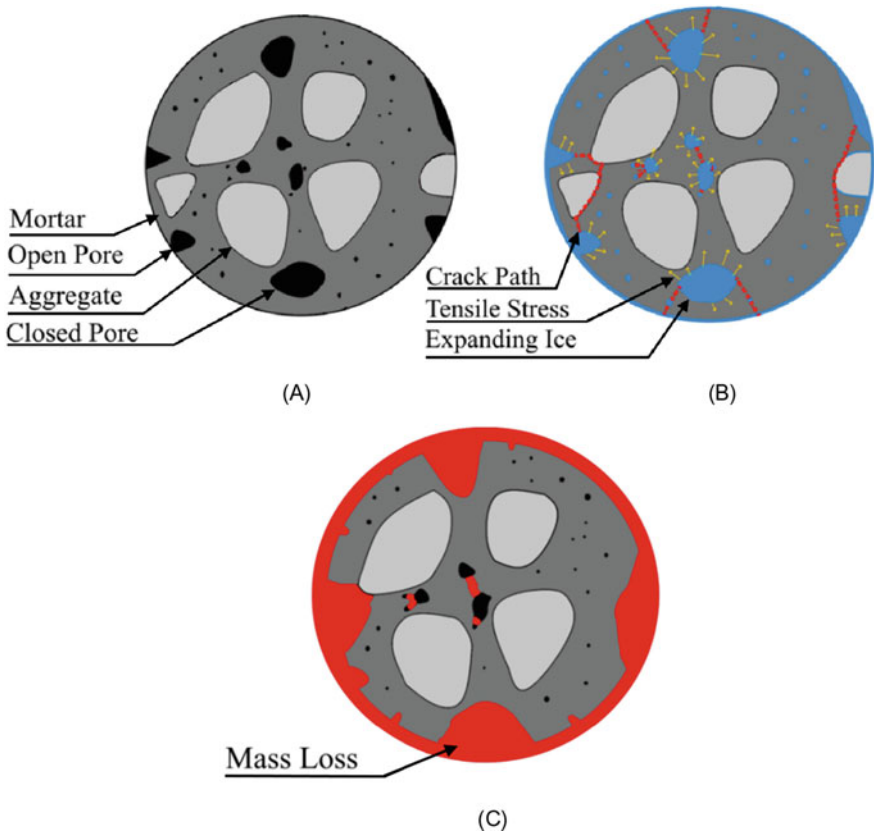


**Fig. 1** Concrete **a** Before wetting, **b** After wetting and frosting, and **c** After frost damage [3]

Extensive research has investigated the frost damage of concrete through experimental testing and finite element (FE) modeling. Experimental testing of the freeze–thaw damage is crucial for examining its severity and mechanisms under different environments and testing conditions; however, it is time-consuming and provides no details on the stress distribution within concrete. Hence, different types of FE models were developed, including solid macroscale [27], mesostructure [4, 16], and microstructure models [6, 15]. Solid macroscale FE models treat concrete as a single homogenous material, ignoring the mechanical interaction between its cement mortar and aggregates. In contrast, mesostructure and microstructure FE models treat concrete as a composite material by modeling its mortar and aggregates with the appropriate contact conditions. The prime difference between mesostructure and microstructure FE models is the process of constructing the 3D models of the aggregates, air voids, and cement mortar. The three-dimensional elements of mesostructured FE models are generated mathematically, whereas the image-based elements of microstructure FE models are created by stacking 2D images of an actual concrete, normally captured using micro-computed tomography ($\mu$CT). Thus, microstructure FE models provide the most realistic representations of the frost damage within concrete, making it an excellent tool for investigating the micro-scale freeze–thaw damage of actual concrete elements in a timely and efficient manner by minimizing the need for applying lengthy frost cycles and expensive CT scans.

The paper's prime objective is to develop a realistic microstructural finite element model to simulate the frost damage, within two actual concrete specimens that were imaged using a high-resolution micro-computed tomography. The severity of freeze–thaw damage was investigated using the concrete's volume loss data, and the damage progression was monitored throughout the applied frost cycles. The severity and progression of the freeze–thaw damage were compared with the experimental results to examine the accuracy of the FE model, and the observed agreement was discussed.

## 2 Finite Element (FE) Model

### 2.1 General

Image-based three-dimensional reconstruction of actual concrete specimens is the first step of developing the microstructural finite element model. A high-resolution micro-computed tomography ($\mu$CT) imaging system, shown in Fig. 2a, was employed to scan two concrete specimens of the same composition with a diameter of 14 mm and a height of about 40 mm. The samples were made using water/cement, sand/cement, and aggregate/cement ratios of 0.5, 1, and 1.5, respectively, after which the specimens were cured for 28 days. It is worth noting that only the 36 mm midsection, illustrated in Fig. 2b, was analyzed and modeled to minimize inconsistencies caused by the non-uniform top and bottom surfaces. The collected CT images were filtered to reduce scanning artifacts and stacked into 3D elements, as

demonstrated in Fig. 2c, after which the images were segmented through thresholding to separate the aggregates from the cement mortar. Also, void detection analysis was conducted to capture the micro-scale air voids, which were later modeled as ice. Three-dimensional mesh elements of the aggregates, voids, and mortar were generated, cleaned, and converted into solid 3D models, as shown in Fig. 3. The mechanical properties, contact conditions, and applied freeze–thaw cycles are discussed in the following sections.



(A)                                                                                                                     (B)



(C)
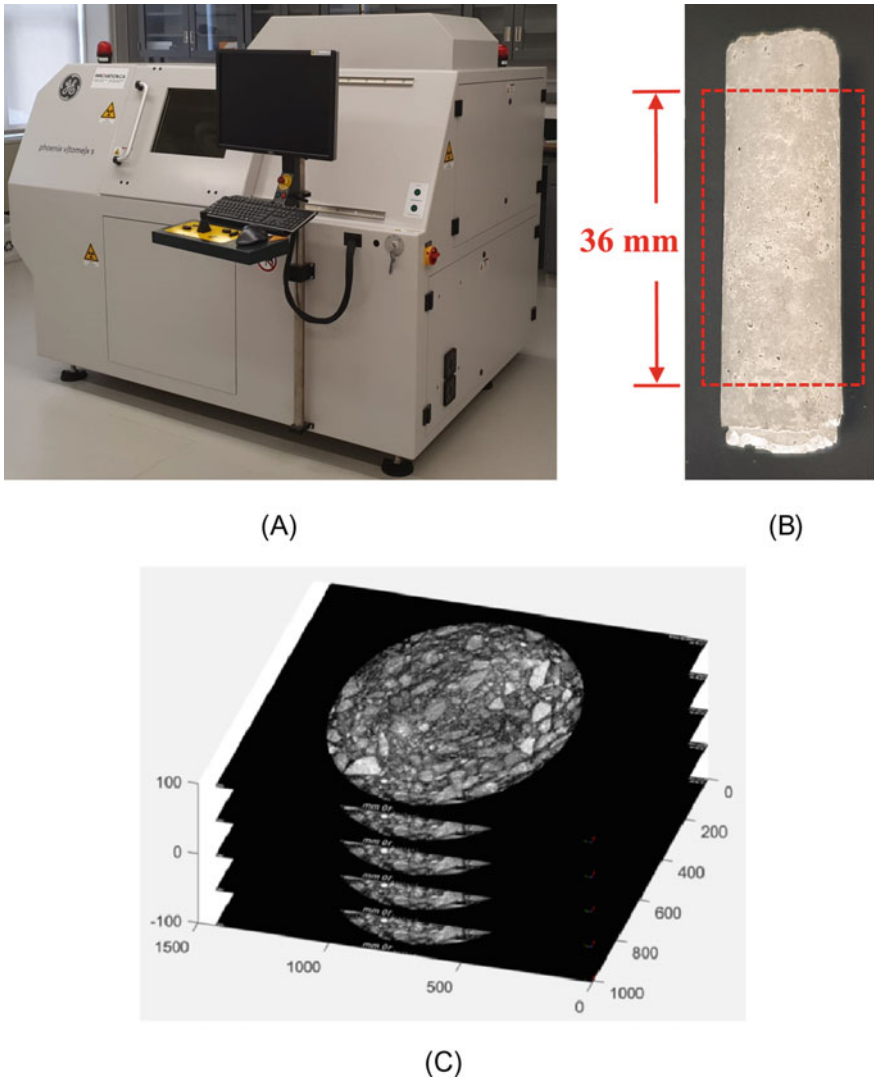
**Fig. 2** **a** μCT imaging system, **b** Analyzed segment of the specimens, and **c** Stacked CT images [2]
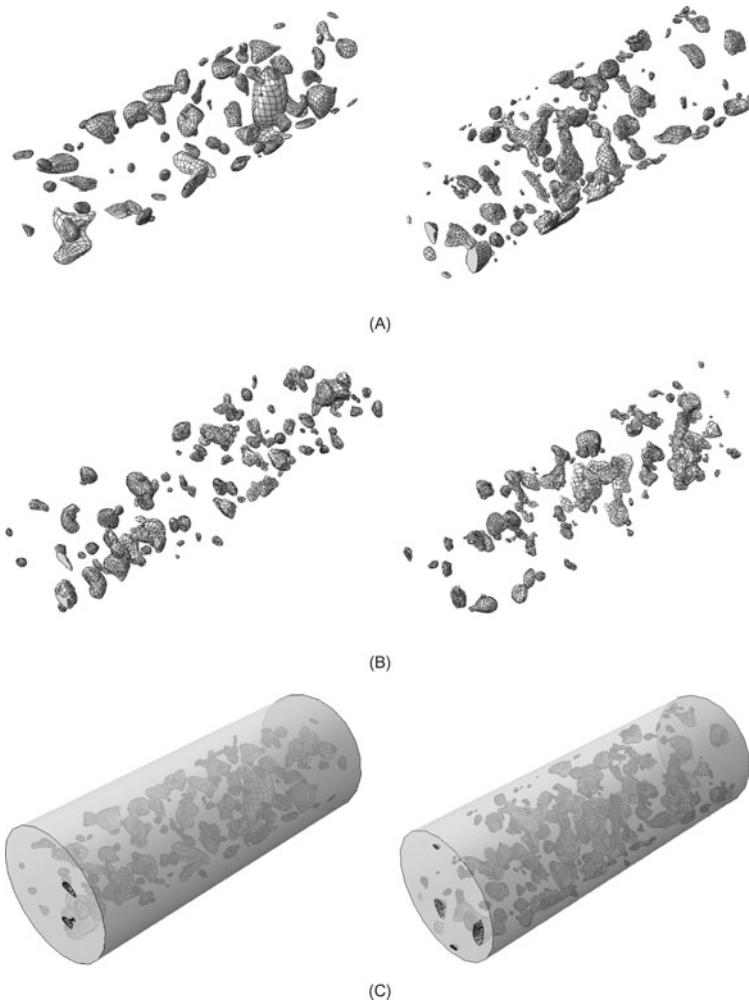
**Fig. 3** 3D models of **a** Aggregates, **b** Ice (voids), and **c** Cement mortar of specimens 1 (left) and 2 (right)

## 2.2 Material Properties

The mechanical properties of the expanding ice are temperature-dependent. The modulus of elasticity, thermal expansion coefficient, density, and Poisson's ratio of the ice are plotted in Fig. 4. In contrast, it is assumed at this stage of the FE modeling that the mechanical properties of mortar and aggregates are temperature-independent; thus, the mechanical properties at room temperature were used throughout the freeze–thaw cycles, as listed in Table 1. Also, the high-strength aggregates normally experience little to no frost damage; hence, the aggregates were modeled as an elastic
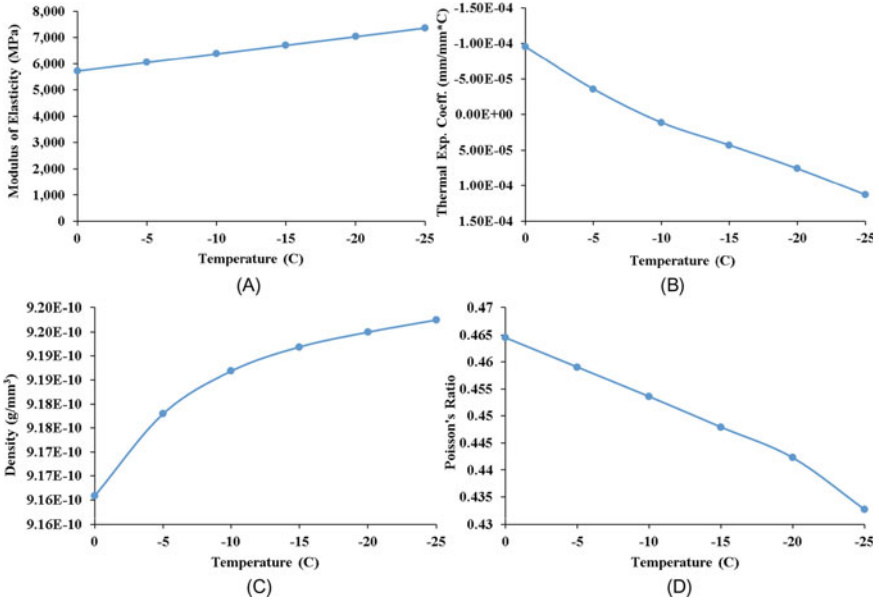
**Fig. 4** **a** Modulus of elasticity, **b** Thermal expansion coefficient, **c** Density, and **d** Poisson's ratio of ice at different freezing temperatures. Recreated from [9, 19, 20, 23]

material with a modulus of elasticity, density, and Poisson's ratio of 47.00 MPa, 2680 kg/m$^3$, and 0.2, respectively. On the other hand, the cement mortar has compressive strength, tensile strength, density, and Poisson's ratio of 25.28 MPa, 3.2 MPa, 2022 kg/m$^3$, and 0.3, respectively. The mortar's modulus of elasticity and shear strength of 23,797.1 MPa and 0.553 MPa were calculated as recommended by ACI 318 (2014). Also, the freeze–thaw damage within the mortar was investigated via the concrete damage plasticity (CDP) model, using the default parameters listed in Table 2. The CDP model utilized the mortar's compressive and tensile stress–strain curves, shown in Fig. 5, which were plotted using the equations of Saenz [22] and Desay and Krishnan [11], respectively.

## 2.3 Contact Conditions

The contact properties of the mortar-aggregate, mortar-ice, and aggregate-ice interfaces are listed in Table 3. The cement mortar's tensile and shear strengths of 3.2 MPa and 0.554 MPa, respectively, were utilized to model the adhesive contact between the mortar and the aggregates. Also, a friction-based slide condition with a friction coefficient of 0.6 was used in the mortar-aggregate interface. On the other hand, a frictionless slide condition was applied in the mortar-ice and aggregate-ice interfaces.

**Table 1** Mechanical properties of cement mortar and aggregates

| Property | Cement mortar[a] | Aggregates[b] |
|---|---|---|
| Compressive strength (MPa) | 25.28 | – |
| Tensile strength (MPa) | 3.2 | – |
| Shear strength (MPa) | 0.553 | – |
| Modulus of elasticity (MPa) | 23,797.1 | 47,200 |
| Density (kg/m$^3$) | 2022 | 2680 |
| Poisson's ratio | 0.3 | 0.2 |

[a] *Sources* Aho and Ndububa [1, 25] and Narayan Swamy [14]
[b] *Sources* Skarżyński et al. [21] and Qiu et al. [18]

**Table 2** Parameters of concrete damage plasticity model

| Dilation angle | Eccentricity | Stress ratio | Shape factor | Viscosity parameter |
|---|---|---|---|---|
| 45 | 0.1 | 1.16 | 0.667 | 0.0005 |
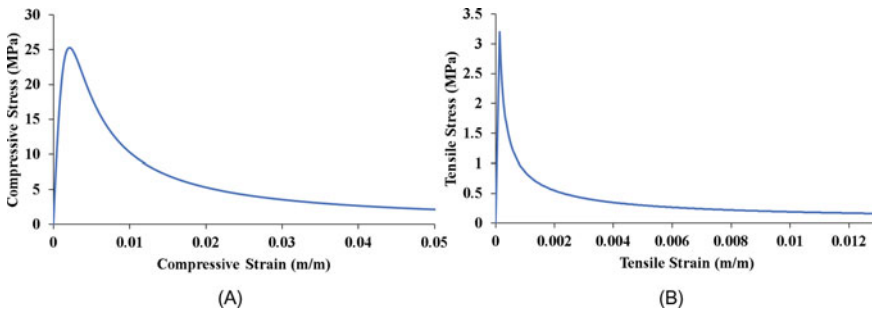


**Fig. 5** **a** Compressive and **b** Tensile stress–strain curves of cement mortar

**Table 3** Contact conditions of the mortar-aggregate, mortar-steel, and aggregate-steel interfaces

| Interface | Adhesive condition[a] | Friction condition[b] |
|---|---|---|
| Mortar-aggregate | Tensile strength = 3.2 MPa<br>Shear strength = 0.554 MPa | Friction coef. = 0.6 |
| Mortar-ice | – | Frictionless |
| Aggregate-ice | – | Frictionless |

[a] *Sources* Yao et al. [25]
[b] *Sources* Yao et al. [26] and Fisher and Kloiber [8]
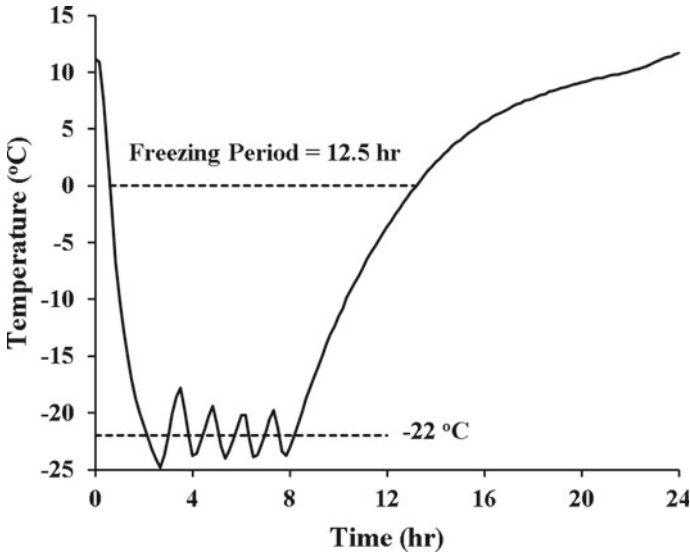
**Fig. 6** Controlled environment temperature of a single freeze–thaw cycle [3]

## 2.4 Freeze–Thaw Cycles

Two actual concrete specimens were subjected to 40 freeze–thaw cycles, each of which had a controlled environment temperature ranging from 11 to − 25 °C, as shown in Fig. 6. The lowest temperature fluctuated around an average temperature of − 22 °C, which is considered the lowest ice temperature. Also, since the frost damage is caused mostly by ice expansion, it is possible to simulate the freeze–thaw damage by modeling only the freezing period of the cycles, significantly decreasing the required computational time. Thus, the temperature of the simulated freeze–thaw cycles fluctuated between 0 and − 22 °C, as illustrated in Fig. 7.

## 3   Results

## 3.1   General

The stress distribution within concrete was studied. It was observed that the stress was concentrated mostly around the expanding ice and within the mortar-aggregate interface. As more cycles were applied, minor cracking occurred around the expanding ice, locally relieving the stress and altering the stress distribution within the concrete element. Also, the severity of frost damage was investigated by analyzing the volume loss of concrete. A good agreement was observed between the volume loss of the FE
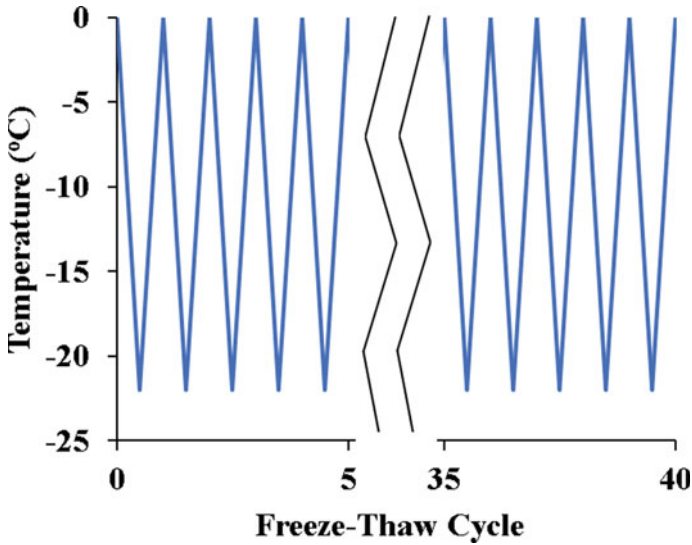
**Fig. 7** Temperature of the applied freeze–thaw cycles

model and the experimental CT imaging data. In terms of the damage progression, it was noted that the frost damage within the actual concrete specimens was not visually detectable, as shown in Fig. 8. Thus, the damage progression of the FE model was compared with the frost-induced pore expansion of the concrete's internal pore structure, and the observed agreement was discussed.

## 3.2 Stress Distribution

The distribution of the von Mises stress within the concrete specimen #1 was analyzed after applying 5, 20, and 40 freeze–thaw cycles, as illustrated in Fig. 9. It was observed after applying five cycles that the stress around the expanding ice was mostly uniform. After applying 20 cycles, the concrete element experienced minor cracking nearby the ice, which partially relieved the surrounding high stress, making it less uniform. It is worth noting that the frost-induced cracks at cycle 20 relieved the high stress at the top and bottom surfaces of concrete, shifting the stress to its side surface, as shown in Fig. 9c. Also, it was noted that subjecting concrete to 20 cycles propagated the stress toward the nearby aggregates, increasing the likelihood of stress concentration within the mortar-aggregate interfacial zone. Exposure to 40 freeze–thaw cycles produced more cracks within the cement mortar, making the stress distribution more localized, as demonstrated in Fig. 9d.

(A)



(B)
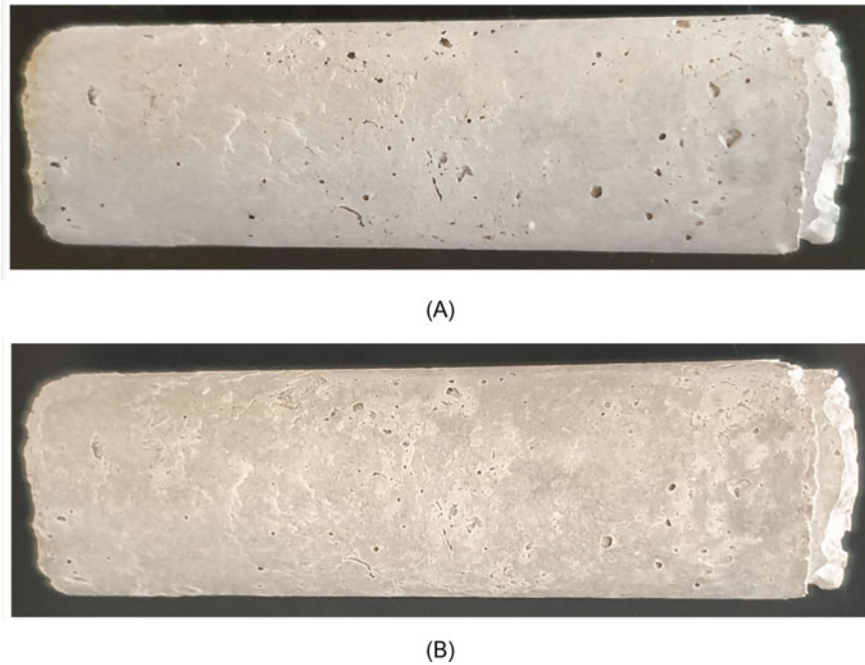
**Fig. 8** Concrete specimen #1 **a** Before and **b** After 40 freeze–thaw cycles

## 3.3 Severity of Concrete Damage

The severity of the simulated frost damage of specimens 1 and 2 was investigated by computing the volume loss of concrete, as demonstrated in Fig. 10. Also, the actual volume loss of the two samples at cycle 40 was measured using the experimental CT imaging data, which was plotted as a polynomial curve. It was observed that the actual volume losses of samples 1 and 2 after 40 freeze–thaw cycles were 5.70 mm$^3$ and 12.99 mm$^3$, respectively, whereas the simulated volume losses of the two specimens were 5.93 mm$^3$ and 12.06 mm$^3$, corresponding to percent errors of 3.96% and 7.21%, respectively. Thus, the developed FE model accurately predicted the frost damage of the two samples even though the volume loss of specimen 2 was over twice that of specimen 1. Also, the simulated volume loss grew exponentially, matching the observations reported by Li et al. [13]. In conclusion, the microstructural FE model successfully utilized the micro-scale configurations of the aggregates and ice (voids) to assess the concrete's frost damage accurately, illustrating its potential for investigating the freeze–thaw damage of concrete.
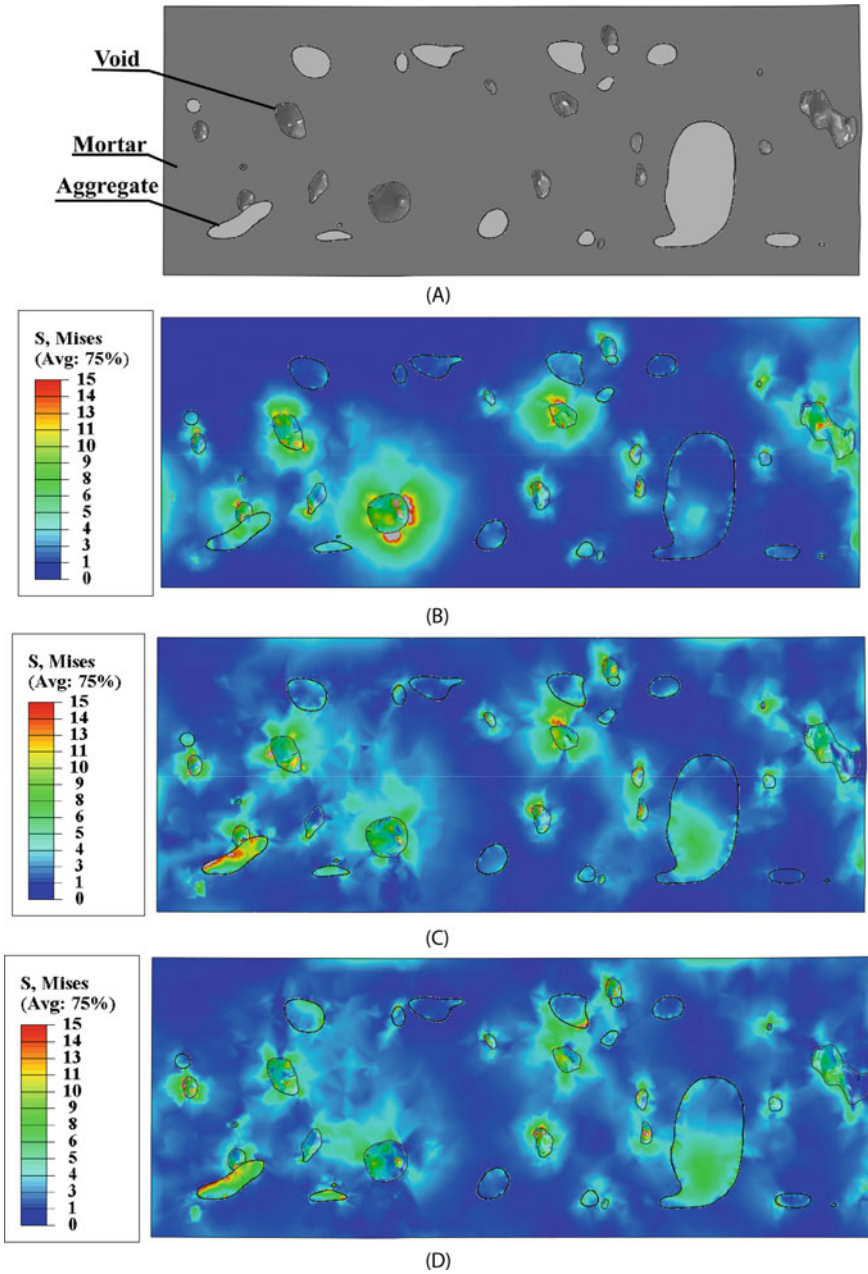
**Fig. 9** von Mises stress distribution within the concrete specimen #1 **a** Before and after **b** 5, **c** 20, and **d** 40 freeze–thaw cycles
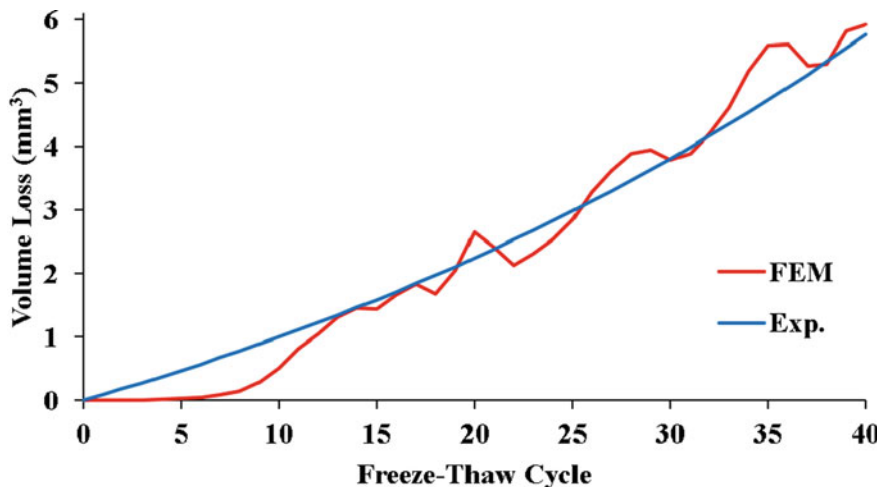
(A)
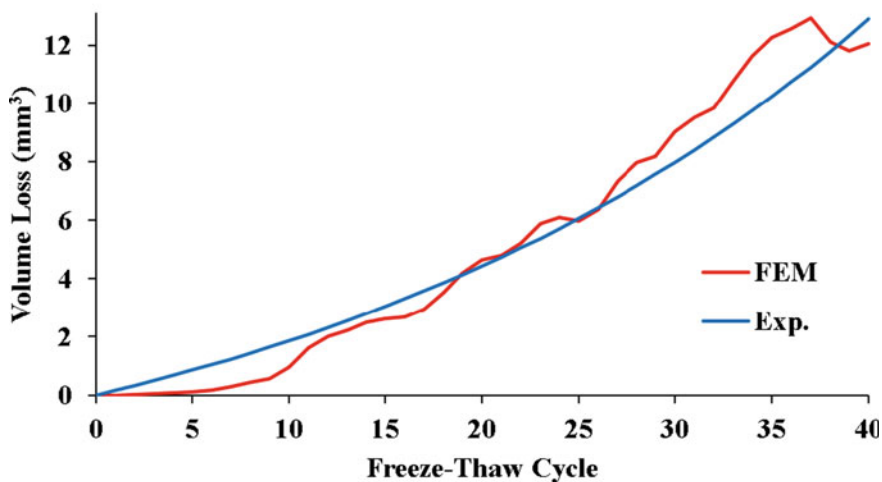


(B)

**Fig. 10** Volume loss of **a** Specimen #1, and **b** Specimen #2 after 40 freeze–thaw cycles

## 3.4 Damage Progression

The progression of the simulated frost damage of specimen #1 was studied after applying 5, 20, and 40 cycles, as illustrated in Fig. 11. It was noted that cracks initiated in the top and bottom surfaces of concrete, which relieved the stress within these surfaces, as discussed in the previous section. As more freeze–thaw cycles were
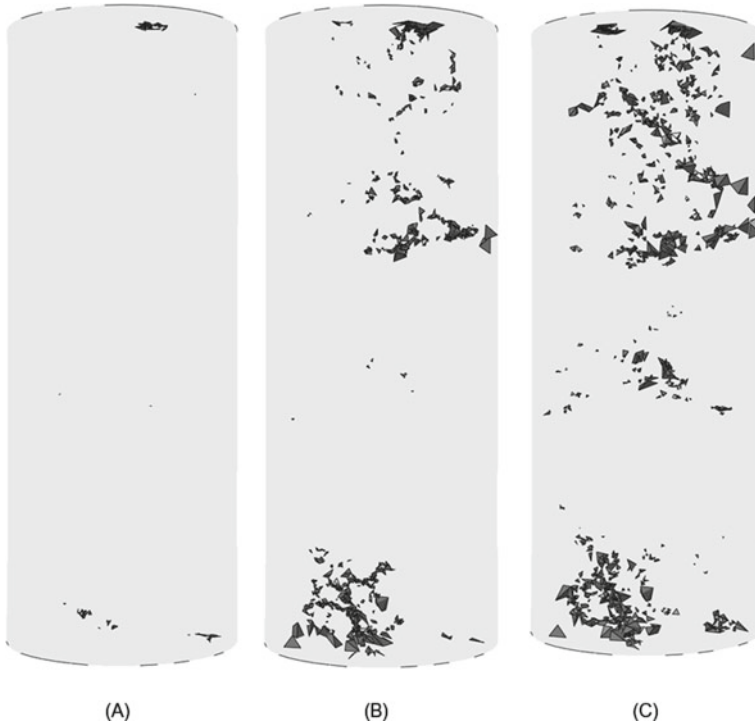
**Fig. 11** Freeze–thaw damage of the modeled concrete after **a** 5, **b** 20, and **c** 40 freeze–thaw cycles

applied, the concrete damage propagated from the top and bottom surfaces to the center of the concrete element.

The accuracy of the simulated frost damage was examined by comparing the concrete damage of the FE model with the expansion of the concrete's internal pore structures, shown in Fig. 12a and b. It was observed that exposure to 40 freeze–thaw cycles produced mostly internal pore expansion, which seems similar to the FE model's frost damage, as indicated by the red and yellow highlights. Based on these results, it appears that the microstructure FE model accurately anticipated the locations of frost damage within the concrete element. However, further investigation is required to determine the accuracy of the simulated mechanisms of frost damage.
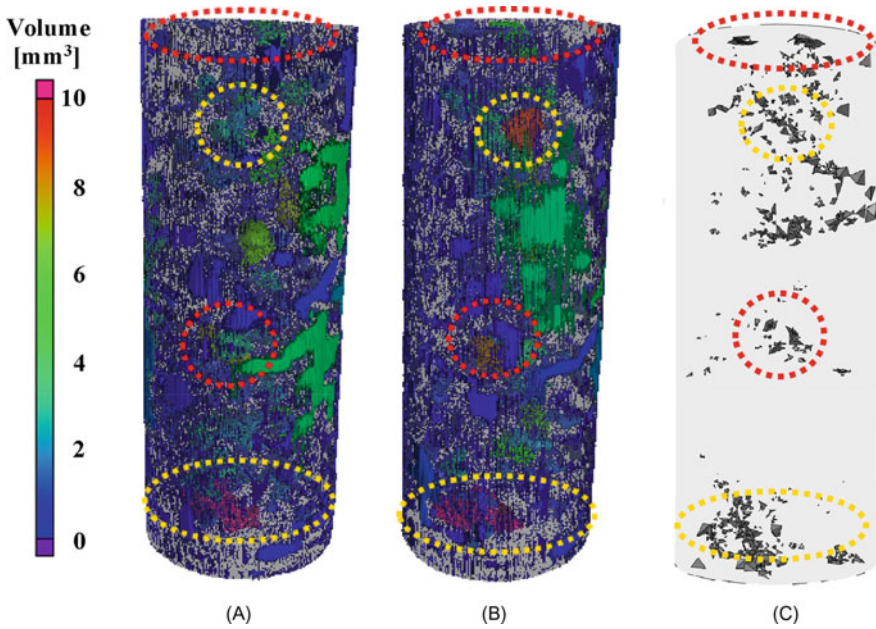
**Fig. 12** Internal pore structures of specimen #1 **a** Before and **b** After 40 freeze–thaw cycles, and **c** Frost damage of the FE model

## 4 Conclusion

An image-based microstructural finite element (FE) model of concrete freeze–thaw damage was developed and tested. The frost-induced stress distribution within the concrete element was examined, and the severity and progression of the freeze–thaw damage were analyzed and compared with the experimental results. Based on the results, the following points were concluded.

- The developed micro-scale FE model accurately anticipated the severity of the frost damage of two actual concrete specimens, as indicated by the volume loss data.
- In the early stages of freeze–thaw damage, the frost-induced stress within concrete was uniformly surrounding the expanding ice. However, further exposure to frost cycles produced minor cracks, which locally relieved the high stress and altered the stress distribution.
- The stress within the mortar-aggregate interfacial zone increased as more cycles were applied, potentially leading to more severe stress concentration and interfacial cracking.

# References

1. Aho IM, Ndububa EE (2015) Compressive and flexural strength of cement mortar stabilized with raffia palm fruit peel (RPEP). Glob J Eng Res 14(1):1–7. https://doi.org/10.4314/gjer.v14i1.1
2. Alhusain M, Al-Mayah A (2021) Three dimensional imaging of reinforcement corrosion using micro-computed tomography: literature review. Constr Build Mater 284:122813. https://doi.org/10.1016/j.conbuildmat.2021.122813
3. Alhusain M, Al-Mayah A (2022) Three-dimensional MCT imaging of pore morphology and freeze-thaw damage mechanisms of different concrete mixtures
4. Chen X, Yu A, Liu G, Chen P, Liang Q (2020) A multi-phase mesoscopic simulation model for the diffusion of chloride in concrete under freeze-thaw cycles. Constr Build Mater 265:120223. https://doi.org/10.1016/j.conbuildmat.2020.120223
5. Deng X, Gao X, Wang R, Gao M, Yan X, Cao W, Liu J (2021) Investigation of microstructural damage in air-entrained recycled concrete under a freeze-thaw environment. Constr Build Mater 268:121219. https://doi.org/10.1016/j.conbuildmat.2020.121219
6. Dong Y, Qiao P (2021) CT image-based synthetic mesostructure generation for multiscale fracture analysis of concrete. Constr Build Mater 296:123582. https://doi.org/10.1016/j.conbuildmat.2021.123582
7. Eriksson D, Wahlbom D, Malm R, Fridh K (2021) Hygro-thermo-mechanical modeling of partially saturated air-entrained concrete containing dissolved salt and exposed to freeze-thaw cycles. Cem Concr Res 141:106314. https://doi.org/10.1016/j.cemconres.2020.106314
8. Fisher JM, Kloiber LA (2006) Steel design guide 1-base plate and anchor rod design. In: AISC, pp 801–806
9. Gold LW (1994) The elastic modulus of columnar-grain fresh-water ice. Ann Glaciol 19:13–18. https://doi.org/10.3189/1994AoG19-1-13-18
10. Yuan J, Liu Y, Li H, Zhang B (2014) Experimental investigation of the variation of concrete pores under the action of freeze-thaw cycles by using X-ray CT. Adv Mater Sci Eng 1–11. https://doi.org/10.1155/2014/571357
11. Kmiecik P, Kamiński M (2011) Modelling of reinforced concrete structures and composite structures with concrete strength degradation taken into consideration. Arch Civ Mech Eng 11(3):623–636. https://doi.org/10.1016/S1644-9665(12)60105-8
12. Lei B, Li W, Tang Z, Tam VWY, Sun Z (2018) Durability of recycled aggregate concrete under coupling mechanical loading and freeze-thaw cycle in salt-solution. Constr Build Mater 163:840–849. https://doi.org/10.1016/j.conbuildmat.2017.12.194
13. Li Y, Li Y, Guan Z, Ding Q (2018) Elastic modulus damage model of cement mortar under salt freezing circumstance based on X-ray CT scanning. Constr Build Mater 191:1201–1209. https://doi.org/10.1016/j.conbuildmat.2018.10.097
14. Narayan Swamy R (1971) Dynamic Poisson's ratio of portland cement paste, mortar and concrete. Cem Concr Res 1(5):559–583. https://doi.org/10.1016/0008-8846(71)90060-3
15. Pan T, Chen C, Yu Q (2017) Three-dimensional micromechanical modeling of concrete degradation under multiphysics fields. Compos Struct 175:7–18. https://doi.org/10.1016/j.compstruct.2017.05.008
16. Peng R-X, Qiu W-L, Teng F (2020) Three-dimensional meso-numerical simulation of heterogeneous concrete under freeze-thaw. Constr Build Mater 250:118573. https://doi.org/10.1016/j.conbuildmat.2020.118573

17. Qin X-c, Meng S-p, Cao D-f, Tu Y-m, Sabourova N, Grip N, Ohlsson U, Blanksvärd T, Sas G, Elfgren L (2016) Evaluation of freeze-thaw damage on concrete material and prestressed concrete specimens. Constr Build Mater 125:892–904. https://doi.org/10.1016/j.conbuildmat.2016.08.098

18. Qiu W, Fu S, Zhu J-h, Zeng C, Ye J (2022) Meso-scale modelling of the thermo-mechanical response for concrete with complex-shaped aggregates in early age. Constr Build Mater 323:126485. https://doi.org/10.1016/j.conbuildmat.2022.126485

19. Rhardane A, Sleiman SAH, Alam SY, Grondin F (2021) A quantitative assessment of the parameters involved in the freeze-thaw damage of cement-based materials through numerical modelling. Constr Build Mater 272:121838. https://doi.org/10.1016/j.conbuildmat.2020.121838

20. Sinha NK (1987) Effective Poisson's ratio of isotropic ice. In: Sixth international offshore mechanics and arctic engineering symposium, 01 Mar 1987, Houston, Texas, USA, vol 4. Collection/Collection: NRC Publications Archive/Archives des publications du CNRC, pp 189–195

21. Skarżyński Ł, Nitka M, Tejchman J (2015) Modelling of concrete fracture at aggregate level using FEM and DEM Based on X-ray MCT images of internal structure. Eng Fract Mech 147:13–35. https://doi.org/10.1016/j.engfracmech.2015.08.010

22. Tao Y, Chen JF (2015) Concrete damage plasticity model for modeling FRP-to-concrete bond behavior. J Compos Constr 19(1):04014026. https://doi.org/10.1061/(ASCE)CC.1943-5614.0000482

23. Wang P, Zhou G (2018) Frost-heaving pressure in geotechnical engineering materials during freezing process. Int J Min Sci Technol 28(2):287–296. https://doi.org/10.1016/j.ijmst.2017.06.003

24. Wang R, Hu Z, Li Y, Wang K, Zhang H (2022) Review on the deterioration and approaches to enhance the durability of concrete in the freeze-thaw environment. Constr Build Mater 321:126371. https://doi.org/10.1016/j.conbuildmat.2022.126371

25. Yao W, Jiang S, Fei W, Cai T (2017) Correlation between the compressive, tensile strength of old concrete under marine environment and prediction of long-term strength. Adv Mater Sci Eng 2017:1–12. https://doi.org/10.1155/2017/8251842

26. Yu Y, Zheng Y, Xu J-j, Wang X-l (2021) Modeling and predicting the mechanical behavior of concrete under uniaxial loading. Constr Build Mater 273:121694. https://doi.org/10.1016/j.conbuildmat.2020.121694

27. Zhang Z-w, Zhang Z-h, Wang X, Zhou C-h (2022) Dynamic and static interfacial bonding properties of CFRP–concrete subjected to freeze-thaw cycles. Structures 37:947–959. https://doi.org/10.1016/j.istruc.2022.01.049

# Finite Element Modeling of Fiber-Reinforced Polymer Composite Tubes Filled with Concrete

Alireza Sadat Hosseini and Pedram Sadeghian

**Abstract**  Sustainable development of Civil Engineering infrastructure has already benefited from the use of fiber-reinforced polymer (FRP) composite materials for different structural applications such as reinforcing existing structures and constructing new ones. Among the various FRP structural elements, $\pm$ 55° filament wound glass FRP (GFRP) tubes, which are typically prefabricated for piping application, have been considered in a number of structural applications. As a load-bearing structural element, filling these tubes with concrete (concrete-filled FRP tubes or CFFTs) can considerably enhance their stiffness and strength under axial and flexural loadings. Although there have been multiple studies on the bending and compressive behavior of CFFTs, studies on the tensile behavior of CFFTs and especially those made of $\pm$ 55° GFRP tubes are quite scarce. Here in this study, in order to take a step toward a better understanding of the behavior of the CFFTs under axial tension, finite element models of the hollow tubes and CFFTs were generated using the ABAQUS software package and verified against the experimental outputs of previous studies. Shell elements were used to model the tube while solid elements formed the concrete. The concrete damaged plasticity (CDP) model was used to introduce the material properties of the concrete to the model. Quasi-static analysis using Dynamic/Explicit solver was implemented due to its capabilities for converging highly nonlinear problems. Good compatibility of the results of the numerical study with the test outputs was seen on both hollow tubes and CFFTs. It can be concluded that the damage criteria used for FRP were capable of predicting matrix cracking as the governing mode of failure in FRP observed in the experiments. Moreover, the CDP model could simulate the tensile cracking of concrete.

**Keywords**  GFRP tube · Concrete · CFFT · Tension · Finite element analysis

A. Sadat Hosseini (✉) · P. Sadeghian
Department of Civil and Resource Engineering, Dalhousie University, Halifax, Canada
e-mail: asadat@dal.ca

# 1 Introduction

Filament wound fiber-reinforced polymer (FRP) tubes have recently been used instead of traditional metallic pipes in municipal sectors. This has improved the importance of these pipes and therefore, they have been extensively studied under internal and external pressure loading by some researchers [18, 22]. However, there are quite scarce studies on the axial behavior of filament wound glass fiber-reinforced polymer (GFRP) tubes and further studies and investigations, which is the purposes of this study, are required to shed more light on the mechanical behavior of these tubes in order to be used in a wide variety of structures. In an experimental study by Bai et al. [4], the mechanical behavior of filament wound GFRP tubes was investigated under pure axial tensile load, pure internal pressure, and combined loading. Results of this study were used to recognize the main damage initiation mechanisms such as micro-cracking and delamination. The researchers of another study, Khalifa et al. [11] experimentally investigated the mechanical behavior of filament wound tubes under axial monotonic loading. Through this study, a non-destructive test was developed whose results were in line with the traditional tensile tests. One of the very recent studies on the axial [5] and flexural [6] behavior of these tubes was conducted in the Department of Civil and Resource Engineering, Dalhousie University. Experimental and analytical investigation of the behavior of these tubes under longitudinal compressive and tensile loading. According to the experiments, it was seen that the failure started with matrix cracking along the direction of the fibers and continued until the specimen fails. Through the analytical studies, nonlinear formulations were presented on the behavior of the tubes and verified against the experiments and the literature. A clear understanding of the material behavior and the response of these tubes under different loading conditions is provided which is the basis of further investigation on these tubes.

Although very good studies have been done so far on the behavior of filament wound GFRP tubes, albeit limited, investigation of the behavior of concrete-filled tubes (CFFTs) is much more limited. The idea of CFFTs was proposed by Mirmiran and Shahawy [16] inspired by the concrete-filled steel tubes to achieve high strength, ductility, and prolonged durability. Fam and Rizkalla [8] conducted large-scale tests on concrete-filled GFRP tubes. They targeted the strength to weight ratio and found that specimens with a central longitudinal hole are the optimum scheme. The contribution of concrete to the flexural strength was studied and a parametric study on the effective parameters was carried on. In another research by Fam et al. [7], the behavior of CFFTs was studied through an experimental program, and an analytical model was proposed. It was found that increasing the ratio of fibers in the axial direction enhances the flexural strength, while axial compressive strength of CFFTs increased when higher ratios of fibers in the hoop direction were used. Shao and Mirmiran [19] studied the cyclic behavior of CFFTs as simple span beam-columns. Half of the specimens were filament wounds and others were centrifuge casting tubes. Thick tubes failed with a brittle compression mode while a ductile tension failure was observed in thin tubes. In another study by Zohrevand and Mirmiran [23], Ultra

high-performance concrete-filled fiber-reinforced polymer tubes (UHPCFFT) were studied to estimate their maximum ground acceleration capacity as column members. Although the ductility of the un-reinforced CFFTs was lower than the reinforced ones, higher ground acceleration capacity was observed for the thinnest CFFT with no steel reinforcement.

More recently, Qasrawi et al. [17] studied the behavior of CFFTs under dynamic impact loads and presented a procedure for the analysis and design of CFFTs under this type of loading. Promising results were achieved regarding the flexural capacity and maximum displacement for CFFTs over the conventional reinforced concrete counterparts. Using existing experimental data [14] on seawater and sea sand concrete (SWSSC) with FRP tubes, Li et al. [13] presented a theoretical model to present the behavior of these CFFTs. The model was developed on an existing dilation model for concrete-filled FRP wraps [20] combined with a biaxial stress analysis to incorporate the effect of the Poisson's ratio of the tubes in the model. Xie et al. [21] investigated the behavior of the CFFTs under axial compressive loading through experiments and developed an analytical model to capture the nonlinear biaxial behavior of concrete-filled filament wound FRP confining tubes. Lu and Fam [15] experimentally investigated the effect of damage on the FRP tubes of CFFTs in form of controlled longitudinal and circumferential linear cuts on the flexural strength of these tubes. Cross-ply tubes were found to be more vulnerable in comparison to the angle-ply commercially used tubes. Moreover, tension side cuts were more effective in strength reduction than compression side cuts. Jawdhari et al. [10] conducted numerical studies CFFTs under axial load and bending moment. ANSYS and LS DYNA software packages were used for the simulations. Although LS DYNA results followed the overall trend of the test results, the model had some deviations regarding the stresses corresponding to concrete splitting crack and stiffness reduction.

An overall review of the past studies reveals that not only our knowledge about the structural behavior of the CFFTs is not enough, but also studies on $\pm 55°$ filament wound GFRP tubes under tensile loading have not yet moved much toward a deeper understanding of their behavior when filled with concrete. This study aims to develop a finite element model using the ABAQUS software package [1] to simulate the behavior of CFFTs under axial tension. The geometrical and mechanical properties of the GFRP and concrete were introduced to the model based on the available experimental data. First, the finite element model of the hollow tube was generated and verified against the experiments. Then the concrete part was added to the model and analyzed. Results of the finite element models were in good agreement with the experiments regarding the prediction of tube stiffness and failure patterns.

## 2 Benchmark Experiments

The experimental outputs were taken from two separate studies, one on the hollow GFRP tubes under tensile loading, and the other one on the CFFTs under tension. An innovative test method of capturing the tensile behavior was proposed [5] to

**Table 1** Structural and geometrical properties of P1050-D76-T

| Nominal pressure rating (kPa) | Inner diameter (mm) | Cross-sectional area (mm$^2$) | Wall thickness (mm) | Filament wind layup (°) |
|---|---|---|---|---|
| 1050 | 76.2 | 964.4 | 3.8 | $[\pm 55]^7$ |

investigate the behavior of hollow tubes under axial tensile loading. In this method, the actual tensile parameters are driven from the full pipe test instead of coupons with some shortcomings such as fiber discontinuity along the edges. Tubes with different diameter to thickness ratios (DTR) and nominal pressure ratings (NPR) were selected for the experiments. Among these tubes, P1050-D76-T with the geometrical properties presented in Table 1 was selected to be filled with concrete in another study [12]. The concrete mix design was designed to reach a compressive strength of about 40 MPa. Concrete cylinder specimens were made of the manufactured concrete mix and tested according to ASTM C39 [3] to determine the compressive strength of concrete. The value of the compressive strain was found to be around 38 MPa which was acceptable. The same concrete was poured inside the tube and cured at room temperature for 28 days while covered with plastic sheets and then tested. Before filling the tubes with concrete, the inside surface of the tube's wall was greased to achieve a smooth and frictionless surface. Two steel cores with steel rods were used on the top and bottom of the tube to make it possible for tensile testing.

The test specimens were fixed inside a 2MN Static Hydraulic Universal Testing System, and the steel rods of the specimen were attached to the plates of the testing machine. The specimens were subjected to tensile loading at a rate of 2 mm/min, and the load–displacement and the strains of the specimen were measured using a data acquisition system collecting data every 1/10 s. The test setup can be found in [5]. The tension tests were continued after peak load up to the point that the load decreased to 80% of the peak load. According to the experiments, the failure in hollow GFRP tubes is in the form of matrix cracking which follows the directions of the fibers at $\pm 55°$. The failure in GFRP for the CFFT sample was mostly at the ends adjacent to the steel cores mainly because of using concrete that controls the biaxial strains. For the concrete core, cracking in the middle due to the tensile failure and crushing in both ends due to the compressive failure were observed.

## 3   Finite Element Simulation

### 3.1   Material Parameters

The material properties of the GFRP based on the manufacturer data were taken from one of the reference studies [5] for this research and are presented in Table 2.

Hashin damage criteria [9] were used in the numerical models to consider the strength of the GFRP tube taking into account the material properties given in Table 2.

**Table 2** Verified material properties of GFRP

| Property | Value | Property | Value |
|----------|-------|----------|-------|
| E1 | 40,000 | SL+ | 1036 |
| E2 | 9500 | SL− | 567 |
| υ12 | 0.28 | ST+ | 50 |
| G12 | 3900 | ST− | 116 |
| G23 | 2700 | SLT | 81 |

E1: longitudinal elastic modulus; E2: transverse elastic modulus; G12: shear modulus; ν12: major Poisson's ratio; ν21: minor Poisson's ratio; SL+: longitudinal tensile strength; SL−: longitudinal compressive strength; ST+: transverse tensile strength; ST−: transverse compressive strength; SLT: shear strength

The post-damage behavior of the FRP elements was considered in the analyses to cater for damage evolution.

The concrete material was modeled using the concrete damaged plasticity (CDP) model in ABAQUS having a compressive strength ($f'_c$) of 38 MPa based on the experimental data. The CDP model is a continuum, plasticity-based, damage model for concrete. It assumes that the main two failure mechanisms are tensile cracking and compressive crushing of the concrete material. The model assumes that the uniaxial tensile and compressive response of concrete is characterized by damaged plasticity. To introduce the concrete damage properties to ABAQUS, it is needed to introduce the modulus of elasticity ($E_c$) and the Poisson's ratio ($\nu$). According to ACI 318-08 [2], for normal-weight concrete, the modulus of elasticity of concrete is:

$$E_c = 4700\sqrt{f'_c} = 4700 \times \sqrt{38} \approx 29{,}000 \text{ MPa} \tag{1}$$

For the design of concrete structures, the most common value of concrete Poisson's ratio is taken as 0.2. To define the compressive behavior and the corresponding compressive crushing or the tensile behavior and its corresponding tensile cracking, two curves are needed to be defined for each compressive and tensile behavior: Yield Stress versus Inelastic Strain and Damage Parameter versus Inelastic Strain. Inelastic Strain is calculated by the following formulation:

$$\varepsilon^{\text{in}} = \varepsilon - \sigma/E_c \tag{2}$$

wherein $\varepsilon$ and $\sigma$ are the concrete strain and stress, respectively. The inelastic strain in the tensile behavior is known as the cracking strain. When extracting the inelastic strain from the initial stress–strain data, the yield stress could be found from the stress–strain curve which is the stress value corresponding to the shift from the linear response to nonlinear. The Damage Parameter ($d$) is calculated using the ratio of concrete stress ($\sigma$) and concrete yield stress ($\sigma_y$):

$$d = 1 - \sigma/\sigma_y \tag{3}$$

**Table 3** Material properties of the concrete core in the finite element model

| Property | Value | Property | Value |
|---|---|---|---|
| Dilation angle | 35° | Mass density (kg/m$^3$) | 2300 |
| Eccentricity | 0.1 | Young's modulus (MPa) | 28,970 |
| $F = \sigma_{bo}/\sigma_{co}$ | 1.16 | Poisson's ratio | 0.2 |
| $K_c$ | 0.667 | Compressive and tensile strength (MPa) | 38 and 3.5 |

In order to introduce the tensile behavior of concrete, its tensile strength can be calculated using the following relationship between the splitting tensile strength and compressive strength according to ACI 318 [2]:

$$f_t = 0.56\sqrt{f_c'} = 0.56 \times \sqrt{38} \approx 3.5 \, \text{MPa} \tag{4}$$

Table 3 presents the material properties of the concrete for the CDP model.

### 3.2  Geometry and Boundary Conditions

The geometries of the finite element models are similar to the experimental samples, P1050-D76-T, presented in Table 1. The Inner Diameter of the tube is 76.2 mm, the wall thickness is 3.8 mm, and its length was assumed 450 mm. Two circular rigid plates were used in the models representing the experimental steel caps of the specimens. Shell elements type S8 in ABAQUS were used to generate the tube, while solid elements type C3D8 in ABAQUS were used for the concrete fill geometry in the finite element models. The finite element models of the hollow tube and CFFT are presented in Fig. 1.

The layup configuration of the filament wound GFRP tube was introduced to the model based on the data obtained from the manufacturer of the filament wound $\pm 55°$ GFRP tubes as per Table 1. Figure 2 presents the GFRP layup of the P1050-D76-T tube in the finite element model.

The boundary conditions of the model were chosen as close as possible to the experimental setup. The plate on the top end acted as the load cell (applying the tensile load). An increasing time-dependent displacement was applied on the top rigid plate, while the bottom one restricted all degrees of freedom of the tube. Since oil was used to cover the inside surface of the tube in the experiments, surface-to-surface contact with frictionless contact material was used to simulate the friction of concrete with the inner surface of the tube in the finite element models. The modeling was conducted using Quasi-static analysis using Dynamic/Explicit solver of ABAQUS which includes the loading speed and the materials' density and is capable of solving nonlinear and complicated problems.
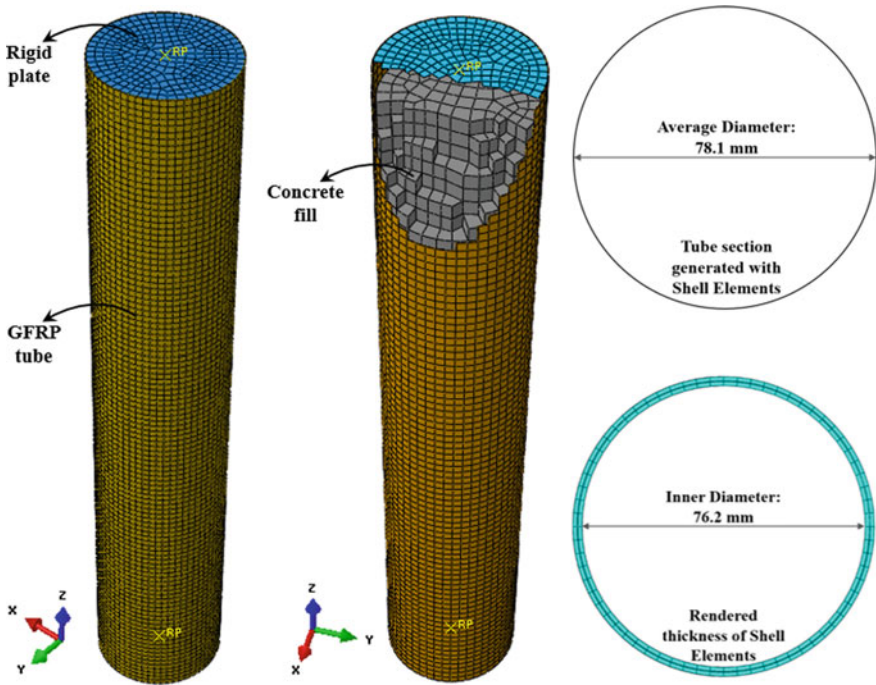
**Fig. 1** Mesh geometry and dimensions of the hollow and concrete-filled GFRP P1050-D76-T tubes in the finite element model
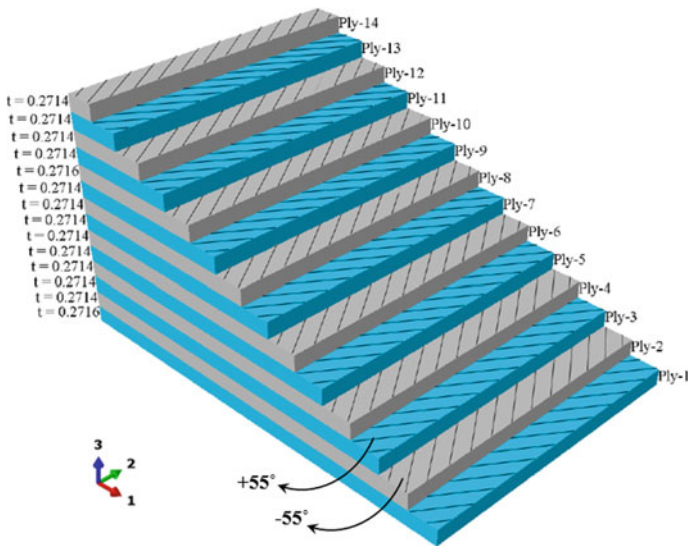


**Fig. 2** The composite layup in the numerical model

# 4 Results and Discussion

This section is divided into two subsections, presenting the results of finite element modeling of the hollow tubes and CFFTs.

## 4.1 Hollow Tube

Figure 3a illustrates the stress–strain curve of the filament wound GFRP tubes resulting from the finite element modeling of the hollow tubes. As can be seen, the model could simulate the tube stiffness, strength and post-failure behavior with good accuracy in comparison to the test result. Figure 3b shows the damage contours of the hollow tubes and the concrete-filled ones under the axial tension. As can be seen in this figure, the numerical finite element model could capture the damage mechanism as similar to the observations of the experiments. The failure in the tube is in the form of matrix cracking along the direction of the fibers which continues until the failure of the tube.
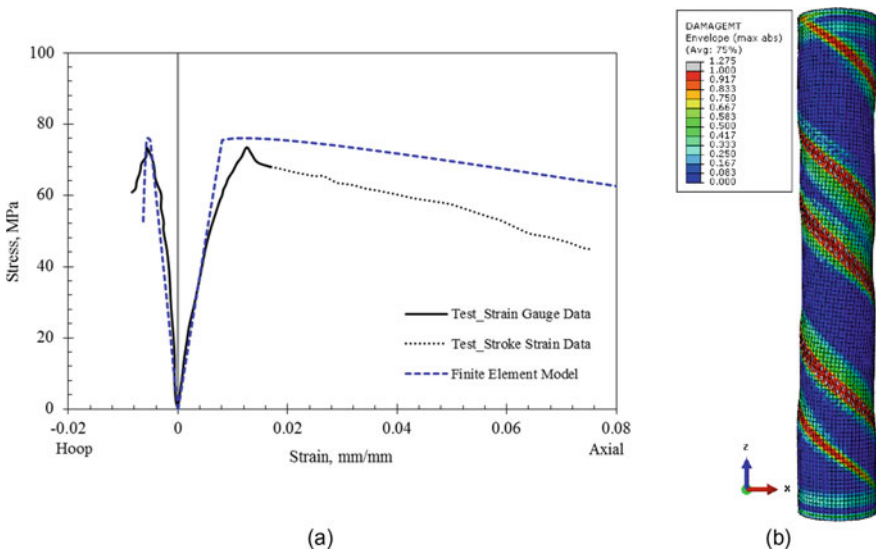


**Fig. 3** Results of the finite element modeling of the hollow GFRP tube: **a** comparing the test results [5] with the ABAQUS numerical model, **b** damage contours of GFRP matrix in tension

## 4.2  Concrete-Filled FRP Tube (CFFT)

Figure 4a illustrates the stress–strain relationship of the finite element model and the experiments on the concrete-filled FRP tubes (CFFT), and Fig. 4b shows the damage contours of the concrete core at the end of the tensile loading. The difference between the two tests is that in Test #2 CFRP wraps were used at the ends of the specimen to prevent premature failure at the end. The numbers inside the circles in these figures correspond to the sequence of damage in the concrete core. Point #1 in Fig. 4b shows the tensile cracking of concrete in the middle which corresponds to the drop of the stress–strain curve of Fig. 4a around 40–60 MPa. As it is seen, the finite element model could capture the load-bearing drop of the CFFT which was observed in the experiments. By increasing the tensile load after the drop point, to about 80 kN (Point #2 in Fig. 4a), the first damage and stiffness degradations in the GFRP tube occurred, and some other parts of the concrete were damaged (Point #2 in Fig. 4b). Therefore, the effectiveness of the concrete in restricting the transverse displacement and necking of the tube decreased. Therefore, the stiffness of the CFFT model dropped to around 80–100 kN. The other interesting result which can be seen in Fig. 4a is that the FE model could be able to capture the post-failure behavior of the CFFT up to the failure point (Point #3) with acceptable precision in comparison with the outputs of the tests. Overall, comparing the stress–strain diagram of the model and the experiments, it can be seen that there is good compatibility between the model and the experiment.
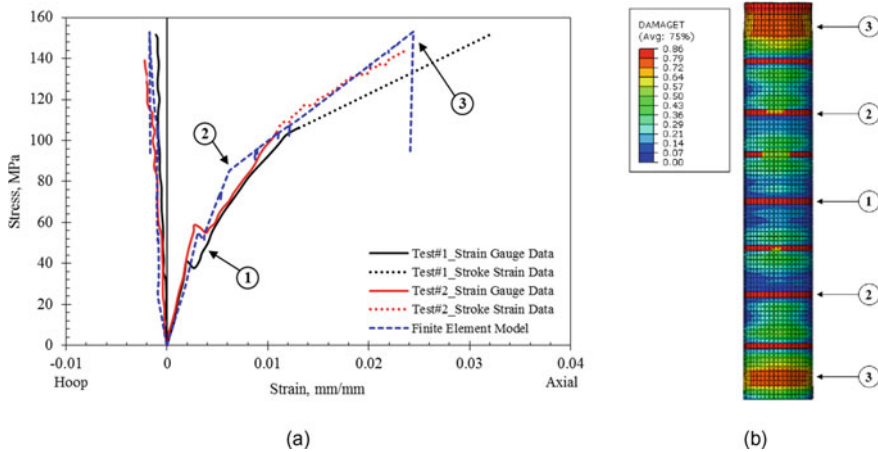


**Fig. 4** Results of the finite element modeling of CFFT: **a** comparing the test results [12] with the numerical model, **b** damage contours of the concrete core in the finite element model

## 5   Summary and Conclusion

This paper presents the results of finite element modeling of the concrete-filled GFRP tubes (CFFT). The study started with numerical modeling of the hollow tubes based on the experiments on these tubes. Results showed that the FE model is capable of simulating the behavior of the tubes under tensile loading. Hashin damage criteria for fiber and matrix failure were introduced to the model which could predict the damage pattern of the tube compatible with the experimental observations. Moreover, the CFFT model was generated using the Concrete Damaged Plasticity model in ABAQUS for the concrete core. Results were in good agreement with the experimental outputs regarding the initial damage and its propagation in the concrete core, failures in the FRP in the form of matrix cracking, and post-failure behavior of the CFFT observed in the stress–strain relationship diagram.

This study can be extended to evaluate the effect of the contributing parameters of GFRP and concrete in the finite element model as future research work.

## References

1. ABAQUS/Standard User's Manual (2014) Version 6.14. Simulia, Providence, RI
2. American Concrete Institute (2008) Building code requirements for structural concrete (ACI 318-08) and commentary. American Concrete Institute
3. American Society for Testing and Materials (2014) ASTM C39/C39M, standard test method for compressive strength of cylindrical concrete specimens
4. Bai J, Seeleuthner P, Bompard P (1997) Mechanical behaviour of $\pm 55°$ filament-wound glass-fibre/epoxy-resin tubes: I. Microstructural analyses, mechanical behaviour and damage mechanisms of composite tubes under pure tensile loading, pure internal pressure, and combined loading. Compos Sci Technol 57:141–153. https://doi.org/10.1016/S0266-3538(96)00124-8
5. Betts D, Sadeghian P, Fam A (2019) Investigation of the stress-strain constitutive behavior of $\pm 55°$ filament wound GFRP pipes in compression and tension. Compos Part B Eng 172:243–252
6. Betts D, Sadeghian P, Fam A (2021) Experimental and analytical investigations of the flexural behavior of hollow $\pm 55°$ filament wound GFRP tubes. Thin-Walled Struct 159:107246
7. Fam A, Flisak B, Rizkalla S (2003) Experimental and analytical modeling of concrete-filled FRP tubes subjected to combined bending and axial loads. ACI Struct J 100:499–509
8. Fam AZ, Rizkalla SH (2002) Flexural behavior of concrete-filled fiber-reinforced polymer circular tubes. J Compos Constr 6:123–132
9. Hashin Z (1980) Failure criteria for unidirectional fiber composites. ASME J Appl Mech
10. Jawdhari A, Fam A, Sadeghian P (2020) Modeling the nonlinear response of $\pm 55$ angle-ply GFRP tube used in CFFT applications. In: 8th international conference on advanced composite materials in bridges and structures, Sherbrooke, Quebec, Canada
11. Khalifa AB, Zidi M, Abdelwahed L (2012) Mechanical characterization of glass/vinylester $\pm 55°$ filament wound pipes by acoustic emission under axial monotonic loading. C R Méc 340:453–460. https://doi.org/10.1016/j.crme.2012.02.006

12. Khan S (2019) Structural properties of commercially used ±55° filament wound GFRP pipes filled with concrete in tension. In: Partial fulfillment of the requirements of the Engineering Co-op Education Program at Dalhousie University
13. Li YL, Teng JG, Zhao XL, Singh Raman RK (2018) Theoretical model for seawater and sea sand concrete-filled circular FRP tubular stub columns under axial compression. Eng Struct 160:71–84. https://doi.org/10.1016/j.engstruct.2018.01.017
14. Li YL, Zhao XL, Singh RKR, Al-Saadi S (2016) Experimental study on seawater and sea sand concrete filled GFRP and stainless steel tubular stub columns. Thin-Walled Struct 106:390–406
15. Lu C, Fam A (2020) The effect of tube damage on flexural strength of±55 angle-ply concrete-filled FRP tubes. Constr Build Mater 240:117948
16. Mirmiran A, Shahawy M (1996) A new concrete-filled hollow FRP composite column. Compos Part B Eng 27:263–268
17. Qasrawi Y, Heffernan PJ, Fam A (2015) Dynamic behaviour of concrete filled FRP tubes subjected to impact loading. Eng Struct 100:212–225
18. Rafiee R (2016) On the mechanical performance of glass-fibre-reinforced thermosetting-resin pipes: a review. Compos Struct 143:151–164. https://doi.org/10.1016/j.compstruct.2016.02.037
19. Shao Y, Mirmiran A (2005) Experimental investigation of cyclic behavior of concrete-filled fiber reinforced polymer tubes. J Compos Constr 9:263–273
20. Teng J, Huang YL, Lam L, Ye LP (2007) Theoretical model for fiber-reinforced polymer-confined concrete. J Compos Constr 11:201–210
21. Xie P, Lin G, Teng JG, Jiang T (2020) Modelling of concrete-filled filament-wound FRP confining tubes considering nonlinear biaxial tube behavior. Eng Struct 218:110762. https://doi.org/10.1016/j.engstruct.2020.110762
22. Xing J, Geng P, Yang T (2015) Stress and deformation of multiple winding angle hybrid filament-wound thick cylinder under axial loading and internal and external pressure. Compos Struct 131:868–877. https://doi.org/10.1016/j.compstruct.2015.05.036
23. Zohrevand P, Mirmiran A (2013) Seismic response of ultra-high performance concrete-filled FRP tube columns. J Earthq Eng 17:155–170

# The Interfacial Bond Stresses in Concrete Filled FRP Tubes

**Ali Alinejad, Pedram Sadeghian, and Amir Fam**

**Abstract**  Composite structures have gained more attention these days due to their advantages, such as high strength (because of complementary performance of core concrete and FRP tube), excellent durability, light weight, and fast erection. One of the composite structures is concrete filled fiber-reinforced polymer (FRP) tubes (CFFTs). The technology has been investigated in the past, but more attention should be paid to some specific problems, such as quantifying an adequate bond between the tube and the concrete core to act as a full-composite structure, which is an important issue, especially in flexural member. This study proposes a new and simple analytical method calculating the bond stress in flexural members. The equilibrium between the tension and the compression forces is used to develop a MATLAB code to calculate the bond stress. The section is divided into some fibers. The force in each fiber is calculated according to the stress distribution. The total tension and compression forces are calculated by the sum of fibers' forces. The bond stress is the total tension or compression force divided by the interface between the concrete core and the FRP tube. However, the ultimate moment capacities given from tests are used in the simplified method to calculate the bond stress. The tension and the compression forces are calculated based on the arm between them. Finally, the bond stress is determined. Furthermore, a comparison between the bond stress calculated according to two methods and the bond strength data derived from push-off tests is made. The results show that although the bond stresses are a bit more than the bond strength at the ultimate condition, there is an adequate bond between the concrete and the FRP tube before reaching the ultimate condition as the differences are not too much.

**Keywords**  Concrete filled FRP tubes (CFFTs) · CFFT flexural members · Interfacial bond stresses

A. Alinejad (✉) · P. Sadeghian
Department of Civil and Resource Engineering, Dalhousie University, Halifax, Canada
e-mail: ali.alinejad@dal.ca

A. Fam
Department of Civil Engineering, Queen's University, Kingston, Canada

# 1 Introduction

The strengthening of concrete members by bonding and wrapping of fiber-reinforced polymer (FRP) straps, sheets, and shells around the concrete members has increased in recent years. FRP is one of the several choices due to its advantages, such as its high strength, lightweight, lower need for maintenance, and resistance against corrosion. Concrete filled FRP tubes (CFFTs) also are known as composite structures. Using FRPs shows a significant increase in strength and ductility of concrete members. However, the exact behavior of composite structures had to be examined. In this regard, experimental and analytical studies have been started since about 1990. As some of the early attempts to evaluate the behavior of composite structures, Mirmiran and Shahawy [11] and Fam and Rizkalla 4 tested many concrete columns confined by fiber composite. The results show that the use of fiber composites is an effective means of confinement. In addition, Fam and Rizkalla [5] and Samaan et al. [10] presented analytical models for confined concrete by fiber composite, which can precisely predict these types of structures' behavior. Composite tubes were examined experimentally and numerically in recent years [1, 8, 14] as well as FRP tubes with fibers in declined direction, which showed a great nonlinear with high ductility behavior. According to some experimental studies, FRP tube with fibers in $\pm 55°$ direction was considered one of the best choices for composite structures [2, 3, 6, 13].

The problem that should be solved is finding an adequate bond between FRP tube and concrete. The bond should be assessed to understand the exact process between the FRP tube and the concrete. This problem has been addressed in concrete filled steel tubes (CFSTs) by considering effective parameters on the bond strength during many push-off tests, and some equations are defined to calculate the bond strength in different codes. However, this problem remains unsolved in CFFTs. In this study, a detailed method using fiber analysis is developed in MATLAB software to calculate the exact bond stress between the FRP tube and concrete, and a simplified method for two extreme hypothetical cases is presented to calculate the approximate bond stress. Also, several push-off tests data, which have been done to calculate the bond strength in CFFTs, have been collected to compare with bond stresses driven from the presented methods.

# 2 Basic Assumptions

The equilibrium between the tension and the compression forces is used in the detailed method to develop a MATLAB code to calculate the bond stress. The section is divided into some fibers, and the force in each fiber is calculated by multiplying the area of the fiber to the stress distribution. The total tension and compression forces are calculated by the sum of fibers' forces in tension and compression zones. The bond stress is the total tension or compression force divided by the interface between the concrete core and the FRP tube. However, the ultimate moment capacities given

from tests are used in the simplified method to calculate the bond stress. The tension and the compression forces are calculated by dividing the moment capacity to the arm between the tension and the compression forces (fiber analysis is used to find the arm). Finally, the bond stress is determined using the same approach used in the detailed method.

The assumptions for two analytical methods are as below:

1. Plane sections remain plane
2. There is no slip between the concrete and the FRP tube
3. There is no local buckling in FRP tube
4. Concrete tensile strength is neglected
5. Strain compatibility is used to determine the stress distribution.

## 2.1 Geometry of the Problem and Stress Distribution

Figure 1 shows the cross section and the geometry defined for the problem. $D_0$ and $t$ are the total diameter and thickness of tube, respectively. $D$ is the average diameter of the tube, and $n$ is the number of fibers by which the section is divided. $hi$ is the thickness of each fiber. The depth of the center of each fiber is shown by $h(i)$. The length of the perimeter of the tube within the fiber on one side is shown by $L(i)$. $\varphi_1(i)$ and $\varphi_2(i)$ are the angles in radians between the vertical center line of the section and the two radiuses bounding the length of the arc $L(i)$, and $\varphi(i)$ is the angle between the vertical center line of the section and the radius reaching to the perimeter at the level of the mid thickness of the fiber. $B(i)$ is half of the width of the fiber. $A_f(i)$ and $A_c(i)$ are the area of the tube and the area of the concrete core at each fiber, respectively. All the parameters are defined as below:

$$D = D_0 - t \tag{1}$$

$$hi = \frac{D}{n} \tag{2}$$

$$h(i) = hi(i - 0.5) \tag{3}$$

$$\varphi_1(i) = \cos^{-1}\left[\frac{0.5D - h(i) + 0.5hi}{0.5D}\right] \tag{4}$$

$$\varphi_2(i) = \cos^{-1}\left[\frac{0.5D - h(i) - 0.5hi}{0.5D}\right] \tag{5}$$

$$\varphi(i) = \cos^{-1}\left[\frac{0.5D - h(i)}{0.5D}\right] \tag{6}$$
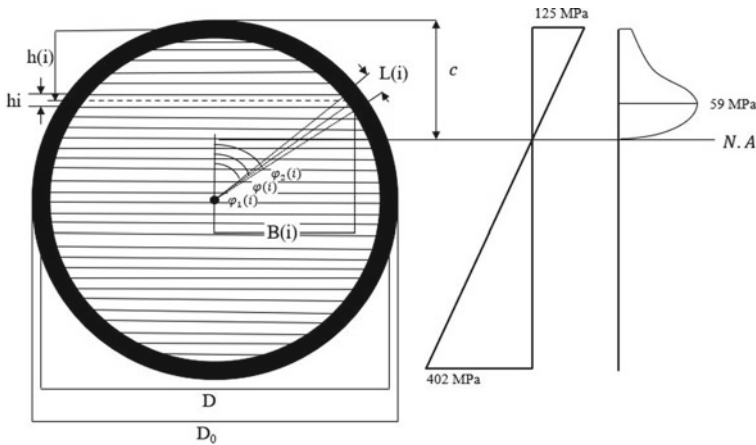
**Fig. 1** Geometries and stresses distributions

$$L(i) = 0.5D(\varphi_2(i) - \varphi_1(i)) \tag{7}$$

$$B(i) = 0.5D \sin \varphi(i) \tag{8}$$

$$A_f(i) = 2L(i)t \tag{9}$$

$$A_c(i) = 2B(i)hi - 0.5A_f(i) \tag{10}$$

The centers of gravity for tension and compression zones are determined according to the stress distribution along the section depth.

To calculate the center of gravity, each fiber is considered a cube. The center of gravity for the compression zone is defined as a weighted mean of the center of gravity of the concrete and the center of gravity of the FRP tube in compression. However, the center of gravity in the tension zone is just the center of gravity of the FRP tube. Finally, the center of gravity of each zone is calculated as below.

For compression zone:

$$\text{COG}_c = \left(\sum (0.5D - h(i))A_c(i)\varepsilon(i)\right) / \left(\sum A_c(i)\varepsilon(i)\right) \tag{11}$$

$$\text{COG}_f = \left(\sum (0.5D - h(i))A_f(i)\varepsilon(i)\right) / \left(\sum A_f(i)\varepsilon(i)\right) \tag{12}$$

$$\text{COG}_{\text{com}} = (\text{CFF} \times \text{COG}_f + \text{CCC} \times \text{COG}_c) / (\text{CFF} + \text{CCC}) \tag{13}$$

For tension zone:

$$\text{COG}_{\text{ten}} = \left(\sum (0.5D - h(i)) A_f(i) \varepsilon(i)\right) / \left(\sum A_f(i) \varepsilon(i)\right) \tag{14}$$

## 2.2 Stress Distribution

The properties of the beam BC given from Helmi et al. study [7] are used for calculations. The model presented by Mander et al. [9] has been selected for the concrete core due to its accurate representation of the material's non-linearity as shown in Fig. 1, while the linear stress–strain relationship is considered for the FRP tube. The stress distributions are defined as below, in which $E_{\text{FRP}}$ is the modulus of elasticity of the FRP tube, $\varepsilon(i)$ is the strain at each fiber, $f_c'$ is the compressive strength of unconfined concrete, $E_c$ and $E_{\text{sec}}$ are tangent and secant modulus of elasticity of concrete.

FRP in tension:

$$f_t(i) = E_{\text{FRP}} \varepsilon(i) \tag{15}$$

FRP in compression:

$$f_f(i) = E_{\text{FRP}} \varepsilon(i) \tag{16}$$

Concrete in compression:

$$f_c(i) = \frac{f_c' x(i) r}{r - 1 + x(i)^r} \tag{17}$$

$$x(i) = \frac{\varepsilon(i)}{\varepsilon_c'} \tag{18}$$

$$r = \frac{E_c}{E_c - E_{\text{sec}}} \tag{19}$$

$$E_c = 4700 \sqrt{f_c'} \tag{20}$$

$$E_{\text{sec}} = \frac{f_c'}{\varepsilon_c'} \tag{21}$$

# 3 Proposed Methods

Two methods are presented in this section. The sample calculations have been done for the beam given from Helmi et al. study [7] (beam with identification BC) using both detailed and simplified methods, and the results for the other beams are presented in the result section.

## 3.1 Detailed Method

The equilibrium between the tension and the compression forces is used to develop a MATLAB code to calculate the bond stress. The beam section is divided into some fibers. The force in each fiber is calculated according to the stress distribution. The total tension and compression forces are calculated by the sum of fibers' forces, and the depth of the neutral axis is determined using the equilibrium between total tension and total compression forces. The bond stress is the total tension or compression force divided by the interface between the concrete core and the FRP tube. The equilibrium equation used in this method is shown below, and the neutral axis depth is equal to 0.239 D according to the equilibrium.

$$\sum \text{Eft}\varepsilon_{\text{ft}}(i)\text{Aft}(i) = \sum \text{Efc}\varepsilon_{\text{fc}}(i)\text{Afc}(i) + \sum A_c(i)f_c(i) \rightarrow c = 0.239\,\text{D} \quad (22)$$

Then, the arcs and the bond stresses between the concrete and the FRP tube are calculated in the tension and the compression zones. The location of the neutral axis and the arm is shown in Fig. 2. The 3D schematic of the parameters used in the detailed method is presented in Fig. 3.
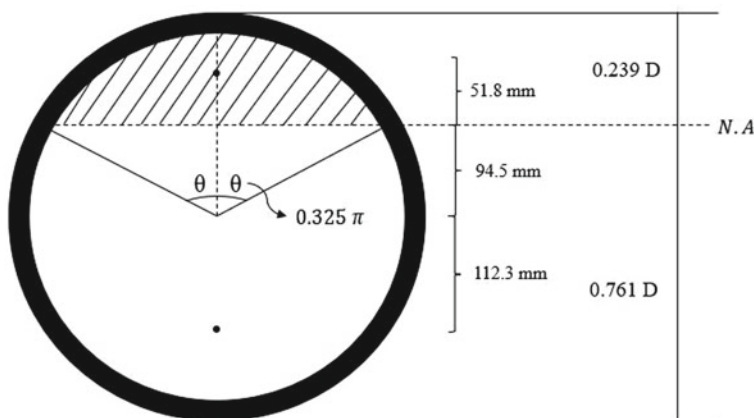


**Fig. 2** Cross section of beam based on the equilibrium of the tension and compression forces
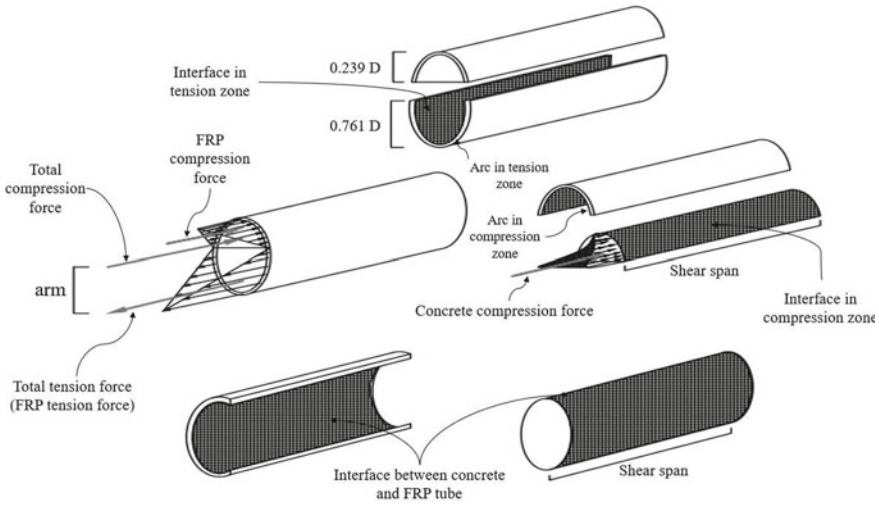
**Fig. 3** 3D schematic of the parameters used in the detailed method

The calculation for one beam given from Helmi et al. study [7] is presented in this section as an example. The beam ID is BC according to the study. The dimensions and mechanical properties of the beam is presented in Table 1.

The calculations for beam BC (the dimensions are given from Helmi et al. study [7]) in compression zone are as follows:

$$C_c = 759 \, \text{kN (according to the fiber analysis have been done in MATLAB)}$$

$$\text{arc}_c = r \times 2 \times \theta = 181.1 \times 2 \times 0.325\pi = 369.8 \, \text{mm}$$

$$\tau_c = \frac{C_c}{\text{arc}_c \times \text{Shear span}} = \frac{759 \times 10^3}{369.8 \times 2000} = 1.026 \, \text{MPa}$$

The same calculations have been done for the tension zone as follows:

**Table 1** Dimensions and mechanical properties of beam BC [7]

| Outer diameter (mm) | Total wall thickness (mm) | Structural wall thickness (mm) | Longitudinal modulus (GPa) | Longitudinal tensile strength (MPa) | Length of the beam (m) | Shear span (m) | Ultimate moment capacity (kN m) | Bond Strength due to push-off test (MPa) |
|---|---|---|---|---|---|---|---|---|
| 367 | 5.7 | 4.8 | 23.1 | 402 | 5 | 2 | 200 | 0.664 |

$T = 837 \, \text{kN}$ (according to the fiber analysis have been done in MATLAB)

$$\text{arc}_T = r \times 2 \times (\pi - \theta) = 181.1 \times 2 \times 0.675\pi = 768.1 \, \text{mm}$$

$$\tau_t = \frac{T}{\text{arc}_t \times \text{Shear span}} = \frac{837 \times 10^3}{768.1 \times 2000} = 0.545 \, \text{MPa}$$

## 3.2 Simplified Method

This section considers two extreme cases for the depth of the neutral axis ($c$). The first case is the least depth of neutral axis, which can happen in tests, and the second one is the most depth of neutral axis. $c$ is equal to 0.2 and 0.45 D for the first and second cases, respectively.

The ultimate capacities of beams are given from experimental studies [7, 12]. The arm between compression and tension forces is calculated according to fiber analysis. Also, the compression force of FRP tube is calculated. The total compression and tension forces are calculated $\left(C = T = \frac{M}{\text{arm}}\right)$. For calculating the bond stress between the FRP tube and the concrete core, the FRP tube force is deducted from the total force ($C$) to calculate the concrete force ($C_c$) in compression zone, while the total force ($T$) is considered for the tension zone. The interface between concrete and FRP tube in compression and tension zones is calculated (arc $\times$ L). Eventually, the bond stresses in compression and tension zones are calculated $\left(\tau = \frac{\text{Force}}{\text{interface}}\right)$.

The equilibrium of tension and compression forces is neglected in this section, and the arm is calculated as the distance between the compression and tension force according to the fiber analysis.

### 3.2.1 C = 0.2 D

The neutral axis and the centers of gravity of tension and compression zones are shown in Fig. 4 when $c$ is equal to 0.2 D.

The arm and arcs in tension and compression zones, the total tension and compression forces, the concrete force in compression, and the bond stress between the concrete and the FRP tube in tension and compression zones can be determined as follows:

$$\text{arm} = 43.2 + 108.7 + 108.1 = 260 \, \text{mm}, \quad M_{BC} = 200 \, \text{kN m},$$

$$C = T = \frac{M_{BC}}{\text{arm}} = \frac{200 \times 10^3}{260} = 769.2 \, \text{kN}$$

$C_{FRP} = 82 \, \text{kN}$ (according to the fiber analysis) $\rightarrow C_c = 769.2 - 82 = 687.2 \, \text{kN}$
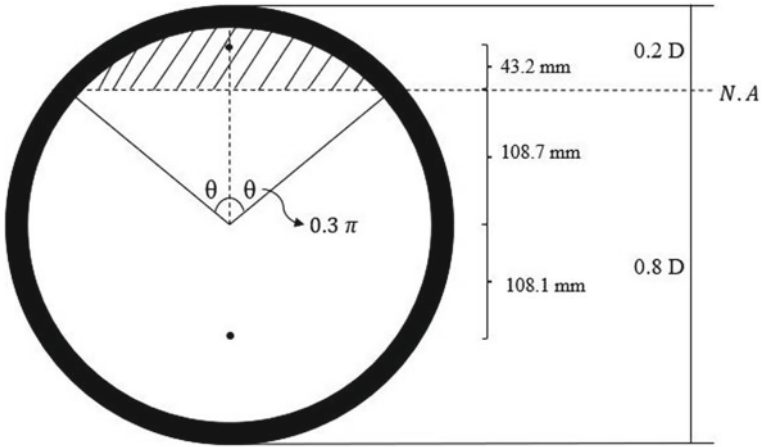
**Fig. 4** Cross section of beam when $c = 0.2$ D

$$\text{arc}_c = 181.1 \times 2 \times 0.3\pi = 341.4 \,\text{mm}, \quad \text{arc}_t = 181.1 \times 2 \times 0.7\pi = 796.5 \,\text{mm}$$

$$\tau_c = \frac{C_c}{\text{arc}_c \times \text{Shear span}} = \frac{687.2 \times 10^3}{341.4 \times 2000} = 1.006 \,\text{MPa},$$

$$\tau_t = \frac{T}{\text{arc}_t \times \text{Shear span}} = \frac{769.2 \times 10^3}{796.5 \times 2000} = 0.483 \,\text{MPa}$$

### 3.2.2  $C = 0.45$ D

The neutral axis and the centers of gravity of tension and compression zones are shown in Fig. 5 when $c$ is equal to 0.45 D.

The same calculations are done when $c$ is equal to 0.45 D.

$$\tau_c = 0.313 \,\text{MPa}, \quad \tau_t = 0.655 \,\text{MPa}$$

## 4  Verification of the Detailed Method

The ultimate moment capacities calculated by MATLAB software are compared with the ultimate moment capacities given from tests to determine the accuracy of the detailed method.
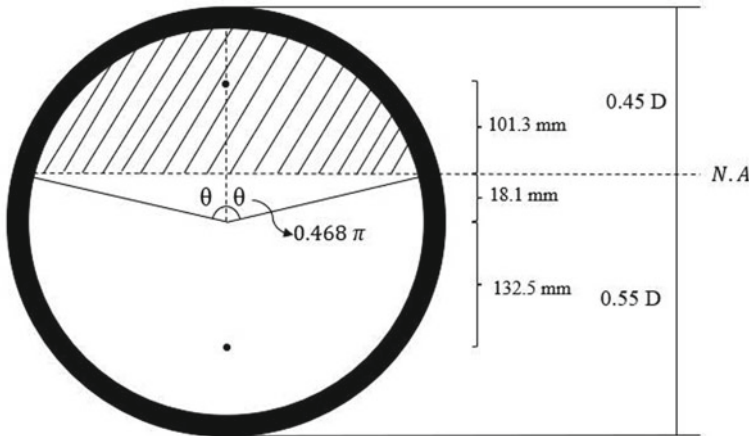
**Fig. 5** Cross section of beam when $c = 0.45$ D

**Table 2** Comparison between ultimate moment capacities given from tests and MATLAB software

|  | Specimen ID | Moment capacity (kN m) using MATLAB code | Moment capacity (kN m) given from tests | Difference between moment capacities (%) |
|---|---|---|---|---|
| Helmi et al. [7] | BC | 217.7 | 200.0 | 8.1 |
|  | BPL | 217.7 | 195.0 | 10.4 |
|  | BPU | 217.7 | 189.0 | 13.2 |
| Qasrawi and Fam [12] | Beam 10 | 162.8 | 155.0 | 4.8 |

The differences between the moment capacities driven from tests and the moment capacities calculated using MATLAB software are presented in Table 2.

## 5 Result and Discussion

The comparison between bond stress calculated according to the detailed method and bond strength given from push-off tests is shown in Table 3. The results show that the bond stresses in the compression zone are greater than the bond strengths, while they are less than bond strengths in the tension zone.

Also, it should be noted that the bond strength given from Qasrawi and Fam's study [12] is related to the hollow section. So, the bond strength is much lower than the bond strength given from another study.

In addition, the comparison between bond stress calculated according to the two hypothesis cases and bond strength given from push-off tests is shown in Table 4.

**Table 3** Comparison between bond stress calculated according to the detailed method and bond strength given from push-off tests

|  | Specimen ID | Moment capacity (kN m) (based on equilibrium) | Bond strength due to push-off test (MPa) | Shear span (m) | Bond stress according to equilibrium According to concrete force in compression | Bond stress according to equilibrium According to GFRP force in tension |
|---|---|---|---|---|---|---|
| Helmi et al. [7] | BC | 217.7 | 0.664 | 2 | 1.025 | 0.538 |
|  | BPL | 217.7 | 0.825 | 2 | 1.025 | 0.538 |
|  | BPU | 217.7 | 0.538 | 2 | 1.025 | 0.538 |
| Qasrawi and Fam [12] | Beam 10 | 162.8 | 0.2 | 2 | 0.984 | 0.563 |

The bond stresses calculated according to the concrete force in the compression zone are more than bond strengths when $c$ equals 0.2 D, while bond stresses in the tension zone are less than bond strength. However, when $c$ is equal to 0.45 D, bond stresses in the compression zone are less than bond strengths, and bond stresses in the tension zone have different situations.

Generally, the decision can be made that there is an adequate bond between the concrete core and the FRP tube as the bond stresses are calculated according to the ultimate moment capacities, which means that there is not enough bond at the ultimate capacities. However, an adequate bond is provided between the concrete core and the FRP tube before reaching the ultimate capacities.

# 6  Conclusions

This paper has presented two detailed and simplified analytical methods. The equilibrium between the tension and the compression forces is used for the detailed method to calculate the bond stress. The bond stress is the total tension or compression force divided by the interface between the concrete and the FRP tube, while moment capacities given from tests are used for calculating the bond stress between the concrete and the FRP tube in the simplified method. The exact tension and compression forces are used in the detailed method while they were assumed in the simplified method.

Comparisons between the predicted moment capacities of CFFRs according to the detailed method using fiber analysis and experimental results available in the literature show good agreement.

Although the detailed method shows a good agreement with the test results for moment capacities, it is not completed as the bond stress distribution is not uniform

**Table 4** Comparison between bond stresses calculated according to the two hypothesis cases and bond strength given from push-off tests

| | Specimen ID | Moment capacity (kN m) | Bond strength due to push-off test (MPa) | Shear span (m) | Bond stress (MPa) N.A = 0.2 D According to concrete force in compression | Bond stress (MPa) N.A = 0.2 D According to GFRP force in tension | Bond stress (MPa) N.A = 0.45 D According to concrete force in compression | Bond stress (MPa) N.A = 0.45 D According to GFRP force in tension |
|---|---|---|---|---|---|---|---|---|
| Helmi et al. [7] | BC | 200 | 0.664 | 2 | 1.006 | 0.483 | 0.313 | 0.655 |
| | BPL | 195 | 0.825 | 2 | 0.978 | 0.471 | 0.295 | 0.639 |
| | BPU | 189 | 0.538 | 2 | 0.945 | 0.456 | 0.272 | 0.619 |
| Qasrawi and Fam [12] | Beam 10 | 155 | 0.2 | 2 | 1.022 | 0.484 | 0.344 | 0.657 |

through the section. As a result, a new method should be described which is more accurate to find the bond stress distribution through the section.

The results given from the detailed method reveal that the tension zone is the safe zone as the bond strength is more than the bond stress in that zone while the bond strength is less than bond stress in the compression zone according to the ultimate condition. Although the bond stresses between the concrete core and the FRP tube in the compression zone are more than the bond strength when the ultimate condition is considered, there is almost enough bond strength in tension and compression zones before reaching the ultimate condition. However, the simplified method's results show that the bond stresses between the concrete core and the FRP tube are more than the bond strength in ultimate conditions.

This research is not completed, and more exact results will be presented at the conference.

# References

1. Alinejad A, Khaloo A, Hassanpour S (2021) Investigating the behavior of circular concrete filled PVC tube columns under concentric and eccentric load using FEM. Asian J Civ Eng 22(4):589–603
2. Betts D, Sadeghian P, Fam A (2019) Investigation of the stress-strain constitutive behavior of ±55° filament wound GFRP pipes in compression and tension. Compos B Eng 172:243–252
3. Betts D, Sadeghian P, Fam A (2021) Experimental and analytical investigations of the flexural behavior of hollow ±55° filament wound GFRP tubes. Thin-Walled Struct 159:107246
4. Fam AZ, Rizkalla SH (2001) Behavior of axially loaded concrete-filled circular fiber-reinforced polymer tubes. ACI Struct J 98(3):280–289
5. Fam AZ, Rizkalla SH (2001) Confinement model for axially loaded concrete confined by circular fiber-reinforced polymer tubes. ACI Struct J 98(4):451–461
6. Gemi L, Köroğlu MA, Ashour A (2018) Experimental study on compressive behavior and failure analysis of composite concrete confined by glass/epoxy ±55° filament wound pipes. Compos Struct 187:157–168
7. Helmi K, Fam A, Mufti A (2005) Field installation, splicing, and flexural testing of hybrid FRP/concrete piles. Special Publication 230:1103–1120
8. Jawdhari A, Fam A, Sadeghian P (2020) Modeling the nonlinear response of ±55 angle-ply GFRP tube used in CFFT applications. In: 8th international conference on advanced composite materials in bridges and structures
9. Mander JB, Priestley MJN, Park R (1989) Theoretical stress-strain model for confined concrete. J Struct Eng 114(8):1804–1826
10. Michel Samaan B, Mirmiran A, Shahawy M (1998) Model of concrete confined by fiber composites. J Struct Eng 124(9):1025–1031
11. Mirmiran A, Shahawy M (1997) Behavior of concrete columns confined by fiber composites. J Struct Eng 123(5):583–590
12. Qasrawi Y, Fam A (2008) Flexural load tests on new spun-cast concrete-filled fiber-reinforced polymer tubular poles. ACI Struct J 105(6):750–759
13. Roy S, Sadeghian P (2021) Shear and bending behaviour of short-span steel-reinforced concrete-filled FRP tubes with ±55° fiber orientation. In: CSCE annual conference. Canadian Society for Civil Engineering
14. Sadeghian P, Asce M, Rahai AR, Ehsani MR (2010) Experimental study of rectangular RC columns strengthened with CFRP composites under eccentric loading. J Compos Constr 14(4):443–450

# Development and Assessment of a Mechanical Strengthening System for Post-tensioned Concrete Bridge Cantilever Wings Using Post-tensioned CFRP Rods

**Faraj Shahrstan and Pedram Sadeghian**

**Abstract** This paper presents the development and experimental assessment of a mechanical strengthening system using post-tensioned (PT) carbon fiber reinforced polymer (CFRP) rods for the rehabilitation of post-tensioned concrete bridge cantilever wings. CFRP rods were selected as a direct parallel to PT steel bars owing to CFRP's superior fatigue, corrosion resistance, and lightweight properties as a composite material. The mechanical strengthening system is a metal anchor comprised of a stainless steel barrel and split aluminum wedges in direct contact with a CFRP rod. The system strictly relies on friction for load-bearing capacity with no adhesives required. The developed CFRP mechanical anchorage system is assessed experimentally as part of a broader experimental program seeking to adequately transfer the CFRP post-tensioning force through bearing at anchorage ends to strengthen PT concrete bridge cantilever wing specimens that exhibit deterioration. The CFRP rods for strengthening will be embedded in near-surface-mounted (NSM) grooves in the negative moment region of the experimental PT concrete bridge cantilever wing specimens. The anchor features a contoured longitudinal profile consisting of a 1650 mm circular radius to minimize the stress concentrators at the loading end of the anchor, pushing the stress toward the back of the anchor. The anchor also features a competitive 80 mm in length stainless steel barrel and 80 mm in length aluminum wedge core. Seven specimens in total were carried out for the experimental assessment of the anchorage system. All prepared specimens measured 1.8 m in total length with a 1.5 m CFRP rod free gauge length in-between the ends of the anchors. Two specimens as proof of concept anchorage testing were carried out with no pre-setting load to observe the behavior of the design concept during loose wedge conditions. Subsequently, anchorage static testing was carried out with five

F. Shahrstan (✉)
Wiss, Janney, Elstner Associates, Inc., Northbrook, Illinois, United States
e-mail: fshahrstan@wje.com

F. Shahrstan · P. Sadeghian
Department of Civil and Resource Engineering, Dalhousie University, Halifax, Nova Scotia, Canada

prepared specimens. Two distinct pre-setting loads were selected to induce initial contact pressure between the wedges and the CFRP rod to reduce slippage. Three specimens were pre-set at 80 kN and two specimens were pre-set at 100 kN before tensioning. The average ultimate capacity of the anchorage system was 97.6 kN, yielding a system efficacy of 63.4% against a guaranteed CFRP tensile strength of 154 kN. Adhering to the Canadian Highway Bridge Design Code, S6-19, the CFRP rods will be post-tensioned up to an effective jacking force of 50 kN at transfer due to the anchorage effect on the CFRP rod.

**Keywords** Carbon fiber-reinforced polymers (CFRP) · Wedge-barrel anchor · Post-tensioning · NSM rehabilitation · Concrete bridge cantilever strengthening

## 1 Introduction

Bridge replacement is expensive; the US Federal Highway Administration (FHWA) has estimated that, in 2016, the total cost for the replacement of all structurally deficient highway bridges is more than 47 billion dollars [6]. Thus, it is economically viable and eco-conscious to develop efficient strengthening systems to rehabilitate existing deteriorated bridges to achieve bridge service life. Strengthening structurally deficient highway bridges results in life cycle economic savings, reduction of negative environmental impacts, and limits traffic detours. Currently, several Departments of Transportation have found compromised transverse post-tensioning steel in bridge cantilever wings requiring a cost-effective rehabilitation strategy to maintain the service life of the bridge structure. Historically and currently, high-strength steel has been utilized for post-tensioning applications for concrete bridges, but harsh ambient environments which include constant freeze and thaw cycles, de-icing salts, de-icing chemicals, and exposure to marine air have reduced the service life of existing public infrastructure. Steel is susceptible to corrosion when in contact or exposed to oxygen and water. Harsh environments and climate change have facilitated an increased haven for the effects of corrosion. Over time as the steel is exposed to the elements, the steel rusts and loses its cross-section, which results in spalled concrete and a reduced structural capacity.

Prestressing steel applications have become a gold standard and common approach for the design of larger span to depth ratios in concrete members and the design of a multitude of concrete members including but not limited to bridge decks, bridge piers, and commercial malls slabs, ground applications, etc. Steel is isotropic and offers great ductility due to its great post-yielding plastic hardening properties. The major concern with steel that has led to investment in FRP materials is the issues regarding fatigue relaxation and corrosion. CFRP material is an alternative to supplement steel, but it has its Achilles Heel. Due to CFRP material's orthotropic properties, reduced ductility, and reduced ability to withstand sharp stress concentrators, conventional mechanical anchors used for post-tensioning steel strand applications are not suitable. A modification to existing mechanical anchorages is required to better suit CFRP.

CFRP is weak in the transverse direction and cannot handle orthogonal compression as greatly as isotropic steel strands. However, when there are concerns related to the long-term durability of prestressed steel in terms of corrosion, fatigue, and relaxation, CFRP materials are a good candidate. CFRP is known for its high strength to weight ratio, non-corrosiveness, high durability, and high stiffness offering improved ultimate limit state and serviceability conditions for bridge infrastructure. Unlike conventional steel strands and bars, to the best knowledge of the authors, there are no available commercial anchorage systems for CFRP rods. Various researchers have experimented with bonded versus mechanical anchorage systems for CFRP materials. However, a mechanical strengthening system is more suitable for heavy civil infrastructure projects. The main concern with mechanical anchorage systems is how to adequately grip the CFRP rod without premature failure. Various experiments have been conducted in the past two decades with differential angles, contoured longitudinal profiles, and different geometry configurations for an optimum mechanical anchorage system. The contact pressure distribution on the rod surface plays a significant role in controlling the level of tensile loading that can be carried by the CFRP anchorage system. High contact pressure on the rod surface combined with high applied tensile stress induces premature failure due to the stress concentration at the loading end of the anchor. On the other hand, low contact pressure on the rod surface causes it to slip as the tensile load increases. Thus, a balance between contact pressure and tensile load capacity would provide for the ideal anchorage system. Optimum contact pressure is needed for a suitable anchor design to ensure no slippage as required by design codes. The contact pressure can be controlled by the profile geometry and the mechanical properties of the anchor components that are in direct contact with the CFRP rod. The competitiveness of a CFRP anchorage system would be to achieve a minimal anchor barrel and wedge length that is adequate to compete with conventional mechanical systems that grip steel strands. In this paper, a mechanical anchorage system is developed and experimentally assessed using 10 mm pultruded CFRP rods. ASTM D7205 FRP tensile tests are conducted on the CFRP rods in addition to proof of concept anchorage testing and anchorage static testing. The purpose of the anchorage experimental testing is to use the developed anchor for experimental strengthening of half-scale PT bridge cantilever wing slabs.

## 2 Experimental Program

A mechanical anchorage system was developed, computer numerical control (CNC) machined, and assessed experimentally to evaluate its suitability and efficacy for the strengthening of post-tensioned concrete bridge cantilever wing slabs exhibiting deteriorated transverse steel post-tensioning. The developed CFRP mechanical anchorage system in this research study is a combination/adaptation from a combination of previous researchers including [1–3, 8, 9, 12, 13]. The experimental program consists of firstly, conducting tensile tests on the selected NO.3 (10 mm) CFRP rod as per the ASTM D7205-21 standard [4] to verify the material properties of the CFRP

rod. Secondly, conducting preliminary proof of concept testing to verify the design concept in-house. Lastly, conducting static anchorage testing on the anchors per a specified load-controlled loading protocol. The goal of the proposed anchorage system is to provide effective means to jack and grip the CFRP rod up to a specified post-tensioning force in order to near-surface mount for strengthening post-tensioned concrete bridge cantilever wing slabs. This paper presents the details regarding the development and assessment of the proposed CFRP mechanical anchorage system. The presentation of the performance and behavior of post-tensioned concrete cantilever specimens that have undergone strengthening with NSM post-tensioned CFRP rods using the proposed mechanical anchorage system are outside the scope of this paper and will be addressed in another research paper.

## 2.1 Anchorage Design and Materials

The proposed mechanical anchorage system is based on existing mechanical anchorage systems used for conventional unbonded steel strand post-tensioning systems. The conventional anchorage design is modified and altered to apply to CFRP rods. In this research study, the proposed CFRP anchor is comprised of a barrel and split wedge system with a contoured longitudinal profile. The outer surface profile of the split wedges and the inner surface profile of the barrel is CNC machined with the same selected longitudinal circular radius of 1650 mm. The wedges are in direct contact with the CFRP rod housed inside the conical barrel and grip the rod relying purely on frictional resistance for load-bearing capacity. The CFRP PT force is transferred to a structural concrete element warranting strengthening via a steel bearing plate. The main design concept of this anchorage system is the utilization of a contoured longitudinal profile within the anchor to prevent premature rupture of the CFRP from the stress concentrators at the loaded end of the anchor. The contoured longitudinal profile (LP) provides a distribution of the differential angles along the anchor, thus facilitating a balance between required contact pressure and the imparted high applied tensile stress concentration. Figure 1 depicts the design concept of the contoured longitudinal profile utilized in the current proposed CFRP anchorage system.

The CFRP material chosen for this research study is a unidirectional pultruded No. 3 (10 mm) CFRP Rod. Table 1 presents the material properties of the selected CFRP rod.

Material selection for the anchorage components was based on the criteria of utilizing cost-effective, locally sourced, commercially available corrosion-resistant materials. Table 2 presents the selected materials for the barrel and wedge components of the anchorage system.

Stainless Steel 316 was selected as the constituent material for the barrel for its exceptionally high resistance in chloride environments and overall corrosion-resistant properties. 316 is the most corrosion-resistant grade of stainless steel
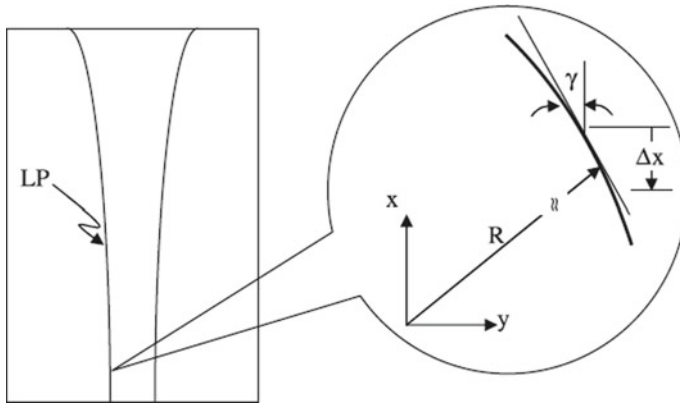
**Fig. 1** Anchor contoured longitudinal profile (obtained from [2])

**Table 1** CFRP rod material properties

| Nominal diameter (mm) | Cross-section area (mm$^2$) | Yield strength (MPa) | Ultimate strength (MPa) | Modulus of elasticity (GPa) |
|---|---|---|---|---|
| 10 | 71.26 | N.A[a] | 2172 | 124 |

[a] Not applicable

**Table 2** Anchorage constituent materials

| Anchorage component | Material |
|---|---|
| Barrel | Stainless Steel 316 |
| Wedges | Aluminum 6061 |

commercially available locally. Aluminum 6061 was selected as the constituent material for the split wedges for its low-cost, corrosion resistance, and great formability as a soft metal. The phenomenon of the plasticization of aluminum as the contact pressure increases results in the aluminum wedges conforming to the shape of the CFRP rod which increases the grip and friction between the wedges and rod resulting in a higher anchorage system tensile load capacity. Table 3 presents the material properties of the selected anchorage components.

For CFRP mechanical anchorage systems to be competitive with existing steel strand post-tensioning anchorage systems, the barrel, and wedge lengths need to

**Table 3** Anchorage material properties

| Material | Tensile strength (MPa) | Modulus of elasticity (GPa) |
|---|---|---|
| Stainless Steel 316 barrel | 515 | 193 |
| Aluminum 6061 wedges | 310 | 68 |

be as minimal as adequately possible. The length of the barrel and wedges of the developed anchor is similar to the anchorage system developed by Heydarinouri et al. [8, 9]. Figure 2 presents the geometric details of the developed split wedge and barrel CFRP anchorage system.

Figure 3 presents the cross-section of the developed split wedge and barrel CFRP anchorage system.
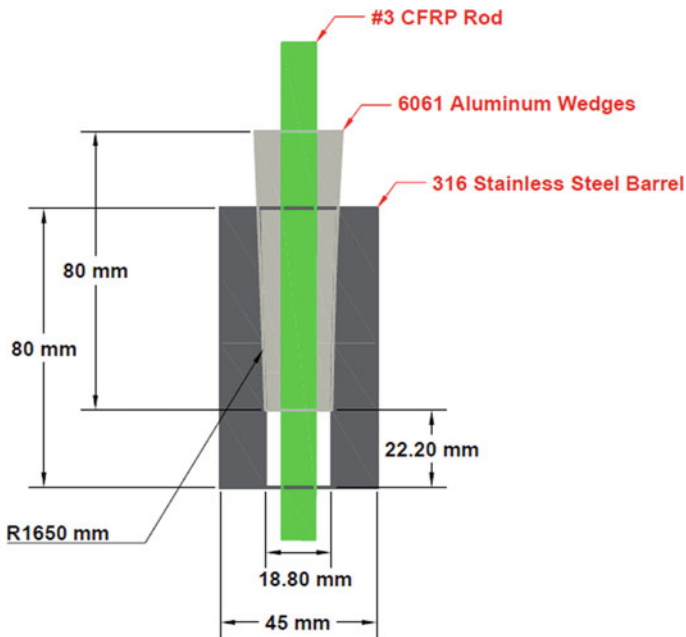


**Fig. 2** Split wedge and barrel anchor geometric details

**Fig. 3** Split wedge and barrel anchor cross-section
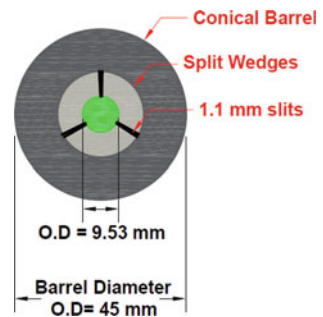
## *2.2   ASTM D7205 FRP Tensile Tests*

The tensile strength of the CFRP specimens was verified by following the ASTM D7205-21 standard [4]. This test method determines the quasi-static longitudinal tensile strength and elongation properties of fiber-reinforced polymer matrix (FRP) composite bars commonly used as tensile elements in reinforced, prestressed, or post-tensioned concrete. This test method was chosen as an internationally recognized testing strategy to verify the material properties of the sourced CFRP rod and to cross-check with the manufacturer's reported values.

### 2.2.1   Test Matrix and Fabrication

The number of prepared specimens, specimen length, and CFRP free gauge length in-between the ends of the anchors were in adherence to the ASTM D7205-21 standard [4] requirements. Five specimens were prepared, and Table 4 presents the observed test matrix.

To observe the ultimate strength of the CFRP rod in which the CFRP rod ruptures within its free gauge length, potted anchors were utilized as a gripping mechanism. Direct gripping of the CFRP rods by the jaws of the testing machine would result in premature failure. The anchors were comprised of ASTM A36 1¼ in. carbon steel schedule 80 pipes and an in-house developed epoxy resin with silica sand filler matrix as the potting material. Each specimen was 1.8 m in total length. Each anchor was 550 mm in length. The free gauge length of the CFRP rod in-between the steel pipe anchors was 650 mm. Two 350-$\Omega$ strain gauges were attached at the midpoint of the CFRP rod's free gauge length. Figure 4 presents a schematic of the fabricated ASTM specimens for tensile strength testing.

Figure 5 presents the cross-section of the steel pipe anchors inclusive of the steel pipe, the potting material, and the concentric CFRP rod.

A wooden jig from ¾ in. plywood was built to align the fabricated specimens. Alignment of the CFRP rod within the potted anchors is required to facilitate a pure tensile test with no induced bending. Figure 6 presents the aligning jig built for the ASTM tensile tests.

**Table 4**   ASTM D7205 tensile test matrix

| Specimen ID | Material | Anchor type | Specimen length (m) |
| --- | --- | --- | --- |
| S1 | #3 CFRP rod | Epoxy potted steel pipe | 1.8 |
| S2 | #3 CFRP rod | Epoxy potted steel pipe | 1.8 |
| S3 | #3 CFRP rod | Epoxy potted steel pipe | 1.8 |
| S4 | #3 CFRP rod | Epoxy potted steel pipe | 1.8 |
| S5 | #3 CFRP rod | Epoxy potted steel pipe | 1.8 |
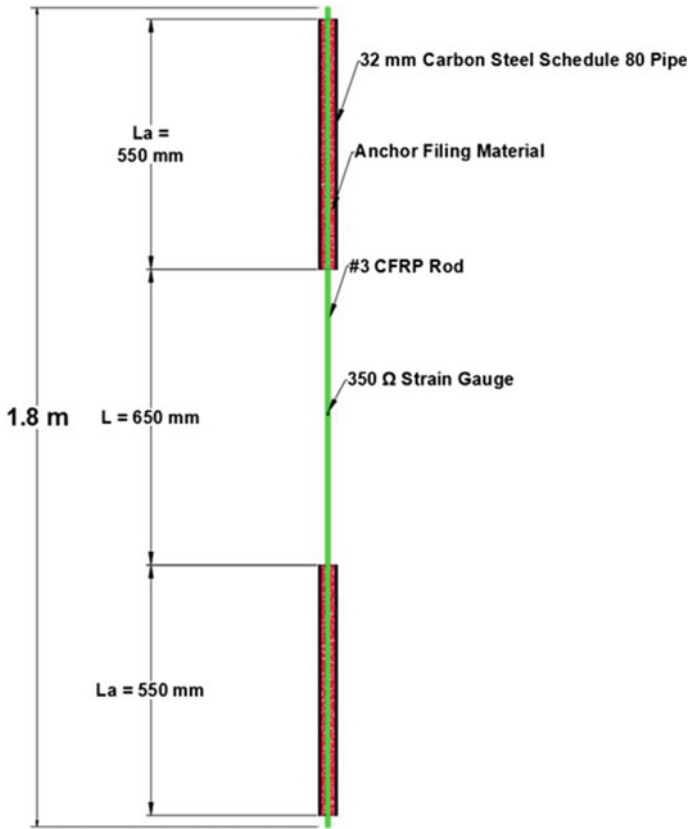
**Fig. 4** ASTM D7205 tensile test specimen

**Fig. 5** ASTM D7205 tensile
test specimen cross-section
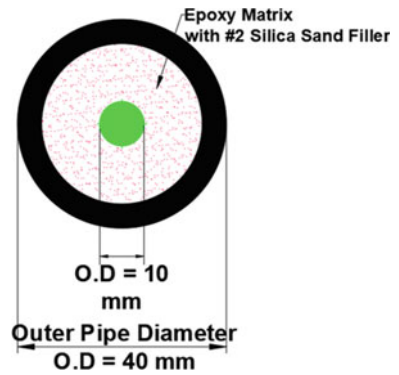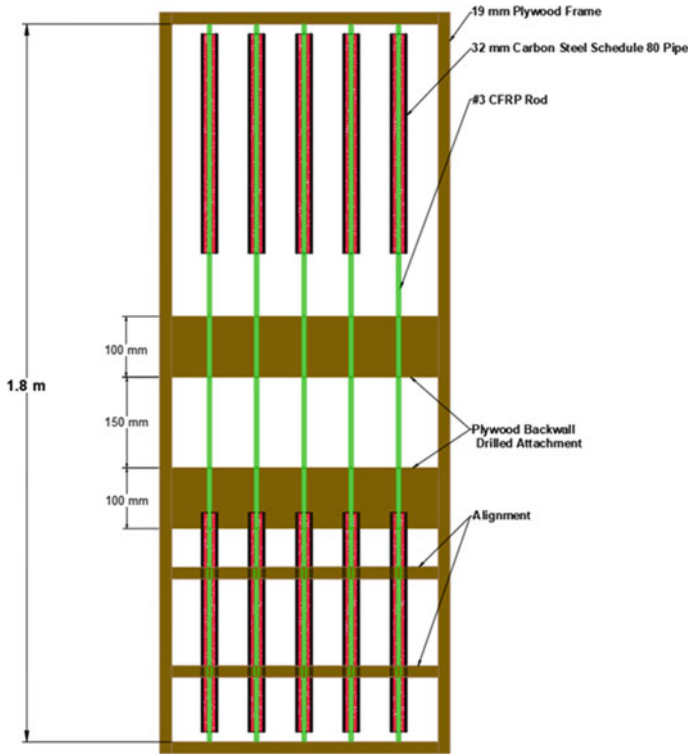
**Fig. 6** Jig for aligning ASTM specimens and anchors

Figure 7 presents a cross-sectional view of the built alignment wooden jig showcasing all five steel pipe anchors.
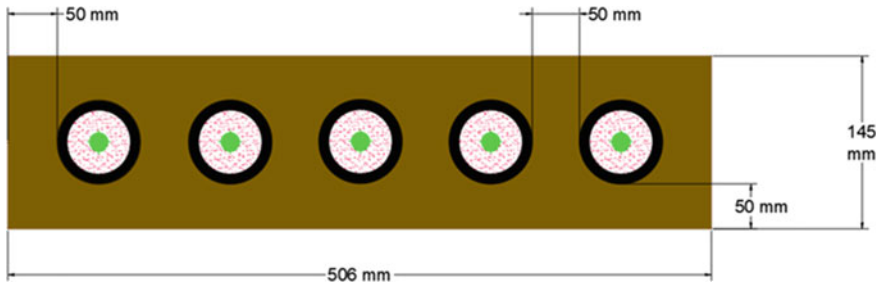


**Fig. 7** Cross-section of wooden alignment

**Table 5** ASTM D7205 tensile test results

| Specimen ID | Ultimate load (kN) | Ultimate strength (MPa) | Elastic modulus (GPa) |
|---|---|---|---|
| S1 | 193 | 2708 | 138 |
| S2 | 193 | 2708 | 139 |
| S3 | 191 | 2680 | 138 |
| S4 | 175 | 2455 | 134 |
| S5 | 163 | 2287 | 124 |

### 2.2.2    Test Results and Discussion

The five specimens were monotonically loaded using a displacement-controlled loading scheme of 2.5 mm/min until ultimate rupture. Table 5 presents the results of the ASTM tensile tests.

The obtained results verify that the CFRP rods meet the manufacturer's guaranteed tensile load of 154 kN and ultimate strength of 2172 MPa, respectively.

## 2.3    *Preliminary Mechanical Anchorage Tests*

Preliminary proof of concept testing was conducted on the anchors to verify the proposed design concept of the contoured longitudinal profile, the geometric details portrayed in Fig. 2, and the selected materials for the respective components of the anchorage system.

### 2.3.1    Test Matrix and Fabrication

The purpose of the preliminary proof of concept tests was threefold. Firstly, to determine the suitability of the proposed anchor. Secondly, evaluate the behavior and performance of each of the anchorage components. Thirdly, determine the overall efficiency of the anchor against the nominal strength of the CFRP rod. Ideally, the proposed anchor would be capable of developing the full ultimate tensile strength of the CFRP material with a rupture of the CFRP within its free gauge length. Since the application of the proposed CFRP anchorage system is intended for CFRP strengthening of a post-tensioned concrete bridge cantilever wing slab exhibiting deteriorated transverse steel post-tensioning in Canada, the Canadian Highway Bridge Design code will be utilized for code requirements. The Canadian Standards Association (CSA) S6-19 code [5], clause 16.8.6.3 on the capacity of FRP anchors stipulates that when tested in an unbonded condition, anchors for post-tensioning tendons shall be capable of developing a tendon force at least 50% higher than the jacking force. Thus, the test criteria for the anchor will be set to meet the CSA S6-19 bridge code. Additionally, after tensioning and seating, anchors shall sustain applied loads without

slippage, distortion, or other changes that result in loss of prestress. The ultimate tensile capacity of the anchorage system and the displacements and slippage of the anchorage components will dictate the maximum permissible jacking force. Two specimens were prepared for preliminary proof of concept testing. Table 6 presents the proof of concept test matrix that was observed.

Two specimens were made for preliminary testing. No pre-setting load was applied onto the barrel anchors at this stage to observe the movements of the anchorage components at the loose state and to record when slippage occurs. The first specimen was comprised of a split wedge and barrel anchor for both the live and dead ends. The second specimen was comprised of a split wedge and barrel anchor for the live end and an epoxy potted steel anchor for the dead end. Both specimens were 1.8 m in total length with different free gauge lengths of CFRP rod owing to the longer length of the potted dead anchor. Figure 8 presents a schematic of the fabrication of the preliminary proof of concept test specimens.

The specimens were loaded based on a load-controlled stepwise loading protocol. The loading protocol was adapted from [7, 10, 11]. Table 7 presents the stepwise loading protocol that was observed.

The loading protocol portrayed in Table 7 was chosen for the movements of the anchorage system components to be observed during stages of applied and sustained loading. The load-controlled stepwise loading protocol was understood as more advantageous than monotonic tensile loading until failure as it could capture the displacements of the anchorage components and is a better simulation of realistic periods of applied and sustained loading that bridge structures undergo. Linear potentiometers (LP) were placed on the top of the CFRP rod, the wedges, and the barrel to measure the draw-ins of each of the anchorage components as the tensile load increased. Figure 9 presents the schematic for placement of the LPs on the anchorage components for draw-in measurements.

**Table 6** Preliminary proof of concept test matrix

| Specimen ID | Material | Anchor type | Pre-setting load (kN) | Specimen length (m) |
|---|---|---|---|---|
| S1-Top | #3 CFRP Rod | Split wedge and barrel | None: loose | 1.8 |
| S1-Bottom | #3 CFRP Rod | Split wedge and barrel | None: loose | |
| S2-Top | #3 CFRP Rod | Split wedge and barrel | None: loose | 1.8 |
| S2-Bottom | #3 CFRP Rod | Epoxy potted steel pipe | None: loose | |
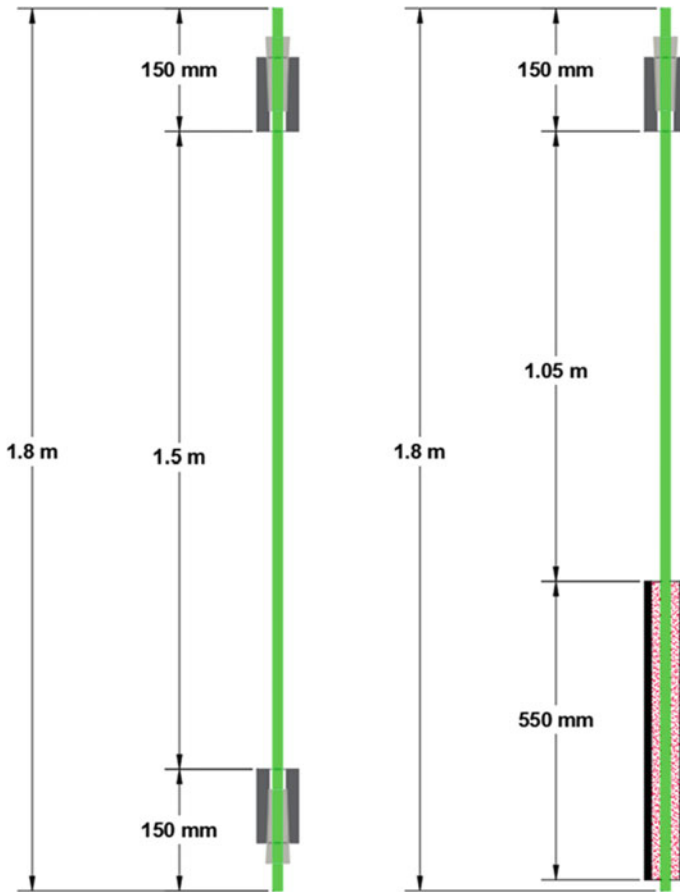
**Fig. 8** Preliminary anchorage static test specimens

**Table 7** CFRP anchorage test loading protocol

| Load state (%) | Load (kN) | Loading rate (kN/min) | Load step |
|---|---|---|---|
| 20 | 30 | 6 | 5 min applied 5 min sustained |
| 40 | 60 | 6 | 5 min applied 5 min sustained |
| 60 | 90 | 6 | 5 min applied 5 min sustained |
| 70 | 105 | 6 | 2.5 min applied 60 min sustained |
| 100 | 150 | 6 | 5–10 min applied |

**Fig. 9** Anchorage components draw-in measurements
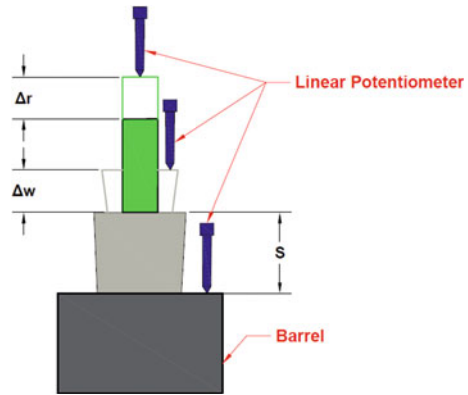


## 2.3.2 Test Results and Discussion

The results of the preliminary proof of concept tests were promising to permit the continuation of the proposed anchorage design and geometric details. The proposed anchorage system was a good preliminary candidate worthwhile pursuing more tests and improvements. Table 8 presents a summary of the preliminary proof of concept test results.

Observing and recording the experimental preliminary anchorage tests yielded many learned lessons. The following points indicate the steps that were undertaken to improve the anchorage design before conducting the anchorage static tests:

- Pre-setting the wedges to the required load to activate the system, increase the contact pressure around the CFRP rod, reduce slippage and overcome wedge seating losses rather than have loose wedges with no pre-setting.
- Arranging the three split wedges evenly around the CFRP rod to ensure a uniformly distributed contact pressure on the CFRP rod.
- Application of metal-free anti-seize lubricant on the outer surface of the aluminum wedges to facilitate better insertion into the barrel and reduce any potential metal galling.
- Rounding off the tips of the wedges to reduce any sharp corners to reduce stress concentrators in the region of high shear and tensile stress.

**Table 8** Preliminary CFRP proof of concept test results

| Specimen | Load (kN) | Failure mode | Slippage | Efficacy (%) |
|---|---|---|---|---|
| S1 | 100.3 | Pinching shear failure near the anchor | Observed around 10 kN | 65 |
| S2 | 102.7 | Pinching shear failure near the anchor | Observed around 15 kN | 66 |

**Table 9** Anchorage static test matrix

| Specimen ID | Material | Anchor type | Pre-setting load (kN) | Specimen length (m) |
|---|---|---|---|---|
| S1 | #3 CFRP Rod | Split wedge and barrel | 80 | 1.8 |
| S2 | #3 CFRP Rod | Split wedge and barrel | 80 | 1.8 |
| S3 | #3 CFRP Rod | Split wedge and barrel | 80 | 1.8 |
| S4 | #3 CFRP Rod | Split wedge and barrel | 100 | 1.8 |
| S5 | #3 CFRP Rod | Split wedge and barrel | 100 | 1.8 |

- Threading of the barrels so a hex nut can thread onto the free end of the barrel to lock the jacking force being transferred to the bridge cantilever concrete specimens from the PT CFRP rod.

## 2.4 Mechanical Anchorage Static Tests

Mechanical anchorage static testing was conducted to evaluate the short-term performance of the proposed CFRP anchorage system under short-term applied and sustained loads. The capacity and efficacy of the anchors were determined in addition to the draw-in measurements of the anchorage components as the tensile load increased.

### 2.4.1 Test Matrix and Fabrication

Five specimens were prepared for experimental anchorage static testing. The specimens were pre-set vertically using an Instron machine. Three specimens were pre-set at a load of 80 kN and two specimens were pre-set at a load of 100 kN. The five specimens were 1.8 m in length utilizing split wedge and barrel anchors for both the live and dead ends. A schematic of the fabrication of the specimens would be similar to the preliminary specimen, S1 in Fig. 7. Table 9 presents the test matrix for the anchorage static testing.

### 2.4.2 Test Results and Discussion

Table 10 presents the ultimate tensile load capacity of the CFRP anchorage system, the load level where slippage was observed, and the efficacy of the anchorage system.

**Table 10**  CFRP anchor static test results

| Specimen | Pre-setting load (kN) | Load (kN) | Observed slippage (kN) | Efficacy (%) |
|----------|----------------------|-----------|------------------------|--------------|
| S1 | 80 | 87.4 | Around 70 | 56.8 |
| S2 | 80 | 98.9 | Around 70 | 64.3 |
| S3 | 80 | 105.9 | Around 70 | 68.9 |
| S4 | 100 | 97.7 | Around 80 | 63.5 |
| S5 | 100 | 90.3 | Around 80 | 58.7 |

**Table 11**  Final CFRP anchorage materials

| Anchorage component | Material |
|---------------------|----------|
| Barrel | Stainless Steel 316 |
| Wedges | Aluminum 6061 |
| Spacer Disc | Plastic |
| Hex Nut | Stainless Steel 316 |

The average ultimate capacity of the anchorage system was 97.6 kN yielding a system efficacy of 63.4% against a guaranteed CFRP tensile strength of 154 kN.

## 2.5 Final CFRP Anchorage Design

Based on the results of the preliminary proof of concept and the anchorage static tests that were conducted, the proposed split wedge and barrel CFRP mechanical anchorage system will be utilized for the strengthening of half-scale post-tensioned concrete bridge cantilever wing specimens exhibiting deterioration in the steel PT. Table 11 presents the materials for the finalized CFRP anchorage design.

The final proposed CFRP anchorage system features the following items:

- 316 Stainless Steel Barrel.
- Three Split 6061 Aluminum Wedges.
- No sleeves or adhesives, pure frictional resistance.
- A longitudinal circular profile with a circular radius of 1650 mm was used for the inner conical hole of the barrel and the outer aluminum wedge core.
- Radial Plastic Spacer Disc.
- Fine Barrel Threading with 25 mm Thick 316 Stainless Steel Hex Nut at the loading end of the barrel.
- Pre-set live and dead end anchors.

Figure 10 presents the final CFRP anchorage system. The system is comprised of live and dead anchors bearing on steel bearing plates that would bear on the PT bridge cantilever concrete specimen.
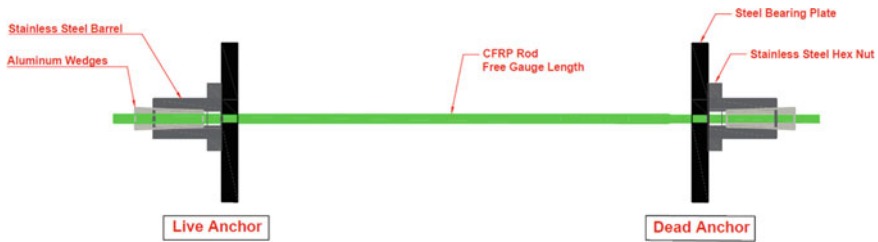
**Fig. 10** CFRP anchorage strengthening system

# 3 Conclusions

The results of the anchorage static tests showcased that the proposed CFRP anchorage system is promising for implementation to strengthen post-tensioned concrete bridge cantilever specimens up to a specified jacking force. Experimental tests yielded a safe effective post-tensioning force of 50 kN. Although it would be highly advantageous and competitive for a mechanical anchorage system to not undergo pre-setting, slippage is prone to occur and was confirmed experimentally. The anchorage system in its loose stage where no pre-setting load is applied resulted in slippage at a very early tensile load. It was observed that no slippage occurred up to 70 kN when pre-setting the anchor to a load level of 80 kN. When pre-setting to a load level of 100 kN, no slippage occurred up to 80 kN. More testing is required to optimize the longitudinal circular profile and the anchorage dimension to be more competitive with steel.

# References

1. Al-Mayah A, Soudki K, Plumtree A (2001) Mechanical behavior of CFRP rod anchors under tensile loading. J Compos Constr 5(2):128–135
2. Al-Mayah A, Soudki K, Plumtree A (2006) Development and assessment of a new CFRP rod–anchor system for prestressed concrete. Appl Compos Mater 13(5):321–334
3. Al-Mayah A, Soudki K, Plumtree A (2013) Simplified anchor system for CFRP rods. J Compos Constr 17(5):584–590
4. ASTM D7205/D7205M-21 (2021) Standard test method for tensile properties of fiber reinforced polymer matrix composite bars. ASTM International, West Conshohocken, PA

5. Canadian Standard Association, CSA S6-19. Canadian Highway Bridge Design Code, Mississauga, Ontario
6. Federal Highway Administration (FHWA) (2016) Count of deficient bridges by functional classification. National Bridge Inventory
7. fib (International Federation for Structural Concrete) (1993) Recommendations for the acceptance of post-tensioning systems. fib, Lausanne, Switzerland
8. Heydarinouri H, Vidovic A, Nussbaumer A, Ghafoori E (2021) FE analysis and experimental validation of mechanical wedge–barrel anchors for CFRP rods. Compos Struct 275:114509
9. Heydarinouri H, Motavalli M, Nussbaumer A, Ghafoori E (2021) Development of a mechanical wedge–barrel anchor for CFRP rods: static and fatigue behaviors. J Compos Constr 25(3):4021015
10. PTI (Post-Tensioning Institute) (2006) Post-tensioning manual. PTI, Phoenix
11. Rostásy FS (1998) Draft guidelines for the acceptance testing of FRP posttensioning tendons. J Compos Constr 2(1):2–6
12. Schmidt JW, Bennitz A, Täljsten B, Pedersen H (2010) Development of mechanical anchor for CFRP tendons using integrated sleeve. J Compos Constr 14(4):397–405
13. Schmidt JW, Smith ST, Täljsten B, Bennitz A, Goltermann P, Pedersen H (2011) Numerical simulation and experimental validation of an integrated sleeve-wedge anchorage for CFRP rods. J Compos Constr 15(3):284–292

# Ultimate Drift Capacity of Flexure-Dominant Reinforced Concrete Masonry Shear Wall

**Yu-Cheng Hsu, Miaoyuan Dou, T. Y. Yang, and Svetlana Brzev**

**Abstract** Reinforced masonry (RM) has been practised in Canada for more than 50 years, mostly for construction of low- to mid-rise buildings. The National Building Code of Canada 2015 [NBCC (2015) National building code of Canada 20 National Research Council, Ottawa, ON, Canada] permits the use of ductile shear wall class for tall masonry buildings with the height limit of 60 m at sites with moderate seismic hazard and 40 m for high seismic hazard sites, but the application of ductile shear wall in tall (more than 40 m high) RM buildings is still very limited in Canada. There is a very limited research evidence related to seismic response of these structures. One of the most important properties for seismic design of ductile RM shear walls is the ultimate drift capacity, which varies significantly depending on failure mechanism(s). This paper reviews past experimental research studies on the subject and presents a database of 66 flexure-dominant RM shear walls. A statistical analysis of the data contained in the database has been performed to determine the governing parameters which are expected to influence the ultimate drift capacity of flexure-dominant RM shear walls. Moreover, this paper also proposes an approach for predicting ultimate drift capacity of RM shear walls, based on the governing parameters determined through experimental studies.

**Keywords** Bridge structures · Brittle fracture · Reliability index · Probabilistic analysis

## 1 Introduction

Reinforced masonry (RM) has been used for construction of low- and mid-rise buildings in Canada for more than 50 years. A few tall reinforced masonry (TRM) buildings were constructed at sites with low to moderate seismic hazard in central and eastern Canada. For example, a 24-storey RM apartment building in Winnipeg, Manitoba,

Y.-C. Hsu (✉) · M. Dou · T. Y. Yang · S. Brzev
The University of British Columbia, Vancouver, Canada
e-mail: ychsu11@mail.ubc.ca

was built in the 1970s, and a few 21-storey RM apartment buildings were built in Hamilton, Ontario [11]. There are also a few TRM applications in high seismic hazard areas of Canada. For example, three 16-storey unreinforced masonry buildings in Vancouver, British Columbia, were constructed in 1960s. Besides Canada, there are a few reported TRM building applications in the USA. For example, a 28-storey Excalibur Hotel in Las Vegas, Nevada, was constructed in 1989 [14]. A few TMR buildings have also been reported in other countries, e.g. several 20-storey buildings in Brazil [9] and a 28-storey office building in Heilongjiang Province, China [24]. It is evident that the application of TRM construction in moderate-to-high seismic hazard areas is limited, which can be attributed to limited compressive strength of commercially available concrete blocks and lack of research studies related to seismic behaviour of TRM buildings [13].

Ductile detailing provisions for RM shear walls contained in the Canadian masonry design standard CSA S304 were last updated in 2014 (CSA S304-14). Provisions related to Moderately Ductile Shear Wall (MDSW) class with ductility force modification factor $R_d = 2.0$ were revised, and a new class Ductile Shear Walls (DSW, $R_d = 3.0$) was introduced. MDSW class is most common for seismic design applications in Canada and is mandatory for all post-disaster buildings according to the National Building Code of Canada 2015 [15] and CSA S304-14. Partially grouted MDSWs can be used at sites with low seismic hazard level, where wall aspect ratio ($h_w/l_w$) is not larger than 2.0, and also at sites with higher seismic hazard with axial pre-compression stress less than $0.1 f'_m$, where $f'_m$ denotes the masonry compressive strength. Fully grouted MDSWs are required at sites with high seismic hazard. The CSA S304-14 seismic design provisions for RM shear walls are explained and illustrated through design examples by [8]. NBCC [15] permits the use of MDSW and DSW classes for RM buildings, but the height limit was set to 60 m (approximately 20 storeys) at sites characterized by moderate seismic hazard, and 40 m (approximately 13 storeys) for high seismic hazard sites.

Asides from the restriction of axial pre-compression stress ($0.1 f'_m$) and height limit, CSA S304-14 Cl.16.8.8 prescribes provisions for ductility verification of RMSWs, which depends on the inelastic rotational capacity ($\theta_{ic}$) of the RMSWs to be larger than the inelastic rotational demand ($\theta_{id}$). The code states that:

$$\theta_{ic} = \frac{\varepsilon_{mu} l_w}{2c} - 0.002 \leq 0.025, \tag{1}$$

where $\varepsilon_{mu}$ denotes as the ultimate compressive masonry strain, which can be taken as 0.0025, $c$ denotes as the depth of neutral axis, and 0.002 is the estimation of elastic rotation of RMSWs.

The $\theta_{id}$ can be calculated as:

$$\theta_{id} = \frac{\Delta_u - \Delta_{f1} \gamma_w}{h_w - \frac{l_w}{2}}, \tag{2}$$

where $\Delta_u$ denotes the ultimate roof displacement, which can be taken as $\Delta_{f1} R_d R_o$, $\Delta_{f1}$ denotes the elastic roof displacement, $\gamma_w$ denotes the overstrength factor, and there is a minimum value of $\theta_{id}$ 0.003 for MDSWs (corresponding to $c/l_w \leq 0.25$) and 0.004 for DSWs (corresponding to $c/l_w \leq 0.208$) to ensure that in the case of applying the minimum $\theta_{id}$, , the corresponding minimum ductility ($\mu$) of walls will be 2.5 and 3 for walls in each category, respectively.

This paper focuses on compiling of an experimental database of 66 flexure-dominant RMSW specimens. Database was used to identify the influence of different key design parameters on the structural behaviour, including identifying the key design parameters that have the highest influence on ultimate lateral drift capacity ($\delta_u$) and the ductility of RMSWs ($\mu$). Lastly, linear regression was applied to develop empirical equation to quantify the ultimate lateral drift capacity $\delta_u$.

## 2 Failure Mechanisms for RMSW Systems

Robazza et al. [18] classified failure mechanisms for RM shear walls (RMSWs) as ductile failure (DF), diagonal shear failure (S), shear-flexure failure (SF), sliding failure (SL), toe-crushing or web-crushing failure (TC), bar-buckling (BB) and bar-fracture failure (BF), rocking (RO), and lateral instability (LI). The type of failure mechanism affects the seismic behaviour of RMSWs in terms of the lateral strength, ductility, ultimate drift capacity, and strength degradation rate. In this paper, failure mechanisms corresponding to two distinct stages, namely the maximum strength and failure, defined as 80% of the maximum strength, are defined as primary failure mechanism (PF) and secondary failure mechanism (SF), respectively. The sequence of development of failure mechanisms in RMSWs is complex, and it is common that more than two failure mechanisms occur before the collapse takes place. For instance, both specimens shown in Fig. 1 experienced ductile failure after reaching the peak lateral strength; also, more failure mechanisms (e.g. LI, SL, RO, BF) were observed in specimen W6 than W1. According to [18], the primary failure mechanism governs the strength of a RMSW, while the secondary failure mechanism characterizes failure after the primary failure mechanism has been initiated, as illustrated in Fig. 1.

## 3 Review of Experimental Research on Slender RMSWs

### 3.1 Summary of Database

Important parameters influencing the behaviour of TRM shear walls have been identified by performing a review of past experimental research studies. In total, 66 wall specimens from 12 experimental studies [2–6, 12, 16, 17, 19–21, 23] were selected based on the following criteria: (i) shear span ratio ($M/Vl_w$) higher than 1.5, (ii)
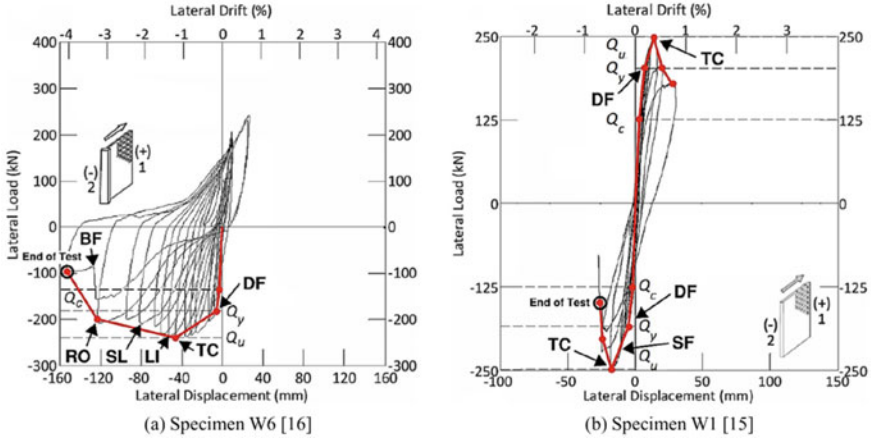
**Fig. 1** Hysteresis loops and failure sequence of RMSWs [18]

ductile failure mode (DF) as the primary failure mechanism, and (iii) reversed cyclic testing until the failure (drift ratio corresponding to 80% maximum lateral strength). Out of the selected specimens, 40 specimens do not have boundary elements (BEs) and 26 have boundary elements. Detailed information related to these specimens is summarized in Appendices 1 and 2. Only six specimens tested by Aly and Galal [3, 4] had applied additional bending moment at the top. Specimen W10 has a shear span ratio of 3.5, while specimens W7, 8, 9, 11, and 12 have a shear span ratio of 7.0. The remaining specimens were tested with cantilever boundary conditions; hence, the aspect ratios were equal to the shear span ratios. Note that the dimensions are shown in Fig. 2. $b$ denotes as the width of compression zone, which is equal to $t_w$ for rectangular cross-sections and $t_{BE}$ for cross-sections with BEs. $\rho_{BE}$ represents the ratio of flexural reinforcement area and the gross cross-sectional area of a BE ($\rho_{BE} = A_{s,BE}/A_{BE}$). The analytical parameter, depth of the neutral axis, $c$, is calculated by Eq. 3a for rectangular sections without BEs, and Eq. 3b for sections having BEs [8].

$$\frac{c}{l_w} = \frac{\omega + \alpha}{2\omega + 0.68},$$

$$\text{where } \omega = \frac{\phi_s f_y}{\phi_m f'_m} \rho_v; \alpha = \frac{P}{\phi_m f'_m A_g} \qquad (3a)$$

$$\frac{c}{l_w} = \frac{a}{\beta_1 l_w}$$

$$a = \frac{P + \phi_s f_{yv} A_d}{t_{BE} 0.85 \phi_m f'_m} \quad \text{for} \quad c \le l_{BE};$$

$$a = \left( \frac{P + \phi_s f_y A_d}{0.85 \phi_m f'_m} - A_{BE} \right)$$
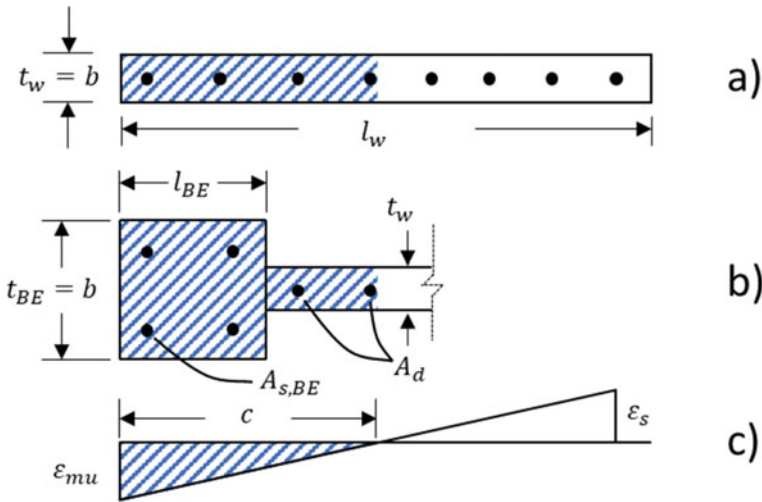
**Fig. 2** Dimensions of **a** rectangular cross-section, **b** wall cross-section with BE, and **c** strain distribution

$$\times \frac{1}{t_{\mathrm{w}}} + l_{\mathrm{BE}} \quad \text{for} \quad c > l_{\mathrm{BE}}, \tag{3b}$$

where $\beta_1$ is taken as 0.8; $\phi_s$ and $\phi_m$ are taken as 1.0; $l_{\mathrm{BE}}$ is the length of boundary elements; $A_{\mathrm{d}}$ is the total area of distributed vertical wall reinforcement; $A_{\mathrm{BE}}$ is the gross cross-sectional area of a BE.

Figure 3 shows histograms of design parameters for selected specimens. Limited field applications of TRM buildings in Canada can be partially attributed to scarcity of past experimental research studies on ductile RMSW specimens with dominant flexural behaviour, and aspect ratio higher than 2.0. Majority of Canadian experimental research studies were performed on ductile RMSWs with a rectangular cross-section [12, 17, 19, 20, 21, 23]. Figure 3d shows that most research studies related to seismic behaviour of RMSWs were focused on testing fully grouted (FG) specimens. Research evidence on partially grouted (PG) RMSWs is very limited [23]. Only 3 slender RMSW specimens are reported in this paper. Figure 3f indicates that most research were focused on the low axial stress level which is not representative of TRM buildings. It can be observed by comparing Fig. 3f, g that adding boundary element to RMSWs will significantly reduce $c/l_{\mathrm{w}}$, because the level of axial stress level in walls with or without BEs is similar, while RMSWs with BEs significantly lower $c/l_{\mathrm{w}}$ values than walls without BEs.
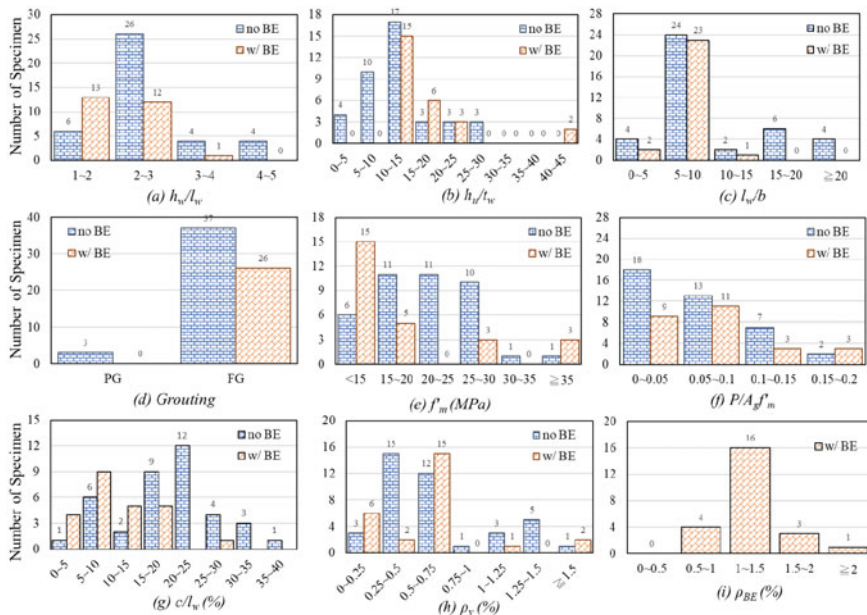
**Fig. 3** Histograms of selected test specimens presented in Appendix 1 and 2

## 3.2 Key Design Parameters Effecting the Lateral Drift Capacity of RMSWs

Key design parameters, as shown in Table 1, have been selected based on the review of Canadian code (CSA S304-14) and previous research [1, 18, 20, 21] to examine the influence on the lateral drift capacity of RMSWs. The correlation coefficient of these parameters with respect to both the ultimate lateral drift capacity ($\delta_u$) and the ductility of RMSWs ($\mu$) for specimen with and without BEs is shown in Table 1.

Based on the correlation coefficients presented in Table 1, the following key parameters are expected to affect the lateral drift capacity of RMSWs with rectangular cross-sections more significantly: (i) the aspect ratio $A_R$, (ii) depth of neutral axis to width of the compression zone ratio $c/b$, and (iii) wall length to width of the compression zone ratio $l_w/b$. It was observed that the depth of neutral axis to wall length ratio $c/l_w$ is not correlated to the drift capacity, but it is positively correlated to the wall ductility. However, for RMSWs with BEs, none of the investigated parameters appeared to have significant impact on the wall's lateral drift capacity and ductility. The limited test results of RMSWs with BEs of varying sizes, shapes (flanged or barbell shaped), and detailing make the seismic behaviour more complicated, causing difficulty to identify and quantify the impact of various design parameters. For RMSWs with BEs, there is no correlation between lateral drift capacity

**Table 1** Correlation coefficients, $R$, for design parameters, $\delta_u$ and $\mu$

| Correlation coefficient | | $\frac{h_w}{l_w}$ | $\frac{h_u}{l_w}$ | $\frac{c}{b}$ | $\frac{l_w}{b}$ | $\frac{V_{peak}}{A_g\sqrt{f'_m}}$ | $\frac{P}{A_g f'_m}$ | $\rho_v$ | $\rho_h$ | $\frac{c}{l_w}$ | $\frac{l_w c}{b^2}$ | $\delta_u$ | $\mu$ |
|---|---|---|---|---|---|---|---|---|---|---|---|---|---|
| RMSWs w/o BEs | $R_{\delta_u}$ | 0.65 | − 0.59 | − 0.64 | − 0.73 | − 0.46 | 0.24 | − 0.36 | − 0.30 | − 0.13 | − 0.54 | 1.00 | 0.37 |
| | $R_\mu$ | 0.07 | − 0.03 | − 0.48 | − 0.19 | − 0.57 | − 0.09 | − 0.54 | − 0.17 | − 0.67 | − 0.43 | 0.37 | 1.00 |
| RMSWs with BEs | $R_{\delta_u}$ | − 0.42 | 0.32 | 0.21 | 0.15 | − 0.17 | 0.15 | − 0.25 | − 0.44 | 0.20 | − 0.41 | 1.00 | 0.38 |
| | $R_\mu$ | − 0.42 | 0.00 | 0.03 | 0.34 | − 0.22 | 0.13 | − 0.47 | − 0.37 | − 0.11 | 0.05 | 0.38 | 1.00 |

and wall ductility, but these walls have higher ductility in the experimental database as shown in Fig. 5a.

Figure 4 shows the key parameters affecting the lateral drift capacity of TRM walls. The definition of lateral drift capacity $\delta_u$ is the drift corresponding to the 80% maximum capacity of walls. Figure 4a shows that the aspect ratio ($h_w/l_w$) is positively correlated with the drift capacity. The behaviour of RMSWs with higher aspect ratios is not governed by the diagonal shear failure and shear-flexure failure; hence, the drift capacity is larger. On the other hand, Fig. 4b, d shows a negative correlation between length to width of the compression zone ratio ($l_w/b$), unsupported height to thickness ratio ($h_u/t_w$), and drift capacity. Robazza et al. [17] indicated that RMSWs with higher $l_w/t_w$ and $h_u/t_w$ ratios may experience lateral instability (LI) failure at relatively small drift levels. As discussed before, depth of neutral axis to width of the compression zone ratio $c/b$ was shown to be negatively correlated with the drift capacity, and a clear trend can be seen in Fig. 4c.

Figure 4e shows the correlation between axial stress ($P/A_g f'_m$) and drift capacity. Based on the results shown, the trend for the axial stress and drift capacity is not clear. However, if all other parameters are kept the same, in this case the test data from [2, 16, 17], Banting and El-Dakhakhni (2019) are selected and presented in Fig. 4f. The result shows that a clear reduction in the drift capacity as the axial stress increases. It can be seen by comparing Fig. 4c, e that the influence of axial stress can be better evaluated using the parameter, $c/b$, because that parameter $c/b$ implicitly accounts for a complicated interaction between the axial stress, material strength and stiffness,
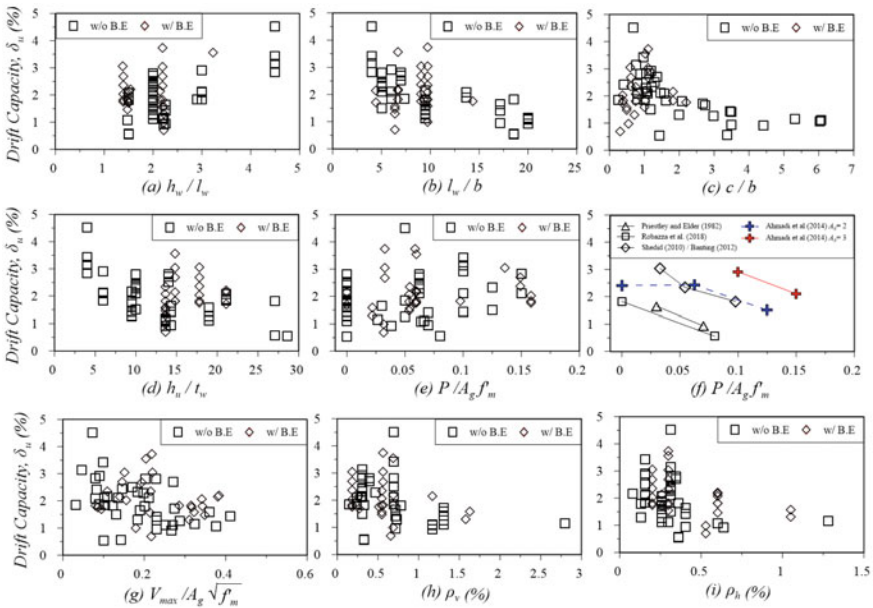


**Fig. 4** Effect of various design parameters on the ultimate drift capacity of RMSWs
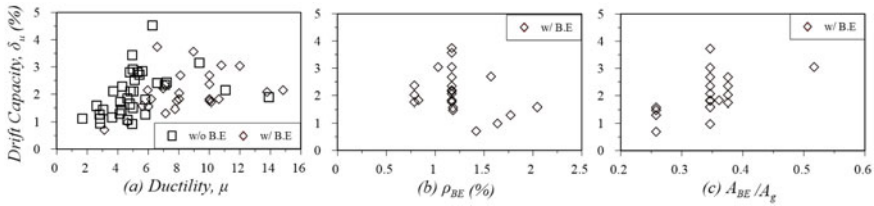
**Fig. 5** Effect of boundary elements on the ultimate drift capacity of RMSWs with and without BEs

and reinforcement layout. It should be note that it is expected that the RMSW in TRM buildings will have high axial stress due to the presence of the gravity load. On the other hand, the experimental data for RMSW with axial stress (higher than $0.1 f'_\mathrm{m}$) is limited. Hence, more research of RMSW with high axial stress is needed for TRM building research.

It can be seen from Fig. 4g that the level of wall shear stress is another important parameter affecting the drift capacity of RMSWs. Furthermore, it can be observed that among the specimens subjected to similar shear stress level, drift capacities are higher for specimens with BEs. The higher the shear stress, the lower the drift capacity. Figure 4h, i presents a slightly negative correlation between the vertical reinforcement ratio $\rho_\mathrm{v}$, the horizontal reinforcement ratio $\rho_\mathrm{h}$, and the drift capacity. Higher $\rho_\mathrm{v}$ prevents RMSWs from sliding failure and results in higher flexural strength of RMSWs but may cause brittle compression-controlled flexural failure mechanism, reducing the wall drift capacity. It is critical to control longitudinal reinforcement to achieve desired high drift capacity in RMSWs.

### 3.3 Impact of Design Parameters on the Drift Capacity of RMSWs with Boundary Elements

Figure 5a indicates that specimens with BEs generally have higher ductility, roughly higher than 6, except two specimens tested by El-Azizy [12]. The two specimens were designed with lower $\rho_\mathrm{v}$ and $\rho_\mathrm{h}$ values, had flanged section and barbell-shaped section, respectively. Concentrated damage was observed at two corners at the wall end zones, resulting in strength degradation at an early stage. Table 2 summarizes correlation coefficients of other parameters related to RMSW with BEs. Note that none of these parameters have shown significant influence on the drift capacity and ductility. Figure 5b, c shows that the longitudinal reinforcement ratio in the boundary elements $\rho_\mathrm{BE}$ is negatively correlated, and the area ratio of boundary elements $A_\mathrm{BE}/A_\mathrm{g}$ is positively correlated with the drift capacity. It is expected that, different shapes, detailing, confinement level, and layout of BEs affect the drift capacity [5] and Banting and El-Dakhakhni (2014), but the impact of these parameters cannot be easily quantified, as shown in Fig. 4e, f.

**Table 2**  Correlation coefficients, $R$, for BE related design parameters, $\delta_\mu$ and $\mu$

| RMSWs with BEs | $\rho_{BE}$ | $\dfrac{\rho_{BE}}{\rho_v}$ | $\dfrac{t_{BE}}{t_w}$ | $\dfrac{A_{BE}}{A_g}$ |
|---|---|---|---|---|
| Correlation coefficient, $R_{\delta_u}$ | − 0.30 | 0.38 | − 0.41 | 0.57 |
| Correlation coefficient, $R_\mu$ | − 0.39 | − 0.76 | 0.05 | 0.49 |

## 4  Prediction of Ultimate Drift Capacity of RMSW Without Boundary Elements

Aspect ratio and combined slenderness parameter show the best correlation to the ultimate drift capacity. In this study, these two key parameters were used to construct an empirical equation to predict the lateral drift capacity of RMSWs without boundary elements. Equation 4 shows the results obtained from linear regression analyses using the database provided on Appendix 1.

$$\delta_u(\%) = 1.16 + 0.48\frac{h_w}{l_w} - 0.012\frac{l_w c}{b^2}. \tag{4}$$

The left-hand side of Eq. 4 represents the ultimate lateral drift capacity of the RMSWs, which is defined as the drift at 80% of the lateral load capacity. The right-hand side of Eq. 4 consists of term related to the aspect ratio ($h_w/l_w$) and the combined slenderness parameter ($l_w c/b^2$). The first term represents the influence of wall geometry, and the second term represents the influence of axial load, geometry of the cross-section and the amount of longitudinal wall reinforcement on the ultimate drift capacity.

Equation 4 firstly implies that an increase in the aspect ratio may result in an increase in the ultimate drift capacity. Secondly, the equation indicates that the drift capacity $\delta_u$ has a negative correlation with the combined slenderness parameter ($l_w c/b^2$). The combined slenderness parameter can be reduced by: (i) reducing the axial load, which will make $c$ smaller, (ii) increasing the compressive masonry strength $f'_m$, which will reduce $c$ as well, (iii) increasing the block thickness, which will reduce $c$ and increase the $b$ at the same time. An additional benefit from reducing compression zone depth $c$ is to avoid the brittle compression-controlled flexural failure mechanism, thereby resulting in a higher wall ductility.

Figure 6 shows the experimental versus the predicted drift capacities. The result shows that the predicted result matches the experimental data very well with mean and the coefficient of variation (COV) are 1.02 and 0.32, respectively.

**Fig. 6** Effect of boundary elements on the ultimate drift capacity of RMSWs without boundary element
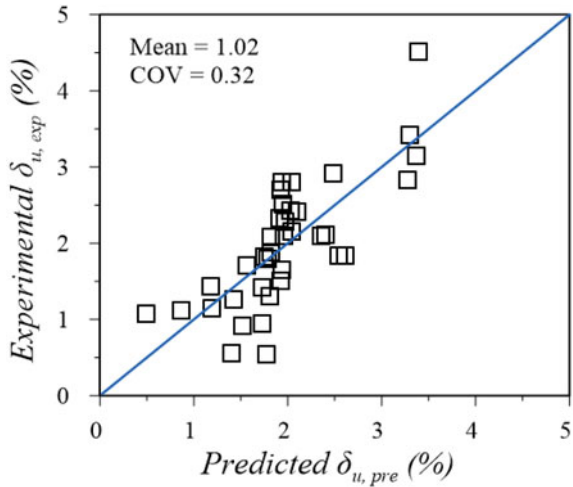


## 5 Conclusion

A review of experimental research studies on RMSWs with flexure-dominant behaviour is presented in the paper. The results of previous experimental studies indicate that the axial aspect ratio ($h_w/l_w$), depth of neutral axis to width of the compression zone ratio ($c/b$), and wall length to width of compression zone ratio ($l_w/b$) are important parameters affecting the behaviour and drift capacity of RMSWs. None of the parameters are found to significantly affect drift capacity of RMSWs with boundary elements. However, provisions of boundary elements in RMSWs increases their ductility and enhance overall seismic performance. The test results showed that the ductility of 6 or higher can be seen in RMSWs with BEs. An empirical equation is proposed to predict the ultimate drift capacity of RMSWs without boundary elements using aspect ratio and a combined slenderness parameter. The result shows the equation can effectively predict the ultimate drift capacity of RMSWs without boundary elements.

## Notations

$V_r =$      shear capacity of GFRP RC beam
$V_c =$      shear strength provided by concrete
$V_s =$      shear strength provided by FRP shear reinforcement
$f'_c =$      concrete compressive strength

$f_{cr} =$      concrete cracking strength
$\epsilon_x =$      mid-depth strain
$M_f =$      factored moment at critical shear section
$V_f =$      factored shear at the critical shear section
$d =$      effective depth of beam cross-section
$d_v =$      effective shear depth
$b_w =$      beam width
$h =$      beam overall depth
$E_f =$      elastic modulus of longitudinal FRP straight bar reinforcement
$A_f =$      area of longitudinal FRP reinforcement
$A_{fv} =$      area of FRP shear reinforcement
$f_{fv} =$      usable stress for the FRP stirrups
$f_{fu} =$      ultimate strength of FRP straight bars
$\theta =$      Angle of compression
$s =$      spacing of stirrups
$s_{xe} =$      crack spacing
$r =$      bend radius
$\rho_f =$      reinforcement ratio
$n_f =$      modular ratio
$k =$      ratio of depth of neutral axis to effective depth

## Appendix 1: Experimental Database of RMSW Specimens Without Boundary Elements

| ID | Geometry | | | | Material (MPa) | | | Detailing (%) | | | Experimental results | | | |
|---|---|---|---|---|---|---|---|---|---|---|---|---|---|---|
| | $h$ (cm) | $\frac{h}{l_w}$ | $\frac{h_w}{t_w}$ | $\frac{l_w}{t_w}$ | $f'_m$ | $f_{yv}$ | $f_{yh}$ | $\rho_v$ | $\rho_h$ | $\frac{P}{A_g f'_m}$ | $V_{peak}$ (kN) | $\delta_u$ (%) | $\mu$ | PF/SF |
| Priestley and Elder [16] | | | | | | | | | | | | | | |
| Wall 1 | 540 | 2.3 | 14.3 | 10.5 | 26.9 | 434 | 322 | 0.72 | 0.40 | 7 | 323 | 0.90 | 2.8 | DF/TC |
| Wall 2 | 540 | 2.3 | 14.3 | 10.5 | 26.9 | 434 | 322 | 0.72 | 0.40 | 7 | 326 | 1.30 | 4.3 | DF/SL |
| Wall 3 | 540 | 2.3 | 14.3 | 10.5 | 26.9 | 434 | 322 | 0.72 | 0.40 | 3 | 268 | 1.60 | 4.8 | DF/TC |
| Shedid et al. [23] | | | | | | | | | | | | | | |
| Wall 1P | 360 | 2.0 | 19.0 | 9.5 | 15.2 | – | – | 1.31 | 0.26 | 0 | 274 | 0.60 | 1.7 | DF/TC |
| Wall 2P | 360 | 2.0 | 19.0 | 9.5 | 15.2 | – | – | 1.31 | 0.26 | 0 | 360 | 1.30 | 2.6 | DF/TC |
| Wall 3P | 360 | 2.0 | 19.0 | 9.5 | 15.2 | – | – | 0.73 | 0.13 | 0 | 242 | 1.80 | 5.8 | DF/TC |
| Shedid et al. [20] | | | | | | | | | | | | | | |
| 1 | 360 | 2.0 | 9.5 | 9.5 | 14.8 | 502 | 491 | 0.29 | 0.08 | 0 | 143 | 2.15 | 11.1 | DF/TC |
| 2 | 360 | 2.0 | 9.5 | 9.5 | 14.8 | 502 | 491 | 0.78 | 0.13 | 0 | 265 | 1.80 | 5.8 | DF/TC |
| 3 | 360 | 2.0 | 9.5 | 9.5 | 14.8 | 502 | 491 | 0.73 | 0.13 | 0 | 242 | 1.30 | 4.1 | DF/TC |
| 4 | 360 | 2.0 | 9.5 | 9.5 | 14.8 | 502 | 491 | 1.31 | 0.26 | 0 | 360 | 1.51 | 4.2 | DF/TC |
| 5 | 360 | 2.0 | 9.5 | 9.5 | 14.8 | 502 | 491 | 1.31 | 0.26 | 5 | 377 | 1.31 | 2.8 | DF/TC |
| 6 | 360 | 2.0 | 9.5 | 9.5 | 14.8 | 624 | 491 | 1.31 | 0.26 | 10 | 541 | 1.73 | 3.1 | DF/TC |
| Shedid et al. [21] | | | | | | | | | | | | | | |
| W1 | 399 | 2.2 | 13.7 | 20.0 | 16.4 | 495 | 534 | 1.17 | 0.30 | 7 | 177 | 1.11 | 2.8 | DF/TC |
| W4 | 266 | 1.5 | 13.7 | 20.0 | 16.4 | 495 | 534 | 1.17 | 0.60 | 6 | 265 | 1.07 | 4.7 | DF/TC |
| Ahmadi et al. [2] | | | | | | | | | | | | | | |
| WSU-W-01A | 203 | 2.0 | 10.0 | 5.0 | 19 | 456 | 456 | 0.70 | 0.31 | 6 | 183 | 2.80 | 5.3 | – |
| WSU-W-01B | 203 | 2.0 | 10.0 | 5.0 | 21 | 446 | 446 | 0.70 | 0.31 | 6 | 201 | 2.10 | 4.8 | – |

(continued)

(continued)

| ID | Geometry | | | | Material (MPa) | | | Detailing (%) | | | Experimental results | | | |
|---|---|---|---|---|---|---|---|---|---|---|---|---|---|---|
| | $h$ (cm) | $\frac{h}{l_w}$ | $\frac{h_u}{l_w}$ | $\frac{l_w}{t_w}$ | $f'_m$ | $f_{yv}$ | $f_{yh}$ | $\rho_v$ | $\rho_h$ | $\frac{P}{A_g f'_m}$ | $V_{peak}$ (kN) | $\delta_u$ (%) | $\mu$ | PF/SF |
| WSU-W-02A | 203 | 2.0 | 10.0 | 5.0 | 19 | 456 | 456 | 0.31 | 0.31 | 13 | 166 | 2.33 | 7.1 | – |
| WSU-W-02B | 203 | 2.0 | 10.0 | 5.0 | 21 | 450 | 450 | 0.31 | 0.31 | 13 | 124 | 1.50 | 5.0 | – |
| UT-W-13 | 366 | 3.0 | 6.0 | 6.0 | 31 | 421 | 421 | 0.70 | 0.16 | 5 | 142 | 1.84 | 4.7 | – |
| UT-W-14 | 366 | 3.0 | 6.0 | 6.0 | 23 | 448 | 448 | 0.31 | 0.16 | 10 | 108 | 2.91 | 5.0 | – |
| UT-W-15 | 366 | 3.0 | 6.0 | 6.0 | 23 | 421 | 421 | 0.70 | 0.16 | 10 | 160 | 2.11 | 3.7 | – |
| UT-W-16 | 366 | 3.0 | 6.0 | 6.0 | 23 | 448 | 448 | 0.31 | 0.16 | 15 | 121 | 2.10 | 5.0 | – |
| UT-W-17 | 366 | 4.5 | 4.0 | 4.0 | 29 | 421 | 421 | 0.70 | 0.31 | 5 | 64 | 4.51 | 6.3 | – |
| UT-W-18 | 366 | 4.5 | 4.0 | 4.0 | 29 | 448 | 448 | 0.31 | 0.31 | 10 | 42 | 3.14 | 9.4 | – |
| UT-W-19 | 366 | 4.5 | 4.0 | 4.0 | 23 | 421 | 421 | 0.70 | 0.16 | 10 | 78 | 3.42 | 5.0 | – |
| UT-W-20 | 366 | 4.5 | 4.0 | 4.0 | 23 | 448 | 448 | 0.31 | 0.16 | 15 | 63 | 2.83 | 5.6 | – |
| WSU-W-07 | 203 | 2.0 | 10.0 | 5.0 | 21 | 450 | 450 | 0.31 | 0.31 | 0 | 79 | 2.41 | 6.6 | – |
| WSU-W-08 | 203 | 2.0 | 10.0 | 5.0 | 21 | 455 | 455 | 0.31 | 0.31 | 6 | 139 | 2.43 | 7.2 | – |
| WSU-W-09 | 203 | 2.0 | 10.0 | 5.0 | 16 | 455 | 455 | 0.47 | 0.31 | 6 | 164 | 2.28 | 4.3 | – |
| WSU-W-31 | 284 | 2.0 | 14.0 | 7.0 | 16 | 465 | 465 | 0.70 | 0.16 | 0 | 196 | 2.51 | 5.1 | DF/SF |
| WSU-W-32 | 284 | 2.0 | 14.0 | 7.0 | 16 | 465 | 465 | 0.39 | 0.34 | 0 | 263 | 2.80 | 4.8 | DF/TC |
| WSU-W-33 | 284 | 2.0 | 14.0 | 7.0 | 16 | 465 | 465 | 0.39 | 0.34 | 6 | 313 | 2.70 | 5.4 | – |
| El-Azizy et al. [12] | | | | | | | | | | | | | | |
| W1 | 399 | 2.2 | 13.7 | 20.0 | 28 | 480 | 510 | 1.17 | 0.64 | 3.8 | 230 | 0.92 | 4.9 | DF/TC |
| W4 | 399 | 2.2 | 13.7 | 20.0 | 41 | 480 | 510 | 2.80 | 1.28 | 2.7 | 336 | 1.15 | 3.6 | DF/TC |
| Robazza et al. [17] | | | | | | | | | | | | | | |

(continued)

(continued)

| ID | Geometry | | | | Material (MPa) | | | Detailing (%) | | | Experimental results | | | |
|---|---|---|---|---|---|---|---|---|---|---|---|---|---|---|
| | $h$ (cm) | $\frac{h}{t_w}$ | $\frac{h_u}{l_w}$ | $\frac{l_w}{t_w}$ | $f'_m$ | $f_{yv}$ | $f_{yh}$ | $\rho_v$ | $\rho_h$ | $\frac{P}{A_g f'_m}$ | $V_{\text{peak}}$ (kN) | $\delta_u$ (%) | $\mu$ | PF/SF |
| W1 | 380 | 15 | 27.1 | 18.6 | 23.4 | 484 | 484 | 0.33 | 0.36 | 8 | 251 | 0.56 | – | DF/SF |
| W2 | 380 | 1.5 | 27.1 | 18.6 | 23.4 | 512 | 512 | 0.33 | 0.36 | 0 | 217 | 1.82 | – | DF/LI |
| W3 | 400 | 1.5 | 21.1 | 13.7 | 27.1 | 508 | 508 | 0.24 | 0.26 | 0 | 206 | 2.08 | – | DF/RO |
| W4 | 400 | 2.9 | 21.1 | 7.4 | 27.1 | 465 | 465 | 0.15 | 0.26 | 0 | 43 | 1.84 | – | DF/BF |
| W5 | 400 | 1.5 | 28.6 | 18.6 | 27.1 | 506 | 506 | 0.33 | 0.36 | 0 | 189 | 0.54 | – | DF/TC |
| Robazza et al. [19] | | | | | | | | | | | | | | |
| W8 | 400 | 1.5 | 21.1 | 13.7 | 26.4 | 499 | 499 | 0.24 | 0.26 | 0 | 225 | 1.88 | 13.9 | DF/TC |

*Notes* $h$—wall height, $l_w$—wall length, $h_u$—unsupported wall height, $t_w$—wall thickness, $f'_m$—masonry compressive strength, $f_{yv}$—yield strength of vertical reinforcement, $f_{yh}$—yield strength of horizontal reinforcement, $\rho_v$—area ratio of vertical reinforcement, $\rho_h$—area ratio of horizontal reinforcement, $P$—axial load, $A_g$—gross area of wall section, $V_{\text{peak}}$—maximum strength and $\delta_u$—drift at 0.8 $V_{\text{peak}}$ also denotes as the drift capacity, $\mu$—ductility, $^P$—Partially grouted, denotes that researchers did not report specific data

# Appendix 2: Experimental Database of RMSW Specimens with Boundary Elements

| ID | Geometry | | | | Material (MPa) | | | | Detailing (%) | | | | Experimental results | | | |
|---|---|---|---|---|---|---|---|---|---|---|---|---|---|---|---|---|
| | $h$ (cm) | $\frac{h}{l_w}$ | $\frac{h_u}{l_w}$ | $\frac{l_w}{t_w}$ | $f'_m$ | $f_{yv}$ | $f_{yh}$ | $f_{yBE}$ | $\rho_v$ | $\rho_h$ | $\rho_{BE}$ | $\frac{P}{A_g f'_m}$ | $V_{\text{peak}}$ (kN) | $\delta_u$ (%) | $\mu$ | PF/SF |
| Shedid et al. [21] | | | | | | | | | | | | | | | | |
| W2$^F$ | 399 | 2.2 | 13.7 | 6.4 | 16.4 | 495 | 534 | 495 | 0.55 | 0.3 | 1.18 | 5 | 151 | 1.56 | 6.0 | DF/BF |
| W3 | 399 | 2.2 | 13.7 | 9.7 | 16.4 | 495 | 534 | 495 | 0.55 | 0.3 | 1.17 | 5 | 152 | 2.34 | 7.1 | DF/TC |
| W5$^F$ | 266 | 1.5 | 13.7 | 6.4 | 16.4 | 495 | 534 | 495 | 0.55 | 0.6 | 1.18 | 5 | 245 | 1.47 | 7.7 | DF/BF |
| W6 | 266 | 1.5 | 13.7 | 9.7 | 16.4 | 495 | 534 | 495 | 0.55 | 0.6 | 1.17 | 5 | 241 | 1.81 | 10.6 | DF/TC |
| W7$^a$ | 266 | 1.5 | 13.7 | 9.7 | 16.4 | 495 | 534 | 495 | 0.55 | 0.6 | 1.17 | 5 | 240 | 2.07 | 13.8 | DF/TC |
| [5] | | | | | | | | | | | | | | | | |
| W1 | 399 | 2.2 | 14.8 | 9.7 | 13.7 | 496 | 583 | 496 | 0.56 | 0.3 | 1.17 | 3 | 143 | 3.04 | 12.0 | DF/BF |
| W2 | 399 | 2.2 | 14.8 | 9.7 | 13.7 | 496 | 583 | 496 | 0.56 | 0.3 | 1.17 | 3 | 126 | 2.68 | 8.1 | DF/TC |
| W3 | 399 | 2.2 | 14.8 | 9.7 | 13.7 | 496 | 583 | 496 | 0.56 | 0.3 | 1.17 | 3 | 141 | 3.73 | 6.6 | DF/TC |
| W4 | 399 | 2.2 | 14.8 | 9.7 | 13.7 | 496 | 583 | 496 | 0.56 | 0.3 | 1.17 | 10 | 203 | 1.82 | 10.0 | DF/TC |
| Banting and El-Dakhakhni (2014) | | | | | | | | | | | | | | | | |
| Wall 1 | 399 | 1.5 | 44.3 | 14.4 | 14.9 | 496 | 583 | 496 | 0.51 | 0.3 | 1.17 | 6 | 314 | 1.75 | 7.9 | DF/TC |
| Wall 2 | 399 | 3.2 | 14.8 | 6.7 | 14.9 | 496 | 583 | 496 | 0.69 | 0.3 | 1.17 | 6 | 94 | 3.56 | 9.0 | DF/BF |
| Wall 3 | 266 | 2.2 | 14.8 | 6.7 | 14.9 | 496 | 583 | 496 | 0.69 | 0.6 | 1.17 | 6 | 132 | 1.82 | 6.2 | DF/TC |
| Wall 4 | 266 | 2.2 | 14.8 | 6.7 | 14.9 | 496 | 583 | 496 | 1.17 | 0.6 | 1.17 | 6 | 176 | 2.15 | 6.0 | DF/TC |
| Wall 5 | 190 | 1.5 | 21.1 | 6.7 | 14.9 | 496 | 583 | 496 | 0.69 | 0.6 | 1.17 | 6 | 177 | 2.20 | 7.0 | DF/TC |
| El-Azizy et al. [12] | | | | | | | | | | | | | | | | |
| W2$^F$ | 399 | 2.2 | 13.7 | 6.4 | 28.3 | 510 | 510 | 480 | 0.66 | 0.53 | 1.42 | 3.2 | 187 | 0.70 | 3.1 | DF/TC |
| W3 | 399 | 2.2 | 13.7 | 9.7 | 36.4 | 480 | 510 | 420 | 0.69 | 0.53 | 1.64 | 3.2 | 176 | 0.98 | 4.6 | DF/TC |
| W5$^F$ | 399 | 2.2 | 13.7 | 6.4 | 41 | 510 | 510 | 480 | 1.58 | 1.05 | 1.77 | 2.2 | 322 | 1.30 | 7.1 | DF/TC |

(continued)

| ID | Geometry | | | | Material (MPa) | | | | Detailing (%) | | | | Experimental results | | | |
|---|---|---|---|---|---|---|---|---|---|---|---|---|---|---|---|---|
| | $h$ (cm) | $\frac{h}{l_w}$ | $\frac{h_u}{l_w}$ | $\frac{l_w}{t_w}$ | $f'_m$ | $f_{yv}$ | $f_{yh}$ | $f_{yBE}$ | $\rho_v$ | $\rho_h$ | $\rho_{BE}$ | $\frac{P}{A_g f'_m}$ | $V_{peak}$ (kN) | $\delta_u$ (%) | $\mu$ | PF/SF |
| W6 | 399 | 2.2 | 13.7 | 9.7 | 41 | 480 | 510 | 420 | 1.63 | 1.05 | 2.05 | 2.2 | 334 | 1.58 | 5.6 | DF/TC |
| Aly and Galal [3, 4] | | | | | | | | | | | | | | | | |
| W7 | 238 | 1.4 | 17.8 | 9.0 | 8.7 | 460 | 535 | 460 | 0.18 | 0.20 | 0.79 | 15 | 62 | 2.36 | 10.0 | DF/TC |
| W8 | 238 | 1.4 | 17.8 | 9.0 | 8.7 | 460 | 535 | 460 | 0.18 | 0.20 | 1.57 | 15 | 83 | 2.69 | 10.0 | DF/TC |
| W9 | 238 | 1.4 | 17.8 | 9.1 | 8.7 | 460 | 535 | 460 | 0.18 | 0.20 | 1.03 | 14 | 87 | 3.05 | 10.8 | DF/TC |
| W10 | 238 | 1.4 | 17.8 | 9.0 | 14.2 | 460 | 535 | 460 | 0.18 | 0.20 | 0.79 | 16 | 113 | 2.02 | 8.0 | DF/TC |
| W11 | 238 | 1.4 | 17.8 | 9.3 | 14.2 | 460 | 535 | 460 | 0.18 | 0.20 | 0.83 | 16 | 57 | 1.82 | 8.0 | DF/TC |
| W12 | 238 | 1.4 | 17.8 | 9.0 | 14.2 | 460 | 535 | 460 | 0.18 | 0.20 | 0.79 | 16 | 62 | 1.75 | 10.0 | DF/TC |
| Robazza et al. [19] | | | | | | | | | | | | | | | | |
| W6[b,T] | 400 | 1.5 | 21.1 | 13.7 | 26.4 | 505 | 505 | 505 | 0.27 | 0.26 | 0.54 | 0 | 241 | 1.70 | 10.1 | DF/LI |
| W7[T] | 400 | 1.5 | 21.1 | 13.7 | 26.4 | 507 | 507 | 507 | 0.27 | 0.26 | 0.54 | 0 | 355 | 2.15 | 14.8 | DF/SL |

*Notes* $f_{yBE}$—yield strength of flexural reinforcement in boundary elements

[a] With spiral lateral reinforcement, [b] asymmetrically loaded, [F] flanged cross-section, [T] T-shaped cross-section. The remaining specimens have a barbell-shaped cross-section.

# References

1. Abdullah S, Wallace J (2019) Drift capacity of RC structural walls with special boundary elements. ACI Struct J 116:183–194. https://doi.org/10.14359/51710864
2. Ahmadi F, Hernandez J, Sherman J, Kapoi C, Klingner RE, McLean DI (2014) Seismic performance of cantilever-reinforced concrete masonry shear walls. J Struct Eng 140(9):04014051. https://doi.org/10.1061/(ASCE)ST.1943-541X.0000941
3. Aly N, Galal K (2020a) Experimental investigation of axial load and detailing effects on the inelastic response of reinforced-concrete masonry structural walls with boundary elements. J Struct Eng 146(12):04020259. https://doi.org/10.1061/(ASCE)ST.1943-541X.0002842
4. Aly N, Galal K (2020) In-plane cyclic response of high-rise reinforced concrete masonry structural walls with boundary elements. Eng Struct 219:110771. https://doi.org/10.1016/j.engstruct.2020.110771
5. Banting BR, El-Dakhakhni WW (2012) Force- and displacement-based seismic performance parameters for reinforced masonry structural walls with boundary elements. J Struct Eng 138(12):1477–1491. https://doi.org/10.1061/(ASCE)ST.1943-541X.0000572
6. Banting BR, El-Dakhakhni WW (2014) Seismic performance quantification of reinforced masonry structural walls with boundary elements. J Struct Eng 140(5):04014001. https://doi.org/10.1061/(ASCE)ST.1943-541X.0000895
7. Banting BR, El-Dakhakhni WW (2014) Seismic design parameters for special masonry structural walls detailed with confined boundary elements. J Struct Eng 140(10):04014067. https://doi.org/10.1061/(ASCE)ST.1943-541X.0000980
8. Brzev S, Anderson DL (2018) Seismic design guide for masonry buildings, 2nd edn. Canadian Concrete Masonry Producers Association, Toronto, Ontario, Canada. www.ccmpa.ca
9. Corrêa MRS (2012) Masonry engineering in brazil: past development, current overview, future improvements. In: Proceedings of 15th international brick and block masonry conference, Florianópolis, Brazil
10. CSA S304-14 (2014) Design of masonry structures. Canadian Standards Association, Mississauga, ON, Canada
11. Drysdale RG, Hamid AA (2005) Masonry structures: behaviour and design, Canadian. Canada Masonry Design Centre, Mississauga, ON, Canada
12. El-Azizy OA, Shedid MT, El-Dakhakhni WW, Drysdale RG (2015) Experimental evaluation of the seismic performance of reinforced concrete structural walls with different end configurations. Eng Struct 101:246–263. https://doi.org/10.1016/j.engstruct.2015.06.042
13. El-Dakhakhni W, Ashour A (2017) Seismic response of reinforced concrete masonry shear-wall components and systems: state of the art. J Struct Eng 143(9):03117001. https://doi.org/10.1061/(ASCE)ST.1943-541X.0001840
14. Hamid A (2018) Masonry structures: behaviour and design, 4th edn. The Masonry Society, USA
15. NBCC (2015) National building code of Canada 2015. National Research Council, Ottawa, ON, Canada
16. Priestley MJN, Elder DM (1982) Cyclic loading tests of slender concrete masonry shear walls. Bull N Z Soc Earthq Eng 15(1):3–21. https://doi.org/10.5459/bnzsee.15.1.3-21
17. Robazza BR, Brzev S, Yang TY, Elwood KJ, Anderson DL, McEwen B (2018) Out-of-plane behavior of slender reinforced masonry shear walls under in-plane loading: experimental investigation. J Struct Eng 144(3):04018008. https://doi.org/10.1061/(ASCE)ST.1943-541X.0001968
18. Robazza BR, Brzev S, Yang TY, Elwood KJ, Anderson DL, McEwen B (2020) Seismic behaviour and design code provisions for predicting the capacity of ductile slender reinforced masonry shear walls. Eng Struct 222:110992. https://doi.org/10.1016/j.engstruct.2020.110992
19. Robazza BR, Yang TY, Brzev S, Elwood KJ, Anderson DL, McEwen W (2019) Response of slender reinforced masonry shear walls with flanged boundary elements under in-plane lateral loading: an experimental study. Eng Struct 190:389–409. https://doi.org/10.1016/j.engstruct.2019.04.035

20. Shedid MT, Drysdale RG, El-Dakhakhni WW (2008) Behavior of fully grouted reinforced concrete masonry shear walls failing in flexure: experimental results. J Struct Eng 134(11):1754–1767. https://doi.org/10.1061/(ASCE)0733-9445(2008)134:11(1754)
21. Shedid MT, El-Dakhakhni WW, Drysdale RG (2010a) Alternative strategies to enhance the seismic performance of reinforced concrete-block shear wall systems. J Struct Eng 136(6):676–689. https://doi.org/10.1061/(ASCE)ST.1943-541X.0000164
22. Shedid MT, El-Dakhakhni WW, Drysdale RG (2010) Characteristics of rectangular, flanged, and end-confined reinforced concrete masonry shear walls for seismic design. J Struct Eng 136(12):1471–1482. https://doi.org/10.1061/(ASCE)ST.1943-541X.0000253
23. Shedid M, Hamid AA, Drysdale RG (2005) Ductility of reinforced masonry shear walls and impact of incomplete grouting. In: Proceedings of 10th Canadian masonry symposium. Banff, Alberta
24. Wang FL, Zhang XC, Zhu F (2016) Research progress and low-carbon property of reinforced concrete block masonry structures in China. In: Proceedings of 16th international brick and block masonry conference. Padova, Italy

# Stress–Strain Behaviour of Boundary Elements in Reinforced Block Masonry Shear Walls Under Uniaxial Compression

**Miaoyuan Dou, Yu-Cheng Hsu, Svetlana Brzev, and T. Y. Yang**

**Abstract** Reinforced masonry shear walls (RMSWs) constructed using hollow concrete blocks are commonly used in medium-rise and high-rise reinforced masonry buildings. Past research has shown that RMSWs can be used as an effective seismic force resisting system (SFRS) as they can dissipate stable energy through ductile inelastic deformations. The seismic performance of RMSWs can be enhanced by special boundary elements, which are either barbell sections connected to the wall or integrated within the wall ends. The knowledge of stress–strain behaviour of boundary elements subjected to uniaxial compression is needed to accurately estimate the inelastic behaviour of RMSWs. This paper presents a detailed review of previous studies on boundary elements in RMSWs. The paper also presents an ongoing experimental programme performed by the authors, which includes testing of 4-course grouted reinforced block masonry prism specimens. The purpose of the testing programme is to study the effect of confinement on uniaxial strength and deformations in boundary elements. The influence of various parameters, including tie spacing, hook details, and grout strength on compressive strength and ultimate compressive strain of the prism specimens is investigated in the study.

**Keywords** Stress–strain relationship · Confinement · Reinforced masonry concrete blocks · Boundary elements

## 1 Introduction

Masonry is one of the oldest construction technologies, which has evolved from early applications of unreinforced stone and clay brickwork (i.e. the Parliament of Canada) to modern Reinforced Masonry (RM) construction. Masonry construction has several advantages: it is durable, requires minimal maintenance, and has superior fire and blast resistance compared to other construction materials and technologies.

M. Dou · Y.-C. Hsu · S. Brzev · T. Y. Yang (✉)
Department of Civil Engineering, The University of British Columbia, Kelowna, Canada
e-mail: yang@civil.ubc.ca

Moreover, masonry buildings are sustainable due to the low carbon emission associated with the masonry materials and excellent thermal performance of masonry walls. Compared to Reinforced Concrete (RC) shear walls, RM structural systems have lower costs, require less steel and concrete, and have less carbon emission [31, 37, 41].

In recent decades, the number of RM buildings in Canada has increased dramatically. However, only a few Tall Reinforced Masonry (TRM) buildings have been constructed. This includes a 24-storey TRM apartment building in Winnipeg, MB and a few 21-storey TRM apartment buildings in Hamilton, ON [10]. These applications are located in low to moderate seismicity. The only reported tall masonry application at a high seismic hazard site in Canada consists of three 16-storey unreinforced masonry buildings located in Vancouver, BC, which were constructed in the 1960s. Outside Canada, there are a few TRM buildings in countries such as the USA [13], Brazil [5], and China [41]. Currently, the [24] restricts the maximum height of masonry buildings with reinforced masonry shear walls (RMSWs) to 40 and 60 m at sites with high and moderate seismicity, respectively. The design is performed based on the provisions of Canadian masonry design standard CSA S304-14.

One of the solutions to enhance the seismic performance of RMSWs, in terms of strength and ductility, is by providing boundary elements that are commonly used in the seismic design of reinforced concrete shear walls (RCSWs). The effect of confinement in the RC members has been studied extensively [2, 23, 30]. CSA A23.3 contains provisions related to reinforcement within the compression end zones in ductile RC shear walls which details the end zones like confined concrete columns. The lateral reinforcement (ties) increase both the peak compressive concrete strength ($f_c'$) and ultimate compressive concrete strain ($\varepsilon_{cu}$) of the confined RC cores. Moreover, confinement can also improve the performance and resilience of RC members subjected to large seismic demand. Lateral confinement around vertical reinforcement also prevents vertical reinforcement from buckling under compressive loads.

Confinement can be achieved in RMSWs by adding boundary elements at wall ends. Reinforced masonry boundary elements (RMBEs) are provided to improve the ductility and strength of RMSWs. This reduces the depth of compression zone and enhanced the curvature capacity of RMSWs. The maximum masonry compressive strain ($\varepsilon_{mu}$), which is set at 0.0025 in CSA S304-14 could be increased if the boundary elements are detailed according to CSA S304-14 requirements. Proper confinement and design of the RMBEs are necessary to improve the overall seismic performance of the RMSWs. However, there are no specifications in the codes regarding the testing. In addition, there is only limited research evidence on the increased compression strain capacity with the addition of the boundary elements [1, 28]. Therefore, there is an urgent need to investigate, experimentally and analytically, the behaviour of RMBEs.

## 2 Maximum Applied Axial Compression Stress Ratio of RMSWs

### 2.1 CSA S304-14

The maximum axial compressive stress for Moderately Ductile RMSWs and Ductile RMSWs is not explicitly addressed by the CSA S304-14. Instead, the limit is represented in terms of the limitation of the ratio of the depth of neutral axis depth to the length of the wall ($c/l_w$) to ensure the enough rotational capacity within the plastic hinge region of RMSWs. The corresponding ductility verification in CSA S304-14 Cl.16.8.8 requires the inelastic rotation capacity ($\theta_{ic}$) to be greater than the inelastic rotational demand ($\theta_{id}$). Since the minimum inelastic rotational demand is defined as 0.003 for Moderately Ductile RMSWs and as 0.004 for Ductile RMSWs, the limitation of $c/l_w$ can be derived as Eqs. 1 and 2, respectively.

$$\frac{c}{l_w} \leq \frac{\varepsilon_{mu}}{0.01} \quad \text{(for Moderate Ductile RMSW)} \tag{1}$$

$$\frac{c}{l_w} \leq \frac{\varepsilon_{mu}}{0.012} \quad \text{(for Ductile RMSW)} \tag{2}$$

where $\varepsilon_{mu}$ should be taken as 0.0025 and the maximum $c/l_w$ ratio for Moderately Ductile RMSWs and Ductile RMSWs are 0.25 and 0.208, respectively. The relationship between maximum axial stress ratio ($P/f'_m A_g$) and $c/l_w$ ratio can be further derived according to [3]. Considering the case of steel yield stress $f_y = 400$ MPa (Steel Grade 400), the maximum axial stress levels for different values of vertical reinforcement ratio $\rho_v$, $c/l_w$ ratio, and maximum masonry compressive strength $f'_m$ are shown in Fig. 1. It can be observed that the permitted compressive stress ratio increases when $\varepsilon_{mu}$ and $f'_m$ increases. For the $\varepsilon_{mu}$ of 0.0025, CSA S304-14 explicitly implies that there are 8% and 10% limitations of axial compressive stress level for Ductile RMSWs and Moderately Ductile RMSWs, respectively. This limitation is set to ensure enough inelastic rotational capacity (i.e. ductility) of RMSWs. In addition, the higher $\varepsilon_{mu}$ can be achieved through confinement in the compression zone if boundary elements are used.

### 2.2 TMS 402/602-16

The limitation of axial compressive stress for RMSWs is implicitly defined in terms of the maximum vertical reinforcement ratio, $\rho_{max}$. For example, TMS 402/602-16 (9.3.3.2) prescribes $\rho_{max}$ for fully grouted RMSWs with only concentrated tension reinforcement as follows:
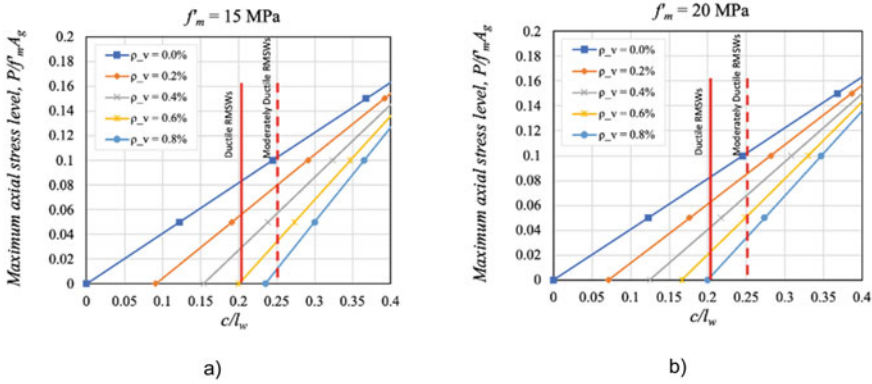
**Fig. 1** Maximum axial compression stress level for different $c/l_w$ values, longitudinal reinforcement ratio $\rho_v$, and masonry compressive strength $f'_m$: **a** $f'_m = 15$ MPa and **b** $f'_m = 20$ MPa

$$\rho_{max} \leq \frac{0.64 f'_m \left( \frac{\varepsilon_{mu}}{\varepsilon_{mu} + \alpha \varepsilon_y} \right) - \frac{P}{A_g}}{f_y} \tag{3}$$

where $\alpha$ is the strain factor, which can be taken as 4 for specially reinforced walls; $\varepsilon_y$ is the yield strain of steel; $P$ is the axial compressive force; $A_g$ is the gross area of the wall section, and $f_y$ is the yield stress of steel.

The above equation implies that axial compressive stress ($P/f'_m A_g$) limit decreases when vertical reinforcement ratio ($\rho_{max}$) increases. The relationships for different $\varepsilon_{mu}$ and $f'_m$ values for $f_y = 400$ MPa are plotted in Fig. 2. It can be observed that the maximum axial compressive stress level increases significantly with higher $\varepsilon_{mu}$, and $f'_m$ also provides positive influence on the maximum applicable axial compressive stress of sections with a certain longitudinal reinforcement ratio. For the minimum $\rho_v$ of 0.07% prescribed in TMS 402/602-16, the corresponding maximum compressive stress limit can be found as 14% for the sections with masonry compressive strength $f'_m = 15$ MPa.

## 2.3 Discussion

CSA S304-14 and TMS 402/602 implicitly propose the limitation of axial stress for RMSWs. The limitations are 8% and 10% for two different RMSWs defined in S304-14, and 14% for special RMSWs defined in TMS 402/602. However, TRM buildings require RMSWs to resist higher axial stress due to the higher gravity load and earthquake lateral forces. To reduce the stress in the RMSW, additional boundary elements have been proposed for RMSWs. Boundary elements enable confinement of the grouted masonry core, resulting in higher maximum compressive strain ($\varepsilon_{mu}$) and
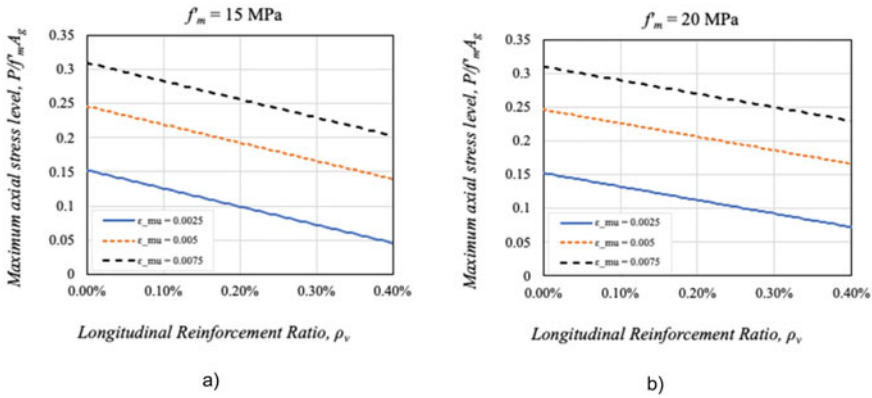
**Fig. 2** Maximum axial compressive stress versus longitudinal reinforcement ratio for different values of $f'_m$ and maximum masonry compressive strain $\varepsilon_{mu}$ (TMS 402/602-16): **a** $f'_m = 15$ MPa and **b** $f'_m = 20$ MPa

higher compressive strength ($f'_m$), which will increase the inelastic rotational capacity of RMSWs from the perspective of code design provisions. However, compressive stress–strain relationship of confined concrete masonry in boundary elements needs to be studied to serve as the basis for seismic analysis and design of RMSWs with boundary elements.

## 3 Review of Experimental Research on Reinforced Masonry Boundary Elements

### 3.1 Steel Plates

One of the first confinement schemes for end zones of RMSWs was in the form of steel plates embedded in bed joints of boundary elements [21, 22, 33]. The tests showed that the plates were effective in preventing splitting and spalling associated with the compressive failure at the toe of the wall, leading to improvement in the inelastic behaviour by making the most use of the longitudinal reinforcement. Further investigations show that confining plates could modify the failure mechanism and improve the ductility of the RMSWs. Average stress–strain curves obtained from the test programme agreed well with a modified form of the Kent-Park curve for confined reinforced concrete prisms. However, the peak strength was almost not influenced by the confining plates [32]. Provision of confining plates is permitted by the New Zealand masonry design code (NZS 4230:2004) with the masonry ultimate compression strain ($\varepsilon_{mu}$) of 0.008 to assess the ductility of RMSWs.

An experimental study including 114 RM prisms evaluated seven different confining methods, including lateral ties placed in cells around a single longitudinal bar used in the centre, steel confining plates placed in the bed joints, steel confining combs placed in the bed joints, steel mesh in the bed joints, and various circular or spiral ties around four longitudinal bars. The confining techniques had no significant influence on the peak strength or the corresponding strain of the masonry elements but could elongate the post-peak progress thus increasing the ultimate strain and ductility capacity [14, 15, 35].

Another proprietary method, named self-reinforced concrete block, proposes reinforcement cages around the cells to provide lateral confinement to the enclosed volume of block and grout material. Due to the presence of the confining elements within the block, the plasticity of the member improved significantly [18]. Welded wire mesh, polymer fibres, steel confinement plates, and seismic reinforcement combs are also effective techniques to increase the masonry compressive strain capacity and, thereby, improve ductility [8, 17, 39].

Although these techniques could efficiently increase the masonry compressive strain and ductility capacity, none of them has been adopted in North American masonry practice. These provisions were not able to provide lateral support to vertical bars. As a result, the longitudinal reinforcing bars would buckle easily and could not sustain high compressive stresses.

## 3.2    Reinforced Masonry Boundary Elements

An alternative approach that mimics boundary elements of RC shear walls was developed to overcome these limitations. Masonry boundary elements are sufficiently large to accommodate two layers of reinforcement (similar to pilasters). At least four longitudinal reinforcing bars with lateral ties are provided at each end of the RMSWs [38].

Ductile RMSWs with column-like boundary elements have been introduced in North American masonry design standards to enhance the ductility of walls. CSA S304-14 states that testing and analysis are required to prove that the proposed confining method can satisfy the necessary requirements for the strain and ductility requirement of the wall when the maximum masonry compressive strain is greater than the maximum strain prescribed by the code. Current American masonry design code TMS 402/602-16 requires that testing be done to verify that the detailing provided is capable of developing a strain capacity in the boundary element that would be in excess of the maximum strain set by the standard. Extensive tests need to be conducted to develop prescriptive detailing requirements for specially confined boundary elements of RMSWs.

There is a need to assess the performance and ductility capacity of confined boundary elements by experiments and analysis. There are many factors that will influence the behaviour of boundary elements, including grout strength, various confinement configurations.

### 3.2.1 Influence of Grout

Since grouting of the block cores increases their cross-sectional area significantly, the load-bearing capacity of masonry members is expected to increase substantially due to grouting. However, a considerable amount of research has shown that increasing the grout strength does not result in increase in the masonry prism compressive strength significantly [9, 27, 43]. Zorainy et al. [43] found that tripling the grout core compressive strength from 15 to 45 MPa, increased the BE's compressive strength by 50%. Similar test results performed by [27] showed that the BE's compressive strength increased by approximately 27% and 49% as the grout strength increased from 15 to 45 MPa for BE having a longitudinal reinforcement ratio of 0.8 and 1.4%, respectively.

The compressive strength of grouted masonry could be smaller than ungrouted masonry [9, 12, 19]. Although the compressive strength of prisms increased uniformly with the increase of grouting concrete strength, the grouted prisms have lower strength compared to the hollow ones (unless very high-strength grout is used), as shown in Fig. 3.

The superposition strength for masonry units (SH-0-5) and grout (GC-N-5-A) fails to capture the actual strength and post-peak behaviour of the prism (BE-N-5), as shown in Fig. 4 [43]. This could be attributed to five main reasons: (1) material incompatibility; (2) effects of block geometry; (3) bond pattern geometry; (4) initial plastic shrinkage; (5) flaws of grout and drying shrinkage. Material incompatibility means that the stress–strain behaviour of masonry units, grout and mortar is different. The grout acts as a wedge inside the masonry, weakening the masonry strength. In the case of running-bond pattern, the webs of blocks do not align vertically which leads
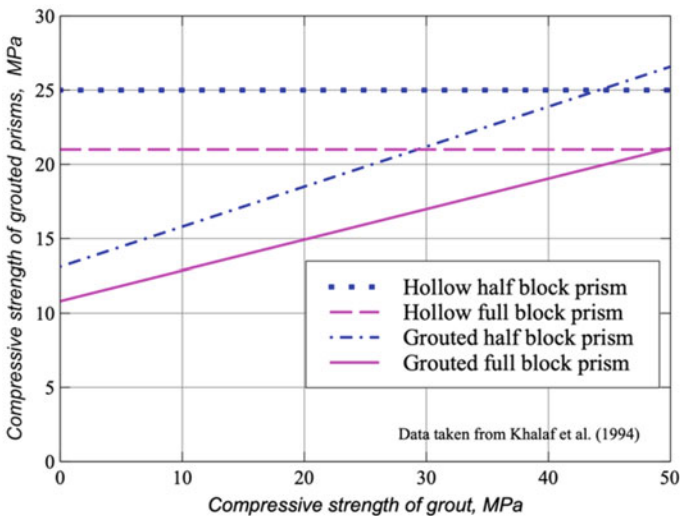


**Fig. 3** Grouted prism strength versus grout strength [19]
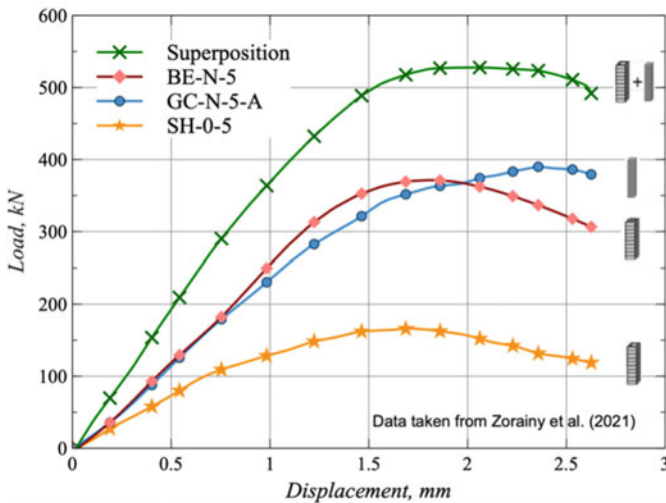
**Fig. 4** Comparison of the load–displacement relationships of hollow masonry prisms, grouted prisms, and their superposition [43]

to sudden changes in the centroids of the grout. Discontinuities and irregularities in the grout could reduce the compressive strength of masonry members. Another reason is the voids in the grouted masonry specimens. When fluid grout is poured into the cells, water is gradually absorbed by blocks, resulting in shrinkage of grout and separation between grout and masonry units. These flaws can be observed at the bed joint location where nonaligned webs cause obstruction to the uniform flow of grout during consolidation. As concrete with high water content shrinks, internal stresses between grout and masonry blocks could introduce negative effects on strength superposition [9, 10, 12, 16, 20, 27, 34, 43]. Several researchers suggested that the highest compressive strength could be attained when the deformation characteristics (such as stiffness and Poisson's ratio) of block and grout were similar [9, 19, 36], however [19] reported that higher strength could be attained when the grout strength (based on testing of cube specimens) was by 45–50% higher than that of the concrete block.

The effect of fine or coarse grout on the compressive strength of grouted concrete block masonry was investigated by [40]. Fine and coarse grout with different strengths were used. Test results show that coarse grout is more effective than fine grout in increasing the compressive capacity of grouted masonry.

### 3.2.2 Influence of Confinement Detailing

Various studies have been carried out to assess the influence of confinement detailing on the behaviour and compressive strength of BEs.

El Ezz et al. [11] conducted axial compression tests on 17 full-scale unconfined and confined masonry BE columns with different bar sizes (10 and 20 M) and tie spacing (100 and 200 mm), resulting in various confinement reinforcement ratios. The influence of the confinement ratio variation (0.008–0.038%) on the compressive behaviour and the strain capacity of BEs was investigated. The results showed that the confining effect on the compressive strength and ductility capacity was significant. The compressive strength of the confined BEs was 1.6–2.4 times higher than that of the unconfined ones, whereas the strain of the confined boundary elements at 50% strength degradation showed an increase, ranging from 2.2 to 7 times compared to that of the unconfined BEs. With the increasing confinement ratio, higher strain ductility was achieved with softening of the post-peak branch of the stress–strain curve.

According to the specimens designed by [11], spacing of standard stretcher blocks only allowed placing the confinement ties at the mortar joints, thus limiting the confinement configuration. Obaidat et al. [26] used innovative C-shaped masonry blocks to satisfy the requirement of different hoop spacings in BEs. Several researchers [1, 11, 26–28] concluded that increasing the confinement ratio had a significant effect on enhancing the axial strength and softening the post-peak branch of the stress–strain curve. It was also found that the confinement ratio had a more noticeable effect on the post-peak branch of the stress–strain curve than on the ascending part [27].

### 3.2.3 Influence of Other Factors

Obaidat et al. [28], Zorainy et al. [43] investigated the effect of the height to thickness ratio on the peak stress, strain corresponding to peak, and post-peak behaviour of MBEs. The result indicated that the compressive strength and ductility capacity of MBEs increased as the aspect ratio decreased.

Moreover, the effect of block geometry was investigated by different researchers [1, 40]. Steadman et al. [40] concluded that prisms made of blocks without flared webs and face shells had higher capacity due to continuous grout. RMBEs with rectangular cross-sections had comparable peak strength, a smaller drop after the spalling of the face shell, and better strain ductility compared to square RMBEs [1].

Abdelrahman and Galal [1] investigated the influence of stack pattern and running-bond, and pre-wetting of dry masonry shell before grouting. It was found that the running-bond pattern had a negative influence on the compressive stress–strain behaviour of dry RMBEs compared to the stack pattern, while wet RMBEs were not affected much by the bond pattern. Pre-wetting of dry masonry units before grouting was found to greatly enhance the peak compressive stress of masonry prisms but caused a decrease in strain values. Dry RMBEs had a more softening post-peak branch than wet ones.

## 3.3 Discussion

A comprehensive literature review indicates that considerable research has been conducted on the stress–strain behaviour of confined concrete masonry elements subjected to axial compression. However, there is limited research evidence related to the compressive behaviour of RMBEs under various confining details, e.g. hook details. There is an urgent need to investigate the compressive strength and ductility capacity of RMBEs by considering various design parameters, including hook details, tie spacing, and grout strength. Improving the peak stress and strain capacity of RMBEs can lead to the higher inelastic rotational capacity of RMSWs, thus enhancing the ductility and seismic performance of RMSWs. Further experimental investigations are required to increase masonry ultimate compressive strains stipulated by the current CSA S304-14 and TMS 402/602 standards. This will help to ensure that adequate inelastic deformation and energy dissipation levels of RMBEs can meet the ductility demands, thus promoting the RMSWs as SFRS used in medium-rise or high-rise buildings in seismic zones.

## 4 Experimental Programme at the UBC

### 4.1 Test Matrix

The research project which is currently at the initial stage at the University of British Columbia (UBC) intends to examine the compressive stress–strain behaviour of reinforced masonry prisms, which represent the embedded boundary elements in RMSWs, as shown in Fig. 5. In total, 108 concrete block masonry prisms will be constructed and tested under uniaxial compressive loading. The test matrix is designed to complement the literature gap and comprehensively investigate the effect of design parameters on the stress–strain behaviour of masonry BEs under uniaxial compressive loading. The influence of tie spacing, hook details, grout strength, block strength, and different configurations of ties on the compressive stress–strain response of grouted masonry prisms will be investigated. Tie spacing is set at 100 or 200 mm. Two different grout strengths are considered: regular strength grout with compressive strength of 15 MPa, and high-strength grout with compressive strength of 30 MPa. Basalt fibre cement will be also considered to replace the conventional grout in order to provide higher tensile capacity for the cores for another set of specimens. Conventional 90° and 135° hooks will be tested. The proposed tie configurations include closed ties, lap splices, and S-shaped ties. The details of the combination of test parameters are presented in Table 1. Note that the first letter (U) represents "Unreinforced prism" while R denotes "Reinforced prism". The middle number (15 and 20) refers to the compressive strength of concrete blocks in MPa. The last two letters (RG, HG, and FG) refer to the type of grout, "regular strength grout", "high-strength grout", and "basalt fibre grout", respectively. Masonry prisms

**Fig. 5** Cross-section of a fully grouted RMSW with embedded boundary elements

**Table 1** Test matrix

| | No ties | 10 M@100 90º hook Closed tie | 10 M@100 135º hook Closed tie | 10 M@200 90º hook Closed tie | 10 M@200 90º hook Lap splice | 10 M@200 135º hook Closed tie | 10 M@200 135º hook S-shaped ties |
|---|---|---|---|---|---|---|---|
| U15 | 5 | – | – | – | – | – | – |
| U15RG | 5 | – | – | – | – | – | – |
| R15RG | – | 5 | 5 | 5 | 5 | 5 | 5 |
| U15HG | 5 | – | – | – | – | – | – |
| R15HG | – | – | – | 3 | – | 3 | 3 |
| U20 | 5 | – | – | – | – | – | – |
| U20HG | 5 | – | – | – | – | – | – |
| R20HG | – | 5 | 5 | 5 | 5 | 5 | 5 |
| U20FG | 5 | – | – | – | – | – | – |
| R20FG | – | – | – | 3 | - | 3 | 3 |

are divided into several sets to investigate the effect of relevant design parameters and each set includes 5 identical specimens to satisfy the CSA S304 requirements for the minimum number of tested prisms. All the prisms will be fully grouted, except for two sets which will be hollow to quantify the compressive strength of hollow concrete blocks as the control sets.

## 4.2 Design of Test Specimens

According to CSA S304-14, masonry prisms built with hollow concrete block units are required to have more than 3 courses and the height to thickness ratio should be larger than 2. Consequently, all prism specimens were designed to be four-course high with a rectangular section of 390 mm × 240 mm in the stacked bond pattern with 10 mm mortar joints. Type S mortar is used for all specimens. Four 20 M longitudinal reinforcing bars will be installed at the four corners of the masonry blocks confined with 10 M lateral ties. The middle web of the masonry units will be fully removed. Thus, ties can be placed anywhere inside the masonry blocks.
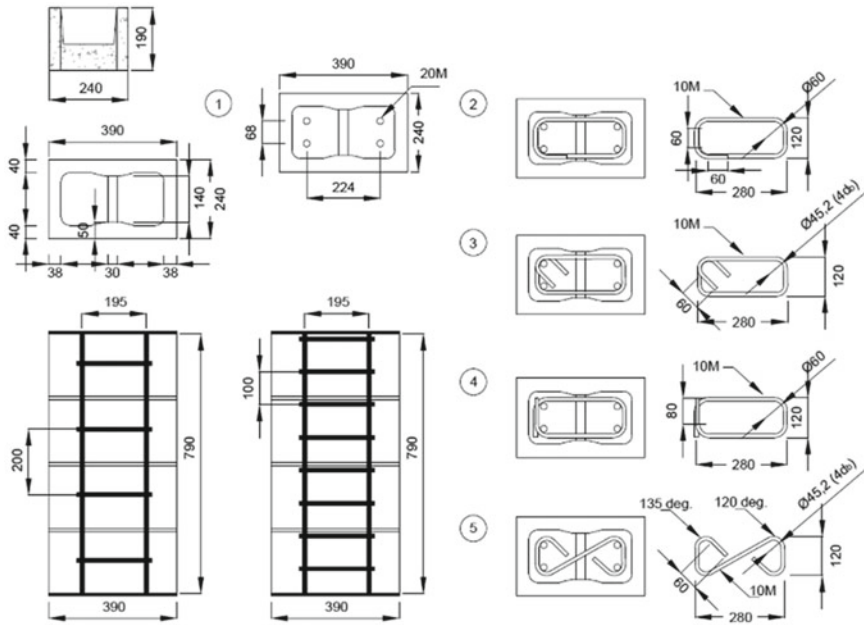
**Fig. 6** Dimensions and confining configurations of tested RMBEs

The ties are 120 mm wide and 280 mm long. The details of dimensions and confining configurations of tested RMBEs are shown in Fig. 6. Configuration ① is for specimens that are reinforced but unconfined. For configuration ② and ③, CSA A23.3-14 Cl.6.6.2.4 stipulates that the bend diameter measured on the inside of the bar shall be at least 4 times the bar diameter, i.e. 45 mm. Either a 90° or 135° bend plus an extension of 60 mm is required. Configuration ④ is the lap slicing tie. Two legs are designed to overlap with each other for 80 mm to maximize the effect of anchorage. For configuration ⑤, S-shaped ties are designed to bend at 135° with a bending diameter of 45 mm and extension of 60 mm. The ties are expected to serve as lateral support and delay the buckling of vertical reinforcement, but will not provide confinement to the grouted cores.

## 4.3 Material Properties

Material properties to be used in experimental programme are tabulated in Table 2. Two different unit strengths and two different grout strengths will be tested.

**Table 2** Summary of material properties

| Concrete unit | Higher compressive strength | 20 MPa |
|---|---|---|
| | Lower compressive strength | 15 MPa |
| | Thickness | 250 mm |
| Mortar | Type | S |
| Grout | Regular strength | 15 MPa |
| | High strength | 30 MPa |
| Vertical reinforcement (20 M) and horizontal ties (10 M) | Yield strength | 400 MPa |

## 4.4  Construction of the Test Specimens

The construction process (Fig. 7) will start with making the capping plate by moulding high-strength gypsum cement in the wooden form. The first block will be put concentrically and vertically on the capping plate. Four longitudinal reinforcing bars will be placed at the corners, extending from the bottom to the top. Longitudinal reinforcing bars will be laterally supported by horizontal ties with various configurations. As the middle webs in each block will be removed, the ties spaced at 100 mm will not be obstructed by the middle webs. The steel cage will then be placed on the capping plate. Subsequently, 10 mm mortar will be placed at the bed joints. Afterwards, the next three masonry blocks and mortar joints will be constructed. The grout will be mixed and poured into the prisms. A mechanical vibrator shall be used to ensure the grout's consistency and flowability and prevent honeycombing along the specimen's height. Finally, wooden forms will be used to cast the top gypsum capping.

## 4.5  Test Setup and Measurements

A servo-controlled 400 kips (2000 kN) Baldwin universal testing machine attached to the rigid steel testing frame will be utilized to apply the uniaxial compressive load in a displacement-controlled loading protocol. The displacement-control system allows for capturing the post-peak response of the tested prisms. The increasing compressive displacement will be applied monotonically to the specimens until failure. A highly precise load cell attached to the hydraulic actuator and connected to a data acquisition system will ensure the precision and accuracy of the real-time reading of the axial loading and displacements. Before attaching the upper and lower rigid spherical steel bearing plates to the specimens' ends, high-strength gypsum cement capping plates will be placed at the top and bottom to eliminate the roughness of the surface and uniformly distribute the applied uniaxial load on the specimens. The bearing plates, the capping plates and the specimens will be aligned vertically and concentrically
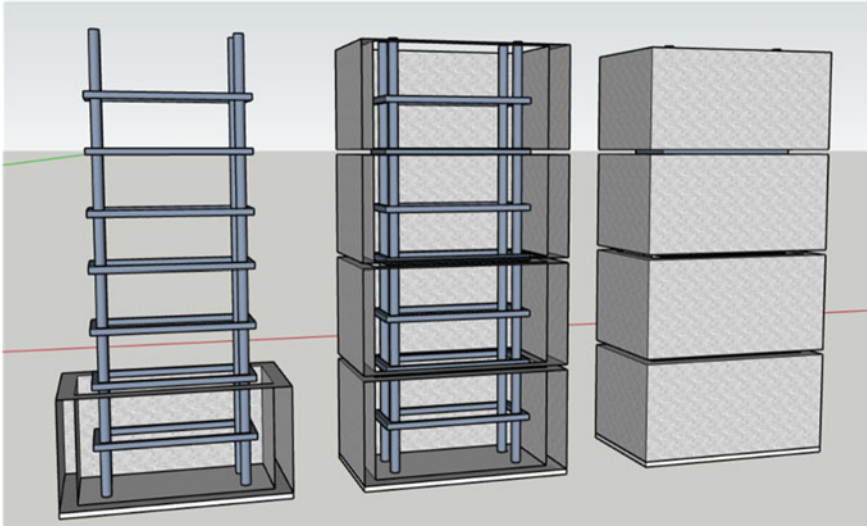
**Fig. 7** Construction process for prism specimens

along with the hydraulic actuator. The incremental monotonic uniaxial loading will be applied at a slow displacement rate of 0.003 mm/s up to the failure of the specimens. This is to ensure that the complete compressive stress–strain curve including the post-peak branch of the RMBEs will be recorded. The whole compression response of the RMBEs will be an important reference for designing the RMBEs and RMSWs.

Four draw-wire displacement transducers (i.e. potentiometers) with an error of 0.0005 of the full strokes will be utilized to monitor axial displacements of the specimens. The potentiometers will be attached to the centre of the four sides of the specimens using epoxy adhesive. The complex stress pattern may lead to crushing of the mortar joints and spalling of sections of the face shells adjacent to the joints [29]. Thus, the measuring devices will be attached at the top and bottom of the specimen, away from the mortar joints. The gauge length will be selected as the full height of the specimens.

It is noteworthy that the compressive strain of masonry boundary elements, including the masonry and the reinforcement, should be considered to ensure strain compatibility and zero slippage between the grout core and longitudinal reinforcement. Therefore, strain gauges will be attached to the longitudinal reinforcement to measure the compression strains. The measured reinforcement strains will be compared to the strains measured on the masonry face shells to validate the compatibility of the strains between the longitudinal reinforcement and the grouted core.

# 5　Conclusions

RMSWs with boundary elements are an effective SFRS for medium- and high-rise buildings. To understand the seismic response of RMSWs with boundary elements, it is necessary to investigate the compressive stress–strain behaviour of RMBEs. North American masonry standards require testing to prove higher masonry compressive strain to be used. Previous research efforts were focused on limited test parameters, such as grout compressive strength and the reinforcement confinement ratio. There are other relevant typical design parameters affecting the compressive stress–strain behaviour of RMBEs to be investigated, such as tie spacing, hook details, and grout strength. This paper presents a detailed literature review of past research on the study of boundary masonry elements. In addition, an experimental programme that is focused on investigating the influence of different parameters on the compressive stress–strain response of RMBEs is presented. Quantifying the influence of those parameters on the compressive strength and strain capacity of RMBEs conducted in this study will contribute to the prediction of the seismic response of RMSWs with boundary elements.

# References

1. Abdelrahman B, Galal K (2021) Experimental investigation of axial compressive behavior of square and rectangular confined concrete-masonry structural wall boundary elements. Eng Struct 243:112584. https://doi.org/10.1016/j.engstruct.2021.112584
2. Berry MP, Eberhard MO (2005) Practical performance model for bar buckling. J Struct Eng 131(7):1060–1070. https://doi.org/10.1061/(ASCE)0733-9445(2005)131:7(1060)
3. Brzev S, Anderson D (2018) Seismic design guide for masonry buildings, 2nd edn. Canadian Concrete Masonry Producers Association
4. Building code requirements and specification for masonry structures: containing TMS 402-16 building code requirements for masonry structures (formerly also designated as ACI 530 and ASCE 5), TMS 602-16 specification for masonry structures (formerly also designated as ACI 530.1 and ASCE 6), and companion commentaries (2016). The Masonry Society
5. Corrêa MRS (2012) Masonry engineering in Brazil: past development, current overview, future improvements. In: 15th international brick and block masonry conference
6. CSA S304-14 Design of Masonry Structures (2014). CSA Group
7. CSA A23.3–14 Design of Concrete Structures (2014). CSA Group
8. Dhanasekar M, Shrive NG (2002) Strength and deformation of confined and unconfined grouted concrete masonry. ACI Struct J 99(6). https://doi.org/10.14359/12347
9. Drysdale RG, Hamid AA (1979) Behavior of concrete block masonry under axial compression. J Proc 76(6):702–722
10. Drysdale RG, Hamid AA (2008) Masonry structures behavior and design, 3rd edn. Masonry Society

11. El Ezz A, Seif Eldin HM, Galal K (2015) Influence of confinement reinforcement on the compression stress-strain of grouted reinforced concrete block masonry boundary elements. Structures 2:32–43. https://doi.org/10.1016/j.istruc.2015.01.001

12. Fortes ES, Parsekian GA, Fonseca FS (2015) Relationship between the compressive strength of concrete masonry and the compressive strength of concrete masonry units. J Mater Civ Eng 27(9):04014238. https://doi.org/10.1061/(ASCE)MT.1943-5533.0001204

13. Hamid AA (2018) Masonry structures: behavior and design, 4th edn. Masonry Society

14. Hart GC, Noland JL, Kingsley JL, Englekirk RE, Sajjad NA (1988) The use of confinement steel to increase the ductility in reinforced masonry shear walls. Masonry Soc J 7(2)

15. Hart GC, Sajjad NA, Kingsley JL, Noland JL (1989) Analytical stress-strain curves for grouted concrete masonry. Masonry Soc J 8(1):T21–T34

16. Hatzinikolas M, Korany Y, Brzev S (2015) Masonry design: for engineers and architects, 4th edn. Canadian Masonry Publications

17. Hervillard TPC (2005) Effectiveness of polymer fibers for improving the ductility of masonry structures [Unpublished master's thesis]. Washington State University

18. Joyal M (2014) Enhanced ductility of masonry shear walls using laterally confined (self-reinforced) concrete block [Unpublished doctoral thesis]. McMaster University

19. Khalaf FM, Hendry AW, Fairbairn DR (1994) Study of the compressive strength of blockwork masonry. ACI Struct J 91(4). https://doi.org/10.14359/4139

20. Long L, Hamid AA, Drysdale RG (2005) Small-scale modelling of concrete masonry using ½-scale units: a preliminary study. In: 10th Canadian masonry symposium

21. Mayes RL, Omote Y, Clough RW (1976) Cyclic shear tests of masonry piers: analysis of test results, vol 2. Earthquake Engineering Research Center, University of California

22. Mayes RL, Omote Y, Clough RW (1976) Cyclic shear tests of masonry piers: test results, vol 1. Earthquake Engineering Research Center, University of California

23. Moyer MJ, Kowalsky M (2003) Influence of tension strain on buckling of reinforcement in concrete columns. ACI Struct J 100:75–85

24. National Building Code of Canada 2015 (2010). National Research Council of Canada

25. NZS 4230 Design of Reinforced Concrete Masonry Structures (2004). Standards New Zealand

26. Obaidat AT, Abo El Ezz A, Galal K (2017) Compression behavior of confined concrete masonry boundary elements. Eng Struct 132:562–575.https://doi.org/10.1016/j.engstruct.2016.11.043

27. Obaidat AT, Ashour A, Galal K (2018) Stress-strain behavior of C-shaped confined concrete masonry boundary elements of reinforced masonry shear walls. J Struct Eng 144(8):04018119. https://doi.org/10.1061/(ASCE)ST.1943-541X.0002120

28. Obaidat AT, Ashour A, Galal K (2019) Stress-strain model for C-shape confined concrete masonry boundary elements of RM shear walls. Eng Struct 183:1059–1071. https://doi.org/10.1016/j.engstruct.2019.01.016

29. Page AW, Kleeman PW, Xie H (2000) A new approach to the prediction of failure of face-shell bedded hollow masonry loaded in eccentric compression. In: 12th international brick/block masonry conference

30. Pantazopoulou SJ (1998) Detailing for reinforcement stability in RC members. J Struct Eng 124(6):623–632. https://doi.org/10.1061/(ASCE)0733-9445(1998)124:6(623)

31. Pohl S (2018) When green marketing meets reality: selected facts about sustainable house building. Mauerwerk 22(4):215–224. https://doi.org/10.1002/dama.201800007

32. Priestley MN, Elder DM (1983) Stress-strain curves for unconfined and confined concrete masonry. ACI J Proc 80(3). https://doi.org/10.14359/10834

33. Priestley MJN, Bridgeman DO (1974) Seismic resistance of brick masonry walls. Bull N Z Soc Earthq Eng 7(4):167–187. https://doi.org/10.5459/bnzsee.7.4.167-187

34. Roman H, Romagna R (2002) Compressive strength of grouted and un-grouted concrete block masonry. In: Proceedings of the british masonry society, 399–404

35. Sajjad NA (1990) Confinement of concrete masonry [Unpublished doctoral thesis]. University of California, Los Angeles

36. Sarhat SR, Sherwood EG (2018) Compressive strength prediction of grouted hollow concrete block masonry. Masonry Soc J 36

37. Sazedj S, José Morais A, Jalali S (2017) Comparison of environmental benchmarks of masonry and concrete structure based on a building model. Constr Build Mater 141:36–43.https://doi.org/10.1016/j.conbuildmat.2017.02.150

38. Shedid MT, El-dakhakhni WW, Drysdale RG (2010) Alternative strategies to enhance the seismic performance of reinforced concrete-block shear wall systems. J Struct Eng 136(6):676–689. https://doi.org/10.1061/(ASCE)ST.1943-541X.0000164

39. Snook M, McLean D, McDaniel C, Pollock D (2005) Effects of confinement reinforcement on the performance of masonry shear walls. In: 10th Canadian masonry symposium

40. Steadman M, Drysdale RG, Khattab MM (1995) Influence of block geometry and grout type on compressive strength of block masonry. In: 7th Canadian masonry symposium

41. Wang Fl, Zhang XC, Zhu F (2016) Research progress and low-carbon property of reinforced concrete block masonry structures in China. Brick and Block Masonry, 2247–2254.https://doi.org/10.1201/b21889-278

42. Williams D (1975) Seismic resistance of brick masonry walls. Bull N Z Soc Earthq Eng 8(3):238–240. https://doi.org/10.5459/bnzsee.8.3.238-240

43. Zorainy M, Ashour A, Obaidat AT, Galal K (2021) Compressive stress-strain behaviour of unreinforced masonry boundary element prisms constructed with C-shaped blocks. In: 14th Canadian masonry symposiums

# Experimental Testing of Partially Grouted Masonry Shear Walls with Different Horizontal Reinforcement Types

Amr Ba Rahim, Carlos 'Lobo' Cruz Noguez, and Clayton Pettit

**Abstract** Partially grouted (PG) masonry shear walls are widely used as lateral force-resisting systems in North America due to their economic value and practicality. Unlike fully grouted (FG) shear walls, only cells containing reinforcing steel are grouted in PG walls leaving the remaining cells hollow. With the wall assemblage consisting of materials such as masonry block, mortar, grout, and reinforcing steel, the overall behaviour is complex. To understand better the in-plane response of PG walls, experimental testing has been used as a viable tool. However, few experimental studies have been carried out to investigate PG walls compared with FG walls. Moreover, if available, some studies lacked full-scale test specimen size, compliance to the actual masonry construction, and well-documented reports. As a result, North American code equations have been obtained based on FG walls data leading to uneconomical designs while being unconservative in some cases. This paper describes the preliminary experimental results of four full-scale partially grouted masonry shear walls. These walls were designed and built to reflect the conventional construction practice, including wall geometry, reinforcement distribution, boundary conditions, and loading scenario. All the walls were subjected to constant vertical load, and reverse in-plane lateral cyclic load incrementally increased. The variable design parameters investigated in this study were: aspect ratio and horizontal reinforcement type (bond beams or bed-Joint reinforcement). These walls' response was evaluated in terms of damage progression, in-plane hysteresis curves of lateral load against drift ratio, and energy dissipation. The experimental results revealed that lateral load capacity attained by walls with similar aspect ratios had no significant difference regardless of the reinforcement type. On the other hand, the aspect ratio had a significant effect. Moreover, the effect of bed-joint reinforcement was more visible in controlling the damage progression by distributing new cracks throughout the wall panel instead of widening the existing cracks.

A. B. Rahim (✉) · C. '. C. Noguez · C. Pettit
Department of Civil and Environmental Engineering, School of Mining and Petroleum Engineering, University of Alberta, Edmonton, Canada
e-mail: abarahim@ualberta.ca

## 1  Introduction

The partially grouted (PG) masonry shear walls are considered one of the common
lateral force-resisting systems in masonry constructions. PG masonry walls are
grouted just when reinforcing bars are inserted, such as vertically aligned cells with
vertical flexural reinforcement or horizontal bond beams with shear reinforcement,
unlike fully grouted (FG) masonry walls. As a result of the lower material and labour
costs, they provide a cost advantage over FG walls [10, 22]. In North America, PG
walls can be found in commercial and school buildings, college dorms, motels, and
residential buildings [5]. However, the shear response of PG walls under in-plane
lateral loading is not yet well understood, unlike that of FG walls, for which there
are more experimental data and mechanics-based capacity equations [2, 3]. To attain
safety levels comparable with FG walls, North American code expressions for PG
wall lateral capacity are based on those produced for FG walls with an arbitrary
reduction factor [11]. Consequently, the current design expressions are of limited
accuracy, and in some cases, non-conservative [4, 10, 16, 17, 20, 22].

There are two horizontal reinforcement types commonly used in masonry walls:
bond beam and bed-joint reinforcement. Bond beam reinforcement consists of hori-
zontal steel bars placed at the centre of the masonry courses, supported on knocked-
out webs and then filled these courses with grout. Bed-joint reinforcement consists of
a ladder-type steel reinforcement that is placed at the top of the masonry joints before
applying mortar. Yancey and Scribner [34], Schultz [27], Schultz et al. [28], Baen-
ziger and Porter [1], Hoque [19], Bolhassani et al. [5], Stathis et al. [30], Schultz and
Johnson [29], Calderon et al. [6] studied the effect of horizontal reinforcement types
on the shear strength of PG walls. Hidalgo and Luders [18], Hoque [19], Wierzbicki
[33] noted that bed-joint reinforcement was less effective than bond beam rein-
forcement as horizontal seismic reinforcement because it can readily fracture when
subjected to several loading and unloading cycles. As a result, walls reinforced with
a bond beam can carry higher lateral capacities than those reinforced with bed-joint
reinforcement. Schultz et al. [28], Baenziger and Porter [1], Ramírez et al. [25],
Sandoval et al. [26], Stathis et al. [30] observed the role of bed-joint reinforcing in
controlling the cracking distribution and improving the post-peak behaviour and wall
ductility when compared with the bond beam reinforcement. This is attributed to the
ability of bed-joint reinforcement to limit the propagation of existing cracks, forcing
the creation of new cracks throughout the wall panel after reaching the peak lateral
load. Bolhassani et al. [5] observed that the peak lateral load attained by all walls was
not significantly different regardless of the horizontal reinforcement type, which was
confirmed recently by [6, 29]. Calderon et al. [6] observed that the grout limited the

development of cracks near the bond beams, resulting in a few wide cracks crossing horizontal reinforcement in bond beams. In contrast, they noticed that the cracks were better distributed throughout the wall panel and the residual deformations were controlled by bed-joint reinforcement. Finally, [6] suggested studying whether the effect of the horizontal reinforcement type on the shear behaviour of PG walls can be similar with different aspect ratios, horizontal reinforcement ratios, and axial stresses.

To expand our comprehension of the in-plane response of PG walls, this paper presents the preliminary experimental results of four full-scale walls made of concrete masonry units (CMUs), which replicate the realistic details of conventional masonry construction, including wall geometry, reinforcement detailing, boundary conditions, and loading settings. These walls were subjected to a combination of constant axial load and reverse cyclic in-plane lateral loads. The aspect ratio and horizontal reinforcement types (bond beams and bed-joint reinforcement) were the variable design parameters in this research. The response of these walls and the role of the variable design parameters were studied in terms of damage development, hysteretic response, and energy dissipation.

## 2 Experimental Programme

### 2.1 Description of Test Specimens

A total of four partially grouted walls were designed and built as a cantilever wall according to CSA S304-14 [8]. This study used two aspect ratios: 1.86 (slender) and 1.00 (squat) by varying the wall length and keeping the wall height constant, which equals 2.6 m. This study implemented two horizontal reinforcement types: bond beam (BB) and bed-joint reinforcement (BJ). All the horizontal reinforcement ratios were approximately equal, except BB slender wall was higher because it complies with the reinforcement regulations according to CSA S304-14 [8]. All the test specimens had the same vertical reinforcement distribution where vertically reinforced of 15 M rebar with 1200 mm spacing. The axial stress applied on all the test specimens was around 1.9 MPa. This applied axial stress is approximately identical to the load coming from mid-rise masonry building [2]. The geometrical dimensions and reinforcement details are summarized and illustrated in Fig. 1 and Table 1.

All the tested walls were constructed by professional masons using hollow concrete masonry units CMUs, following the running bond approach. The construction process of the test specimens consisted of three stages; (1) construction of reinforced concrete base, (2) construction of wall panels on the base using CMUs with nominal dimensions $(400 \times 200 \times 200)$ mm, and (3) construction and placing of capping beam on the top of wall panels. Twenty cm standard, half standard, and knock-out lintel blocks were used to build the walls, where knock-out lintel was used throughout the wall height to allow the bond beam reinforcement placement
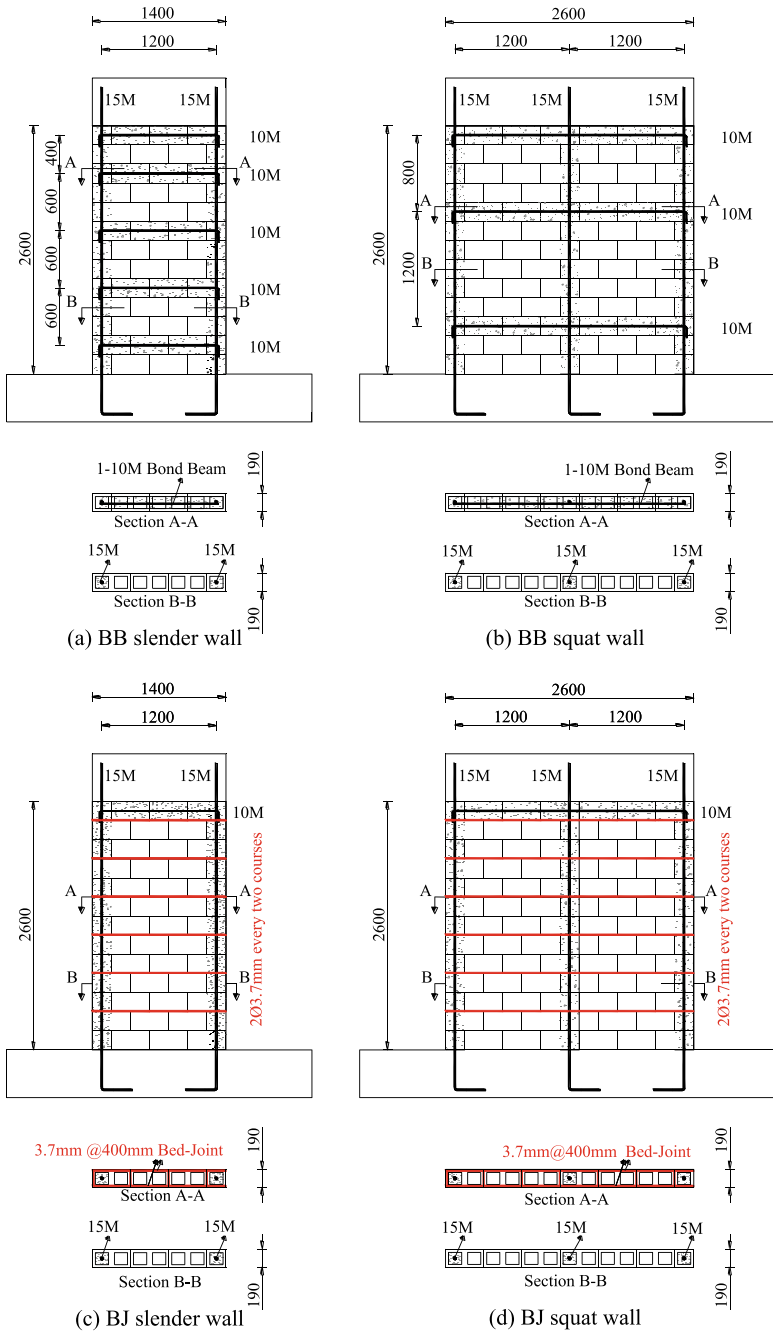
**Fig. 1** Reinforcement details of the wall specimens

**Table 1** Design details of test specimens

| | Specimen ID | Specimen dimensions | | | Aspect ratio | Vertical reinforcement | | Horizontal reinforcement | | Axial stress |
|---|---|---|---|---|---|---|---|---|---|---|
| | | $h$ (mm) | $l$ (mm) | $t$ (mm) | $h/l$ | Vertical layout | $\rho_v$ (%) | Horizontal layout | $\rho_h$ (%) | $\sigma_g$ MPa |
| Slender walls | BB slender | 2600 | 1400 | 190 | 1.86 | 15 M@1200 | 0.09 | 10 M@600 | 0.09 | 1.9 |
| | BJ slender | 2600 | 1400 | 190 | 1.86 | 15 M@1200 | 0.09 | 3.7 mm@400 + 1–10 M | 0.05 | 1.9 |
| Squat walls | BB squat | 2600 | 2600 | 190 | 1.00 | 15 M@1200 | 0.09 | 10 M@1200 | 0.04 | 1.9 |
| | BJ squat | 2600 | 2600 | 190 | 1.00 | 15 M@1200 | 0.09 | 3.7 mm@400 + 1–10 M | 0.05 | 1.9 |
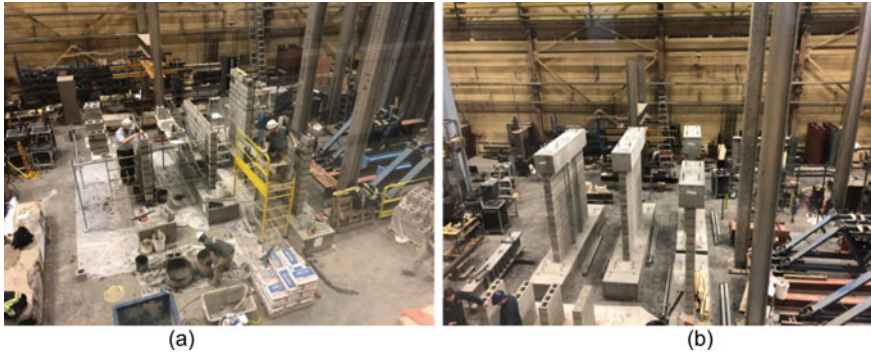
**Fig. 2** **a** Walls during construction, **b** Walls after construction

and the grout continuity. Head and bed-joint thickness of approximately 10 mm was implemented where Type S Portland Lime and Sand premixed mortar, which is commonly used in the masonry construction, was used throughout the joints. Core Fill Grout-Coarse was used to fill the vertical cells where vertical reinforcement was placed and the bond beams along the whole length. The bond beam reinforcement consisted of a single 10 M rebar, placed continuously throughout the wall length where it hooked using a 90° hook around the edge of vertical rebars, according to CSA S304-14 [8]. The bed-joint reinforcement consisted of a Standard (9 Gauge) Ladder of 3.7 mm diameter, which is commonly used to horizontally reinforce the bed joints of the masonry structures, placed embedded at the bed joints of the wall panels. The vertical reinforcement was continuously placed along the test specimen height without a lab splice. The RC base was designed specifically to replicate the intended boundary conditions and connect the specimens to the strong floor of the laboratory to securely fix the specimen at the set-up during the test. In addition, the RC capping beam was designed to impose and transfer the vertical and lateral loads to the top of the wall panel. Finally, all the test specimens were cured under laboratory environment control. Figure 2 shows the construction process of the test specimens.

## 2.2 Material Properties

Five samples of hollow concrete masonry units (CMUs) were tested to obtain the uniaxial compressive strength. The average compressive strength was 19 MPa with a coefficient of variation, CV of 6.8%. Seven 50 mm mortar cubes were sampled from the same batch used to build the wall panels. The average compressive strength was 14.8 MPa with CV of 16.7%. Seven samples of the grout used to fill the vertical cells where vertical bars were placed and to fill the bond beams were tested. The average compressive strength was 30.6 MPa with CV of 8.1%. Grade 400 steel bars of 10 M

(11.3 mm) and 15 M (16.2 mm) were used to reinforce the wall panels horizontally and vertically, respectively. The average yield strength of three 10 M and three 15 M bars were 521 MPa and 455 MPa with CV of 0.9% and 0.4%, respectively. Standard 9 gauge bed-joint reinforcement with 3.7 mm diameter was tested to obtain the yield strength of 617 MPa with CV 2.6%. To determine the compressive strength of the masonry material, six 5-course prisms (three of them were ungrouted and three were grouted) were tested under uniaxial compression force. The average ungrouted and grouted compressive strengths were 22.0 MPa and 16.4 MPa, with CV of 15.8% and 16.1%, respectively.

## 2.3 Test Set-up and Instrumentation

The test set-up is depicted in Fig. 3. This set-up was mainly comprised of base system, lateral load assembly, vertical load assembly, and out-of-plane restraining system. The base system was made of reinforced concrete base, which connected to the strong floor of the laboratory through post-tensioned high-strength rods of 38 mm diameter. This connection induced the cantilever boundary condition by considering the bottom side of the specimen as a fixed point. The lateral load assembly was made up of double-acting hydraulic jacks of 800 kN capacity (push–pull). These jacks were connected at one end to a strong steel shear wall while connected at another end to two C-channels that were attached to both sides of the capping beam through high-strength rods of 19 mm diameter. This connection allowed even distribution of lateral load transfer to the wall panel. Vertical loads were applied to the test specimen employing four gravity load simulators (GLS) of 350 kN capacity of each one, two at each side of the wall specimen that simultaneously worked through the same oil pump. These GLSs were connected to the cruciform shape beam at the top of the wall panel by means of tension tie rods. This assembly had the advantage of maintaining the vertical loads throughout the lateral movement of the wall panel [9, 23, 24]. Finally, four rectangular steel frames were used to prevent any out-of-plane displacement, two at each side of the specimen. These frames were connected at one end to the capping beam and at another end to the steel frame.

Instrumentation layout of all test specimens is illustrated in Fig. 4. There were 16 channels in order to capture and measure the loads and displacements that resulted during the test—these channels comprised of load cells, cable transducers, and linear variable differential transformers (LVDTs). Vertical and lateral loads were registered via channels 0 and 1, respectively. Lateral displacement at the mid-capping beam, top wall panel, and mid-wall panel were measured via channels 2, 3, and 4, respectively. The slip of the wall base and RC base were recorded using channels 5 and 6, respectively. Channel pairs of 7 and 8, 9 and 10, and 11 and 12 were used to measure the vertical displacement at two-course height, four-course height, and between base and capping beam. Channels 13 and 14 were used to measure the diagonal displacement within the whole wall panel. Out-of-plane displacement at the mid-wall panel was registered using channel 15. In addition, several strain gauges were installed at the
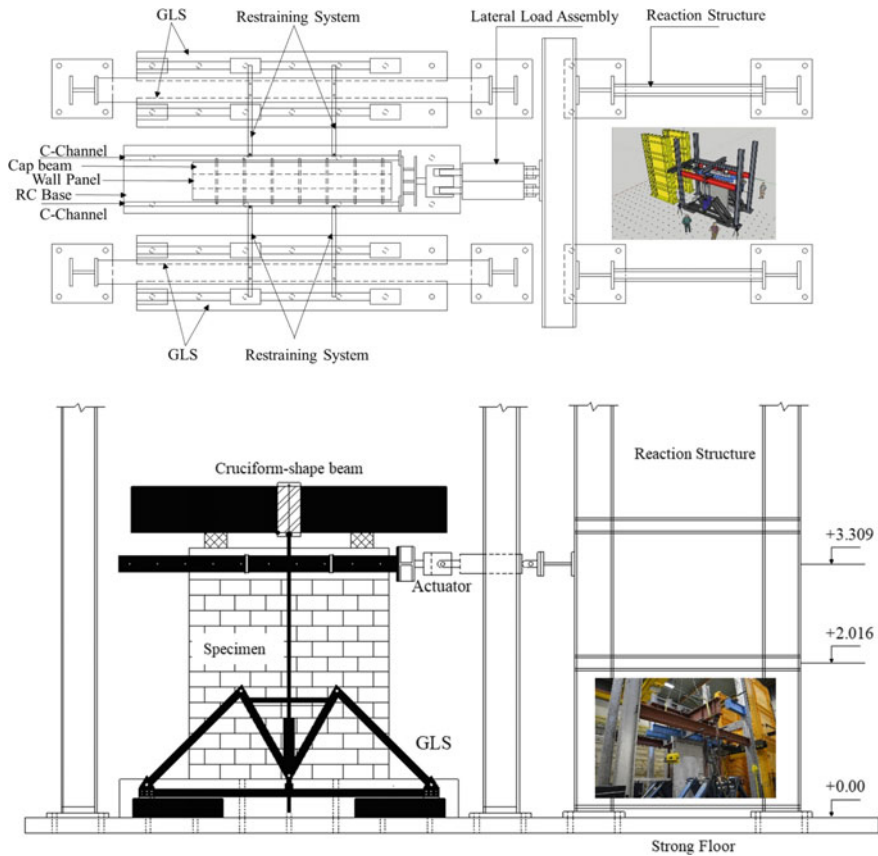
**Fig. 3** Test set-up

vertical and horizontal bars before construction, in order to measure the strain of the steel bars during the cyclic test. These gauges were positioned at various locations of steel bars so that they could capture the cyclic response of the reinforcement. Finally, digital image correlation (DIC) system was implemented to measure the strains of the test specimens. This innovative system enhanced the ability to capture the strains at different directions, which enabled comprehending the cyclic performance of the wall panels.

## 2.4  Testing Procedure

Test specimens were subjected first to vertical loads up to a certain limit, and then they were kept constant during the test using force control load. The total applied vertical loads on the top of the test specimens were 516 kN and 973 kN for wall panels with
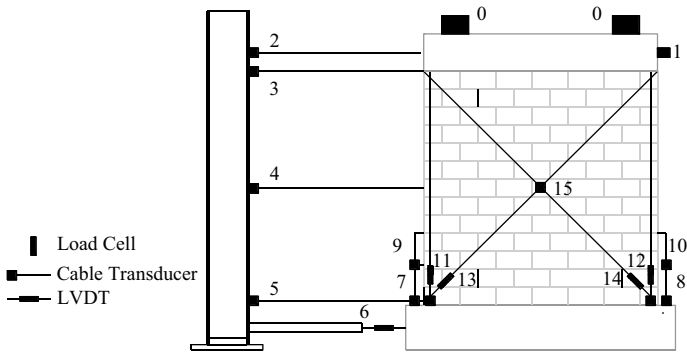
**Fig. 4** Instrumentation layout

an aspect ratio of 1.86 and an aspect ratio of 1.00, respectively. Lateral loads were then applied in a reversal mode (push then pull at each displacement level) using a displacement control load. Each displacement level was repeated twice to capture the stiffness degradation clearly [12]. It should be noticed that the lateral loading depended on the ratio of the top central displacement to the height of the wall panel, which is called a drift ratio. Loading rate was 6 mm/min at the first displacement levels and then increased to 12 mm/min at latter levels. The protocol of cyclic lateral loading is depicted in Fig. 5. Finally, the test was stopped when the lateral loads reached 80% of the peak lateral load that resulted during the test, which is defined as the test specimen's failure point.

**Fig. 5** Loading protocol
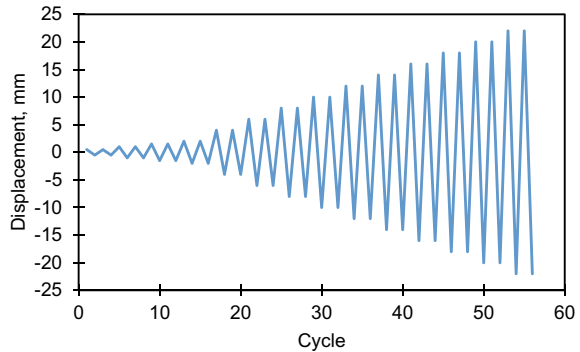
# 3 Test Results

## 3.1 Cracks and Failure Modes

The instruments and digital image correlation (DIC) were used to monitor and record the progression of the wall cracks. All of the recorded data has been processed to show how the tested walls behaved during the cyclic test and how they responded to the applied loads. At the completion of the test, Fig. 6 depicts the cracking patterns of all tested specimens. These patterns, it should be noted, are dependent on the unique characteristics of each wall. The failure mode was diagonal cracking in both directions, diagonally propagated from the upper corner to the toe for squat walls. On the other hand, BJ slender wall showed mixed shear-flexure failure, while BB slender wall experienced flexure failure due to the higher horizontal reinforcement ratio compared with BJ slender wall. Two common types of diagonal cracks were observed throughout wall panels. The first type was stair-stepped type, where the shear stresses coming from the applied loads exceeded bond strength between the blocks and the mortar. The second one was diagonal cracking through blocks and mortar, where the principal stresses coming from the applied loads surpassed the tensile strength of the masonry.

In addition, the vertical reinforcement has been yielded in the slender wall reinforced with bond beam due to the higher horizontal reinforcement ratio, which induced the flexural failure despite diagonal cracks occurring throughout the wall
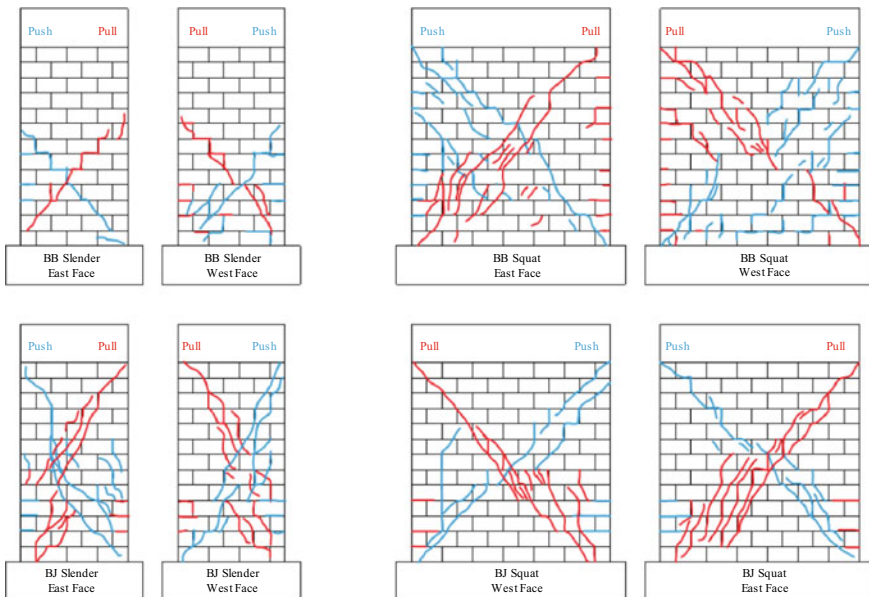


**Fig. 6** Cracking patterns of tested walls at the final stage
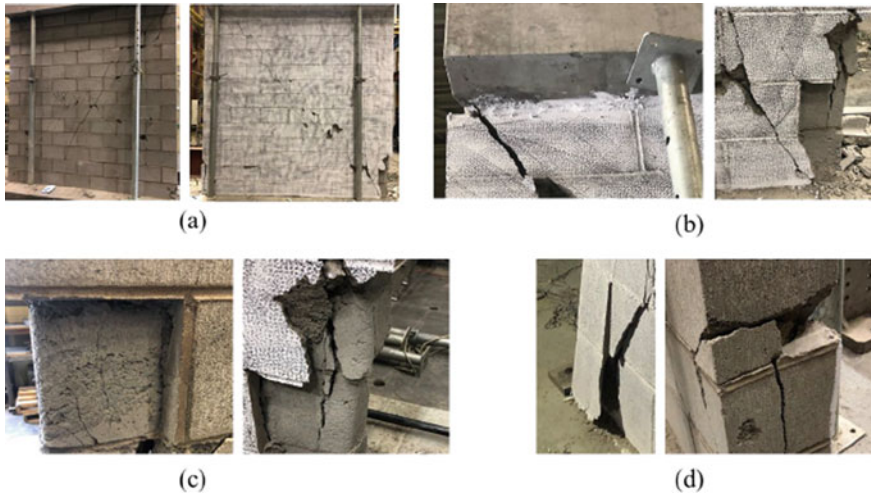
**Fig. 7** Typical damage observed during the cyclic test: **a** Stair-stepped and diagonal cracking, **b** Upper end and toe penetration cracking, **c** Vertical grout cracking, and **d** Spalling of face-shell

surface. On the other hand, horizontal reinforcement has been yielded in the squat walls due to the lower aspect ratio, which promoted the shear failure for such walls. This failure caused damage to the tested wall in terms of stair-stepped and diagonal cracking, upper end and toe penetration cracking, vertical grout cracking, and spalling of face-shell, as demonstrated in Fig. 7.

## 3.2 Lateral Load-Drift Ratio Response

The relationship between the lateral load and both lateral displacement and drift ratio is depicted in Fig. 8, including all the plots of the tested walls. These plots demonstrate milestones that all walls went through during the test. These millstones are initial cracking, strut formation, and peak load. The initial cracking is identified as the first slope change on the in-plane hysteresis curve. Following initial cracking, the next noticeable slope change in the in-plane hysteresis curve corresponds to the strut formation. The maximum load in the lateral load–drift ratio diagram is called the peak load. Data pertaining to these plots, such as lateral load associated with these milestones and their associated displacements and drifts in both push and pull directions, are summarized in Table 2.

According to Fig. 8, it can be observed that all walls experienced a linear-elastic behaviour up to the occurrence of the first crack. This behaviour was characterized by narrow cycles and approximately symmetric response with low dissipated energy. After the first crack, nonlinear behaviour started, but the energy dissipation was still low. When the first diagonal crack occurred, all walls started to have wider cycles
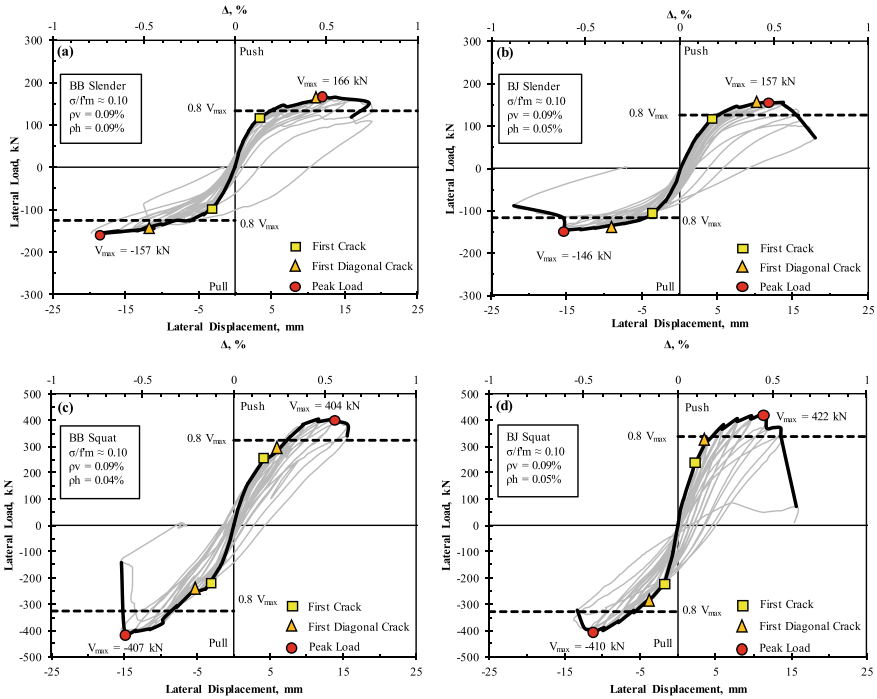
**Fig. 8** Load–displacement hysteresis loop diagram of tested walls

indicating that more energy was dissipated due to the occurrence of more cracks. This was more visible in squat walls than in slender ones.

With regard to slender walls, it was observed that BB slender wall did not show any signs of strength deterioration after reaching the peak lateral load for three cycles, until suddenly it showed rapid degradation of strength (37% drop) with visible wide and major cracks concentrated at the bottom half, particularly in the area between the bond beams. This is attributed to the large difference in stiffness (23% difference) between the grouted and ungrouted zones around the bond beams [6]. On the other hand, BJ slender wall showed a better distribution of cracks throughout the wall height. The gradual degradation of strength confirmed this observation after reaching the peak lateral load. The reason for this is due to the distribution of the bed-joint reinforcement every two courses, which contributes largely to controlling the damage by allowing the cracks to distribute evenly throughout the wall surface and preventing the cracks to concentrate in specific regions. In addition, it was observed that both walls attained nearly equal peak lateral load regardless of the horizontal reinforcement types in both loading directions with a maximum of 8% difference. This finding was also observed by [32].

In the case of squat walls, the deterioration was gradual in both walls after reaching the peak lateral load, but the wall reinforced with a bond beam showed a sudden drop in the lateral load by 63% of the peak load at the subsequent cycle. In comparison,

**Table 2** Results of tested walls

| Specimen ID | Load direction | Initial crack | | | Strut formation | | | Peak lateral load | | |
|---|---|---|---|---|---|---|---|---|---|---|
| | | Lateral displacement (mm) | Drift Δ (%) | Lateral force (kN) | Lateral displacement (mm) | Drift Δ (%) | Lateral force (kN) | Lateral displacement (mm) | Drift Δ (%) | Lateral force (kN) |
| BB slender | Push | 3.5 | 0.13 | 117 | 11.5 | 0.44 | 156 | 12.3 | 0.47 | 166 |
| | Pull | 3.4 | 0.13 | 98 | 12.4 | 0.48 | 142 | 19.5 | 0.75 | 157 |
| BJ slender | Push | 4.3 | 0.17 | 116 | 10.3 | 0.40 | 153 | 12.2 | 0.47 | 157 |
| | Pull | 3.7 | 0.14 | 109 | 9.7 | 0.37 | 136 | 16.0 | 0.62 | 146 |
| BB squat | Push | 4.0 | 0.16 | 240 | 6.1 | 0.23 | 279 | 14.2 | 0.55 | 404 |
| | Pull | 4.0 | 0.15 | 243 | 6.0 | 0.23 | 258 | 15.6 | 0.60 | 407 |
| BJ squat | Push | 2.3 | 0.09 | 228 | 4.1 | 0.16 | 319 | 11.9 | 0.46 | 422 |
| | Pull | 2.0 | 0.08 | 226 | 4.1 | 0.16 | 289 | 12.1 | 0.46 | 410 |

the wall reinforced with bed-joint reinforcement showed gradual degradation in the peak lateral load by 12% at the next cycle. This may be attributed to the improved post-peak behaviour of walls reinforced with bed-joint reinforcement [1, 6, 30]. This is indicated that the wall reinforced with bed-joint reinforcement continued to sustain damage in terms of new cracks throughout the wall panel, in contrast to the wall reinforced with bond beam where the grout limited the development of new cracking around the bond beam but promoted widening of the existing cracks [6]. In addition, both walls attained nearly similar peak lateral load (2% difference). This corresponded well with the observations by [5, 6, 29].

### 3.3  Comparison Between Predicted and Measured Strength

The predicted capacity of the tested walls, calculated based on the measured materials properties, is given in Table 3. It is seen that the predicted mode of failure for the squat walls was in-plane shear, as the flexural capacity or STM developed by [7] was greater than the predicted in-plane shear strength. For slender walls, the predicted mode of failure was flexural, however, the in-plane shear and flexural capacities were very close (8%) difference and thus, the failure mode could be defined as mixed shear-flexural [13, 15].

From the comparison between the predicted and the experimental diagonal shear strength for squat walls, the CSA equation [8] was more conservative than the TMS equation [21] by 22%.

### 3.4  Energy Dissipation

This parameter indicates how much the system withstands the applied loads without significant damage. The dissipated energy is the area enclosed by the hysteric loop in a one complete cycle, as shown in Fig. 9. Therefore, this energy was evaluated as a summation of the two repetitive cycles for each displacement level until reaching the peak lateral load because some walls experienced sudden deterioration of strength, leading to brittle failure after reaching the peak load.

Figure 10 shows the development of the dissipated energy with respect to the drift ratio and how the variation of the aspect ratio and horizontal reinforcement types affect this parameter. Generally, walls with a lower aspect ratio show a higher amount of energy than those with a higher aspect ratio. This finding was agreed with [25], implying that walls with lower aspect ratio experienced a wide range of damage even during the first imposed displacement levels. Basically, walls reinforced with horizontal reinforcement attain higher resistance and dissipated energy than the un-reinforced ones [14, 31]. Slender walls either reinforced by bond beam or bed-joint reinforcement presented similar levels of dissipated energy. On the other hand, BJ squat wall showed higher dissipation of energy than BB squat wall by 45%. Finally,

**Table 3** Test specimens capacity calculation based on measured materials properties

| Specimen ID | Strut-and-tie model (STM) (kN) | Flexural (kN) | Diagonal shear (kN) | | $V_{r,\max}$ (kN) | | Sliding shear (kN) | | Exp. peak strength (average push–pull, kN) |
|---|---|---|---|---|---|---|---|---|---|
| | [7] | Compatibility analysis | CSA | TMS | CSA | TMS | CSA | TMS | |
| BB slender | 160 | 166 | 200 | 230 | 192 | 155 | 489 | 660 | 162 |
| BJ slender | 160 | 166 | 178 | 213 | 192 | 155 | 489 | 660 | 152 |
| BB squat | 448 | 544* | 312 | 378 | 350 | 271 | 872 | 1317 | 406 |
| BJ squat | 448 | 554* | 327 | 389 | 350 | 271 | 872 | 1317 | 416 |

* Strain compatibility analysis is not completely applicable to deep members
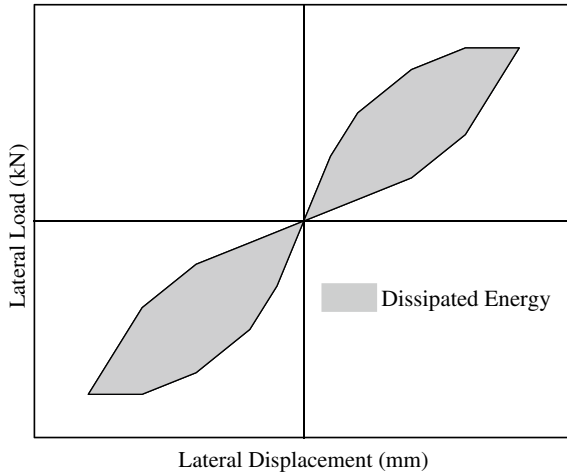
**Fig. 9** Computation of dissipated energy in one completed cycle

it is noted that, walls with a lower aspect ratio started showing higher increments of dissipated energy from an approximately drift ratio of 0.15%. At this drift ratio, either visible cracks were observed or a significant change in the stiffness occurred. This implies that the horizontal reinforcement started contributing to the wall system.
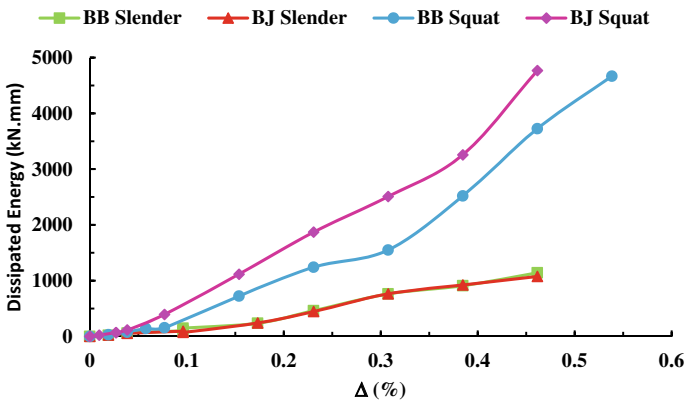


**Fig. 10** Dissipated energy of all tested walls

# 4 Conclusions

Preliminary experimental results of four full-scale PG masonry shear walls subjected to a combination of reversal cyclic lateral load and constant vertical load were described. The actual practice and conventional masonry buildings construction were reflected in the design and construction of the tested specimens. Damage progression, hysteretic response, and energy dissipation were utilized to investigate the effect of the variable design parameters considered in this study (aspect ratio and horizontal reinforcement type) on the performance of PG walls during cyclic loading. From all of the above, the following conclusions can be drawn:

- Diagonal shear was the dominant failure mode for the squat walls. On the other hand, slender walls exhibited a mixed flexure-shear failure mode.
- Walls with similar aspect ratios attained approximately equal peak lateral loads regardless of the horizontal reinforcement types.
- Bed-joint reinforcement proved to be a superior reinforcement in controlling cracks, specifically after reaching the peak load. On the other hand, the presence of grout in bond beams limited the development of cracks, and hence not allowing the cracks to distribute evenly throughout the wall surface in contrast to the bed-joint reinforcement.
- CSA equation is more conservative in predicting the diagonal shear strength than the TMS equation when compared with the experimental peak load of squat walls by 22%.
- Squat wall reinforced with bed-joint reinforcement showed higher dissipation of energy than squat wall reinforced with bond beam by 45%. On the other hand, slender walls reinforced either by bond beam or bed-joint reinforcement presented similar levels of dissipated energy.

# References

1. Baenziger G, Porter ML (2011) Joint reinforcement for masonry shear walls. In: Eleventh North American masonry conference. The Masonry Society, Minneapolis, MN
2. Banting BR, El-Dakhakhni WW (2012) Force- and displacement-based seismic performance parameters for reinforced masonry structural walls with boundary elements. J Struct Eng 138(12):1477–1491
3. Banting BR, El-Dakhakhni WW (2013) Seismic performance quantification of reinforced masonry structural walls with boundary elements. J Struct Eng 140(5)
4. Bolhassani M, Hamid AA, Johnson C, Schultz AE (2016) Shear strength expression for partially grouted masonry walls. Eng Struct 127:475–494

5. Bolhassani M, Hamid AA, Moon FL (2015) Enhancement of lateral in-plane capacity of partially grouted concrete masonry shear walls. Eng Struct 108:59–76

6. Calderon S, Sandoval C, Araya-Letelier G, Inzunza E (2021) Quasi-static testing of concrete masonry shear walls with different horizontal reinforcement schemes b. J Build Eng 38

7. Calderón S, Sandoval C, Inzunza E, Cruz-Noguez C (2019) Influence of a window-type opening on the shear response of partially-grouted masonry shear walls. 201

8. CSA.S304-14 (2014) Design of masonry structures S304-14. Canadian Standards Association, 5060 Spectrum Way, Suite 100, Ontario, Canada

9. Dastfan M, Driver RG (2015) Large scale test of a modular steel plate shear wall with partially encased composite columns. J Struct Eng 2(142)

10. Dhanasekar M (2011) Shear in reinforced and unreinforced masonry: response, design and construction. Proc Eng: 2069–2076

11. Dillon P, Fonseca FS (2017) Uncertainty in partially grouted masonry shear strength predictions. In: 13th Canadian masonry symposium, Halifax

12. FEMA 461 (2007) Interim testing protocols for determining the seismic performance characteristics of structural and nonstructural components. FEMA Rep. No. 461, Applied Technology Council, Washington, DC

13. Haach VG (2009) Development of a design method for reinforced masonry subjected to in-plane loading based on experimental and numerical analysis. University of Minho

14. Haach VG, Vasconcelos G, Lourenço PB (2010) Experimental analysis of reinforced concrete block masonry walls subjected to in-plane cyclic loading. J Struct Eng 136(4):452–462

15. Haach VG, Vasconcelos G, Lourenço PB (2013) Proposal of a design model for masonry walls subjected to in-plane loading. J Struct Eng 139(4):537–547

16. Haider W (2007) Haider—2007—inplane response of wide spaced reinforced masonry shear walls.pdf. Central Queensland University

17. Hassanli R, ElGawady MA, Mills JE (2014) An evaluation of design code expressions for in-plane shear strength of partially grouted masonry walls. Aust J Struct Eng 15(3):299–320. https://doi.org/10.7158/S13-031.2014.15.3

18. Hidalgo P, Luders C (1986) Shear strength of reinforced masonry walls under earthquake excitation. In: Proceedings of 3rd U.S. National conference on earthquake engineering, vol 2. Earthquake Engineering Research Institute, Oakland, CA, 1335–1546

19. Hoque N (2013) In-plane cyclic testing of reinforced concrete masonry walls to assess the effect of varying reinforcement anchorage and boun- dary conditions. Ph.D. thesis, Univ. of Calgary, Calgary, AL, Canada

20. Izquierdo K (2021) Statistical prediction methods for the in-plane shear strength of partially grouted masonry walls. M.Sc. thesis, University of Alberta

21. TMS (2016) Building code requirements and specifications for masonry structures. The Masonry Society

22. Minaie E, Mota M, Moon FL, Hamid AA (2010) In-plane behavior of partially grouted reinforced concrete masonry shear walls. J Struct Eng 136(9):1089–1097

23. Mobeen SS (2002) Cyclic tests of shear walls confined with double head studs. M.Sc. thesis, University of Alberta

24. Moghimi H (2013) Steel plate shear walls for low and moderate seismic regions and industrial plants structural engineering Department of Civil and Environmental Engineering. Ph.D. thesis, University of Alberta

25. Ramírez P, Sandoval C, Almazán JL (2016) Experimental study on in-plane cyclic response of partially grouted reinforced concrete masonry shear walls. Eng Struct 126:598–617

26. Sandoval C, Calderon S, Almazan JL (2018) Experimental cyclic response assessment of partially grouted reinforced clay brick masonry walls. Bull Earthq Eng 16(7):3127–3152

27. Schultz A (1996) Seismic performance of partially-grouted masonry shear walls. In: Proceedings of 11th world conference on earthquake engineering, international association for earthquake engineering, Tokyo, 246–256

28. Schultz AE, Hutchinson RS, Cheok GC (1998) Seismic performance of masonry walls with bed joint reinforcement. In: Proceedings of structural engineers world congress, Elsevier Science, New York, 18–23

29. Schultz AE, Johnson CA (2019) Seismic resistance mechanisms in partially grouted shear walls with new design details. In: 13th North American masonry conference, Salt lake City,UT,USA, 1274–1286
30. Stathis O, Fischer O, Lissel SL (2018) Effects of horizontal reinforcement distribution on in-plane performance and post-peak behaviour of masonry shear walls. In: 10th Australian masonry conference, Sydney, Australia, 467–478
31. Tomaževič M (1999) Earthquake resistant design of masonry buildings. Advances in Indian earthquake engineering and seismology: contributions in honour of Jai Krishna, Imperial College Press
32. Tomaževič M, Lutman M (1988) Seismic resistance of reinforced masonry walls. In: 9th world conference on earthquake engineering, Tokyo-Kyoto, Japan, 97–102
33. Wierzbicki CJ (2010) Behaviour of reduced-scale fully-grouted concrete block shear walls. M.Sc. thesis, McMaster Univ., Hamilton, ON, Canada
34. Yancey CWC, Scribner CF (1989) Influence of horizontal reinforcement on shear resistance of concrete block masonry walls (NISTIR 4202)

# Structural Specialty: Innovation in Structural Engineering

# A New Methodology to Predict Cumulative Plastic Ductility Capacity of Steel Buckling-Restrained Braces

**Ali Sadrara, Siamak Epackachi, and Ali Imanpour**

**Abstract** This paper presents a database of buckling-restrained brace (BRB) cyclic tests and predicts the cumulative plastic ductility (CPD) capacity of BRBs by using a regression-based machine learning (ML) model trained using the collected data. A summary of the past cyclic tests performed on BRBs is first presented. The hysteretic responses obtained from the test data along with influential, constitutional, and geometrical properties of tested BRBs are leveraged to develop the predictive model for the CPD capacity. The CPD capacity of prototype BRBs predicted using the predictive model proposed here agrees well with the test data, confirming the accuracy and efficiency of the ML-based technique employed here. Such a predictive model can be used in practice to size BRB cores in the preliminary design stage.

**Keywords** Buckling-restrained brace · Cumulative plastic ductility · Machine learning · Support vector regression

## 1 Introduction

Steel buckling-restrained braced frames (BRBF) are extensively used as the lateral load-resisting system of multi-story building structures, in particular, in high seismic zones. Unlike braces in concentrically braced frames (CBFs), buckling resisting braces (BRBs) are expected to yield in tension and compression under seismic loads offering a significant energy dissipation and high ductility capacities, while providing robust inelastic cyclic behavior [7, 22, 29, 30]. However, owing to the limited yielding

A. Sadrara (✉)
Sharif University of Technology, Tehran, Iran
e-mail: ali.sadrara@sharif.edu

S. Epackachi
Amirkabir University of Technology, Tehran, Iran

A. Imanpour
University of Alberta, Edmonton, AB, Canada

length of BRBs compared with the full BRB length, e.g., 0.6, significant plastic strains are developed in the BRB core while the brace undergoes large tension and compression cycles. The resulted accumulated plastic strains may however become problematic and compromise the load-carrying and inelastic deformation capacities of the BRB due to low cycle fatigue fracture [15]. The prediction and verification of the plastic strain or ductility capacity of BRBs are, therefore, considered as a critical design consideration by BRB manufacturers and designers.

Cumulative plastic ductility (CPD) capacity is defined as the cumulative plastic deformation sustained before fracture initiation in the member under extreme loading conditions. This parameter plays a key role in the design of steel BRBs and the evaluation of the seismic behavior of BRBFs. Despite significant advancement in the understanding of BRB seismic behavior and design of BRBs, predicting their CPD capacity, which is a key design parameter when sizing the BRB core, remained a crucial and yet challenging problem. Several predictive models have been proposed in the past, in particular over the past decade, however, a comprehensive method to predict the BRB CPD that can be used as a design tool in sizing BRBs has not been developed systematically yet.

## 2  Existing Predictive Models

Several methods have been developed by the research community to predict the CPD in steel BRBs manufactured in North America. These methods can be grouped into four families:

*Finite element-based models*: The first approach to predict the CPD of steel BRBS exploits an appropriate damage model [16, 27] incorporated into a high-fidelity finite element model (FEM). The accuracy and applicability of this method have been verified in past studies [27]. However, modeling difficulties and high computational cost limit the applicability of such models, particularly when large-scale structural components or systems are to be evaluated under a seismic ground motion.

*Phenomenological models*: This regression-based method predicts the CPD using past BRB test data [1]. However, the inclusiveness of the databases used to develop such models remains the key challenge [27].

*Strain-based models*: This approach aims to determine the relationship between the number of cycles to failure and the core strain amplitudes, e.g., Coffin- Manson relationship, which is typically obtained by curve-fitting to past test data and represent the fatigue life of the BRB core under cyclic loading [9, 28, 33, 34]. Miner's model is an example of this approach, which can be used to predict fracture of BRBs under random loading.

*Semi-analytical models*: These models determine the relationship between local and global strains [11]. The accumulation of local strains, so-called the actual local strain,

leads to fracture initiation. Global strain is the normalized end displacement of the brace. The predicted history of the local strain is used to estimate the damage.

Given that emerging machine learning-based (ML) methods are increasingly used in various disciplines to solve problems involving uncertainties such as solid mechanics, structural dynamics, structural health monitoring, computational fluid dynamics, electromagnetism, biomechanics, heat transfer, and even finance [6, 20–22, 24, 26, 35], there is an ample opportunity to leverage the power of advanced statistical tools to achieve a more accurate and efficient predictive model for CPD of steel BRBs. The current study attempts to propose a new methodology to tackle this complex problem involving a large number of uncertainties.

## 3 Database Development

A database of available BRB test data was collected. The database contains 99 large-scale BRB specimens that experienced fracture at the end of the test. It should be noted that of 99 specimens, 14 specimens lack sufficient test information and therefore the data associated with the remaining 85 specimens were used here to develop the model. The key test results are summarized in Table 1. Five parameters deemed to heavily influence CPD in BRBs were defined that include the normalized length of the yielding zone, area of the core, normalized core yield stress, and maximum BRB ductility in tension and compression. These parameters are represented by $A_c$, $L_y$, normalized $F_y$, $M_{ut}$, and $M_{uc}$, respectively. The maximum brace ductility in tension and compression are defined as the ratio of maximum deformation in tension and compression to the yield deformation, respectively. The normalized yield stress equals yield stress of the core divided by 290 MPa, which corresponds to ASTM A36 steel typically used to manufacture steel BRBs in North America.

Figure 1 shows four examples of the BRB specimens listed in Table 1.

The distributions of the input parameters are shown in Fig. 2. There exists a number of data gaps in the database for the normalized $F_y$, $A_c$, $L_y$, $M_{ut}$ input parameters, namely in the following ranges: (0.5, 0.67], (13,300, 16500], (5020,5930], and (4.5, 6.26], for normalized $F_y$, $A_c$, $L_y$, $M_{ut}$, respectively. Furthermore, data gaps can be observed within (4.1, 5.1] and (6.1, 8.1] for $M_{uc}$ parameter.

The cumulative plastic ductility in this study is defined as [9]

$$\text{CPD} = \sum_i \left[ \frac{2(|\varepsilon_i^{\max}| + |\varepsilon_i^{\min}|)}{\varepsilon_y} - 4 \right] \tag{1}$$

in which the $\varepsilon_i^{\max}$ and $\varepsilon_i^{\min}$ are the maximum and minimum of global strain during $i$-th loading cycle, respectively. The CPD capacities calculated for the BRB database are presented in Fig. 3a–e against the selected influential parameters including the length of the yielding zone, the area of the core, the normalized yield strength of the

**Table 1** Summary of BRB test data

| Study | Specimen ID | $L_y$ (mm) | $A_c$ (mm$^2$) | Normalized $F_y$ | $M_{ut}$ | $M_{uc}$ | CPD |
|---|---|---|---|---|---|---|---|
| [23] | No. 2 | 1291.00 | 2860.00 | 0.94 | 7.20 | NR | 1420.00 |
| [17] | 100 − 150 | 960.00 | 2500.00 | 0.33 | 0.80 | 0.80 | 17,504.00 |
| | 100 − 016 | 960.00 | 2500.00 | 0.33 | 0.10 | 0.10 | 27,208.00 |
| | 100 − 040 | 960.00 | 2500.00 | 0.33 | 0.20 | 0.20 | 98,085.00 |
| | 100 + 150 | 1180.00 | 4400.00 | 0.33 | 0.70 | 0.80 | 10,734.00 |
| | 400 − 200 | 960.00 | 2500.00 | 0.89 | 1.00 | 1.00 | 3894.00 |
| | 400 − 150 | 960.00 | 2500.00 | 0.89 | 0.80 | 0.80 | 4186.00 |
| | 235 + 150 | 470.00 | 2900.00 | 0.82 | 2.10 | 2.30 | 1261.00 |
| | 235 − 150 | 470.00 | 2800.00 | 0.77 | 2.20 | 2.40 | 2621.00 |
| [2] | 99 − 2 | 2990.00 | 3876.00 | 1.09 | 1.50 | 1.50 | 879.00 |
| | 00 − 11 | 3410.00 | 7125.00 | 1.02 | 2.30 | 2.30 | 1045.00 |
| [12] | 1.00 | 4470.40 | 2451.00 | 1.00 | 2.25 | 2.25 | 900.00 |
| | 2.00 | 4556.76 | 3845.00 | 1.00 | 2.25 | 2.25 | 600.00 |
| [19] | B-1 | 2907.00 | 11,648.00 | 1.03 | 3.40 | 3.40 | 864.00 |
| | B-2 | 6178.00 | 11,648.00 | 1.03 | 2.20 | 2.20 | 599.00 |
| [18] | 3G | 3670.30 | 17,419.00 | 0.89 | 3.19 | 3.13 | 631.00 |
| [5] | BRB60-North | 1625.60 | 838.00 | 1.09 | 2.90 | 3.50 | 389.00 |
| | BRB60-South | 1625.60 | 838.00 | 1.09 | 3.30 | 2.90 | 453.00 |
| | BRB80-North | 1651.00 | 1122.00 | 1.09 | 2.60 | 3.60 | 439.00 |
| | BRB80-South | 1651.00 | 1122.00 | 1.09 | 3.90 | 2.40 | 444.00 |
| | BRB100-North | 1981.20 | 1399.00 | 1.09 | 3.40 | 2.40 | 372.00 |
| [31, 32] | 2UBN | 2628.00 | 2512.00 | 1.18 | 0.80 | 1.70 | 255.00 |
| | 2UBS | 2628.00 | 2512.00 | 1.18 | 1.80 | 0.80 | 245.00 |
| | 1BRBN | 2605.00 | 2592.00 | 1.38 | 1.60 | 1.60 | 260.00 |
| | 1BRBS | 2605.00 | 2592.00 | 1.38 | 2.00 | 1.40 | 290.00 |
| | 2BRBN | 2658.00 | 2160.00 | 1.38 | 1.70 | 1.70 | 290.00 |
| | 2BRBS | 2658.00 | 2160.00 | 1.38 | 1.80 | 1.60 | 285.00 |
| | 3BRBN | 2660.00 | 1296.00 | 1.37 | 1.20 | 1.40 | 340.00 |
| | 3BRBS | 2660.00 | 1296.00 | 1.37 | 1.50 | 1.20 | 350.00 |
| [36] | C500WI | 2000.00 | 500.00 | 0.94 | 2.26 | 2.25 | 1403.00 |
| | C500WII | 2000.00 | 500.00 | 0.94 | 2.13 | 2.32 | 562.00 |
| | C800WI | 2000.00 | 800.00 | 0.97 | 2.04 | 2.03 | 2727.00 |
| | C800WII | 2000.00 | 800.00 | 0.97 | 2.14 | 2.22 | 2802.00 |
| | C600B | 1802.00 | 600.00 | 0.89 | 2.24 | 2.22 | 1875.00 |
| | C825B | 2198.00 | 825.00 | 0.89 | 1.88 | 1.82 | 2412.00 |
| | WC150B | 3879.00 | 2375.00 | 1.04 | 2.28 | 2.29 | 477.00 |

**Table 1** (continued)

| Study | Specimen ID | $L_y$ (mm) | $A_c$ (mm²) | Normalized $F_y$ | $M_{ut}$ | $M_{uc}$ | CPD |
|-------|-------------|-----------|-------------|------------------|----------|----------|-----|
|  | WC150C | 3879.00 | 2375.00 | 1.04 | 3.15 | 3.14 | 868.00 |
|  | WC250B | 3421.00 | 3650.00 | 0.95 | 2.91 | 2.86 | 804.00 |
|  | WC250C | 3421.00 | 3650.00 | 0.95 | 2.90 | 2.89 | 822.00 |
| [36] | WC500B | 3421.00 | 7446.00 | 0.95 | 1.46 | 1.52 | 206.00 |
|  | WC500C | 3421.00 | 7446.00 | 0.95 | 1.90 | 1.81 | 319.00 |
|  | PC160 | 4470.00 | 2451.00 | 1.00 | 2.40 | 2.34 | 1185.00 |
|  | PC250 | 4557.00 | 3845.00 | 1.00 | 2.46 | 2.40 | 750.00 |
|  | PC350 | 4656.00 | 5380.00 | 1.00 | 1.81 | 1.71 | 1239.00 |
|  | PC500 | 4702.00 | 8167.00 | 0.94 | 2.32 | 2.36 | 1564.00 |
|  | PC750A | 4679.00 | 11,516.00 | 1.00 | 2.52 | 2.43 | 1639.00 |
|  | PC750B | 4557.00 | 11,529.00 | 1.00 | 2.33 | 2.27 | 1085.00 |
|  | PC1200A | 4704.00 | 16,664.00 | 1.00 | 1.69 | 1.69 | 1211.00 |
|  | PC1200B | 4605.00 | 18,464.00 | 1.00 | 1.69 | 1.64 | 1305.00 |
| [8, 10] | 3.00 | 3800.00 | 5200.00 | 0.79 | 3.70 | 5.50 | 1221.00 |
|  | 6.00 | 3800.00 | 5200.00 | 0.97 | 3.70 | 5.40 | 733.00 |
|  | W15G2-74-IN | 1677.00 | 1110.00 | 1.31 | 4.00 | 4.00 | 391.00 |
|  | W18G2-90-IN | 1677.00 | 1620.00 | 1.24 | 4.00 | 4.00 | 491.00 |
|  | W20G2-90-IN | 2000.00 | 1800.00 | 1.04 | 3.50 | 3.50 | 669.00 |
|  | W20G2-110-IN | 2000.00 | 2200.00 | 1.04 | 3.50 | 3.50 | 661.00 |
|  | R40G2-200-IN | 1860.00 | 8000.00 | 1.37 | 3.50 | 3.50 | 583.00 |
|  | R25G1-250-IN | 1860.00 | 6250.00 | 1.36 | 3.50 | 3.50 | 767.00 |
|  | W16G2-85-IH | 1520.00 | 1360.00 | 1.35 | 3.50 | 3.50 | 486.00 |
|  | W16G2-95-IH | 1520.00 | 1520.00 | 1.34 | 3.50 | 3.50 | 491.00 |
|  | W16G2-85-CN | 2000.00 | 1360.00 | 0.93 | 3.00 | 3.00 | 1922.00 |
| [4] | 2.00 | 3000.00 | 2874.50 | 1.33 | 3.00 | 3.00 | 672.00 |
|  | 3.00 | 3000.00 | 2862.45 | 1.33 | 3.00 | 3.00 | 965.00 |
|  | 4.00 | 3000.00 | 2876.41 | 1.33 | 3.00 | 3.00 | 1228.00 |
|  | 5.00 | 3000.00 | 2852.15 | 1.33 | 3.00 | 3.00 | 765.00 |
|  | 7.00 | 3000.00 | 2843.30 | 1.33 | 1.50 | 2.20 | 1657.00 |
|  | 9.00 | 3000.00 | 2840.27 | 1.33 | 3.00 | 3.00 | 859.00 |
|  | 10.00 | 3000.00 | 2827.20 | 1.33 | 3.00 | 3.00 | 795.00 |
| [27] | UBB-1 | NR | NR | NR | 3.30 | 3.30 | 805.00 |
|  | UBB-1 | NR | NR | NR | 3.00 | 3.00 | 1103.00 |
|  | UBB-2M | NR | NR | NR | 3.29 | 3.29 | 752.00 |
|  | UBB-3M | NR | NR | NR | 3.30 | 3.30 | 882.00 |
|  | UBB-4M | NR | NR | NR | 3.45 | 3.45 | 550.00 |

**Table 1** (continued)

| Study | Specimen ID | $L_y$ (mm) | $A_c$ (mm$^2$) | Normalized $F_y$ | $M_{ut}$ | $M_{uc}$ | CPD |
|-------|-------------|-----------|----------------|------------------|----------|----------|-----|
|       | UBB-5M      | NR        | NR             | NR               | 3.28     | 3.28     | 526.00 |
|       | UBB-P1      | NR        | NR             | NR               | 3.50     | 3.50     | 1096.00 |
|       | UBB-P2      | NR        | NR             | NR               | 3.50     | 3.50     | 734.00 |
|       | UBB-P3      | NR        | NR             | NR               | 3.00     | 3.00     | 373.00 |
|       | UBB-P4      | NR        | NR             | NR               | 3.00     | 3.00     | 373.00 |
|       | WPSC1       | 3530.60   | 1300.35        | 0.99             | 3.50     | 3.50     | 1383.00 |
|       | WPSC2       | 3530.60   | 1935.48        | 0.99             | 3.50     | 3.50     | 2043.00 |
|       | WPSC3       | 3276.60   | 5846.76        | 0.98             | 2.25     | 2.25     | 1810.00 |
|       | PN1         | 771.53    | 1451.61        | 1.01             | 6.80     | 8.80     | 720.00 |
|       | WPSC4       | 3028.95   | 8588.50        | 1.04             | 3.50     | 3.50     | 591.00 |
|       | WPSC3A      | 3006.00   | 3749.80        | 1.03             | 3.50     | 3.50     | 815.00 |
|       | WPSC5       | NR        | NR             | NR               | 3.50     | 3.50     | 1708.00 |
|       | WPSC6       | NR        | NR             | NR               | 3.50     | 3.50     | 1261.00 |
|       | WPSC7       | NR        | NR             | NR               | 3.50     | 3.50     | 547.00 |
| [9]   | A1          | 3777.00   | 3600.00        | 1.04             | 0.28     | 0.30     | 5573.00 |
|       | B1          | 3048.00   | 7258.00        | 1.06             | 0.30     | 0.31     | 6780.00 |
|       | C1          | 2883.00   | 11,044.00      | 1.03             | 0.37     | 0.32     | 6719.00 |
|       | A2          | 3777.00   | 3600.00        | 1.04             | 0.78     | 0.88     | 3346.00 |
|       | B2          | 3048.00   | 7258.00        | 1.06             | 0.91     | 0.89     | 2867.00 |
|       | C2          | 2883.00   | 11,044.00      | 1.03             | 0.87     | 0.80     | 3957.00 |
|       | A3          | 3777.00   | 3600.00        | 1.04             | 2.15     | 2.09     | 808.00 |
|       | B3          | 3048.00   | 7258.00        | 1.06             | 2.18     | 2.13     | 1126.00 |
|       | C3          | 2883.00   | 11,044.00      | 1.03             | 2.06     | 2.14     | 1542.00 |
|       | B6          | 3048.00   | 7258.00        | 1.06             | 2.65     | 2.60     | 694.00 |
|       | B7          | 3048.00   | 7258.00        | 1.06             | 3.66     | 1.59     | 875.00 |
|       | B8          | 3048.00   | 7258.00        | 1.06             | 1.57     | 3.64     | 624.00 |
|       | B5          | 3048.00   | 7258.00        | 1.06             | 3.22     | 3.05     | 687.00 |

\* *NR* not reported

core, the maximum brace ductility in tension, and the maximum brace ductility in compression, respectively.

The range of input parameters and CPD capacities are given in a tabular format in Table 2 along with their minimum, maximum, average, and coefficient of variation values. The coefficient of variation of input parameters falls within the range of [20, 86.7%]. It can be seen that the yield stress has the least coefficient of variation. This is due to the fact that most of the specimens in the database are made of ASTM A36 steel. Besides, the coefficient of variation of the CPD parameter equals 191.8% which indicates the high variability of CPD within the database.
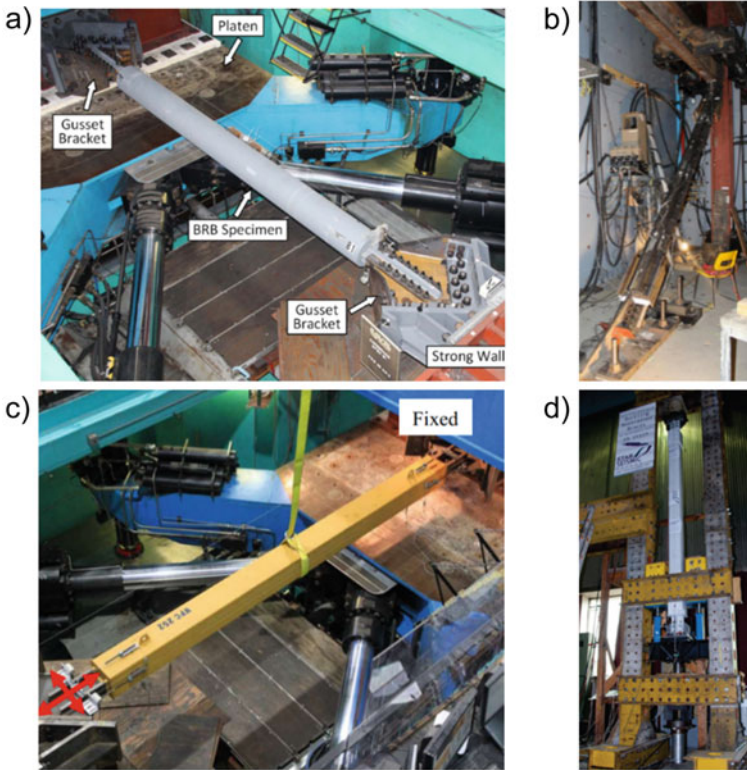
**Fig. 1** Test setup and BRB specimen: **a** [9], **b** [4], **c** [27], and **d** [36]

The correlation parameters are of most importance in machine learning problems. Figure 4 shows the correlation among the input CPD parameters. In this figure, each cell represents the Pearson correlation coefficient between two input parameters [3]. The correlation coefficient between two sets of data such as $\{(x_1, y_1), \ldots, (x_n, y_n)\}$ is calculated as follows:

$$r_{xy} = \frac{\sum_{i=1}^{n} (x_i - \overline{x})(y_i - \overline{y})}{\sqrt{\sum_{i=1}^{n} (x_i - \overline{x})^2}\sqrt{\sum_{i=1}^{n} (y_i - \overline{y})^2}} \tag{2}$$

$$\overline{x} = \frac{1}{n} \sum_{i=1}^{n} x_i, \, \overline{y} = \frac{1}{n} \sum_{i=1}^{n} y_i \tag{3}$$

As shown in Fig. 4, the correlation coefficients range from $-1$ to $+1$. The values of linear correlation near $+1$ and $-1$ show a higher correlation between the two input parameters. The input parameters with a high correlation coefficient
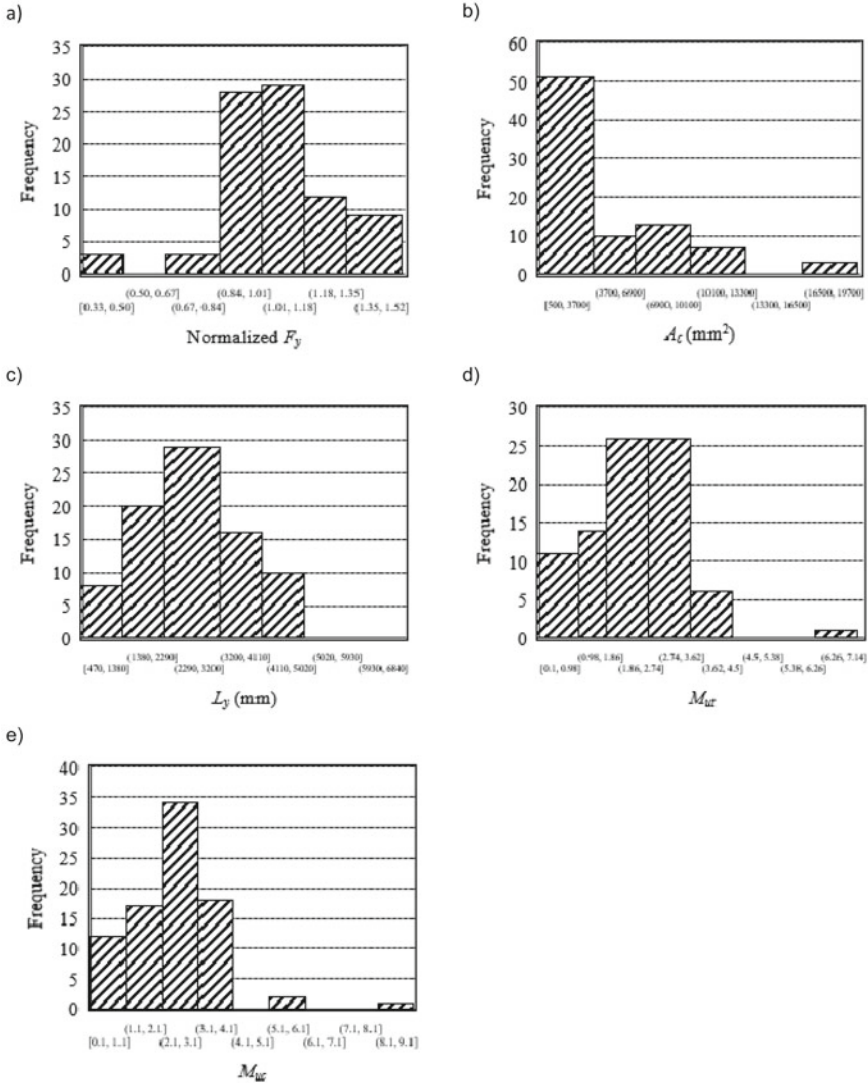
**Fig. 2** Distribution of input parameters: **a** Normalized yield stress, **b** Core area, **c** Length of the yielding zone, **d** Maximum brace ductility in tension, and **e** Maximum brace ductility in compression

can be eliminated to reduce the dimensionality of the inputs. As shown in Fig. 4, there are low correlation coefficient parameters between input parameters, but a high correlation coefficient is observed for $M_{ut}$ and $M_{uc}$, which stems from the fact that most of the specimens in the database are subjected to the AISC 341–16—Chapter K loading protocol.
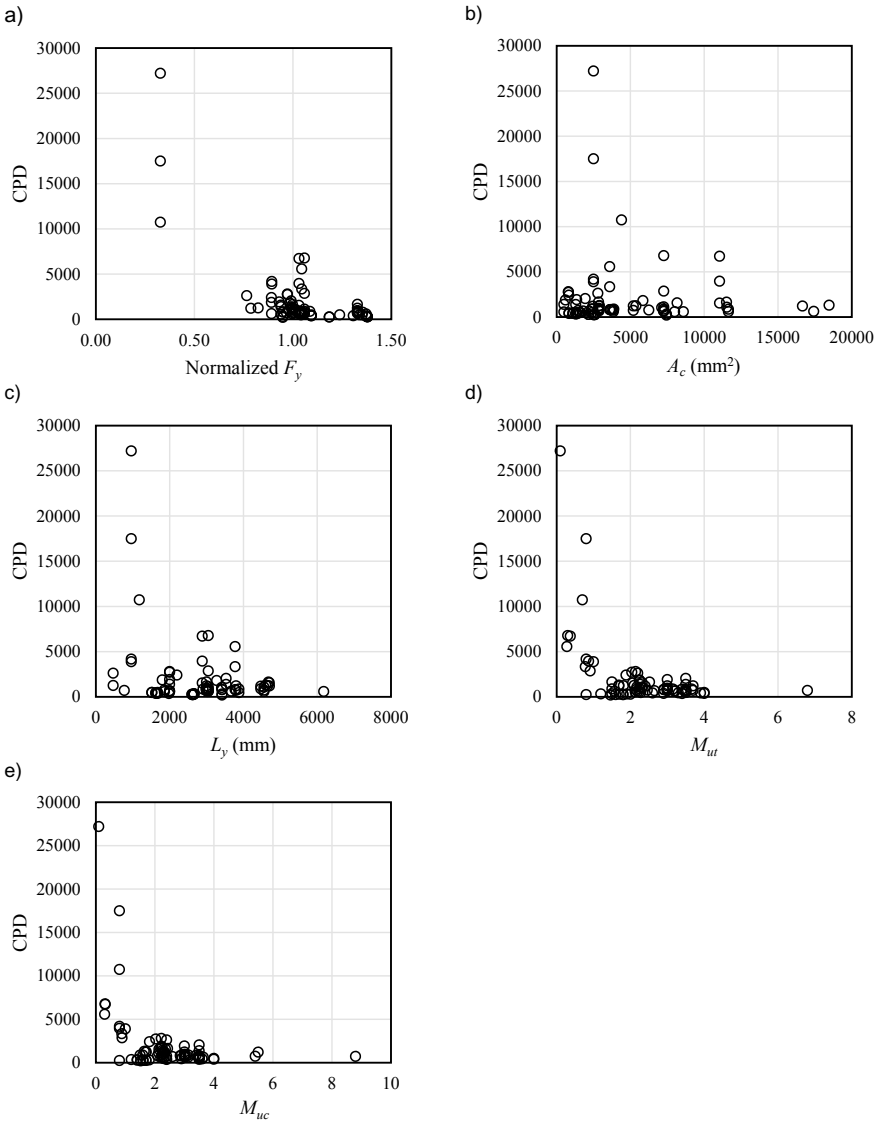
**Fig. 3** Distribution of CPD capacity against input parameters: **a** Normalized yield stress, **b** Core area, **c** Length of the yielding zone, **d** Maximum brace ductility in tension, and **e** Maximum brace ductility in compression

**Table 2** Statistics of input and output parameters

| | Parameters | Minimum | Maximum | Mean | Coefficient of variation (%) |
|---|---|---|---|---|---|
| Input parameters | *Normalized* $F_y$ | 0.33 | 1.38 | 1.06 | 20.0 |
| | $A_c$ (mm$^2$) | 500 | 18,464 | 4556.4 | 86.7 |
| | $L_y$ (mm) | 470 | 6178 | 2825.3 | 39.9 |
| | $M_{ut}$ | 0.1 | 6.8 | 2.4 | 45.7 |
| | $M_{uc}$ | 0.1 | 8.8 | 2.4 | 52.1 |
| Output parameter | CPD | 206.0 | 27,208 | 1915.6 | 191.8 |
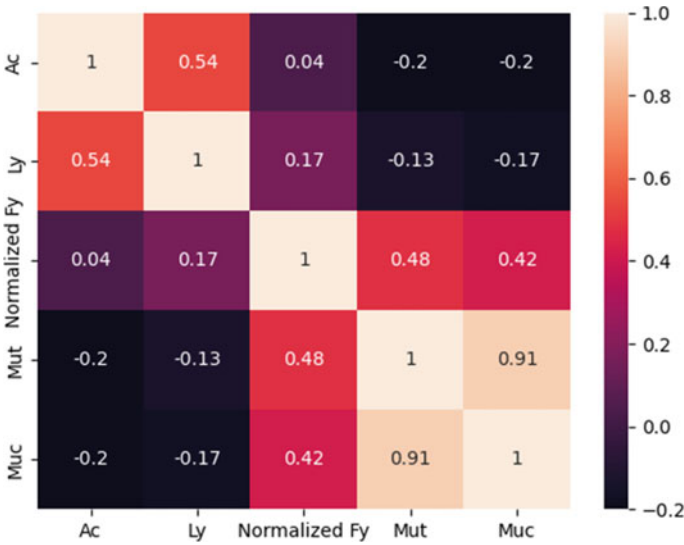


**Fig. 4** Pearson correlation coefficients for the CPD input parameters

## 4 Support Vector Regression-Based CPD Model

Rooted in the support vector machine, support vector regression (SVR) is a machine learning-based method that enjoys the maximal margin classifier. In this method, the linear regression is conducted on the mapped input parameters. The output of SVR is defined as:

$$f(x) = \phi(x)^{\mathrm{T}} w + b \tag{4}$$

where $b$ is the bias of the model, $\Phi(x)$ is a function that maps the input data into a higher dimension. The minimum value of $w$ is found by minimizing:

$$\min\left[\frac{1}{2}w^{\mathrm{T}}w + C\sum_{i=1}^{n}\left(\varsigma_i + \varsigma_i^*\right)\right] \quad (5)$$

in which $\varsigma_i$ and $\varsigma_i^*$ are slack variables, $C$ is the penalty parameter which is imposed to predict beyond the acceptable error margin. The predicted function based on SVR is defined as:

$$f\left(x, \alpha_i, \alpha_i^*\right) = \sum_{j=1}^{N}\left(\alpha_j - \alpha_j^*\right)K\left(x_j, x\right) + b \quad (6)$$

where $\alpha_i$ and $\alpha_i^*$ are Lagrange multipliers, $K(x_i, x)$ is the kernel function. The SVR in Eq. 6 can be adjusted using the different kernel functions. In this study, three kernel functions including radial basis function (RBF), linear function (linear), and polynomial function (poly) were used. To develop the ML-based model for predicting CPD, the input and output parameters were normalized. The data were then randomly broken down into training and testing data categories. Accordingly, 85% and 15% of data were considered as training and testing data, respectively. The training data were used to train the ML models and the accuracy of the proposed model was assessed using the test data. To examine the error, the mean absolute error (MAE) parameter was used:

$$\mathrm{MAE} = \frac{1}{n}\sum_{i=1}^{n}|y_i - f(x_i)| \quad (7)$$

in which $f(x_i)$ and $y_i$ are the predicted and experimental values of CPD. In ML models, the hyperparameters parameters control the learning process. These parameters should be chosen carefully to improve the accuracy of the model.

The ranges of hyperparameters in this study were chosen as suggested by [25]. The ranges of hyperparameters were then evaluated for each kernel function and the hyperparameters that led to the least error were finally shortlisted. There are three hyperparameters in radial basis kernel function including $C$, $\Upsilon$, and $\varepsilon$ for which the ranges [0.1, 1000], [0.0001, 5], and [0.0001, 5] were evaluated, respectively. The polynomial kernel function's hyperparameters include $C$, $\Upsilon$, $\varepsilon$, Coeff$_0$, and the degree of the polynomial. The ranges consisting of [0.1, 100], [0.005, 1], and [0.01, 0.1] were interrogated for $C$, $\Upsilon$, and $\varepsilon$, respectively. The degree of the polynomial and *Coeff$_0$* were taken as 4 and 1, respectively.

In Table 3, the optimum values of hyperparameters and their corresponding MAE are presented for each kernel function. Referring to Table 3, the MAE of polynomial and radial basis kernel functions equal 0.02 and these kernel functions yield the results with an acceptable error range. The MAE of the linear kernel function is equal to 0.05, which is higher than that of two other kernel functions, yet this function offers a simpler solution.

**Table 3** Selected optimum hyperparameters and respective errors

| Kernel function | Hyperparameters | MAE |
|---|---|---|
| Linear | $C = 1$, $\Upsilon = 0.0001$ | 0.05 |
| Radial basis | $C = 1000$, $\Upsilon = 0.005$, $\varepsilon = 0.001$ | 0.02 |
| Polynomial | $C = 1$, $\Upsilon = 0.1$, $\varepsilon = 0.01$, $Coeff_0 = 1$ and degree $= 4$ | 0.02 |
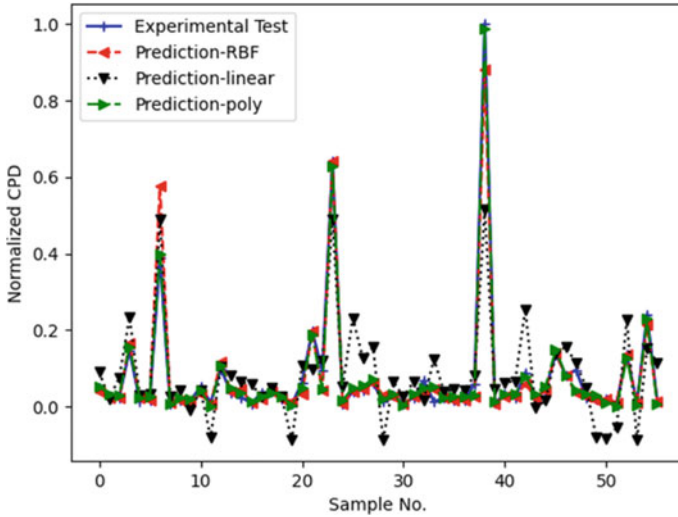


**Fig. 5** Predicted CPD versus training data

In Figs. 5 and 6, the CPD calculated by three different kernel functions are compared with the training and testing data, respectively. Overall, all proposed models can predict the CPD with acceptable accuracy. Referring to Figs. 5 and 6, the polynomial and radial basis kernel functions result in the CPD prediction with the most accuracy when compared with the testing data, i.e., experimental test data. As shown in Fig. 5, the proposed models are not overfitted to the training data. This suggests the generalization capability of the proposed models in predicting testing data.

## 5   Conclusions

This study presents a machine learning-based methodology for predicting the cumulative plastic ductility (CPD) of buckling-restrained braces (BRB) by leveraging experimental test data. A large number of available experimental test data involving steel BRBs were first collected. The data associated with 85 test specimens having
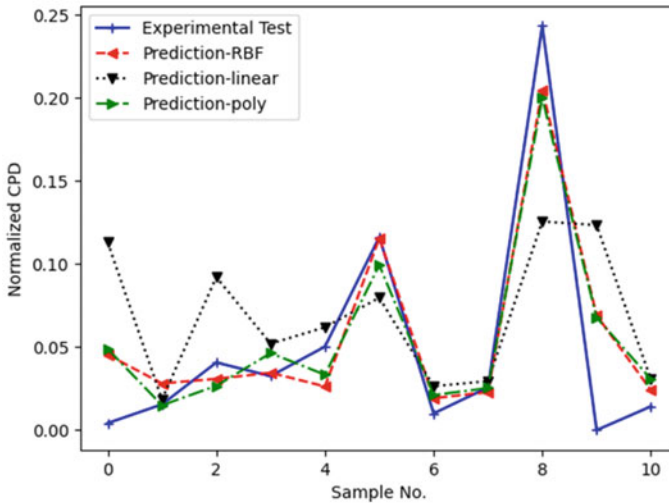
**Fig. 6** Predicted CPD versus experimental test data

sufficient input and output parameters (features) were used to develop the ML-based models. Five influential parameters including the normalized yield stress, core area, yielding zone length, and maximum ductility in tension and compression were found as effective input parameters. The support vector regression-based models were proposed to predict CPD using three different kernel functions including linear, polynomial, and radial basis functions through tuning hyperparameters of the SVR-based models to minimize the error parameter. The preliminary results of the proposed methodology confirm the proposed data-driven models can well predict the CPD capacity of steel BRBs. The proposed models should be improved in future studies by incorporating physics-based techniques, with the objective of achieving an easy-to-use tool for the design and evaluation of steel BRBs.

# References

1. Andrews BM, Fahnestock L, Song J (2008) Performance-based engineering framework and ductility capacity models for buckling-restrained braces. Newmark Structural Engineering Laboratory. University of Illinois at Urbana
2. Black C, Aiken ID, Makris N (2002) Component testing, stability analysis, and characterization of buckling-restrained unbonded braces (TM). Pacific Earthquake Engineering Research Center
3. Dangeti P (2017) Statistics for machine learning: techniques for exploring supervised, unsupervised, and reinforcement learning models with python and R. Packt Publ: 442/438
4. Dehghani M, Tremblay R (2018) Design and full-scale experimental evaluation of a seismically endurant steel buckling-restrained brace system. Earthq Eng Struct Dyn 47(1):105–129. https://doi.org/10.1002/EQE.2941. Accessed 16 Mar 2022
5. Fahnestock LA (2006) Analytical and large-scale experimental studies of earthquake-resistant buckling-restrained braced frame systems. Lehigh University

6. Geske R, Shastri K (1985) Valuation by approximation: a comparison of alternative option valuation techniques. J Financ Quant Anal 20(1):45. https://doi.org/10.2307/2330677
7. Kim J, Choi H (2004) Behavior and design of structures with buckling-restrained braces. Eng Struct 26(6):693–706. https://doi.org/10.1016/J.ENGSTRUCT.2003.09.010
8. Lanning J, Uang C-M (2014) Testing and modeling of A36 and stainless steel buckling-restrained braces under near-fault loading conditions
9. Li C-H, Vidmar Z, Saxey B, Reynolds M, Uang C-M (2022) A procedure for assessing low-cycle fatigue life of buckling-restrained braces. J Struct Eng 148(2):4021259
10. Lin P, Tsai K, Chang C, Hsiao Y, Wu A (2016) Seismic design and testing of buckling-restrained braces with a thin profile. Earthq Eng Struct Dyn 45(3):339–358
11. Matsui R, Takeuchi T (2012) Cumulative deformation capacity of buckling restrained braces taking buckling of core plates into account. In: 15th world conference on earthquake engineering
12. Merritt S, Uang C-M, Benzoni G (2003) Subassemblage testing of star seismic buckling restrained braces. Struct Syst Res Proj Rep No TR-2003/04, Univ Calif San Diego, San Diego
13. Moghaddam H, Sadrara A. Experimental and numerical evaluation of the mechanical characteristics of semi-rigid saddle connections. Struct Des Tall Spec Build n/a(n/a):e1923. https://doi.org/10.1002/tal.1923. https://doi.org/10.1002/tal.1923
14. Moghaddam H, Sadrara A (2021) Improving the mechanical characteristics of semi-rigid saddle connections. J Constr Steel Res 186:106917. https://doi.org/10.1016/J.JCSR.2021.106917
15. Moghaddam H, Sadrara A, Jalali SR (2021) Seismic performance of stainless-steel built-up box columns subjected to constant axial loads and cyclic lateral deformations. Structures 33:4080–4095. https://doi.org/10.1016/J.ISTRUC.2021.07.014. Accessed 14 July 2021. https://linkinghub.elsevier.com/retrieve/pii/S2352012421006299
16. Mortezagholi MH, Zahrai SM (2020) Evaluating ultra low cycle fatigue based on ductile fracture model in double core BRBs. Eng Struct 223:111158
17. Nakamura H, Takeuchi T, Maeda Y, Nakata Y, Sasaki T, Iwata M, Wada A (2000) Fatigue properties of practical-scale unbonded braces. Nippon steel Tech Rep 82
18. Newell J (2006) Subassemblage testing of CoreBrace buckling-restrained braces (G series)
19. Nishimoto K, Nakata Y, Kimura I, Aiken I, Yamada S, Wada A (2004) Sub-assembly testing of large buckling-restrained unbonded braces. In: 13th world conference on earthquake engineering. Vancouver Canada
20. Rao SS (2017 Oct 31) The finite element method in engineering. Finite Elem Method Eng: 1–763. https://doi.org/10.1115/1.3167179
21. Razavi Setvati M, Hicks SJ (2022) Machine learning models for predicting resistance of headed studs embedded in concrete. Eng Struct 254:113803. https://doi.org/10.1016/J.ENGSTRUCT.2021.113803
22. Sabelli R, Mahin S, Chang C (2003) Seismic demands on steel braced frame buildings with buckling-restrained braces. Eng Struct 25(5):655–666. https://doi.org/10.1016/S0141-0296(02)00175-X
23. Saeki E, Maeda Y, Iwamatsu K, Wada A, Iwata M, Mamor I (1999) Experimental study on dynamic behavior of unbonded braces. Collect Tech Reports Archit Soc Jpn 476(9):103–1G6
24. Salehi H, Burgueño R (2018) Emerging artificial intelligence methods in structural engineering. Eng Struct 171:170–189. https://doi.org/10.1016/J.ENGSTRUCT.2018.05.084
25. Smets K, Verdonk B, Jordaan EM (2007) Evaluation of performance measures for SVR hyperparameter selection. In: IEEE international conference on neural networks—conference proceedings, 637–642. https://doi.org/10.1109/IJCNN.2007.4371031
26. Solhmirzaei R, Salehi H, Kodur V, Naser MZ (2020) Machine learning framework for predicting failure mode and shear capacity of ultra high performance concrete beams. Eng Struct 224:111221. https://doi.org/10.1016/J.ENGSTRUCT.2020.111221
27. Terashima M (2018) Ductile fracture simulation and risk quantification of buckling-restrained braces under earthquakes. Stanford University
28. Tong C, Wu J, Hua K, Tian H (2021) Low-cycle fatigue life evaluation of buckling-restrained braces based on cumulative plastic deformation curves. 25(2):336–354. Accessed 16 Mar 2022. https://doi.org/10.1177/13694332211049991

29. Tremblay R, Bolduc P, Neville R, DeVall R (2006) Seismic testing and performance of buckling-restrained bracing systems. Can J Civ Eng 33(2):183–198
30. Tsai K-C, Lai JW, Chen C-H, Hsiao BC, Weng YT, Lin ML (2004) Pseudo dynamic tests of a full scale CFT/BRB composite frame. In: Structures 2004: building on the past, securing the future, pp 1–10
31. Tsai K, Hsiao P (2008) Pseudo-dynamic test of a full-scale CFT/BRB frame—part II: seismic performance of buckling-restrained braces and connections. Earthq Eng Struct Dyn 37(7):1099–1115
32. Tsai K, Hsiao P, Wang K, Weng Y, Lin M, Lin K, Chen C, Lai J, Lin S (2008) Pseudo-dynamic tests of a full-scale CFT/BRB frame—part I: specimen design, experiment and analysis. Earthq Eng Struct Dyn 37(7):1081–1098
33. Wang C-L, Usami T, Funayama J (2012) Improving low-cycle fatigue performance of high-performance buckling-restrained braces by toe-finished method. J Earthq Eng 16(8):1248–1268
34. Xie L, Wu J, Huang Q (2018) Experimental study on low-cycle fatigue performance of weld-free buckling-restrained braces. J Earthq Eng 22(8):1392–1414
35. Zilan Z, Zhizhou Z, Di Caprio F, Gu GX (2022) Machine learning for accelerating the design process of double-double composite structures. Compos Struct 285:115233. https://doi.org/10.1016/J.COMPSTRUCT.2022.115233
36. Zsarnoczay A (2013) Experimental and numerical investigation of buckling restrained braced frames for Eurocode conform design procedure development.

# Reliability Based Optimal Design of Magnetic Negative Stiffness Damper Based Inerter for Efficient Energy Harvesting

**Sourav Das and Solomon Tesfamariam**

**Abstract** This study proposes a magnetic negative stiffness damper-based inerter (MNSDI) for mitigating wind-induced vibration of tall structures and energy harvesting. The proposed control system has a nonlinear magnetic negative stiffness damper which does not add any additional stiffness into the combined system by which the adjoining members of the proposed control system do not experience any additional force demand. Due to the movement of the magnets inside a conductive pipe, MNSDI introduces eddy current damping into the structural system. An electromagnetic transducer is attached to MNSDI to convert vibrational energy to electrical energy. As the proposed system is a passive damper, the design parameters related to the damper are needed to estimate before installation. In this context, a reliability-based design optimization (RBDO) is used to estimate the design parameters of MNSDI, so that maximum energy harvesting can be achieved. As the RBDO framework is computationally expensive, Kriging is used as a surrogate model. For the numerical demonstration, a 76-storys high-rise benchmark building is considered. The stationary wind loads are used where fluctuating components of wind loads are simulated from the Davenport spectrum. The numerical results show the effectiveness of the proposed control system to reduce the structural vibration as well as enhance its energy harvesting capability simultaneously.

**Keywords** Inerter · Negative stiffness · Energy harvesting · Reliability-based optimization · Stationary wind

S. Das (✉) · S. Tesfamariam
School of Engineering, The University of British Columbia, Okanagan Campus, Kelowna, BC V1V 1V7, Canada
e-mail: sds2019@mail.ubc.ca

# 1    Introduction

Due to the development of technology, civil engineering structures have become slenderer and are more prone to excessive vibration due to dynamic loads, which leads to occupant discomfort and structural instability. To mitigate the excessive vibration in tall structures, tuned mass dampers (TMD), one of the oldest vibration absorbers are used. They consist of a lumped mass connected to the structure by a spring and a viscous damper [4]. The TMD is designed in such a way that the natural frequency of the TMD coincides with the natural frequency of the superstructure, which results in resonance and hence energy due to external loads is dissipated. It is noticed that the performance of TMD relies on the mass of the TMD, i.e., a higher mass provides better energy dissipation. However, the larger mass may have an adverse effect on high-rise buildings. Also, the length of the viscous damper should be at least four times the stroke length.

In the recent past, inerters have gained popularity among researchers as an alternative to TMD, where the inertance of an inerter is significantly larger than its actual weight [18]. It consists of flywheels that transform the linear displacement into rotational motion, by which the effective mass of the system is increased. Many variants of inerter have been proposed by researchers. Lazar et al. [8] proposed a tuned inerter damper which is connected to the structure by a spring and damper in series. A combination of inerter and TMD was proposed by [11] and showed the enhancement of energy dissipation under seismic events compared with the traditional TMD. Wen et al. [20] showed the effectiveness of multiple tuned inerter-based dampers using $H_2$ control theory. A rotational inertia double-tuned mass damper, which is an improved version of the tuned viscous mass damper, was proposed by [5]. Xie et al. [21] developed a cable-braced inerter system that is composed of a pair of bracing cables, a flywheel, and a shaft. When the structure experiences displacement, one of the cables is shortened by which shaft starts to rotate, and results the translational motion is transformed into rotational motion.

Despite the advantages of a tuned inerter damper (TID), few modifications are needed, such as the configuration of the TID. The TID consists of a spring, so that additional stiffness is added into the system, and hence the force demand on the member which is connected with the TID increases. In this view, a magnetic negative stiffness damper (MNSD) has been proposed in this study. The main advantage of this damper is that the additional stiffness is not added to the system. A few literatures are available on MNSD. Shi and Zhu [14] proposed MNSD and the effectiveness of the damper was investigated by experimental simulation. Furthermore, they studied the design optimization of MNSD through parametric studies [15]. Liu and Lui [10] proposed the mathematical expression for the nonlinear force–displacement hysteresis of MNSD, which was evaluated in the deterministic framework.

Energy harvesting has gained popularity in this decade where mechanical vibration energy of the controller can be transformed into electrical energy using an electromagnetic transducer. For energy harvesting, tuned inertial mass with an electromagnetic transducer was proposed by [1]. Marian and Giaralis [12] investigated the

potential of energy harvesting using a tuned mass damper-inerter system for harmonically excited structures. Petrini [13] proposed a tuned mass inerter damper with an electromagnetic transducer for wind-excited tall buildings. A back-driven ball screw mechanism combined with a rotary transducer was proposed by [2]. Gonzalez-Buelga [6] developed a combined system consisting of a tuned mass damper and an electromagnetic motor for mitigation of a structure's vibration and energy harvesting simultaneously. Tai and Zuo [19] studied the optimal performance of the energy harvester for base-excited structures. Das et al. [3] investigated the optimal performance of a shape memory alloy-based inerter system for simultaneous mitigation of wind-induced vibration of tall structures and energy harvesting.

The literature presented above mainly focuses on the different advancements of inerter systems for the reduction of structural vibration, due to earthquakes or winds and the potential for energy harvesting. This work investigated the performance of a modified inerter system, which enables to reduce vibrational energy of the structure and converts it into electrical energy. With this in view, the following objectives are set for the present study-

- Develop an inerter system which combines a magnetic negative stiffness damper (MNSD) and an electromagnetic transducer. The purpose of using MNSD is that additional stiffness is not added into the system and also the nonlinear load-deformation hysteresis can absorb the vibrational energy.
- To produce the maximum electrical energy, a surrogate-assisted optimization has been carried out to reduce the computational burden. Kriging is used as a surrogate model.
- To establish the potential of the proposed control system for simultaneous vibration control and energy harvesting, a 76-story building is being considered for numerical demonstration purposes.

## 2 Coupled Dynamics of Structure, Inerter, and Energy Harvesting System

In this section, a high-rise benchmark building is used to demonstrate the proposed control system to mitigate the wind-induced vibration. The governing equations of motion and modeling details of the magnetic negative stiffness damper are elaborated in detail in the following subsections.

### 2.1 Governing Equations of Motion for Coupled System

Figure 1 illustrates the layout of the proposed control system, where an inerter is installed on the top floor of the building and the ineter is coupled with a magnetic negative stiffness damper (MNSD) for energy dissipation and an electromagnetic
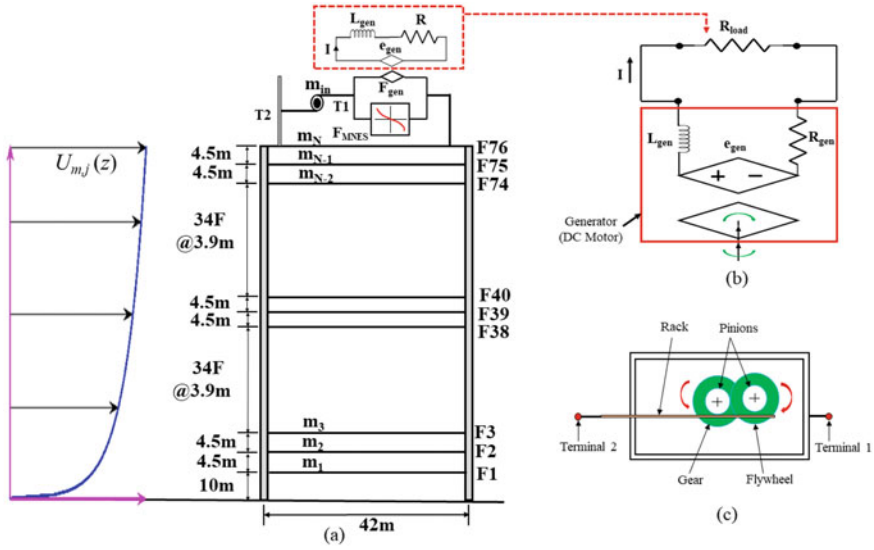
**Fig. 1** Architecture of the proposed control system; **a** Layout of 76-story benchmark building, **b** Modeling of a DC motor connected with a resistor in series and **c** Configuration of inerter

transducer for energy harvesting. In this proposed control system, the MNSD and the transducer are connected in parallel, whereas the entire system is connected with the inerter in series. The configuration of the inerter is shown in Fig. 1c, which consists of a rack, pinions, gears, and flywheels. The force induced by the inerter is expressed as

$$F_{in} = \frac{J_{in}}{r_{in}^2}\left(\ddot{x}_i - \ddot{x}_j\right) = M_{in}\ddot{x}_{in} \tag{1}$$

where $J_{in}$ is the moment of inertia of the flywheel, $r_{in}$ is the radius of the gear, $x_{in}$ denotes the displacement of the inerter which is the relative displacement of two terminals, (i.e., T1 and T2 in Fig. 1a) of the inerter, i.e., $x_{in} = (x_i - x_j)$. Also, the over-dot in Eq. (1) shows the differentiation with respect to time. Therefore, the inertance of the inerter ($M_{in}$) equals to $\left(J_{in}/r_{in}^2\right)$.

The governing equations of motion of the coupled system subjected to wind loads ($F_{wind}$) can be written as

$$M\ddot{x} + C\dot{x} + Kx - F_{MNSD} + K_f I = F_{wind} \tag{2}$$

$$M_{in}\ddot{x}_{in} + F_{MNSD} - K_f I = 0 \tag{3}$$

$$K_v(\dot{x}_{in} - \dot{x}_N) + RI + L_{gen}\dot{I} = 0 \tag{4}$$

where $M$, $C$, and $K$ are the mass, damping, and stiffness matrices of the primary structure, respectively. $x$ is a vector of floor displacement, i.e., $x = [x_1, x_2, …, x_N]^{\mathrm{T}}$, where $N$ is the total number of floors in the primary structure. $F_{\mathrm{MNSD}}$ in Eq. (2) represents the force induced by the magnetic negative stiffness damper, whose details are provided in the following subsection. Also, in Eq. (3), $R$ denotes the resistance of the electromagnetic transducer, which is equivalent to $R = (R_{\mathrm{gen}} + R_{\mathrm{load}})$, where $R_{\mathrm{gen}}$ and $R_{\mathrm{load}}$ are the resistance of the generator and the external resistance, respectively. The inductance of the generator is denoted by $L_{\mathrm{gen}}$. According to Faraday's law of electromagnetic induction, when the generator is attached to a rotating mechanical system, the electromotive force (EMF) induced in the generator, i.e., $e_{\mathrm{gen}}$ is proportional to the relative angular velocity of the mechanical system $(\dot{\theta}_{\mathrm{gen}})$, which is expressed as

$$e_{\mathrm{gen}}(t) = K_v \dot{\theta}_{\mathrm{gen}}(t) \tag{5}$$

where $K_v$ is the motor's back-EMF constant. Also, from Lorentz's force law, the torque produced in the mechanical system depends on the electric current $(I)$ induced in the coil of the generator, which is given by

$$\tau_{\mathrm{gen}}(t) = K_f I(t) \tag{6}$$

where $K_f$ is the motor torque constant. From Eqs. (5) and (6), the relation between torque and the angular velocity of the generator can be expressed as [9].

$$\tau_{\mathrm{gen}}(t) = \frac{K_v K_f}{R_{\mathrm{gen}} + R_{\mathrm{load}}} \dot{\theta}_{\mathrm{gen}}(t) \tag{7}$$

The power generated by the electromagnetic transducer is expressed as

$$P_g(t) = I^2(t) R_{\mathrm{load}} \tag{8}$$

## 2.2 Modeling Details of Magnetic Negative Stiffness Damper

In this study, a magnetic negative stiffness damper (MNSD) is used as a passive vibration absorber, as proposed by [14]. As shown in Fig. 2, the MNSD consists of three magnets placed in a non-ferromagnetic (e.g., copper) conductive pipe. One of these is movable. Two magnets are stationary at opposite ends of the conductive pipe. When the structure experiences displacement due to external dynamic loads, the movable magnet is displaced from the equilibrium position. To maintain the equilibrium position of the movable magnets, an opposite force is exerted by one of the stationary magnets, which is opposite to the motion of the movable magnet. Thus, negative stiffness is experienced. Also, as the conductive pipe is made of non-ferromagnetic material, an eddy current is induced due to the change in magnetic flux

**Fig. 2** Architecture of the proposed control system
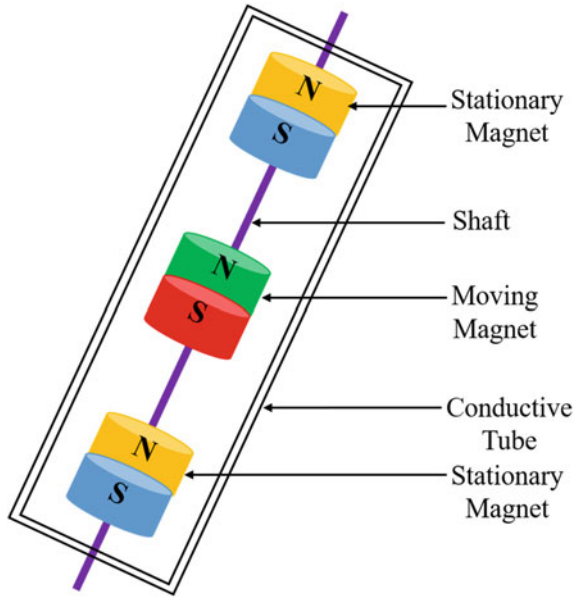
when the magnet is moving, thus damping is induced in the system. There are different phenomenological models available to define the load–deformation hysteresis of the MNSD. In this study, [10] is used to represent the nonlinear hysteresis of the MNSD, which is derived within the deterministic framework. The force exerted by the MNSD is expressed as

$$F_{\text{MNSD}} = C_{\text{MNSD}} \dot{x}_{\text{in}} \qquad (9)$$

where the damping coefficient, $C_{\text{MNSD}}$ is written as

$$C_{\text{MNSD}} = M_0^2 \mu_0^2 R^3 \sigma \varepsilon \left[ \frac{a}{1 + \left(\frac{\varepsilon}{b}\right)^c} \right] \qquad (10)$$

where $M_0$ is the magnetization, $\mu_0$ is the magnetic constant, and $\sigma$ is the conductivity of the pipe. In the above equation, $R$ denotes the magnetic radius and $\varepsilon = (R_2 - R_1)/R_1$, where $R_1$ and $R_2$ are the inner and outer radii of the conductive pipe. The constants $a$, $b$, and $c$ are expressed as follows

$$a = -\theta_1 \zeta^2 + \theta_2 \zeta + \theta_3 \qquad (11)$$

$$b = -\theta_4 \zeta^2 + \theta_5 \zeta + \theta_6 \qquad (12)$$

$$c = -\theta_7 \zeta^2 - \theta_8 \zeta + \theta_9 \qquad (13)$$

where $\zeta$ is the aspect ratio of the magnet. In the above equations, the constants $\theta_1$, …, $\theta_9$ depend on the manufacturing process, which helps the designer to tune the MNSD against the stochastic loads.

## 3    Simulation of Stochastic Wind Loads

In this study, the wind loads are simulated for the along-direction of the building floors, which are assumed to be quasi-steady. It has two components, i.e., mean and fluctuating components. The wind force acting on the $i$-th floor is expressed as

$$W_i = \frac{1}{2}\rho C_D A_i \big[U_{m,i}(t) + U_{f,i}(t)\big]^2 \lambda_D(f) \approx \rho C_D A_i U_{m,i}(t)U_{f,i}(t) \tag{14}$$

In the above equation, $\rho$ is the air density, $C_D$ is the drag coefficient, which depends on the shape of the building, and $A_i$ is the projected frontal area of the building perpendicular to the wind flow. The mean and fluctuating components of the wind velocity at the $i$-th floor of the building are represented by $U_{m,i}$ and $U_{f,i}$. In Eq. (14), $\lambda_D$ is the aerodynamic admittance for drag, which depends on the frequency ($f$) and equals 1.0 for quasi-static conditions. The mean component of the wind velocity, $U_{m,i}(t)$, at the $i$-th floor of the building is expressed using the logarithmic law [17], given by

$$U_{m,i}(z) = U_m(z_{10})\frac{\ln(z/z_0)}{\ln(10/z_0)} \tag{15}$$

where $z$ is the height measured from ground level, $U_m(z_{10})$ is the mean wind velocity at $z = 10$ m, and $z_0$ is the terrain roughness length. In Eq. (14), the fluctuating component of the wind velocity, $U_{f,i}$ is estimated using the spectral method, proposed by [16]. The power spectral density matrix for the stochastic wind field of a $N$-storys building is written as

$$S(\omega) = \begin{bmatrix} S_{11}(\omega) & \cdots & S_{1N}(\omega) \\ \vdots & \ddots & \vdots \\ S_{N1}(\omega) & \cdots & S_{NN}(\omega) \end{bmatrix} \tag{16}$$

where $\omega$ is the frequency in rad/s. The elements of $S(\omega)$ in Eq. (16), i.e., $S_{ij}(\omega)$ is expressed as

$$S_{ij}(\omega) = \begin{cases} S_i(\omega), & \text{if } i = j \\ \sqrt{S_i(\omega)S_j(\omega)}\psi_{ij}(\omega), & \text{if } i \neq j \end{cases} \tag{17}$$

where $S_i(\omega)$ denotes the power spectral density function (PSDF) and $\psi_{ij}(\omega)$ is the coherence function between the turbulence between the $i$-th floor and the $j$-th floor, corresponding to $z_i$ and $z_j$ heights, respectively. The coherence function, $\psi_{ij}(\omega)$ is given by

$$\psi_{ij}(\omega) = \exp\left[-\frac{\omega}{2\pi}\frac{C_z|z_i - z_j|}{0.5(U_{m,i} + U_{m,j})}\right] \tag{18}$$

where $C_z$ is the correlation coefficient. The power spectral density function, $S(\omega)$ in Eq. (16) is decomposed using Cholesky decomposition and is expressed as

$$S(\omega) = L(\omega)L^{T*}(\omega) \tag{19}$$

In the above equation, $L(\omega)$ is the lower triangular matrix for every $\omega$ whose complex conjugate is denoted by $L^*(\omega)$. The matrix $L(\omega)$ is expressed as follows

$$L(\omega) = \begin{bmatrix} L_{11}(\omega) & \cdots & 0 \\ \vdots & \ddots & \vdots \\ L_{N1}(\omega) & \cdots & L_{NN}(\omega) \end{bmatrix} \tag{20}$$

In this study, fluctuating component of the wind velocity are modeled as a stationary process, where the standard deviation of the fluctuating wind velocity is independent of time. The Davenport spectrum is used to simulate the stationary fluctuating wind speed, which is expressed as

$$S_i(\omega) = \frac{\left[\sigma^S(z)\right]^2}{6}\frac{2\pi}{\omega}\frac{4P^2}{\left(1 + P^2\right)^{4/3}} = \frac{1}{2}\frac{u_*^2}{\omega}\frac{4P^2}{\left(1 + P^2\right)^{4/3}} \tag{21}$$

where $P = \frac{1200\omega}{2\pi U_m(z_{10})}$ and the wind shear ($u_*$) in the above equation is written in the following form

$$u_* = \frac{k_0 U_{m,i}(z)}{\ln(z/z_0)} \tag{22}$$

where $k_0$ is the von-Karman constant, which is assumed to be 0.4 in this study. Once the PSDF for the stationary process is defined, the fluctuating wind velocity time history $U_{f,i}$ at the $i$-th floor of the building is simulated by using the superposition of trigonometric functions with random phase angles, which is expressed as

$$U_{f,i}^S(t) = 2\sum_{m=1}^{N}\sum_{l=1}^{N_\omega}|L_{im}(\omega_{ml})|\sqrt{\Delta\omega}\cos[\omega_{ml}t - \theta_{ml}(\omega_{ml}) + \Phi_{ml}] \tag{23}$$

where $L_{\mathrm{im}}$ is the element of the matrix $L(\omega)$ defined in Eq. (20). Also, $\Delta\omega$ is the frequency step, which is equal to $(\omega_u/N_\omega)$. The cut-off frequency is denoted by $\omega_u$ and $N_\omega$ is the total number of divisions in the frequency scale which is equal to $\omega_{\mathrm{ml}} = l\Delta\omega - \left(\frac{m-l}{m}\right)\Delta\omega$. In Eq. (23), $\Phi_{\mathrm{ml}}$ is the random phase angle which is uniformly distributed between 0 and $2\pi$. Also, $\theta_{\mathrm{ml}}(\omega_{\mathrm{ml}}) = \tan^{-1}\left\{\frac{\mathrm{Im}[L_{\mathrm{im}}(\omega_{\mathrm{ml}})]}{\mathrm{Re}[L_{\mathrm{im}}(\omega_{\mathrm{ml}})]}\right\}$, where Im[.] and Re[.] are the imaginary and real components, respectively.

# 4 Reliability-Based Optimal Tuning of Proposed Control System

The nonlinear model of the combined structural system coupled with the magnetic negative stiffness damper-based inerter system is elaborated in the previous section, which is exposed to stochastic wind loads. The purpose of the proposed control system is to maximize energy harvesting. Thus, the optimization of the proposed control system is needed to ensure the maximum power generated. Monte Carlo simulation is one of the oldest and most robust method for optimization. In reality, this method is not suitable for high-fidelity models where many samples are required to capture the nonlinearity of the structural system, and thus, it becomes computationally expensive. To reduce the computational cost, surrogate-assisted optimization has gained popularity in recent decades. In this study, Kriging, a well-known surrogate model, is used, whose details are provided in the following subsection.

## 4.1 Kriging Surrogate Model

Kriging is a stochastic modeling technique that produces the probabilistic responses from data samples using an interpolation scheme by minimizing the mean squared error. It approximates the original response surface with the assumption that the output from the Kriging is evaluated by a Gaussian process whose mean and autocorrelation are unknown and computed from the training dataset. The output response, which is a function of input design variables, is expressed as follows

$$Y \approx \sum_{i=1}^{m} \eta_i f_i(X) + \psi(X) = f(X)^T \eta + \psi(X) \tag{24}$$

where $X$ is the vector of design variables, $f(X)$ is the vector of m numbers of known regression functions, and $\eta$ is the regression coefficient vector. Also, in the above equation, $\psi(X)$ is the error function, which is assumed to be a stationary Gaussian process with a zero mean, constant variance $\sigma^2$ and the auto-correlation function $Q$. The autocovariance function of $\psi(X)$ is expressed as follows

$$E\big[\psi(X_i)\psi(X_j)\big] = \sigma^2 Q(X_i, X_j; \theta) \tag{25}$$

where $E[.]$ is the expectation operator and $Q(X_i, X_j; \theta)$ is the correlation between the samples $X_i$ and $X_j$ with respect to hyperparameter $\theta$. In this study, the Gaussian correlation function is used, which is written as

$$Q(X_i, X_j; \theta) = \prod_{k=1}^{m} \exp\Big\{-\theta_k(X_{i,k} - X_{j,k})^2\Big\} \tag{26}$$

where $X_{i,k}$ and $X_{j,k}$ are the $k$-th components of $X_i$ and $X_j$, respectively. The hyperparameter $\theta$ is estimated using a maximum likelihood estimate. Also, the regression coefficient $\eta$ in Eq. (24) is estimated by the least-square method. The details of the entire procedure of Kriging are found in [3].

## 4.2   Optimization of the Proposed Control System

In this study, Kriging is adopted for reliability-based optimization of the combined inerter system. The tuning parameters of the proposed control system are designed so that maximum power can be generated. In this case, the uncertainty is associated with the wind loads. The performance function for the optimization is considered as follows

$$\beta = \frac{\mu_{\text{Pg}}}{\sigma_{\text{Pg}}} \tag{27}$$

where $\beta$ is the reliability index, which is a ratio of the mean ($\mu_{\text{Pg}}$) and standard deviation ($\sigma_{\text{Pg}}$) of the maximum value of power generated from an ensemble of wind load time histories. Within this view, the RBDO problem is formulated as

$$X^* = \arg\max_X[\beta(X, \kappa)]$$
$$\text{s.t. } X_{\text{LL}} \leq X \leq X_{\text{UL}} \tag{28}$$

where $X = [R, \zeta, R_1, R_2, \theta_1, \ldots, \theta_9]$ are the design variables which are bounded by lower and upper limits, $X_{\text{LL}}$ and $X_{\text{UL}}$, respectively, $R$ and $\zeta$ are the radius and aspect ratio of the magnet, $R_1$ and $R_2$ are the inner and outer radii of the conductive pipe, and $\theta_1, \ldots, \theta_9$ are parameters which control the hysteresis of the MNSD, as defined in Eqs. (11)–(13). In Eq. (28), $\kappa$ is the uncertainty related to the wind loads. The entire framework of the optimization is shown in Fig. 3.
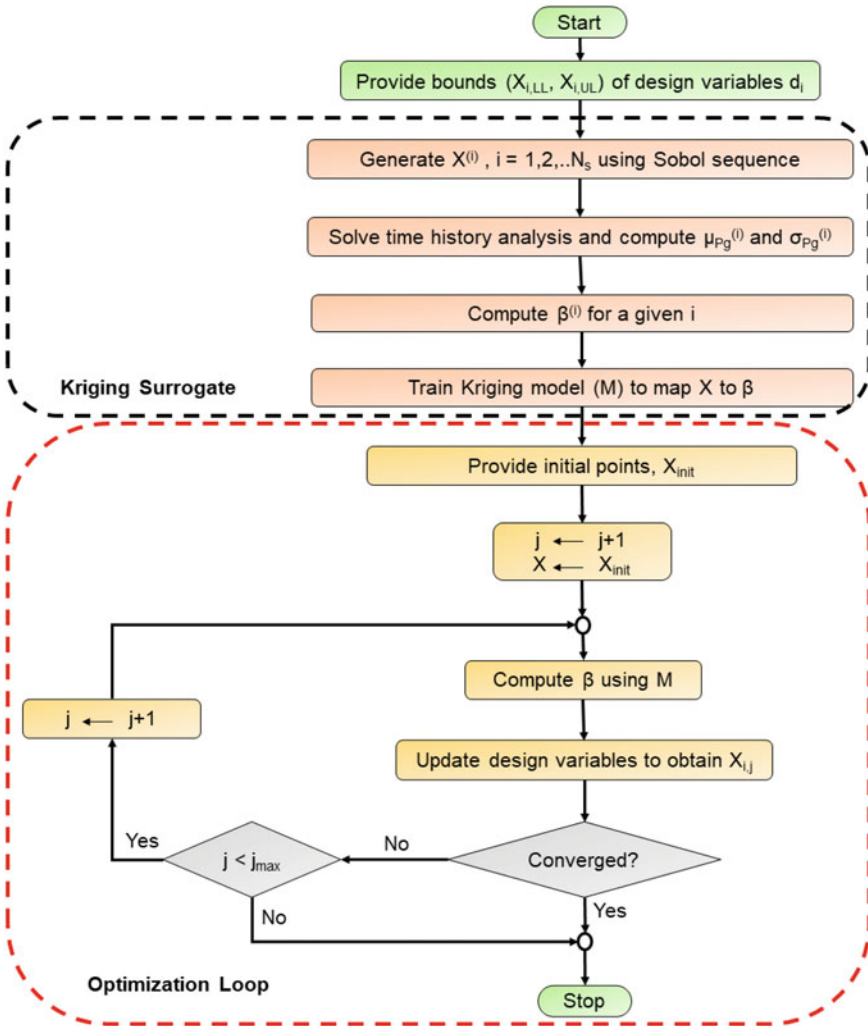
**Fig. 3** Flowchart representing kriging-based RBDO

## 5 Numerical Results

In this study, a 76-storys high-rise benchmark building is taken [22] for demonstration purposes. The building is located in Melbourne, Australia. It was made of reinforced concrete, consisting of a concrete core and a concrete frame. The total height of the structure is 306 m, where the first story is 10 m high from ground level, the story heights for the second and third floors, 38th to 40th, and 74th to 76th, are 4.5 m, and the other story heights are 3.9 m, as shown in Fig. 1. The total mass of the structure is 153,000 metric tons, including heavy machinery in plant rooms. The aspect ratio
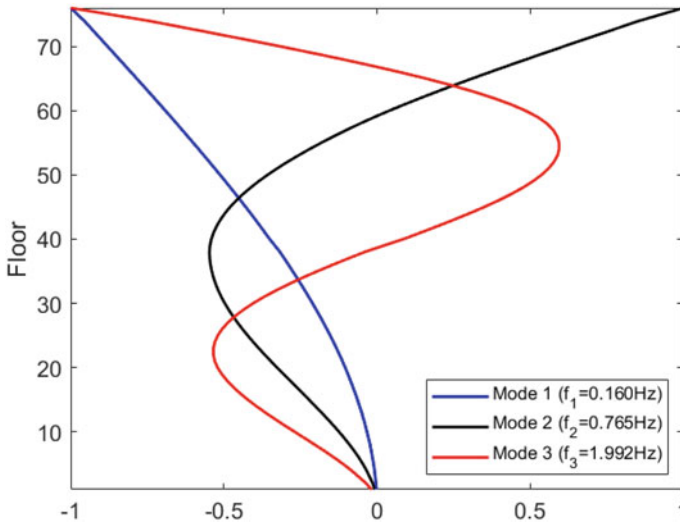
**Fig. 4** Mode shape and modal frequencies of 76-story benchmark building

(i.e., the height to width ratio) is 7.3, which means the structure is slender and highly sensitive to wind-induced vibration. The core of the structure is designed to resist the wind loads and the gravitational loads and part of wind loads are carried by concrete frames. In this study, all rotational degrees of freedom are eliminated by using a static condensation procedure, and only translational degrees of freedom are considered, i.e., one for each floor. The natural frequencies of the building are found to be 0.16, 0.765, and 1.992 Hz. The damping ratio is 1% in all modes following Rayleigh's model. Figure 4 shows the first three modal frequencies and mode shapes of the benchmark building.

Once the structural properties are defined, the wind loads are estimated for different floors of the building using the quasi-steady model, described in Sect. 3. The air density ($\rho$) is assumed to be 1.226 kg/m$^3$. The random wind loads have mean and fluctuating components, where the mean component of the wind loads at every floor is computed using the logarithmic power law and the stationary fluctuating part is simulated using the Davenport spectrum. The mean wind speed at 10 m above ground level is assumed to be 25 m/s. The ground roughness coefficient is assumed to be 0.3. Figure 5 shows the wind velocity acting on different floors of the building considering stationary fluctuating components. Also wind force time history for two cases at 70th and 76th floors are shown in Fig. 6a, b, respectively. Figure 6c depicts the auto power spectral density function (PSDF) at the 76th floor. Similarly, Fig. 6d illustrates the cross PSDF between 70th and 76th floors. It is seen that the target PSDF and the ensemble average of PSDF of fluctuating components of stationary wind loads simulated from the target PSDF match well.
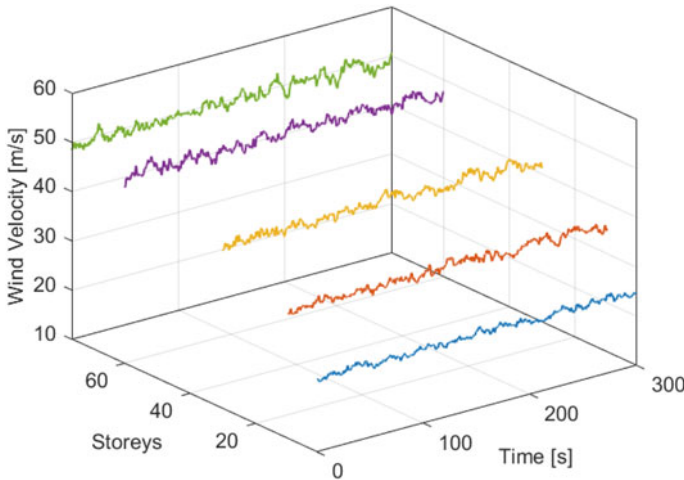
**Fig. 5** Wind velocity time histories at different floors considering stationary fluctuating component

Once the wind loads are simulated, attention is focused on the reliability-based optimization of the proposed controller, which is achieved by the tuning of the parameters of the proposed controller. The wind loads are assumed to be the only source of the uncertainty. The mean value of design parameters are taken: $\mu_R$ (radius of the magnet) = 10 mm, aspect ratio ($\zeta$) of the magnet = [0.05, 2], $\mu_{R1}$ (inner radius of the conductive pipe) = 11 mm, $\mu_{R2}$ (outer radius of the conductive pipe) = 17 mm, the constants related to the hysteresis of the MNSD, $[\mu_{\theta1}, …, \mu_{\theta9}]$ = [0.39,1.213, 0.19, 0.1375, 0.5043, 0.14, 0.033, 0.006, 1.1146]. The mean value is denoted by $\mu$ in the above. All the design variables are assumed to be uniformly distributed with coefficient of variation of 20%. As Kriging is the approximate model which predicts the output responses based on few observations called design of experiment (DoE). Therefore, attention is devoted to the accuracy of the surrogate model. Different sizes of DoE set, i.e., from 75 to 200 samples with an increment of 25 samples, are considered, which are generated using the Sobol sequence. With the DoE samples, a Kriging model is trained, and 50,000 prediction points of design variables are passed through the trained Kriging model to obtain the predicted outputs. The same prediction points are used for estimating the accuracy. Figure 7 shows the convergence history for different sizes of the DoE set. It is seen that a minimum of 125 DoE samples is needed in this case. With this DoE set, the optimization is carried out. The optimum design parameters are obtained as: $R = 9.6$ mm, $\zeta = 1.99$, $R_1 = 10.8$ mm, $R_2 = 13.6$ mm, the constants related to the hysteresis of the MNSD, $[\theta_1, …, \theta_9]$ = [0.51,1.06, 0.25, 0.16, 0.39, 0.11, 0.04, 0.0074, 0.898].

With the optimized design parameters, time history analysis is performed. Figure 8 shows the top floor displacement time history without and with controller. It is seen that the peak displacement of the top floor is reduced by 56% while using the proposed controller. The rms reduction is found to be 49%. Besides the reduction of peak and
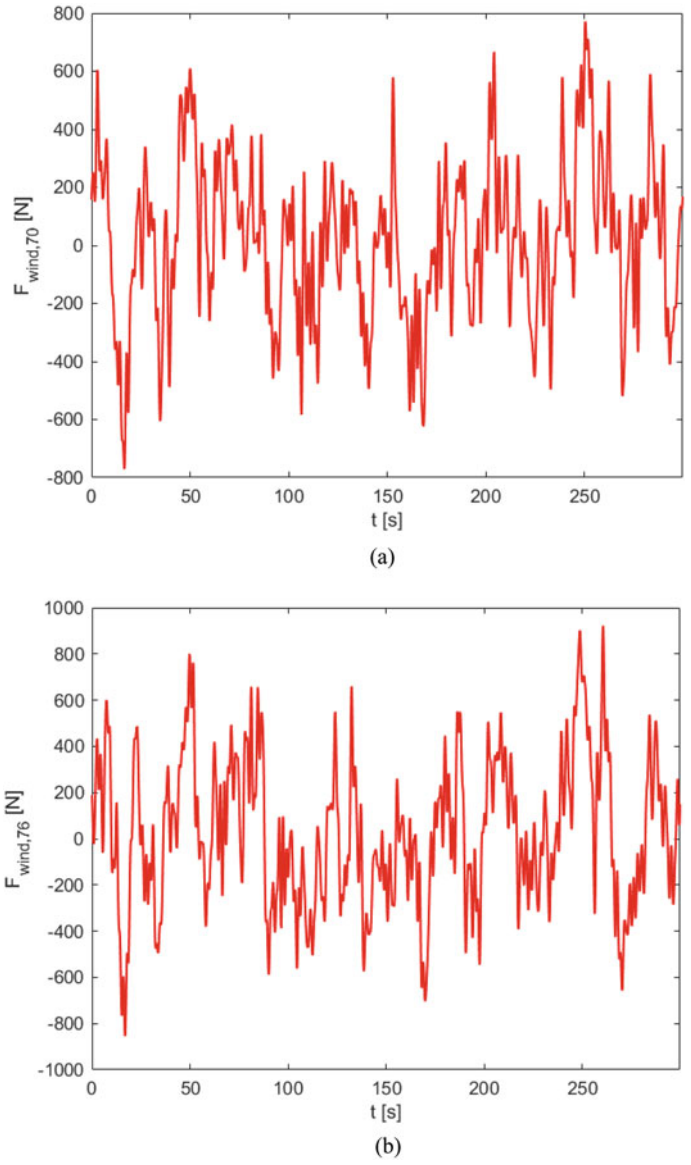
Fig. 6 Wind force simulation; **a** Time history at 70th floor, **b** Time history at 76th floor, **c** Auto PSDF at 76th floor and **c** Cross PSDF between 70th and 76th floor

(c)



(d)
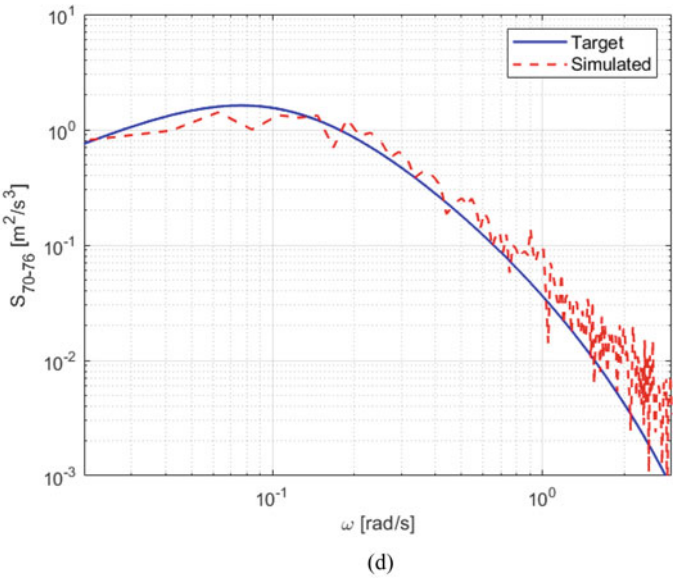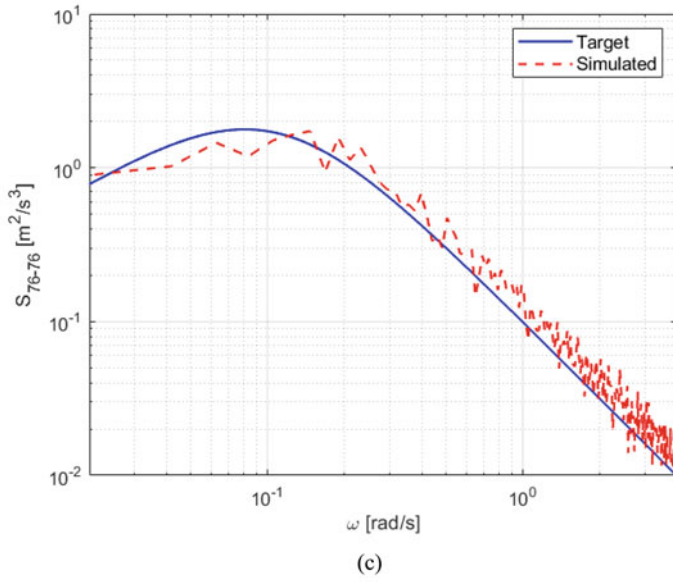
**Fig. 6** (continued)
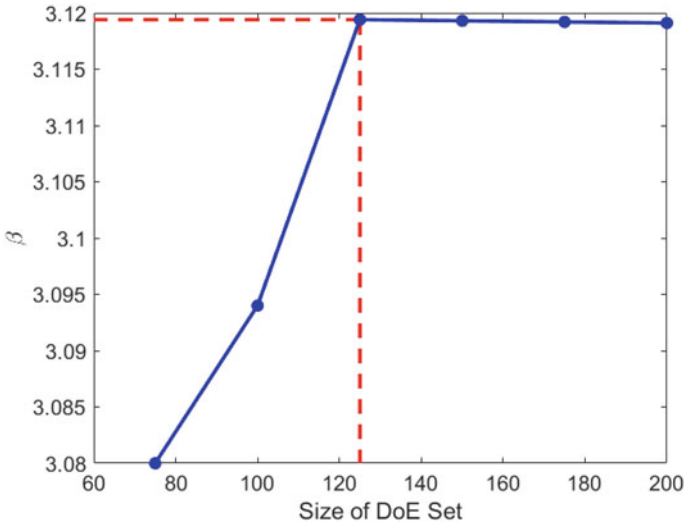
**Fig. 7** Convergence history for different sizes of DoE sets

rms displacement of the top floor, the generated power time history is shown in Fig. 9a. It is seen that the maximum power generated is found to be 716 W. Also, the ensemble average of power generated using the proposed control strategy is shown in Fig. 9b.
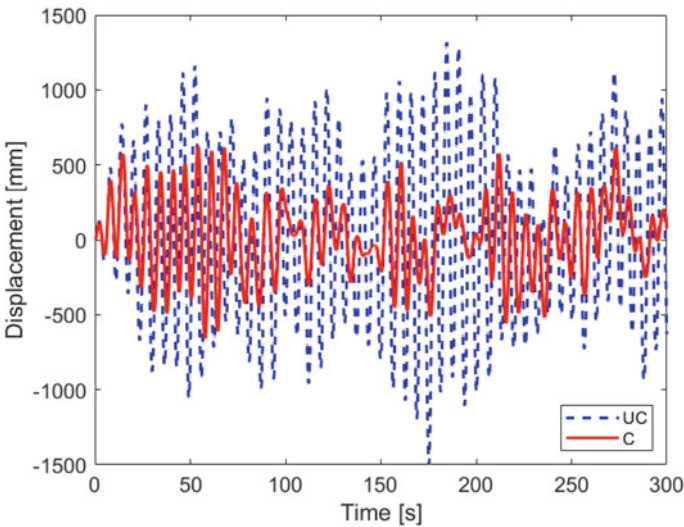


**Fig. 8** Top floor displacement without and with controller for stationary winds

(a)



(b)
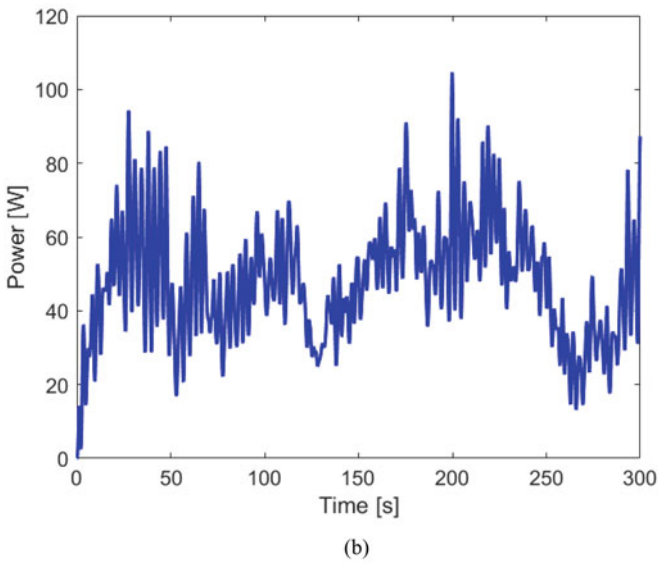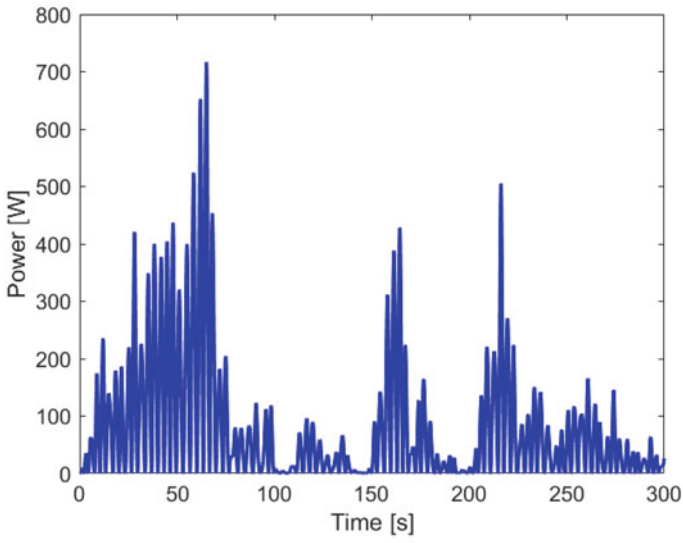
**Fig. 9** **a** Power generated for single wind load time history and **b** Ensemble average of power generated

# 6   Conclusions

The theoretical study presented in this paper is focused on the performance of the magnetic negative stiffness damper-based inerter system for mitigating the wind-induced vibration of tall structures. It also investigates the potential of energy harvesting using the proposed control system. The major contributions of the present study are listed below:

- The numerical results presented in the previous section establish the effectiveness of the proposed control system for mitigating the wind-induced vibration of the structure and energy harvesting, i.e., the conversion of vibrational energy into electrical energy. It shows the effectiveness of the proposed control system in terms of reducing the peak and rms values of the floor displacement.
- To generate the maximum power, the parameters associated with the proposed control system are tuned using stochastic optimization. Kriging is used as a surrogate model for optimization. It is seen that the optimization technique is very efficient at reducing the computational cost while operating in a stochastic environment.

All these aspects clearly indicate the effectiveness of the proposed control system for reducing the wind-induced vibration of high-rise buildings, and the dissipated energy is converted into power.

# References

1. Asai T, Araki Y, Ikago K (2018) Structural control with tuned inertial mass electromagnetic transducers. Struct Control Health Monit 25(2):e2059
2. Cassidy IL, Scruggs JT, Behrens S, Gavin HP (2011) Design and experimental characterization of an electromagnetic transducer for large-scale vibratory energy harvesting applications. J Intell Mater Syst Struct 22(17):2009–2024
3. Das S, Chakraborty A, Barua I (2021) Optimal tuning of SMA inerter for simultaneous wind induced vibration control of high-rise building and energy harvesting. Smart Mater Struct 30(2):025027
4. Den Hartog JP (1956) Mechanical vibrations, 4th edn. McGraw-Hill, New York
5. Garrido H, Curadelli O, Ambrosini D (2013) Improvement of tuned mass damper by using rotational inertia through tuned viscous mass damper. Eng Struct 56:2149–2153
6. Gonzalez-Buelga A, Clare LR, Cammarano A, Neild SA, Burrow SG, Inman DJ (2014) An optimised tuned mass damper/harvester device. Struct Control Health Monit 21(8):1154–1169
7. Hong HP (2016) Modeling of nonstationary winds and its applications. J Eng Mech 142(4):04016004
8. Lazar IF, Neild SA, Wagg DJ (2014) Using an inerter-based device for structural vibration suppression. Earthquake Eng Struct Dynam 43(8):1129–1147

9. Lin GL, Lin CC, Chen YJ, Hung TC (2021) Experimental verification of electromagnetic multiple tuned mass dampers for energy harvesting and structural control. Earthquake Eng Struct Dynam 50(13):3483–3504

10. Liu W, Lui EM (2020) Mathematical modeling and parametric study of magnetic negative stiffness dampers. Adv Struct Eng 23(8):1702–1714

11. Marian L, Giaralis A (2014) Optimal design of a novel tuned mass-damper–inerter (TMDI) passive vibration control configuration for stochastically support-excited structural systems. Probab Eng Mech 38:156–164

12. Marian L, Giaralis A (2017) The tuned mass-damper-inerter for harmonic vibrations suppression, attached mass reduction, and energy harvesting. Smart Struct Syst 19(6):665–678

13. Petrini F, Giaralis A, Wang Z (2020) Optimal tuned mass-damper-inerter (TMDI) design in wind-excited tall buildings for occupants' comfort serviceability performance and energy harvesting. Eng Struct 204:109904

14. Shi X, Zhu S (2015) Magnetic negative stiffness dampers. Smart Mater Struct 24(7):072002

15. Shi X, Zhu S (2017) Simulation and optimization of magnetic negative stiffness dampers. Sens Actuators, A 259:14–33

16. Shinozuka M, Deodatis G (1991) Simulation of stochastic processes by spectral representation. Appl Mech Rev 4(44):191–204

17. Simiu E, Scanlan RH (1996) Wind effects on structures: fundamentals and applications to design, vol 688. John Wiley, New York

18. Smith MC (2002) Synthesis of mechanical networks: the inerter. IEEE Trans Autom Control 47(10):1648–1662

19. Tai WC, Zuo L (2017) On optimization of energy harvesting from base-excited vibration. J Sound Vib 411:47–59

20. Wen Y, Chen Z, Hua X (2017) Design and evaluation of tuned inerter-based dampers for the seismic control of MDOF structures. J Struct Eng 143(4):04016207

21. Xie L, Ban X, Xue S, Ikago K, Kang J, Tang H (2019) Theoretical study on a cable-bracing inerter system for seismic mitigation. Appl Sci 9(19):4096

22. Yang JN, Agrawal AK, Samali B, Wu JC (2004) Benchmark problem for response control of wind-excited tall buildings. J Eng Mech 130(4):437–446

# Computational Wind Load Evaluation and Aerodynamic Mitigation of Low-Rise Building with Complex Roof Geometry

**Raghdah Al-Chalabi, Muhammad Ibrahim, and Ahmed Elshaer**

**Abstract** Climate change is the leading cause of the increasing intensity and occurrence frequency of wind events, inducing significant environmental, and economic consequences on communities and cities. A significant wind-induced load is initiated during a windstorm, mainly impacting the roof, leading to extensive roof damages or even roof total failure. Typical roof shapes (i.e., gable/hip) are generally designed using provision codes and standards. The wind tunnel test is required when designing complex roofs of low-rise buildings, as it experiences complex loading patterns attributed to the various possible roofing shapes and turbulent characteristics within the atmospheric boundary layer. This roof can be efficiently improved using computational modeling, including high-fidelity large eddy simulation (LES) to provide quantitative assessment for wind load in the primary stage of the design process to narrow down the design alternatives. The current study targets an isolated complex roof shape and utilizes LES and consistent discrete random flow generator (CDRFG) technique to simulate a model size of 1:50 to assess numerically wind load prediction by validating it with wind tunnel results. The current study aims to numerically (i) evaluate wind load on an isolated low-rise building with complex roof geometry for various angles of attack and (ii) mitigate the roof aerodynamically using parapets added corners to reduce the wind impact on the roof. The validation shows that both the mean and RMS pressure coefficients agree with the wind tunnel. The latter is evident for the effectiveness of that numerical evaluations as a precautionary method for the preliminary stage of the design of buildings. It was found that roof surfaces with solid parapets added to the corners can effectively reduce wind uplift forces on average by 15%.

**Keywords** Wind engineering · Aerodynamics · Computational fluid dynamics · Wind load · Low-rise buildings

R. Al-Chalabi (✉) · M. Ibrahim · A. Elshaer
Department of Civil Engineering, Lakehead University, Thunder Bay, ON, Canada
e-mail: ralchal@lakeheadu.ca

M. Ibrahim
Department of Aerospace Engineering, Queen's University, Belfast, UK

# 1   Introduction

Windstorms, among other factors such as aging infrastructure and the increasing population, have led to an increase in the damages to structures worldwide. According to post damage surveys, the wind is considered one of the major forces responsible for the catastrophic economic and life loss. In the past 40 years, windstorm-induced losses are estimated to represent 60% of the total insured losses due to natural catastrophes [18]. Barrie's recent tornado in July 2021 is a sobering reminder of the catastrophic damages that wind may cause. The majority of structures built in Canada are categorized as low-rise buildings used mainly for residential and commercial purposes. In fact, according to census Canada, in 2016, the overall housing stock was classified as single detached houses with more than 53%. The latter building category is considered the most susceptible to wind damage due to the development of high suction regions caused by flow separations at sharp edges, where worst wind suctions occur at corners for oblique wind directions. In addition, low-rise building is located within the atmospheric boundary layers where they may endure the complex turbulent characteristics [3]. Although uplift forces may not impose a significant threat to the structural building system due to the improvements in building codes over the last decades, they can still inflict severe damages to the building envelope, especially to roofing components such as roof sheathing and roof covering [5].

Since buildings are bluff bodies where the roof is the first line of defense that keeps the building intact during a wind event, many studies have investigated modifying the roof edges and corners using aerodynamic modification techniques (e.g., pergolas and parapets). These techniques can be installed as permanent architectural features or used for rehabilitation purposes. The aerodynamic modifications can be located at the roof edge/corner aim to change the wind flow pattern on the roof, by disrupting the formation of corner vortices or diverting the flows in the separation zone away. Previous studies showed the efficiency of modifying the roof corners or edges, by adding varieties of aerodynamic modifications to reduce both the extreme negative pressures caused by conical vortices and the uplift forces on the roof, such as [3, 8, 15, 19, 20]. It was found that the modifications techniques can effectively reduce the magnitude of wind load during wind events, subsequently reducing the wind-induced risk of damages on roofs of low-rise buildings in addition to the building cost. Furthermore, many studies have linked the mitigation technique to an optimization procedure to find the optimal configuration that maximizes wind load reduction, such as [7, 9, 12, 13].

Parapets are considered a commonly employed aerodynamic modification technique that has been used as a standard architectural feature for decades, where they can be retrofitted to an existing building structure. They are often mounted on edge and corner areas, as shown in Fig. 1, where their height and orientation are crucial factors impacting their efficiency. Their mechanism works by lifting the separated wind shear layers of the roof surface and dissipating the high local corner or edge suctions over a larger area [4]. One of the early studies investigating the aerodynamic impact of solid parapets on low-rise buildings was presented by [6]. Their results

Solid parapets          Discontinues corner          Full-length roof-edge
                        parapets                     parapets
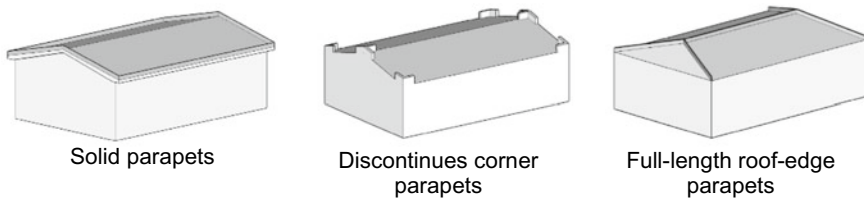
**Fig. 1** Roof aerodynamic modification techniques

show that tall parapets reduce the high suction on roofs, while short parapets are found to aggravate the edge and corner suction. Furthermore, the National Building Code of Canada (NBCC) has also allowed reductions for suction coefficients by up to 27%, depending on the reference roof height and the distance to the nearest edge. Also, codes such as the ASCE allow the corner zone to be treated as an edge zone for component and cladding design if a parapet equal to, or higher than 0.9 m is present, effectively reducing the corner suction coefficients by 35% in that standard.

Suaris and Irwin [19] have studied the parapet's porosity and location impact on the parapet's efficiency in reducing peak suctions. They have found that corner parapets with a porosity of 33% can lead to a total reduction in the peak corner suction of 60%. Bitsuamlak et al. [8] investigated architectural elements' efficiency, including gable end, ridgeline extensions, and wall extensions to reduce roof and wall corner suction. The study concluded that the 200 mm height ridgeline extension reduced peak suction for a roof slope of 3:12 at zones close to the roof ridge by 60%, while the gable-end extensions reduced peak suction close to the roof's gable-end zone by 65%. A similar study has been conducted by [2], where various corner, edge, and ridgeline modifications are applied to a gable roof sloped at 3:12. It was found that discontinued parapets with a height of 750 mm led to an 8% reduction of the uplift forces on the entire roof.

While the impact of parapets on the uplift forces for typical roof geometry (i.e., gable or hip) has been the topic of numerous experimental studies, the effect of parapets on complex roof structures has remained largely unexamined. Therefore, the current study aims to (i) validate the numerical wind load estimation on complex roofs geometry utilizing the consistent discrete random flow generator (CDRFG) technique as an inflow generator for a suburban terrain using experimentally obtained data (i.e., wind tunnel) to validate the numerical large eddy simulation (LES) and (ii) examine the effectiveness of using solid corner parapets to reduce the wind impact on low-rise building roofs with complex roof geometry. These objectives will be achieved by comparing the wind-induced forces and pressure on the roof surfaces. A modified model was compared with a non-modified model using computational fluid dynamics (CFD) at different wind angles of attack. The current study is divided into four sections. Section 1 (this section) presents an introduction and a review of the literature examining the impact of adding an aerodynamic modification to the roof perimeter at different wind angles of attack. Section 2 presents a description of the study, building's geometry, the utilized modifications techniques, the validation
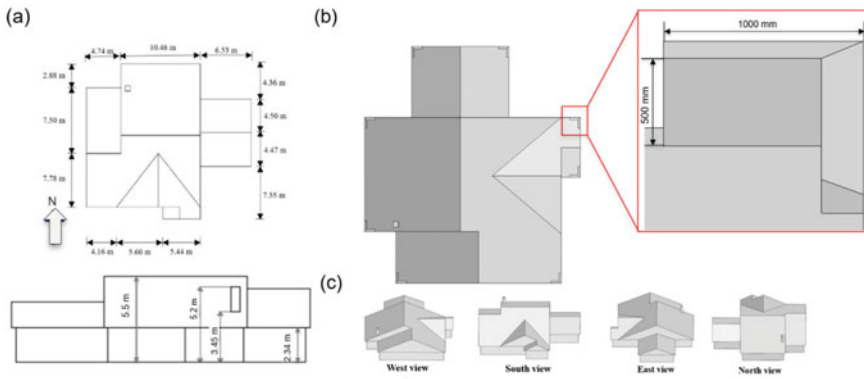
**Fig. 2** Non-modified model **a** Dimensions, **b** Solid parapet locations, and **c** Three-dimensional views

model, and the adopted CFD model used in assessing the different building shapes. Section 3 examines the impact of introducing the solid corner parapets on the wind-induced forces acting on the roof. Section 4 summarizes the conclusion and the main findings of this study.

## 2 Numerical Model Details

### 2.1 Study Case

The non-modified model has a complex roof geometry with varieties of roof slopes and one chimney, occupying a total footprint of 20.88 m × 21.7 m with a total height of 5.5 m and an eave height (H) of 2.34 m, in full scale. The overall model dimensions are illustrated in Fig. 2a. The study model was modified using parapets located at the perimeter corners of the roof with a height of 500 mm and width of 200 mm, while the length is 1000 mm, as shown in Fig. 2b.

To study the impact of the eight corner parapets on the forces acting on the roof, the roof surfaces parallel to the wind flow were denoted as R1–R6 while the roof surfaces that are perpendicular to the wind flow are denoted by S1–S6, as presented in Fig. 3.

### 2.2 Numerical Simulation

The adopted CFD model, employed Star CCM+ (15.04.008-R8), utilized the LES turbulence model, while using WALE sub-grid scale as previous studies found that
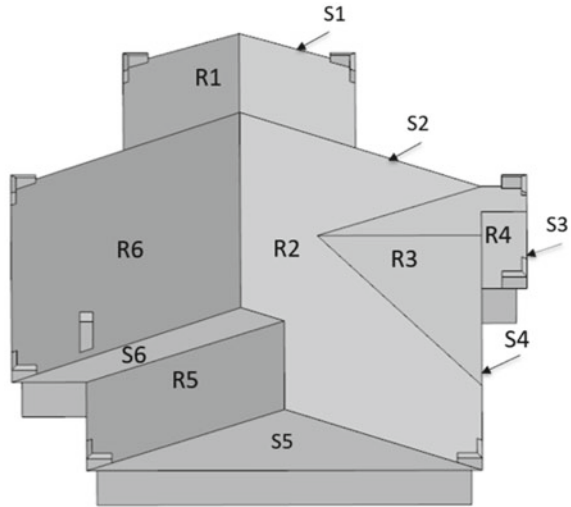
it can reduce the computational time by up to 64% [16]. The computational domain dimensions and boundary conditions are shown in Fig. 4. As observed from Table 1, the size of the computational domain satisfied the minimum values set by [14]. The boundary conditions at the top and side surfaces of the computational study domain were set as symmetry plane boundary conditions. The ground and building surfaces were defined as a non-slip wall boundary condition, while the outlet surface was defined as an outflow. The inlet wall was defined as a time-varying inlet velocity boundary condition using the CDRFG technique described by [1, 11].
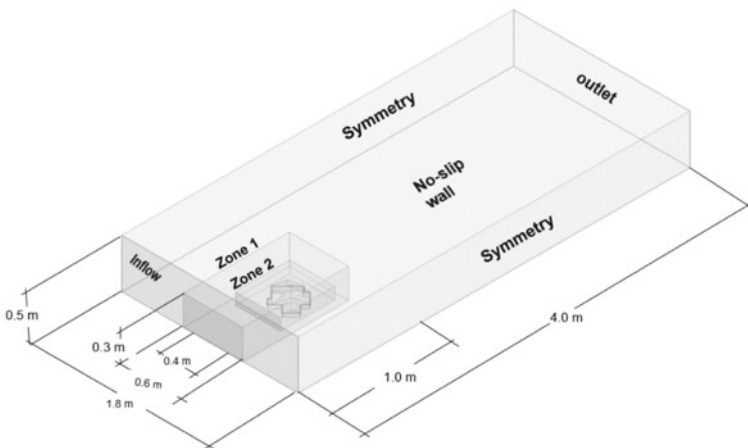


**Fig. 4** Computational domain dimensions and boundary conditions

**Table 1** Computational domain description

| $H_{max}$ | Current study | | Recommendations by [14] |
|---|---|---|---|
| 0.11 m | Vertical extension of the CD | 0.5 m | $5H_{max.}$ (0.55 m) |
| | The lateral extension of the CD | 1.8 m | $5H_{max}$ 0.55 m) |
| | Distance between inflow boundary and building | 0.6 m | $5H_{max}$ (0.55 m) |
| | Distance between outflow boundary and building | 3.04 m | $15H_{max}$ (1.65 m) |

The computational domain was discretized to a hexahedral ranging from 10 to 40 mm and further refined near the building to a mesh size of 4 mm to capture smaller scale turbulence near the building of interest, yielding a total mesh of 202 M cells as shown in Fig. 5. Conditional transient analysis with LES is crucial to ensure the convergence of a numerical method for partial differential equations. This condition is known as the Courant-Friedrichs-Lewy (CFL) [10]. The latter aims to provide numerical convergence within each time-steps by maintaining the Courant-Friedrichs-Lewy (CFL) below 1.0. CFL is calculated based on velocity, cell size, and the time step at each cell. Accordingly, the time step was chosen to be equal to 0.5 ms. The numerical simulations are conducted for 16,000 time-steps and 4 inner iterations.

The study's model was tested at eight wind angles of attack ranging from 0° to 315° with an increment of 45°, where the north is 0° and 90° is at east. The current study compares all dels' critical forces in *x*, *y*, and *z* directions. The data were processed and extracted in the sequence shown in Fig. 6. It is worth mentioning that surfaces generating negligible wind forces in specific directions have been eliminated from comparison. For instance, vertical surfaces, S1–S6, will not generate any uplift forces in the *z*-direction as they are vertical surfaces. Thus, uplift forces time histories have not been presented in the comparison.
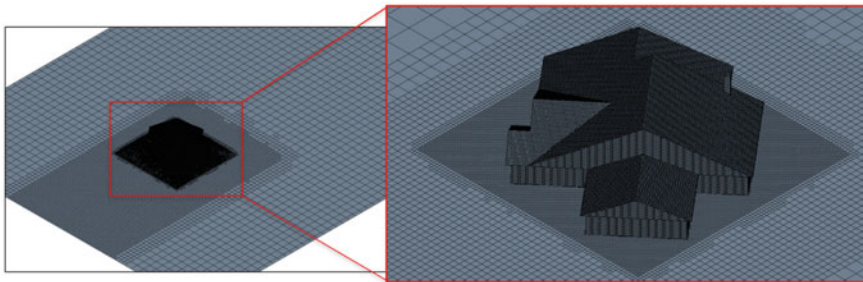


**Fig. 5** Mesh grid resolution utilized in the CFD simulations
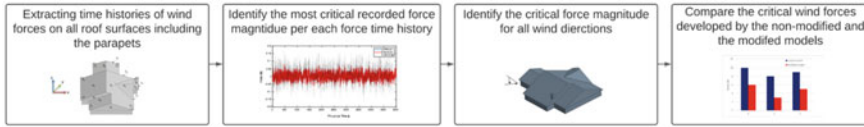
**Fig. 6**　Procedure of data extraction, processed, and analysis

## 2.3　Validation Simulation

The adopted CFD model was validated by comparing the mean and RMS of pressure coefficients with the experimentally obtained data presented by [17]. The validation process aims to assess the fidelity and accuracy of the numerical technique, evaluating wind load for a complex roof of a low-rise building. The mean velocity profile obtained from the wind tunnel measurements compared well with the velocity profile corresponding to suburban terrain roughness, $z_o$, of 230 mm and $1/\alpha$ is 0.14, as given in Eq. (1) and shown in Fig. 7a. The turbulence intensity profile demonstrated in Fig. 7b obtained from wind tunnel measurements is also compared well with the turbulence profile as shown in Eq. (2).

$$U_z = \overline{U}_{10}\left(\frac{z}{10}\right)^{1/\alpha} \tag{1}$$

$$I_u = c_u\left(\frac{z_{\text{ref}}}{z}\right)^{bu} \tag{2}$$

The CFD was modeled at a scale of 1:50 where the surface pressure acting on the roof was measured at a reference wind velocity ($V_{\text{ref}}$) of 1.6 m/s (8.2 m/s in full scale) corresponding to a mean roof height of 0.086 m (4.3 m in full scale). The validation
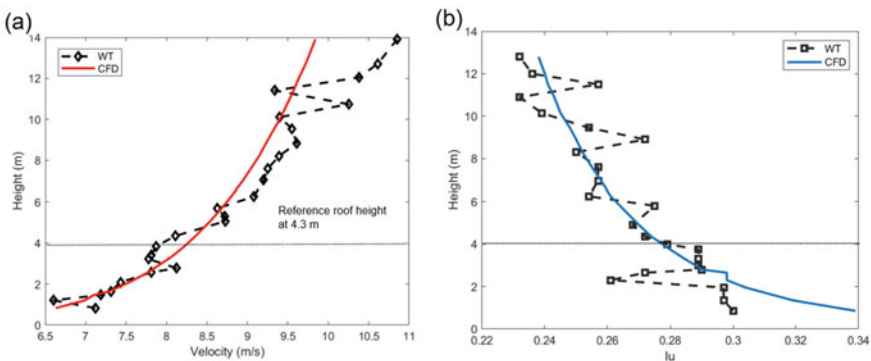


**Fig. 7**　Comparison of CFD and target profiles at mean roof height of 4.3 m in full scale **a** Mean velocity profile and **b** Turbulence intensity profile

**Fig. 8** Probes layout for
validation
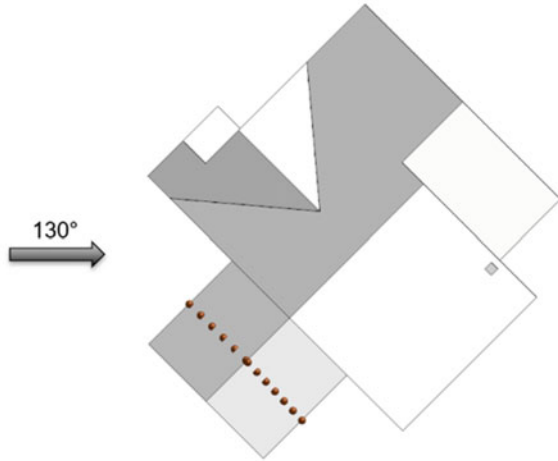


was performed to the tested model corresponding to a wind angle of attack of 130°,
which was repeated 30 times where each test lasted for 360 s, with a time scale of
1:10.

The mean velocity and turbulence intensity profile generated to match a suburban
terrain exposure were later adopted in the current study. Twelve pressure probes were
located in the middle of the gable roof at the east side of the building to extract mean
and RMS pressure coefficients, as shown in Fig. 8. The contours of both mean and
pressure coefficients for the validation model are shown in Fig. 9. Figure 10 presents
a comparison of the mean and RMS resulting from the current numerical simulation
to the experimental data. The mean and RMS pressure coefficient were found to
have an average difference of 14% and 10%, respectively. The pressure coefficient at
the side behind the separation point is lower than the experimental values. The latter
may be due to the insufficient power of incident flows in the relatively low-frequency
region.

## 3   Results and Discussion

It is crucial to perceive wind force characteristics as an influential climate factor in a
formed man-made environment, specifically in residential areas, to maximize wind-
resilience designs in low-rise buildings, considering structural safety and afford-
ability. Therefore, the current study addresses the impact of employing solid corner
parapets on stand-alone models in suburban terrain, by reducing the flow separation
at the corners to allow for an economical design for the low-rise buildings. During
wind events, the corner parapets aim to displace the vortex from the roof, therefore
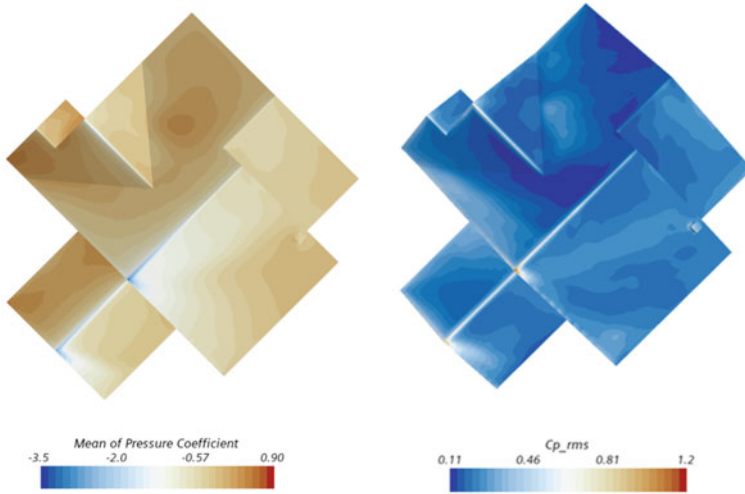
**Fig. 9** Mean and RMS of the pressure coefficients for wind angle of attack of 130°
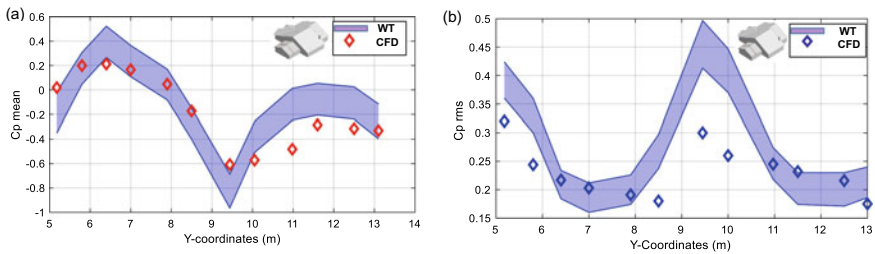


**Fig. 10** Mean and fluctuation pressure coefficient wind angle of attack of 130°

reducing the critical forces that govern the roof design. Ideally, the mitigation techniques (i.e., parapets) would have minimal loads to avoid them becoming wind-borne debris, or bring significant uplift, lateral forces to the host building.

The current study investigates the effectiveness of corner modification techniques in reducing wind load for low-rise buildings, with complex roof geometry during wind events. The parapets' orientation was chosen where the wind-induced damages were frequently reported in the post damage assessment locations. The results are based on extracting the time histories for the uplift, along- and across-wind forces for both the non-modified and the modified model at wind angles of attack ranging from 0° to 315° with an increment of 45°.

## 3.1 Critical Forces Acting on the Roof

### 3.1.1 Uplift Wind Forces

Solid corner parapets offer an effective wind pressure mitigation for complex roof surfaces. In the current study, the corner parapets effectively reduced the critical uplift forces up to 21% on the roof surface R1 (i.e., east side) as shown in Fig. 11. It can be noted from Fig. 12: that the reduction is not only applied to the most critical uplift force at an of the wind loading but also reduced the peaked uplift forces for the entire time history and increased instance the downward acting force (i.e., stabilizing the roof). Similarly, uplift forces on roof surfaces R5 and R6 were reduced by 12% and 32%, respectively.

On the contrary, it was noticed that part of the roof denoted by $R3$ experienced a rise in the uplift forces compared with the non-modified model. The latter is probably due to not modifying the middle zones of the complex roof geometry roof surfaces.
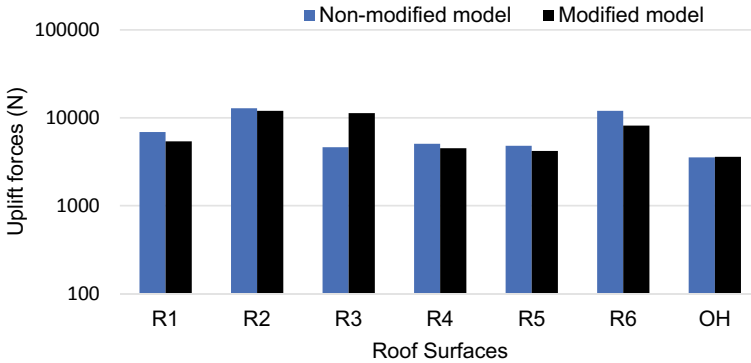


**Fig. 11** Critical full-scale uplift forces acting on roof surfaces
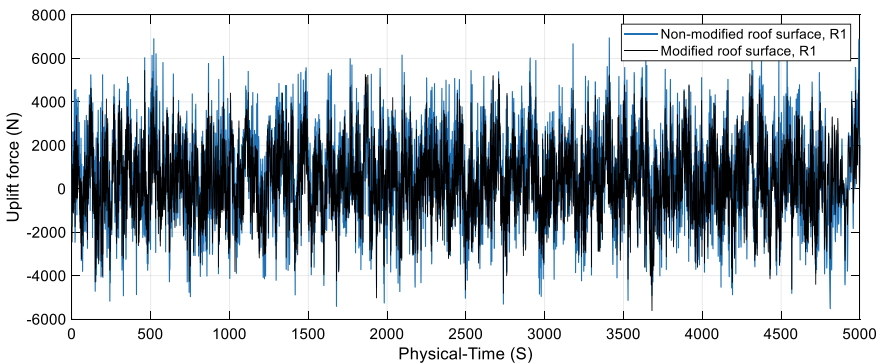


**Fig. 12** Uplift force time histories of non-modified and the modified models for R1
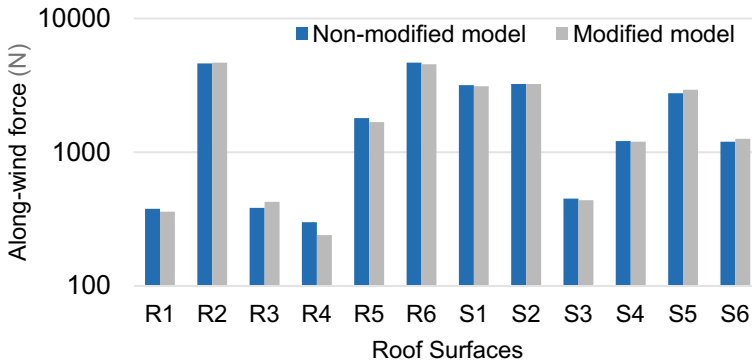
**Fig. 13** Critical full-scale along-wind forces acting on roof surfaces

This increase in the uplift forces can be reduced effectively by adding a ridgeline extension to displace the wind flow on the middle zones of the roof, as many previous studies concluded [2, 8]. On another note, Fig. 12 shows that parapets did not influence the uplift forces attributed to the overhang (i.e., OH) when the modified model compared with the non-modified model. The reason is that most incident flow of the wind at the building eave height depends on the wind pressure, which was not impacted by the presence of the parapets.

### 3.1.2 Along-Wind Forces

During wind events, structures experience wind forces, including the along-wind forces acting in the wind direction. In the current study, the along-wind forces are used as criteria for examining the effectiveness of the mitigation techniques. It can be noted from Fig. 13 that, the presence of the parapets did not reduce the along-wind forces attributed to the surface denoted by S. The along-wind forces for the surface perpendicular to the wind flow may be reduced by adding a gable-end extension. As for roof surface R4, it was found to have a 20% reduction in the along-wind force compared with the non-modified model. The latter reduction is achieved by the presence of the corner parapets at a wind angle of attack (i.e., 90° in this case). It can be noted from Fig. 14 that, although the minimum reduction in the along-wind forces for roof surface R1, however, adding parapets to the east end of the building led to reducing the peak of along-wind forces for the entire time history.

### 3.1.3 Across-Wind Forces

The term across wind refers to the transverse wind flow, which causes wind-induced forces in a plane perpendicular to the wind direction. In the design of low-rise buildings, the across wind-wind forces are typically dominant by the along-wind response,
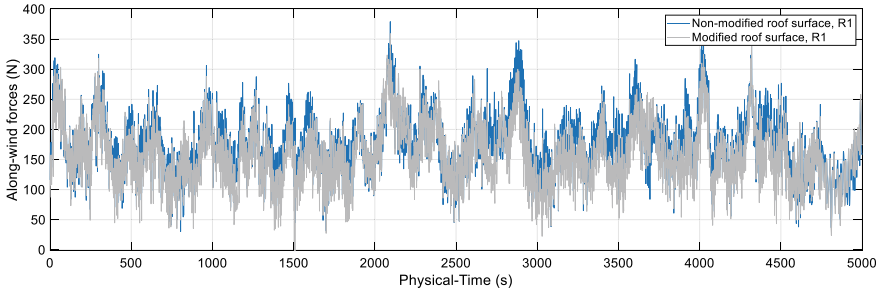
**Fig. 14** Along-wind force time histories of non-modified and the modified models
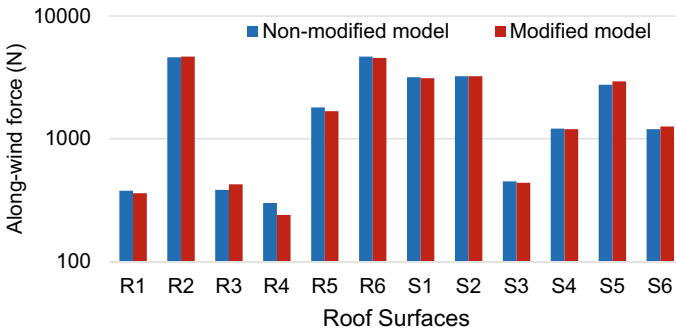


**Fig. 15** Critical full-scale across-wind forces acting on roof surfaces

unlike the tall buildings. The along-wind forces on the entire roof for the study complex roof geometry are, on average, 22 times higher than the across-wind forces. It can be noted from Fig. 15 that the across-wind forces impacted the multiple roof surfaces, where it produced a maximum reduction, for example of roof surface R1, of 31%. The entire time histories for across forces for both non-modified and modified models are presented in Fig. 16.

## 4 Summary and Conclusions

The study presented in the current paper investigates the performance of an aerodynamic mitigation technique (i.e., corner parapets) on reducing uplift, along-wind, and across-wind forces produced by wind in a suburban intensity setup on a complex roof of low-rise buildings. Parapets were added to the corners at the roof's perimeter to displace the wind shear layers away from the separation zones, where the damage is typically initiated due to high-pressure magnitudes. According to the comparative assessment between the non-modified and the modified model at a wind angle of attack ranging from 0° to 315° with an increment of 45°, corner parapets were found
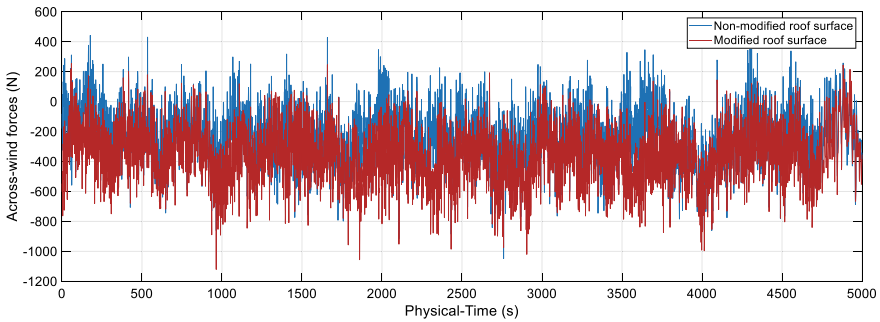
**Fig. 16** Across-wind force time histories of non-modified and the modified models

to reduce the uplift forces for multiple roof surfaces, where the maximum reduction for the critical uplift forces reached up to 32%, and on average 15% for the modified roof surfaces. In addition, it was noted that the total uplift forces induced by the overhang were not impacted by the presence of the parapets. Overall, it can be concluded that parapets located on a corner with a height ratio $(h_p/H)$ of 0.21 did produce a significant reduction in the uplift forces to multiple parts of the roof surfaces. These results encourage the continuation of research in this area, focusing on the mitigation feature's size, shape, and location. The parapets have a simple geometry and can be retrofitted to an existing building; therefore, it offers a great solution for reducing the uplift forces on the complex roof of low-rise buildings, providing an easy and economical solution for wind-induced damaged.

# References

1. Aboshosha H, Elshaer A, Bitsuamlak GT, El Damatty A (2015) Consistent inflow turbulence generator for LES evaluation of wind-induced responses for tall buildings. J Wind Eng Ind Aerodyn 142:198–216. https://doi.org/10.1016/j.jweia.2015.04.004
2. Al-Chalabi R, Elshaer A (2021) Aerodynamic mitigation of low-rise building roofs. In: CSCE confrence, Nigra Falls
3. Aly AM, Bresowar J (2016) Aerodynamic mitigation of wind-induced uplift forces on low-rise buildings: a comparative study. J Build Eng 5:267–276. https://doi.org/10.1016/j.jobe.2016.01.007
4. Asghari Mooneghi M, Kargarmoakhar R (2016) Aerodynamic mitigation and shape optimization of buildings: review. J Build Eng
5. Azzi Z, Habte F, Elawady A, Chowdhury AG, Moravej M (2020) Aerodynamic mitigation of wind uplift on low-rise building roof using large-scale testing. Front Built Environ 5. https://doi.org/10.3389/fbuil.2019.00149.
6. Baskaran A, Stathopoulos T (1988) Roof corner wind loads and parapet configurations. J Wind Eng Ind Aerodyn 29(1–3):79–88. https://doi.org/10.1016/0167-6105(88)90147-X
7. Bernardini E, Spence SMJ, Wei D, Kareem A (2015) Aerodynamic shape optimization of civil structures: a CFD-enabled kriging-based approach. J Wind Eng Ind Aerodyn 144:154–164. https://doi.org/10.1016/J.JWEIA.2015.03.011

8. Bitsuamlak GT, Asce M, Warsido W, Ledesma E, Chowdhury AG (2013) Aerodynamic mitigation of roof and wall corner suctions using simple architectural elements. Ascelibrary.Org 139(3):396–408.https://doi.org/10.1061/(ASCE)EM.1943-7889.0000505

9. Bobby S, Spence SMJ, Bernardini E, Kareem A (2014) Performance-based topology optimization for wind-excited tall buildings: a framework. Eng Struct 74:242–255. https://doi.org/10.1016/J.ENGSTRUCT.2014.05.043

10. Courant R, Friedrichs K, Lewy H (1928) Über Die Partiellen Differenzengleichungen Der Mathematischen Physik. Math Ann 100(1):32–74. https://doi.org/10.1007/BF01448839

11. Elshaer A, Aboshosha H, Bitsuamlak G, El Damatty A, Dagnew A (2016) LES evaluation of wind-induced responses for an isolated and a surrounded tall building. Eng Struct 115:179–195. https://doi.org/10.1016/J.ENGSTRUCT.2016.02.026

12. Elshaer A, Asce AM, Bitsuamlak G (2018) Multiobjective aerodynamic optimization of tall building openings for wind-induced load reduction. J Struct Eng 144(10):04018198. https://doi.org/10.1061/(ASCE)ST.1943-541X.0002199

13. Elshaer A, Bitsuamlak G, El Damatty A (2017) Enhancing wind performance of tall buildings using corner aerodynamic optimization. Eng Struct 136:133–148. https://doi.org/10.1016/J.ENGSTRUCT.2017.01.019

14. Franke J, Antti Hellsten K, Schlünzen H, Carissimo B (2011) The COST 732 best practice guideline for CFD simulation of flows in the urban environment: a summary. Int J Environ Pollut 44(1–4):419–427. https://doi.org/10.1504/IJEP.2011.038443

15. Huang P, Peng X, Ming G (2017) Wind tunnel study on effects of various parapets on wind load of a flat-roofed low-rise building. Adv Struct Eng 20(12):1907–1919. https://doi.org/10.1177/1369433217700425

16. Khaled MF, Aly AM, Elshaer A (2021) Computational efficiency of CFD modeling for building engineering: an empty domain study. J Build Eng 42:102792. https://doi.org/10.1016/J.JOBE.2021.102792

17. Kopp GA, Gavanski E (2010) Wind tunnel pressure measurements on two FCMP houses, pp 1–30

18. Sandink D, Kopp G, Stevenson S, Dale N (2019) Increasing high wind safety for Canadian homes: a foundational document for low-rise residential and small buildings institute for catastrophic loss reduction building resilient communities

19. Suaris W, Irwin P (2010) Effect of roof-edge parapets on mitigating extreme roof suctions. J Wind Eng Ind Aerodyn 98(10–11):483–491. https://doi.org/10.1016/j.jweia.2010.03.001

20. Surry D, Lin JX (1995) The effect of surroundings and roof corner geometric modifications on roof pressures on low-rise buildings. J Wind Eng Ind Aerodyn 58(1–2):113–138. https://doi.org/10.1016/0167-6105(95)00016-K

# Structural Specialty: Seismic and Structural Analysis

# Parametric Study of a Cable Dome of Geiger-Type

**Hannah Tulloch, Elshaimaa Ahmed, and Ashraf El Damatty**

**Abstract** Cable and membrane structures are typically geometrically flexible and are subject to larger deflections under loads when compared to geometrically rigid structures. As one of the well-known types of cable roofs, the preliminary design of cable domes requires assigning appropriate prestress to the cables and struts taking into account the strength, stability, and serviceability requirements under different load conditions according to design codes. The ideal prestress is assigned initially based on the geometrical arrangements of cables and struts then magnified according to the load carrying capacity of the dome. The arrangement of cables and struts can affect the ideal prestress and, eventually, the total weight and maximum displacement of the dome under service loads. In this regard, this study performs a parametric study to investigate the sensitivity of some geometrical parameters (radial divisions and number of sectors) to the maximum displacement and total weight of a cable dome of Geiger-type. A code was developed to determine the initial prestress of 12 domes (with configurations of 2 hoops and 10 sectors up to 4 hoops and 20 sectors) using singular value decomposition technique. Then, 12 domes were modeled using SAP2000 and subjected to service loads according to the NBCC code. The results of this study showed that the total weight and maximum displacement remain relatively constant when increasing the number of sectors. On the other hand, increasing the number of hoops leads to significantly less displacement and a heavier dome. Based on these results, it can be concluded that domes with a larger number of hoops perform better under external loading but resultantly are heavier and therefore more expensive.

**Keywords** Parametric study · Geiger cable dome · Ideal prestress

H. Tulloch · E. Ahmed · A. El Damatty (✉)
The University of Western Ontario, London, Canada
e-mail: damatty@uwo.ca

# 1   Introduction

Cable structures are incorporated in the design of long-span buildings due to their lightweight and versatile nature and can be classified into three categories [7]. The first is the pure tensile structure, in which one set of cables provides support, while the other is for stabilization. The second is the tensegrity structure, a combination of both cables and struts that are self-equilibrated through prestressing and do not require the stiffness provided by supports. The third category of cable structures is the hybrid tensile structure, which is considered a tensegrity structure, but with perimeter support [7]. Cable domes, as a hybrid tensile structure, attain their stability by assigning the appropriate level of prestress. Meanwhile, the initial geometry can affect greatly the prestress distribution and, consequently, the static behavior of cable domes under external loads. This phenomenon was touched on in some past studies, such as Kawaguchi [3] who studied the effects of changing the length of the outermost post and found that increasing the length would decrease the vertical displacement of cable domes. Also, Quagliaroli et al. [7], Yuan and Dong [10], and Pollini [6] investigated effects of the member's weight on the dome feasibility and determined the optimal weight for a feasible design. Castro and Levy [1] found that increasing the strut height ultimately minimized the cost of the Georgia Olympic Dome, and that a two-hoop dome was more economical than a three-hoop one. Fu [2] determined that a wedge-shaped cable network resulted in a lighter weight structure than a triangulated network as there was a smaller number of cable elements. Krishnan [4] investigated the effects of the number polygon sides on torsional stiffness and found that domes with fewer sides were prone to torsional distortion. Based on the above and due to the growing demand in the market on this type of lightweight roofing, more research is required to cover further aspects in this domain.

The objective of the current research is to determine the optimal member arrangement for the design of long-span cable dome structures to the minimum weight and displacement. In this regard, this paper investigates the results of twelve cable dome models, each with different numbers of sectors and hoop cables and is subjected to various load combinations. The paper is organized as follows. Section 2 includes the design of positive curvature cables domes by, first, determining prestresses using the singular value decomposition method, then, calculating the required cross-sectional areas under different load conditions according to the NBCC code. Twelve study cases are presented. Section 3 presents and discusses the results of the numerical model. Finally, Sect. 4 concludes the results.

## 2  Design Procedure of a Cable Dome of Geiger-Type

### 2.1  Calculating Prestress of Cable Domes Using Singular Value Decomposition

The fundamental contributions of matrix analysis of pin-jointed tensegrities using the singular value decomposition (SVD) method are due to the work done by [5]. This method is based on calculating the connectivity matrix of the dome as illustrated in [8], then calculating the projected lengths of all members in the $x$-, $y$-, and $z$-directions as follows:

$$l^x = Cx + C_f x_f \tag{1}$$

$$l^y = Cy + C_f y \tag{2}$$

$$l^z = Cz + C_f z_f \tag{3}$$

where $(x, y, z)$ and $(x_f, y_f, z_f)$ are the nodal coordinates for the free and fixed nodes in $x, y, z$ directions, respectively. $C$ and $C_f$ describe the connectivity of the members to the free and fixed nodes, respectively. The members lengths are then calculated using

$$l = \sqrt{lx^2 + ly^2 + lz^2} \tag{4}$$

The equilibrium matrix A can be formed using the project lengths as defined by

$$A = \begin{pmatrix} C^T \operatorname{diag}(l^x) \\ C^T \operatorname{diag}(l^y) \\ C^T \operatorname{diag}(l^z) \end{pmatrix} L^{-1} \tag{5}$$

where $L$ is diagonal $l$. By applying the SVD technique on the equilibrium matrix, the vector of prestress of all members can be retrieved. The unilateral conditions of all members, i.e., struts are under compression and cables under tension, should be checked; otherwise, the geometry should be changed. A code was developed using MATLAB that reads the connectivity matrix of the dome, constructs the equilibrium matrix, and performs SVD technique to determine prestresses for all domes.

The prestress of one of the elements in the inner ring of the dome is scaled to 1, then the prestresses of all other elements are proportionally scaled up by the same ratio. Those values are then magnified to $10^8$ N which achieves the minimum displacement of the dome under external loads.

**Table 1** Load combinations from NBCC

| Case | Principal loads | Companion loads |
|------|-----------------|-----------------|
| 1 | 1.4D + St | – |
| 2 | (1.25D or 0.9D) + 1.5L + St | 1.0S or 0.4W |
| 3 | (1.25D or 0.9D) + 1.5S + St | 1.0L or 0.4W |
| 4 | (1.25D or 0.9D) + 1.4W + St | 0.5L or 0.5S |

## 2.2  Load Cases

Krishnan [4] examined the various loads and load combinations that cable domes are designed to withstand. These loads include prestressing forces, dead and live loads, snow loads, and wind loads, which are included in the design of twelve cable domes. Prestressing forces are necessary to ensure that all cables remain in tension, and that the deflections are within the designated limits. Prestressing loads depend on the geometry, member size, and deflection limits of the structure. The dead loads, live loads, snow loads, and wind loads are applied at the upper joints based on the tributary area each node supports.

Loads considered:

(1)  live load L $= 1.0$ kN/m$^2$
(2)  snow load S $= 0.85$ kN/m$^2$
(3)  wind load W $= 0.9$ kN/m$^2$ in suction
(4)  prestress load St.

Load combinations:

The dome models are subject to load combinations from 4.1.3.2.-A of the National Building Code of Canada as presented in Table 1, with the addition of the prestress load to each combination. The allowable stress was taken as 30% of critical tensile strength for cables and 60% of critical compressive strength for the struts [9]. The critical strength of cables and struts is $\sigma_c = 1.67 \times 10^6$ kN/m$^2$ and $\sigma_s = 3.45 \times 10^5$ kN/m$^2$, respectively, and the Young's modulus for cables and struts is $E_c = 1.9 \times 10^8$ kN/m$^2$ and $E_s = 2.06 \times 10^8$ kN/m$^2$, respectively.

## 2.3  Case Studies

Twelve cable domes are considered in the current study. The domes range from two hoops and ten sectors (2H10S) to four hoops and twenty sectors (4H20S), as shown in Fig. 1a–l. The prestresses for the domes are first determined using a code developed in MATLAB based on SVD method as outlined in Sect. 2.1. All domes were then designed using the commercial software SAP2000 according to the envelope of all load combinations outlined in Sect. 2.2.
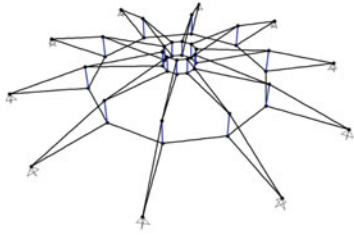
(a) 2 Hoops 10 Sectors
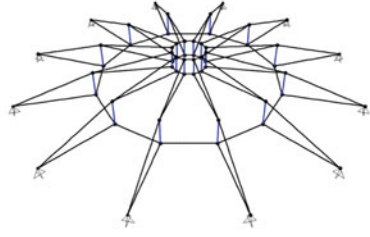
(b) 2 Hoops 12 Sectors
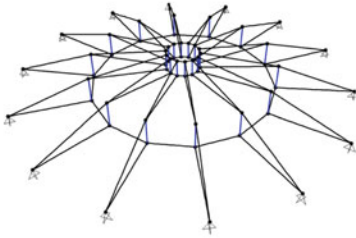
(c) 2 Hoops 14 Sectors
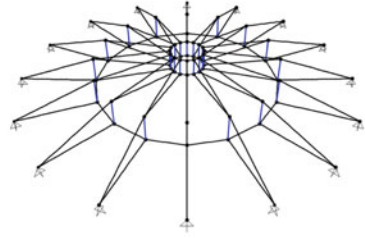
(d) 2 Hoops 16 Sectors
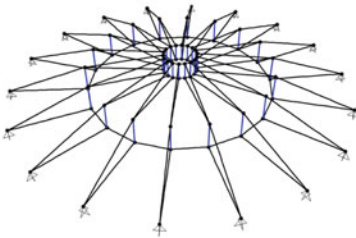
(e) 2 Hoops 18 Sectors
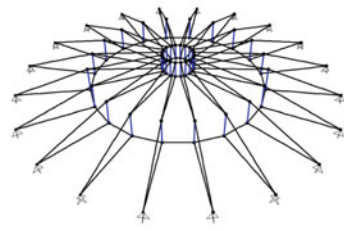
(f) 2 Hoops 20 Sectors
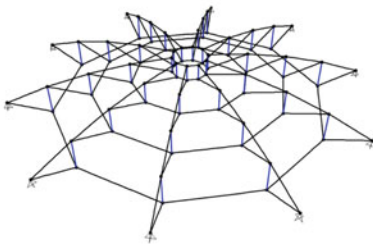
(g) 4 Hoops 10 Sectors
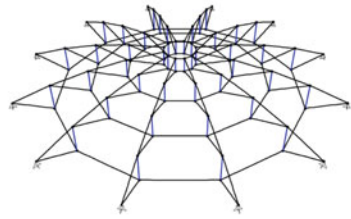
(h) 4 Hoops 12 Sectors

**Fig. 1** 3D view of twelve case studies of cable dome

(i) 4 Hoops 14 Sectors                                    (j) 4 Hoops 16 Sectors

(k) 4 Hoops 18 Sectors                                    (l) 4 Hoops 20 Sectors
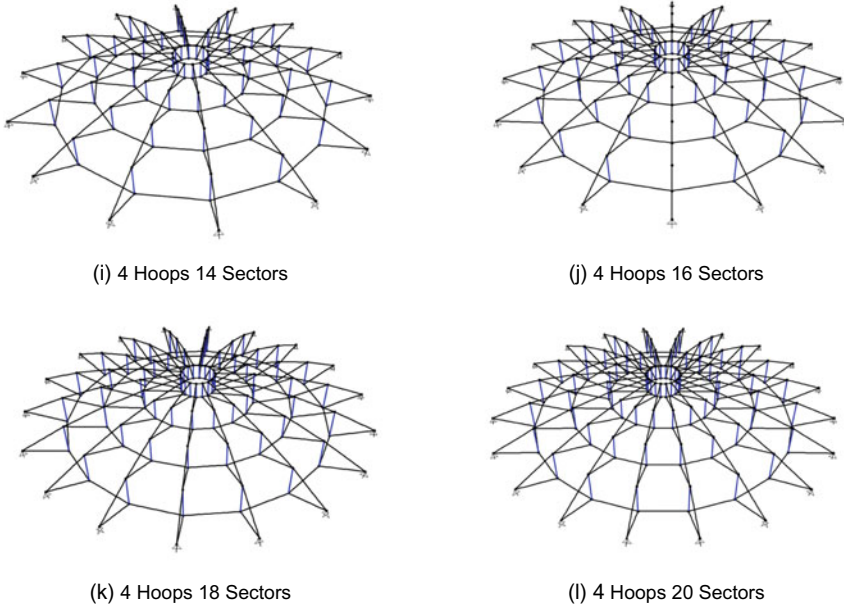
**Fig. 1**  (continued)

## 3   Results and Discussion

### 3.1   *Prestress Results*

As the first step in designing cable domes, the feasible prestress of all members should be determined before external loads can be applied and then magnified according to the load carrying capacity of the domes. Tables 2 and 3 compare the prestresses of all groups of members in models with 2 hoops and 4 hoops, respectively. This comparison showed that the prestress distribution in the hoop cables does not change significantly when changing the number of sectors. However, the prestresses in both diagonal and ridge cables decrease with the increase in the number of sectors. For example, the prestress for the HS0 cable in two hoops and ten sectors (2H10S) is 1.37778, and for two hoops and twenty sectors (2H20S), the prestress is 1.375. Figure 2 illustrates the geometry and group members of cable domes with two and four hoops. Contrary to this, the number of hoops does affect the prestress distribution. For example, HS0 cable in two hoops and fourteen sectors (2H14S) dome has a prestress of 1.37805, while the same cable in four hoops and fourteen sectors (4H14S) has a prestress of 0.25993.

**Table 2** Prestress modes for two hoop cases

| Member | 10S | 12S | 14S | 16S | 18S | 20S |
|---|---|---|---|---|---|---|
| HS0P | 1 | 1 | 1 | 1 | 1 | 1 |
| HS0 | 1.37778 | 1.38372 | 1.37805 | 1.38462 | 1.37333 | 1.375 |
| HS1 | 29.8111 | 29.7326 | 29.7073 | 29.7949 | 29.6267 | 29.5833 |
| JS1 | 0.62222 | 0.52326 | 0.45122 | 0.39744 | 0.34667 | 0.31944 |
| JS2 | 1.54444 | 1.2907 | 1.10976 | 0.97436 | 0.86667 | 0.77778 |
| XS1 | 0.85556 | 0.72093 | 0.60976 | 0.53846 | 0.48 | 0.43056 |
| XS2 | 18.4222 | 15.3953 | 13.2195 | 11.6282 | 10.2933 | 9.26389 |
| G0 | − 0.07778 | − 0.06977 | − 0.06098 | − 0.05128 | − 0.04 | − 0.04167 |
| G1 | − 0.46667 | − 0.39535 | − 0.32927 | − 0.29487 | − 0.26667 | − 0.23611 |

**Table 3** Prestress modes for four hoop cases

| Member | 10S | 12S | 14S | 16S | 18S | 20S |
|---|---|---|---|---|---|---|
| HS0P | 1 | 1 | 1 | 1 | 1 | 1 |
| HS0 | 0.26003 | 0.26094 | 0.25993 | 0.25976 | 0.26003 | 0.26079 |
| HS1 | 0.60193 | 0.6013 | 0.60265 | 0.60272 | 0.60209 | 0.60252 |
| HS2 | 1.39647 | 1.39546 | 1.39735 | 1.39728 | 1.39616 | 1.39748 |
| HS3 | 3.08026 | 3.07942 | 3.08278 | 3.08149 | 3.07853 | 3.08094 |
| JS1 | 0.61958 | 0.51864 | 0.44702 | 0.39219 | 0.34904 | 0.31475 |
| JS2 | 0.78973 | 0.66126 | 0.56954 | 0.49915 | 0.44328 | 0.39928 |
| JS3 | 1.19101 | 0.99676 | 0.85762 | 0.75212 | 0.66841 | 0.60252 |
| JS4 | 2.14607 | 1.79579 | 1.54636 | 1.35484 | 1.20593 | 1.08633 |
| XS1 | 0.16854 | 0.141 | 0.12252 | 0.10696 | 0.09424 | 0.08633 |
| XS2 | 0.39647 | 0.33063 | 0.28477 | 0.24958 | 0.22164 | 0.19964 |
| XS3 | 0.91653 | 0.76661 | 0.6606 | 0.57895 | 0.51483 | 0.46403 |
| XS4 | 2.04173 | 1.70989 | 1.47185 | 1.29032 | 1.1466 | 1.03417 |
| G0 | − 0.05136 | − 0.04214 | − 0.03642 | − 0.03226 | − 0.02792 | − 0.02518 |
| G1 | − 0.13483 | − 0.11183 | − 0.09603 | − 0.08489 | − 0.07504 | − 0.06835 |
| G2 | − 0.30658 | − 0.2577 | − 0.22185 | − 0.19355 | − 0.17277 | − 0.15468 |
| G3 | − 0.73997 | − 0.61912 | − 0.53311 | − 0.46689 | − 0.41536 | − 0.3741 |

## 3.2 Total Weight Results

By comparing the total weight of all models, it can be seen that the weight is almost the same for all models with the same number of hoop cables as shown in Fig. 3a and shown in Table 4. This equivalency is due to the fact that increasing the number of sectors decreases the tributary area each node supports, and this decreases the cross-sectional areas of the elements in each sector. As a result, the total weight of the dome
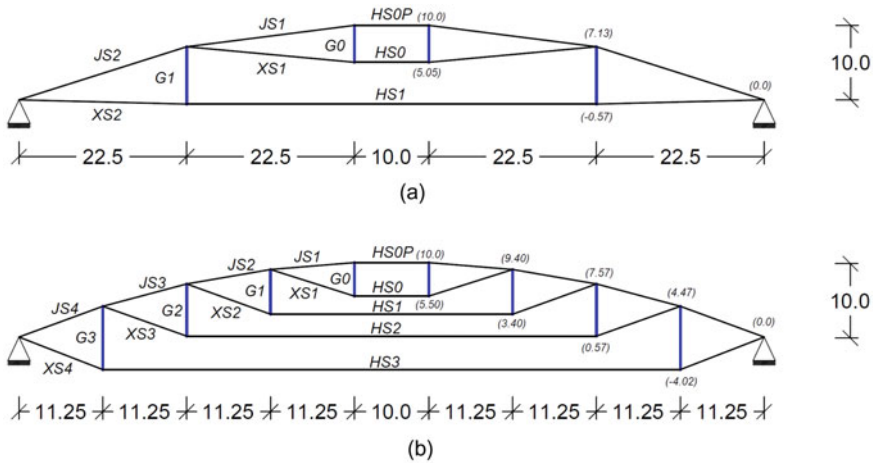
**Fig. 2** Geometry and group members of **a** two hoop cases and **b** four hoop cases

remains almost the same when increasing the number of sectors keeping the number of hoops unchanged. In other words, the increased number of sectors balances the decreased values of cross-sectional areas. For example, the total weight of the dome with four hoops and ten sectors (4H10S) is 11800.73 KN, meanwhile the dome with four hoops and twenty sectors (4H20S) weighs 12,358.71 KN. Although they differ significantly in the number of members, they have very similar total weights.

### 3.3 Total Displacement Results

By comparing the total displacement of all domes, the number of hoop cables has the greatest effect on the total displacement as shown in Table 4 and Fig. 3b. As the number of hoops increases, the total weight increases, while the maximum displacement decreases. This can be interpreted as that the dome becomes stiffer when increasing the number of hoops, which confines the domes. For example, the max displacement for the dome with two hoops and sectors (2H14S) is 0.028921 m, while the dome with four hoops and fourteen sectors (4H14S) undergoes a max displacement of 0.005015 m. Although both domes have the same number of sectors, the dome with four hoops has a significantly smaller max displacement. On the other hand, the number of sectors does not affect greatly the max displacement. As shown in Table 4, four hoops and ten sectors (4H10S) dome has a maximum displacement of 0.005232 m, while the dome with four hoops and twenty sectors (4H20S) has a maximum displacement of 0.005624 m. Although the number of sectors has changed, the maximum displacement remained nearly constant.

(a)



(b)
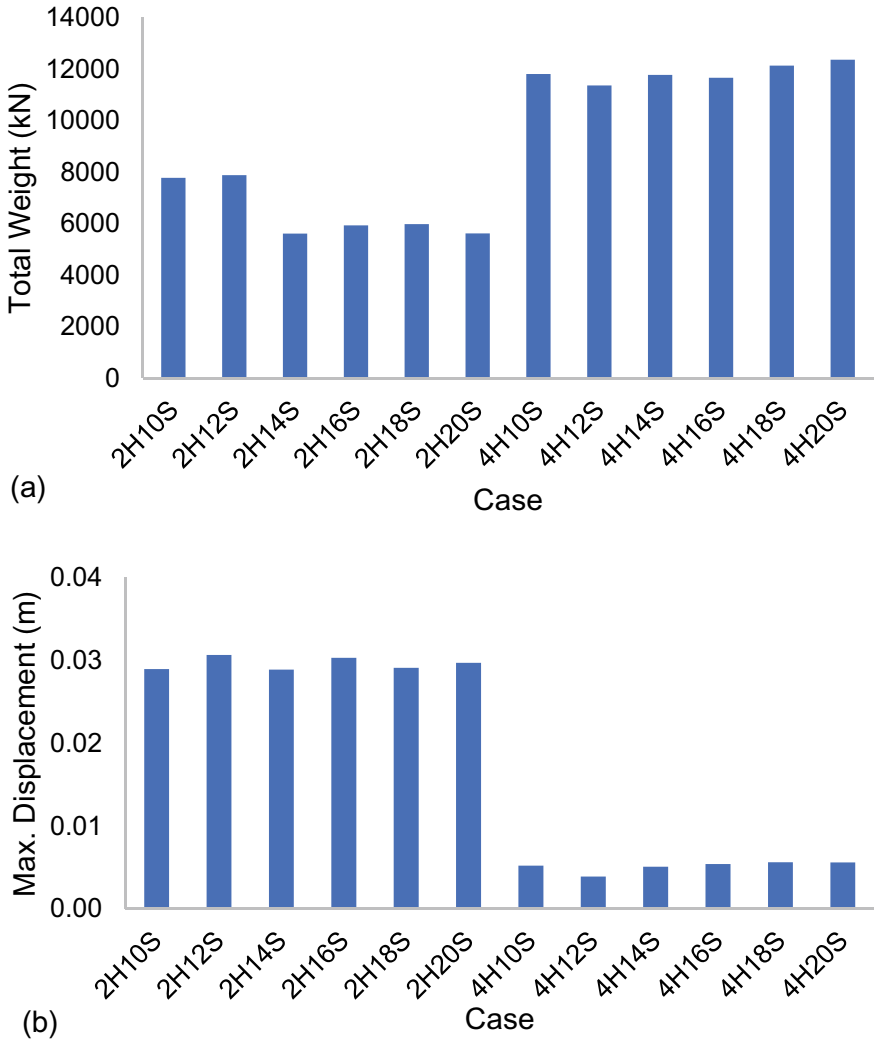
**Fig. 3** **a** Total weight and **b** maximum displacement of 12 case studies

**Table 4** Model total weights and maximum displacement

| Model | Weight (kN) | Max. Disp. (m) | Model | Weight (kN) | Max. Disp. (m) |
|-------|-------------|----------------|-------|-------------|----------------|
| 2H10S | 7775.255 | 0.028975 | 4H10S | 11,800.73 | 0.005232 |
| 2H12S | 7876.44 | 0.030687 | 4H12S | 11,358.88 | 0.003917 |
| 2H14S | 5609.393 | 0.028921 | 4H14S | 11,772.08 | 0.005104 |
| 2H16S | 5930.314 | 0.030327 | 4H16S | 11,659.94 | 0.005427 |
| 2H18S | 5977.006 | 0.029123 | 4H18S | 12,130.15 | 0.005634 |
| 2H20S | 5616.371 | 0.029741 | 4H20S | 12,358.71 | 0.005624 |

### *3.4   Effect of Outermost Struts' Length*

When comparing the length of outermost struts in two hoop and four hoop domes shown in Fig. 2, it is obvious that the outermost struts in the domes with two hoops are relatively short compared to vertical elevation of supports. Therefore, the diagonal cables are carrying excessive stresses and have higher prestresses compared to the ridge cables. To illustrate further, the diagonal cable XS2 in the dome with two hoops and ten sectors has a prestress of 18.4222, whereas the ridge cable JS2 has a prestress of only 1.54444, as shown in Table 2. As a result, cable XS2 is carrying much of the load and, accordingly, must have a larger cross section than if the outer post dropped lower. On the same line, increasing the length of the outermost struts can redistribute the forces among the diagonal cables, ridge cables, and the outermost struts. This reflects the sensitivity of this type of structures to the geometry configuration, in general, and the length of struts, in particular. The effects of the lengths of the outermost struts were investigated by [3], where they illustrated that increasing the lengths of the outermost struts can decrease the vertical displacement by 25–35%.

## 4   Conclusion

This paper investigated the effects of the number of hoops and sectors on the total weight and maximum displacement of long-span cable dome structures. Twelve domes were designed under different load combinations and compared in terms of the max displacement, total weight, and prestress distribution. By analyzing the results, it can be concluded that changing the number of sectors has the least effect on the total weight and the maximum displacement of the dome, rather, increasing the number of hoops stiffens the structure by decreasing the total displacement, despite the increase in weight. Moreover, the behavior of the dome is highly affected by the length of struts, especially when the outermost struts are relatively short compared to the vertical elevation of supports, leading to excessive stresses in the diagonal cables compared to the ridge cables. This reflects the sensitivity of this type of structures to the geometry configuration, in general, and the length of struts, in particular.

# References

1. Castro G, Levy MP (1992) Analysis of the Georgia Dome cable roof. In: Computing in civil engineering and geographic information systems symposium. ASCE, pp 566–573
2. Fu F (2005) Structural behavior and design methods of tensegrity domes. J Constr Steel Res 61(1):23–35
3. Kawaguchi M, Tatemichi I, Chen PS (1999) Optimum shapes of a cable dome structure. Eng Struct 21(8):719–725
4. Krishnan S (2015) Prestressed cable domes: structural behavior and design. University of Illinois at Urbana-Champaign
5. Pellegrino S (1993) Structural computations with the singular value decomposition of the equilibrium matrix. Int J Solids Struct 30(21):3025–3035
6. Pollini N (2021) Gradient-based prestress and size optimization for the design of cable domes. Int J Solids Struct 222:111028
7. Quagliaroli M, Malerba PG, Albertin A, Pollini N (2015) The role of prestress and its optimization in cable domes design. Comput Struct 161:17–30
8. Tran HC, Park HS, Lee J (2012) A unique feasible mode of prestress design for cable domes. Finite Elem Anal Des 59:44–54
9. Wang Z, Yuan X, Dong S (2010) Simple approach for force finding analysis of circular Geiger domes with consideration of self-weight. J Constr Steel Res 66(2):317–322
10. Yuan XF, Dong SU (2002) Nonlinear analysis and optimum design of cable domes. Eng Struct 24(7): 965–977

# Seismic Fragility of Using Friction Dampers to Retrofit Non-ductile Reinforced Concrete Shear Wall Buildings in Western Canada

**Chunxiao Ning and Yazhou Xie**

**Abstract** Reinforced concrete (RC) shear wall buildings designed pre-1980 in Canada are vulnerable to earthquake hazards due to insufficient ductility and brittle failure mechanism of the shear wall. Energy dissipation devices, such as friction dampers, bear the potential to enhance the earthquake resistance of civil engineering structures, while their applicability to shear wall buildings remains unclear. One fundamental challenge lies in the lack of a viable layout design of damper devices to fully engage their stroke capacity to dissipate sufficient earthquake energy. This challenge is aggravated in western Canada because of its elevated level of seismicity. To address these issues, this study relies on seismic fragility analyses to explore the effectiveness of using friction dampers to retrofit non-ductile RC shear wall buildings in western Canada. Finite element models are developed to integrate nonlinear behaviours of shear wall buildings, different layout designs of friction dampers, and their hysteretic force–displacement relationships. Site-consistent seismic hazard model is developed for a benchmark site in western Canada, namely the city of Victoria, from which a large suite of spectra-consistent ground motions is selected for nonlinear time history analyses. By comparing seismic demand with the shear wall's capacity, different sets of seismic fragility models are developed to assess to what degree each proposed damper design would change the seismic fragility of shear wall building.

**Keywords** Shear wall · Friction damper · Seismic hazard model · Seismic fragility assessment

C. Ning · Y. Xie (✉)
Department of Civil Engineering, McGill University, Montreal, QC, Canada
e-mail: tim.xie@mcgill.ca

# 1 Introduction

Western Canada is susceptible to three kinds of earthquakes—crustal, in-slab, and interface earthquakes. The shallow crustal earthquake is originated from the crust of the North American continental plate. The in-slab earthquake and interface earthquake are triggered by the relative convergent movement between Juan de Fuca Plate and the North American continental plate at the Cascadia subduction zone [9]. Both slab and interface seismic events feature large source-to-site distances, and their magnitudes are generally above Mw 8.0 [34, 51]. Historical evidence illustrates that destructive earthquakes repeatedly happened in this area during the last 3500 years, hitting both Vancouver Island in Canada and Washington state in the United States [34, 42]. Moreover, Goldfinger et al. [19] recently found that the reoccurrence period of the subduction earthquake is approximately 430 years, and a devastative earthquake is expected to hit the west coast of Canada in the near future.

The west coast is built with a large inventory of non-ductile RC structures. These pre-1980s RC buildings are believed to have the following deficiencies: insufficient strength and lateral stiffness, structural discontinuity and irregularity, and brittle behaviour in key elements [38, 56]. In particular, non-ductile shear wall buildings constitute a major proportion of early-designed RC buildings in western Canada. Recent earthquake events, such as the 2021 Maule earthquake [52] and the 2011 Christchurch earthquake [27] have witnessed extensive damage and even complete collapse of deficient RC shear wall buildings due to their unsatisfactory seismic design and non-ductile failure mechanism [56].

Seismic protective devices, such as dampers and isolation bearings, show promise in mitigating the seismic risk of infrastructures and buildings. For instance, installing viscous dampers and isolation bearings can effectively reduce the seismic demand of bridge components (e.g. columns, unseating), thereby minimizing the repair cost ratio of the entire bridge [53, 44]. Likewise, seismic performance of building structures can be significantly enhanced through retrofit actions that engage various types of energy dissipation devices, including fluid viscous dampers [13, 40], shape memory alloy dampers [20, 21, 57], friction dampers [24, 47], yielding dampers [14, 21], etc. These devices introduce new energy dissipation mechanisms (e.g. friction, yielding, and viscous dissipation) and localized seismic damage in dampers/isolators [1], which permits the accurate control and estimation of seismic risk. In addition to widely investigated seismic performance, the durability of seismic protective devices also deserves careful estimation before application. For example, yielding damper and buckling restrained braces would be replaced after a major earthquake event due to metallic yielding. Tuned mass dampers control the structure by attaching a mass that is synchronized with the structure's natural period, and later system tuning would be required if the structural period changes (e.g. structural softening due to damage) [6]. Moreover, seismic protective devices usually require monitoring and maintenance during the service life, thus the associated life-cycle cost is increased.

Despite the proven effectiveness, previous studies regarding seismic retrofits of buildings have mainly focussed on moment-resisting frames. Because of their overall

brittle behaviour, non-ductile RC shear walls would experience significant seismic damage at small drift levels. In this respect, viable layout designs are required for energy dissipation devices to have sufficient displacement responses to fully engage their stroke capacity for dissipating earthquake energy. This added challenge renders the absence of literature, investigating the feasibility of using damper devices to retrofit non-ductile shear wall buildings. Moreover, the effectiveness of using damper devices is also influenced by the dynamic properties of the base structure and the uncertainty in seismic hazards, particularly in western Canada under different types of earthquakes.

To fill these research gaps, this study investigates the soundness of installing friction dampers to reduce the seismic fragilities of non-ductile RC shear wall buildings. After an overall investigation of the shear wall building inventory in western Canada, two design layouts of friction devices are proposed to retrofit a three-storey non-ductile shear wall in the city of Victoria. Details of finite element models are presented to simulate the seismic behaviours of the shear wall and friction damper. A large suite of site-consistent ground motions is selected to excite the benchmark wall structure. Finally, the seismic performance of the shear wall installed with different damper design schemes is assessed by comparing the fragility curves with different damage states.

## 2 Non-ductile Shear Wall Buildings and the Numerical Modelling

### 2.1 Inventory Analysis of Non-ductile Shear Wall Buildings in West Canada

Most of the RC buildings constructed prior to 1980 are shear wall buildings in western Canada [56], following the design code of *National Building Code of Canada 1965* [41, 39]. These early-designed buildings fell short in seismic design and detailing because Canada's seismic design provisions were formally introduced in 1973 [7, 18, 37]. In a recent study by Yathon et al. [56], more than 350 non-ductile RC shear wall buildings have been reviewed to feature the following common deficiencies: (1) poor detailing in thin walls; (2) inadequate or/and bad arrangement of walls; and (3) low flexural capacities for multi-storey buildings. In addition, the pre-1980 RC shear walls have no confined boundary elements; their use in low-rise buildings may also cause shear failure due to the lack of buckling prevention ties and inadequate transverse reinforcements [41].

## 2.2 Benchmark Design of Shear Wall and Its Numerical Modelling

As illustrated in Fig. 1, a three-storey non-ductile RC shear wall is benchmarked from the inventory analysis. The structure is 36 ft (10.97 m) in height, 8 in. (0.20 m) in thickness, and has an elevation aspect ratio (height over width) of 6. These values are determined according to the work of Yathon et al. [56], who offered geometric statistics of non-ductile RC shear wall buildings on the west coast. The wall's horizontal reinforcement ratio is considered 0.18%, whereas its vertical reinforcement ratio is assumed as 0.21% with no confined boundary element [11]. The compressive strength of concrete and tensile strength of steel rebars are selected as 21 and 280 MPa, respectively [11].

Shear wall structures can be simulated using different types of elements, including nonlinear beam-column elements (NBCE), plastic zone elements [48], multiple-vertical-line-element-model (MVLEM) [46], and shear-flexural interaction MVLEM (SFI-MVLEM) [30, 32]. NBCE assumes the nonlinear behaviour of the shear wall is the same as that of a beam, in which the plane section assumption holds. Plastic zone elements assume the plastic hinge happens at the bottom of the wall and simulate it using concentrated nonlinear springs. MVLEM models the flexural-dominated RC shear wall by having multiple strips of macro-fibres connected to rigid beams at the top and bottom. The shear stiffness of MVLEM is described by a horizontal shear
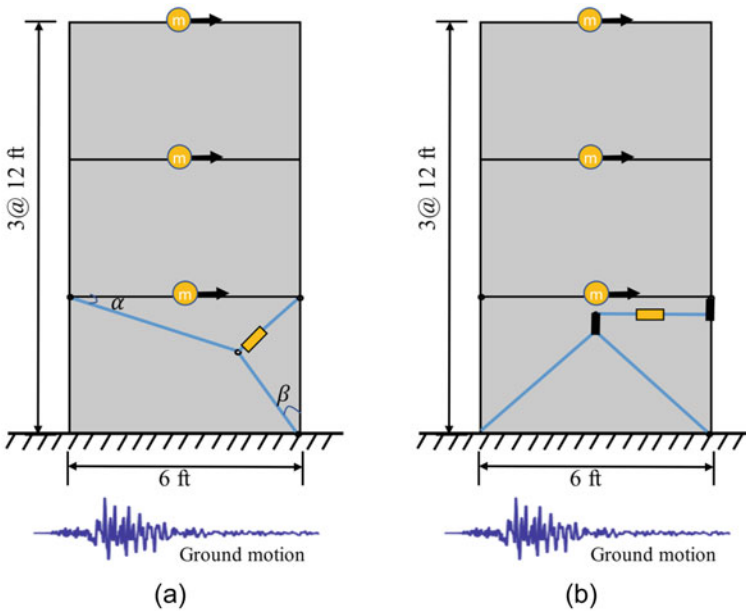


**Fig. 1** Elevation view of the benchmark shear wall with two layouts of friction damper, **a** layout 1: toggle-brace system; **b** layout 2: chevron-brace system

**Fig. 2** SFI-MVLEM element for modelling the shear wall
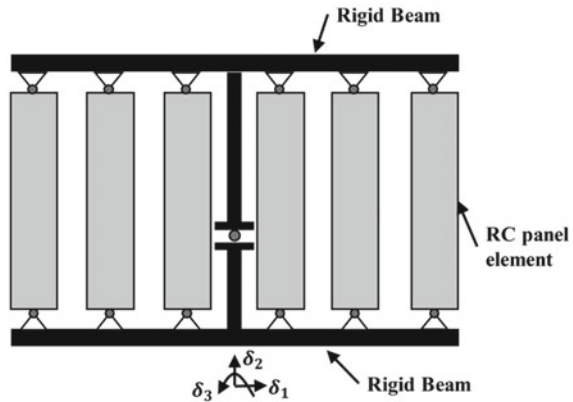
spring located between the two beams, which are allowed to rotate and displace relative to the spring. As such, the MVLEM model captures the interaction between axial and flexural deformations. SFI-MVLEM shown in Fig. 2 is the most advanced one for modelling walls with moderate aspect ratios. It captures both axial-flexural interaction and shear-flexural interaction in the wall [31, 32]. Essentially, the SFI-MVLEM is an extension of the MVLEM by replacing its uniaxial macro-fibres with panel elements subjected to membrane actions. The comparison between experimental results and outcomes from the SFI-MVLEM shows its superior performance in simulating non-ductile shear walls under reversed cyclic loading. This study adopts the SFI-MVLEM to model the seismic behaviour of non-ductile shear walls, as both brittle shear failure and flexural failure mechanisms are possible due to the design of insufficient reinforcements.

## 3 Retrofitting Shear Walls Using Friction Dampers

### 3.1 Proposed Design Layouts of Friction Dampers

Friction dampers have been widely used in steel frame buildings [47, 50], RC frame buildings [28], and wood structures [55]. The friction damper is designed with two frictional contact surfaces to engage relative movement under earthquake loading. As a result, input energy is dissipated through the friction effect of the damper [35]. Namely, the energy dissipated by the friction damper is proportional to its slip distance and slip force. A relatively large slip displacement is needed for the damper to dissipate sufficient earthquake energy. However, limited ductility is commonly expected in stiff structures such as shear walls. The protection effectiveness of friction dampers will be limited if they are connected to the wall using conventional layouts [33]. To tackle this issue, two different damper layouts are proposed to explore the

displacement amplification effect of dampers. As shown in Fig. 1, the toggle-brace system bears the potential to amplify the damper displacement to 2.5–3.0 times the wall's inter-storey drift, while the chevron-brace layout would share the same level of displacement as that of the wall [10]. Besides, the amplification effect of the toggle-brace system depends on the angle layout of the connecting braces (i.e. $\alpha$ and $\beta$ in Fig. 1a) [10]. This study considers $\alpha = 45°$ and $\beta = 14°$. It is worth mentioning that the brace flexibility would also affect the damper's displacement magnification effect, as a proportion of the deformation would be elastically concentrated in the connecting braces. Strategies to deal with this issue include designing stiffened braces or further optimizing damper layouts [49].

## 3.2 Numerical Modelling of Friction Dampers

A bilinear model [5, 45] is usually used to simulate the axial behaviour of the friction damper assembly—its elastic stiffness is determined by the stiffness of the connecting braces, while its yielding strength equals the damper force at sliding. However, the damper assembly may undergo additional phases after the slip distance exceeds certain limits. Such post-sliding phases include the bearing or shear failure of the connecting bolts [47]. In this regard, a multilinear material model is adopted to simulate the seismic performance of the friction damper assembly [47]. As shown in Fig. 3, the multilinear model features three distinct stages—the elastic deformation stage, friction slipping stage, and bolt bearing stage. When the earthquake is of small intensity, the force in the damper assembly is below the slipping strength, and braces are the only components to deform elastically. In this elastic stage, the deformation of braces will restore completely after the earthquake excitation, and no seismic energy will be dissipated. By contrast, a strong earthquake will make the damper reach its slipping force, trigger the sliding mode, and dissipate external energy. In certain extreme cases, when the damper reaches its slipping limit, additional strength and stiffness will be provided through the bearing force of the post-tensioned bolts.

As presented in Fig. 3, modelling parameters of the damper assembly include slip strength ($P_s$), stiffness of brace ($k_e = P_s/u_y$), slip slot length ($u_a$) and bearing strength ($f_d$). Large $k_e$ is preferred to maximize the protection effectiveness of the friction damper. However, increasing $k_e$ requires designing a larger cross-section of the brace, thereby increasing its initial cost. Meanwhile, having enormous slip strength $P_s$ is not applicable as, (1) the damper may not be able to slip under medium-level earthquakes and (2) braces may buckle before the slip of the damper. This study selects HSS 508 × 508 × 22 ($F_y = 350$ MPa and $E = 200$ GPa) [8] for designing the brace elements. Furthermore, the slip strength ($P_s$) of the damper is considered to be smaller than the brace's buckling strength to ensure its elastic performance [47]. These considerations finally lead to $P_s = 180$ kN in the current study. Recommended values for other parameters can be found in the work from Ramirez and Tirca [47], who suggested using $u_a = 24$ mm and $f_d = 150$ kN. Given these modelling parameters, the *hardening material* and *elastic-perfectly plastic gap material* are

**Fig. 3** Numerical model of friction damper
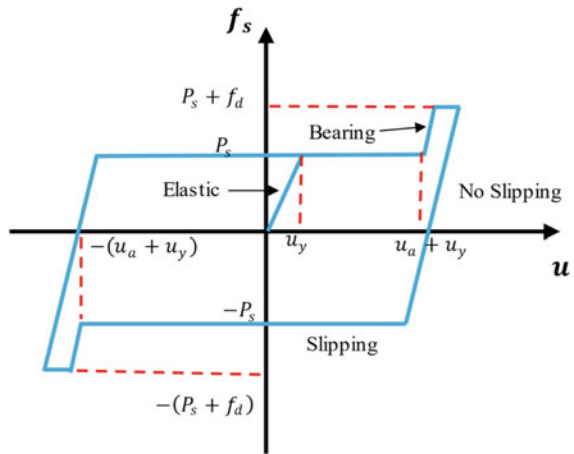


connected in parallel to simulate the friction damper using the software platform of OpenSees [36].

## 4 Seismic Hazard in Western Canada and Ground Motion Selection

### 4.1 Seismic Hazard Model for the City of Victoria

The benchmark structure represents many existing non-ductile RC shear wall buildings in Victoria, British Columbia [56]. In this study, results from the seismic deaggregation analysis are relied upon to pinpoint the relative contribution of the three types of earthquakes (e.g. crustal, interface, and in-slab earthquake) to the seismicity in Victoria [4]. Geological Survey of Canada has developed uniform hazard spectra (UHS) for all locations across Canada, while no associated deaggregation information is currently available [29]. To this end, Goda et al. [17] used the updated seismic information to calculate the seismic hazard and UHS for western Canada, from which seismic deaggregation analysis is further performed for Vancouver [16]. Recently, Halchuk et al. generated seismic deaggregation results for Montreal and Vancouver. Their results are consistent with the seismic hazard model in the *2015 National Building Code of Canada* [22] and are used in the current study to develop the conditional mean spectra (CMS) [3, 12] quantifying proper contributions of different earthquake scenarios at the building site.

## 4.2   Selection of Ground Motions

As recommended by Goda and Atkinson [16], this study computes the CMS for different types of earthquake hazards in Victoria and selects 125 ground motions from the NGA-West2 strong motion database [2]. Figure 4a shows distributions of some physical features of the selected ground motions, including earthquake magnitude, duration, spectral acceleration at the first period of the structure ($S_a(T_1)$), field distance ($R_{jb}$), shear wave velocity ($V_s$ (m/s)), and the associated complete response spectra. Besides, Fig. 4b shows the magnitude-site distance distribution for the selected ground motions. As shown in the figure, earthquake magnitudes for most ground motions are larger than 7.5, which is consistent with the region's overall seismicity [9, 23, 42]. Also, a wide range of distributions can be observed for other features.

For each case (i.e. as-built wall, damper layout 1 and layout 2), 125 nonlinear time history analyses are conducted to obtain the shear wall's seismic demands. Ground motion excitations are applied to the structures in horizontal directions, and the Newmark integration [43] method with $\gamma = 0.5, \beta = 0.25$ is used to solve the transient problem. Structural responses, including force and deformation of the damper and the shear walls, are monitored and recorded during these analyses.
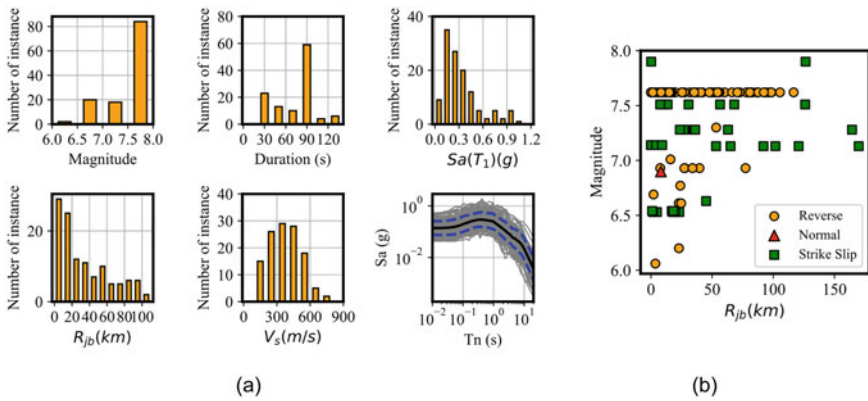


**Fig. 4**   Distributions of the selected ground motions: **a** physical features; **b** magnitude-site distance

## 5 Seismic Fragility Analyses of As-Built Versus Retrofitted Shear Walls

### 5.1 Deterministic Comparison of Time History Responses Under Given Ground Motions

Time history responses of the as-built and retrofitted shear walls are first compared deterministically. Figure 5 shows the comparisons of some critical response parameters, such as the force–displacement curves of the damper, base shear-drift and base moment–curvature relationships of the wall, and time histories of the wall's first-storey drift ratio. The input ground motion with a PGA of 0.36 g is also provided in Fig. 5e. Figure 5a indicates that damper assemblies with the toggle-brace layout (i.e. layout 1) and chevron-brace layout (i.e. layout 2) share similar force–displacement hysteresis curves. Dampers with both design layouts can effectively dissipate earthquake energies. Figure 5b, c also indicate that the shear wall's drift ratio and base curvature can be significantly reduced by installing friction dampers. As further compared in Fig. 5d, the peak drift ratios for the as-built and protected walls with damper layouts 1 and 2 are 1.65%, 0.81% and 0.65%, respectively. Namely, damper layout 1 can reduce the wall's peak drift ratio by 50.9%, whereas layout 2 can further reduce the peak ratio by 60.6% under the given ground motion input.

### 5.2 Seismic Capacity Models of Shear Walls

The seismic demands of shear walls in Fig. 1 are further convolved with the corresponding capacity models for seismic fragility development. As listed in Table 1, two engineering demand parameters (EDPs) are considered to describe different damage states of the RC shear wall. In particular, the peak inter-storey drift ratio and peak floor acceleration quantify the damage potential of structural and non-structural components, respectively [15, 21]. The capacity limit state models and their references for these two EDPs reaching slight, moderate, extensive, and complete damage states are provided in Table 1.

### 5.3 Comparisons of Seismic Fragility Models

This study assesses the shear wall's seismic fragility through the cloud analysis method, which convolves seismic demands with capacities using a log-normal distribution function [25, 26]:

$$P[\text{EDP} \geq C \,|\, S_a(T_1)] = \Phi\left[\frac{\log(\mu_{\text{EDP}}) - \log(C)}{\beta_{\text{EDP|IM}}}\right] \tag{1a}$$
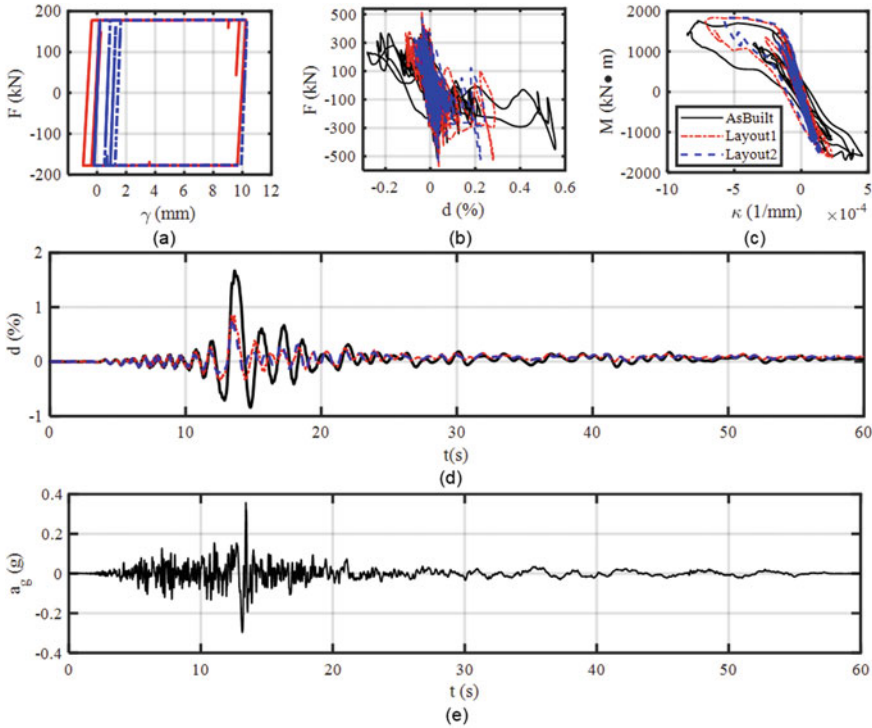
**Fig. 5** Deterministic response comparisons of **a** damper hysteresis curves, **b** shear wall base shear-drift hysteresis curves, **c** shear wall moment–curvature hysteresis curves, **d** time history of first-storey drift ratios under, **e** given ground motion input

$$\log(\mu_{\text{EDP}}) = a + b \cdot \log(S_a(T_1)) \tag{1b}$$

$$\beta_{\text{EDP}|\text{IM}} = \sqrt{\frac{1}{N-2} \sum_{1}^{N} \left[\log(\text{edp}_i) - \log(\mu_{\text{EDP}})\right]^2} \tag{1c}$$

where $C$ is the seismic capacity model in Table 1; $\mu_{\text{EDP}}$ is the mean value of the seismic demand assumed as a linear function of the spectral acceleration $S_a(T_1)$ in the logarithmic space, as given in Eq. (1b). $a$ and $b$ are regression coefficients, and $\beta_{\text{EDP}|S_a(T_1)}$ is the associated logarithmic dispersion, $N$ is the number of $S_a(T_1) -$

**Table 1** Seismic capacity models for shear wall

| EDPs | Slight | Moderate | Extensive | Complete | References |
|---|---|---|---|---|---|
| Inter-storey drift ratio (%) | 0.50 | 1.00 | 2.00 | 5.33 | [41] |
| Floor acceleration (g) | 0.30 | 0.60 | 1.20 | 2.00 | [15, 21] |

EDP samples for the analysis, and $edp_i$ represents the $i$th seismic demand parameter obtained from the nonlinear time history analysis.

Figure 6 presents the final comparisons of seismic fragilities for the as-built shear wall, and the wall equipped with damper design layout 1 and design layout 2. The solid lines in Fig. 6a–d indicate the overall seismic vulnerability of the as-built shear wall, as the median spectral accelerations $S_a(T_1)$ (i.e. the spectral acceleration corresponding to 50% failure probability) will be 0.03, 0.10, 0.40, and 1.60 g for reaching slight, moderate, extensive, and complete damage states if no seismic retrofit is conducted. However, installing friction dampers can effectively mitigate the seismic fragility of the non-ductile shear wall. Designed with the toggle-brace layout, friction dampers can increase the median spectral accelerations $S_a(T_1)$ to be 0.08 g, 0.25 g, 0.95 g, and 3.20 g for the slight, moderate, extensive, and complete damage states, respectively. This value is further increased to 0.15, 0.53, 1.80, and 5.02 g correspondingly when the chevron-brace layout is utilized. In general, friction dampers show limited effectiveness in preventing the shear wall from reaching the slight damage state. However, damage probabilities for the wall to reach extensive and complete damage stages are significantly reduced through the proper installation of friction dampers.

The use of damper devices is commonly associated with enlarged seismic fragilities regarding damage to non-structural components through amplified floor accelerations [54]. However, as proved from Fig. 6e, f, this is not the case for installing friction dampers, as close fragility curves can be observed across the three considered case scenarios. It is noted that seismic fragilities for floor accelerations are
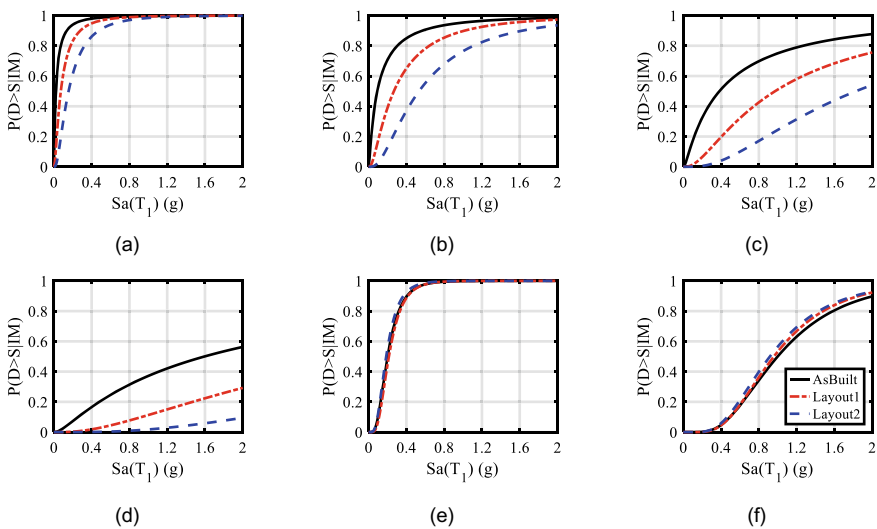


**Fig. 6** Comparison of seismic fragility curves for **a–d** peak inter-storey drift ratio and **e–f** peak floor acceleration

not shown in Fig. 6 regarding the extensive and complete damage states, because negligible fragility values have been observed in these two damage states.

## 6   Conclusions

This study examines the effectiveness of implementing friction dampers to reduce the seismic fragility of non-ductile RC shear wall buildings in western Canada. By proposing two viable design layouts and using state-of-the-art nonlinear modelling schemes for the RC shear wall and friction damper, nonlinear time history analyses are performed for a benchmark shear wall retrofitted with friction dampers. Moreover, site-consistent ground motions are selected for the city of Victoria, from which probabilistic seismic demand models and seismic capacity models are developed for seismic fragility assessment. By comparing the time history responses and fragility curves of the as-built and retrofitted shear walls, the effectiveness of installing friction dampers is verified. This study concludes the following:

(1)   SFI-MVLEM and multilinear material model capture the hysteretic behaviours of the non-ductile RC shear wall and friction damper, respectively.
(2)   Friction dampers can effectively reduce the shear wall's shear deformation and base curvature; the proposed two damper layouts are able to dissipate the input seismic energy and decrease the inter-storey drift of the shear wall.
(3)   Seismic fragility comparison indicates that the chevron-brace damper system outperforms the current toggle-brace system in mitigating the inter-storey drift of the shear wall.
(4)   Unlike other types of damper devices, such as the viscous damper, the friction damper has negligible influence on the peak floor acceleration of the shear wall.

It is worth mentioning that this study focusses on retrofitting one benchmark structure using friction dampers, and their applicability to shear wall structures with different aspect ratios and heights deserves further investigation. Moreover, the damper's effectiveness in seismic protection when subjected to different design parameters (e.g. brace angles) and mechanical properties (e.g. slip strength and slip limit) is the subject of an ongoing study.

# References

1. Agrawal AK, Amjadian M (2022) Seismic component devices. In: Innovative bridge design handbook, 2nd edn. Elsevier, pp 637–662. https://doi.org/10.1016/B978-0-12-823550-8.000 27-5
2. Ancheta TD et al (2014) NGA-West2 database. Earthq Spectra 30(3):989–1005
3. Baker JW (2011) Conditional mean spectrum: tool for ground-motion selection. J Struct Eng 137(3):322–331
4. Baker JW (2008) An introduction to probabilistic seismic hazard analysis (PSHA). White paper, version, vol 1, p 72
5. Berger EJ, Krousgrill CM (2002) On friction damping modeling using bilinear hysteresis elements. J Vib Acoust 124(3):367–375
6. Berquist M, DePasquale R (2020) Fluid viscous dampers: general guidelines for engineers including a brief history. Taylor Devices Inc., North Tonawanda, NY
7. CSA (1973) Code for the design of concrete structures for buildings. Canadian Standards Association, Mississauga, ON
8. CSA (2009) Design of steel structures (CSA S16-09). Canadian Standards Association, Mississauga, ON
9. Clague JJ (1997) Evidence for large earthquakes at the Cascadia subduction zone. Rev Geophys 35(4):439–460
10. Constantinou MC et al (2001) Toggle-brace-damper seismic energy dissipation systems. J Struct Eng 127(2):105–112
11. Cortés-Puentes WL, Palermo D (2017) SMA tension brace for retrofitting concrete shear walls. Eng Struct 140:177–188
12. Daneshvar P, Bouaanani N, Godia A (2015) On computation of conditional mean spectrum in Eastern Canada. J Seismol 19(2):443–467
13. De Domenico D, Ricciardi G, Takewaki I (2019) Design strategies of viscous dampers for seismic protection of building structures: a review. Soil Dyn Earthq Eng 118:144–165
14. Ebadi Jamkhaneh M, Ebrahimi AH, Shokri Amiri M (2019) Experimental and numerical investigation of steel moment resisting frame with U-shaped metallic yielding damper. Int J Steel Struct 19(3):806–818
15. FEMA (2021) Hazus-MH 2.1 advanced engineering building module (AEBM). Federal Emergency Management Agency
16. Goda K, Atkinson GM (2011) Seismic performance of wood-frame houses in south-western British Columbia. Earthq Eng Struct Dyn 40(8):903–924
17. Goda K, Hong HP, Atkinson GM (2010) Impact of using updated seismic information on seismic hazard in western Canada. Can J Civ Eng 37(4):562–575
18. Goda K, Tesfamariam S (2015) Multi-variate seismic demand modelling using copulas: application to non-ductile reinforced concrete frame in Victoria, Canada. Struct Saf 56:39–51
19. Goldfinger C et al (2017) The importance of site selection, sediment supply, and hydro-dynamics: a case study of submarine paleoseismology on the northern Cascadia margin, Washington USA. Mar Geol 384:4–46
20. Gur S, Mishra SK, Roy K (2016) Stochastic seismic response of building with super-elastic damper. Mech Syst Signal Process 72–73:642–659
21. Gur S, Xie Y, DesRoches R (2019) Seismic fragility analyses of steel building frames installed with superelastic shape memory alloy dampers: comparison with yielding dampers. J Intell Mater Syst Struct 30(18–19):2670–2687
22. Halchuk S et al (2019) Deaggregation of NBCC 2015 seismic hazard for selected Canadian cities. In: 12th Canadian conference on earthquake engineering, p 9
23. Heaton TH, Hartzell SH (1987) Earthquake hazards on the Cascadia subduction zone. Science 236:162–168
24. Jafarzadeh K, Lotfollahi-Yaghin M, Sabetahd R (2012) Evaluation of pall friction damper performance in near-fault earthquakes by using of nonlineartime history analysis. World Appl Sci J 20(2):259–263

25. Jalayer F (2003) Direct probabilistic seismic analysis: implementing non-linear dynamic assessments. Stanford University, Stanford, CA
26. Jalayer F et al (2014) Cloud analysis revisited: efficient fragility calculation and uncertainty propagation using simple linear regression. In: NCEE 2014—10th U.S. national conference on earthquake engineering: frontiers of earthquake engineering
27. Kam WY, Pampanin S, Elwood K (2011) Seismic performance of reinforced concrete buildings in the 22 February Christchurch (Lyttleton) earthquake. Bull New Zealand Soc Earthq Eng 44(4):239–279
28. Kiris SS, Boduroglu MH (2013) Earthquake parameters affecting the performance of an RC frame with friction damper. Soil Dyn Earthq Eng 55:148–160
29. Kolaj M et al (2019) Ground-motion models for the 6th generation seismic hazard model of Canada. In: 12th Canadian conference on earthquake engineering, Quebec City
30. Kolozvari K et al (2015) Modeling of cyclic shear-flexure interaction in reinforced concrete structural walls. II: Experimental validation. J Struct Eng 141(5):04014135
31. Kolozvari K, Orakcal K, Wallace JW (2015) Modeling of cyclic shear-flexure interaction in reinforced concrete structural walls. I: Theory. J Struct Eng 141(5):04014135
32. Kolozvari K, Wallace JW (2016) Practical nonlinear modeling of reinforced concrete structural walls. J Struct Eng 142(12)
33. Lee D, Taylor DP (2001) Viscous damper development and future trends. Struct Des Tall Buildings 10(5):311–320
34. Liel A, Raghunandan M (2011) Investigation of structural collapse risk in the cascadia subduction zone. Technical report G11AP20134, US Geological Survey
35. López I, Busturia JM, Nijmeijer H (2004) Energy dissipation of a friction damper. J Sound Vib 278(3):539–561
36. McKenna F (2011) OpenSees: a framework for earthquake engineering simulation. Comput Sci Eng 13(4)
37. Mitchell D et al (2010) Evolution of seismic design provisions in the national building code of Canada. Can J Civ Eng 37(9):1157–1170
38. Moehle JP (2008) Earthquake collapse risk of older concrete buildings. In: Proceedings of Luis Garcia symposium. CiteSeer, pp 1–12
39. NRCC (1965) National building code of Canada. National Research Council of Canada, Ottawa
40. Narkhede DI, Sinha R (2014) Behavior of nonlinear fluid viscous dampers for control of shock vibrations. J Sound Vib 333(1):80–98
41. Nazari YR, Saatcioglu M (2017) Seismic vulnerability assessment of concrete shear wall buildings through fragility analysis. J Build Eng 12:202–209
42. Nelson AR, Kelsey HM, Witter RC (2006) Great earthquakes of variable magnitude at the Cascadia subduction zone. Quatern Res 65(3):354–365
43. Newmark NM (1959) A method of computation for structural dynamics. J Eng Mech Div 85(3):67–94
44. Ning C, Xie Y (2022) Risk-based optimal design of seismic protective devices for a multicomponent bridge system using parameterized annual repair cost ratio. J Struct Eng 148(5):04022044
45. Nishitani A et al (2000) Semiactive variable-friction damper control with simple algorithm. In: Proceedings of the 2000 American control conference. ACC (IEEE Cat. No.00CH36334), vol 1. IEEE, pp 503–507
46. Orakcal K, Sanchez LMM, Wallace JW (2006) Analytical modeling of reinforced concrete walls for predicting flexural and coupled-shear-flexural responses. Pacific Earthquake Engineering Research Center
47. Ramirez JDM, Tirca L (2012) Numerical simulation and design of friction- damped steel frame structures damped. In: 15th World conference in earthquake engineering
48. Scott MH, Fenves GL (2006) Plastic hinge integration methods for force-based beam-column elements. J Struct Eng 132(2):244–252
49. Symans MD et al (2008) Energy dissipation systems for seismic applications: current practice and recent developments. J Struct Eng 134(1):3–21

50. Taiyari F, Mazzolani FM, Bagheri S (2019) Damage-based optimal design of friction dampers in multistory chevron braced steel frames. Soil Dyn Earthq Eng 119:11–20
51. Tesfamariam S, Goda K (2017) Impact of earthquake types and aftershocks on loss assessment of non-code-conforming buildings: case study with Victoria, British Columbia. Earthq Spectra 33(2):551–579
52. Wallace JW et al (2012) Damage and implications for seismic design of RC structural wall buildings. Earthq Spectra 28:281–299
53. Xie Y, Zhang J (2017) optimal design of seismic protective devices for highway bridges using performance-based methodology and multiobjective genetic optimization. J Bridg Eng 22(3):04016129
54. Xie Y, Zhang J, Xi W (2018) Effectiveness evaluation and optimal design of nonlinear viscous dampers for inelastic structures under pulse-type ground motions. Earthq Eng Struct Dyn 47(14):2802–2820
55. Xue J et al (2021) Experimental and numerical study of mortise-tenon joints reinforced with innovative friction damper. Eng Struct 230:111701
56. Yathon J, Adebar P, Elwood KJ (2017) A detailed inventory of non-ductile concrete shear wall buildings. Earthq Spectra 33(2):605–622
57. Zhang Z et al (2020) Development of a novel deformation-amplified shape memory alloy-friction damper for mitigating seismic responses of RC frame buildings. Eng Struct 216:110751

# Seismic Response of Single-Layer Lattice Domes Made from Steel and Aluminium

**Akossiwa Constance Efio-Akolly and Charles-Darwin Annan**

**Abstract** Lattice domes are used in the construction of stadiums and airports to accommodate many people. These structures fit into the high seismic importance category because they serve as shelters in case of seismic events. Information based on research regarding the seismic design of domes exists; however, the practical application of this information by the designer remains a daunting challenge. Essentially, there are no established guidelines for the seismic design of domes. Given that aluminium is fast evolving as an effective alternative to steel in the construction of domes, the objective of this study is to assess the seismic performance of an aluminium dome in comparison with a steel dome using modal analyses, modal pushover analyses and nonlinear time history analyses. The selected ground motion for the time history analyses is the 1995 Kobe earthquake with a peak ground acceleration of 0.48 g. It was observed that the modal characteristics of both domes were similar. There was no permanent deformation in both domes under the unscaled ground motion. However, at higher seismic intensities, permanent deformations occurred, and both domes had about the same residual displacement. For all levels of seismic intensities considered, the aluminium dome experienced more displacements than the steel dome.

**Keywords** Aluminium alloys · Carbon steel · Lattice dome · Seismic response · Seismic design

## 1 Introduction

A lattice dome is a space frame constructed by assembling profile members to form the approximate shape of a cut sphere. According to surveys carried out right after the Kobe earthquake in 1995, no complete collapse was reported for domes, and the recorded damages were minor. This later prompted their use as refuge shelters for

A. C. Efio-Akolly (✉) · C.-D. Annan
Department of Civil and Water Engineering, Laval University, Quebec City, QC, Canada
e-mail: akossiwa-constance.efio-akolly.1@ulaval.ca

thousands of people who lost their homes in this devastating earthquake [12]. The same observation was made during the Wenchuan earthquake in 2008, where among numerous spatial structures located in the earthquake-hit area, no major collapse was reported [10]. Among the partially damaged spatial structures, those with a reinforced concrete slab roof suffered the most damage. This was due to the additional self-weight of the concrete roofing material that attracted considerable seismic forces into the system. Experience gained from these two earthquakes shows that lattice domes may deliver superior seismic performance compared with other structures, provided that the self-weight of the roofing material is kept to a safe minimum. This satisfactory seismic performance is attributable to the three-dimensional load-bearing mechanism of domes, which allows the full participation of its constituent members. Lattice domes also have an inherent lightness and high stiffness, but they can also sustain large deformations [14]. Numerical and experimental research results on the seismic performance of steel domes confirmed this observation. For instance, a 40-m medium-rise dome with a seismic mass of 200 kg/m$^2$ subjected to the El Centro ground motion scaled to higher intensities failed when the peak ground acceleration reached 8 m/s$^2$ [9]. Fan et al. [9] and Zhongxue and Zuyan [20] contributed significantly to the identification of the dynamic modes of failure for single-layer domes. It is now well established in the literature that domes have two main failure modes, namely dynamic strength failure and dynamic instability failure. The dynamic instability collapse mechanism is characterized by dynamic buckling or coupled instability with member buckling and the overall buckling of the system. The dynamic collapse mechanism is revealed in a drastic increase of the nodal displacement of the system, which results in the sudden collapse of the system. Therefore, it is recommended in the literature to prevent this mode of failure by ensuring that the prevalent dynamic collapse mechanism of a lattice dome is the dynamic strength failure mechanism. For example, [9] recommended that the domes have a safety factor of 2.5 against elastic buckling to avoid the dynamic instability collapse mechanism. The dynamic strength failure mechanism mainly results from yielding and material damage accumulation. This failure is evident in the rapid development of plastic regions or the rapid increase in the ratio of yielded members. Although much progress has been made through research that sets the foundation with concepts and recommendations for the seismic evaluation of lattice domes, there are no established guidelines for the seismic design of domes. Moreover, the available research-based data on the seismic design of domes was established based on steel dome models.

Aluminium is becoming a very competitive material that is gradually replacing structural steel and stainless steel in the construction of space structures such as domes [16]. The preference for aluminium as a material for load-bearing and non-load-bearing elements of domes is justified by its advantageous physical and mechanical properties. In fact, aluminium alloys are very promising ecological material for the construction of load-bearing structural elements and compared with steel, they have high strength-to-weight ratio and high resistance to atmospheric corrosion, are durable and extrudable and have superior aesthetic appearance. Only very few results are present on the dynamic behaviour of aluminium domes.

## 2  Research Objectives

Since aluminium and steel have different mechanical and cyclic properties, it is necessary to study the influence of the material on the nonlinear dynamic response of domes subjected to severe earthquake ground motions. A study of the seismic response of aluminium domes will therefore validate or redefine the failure mechanisms of aluminium domes and assess the seismic performance of aluminium domes under cyclic loads. According to the study conducted by [19], "aluminium domes are more suitable to be used in zones of high seismic activity". The study showed that the seismic effect on steel was always more significant than the one on aluminium domes because of the reduced structural self-weight due to the lightness of aluminium. These conclusions were obtained for earthquake acceleration between 0.05 and 1 g. However, the hysteretic and damage behaviour of the material was not taken into account, so this must be investigated further. Therefore, when investigating the dynamic strength failure mechanism of an aluminium or steel single layer dome under earthquakes, low cycle fatigue is essential to obtain accurate results and predictions. The objectives of the present study are to identify a suitable aluminium alloy with comparable hardening and fatigue properties to steel and to assess the seismic performance of an aluminium dome and a steel dome, designed based on the design recommendations available in the literature and the Canadian building code.

## 3  Selection of Aluminium Alloys

Single-layer lattice domes suffer yielding and cyclic inelastic strains leading to low cycle fatigue rupture under severe earthquakes. Since yielding and fracture are expected in single-layer domes under severe earthquakes loadings, the material model should capture the expected plasticity mechanism under cyclic inelastic loadings. This is achieved by defining the hysteretic behaviour of members under cyclic loading in the material model. The hysteresis of steel and aluminium is mainly controlled by the combined isotropic and kinematic hardening properties and the material's low cycle fatigue properties. Therefore, the Chaboche model and the Coffin Mason model were considered to simulate the hysteresis behaviour of the material in the numerical analyses conducted. The calibrated model parameters of all the aluminium alloys for which experimental data was available were screened, and an aluminium alloy with comparable cyclic mechanical properties to low carbon steel was selected. Low carbon steel 350WT was selected as the reference material, and its mechanical properties were obtained from the work of [1].

The monotonic stress–strain curves in dashed lines and the cyclic stress–strain curves in solid lines of the materials are presented in Fig. 1. This graph shows that low carbon steel experiences significant cyclic hardening, followed by the aluminium alloys 5083 H111 [17] and 6082 T6 [2, 6], whereas the aluminium alloys 6061 T6 [3, 4] and 2024 T3 [13, 18] experience cyclic softening. The aluminium alloy 6061
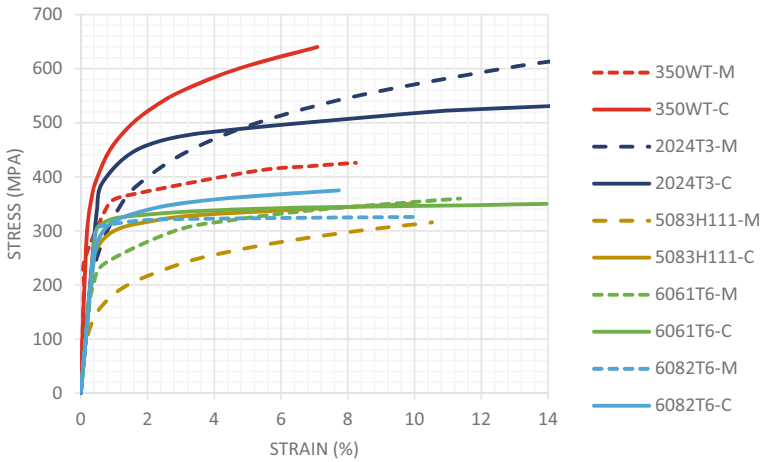
**Fig. 1** Monotonic and cyclic stress–strain curves of the materials

T6 was first eliminated since this alloy is very sensible to strain rate and amplitude, hence the large variability observed in the existing literature [3, 4, 8]. At this stage, the alloys with acceptable cyclic strength properties are 2024T3, 5083H111 and 6082T6. A comparison of the low cycle fatigue properties of the aluminium alloys was also conducted, as shown in Fig. 2. It can be noticed that the alloy 5083 H111 has the least fatigue strength, whereas the alloy 2024 T3 has a good fatigue resistance similar to that of low carbon steel. However, the alloy 2024T3 has the least corrosion resistance among the aluminium alloys screened [5]. Since corrosion resistance is one great advantage of interest when aluminium replaces steel in the construction industry, the alloy 2024T3 was eliminated. Therefore the alloy 6082T6 was selected for its acceptable cyclic hardening and low cycle fatigue strength, in addition to a good corrosion resistance.

## 4  Numerical Model Definition

The pilot dome considered in this study is a single-layer lattice diamatic dome, as shown in Fig. 3. The dome is a 40-m medium-rise single-layer diamatic dome with a rise-to-span ratio of 1/3. The average member length was determined to prevent buckling of the aluminium members under the factored load. Since aluminium is more prone to buckling than steel, selecting an adequate member length was made based on the critical buckling strength of the selected aluminium alloy, 6082T6. As a result, the average member length was 2.38 m. The pilot dome is assumed to connect directly to a firm foundation. The boundary conditions of the dome are modelled as three-way pinned supports. Connections between members are assumed to be rigid. Both aluminium and steel domes were designed according to the Canadian standards
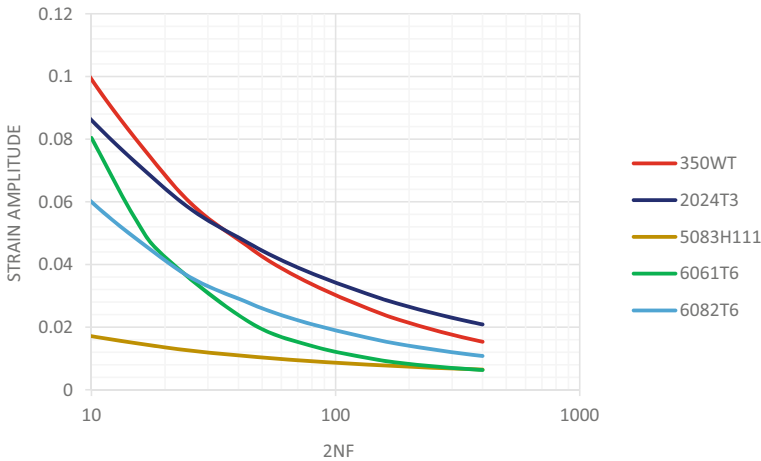
**Fig. 2** Low cycle fatigue curves of the materials

for a dead load of 0.5kN/m$^2$, a snow load of 1.82 kN/m$^2$ and a roof load of 1 kN/ m$^2$. The nominal dead load includes the weight of the various accessories (cladding, lighting, heat and ventilation equipment) and the self-weight of the structural frame. The nominal live load and snow loads were determined based on the specifications in the Canadian building code [7]. The seismic mass was estimated as 100% the dead load plus 25% of the snow load and 25% the live load. The sizing of the members was performed to prevent collapse by instability and sufficient strength at the ultimate limit states. Moreover, a nonlinear buckling analysis was conducted to ensure that the ratio of the buckling load to the design load is greater than 2.5, as recommended in the literature [9, 11]. At the end of the design process, the selected tubular profiles were 4.00″ OD × 0.125″ WALL, with an outside diameter of 101.6 mm and a wall thickness of 3.2 mm for the aluminium dome members, and HSS73 × 3.2 with an outside diameter of 73 mm and a wall thickness of 3.2 mm for the steel dome members.

The designed domes were modelled in OpenSees, considering geometrical and material imperfections. To do so, each structural member of the dome was discretized into four displacement-based beam-column elements and arranged in the shape of the first member buckling mode shape of the member scaled to 1/300 of the span of the dome. This beam element model uses the fibre-based frame elements approach, which divides the cross section of the element into fibres to capture local axial stresses and strains. The uniaxial cyclic stress–strain behaviour assigned to each fibre included the calibrated material properties of the Chaboche combined hardening model and the Coffin Manson low cycle fatigue model. The calibrated material model properties input in the uniaxial material objects for the 6082T6 alloy and the low carbon steel 350WT were obtained from Borrego et al. [6], Arslan et al. [2], Annan and Beaumont [1]. The strength properties and Coffin Manson low cycle fatigue model parameters

**Fig. 3** Pilot dome model
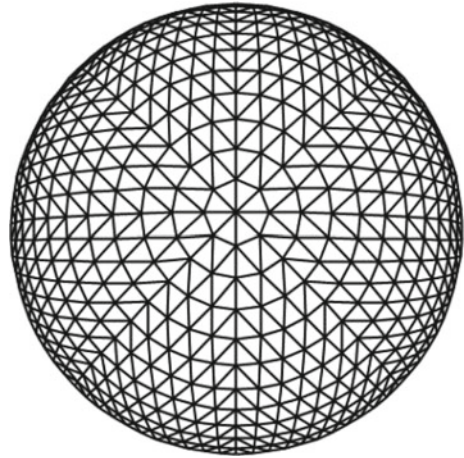


of 6082T6 alloy and low carbon steel 350WT are given in Table 1. In addition, a P-Delta coordinate transformation object was assigned to the dome model to consider the second-order effects. For the dynamic analyses, damping was applied in the model using the Rayleigh damping formulation with a damping ratio of 2%.

Modal analyses, nonlinear time history analyses and modal pushover analyses were carried out. For the modal analyses, it was assumed that the first 200 modes cover all the modes that are likely to be excited by any ground motions. Therefore, the first 200 modes were requested. For the nonlinear time history analyses, three engineering demand parameters were requested: the maximum nodal displacement, the normalized yield element ratio, and the fractured member ratio. Although the maximum nodal displacement varies from one node to the other during the analysis, the maximum values of this quantity recorded among all nodes would be more representative than that recorded at a particular node. For the modal pushover analyses, the gravity load was first applied. Subsequently, the lateral loads were gradually applied at each joint in a pattern proportional to a selected mode shape. The first three modes having the most significant mass participation ratio in the horizontal direction were considered to determine the lateral load in each modal pushover analysis. The recorded demand measure was the maximum nodal displacement of the dome. The total response was obtained by combining the individual response of each of the three

**Table 1** Low cycle fatigue properties of 350WT and 6082T6

| Material name | Modulus of elasticity, $E$ (MPa) | Yield strength $F_y$ (MPa) | Ultimate strength $F_u$ (MPa) | Coffin Mason fatigue ductility coefficient, $\varepsilon_f$ | Coffin Mason fatigue ductility exponent, $c$ |
|---|---|---|---|---|---|
| 350 WT | 211,180 | 364 | 503 | 0.33 | $-0.54$ |
| 6082T6 | 66,500 | 307 | 330 | 0.209 | $-0.593$ |

modal pushover analyses using the complete quadratic combination (CQC) method. The CQC method was preferred to the square root sum of square method (SRSS) since the frequencies of the domes were closely spaced.

## 5 Seismic Performance of Domes

This section presents the results of the modal analyses, the modal pushover analyses, and the nonlinear time history analyses. For ease of reference, the aluminium dome and the steel dome are referred to as AD40f3 and SD40f3, respectively.

### 5.1 Dynamic Characteristics of the Domes

Modal analyses were conducted on AD40f3 and SD40f3 to compare the dynamic characteristics of both domes. For each dome, the vibration mode numbers and their corresponding frequencies are shown in Fig. 4. This figure shows that the frequency distribution curves of both domes are very close and similar in shape. Since both domes have the same geometrical particulars and support conditions but different materials, it can be inferred that the material does not influence the frequency distribution of the dome. It can also be noticed that the frequencies in each frequency distribution curve are closely spaced. This corroborates the existing literature [11, 15]. The shape of each frequency distribution curve can be divided into two segments, the first one having a nearly flat slope with frequencies lesser than 10 Hz and the next one having a steep slope with frequencies greater than 10 Hz. The frequencies greater than 10 Hz were associated with localized vibration modes. On the other hand, frequencies less than 10 Hz were associated with global vibration modes. The latter has more influence on the dynamic characteristics of the dome. The influence of these global vibration modes is seen in the horizontal and vertical cumulative mass participation ratio distribution shown in Fig. 5. This figure shows that 90% of the total mass participation ratio is achieved by considering the first three modes with the highest mass participation ratio. The fundamental mode contributes to nearly 68%. The first two modes are symmetrical and are obtained by rotating the other to 90°. This was expected given the complete symmetry of the dome. It is also observed that the first three modes having the most significant mass participation ratio in the horizontal direction have nearly no participation in the vertical direction. The two main modes in the vertical direction have a purely vertical response. Therefore, it can be concluded that the first three horizontal modes govern the dynamic response of these domes, and the vertical response would have less influence on the total seismic response of the domes. Figure 6 shows that the fundamental mode shapes of both domes are similar. However, the first mode periods of both domes are different (0.29 s for the steel dome and 0.38 s for the aluminium dome), suggesting here that the steel dome is stiffer than the aluminium dome.
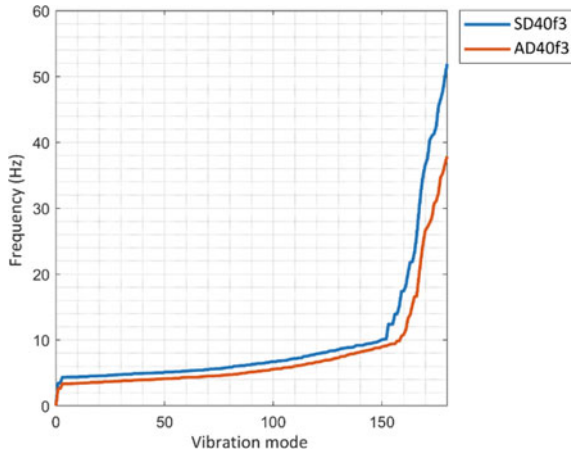
**Fig. 4** Frequency distribution curves of the steel and aluminium domes
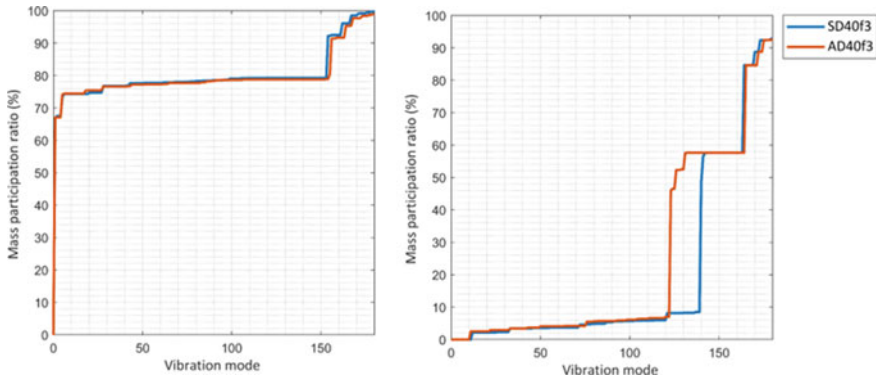


**Fig. 5** Cumulative mass participation ratio in the horizontal direction (left) and the vertical direction (right)

## 5.2 Seismic Response of the Domes

The steel and aluminium domes were subjected to the 1995 Kobe ground motions scaled to higher seismic intensity levels. A first evaluation of the global behaviour of the domes is achieved by comparing the time history of the maximum nodal displacement shown in Fig. 7. The time histories corresponding to lower seismic intensities are clearly at the bottom of the figure, and those corresponding to higher seismic intensities are at the top, as shown in the legend of the figure. It can be observed that the structural members of both domes remained elastic when the earthquake was scaled with factors lesser than 2. This is clearly evident in the figure, as the maximum nodal displacement values of the domes at the end of the earthquake are
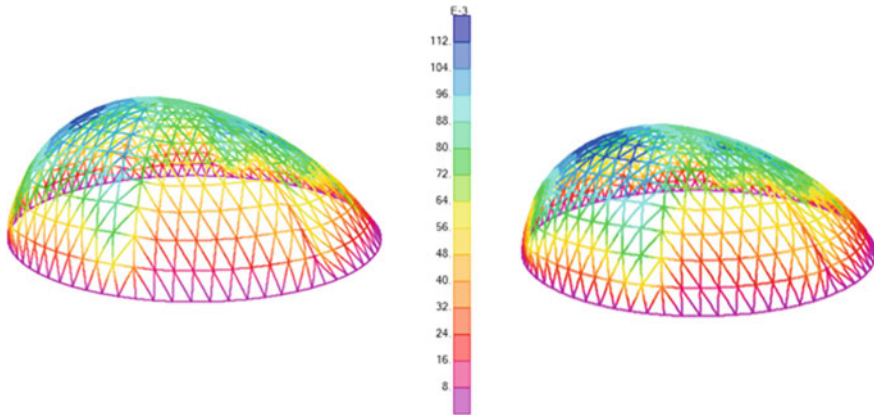
**Fig. 6** Fundamental mode shapes of the steel dome (left) and the aluminium dome (right)

equal to the initial maximum nodal displacement values of the domes before the ground motion was applied. The nodal displacements in the aluminium dome were always greater than those in the steel dome. However, the permanent deformations of the dome were about the same in both domes. At the end of the time history, the joint with the maximum nodal displacement was closest to the members with the most plasticity. It was also observed that most of the yielded elements were in the first ring members and diagonal members close to the supports of the steel and aluminium domes. However, there were also yielded elements at various areas in the members, further from the base in the aluminium dome. The spread of plasticity and the fatigue failure of the members were also investigated. Table 2 shows that the steel dome and the aluminium dome remained elastic when subjected to the ground motion scaled with a factor of lesser or equal to 2. In both domes, when the ground motion is scaled with factors greater than 3, plastic regions developed, and the degree of plasticity in the aluminium domes was always greater than that in the steel domes. Increasing plastic deformations in the members, close to the base, led to the collapse of the domes. This failure is characteristic of the dynamic strength failure mechanism. Dynamic buckling was not observed in both domes subjected to the Kobe earthquake.

To further investigate the influence of the material on the lateral load resisting mechanism of the domes, the modal pushover curves of the steel dome and the aluminium dome are presented in Fig. 8. This figure shows that the steel dome is laterally stiffer than the aluminium dome. The same observation was made on the ground of the values of the fundamental periods of the domes presented above. Moreover, a gradual progression from the elastic to plastic behaviour is observed in the modal pushover curve of the steel dome. In contrast, the progression from elastic to plastic behaviour is quite abrupt in the aluminium dome. In other words, the post-yield stiffness of the steel dome is also greater than that of the aluminium dome. This can be justified because the aluminium dome was more flexible and could
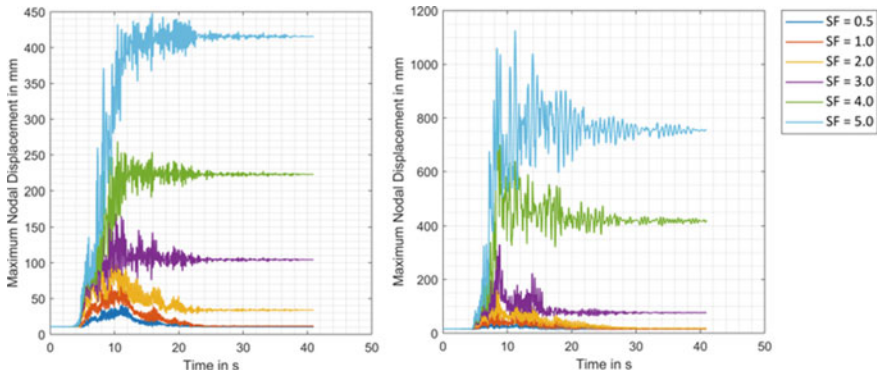
**Fig. 7** Time history of the maximum nodal displacement in the steel dome (left) and the aluminium dome (right)

**Table 2** Variation of the normalized yield element and fractured element ratios for both domes

| Scale factor | Normalized yield element ratio | | | | | Fractured member ratio | | | | |
|---|---|---|---|---|---|---|---|---|---|---|
| | 1.0 | 2.0 | 3.0 | 4.0 | 5.0 | 1.0 | 2.0 | 3.0 | 4.0 | 5.0 |
| Steel dome (%) | 0 | 0 | 0 | 0.06 | 1.4 | 0 | 0 | 0 | 0 | 0.6 |
| Aluminium dome (%) | 0 | 0 | 0.9 | 7.21 | 18.98 | 0 | 0 | 1.07 | 8.1 | 19.65 |

undergo plastic deformation quickly. Therefore, the aluminium dome could deform more globally and accept greater lateral forces, as shown in Fig. 9. The combined influence of the material properties and the system configuration is responsible for this observed behaviour.
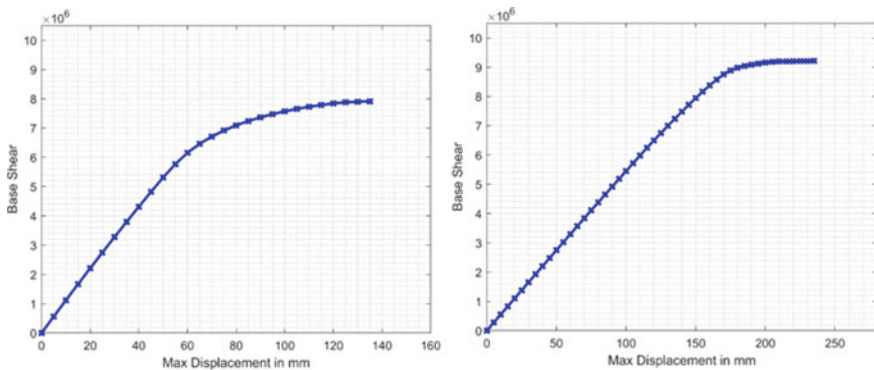


**Fig. 8** Modal pushover curve for the steel dome (left) and the aluminium dome (right)
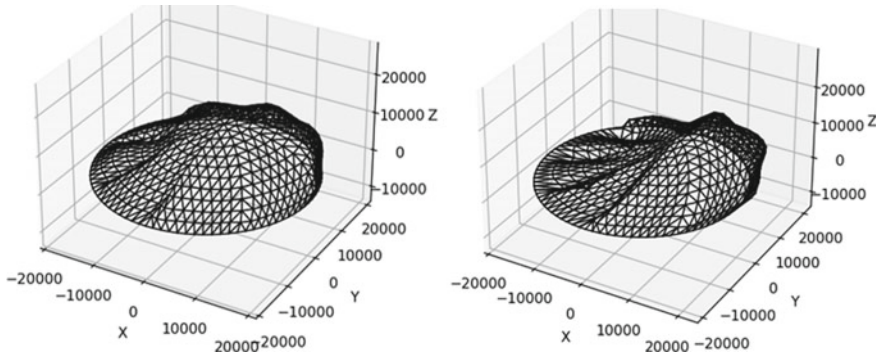
**Fig. 9** Final deformed shape of the steel dome (left) and the aluminium dome (right) at the end of the first mode modal pushover analysis

## 6 Conclusion

The seismic design of domes poses a challenge in the absence of codified seismic design methods, because latticed domes exhibit a nonlinear dynamic behaviour highly influenced by the geometrical configuration and the geometrical and material nonlinearities. Although research-based information is available for the seismic design of domes, these recommendations were made based on research on steel latticed domes. Given that aluminium has become an alternative material to steel in the construction of domes, this paper evaluates the seismic response of an aluminium dome and a steel dome designed for the same gravity loadings and design considerations. The results obtained from modal analyses, modal pushover analyses and the nonlinear time history analyses shed light on the dynamic characteristics and the seismic performance of the domes. The modal characteristics of the steel dome and the aluminium dome were similar. Therefore the material does not influence the modal characteristics of the dome. Moreover, the steel dome and the aluminium dome exhibited a good performance when subjected to the Kobe earthquake. This good seismic performance is attributable to the fact that the domes were initially designed to avoid dynamic instability by ensuring a safety factor of 2.5. However, this safety factor applied to aluminium domes is insufficient to ensure a seismic performance comparable with the steel dome. Therefore, it is recommended to use a displacement-based or a performance-based design approach for aluminium domes in earthquake-prone areas. Finally, the ductility of aluminium domes allows load redistributions in the members and more uniform distribution of plasticity in the members close to the base, which can be considered an advantage of the material. As a result, the aluminium dome could deform more globally and accept greater monotonic lateral forces. This observed behaviour is due to the combined influence of the material properties and the system configuration. However, under cyclic inelastic strains, the low cycle fatigue resistance of the material reduces this structural performance.

# References

1. Annan CD, Beaumont E (2020) Low-cycle fatigue of stainless steel plates under large plastic strain demands. J Build Eng 29:101160. https://doi.org/10.1016/j.jobe.2019.101160
2. Arslan E, Zigo M, Kepplinger G (2020) A novel approach for determination of hardening parameters of an aluminum alloy under cyclic loading with high amplitudes. IOP Conf Ser Mater Sci Eng 947(1):6–11. https://doi.org/10.1088/1757-899X/947/1/012009
3. Azizian-Farsani E, Ghodsiyeh D, Akbarzadeh S, Khonsari MM (2020) Theoretical and experimental analysis of relation between entropy and tension–compression fatigue of aluminum 6061–T6. J Braz Soc Mech Sci Eng 42(2):1–10. https://doi.org/10.1007/s40430-020-2194-9
4. Badaruddin M, Zulhanif, Supriadi H (2019) Low cycle fatigue properties of extruded 6061-T6 aluminum alloy. J Phys Conf Seri 1198(3). https://doi.org/10.1088/1742-6596/1198/3/032002
5. Beaulieu D (2006) Design of aluminium structures. Les Presses de l'aluminium
6. Borrego LP, Abreu LM, Costa JM, Ferreira JM (2004) Analysis of low cycle fatigue in AlMgSi aluminium alloys. Eng Fail Anal 11(5):715–725. https://doi.org/10.1016/j.engfailanal.2003.09.003
7. CNRC (2015) Code national du bâtiment, vol 1. Canada
8. Mirza FA, Liu K, Chen X-G (2017) Cyclic stress-strain behavior and low cycle fatigue life of AA6061 aluminum alloy. Miner Metals Mater Soc 210819. https://doi.org/10.1007/978-3-319-51541-0_172
9. Fan F, Shen SZ, Parke GAR (2005) Study of the dynamic strength of reticulated domes under severe earthquake loading. Int J Space Struct 20(4):235–244. https://doi.org/10.1260/026635105775870251
10. Feng Y, Liu Y, Xia X (2009) Grid structures in Wenchuan Earthquake. In: Proceedings of the international association for shell and spatial structures, October, 289–295
11. Hosseinizad (2018) Seismic response of lattice domes 47. https://doi.org/10.1503/cmaj.180710
12. Ishikawa K, Kawaguchi K, Kengo T, Sakai T (1997) Report on gymnasium and spatial structures damaged by Hyogoken-Nanbu earthquake. Architect Inst Jpn J Technol Des 3(5):96–101. https://doi.org/10.3130/aijt.3.96
13. Karakaş, & Szusta, J. (2016) Monotonic and low cycle fatigue behaviour of 2024–T3 aluminium alloy between room temperature and 300 °c for designing VAWT components. Fatigue Fract Eng Mater Struct 39(1):95–109. https://doi.org/10.1111/ffe.12336
14. Lan T (2005) Space frame structures, 2nd edn. In: Handbook of structural engineering.https://doi.org/10.1201/9781420039931.ch24
15. Li YG, Fan F, Hong HP (2017) Reliability of lattice dome with and without the effect of using small number of ground motion records in seismic design. Eng Struct 151:381–390. https://doi.org/10.1016/j.engstruct.2017.07.038
16. Mazzolani FM (2006) New challenges for aluminium structures: an introduction structural applications of aluminium in civil engineering fields of application. Struct Eng Int 4:1–4
17. Nečemer B, Zupanič F, Gabriel D, Tarquino EA, Šraml M, Glodež S (2021) Low cycle fatigue behaviour of ductile aluminium alloys using the inelastic energy approach. Mater Sci Eng A 800. https://doi.org/10.1016/j.msea.2020.140385
18. Peč M, Šebek F, Zapletal J, Petruška J, Hassan T (2019) Automated calibration of advanced cyclic plasticity model parameters with sensitivity analysis for aluminium alloy 2024–T351. Adv Mech Eng 11(3):1–14. https://doi.org/10.1177/1687814019829982

19. Xu S, Chen Z, Mazzolani FM (2015) The behavior of spherical domes under wind and earthquake action
20. Zhongxue L, Zuyan S (2001) Shaking table tests of two shallow reticulated shells. Int J Solids Struct 38(44–45):7875–7884. https://doi.org/10.1016/S0020-7683(01)00075-0

# Multi-Dimensional Seismic Vulnerability Assessment of CLT Coupled Wall System

**Biniam Tekle Teweldebrhan and Solomon Tesfamariam**

**Abstract** In this paper, multi-dimensional seismic vulnerability assessment is performed for a cross-laminated timber (CLT) coupled wall (CLT-CW) system. The CLT-CW structural system uses multiple balloon type CLT shear walls connected, at every story, with replaceable coupling beams. For the seismicity of Vancouver, British Columbia–Canada, five 10-story CLT-CW buildings with coupling ratio (CR) values 10–50%, are examined. Two-dimensional numerical model of the system is developed in OpenSees, and incremental dynamic analysis (IDA) is performed using 30 (bi-directional) ground motion records. Bi-dimensional damage demands, maximum inter-storey drift ratio, and residual drift ratio are used to compute the corresponding fragility curves at three different limit state capacities, namely immediate occupancy (IO), life safety (LS), and collapse prevention (CP). From the analyses, it is shown that CLT-CW systems with higher CR values are less vulnerable when compared with those of lower CR values. Moreover, this study has investigated the effect of different combinations of the limit state functions on the resulting fragility curves and seismic vulnerability of the systems.

**Keywords** Coupling ratio · Fragility curves · Limit state functions · Shear-links · Timber

B. T. Teweldebrhan (✉)
School of Engineering, The University of British Columbia, Okanagan Campus, 3333 University Way, Kelowna, BC V1V 1V7, Canada
e-mail: binitek@mail.ubc.ca

B. T. Teweldebrhan · S. Tesfamariam
Department of Civil and Environmental Engineering, University of Waterloo, 200 University Ave W, Waterloo, ON N2L 3G1, Canada

# 1   Introduction

With the increasing interest in tall structures, the provision of seismic resistance becomes a critical design factor [1]. Design decisions, such as selection of an appropriate structural material and provision of an innovative lateral load resisting system (LLRS) are vital to achieve a resilience structural system [40]. Traditionally, non-combustible materials, such as steel and concrete were the front-runners as the material of choice for high-rise structures [28]. However, due to the ecological trend, a wide range of economic factors, and rapid development of high-performance engineered wood products, timber-based constructions have had a resurgence in popularity over the past years [15, 29]. Specifically, cross-laminated timber (CLT) has been playing a radical impact on the construction of tall buildings in recent years [4, 6]. In literature, innovative CLT-based LLRS is proposed (e.g., [21, 24, 34, 39]). One novel contribution to the state-of-the-art knowledge in CLT construction is the recently proposed CLT coupled wall (CLT-CW) system [32, 33].

Coupled wall system is a LLRS that comprises multiple structural walls connected at all storys with coupling beams [11]. The coupling system enables the building to respond in-elastically when subjected to design seismic loads, where the coupling beams yield first and incur the largest portion of ductility and energy dissipation demand of the system [11, 27]. This ductile response of the coupling beam in return reduces the seismic demand of the structural system [11]. CW systems have been widely used in conventional coupled wall (e.g., [27]), hybrid coupled wall (e.g., [11]), replaceable coupled wall (e.g., [13]), and post-tensioned coupled wall (e.g., [26]) systems. Tesfamariam et al. [32] recently extended the CW system to timber buildings by using CLT shear-walls. Prior to this study, Pei et al. [23] and Tesfamariam et al. [31] have studied CLT-CW system considering CLT floors and reinforced concrete coupling beam as coupling elements, respectively. To improve the earthquake resilience of CLT-CW system, Tesfamariam et al. [32] used steel coupling beams (SCBs) with reparable or replaceable shear-links. Moreover, for tall buildings, platform construction is not preferable due to the large perpendicular to grain compressive loads that are transferred to the CLT floor panels at the lower story levels [7]. Accordingly, the system examined by Tesfamariam et al. [30] uses a balloon type of CLT shear-walls with buckling-restrained brace (BRB) hold-downs. In this article, a multi-dimensional probabilistic seismic vulnerability assessment is carried out on a 10-story CLT-CW system with five coupling ratio (CR) values 10–50%. Two-dimensional (2D) numerical model of the system is developed in OpenSees, and incremental dynamic analyses (IDA) are performed using suitable set of 30 ground motion records that reflects the seismicity of Vancouver, British Columbia (BC)—Canada. Engineering demand parameters, maximum inter-story drift ratio (MaxISDR), and residual inter-story drift ratio (ResISDR) are selected as seismic damage measuring parameters. Three limit state surfaces (linear, circular, and square) are considered to compute the fragility curves at three different non-collapse limit state capacities, namely immediate occupancy (IO), life safety (LS), and collapse prevention (CP). Moreover, collapse fragility curves are computed, and

the performance of the 10 story CLT-CW system is investigated under the considered CR values.

The rest of this document is organized in six sections. Section 2 presents the system details and design considerations followed by Sect. 3, that defines the methodology of the study. Section 4 discusses the finite element model and ground motion selection method, and Sect. 5 presents the result and discussion of the study. Finally, Sect. 6 provides some concluding remarks.

## 2 Building Details and Design Consideration

### 2.1 System Design and Details

The 2D view of the considered 10-story CLT-CW system is shown in Fig. 1. The structural model comprises glulam beams and columns, CLT floor panels, CLT core shear-walls, and SCBs with replaceable shear-links. The glulam beams and columns are designed to support the vertical gravity load of the system, while the balloon CLT shear-walls and coupling beams resist the lateral loads. The complete 3D view and structural components of the system are provided in Tesfamariam et al. [32]. The first story height of the building is taken as 3.8 m, and height of all other stories are 3.0 m. The length of the two symmetrical 7-ply Grade E1 CLT balloon shear-walls and coupling beams are 4 m and 1 m, respectively. The building is designed with a live load of 2.4 kPa and a superimposed load of 2.8 kPa. The snow and seismic loads are determined based on the provisions of NBC [20] considering class C soil condition. The CLT floor panels are designed as a one-way slab using a 5-ply CLT Grade E1 per CSA 086-14 standard [6]. The force parameters for the gravity load design were determined using ETABS, and system's glulam frame members (columns and beams) are designed following the CSA 086-14 [5] standard. The summary for the gravity load design and details of the system is presented in [30].

### 2.2 Coupling Ratio

CR is the parameter that governs the behavior of the CW system, and its value indicates the part of the total base moment converted into wall axial forces by means of the shear forces developed in the coupling beams (Fig. 2). The CR has a significant impact on the structural performance of CW systems, and analytically, for a two-wall system, the value of CR is defined as:

$$CR = \frac{TL_w}{M_{max}} = \frac{TL_w}{TL_w + \sum M_{wall}} = \frac{L_w \sum V_{z,i}}{TL_w + \sum M_{wall}} \quad (1)$$
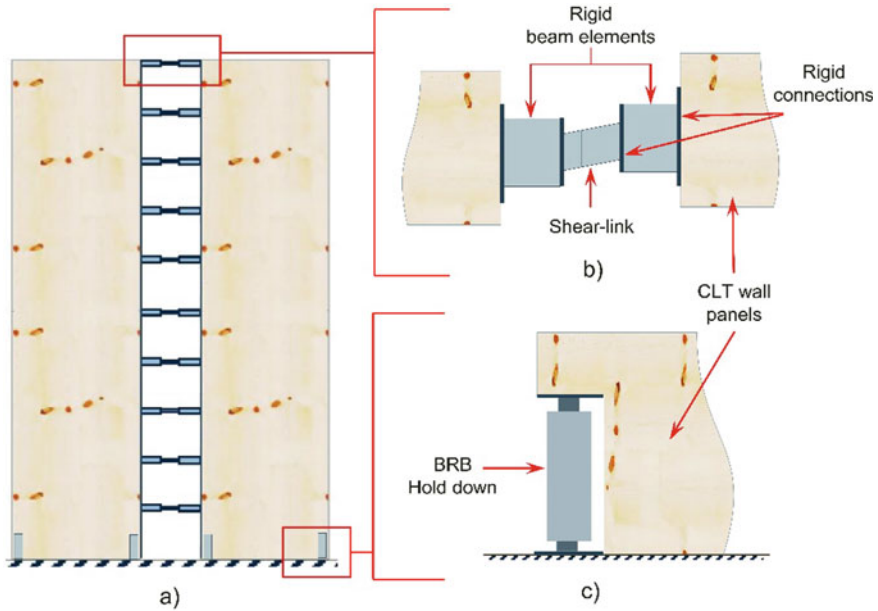
**Fig. 1** CLT-CW system: **a** Coupling system, **b** Coupling beam, and **c** Hold-down

where $M_{max} = M_1 + M_2 =$ total overturning moment due to lateral forces, $T = C =$ axial load induced by the shear forces of the coupling beams, $L_w =$ distance between the centroid of the two walls, $M_{wall} =$ reduced base moment of the individual walls ($M_1 = M_2$ for symmetrical walls), and $\sum V_{z,i} =$ accumulation of coupling beam shears acting at the edge of all piers.
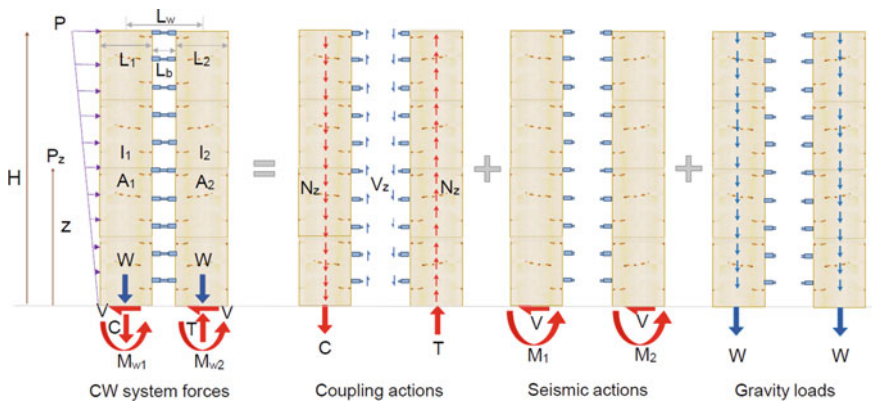


**Fig. 2** CW system force distributions

The behavior of CW is classified as low, intermediate, and high based on the values of CR. Among the three classes, the intermediate coupling (CR value 30–45%) is the most optimal. For ordinary CW systems, CR values of 30–80% were used under different design conditions. Unlike the reinforced concrete and hybrid structures, the behavior of coupling action in mass timber structures with CLT wall pier is a new area of research. Owing the relatively lower axial strength of CLT walls (compared with RC walls), smaller values of CR are expected to work for CLT-CW system. Accordingly, CR values of 10–50% are selected in this paper.

## 2.3 Seismic Design

The seismic design of the CLT-CW system is carried out using continuous medium method (CMM). The method is a simplified elastic method that can be used to analyze and design the preliminary geometries of CW systems for a uniform or quasi-uniform structures [27]. The method reduces the statically indeterminate CW system into a problem modeled as single fourth-order differential equation [27]. Smith and Coull [27] provide closed form solutions that depend on the type of lateral loads. The design, using the closed form solutions, provide a good approximation for preliminary designs of regular CW systems and should be accompanied by a more accurate nonlinear analysis method to evaluate the system's performance. Accordingly, in this paper, the CMM and FEM are used to design the LLRS parameters and study the nonlinear responses of the structure under the action of different GMs, respectively. The complete design procedure, along with a numerical example, is provided in Tesfamariam et al. [32, 33].

## 3 Multi-Dimensional Seismic Vulnerability Assessment

### 3.1 Damage Measuring Parameters

In this study, two engineering demand parameters are used, MaxISDR and ResISDR, to access the performance of the CLT-CW system. MaxISDR is a direct measure of building's performance, and it denotes the maximum (absolute) difference in lateral displacement between two consecutive floors divided by the story height [22]. ResISDR, on the other hand, represents the maximum story drift ratio recorded at the end of the GM time history [22]. For decision-making and an appropriate understanding on the performance of the system, the relationship between demand and capacity of the system should be explored [25]. Accordingly, in this study, demand-to-capacity ratio ($Y = $ D/C) is used to indicate the relative performance of the CLT-CW system under the action of seismic excitation. The demand and capacity values represent the outcomes of the structural analyses and the threshold

| Performance limit state | MaxISDR (%) | ResISDR (%) |
|---|---|---|
| IO | 0.5 | 0.2 |
| LS | 1.5 | 0.5 |
| CP | 2.5 | 1 |

**Table 1** Limit state capacities for MaxISDR and ResISDR [10, 12]

of the performance of limit states considered, respectively. As stated earlier, three limit states (IO, LS, and CP) are considered in this study, and the performance limit state capacity values are summarized in Table 1.

## 3.2   Limit State Functions

To perform a multi-dimensional seismic vulnerability assessment of a system, multi-dimensional limit state functions (MLSFs) should be defined [8, 35]. These functions can combine two or more demand-to-capacity ratios in terms of nonlinear combination of the ratios or as union or intersection of MLSFs [8, 19]. The generic expression that demonstrates the stated relationships is given as [8]:

$$G(\mathbf{Y}, \text{IM}) = \sum_{i=1}^{N} \left( a_i \cdot Y_i^b - 1 \right) \text{ with } a_i = 1 \text{ or } 0 \tag{2}$$

$$G(\mathbf{Y}, \text{IM}) = \bigcup_{j=1}^{N} (G_j \le 0) \cdot G(\mathbf{Y}, \text{IM}) = \bigcap_{j=1}^{N} (G_j \le 0) \tag{3}$$

where $G(\mathbf{Y}, \text{IM})$ = the multi-dimensional limit state function, IM = intensity measure, $b$ = power term that defines the shapes of the limit state function, and $N$ = number or dimensions of the damage measures ($Y_i$ values).

In this study, three limit state surfaces are defined and used. Equations (2) and (3) can be simplified to the forms shown in Eqs. (4), (5), and (6), to represent the chosen limit state surfaces linear, circular, and square, respectively [8]. The 3D and 2D view of the limit state surfaces are demonstrated in Fig. 3.

$$G(\mathbf{Y}) = Y_1 + Y_2 - 1 \tag{4}$$

$$G(\mathbf{Y}) = Y_1^2 + Y_2^2 - 1 \tag{5}$$

$$G(\mathbf{Y}) = G_1(\mathbf{Y}) \cap G_2(\mathbf{Y}) = (Y_1 - 1) \cap (Y_2 - 1) \tag{6}$$
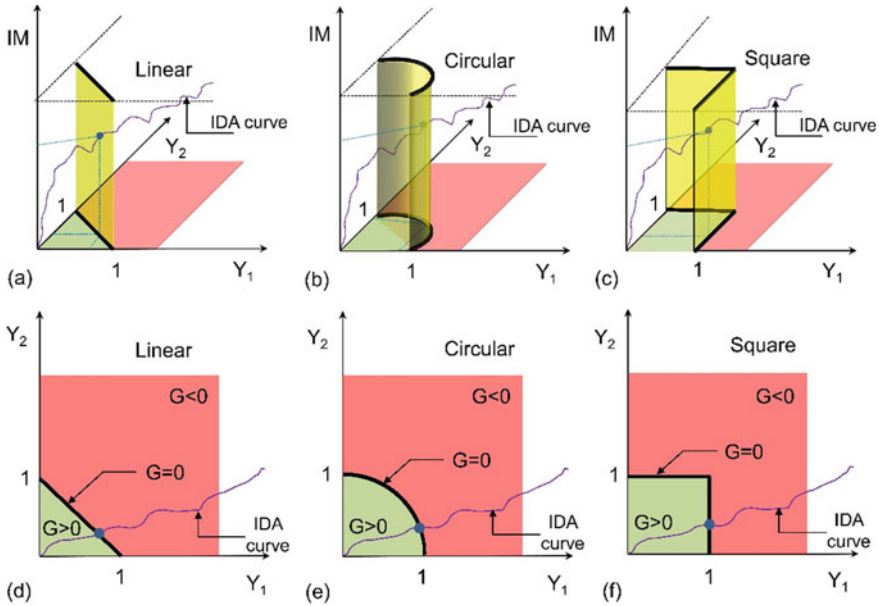
**Fig. 3** Limit state functions, adapted from De Risi et al. [8]

## 4 Numerical Model and Ground Motion Selection

A finite element (FE) model for a 2D CW frame of the buildings was developed using Open System for Earthquake Engineering Simulation [18]. In this FE framework, the global system is formed by assembling the model components: CLT shearwall elements, hold-downs, and coupling beams (Fig. 4). The CLT wall panels are modeled using *ElasticIsotropic* material and *quad* elements [9]. The two ends and central "fuse" of the coupling beams are modeled using OpenSees *elasticBeamColumn* elements as rigid offsets and *Steel01 UniaxialMaterial* with *zeroLength* nonlinear vertical springs, respectively [16]. To satisfy the high axial demand, BRB hold-down [31] is modeled using OpenSees *Steel01 uniaxialMaterial*. The contact between the CLT wall and the base is modeled using OpenSees *uniaxial elastic notension* (ENT) material and a large elastic stiffness value is assigned to the *ENT* spring under compression. Besides, to take account the effect of P-delta, a leaning column is introduced and modeled as *elasticBeamColumn* element. Elastic *UniaxialMaterial* and *truss* elements are used to link the CLT shear-walls and leaning column and transfer the P-delta effect. A load (equivalent to the gravity load carried by the gravity columns) is applied in the provided lean column at each story level. The detail modeling parameters can be obtained in Tesfamariam et al. [32].

Modal analysis was performed, and the first three fundamental periods are summarized in Table 2. To develop the seismic fragility curves of the systems, GM selection is carried out by matching the response spectra of the selected records to a target
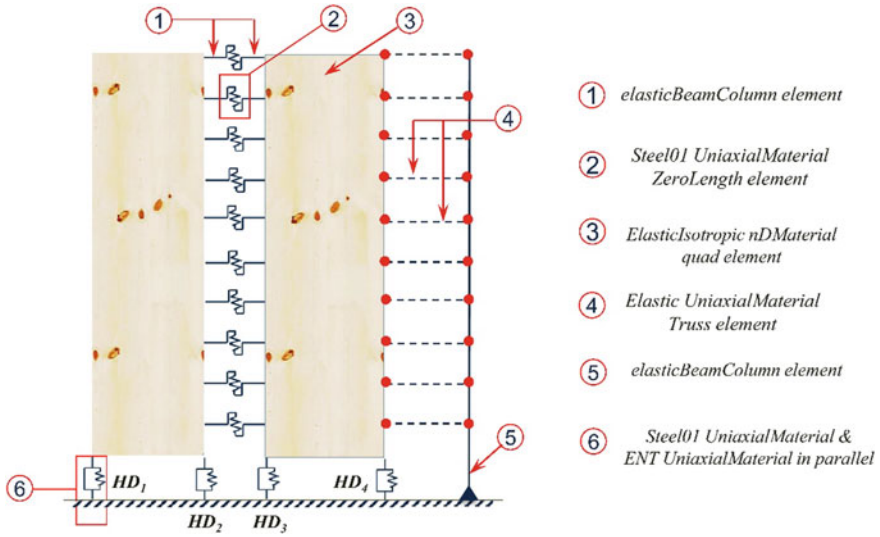
**Fig. 4** Details of the numerical model

response spectrum of Vancouver, BC—Canada. Using multiple CMS-based record selection method [2, 14], a set of 30 GM records (bi-directional) is selected at the anchor period of 1.0 s, considering the 2% probability of exceedance (PE) in 50-year design level earthquake. Vibration periods of 0.1 and 2.0 s are considered as the lower and upper limits for the GM selection, and the match is satisfied within these lower and upper limits vibration period ranges.

**Table 2** Natural periods of the CLT-CW system under different CR values

| CR (%) | Fundamental periods (s) | | |
|--------|-------|-------|-------|
|        | $T_1$ | $T_2$ | $T_3$ |
| 10     | 1.21  | 0.27  | 0.11  |
| 20     | 1.10  | 0.26  | 0.11  |
| 30     | 1.04  | 0.24  | 0.11  |
| 40     | 1.00  | 0.23  | 0.10  |
| 50     | 0.98  | 0.23  | 0.10  |

# 5 Result and Discussion

## 5.1 Incremental Dynamic Analysis

IDA is a series of dynamic analyses performed by repeatedly scaling a GM record until a specific damage on the structure is attained [37]. The resulting curve (IDA curve) relates the scaled IM values with one or more structural demand parameters EDPs or alternatively damage measures. In this study, the 5% spectral acceleration at the fundamental period of the system ($S_a(T_1)$) is considered as the IM, and two EDPs, MaxISDR and ResISDR are considered as the damage measuring parameters. The typical 3D IDA curves for the CLT-CW systems (with CR = 10%) are shown in Fig. 5. As seen in the figure, the systems first behave elastically and then, the slope falls as the $S_a(T_1)$ level raises, indicating that the systems have suffered significant drift damage before reaching the collapse points. Moreover, it can be noticed that though the systems are subjected to significantly higher MaxISDR, the ResISDR remains well below 1%, a threshold value to protect excessive post-earthquake deformations [22]. Besides, the figure demonstrates the performance points and the $S_a(T_1)$ values corresponding to the onset of a specific limit state capacities. It is worth noting that the distributions of the limit state capacity points are almost the same for the LS and CP limit states (Fig. 5b, c). On the other hand, a significant difference can be seen between the IO and the other two limit state capacities. Note that Fig. 5 shows the case for CLT-CW system with CR = 10%. Similar observations can be made for the other CR cases as well.

The bi-dimensional representation of the same IDAs, in terms of $Y$'s, is shown in Fig. 6. The vertical and horizontal axes of the figure represent the normalized, the ratio between the demand and corresponding capacity, of MaxISDR and ResISDR, respectively. From the figure, it can be shown that as the IDA passes from IO to CP, there is a larger part of the limit state surface intersected by the IDA curves, leading to a larger dispersion of the response. Moreover, for the case of the square limit state
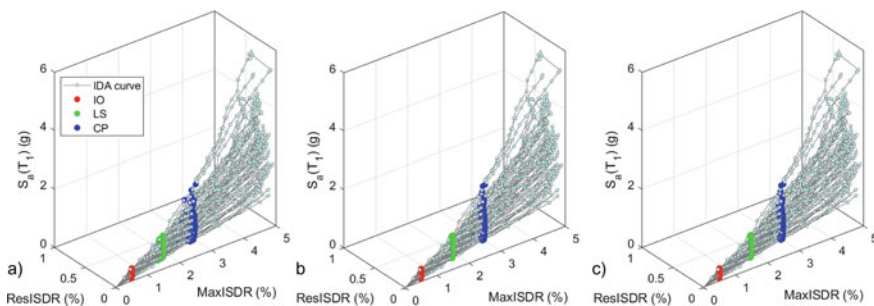


**Fig. 5** 3D IDA curves for CLT-CW system with CR = 10% considering: **a** Linear, **b** Circular, and **c** Square limit state functions
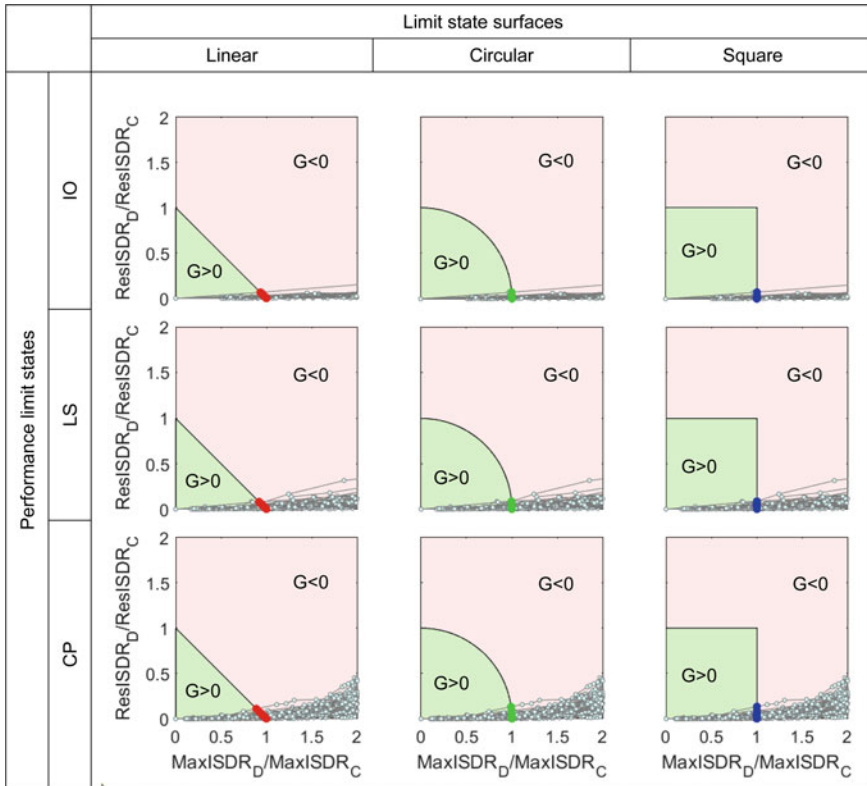
**Fig. 6** Bi-dimensional IDA curves

functions the proposed procedure is almost coincident with the classic procedure adopted for the case of scalar damage measure.

## 5.2 Fragility Curves

In literature, different parametric and nonparametric fitting models exist to develop seismic fragility curves. Considering its simplicity, good representation, and convenient characteristics, the lognormal cumulative distribution function (CDF) has often been used [17]. Accordingly, in this study the lognormal CDF is used, and the method of moments is applied to obtain the parameters of the distribution function at the damage threshold of interest (e.g., IO). These parameters (the mean and standard deviation) are then used to develop the fragility curves at the specific limit state condition. Analytically, for a single scalar damage measuring index, the resulting fragility curve is described by the following equation [3, 8]:

$$P(D > C/\text{IM} = \text{IM}_i) = P(G(Y) \leq 0/\text{IM} = \text{IM}_i)$$

$$= \Phi\left(\frac{\ln(\text{IM}_i) - \overline{\mu}}{\overline{\beta}}\right) \tag{6}$$

where $\text{IM}_i = \text{IM}$ for the $i$th GM at the damage threshold of interest ($i$ ranges from 1 to $N$, the number of GM records), $\Phi =$ the standard cumulative normal distribution function, $\overline{\mu}$ and $\overline{\beta}$ are the sample mean and standard deviation, respectively, which are calculated as:

$$\overline{\mu} = \frac{1}{N} \sum_{1}^{N} \ln(\text{IM}_i) \tag{7}$$

$$\overline{\beta} = \sqrt{\left(\frac{\sum_{1}^{N} (\ln(\text{IM}_i) - \ln(\overline{\mu}))^2}{N - 1}\right)} \tag{8}$$

In this study, however, the fragility methodology is applied based on the bi-dimensional damage indices. For the case of a multi-dimensional limit state surface, the calculation of IM values corresponding to the onset of a specific limit state is not straightforward [8]. It is necessary to obtain the performance point ($G = 0$) by interpolating the closest points that are a little smaller and bigger than the performance point. When the IM is obtained by interpolation, the same procedure (i.e., the method of moments) is applied to predict the fragility curve parameters of the lognormal CDF. The detail formulation and implementation of the performed calculation on to get the performance point are provided in [8].

### 5.2.1 Non-collapse Fragility Curves

As discussed in the previous sections, the seismic vulnerability of the designed CLT-CW systems is examined under the three non-collapse limit states: IO, LS, and CP. The performance points are first estimated considering the three limit state functions. Once the $S_a(T_1)$ at the damage threshold of interest (e.g., IO) is obtained for all the GMs and the limit state functions, the logarithmic moments of the distribution of $S_a$ are easily computed. The resulting non-collapse fragility curve is shown in Fig. 7 for the case CR $= 10\%$. Two important points can be noticed. First, the resulting fragility curve shows that the circular and square limit state function yields the same result, and as expected, the linear limit state function gives a critical fragility curve. Second, the fragility curves in Fig. 7b, c have bigger standard deviation, and this corresponds to the fact that the damage data are largely dispersed in the nonlinear response zone of the system. However, in the case of IO, where there is a moderate earthquake intensity and system's response is almost linear, the fragility curve has a smaller standard
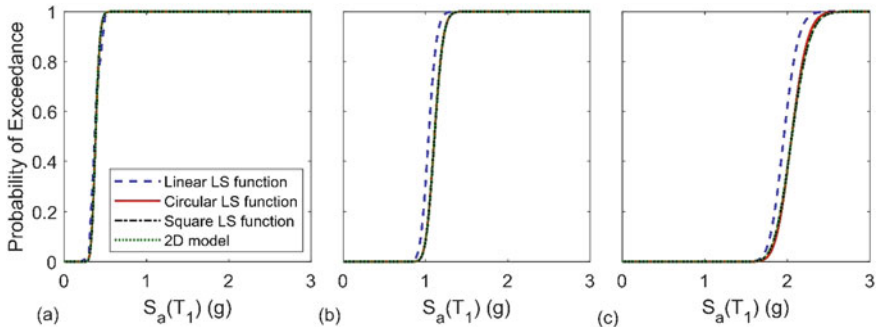
**Fig. 7** Non-collapse fragility curves for CR = 10% considering **a** IO, **b** LS, and **c** CP

deviation. Overall, the MaxISDR damage index is found to govern the fragility curves with a marginal impact from the ResISDR. As all the performance points are intercepted by the MaxISDR (Fig. 6), the fragility curve obtained from the square limit state function overlaps with the one developed considering the MaxISDR only (i.e., the 2D fragility curve model obtained from the 2D IDA curves). Nonetheless, the use of the 3D model yields a critical fragility curve (especially for the LS and CP limit states) since ResISDR has a contribution on the overall vulnerability of the system at the linear limit state function (Fig. 7). Because timber structures are prone to residual deformations due to the slip in connections and may contribute to the global performance of the system, bi-dimensional damage demands can give a better result. Note that though Fig. 7 shows the result for the case with CR = 10%, the same observations are noted to the other four cases (CR = 20–50%).

REF _Ref97209191 \h \* MERGEFORMAT Figure 8 demonstrates the non-collapse fragility curves for the case CR =10, 30, and 50%. Each curve in REF _Ref97209191 \h \* MERGEFORMAT Fig. 8 represents the combined equivalent fragility curve which is the median curve of the fragility curves of the three considered limit state functions [8]. As expected, CLT-CW systems with higher CR value exhibit better seismic performance with lower PE under a given hazard level, than those with lower CR values. This contributes to the fact that systems with higher CR values have greater coupling beam strength, higher reduction in the seismic demand of the individual walls, and hence are stronger. The relative difference in the seismic performance of the systems is more pronounced for the LS and CP limit states, where the systems exhibit nonlinearity.

### 5.2.2 Collapse Fragility Curves

To extend the vulnerability assessment of the considered system with respect to the probability of collapse, collapse fragility curves are developed from the IDA results (considering only the MaxISDR). For this system, collapse is considered to occur at a MaxISDR = 5% [38]. Figure 9 shows the IDA curve based on the MaxISDR damage
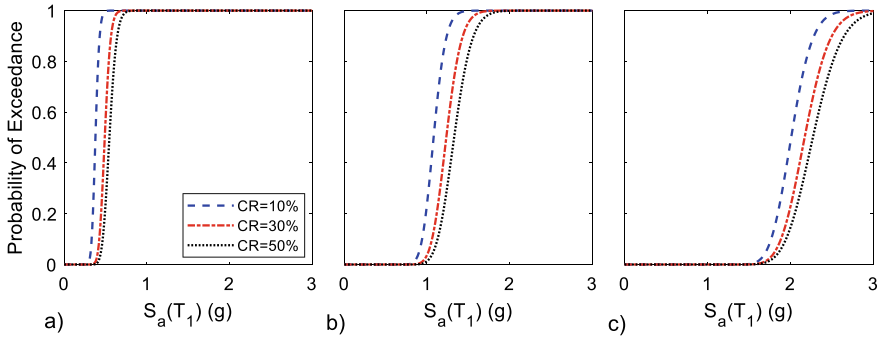
**Fig. 8** Equivalent non-collapse fragility curves: **a** IO, **b** LS, and **c** CP

indices. As can be seen from the figure, collapse is achieved at higher $S_a(T_1)$ value for systems with higher CR values. Accordingly, the collapse fragility curves for the case with CR values 10, 30, and 50% are developed (Fig. 10). As can be seen from the figure, CLT-CW systems with higher CR values are less vulnerable compared with those of lower CR values. It can also be noticed that the dispersion of the spectral acceleration at collapse state (MaxISDR = 5%) is greater than the spectral acceleration values at the other limit state capacities (e.g., IO). The discussion also holds true for systems with CR = 20% and 40%, in which their non-collapse and collapse fragility curves lie between the corresponding systems, 10% and 30%, and 30% and 50%, respectively [33, 36].
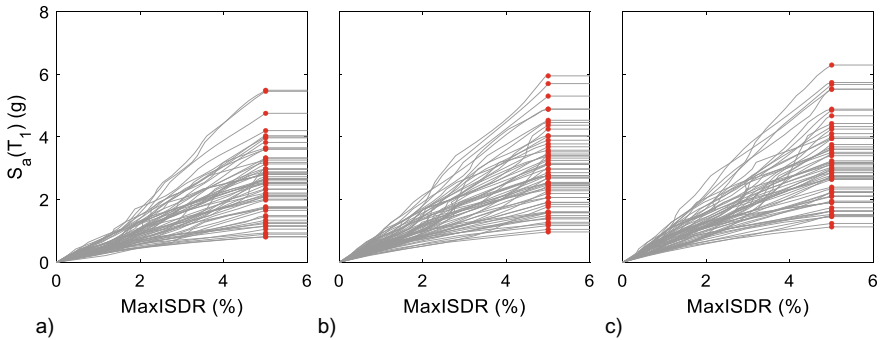


**Fig. 9** IDA curves for CR = **a** 10%, **b** 30%, and **c** 50%

**Fig. 10** Collapse fragility
curves
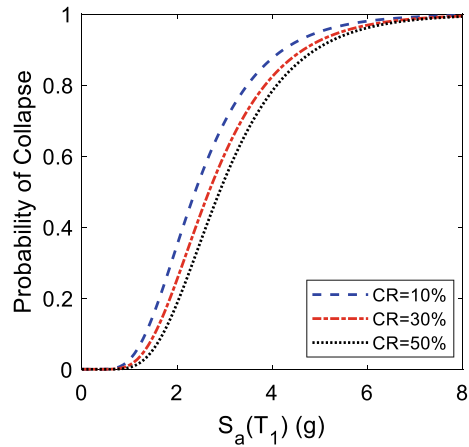


# 6   Conclusion

As buildings are built taller and slender, the provision of seismic and wind resistance
becomes a critical design consideration. Design consideration such as selection of an
appropriate structural material and provision of an innovative lateral load resisting
system are important to achieve a resilience structural system. Currently, the desire
for a sustainable material has reignited the interest in timber-based construction.
Even though this timber-based construction is becoming common for residential and
low-rise apartment buildings, new innovative building system may offer better oppor-
tunities as code revisions allow for increasing heights in timber construction. One
possible innovative and readily available structural system, proposed by Tesfamariam
et al. [32], is cross-laminated timber coupled-wall (CLT-CW) systems. The proposed
system comprises CLT balloon shear-walls, BRB hold-downs, and coupling beams.
As an extension to the study, in this paper, a multi-dimensional probabilistic seismic
vulnerability assessment is carried out on a 10-story CLT-CW system, consid-
ering five coupling ratio (CR) values 10% to 50%. Incremental dynamic analyses
(IDA) are performed in OpenSees using suitable set of 30 (bi-directional) ground
motion records that reflect the seismicity of Vancouver, BC—Canada. Two damage
indices (MaxISDR and ResISDR) and three limit state surfaces (linear, circular, and
square) are considered to compute the fragility curves at three different performance
limit state levels, namely: immediate occupancy (IO), life safety (LS), and collapse
prevention (CP). From this study, the following conclusions can be drawn:

- For the given system, the non-collapse fragility curves showed that the circular
  and square limit state function yields the same result and as expected, the linear
  limit state function gives a critical fragility curve. The MaxISDR damage index
  is found to govern the fragility curve with a marginal impact from the ResISDR.
  Consequently, the square limit state function coincides with the fragility curve
  developed considering the MaxISDR only. Nonetheless, the use of the 3D model

yields a critical fragility curve (especially for the LS and CP limit states) due to the fact that ResISDR has a contribution on the overall vulnerability of the system at the linear limit state function. Because timber structures are prone to residual deformations due to the slip in connections and may contribute to the global performance of the system, 3D model can give a better result.

- As the IDA passes from IO to CP, there is a larger part of the limit state surface intersected by the IDA curves, leading to a larger dispersion of the response in the nonlinear response zone of the system. Consequently, LS and CP fragility curves exhibit larger standard deviation. However, in the case of IO, where there is a moderate earthquake intensity and system's response is almost linear, the fragility curve has a smaller standard deviation.

- The equivalent fragility curve, the median curve of the fragility curves of the three considered limit state functions, showed that CLT-CW systems with higher CR value exhibit better seismic performance, with lower PE under a given hazard level, than those with lower CR values. This contributes to the fact that systems with higher CR values have greater coupling beam strength and higher reduction in the seismic demand of the individual walls. The relative difference in the seismic performance of the systems is more pronounced for the LS and CP limit states, where the systems exhibit nonlinearity.

- The vulnerability assessment of the system is extended to the collapse limit state. From the analyses, it is shown that CLT-CW systems with higher CR values are less vulnerable compared with those of lower CR values. Moreover, it is found that the dispersion of the spectral acceleration at collapse state is greater than the spectral acceleration values at the other limit state capacities.

In summary, it can be concluded that the structural behavior of the CLT-CW system is enhanced by providing coupling beams with higher shear strengths. This study, however, has some limitations. The CLT to hold-down and CLT to coupling beams connections are modeled as rigid connections. Moreover, the CLT shear-walls are modeled as single walls. The stated limitation warrants further investigation and potentially, the analyses can also be extended for three wall systems and different coupling beam shear force profiles.

# References

1. Ali MM, Moon KS (2018) Advances in structural systems for tall buildings: emerging developments for contemporary urban giants. Buildings 8(8):104–138
2. Baker JW (2011) Conditional mean spectrum: tool for ground-motion selection. J Struct Eng 137(3):322–331

3. Baker JW (2015) Efficient analytical fragility function fitting using dynamic structural analysis. Earthq Spectra 31(1):579–599

4. Brandner R, Flatscher G, Ringhofer A, Schickhofer G, Thiel A (2016) Cross laminated timber (CLT): overview and development. Euro J Wood Prod 74(3):331–351

5. Canadian Standards Association (CSA) (2016) Standard CSA 086-14: engineering design in wood (supplement). Canadian Standards Association, Mississauga, Canada

6. Casagrande D, Doudak G, Mauro L, Polastri A (2018) Analytical approach to establishing the elastic behavior of multipanel CLT shear walls subjected to lateral loads. J Struct Eng 144(2):04017193

7. Chen Z, Popovski M (2020) Mechanics-based analytical models for balloon-type cross-laminated timber (CLT) shear walls under lateral loads. Eng Struct 208:109916

8. De Risi R, Goda K, Tesfamariam S (2019) Multi-dimensional damage measure for seismic reliability analysis. Struct Saf 78:1–11

9. Demirci C, Málaga-Chuquitaype C, Macorini L (2018) Seismic drift demands in multi-storey cross-laminated timber buildings. Earthquake Eng Struct Dynam 47(4):1014–1031

10. DeVall RH (2003) Background information for some of the proposed earthquake design provisions for the 2005 edition of the National Building Code of Canada. Can J Civ Eng 30(2):279–286

11. El-Tawil S, Harries KA, Fortney PJ, Shahrooz BM, Kurama Y (2010) Seismic design of hybrid coupled wall systems: state of the art. J Struct Eng 136(7):755–769

12. Federal Emergency Management Agency (FEMA) (2012) Seismic performance assessment of buildings: vol. 1-methodology, FEMA P-58-1. Federal Emergency Management Agency, Washington, DC

13. Fortney PJ, Shahrooz BM, Rassati GA (2007) Large-scale testing of a replaceable "fuse" steel coupling beam. J Struct Eng 133(12):1801–1807

14. Goda K (2019) Nationwide earthquake risk model for wood-frame houses in Canada. Front Built Environ 5:128

15. Izzi M, Casagrande D, Bezzi S, Pasca D, Follesa M, Tomasi R (2018) Seismic behaviour of cross-laminated timber structures: a state-of-the-art review. Eng Struct 170:42–52

16. Ji X, Liu D, Hutt CM (2018) Seismic performance evaluation of a high-rise building with novel hybrid coupled walls. Eng Struct 169:216–225

17. Lallement D, Kiremidjian A, Burton H (2015) Statistical procedures for developing earthquake damage fragility curves. Earthquake Eng Struct Dynam 44(9):1373–1389

18. McKenna F, Fenves GL, Scott MH (2000) Open system for earthquake engineering simulation (OpenSees). University of California, Berkeley, CA

19. Melchers RE, Beck AT (2018) Structural reliability analysis and prediction. Wiley

20. National Building Code of Canada (NBC) (2015) National building code of Canada 2015. National Research Council of Canada (NRCC), Ottawa, Canada

21. Pacchioli S, Pozza L, Trutalli D, Polastri A (2021) Earthquake-resistant CLT buildings stiffened with vertical steel ties. J Build Eng 40:102334

22. Pacific Earthquake Engineering Research Center (PEER) (2017) Guidelines for performance-based seismic design of tall buildings. Pacific Earthquake Engineering Research Center, University of California, Berkeley (PEER Report 2017/06)

23. Pei S, Lenon C, Kingsley G, Deng P (2017) Seismic design of cross-laminated timber platform buildings using a coupled shearwall concept. J Archit Eng 23(3):06017001

24. Polastri A, Izzi M, Pozza L, Loss C, Smith I (2019) Seismic analysis of multi-storey timber buildings braced with a CLT core and perimeter shear-walls. Bull Earthq Eng 17(2):1009–1028

25. Powell GH (2010) Modeling for structural analysis: behavior and basics. Computers and Structures

26. Shen Q, Kurama YC, Weldon BD (2006) Seismic design and analytical modeling of posttensioned hybrid coupled wall subassemblages. J Struct Eng 132(7):1030–1040

27. Smith BS, Coull A (1991) Tall building structures: analysis and design, vol 5. Wiley, New York

28. Smith I, Frangi A (2014) Use of timber in tall multi-storey buildings. International Association for Bridge and Structural Engineering (IABSE)

29. Stepinac M, Šušteršič I, Gavrić I, Rajčić V (2020) Seismic design of timber buildings: Highlighted challenges and future trends. Appl Sci 10(4):1380
30. Tesfamariam S, Das S (2021) Resilient tall timber building design: damped-outrigger system. UBC Faculty Research and Publications. https://doi.org/10.14288/1.0403816
31. Tesfamariam S, Skandalos K, Goda K, Bezabeh MA, Bitsuamlak G, Popovski M (2021) Quantifying the ductility-related force modification factor for 10-story timber-RC hybrid building using FEMA P695 procedure and considering the 2015 NBC seismic hazard. J Struct Eng 147(5):4021052
32. Tesfamariam S, Skandalos K, Teweldebrhan BT (2021) Design of tall coupled-wall timber building: energy dissipating coupling beams. UBC Faculty Research and Publications. https://doi.org/10.14288/1.0403817
33. Teweldebrhan BT, Tesfamariam S (2022) Performance-based design of tall-coupled cross-laminated timber wall building. Earthquake Eng Struct Dynam 51(7):1677–1696. https://doi.org/10.1002/eqe.3633
34. Tesfamariam S, Teweldebrhan BT (2023) Seismic design of tall timber building with dual CLT-shear wall and glulam moment resisting frame systems. UBC Faculty Research and Publications. https://doi.org/10.14288/1.0431446
35. Teweldebrhan BT, Goda K, De Risi R, Tesfamariam S (2023) Multi-variate seismic fragility assessment of CLT coupled wall systems. Earthq Spectra. https://doi.org/10.1177/87552930231190687
36. Teweldebrhan BT, Popovski M, McFadden JBW, Tesfamariam S (2022) Development of ductility-related modification factor for CLT-coupled wall buildings with replaceable shear link coupling beams. Can J Civ Eng 50(5):362–374. https://doi.org/10.1139/cjce-2022-0257
37. Vamvatsikos D, Cornell CA (2002) Incremental dynamic analysis. Earthquake Eng Struct Dynam 31(3):491–514
38. van de Lindt JW, Amini MO, Rammer D, Line P, Pei S, Popovski M (2020) Seismic performance factors for cross-laminated timber shear wall systems in the United States. J Struct Eng 146(9):4020172
39. Wilson AW, Motter CJ, Phillips AR, Dolan JD (2020) Seismic response of post-tensioned cross-laminated timber rocking wall buildings. J Struct Eng 146(7):4020123
40. You T, Teweldebrhan BT, Wang W, Tesfamariam S (2023) Seismic loss and resilience assessment of tall-coupled cross-laminated timber wall building. Earthq Spectra 39(2):727–747. https://doi.org/10.1177/87552930231152512

# Structural Layout Optimization of Tall Buildings Against Wind Load

**Magdy Alanani and Ahmed Elshaer**

**Abstract** Nowadays, tall buildings are playing an important role in fulfilling the increasing demand for housing in urban cities. The design process of tall buildings is quite complex, and it requires continuous collaboration between different engineering fields and architects to satisfy the target functionality at a suitable cost. Since tall buildings are sensitive to lateral loads, a change in their layout, size, or shape will affect their cost and behaviour. In this paper, a case study for topology optimization is presented to find the optimal lateral resisting system layout against dynamic wind load for tall buildings, by altering the configuration of shear wall segments. First, an automated finite element (FE) model is adopted to assess the structural performance against static wind loads provided by the National Building Code of Canada. These models are integrated with a genetic algorithm, in order to identify the optimal configuration of the structural system. A comparison is held between dynamic time history wind loads and equivalent static wind loads to investigate the effect of including dynamic loads within the optimization framework. This study demonstrates the potential capability of topology optimization in tall buildings, which can increase the wind performance of the tall building, while reducing the overall cost of the structure within predefined architectural and structural constraints.

**Keywords** Structural optimization · Topology optimization · Tall buildings · Wind load · Genetic algorithm · Neural networks · CFD · Shear walls

## 1 Introduction

The number of climate-related natural disasters increased in the last three decades, especially extreme wind events resulting from climate change [15]. These changes require an increase in the wind resilience of residential buildings, which increases the

M. Alanani (✉) · A. Elshaer
Department Civil Engineering, Lakehead University, Thunder Bay, ON, Canada
e-mail: malanani@lakeheadu.ca

cost of construction and leads to further increases in the cost of housing. Tall buildings, with number of storeys more than 10 [14], can be considered a vital component in modern urban cities. This type of buildings is sensitive to dynamic loads like wind events. The design of those buildings relies on their lateral load resisting system (LLRS) that supports the building and composes its stiffness. This design process starts with an initial proposal for the location and orientation of the main LLRS. Then, it goes through numerous iterations to reduce the cost of these systems and increase their efficiency. However, it never guarantees that the final product of this process is the optimal solution. With these current design practices, the construction industry becomes responsible for almost 40% of global energy-related carbon emissions [17]. Consequently, structural optimization becomes a crucial objective for futuristic buildings. Structural topology optimization (STO) is one of the aspects addressing the problem of structural optimization. STO can be defined as finding the best distribution of material within a design domain [4]. In the last few decades, STO has been introduced to tall building designs, especially in the conceptual phase of the design process [3]. For tall buildings, STO is assessing mostly the LLRS system layout. Most of the previous research focused on tackling the vertical layout of the structure. For instance, [16] adopted a continuous approach in using an experimented pattern gradation with topology optimization, and it achieved a good balance between aesthetics and structural requirements as shown in Fig. 1, while the discrete approach using modified pattern search was used by [2] to find optimal bracing system design for tall buildings. Some research work was concerned about the LLRS horizontal layout optimization by altering the location and orientation of LLRS elements in the plan layout. For example, a computational method was developed by [18] to find the optimal shear wall location within an architectural layout with more flexible shape formations. The aforementioned research simplified the lateral load behaviour into equivalent static loads. However, lateral loads have stochastic dynamic behaviours that affect the structural vibrational modes. Thus, some researches started to consider the dynamic nature of lateral loads. For instance, [5] used Monte Carlo simulations to develop a performance-based topology optimization framework for tall buildings. This framework relies on an approximate static sub problem for the 2D vertical layout of the bracing system. [11] developed this framework to consider 3D performance-based topology optimization problems using dynamic wind loads extracted from boundary layer wind tunnel tests. [9] used the equation of motion within the topology optimization algorithm against dynamic wind loads correlated to known stationary wind power spectral densities. Most of this research focussed on the vertical layout of the LLRS. However, a limited contribution was found to consider the dynamic wind load for the horizontal layout of the LLRS.

Accordingly, this work aims to tackle the topology optimization of the horizontal layout of LLRS of tall buildings. An optimization framework is developed for LLRS layout within tall buildings against gravity and wind loads based on [13]. A surrogate model is built using artificial neural networks (ANN), which is able to estimate the structural response of structures after being trained by results generated by the finite element analysis. This model is coupled with a genetic algorithm to identify the optimum layout of shear walls within predefined architectural constraints. Finally,

**Fig. 1** Topology
optimization continuous
approach for tall buildings
[16]
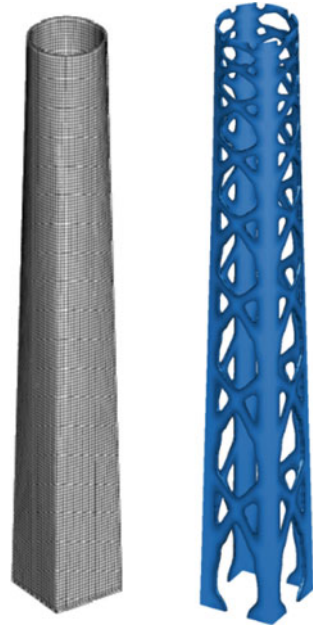
the response of a tall building was assessed using both the equivalent static method
and time history method to highlight the accuracy achieved through the latter method.

## 2 Structural Optimization Framework

The main purpose of the structural optimization framework (SOF) proposed in this
study is to increase the efficiency of the LLRS used, within our predefined layout
to enhance the structure wind performance without changing the amount of mate-
rials used. As shown in Fig. 2, a flowchart represents the procedure of structural
optimization. The procedure starts with defining the optimization problem objective
function, which is minimizing the maximum interstorey drift in both $X$ and $Y$ direc-
tions against wind and gravity loads for tall buildings. The finite element method
(FEM) is used for modelling and analyzing the structure under the selected load
cases using ETABS [7]. In this study, the optimization problem was tackled through
a stochastic approach which is a genetic algorithm (GA). GA relies on numerous eval-
uations of the objective function through altering design variables till an optimum
value is reached. In this case study, the design variables are identified as a discrete
binary value for all possible locations of shear walls based on a predefined domain.
The execution of the evaluation function through FEM is computationally costly.
Consequently, a surrogate model will be used to estimate the structural response of
tall buildings after being trained with a database of building alternatives with their
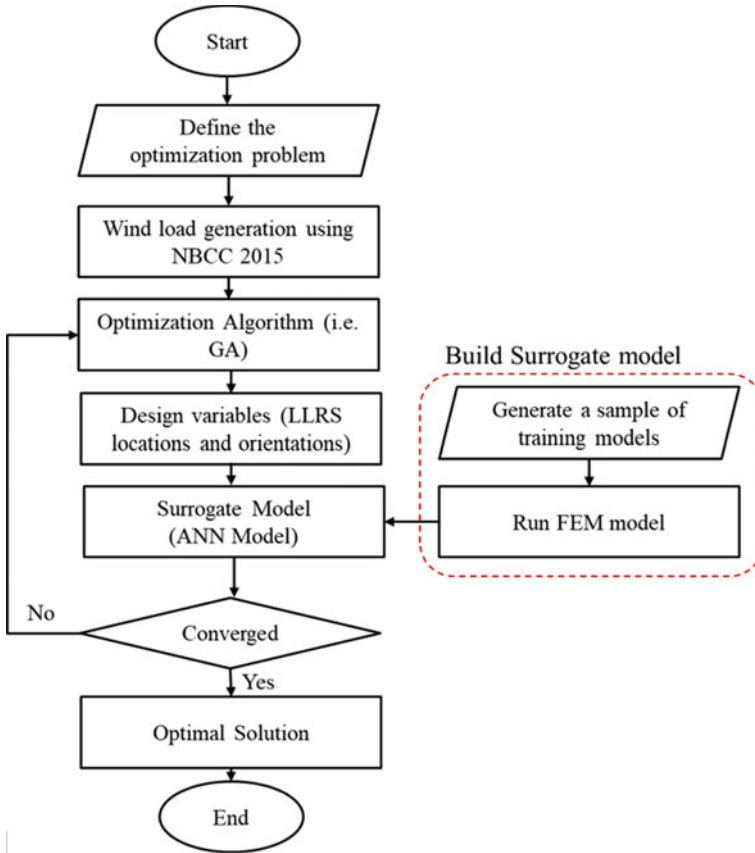
**Fig. 2** Structural optimization framework flowchart

corresponding performances. The surrogate model used in the SOF is an artificial neural network (ANN). In order to build this surrogate model, a group of random training models was prepared using FEM in order to train the ANN for interstorey drift evaluation.

## 3 Case Study

In this study, a multistorey residential building of 20 floors, with a storey height of 3.5 m, is adopted, which follows the structure described in [1]. A single symmetric layout of rectangular-shaped flat slabs with dimensions of 24.75 m × 18.75 m is used. A superimposed dead load of 5 kN/m$^2$ and a live load of 1.9 kN/m$^2$ are applied to all slabs. The layout is designed according to the Canadian Standards Association (CSA) 23.3-14 [6] using concrete of $f_c' = 35$ MPa and steel reinforcement ASTM992

of grade 50. The ultimate limit state and serviceability limit load combinations are used for designing structural elements. The selected building is designed to resist a mean-hourly wind velocity pressure, $q$, of 0.39 kPa, importance factor, $I_w$, of 1.0, and topographic factor, $C_t$ of 1.0. The terrain is considered open terrain with no topology effect. An architectural layout is proposed for two flats per storey, as shown in Fig. 3a. Based on the proposed architectural layout, possible locations for shear walls are identified to fulfil architectural objectives as illustrated in Fig. 3b. A preprocessing stage is implemented to prepare the optimization problem that will be described in detail in the following sections. The blue lines in the below figure are considered the domain for shear walls. To identify the length and the shape of shear walls, a discretization of this domain is performed based on a rectangular mesh of predefined base size which is 1.0 m. As a result of this process, the domain will be divided into 170 segments of shear walls, each of 1.0 m. In this study, 45 shear wall segments will be selected for the optimization problem. For each model, different locations of columns will be identified to avoid overlapping between shear wall segments and columns. Each shear wall segment is of 1000 mm length and 300 mm thickness, as illustrated in Fig. 4b. Each floor is supported by a certain number of columns of 750 × 750 mm cross-section dimensions and 2.5% steel reinforcement, as shown in Fig. 4c. In order to assess the effect of shear walls' location alteration around the plan, all scenarios will have the same quantity of materials by maintaining the predefined reinforced concrete dimensions and steel reinforcement ratios. Also, the same number of columns, shear walls, reinforcement bars, and slabs are maintained.
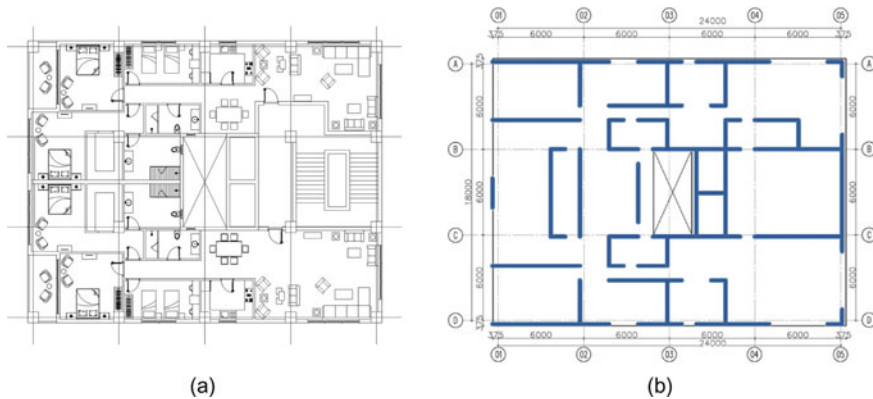


**Fig. 3** **a** Architectural plan view, **b** Possible shear wall locations
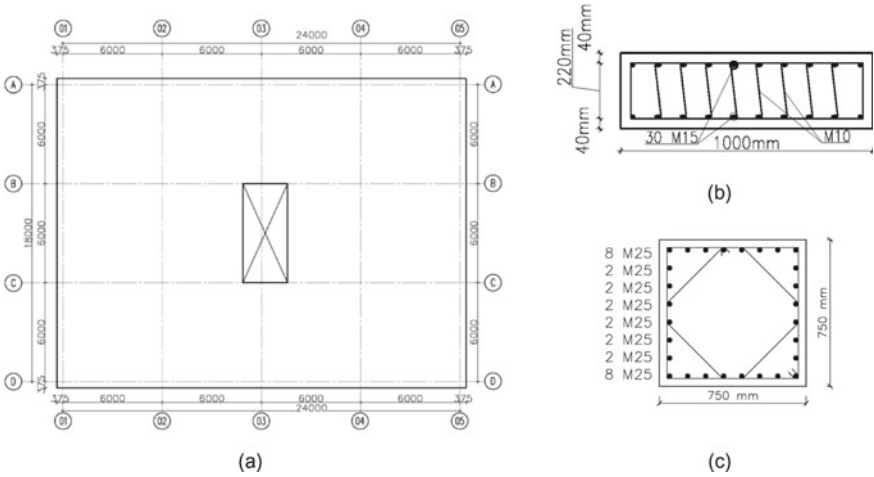
**Fig. 4** **a** Benchmark plan layout, concrete dimensions, and reinforcement detailing for cross-sections of **b** Shear wall segment and **c** Column

## 4 Validation

Since this study will be a first step in considering dynamic wind load and correlating it to the NBCC through optimization framework, previous studies should be considered for validating the computational fluid dynamic (CFD) model and the FEM model.

### 4.1 Computational Fluid Dynamics Model

Regarding the CFD model, a well-established standard tall building is adopted in the validation process, known as the Commonwealth Advisory Aeronautical Research Council (CAARC) building [12]. Various boundary layer wind tunnel (BLWT) tests and CFD simulations studied that building. In order to validate our model, the mean pressure coefficient ($C_p$ mean) and root mean square of the pressure coefficient (RMS $C_p$) will be compared with two main BLWT tests on the CAARC building held in Monash University and the National Physics Laboratory (NPL). Large eddy simulation (LES) is conducted for a scaled model of the CAARC building similar to the BLWT. Based on [8] study, the time scale and length scale are 1:100 and 1:400, respectively. The building and computational domain full-scale dimensions are provided in Table 1. As shown in Fig. 5, three zones are used for grid discretization with different base mesh sizes: zone 1, zone 2, and zone 3 grid sizes are H/5, H/10 and H/25, respectively, producing a total number of ~ 1,730,000 cells, as shown in Fig. 6. In addition, 10 prism layers are used around wall regions with a stretching factor of 1.30. In order to generate a turbulent inflow, the consistent discrete random

flow generation (CDRFG) technique is utilized with a mean wind speed of 10 m/s at the building's height. Turbulent intensity, turbulence length scale, and velocity profile regression coefficients are used as per [8]. For representing the wind power spectral density (PSD), a range of frequencies is utilized from 1.0 to 3500 Hz. Velocity streamlines in Fig. 7 show a very reasonable behaviour with velocity magnitude similar to what is conducted by [8] study. As shown in Fig. 8, $C_{p\,mean}$ and $C_{p\,RMS}$ are compared with Monash University and NPL results, and they showed a good agreement with a maximum variation of less than 6% in both parameters.

Based on the previous results, this computational domain with wind flow properties proved the validity to be used in future investigations of tall buildings. In a further publication, in this case study tall building will be inserted into this computational domain to extract wind load time histories on each floor. Afterwards, those

**Table 1** Building and computational domain dimensions

|          | Length ($X$-direction) | Width ($Y$-direction)     | Height ($Z$-diection)       |
|----------|------------------------|---------------------------|-----------------------------|
| Building | 30.5                   | 45.7                      | 182.5                       |
| Zone 1   | 20 H                   | Wind tunnel width (2.1 m) | Wind tunnel height (2.6 m)  |
| Zone 2   | 15 H                   | 2.4 H                     | 2.25 H                      |
| Zone 3   | 12 H                   | 0.8 H                     | 1.75 H                      |
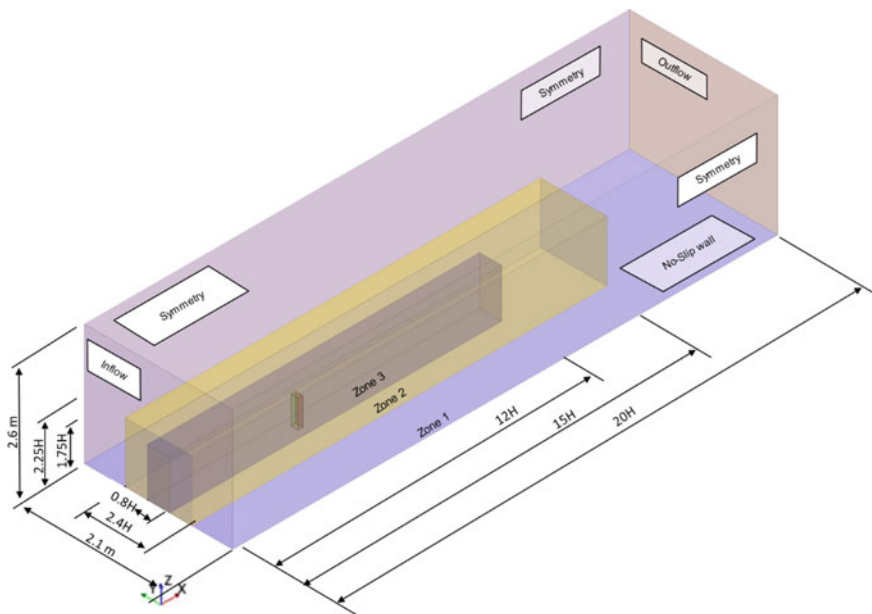


**Fig. 5** Computational domain details and boundary conditions
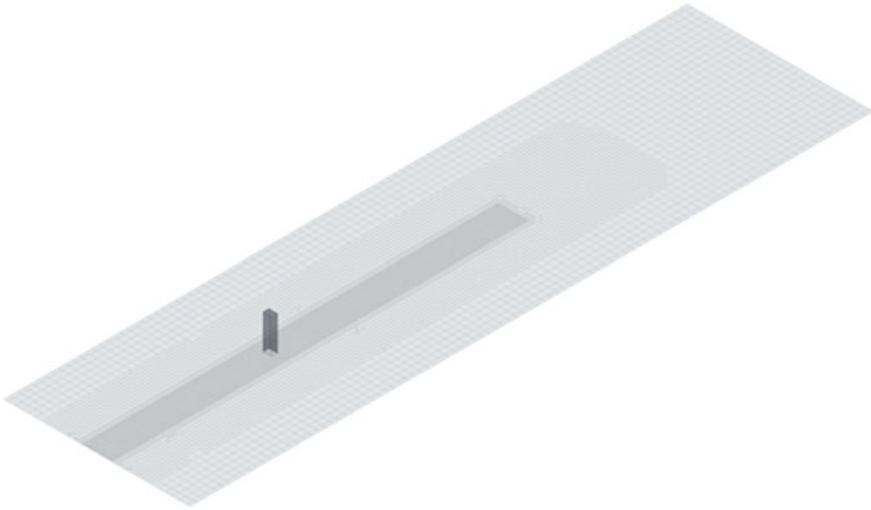
**Fig. 6** Grid resolution for CFD computational domain
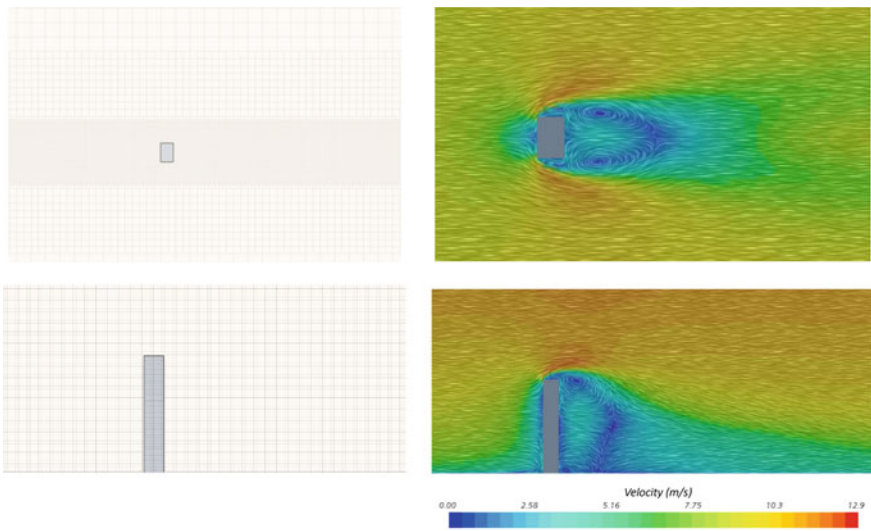


**Fig. 7** Mean velocity magnitude with flow streamlines and corresponding grid resolution

time histories will be applied to the FEM model to evaluate the wind performance of the structure.
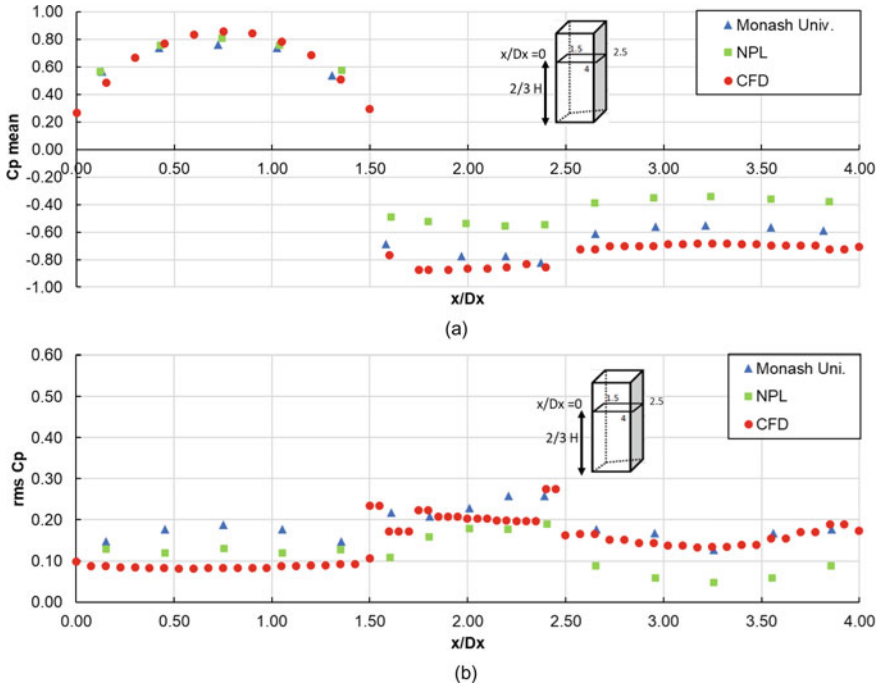
**Fig. 8** **a** $C_p$ mean, **b** RMS $C_p$ distribution over the horizontal section of the building at 2/3 H against BLWT tests' results

## 4.2 Finite Element Method Model

In order to validate the FEM adopted in this study, CAARC building was used as a benchmark to apply the structure topology optimization on this case study tall building. Building geometry consists of plan dimensions of 30 m × 45 m with an overall height of 180 m. The building consisted of 45 storeys and was made up of 10 bays × 15 bays steel frame with a storey height of 4 m and a bay width of 3 m as shown in Fig. 9. The initial member sizes considered for this building are summarized in Table 2 as adopted in [10]. The ground supports are considered fixed-end support, giving the structure a rigid floor connection. The structure's natural frequency is 0.15 Hz, with a damping ratio of 2%. Steel has a density of 7850 kg/m³, Young's Modulus of 200,000 MPa, and Poison's ratio of 0.25. As shown in Fig. 10, a comparison between the validation model and the [10] model in both deflection and interstorey drift shows a significant agreement between both models.

**Fig. 9** Framework of the 45
storey CAARC structure
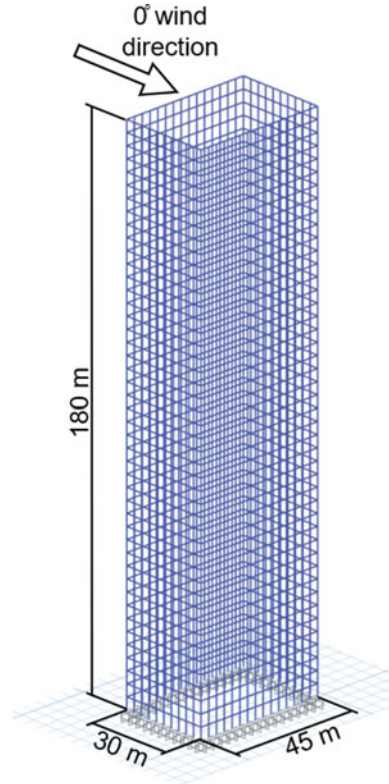


**Table 2** Initial member sizes
for the CAARC building
framework

| Floor zone | Colum | Beam |
| --- | --- | --- |
| 1–9 | W14 × 550 | W30 × 357 |
| 10–18 | W14 × 500 | W30 × 326 |
| 19–27 | W14 × 370 | W30 × 292 |
| 28–36 | W14 × 257 | W30 × 261 |
| 37–45 | W14 × 159 | W30 × 211 |

## 5   Surrogate Model

A surrogate model can be defined as an estimation model for computationally compli-
cated and costly simulations. In this study, FEM analysis through ETABS could take
between a couple of minutes to 30 min. In order to evaluate the objective function
through real-time simulation, this will be very time-consuming. ANN is used in this
study as a surrogate model. ANN is a regression model that consists of inputs, hidden
layers, and outputs. The quality of the neural network outputs (objective function)
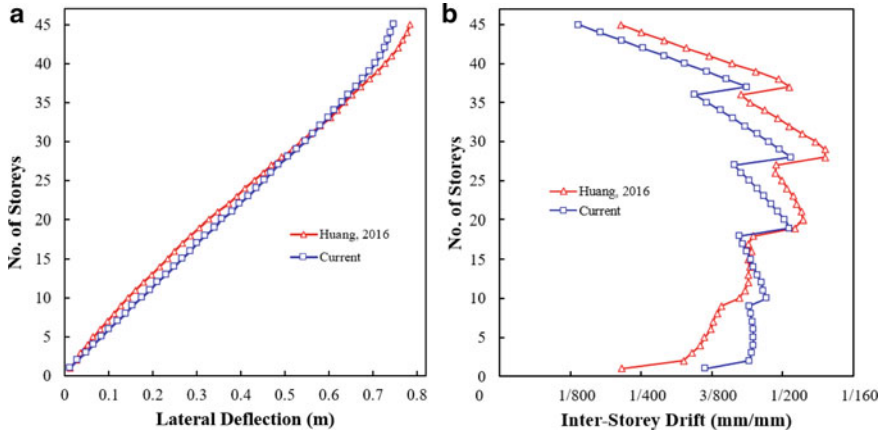
**Fig. 10** **a** Maximum top deflection and **b** Maximum interstorey drift in the along-wind direction

relies on the training process effectiveness, through various training sample models that can cover most of the search space required in the optimization problem.

In this study, a feedforward neural network is used to determine the interstorey drift in Y-direction as an output based on an input of shear wall locations. The input layer is one layer of size equal to 170 nodes that accepts binary values (i.e., 0 or 1). These nodes represent possible locations of shear wall segments. This ANN also consists of two hidden layers, one of 170 nodes and the other one of 20 nodes. It is recommended to use the first hidden layer size similar to or greater than the input layer size. Regarding the second hidden layer, the number of nodes is chosen based on the number of storeys within the tall structure. Both layers have a hyperbolic tangent sigmoid transfer function (Tansig) that transfers inputs into values belonging to [− 1 1]. The output layer size is 20 nodes, which equals the interstorey drift of each floor. This surrogate model represents the scenario of having 45 shear wall segments out of 170 possible locations. A total of 100 random configurations of the 45 shear wall segments out of the possible 170 segments are prepared using MATLAB code that automates the process of building models and extracting results on ETABS through the open application programming interface (OAPI). This code also generates columns' locations based on the predefined locations and avoids any overriding or intersections with the generated shear walls. After using 70% of the samples in training and 30% in testing and validation, the correlation coefficient between the FEM database and the ANN model is 92.66%, as shown in Fig. 11. As shown in Fig. 12, 95% of the samples produced an error of less than 4%, while 5% of the samples exceeded this ratio. All of the previously mentioned percentages support the adequacy of the ANN surrogate model in mapping complex relations between inputs and outputs.
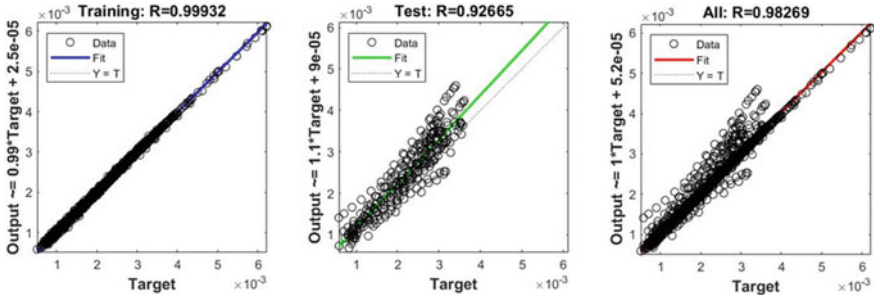
**Fig. 11** Regression plots for training and validation samples
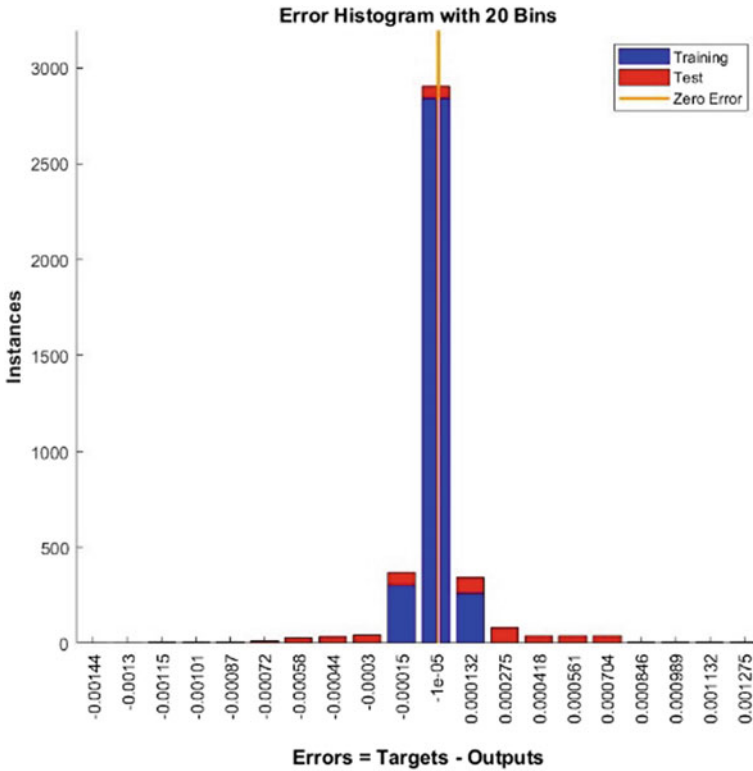


**Fig. 12** Error histogram for training and validation

## 6 Optimization Problem and Results

Two optimization problems are conducted in this study, which are the interstorey drift in $X$-direction and $Y$-direction. The following section will only describe the $Y$-direction as the $X$-direction will be similar but with different output and objective functions. The optimization problem can be mathematically modelled as shown in Eq. (1), where $S$ represents the shear wall segment's location, $\delta_{ix}$ represents the maximum interstorey drift in $X$-direction and, $\delta_{iy}$ represents the maximum interstorey drift in $Y$-direction. Both values should not exceed 0.2% based on the [13], $T$ is the total number of shear wall segments used which is 45, and $N$ is the total number of possible shear wall segments locations which is 170 locations in this study.

$$
\begin{aligned}
&\text{Find } S = (S_1, S_2, \ldots, S_N) \\
&\text{Minimize: } \delta_{iy} \\
&\text{Subjected to Sum } S = T, \delta_{ix} \,\&\, \delta_{iy} \leq 0.2\% \\
&\text{Where } S_i\{0, 1\}, i = (1, 2, \ldots, N)
\end{aligned} \tag{1}
$$

The genetic algorithm code is adopted where four different sizes of the initial population are chosen to check the adequate population sample. As shown in Fig. 13, a random configuration is selected for each population sample. The fitness curve is plotted in Fig. 14, and it can be concluded that a population size of 40 will be enough to converge to the most optimal configuration of shear wall segments to get the least interstorey drift in $X$-direction and $Y$-direction, which were found to be 0.27% and 0.32%, respectively. This framework managed to reduce the interstorey drift in both directions by ~ 30% compared with the initial configuration.

The GA code starts by generating a population of size 40; each sample consists of a random configuration of 45 shear wall segments within 170 possible locations. This is represented in the form of binary values for 170 variables for the optimization function. The optimization function used is the ANN model of interstorey drift in $X$-direction. Through generations and after evaluation of each objective value, mutations and crossover operators are applied based on the GA parameters mentioned in Table 3. The mutation is generated from a single parent by switching the order of identified variables, while crossover is done between two parents through exchanging parts of the configuration. The optimization procedure is repeated several times to avoid getting trapped in local minima. Two different layouts resulted from this optimization procedure, which are corresponding to the optimization of the interstorey drift in $X$-direction and $Y$-direction, as shown in Fig. 15.

In order to assure wind performance improvement through this framework, a 3D FEM analysis is conducted using the resulted optimal layout, as shown in Fig. 16. In this step, a comparison is held between the interstorey drift of the tall building due to dynamic loads and static loads. Dynamic loads are time histories of forces extracted from the CFD model for each floor using derived surfaces with monitors that record forces with respect to time, as illustrated in Fig. 17b. These forces are applied to
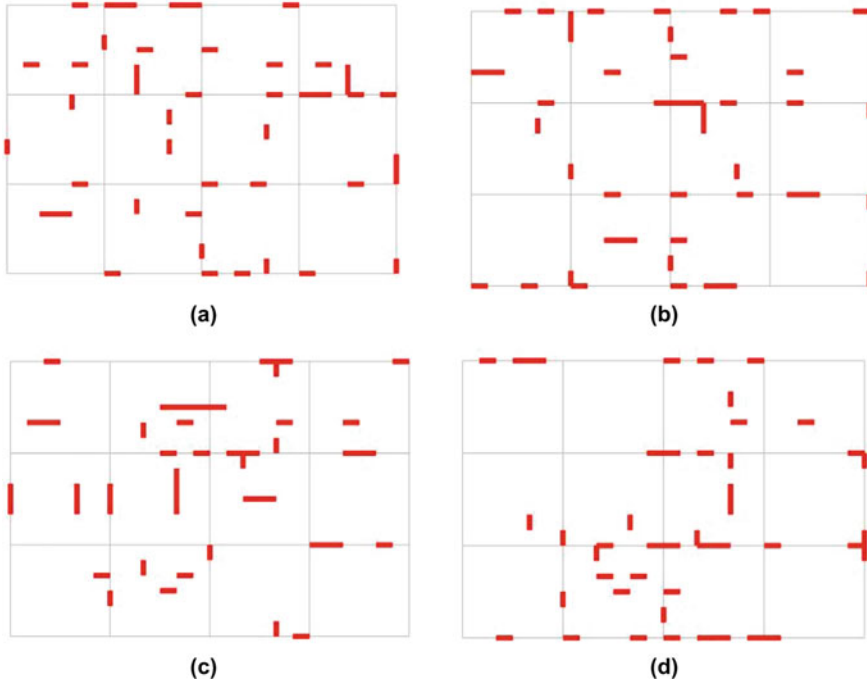
**Fig. 13** Different initial population for 45 shear walls segments: **a** 40 population samples, **b** 70 population samples, **c** 100 population samples, **d** 120 population samples

the FEM model as time history functions, as shown in Fig. 17, while equivalent static loads are applied based on [13]. To assure correlation between dynamic loads FEM model and static loads model, the mean-hourly wind velocity pressure, $q$. value is maintained at 0.74 kPa, based on the wind speed at the building's height in the CFD model, which is 33.98 m/s. Interstorey drift and displacement for both FEM models are presented in Fig. 18. It is noticed that the dynamic loads model shows lower responses with a difference of 42% in both parameters compared with the static loads model. Consequently, embedding dynamic loads within the optimization framework, instead of equivalent static loads, can provide a better representation of tall buildings' behaviour against wind loads.
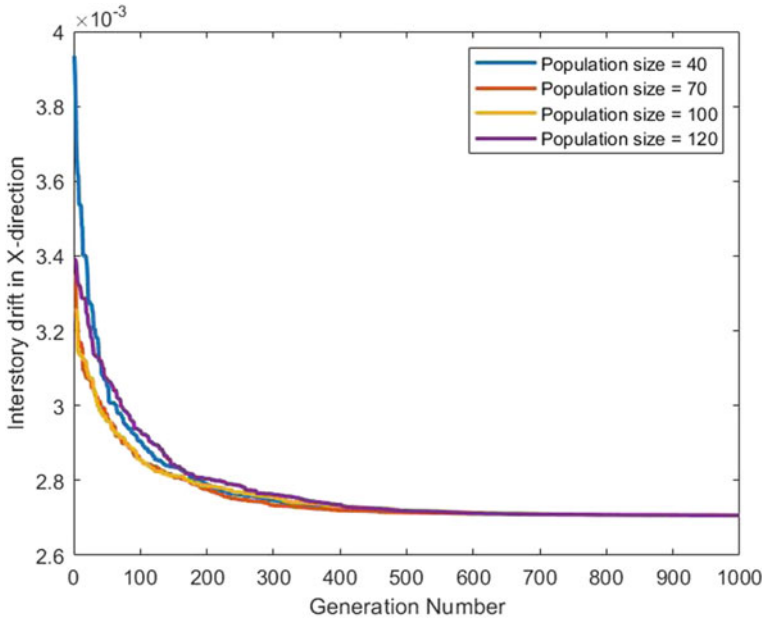
**Fig. 14** Fitness curve for interstorey drift in *X*-direction

**Table 3** Genetic algorithm parameters

| Number of variables | Population size | Number of generations | Number of times to apply mutation | Number of times to apply simple crossover |
|---|---|---|---|---|
| 170 | 40 | 1000 | 4 | 10 |

**Fig. 15** Optimal shear wall layout configuration
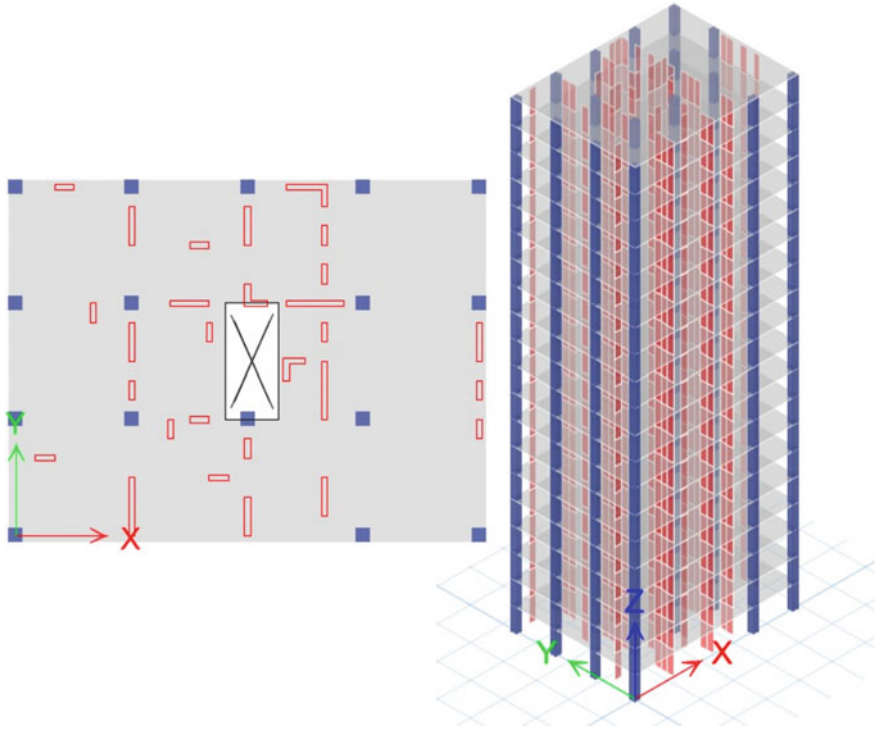
**Fig. 16** 3D FEM of resulted optimal layout in *Y*-direction
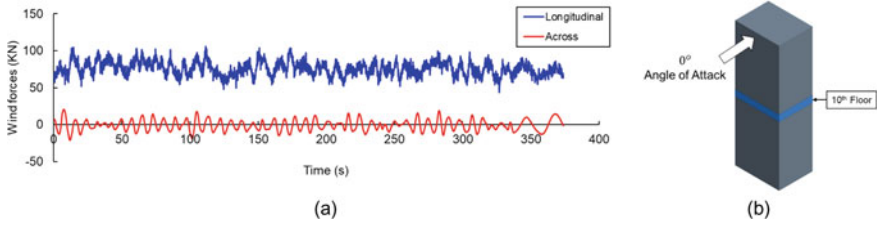


**Fig. 17** **a** Longitudinal and across-wind forces time history at 10th floor, **b** Highlighted derived surface for the 10th floor
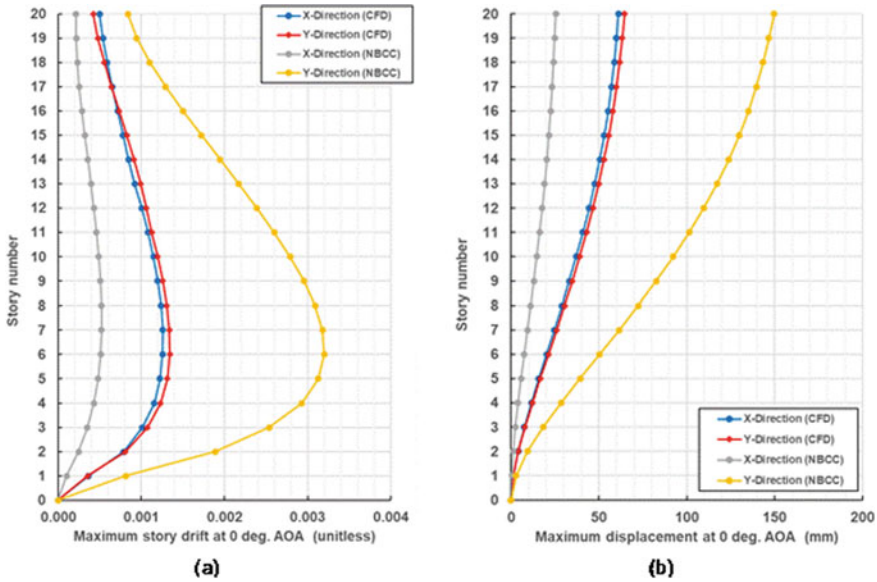
**Fig. 18** Comparison between dynamic and static wind loads **a** Interstorey drifts, **b** Lateral deflection

## 7 Conclusion

In this study, a structural optimization framework (SOF) is developed to enhance the wind performance of tall buildings by altering the location of shear wall segments. SOF is considered a combination of finite element method (FEM) analysis, artificial neural networks (ANN), genetic algorithm (GA), and computational fluid dynamics (CFD). The SOF relies on a training dataset prepared using the FEM analysis automated by an OAPI MATLAB code. This training dataset is used to build and train the surrogate model for the objective function, which is in the form of ANN in this study. In the current framework, the objective function is to minimize the interstorey drift without changing the number or the dimensions of the LLRS. A typical tall building is adopted as a case study to apply the STO and check its validity. By choosing 45 shear wall segments out of 170 possible shear wall segments, STO showed a noticeable capability to reduce the interstorey drift by 30% in both $X$ and $Y$ directions. It is also noted that this ANN model showed efficiency in capturing the complex behaviour of the tall building subjected to wind loads by a correlation coefficient of ~ 92%. The final output of the STO is validated by a FEM model to check the improvement of the wind performance. In addition, the FEM model subjected to dynamic wind loads resulting from CFD shows a significant reduction in interstorey drift and lateral deflection by almost 42%, which highlights the ability to improve the accuracy in evaluating the structural performance based on dynamic loads.

# References

1. Alanani M, Elshaer A (2021) Improving wind performance of structural systems of tall buildings using topology modifications. CSCE annual conference, 1–9
2. Baldock R, Shea K, Eley D (2005) Evolving optimized braced steel frameworks for tall buildings using modified pattern search. In: Proceedings of the 2005 ASCE international conference on computing in civil engineering, 631–642
3. Beghini A, Stromberg LL, Baker WF, Paulino GH, Mazurek A (2011) A new frontier in modern architecture: optimal structural topologies. Taller, longer, lighter-meeting growing demand with limited resources, 3–8
4. Bendsøe MP, Sigmund O (2004) Topology optimization. Topology Optimization, Springer, Berlin
5. Bobby S, Spence SMJ, Bernardini E, Kareem A (2014) Performance-based topology optimization for wind-excited tall buildings: a framework. Eng Struct 74:242–255
6. CSA (2019) Design of concrete structures. CSA Group
7. CSI (2018) ETABS. Computers and Structures, Inc.
8. Elshaer A, Aboshosha H, Bitsuamlak G, El Damatty A, Dagnew A (2016) LES evaluation of wind-induced responses for an isolated and a surrounded tall building. Eng Struct 115:179–195
9. Gomez F, Spencer BF, Carrion J (2021) Topology optimization of buildings subjected to stochastic wind loads. Probabil Eng Mechan 64:103127
10. Huang M (2017) High-rise buildings under multi-hazard environment. Springer, Singapore
11. Luo X, Suksuwan A, Spence SMJ, Kareem A (2017) Topology optimization and performance-based design of tall buildings: a spatial framework. In: Structures congress 2017, American Society of Civil Engineers, Reston, VA, 447–458
12. Melbourne WH (1980) Comparison of measurements on the CAARC standard tall building model in simulated model wind flows. J Wind Eng Ind Aerodyn 6(1–2):73–88
13. National Building Code of Canada (2015) Canadian commission on building and fire codes National Research Council of Canada
14. Council O (2003) Urban design guidelines for high rise buildings. Management 8(3):119–133
15. Reidmiller D, Avery C, Easterling D, Kunkel K, Lewis K (2018) Fourth national climate assessment: report-in-brief. US Global Change Research Program, Washington, D.C.
16. Stromberg LL, Beghini A, Baker WF, Paulino GH (2011) Application of layout and topology optimization using pattern gradation for the conceptual design of buildings. Struct Multidisc Optim 43(2):165–180
17. WGBC (2019) Embodied carbon call to action report. World Green Building Council
18. Zhang Y, Mueller C (2017) Shear wall layout optimization for conceptual design of tall buildings. Eng Struct 140:225–240

# Structural Fatigue Crack Localization Based on EMD and Sample Entropy

**Shihao Cui, Pooneh Maghoul, and Nan Wu**

**Abstract** During structural vibration, fatigue cracks, especially at their initial stage, introduce a repetitive crack open-close breathing-like phenomenon. Breathing cracks cause irregularities, bi-linearity, or perturbations in the vibration response of a structural system. Entropy can be used to quantify the irregularity or bi-linearity in those responses, and the crack position can be determined since on the two sides of the breathing crack, there is an apparent variation of entropy values. Here, we present a new breathing crack localization method based on a spatially distributed entropy approach coupled with the empirical mode decomposition (EMD). EMD is used as a pre-processing tool to extract the characteristics caused by breathing phenomenon in the vibration signal, and the reconstructed signal is used for entropy calculation. The location of the crack can be estimated by entropy values at different positions of the test structure. To verify the accuracy of the proposed method in localizing the breathing crack, the results were compared with a series of laboratory experiments in a beam. It is concluded that the proposed approach can be effectively used for breathing crack localization in a structural system.

**Keywords** Fatigue cracks · Entropy · Emprical mode decomposition · Breathing phenomenon

## 1 Introduction

Fatigue crack detection plays an important role in the field of structural health monitoring (SHM). The crack at its initial stage is closed and can undergo the open-to-close and close-to-open statuses alternatively during vibration. The breathing

S. Cui · P. Maghoul (✉)
Department of Civil, Geological and Mining Engineering, Polytechnique Montréal, Montréal, Canada
e-mail: Pooneh.Maghoul@polymtl.ca

N. Wu
Department of Mechanical Engineering, University of Manitoba, Winnipeg, Canada

crack can introduce irregularities, perturbations, disorder or bi-linearity into vibration responses.

There are different methods that have been used for crack identification. Some methods achieve crack identification by key features such as natural frequencies, modal shapes, modal curvatures, and so on [1–3]. However, those features are hard to be measured in real systems. Some signal processing methods are also used for crack identification. For example, wavelet transform (WT), empirical mode decomposition (EMD), and entropy have been used in SHM [4–7]. Recently, big data technology has also become popular in this regard. However, it is still hard to gain a large volume of data in some specific problems, and the application of artificial intelligence in practice is still limited [8, 9].

By quantifying the disorder or perturbations in a system, entropy can be used for crack identification. Yang et al. [10] firstly used entropy for open crack detection. Wimarshana et al. [7, 11–13] used entropy to detect the depth of breathing crack. In their work, WT is used to amplify the characteristics in the vibration signal caused by the breathing phenomenon before entropy calculation. Cui et al. [14, 15] used WT and entropy for crack localization. In this research, the entropy distribution on the structure is shown, and on the two sides of the crack, there is a clear variation in the entropy value. However, there are two disadvantages of WT as a signal pre-processing tool. The basis function should be determined, and the scale parameter of WT needs to be tuned ahead. It causes difficulties for the usage of WT in practice. There are different kinds of entropy methods, such as Shannon entropy, approximate entropy, sample entropy (SampEn), and fuzzy entropy [16–19]. In this work, SampEn is used for crack localization owing to its robustness in data length and noised data [13].

EMD can decompose a given signal into a series of waveforms defined as intrinsic mode functions (IMFs). As a signal processing method, EMD and its variants have been widely used for SHM. For example, Alejandro et al. [5] applied EMD and entropy to detect the corrosion severity in a truss structure. Rezaei and Taheri [20] used EMD to identify damages using only one sensor. The research using EMD and its variants in the field of SHM has been reviewed by Barbosh et al. [21]. As a signal processing or pre-processing tool, especially compared with WT, EMD has advantages: No basis function is needed, it is a self-adaptive method, and no parameters are needed to be selected ahead.

In light of the above, this research proposes a crack localization method based on spatially distributed entropy combined with EMD. EMD is used to decompose the vibration signal into different components. In order to extract characteristics caused by breathing crack, the IMF with the characteristics caused by the crack and the rest components are used to reconstruct the signal for post entropy calculation. The proposed method is validated on a cantilever beam with a pre-defined crack.

## 2   Methodology

The flowchart of the proposed method based on EMD and entropy is illustrated in Fig. 1. This method encompasses three steps. The first step is data acquisition. As Fig. 1a is shown, sensors or signal receivers are placed on different positions of the test structure. The second step is signal pre-processing based on EMD. During vibration, the breathing phenomenon, in which the crack experiences close-to-open and open-to-close states repeatedly, can result in irregularities or perturbations into the vibration signals. The EMD-based signal pre-processing method is used to extract the characteristics caused by the breathing phenomenon. Because breathing crack can induce super-harmonics into vibration signals. The crack's feature may be contained in the component of those super-harmonics. Here, we use the spectral center of gravity (FC) to select the IMFs containing the characteristics in the vibration signal. Those chosen IMFs are used to reconstruct the signal for entropy value calculation. As Fig. 1b shows, in this step, the signal collected at each position of the test structure is pre-processed by the EMD based method. The third step is entropy value calculation using the sample entropy. Each slice signal at a specific acquisition position is used for entropy calculation, and then, a curve of entropy values at different positions can be obtained. As Fig. 1c shows, by comparing the entropy value at different positions, on the two sides of the crack, there is a variation, so the location of the crack can be estimated. In Fig. 1c, there is a schematic diagram of the entropy value curve, where $L_c^*$ refers to the estimated location of the crack. The details of the theory of EMD-based signal pre-processing, SampEn, and the experimental setup are explained in the following sections.

### 2.1   EMD-Based Pre-processing Method

EMD is an approach that can decompose non-linear or non-stationary signals into several intrinsic mode functions IMFs without the requirement of any prior basis. IMF is defined as the function that satisfies the two criteria [22]. For a given time-series signal composed of $N$ samples, it is denoted by $x(n) = \{x(1), x(2), \ldots, x(N)\}$. The algorithm process of EMD is elaborated as follows:

1. All the local maxima and minima of the input original signal $x(n)$ can be marked.
2. The upper envelope $E_{\max}(n)$ and the lower envelope $E_{\min}(n)$ can be established by the local maxima and local minima.
3. The local mean based on upper and lower envelopes can be obtained as $m(n) = (E_{\max}(n) + E_{\min}(n))/2$.
4. The difference $d(n)$ between $x(n)$ and $m(n)$ is $d(n) = x(n) - m(n)$.
5. Judging if $d(n)$ satisfies the definition of IMF. If not, $d(n)$ is set as the input signal, and the algorithm returns to Step 1.
6. If $d(n)$ meets the convergence condition, $d(n)$ is recorded as an IMF, denoted by $\text{imf}^i(n)$, in which $i$ refers to the $i$th IMF.
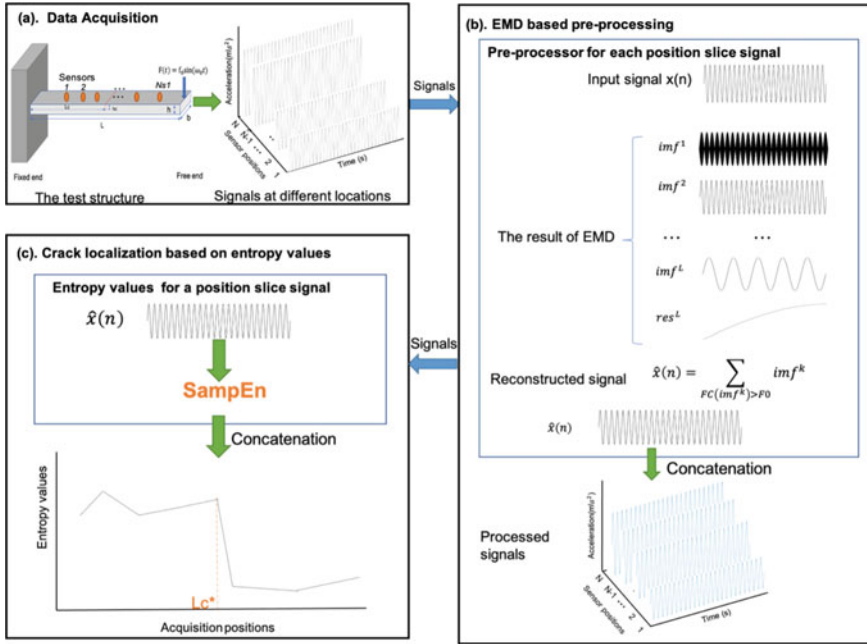
**Fig. 1** Flowchart of the proposed method. **a** Data acquisition. **b** EMD-based pre-processing. **c** entropy calculation for crack localization

7. The residue $\text{res}(n) = x(n) - \text{imf}^i(n)$. Judging whether $\text{res}(n)$ is a constant or monotonic function. If so, all the IMFs of the original signal $x(n)$, denoted by $\{\text{imf}^1, \text{imf}^2, \text{imf}^3, \ldots, \text{imf}^L\}$, and the final residue $\text{res}^L$, where $L$ refers to the number of IMFs, are output, and the algorithm is ended. If not, $\text{res}(n)$ is set as the input signal, and the algorithm returns to Step 1.

Therefore, for a given signal $x(n)$, the result of EMD can be expressed as Eq. (1). Among the decomposition result $\text{imf}(n) = \{\text{imf}^1(n), \text{imf}^2(n), \text{imf}^3(n), \ldots, \text{imf}^L(n)\}$, where $1 \leq i \leq L$, the frequency of $\text{imf}^i(n)$ decreases with regards to the mode number $i$. That means the first IMF $\text{imf}^1(n)$ of the result of EMD has the highest frequency among all the decomposition components.

$$x(n) = \sum_{i=1}^{L} \text{imf}^i(n) + \text{res}^L. \tag{1}$$

More details of EMD can be found in Barbosh et al. [21]. The result of the pre-processing $\hat{x}(n)$ is

$$\hat{x}(n) = \sum_{FC(\mathrm{imf}^k) > F_0} (\mathrm{imf}^k). \tag{2}$$

Here, $\mathrm{imf}^k$ is the $k$-th IMF, and $F_0$ is the excitation frequency (Hz).

## 2.2 *SampEn*

SampEn can be used as a tool to measure the disorder or irregularities in a time series. For a given time-series signal $S(n)$ including $N$ number of data points, it is denoted by $S(n) = \{S(1), S(2), \ldots, S(N)\}$. Its SampEn value can be calculated as follows. First, template vectors of length $m$ are denoted by

$$S(1) = \{S(1), S(2), \ldots, S(m)\}, S(2) = \{S(2), S(3), \ldots, S(m+1)\}, \ldots,$$
$$S(N - m + 1) = \{S(N - m + 1), S(N - m + 2), \ldots, S(N)\}.$$

Then, the statistics is made leading to

$$B_i^m(r) = \frac{\text{The number of } j \text{ such that } d[S_m(i), S_m(j)] \le r}{N - m - 1}, \tag{3}$$

$$B^m(r) = \frac{\sum_{i=1}^{N-m} B_i^m(r)}{N - m}, \tag{4}$$

where $1 \le j \le N - m$, $j \ne i$ and $d[S_m(i), S_m(j)]$ is the Chebyshev distance; $r$ is the pre-defined tolerance value; $r = k * \mathrm{SD}(S)$, and SD means the standard deviation. Then, similar to the second step, we can have

$$A_i^{m+1}(r) = \frac{\text{The number of } j \text{ such that } d\left[S_{m+1}(i), S_{m+1}(j)\right] \le r}{N - m - 1}, \tag{5}$$

$$A^{m+1}(r) = \frac{\sum_{i=1}^{N-m} A_i^{m+1}(r)}{N - m}. \tag{6}$$

Finally, $\mathrm{SampEn}(m, r, N) = -\ln\left[\frac{A^{m+1}(r)}{B^m(r)}\right]$.

The details of SampEn calculation can be found in the work [7]. According to the previous research, in SHM, the parameters of SampEn can be set as: $m = 2$ and $r = 0.2$.

346 S. Cui et al.

## *2.3 Experimental Setup*

In this work, a cantilever beam with a pre-defined crack is used to validate the proposed method for crack localization. The test beam is made by joining two identical aluminum 6063-T6 steel beam using the J-B weld glue. The schematic diagram of the cantilever beam is shown in Fig. 2. The relative crack location $RL_c$ is defined as the ratio of the crack location $L_c$ to the total length of the beam $L$. 19 accelerometers are evenly distributed along the beam length and the location of a sensor, denoted by $RL_s$ defined as the ratio of the sensor location, $L_s$, to $L$. The $RL_s$ of the accelerometers used in this case is from 5 to 95 with a spacing of 5. The excitation is $F(x_0, t) = f_0 \sin(\omega_0 t)$, where $f_0$ is the amplitude; $\omega_0$ is the excitation frequency; $t$ is time; $x_0$ is the position where the load applies, and here, the base motion is used for excitation. In this paper, two beams are tested; the depth of the crack is both $Rh_c = 50\%$, and the location of the crack $RL_c$ is 40% and 50%, respectively. The basic property parameters are shown in Table 1.

The experimental setup is shown in Fig. 3. The test beam is excited by a shaker (2100E11, Modal shop). The signal generator (33210A Waveform) is used to generate the sinusoidal excitation signal, and then, the excitation signal is magnified by the 2050E05 linear power amplifier. The accelerometer (352A24, PCB Piezotronics)
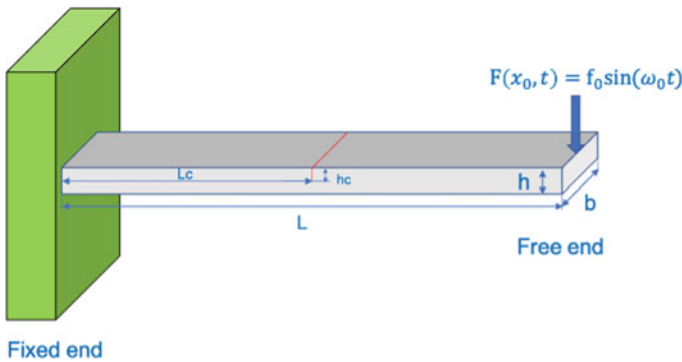


**Fig. 2** Schematic diagram of the cantilever beam

**Table 1** Basic parameters of the test beam

| Parameters (Unit) | Value |
|---|---|
| Length, $L$ (m) | 0.5 |
| Width, $b$ (m) | 0.0254 |
| Thickness, $h$ (m) | 0.00635 |
| Young's modulus, $E$ (GPA) | 68.3 |
| Density, $\rho$ (kg/m$^3$) | 2690 |
| The first natural frequency, $NF_1$ (Hz) | 21 |
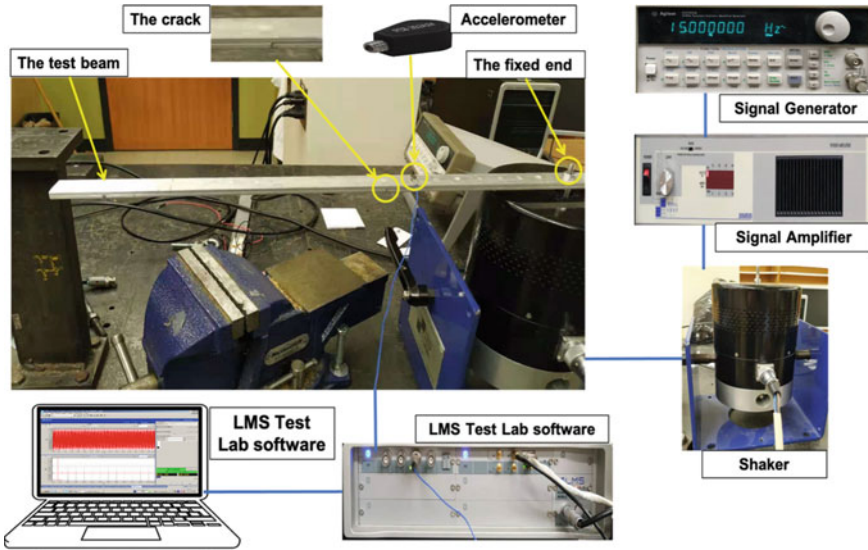
**Fig. 3** Experimental setup

is placed on the top surface for acceleration data collection. The LMS SCADAS mobile system (SCM05) is used to record the collected data acquisition. The excitation frequency can be selected from the values close to the first natural frequency which leads to a monotonic and non-symmetric deflection curve. Therefore, here, the excitation frequency is 15 Hz.

## 3 Result and Discussion

Figure 4 shows the result of EMD for a signal collected on a test beam, where the result of EMD, including IMFs and the residue, is transformed into the spetral dmoain using fast Fourier transform (FFT). From the spectra, it can be observed that the FC of the component of the first IMF is higher than the excitation frequency (15 Hz here), so it can be regarded as the component which contains the characteristics caused by the breathing crack. The components selected by the FC are used for the signal reconstruction.

Figure 5 compares entropy values at different $RL_s$ of the pre-processed signals, the removed components, and the original signals, in which pre-processed signals indicate signals processed by the EMD based pre-processing method, signals of the removed components indicate the components removed from the signal, and the original signal is the signal without processing. The entropy value NmEnt(%) is defined as follows:
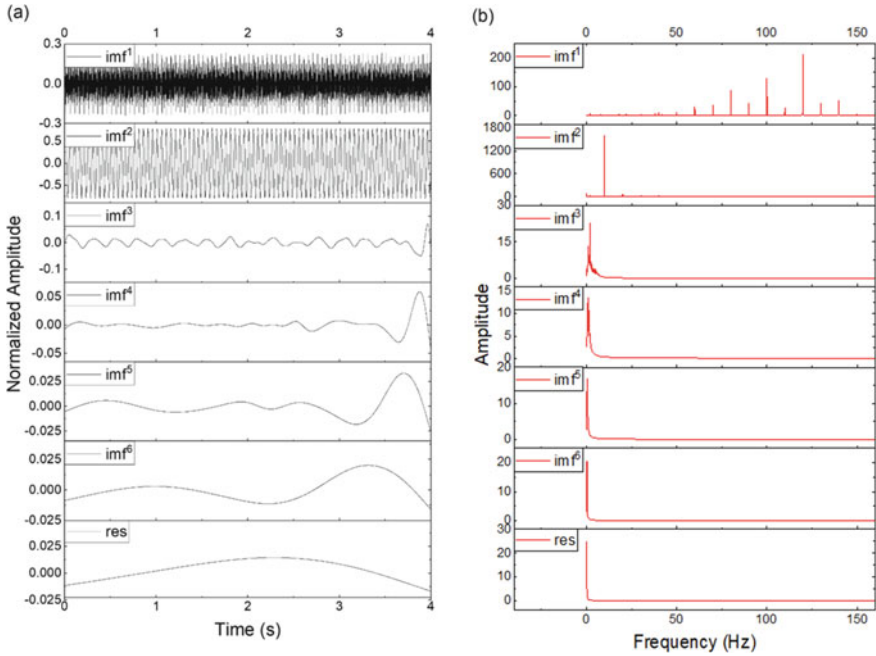
**Fig. 4** Result of EMD in time and frequency domains

$$\text{NmEnt}(\%) = \frac{\text{Ent} - \text{Ent}_{\min}}{\text{Ent}_{\max} - \text{Ent}_{\min}} * 100, \tag{7}$$

where Ent represents the entropy values at a certain position, and $\text{Ent}_{\max}$ and $\text{Ent}_{\min}$, respectively, represent the minimum and maximum value among all positions in the test beam. From Fig. 4, we can see that the entropy value of the removed components and the original signal cannot be used for crack localization, while the entropy value of the pre-processed signal works for crack localization. It shows the EMD-based pre-processing can be used to extract characteristics caused by the breathing crack. Figure 6 shows the result of crack localization on the beams with $\text{RL}_c = 40\%$ and $\text{RL}_c = 50\%$, respectively. In this figure, we can see that the proposed method can achieve crack localization, which illustrates the effectiveness of the proposed method.
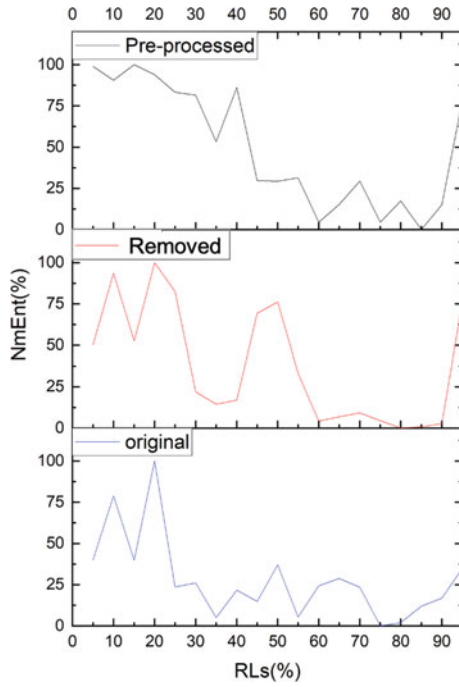
**Fig. 5** Entropy values of the pre-processed signal, the removed component, and the original signal
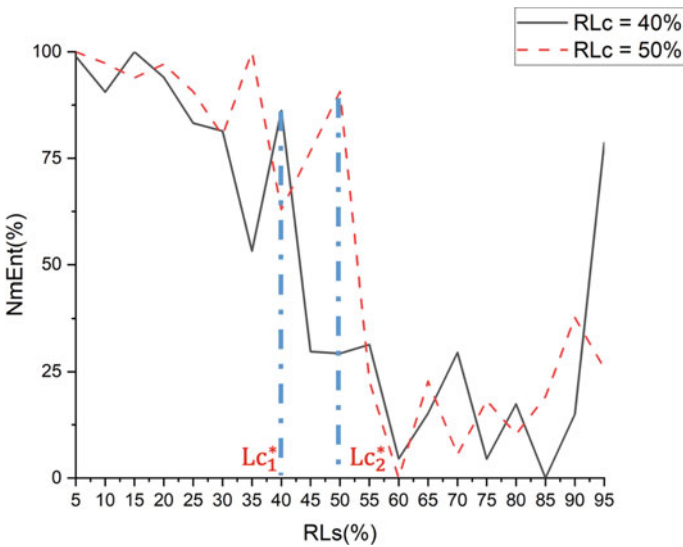


**Fig. 6** Result of crack localization for the beams: $RL_c = 40\%$ and $RL_c = 50\%$

# 4   Conclusion

A new crack localization method based on EMD and entropy is proposed in this paper. An EMD-based signal pre-processing method is proposed to extract characteristics caused by the breathing phenomenon. This method is self-adaptive, and no additional parameters are needed ahead of time. The entropy value calculated by SampEn at different acquisition positions is used to determine the breathing crack location. The proposed method is validated by the cantilever beam structure. Future work should be focused on microcrack identification and parameter optimization for the selected entropy methods. The proposed method can also be extended to other structures with more complex loading conditions.

# References

1. Moughty J, Casas J (2017) A state of the art review of modal-based damage detection in bridges: development, challenges, and solutions. Appl Sci 7:510–535
2. Hou R, Xia Y (2020) Review on the new development of vibration-based damage identification for civil engineering structures: 2010–2019. J Sound Vib 115741
3. Alfredo G, Antonio FL, Renato PA, Julian SP (2020) Structural health monitoring for advanced composite structures: a review. J Compos Sci 4(1):13–29
4. Kim H, Melhem H (2004) Damage detection of structures by wavelet analysis. Eng Struct 26(3):347–362
5. Alejandro MG, Amezquita-Sanchez JP, Martin VR, Carlos PR, Aurelio DG, Omar CA (2018) EMD-Shannon entropy-based methodology to detect incipient damages in a truss structure. Appl Sci 6858(11):2068
6. Xu Y, Chen J (2004) Structural damage detection using empirical mode decomposition: experimental investigation. J Eng Mech 130(11):1279–1288
7. Wimarshana B, Wu N, Wu C (2017) Crack identification with parametric optimization of entropy and wavelet transformation. Struct Monit Maintenance 4(1):33–52
8. Sheerin SN, Kavitha S, Raghuraman G (2018) Review and analysis of crack detection and classification techniques based on crack types. Int J Appl Eng Res 13(8):6056–6062
9. Ye X, Jin T, Yun C (2019) A review on deep learning-based structural health monitoring of civil infrastructures. Smart Struct Syst 59924(5):567–586
10. Yang Z, Chen X, Jiang Y, He Z (2014) Generalised local entropy analysis for crack detection in beam-like structures. Nondestr Test Eval 29(2):133–153
11. Wimarshana B, Wu N, Wu C (2017) Application of entropy in identification of breathing cracks in a beam structure: simulations and experimental studies. Struct Health Monit 17(3):549–564
12. Wimarshana B, Goes F, Wu N, Wu C (2017) Experimental study on breathing crack detection and evaluation under random loading with entropy. Trans Can Soc Mech Eng 65241(5):669–680
13. Wimarshana B, Wu N, Wu C (2016) Identification of breathing cracks in a beam structure with entropy. In: Smart structures and materials+ nondestructive evaluation and health monitoring, p 98042

14. Cui S, Wu N, Maghoul P, Liang X, Wang Q (2021) Fatigue crack localization based on entropy and wavelet transformation. In: 8th International conference on vibration engineering, Shanghai, China
15. Cui S, Maghoul P, Liang X, Wu N, Wang Q (2022) Fatigue crack localization based on spatially distributed entropy and wavelet transform. Eng Struct 266,114544
16. Shannon CE (1948) A mathematical theory of communication. Bell Syst Tech J 27(3):379–423
17. Pincus S (1995) Approximate entropy (ApEn) as a complexity measure chaos. Interdisc J Nonlinear Sci 5(1):110–117
18. Richman JS, Moorman JR (2000) Physiological time-series analysis using approximate entropy and sample entropy. Am J Physiol-Heart Circulatory Physiol 278(6):2039–2049
19. Chen W, Zhuang J, Yu W, Wang Z (2009) Measuring complexity using FuzzyEn, ApEn, and SampEn. Med Eng Phys 311:61–81
20. Rezaei D, Taheri F (2009) Experimental validation of a novel structural damage detection method based on empirical mode decomposition. Smart Mater Struct 18(4):045004
21. Barbosh M, Singh P, Sadhu A (2020) Empirical mode decomposition and its variants: a review with applications in structural health monitoring. Smart Mater Struct 29(9):093001
22. Lu Z, Smith JS, Wu QH, Fitch J (2005) Empirical mode decomposition for power quality monitoring. In: 2005 IEEE/PES Transmission & distribution conference & exposition, Asia and Pacific

# A Time-Dependent Probabilistic Approach for Safety Assessment of Brittle Elements in Bridge Structures

**Mohammad J. Tolou Kian, Michelle Y. X. Chien, and Scott Walbridge**

**Abstract**  As bridge structures age, their metallic members deteriorate due to corrosion and cyclic stress. Over time, this deterioration can lead to failure of various bridge members, either due to yielding, buckling, or brittle fracture, which can potentially cause the collapse of the bridge structure. For this reason, routine assessment and maintenance procedures, including finding, monitoring, and retrofitting defects in early stages, are essential to the safety of bridge structures. However, there are elements in bridge structures that are either hardly accessible or inaccessible, rendering visual inspection hard or impossible. Pins in pinned connections of truss bridges are examples of such members. This situation can be even more problematic when brittle fracture, which can occur with little warning, is a potential failure mode. In the case where inspections cannot be efficiently conducted, numerical approaches such as probabilistic fracture mechanics methods can be effectively employed to assess the safety of such bridge elements and provide useful information on such things as the critical defect size. This information can be useful for assessing the suitability of more drastic non-destructive evaluation (NDE) measures or making decisions regarding retrofitting. In this regard, a probabilistic approach based on the Eurocode EN1993-1-10 fracture mechanics method is used in this paper to assess the probability of failure of a typical pin used in large steel truss bridges. With this information, this paper presents a comprehensive methodology for assessing critical crack sizes for the pins of the bridge example, which considers the probability of brittle fracture.

**Keywords**  Bridge structures · Brittle fracture · Reliability index · Probabilistic analysis

M. J. Tolou Kian (✉) · M. Y. X. Chien · S. Walbridge
University of Waterloo, Waterloo, Canada
e-mail: mj2toloukian@uwaterloo.ca

# 1   Introduction

Maintenance is essential to guarantee the safety of existing bridge structures, especially for old bridges built in the early twentieth century, which can be more susceptible to damage as they were not designed for today's traffic load and fatigue considerations. Fatigue damage and brittle fracture are significant concerns in bridges and threaten public safety [8]. For instance, in 1967, the collapse of the Silver Bridge after 40 years of service tolled 46 lives. The catastrophic event was triggered by the failure of a single eye-bar member of the bridge, causing instability in a joint and the whole bridge superstructure as it lacked an appropriate level of redundancy [4, 15, 24].

The fatigue lifetime of structural members can be estimated using stress-based methods or strain-based approaches. The stress-based or S–N method relates the applied stress range with the number of cycles applied that cause failure in a bridge member, while in strain-based approaches, strain–life curves are obtained, and for that, the cyclic stress–strain curve of the material is required [9, 14, 25]. An alternative method to estimate the fatigue life of bridge members is fracture mechanics with a crack initiation procedure or assuming an initial crack on the member [7, 10]. In this method, finite element (FE) analysis can assess the member fracture mechanics parameters, such as the elastic stress concentration and associated stress intensity factors. Then, the calculated parameters can predict fatigue crack initiation and the number of cycles to propagate the crack through failure in the bridge member using strain-related approaches, according to relations discussed in [2, 5, 16].

Furthermore, the strength and loading parameters of structural members have a probabilistic nature. For this reason, the fracture and fatigue calculations of bridge members can be performed in a probabilistic fashion, in which the reliability index or the probability of failure of members is calculated using probabilistic loading and strength data [13, 21]. In addition, the analysis can be performed in a time-dependent fashion as the coldest hour and the highest live load of the year do not necessarily coincide.

In this regard, a time-dependent probabilistic approach based on the Eurocode EN1993-1-10 [6] fracture mechanics method is used in this paper to assess the probability of failure of pins commonly used in large steel truss bridges. This paper presents a methodology for assessing critical crack sizes in bridge pins considering an appropriate reliability index for the pins.

# 2   Methodology

According to CSA S6-19 [3], the demand–capacity ratio of pins in bridge structures is calculated according to Eq. 1, in which $M_r$ and $V_r$ are bending moment and shear force resistance of the pin, and $M_f$ and $V_f$ are factored bending moment and shear force of the pin under a factored load of $P_f$. The factored load is calculated based on
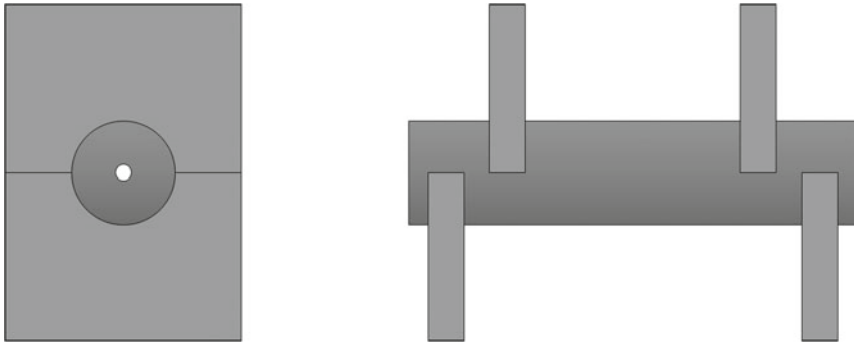
**Fig. 1** Schematic of a simple pinned connection

Eq. 2, where $D1$, $D2$, and $D3$ represent the self-weight, the weight of non-structural elements, and the weight of surface wearing, while $L$ is the live load.

$$\frac{M_f}{M_r} + \left[\frac{V_f}{V_r}\right]^3 \leq 1.0, \tag{1}$$

$$P_f = 1.1D_1 + 1.2D_2 + 1.5D_3 + 1.7L. \tag{2}$$

The most straightforward symmetrical pinned connection commonly used in truss bridge structures has four elements that exert force on the pin, as shown in Fig. 1. In this type of connection, the critical cross-section of the pin generally occurs at the middle part of the pin, where the bending moment is at its maximum, and the shear force is zero.

In this study, it is assumed that the demand–capacity ratio of the pin is equal to 0.9, and the unfactored live load applied on the pin is 20% of its unfactored dead load. Also, it was assumed that $D1$, $D2$, and $D3$ correspond to 80%, 10%, and 10% of the dead load, respectively. As a result, now, the dead load and live load bending moments and stresses at the mid-length of the pin can be derived as displayed in Eqs. 3–6.

$$M_f = 0.9M_r \rightarrow M_f = 0.9\sigma_y/S, \tag{3}$$

$$M_f/M_D = 1.1 \times 0.8 + 1.2 \times 0.1 + 1.5 \times 0.1 + 1.7 \times 0.2 = 1.5, \tag{4}$$

$$M_D = 0.67M_f = 0.67 \times 0.9 \times \sigma_y/S \rightarrow \sigma_D = 0.67 \times 0.9 \times \sigma_y = 0.54\sigma_y, \tag{5}$$

$$M_L = 0.2M_D = 0.13M_f \rightarrow \sigma_D = 0.13 \times 0.9 \times \sigma_y = 0.12\sigma_y. \tag{6}$$

## 2.1 Fracture Analysis

### 2.1.1 Ture Toughness

It was shown by [23] that a unique empirical relationship, termed the master curve, can be derived between the fracture toughness and temperature for most ferric steels. The master curve is calibrated at a fracture toughness of $100\,\mathrm{MPa\cdot m^{0.5}}$, corresponding to a temperature of $T_{100}$ °C. Equation 7 shows the master curve relationship.

$$K_{Jc(\text{median})} = 30 + 70 \exp(0.019 \cdot (T - T_{100})). \tag{7}$$

In the next step, the parameter $T_{100}$ is defined according to the modified Sanz correlation [17, 19], as shown in Eq. 8. In modified Sanz correlation, $T_{100}$ is defined based on $T_{27J}$, the temperature at which the Charpy test has 27 J impact energy.

$$T_{100} = T_{27J} - 18. \tag{8}$$

Eurocode has a more sophisticated approach toward fracture toughness than other codes, with Eurocode EN1993-1-10 employing the above relationships to determine the fracture toughness of steel, as shown in Eq. 9.

$$K_{\text{mat}} = 20 + \left[ 70 \left\{ \exp\left( \frac{T_{\text{Ed}} - [T_{27J} - 18\,^{\circ}\mathrm{C}] + \Delta T_R}{52} \right) \right\} + 10 \right] \cdot \left( \frac{25}{b_{\text{eff}}} \right)^{0.25}. \tag{9}$$

In Eq. 9, $T_{\text{Ed}}$ is a reference temperature calculated using Eq. 11, $\Delta T_R$ is a safety allowance, and $b_{\text{eff}}$ is a measure of the effective crack front length incorporated in the formulation to address the effect of the crack front on the probability of failure. In Eq. 10, $T_{\text{md}}$ is the lowest air temperature with a suitable return period of 50 years for Waterloo, Ontario. $\Delta T_r$ is the temperature change due to radiation loss, $\Delta T_\sigma$ is the temperature change due to applied stresses, $\Delta T_{\dot{\varepsilon}}$ is the temperature adjustment due to strain rate, and $\Delta T_{\text{cf}}$ is the temperature adjustment due to cold-forming. Parameters $\Delta T_r$, $\Delta T_\sigma$, $\Delta T_{\dot{\varepsilon}}$, and $\Delta T_{\text{cf}}$ were input $-5$, 0, 0, and 0.

$$T_{\text{Ed}} = T_{\text{md}} + \Delta T_r + \Delta T_\sigma + \Delta T_{\dot{\varepsilon}} + \Delta T_{\text{cf}}. \tag{10}$$

### 2.1.2 Stress Intensity

Classically, the applied stress intensity factor is calculated using Eq. 11, in which $K$ is the stress intensity factor, $S$ is the stress normal to the crack plane, and $a$ is the crack width. Since the stress distribution and, consequently, the stress intensity vary by the shape, crack size, and crack location of a member, a geometry correction factor, $Y$, is defined as displayed in Eq. 11. This correction factor can be calculated

as the normalized stress intensity, $Y = K/(S\sqrt{\pi a})$.

$$K = YS\sqrt{\pi a}. \qquad (11)$$

Raju and Newman [18] calculated the normalized stress intensity for the geometry of rods with different cracks shapes and widths using advanced FE models. This paper is used in the fracture toughness calculations of pins. This study used elliptical curves to define the crack front, as shown in Fig. 2. Then, the study offered geometry modification factors for stress intensity on rods with different crack width to diameter, $a/D$, and different crack shapes defined with $a/c$, crack width over half of the crack length (Fig. 2).

Table 1 summarizes the normalized stress intensity factors, which is another way of describing the geometry modification factor. The normalized stress intensity factors were calculated for rods with different $a/c$ and $a/D$ values under bending stresses.

In fracture mechanics, the stress intensity in elastic materials is calculated using Eq. 11. Therefore, the calculated stress intensity factor is corrected using a factor of $K_{R6} - \rho$ from the CEB6-R6 Failure Assessment Diagram (FAD), as shown in Eq. 12.

**Fig. 2** Surface crack geometrical properties of a typical rod based on [18]
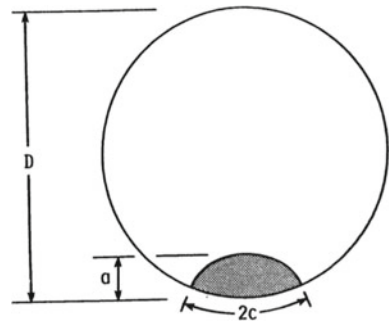


**Table 1** Normalized stress intensity factor for surface cracks in rods subjected to bending loads, based on [18]

| $a/D$ | Bending loads | | | | | |
|---|---|---|---|---|---|---|
| | $a/c = 1.0$ | | $a/c = 0.8$ | | $a/c = 0.6$ | |
| | A | B | A | B | A | B |
| 005 | 0.938 | 1.129 | 0.984 | 1.029 | 1.035 | 0.907 |
| 0.125 | 0.836 | 1.114 | 0.901 | 1.019 | 0.987 | 0.903 |
| 0.20 | 0.749 | 1.112 | 0.830 | 1.028 | 0.985 | 0.909 |
| 0.275 | 0.683 | 1.109 | 0.795 | 1.040 | 1.041 | 0.924 |
| 0.35 | 0.629 | 1.106 | 0.782 | 1.039 | 1.056 | 0.876 |

$A$ = maximum depth point
$B$ = free surface point

$$K_{\text{appld}}^* = \frac{K_{\text{appld}}}{k_{R6} - \rho}.$$ (12)

In Eq. 12, $K_{R6}$ is the plasticity correction factor from the R6-Failure Assessment Diagram, and $\rho$ is the correction factor for residual stresses produced due to welding. $K_{R6}$ ranges between 0.816 and 1.0 and is calculated using Eq. 13, where $L_r$ is $\sigma_p/\sigma_{gy} \leq 1.0$. In the calculation of $L_r$, $\sigma_p$ is the stress applied to the gross section from applied loads, and $\sigma_{gy}$ is the stress required to obtain yielding in the net section.

$$k_{R6} = \frac{1}{\sqrt{1 + 0.5L_r^2}}.$$ (13)

## 2.2 Probabilistic Fracture Analysis

Since the strength and loading parameters of structural members have a probabilistic nature, a Monte Carlo simulation (MCS) with 10,000 analyses was used to calculate the fracture probability for the pin as shown in Fig. 1. For this reason, a distribution was defined for each parameter used in fracture calculations. For each probabilistic parameter, the value, the bias factor mean and coefficient of variation, the type of distribution, and the appropriate reference are summarized in Table 2.

**Table 2** Parameters used in probabilistic fracture analysis

| Parameter | Unit | Value | $\mu_{\text{Bias}}$ | $\text{COV}_{\text{Bias}}$ | Distribution | References |
|---|---|---|---|---|---|---|
| $F_y$ | MPa | 358.0 | 1.10 | 0.091 | Lognormal | [11] |
| $t$ | mm | 330.2 | 1.02 | 0.012 | Lognormal | [12] |
| $T_{\text{md}}$ | °C | − 33.0 | 1 | 3.244 | Normal | [1] |
| $a$ | m | 0.022 | 1 | 0.198 | Lognormal | [22] |
| $\sigma_{DL}$ | MPa | 193.3 | 1.03 | 0.080 | Lognormal | [1] |
| $\sigma_{LL}$ | MPa | 42.96 | 1.52 | 0.030 | Lognormal | [1] |
| $\Delta_1^*$ | – | 1.0 | 1 | 0.250 | Normal | [20] |
| $\Delta_2^{**}$ | – | 0.0 | 0 | 13 | Normal | [20] |

$\Delta_1^*$Factor to account for uncertainties in the brittle fracture master curve formula

$\Delta_2^{**}$Factor to account for uncertainties in the CVN to facture toughness conversion formula
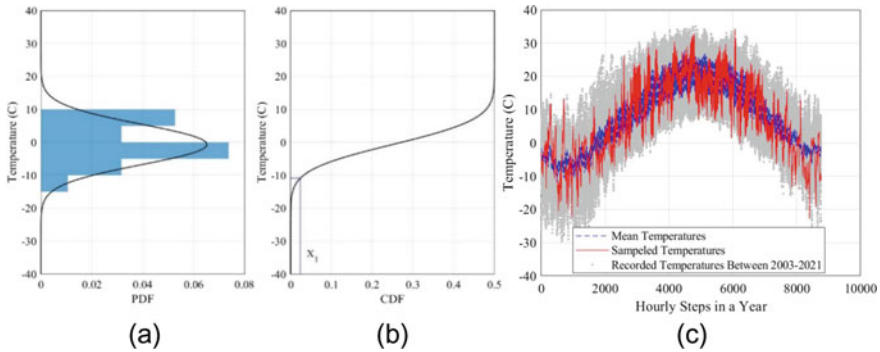
**Fig. 3** Procedure for sampling temperature **a** normal distribution fitted to recorded temperatures PDF at a random time step, **b** CDF of temperature distribution at a random time step, **c** sampled hourly temperature in a year

## 2.3 Time-Dependent Probabilistic Fracture Analysis

The probabilistic fracture mechanics analysis can be more accurate if performed in a time-dependent fashion as the yearly coldest hour and the highest live load do not necessarily coincide. In the time-dependent probabilistic approach presented in this paper, a one-hour time step was used to incorporate time-varying parameters, consisting of the temperature and live load stress, into the analysis.

The hourly temperature inputs were calculated by employing a random number $X_1$ and sampling from a normal distribution fitted to recorded temperatures between 2003 and 2021 at every specific hour, as shown in Fig. 3.

Regarding the live load stress, it was assumed that the average daily truck traffic (ADTT) of the bridge is 4000, according to [1]. Then, a Gumbel distribution per [1] was used to calculate an extreme hourly force effect by employing a random number, $X_2$, as illustrated in Fig. 4.

The time-dependent probabilistic analysis is performed as follows:

1. $K_{mat}$—CDF curves for various temperatures—and $K_{appld}^*$—CDF curves for various live load stresses—are calculated using the probabilistic fracture analysis method.
2. For each hourly time step in a one-year analysis, the $K_{mat}$ is calculated based on the temperature of the time step and appropriate $K_{mat}$—CDF curves. First, a random number, $X_3$, is employed to select a trial resistance value. Then, the $K_{mat}$ of the step is determined by interpolating the two curves with the closest temperatures to the step temperature value at $X_3$ (Fig. 5).
3. For each hourly time step in a one-year analysis, the $K_{appld}^*$ is calculated based on the live load stress of the time step and appropriate $K_{appld}^*$—CDF curves. First, a random number, $X_4$, is employed to select a trial demand value. Then, the $K_{appld}$ of the step is determined by interpolating the two curves with the closest live load stresses to the step stress value at $X_4$ (Fig. 5).
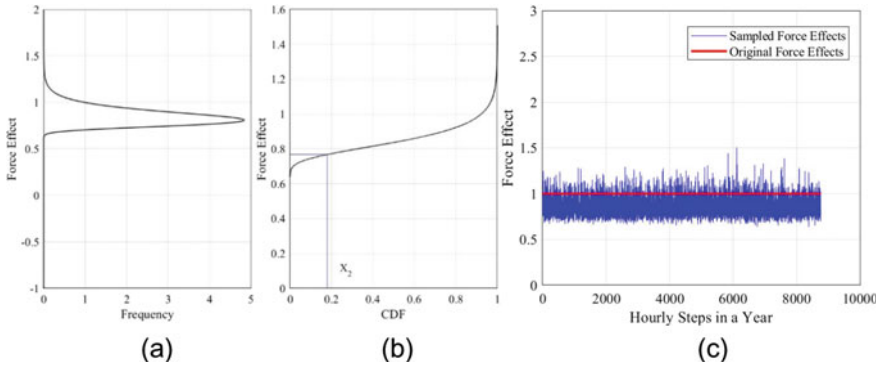
**Fig. 4** Procedure for sampling live load stress **a** live load stress Gumbel distribution at every time step, **b** CDF of live load stress distribution at every time step, **c** sampled hourly live load stress in a year
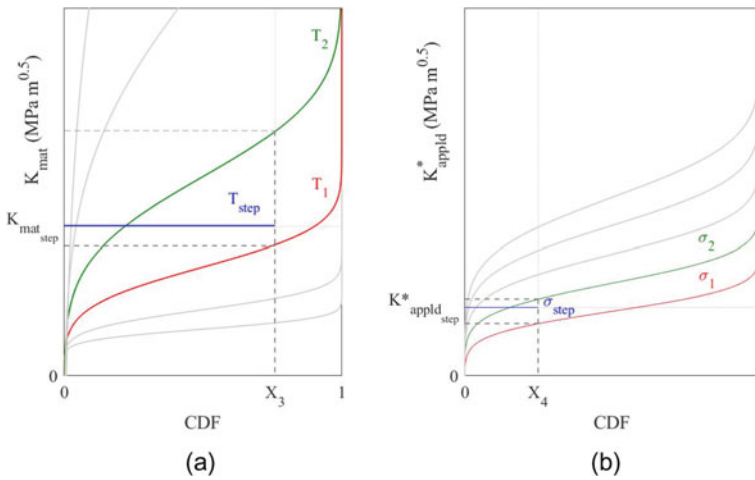


**Fig. 5** Procedure for calculating **a** fracture toughness, **b** stress intensity at each time step

4. The fracture occurs in a year if, at any time steps of the year, $K^*_{appld}$ surpasses $K_{mat}$. Then, in a Monte Carlo simulation, this one-year time-dependent probabilistic fracture analysis is repeated many times to accurately reflect the annual probability of brittle fracture failure in the member.

# 3 Results

This section shows the results of the time-dependent probabilistic approach based on the Eurocode EN1993-1-10 (2005) fracture mechanics method for different crack sizes in a pin of a bridge located in Waterloo, Ontario. First, the probability and cumulative distribution functions for $K_{mat}$ and $K_{appld}^*$ for the fracture mechanics parameters are summarized in Table 2, and different crack widths were calculated, as shown in Fig. 6.

Next, the probability of failure was calculated using the time-dependent probabilistic approach discussed above for different crack widths over 100 one-year analyses. The calculated probabilities of failure showed notable convergence after 50 iterations, and the converged annual probability of failure was directly related to the crack width of the pin, as shown in Fig. 7.
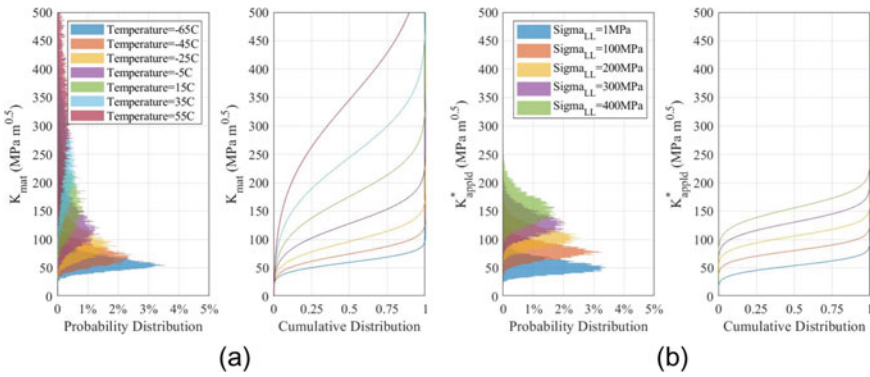


**Fig. 6** Calculated **a** $K_{mat}$—PDF distributions—and $K_{mat}$—CDF curves for various temperatures, **b** $K_{appld}^*$—PDF distributions—and $K_{appld}^*$—CDF curves for various live load stresses, and 6 mm crack width



**Fig. 7** Annual probability of failure versus the number of iterations for different crack widths
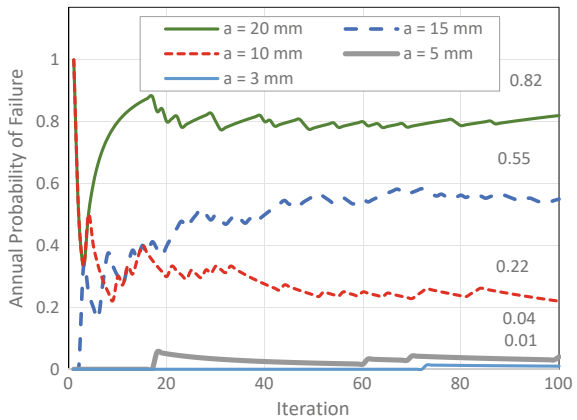
**Fig. 8** Reliability index for
different crack widths
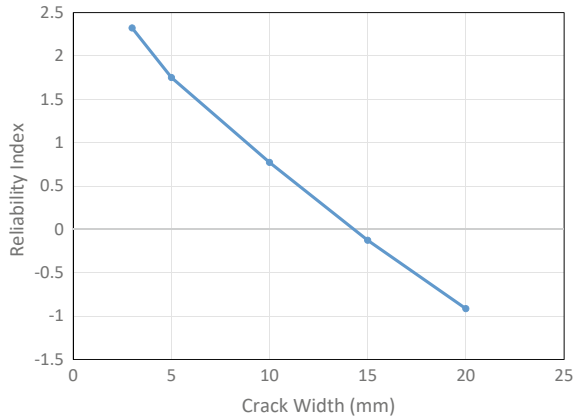


Figure 8 displays the reliability index versus the crack width of the pin. The
reliability index corresponding to each crack width was determined as the negative
of the inverse of the standard normal cumulative distribution function, evaluated at
the calculated failure probability.

## 4   Conclusions

The developed time-dependent analysis method calculates a more realistic failure
probability and reliability index than methods that use time-independent approaches.
Time-independent approaches yield more conservative failure probability and relia-
bility index values since these methods use the minimum temperature and maximum
stress in every time step.

Larger crack widths are associated with higher stress intensity factors, resulting
in higher failure probabilities and lower reliability indices. As shown in Fig. 8, a
critical crack width that conforms with the selected reliability index of the bridge
structure can be calculated. Then, an inspection routine can be established to detect
and monitor cracks with a smaller width than the calculated critical crack width, as
larger crack widths compromise the bridge's safety, while smaller crack widths can
be tolerated and scheduled for retrofitting.

The calculated probability of failure of each crack width converged to a number
as the number of iterations increased. As shown in Fig. 7, 100 iterations are enough
for cracks with larger widths, 10 mm or greater. However, for smaller crack widths,
5 and 3 mm, more iterations are needed to have accurate failure probabilities since
the calculated values are relatively small.

# References

1. Agarwal A, Au A, Becker D, Foschi R, Gagnon D, Hong H, Nowak A (2007) Calibration report for CAN/CSA-S6-06 Canadian Highway Bridge Design Code
2. Basquin OH (1910) The exponential law of endurance tests. Proc Am Soc Testing Mater 10:625–630
3. Canadian Standards Association (CSA) (2019) Canadian Highway Bridge Design Code, CSA S6-19. Toronto, ON
4. Choudhury JR, Hasnat A (2015) Bridge collapses around the world: causes and mechanisms. In: IABSE-JSCE joint conference on advances in bridge engineering-III, p 34
5. Coffin LF Jr (1954) A study of the effects of cyclic thermal stresses on a ductile metal. Trans Am Soc Mechan Eng 76:931–950
6. Comité Européen de Normalisation (CEN) (2005) Eurocode 3: design of steel structures—part-10: material toughness and through-thickness properties, EN 1993-1-10, Comité Européen de Normalisation, Brussels
7. Correia JAFO, De Jesus AMP, Da Silva ALL, Da Silva JFN (2010, July) A procedure to derive probabilistic fatigue strength data for riveted joints. In: The fifth international conference on bridge maintenance, safety and management (IABMAS2010), Philadelphia, Pennsylvania, USA, pp 11–15
8. De Jesus AM, da Silva AL, Figueiredo MV, Correia JA, Ribeiro AS, Fernandes AA (2011) Strain-life and crack propagation fatigue data from several Portuguese old metallic riveted bridges. Eng Fail Anal 18(1):148–163
9. Dowling NE, Thangjitham S (2000) An overview and discussion of basic methodology for fatigue. Fatigue Fracture Mechan 31:3–36
10. Jesus AMP, Correia JAFO (2008) Fatigue assessment of riveted railway bridge connections. Part II: numerical investigations. In: Steel bridges. Advances solutions & technologies, proceedings of the 7th international conference on steel bridges
11. Kennedy D, Baker K (1984) Resistance factors for steel highway bridges. Can J Civ Eng 11:324–334
12. Kennedy D, Gad Aly M (1980) Limit states design of steel structures—performance factors. Can J Civ Eng: 45–77
13. Kunz P, Hirt MA (1993) Reliability analysis of steel railway bridges under fatigue loading. IABSE Colloquium Copenhagen 1993 on remaining structural capacity, IABSE Report 67 (No. CONF, pp 53–60)
14. Lee YL, Pan J, Hathaway R, Barkey M (2005) Fatigue testing and analysis: theory and practice, vol 13. Butterworth-Heinemann
15. Lichtenstein AG (1993) The silver bridge collapse recounted. J Perform Constr Facil 7(4):249–261
16. Manson SS (1953) Behavior of materials under conditions of thermal stress, vol 2933. National Advisory Committee for Aeronautics
17. Marandet B, Sanz G (1976) Étude par la mécanique de la rupture de la ténacité d'aciers à résistance moyenne fournis en forte épaisseur. Revue de Métallurgie 73(4):359–384. https://doi.org/10.1051/metal/197673040359
18. Raju IS, Newman JC (1986) Stress-intensity factors for circumferential surface cracks in pipes and rods under tension and bending loads. In: Fracture mechanics: seventeenth volume. ASTM International
19. Sanz G (1980) Essai de mise au point d'une méthode quantitative de choix des qualités d'aciers vis-à-vis du risque de rupture fragile. Revue de Métallurgie 77(7):621–642. https://doi.org/10.1051/metal/198077070621
20. Sedlacek G, Feldmann M, Kühn B, Tschickardt D, Höhler S, Müller C, Hensen W, Stranghöner N, Dahl W, Langenberg P, Münstermann S, Bijlaard F (2008) EUR 23510 EN: commentary and worked examples to EN 1993-1-10 "material toughness and through thickness properties" and other toughness oriented rules in EN 1993. European Commission Joint Research Centre. European Communities, Luxembourg

21. Tobias DH, Foutch DA (1997) Reliability-based method for fatigue evaluation of railway bridges. J Bridg Eng 2(2):53–60
22. Vojdani A, Farrahi GH, Mehmanparast A, Wang B (2018) Probabilistic assessment of creep-fatigue crack propagation in austenitic stainless steel cracked plates. Eng Fract Mech 200:50–63
23. Wallin K (1998) Master curve analysis of ductile to brittle transition region fracture toughness round robin data: the "EURO" fracture toughness curve. Technical Research Centre of Finland (VTT)
24. Witcher TR (2017) From disaster to prevention: the silver bridge. Civ Eng Mag Archive 87(11):44–47
25. Williams CR, Lee YL, Rilly JT (2003) A practical method for statistical analysis of strain–life fatigue data. Int J Fatigue 25(5):427–436

# Structural Specialty: Durability of Structures

# Condition-Based Maintenance of Highway Bridges Using Q-learning and Considering Component Dependency

**Gaowei Xu and Fae Azhari**

**Abstract**  A bridge comprises many structural components, most of which are critical to its safety and must be maintained periodically. Finding the optimal maintenance policy for a bridge is challenging as each component has a unique deterioration process, and component failures interdepend. Moreover, the components have specific repair schemes with different effects. Maintenance work may involve various combinations of these repair schemes. In this study, we develop a bridge management approach that recommends repair schemes based on routine inspection results. The proposed method uses Q-learning to determine optimal maintenance decisions. The objective is to minimize the total maintenance and user costs in a given planning horizon. Deterioration models for the structural components are obtained using routine inspection data. Q-learning intelligently discovers available repair schemes while repeatedly simulating possible trajectories of bridge states throughout the planning horizon, and eventually summarizes the optimal repair schemes for a given bridge state. This approach eliminates the need for elaborate modeling of structural degradations and repair effects. The proposed decision-making framework is illustrated using an example steel girder bridge.

**Keywords**  Bridge deterioration · Condition-based maintenance · Q-learning · Markov chain · Life-cycle cost

## 1 Introduction

Bridge management systems (BMS) are designed for maintenance scheduling and budget allocation for bridge networks. In the U.S., for example, bridge managers use AASHTO BrM (previously called Pontis) for decision-making and select predetermined repair schemes with minimum long-term costs based on inspection results

G. Xu · F. Azhari (✉)

Department of Mechanical and Industrial Engineering, University of Toronto, 27 King's College Circle, Toronto, ON M5S 1A1, Canada

e-mail: azhari@mie.utoronto.ca

[3, 7, 12]. BMS adopts a bottom-up management approach: given bridge health conditions, the optimal repair scheme of each bridge is determined and maintenance budgets are then allocated to the bridges in order of priority [13]. Bridge health conditions are represented by condition ratings (CR) obtained through routine inspections. The CR of a bridge will have a decreasing trend over time unless the bridge is repaired [2, 9]. For single-bridge maintenance optimization, the AASHTO BrM uses Markov chains to model the temporal CR drops and uses Markov decision processes (MDP) to find optimal repair schemes [13].

A bridge can be regarded as a system comprising various structural components such as the deck, superstructure, and substructure (Fig. 1). However, existing BMS fail to consider the failure interdependencies among bridge components. Here, component failure is defined as a severe loss of function such that performing repairs are no longer economical. Superstructure failures lead to the replacement of both the deck and the superstructure, and substructure failures can result in the reconstruction of the entire bridge. Moreover, multiple types of repair schemes can simultaneously occur on the same bridge, and the repair schemes may affect each other, which leads to cost interdependency. If all the three components only require repairs (i.e., not replacement), then the repairs may not affect each other and existing BMS can provide optimal repair schemes for each component. Yet, by neglecting failure and cost dependencies, the maintenance policies would not be realistic.

From a reliability engineering viewpoint, a bridge may be categorized as a three-component coherent series system [8], where the failure of any component will result in the dysfunction of the entire bridge, causing traffic detours [17]. MDP-based maintenance optimization methods rely on bridge reliability analyses [11]. While the reliability calculations for a three-component series system is not complex, the repair scheme combinations for the components complicate the decision-making process. The primary reason is that the MDP transition probabilities are difficult to obtain [1]; thus, conventional methods (e.g., dynamic programming) cannot handle the problem [18]. In recent years, reinforcement learning algorithms have been applied to infrastructure maintenance management; specifically, model-free learning approaches, such as Q-learning and its variants [10, 15, 18]. This paper develops a condition-based BMS using Q-learning that accounts for component dependency. For demonstration purposes, we use steel bridges with concrete decks to describe



**Fig. 1** Typical highway bridge comprises three main components: substructure, superstructure, and deck
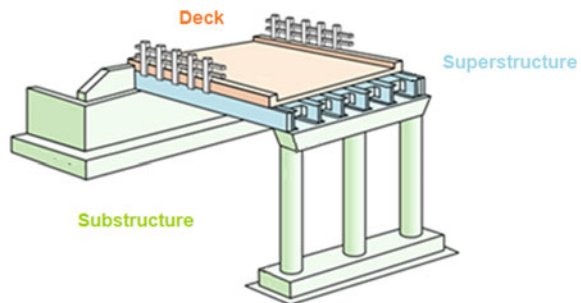
the optimization process. In addition, we use the CR scheme specified by the U.S. National Bridge Inventory (NBI) database [6]—where CRs are integers ranging from 0 (failed) to 9 (excellent)—as an example CR system. Note that other bridge types and CR schemes can easily fit within the same framework.

## 2 Representation of Bridge Health Condition

The health condition of a bridge is associated with the health conditions of the deck, superstructure, and substructure components. Therefore, we use their combined condition rating to represent the bridge health condition. Moreover, as aging structures tend to have higher failure probabilities, we also include time as a variable in bridge health conditions. In a given planning horizon $N$, the set of bridge health conditions in year $t$ is represented by:

$$S = \big\{ (t, \mathrm{CR_{deck}}, \mathrm{CR_{sup}}, \mathrm{CR_{sub}}, \mathrm{IA}) | t \in \{0, 1, \ldots, N\},$$
$$\mathrm{CR_{deck}}, \mathrm{CR_{sup}}, \mathrm{CR_{sub}} \in \{9, 8, \ldots, 3, F\}, IA \in \mathbb{Z} \geq 0 \big\} \tag{1}$$

where $\mathrm{CR_{deck}}$, $\mathrm{CR_{sup}}$, and $\mathrm{CR_{sub}}$ are condition ratings of the deck, superstructure, and substructure in year $t$; the notation $F$ denotes "failure" or $CR \leq 2$ [5]; deck initial age, IA, is the deck age at the beginning of the planning horizon and accounts for history effects; and if the deck has just been replaced, IA would be zero, and IA is not considered for superstructures and substructures as the effects of history can be neglected for those components [16].

## 3 Bridge Reliability Analyses

This section associates bridge state $s \in S$ and the probability of bridge malfunction. First, we calculate the failure probability of each in-service component [16]:

$$F(t, \mathrm{CR}, \mathrm{IA}) = 1 - \exp\left(-\int_0^t h(\tau, \mathrm{CR}, \mathrm{IA})\mathrm{d}\tau\right)(\mathrm{CR} > 2) \tag{2}$$

where $h(t, \mathrm{CR}, \mathrm{IA})$ is the failure rate of the component given its CR and IA in year $t$, obtained by the Weibull-baseline proportional hazard model (WPHM):

$$h(t, CR, IA) = \frac{\beta}{\eta}\left(\frac{t}{\eta}\right)^{\beta-1} \exp(\gamma_1 CR + \gamma_2 IA) \tag{3}$$

where $\beta$ is the shape parameter, $\eta$ is the scale parameter; $\gamma_1$ and $\gamma_2$ are the weights of CR and IA, respectively. "In-service" refers to CR > 2.

Next, we must calculate a conditional failure probability as Eq. (1) does not indicate how long the component has survived before the year $t$. In other words, given the component CR and years of in-service history, $n$, the failure probability of the component in the next year is:

$$F_{\text{component}} = F(r|n, \text{CR}) = \kappa(n, \text{CR})(\boldsymbol{I} - \boldsymbol{R})1_{7N \times 1} \tag{3}$$

$$\boldsymbol{R} = \begin{pmatrix} 0 & \boldsymbol{\Lambda}(0) & 0 & \dots & 0 \\ 0 & 0 & \boldsymbol{\Lambda}(1) & \dots & 0 \\ \vdots & \vdots & \vdots & \ddots & \vdots \\ 0 & 0 & 0 & \dots & \boldsymbol{\Lambda}(N-2) \\ 0 & 0 & 0 & \dots & \boldsymbol{\Lambda}(N-1) \end{pmatrix} \tag{4}$$

$\kappa(n, \text{CR})$ is a special row vector of length $7 \times N$, where only the $(7n + (10\text{-CR}))$th element is nonzero and equals one. $\boldsymbol{\Lambda}(n)$ is a $7 \times 7$ matrix, the elements of which are the annual transition probabilities from the $n$th year with CR $= i$ to the $(n + 1)$th year with CR $= j$:

$$\Lambda_{ij}(n) = p_{ij} \cdot \exp\left(-\int_n^{n+1} h(t, i) \mathrm{d}t\right)(i, j \in \{9, 8 \dots, 3\}; n = 0, 1, \dots, N - 1) \tag{5}$$

Finally, having calculated the component failure probabilities, $F_{\text{deck}}$, $F_{\text{sup}}$, and $F_{\text{sub}}$, we can obtain the probability of the bridge malfunction [8]:

$$F_{\text{bridge}} = 1 - (1 - F_{\text{deck}})(1 - F_{\text{sup}})(1 - F_{\text{sub}}) \tag{6}$$

## 4  Q-learning Concept

This section describes the maintenance optimization framework. As a typical model-free reinforcement learning algorithm, Q-learning is different from dynamic programming [14]. Q-learning creates a virtual agent that repetitively takes actions to explore and receive rewards from its environment (Fig. 2). In bridge management, the "agent" refers to a decision-maker, the "actions" refer to repair schemes, the "rewards" refer to inspection or maintenance costs, and the "environment" refers to bridge health degradations. While exploring, the agent is constantly looking for the optimal action given each possible environmental condition. Therefore, Q-learning can discover possible degradation trajectories in the planning horizon and prepare corresponding optimal maintenance policies. This process is similar to the

Fig. 2 Concept of
Q-learning
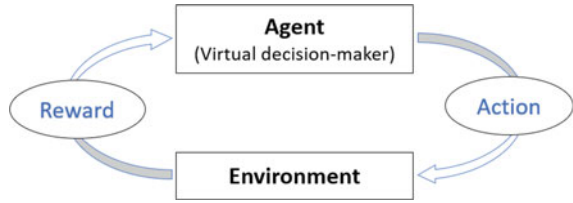
Monte Carlo simulation in that it avoids the elaborate calculations of the transition probabilities between bridge states (defined in Sect. 2) required in dynamic programming.

## 5 Illustrative Example

The following demonstrates the use of Q-learning for maintenance management of an example bridge in New York. The selected bridge (#000000001058920), built in 1961, has steel girders and a concrete deck (Fig. 3). The deck is 20.1 m long and 11.3 m wide. The average daily traffic (ADT) on the bridge is 15,496 veh/d with 3% of trucks [6]. If the bridge fails, its traffic will detour 3 km for one year. According to the latest routine inspection [6], the deck, superstructure, and substructure condition ratings are $CR_{deck} = 6$, $CR_{sup} = 6$, and $CR_{sub} = 6$, respectively, indicating the current bridge condition rating is 6.



Fig. 3 Photograph of the example bridge (retrieved from https://www.google.ca/maps)

**Table 1** Available actions for the example bridge

| Action code | Deck | Superstructure | Substructure |
|---|---|---|---|
| 0 | NA | NA | NA |
| 1 | GE | NA | NA |
| 2 | ES | NA | NA |
| 3 | RE | NA | NA |
| 4 | NA | PR | NA |
| 5 | GE | PR | NA |
| 6 | ES | PR | NA |
| 7 | RE | PR | NA |
| 8 | NA | NA | PR |
| 9 | GE | NA | PR |
| 10 | ES | NA | PR |
| 11 | RE | NA | PR |
| 12 | NA | PR | PR |
| 13 | GE | PR | PR |
| 14 | ES | PR | PR |
| 15 | RE | PR | PR |
| 16 | RE | RE | NA |
| 17 | RE | RE | PR |
| 18 | RE | RE | RE |

## 5.1 Defining Actions (Repair Schemes)

To simplify the problem, we define five repair schemes—no action (NA), preventive repair (PR), general repair (GE), essential repair (ES), and replacement (RE). GE and ES are specific to the deck, and PR is specific to the superstructure and substructure [16, 17]. The possible actions for the bridge are combinations of these component-level repair schemes. Due to component dependency, some combinations are impossible (for instance, deck NA + superstructure RE). We first list all permutations of the repair schemes and then exclude impossible ones [18]. Hence, the state space of possible bridge actions has 19 elements (presented in Table 1): $A$ = {0, 1, …, 18}.

## 5.2 Defining Rewards (Costs)

We assumed that each routine inspection costs $C_I = \$7,000$. The costs of PR, GE, and ES, listed in Table 2, depend on component CRs [16, 17]. Using the same analysis approach, we also obtained the replacement costs of the three components: $C_{RE, deck}$ = 4500 \$/m$^2$, $C_{RE, sup}$ = 5500 \$/m$^2$, and $C_{RE, sub}$ = 5500 \$/m$^2$.

**Table 2** Summary of unit repair costs ($/m²)

| Prior CR, $i$ | General repair $C_{GE, deck}$ | Essential repair $C_{ES, deck}$ | Preventive repair $C_{PR, superstructure}$ | Preventive repair $C_{PR, substructure}$ |
|---|---|---|---|---|
| 7 | 1190 | 3560 | 2700 | 2100 |
| 6 | 1080 | 3530 | 2700 | 2540 |
| 5 | 1190 | 3780 | 2400 | 2850 |
| 4 | 1300 | 3710 | 2300 | 2900 |
| 3 | 1140 | 3500 | 2400 | 2900 |

The detour cost was determined by:

$$C_{DT} = ADT \times 365 \times (\alpha_c FC_c FP_c + \alpha_t FC_t FP_t) \times DL \tag{7}$$

where $\alpha_c$ and $\alpha_t$ represent the percentage of cars and trucks, respectively; $FC_c$ and $FC_t$ are the average fuel consumption of a car (assumed to be 0.1 L/km) and a truck (assumed to be 0.4 L/km), respectively; $FP_c$ and $FP_t$ are the fuel prices of cars (assumed to be 1.02 \$/L) and trucks (assumed to be 1.04 \$/L), respectively; and DL is the detour length in km.

As component failures lead to traffic detours, the corresponding failure costs include both replacement and detour costs:

Deck failure: $C_{F, deck} = C_{RE, deck} + C_{DT}$
Superstructure failure: $C_{F, sup} = C_{RE, deck} + C_{RE, sup} + C_{DT}$
Substructure failure: $C_{F, sub} = C_{RE, deck} + C_{RE, sup} + C_{RE, sub} + C_{DT}.$

Component failure probabilities, defined in Sect. 3, were used to calculate the expected cost of NA given a component failure as the product of the component failure cost and its failure probability: $E(C_{NA,F}) = C_{F,component} \times F_{component}$.

## 5.3 Defining the Environment (Deterioration Model)

Table 3 presents estimated CR transition probabilities, $p_{ij}$, obtained through maximum likelihood estimation in a previous study [16, 17] that explored the use of the Weibull-based proportional hazard model (WPHM) for maintenance management of similar bridges in New York. The WPHM parameters ($\beta$, $\eta$, and $\gamma$) were estimated to be:

Deck: $\beta_{deck} = 1.55$, $\eta_{deck} = 0.61$, $\gamma_{1, deck} = -2.81$, $\gamma_{2, deck} = -0.03$
Superstructure: $\beta_{sup} = 1.36$, $\eta_{sup} = 0.42$, $\gamma_{sup} = -1.89$
Substructure: $\beta_{sub} = 1.22$, $\eta_{sub} = 4.31$, $\gamma_{sub} = -1.17$

We must also consider the improvements in CR due to repairs. $r_{ij}$ denotes the probability of component health condition improvement from $CR = i$ to $CR = j$

**Table 3** Transition probability matrix of substructure condition ratings—$p_{ij,\text{sub}}$

| | j | | | | | | |
|---|---|---|---|---|---|---|---|
| i | 9 | 8 | 7 | 6 | 5 | 4 | 3 |
| 9 | 0.875 | 0.097 | 0.024 | 0.003 | 0.001 | | |
| 8 | | 0.891 | 0.088 | 0.017 | 0.004 | | |
| 7 | | | 0.917 | 0.068 | 0.013 | 0.001 | 0.001 |
| 6 | | | | 0.934 | 0.06 | 0.005 | 0.002 |
| 5 | | | | | 0.954 | 0.041 | 0.005 |
| 4 | | | | | | 0.978 | 0.022 |
| 3 | | | | | | | 1 |

**Table 4** Probability of deck CR improving from $i$ to $j$ following a general repair, $r_{ij,\text{ GE, Deck}}$

| | j | | | | | |
|---|---|---|---|---|---|---|
| i | 9 | 8 | 7 | 6 | 5 | 4 |
| 8 | 1 | | | | | |
| 7 | 0.2 | 0.8 | | | | |
| 6 | | 0.12 | 0.88 | | | |
| 5 | | 0.12 | 0.17 | 0.71 | | |
| 4 | | | 0.04 | 0.14 | 0.82 | |
| 3 | | | 0.01 | 0.02 | 0.13 | 0.83 |

**Table 5** Probability of deck CR improving from $i$ to $j$ following an essential repair, $r_{ij,\text{ ES, Deck}}$

| | j | |
|---|---|---|
| i | 9 | 8 |
| 5–8 | 1 | |
| 4 | 0.72 | 0.28 |
| 3 | 0.84 | 0.16 |

[16, 17]. As an example, Tables 4 and 5 present how general and essential repairs, respectively, improve the deck *CR*. A replacement will restore the component *CR* to 9.

## 5.4 Implementing the Q-learning Algorithm

We first set a planning horizon of $N = 20$ years. As the first year of the horizon is 2021, the deck initiation age, IA, is $2021 - 1961 = 60$ years. A lookup table, called *Q*-table, stores maintenance policies for the next 20 years. The *Q*-table rows are bridge states, and the columns are actions. Each element of the *Q*-table is a *Q* value,

**Fig. 4** Convergence of $Q$ values
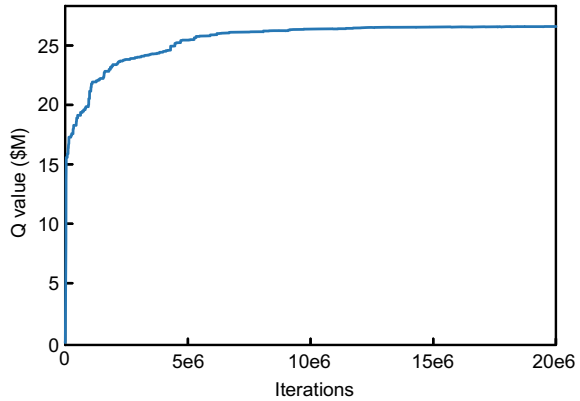


denoted by $Q(s, a)$, indicating the total future cumulative rewards when taking action $a \in A$ given the environment state $s \in S$. For the example bridge we investigated, the $Q$-table has 21,504 rows and 19 columns. Each $Q$ value refers to the total cumulative costs by implementing a specific repair scheme given a certain bridge state. The goal of Q-learning is to obtain the $Q$-table via the following pseudocodes:

```
(1) Initializing all Q values to be 0
(2) Setting the bridge initial state s (in 2021) as the current state
(3) For iteration = 1,2,…
(4)    While time ≤ final year of the planning horizon
(5)      ε-greedy search: Randomly selecting an action a ∈ A with probability ε or selecting the action a =
argmin(Q(s, a))
(6)      Calculating the corresponding reward − r(s, a)
(7)      Determining the next state s' due to taking the action a
(8)      Find the minimal Q value in state s'− Q(s', a')
(9)      Updating the Q value using:
   Q(s,a) ← (1 − α)Q(s,a) + α(r(s, a) + γQ(s',a'))   (8)
where α ∈ (0, 1) is the learning rate, and γ ∈ (0, 1) is the discount factor. Equation (8) implies that Q
values are updated partially by current Q value and partially by future total expected rewards.
(10)    current state = s', time ← time + 1
(10)  End While
(11)  break the for loop if Q values are converged
(11) End For
```

Tuning the hyperparameters, we obtained the optimal values: $\varepsilon = 0.3$, $\gamma = 0.9$, and $\alpha = 1/m^{0.3}$ where $m$ is the number of iterations [4]. The programming was completed using Python. Figure 4 shows the convergence of $Q$ values for the example bridge during the learning process. The $Q$ values approximately converged after 10,000,000 iterations.

## 5.5 Planning Future Maintenance

Using the $Q$-table, we can predict future bridge health conditions and recommend repair schemes every year. Table 6 shows a simulated trajectory of bridge states for

the example bridge in the 20-year planning horizon. The first four columns indicate the bridge states, the fifth column lists the optimal actions corresponding to each year, and the following columns present the details of repair schemes for each component. In 2021, no repair was required. Two repairs occur in 2026 and 2040. Only the superstructure repair would occur in 2026, whereas all components must be repaired in 2040. Moreover, the criterion of performing substructure repair (when $CR_{sub} \leq 5$) is harsher than that of superstructure (when $CR_{sub} \leq 3$) and deck (when $CR_{sub} \leq 4$), because the substructure has a higher failure cost than other components. Though $C_{F, deck}$ is the lowest among all failure costs, the 60-year initiation age apparently increases the need for performing deck repairs. The $CR_{sub}$ remains at five between 2031 and 2040, but it is not recommended to repair it until 2040, which means the substructure hazard rises as the bridge ages, and the hazard in 2040 is high enough to trigger the PR.

**Table 6** Simulated maintenance recommendations between 2021 and 2041

| (1) | (2) | (3) | (4) | (5) | (6) | (7) | (8) |
|---|---|---|---|---|---|---|---|
| Year | $CR_{deck}$ | $CR_{sup}$ | $CR_{sub}$ | Recommended action $a$ | Deck repair | Superstructure repair | Substructure repair |
| 2021 | 6 | 6 | 6 | 0 | NA | NA | NA |
| 2022 | 6 | 5 | 6 | 0 | NA | NA | NA |
| 2023 | 6 | 5 | 6 | 0 | NA | NA | NA |
| 2024 | 6 | 5 | 6 | 0 | NA | NA | NA |
| 2025 | 6 | 5 | 6 | 0 | NA | NA | NA |
| 2026 | 6 | 3 | 6 | 4 | NA | PR | NA |
| 2027 | 6 | 4 | 6 | 0 | NA | NA | NA |
| 2028 | 6 | 4 | 6 | 0 | NA | NA | NA |
| 2029 | 6 | 4 | 6 | 0 | NA | NA | NA |
| 2030 | 6 | 4 | 6 | 0 | NA | NA | NA |
| 2031 | 6 | 4 | 5 | 0 | NA | NA | NA |
| 2032 | 5 | 4 | 5 | 0 | NA | NA | NA |
| 2033 | 5 | 4 | 5 | 0 | NA | NA | NA |
| 2034 | 5 | 4 | 5 | 0 | NA | NA | NA |
| 2035 | 5 | 4 | 5 | 0 | NA | NA | NA |
| 2036 | 5 | 4 | 5 | 0 | NA | NA | NA |
| 2037 | 5 | 4 | 5 | 0 | NA | NA | NA |
| 2038 | 5 | 4 | 5 | 0 | NA | NA | NA |
| 2039 | 5 | 4 | 5 | 0 | NA | NA | NA |
| 2040 | 4 | 3 | 5 | 13 | GE | PR | PR |
| 2041 | 6 | 4 | 8 | 0 | NA | NA | NA |

# 6    Conclusions

A condition-based maintenance algorithm was proposed to improve existing bridge management systems. A bridge was considered as an engineering system comprising three components—deck, superstructure, and substructure. Bridge health conditions were represented by a five-dimensional variable that included time, condition ratings of the three components, and the deck initiation age. Unlike existing bridge management approaches, the proposed method accounts for the interdependency among component failures and deals with the complexity in finding the optimal maintenance policy using Q-learning. Q-learning avoids the need for intricate modeling of temporal degradations of bridge health conditions. The proposed condition-based maintenance optimization framework was demonstrated using an example highway bridge with steel girders and a concrete deck. The practical use of the framework was described through a simulated trajectory of bridge deteriorations and recommended repair schemes during a 20-year planning horizon.

# References

1. Andriotis CP, Papakonstantinou KG (2019) Managing engineering systems with large state and action spaces through deep reinforcement learning. Reliab Eng Syst Saf 191:106483
2. Cesare MA, Santamarina C, Turkstra C, Vanmarcke EH (1992) Modeling bridge deterioration with Markov chains. J Transp Eng 118(6):820–833
3. Dai K, Smith BH, Chen S-E, Sun L (2014) Comparative study of bridge management programmes and practices in the USA and China. Struct Infrastruct Eng 10(5):577–588
4. Even-Dar E, Mansour Y, Bartlett P (2003) Learning rates for Q-learning. J Mach Learn Res 5(1):1–25
5. FHWA (1995) Recording and coding guide for the structure inventory and appraisal of the nation's bridges, US Dept. of Transportation Washington, DC
6. FHWA (2020) National bridge inventory database. Retrieved November 15, 2020, from https://www.fhwa.dot.gov/bridge/nbi.cfm
7. Jeong Y, Kim W, Lee I, Lee J (2018) Bridge inspection practices and bridge management programs in China, Japan, Korea, and U.S. J Struct Integr Maintenance 3(2):126–135
8. Leemis LM (1995) Reliability: probabilistic models and statistical methods, Prentice Hall New Jersey
9. Morcous G (2006) Performance prediction of bridge deck systems using Markov chains. J Perform Constr Facil 20(2):146–155
10. Renard S, Corbett B, Swei O (2021) Minimizing the global warming impact of pavement infrastructure through reinforcement learning. Resour Conserv Recycl 167:105240
11. Robelin C-A, Madanat Samer M (2007) History-dependent bridge deck maintenance and replacement optimization with Markov decision processes. J Infrastruct Syst 13(3):195–201
12. Small EP, Philbin T, Fraher M, Romack GP (1999) Current status of bridge management system implementation in the United States. In: 8th international bridge management conference, transportation research board

13. Thompson PD, Small EP, Johnson M, Marshall AR (1998) The pontis bridge management system. Struct Eng Int 8(4):303–308
14. Watkins CJ, Dayan P (1992) Q-learning. Mach Learn 8(3–4):279–292
15. Wei S, Bao Y, Li H (2020) Optimal policy for structure maintenance: a deep reinforcement learning framework. Struct Saf 83:101906
16. Xu G, Azhari F (2021) Bridge maintenance management based on routine inspection data: a quantitative approach. engrxiv.org.
17. Xu G, Jardine AK, Azhari F (2022) Dynamic bridge maintenance management in smart cities using routine inspection data and hazard modelling. In: Alavi A, Feng M, Jiao P, Sharif-Khodaei Z (eds) The rise of smart cities: advanced structural sensing and monitoring systems. Elsevier
18. Yao L, Dong Q, Jiang J, Ni F (2020) Deep reinforcement learning for long-term pavement maintenance planning. Comput-Aided Civ Infrastruct Eng 35(11):1230–1245

# Long-Term Durability of Shear Critical GFRP RC Beams

**Jahanzaib and Shamim A. Sheikh**

**Abstract**  An extensive experimental and analytical research programme underway at the University of Toronto includes 12 GFRP-reinforced beams (10 flexural critical and 2 shear critical) with 3000 mm span length. Due to the space limitation, only the detailed results of shear critical beams are discussed in this paper. Both the beams were completely reinforced with GFRP straight and bent bars. One beam was tested at room temperature and the second beam was subjected to accelerated thermal conditioning to simulate long-term behaviour of GFRP RC beams considering the recent climate challenges leading to increasing temperatures across the world. Conditioning of the beam was carried out at 50 °C for four months under 60% relative humidity while subjected to sustained load throughout the conditioning period. No significant reduction in the capacity was observed because of the conditioning.

**Keywords**  Durability · GFRP · Shear · Temperature · Beams

## 1  Introduction

Recently, there has been a significant research focus towards understanding the behaviour of fibre-reinforced polymer (FRP) bars in reinforced concrete members. Several design codes and standards have now allowed the use of glass fibre-reinforced polymer (GFRP) bars for flexural, compression and shear resistance. ACI 440.1R-15 [1] allows the use of GFRP straight bars in flexural members and bent bars in shear members; however, it ignores the strength of GFRP bars in compression. Likewise, CSA S806-12 [4] provides design guidelines to use FRP bars in members subjected to flexure and shear and ignores the strength of FRP bars in compression. CSA S6, by contrast, recently allowed the use of FRP bars in compression in columns (CSA S6-19).

Jahanzaib (✉) · S. A. Sheikh
Department of Civil and Mineral Engineering, University of Toronto, Toronto, Canada
e-mail: jahanzaib@mail.utoronto.ca

Although most design codes and guides have allowed the use of bent bars as transverse reinforcement, strength at the bend location has been a persistent design concern. Bending of fibres in GFRP bent bars causes a significant reduction in the bend strength in comparison with the straight portion strength [7, 12]. Most of the researchers conducted the laboratory testing on bare stirrups to evaluate the performance of bent bars. Earlier research found that the bend strength was between 30 and 80% of the straight portion strength [9]. Jeremic and Sheikh [6] tested 24 stirrups in the standardized testing procedure (CSA S806-12 Annex D) and found that the bend strength of GFRP stirrups varied from 35 to 55% of the straight portion strength.

Due to the uncertainty in the bend strength, design guidelines put a limit on the usable strain of GFRP stirrups. ACI 440.1R and CSA S6 limit the strain to 0.004 mm/mm, and CSA S806 standard increases this limit to 0.005 mm/mm. To design the shear members, CSA A23.3-19 [3] provides a general design model of shear behaviour for steel-reinforced concrete members. The model was developed based on the modified compression field theory (MCFT) [11] and considers the member size and strain effect on the shear strength. In previous years, different modifications have been made into these steel-based design provisions to predict the shear strength of GFRP RC members [2, 4, 5, 8]. A comprehensive investigation is needed to evaluate the accuracy of existing models in predicting the shear strength of the RC members reinforced with GFRP stirrups.

Another important aspect of GFRP bent bars that requires further investigation is their long-term durability under increased surface temperatures resulting from the recent climate changes. Park et al. [10] studied the long-term flexural behaviour of GFRP RC beams by conditioning them inside a chamber at an average temperature of 47 °C and an average relative humidity of 80% for 300 days. A maximum reduction of about 9% was observed in the moment capacity. However, no such test results are available in literature that investigated the long-term durability of shear critical beams reinforced with GFRP stirrups. ACI 440.1R-15 highlights that the effects of elevated temperature exposure on the shear capacity of FRP-reinforced members are not well known, and the additional research is warranted in this area.

## 2 Research Significance

The work presented in this paper investigates the shear behaviour of reinforced concrete beams completely reinforced with GFRP bars. Experimentally determined rupture strains of the stirrups due to shear failure of the beam are discussed. The work presented herein further provides an insight into the shear behaviour of beam after accelerated laboratory conditioning for four months at 50 °C and 60% relative humidity while subjected to sustained load. The conditioned beam was tested at the specified temperature.

## 3 Experimental Programme

Experimental programme of the current study consisted of several concrete beams, bond specimens and material specimens. Results from two shear critical beams (320 × 740 × 3000 mm) reinforced with GFRP straight and bent bars are reported in this paper. GFRP stirrups were anchored into the concrete core with 135° hooks at the corner. Reinforcement details and the geometry of the specimens are shown in Fig. 1 and Table 1.

### 3.1 Material Properties

#### 3.1.1 Concrete

Concrete was provided by a local supplier. The two beams were cast in same batch, along with several 100 × 200 mm cylinders. Strength at the time of testing of beams is listed in Table 2. Values in the table represent the average of at least three-cylinder specimens. Group-AS in Table 2 represents the test results of the cylinders cured beside the control beam at ambient temperature, and group-CS cylinders were cured under the studied thermal exposure beside the conditioned beams and were tested at 50 °C.

The development of the concrete compressive strength with time under two exposures—ambient conditions and 50 °C thermal exposure—from the results of 24-cylinders tested under compression is plotted in Fig. 2. It was found that the concrete cured under ambient conditions gained slightly higher strength over time than the concrete cured at higher temperature of 50 °C.
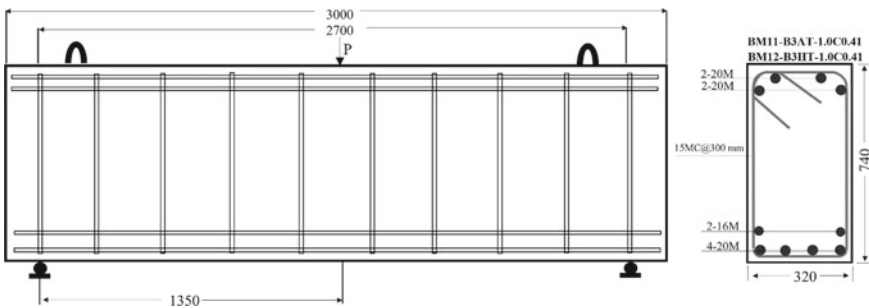


**Fig. 1** Design of two deep beams

**Table 1** Summary of specimen's details

| Nomenclature | Beam no. | $h$ (mm) | $b$ (mm) | Longitudinal reinforcement | Spacing of ties (mm) | $\rho_L$ (%) | $d$ (mm) | $\rho_T$ (%) | Test temperature (C) |
|---|---|---|---|---|---|---|---|---|---|
| Beam 1 | 11 | 740 | 320 | 4–20 M + 2–15 M | 300 | 0.78 | 670 | 0.41 | Ambient |
| Beam 2 | 12 | 740 | 320 | 4–20 M + 2–15 M | 300 | 0.78 | 670 | 0.41 | 50 |

**Table 2** Concrete cylinders test result at the time of testing

| Group name | Test age | $f'_c$ (MPa) | $E_c$ (MPa) | $\epsilon'_c$ (mm/mm) |
|---|---|---|---|---|
| AS | 163 | 46.72 | 30,518 | 0.00215 |
| CS | 163 | 42.20 | 23,645 | 0.00229 |
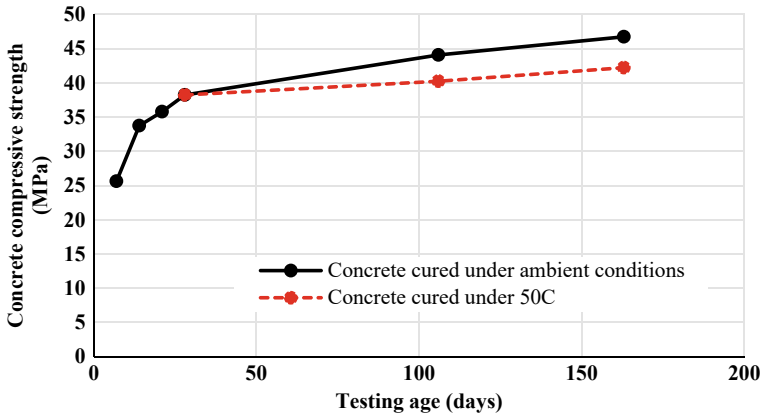


**Fig. 2** Development of concrete compressive strength for Batch 3 concrete

### 3.1.2 GFRP Mechanical Properties

Mechanical properties of all GFRP bars are listed in Table 3. Tensile properties of GFRP straight bars were determined through lab testing in accordance with the test procedure in ASTM D7205 as recommended in CSA S807-19. Actual cross-sectional areas were used for the calculation of mechanical properties of straight bars. Properties of GFRP stirrups were determined in a parallel study conducted at the University of Toronto [6] and are also provided in Table 3.

## 3.2 Instrumentation

Overall instrumentation plan consisted of both internal and external measurement tools. Internally, several electrical resistance strain gauges of 5 mm gauge length were installed on both the longitudinal and transverse reinforcing bars. Locations of strain gauges mounted on the straight bars and stirrups are shown in Fig. 3.

Externally, vertical displacements along the length of the beams were measured using linear variable displacement transformers (LVDTs). In total, five LVDTs were used during the testing in each beam. Two of them were located at the supports (one on each end of the beam) to measure support movements. In addition to the above-mentioned instrumentation, a three-dimensional LED targeting system was

**Table 3** Mechanical properties of GFRP bars

| Material properties | 15 M | 20 M | 15 M stirrup |
|---|---|---|---|
| Nominal core diameter, mm | 16 | 19 | 16 |
| Nominal area, mm$^2$ | 199 | 285 | 199 |
| Actual area, mm$^2$ | 214 | 314 | 202 |
| Ultimate tensile strength, MPa | 1338 | 1336 | 1153 |
| Modulus of elasticity, GPa | 57.7 | 55.7 | 53.1 |
| Elongation at failure, % | 2.32 | 2.40 | 2.17 |
| Bend radius, mm | – | – | 56$^{**}$ |
| Bend strength, MPa | – | – | 14,700 $\mu\epsilon$ |
| Glass transition temperature, C* | 114 | 125 | 109 |
| Fibre content by weight, % | 82.2 | 82.9 | 71.0 |

$^*$Properties specified by the manufacturer
$^{**}$Properties reported by Jeremic and Sheikh [6]
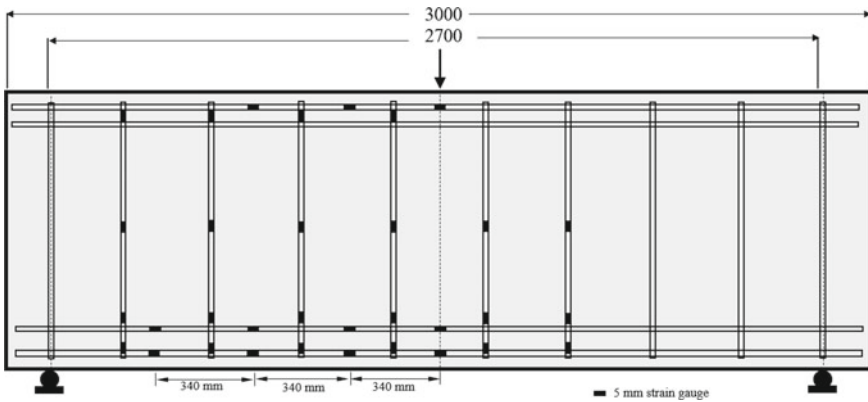


**Fig. 3** Internal instrumentation of the two shear critical beams

used to measure the surface strains. LED targets were affixed to the surface, creating a grid with intervals of 225 mm x 225 mm. Complete external instrumentation is summarized in Fig. 4. It is to be noted that one additional LED target was mounted on the left support to measure the support settlement.
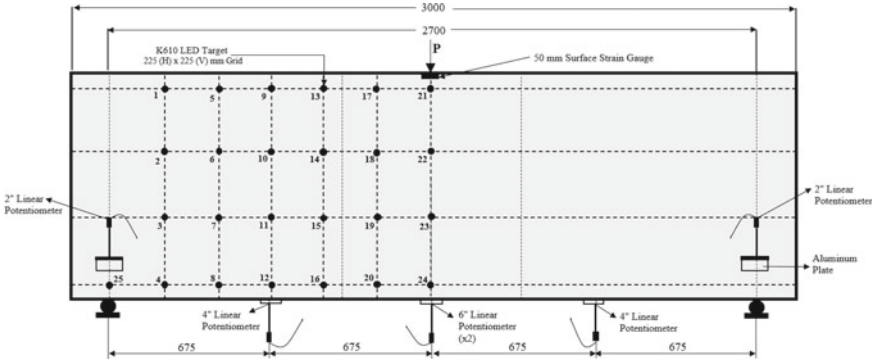
**Fig. 4** External instrumentation for shear critical control beam
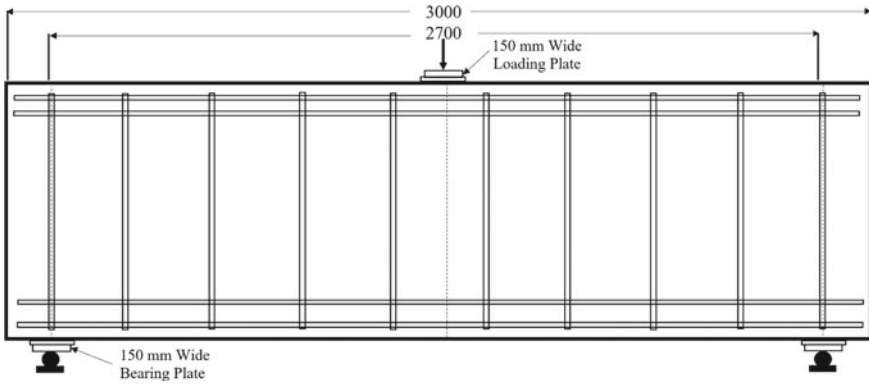


**Fig. 5** Three-point bending test of the deep beams

## 3.3 Test Set-up

### 3.3.1 Test Set-up for Control Beam

Control shear beam was tested under three-point bending test. Testing was conducted in a monotonic displacement-controlled manner with the loading rate varying from 0.008 to 0.025 mm/s. The loading mechanism is shown in Fig. 5.

### 3.3.2 Test Set-up for Conditioned Beam

Conditioned beam was exposed to a temperature of 50 °C for four months under 60% relative humidity. In addition to the temperature exposure, beam was also subjected to the sustained load throughout the conditioning duration to replicate service loads. Load level applied to this shear critical beam was 190 kN (19% of ultimate failure

**Fig. 6** Power-blankets wrapped on a shear beam for heating before start of test

load), and the maximum average stain recorded in bottom layer of the longitudinal reinforcement was 1500 µϵ.

After conditioning, the beam was tested at 50 °C. To ensure the temperature of GFRP bars embedded in concrete at the time of testing to be equal to that in the conditioning chamber, beam was installed in the machine 24 h prior to testing and was wrapped with heating blankets as shown in Fig. 6. On the day of the test, the blankets were removed just before commencing the load.

## 3.4   Test Results and Discussion

As expected, both the beams failed in pure shear failure due to the rupture of GFRP stirrups. Beams were internally instrumented with several strain gauges, and assigned a particular name based on their location as shown in Fig. 7.

The location of strain gauges attached on the stirrups is defined according to the following convention: **SXY**; S stands for stirrup; X refers to the stirrup's number which varies from 1 to 7 and represents the location of the stirrup along the length of the beam; and the letter Y denotes the location of strain gauge on the stirrup (T for top, M for mid-height, B for bottom corner, and B′ for the location where transitioning of the stirrup from the straight portion to the bent portion occurs).
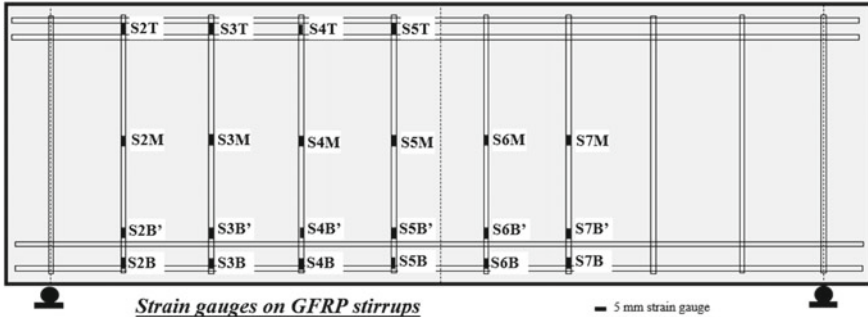
**Fig. 7** Locations and nomenclatures of the strain gauges

### 3.4.1 Test Results of Control Beam

Control beam failed in shear with a shear crack running diagonally from the loading plate towards the left span crossing three instrumented stirrups. Ultimate failure occurred on the instrumented side and hence, recorded stirrups' strains from strain gauges provided a clear picture of the actual failure. Cracking at the tension face of the beam was first noticed at 187.6 kN followed by a slight drop in the load and a noticeable reduction in the stiffness. Further increase in the load resulted into the formation of shear cracks in both of the shear spans. At higher load levels, width of the major shear crack started increasing significantly, and the failure occurred at a load of 958.7 kN with 28.92 mm midspan deflection. Failure happened due to the rupture of stirrup located at 450 mm (strain gauge location: S4B′) from the midspan. It was noticed after the test that the stirrup ruptured at the transitioning point from the straight portion to the bent portion starts.

Load deflection behaviour of the beam is shown in Fig. 8, and the failure crack is shown in Fig. 9. Beam failure and the rupture of the stirrup are shown in Fig. 10.

**Fig. 8** Load deflection curve of the control beam (beam 1)
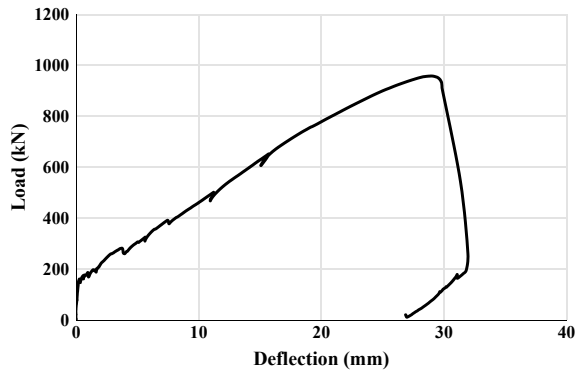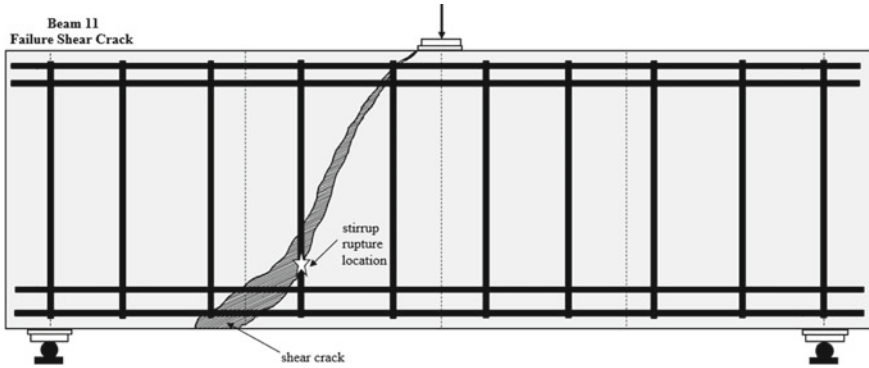
**Fig. 9** Failure crack of beam 1 (east side of the beam failed which was instrumented)



**Fig. 10** Control beam failure and stirrup rupture (north face of the beam)

Recorded Strains in the Stirrups

Most of the strain gauges functioned adequately during the test. Only a few of them failed before the peak load due to either saturation or crack passing through the gauge causing the damage. As shown in Fig. 9, failure crack crossed the stirrup number 3 and the stirrup number 4 below the mid-depth. Therefore, recorded strains with the increasing load for the gauges S3T, S3M, S3B, S3B′, S4T, S4M, S4B, and S4B′ are shown in Fig. 11. Close to the failure point, strain values at the transitioning point (B') in two of the stirrups (S3B′ and S4B′) were found to be the highest with maximum recorded strains of 14,410 με and 12,830 με, respectively.

It is important to note that the strains at the beginning of the bend increased at a faster rate with increasing load than the strains at the bent location (corner), and the stirrup ruptured at the beginning of the bend instead of critical corner location. Therefore, the rupture stirrup strain in this beam test was defined as the maximum strain recorded at the beginning of bends before failure as shown in Fig. 11, and
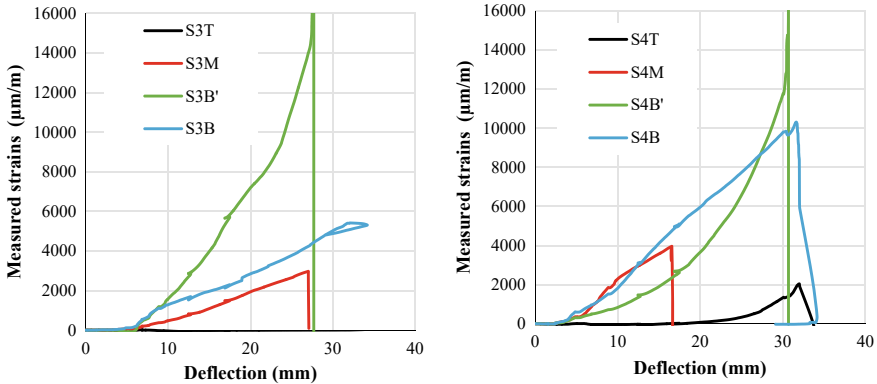
**Fig. 11** Recorded strains in the stirrups (control beam)

were found to be 14,410 με and 12,830 με for stirrup number 3 and 4, respectively, with an average value of 13,620 με. Material tests on the same stirrups conducted in a parallel study by [6] reported average rupture strain of 14,700 με which was considered to be reasonably close to the experimentally determined strain of 13,620 με from the current beam test. It should be noted that the actual strain may likely be higher than recorded.

The reason behind the rupture of the stirrup at the transitioning point (B′) instead of the bottom corner (B, precisely where the weak point is located due to the bending of fibres) can perhaps be attributed to the presence of multiple layers of longitudinal bars. Bentz et al. [2] found that with only one layer of longitudinal bars, the highest shear stress demand is predicted near the bottom of the stirrup (weak corner location); however, with multiple layers of longitudinal bars, the shear stress demand reduces in a more gradual fashion at the bottom. Therefore, stirrup rupture in the beam with multiple layers did not occur at the critical corner location. To experimentally determine this gradual reduction, strain gauges were attached at both of the locations (B: bottom corner; and B′: above longitudinal layers) in the current study. As expected, strain gauge values showed a decrease in the recorded strains going from beginning of bend location to corner location as shown in Fig. 12. This interesting finding can be helpful to protect weaker corner location in GFRP stirrups and allow the stirrup failure to happen away from the bend by providing multiple layers of longitudinal bars.

### 3.4.2 Test Results of Conditioned Beam (Beam 2)

As detailed above, beam 2 was conditioned for four months at 50 °C and tested at 50 °C. Load–deflection behaviour of the beam 2 is shown in the Fig. 13. Beam failed in pure shear with the peak load of 936.2 kN and midspan deflection of 27 mm. Failure at the peak load initiated because of the rupture of GFRP stirrup on the top
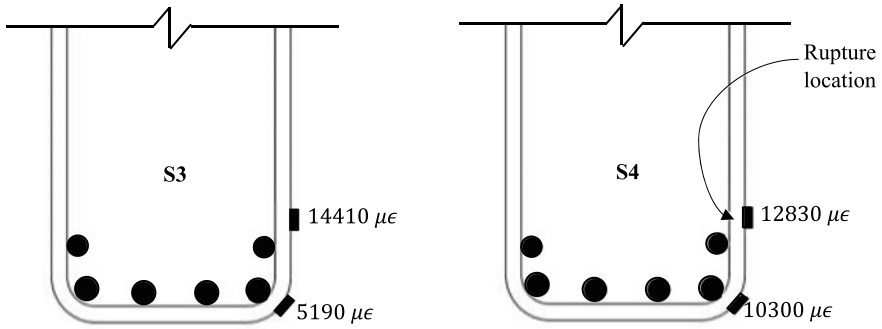
**Fig. 12** Maximum recorded strains in stirrups S3 and S4 at the bottom (beam 1)
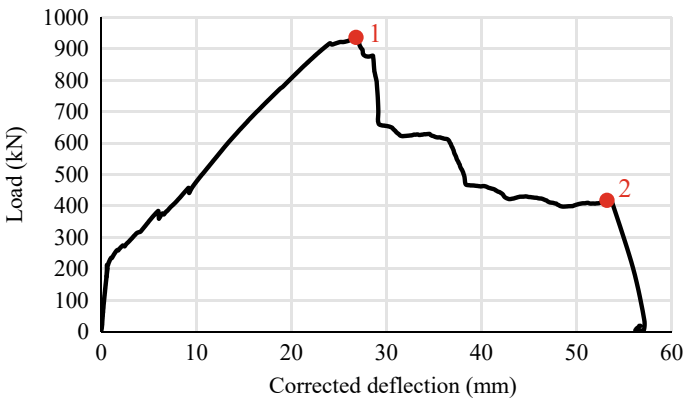


**Fig. 13** Load versus midspan deflection curve of conditioned beam (beam 2)

bend location just beside the loading plate (marked as location 1 on Fig. 14). Peak load was accompanied by a significant drop in the load, but the beam did not fail. This drop in the load was followed by a significant increase in the midspan deflection, and the opening of the major shear crack. Finally, ultimate failure occurred because of the rupture of GFRP stirrups at the bottom corners (marked as location 2 on Figs. 13 and 14). Failure pictures from the beam 2 test are shown in Fig. 15. This beam failed in un-instrumented shear span and therefore, exact strain information for the failed span could not be determined.

### 3.4.3 Effect of Thermal Conditioning on Shear Behaviour

Comparison between load deflection curves of the control and the conditioned shear critical beams (beam 1 and beam 2) is shown in Fig. 16. A slight reduction in the peak load was observed in the thermally conditioned beam. Beam 1 failed at 958.7
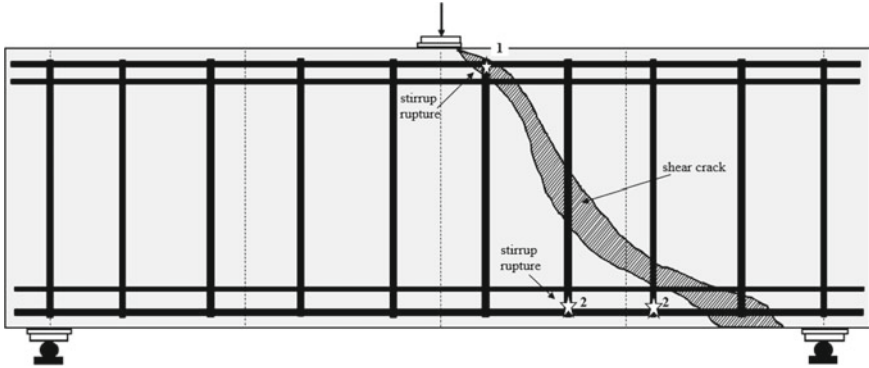
**Fig. 14** Failure crack of conditioned beam (beam 2) (north face of the beam)



**Fig. 15** Failure of beam 2 (shear critical conditioned beam) south face of the beam

kN, and the beam 2 at 936.2 kN, showing only 1% reduction in the peak load. This can be due to the normal scatter in the experimental data. It can be concluded that the beam shear behaviour was not affected much because of the long-term thermal conditioning. Failure modes of the stirrups were different in the two beams. Stirrups in control beam failed due to rupture at beginning of the bend (B' location). However, stirrups in the conditioned beam failed at the corner locations of the stirrups. This variation in the failure mode may be attributed to the fact that thermal conditioning induced relatively more damage to the bent locations (corners) of the stirrups than the straight portion, and consequently, stirrups prematurely failed showing a drop in the peak load.
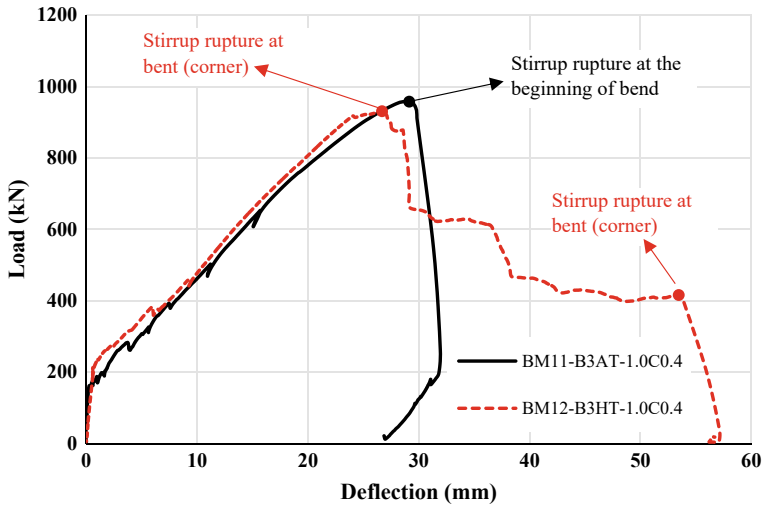
**Fig. 16** Load deflection of shear critical control and conditioned beams (beam 1 and beam 2)

## 4 Conclusions

Based on the results of this experimental and analytical investigation, the following concluding remarks can be made:

1. Conditioned shear critical beam observed only 1% reduction in the ultimate shear capacity that can be considered to be within the normal scatter in the experimental data. It can be stated that long-term thermal exposure to elevated temperatures in the range of 50 °C would not induce any significant deterioration in the shear behaviour.
2. Strain values recorded around the bent location showed that the presence of multiple layers of longitudinal bar appears to protect the weak corner location of the bend due to the gradual reduction in the strain values.

## References

1. ACI Committee 440.1R (2015) Guide test methods for fiber-reinforces polymers (FRPs) for reinforcing or strengthening concrete structures (ACI 440.1R-15). American Concrete Institute, Farmington Hill, MI, United States, 3 pp

2. Bentz EC, Massam L, Collins MP (2010) Shear strength of large concrete member with FRP reinforcement. ASCE J Compos Constr 14(6):637–646
3. CSA A23.3 (2019) Design of concrete structures. Canadian Standards Association, Rexdale, Ontario, Canada
4. CSA S806 (2012) Specification for fiber-reinforced polymers. Canadian Standard Association, Mississauga, ON, Canada
5. CSA S6 (2019) Canadian highway bridge design code. Canadian Standards Association, Toronto, ON, Canada
6. Jeremic N, Sheikh SA (2021) Performance of glass fiber-reinforced polymer bent bars. ACI Struct J 118(2):273–285
7. Johal KS (2016) Investigation of creep rupture phenomenon in glass fibre reinforced polymer (GFRP) stirrups. M.Sc. thesis, Department of Civil Engineering, University of Toronto
8. Johnson DT, Sheikh SA (2014) Investigation of glass fiber reinforced polymer (GFRP) bars as internal reinforcement for concrete structures. Research report JS-14-1, Department of Civil and Mineral Engineering, University of Toronto
9. Nagasaka T, Fukuyama H, Tanigaki M (1993) Shear performance of concrete beams reinforced with FRP stirrups. ACI Special Publication, SP-138-47, pp 789–811
10. Park Y, Kim YH, Lee SH (2014) Long-term flexural behavior of GFRP reinforced concrete beams exposed to accelerated aging exposure conditions. Polymers 6:1773–1793
11. Vecchio FJ, Collins MP (1986) The modified compression field theory for reinforced concrete elements subject to shear. ACI Struct J 83(2):219–231
12. Vint L, Sheikh SA (2015) Investigation of bond properties of alternate anchorage schemes for glass fiber-reinforced polymer bars. ACI Struct J 112(1):59–68

# Simplified Analysis of RC Beams Exposed to Fire

**Lochlan R. Medeiros, M. A. Youssef, and S. F. El-Fitiany**

**Abstract**  With performance-based design becoming more prevalent in today's standards, practical and simplified methods are needed to model and analyze reinforced concrete (RC) structures. These methods must meet the time and cost constraints for the practitioners, while maintaining a high degree of accuracy. Fire incidents are initiated by the ignition of combustible materials and can spread vertically and horizontally based on the specific compartment boundary conditions. RC elements, which are exposed to fire, develop a time-dependent three-dimensional temperature gradient. The developed temperatures cause the element's stiffness to degrade and result in thermal induced deformations. This research introduces two simplified numerical methods to analyze continuous RC beams during fire exposure. The first method divides the beam into predefined segments and uses iterations to define the stiffness for each segment. An automated program was developed to conduct the iterations and redistribute the moments until convergence is achieved. The second approach assigns nonlinear plastic hinges to the predefined segments. The moment–curvature diagrams for these hinges account for the effect of fire exposure. Predictions of both methods were validated using published research by others.

**Keywords**  Reinforced concrete · Elevated temperature · Fire · Sectional analysis · Flexural stiffness · Moment–curvature relationship · Moment redistribution · Nonlinear plastic hinge

## 1   Introduction

Figure 1 shows an example for fire damage in the Newhall tunnel in Santa Clarita, California. The fire was so severe, that it led to visible damage in the concrete and jeopardized the tunnel safety [1]. Prescriptive methods, which are widely used to

L. R. Medeiros (✉) · M. A. Youssef · S. F. El-Fitiany
Department of Civil and Environmental Engineering, Western University, London, ON N6A 5B9, Canada
e-mail: lmedeir3@uwo.ca

design structures for fire safety, are out of date, un-realistic, and based on tests conducted on individual elements, which ignored significant parameters including fire scenarios, failure criteria, boundary conditions, load cases, and system behavior [2–5]. North American design standards, including ASCE 7 [6], allowed the switch from the prescriptive approach to the performance-based approach, which requires simulation and analysis of a structure under realistic fire loading [5]. The benefits of this switch include establishing specific safety goals, permitting structural engineers to use innovative design solutions that meet specific performance criteria, allowing cost-effectiveness and flexibility in design, improving the harmonization between international regulations/codes, providing better knowledge of the implied structural safety level, and adopting to changes in construction technology [7, 8].

Steel bars and concrete experience mechanical and chemical changes at elevated temperatures. Throughout a fire incident, the concrete mechanical properties, including concrete compressive strength ($f'_{cT}$), tensile strength, and modulus of elasticity, continuously degrade [4]. On the other hand, concrete strains increase during fire exposure [4]. Similarly, for steel, it has been proven through experimental tests that elevated temperatures reduce its yield strength ($f_{yT}$) [9]. The yield strength for steel at ambient temperature ($f_y$) usually corresponds to a strain of 0.20%, whereas, at elevated temperatures the steel tends to yield at 1.00–2.00% strain [10].

Current techniques for the analysis of RC beams during fire exposure can only be conducted at the research level [11]. Finite element modeling (FEM) is proven to be a powerful method to analyze and predict the response of RC structures during fire incidents [5]. Drawbacks of this method include the requirement of a thermal-stress analysis and expertise in the subject area itself. Ellingwood and Lin [5] and Huang and Platten [12] developed finite element modeling software for RC sections exposed to fire. Lie and Celikkod [13] simplified this software for RC columns at elevated temperatures. The developed software is very general and assumes simplified models for material degradation, which make it only valid for a limited number of cases. El-Fitiany and Youssef [3] developed a simplified approach that can efficiently predict
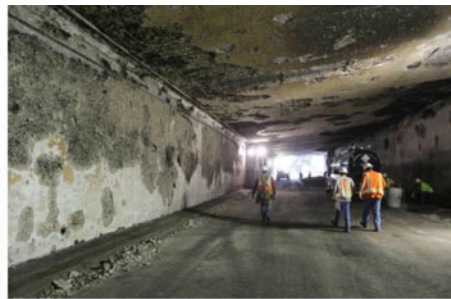


(a) Fire Event                            (b) Post-Fire Condition

**Fig. 1**  Newhall pass tunnel fire event [1]

the moment curvature of RC sections at elevated temperatures, while accurately accounting for the degradation of material properties and the fire-induced strains.

Complexities, associated with analysis of structures during fire exposure, highlighted the need for simplified methods of analysis to satisfy safety. Prescriptive methods meet this need by specifying minimum cross-sectional dimensions and minimum concrete clear cover [5, 12, 13]. This research aims at introducing two structural analysis methods, which facilitate the use of performance-based design of RC beams exposed to fire.

## 2 Analysis of RC Sections at Elevated Temperatures

The sectional analysis approach proposed by El-Fitiany and Youssef [14, 15] is utilized in this paper. Figure 2a shows a section exposed to fire from three faces: left, bottom, and right. Thermal analysis is conducted first. It involves specifying the temperature–time curve for the fire. The temperature distribution within the RC cross section is predicted using the finite difference method [4]. The RC cross section is then divided into horizontal layers. Two average temperatures are defined for each layer: "$T_{th}$", which is the algebraic average of all element's temperatures within the layer and is used for thermal and transient strain calculations [3, 11], and "$T_\sigma$", which is the temperature that produces the same average concrete compressive strength for each layer and is used for strength calculations [11]. "$T_{th}$" is then utilized to evaluate the nonlinear thermal strain, Fig. 2f. To maintain the concept "plane sections remain plane", self-induced stresses, which are in self-equilibrium, are developed. The corresponding self-induced strains are shown in Fig. 2e, and the final unrestrained thermal strain ($\overline{\varepsilon_{th}}$) is shown in Fig. 2f. Mechanical analysis is then conducted. The degradation of the properties of steel and concrete with respect to temperature is calculated using the stress–strain relationships recommended by Youssef and Moftah [4]. For each curvature value, the corresponding moment can be calculated by considering equilibrium of stresses, which allows for the evaluation of the Moment–Curvature ($M$--$\psi$) diagram.

Figure 3a illustrates the typical ($M$--$\psi$) relationship for an RC section exposed to fire for a specific duration [11, 15, 16]. The curvature $\psi$ at any point is composed of a thermal curvature $\psi_i$ and a load-induced curvature $\psi_{cT}$. The nominal moment capacity ($M_n$) represents the flexural capacity for the RC section [4, 11]. At moment $M_{app}$, the secant stiffness ($EI_{eff}$) can be evaluated from the $M$--$\psi$ diagram [11]. The initial flexural stiffness, $E_c I_o$, defines the initial slope of the $M$--$\psi$ diagram. Figure 3b illustrates a simplified version of the $M$--$\psi$ relationship, which is defined based on three points: cracking ($\psi_{cr}$, $M_{cr}$), yielding ($\psi_y$, $M_y$), and ultimate ($\psi_u$, $M_u$).
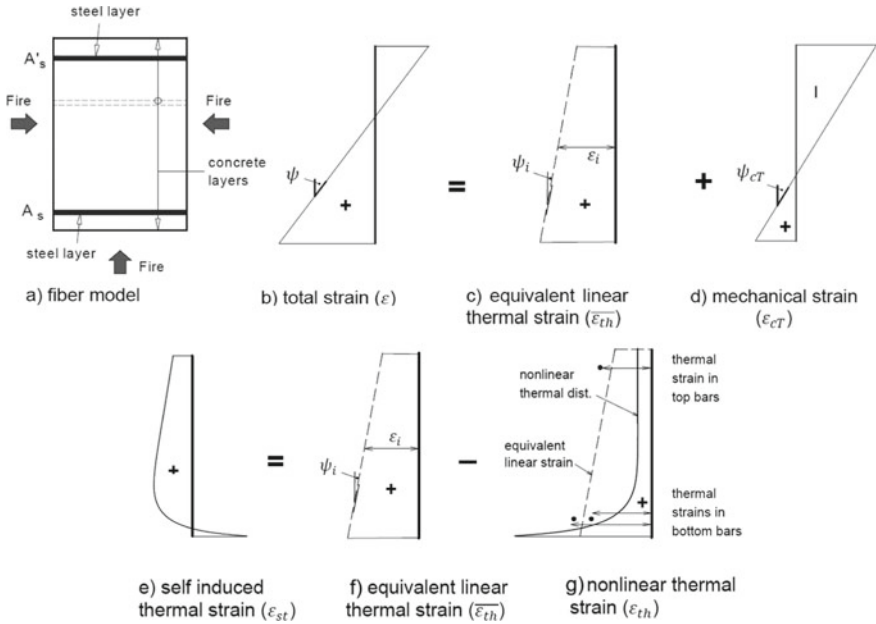
**Fig. 2** Sectional analysis for RC sections exposed to fire on three faces [11]
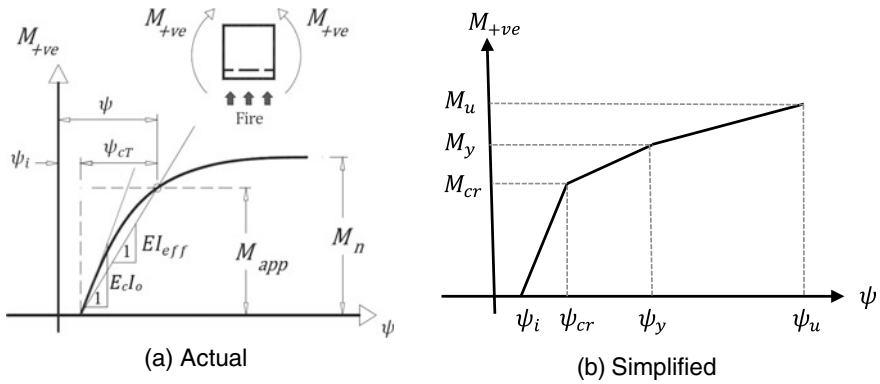


**Fig. 3** RC Sectional moment curvature at elevated temperatures

# 3 Proposed Methodologies for RC Beams at Elevated Temperature

The following sub-sections provide details about the two proposed approaches. The following assumptions were made for the two approaches:

1. Effects of shear, concrete spalling, and slippage between the reinforcing bars and the concrete are not considered.
2. Concrete tensile strength is neglected.
3. Strain hardening of steel bars is ignored.
4. Heat transfer along the longitudinal axis of the beam is neglected [11].
5. Concrete cracking is assumed to have no effect on heat transfer calculations [11].
6. Plane sections are assumed to remain plane [11].
7. The concrete stress–strain curve proposed by Youssef and Moftah [4] is utilized.
8. Terro's model [17] is used to calculate the transient strains.

## 3.1 Secant Stiffness Method

The beam sections behave elastically with an un-cracked flexural stiffness of $(E_c I_o)$ up to a moment value of $M_{cr}$, which corresponds to a curvature of $\psi_{cr}$. The flexural stiffness of the beam elements will then start to reduce, which will lead to moment redistribution if the beam is indeterminant. Iterations will be needed to define the flexural stiffness corresponding to the final moment diagram. These iterations were conducted by utilizing the OAPI programming function in SAP2000 combined with Excel VAB code. The developed program beings by assigning the initial stiffness $E_c I_o$ to all elements. The moment diagram resulting from the applied loads is evaluated using SAP2000. The flexural stiffness for each segment is then evaluated using its average moment value and the moment curvature relationship. This process then continues until the change in the EI value for each of the segments is lower than a predefined tolerance. The following steps can summarize the first proposed approach.

1. Develop trilinear moment–curvature relationships for all sections of the beam at different fire durations.
2. Divide each span of the beam into segments that are 2.50–5.00% of the span and model each segment in SAP2000 as a linear frame element.
3. Assign a flexural stiffness value for these segments equal to $(E_c I_o)$, see Fig. 3.
4. The equivalent linear thermal strain is applied to the model by applying a temperature gradient, which corresponds to the initial axial strain ($\varepsilon_{i,axial}$) and initial curvature ($\psi_i$) for the considered fire duration.
5. SAP2000 model is unlocked, and the loads are incrementally applied to the structure in parallel with the Excel VBA program.

## 3.2 Plastic Hinge Method

The second proposed method starts by using step 1 to step 4 of the first method, the remaining steps are:

1. Define plastic hinges for all segments and assign them the $M$--$\psi$ diagram, which corresponds to the beam section and considered fire duration.
2. The plastic hinge length is set equal to the element length. The plastic hinges can be assigned at: (a) the middle of every segment or (b) at the ends of each segment. Both approaches were examined and found to lead to similar results.
3. An incremental "*Force Controlled*" load case is defined and applied to the beam.

## 4 Case Study—Simply Supported Beam Exposed to Fire

The selected beam for this case study is a simply supported beam (B-124), which was tested by Lin et al. [18]. Figure 4 shows the details of this beam. The yield strength for the #19 longitudinal reinforcing bars is 435.80 MPa. The concrete is fabricated with carbonate aggregate with a maximum concrete compressive strength at ambient temperature of 30 MPa. The initial modulus of elasticity for the concrete was assumed to be 30,000 MPa.
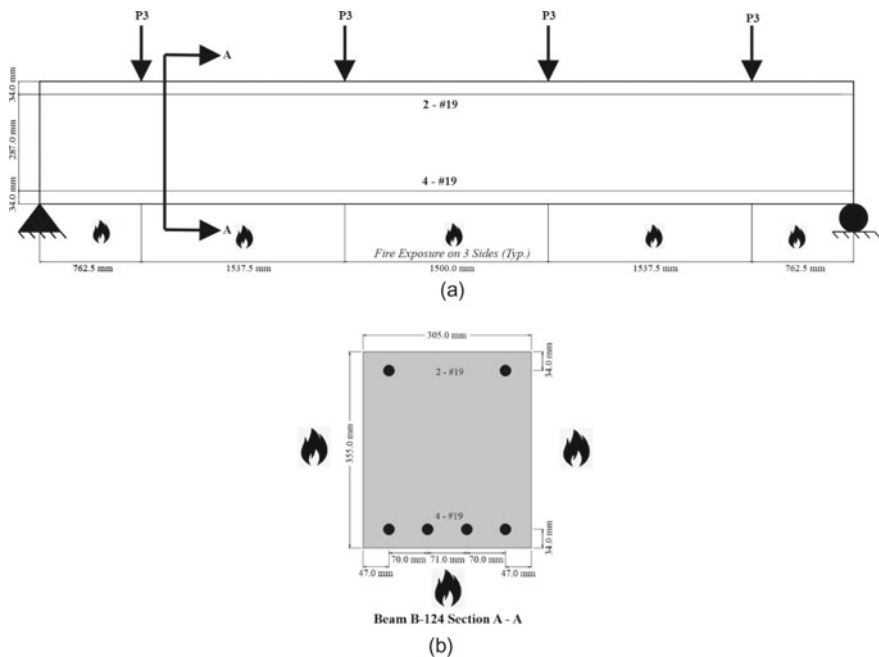


**Fig. 4** Experimental setup for B-124
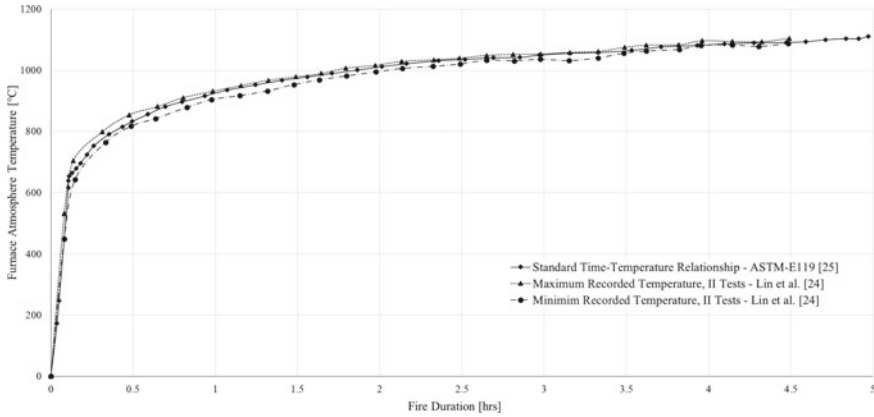
**Fig. 5** B-124 temperature versus time curves

The beam was exposed to fire from three faces: left, bottom, and right. During experimentation, the furnace temperature was programmed to follow the ASTM-E119 [19] temperature–time relationship. Figure 5 shows the maximum and minimum average temperatures obtained during the tests [18], illustrating a nearly exact match with the ASTM-E119 temperature vs. time relationship standard [19].

The moment curvature plots at ambient and elevated temperatures for beam B-124 were evaluated and are shown in Fig. 6. The three points, ($\psi_{cr}$, $M_{cr}$), ($\psi_y$, $M_y$) and ($\psi_u$, $M_u$), defining each diagram were identified and used to develop a trilinear $M$--$\psi$ diagrams, which are shown as red lines in Fig. 6. Values of $\varepsilon_i$ and $\psi_i$ used to determine the equivalent thermal strains are shown in Table 1 considering different fire durations. The corresponding uniform and varying temperatures, which need to be applied to the SAP2000 model to induce these strains, are also shown. They were calculated based on a concrete thermal expansion coefficient ($\alpha_{concrete}$) of 0.000010 °C/m.

A SAP2000 model was constructed for each time increment. The SAP2000 models consisted of a "pin restraint" at the left support and a "roller restraint" at the right support. Beam B-124 was divided into 246 frame segments, and each was assigned its corresponding flexural stiffness ($E_c I_o$). The temperatures corresponding to the thermal strains are then applied to the model. For example, at 2.00 h. of ASTM-E119 fire, a uniform temperature distribution ($\Delta T_U$) of 685.64 °C was assigned as "*Type – Temperature*". Also, the linear temperature distribution ($\Delta T_L$) of 389.72 °C/ m was assigned as: "*Type – Temperature Gradient 3-3*".

Regarding the secant stiffness approach, Table 2 shows the developed Excel spreadsheet, which includes the VBA macro, for 2.00 h ASTM-E119 fire exposure. For each segment, the table shows the values of the EI modifier ($I_{33}$), the EI initial at the considered temperature, and the average moment for the segment. For the first iteration, $I_{33}$ is set equal to 1. The average moments for each segment are then read from SAP2000 analysis and used to find the EI values using the moment curvature diagram. Iterations then continued until the changes in EI values are below
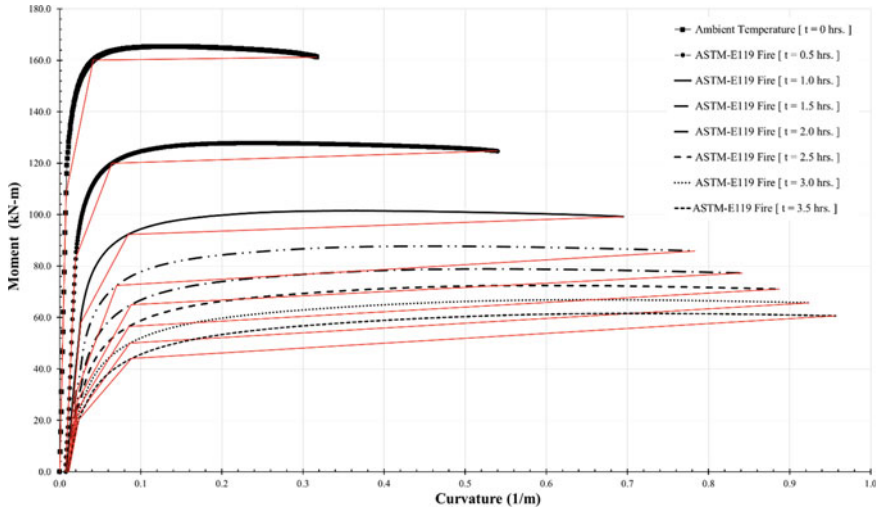
**Fig. 6** B-124 moment—curvature at ambient and elevated temperatures

**Table 1** Thermal strains modeling for B-124

| ASTM-E119 fire duration [h] | Initial axial strain $\left[\frac{mm}{mm}\right]$ $\varepsilon_i$ | Initial curvature $\left[\frac{1}{m}\right]$ $\psi_i$ | Uniform temperature distribution [°C] $\Delta T_U$ | Linear temperature distribution [°C/ m] $\Delta T_L$ |
|---|---|---|---|---|
| 0.0 | 0.0000000 | 0.0000000 | 0.0000 | 0.0000 |
| 0.5 | 0.0024666 | 0.0072725 | 246.66 | 258.17 |
| 1.0 | 0.0046374 | 0.0093892 | 463.75 | 333.32 |
| 1.5 | 0.0059372 | 0.0103790 | 593.72 | 368.45 |
| 2.0 | 0.0068564 | 0.0109780 | 685.64 | 389.72 |
| 2.5 | 0.0075941 | 0.0111640 | 759.41 | 396.32 |
| 3.0 | 0.0082222 | 0.0112380 | 822.22 | 398.95 |
| 3.5 | 0.0087883 | 0.0113600 | 878.83 | 403.28 |

the specified tolerance. As the beam is simply supported, the program converged after two iterations. The applied moment, $M_{app} = 73.12$ kN m at $t = 2.00$ h, is slightly higher than the moment at cracking, $M_{cr} = 73.10$ kN m. Therefore, the EI values for the middle segments were the only values affected, as shown by the yellow high-lighted cells in Table 2. The maximum mid-span deflection at this fire duration was 83.40 mm. This value is having + 16.89% error at as compared to the experimental results by Lin et al. [18].

For the plastic hinge approach, hinges were assigned at the middle of each frame segment. The plastic hinge length was taken equal to the element length. A nonlinear

**Table 2** B-124 Secant stiffness spreadsheet [fire duration = 2.00 h]

| | Iteration (1) | | | | Iteration (2) | | |
|---|---|---|---|---|---|---|---|
| Element No. | Sec. Mod | EI – T = 2.00 h | M − Avg | EI-eff | Sec. Mod | M − Avg | EI-eff |
| (0.025/ 0.0125 m each) | $(I_{33})$ | (SAP2000) (kN/m$^2$) | (kN m) | (M−C) (kN/ m$^2$) | $(I_{33})$ | (kN m) | (M−C) (kN/m$^2$) |
| 108 | 1 | 2613.492063 | 72.92497 | 2613.49206 | 1.00000 | Converged | Converged |
| 109 | 1 | 2613.492063 | 72.94889 | 2613.49206 | 1.00000 | Converged | Converged |
| 110 | 1 | 2613.492063 | 72.97122 | 2613.49206 | 1.00000 | Converged | Converged |
| 111 | 1 | 2613.492063 | 72.99195 | 2613.49206 | 1.00000 | Converged | Converged |
| 112 | 1 | 2613.492063 | 73.01108 | 2613.49206 | 1.00000 | Converged | Converged |
| 113 | 1 | 2613.492063 | 73.02862 | 2613.49206 | 1.00000 | Converged | Converged |
| 114 | 1 | 2613.492063 | 73.04457 | 2613.49206 | 1.00000 | Converged | Converged |
| 115 | 1 | 2613.492063 | 73.05892 | 2613.49206 | 1.00000 | Converged | Converged |
| 116 | 1 | 2613.492063 | 73.07167 | 2613.49206 | 1.00000 | Converged | Converged |
| 117 | 1 | 2613.492063 | 73.08284 | 2613.49206 | 1.00000 | Converged | Converged |
| 118 | 1 | 2613.492063 | 73.09240 | 2613.49206 | 1.00000 | Converged | Converged |
| 119 | 1 | 2613.492063 | 73.10038 | 2605.75978 | 0.99704 | Converged | Converged |
| 120 | 1 | 2613.492063 | 73.10675 | 2598.45840 | 0.99425 | Converged | Converged |
| 121 | 1 | 2613.492063 | 73.11154 | 2580.75869 | 0.98748 | Converged | Converged |
| 122 | 1 | 2613.492063 | 73.11473 | 2575.35295 | 0.98541 | Converged | Converged |
| 123 (mid-span) | 1 | 2613.492063 | 73.11632 | 2568.58459 | 0.98282 | Converged | Converged |
| 124 (mid-span) | 1 | 2613.492063 | 73.11632 | 2568.58459 | 0.98282 | Converged | Converged |
| 125 | 1 | 2613.492063 | 73.11473 | 2575.35295 | 0.98541 | Converged | Converged |
| 126 | 1 | 2613.492063 | 73.11154 | 2580.75869 | 0.98748 | Converged | Converged |
| 127 | 1 | 2613.492063 | 73.10675 | 2598.45840 | 0.99425 | Converged | Converged |
| 128 | 1 | 2613.492063 | 73.10038 | 2605.75978 | 0.99704 | Converged | Converged |
| 129 | 1 | 2613.492063 | 73.09240 | 2613.49206 | 1.00000 | Converged | Converged |
| 130 | 1 | 2613.492063 | 73.08284 | 2613.49206 | 1.00000 | Converged | Converged |
| 131 | 1 | 2613.492063 | 73.07167 | 2613.49206 | 1.00000 | Converged | Converged |
| 132 | 1 | 2613.492063 | 73.05892 | 2613.49206 | 1.00000 | Converged | Converged |
| 133 | 1 | 2613.492063 | 73.04457 | 2613.49206 | 1.00000 | Converged | Converged |
| 134 | 1 | 2613.492063 | 73.02862 | 2613.49206 | 1.00000 | Converged | Converged |
| 135 | 1 | 2613.492063 | 73.01108 | 2613.49206 | 1.00000 | Converged | Converged |
| 136 | 1 | 2613.492063 | 72.99195 | 2613.49206 | 1.00000 | Converged | Converged |
| 137 | 1 | 2613.492063 | 72.97122 | 2613.49206 | 1.00000 | Converged | Converged |
| 138 | 1 | 2613.492063 | 72.94889 | 2613.49206 | 1.00000 | Converged | Converged |

(continued)

**Table 2** (continued)

| | Iteration (1) | | | | Iteration (2) | | |
|---|---|---|---|---|---|---|---|
| Element No. | Sec. Mod | EI $- T =$ 2.00 h | $M -$ Avg | EI-eff | Sec. Mod | $M -$ Avg | EI-eff |
| (0.025/ 0.0125 m each) | ($I_{33}$) | (SAP2000) (kN/m$^2$) | (kN m) | ($M$–$C$) (kN/ m$^2$) | ($I_{33}$) | (kN m) | ($M$–$C$) (kN/m$^2$) |
| 139 | 1 | 2613.492063 | 72.92497 | 2613.49206 | 1.00000 | Converged | Converged |

static load case was then applied with 0.50 kN load increments. The maximum mid-span deflection was found to be 83.40 mm. This deflection has and error of + 4.84% as compared to the experimental results by Lin et al. [18].

Predictions of the secant stiffness approach and the plastic hinge approach were then compared with the experimental results by Lin et al. [18], as shown in Fig. 7. In general, predictions of both methods agree well with the experimental results.
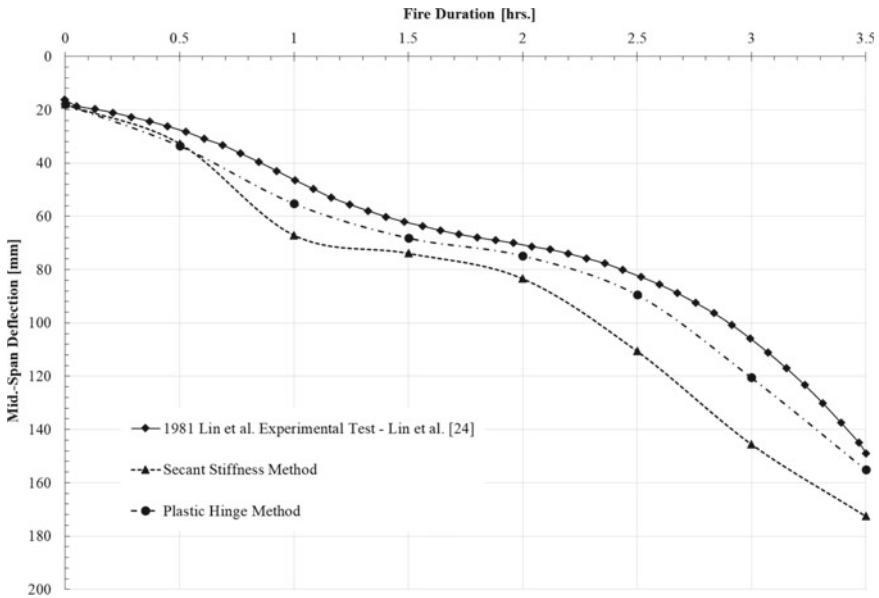


**Fig. 7** Fire duration versus deflection of case study beam

# 5   Summary and Conclusions

To enable the use of performance-based design in structural fire engineering, this paper proposes two simplified methods to analyze RC beams exposed to fire. The secant stiffness and plastic hinge methodologies can be valuable tools for the flexural analysis of RC beams at both ambient and elevated temperatures. The application of both methodologies is explained in view of a simply supported beam exposed to fire. The two methods incorporate the effects of material degradation and thermal strains. They start by applying initial temperatures to the structural model to simulate the effects of the thermal strains. Material degradation is accounted for using the effective flexural strength ($EI_{eff}$). The secant stiffness method then utilizes iterations to evaluate the final $EI_{eff}$ values. On the other hand, the plastic hinge approach models the nonlinearity by utilizing plastic hinges along the beam length. Both methods have shown to provide results with good accuracy as compared to experimental results by others. Future work is required to further validate both methods at ambient and elevated temperatures for beams with varying reinforcement details as well as for framed structures.

# References

1. Gerasimidis S, Civjan S, Menz N (2021) Post-fire damage inspection of concrete structures: final report. In: U. D.- F. Administration (ed) masssDOT Massachusetts Department of Transportation, Massachusetts, The United States of America, p 65. Retrieved 28 Sept 2021, from: https://www.mass.gov/doc/post-fire-damage-inspection-ofconcrete-structures-final-report/download

2. Lie TT (1992) Structural fire protection. ASCE manuals and reports on engineering practice, New York, United States of America, no. 78, p 241

3. El-Fitiany SF, Youssef MA (2009) Assessing the flexural and axial behaviour of reinforced concrete members at elevated temperatures using sectional analysis. Fire Saf J 44(5):691–703

4. Youssef MA, Moftah M (2007) General stress-strain relationship for concrete at elevated temperature. Eng Struct 29(10):2618–2634

5. Ellingwood B, Lin TD (1991) Flexure and shear behaviour of concrete beams during fires. J Struct Eng ASCE 117(2):440–458

6. Cook AC, Vel SS, Johnson SE (2018) Pervasive cracking of heterogeneous brittle materials using a multi-directional smeared crack band model. Int J Mech Sci 149:459–474

7. Branson DE (1965) Instantaneous and time-dependent deflections on simple and continuous reinforced concrete beams. HPR report no. 7, Part 1, Alabama Highway Department, Bureau of Public Roads, pp 1–78

8. ASCE/SEI 7-16 (2016) Minimum design loads and associated criteria for building and other structures. American Society of Civil Engineers & Structural Engineering Institute, Reston, Virginia, United States of America

9. Lie TT (1972) Fire and buildings. Applied Science Publishers Ltd., London

10. Purkiss JA (1996) Fire safety engineering design of structures. Butterworth-Heinemann, Oxford

11. El-Fitiany S (2013) Simplified tools for performance-based design of reinforced concrete frames exposed to fire. PhD thesis, University of Western Ontario.
12. Huang Z, Platten A (1997) Non-linear finite element analysis of planar reinforced concrete members subjected to fire. ACI Struct J 94(3):272–282
13. Lie TT, Celikkod B (1991) Method to calculate the fire resistance of circular reinforced concrete columns. ACI Mater J 88(1):84–91
14. El-Fitiany SF, Youssef MA (2010) A simplified sectional analysis approach for RC elements during fire events. In: 6th International conference on structures in fire, Michigan State University in East Lansing, MI, United States of America, pp 239–246
15. El-Fitiany SF, Youssef MA (2011) Stress block parameters for reinforced concrete beams during fire events, innovations in fire design of concrete structures. ACI SP-279, pp 1–39
16. Kodur VKR, Dwaikat M (2007) Performance-based fire safety design of reinforced concrete beams. J Fire Prot Eng 17(4):293–320
17. Terro MJ (1998) Numerical modeling of the behavior of concrete structures in fire. ACI Struct J 95(2):183–193
18. Lin TD, Gustaferro AH, Abrams MS (1981) Fire endurance of continuous reinforced concrete beam. Portland Cement Association (PCA), Bulletin RD072.01B, Skokie. PCA R&D Ser. No. 1624
19. ASTM-E119 (2020) Standard test methods for fire tests of building construction and materials. ASTM International, West Conshohocken, Pennsylvania, United States

# Structural Specialty: Analysis and Design of Bridges

# Seismic Retrofitting Strategies and Engineering Solutions of Kanaka Creek Bridge on Highway 7

**Lihua Zou, Kai Li, Yuming Ding, and Samson Chan**

**Abstract** Kanaka Creek Bridge carries Highway 7 over Kanaka Creek in Maple Ridge, British Columbia. This paper presents the seismic evaluation and retrofit design adopted for the Kanaka Creek Bridge. Response spectrum analysis was performed under three seismic hazard levels to evaluate seismic performance of the bridge structure. Capacity over demand ratios were employed as main indicators for seismic assessment of critical bridge structural components and connection elements in the seismic load path. Pushover analysis was performed at the abutments to understand the structural performance of the steel pipe piles after yielding. Given the potential of abutment soil liquefaction during seismic events, soil lateral spreading effects and vertical downdrag effects on steel pipe piles were evaluated. After identifying the potential structural failure mechanism, the designers proposed performance-based seismic retrofitting solutions with additional drilled-in steel dowel at bridge abutments and link slabs at bridge deck over piers. This seismic retrofitting scheme provides deck continuity, improves the longitudinal load path and strengthens the connections between superstructure and substructure. The project was completed on time and within the approved budget.

**Keywords** Seismic evaluation · Seismic retrofit · Soil liquefaction · Downdrag · Link slab

L. Zou (✉) · K. Li · Y. Ding · S. Chan
SNC Lavalin Inc., Montreal, Canada
e-mail: Lihua.Zou@snclavalin.com

**Fig. 1** Bird eye view of Kanaka Creek Bridge (left); substructure and steel pipe piles (right)

# 1 Introduction

## 1.1 Bridge Information

Kanaka Creek Bridge carries Highway 7 over Kanaka Creek in Maple Ridge, B.C, with two northbound lanes to Maple Ridge and three southbound lanes to Albion, as shown in Fig. 1 (left photo). Built in 1984, the bridge consists of three 13.8 m long simply-supported spans for a total bridge length of about 42 m. The superstructure consists of twenty-four 600 mm deep BC Ministry of Transportation and Infrastructure (MoTI) prestressed twin cell box stringers joined side-by-side with grouted shear keys. Each pier consists of a conventional concrete pier cap with one row of 305 mm diameter vertical steel pipe piles. There are sixteen and twenty-two steel pipe pile for each abutment and pier respectively, see Fig. 1 (right photo). The steel pipe piles are filled with concrete all the way from the bottom of cap beams down to the riverbed 7 at the piers and only partially for 1.2 m long below the cap beams at the abutments. The rest of the piles below are filled with sand. The bridge structure is in good condition except a few localized concrete delamination in pier caps. Deck expansion joint sealers were pushed out and frayed within the traffic lanes over the piers, and stains on the pier caps indicate water can leak from the deck expansion joint.

## 1.2 Seismic Performance Criteria

The bridge is designated as a Major Route structure as defined in CAN/CSA S6-14 [1] and forms part of the BC MoTI critical route in response to a disaster. The goal of seismic retrofitting for Kanaka Creek bridge is to enhance its seismic performance to meet current design code criteria. Nonetheless, the BC MoTI recognizes this goal may be beyond current funding available. Since the bridge has been in service for more than 35 years, a full retrofit might not provide the best value to the BC MoTI.

**Table 1** Seismic performance criteria options

| Option | Seismic hazard level | Service | Damage | Description of options |
|---|---|---|---|---|
| 1 | 975 years | Service disruption | Extensive damage | Baseline option |
| 2a | 975 years | Life-safety | Probable replacement | Comparison with option 1 |
| 2b | 475 years | Life-safety | Probable replacement | Comparison with option 1 |
| 3 | 2475 years | Life-safety | Probable replacement | Comparison with option 1 |

- Service disruption: The bridge shall be usable for restricted emergency traffic after inspection. The bridge shall be repairable. Repairs to restore the bridge to full service might require bridge closure
- Life-safety: The structure shall not collapse, and it shall be possible to evacuate the bridge safely

The four seismic performance criteria options are listed in Table 1. The damage performance criteria are primarily based on S6-14 [1] and BC Supplement to S6-14 [2], with modifications to address applicable bridge components of the Kanaka Creek Bridge.

## 2 Retrofitting Challenges and Constraints

### 2.1 Existing Bridge Seismic Load Path

The bridge superstructures are simply supported for gravity loads with an expansion joint over the two piers. The steel pipe piles at the abutments are fully embedded into the ground, whereas the pipe piles at the piers have unsupported free length of about 6 m above the riverbed (shown in Fig. 2 Top), which makes the piers relatively flexible and attract less seismic loads. The twin cell box stringers are dowelled to the pier cap at each end with 25 mm diameter rebars as shown Fig. 2 (bottom). These dowels act as horizontal shear connectors between the box stringers and the substructure cap beams, providing the continuous horizontal load transferring mechanism from the deck to the abutments and piers.

In the longitudinal direction, the seismic inertia force on the superstructure is transferred through steel dowels over the piers from one span to the adjacent span, and resisted by the abutments and approach embankment. The condition is analogous to an integral abutment where the girder end diaphragm can push against the approach fill and engage the soil passive resistance. Similarly, in the transverse direction, both abutments and piers would resist lateral loads. The seismic inertia force is transferred by the steel dowels onto the abutments and piers. Wingwalls on abutments will also provide lateral resistance to the superstructure if the steel dowels fail.
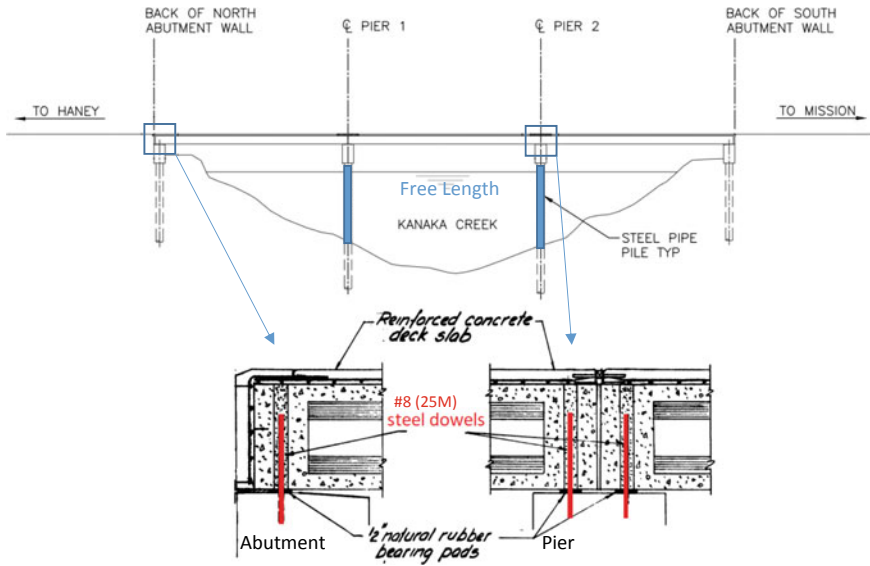
**Fig. 2** Bridge elevation view (top) and dowels connecting girders to abutments and piers (bottom)

## 2.2 Soil Liquefaction

According to the geotechnical investigation report, liquefaction is anticipated at the bridge site for 475-, 975- and 2475-year return period earthquakes. The ground settlement associated with the liquefaction will add downdrag forces in the piles, while the embankment lateral spreading at the two abutments will push against and may damage the piles. The structural integrities of the piles need to be evaluated for both the vertical downdrag and lateral spreading.

## 2.3 Environmental Sensitivity

The bridge is located within identified critical habitat for painted turtle (*Chrysemys picta*), a species listed in the federal Species at Risk Act (SARA). Fourteen fish species are known to be present in Kanaka Creek. Several bat species, all of which are protected under the provincial Wildlife Act and some of which are listed in SARA, may roost in the crevices of the bridge. Nearby, Kanaka Creek Regional Park provides habitat for wildlife and trails for a variety of outdoor experiences. The retrofit design must balance the environmental sensitivities of the site and the potential environmental permits required for retrofit construction and mitigation required.

## 3 Seismic Evaluation Approach

### 3.1 Elastic Dynamic Responses Spectral Analysis

Elastic dynamic response spectral analysis was performed to evaluate the demand and capacity ratio of the structural components located in the critical load path. A 3D finite element analysis model was set-up for the purpose of elastic dynamic analysis (see Fig. 3 left). The superstructure was modelled using shell elements to represent the deck overlay and beam elements to represent box stringers jointed side-by-side with grouted share keys. The superstructure was linked to the abutment and pier caps by elastic link elements. Pile foundations were supported by compliance springs to simulate the soil-structural interaction effects. Effects of abutment backfill on the structural responses was captured by near-field lateral stiffness using Carvajal's equation in CSA S6 [1]. The superstructure is discontinued over the piers due to the existing deck expansion joint (see Fig. 3 right).

The response spectra for earthquake return period of 475, 975 and 2475 years are presented in Fig. 4 based on geotechnical input for site classification.

According to the Caltrans [3] recommendation for existing bridges, the effects of lateral spreading and ground shaking are unlikely to occur simultaneously. Therefore, the results from response spectral analysis do not need to be combined with the effects due to liquefaction. Lateral spreading analysis on piles will be considered separately in the next section.

#### 3.1.1 Pile Foundation Evaluation from Elastic Dynamic Analysis

At the abutments, the lateral seismic responses of the pile foundations primarily occur at the top part and become insignificant below 6 m from the cap beams. The analysis shows that the elastic seismic forces in the piles due to the 475-year and 975-year earthquake are less than the structural capacity of the steel pipe piles in the
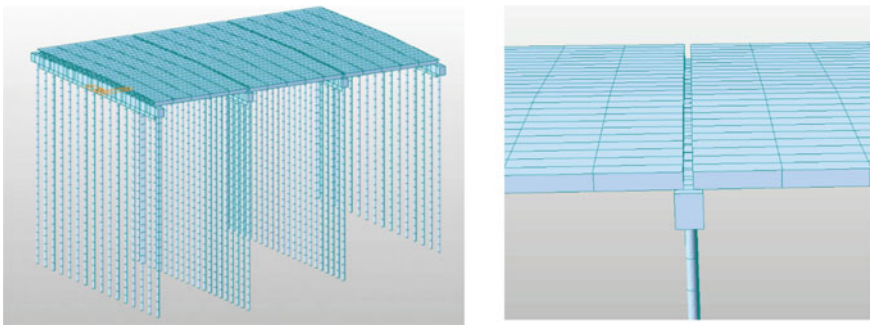


**Fig. 3** Structural analytical model (left) and deck discontinuity over pier (right)

**Fig. 4** Seismic design response spectra
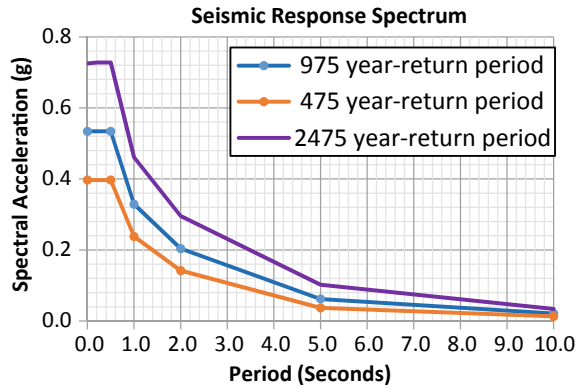


longitudinal direction. In other words, the piles remain elastic under the longitudinal design earthquake. However, in the transverse direction, elastic seismic forces in the piles, particularly at the pile-to-pile cap connection, exceed the structural capacities, meaning the piles will experience plastic deformation. In this case, pushover analysis was performed to verify the displacement capacity of the substructure and foundation in the transverse direction.

At the two piers, piles are quite flexible and attract less seismic lateral loads compared with the abutment piles. The analysis in both longitudinal and transverse directions confirms that all piles remain elastic.

### 3.1.2 Capacity-to-Demand Ratio for Critical Components

According to the existing seismic load path described in Sect. 2.1, critical components for the lateral seismic load transferring include girder-to-cap-beam steel dowels, the abutment and pier cap beams and the pile-to-cap beam connections. The capacity-to-demand ratio of the structural components is summarized in Table 2. A capacity-to-demand ratio greater than 1.0 is considered acceptable. From the table and analysis results, the steel dowel is not structurally adequate because 2475-year seismic event would fail the steel dowel in both longitudinal and transverse directions. The pile cap has sufficient breakout capacity, embedment length and flexural resistance given the greater than 1.0 capacity-to-demand ratios.

**Table 2** Summary of capacity-to-demand ratio

| Structural component | Capacity-to-demand ratio | Remarks |
|---|---|---|
| Steel dowel shear capacity | 0.91 pier/0.75 abutment | 2475-year earthquake |
| Pile-to-pile cap connection | 1.00 | Pile head embedment |
| Pile cap beam | 1.85 | Flexural bending |
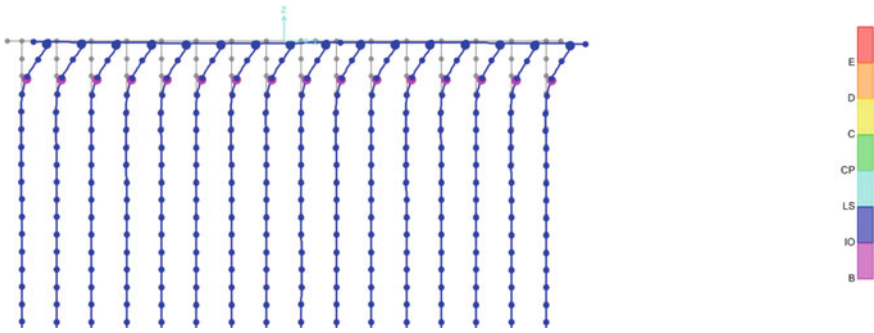
**Fig. 5** Plastic hinge status at displacement demand of 975-year earthquake

## 3.2 Static Pushover Analysis

The static pushover analysis was performed at the abutments to further demonstrate the predicted seismic performance after piles yield due to the displacement demand from the elastic dynamic analysis. It is assumed that plastic hinges may form in the steel pipe piles once the yield strength of the material is exceeded. Plastic hinge properties are assigned to the pile elements in the analysis model.

The abutment frame is pushed slightly to the displacement demand from the response spectral analysis in transverse direction so that the hinge development in the piles can be examined. Figure 5 shows an example of plastic hinge status at the displacement demand of 975-year earthquake. Pushover analysis confirmed that the plastic rotations in the abutments are within the 0.02 radian limit for all performance criteria options. It should be noted that the piles are laterally supported by surrounding soils up to the pier caps at both abutments. Therefore, collapse of the superstructure is unlikely even if the in-ground plastic hinge reaches the rotation limit.

## 3.3 Pile Foundation Assessment Under Soil Liquefaction

According to the geotechnical investigation, liquefaction is anticipated at the bridge site for 475-, 975- and 2475-year return period earthquakes. The embankment lateral spreading at the two abutments will push against the piles and may damage the piles. Ground settlement associated with the liquefaction will impose downdrag forces along the piles. The structural integrities of the piles were evaluated for both lateral spreading and downdrag.

### 3.3.1    Lateral Spreading Assessment

Lateral soil spreading pushes against the steel pipe piles at the abutments and imposes lateral forces to the piles. The effects of lateral spreading on piles were evaluated through a single pile pushover analysis model, incorporating non-linear link elements connecting the pile to the ground. The ground displacement or lateral spreading provided by geotechnical engineer was assigned to the fixed end of the link elements. Plastic hinges were assigned along the length of the pile.

According to the analysis, the piles remain elastic at both abutments at the 475-year earthquake event. However, the bending moment demand in the steel pile exceed its yielding capacity at both 975-year and 2475-year earthquakes. Figure 6 shows multiple plastic hinges are developed along the length of the piles due to lateral spreading up to 0.70 m in the 2475-year earthquake. According to Caltrans Memo 20-15 [4], the crust and liquefied soil are expected to provide lateral support and the damaged steel piles are still able to carry the permanent loads if the drift ratio is less than or equal to 0.20 for steel pipe piles. Based on this, it was found that estimated drift ratio in the steel piles at both level of earthquakes is within the acceptable limit, and the steel pipe piles are considered to have vertical capacity to support the superstructure without collapse.

In addition, lateral soil spreading also impose lateral force in the steel dowels connecting abutment cap beam and superstructure. The evaluation indicates that the lateral force demand in steel dowels exceed their capacity at both 975-year and 2475-year earthquakes, requiring the steel dowels to be retrofitted/strengthen to meet the performance objectives.

### 3.3.2    Axial Pile Capacity Assessment

The steel piles were evaluated for the added downdrag force due to liquefaction. It was found that both geotechnical and structural resistance are adequate for three levels of earthquake events and meet the performance criteria.

## 4    Seismic Retrofitting Solutions

## 4.1    *Retrofitting Solution Discussion*

Conceptual retrofit solutions for all four seismic performance options required by the BC MoTI are discussed below. Based on the seismic evaluation, several retrofit solutions were proposed to achieve better seismic performance with consideration of constructability and cost.
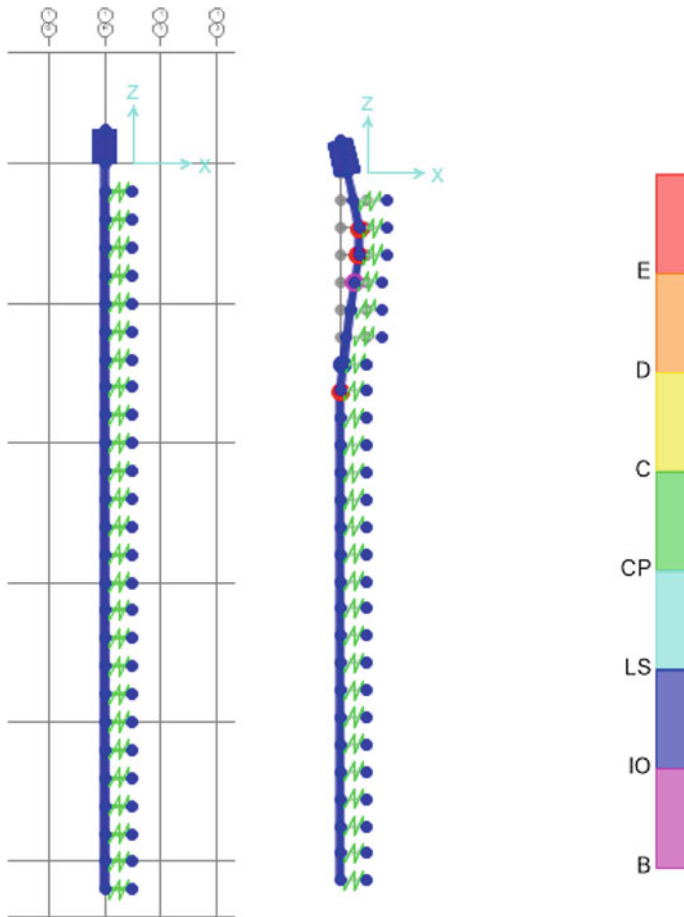
**Fig. 6** Lateral spreading analysis model, deformed shape with formation of plastic hinges

For a 475-year earthquake, under seismic performance criteria Option 2b Life-safety, the expected performance objectives can all be satisfied without seismic retrofit work.

For a 975-year earthquake, either Option 1, Service Disruption (baseline option), or Option 2a Life-safety, the performance objectives of the bridge, except foundation, can be met by strengthening the abutment to superstructure connections in the event of soil liquefaction. The proposed retrofit solutions include:

- At abutments: Add additional dowels by drilling through the end of girders to abutment cap beam; or add concrete back wall and wingwall. The goal is to increase lateral force transferring capacity between the abutments and superstructure.
- At piers: Add additional dowels at the piers to connect girders with pier cap. The goal is to increase lateral force transferring capacity between the piers and

superstructure. Alternatively, replace deck expansion joint by link slabs over the piers. The link slabs provide alternate lateral force transferring path and reduce the force demand in existing steel dowels.

It is important to note that ground improvement is required to achieve seismic performance Option 1. This is due to the excessive horizontal ground movements predicted at both abutments and the required level of foundation performance to satisfy service disruption performance criteria. However, any ground improvement near this bridge is considered costly with significant environmental impact.

For a 2475-year earthquake, under seismic performance criteria Option 3 Life-safety, the same retrofit solutions are required to satisfy this seismic performance.

After comprehensive review, it was concluded that Option 3 for 2475-year Life-safety, performance is the preferred option for the seismic retrofit solution, as it represents the best value for budget among the four seismic performance options required by the BC MoTI. Option 1, with the highest level of seismic performance, will require expensive ground improvements. Option 3 is the second highest level of seismic performance and can be achieved with reasonable amount of construction cost focussed on the bridge deck level. Combining retrofit solutions Option 3, to add dowels at the abutments and to add link slabs at the piers, can provide satisfactory seismic performance with a best value of construction cost. In addition, replacing the expansion joint with concrete link slabs will improve the rideability and minimize water leakage into the bridge substructure below.

## 4.2   Retrofit Design at Abutment—Steel Dowels

The seismic deficiency at both abutments is inadequate shear capacity across the interface between the box girder superstructure and the pile cap-beam substructure, especially in the longitudinal direction. Additional steel dowels are introduced to increase the shear capacity across this interface. The 25 M stainless steel dowel is proposed to be installed at every second box girder as shown in Fig. 7. The proposed doweling position shall not conflict with the existing reinforcing steel and pre-stressing strands based on as-built information. Geometric review of the existing rebars and pre-stressing strands was conducted based on the as-built information. Ground penetration radar is proposed to map the existing rebar and mitigate conflicts during dowel installation.

## 4.3   Retrofit Design Over Pier—Link Slab

The new link slabs were designed for the seismic force extracted from the analysis. Since the new link slabs replace the existing deck expansion joint and create deck continuity longitudinally, the link slab will also subject to forces induced by stringer
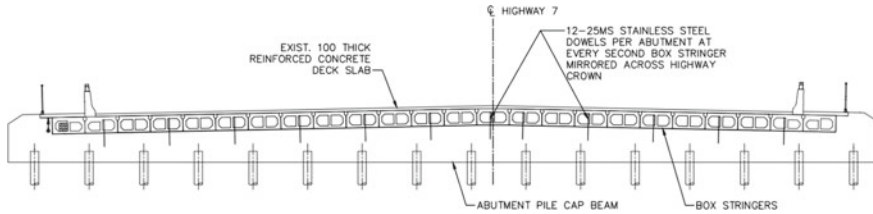
**Fig. 7** Proposed steel dowel location at bridge abutment
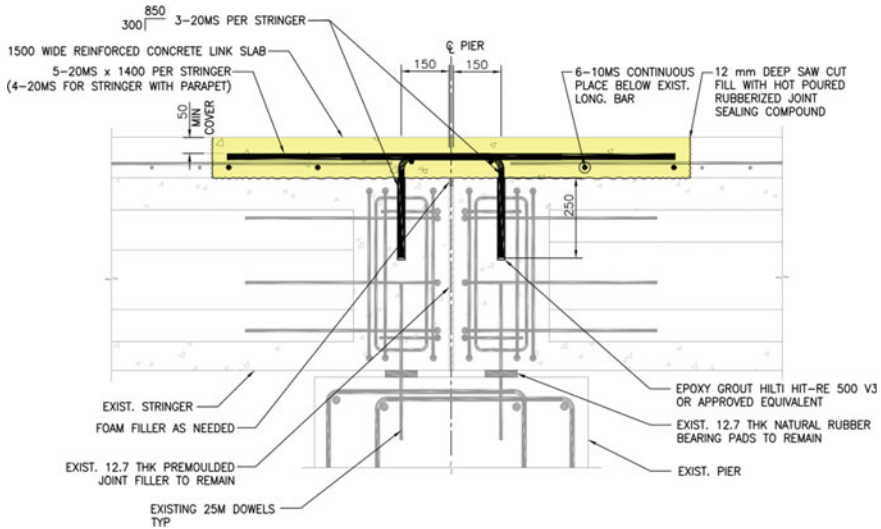


**Fig. 8** Proposed link slab with L-shape rebar embedded in the box stringer

end rotation due to service live load. The reinforcement design includes straight rebar as well as L-shaped rebars that transfers forces between the deck spans on both sides of the piers (see Fig. 8). The link slab construction requires drilling rebar dowels into the existing stringer end diaphragm. To avoid damage to the existing rebar, the stringer ends need to be scanned and all existing rebars shall be identified prior drilling.

## 4.4 Seismic Retrofit Design Achievements

In addition to meet the seismic performance objectives, the recommended seismic retrofit design also has the following benefits:

**Fig. 9** Link slab rebar placement (left), finished link slab open to traffic (middle) and steel dowel drilling at abutment (right)

- The recommended retrofit design scheme requires work primarily on the deck level and does not require work on the substructures in the creek, minimizing environmental impact and the risk of contaminating the creek.
- The retrofit work is a neat solution, requiring dowels and link slabs which are embedded in the deck, and does not alter the existing appearance of the structure.
- The seismic retrofit design allows construction to be done on half width of the bridge at a time, with proper traffic management to ensure traffic flow during the construction period.

## 5 Seismic Retrofit Construction

The seismic retrofit construction occurs in summer of 2021 and was completed within the approved budget. The success of the project is a result of excellent collaboration between BC MoTI, SNC Lavalin design team and the contractor. Figure 9 shows the photos during construction.

## 6 Conclusion

Kanaka Creek Bridge on Highway 7 over Kanaka Creek in Maple Ridge, BC, is designated as a Major Route structure, and forms part of the BC MoTI's critical route in response to a disaster. The seismic retrofit work is required after identifying the structural deficiencies and potential structural failure mechanism. To overcome the retrofitting challenges including the weakness of the existing seismic load path, the potential effects of soil liquefaction and the high environmental sensitivity, SNC Lavalin proposed efficient seismic retrofitting solutions with additional steel dowels at bridge abutment and link slab at bridge deck over piers. The seismic retrofitting

method improves the bridge's seismic performance and provides good value for the BC MoTI. The project was delivered on time and within the budget, and the construction work was completed in the summer of 2021.

# References

1. Canadian Standards Association (CSA) (2014) CSA S6-14 Canadian highway bridge design code, Toronto, Ontario, Canada
2. BC Ministry of Transportation and Infrastructure (BC MoTI) (2016) BC MoTI supplement to S6-14, Victoria, British Columbia, Canada
3. California Department of Transportation (Caltrans) (2016) Seismic Retrofit Guidelines For Bridges in California. Sacramento, California, USA
4. California Department of Transportation (Caltrans) (2017) Lateral spreading analysis for new and existing bridges. Memo to designers, Sacramento, California, USA

# Time-Dependent Probabilistic Analysis of Steel Bridge Brittle Fracture

**Michelle Y. X. Chien, Mohammad Javad Tolou Kian, and Scott Walbridge**

**Abstract**  Brittle fracture is a major concern to structural engineers as it has significant consequences in terms of safety and cost. Although modern day occurrences are rare, it is well known that they can occur without warning and may lead to the sudden closure of a bridge, loss of service, expensive repairs, and/or loss of property or life. In Canada, steel bridge fracture is a more significant concern due to the harsh climate, which, if the toughness properties are improperly specified, could put many steels on the lower shelf of the toughness-temperature curve. In the existing CSA standards, design against brittle fracture solely depends on the temperature of the location of interest, and other factors impacting fracture, such as stress level and plate thickness are currently neglected. A previous comparison of brittle fracture design provisions around the world revealed that more sophisticated approaches have been developed in terms of modelling and understanding brittle fracture than the ones currently in use in North America. One of these procedures is the fracture mechanics method in the European EN 1993-1-10 standard. This paper briefly describes this method and then shows how it can be implemented in a probabilistic framework, using historical temperature and truck data to determine the failure probability with respect to temperature and traffic loadings fluctuating on a time scale throughout the year.

**Keywords**  Steel bridge · Brittle fracture · Probabilistic analysis · Monteo carlo simulation

## 1   Introduction

As Europe made significant advances in the sophistication of the tools available for modelling and understanding brittle fracture, adaptation of similar approaches in North America to assess these situations may be of interest. However, it is worth

M. Y. X. Chien (✉) · M. J. Tolou Kian · S. Walbridge
University of Waterloo, Waterloo, Canada
e-mail: michelle.chien@uwaterloo.ca

noting that in no part of the world has a rigorous probabilistic assessment been performed to assess the reliability levels being achieved, using the various existing brittle fracture design methods. A previous study presented in CSCE 2021 [2] entailed varying the input parameters of the Eurocode fracture mechanics method to study the effects on the probability of failure and the sensitivity of these parameters. In this study, it was observed that the probability of failure by brittle fracture is affected by the crack size, load level, and plate thickness. With the simplistic model employed, the research only considered bias factors for the variability of the master curve and temperature correction on the resistance side of the limit state function. It was noted that more statistical variables should have been considered for a more comprehensive representation of the limit state function, and additionally that the treatment of traffic and temperature in the analysis (assuming the highest load occurs at the lowest temperature) was highly simplistic and overly conservative.

This paper is a continuation of the previous research. It entails casting the problem as a time-dependent reliability problem, with extreme traffic and temperature loads fluctuating over time. In order to model this fluctuation realistically, hourly temperature data was gathered from Environment Canada for a specific location (Waterloo, ON), and truck load data for Ontario highways gathered by the Ontario Ministry of Transportation (MTO) was used to model realistic load fluctuation over time.

## 2 Literature Review

### 2.1 Previous Work on Code Calibration and Reliability Analysis

A study done by Kennedy and Gad Aly in 1980 remains among the notable for making recommendations to the limit states design provisions in CSA S16. Geometric and material properties for W shapes, including their mean and coefficient of variation (COV) for steel columns and beams, were calibrated based on measurements and coupon tests from Canadian mills [6]. The study related the tested capacity to the theoretical capacity to establish a professional ratio, $\rho$, which was then used along with the coefficient of variation, $V$ in an exponential model to determine a performance factor, $\phi$ for steels, which captures the uncertainty in the prediction of structural resistance. It was found in this study that the performance factor of 0.9 previously established for steels in S16 was conservative except for the cases of buckling for W and HSS shapes, where a lower performance factor was recommended.

Two decades later in 2002, Schmidt and Bartlett reassessed the resistance factors from the Kennedy and Gad Aly study. One of the key driving factors for this reassessment was that the manufacturer that supplied materials for the previous study had ceased to produce W shapes in Canada, and it was beneficial to perform a reassessment from steels manufactured in Canada and imported from the United States to obtain a more comprehensive dataset. Additionally, the resistance factors from CSA

S16 needed to be reviewed, as over the decades, there had been changes in the industry and how steels are manufactured and undergo quality control procedures. New material tests were performed, and data was gathered based on steel from numerous major steel suppliers across North America. Yield strength, ultimate strength, and modulus of elasticity were investigated. In this study, it was found that the ratio of actual to nominal dimensions had improved (i.e. a reduction in the scatter was observed), and the yield strength bias factor increased and COV decreased for HSS and WWF shapes compared with the Kennedy and Gad Aly study. However, statistical parameters were slightly worse for W shapes [7]. It is noteworthy that in both aforementioned studies, brittle fracture was not assessed as a mode of failure.

In more recent developments, a fatigue reliability analysis was performed on steel-concrete composite shear connectors, as it was known that welded shear studs tend to fail at low loads due to fatigue. Sjaarda et al. [9] performed tests on composite beams with welded shear studs and bolted shear connectors for static and fatigue performance tests. It was found that the bolted detail was superior in terms of fatigue resistance than the welded studs. Additionally, finite element models were produced to verify the results of the laboratory testing [10].

Based on these studies and others like them, it can be concluded that a significant amount of work has been done to assess reliability with respect to failure modes other than brittle fracture. A major motivation for the work presented in this paper is the need to improve the state of knowledge in this area.

## 2.2 Eurocode Fracture Mechanics: Stress Intensity Factor Based Method

The Eurocode EN 1993-1-10 contains two methods of assessing brittle fracture, a simplified method using design tables, and a fracture mechanics method. The latter is the method that is presented in a plane strain stress intensity factor framework, expressed in terms of $K$-values, and is the method that is modified and applied in the subsequent probabilistic analysis. The basis of the fracture mechanics method is setting a requirement such that the toughness of the material ($K_{\text{Mat,d}}$, which is a function of temperature) must be greater than the applied effects (expressed as the stress intensity factor, $K_{\text{appl,d}}$). This is shown in Eq. 1 [8].

$$K_{\text{appl,d}}^* = \frac{K_{\text{appl,d}}}{k_{R6} - \rho} \leq 20 + \left[70\left\{\text{EXP}\left(\frac{T_{\text{Ed}} - [T_{27\,\text{J}} - 18\,^\circ\text{C}] + \Delta T_{\text{R}}}{52}\right)\right\} + 10\right] \cdot \left(\frac{25}{b_{\text{eff}}}\right)^{1/4} \quad (1)$$

The original master curve, which forms the basis of this method and is used to calculate the material resistance $K_{\text{mat,d}}$, was developed in Wallin [15]. This is shown on the right-hand side of the inequality, which is representative of material behaviour on the lower shelf of the toughness-temperature transition curve. It is noted that the Wallin master curve cannot be used to predict material upper shelf behaviour.

It is well known that the fracture behaviour of steel is dependent on temperature. $T_{\text{Ed}}$, the reference temperature, is a key component in calculating $K_{\text{mat,d}}$, the material toughness. It is dependent on the lowest daily air temperature of the location of interest, plus any applicable temperature corrections for applied stresses, radiation losses, strain rate, and cold forming. Not all of the adjustments are required and may be designated as zero in some cases. It is also noted that many of these effects are not directly measured in units of temperature, but are converted to a temperature equivalent to be used in the master curve to capture their impacts on the material's resistance to brittle fracture.

The left-hand side of the inequality is calculated using Eq. 2, representing the applied effects acting on the component.

$$K_{\text{appl,d}}^{*} = \frac{K_{\text{appl,d}}}{k_{R6} - \rho} = \frac{\sigma_{\text{Ed}}\sqrt{\pi \cdot a_{\text{d}}} \cdot Y \cdot M_{\text{k}}}{k_{R6} - \rho} \left[\text{MPa} \sqrt{\text{m}}\right] \tag{2}$$

It is observed in Eq. 2 that the general form equation for plane strain stress intensity factor, $K = \sigma \sqrt{(\pi a)}$ is present, where $K$ is a measure of crack driving force and is dependent on stress from external loads and crack size. This equation is then modified by several correction factors, for $Y$ and $M_{\text{k}}$ for crack shape, $k_{R6}$ for plasticity, and $\rho$ for local residual stresses. Similar to the right-hand side of the inequality, not all of these correction factors are applicable, and some may be taken as unity or zero depending on the case.

A more comprehensive description of the parameters that are used in Eqs. 1 and 2 have been described in the Eurocode background document EUR 23010 EN [8]. Further diagrams and tables on the determination of the correction factors are also detailed in this source.

## 2.3 Monte Carlo Simulation

Monte Carlo simulation (MCS) is now a common tool for scientific research, which uses random sampling and statistical evaluation where individual trials are independent of each other. One of the major benefits is that it can be used for circumstances in which sampling would be too time-consuming or impractical. However, it also has downsides which include requiring a significant amount of computing energy, and the model used can have imperfections or the code may have bugs [3]. Thus, spending much effort in correctly setting up the models, input parameters, and debugging is crucial.

A common use of this is random sampling from a PDF function, or alternately, using the inverse CDF method. The basis of the process is summarized in the following:

1. Sample a value between 0 and 1 to represent a probability, which can then be correlated back to the value of the parameter based on the distribution type and its mean and COV (statistical parameters).
2. Evaluate the model.
3. Tally the simulation results.
4. Re-evaluate $n$ times.
5. Construct histogram and determine probability of failure.

It is noted that the larger number of trials, the more accurate the simulation is.

## 3 Time-Dependent Probabilistic Analysis

### 3.1 Methodology

The original contribution presented in this paper involves a first attempt to develop automated code, to perform reliability analysis on a time-dependent scale with traffic load and temperature fluctuating hourly. MATLAB was the primary programme used to generate the code, and it was verified by generating an equivalent procedure in Excel to evaluate the accuracy of the results generated.

The main procedure of the code is as follows:

1. Generate $K_{mat}$ cumulative distribution functions (CDFs) for different deterministic temperatures in Waterloo, ON (range between $-55$ and $+55$ °C, using 10 °C increments).
2. Generate $K_{appld}$ CDFs for different deterministic stress levels for highway bridge traffic in Waterloo, ON (ranging between 1 and 400 MPa, with 50 MPa increments).
3. Using historical temperature data between 2003 and 2021 for Waterloo, Ontario, a random number is generated to select the year. In essence, this means assuming temperature is stationary and can be modelled by assuming the hourly temperature history in a given year can only follow one of the annual histories between 2003 and 2021 for which hourly temperature data is available*. (*Note: This is an approximation made in this paper. An alternative would be to employ a probabilistic temperature model wherein the hourly temperature fluctuates realistically but randomly throughout the year.)
4. For each time step (hour) in a one-year simulation:

   (a) Pick random number $X_1$ to get trial value for resistance uncertainty associated with the bridge detail of interest. Obtain the temperature for the time step from the annual temperature history that was randomly selected in Step
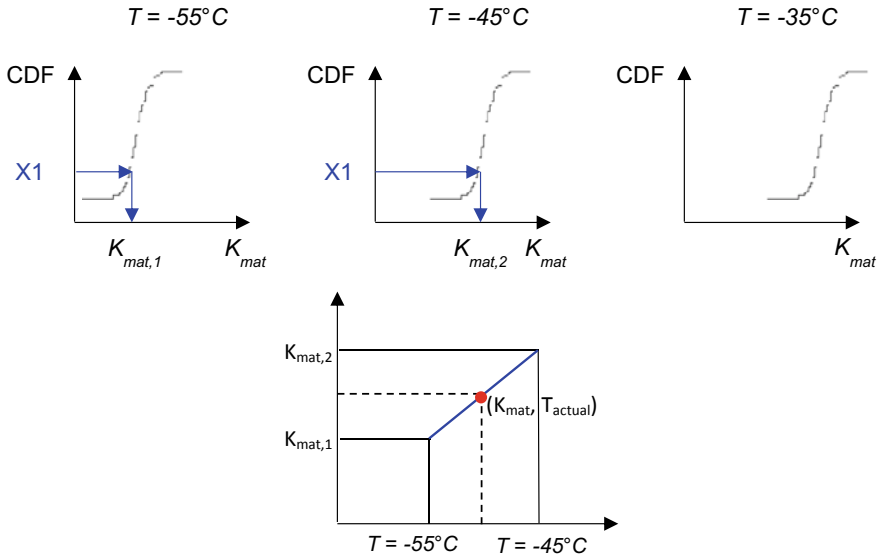
**Fig. 1** Sample schematic of determining $K_{mat}$

3, and determine $K_{mat}$ for that time step by linearly interpolating between the two $K_{mat}$ CDFs generated in Step 1 bounding the actual temperature at the time step with ordinate $= X_1$. This is illustrated in Fig. 1.

(b) Pick random number $X_2$ to get trial value for the "solicitation" uncertainty associated with the bridge detail of interest**. (**Note: $X_2$ accounts for the bridge detail parameters such as the actual weld geometry, crack size, etc., which affects $K_{appld}$ but does not vary from one hour to the next over the year.) Using historical traffic data for Ontario, obtain the stress level for the time step*** and determine $K_{appld}$ by interpolating between the two $K_{appld}$ CDFs generated in Step 2 bounding the actual stress level at the time step with ordinate $= X_2$. This is illustrated in Fig. 2. (***Note: there are several ways this can be done: (1) a similar approach to the one use for temperature can be used for a site where hourly peak stress or load levels are available for an entire year, or (2) peak hourly stress or load level due to traffic can be simulated using a truck weight or load effect histogram, fitted to a continuous distribution, which can then be sampled using extreme value statistics theory in a manner similar to the one used to calibrate the live load factors in CSA S6 (see Agarwal et al. [1]) and MCS sampling with an additional parameter ($X_3$) which accounts for hourly fluctuation in the live load. For the current paper, the latter approach was employed.)

(c) Determine whether failure occurs by checking if $K_{appld} > K_{mat}$ for that time step. If yes, record failure, and if not, go to the next time step.
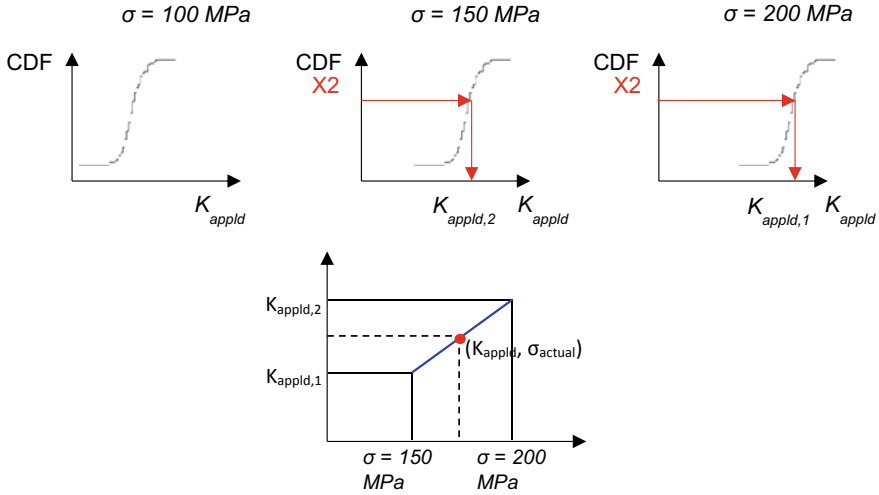
**Fig. 2** Sample schematic of determining $K_{appld}$

5. This process is repeated for each time step (hour) throughout the year to determine if the detail will fail within the year or not for the one-year simulation or "trial".

Repeat for many one-year simulations to determine the annual probability of failure of the detail.

## 3.2 Distribution Types and Statistical Parameters

In the previous probabilistic implementation of the Eurocode fracture mechanics method [2], bias factors were applied to the deterministic input parameters, typically in the form of "multipliers", which are defined to account for the various sources of uncertainty associated with each parameter. It was identified that further investigation was needed to capture the uncertainties in the other parameters embedded in the Eurocode fracture mechanics method, including some theoretical functions for parameters, such as the correction factors on the action side of the limit states function.

Table 1 summarizes the updated bias factors and their distribution type, mean, and coefficient of variation (COV), with sources given where appropriate. The new parameters that are being treated probabilistically from the previous study are indicated by $Z_{11}$ through $Z_{15}$ in Table 1.

Concerning parameters in Table 1, the following additional information is noteworthy:

- In this table, $t$ is the girder flange thickness, flange stresses at the location of interest are denoted with a $\sigma$, and $H_w$ and $W_w$ are the weld height and width associated

**Table 1** Statistical variables and distribution types

| $Z$ | Modifies | Z_bar | $V_Z$ ($\sigma_Z$) | Distribution | Source |
|---|---|---|---|---|---|
| $Z_1$ | $F_y$ | 1.101 | 0.0915 | Lognormal | [6] |
| $Z_2$ | $T$ | 1.02 | 0.0120 | Lognormal | [7] |
| $Z_3$ | $T_{md}$ | 1 | 0.0574 | Normal | 50-year service period, calculated based on Agarwal et al. [1] |
| $Z_4$ | $A$ | 1 | 0.2000 | Lognormal | Vojdani et al. [11] |
| $Z_5$ | $\sigma_{D1}$ | 1.03 | 0.0800 | Lognormal | [1] |
| $Z_6$ | $\sigma_{LL}$ | 1.5228 | 0.0304 | Lognormal | 50-year service period, calculated based on Agarwal et al. [1] |
| $Z_7$ | $H_w$ | 1 | 0.1600 | Lognormal | [5] |
| $Z_8$ | $W_w$ | 1 | 0.1600 | Lognormal | [5] |
| $Z_9$ | Master curve | 1 | 0.2500 | Lognormal | [10] |
| $Z_{10}$ | CVN to SIF conversion | 0 | (13 °C) | Normal | [10] |
| $Z_{11}$ | $\sigma_s$ | 1 | 0.25 | Lognormal | [15] |
| $Z_{12}$ | $\sigma_{Ed}$ | 0.93 | 0.12 | Lognormal | [1] |
| $Z_{13}$ | $a/c$ ratio (crack shape) | 1 | 0.32 | Lognormal | Walbridge and Nussbaumer [14] |
| $Z_{14}$ | $M_k$ | 1 | 0.05 | Lognormal | [15] |
| $Z_{15}$ | SCF | 1 | 0.04 | Lognormal | [15] |

with the critical detail. The $a/c$ ratio is the ratio between the crack depth to width, $M_k$ is a weld toe correction factor, and SCF is the stress concentration factor relating the local stress to the far field (nominal) stress.

- The weld parameters are used to calculate the local stress intensity factor, using equations not shown here for reasons of brevity. To apply these equations, a weld detail geometry must be assumed. In the calibration of the Eurocode simplified method, a longitudinal plate attachment detail was assumed, due to its relative severity. Thus, a similar detail is assumed in the current analysis.
- Uncertainties in the brittle fracture resistance can be captured using bias factors $Z_9$ and $Z_{10}$, to consider uncertainties associated with the brittle fracture "master curve" formula and the notch to fracture toughness conversion, based on raw test data in EUR 23510 EN [10]. Steel grades S355, S460, S690, and S890 were tested (and are reported in this reference) and the lower shelf of the master curve was fitted. Since the master curve was fitted to the average of the data, $Z_9$ is a multiplicative factor to model the scatter of test data for the fitting, which has been assigned a mean of 1.0 and standard deviation of 25%. Using this value, a close replication of the 50, 95, and 5% failure probability curves for the raw test data from Fig. 2.7 in EUR 23510 EN [10] could be produced. Note that the 20 MPa $\sqrt{m}$ term is not multiplied by $Z_9$ because $K = 20$ MPa $\sqrt{m}$ represents

the lower bound for cleavage fracture in steels, and therefore the stress intensity factor cannot be lower than that value [14].

- $Z_{10}$ is an additive factor to model the scatter in test data correlating the fracture mechanics transition temperature, $T_{100}$, to the Charpy test temperature, $T_{27\,J}$. which has been assigned a mean of 0 and standard deviation of 0.13 (the transition temperature standard deviation is 13 °C), based on the raw data from Fig. 2.8 in EUR 23510 EN [10].

## 3.3 Results

PDFs and CDFs generated for $K_{mat}$, which capture uncertainty in the toughness of the material (Step 1 in the procedure described in Sect. 3.1 of this paper), are shown in Fig. 3. The CDFs are used to for the interpolation of a value of $K_{mat}$ based on the hourly temperature (Step 4a).

The PDFs and CDFs for $K_{appld}$, which capture uncertainty in the stress intensity factor due to applied loads (Step 2 in the procedure described in Sect. 3.1 of this paper), are shown in Fig. 4. The CDFs are used for the interpolation of $K_{appld}$ based on the maximum hourly live load (Step 4b).

Figure 5 shows examples of the fluctuation of the minimum hourly temperature (left) and maximum live stress (right) for each time step, in one-hour increments, over the course of one year (8760 h). The input hourly temperature was calculated by random sampling from a normal distribution of recorded temperatures at each hour between 2003 and 2021. Furthermore, the live load was sampled at each hour using the Gumbel distribution method discussed in Agarwal et al. [1].
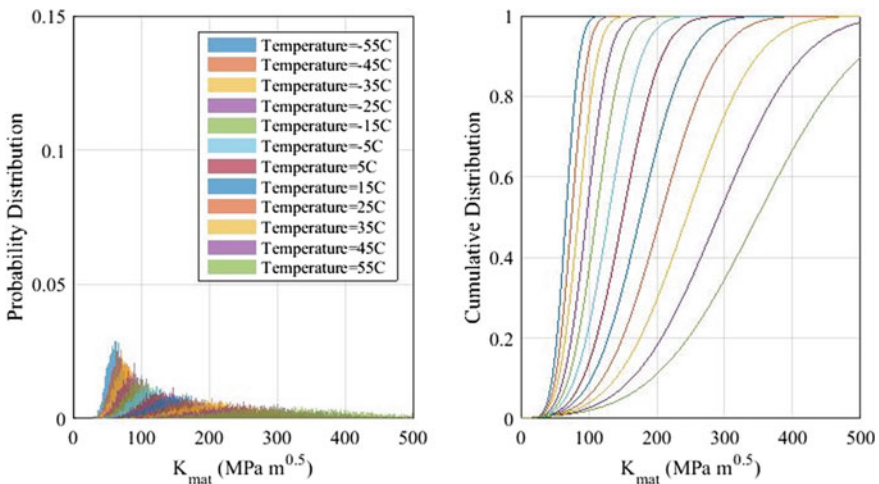


Fig. 3 Probability and cumulative distributions for $K_{mat}$
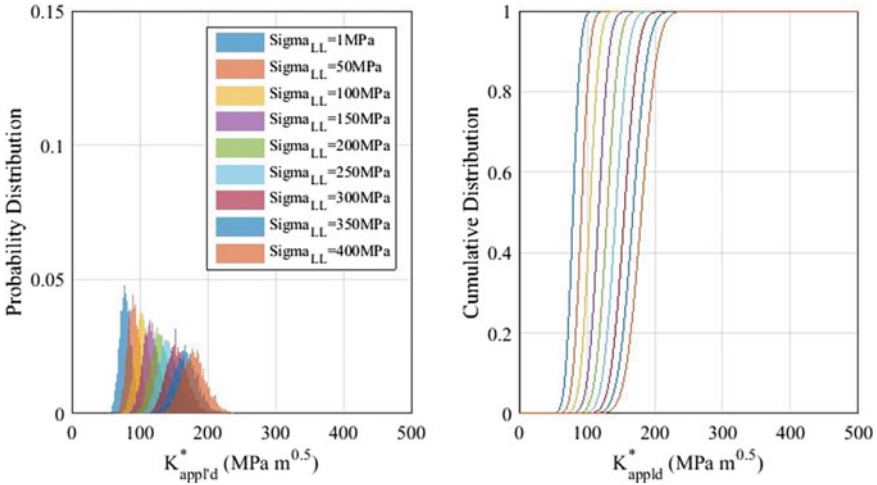
**Fig. 4** Probability and cumulative distributions for $K_{appld}$
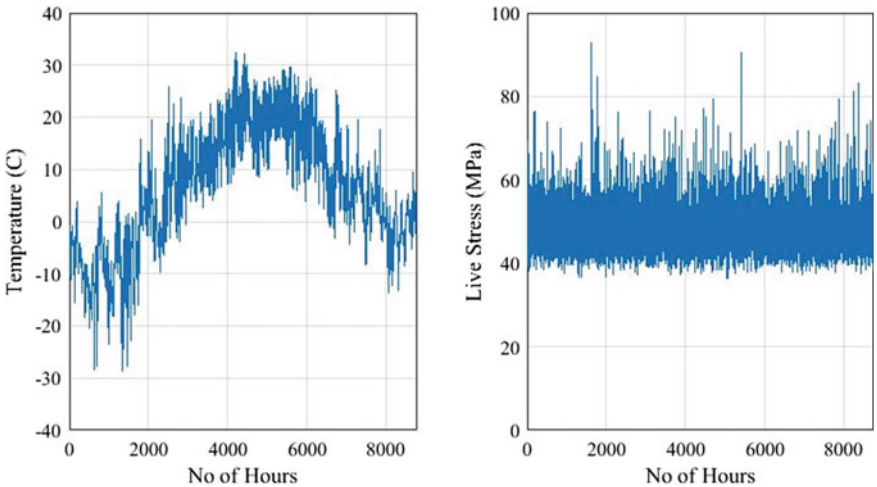


**Fig. 5** Sample temperature and live load stress fluctuations over one year

Figure 6 shows the results of a set of MCS trials simulating 100 years of service, for an assumed crack size of 22 mm. In each time step, 10,000 MCS trials are run, repeated for 8760 h (time steps) per year, which is then repeated for 100 service years. It is observed that the annual probability of failure is converging on approximately 0.45 after the first few years.
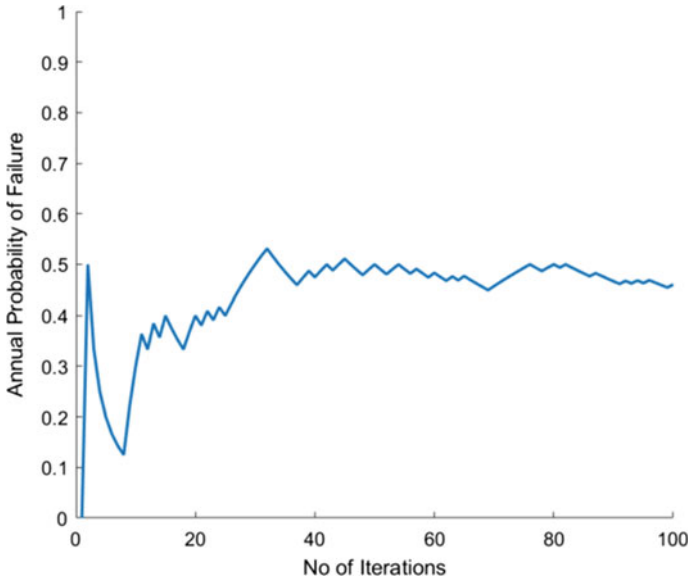
**Fig. 6** Annual probability of failure over number of iterations (100 years)

## 4 Conclusions and Future Work

This paper describes a time-dependent probabilistic analysis performed for Waterloo, ON, to determine the yearly probability of failure. For an assumed crack size of 22 mm in this study, and the resulting yearly probability of failure appeared to plateau at around 0.45. It is noted that while this probability of failure is quite high, it is associated with a fairly large crack size. The development of this MATLAB code means that further time-dependent analyses can be done for different input parameters, such as different crack sizes, weld configurations, temperature data, and traffic data from other locations.

An important next step of the work will be to apply the code in different scenarios in future studies. Effects of different factors on the probability of failure may be beneficial to making recommendations to future iterations of CSA S6, the Canadian Highway Bridge Design Code.

# References

1. Agarwal A, Au A, Becker D, Foschi R, Gagnon D, Hong H et al (2007) Calibration report for CAN/CSA-S6-06 Canadian highway bridge design code
2. Chien MY, Walbridge S, Kühn B (2021) Probabilistic analysis of brittle fracture design code provisions for steel bridges. In: CSCE 2021 annual conference. Springer Nature, Virtual
3. Harrison RL (2010) Introduction To monte carlo simulation. In: AIP conference proceedings. American Institute of Physics, pp 17–21
4. Kala Z, Melcher J, Puklický L (2009) Material and geometrical characteristics of structural steels based on statistical analysis of metallurgical products. J Civ Eng Manag 15(3):299–307
5. Kennedy D, Baker K (1984) Resistance factors for steel highway bridges. Can J Civ Eng 11:324–334
6. Kennedy D, Gad Aly M (1980) Limit states design of steel structures—performance factors. Can J Civ Eng 45–77
7. Schmidt B, Bartlett F (2002) Review of resistance factor for steel: data collection. Can J Civ Eng 29:98–108
8. Sedlacek G, Feldmann M, Kühn B, Tschickardt D, Höhler S, Müller C, Hensen W, Stranghöner N, Dahl W, Langenberg P, Münstermann S, Brozetti J, Raoul J, Pope R, Bijlaard F (2008) EUR 23510 EN: commentary and worked examples to EN 1993-1-10 "material toughness and through thickness properties" and other toughness oriented rules in EN 1993. European Commission Joint Research Centre. European Communities, Luxembourg
9. Sjaarda M, Porter T, West JS, Walbridge S (2017) Fatigue behavior of welded shear studs in precast composite beams. J Bridge Eng 22(11)
10. Sjaarda M, Walbridge S, West JS (2018) Assessment of shear connection through composite beam modeling. Transp Res Rec 2672(41):177–185
11. Vojdani A, Farrahia G, Mehmanparast A, Wang B (2018) Probabilistic assessment of creep-fatigue crack propagation in austenitic stainless steel cracked plates. Eng Fract Mech 200:50–63
12. Walbridge S (2005) A probabilistic study of fatigue in post-weld treated tubular bridge structures. EPFL, Lausanne
13. Wallin K (1992) Guidelines for deriving fracture toughness estimates from normal and miniature size Charpy-V specimen data. Rakenteiden Mekaniikka (J Struct Mech) 25:24–40
14. Walbridge S, Nussbaumer A (2007) A probabilistic model for determining the effect of post-weld treatment on the fatigue performance of tubular bridge joints. Int J Fatigue 29(3) 516–532
15. Wallin K (1998) Master curve analysis of ductile to brittle transition region fracture toughness round robin data: the "EURO" fracture toughness curve. Technical Research Centre of Finland (VTT)

# Unified Seismic Capacity Limit State Models of Reinforced Concrete Bridge Columns

**Yihan Shao and Yazhou Xie**

**Abstract** Highway bridges are crucial links in the transportation network. Their seismic damage and failure have caused casualties, economic losses, and long-term impacts to the affected regions. To date, extensive studies have made efforts to understand the seismic behavior of bridge column, given its vulnerability in affecting seismic fragility/risk assessment of existing bridges and performance-based seismic design (PBSD) of new bridges. In both regards, seismic capacity models constitute an essential element indicating various limit state criteria under increasing levels of earthquake loading. The capacity models of reinforced concrete (RC) columns describe discrete observable material behaviors as damage states, which are further quantified into numerical limit states through various engineering demand parameters (EDPs), including drift ratio, displacement ductility, curvature ductility, and local strains of longitudinal steel, and unconfined and confined concrete. Despite abundant publications, research findings by using various types of EDPs are often scattered and sometimes conflicting, thereby preventing a direct comparison toward a unified column capacity model. Also, different limit state models have been found when the same EDP is used. Such inconsistency motivates the current study to develop a unified column capacity model, where the benchmark case is considered for the modern-designed circular RC columns with ductile seismic behaviors. In doing so, a comprehensive literature review is carried out to synthesize different RC column capacity models used by both researchers and practitioners. Furthermore, cyclic pushover analyses are conducted to convert these models into those used by a shared EDP type—the maximum local strains of concrete and steel. As such, a unified set of capacity models will be developed by incorporating all sources of variations embedded in the literature. The developed model will be the first-of-its-kind and will lay a solid foundation for stakeholders to conduct more reliable seismic fragility/risk assessment of existing bridges and PBSD of new bridges.

**Keywords** Seismic capacity · Damage state · Unified limit state model · Bridge column · Literature review · Cyclic pushover analysis

Y. Shao · Y. Xie (✉)

Department of Civil Engineering, McGill University, Montreal, QC H3A 0C3, Canada
e-mail: tim.xie@mcgill.ca

# 1  Introduction

As crucial links in the transportation network, highway bridges are essential to ensure traffic mobility and timely emergency response after extreme events. Bridges' seismic vulnerability has been well recognized during previous earthquakes, including the 1994 Northridge earthquake [6] and the 2010 Chile earthquake [24, 33], etc. Reconnaissance reports for these earthquakes also reveal that the column is the most vulnerable component in a bridge system. The bridge column has become a subject of significant interest for seismic fragility assessment and PBSD.

Both fragility assessment and PBSD require a proper definition of column capacity models. The limit state (LS) values of column capacity are typically obtained through a physics-based prescriptive approach [30] or a judgment-based descriptive approach [20]. In particular, the prescriptive approach develops the column LS models using the damage data from past earthquakes and experimental studies [4]. Although several experimental tests have been carried out in the past, comprehensive reports presenting detailed measurements of columns under different levels of visual damage are scarce [47], and certain parameters of interest are not always accessible [49].

Researchers and practitioners also lack consensus on the definition of column damage states [1]. For example, the damage state of concrete spalling is referred to as the onset of spalling in some studies [8, 19, 28], but a certain spalling height or pattern in other studies [10, 23]. In addition, this challenge is aggravated by recognizing the variety of EDPs used in the literature to quantify the column LS values. These include component-level EDPs such as drift ratio and displacement ductility, section-based EDP such as curvature ductility, and strain-based EDPs that quantify the column behavior at the material level. Even under the same damage level for the same EDP, uncertainties in column specimens and loading protocols, as well as measurement limitations and errors, have also led to inconsistent LS models. For example, the concrete cover compressive strain for the damage state of concrete spalling shows a considerable spread from 0.002 to 0.018 in the literature [19, 28].

Such inconsistencies motivate the current study to develop a uniform set of column capacity LS models. Numerical simulations supported by high-fidelity finite-element modeling are adopted herein. They can capture realistic seismic behaviors of bridge columns, interconnect different types of EDPs (e.g., drift ratio to displacement ductility to material strains), and take into account all sources of uncertainties. As shown in Fig. 1, a multi-step workflow is utilized to develop the proposed unified capacity LS model. First, different capacity models are reviewed from the literature for modern-designed circular RC columns. These capacity LS models are found to be defined through displacement ductility ($\mu_\Delta$), curvature ductility ($\mu_\varphi$), drift ratio ($\Delta/H$), and material strains ($\varepsilon$). To examine the consistency among the LS models defined by these EDPs, cyclic pushover analyses are conducted in OpenSees [32] to transform the lognormal (LN) medians of different EDPs into their equivalent $\varepsilon$ values (e.g., drift ratio at moderate damage to its corresponding maximum steel strain). As such, all different capacity models in the literature are converted using
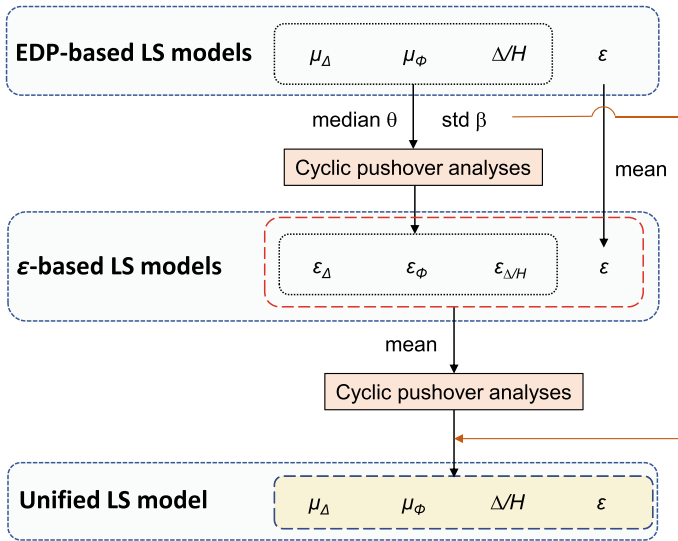
**Fig. 1** Schematic flowchart for developing the unified capacity LS model of column

the same EDP, which further enables comparison and determination of the median ($\theta$) and dispersion ($\beta$) of the unified capacity model.

# 2 Existing Seismic Capacity Limit State Models of Bridge Columns

## 2.1 Definition of Column Damage States

Investigation of seismic capacity models starts with defining the expected degree of observed damage under different damage states (DSs), such as slight, moderate, extensive, and complete [2, 15]. Such DS definitions for bridge columns are summarized in Table 1, where differences emerge across the literature because of the embedded variances in objectives and needs. For example, Ramanathan [40] proposed the column capacity models based on repair strategies from the California Department of Transportation, whereas those established by CSA S6-14 [12] considered bridge operational functionality, traffic volume restriction, and bridge collapse prohibition. To develop a unified capacity model, this study considers those different definitions given in Table 1 and proposes one set of converged DS descriptions. In particular, slight damage ($DS_1$) corresponds to reinforcement yielding and minor concrete cracking and spalling. Moderate damage ($DS_2$) exhibits propagated spalling, more significant numbers and widths of the cracks, and substantial rebar yielding. Extensive damage ($DS_3$) denotes exposed reinforcement and core, and degraded

column strength without a complete collapse. Under the complete damage state
($DS_4$), column strength is significantly degraded; core concrete starts to crush due to
severe reinforcement buckling and fracturing, and immediate column failure should
be expected. Based on these DS definitions, the following sections provide a litera-
ture review on previous experimental results that quantify different DSs into the LS
thresholds using different types of EDPs, including $\mu_\Delta$, $\mu_\varphi$, $\Delta/H$, and $\varepsilon$.

**Table 1** Different definitions of column DS models

| Reference | Slight ($DS_1$) | Moderate ($DS_2$) | Extensive ($DS_3$) | Complete ($DS_4$) |
|---|---|---|---|---|
| Dutta and Mander [13] | Cracking; spalling | Loss of anchorage | Incipient column collapse | Column collapse |
| FEMA [15] | Minor cracking and spalling at hinges | Moderate cracking; spalling of column | Column degrading without collapse | Column collapse |
| Hose and Seible [18] | Cracking and yielding | Initiation of local mechanism | Full development of local mechanism | Strength degradation |
| Hose et al. [19] | Onset of cracks | Theoretical first yield of longitudinal rebar | Onset of concrete spalling | Crushing of core concrete |
| Hwang et al. [21] | Reinforcement yielding | Concrete cracking | Concrete spalling | Reinforcement buckling |
| Nielson [34] | Minor spalling of cover concrete | Moderate cracking and spalling of cover concrete | Degradation without collapse | Collapse |
| Li et al. [29] | Column yielding | Maximum strength | 20% strength degradation | 80% strength degradation |
| CSA S6-14 [12] | Bridge shall remain elastic | Possible occurrence of inelastic behavior | Spalling of concrete; core concrete shall not crush | Extensive distortion of column; collapse not allowed |
| BC MoTI [7] | No concrete spalling; residual crack width not exceeding 1 mm | Reinforcement not exceeding half of the buckling strain limit | Core concrete not exceeding 80% crushing strain; no reinforcement buckling | Core concrete not crushing; reinforcement not fracturing |
| Ramanathan [40] | Minor cracking | Spalling of cover concrete | Exposed core; confinement yielding | Rebar buckling; large drift; core crushing |
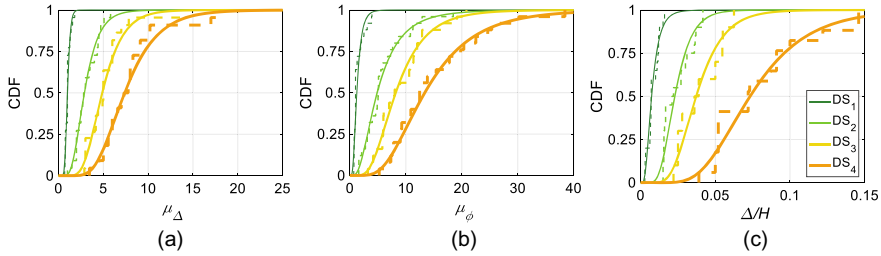
**Fig. 2** Empirical and fitted CDFs of LS models based on **a** $\mu_\Delta$, **b** $\mu_\varphi$, and **c** $\Delta/H$

## 2.2 Capacity LS Models Based on Displacement Ductility, $\mu_\Delta$

Relevant studies that use $\mu_\Delta$ as the EDP for defining capacity LS models are listed in Table 8 in the Appendix. The LS value from each experimental test is further synthesized in Fig. 2a using the cumulative distribution function (CDF), whereas its lognormal fit is also provided in the same figure. It is noted that Fig. 2a also includes the LS model results for post-1971 circular columns summarized by Mangalathu [31]. Despite merely considering circular bridge columns designed after 1971, Fig. 2a still features a wide range of CDF distributions. A closer look at all previous experimental studies indicates significant variances in column dimension, scaling factor, loading protocol, material property, design detail (e.g., reinforcement ratio), axial load ratio, etc. For instance, the steel yielding strength ($f_y$) and concrete compressive strength ($f_c'$) span from 414 MPa to 607 MPa, and 29 MPa to 49 MPa, respectively, whereas the longitudinal reinforcement ratio ($\rho_l$) varies from 1.7 to 5.4%. As a result, $\mu_\Delta$ varies between 0.7 to 1.6, 1.0 to 5.8, 2.9 to 13.8, and 3.5 to 18.0, for $DS_1$, $DS_2$, $DS_3$, and $DS_4$, respectively.

## 2.3 Capacity LS Models Based on Curvature Ductility, $\mu_\varphi$

The $\mu_\varphi$-based capacity LS models documented in various studies are summarized in Table 9, and their CDFs, along with the lognormal fits, are illustrated in Fig. 2b. Note that Fig. 2b also includes datasets provided by Mangalathu [31], Nielson [34], Padgett [36], Ramanathan et al. [41], and Ramanathan [40]. In general, the use of curvature ductility as the EDP shows broader ranges of CDF distributions, which might attribute to the additional challenge and error of measuring the columns' curvatures in plastic regions. In particular, the $\mu_\varphi$ values span from 0.7 to 3.9, 1.6 to 18.5, 3.2 to 20.8, and 5.2 to 38.4, for $DS_1$, $DS_2$, $DS_3$, and $DS_4$, respectively.

## 2.4 Capacity LS Models Based on Drift Ratio, Δ/H

Table 10 summarizes the values of $\Delta/H$ under each LS documented in relevant studies, and Fig. 2c illustrates the empirical and fitted CDFs of the data. Uncertainties in the $\Delta/H$-based LS data result from different attributes in column geometry, material property, design detail, DS definition, etc. For example, $f_y$ and $f_c'$ in the tested column specimens vary from 414 MPa to 607 MPa and 27.6 MPa to 51.8 MPa, respectively, while $\rho_l$ and the transverse reinforcement ratio ($\rho_s$) range from 0.75% to 2.8% and 0.35% to 1.2%, respectively. As mentioned, the relevant literature also exhibits uncertainty in defining the DSs. For instance, $DS_1$ corresponds to a certain level of cracking in Calderone et al. [10], spalling initiation in Dutta and Mander [13] and Kim and Shinozuka [25], while rebar yielding in other studies [3, 18, 28]. As a result, $\Delta/H$-based LS models differ from 0.003 to 0.16, 0.015 to 0.042, 0.022 to 0.063, and 0.039 to 0.15, for $DS_1$ to $DS_4$, respectively.

## 2.5 Capacity LS Models Based on Material Strains, ε

Few studies exist to define LS models based on material strains, as extracting the local strains of longitudinal steel ($\varepsilon_s$), unconfined cover ($\varepsilon_c$), and confined core concrete ($\varepsilon_{cc}$) is not always feasible for a seismically damaged bridge column. Table 2 summarizes the existing LS models defined by material strains from CSA S6-14 [12], BC MoTI supplement [7], and Hose and Seible [18]. It is noted that CSA S6-14 [12] and BC MoTI supplement [7] have more conservative DS descriptions, where the complete collapse of bridge columns is prohibited from a design perspective. As a result, Table 2 lists the rearranged thresholds for different material strains, being consistent with the converged DS descriptions.

## 2.6 Consistency Across Different Types of EDPs

It remains unclear whether the LS models defined by each type of EDP are consistent with each other. To this end, cyclic pushover analyses are utilized to convert the $\mu_\Delta$, $\mu_\varphi$, and $\Delta/H$-based LS models into the equivalent material strains (Fig. 1). In particular, the fitted CDF curves shown in Fig. 2 are used to extract the corresponding lognormal median values, being fed into the numerical models for computing the corresponding material strains. Model consistency is then examined by comparing these equivalent material strains with the mean values of strain-based LS models listed in Table 2. Table 3 lists the lognormal median values extracted from Fig. 2 and the mean values from Table 2.

**Table 2** Summary of capacity LS models based on $\varepsilon$

| Reference | Material | Slight (DS$_1$) | Moderate (DS$_2$) | Extensive (DS$_3$) | Complete (DS$_4$) |
|---|---|---|---|---|---|
| Hose and Seible [18] | Steel | 0.005 | 0.019 | 0.048 | 0.063 |
| | Cover concrete | − 0.0032 | − 0.01 | * | * |
| | Core concrete | * | * | − 0.027 | − 0.036 |
| CSA S6-14 [12] | Steel | $\varepsilon_y$[c] | 0.015 | 0.050 | NS[a] |
| | Cover concrete | − 0.004 | NS | * | * |
| | Core concrete | * | * | $\varepsilon_{cu}$ | NS |
| BC MoTI [7] | Steel | 0.010 | 0.025 | 0.050 | 0.075 (0.060)[d] |
| | Cover concrete | − 0.006 | NS | * | * |
| | Core concrete | * | * | $0.8\varepsilon_{cu}$[b] | $\varepsilon_{cu}$ |

[a]NS: not specified; [b]$\varepsilon_{cu}$: ultimate strain of core concrete; [c]$\varepsilon_y$: yielding strain of reinforcing steel; [d]0.075 is for 30 M or smaller, and 0.060 is for 35 M or larger; *: not applicable

**Table 3** Median and mean capacity LS models used for examining across-EDP consistency

| EDP | | Slight (DS$_1$) | Moderate (DS$_2$) | Extensive (DS$_3$) | Complete (DS$_4$) |
|---|---|---|---|---|---|
| $\mu_\Delta$ | | 1.0 | 2.9 | 4.9 | 7.4 |
| $\mu_\varphi$ | | 1.2 | 4.9 | 8.2 | 13.4 |
| $\Delta/H$ (%) | | 0.73 | 2.3 | 3.7 | 7.3 |
| $\varepsilon$ | $\varepsilon_s$ | 0.0058 | 0.020 | 0.049 | 0.069 |
| | $\varepsilon_c$ | − 0.0044 | − 0.010 | * | * |
| | $\varepsilon_{cc}$ | * | * | − 0.022 | − 0.029 |

*: not applicable

# 3 Numerical Modeling, Cyclic Pushover Analyses, and Yielding Displacement

Cyclic pushover analyses are conducted in OpenSees [32]. As illustrated in Fig. 3a and b, the RC column is modeled using fiber-discretized force-based elements along with a zero-length section element to account for the strain-penetration effect at the bottom of the column. Specifically, the *Concrete02* material [48] is used to simulate both cover and core concrete. The confined concrete strength induced by the effective lateral confining stresses is given by Chang and Mander [11]. Moreover,

the *hysteretic* material simulates the longitudinal reinforcement accounting for reinforcement rupture and buckling. In particular, steel's ultimate strength to yielding strength ratio ($f_u/f_y$) is taken as 1.5, per the recommendations by Bozorgzadeh et al. [9, 39]. The *MinMax* material is wrapped around the *hysteretic* material to simulate the fracture behavior of the reinforcement. This study sets the maximum fracture strain to be 0.2, which lies within the range of fracture strain revealed by various coupon test results [5, 37, 39, 43]. Additionally, the buckling behavior is incorporated in the compression side of the steel, where the model proposed by Zong et al. [50] is adopted. The schematic plots of the constitutive models used for both types of material are illustrated in Fig. 3c, d. Also, the column model takes into account the strain localization issue by introducing a plastic hinge region at the bottom.

As shown in Fig. 4, this study adopts the cyclic loading protocol proposed by Goodnight et al. [16] for the cyclic pushover analyses. The load history begins with elastic cycles until the first rebar yield—$f_y$, and is followed by nonlinear cycles that reach different levels of displacement ductility, $\mu_\Delta$. Note that the high $\mu_\Delta$ levels (i.e., $\mu_\Delta = 15$ and 20) are used for the column to experience a complete failure.

A critical parameter in the pushover analyses lies in the column's yielding displacement, $\Delta_y$. The existing literature has shown different preferences in defining the yielding displacement. For example, some studies consider $\Delta_y$ to be the displacement corresponding to the yielding of the first rebar or the outermost rebar [3, 22, 46].
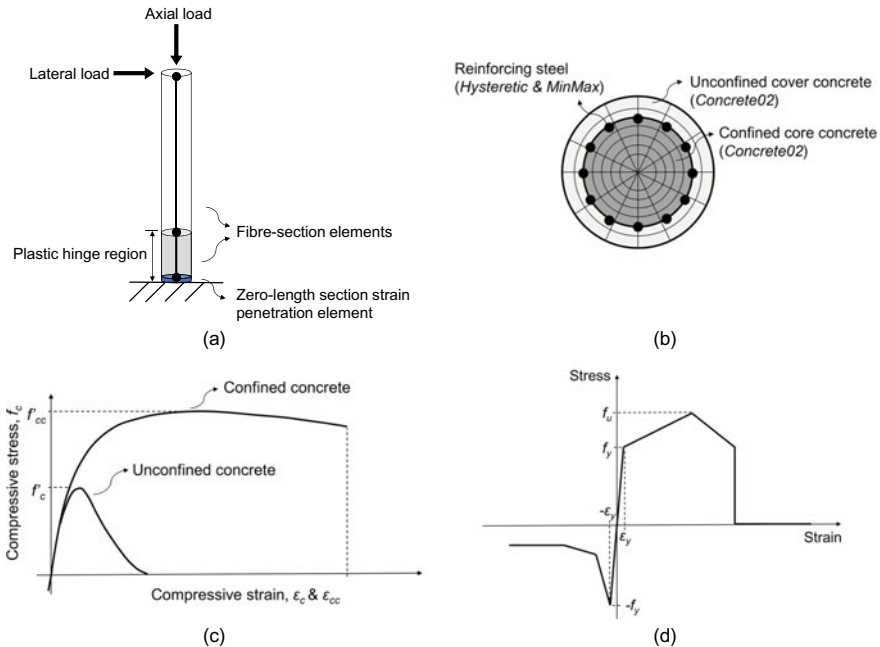


**Fig. 3** Numerical modeling scheme considered in this study: **a** nonlinear elements; **b** fiber-base cross section; **c** concrete material model; **d** steel material model

**Fig. 4** Loading history of the cyclic pushover analyses
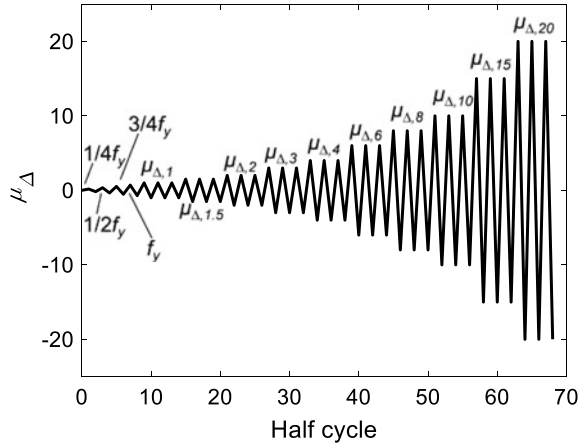


To capture the continuous stiffness change due to progressive yielding of several steel rebars in the circular column, FEMA [15] treats $\Delta_y$ as the displacement point at significant yielding of the column, such as when half of the rebars have yielded. In other studies, $\Delta_y$ is estimated by using an equivalent bi-linear force–displacement relationship [29, 38, 49]. $\Delta_y$ has also been estimated as the displacement when the moment demand equals the nominal moment capacity of the cross section [10, 16, 18, 26].

The locations of $\Delta_y$ determined through the abovementioned approaches are labeled in a monotonic pushover curve, shown in Fig. 5. It has been observed that, among the approaches that incorporate the continuous change of column stiffness, the bi-linear model and the moment factor, respectively, provide the highest and the lowest estimates on $\Delta_y$, while the point where half of the rebars have yielded lies between them. Thus, this study refers $\Delta_y$ to the point where half of the rebars have yielded for its reasonable approximation.

**Fig. 5** Identifications of column's yielding displacement, $\Delta_y$
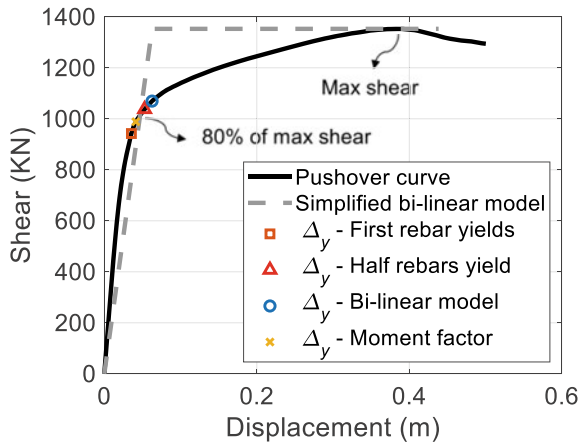
# 4    Developing Unified Seismic Capacity Limit State Models

This study focuses on post-1971, circular RC columns designed for California bridges. As listed in Table 4, these columns vary in geometric parameters and design details [31]. Their corresponding distributions are used to generate random numerical simulations in OpenSees. In addition, a few assumptions are made during the simulations, including: (1) #8 longitudinal rebars and #4 spirals are used in all column samples; (2) a clear cover of 30 mm is applied in all columns; (3) both longitudinal and transverse reinforcements in a column share the same $f_y$; and (4) the axial load is estimated to be 10% of the column's capacity.

The Latin hypercube sampling process is used to randomly generate 80 stochastic realizations for the cyclic pushover analyses, whereas an example of the column hysteretic response is presented in Fig. 6a. The cyclic response of the column is monitored numerically through different EDPs, including the displacements at end nodes, the curvature at the bottom section, and maximum material strains throughout the column. As such, a cross-EDP mapping is established to intercorrelate $\mu_\Delta$, $\mu_\varphi$, and $\Delta/H$ with the corresponding equivalent axial strains in longitudinal steel, cover concrete, and core concrete at every loading step. For a given median LS value defined through $\mu_\Delta$, $\mu_\varphi$, and $\Delta/H$ in Table 3, the pushover analyses provide stochastic distributions of the equivalent material strains through 80 analysis scenarios. One example is shown in Fig. 6b for the equivalent strains of the longitudinal steel at $\mu_\Delta$ equals 1.0 (DS$_1$), 2.9 (DS$_2$), 4.9 (DS$_3$), and 7.4 (DS$_4$), respectively. The empirical CDFs shown in Fig. 6b are further fitted as lognormal distributions to obtain the corresponding median and standard deviation. It is noted that the standard deviation represents $\mu_\Delta$-conditional uncertainties stemming from material properties, column dimensions,

**Table 4** Input parameters and their distributions for the nonlinear pushover analyses

| Parameter | Distribution ($\mu$, $\sigma$)[a] | Lower bound | Upper bound |
|---|---|---|---|
| $D$ (m) | Mixed LN (1.62, 0.21)[b] | 1.22 | 2.74 |
| $H$ (m) | Mixed LN (7.10, 0.15)[b] | 5.18 | 11.0 |
| $f_c{}'$ (MPa) | Normal (31.4, 3.9) | 23.6 | 39.1 |
| $f_y$ (MPa) | Normal (476, 38) | 400 | 552 |
| $\rho_l$ (%) | Uniform (2.00, 0.33) | 1.0 | 3.0 |
| $\rho_s$ (%) | Uniform (0.85, 0.070) | 0.4 | 1.3 |

[a]Median ($\mu$) and standard deviation ($\sigma$) are shown in the parentheses following each distribution
[b]Column diameter ($D$) and height ($H$) feature a mixed combination of different lognormal (LN) distributions

and design details in the numerical modeling. Conversely, the lognormal medians of the equivalent material strains can be synthesized across different EDPs ($\mu_\Delta$, $\mu_\varphi$, $\Delta/H$, and $\varepsilon$ in Table 3) to check the consistency in the LS model quantification. Table 5 lists the equivalent median strain values, where subscripts s, c, and cc denote steel, cover concrete, and core concrete, respectively, and $\Delta$, $\varphi$, $\Delta/H$, and $\varepsilon$ represent that the strain values are conditional to the given displacement ductility ($\mu_\Delta$), curvature ductility ($\mu_\varphi$), drift ratio ($\Delta/H$), and material strain ($\varepsilon$) in Table 3, respectively. It is observed that (1) the LS model defined by drift ratio gives the maximum equivalent steel strains, $\varepsilon_{s,\Delta/H}$; (2) displacement ductility- and curvature ductility-based LS models provide comparable steel strains between $\varepsilon_{s,\Delta}$ and $\varepsilon_{s,\varphi}$; and (3) strain-based LS model shows a conservative estimate on the steel strain capacity, $\varepsilon_{s,\varepsilon}$. The equivalent concrete strains show a consistent trend, where the drift ratio-based model shows large equivalent strains (i.e., $\varepsilon_{c,\Delta/H}$ and $\varepsilon_{cc,\Delta/H}$) and displacement ductility- and curvature ductility-based LS models exhibit comparable concrete strains. However, the strain-based LS model tends to overestimate the concrete strains on $\varepsilon_{c,\varepsilon}$ and $\varepsilon_{cc,\varepsilon}$.

The unified capacity LS models are developed by first taking the mean values of the equivalent strain limits computed from different sources. These mean values are listed in Table 5 with a subscript of *unified*. Because local axial strains are in general difficult to measure, this study further leverages the abovementioned 80 pushover analyses to relate them back to the equivalent $\mu_\Delta$, $\mu_\varphi$, and $\Delta/H$ values. Namely, CDF functions are developed for $\mu_\Delta$, $\mu_\varphi$, and $\Delta/H$ under each unified LS strain value given in Table 5. As shown in Fig. 7, the empirical CDF curves can be further fitted as lognormal functions to identify the median and standard deviation. It is worth mentioning that the standard deviations shown in Fig. 7 are still conditional to the given LS thresholds and, therefore, cannot capture all different sources of uncertainties. However, the associated lognormal medians ($\theta$) are adopted for constituting the final unified LS model. These median values are summarized in Table 6.
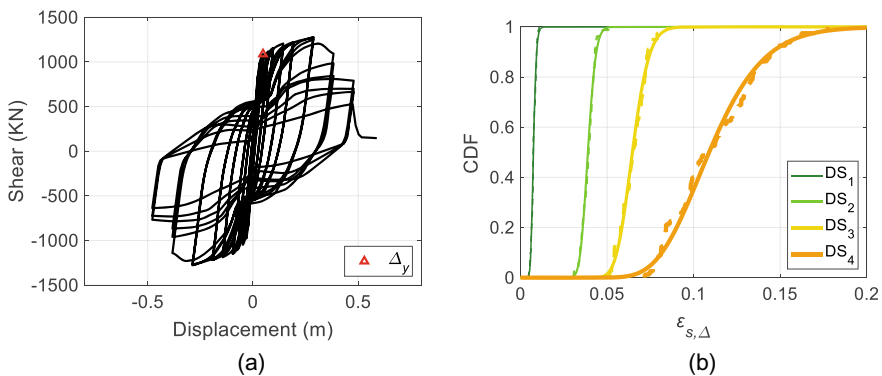


**Fig. 6** **a** Hysteretic response of one column example; and **b** empirical and fitted CDFs of equivalent $\varepsilon_{s,\Delta}$ under given $\mu_\Delta$

**Table 5** Comparisons of equivalent material strain thresholds under different EDPs

| EDP | Slight (LS$_1$) | Moderate (LS$_2$) | Extensive (LS$_3$) | Complete (LS$_4$) |
|---|---|---|---|---|
| $\varepsilon_{s,\Delta}$ | 0.0074 | 0.039 | 0.065 | 0.10 |
| $\varepsilon_{s,\varphi}$ | 0.0081 | 0.035 | 0.059 | 0.095 |
| $\varepsilon_{s,\Delta/H}$ | 0.0091 | 0.046 | 0.078 | 0.16 |
| $\varepsilon_{s,\varepsilon}$ | 0.0058 | 0.020 | 0.049 | 0.069 |
| $\varepsilon_{s,\text{unified}}$ | 0.0076 | 0.035 | 0.063 | 0.11 |
| $\varepsilon_{c,\Delta}$ | $-0.0019$ | $-0.0063$ | * | * |
| $\varepsilon_{c,\varphi}$ | $-0.0020$ | $-0.0057$ | * | * |
| $\varepsilon_{c,\Delta/H}$ | $-0.0021$ | $-0.0076$ | * | * |
| $\varepsilon_{c,\varepsilon}$ | $-0.0044$ | $-0.010$ | * | * |
| $\varepsilon_{c,\text{unified}}$ | $-0.0026$ | $-0.0074$ | * | * |
| $\varepsilon_{cc,\Delta}$ | * | * | $-0.0090$ | $-0.016$ |
| $\varepsilon_{cc,\varphi}$ | * | * | $-0.0081$ | $-0.014$ |
| $\varepsilon_{cc,\Delta/H}$ | * | * | $-0.011$ | $-0.023$ |
| $\varepsilon_{cc,\varepsilon}$ | * | * | $-0.022$ | $-0.029$ |
| $\varepsilon_{cc,\text{unified}}$ | * | * | $-0.013$ | $-0.021$ |

*: not applicable
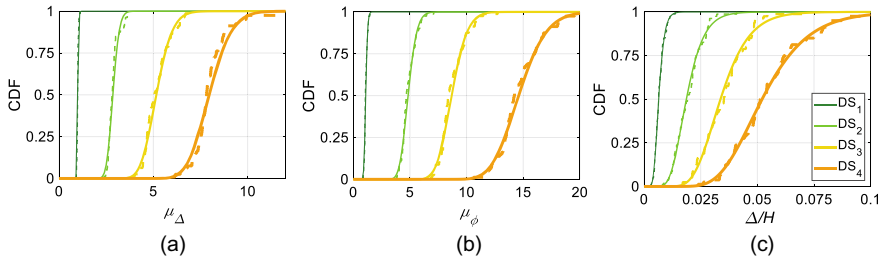


**Fig. 7** CDFs of $\mu_\Delta$, $\mu_\varphi$, and $\Delta/H$ under unified capacity LS models

**Table 6** Medians of the unified seismic capacity LS models based on $\mu_\Delta$, $\mu_\varphi$, $\Delta/H$, and $\varepsilon$

| DS | $\mu_\Delta$ | $\mu_\varphi$ | $\Delta/H$ (%) | $\varepsilon$ | | |
|---|---|---|---|---|---|---|
| | | | | $\varepsilon_s$ | $\varepsilon_c$ | $\varepsilon_{cc}$ |
| Slight (DS$_1$) | 1.0 | 1.0 | 0.65 | 0.0076 | $-0.0026$ | * |
| Moderate (DS$_2$) | 2.9 | 4.8 | 1.9 | 0.035 | $-0.0074$ | * |
| Extensive (DS$_3$) | 5.0 | 8.7 | 3.4 | 0.063 | * | $-0.013$ |
| Complete (DS$_4$) | 8.0 | 14.6 | 5.2 | 0.11 | * | $-0.021$ |

*: not applicable

**Table 7** Lognormal standard deviations of the unified seismic capacity LS models

| DS | $\mu_\Delta$ | $\mu_\varphi$ | $\Delta/H$ | Nielson [34] | Proposed |
|---|---|---|---|---|---|
| Slight (DS$_1$) | 0.25 | 0.53 | 0.55 | 0.25 | 0.40 |
| Moderate (DS$_2$) | 0.43 | 0.65 | 0.39 | 0.25 | 0.45 |
| Extensive (DS$_3$) | 0.38 | 0.50 | 0.39 | 0.46 | 0.45 |
| Complete (DS$_4$) | 0.39 | 0.51 | 0.40 | 0.46 | 0.45 |

Experimental results shown in Fig. 2 confirm that the capacity LS models of bridge columns can be treated as lognormal distributions, where the associated lognormal standard deviations ($\beta$) are extracted and summarized in Table 7. The $\beta$ values account for different sources of uncertainties that emerge during experimental testing, including geometric and material properties, design details, loading protocols, measurement errors, and depictions and damage observations at each DS. Table 7 also includes the $\beta$ provided by Nielson [34], which has been employed in multiple studies. Finally, the proposed $\beta$ values of the unified column capacity LS models are developed by taking the mean values and rounding them to the nearest 0.05. Therefore, the lognormal medians in Table 6 and the proposed standard deviations in Table 7 constitute the finally converged unified LS models.

## 5    Conclusions

A comprehensive study is carried out to develop a set of unified seismic capacity LS models for modern-designed circular RC bridge columns. Different descriptions of DSs within the literature are summarized toward converged definitions of column DSs. The corresponding LS models defined by four commonly-used EDPs (i.e., $\mu_\Delta$, $\mu_\varphi$, $\Delta/H$, and $\varepsilon$) are extracted from previous experimental outcomes. Cyclic pushover analyses are further performed to identify the equivalent material strains under each given LS model defined by $\mu_\Delta$, $\mu_\varphi$, and $\Delta/H$. Hence, these EDP-dependent LS models are converted to their equivalent material strains to examine model consistency across different EDPs. The LS models defined by the drift ratio provide larger capacities than those specified by displacement ductility and curvature ductility. The strain-based LS models show small estimates on steel strains but large predictions on concrete strains. By taking the mean values of the equivalent material strains from all resources and mapping them back to the corresponding EDPs through the cyclic pushover analyses, median values of the unified seismic capacity LS models are identified. Moreover, lognormal standard deviations extracted from previous test outcomes are used to develop converged dispersion models to account for all sources of uncertainties. The developed unified seismic capacity LS models serve as a solid reference for stakeholders to conduct more consistent and reliable seismic fragility/risk assessment of existing bridges and PBSD of new bridges.

# 6  Appendix

See Tables 8, 9 and 10.

**Table 8**  Summary of capacity LS models based on $\mu_\Delta$

| Reference | Slight ($DS_1$) | Moderate ($DS_2$) | Extensive ($DS_3$) | Complete ($DS_4$) |
|---|---|---|---|---|
| Stone and Cheok [45] | 1.0 | 3.0 | 5.0 | 6.6 |
| | 1.0 | 4.0 | 6.0 | 10.0 |
| Hose et al. [17] | 0.8 | 1.0 | 6.0 | 8.0 |
| | 0.7 | 1.5 | 3.0 | 4.5 |
| | 0.7 | 2.5 | 5.0 | 7.3 |
| | 0.8 | 2.0 | 4.0 | 6.0 |
| Sanchez et al. [42] | 0.9 | 2.3 | 2.9 | 3.5 |
| Hose and Seible [18] | 1.0 | 2.0 | 6.0 | 8.0 |
| Lehman and Moehle [27] | 1.0 | 2.7 | 5.0 | 8.0 |
| | 1.0 | 2.5 | 3.0 | 6.0 |
| | 1.0 | 3.0 | 5.0 | 7.0 |
| | 1.0 | 2.0 | 3.0 | 5.0 |
| | 1.0 | 2.0 | 3.0 | 5.0 |
| Calderone et al. [10] | 1.4 | 3.5 | 4.9 | 9.1 |
| | 1.6 | 4.7 | 7.8 | 10.2 |
| | 1.3 | 4.4 | 4.4 | 7.8 |
| | 1.8 | 5.8 | 6.5 | 9.0 |
| Orozco and Ashford [35] | 1.0 | 3.4 | 7.0 | 8.3 |
| Esmaeily and Xiao [14] | 1.3 | 5.1 | 4.2 | 5.6 |
| | 1.1 | 2.8 | 4.2 | 5.6 |
| Shanmugam [44] | 0.8 | 4.5 | 6.0 | 18.0 |
| | 0.8 | 4.3 | 13.8 | 17.0 |

**Table 9** Summary of capacity LS models based on $\mu_\varphi$

| Reference | Slight (DS$_1$) | Moderate (DS$_2$) | Extensive (DS$_3$) | Complete (DS$_4$) |
|---|---|---|---|---|
| Stone and Cheok [45] | 3.9 | 6.7 | 12.5 | 17.1 |
| | 3.1 | 7.3 | 11.4 | 19.8 |
| Hose et al. [17] | 0.8 | 2.8 | 7.0 | 9.3 |
| | 0.7 | 1.6 | 4.2 | 7.8 |
| | 0.7 | 3.1 | 5.8 | 9.2 |
| | 0.8 | 1.6 | 4.6 | 7.3 |
| Sanchez et al. [42] | 0.9 | 4.5 | 6.0 | 7.6 |
| Lehman and Moehle [27] | 1.0 | 5.0 | 10.6 | 17.8 |
| | 1.0 | 4.6 | 5.8 | 13.0 |
| | 1.0 | 5.9 | 10.6 | 15.4 |
| | 1.0 | 3.5 | 6.0 | 10.9 |
| | 1.0 | 3.5 | 6.0 | 10.9 |
| Calderone et al. [10] | 2.1 | 7.6 | 11.4 | 22.5 |
| | 2.5 | 10.9 | 19.1 | 25.4 |
| | 1.9 | 13.0 | 13.0 | 24.6 |
| | 3.9 | 18.5 | 20.8 | 30.2 |
| Orozco and Ashford [35] | 1.0 | 5.1 | 10.8 | 13.9 |
| Esmaeily and Xiao [14] | 1.8 | 11.3 | 9.0 | 12.5 |
| | 1.3 | 5.5 | 6.0 | 12.5 |
| Nielson [34] | 1.0 | 1.6 | 3.2 | 6.8 |
| Padgett [36] | 1.3 | 2.1 | 3.5 | 5.2 |
| Shanmugam [44] | 0.8 | 8.7 | 12.0 | 38.4 |
| | 0.8 | 5.0 | 16.4 | 20.4 |
| Ramanathan [40] | 1.0 | 4.0 | 8.0 | 12.0 |
| Ramanathan et al. [41] | 1.0 | 5.1 | 7.5 | 9.0 |

**Table 10** Summary of capacity LS models based on $\Delta/H$

| Reference | Slight ($DS_1$) | Moderate ($DS_2$) | Extensive ($DS_3$) | Complete ($DS_4$) |
|---|---|---|---|---|
| Dutta and Mander [13] | 0.007 | 0.015 | 0.025 | 0.050 |
| Hose and Seible [18] | 0.010 | 0.030 | 0.050 | 0.087 |
| Calderone et al. [10] | 0.003 | 0.017 | 0.028 | 0.072 |
| | 0.003 | 0.017 | 0.039 | 0.072 |
| | 0.003 | 0.036 | 0.055 | 0.12 |
| | 0.003 | 0.042 | 0.063 | 0.15 |
| Kim and Shinozuka [25] | 0.007 | 0.015 | 0.025 | 0.050 |
| Lehman et al. [28] | 0.007 | 0.016 | NS[a] | 0.052 |
| | 0.006 | 0.016 | NS | 0.052 |
| | 0.007 | 0.021 | NS | 0.073 |
| | 0.007 | 0.016 | NS | 0.052 |
| | 0.007 | 0.016 | NS | 0.052 |
| | 0.012 | 0.027 | NS | 0.091 |
| | 0.013 | 0.031 | NS | 0.10 |
| | 0.007 | 0.016 | NS | 0.039 |
| | 0.012 | 0.036 | NS | 0.091 |
| | 0.016 | 0.042 | NS | 0.15 |
| Babazadeh et al. [3] | 0.011 | 0.022 | 0.022 | NS |
| | 0.012 | 0.027 | 0.036 | NS |
| | 0.015 | 0.037 | 0.055 | NS |

[a]NS: not specified

# References

1. Aldabagh S, Alam MS (2022) Drift ratio limit states for circular concrete columns reinforced with different types of high-strength steel reinforcing bars. J Bridg Eng 27(4):1–16
2. ATC 32 (1996) Improved seismic design criteria for California bridges: provisional recommendations
3. Babazadeh A, Burgueño R, Silva PF (2015) Use of 3D finite-element models for predicting intermediate damage limit states in RC bridge columns. J Struct Eng 141(10):04015012
4. Banerjee S, Shinozuka M (2008) Experimental verification of bridge seismic damage states quantified by calibrating analytical models with empirical field data. Earthq Eng Eng Vib 7(4):383–393

5. Bao Y, Main JA, Lew HS, Sadek F (2017) Performance of precast concrete moment frames subjected to column removal: part 2, computational analysis. PCI J 62(5)
6. Basöz NI, Kiremidjian AS, King SA, Law KH (2019) Statistical analysis of bridge damage data from the 1994 northridge, CA, earthquake. Earthq Spectra 15(1):25–54
7. BC MoTI (2016) Section-4 seismic design, vol 1-supplement to CHBDC S6-14
8. Billah AHMM, Kabir MAB (2021) Development of performance limit states for concrete bridge piers with high strength concrete and high strength steel reinforcement. Can J Civ Eng 48(11):1454–1466
9. Bozorgzadeh A, Megally S, Restrepo JI, Ashford SA (2006) Capacity evaluation of exterior sacrificial shear keys of bridge abutments. J Bridg Eng 11(5):555–565
10. Calderone AJ, Lehman DE, Moehle JP (2001) Behavior of reinforced concrete bridge columns having varying aspect ratios and varying lengths of confinement. Pacific Earthquake Engineering Research Center
11. Chang GA, Mander JB (1994) Seismic energy based fatigue damage analysis of bridge columns: part 1-evaluation of seismic capacity. National Center for Earthquake Engineering Research, 230
12. CSA (2014) S6-14 Canadian highway bridge design code. CSA Group
13. Dutta A, Mander JB (1999) Seismic fragility analysis of highway bridges. In: Proceedings of the center-to-center project workshop on earthquake engineering in transportation systems
14. Esmaeily A, Xiao Y (2005) Behavior of reinforced concrete columns under variable axial loads: analysis. ACI Struct J 102(5):736–744
15. FEMA (1999) Earthquake loss estimation methodology: user's manual. Federal Emergency Management Agency
16. Goodnight JC, Kowalsky MJ, Nau JM (2016) Strain limit states for circular RC bridge columns. Earthq Spectra 32(3):1627–1652
17. Hose Y, Priestley M, Seible F (1997) Strategic relocation of plastic hinges in bridge columns. Structural systems research project
18. Hose Y, Seible F (1999) Performance evaluation database for concrete bridge components and systems under simulated seismic loads. Pacific Earthquake Engineering Research Center
19. Hose Y, Silva P, Seible F (2000) Development of a performance evaluation database for concrete bridge components and systems under simulated seismic loads. Earthq Spectra 16(2):413–442
20. Hwang H, Jernigan JB, Billings S, Werner SD (2000) Expert opinion survey on bridge repair strategy and traffic impact. In: Proceedings of the post earthquake highway response and recovery seminar
21. Hwang H, Jernigan JB, Lin Y-W (2000) Evaluation of seismic damage to Memphis bridges and highway systems. J Bridg Eng 5(4):322–330
22. Hwang H, Liu JB, Chiu YH (2001) Seismic fragility analysis of highway bridges. Mid-America Earthquake Center PR-4 project
23. Johnson NS, Saiidi M, Sanders DH (2006) Large-scale experimental and analytical studies of a two-span reinforced concrete bridge system. Report No. CCEER-06-02, Center For Earthquake Engineering Research
24. Kawashima K, Unjoh S, Hoshikuma JI, Kosa K (2011) Damage of bridges due to the 2010 Maule, Chile, earthquake. J Earthq Eng 15(7):1036–1068
25. Kim S-H, Shinozuka M (2004) Development of fragility curves of bridges retrofitted by column jacketing. Probab Eng Mech 19(2004):105–112
26. Lehman D, Calderone AJ, Moehle JP (1998) Behavior and design of slender columns subjected to lateral loading. In: Proceedings 6th U.S. national conference on earthquake engineering
27. Lehman D, Moehle J (2000) Seismic performance of well-confined concrete bridge columns. Pacific Earthquake Engineering Research Center
28. Lehman D, Moehle J, Mahin S, Calderone A, Henry L (2004) Experimental evaluation of the seismic performance of reinforced concrete bridge columns. J Struct Eng 130(6):869–879
29. Li J, Spencer BF, Asce F, Elnashai AS (2013) Bayesian updating of fragility functions using hybrid simulation. J Struct Eng 139(7):1160–1171

30. Mackie KR, Stojadinović B (2006) Post-earthquake functionality of highway overpass bridges. Earthquake Eng Struct Dynam 35(1):77–93
31. Mangalathu S (2017) Performance based grouping and fragility analysis of box-girder bridges in california. PhD thesis, Georgia Institute of Technology
32. McKenna F (2011) OpenSees: a framework for earthquake engineering simulation. Comput Sci Eng 13(4):58–66
33. Mitchell D, Huffman S, Tremblay R, Saatcioglu M, Palermo D, Tinawi R, Lau D (2012) Damage to bridges due to the 27 Feb 2010 Chile earthquake 1. Can J Civ Eng 40(8):675–692
34. Nielson BG (2005) Analytical fragility curves for highway bridges in moderate seismic zones. PhD thesis, Georgia Institute of Technology
35. Orozco GL, Ashford SA (2002) Effects of large velocity pulses on reinforced concrete bridge columns. Pacific Earthquake Engineering Research Center
36. Padgett JE (2007) Seismic vulnerability assessment of retrofitted bridges using probabilistic methods. PhD thesis, Georgia Institute of Technology
37. Paik JK, Kim KJ, Lee JH, Jung BG, Kim SJ (2017) Test database of the mechanical properties of mild, high-tensile and stainless steel and aluminium alloy associated with cold temperatures and strain rates. Ships Offshore Struct 12(sup1):S230–S256
38. Park R (1989) Evaluation of ductility of structures and structural assemblages from laboratory testing. Bull N Z Soc Earthq Eng 22(3):155–166
39. Priestley MN, Seible F, Calvi GM (1996) Seismic design and retrofit of bridges. Wiley
40. Ramanathan K (2012) Next generation seismic fragility curves for california bridges incorporating the evolution in seismic design philosophy. PhD thesis, Georgia Institute of Technology
41. Ramanathan K, DesRoches R, Padgett JE (2012) A comparison of pre- and post-seismic design considerations in moderate seismic zones through the fragility assessment of multispan bridge classes. Eng Struct 45:559–573
42. Sanchez AV, Priestley M, Seible F (1997) Seismic performance of flared bridge columns. UC San Diago test report
43. Schoettler MJ, Restrepo JI, Guerrini G, Duck DE, Carrea F (2015) A full-scale, single-column bridge bent tested by shake-table excitation. Pacific Earthquake Engineering Research Center
44. Shanmugam SP (2009) Seismic behavior of circular reinforced concrete bridge columns under combined loading including torsion. PhD thesis, Missouri University of Science and Technology
45. Stone WC, Cheok GS (1989) Inelastic behavior of full-scale bridge columns subjected to cyclic loading. National Institute of Science and Technology
46. Tavares DH, Suescun JR, Paultre P, Padgett JE (2013) Seismic fragility of a highway bridge in Quebec. J Bridg Eng 18(11):1131–1139
47. Vosooghi A, Saiidi MS (2012) Experimental fragility curves for seismic response of reinforced concrete bridge columns. ACI Struct J 109(6):825–834
48. Yassin M, Hisham M (1994) Nonlinear analysis of prestressed concrete structures under monotonic and cyclic loads. PhD thesis, University of California, Berkeley
49. Zheng Q (2021) Advanced seismic risk assessment of california box-girder bridges using emerging modeling techniques and innovative risk models. PhD thesis, Georgia Institute of Technology
50. Zong Z, Kunnath S, Monti G (2013) Material model incorporating buckling of reinforcing bars in RC columns. J Struct Eng 140(1):04013032

# Development of Canadian Design Standards for Traffic Barriers for Bridge Applications

**Khaled Sennah**

**Abstract** This paper summarizes the research work done in Canada on steel- and GFRP-reinforced concrete barriers. AASHTO LRFD Bridge Design Specifications specify a triangular yield line failure pattern for steel-reinforced concrete barrier design. However, no evidence was found in the literature to support this failure shape. Recent experimental tests on steel-reinforced barriers showed a trapezoidal crack pattern within the barrier that led to the development of new equations for the barrier transverse flexural capacity using the yield line theory. These equations along with conditions for their use were included in the 2019 Canadian Highway Bridge Design Code (CSA-S6.19). Also, a new punching shear equation for the barrier transverse capacity was developed based on the experimental findings. Due to the use of de-icing salt in winter times, GFRP bars have been used in Canada as a cost-effective alternative to corroded steel reinforcement. Recent design work on a GFRP-reinforced barrier was qualified by conducting three vehicle crash tests using different types of GFRP bars. Then, static load tests to collapse were conducted on the constructed barriers to study their structural behaviour. Test results showed that their failure mode was punching shear at the transverse load location, with trapezoidal-shape flexural cracks appearing at the tapered faces of the barrier during loading. Experimental findings were incorporated in CSA-S6.19 in the form of GFRP bar size, and arrangement to satisfy the crash test acceptance criteria and equation for the punching shear capacity of GFRP-reinforced barrier subjected due to transverse vehicle impact loading.

**Keywords** Traffic barrier · Yield-line analysis · Punching shear · Experimental testing · GFRP-reinforced concrete barrier · Steel-reinforced barrier

K. Sennah (✉)
Civil Engineering Department, Toronto Metropolitan University, Toronto, ON, Canada
e-mail: ksennah@torontomu.ca

# 1 Introduction

AASHTO LRFD Bridge Design Specifications [1] specify an equation for the transverse flexural capacity of steel-reinforced barrier based on a triangular yield line failure pattern. However, no evidence was found in the literature to support this failure shape. Recently, Khedrzadeh and Sennah [16, 18] conducted static load tests to collapse on constructed TL-5 and TL-4 steel-reinforced concrete barriers at Texas A&M Transportation Institute (TTI) to obtain research data on their behaviour under transverse loading. In contrast to the AASHTO triangular yield line pattern, the observed crack pattern during loading the barrier transversely was trapezoidal in shape as depicted in Fig. 1a, b for TL-4 barrier for example. Details of the developed transverse flexural capacity of the barrier based on this crack pattern using the yield line theory are explained in this paper. Punching shear failure could be a potential failure mode at the contact area between the barrier and the applied transverse loading simulating vehicle impact. This was observed in the tested TL-4 barrier as depicted in Fig. 1c, d when loaded at the end location and interior segment, respectively. More details of static tests on these TL-5 and TL-4 barriers can be found elsewhere [17]. Such failure mode was observed in actual vehicle collisions with steel-reinforced concrete barriers [5, 29] and experimental tests to collapse on constructed actual-size TL-5 and TL-4 reinforced concrete bridge barriers [2]. Khederzadeh [17] developed an empirical equation for the barrier resistance to punching shear failure that can be used to determine the minimum thickness of the steel-reinforced concrete barrier subjected to vehicle impact. Figure 2a, b showed views of the punching shear failure shapes of the tested TL-5 GFRP-reinforced barrier at its front and back face, respectively. Similar to the steel-reinforced barrier, trapezoidal-shape flexural cracks appeared on the tapered faces of the barrier during loading. Within the portion of the loaded length of the barrier, a horizontal crack appeared at the barrier-deck junction and at different levels in the top and bottom tapered portions of the wall, extending diagonally outside the loaded length of the wall. This paper presents a summary of the recent research on the development of a GFRP-reinforced barrier at Ryerson University and associated vehicle crash tests and static load tests to collapse conducted at Texas A&M Transportation Institute. In addition, this paper provides more details of the methodology for the design of the barrier thickness based on the experimental findings.

# 2 Yield Line Analysis of Barrier Wall Due to Vehicle Impact

This section applies to the calculation of flexural resistance of steel-reinforced concrete barrier to transverse traffic barrier load based on the trapezoidal yield line pattern shown in Fig. 3.

(a) Crack pattern at end location



(b) Crack pattern at interior segment



(c) Punching shear crack at end location



(d) Punching shear crack at interior segment
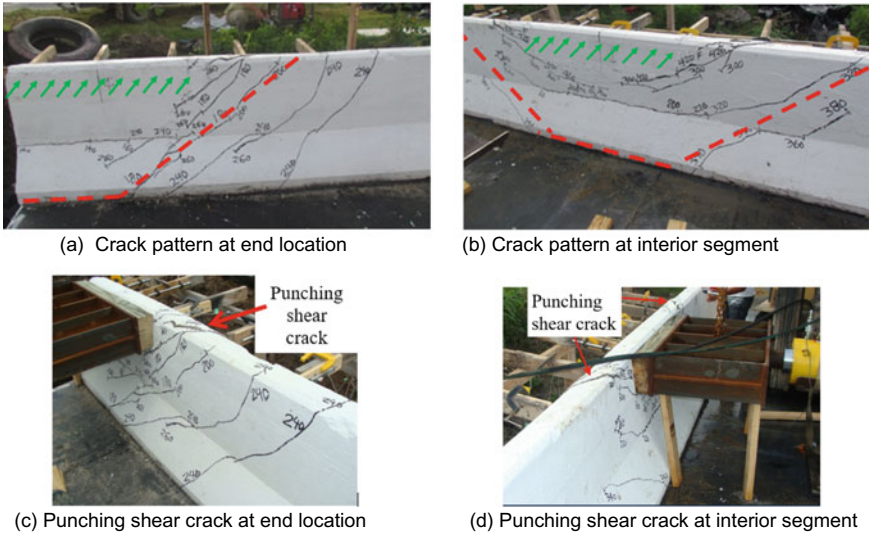
**Fig. 1** Crack pattern and punching shear failure of a TL-4 steel-reinforced barrier



(a)  View from the traffic side



(b) View from the back side
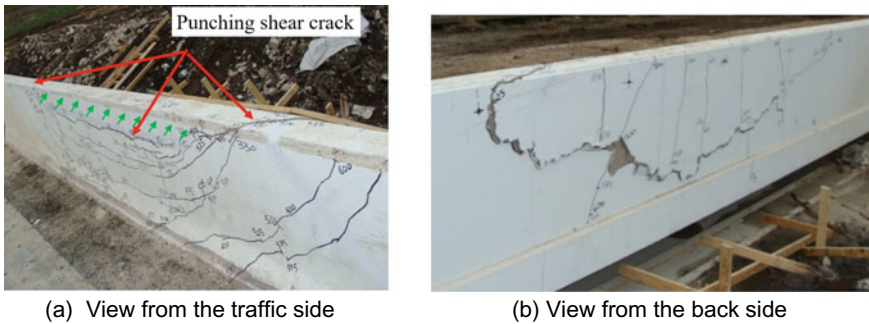
**Fig. 2** Crack pattern and punching shear failure of a TL-5 GFRP-reinforced barrier



(a) For barrier load applied within a barrier segment

(b) For barrier load applied at barrier end
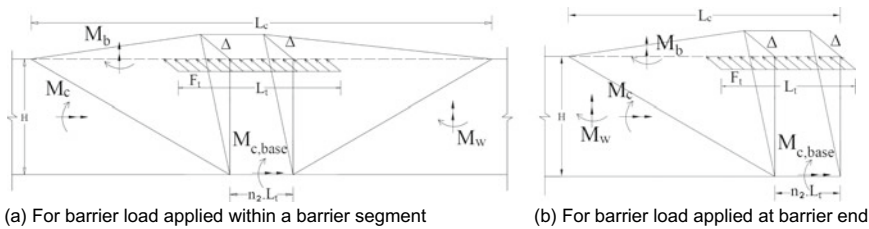
**Fig. 3** Yield line analysis of steel-reinforced concrete barriers

## 2.1 Factored Flexural Resistance of Steel-Reinforced Concrete Barrier to the Transverse Traffic Load

The value of the factored flexural resistance, $R_w$, shall be the lowest value calculated in accordance with (a) and (b) below [15].

(a) **For barrier loads applied within a wall segment**:

$$R_w = \left\{ \frac{1}{2L_c - L_t - n_2^2.L_t} \right\}$$
$$\left\{ 16M_b + 16M_w.H + \frac{2M_c(L_c^2 - n_2.L_t.L_c)}{H} + \frac{2(M_{c,base} - M_c)(n_2 L_t L_c - n_2^2 L_t^2)}{H} \right\} \qquad (1)$$

where the critical barrier length over which the yield line mechanism occurs, $L_c$, shall be taken as:

$$L_c = 0.5L_t(1 + n_2^2)$$
$$+ \sqrt{\frac{1}{4}L_t^2(1 + n_2^2)^2 + \frac{16M_b H + 16M_w H^2 - M_c\left(n_2 L_t^2 + n_2^3.L_t^2\right) - (M_{c,base} - M_c)\left(2n_2^2 L_t^2 - n_2 L_t^2 - n_2^3 L_t^2\right)}{2M_c}} \qquad (2)$$

(b) **For barrier loads applied at barrier ends**:

$$R_w = \left\{ \frac{1}{2L_c - L_t - n_2^2.L_t} \right\}$$
$$\left\{ 2M_b + 2M_w.H + \frac{2M_c(L_c^2 - n_2.L_t.L_c)}{H} + \frac{2(M_{c,base} - M_c)\left(n_2 L_t L_c - n_2^2 L_t^2\right)}{H} \right\} \qquad (3)$$

where the critical barrier length over which the yield line mechanism occurs, $L_c$, shall be taken as:

$$L_c = 0.5L_t(1 + n_2^2)$$
$$+ \sqrt{\frac{1}{4}L_t(1 + n_2^2)^2 + \frac{2M_b H + 2M_w H^2 - M_c(n_2 L_t^2 + n_2^3.L_t^2) - (M_{c,base} - M_c)(2n_2^2 L_t^2 - n_2 L_t^2 - n_2^3 L_t^2)}{2M_c}} \qquad (4)$$

The symbols in the above equations are defined as follows: $F_t$ is the transverse traffic barrier load applied as specified for barrier test level (i.e. TL-1 to TL-5); $H$ is the distance from top of barrier wall to bottom of assumed yield line mechanism; $L_c$ is the critical length of yield line failure pattern, mm; $L_t$ is the longitudinal length of application of transverse load as specified for barrier test level, mm; $M_b$ is the factored flexural resistance of horizontal beam, if any, about its vertical axis in addition to $M_w$ at top of wall, N mm; $M_{c,base}$ is the flexural resistance of the barrier at the bottom of the assumed yield line mechanism about an axis parallel to the longitudinal axis of the bridge, N mm/mm; $M_c$ is the average factored flexural resistance of barrier

over height, $H$, about an axis parallel to the longitudinal axis of the bridge, N mm/mm; $M_w$ is the average factored flexural resistance of the barrier over height, $H$, about its vertical axis, N mm/mm; $n_2$ is a variable ranging from 0 to 1. The critical value of $n_2$ shall be the value resulting in the lowest value of $R_w$ in $N$. In Fig. 3, the lateral deflection of the barrier at its top surface is $\Delta$. It should be mentioned that substituting $n_2$ as zero in the below equations yields the available yield line equations in AASHTO LRFD Bridge Design Specifications [1].

## 2.2 Conditions of Use of the Developed Yield Line Equations

The factored transverse flexural resistance, $R_w$, of a steel-reinforced concrete barrier resulting from the traffic barrier loads applied in accordance with test levels (TL-1 through TL-5) may be determined using the yield line approach per Eqs. 1 through 4 provided that the following conditions are met:

1. Locations where the steel reinforcing bars contributing to $M_w$ or $M_b$ is discontinuous, e.g. at control joints are treated as barrier ends;
2. The yield line mechanisms considered include a yield line mechanism extending from the top of the barrier to the top of the bridge deck as well as yield line mechanisms extending from the top of the barrier to any discontinuities in the barrier thickness, e.g. slope break in roadway face of safety shape barrier, or reinforcing, e.g. rebar cutoffs. The critical value of $R_w$ shall be taken to be the lowest value of $R_w$ determined from the yield line mechanisms;
3. The maximum value of $c/d$ for the vertical and horizontal barrier reinforcement, determined in accordance with basics in reinforced concrete section analysis, does not exceed 0.15 where $c$ is the distance from extreme compression fibre to the neutral axis in a concrete section, mm; $d$ is the effective depth (being the distance from the extreme compression fibre to the centroid of the tensile force), mm;
4. Minimum barrier length with continuous horizontal reinforcement shall be taken as ($L_c + 2H_b$) to result in the yield line failure pattern, where $H_b$ is the height of the barrier. For shorter lengths of barrier, a single yield line may form along the junction of the barrier and deck. Such a failure pattern is permissible, and the resistance of the barrier should be computed using an appropriate analysis;
5. For a barrier with constant width along its height, $M_c$ equals $M_{c,base}$, where width of the barrier and/or the amount of reinforcing steel vary along its height, $M_c$ and $M_w$ for wall resistance shall be taken as the average of their values along the height of the barrier; and
6. The deck overhang region shall be designed to have a resistance larger than the actual resistance of the concrete barrier under transverse loading to ensure that the barrier yield line failure pattern occurs before deck failure.

## 2.3 Background of the Developed Yield Line Equations and Conditions of Use

This subsection covers brief background and limitations of use of the developed yield line equations for the factored transverse flexural resistance of steel-reinforced concrete bridge barrier walls due to vehicle impact. Hirsch [12] developed equations for the transverse flexural capacity of steel-reinforced concrete barrier due to vehicle impact based on triangular yield line failure patterns at interior and end segments, on the basis of the yield line theory. It was assumed that two diagonal yield lines meet at a point at the barrier-deck joint, with a vertical yield line extending from this point to the top of the barrier wall. Hirsch's equations were then included in the AASHTO LRFD Bridge Design Specifications for steel-reinforced barrier design. However, no experimental basis was found in the literature to support such yield line patterns. Recent experimental research [13, 14, 29, 16] showed a different failure pattern in the form of trapezoidal shape rather than the AASHTO LRFD triangular crack pattern at failure. Based on this observed failure shape, it is assumed that two diagonal yield lines extend from the top of the barrier wall down to the deck-wall joint and are connected by a horizontal yield line along this joint. This is in addition to two vertical yield lines extending from the ends of the horizontal yield line at the barrier-deck joint to the top of the barrier wall, as depicted in Fig. 3.

Khedrzadeh and Sennah [15] outlined the procedure for the development of the transverse flexural resistance of steel-reinforced concrete barrier wall based on the trapezoidal yield line failure patterns at interior and end segments. In barrier analysis, the length of horizontal yield line at the barrier-deck joint was considered equal, greater than, and less than the loaded length ($L_t$). Analysis proved that critical transverse flexural resistance of the barrier based on the trapezoidal yield line pattern occurs when the horizontal yield line length at barrier-deck joint is less than the loaded length, through a parameter $n_2$ in Eqs. 1 through 4 with a value between 0 and 1. Figure 4 shows several conceivable alternative yield lines (failure modes) for steel-reinforced concrete barriers when subjected to vehicle collision. Yield lines YL6 and YL7 can develop in short barriers, while other yield lines can develop in long barriers. Yield lines YL1, YL2, and YL3 represent the triangular failure shape as presented in AASHTO LRFD[1] to calculate the barrier transverse flexural resistance. While yield lines YL2 and YL3 have a similar triangular failure shape to that of yield line YL1, it is assumed that yield lines develop above the points of slope discontinuity of the barrier height, taking into account the characteristics of the shape and the amount of reinforcement at each slope discontinuity. Yield lines YL4 and YL5, alternative yield lines, have more similarity with the test results reported by the author's research team on long barriers than any of the other yield lines. It should be noted that yield line YL4 can also be regarded as a geometrically possible failure mechanism based on the difference in barrier width and amount of reinforcement in each of the tapered portions of the barrier wall. Considering the upper-bound theorem of the yield line theory, it is plausible that the yield line that provides the minimum strength is most likely to occur.
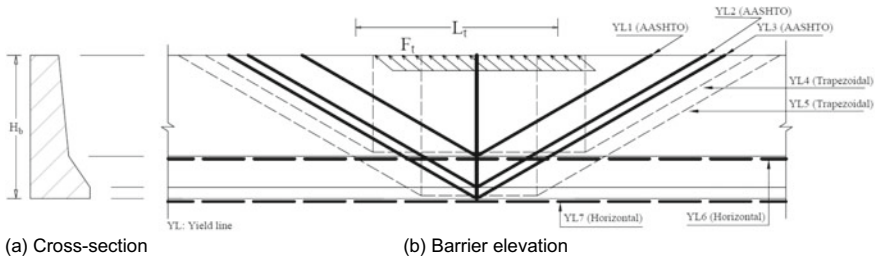
Fig. 4 Alternatives for barrier yield line failure patterns

In applying the yield line theory, steel reinforcement should be fully yielded along the yield lines at failure. In this case, barrier reinforcement is well below that in the balanced condition. Also, reinforcement response should be elastic-perfectly plastic with significant steel strain at failure compared with the elastic strain limit. A $c/d$ ratio of 0.15 yields a 0.02 steel strain at failure, leading to a significant yield plateau before failure. For a barrier with constant width and vertical bars along its height, $M_c$ equals $M_{c,base}$, where width of the barrier varies along its height, $M_c$ and $M_w$ for wall resistance shall be taken as the average of their values along the height of the barrier. In this case, $M_w$ and $M_c$ are approximately calculated by dividing the barrier into a minimum of four segments with constant thickness each, while $M_{c,base}$ is calculated based on the barrier width and reinforcement at the level of the horizontal yield line in the trapezoidal yield line failure pattern.

The analysis is based on the assumption that the positive and negative wall resisting moments ($M_w$) are equal and that the negative and positive beam resisting moments are equal. Unequal negative and positive moments may occur as a result of using different concrete cover in the front and back side of the barrier wall. In the case of unequal negative and positive moments, an average value can be used. Reinforcing steel for concrete barriers shall have sufficient embedment length into the supporting deck slab to develop the yield strength. To avoid an undesirable horizontal yield line, the barrier should be of enough length to ensure that the trapezoidal yield line failure occurs at the general part of the barrier. Such minimum length can be obtained by equation $R_w$ for a horizontal yield line failure pattern (i.e. yield line YL7 in Fig. 4) at barrier-deck joint and $R_w$ based on the trapezoidal yield line failure pattern. Jeon et al. [13] equated AASHTO $R_w$ with that for the horizontal yield line failure pattern at barrier-deck joint, considering the transverse impact load as point load (i.e. $L_t = 0$) and equal resisting moments in the vertical and horizontal directions of the barrier wall (i.e. $M_c = M_w$). This led to a minimum barrier length $L_c = 4\sqrt{2H_b}$. AASHTO LRFD Bridge Design Specifications (1) imply that barrier length should be over a length equal or greater than ($L_c + 2H_b$) to develop the triangular yield line failure pattern and to transfer the developed forces at the barrier-deck joint to the deck slab overhang.

The yield line analysis is based on the assumption that a sufficient longitudinal length of the barrier exists to result in the trapezoidal yield line pattern. For short

lengths of barrier, a single horizontal yield line may form at barrier-deck joint and its flexural resistance should be calculated as $[L_b(M_{c,base})/(H_b)]$ when $L_b = L_t$. For barrier length greater than $L_t$ and shorter than $(L_c + 2H_b)$, the applied moment at the barrier-deck joint depends on the dispersion angle of the applied transverse loading within the barrier wall. Also, horizontal reinforcement will play a greater role in distributing transverse loading over a barrier length greater than $L_t$. Therefore, the applied factored moments required to design barrier width, as well as the vertical and horizontal reinforcement, should be computed using a refined analysis such as the finite element method and orthotropic plate theory. In the yield line analysis, it is assumed that the yield line failure pattern occurs within the barrier only and does not extend into the deck slab. This means that the deck must have sufficient resistance to force the yield line failure pattern to remain within the barrier wall. If the failure pattern extends into the deck, the yield line equations for transverse flexural resistance of the barrier are not valid.

## 3 Transverse Punching Shear Capacity of Steel-Reinforced Barrier

The factored punching shear resistance, $V_c$, of steel-reinforced concrete barrier resulting from the traffic barrier loads specified and applied in accordance with the defined test level (TL-1 through TL-5) shall be determined as [17].

$$V_c = (1 + 2/\beta_c)0.15\lambda\varphi_c\sqrt{f'}b_o.d \tag{5}$$

where $b_o$ is the perimeter of the critical section measured at $1.5d$ from the loading patch ad depicted in Fig. 5; $d$ is the effective slab depth measured at critical perimeter; $f_c'$ is the concrete compressive strength, MPa; $V_c$ is the punching shear capacity of barrier wall at transverse load location, $N$; and $\beta_c$ is the ratio of the long side to the short side of the transverse loading patch.



(a) For load applied within a barrier segment          (b) For load applied at barrier end
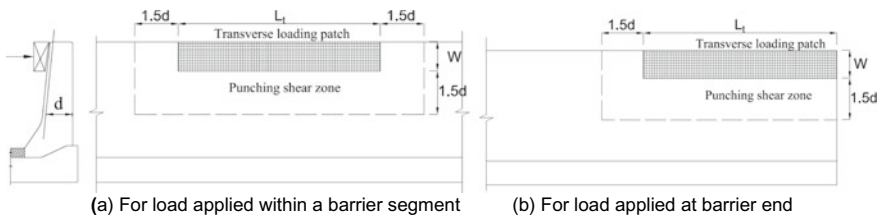
**Fig. 5** Critical perimeter of punching shear failure in concrete barrier walls

## 3.1 Background of the Developed Equation and Conditions of Use

Punching shear failure could be a potential failure mode at the contact area between the barrier and the applied transverse loading simulating vehicle impact. Such failure mode was observed in actual vehicle collisions with steel-reinforced concrete barriers [29] and experimental tests to collapse of constructed actual-size TL-5 and TL-4 reinforced concrete bridge barriers [2, 15, 16, 18]. Khederzadeh [17] developed an empirical equation for the barrier resistance to punching shear failure which can be used to determine the minimum thickness of the steel-reinforced concrete barrier subjected to vehicle impact. This equation is limited to barrier wall supported over deck slab cantilever. The punching shear capacity of the barrier wall mounted over a non-deformable base compared with the deformed deck slab cantilever is as yet unavailable. Section 16 of CSA-S6.19 [6], specifies reinforcing bridge barriers with glass fibre-reinforced polymer (GFRP) bars to eliminate corrosion of reinforcing steel and concrete spalling as result of the use of de-icing salt in winter times. Due to differences in mechanical properties of GFRP bars compared with steel reinforcement, it was found that yield line theory is not applicable to bridge barrier reinforced with GFRP bars. Since GFRP are characterized by elastic behaviour to rupture and low stiffness, plastic moments cannot be developed in the barrier walls. As such, punching shear failure at the impacted area of the barrier wall may occur. Section 16 of CSA-S6.19 specifies an equation to determine the punching shear resistance of GFRP-reinforced concrete barrier based on experimental findings from tests to collapse of actual-size TL-5 and TL-4 GFRP-reinforced barriers which will be explained later.

## 3.2 Conditions for Use of the Punching Shear Resistance and Yield Line Capacity Equations

The following conditions shall be met when designing the barrier using the aforementioned methodologies as specified in CSA-S6-19.

1. Flexural resistance shall be calculated in accordance with the applicable code for concrete bridges;
2. The spacing of the vertical and horizontal bars in the barrier wall is not more than 300 mm;
3. Concrete cover to bars meets the requirements of the applicable code for concrete bridges; and
4. The spacing of the vertical bars and anchors on the traffic side is reduced by half for the following lengths of the wall on (i) each side of a joint in the wall; (ii) each side of a luminaire embedded in the wall; and (iii) from the free vertical edges of the wall: 1.2 m for barriers meeting crash test requirements for test levels 1, 2 and 4; and 2.5 m for barriers meeting crash test requirements for test level 5.

# 4 Design of GFRP-Reinforced Barrier Wall Due to Vehicle Impact

Based on the crash test results referred to in this paper, CSA-S6:19 specifies that a barrier wall that has the details shown in Fig. 6d and whose performance has been established by full-scale crash test level 5 approved by the owner shall satisfy the following minimum conditions:

(a) The wall has vertical GFRP bars of 15 and 13 M at 300 mm spacing in the front and back faces, respectively, with 15 M GFRP bars as horizontal reinforcement;



(a) TL-4 barrier wall with Grade I GFRP bars      (b) TL-5 barrier wall with Grade I GFRP bars

(c) TL-4 barrier wall with Grade III GFRP bars      (d) TL-5 barrier wall with Grade III GFRP bars
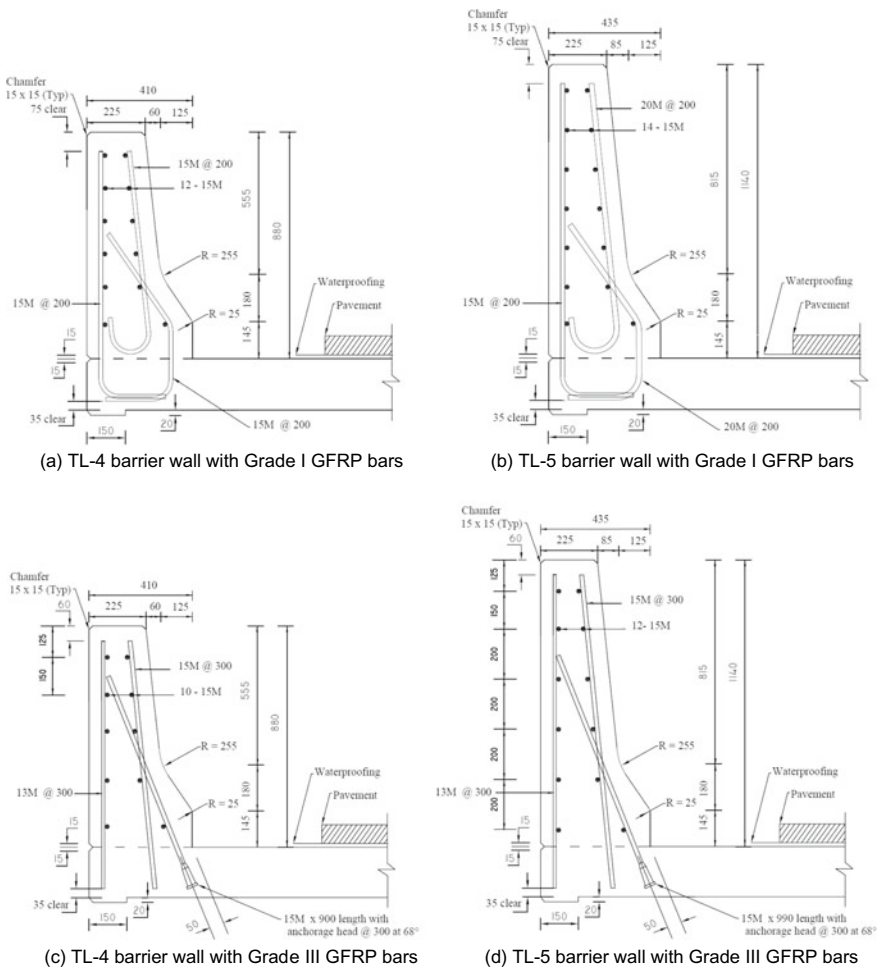
**Fig. 6** GFRP-reinforced barrier wall details (measurements are in mm)

(b) GFRP bar arrangement has 1100 MPa minimum specified longitudinal tensile strength and 60 GPa guaranteed longitudinal modulus of elasticity. Alternative GFRP bars of equivalent strength, stiffness and anchorage capacity produced by the same manufacturer using fibre and resin types identical to those used in the crash-tested bars and approved by the bridge owner shall be used;

(c) The wall is anchored to the slab by GFRP bars with headed ends, bents or 180° hooks whose performance has been established by full-scale crash tests approved by the owner. Other anchorage details at the barrier-slab joint whose performance has been established by approved manual calculations, numerical modelling and/or full-size experimental testing shall be used as an alternative for a crash-tested anchorage.

## 4.1 Punching Shear Resistance of GFRP-Reinforced Concrete Barrier

For a concrete barrier wall with front and back GFRP bar assemblies, the factored punching shear resistance, $V_c$, from the traffic barrier loads specified and applied in accordance with the associated test level (TL-1 through TL-5) and punching shear perimeter shown in Fig. 5 shall be determined as:

$$V_c = (1 + 2/\beta_c)0.13\lambda\varphi_c\frac{\sqrt[3]{\rho_f.E_f.f'_c}}{\sqrt[4]{d}}b_{o,1.5d}.d \qquad (6)$$

where $b_{o,1.5d}$ is the critical perimeter length measured at $1.5d$ from the loading patch; $d$ is the effective slab depth measured at critical perimeter; $E_f$ is modulus of elasticity of GFRP bars; $f_c'$ is concrete compressive strength, MPa; $V_c$ is the punching shear capacity of barrier wall at transverse load location, $N$; $\beta_c$ is the ratio of long-to-short side of the transverse loading patch; $\lambda$ is the concrete density factor; $\varphi_c$ is concrete resistance factor; and $\rho_f$ is the GFRP tensile reinforcement ratio.

## 4.2 Background of the Developed Methodology for GFRP-Reinforced Barrier Design

The barriers shown in Fig. 6a, b were developed, tested, and approved by the Ministère des Transports du Québec (MTQ). Pendulum impact tests were carried out [4, 10] on full-scale type TL-2 and TL-3 barriers reinforced with GFRP bars. The strength of the bent GFRP bars was determined in accordance with the test method in Appendix E of CSA-S806-02 [8]. For the design illustrated in Fig. 6a and b, the mean tensile strength at the bent, in accordance with the test method in Appendix E of CSA-S806-02, should not be less than 390 MPa for 15 M bars and 300 MPa for 20 M bars. The mean tensile strength of the straight portion of the bent GFRP bars in accordance with

the test method in Appendix C of CSA-S806-02 should not be less than 590 MPa for 15 M bars and 510 MPa for 20 M bars. This leads to tensile strength ratios of bent and straight bar portions of 66% and 59% for the 15 M and 20 M bars, respectively. As a result, the number of bent low-modulus GFRP bars is increased and even doubled at such locations where bar bents are required. Most recently, GFRP manufacturers developed GFRP bars with a higher modulus of elasticity than that used to develop barrier details in Fig. 6a, b considering the first generation of GFRP bars which were of low modulus. Over the years, GFRP bars were manufactured with a variety of tensile strengths and modulus of elasticity. Therefore, CSA S807-10 [9] specified three grades of GFRP bars based on the varying productions among the manufacturers that are affected by the fibre content by volume and the presence of secondary fibres and fillers. CSA S807-10 allows an inert fibre material added to the matrix without significantly changing the properties of the FRP. Also, it allows an inert material added to the matrix to reduce the volume of polymer without significantly changing the properties of the FRP. So, the primary factor on deciding on the GFRP grade is the fibre content by volume. CSA S807-10 specifies GFRP bar Grades I, II and III with moduli of elasticity of 40, 50 and 60 GPa, respectively. MTO Special Provision for GFRP bars [20] specifies similar grades based on the modulus of elasticity but with added limiting tensile strength of the bars based on their nominal cross-sectional area as 651, 798 and 1008 MPa for Grades I, II and III, respectively, for 13 M bars. Also, it specifies minimum tensile strength for 15 M GFRP bars of 653, 799 and 1005 MPa for Grades I, II and III, respectively, based on the nominal cross-sectional areas. CSA S807-10 specified the nominal diameter and nominal cross-sectional areas of the 15 MPa and 13 M bars.

Using Grade III GFRP bars, TL-5 barrier wall shown in Fig. 6d was developed, crash-tested, statically-tested to collapse and then adopted by Ontario Ministry of Transportation (MTO) and Ministère des Transports du Québec (MTQ) with slight changes. Two crash tests were conducted on constructed TL-5 barrier-deck systems using ribbed-surface and sand-coated bars considering bars with headed ends at the barrier-deck connection [25, 26]. A third crash test was conducted using GFRP bars with 180° hooks at the barrier-deck connection [27]. Further research was conducted to justify the use of 435 mm width at the barrier base in lieu of the 475 mm width considered in the crash-tested barrier [23]. Then, MTQ adopted this change that resulted in the barrier configuration shown in Fig. 6d and adopted a similar design using Grade III GFRP bars in the TL-4 barrier as shown in Fig. 6c with slight changes [21].

Alternative GFRP bars produced by other manufacturers should be crash-tested for TL-5 barrier, given the fact that a standard test method for the dynamic behaviour of the GFRP bars and approved by the bridge owner is yet unavailable. For an anchorage at the barrier-deck slab region to be considered acceptable, significant damage shall not occur in the anchorage or deck during crash testing. If crash testing cannot be conducted to qualify an anchorage design, the anchorage and deck shall be designed to resist the applied factored loads that can be transmitted to them by the traffic barrier. Clause C12.4.3.4.5 in CSA-S6-14 Commentary [7] suggests the following examples where changes may potentially be acceptable: (i) changes to an anchorage

system, where the failure of the anchorage is not exhibited during crash testing and the strength of the replacement anchorage is determined to be equivalent to that of the original; and (ii) substituting materials with properties identical or superior to the original material as far as behaviour during crash testing is concerned. The longitudinal reinforcement in the concrete barrier wall must be continuous through the control joints. Unsupported ends of the barrier wall (including those at expansion joints) must, for a specific distance from the unsupported end, be provided with double the amount of vertical reinforcement required for the bending moment at the traffic side for the remainder of the wall. This is normally done by doubling up the number of bars at the unsupported end thereby reducing the spacing to one-half of the normal spacing. This is supported by Section 10.4.1 of MTO Structural Manual [22] and Chaps. 12 and 16 of MTQ Structural Manual [21]. The distance over which the number of the vertical GFRP bars at the traffic side is doubled represents the contact length between the vehicle wheels and the barrier wall during the collision. The increase in the amount of vertical bars at the traffic side may reflect the fact that results of crash testing of a steel- or GFRP-reinforced barrier end are as yet unavailable. In addition, the vertical bending moment at the barrier-deck connection at the barrier unsupported end is much greater than that within the internal segment of the barrier wall due to similar transverse loading pattern [3].

GFRP-reinforced barrier configurations in Fig. 6 are based on the assumption that sufficient longitudinal length of the barrier, with continuous horizontal reinforcement, exists to behave as the crash-tested barriers. For short lengths of barrier, a flexural failure with a single horizontal crack may form at the barrier-deck connection. As such, the barrier configurations in Fig. 6 cannot be used. The deck overhang region shall be designed to have a resistance larger than the actual resistance of the concrete barrier under transverse loading, to ensure that the barrier failure pattern occurs before deck failure. Static tests to collapse conducted on actual-size TL-5 bridge barriers resulted in punching shear failure at the transverse load location within the barrier segment and at barrier ends [24, 28]. The punching shear equation mentioned earlier was developed from this research. Similar punching shear failure was observed elsewhere for GFRP-reinforced TL-4 barrier [11]. Barrier walls for test levels 1, 2, 4 and 5 with details other than those shown in Fig. 6d may be used if their performance has been established by full-scale tests per the MASH crash test requirements [19] and approved by the owner.

## 5   Conclusions

This paper presents a summary of the findings of extensive research on steel- and GFRP-reinforced concrete bridge barriers over the last decade. New equations for the transverse flexural resistance of steel-reinforced barriers were developed based on observed experimental crack patterns and using the yield line theory. Punching shear resistance equations for steel- and GFRP-reinforced concrete barriers mounted over

deck slab cantilevers were developed based on experimental findings. Background and limitations of the use of the developed methodologies are presented.

# References

1. AASHTO (2020) AASHTO LRFD bridge design specifications, 8th edn. American Association of State Highway and Transportation Officials, Washington D.C., USA
2. Alberson D, Williams W, Bloschock M, Boyd C (2011) Analysis and design of concrete traffic railings. TRB annual meeting, Transportation Research Board, USA, pp 1–12
3. Azimi H, Sennah K, Tropynina E, Goremykin S, Lucic S, Lam M (2014) Anchorage capacity of concrete bridge barriers reinforced with GFRP bars with headed ends. ASCE J Bridge Eng 19(9):1–15
4. Benmokrane B, El-Gamal S, Tobbi H, El-Sayed A (2007) Essais dynamiques sur glissières de types 201 et 301 renforcées avec de l'armature de PRFV. Rapport final, soumis au ministère des Transports du Québec (Direction des structures), Octobre, 79 pp
5. Bligh R, Briaud J, Kim K, Abu-Odeh A (2010) Design of roadside barrier systems placed on MSE retaining walls. NCHRP REPORT 663. National Cooperative Highway Research Program, Transportation Research Board, Washington, D.C., p 194
6. CSA (2019) Canadian highway bridge design code, CAN/CSA-S6-19. Canadian Standard Association, Toronto, Ontario, Canada
7. CSA (2014) Commentary of the Canadian highway bridge design code. Canadian Standard Association, Toronto, Ontario, Canada
8. CSA (2002) Design and construction of building structures with fibre-reinforced polymers, CAN/CSA-S806-02. Canadian Standard Association (CSA), Toronto, Ontario, Canada
9. CSA (2010) Specification for fibre-reinforced polymers, CAN/CSA-S807-10. Canadian Standard Association (CSA), Toronto, Ontario, Canada
10. El-Gamal S, Benmokrane B (2008) Testing of concrete bridge barriers reinforced with new GFRP bars. In: Proceedings, CSCE annual conference, Quebec City, Quebec, 10–13 June, GC-435, pp 1–10
11. El-Salakawy E, Islam M (2014) Repair of GFRP-reinforced concrete bridge barriers. ASCE J Bridge Eng 1–11. https://doi.org/10.1061/(ASCE)BE.1943-5592.0000584
12. Hirsch T (1978) Analytical evaluation of Texas bridge rails to contain buses and trucks. Research report 20-2, Texas Transportation Institute, Texas A&M University, p 105
13. Jeon SJ, Choi MS, Kim YJ (2008) Ultimate strength of concrete barrier by the yield line theory. Int J Concr Struct Mater 2(1):57–62
14. Jeon SJ, Choi MS, Kim YJ (2011) Failure mode and ultimate strength of precast concrete barrier. ACI Struct J 108(1):99–107
15. Khederzadeh H, Sennah K (2018) Development of transverse ultimate load carrying capacity of concrete bridge barrier using yield-line theory for CHBDC 2019. In: Proceedings of the 10th international conference on short and medium span bridges, Quebec City, pp 1–10
16. Khederzadeh H, Sennah K (2014) Experimental investigation of steel-reinforced PL-3 bridge barriers subjected to transverse static loading. In: Proceedings of the 9th international conference on short and medium span bridges, Calgary, Alberta, pp 1–9
17. Khederzadeh H (2014) Development of innovative designs of bridge barrier systems incorporating reinforcing steel or GFRP bars. Ph.D. dissertation, Civil Engineering Department, Ryerson University, Toronto, Ontario, Canada
18. Khederzadeh H, Sennah K (2014) Development of cost-effective PL-3 concrete bridge barrier reinforced with sand-coated GFRP bars: static load tests. Can J. for Civil Eng 41(4):368–379
19. MASH (2016) Manual for assessing safety hardware, MASH. American Association of State Highway and Transportation Officials, Washington. D.C.

20. MTO (2014) MTO special provision, glass fibre reinforced polymer reinforcing bars-NSSP-2014. Ontario Ministry of Transportation, St. Catherine, Ontario, Canada, 9 pp
21. MTQ (2017) Manuel de conception des structures. Direction Générale des Structures, Ministère des Transports, de la Mobilité Durable et de l'Électrification des Transports, Montréal, Québec
22. MTO (2008) Structural manual. Highway Standards Branch, Bridge Office, Ontario Ministry of Transportation, St. Catharines, Ontario, Canada
23. Rostami M, Sennah K, Afefy H (2017) Ultimate capacity of barrier-deck anchorage in MTQ TL-5 barrier reinforced with headed-end, high-modulus, sand-coated GFRP bars. Can J Civ Eng 45:263–278
24. Rostami M, Sennah M, Mostafa A (2019) Experimental study on the transverse load carrying capacity of TL-5 bridge barrier reinforced with special profile GFRP bars. ASCE J Compos Constr 23(4):1–16, 04019027
25. Sennah K, Hedjazi S (2018) Structural qualification of a developed GFRP-reinforced PL-3 concrete bridge barrier using vehicle crash testing. Int J Crashworthiness 1–18. https://doi.org/10.1080/13588265.2018.1480582
26. Sennah K, Khederzadeh H (2014) Development of cost-effective PL-3 concrete bridge barrier reinforced with sand-coated GFRP bars: vehicle crash test. Can J Civil Eng 41(4):357–367
27. Sennah K, Mostafa A (2018) Performance of a developed TL-5 concrete bridge barrier reinforced with GFRP hooked bars: vehicle crash testing. ASCE J Bridge Eng 23(2):1–20
28. Sennah K, Tropynina E, Ibrahim Z, Hedjazi S (2018) Structural qualification of a developed GFRP-reinforced PL-3 concrete bridge barrier using ultimate load testing. Int J Concr Struct Mater 12(63):1–22
29. Williams W, Buth CE, Menges W (2006) Repair/Retrofit anchorage designs for bridge rails. Report No FHWA/TX-06/0-4823-T1-1, Texas Transportation Institute, Texas A&M University System, College Station, Texas, 161 pp

# Structural Specialty: Ground Structures

# Estimation of Permanent Ground Displacement Capacities for Corroded Pipelines

**Prajakta Jadhav and Dharma Wijewickreme**

**Abstract** Permanent ground displacements (PGD) occur either due to earthquake-induced ground failures, such as lateral spreading, or due to landslides, and in turn, could induce significant strains in buried pipelines. When the induced strains exceed the strain capacity, buried pipelines could suffer potential rupture or compression/buckling failures as evidenced from past earthquake events. Research efforts, including rigorous experimentation and numerical analyses, have led to procedures for evaluating and quantifying pipe stress/strain capacities to withstand PGDs of intact pipelines subjected to ground movements. When pipelines that have experienced corrosion are encountered, their PGD capacities would be certainly different from those of intact pipelines. In pipeline risk assessments, there is a need to account for the corrosion effects on the PGD capacity—in particular, this requires having relatively simpler ways to without resorting to rigorous analyses to address this multi-hazard problem. With this impetus, in the present study, different available approaches were explored to obtain the PGD capacities of corroded pipelines. As the response is dependent on the orientation of pipelines with respect to the ground movements, the PGD capacities were determined considering several cases of straight steel pipe sections subjected to PGDs in both longitudinal and transverse direction to the pipe alignment. Assuming that corrosion effects could be represented by an equivalent pipe wall thickness (i.e., uniform reduction in pipe wall thickness due to corrosion), modification factors were developed to adjust the PGD capacities of intact pipelines to account for different degrees of corrosion.

**Keywords** Pipelines · Permanent ground displacements · Corrosion · Pipeline strain capacity

P. Jadhav · D. Wijewickreme (✉)
Department of Civil Engineering, University of British Columbia, Vancouver, BC, Canada
e-mail: dharmaw@civil.ubc.ca

471

# 1   Introduction

Pipelines are one of the safest ways of transporting fluids over long distances, and it is in everyone's best interest to ensure integrity of pipelines to safeguard our health and quality life, protect communities and environment, and promote economic growth and value creation. Permanent ground displacements hazards, arising from liquefaction-induced lateral spread displacements and landslides, have been noted as one of the major cause of earthquake damage leading to loss of pressure integrity of buried energy pipelines [9]. Under seismic loading, several studies have reported these pipelines to have suffered damage and undergone failures. In 1971, San Fernando earthquake, 11 pipelines got damaged and 80 breaks have been reported. These pipes were primarily subjected to liquefaction-induced lateral spread displacements and landslides. Similar failure cases have been reported in the literature, wherein the pipelines have undergone failures essentially due to permanent ground displacements [2, 6–8]. Typically, under seismic loading, induced ground displacements can manifest in the form of (a) transient ground displacements (TGD) wherein the ground undergoes transient shaking as a result of (during) seismic wave propagation and (b) permanent ground displacements (PGDs) where the ground deforms irreversibly. Damage due to TGDs has been noted to be insignificant compared to PGDs as the TGD-induced strains can be usually accommodated by the good ductility of welded steel pipes (PRCI 2009). Another factor that is of concern is the degradation of pipe strain capacity due to corrosion. As documented in the BCOGC [1] report, except for those cases involving human intervention, occurrence of pipeline failures in Canada can be mainly attributed to those due to corrosion and geotechnical hazard. The performance of the pipeline under geotechnical hazard depends upon the pipeline condition; hence, it is of importance to recognize that corroded pipes can undergo significant damage even underground displacements of relatively lesser magnitude—i.e., reduced pipe stress/strain capacities to withstand PGDs. The capacity of buried pipelines to withstand permanent ground displacements would depend on several factors such as geometrical (cross-sectional) and material properties of pipe and orientation of pipeline with respect to the ground displacements. There is a need to account for the corrosion effects on the PGD capacity, particularly, in pipeline risk assessments through relatively simpler ways without resorting to rigorous analyses to address this multi-hazard problem.

In the present study, different available approaches were explored to obtain the strain/PGD capacities of corroded pipelines. Studies performed in all the three research domains, viz. experimental, numerical and statistical, were explored. It was realized that there is a need of a simplistic methodology to adjust approximately the PGD capacities of intact pipelines to account for the reduction in thickness due to corrosion. The ability to arrive at potential modification factors to the intact-pipe PGD capacities in order to account for the corrosion effects was examined; in essence, the idea to develop/suggest modification factors to account for the changes in PGD capacity of intact pipelines under different degrees of corrosion—established

via an equivalent pipe wall thickness accounting for corrosion, in turn, resulting in equivalent pipeline cross-sectional area ($A$) and second moment of area ($I$).

## 2 Liquefaction-Induced Lateral Spread Displacements Loading

The term lateral spreading is used to describe permanent finite lateral displacements that a gently sloping ground experiences as a result of earthquake-induced liquefaction. The strains induced in buried pipelines would differ based on the direction of ground movement with respect to the orientation of pipeline (see Fig. 1). Accordingly, two types of PGD capacities can be obtainable: longitudinal PGD capacity and transverse PGD capacity. These ground displacements can be characterized by the dimensions of the lateral spread zone and magnitude of the ground displacements.

Buried pipelines will have different components, viz. straight pipe segments, T-section, elbows, etc. In this study, the focus is on straight pipe segments only. Further, the pipelines are susceptible to different types of pitting corrosion patterns; single pit, multiple non-interacting pit clusters, and multiple interacting pit clusters are some examples in this regard. However, typically available models estimate corrosion rates reflecting uniform reduction of pipe wall thickness. Accordingly, in the present study, it was considered reasonable to assess PGD capacities only assuming an equivalent reduced pipe wall thickness. As the response is dependent on the orientation of pipelines with respect to the ground movements, the PGD capacities were determined considering several cases of straight steel pipe sections subjected to PGDs in both longitudinal and transverse direction to the pipe alignment.



(a)  (b)
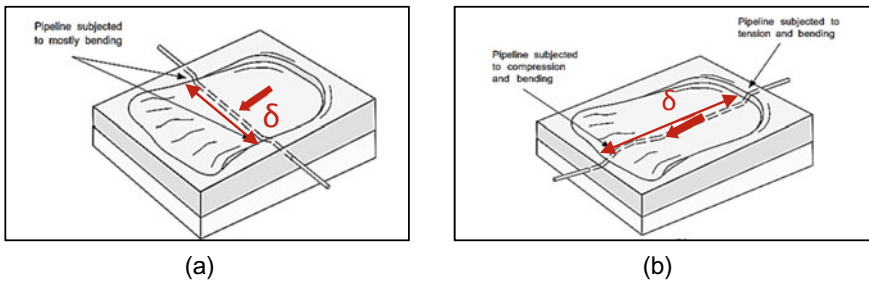
**Fig. 1** Pipeline subjected to: **a** transverse ground movement and **b** longitudinal ground movement

# 3 Estimation of Longitudinal PGD Capacities

When a buried pipeline is subjected to longitudinal ground displacements, the pipeline experiences tension on one end of the lateral spread zone, and compression at the other end of this zone, as shown in Fig. 2. The buried pipeline would offer resistance to these longitudinal (axial) ground displacements as a result of the frictional forces developed along the length of the pipeline to accommodate the ground displacements.

Although this length of the pipeline would depend upon the pipeline alignment, it is important to ensure that the length of the pipeline is sufficient enough to accommodate the ground displacements as well as provide the required anchorage outside the zone of ground movement. This equivalent anchor length of the pipe ($L_{EA}$) can be obtained by equating the axial forces due to the axial soil restraint force acting along $L_{EA}$ with the axial force corresponding to the axial stress of 110% of the minimum specified yield strength (Terasen 2010). See Fig. 2 for the definition of $L_{EA}$.

$$L_{EA} = \frac{1.1\pi \, Dt\sigma_y}{T_u} \tag{1}$$

Here,

$D$ = outer diameter of pipe
$t$ = pipe wall thickness
$T_u$ = maximum axial soil restraint
$\sigma_y$ = minimum specified yield strength.

In other words, the equivalent length, $L_{EA}$ is the length required for the soil restraint force, $T_u$, to induce axial yield in the pipeline. Based on the length of PGD zone, relative to this $L_{EA}$, following cases are possible:

Case A: length of lateral spread zone < 2 $L_{EA}$. In this case, the probability of failure due to axial PGD is considered 0%.

Case B: length of lateral spread zone > 2 $L_{EA}$. This condition signifies that the soil restraint forces, $T_u$, acting along the length, $L_{EA}$, would result in yielding and that the pipe would have negligible additional capacity. Under such circumstances, the
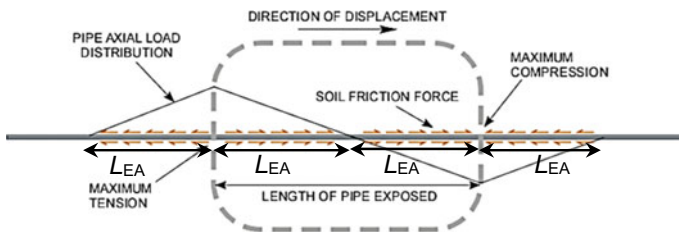


**Fig. 2** Load distribution on pipeline subjected to axial ground movement

probability of failure would depend upon the likelihood that the length of PGD zone is actually greater than 2 $L_{EA}$ and that the axial displacements induced are greater than the maximum displacements induced due to tension and compression at the ends of the PGD zone. Further, for yield strain of 0.5% assuming triangular distribution for axial soil restraint forces, the axial pipe displacement capacities, $D_{A\max}$, have been estimated using Eq. (2) (Terasen 2010).

$$D_{A\max} = 0.005 L_{EA} \tag{2}$$

The steps/procedure mentioned above for intact pipelines was adopted for corroded pipelines. The $L_{EA}$ and the corresponding $D_{A\max}$ were calculated for assuming Grade X60 steel pipeline for different pipe sections: viz. NPS 4, 8, 12, 24, 30, and 42. One soil type with the following soil parameters were assumed for the estimation of the soil restraint forces ($T_u$) using Eq. (3) as per (2009) are unit weight ($\gamma$) = 18 kN/m$^3$, internal friction angle ($\phi$) = 32°, coefficient of lateral earth pressure ($K$) = 0.6 and burial depth of 1 m.

$$T_u = \pi.D.h.\gamma'.\left(\frac{1+K}{2}\right).\tan\delta \tag{3}$$

The longitudinal PGD capacities for intact pipelines as well as those for the cases corresponding to 10–30% reduction in pipe wall thickness due to corrosion are given in Table 1. It can be observed that the anchor length ($L_{EA}$) required for resisting the PGDs increases with the decreasing pipe wall thickness due to corrosion. As such, there is increase in the probability of exceeding the $L_{EA}$ (in other words, reducing longitudinal PGD capacity) a result of increasing degree of corrosion.

## 4 Estimation of Transverse PGD Capacities

A buried pipeline when subjected to transverse PGD would stretch and bend to accommodate the transverse ground displacements. Under this scenario, the failure mode will be governed by the relative amount of axial tension and flexural/bending strain. The pipeline would rupture due to the combined effects of the axial tension and flexure, if axial strains in pipe are considerable; whereas, if the axial strains are low, alternatively, the pipeline may buckle in compression due to excessive bending. Based on the observations made from the past earthquakes, the PGD patterns/profiles (in plan view) can manifest primarily in the form of the following categories: gradually varying PGD profile and abrupt PGD profile, as shown in Fig. 3. It was decided to explore and examine existing analytical methodologies for estimating the transverse PGD capacities of buried pipelines under both the ground displacement profiles and assess how these can be extended for estimating those capacities for the cases of corroded pipelines. Based on the employment of these analytical models, the idea

**Table 1** Longitudinal PGD capacities of buried pipelines of different NPS sizes

| NPS | % corrosion | $D$ (in) | $D$ (m) | $t$ (m) | $L_{EA}$ (m) | Dmax ~ 0.5% yield strain |
|-----|-----|-----|-----|-----|-----|-----|
| 4 | 0 | 4.5 | 0.114 | 0.0054 | 532 | 2.7 |
| 4 | 10 | 4.5 | 0.114 | 0.00486 | 479 | 2.4 |
| 4 | 20 | 4.5 | 0.114 | 0.00432 | 426 | 2.1 |
| 4 | 30 | 4.5 | 0.114 | 0.00378 | 373 | 1.9 |
| 8 | 0 | 8.625 | 0.219 | 0.0055 | 542 | 2.7 |
| 8 | 10 | 8.625 | 0.219 | 0.00495 | 488 | 2.4 |
| 8 | 20 | 8.625 | 0.219 | 0.0044 | 434 | 2.2 |
| 8 | 30 | 8.625 | 0.219 | 0.00385 | 380 | 1.9 |
| 12 | 0 | 12.75 | 0.324 | 0.0064 | 631 | 3.2 |
| 12 | 10 | 12.75 | 0.324 | 0.00576 | 568 | 2.8 |
| 12 | 20 | 12.75 | 0.324 | 0.00512 | 505 | 2.5 |
| 12 | 30 | 12.75 | 0.324 | 0.00448 | 442 | 2.2 |
| 24 | 0 | 24 | 0.610 | 0.0071 | 700 | 3.5 |
| 24 | 10 | 24 | 0.610 | 0.00639 | 630 | 3.2 |
| 24 | 20 | 24 | 0.610 | 0.00568 | 560 | 2.8 |
| 24 | 30 | 24 | 0.610 | 0.00497 | 490 | 2.5 |
| 30 | 0 | 30 | 0.762 | 0.0105 | 1035 | 5.2 |
| 30 | 10 | 30 | 0.762 | 0.00945 | 932 | 4.7 |
| 30 | 20 | 30 | 0.762 | 0.0084 | 828 | 4.1 |
| 30 | 30 | 30 | 0.762 | 0.00735 | 725 | 3.6 |
| 42 | 0 | 42 | 1.067 | 0.0091 | 897 | 4.5 |
| 42 | 10 | 42 | 1.067 | 0.00819 | 808 | 4.0 |
| 42 | 20 | 42 | 1.067 | 0.00728 | 718 | 3.6 |
| 42 | 30 | 42 | 1.067 | 0.00637 | 628 | 3.1 |

was to develop corrosion modification factors which can be directly applied to the PGD capacities of the intact pipelines.

## 4.1 Transverse PGD Capacity for Buried Pipelines Subjected to Gradual PGD Profile

Liu and O' Rourke [5] have proposed analytical expressions for estimating strains in the pipe corresponding to different values of PGDs. According to their model, the pipe is modeled as elastic and subjected to a PGD profile extending as a cosine wave function (in plan) over the lateral spread zone. According to Liu and O' Rourke [5] as shown in Fig. 4, during PGD, the pipe displaces by the same magnitude as

(a)                                           (b)
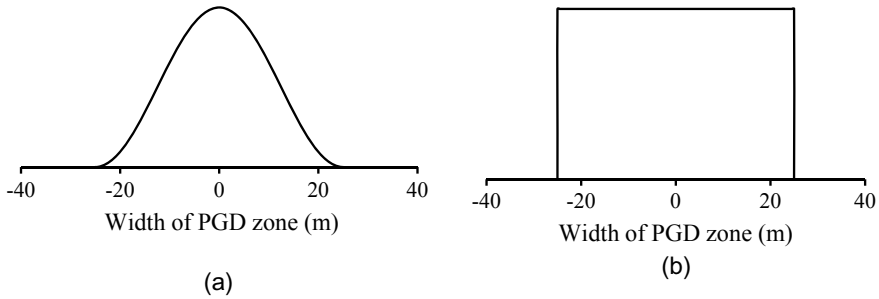
**Fig. 3** Lateral PGD (plan view) profiles considered in the analyses: **a** gradually varying PGD profile and **b** abrupt PGD profile

that of ground up to certain magnitude of PGD, denoted as critical displacement ($\delta_{cr}$); beyond this point, with increasing PGD, the strains induced in the pipe stay nearly constant and with essentially no change in the pipe displacements. Based on this theory, Liu and O' Rourke [5] proposed the expressions to estimate $\delta_{cr}$ while accounting for the flexural (beam) as well as axial (cable) effects. In the present study, these equations were embedded in a computer code to obtain longitudinal strain versus ground displacements for all the NPS sizes.

For the present exercise, the width of PGD zone as shown in Fig. 3 in this study was assumed 100 m represent cross-sectional properties of the corresponding NPS pipe section, viz. the chosen pipe sizes [diameter ($D$) and thickness ($t$)] are given in Table 2. The cross-sectional area ($A$) and second moment of area ($I$) were computed accordingly. Young's modulus of steel pipe ($E$) was considered as 210 GPA. The soil restraint forces, axial soil restraint ($T_u$), and lateral soil restraint ($P_u$) were calculated using the equations given in PRCI (2009) guidelines; the soil parameters
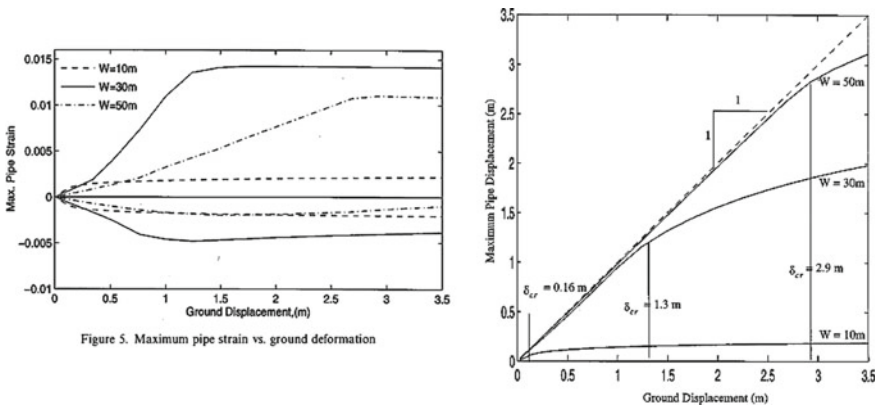


**Fig. 4** Maximum pipe strains and maximum pipe displacements versus ground displacements curve (after Liu and O' Rourke [5])

were identical to those used for the estimation of longitudinal PGD capacities: $\gamma = 18 \text{ kN/m}^3$; $\phi = 32°$. A pipe burial depth of 1 m was used.

Typical variation of longitudinal strains with permanent ground displacements, computed for NPS 12 pipe for different levels of corrosion using the analytical model, shown in Fig. 5. In this study, these curves were obtained for reduced equivalent pipe wall thickness of the pipe for each NPS size, to different levels of corrosion, viz. 10, 20, and 30%. The magnitude of displacements resulting in same magnitude of strain can be observed to decrease with increase in the degree of corrosion. As the curve follows linear trend up to the $\delta_{cr}$ value, the modification factors were calculated as the ratio of displacement capacity for the corroded pipe to that of an intact pipe for a particular strain value. The computed modification factors for different levels of corrosion are given in Table 2.

## 4.2 Transverse PGD Capacity for Buried Pipelines Subjected to Abrupt PGD Profile

Unlike for the case of gradually changing PGD profile (Fig. 3), analytical studies reporting the expressions for estimating strains in buried pipeline due to abrupt PGD profile are limited. Instead, through numerical modeling (typically using finite element method), the strains induced in a buried pipeline as a result of abrupt ground displacement profile can be computed, and in turn, the PGD capacities for intact pipelines can be estimated. In order to simplistically estimate the PGD capacities for a corroded pipe using the PGD capacities for intact pipelines, in the present study, it was explored whether the modification factors obtained for the gradual PGD profile (discussed in the previous section) could be adopted for abrupt PGD profile as well.

In view of this, a three-dimensional numerical model of pipe was developed using ABAQUS software [10], wherein the soil was modeled using springs in all the three directions, viz. horizontal, lateral/transverse, and vertical. The lateral spread zone width of 100 m was considered for the model. The pipe has been modeled using deformation plasticity model in ABAQUS with Ramberg–Osgood parameters [11]. The far ends were modeled as fixed. The numerical analyses were performed considering the cases of 0, 20, and 40% reduction in equivalent pipe wall thickness due to corrosion. Figure 6 shows the variation of computed longitudinal strains versus permanent lateral ground displacements for NPS 12 pipe for the three different levels of corrosion considered in the analyses. The modification factors were obtained using the above-mentioned exercise. Slight deviation in the factors was observed owing to the different set of boundary conditions than those considered in the analytical model. Liu and O' Rourke [5] considered gradually applied transverse displacements following cosine wave pattern which would result in different magnitude of strains than with abrupt displacements. As a result, the PGD capacity for the case of abrupt PGD profile got reduced further as the pipeline would have reduced capability to accommodate abrupt displacements. Based on this examination, it was deduced that

**Table 2** Modification factors to account for corrosion for different pipe sizes using analytical model

| % Corrosion | D (m) | t (m) | δ$_{cr}$ (m) | Strain | Factor | % Corrosion | D (m) | t (m) | δ$_{cr}$ (m) | Strain | Factor |
|---|---|---|---|---|---|---|---|---|---|---|---|
| NPS 4 | | | | | | NPS 24 | | | | | |
| 0 | 0.102 | 0.0054 | 11.6 | 0.007 | 1.000 | 0 | 0.610 | 0.0071 | 7.6 | 0.009 | 1.000 |
| 10 | 0.101 | 0.0049 | 12.0 | 0.008 | 0.960 | 10 | 0.608 | 0.0064 | 7.8 | 0.009 | 0.978 |
| 20 | 0.099 | 0.0043 | 12.4 | 0.008 | 0.916 | 20 | 0.607 | 0.0057 | 8.0 | 0.009 | 0.953 |
| 30 | 0.098 | 0.0038 | 12.8 | 0.009 | 0.867 | 30 | 0.605 | 0.0050 | 8.3 | 0.010 | 0.924 |
| NPS 8 | | | | | | NPS 30 | | | | | |
| 0 | 0.203 | 0.0055 | 9.6 | 0.007 | 1.000 | 0 | 0.762 | 0.0105 | 6.6 | 0.008 | 1.000 |
| 10 | 0.202 | 0.0050 | 9.9 | 0.007 | 0.965 | 10 | 0.760 | 0.0095 | 6.8 | 0.008 | 0.983 |
| 20 | 0.201 | 0.0044 | 10.2 | 0.008 | 0.926 | 20 | 0.758 | 0.0084 | 7.0 | 0.009 | 0.964 |
| 30 | 0.200 | 0.0039 | 10.6 | 0.009 | 0.882 | 30 | 0.756 | 0.0074 | 7.3 | 0.009 | 0.941 |
| NPS 12 | | | | | | NPS 42 | | | | | |
| 0 | 0.305 | 0.0064 | 8.5 | 0.007 | 1.000 | 0 | 1.067 | 0.0091 | 6.6 | 0.010 | 1.000 |
| 10 | 0.304 | 0.0058 | 8.8 | 0.007 | 0.970 | 10 | 1.065 | 0.0082 | 6.9 | 0.011 | 0.985 |
| 20 | 0.302 | 0.0051 | 9.0 | 0.008 | 0.936 | 20 | 1.063 | 0.0073 | 7.1 | 0.011 | 0.968 |
| 30 | 0.301 | 0.0045 | 9.4 | 0.009 | 0.898 | 30 | 1.061 | 0.0064 | 7.4 | 0.012 | 0.947 |

**Fig. 5** Variation of longitudinal strains with permanent lateral ground displacements for NPS 12 pipe for different levels of corrosion using analytical model
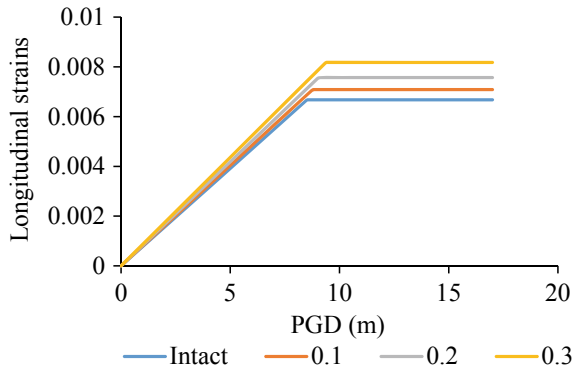


**Fig. 6** Variation of longitudinal strains with permanent lateral ground displacements for NPS 12 pipe for different levels of corrosion using FE model
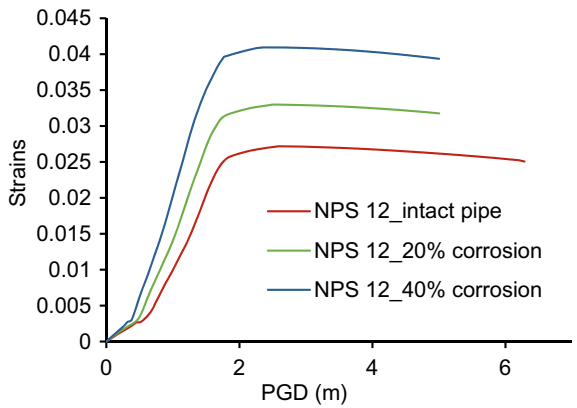


the modification factor in the event of abrupt displacements is ~ 0.86 times the factor obtained based on analytical model that considers gradual cosine wave displacement pattern. Further, it is to be noted that the modification factors proposed herein should be only used for prorating the linear part of the curve (as shown on Fig. 6) only, as prorating for higher displacements is beyond the scope as it will involves high nonlinearity.

## 5   Conclusion

There is a need to account for the corrosion effects on the PGD capacity. In this study, relatively simple way to account for the complex problem of corroded pipelines subject to ground movements, without rigorous analyses, is proposed. Since the failure mode in buried pipelines would differ based on the direction of orientation of pipeline with respect to the ground movement, PGD capacities have been computed

for PGD longitudinal and transverse to the buried pipelines for pipes experiencing equivalent wall thickness reductions from 0 to 30% due to corrosion. Accordingly, some of the key outcomes are as follows:

1. For pipes experiencing longitudinal ground movement, the equivalent anchor length ($L_{EA}$), and hence, the PGD capacity reduces with increase in corrosion.
2. For pipes subjected to gradually varying transverse ground movement, modification factors corresponding to different levels of corrosion were calculated based on available analytical model for different pipe sizes. The computed PGD capacities of intact pipelines can be multiplied by the modification factors to obtain the PGD capacities of corroded pipelines.
3. When estimating PGD capacities of corroded pipelines under abrupt transverse ground movements, the modification factors obtained for gradually varying transverse ground movements should be further reduced by about 0.86 (obtained based on FE analyses).

# References

1. (BCOGC), B.O. and G.C. (2018) Pipeline Performance Summary 2016 Annual Report
2. Ariman T, Lee BJ, Chen Q (1987) Failure of buried pipelines under large ground deformations. In: Developments in geotechnical engineering. Elsevier, pp 63–75
3. C-CORE, D.G. Honegger Consulting SSD, I. (2009) Guidelines for constructing natural gas and liquid hydrocarbon pipelines through areas prone to landslide and subsidence hazards. Design, Materials, and Construction Committee of Pipeline Research Council International, Inc. (January)
4. D.G. Honegger Consulting (2010) Regional seismic risk assessment of terasen natural gas pipelines
5. Liu X, O'Rourke MJ (1997) Behaviour of continuous pipeline subject to transverse PGD. Earthquake Eng Struct Dyn 26(10):989–1003. Wiley Online Library
6. Lund LV (1994) Lifelines performance in the landers and big bear (California) earthquakes of 28 June 1992. Bull Seismol Soc Am 84(3):562–572. The Seismological Society of America
7. Lund LV (1996) Lifeline utilities performance in the 17 January 1994 Northridge, California, earthquake. Bull Seismol Soc Am 86(1B):S350–S361. The Seismological Society of America
8. Mori S, Chiba K, Koike T (2012) Seismic performance analysis of the transmission Gas pipeline in the 2011 Great East Japan earthquake. In: 15th world conference on earthquake engineering (15WCEE), pp 24–28
9. O'Rourke TD, Stewart HE, Gowdy TE, Pease JW (1991) Lifeline and geotechnical aspects of the 1989 Loma Prieta earthquake. University of Missouri–Rolla
10. Smith M (2018) ABAQUS/Standard User's Manual, Version 2018. Dassault Systèmes Simulia Corp, United States
11. Walker AC, Williams KAJ (1995) Strain based design of pipelines

# Analyzing Geosystems with Deployable Compliant Mechanisms for Enhanced Tension Capacity

**Kaylee A. Tucker and Ann C. Sychterz**

**Abstract**  Current research into deployable and compliant structures focuses on their applications above-ground. Deployable structures have benefits in the construction industry because they can be transported compactly and installed easily on site. These benefits can be extended to underground applications which have not been widely investigated experimentally. Geotechnical structures, loaded primarily in tension, risk brittle collapse or displacement accumulation under extreme loading. To address this concern, members are oversized or components are added. Deployable structures offer a way to resist extreme design loading while increasing system resiliency and decreasing material cost, transport, construction time, and environmental impact. The goal of this work is to develop compliant attachments to the exterior of tension-loaded geostructures that deploy passively and increase the bearing area and capacity. This novel arrangement consists of a tension-loaded member (a pile) and compliant components (awns). When twisted, the awns deploy, entrapping soil and increasing surface friction. This increases the tensile capacity of the pile. Test members are fabricated via additive manufacturing using rigid polymer and rubber from Stratasys. They are rotated in clear sand by manually pulling cables with a load cell to measure applied tension. Using a machine vision plugin, rotation data is collected from video footage during experimental tests. The performance of the geometry is evaluated based on predictable awn deployability and the tension load of the geosystem. This paper presents parametric studies and experimental tests of adaptive torque-driven underground structures at small scale. With both structural and sustainability benefits, the deployable attachments increase the tension capacity of ground anchors while decreasing the embodied energy of the anchors.

**Keywords**  Adaptive structures · Deployable structures · Compliant structures · Additive manufacturing · Tension piles · Parametric design · Experimental validation

K. A. Tucker (✉) · A. C. Sychterz
Civil and Environmental Engineering, University of Illinois at Urbana-Champaign, Champaign, USA
e-mail: katucke2@illinois.edu

# 1 Overview

A key feature of deployable structures is that they change shape as they change size. These structures deploy by expanding in shape when their size is increased [15]. Deployable and compliant structures have potential within the field of civil engineering thanks to their potential for increased capacity and decreased embodied energy.

Two common applications of deployable structures take advantage of these features. For temporary installments—like emergency shelters [3]—lightweight, movable, and easy to erect structures are required. Larger scale systems, like scissor structures [7] and space applications such as masts, solar arrays, and antennae [5, 26], are designed to be lightweight and compact for ease of transportation [25]. In practice, many contemporary structures use preconnected parts for easier deployment. Locking mechanisms may also be necessary for deployable structures that are stress-free before, during, and after deployment [6]. Construction of deployable structures has focused on these aboveground structures but have not yet been expanded to underground use.

Compliant structures are similar to deployable structures in that they change shape. However, instead of changing shape by changing size, compliant structures change shape through elastic or plastic material deformation. Compliant elements are singular elements that deform to perform their functions [9]. These biologically inspired mechanisms function without joints and like natural elements are flexible [11]. Compliant structures also have advantages in assembly and manufacturing because as singular elements, there is little assembly or pre-connection required [29]. While new work has been done to scale up compliant structures to the building scale for use in façades [10, 20], compliant structures tend to be used in small scale applications such as microelectromechanical systems [16].

Although most geotechnical engineering systems do not change shape, this is beginning to change within the area of pile-based anchors [8, 13, 28]. Existing work has been done regarding underground geostructures that involve fins. Static radial fins were found to better resist uplift loads when installed in sand and varied with fin configuration and geometry [27]. Piles that have anchor wings have also been explored. After a pile is rotated into sand, wings hinge outward into sand and provide improved resistance to uplift loads [19]. In addition, static piles with snakeskin inspired geometries have been tested [14]. While these studies have explored the advantages of deployability or biological inspiration, they either have no motion involved or work through rigid body motion. Compliant and deployable systems, which change shape and size elastically, have not yet been explored within geotechnical engineering.

This paper presents parametric studies and experimental tests of adaptive torque-driven underground structures at small scale to increase the tension capacity of ground anchors. This adaptive structure combines elements of deployable and compliant structures with existing work in increasing capacity of underground geostructures

via protrusions. This new work stems from the authors' publication on hammer-driven deployable compliant piles, but focuses on a torque-based deployment and a radial arrangement of compliant components [23].

## 2 Structure Description

This work focuses on a geosystem (Fig. 1) comprised of a cylindrical tension-loaded member—a pile—and a specified number of compliant components. These compliant elements, or awns, deploy into sand via rotation. When deployed by twisting, the awns change shape and size and undergo bending. This combination of deployable and compliant structures entraps soil and increases surface friction. This paper first presents an exploration of parameters that contribute to the geometry of the awn and then determines how changing one geometric parameter—the number of awns—impacts the tensile capacity of the geosystem.

The geosystem test members were fabricated via additive manufacturing on a Stratasys Objet500 Connex3 resin 3D printer [22]. This machine has a build volume of 0.5 m × 0.4 m × 0.3 m and prints multi-material parts with a layer thickness of 25 microns. The piles were printed using the rigid polymer VeroMagentaV and
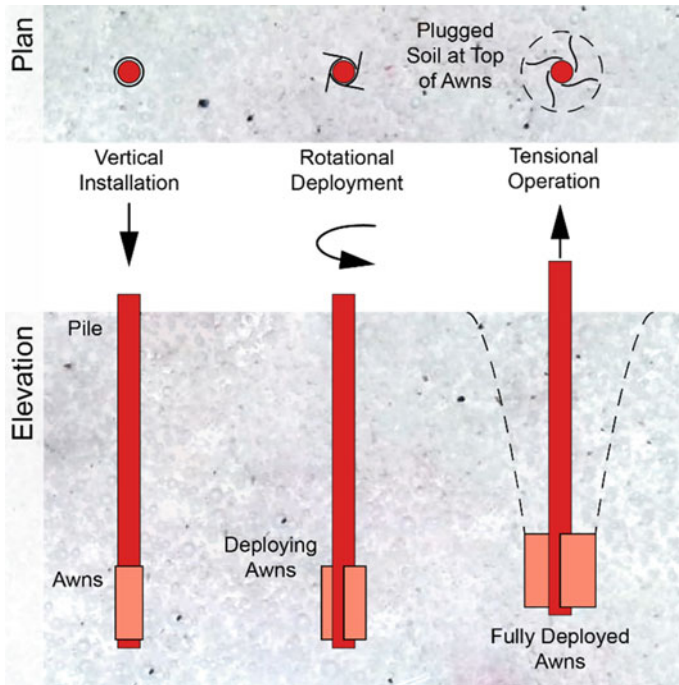


**Fig. 1** Schematic illustration of geosystem before, during, and after deployment

VeroCyan. Both of these materials are 100% rigid polymer with a Young's modulus of 3 GPa and a tensile strength of 65 MPa. The awns were a mixture between rigid polymer (VeroMagentaV) and rubber (Agilus30) materials at a proportion of 95% rigid polymer and 5% rubber. This combination of materials has a tensile strength of 62 MPa.

## 3   Methodology

### 3.1   Overview

This work began with defining the parameters and parametrically modeling the geosystem and its geometry. This was accomplished in Grasshopper, a computational design environment within Rhinoceros 7 [18]. External plugins—Pufferfish, Telepathy, and TT Toolbox [4, 12, 24]—were used in the Grasshopper definition as well.

The geosystem members were then fabricated using the printer and the parameters as described in Sect. 2. Each pile was printed at a height of 75 mm and a diameter of 25 mm with awns attached. Each member was printed vertically to mitigate unequal prestressing on the awns. After fabrication, the test members were deployed in clear sand by manually pulling cables with a load cell to measure applied tension. Data was obtained by recording videos of the awns deploying and the load cell readout. These videos were synchronized and analyzed to find the maximum force, the deployment of the awns, and the rotation of the pile.

### 3.2   Geometry

The basic geometry of the geosystem is a cylinder (the pile) with one or more awns attached. These awns are comprised of two connected arcs—the first arc is exactly the radius of the pile and the second arc can be any radius larger than the first. The first arc ensures that the awn is smoothly attached to the pile. The second arc has a larger radius than the first to ensure that the awn can be separated from the pile after printing.

The arcs are defined by their radii and arc length. Once both arcs are defined (i, ii), the second arc is repositioned at the end of the first arc and is rotated into a neutral position (iii). If desired, the angle between the arcs can be adjusted further. After any adjustments, the first arc and second arc are joined (iv) and optionally filleted for smoothness.

To ensure a smooth attachment to the pile, the awns are thickened by offsetting different parts of the joined curve. This is achieved by creating horizontal lines along the curve in varying lengths—one at each end and a specified number (here, one) in

the middle (v). These lines are used as cross section curves for the joined curve to pass through (vi), allowing for the definition of the outer curve [21].

After obtaining the basic shape of the inner and outer curves, they are closed together (with various options for the cap type and size) (vii). The final footprints are then extruded in the $z$ direction and arrayed around the pile (ix). The definition also records and saves data about each iteration to an Excel file. In addition, it generates annotations to embed in the print in a different color. In addition to printing the name of the iteration on the final print, it also prints colored points and lines to improve motion tracking during testing (viii).

## 3.3  Experimental Testing

Testing consisted of awns being deployed in Ranco-Sil™ B (30/50 mesh) fused silica sand [17] to determine performance. When a solution of sugar water (198 g sugar to 100 mL water) is added to the sand in a ratio of 42 g solution to 100 g sand, the resulting mixture becomes translucent.

The testing setup (Fig. 3) is comprised of a clear acrylic box raised above a document camera by a wooden crate. Two pieces of wood are clamped to the top of the crate to constrain the box from moving in one direction. Along the same axis, two small pulley clamps are attached to the edges of the crate, aligning with the centerline of the acrylic box.

The test member is placed in the center of the acrylic box. When testing, petroleum jelly (sufficient to create a 1 mm thick layer between the pile and the acrylic box) is added to the bottom of the pile. This ensures that the member stays in place during setup and keeps the bottom of the box clear of sand so that test data can be recorded via video from the document camera.

Next, the clear sand is added until it fills the box up to a 25 cm mark, just covering the awns. An acrylic plate was fabricated with a hole in the center to help keep the awn in place during testing. After the plate is placed on top of the sand, a nylon cord is coiled around the pile and is laid on the pulleys. To account for the uneven placement of the clear box on the table, the cord's midpoint is placed at the center of the pile. Under the table, the ends of the cord are connected by matching their ends and tying them in a knot to the measurement device. A load cell with a capacity of 4500 N and a resolution of 4.5 N was used for this experiment. The pulley system setup allows for the positions of the awns to be recorded via video from the document camera while simultaneously tracking the force applied to the geosystem as it deploys to measure applied tension.

### 3.4 Tracking

To record the movement of the awns during testing, blue polymer points were embedded into the bottoms of the pile and the awns. The main geometry of the geosystems was printed with the VeroMagentaV polymer, but these tracking points were printed in the VeroCyan polymer. Videos recorded during testing showed the movement of these tracking points. At the same time, the load cell's digital readout was videotaped to record the force applied to the system.

The position of the awns was recorded by embedding two trackers—one on the awn and one on the pile (Fig. 4). For each set of these position trackers, the distance between the two points was calculated to give information on the awns' deployment. A line was also embedded into the pile to allow for rotation tracking. For this type of tracking, two points along the line are analyzed simultaneously, allowing for rotation data to be recorded.

Two methods for processing the raw data were explored. Both methods began with matching the videos recorded during the experiment (Fig. 5). Using the native synchronization feature in Adobe Premiere Pro [2], video sound was used as a reference to synchronize the videos. A loud clap and ambient noise were used as reference sounds.

The first method of data processing provided static information about the maximum force and the distances the awns deployed to. For this method, the videos were marked at the maximum force and the maximum angle. The frames at those times were exported to images and imported into Rhinoceros 7. Then, the distance associated with the position trackers and the angle associated with the rotation tracker were dimensioned and recorded in a spreadsheet.

The second method provided dynamic data of how the awns move throughout the test. After synchronizing the videos, the video recorded from the document camera was imported into Adobe After Effects [1]. To track both the position and rotation movements, the native Track Motion function was used. For this method, the contrasting color of the blue tracking points against the magenta geosystem allowed for the tracking to be analyzed through the RGB channel, a more accurate tracking method than the Luminance channel. The tracked information was brought back into Adobe Premiere Pro and displayed on the video canvas so that it can be analyzed in real time with the movement of the awn and the force applied.

### 3.5 Awn Count Tests

In this experiment, three versions of the geosystem were tested with different numbers of awns. The following tests (Table 1) allowed for determining the impact of the number of awns on the force required for deployment.

Awn geometry and fabrication for the three cases were identical. They were all comprised of two arcs, the first one was a 12.5 mm radius arc measuring 17 mm

**Table 1**  Tested awn arrangements and their parameters

| Parameter | Units | AwnCount1 | AwnCount2 | AwnCount3 |
|---|---|---|---|---|
| Awn count | — | 1 | 2 | 3 |
| Pile height | mm | 50 | 50 | 50 |
| Pile diameter | mm | 25 | 25 | 25 |
| Radius 1 | mm | 12.5 | 12.5 | 12.5 |
| Arc length 1 | mm | 17 | 17 | 17 |
| Radius 2 | mm | 25 | 25 | 25 |
| Arc length 2 | mm | 25 | 25 | 25 |
| Awn thickness (attachment point, midpoint, free end) | mm | 0, 1.6, 2 | 0, 1.6, 2 | 0, 1.6, 2 |
| Angle between arcs | deg (°) | 0 | 0 | 0 |
| Fillet | mm | 10 | 10 | 10 |
| Cap type | – | Rounded | Rounded | Rounded |
| Curve bulge | mm | 1.0 | 1.0 | 1.0 |
| Plan | – |  |  |  |

in length and the second one was a 25 mm arc measuring 25 mm in length. The awn profile was defined using the guideline and rail method as seen in steps (v) and (vi) from Fig. 2. In this test, the attached end's guideline was set to 0.0 mm, the midpoint's was set to 1.6 mm, and the unattached end's guideline was set to 2.0 mm. This provides an awn profile that attaches smoothly to the pile and increases in thickness smoothly to the tip of the awn.

Each awn arrangement was printed three times, and each print was tested three times using the testing setup from Sect. 3.3. The six trials' data was processed using the static method from Sect. 3.4. During the tests, the awns started in the neutral position they were printed in, as seen in Fig. 6. During deployment, they separated further from the pile. The tests were stopped when awns reached an angle of 90° to the pile at the attachment point (Fig. 6).

Results (Table 2) were obtained by averaging the six trials for each type of geostructure. The rotation angle was found directly through the static data processing method. The average awn deployment was calculated by finding the difference between the initial awn position and the final awn position, measured between the end point of the awn and a static point on the pile. For the geostructures with more than one awn, those deployment values were averaged to find an overall measurement. To find the rate of deployment with respect to rotation, the average deployment value in each trial was divided by the rotation angle for that trial. The average between the six trials of each type of geostructure was then calculated.
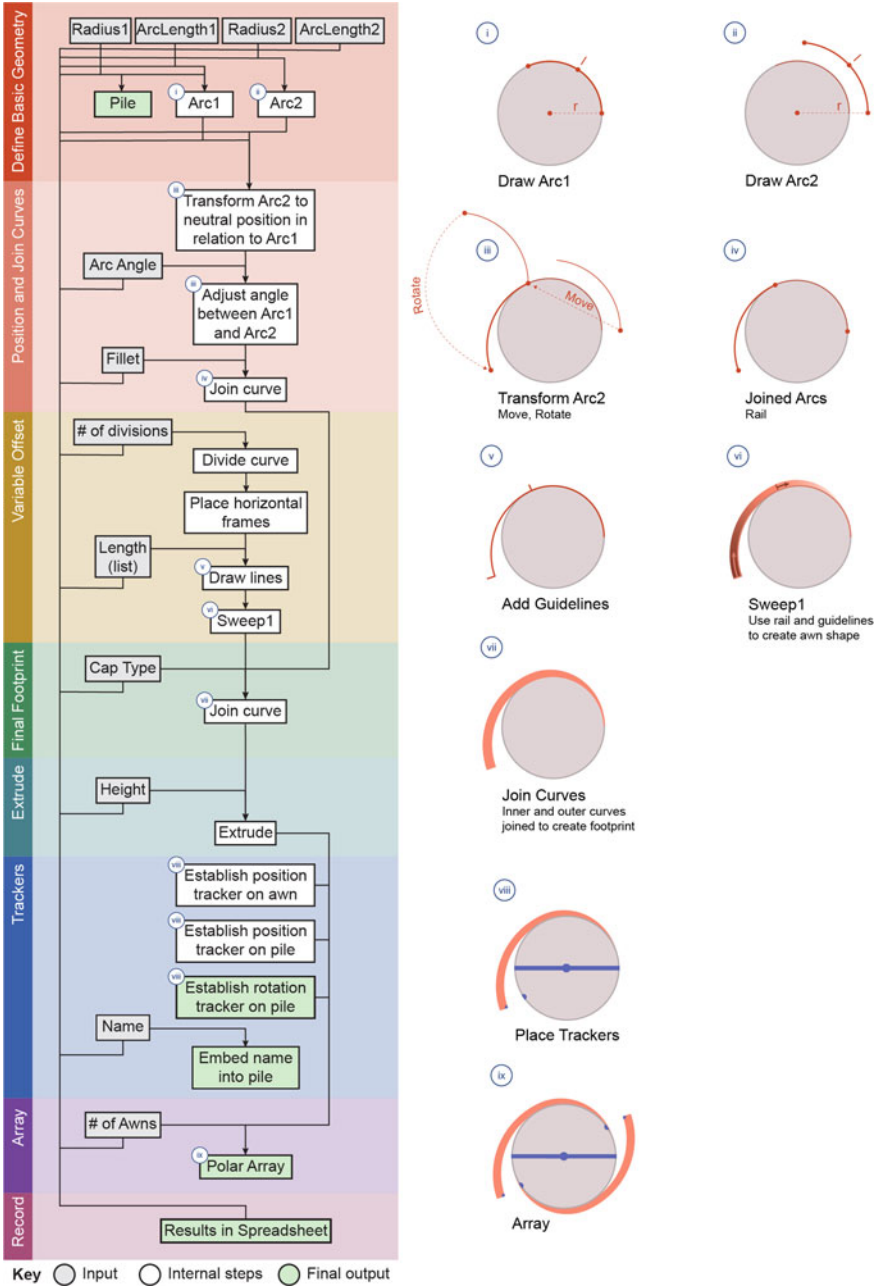
**Fig. 2** Grasshopper definition logic for defining and generating awn geometry with step-by-step images
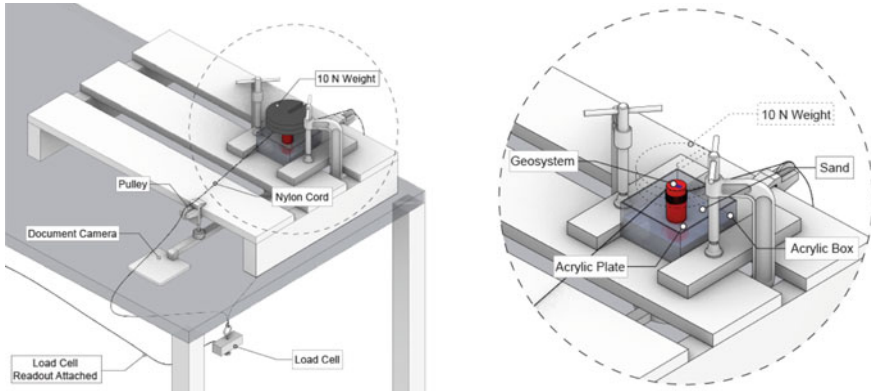
**Fig. 3** Representation of testing setup showing data collection methods [left] and geosystem setup [right]
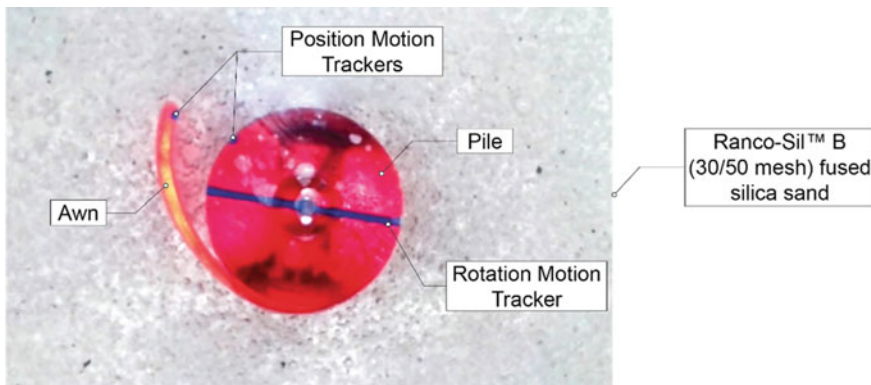


**Fig. 4** 3D printed geosystem being tested in Ranco-Sil silica sand with embedded motion trackers
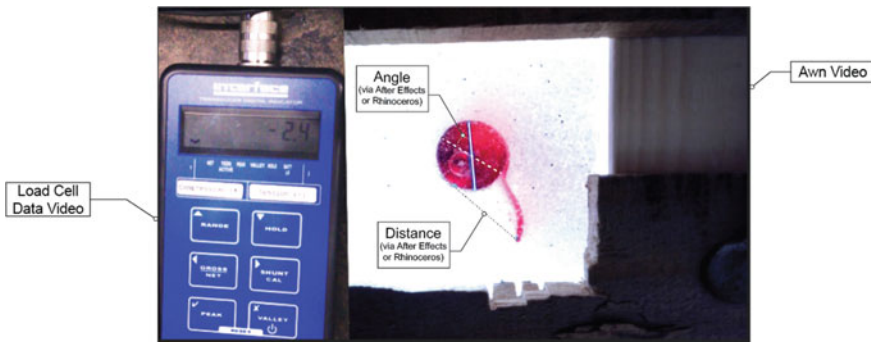


**Fig. 5** Adobe Premiere Pro video editing setup with load cell data [left] and awn videos [right]
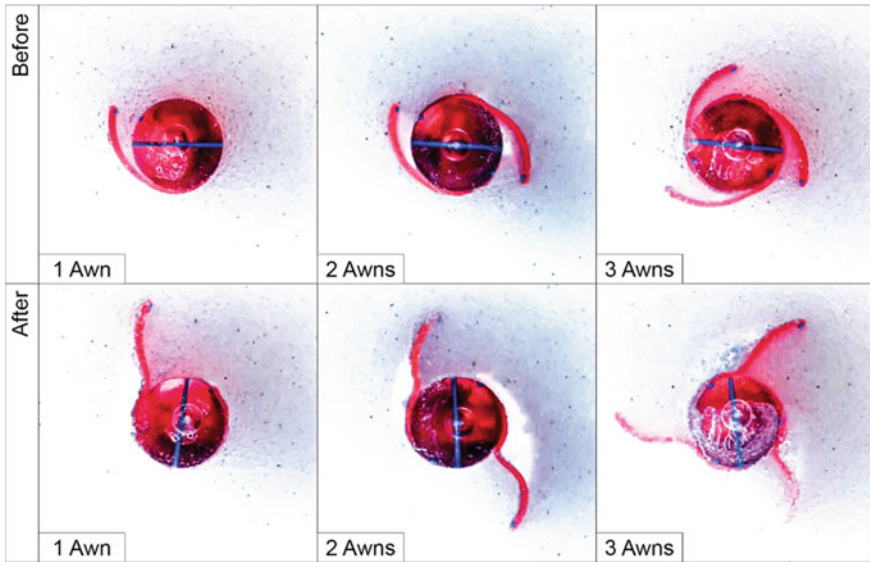
**Fig. 6** 3D printed geosystems before and after testing in Ranco-Sil silica sand

**Table 2** Average results at maximum force

| Awn count | Rotation angle (°) | Average awn deployment (mm) | Awn deployment/ degree rotation (mm/°) | Maximum force (N) | Difference from AwnCount1 force (%) |
|---|---|---|---|---|---|
| 1 | 66.0 | 14.6 | 0.23 | 12.2 | 0 |
| 2 | 61.9 | 12.4 | 0.19 | 20.8 | 71.3 |
| 3 | 79.1 | 16.0 | 0.21 | 23.3 | 91.3 |

## 4  Discussion

While all tests were run until the awn was at 90° to the pile at the attachment point, the behavior of the awns at their endpoints changed with the number of the awns. These tests show that the awns deploy most when they are in an arrangement of three awns. While the awn deployment is largest for the three-awn version of the geosystem, it also required more rotation. All three geosystems tested had a similar rate of deployment per degree of rotation, illustrating that the awns deploy in the same method. In all of the tests, the amount of rotation the geosystem undergoes is correlated to the amount of deployment the awns undergo. A two-awn arrangement showed the smallest rotation and thus the least amount of awn deployment.

Adding more awns increased the force the geosystem. However, the effect was greatest after adding the second awn. In the one-awn system, the asymmetry of the

geometry may have contributed to the low force recorded. However, when a second awn is added to the first, there is an 8.6 N increase in force. The effect is less pronounced when a third awn is added, with only a 2.5 N increase in force.

Each awn was composed of 1770 mm$^3$ of material. In comparison to the 34,040 mm$^3$ of material required for the pile, a single awn is approximately 5% of the total geosystem volume. While adding additional awns does correlate with increased force, the effect should be considered in combination with the volume of material used. Because the awns are intended to increase the tensile capacity in order to decrease the volume of the geosystem, balancing the increase in force with the increase in volume (and thus weight and cost) is essential to their utility in practice.

## 5   Conclusions and Future Work

The parametric modeling method presented in this paper provides a straightforward definition of the awn geometry studied. This method is flexible enough to allow for a full range of user-controlled variables while remaining structured enough to allow the user to determine how changing one variable impacts the system.

Future work includes testing of other the awn geometry parameters defined in this paper, explorations into texturing of the exterior of the awn, and expansion of the system at a larger scale.

## References

1. Adobe After Effects (version 22.0). 2022. Adobe
2. Adobe Premiere Pro (version 22.0). 2022. Adobe
3. Cai J, Deng X, Xu Y, Feng J (2015) Geometry and motion analysis of origami-based deployable shelter structures. J Struct Eng 141(10):06015001. https://doi.org/10.1061/(ASCE)ST.1943-541X.0001238
4. CORE studio (2017) TT TOOLBOX (by CORE Studio) (version 1.9). Thornton Tomasetti. https://www.food4rhino.com/en/app/tt-toolbox
5. Furuya H (1992) Concept of deployable tensegrity structures in space application. Int J Space Struct 7(2):143–151. https://doi.org/10.1177/026635119200700207
6. Gantes CJ, Connor JJ, Logcher RD, Rosenfeld Y (1989) Structural analysis and design of deployable structures. Comput Struct 32(3):661–669. https://doi.org/10.1016/0045-7949(89)90354-4
7. García-Mora CJ, Sánchez-Sánchez J (2021) Actuation methods for deployable scissor structures. Autom Constr 131:103894. https://doi.org/10.1016/j.autcon.2021.103894
8. Giampa JR, Bradshaw AS, Schneider JA (2017) Influence of dilation angle on drained shallow circular anchor uplift capacity. Int J Geomech 17(2):04016056. https://doi.org/10.1061/(ASCE)GM.1943-5622.0000725

9. Howell LL, Magleby SP, Olsen BM (2013) Handbook of compliant mechanisms. Wiley, Chichester, West Sussex, United Kingdom Hoboken, New Jersey

10. Korner A, Mader A (2016) Bio-inspired kinetic curved-line folding for architectural applications. In: ACADIA//2016: POSTHUMAN FRONTIERS: data, designers, and cognitive machines [Proceedings of the 36th annual conference of the association for computer aided design in architecture (ACADIA). ISBN 978-0-692-77095-5], Ann Arbor, 27–29 Oct 2016. CUMINCAD, pp 270–279. http://papers.cumincad.org/cgi-bin/works/paper/acadia16_270

11. Kota S, Joo J, Li Z, Rodgers SM, Sniegowski J (2001) Design of compliant mechanisms: applications to MEMS. Analog Integr Circ Sig Process 29(1):7–15. https://doi.org/10.1023/A:1011265810471

12. Pryor M (2021) Pufferfish (by Ekimroyrp) (version 3.0). https://www.food4rhino.com/en/app/pufferfish

13. Neubecker SR, Randolph MF (1996) The kinematic behaviour of drag anchors in sand. Can Geotech J 33(4):584–594. https://doi.org/10.1139/t96-084-306

14. O'Hara KB, Martinez A (2020) Monotonic and cyclic frictional resistance directionality in snakeskin-inspired surfaces and piles. J Geotech Geoenviron Eng 146(11):04020116. https://doi.org/10.1061/(ASCE)GT.1943-5606.0002368

15. Pellegrino S (2001) Deployable structures. Springer, Wien-New York

16. Poppinga S, Körner A, Sachse R, Born L, Westermeier A, Hesse L, Knippers J, Bischoff M, Gresser GT, Speck T (2016) Compliant mechanisms in plants and architecture. In: Knippers J, Nickel KG, Speck T (eds) Biomimetic research for architecture and building construction: biological design and integrative structures. Biologically-inspired systems. Springer International Publishing Cham, pp 169–93. https://doi.org/10.1007/978-3-319-46374-2_9

17. Ransom & Randolph (2022) Ransom-Randolph. https://www.ransom-randolph.com/ranco-sil

18. Rhinoceros (version 7.15) (2022) Robert McNeel & Associates, Seattle, Washington

19. Sakr M, Nazir A, Azzam W, Sallam A (2020) Model study of single pile with wings under uplift loads. Appl Ocean Res 100:102187. https://doi.org/10.1016/j.apor.2020.102187

20. Schleicher S (2015) Bio-inspired compliant mechanisms for architectural design: transferring bending and folding principles of plant leaves to flexible kinetic structures

21. Khaled S (2020) Variable Offset.Gh. https://discourse.mcneel.com/t/variable-offset-curves/98075.

22. "Stratasys." 2022. 2022. https://www.stratasys.com/en/3d-printers/printer-catalog/objet-350-500-connex3-printers

23. Sychterz AC, Bernardi I, Tom J, Beemer R (2021) Nonlinear soil-structure behavior of a deployable and compliant anchor system. Can J Civil Eng

24. Syp M, Heumann A (2017) Telepathy (version 1.0.0.0). nbbj digital. https://www.food4rhino.com/en/app/telepathy

25. Tibert AG, Pellegrino SRM (2003) Deployable tensegrity masts

26. Tibert G (2002) Deployable tensegrity structures for space applications. Royal Institute of Technology

27. Tom J, O'Loughlin C, White D, Haghighi A, Maconochie A (2017) The effect of radial fins on the uplift resistance of buried pipelines. Géotech Lett 7. https://doi.org/10.1680/jgele.16.00142

28. Wilde B, Treu H, Fulton T (2001) Field testing of suction embedded plate anchors. In: OnePetro. https://onepetro.org/ISOPEIOPEC/proceedings/ISOPE01/All-ISOPE01/ISOPE-I-01-208/7989

29. Zentner L, Böhm V (2009) On the classification of compliant mechanisms. In: Ceccarelli M (ed) Proceedings of EUCOMES 08. Springer Netherlands, Dordrecht, pp 431–38. https://doi.org/10.1007/978-1-4020-8915-2_52

# Structural Specialty: Modular Structures

# Prefabrication and Modular Construction—A Potential Solution to Affordable and Temporary Housing in Ontario?

**Daniela Roscetti, Andrea Atkins, and Daniel Lacroix**

**Abstract** Canada's housing crisis, and particularly Ontario's, has reached an all-time high in recent years. Due to the lack of affordable housing, the federal government created the Rapid Housing Initiative (RHI) to fund the construction of affordable housing units. The RHI has a twelve-month delivery date from funding requirement which has contributed to partners turning to the use of prefabrication and modular construction methods to produce housing units in large quantities and in a timely manner. The current study investigates successful modular projects in Ontario in order to identify their key success-driving factors as well as limitations. These success drivers included the structure durability, ability to deploy and relocate, ability to flat-pack the structure for transportation, and the primary funding source for the project. Based on these factors, it is concluded that there is a gap in the industry in panelized relocatable housing structures. Whereas prefabrication and modular construction have been successful thus far in major cities, the study highlighted the need for a prefabricated or modular sustainable assembly using either light-frame wood or mass timber that can be easily deployed, assembled, and transported to meet the housing demand in remote communities in Ontario.

**Keywords** Modular construction · Prefabrication · Relocatable housing · Affordable housing · Deployable housing

D. Roscetti (✉) · A. Atkins · D. Lacroix
University of Waterloo, Waterloo, Canada
e-mail: dnroscetti@uwaterloo.ca

A. Atkins
e-mail: andrea.atkins@uwaterloo.ca

D. Lacroix
e-mail: daniel.lacroix@uwaterloo.ca

497

# 1   Introduction

For decades, Canada has been experiencing a housing crisis due to the lack of housing available to meet the needs of a growing population. In 2020, Canada had the lowest average housing supply per capita among the G7 countries, with Ontario's supply falling below the country's average [1]. The lack of housing supply across Canada, and more specifically within Ontario, combined with the increased demand continues to drive rising housing prices. As a response to the lack of affordable housing, the Canada Mortgage and Housing Corporation (CMHC) announced a $1 billion Rapid Housing Initiative (RHI) in 2020 to help address the existing crisis [2] and followed up with a second round of funding in the amount of $1.5 billion in 2021 [3].

The first two rounds of the RHI aim to support the creation of new affordable housing and rental units, acquisition of land and to rehabilitate existing buildings into affordable housing within a twelve-month period of the funds being committed [3]. The RHI will provide 10,254 units across Canada with a total of 2870 (28%) units planned for Ontario. The twelve-month funding period seems to be paying dividends: several projects are already completed and occupied, including new builds and rehabilitation projects. Although the RHI provides fund to acquire old properties to rehabilitate them into permanent affordable housing units [e.g., 4–6], the focus of the current paper is to investigate the modular methods used in different projects to reduce the time to occupancy within the Ontario jurisdiction.

Successful new builds [e.g., 7–9] have turned to construction methods that involve some level of prefabrication and modularity. The urgency in providing affordable housing combined with the fact that most often the entities responsible for undertaking these projects are non-profit or have limited resources highlights the need to avoid unforeseen additional costs with the materials and construction as well as delays in the delivery of the projects. Prefabrication and modular construction are not novel methods of construction and have been around for decades. However, these methods have been gaining traction in the housing industry in recent years with various successful projects completed to show for it.

The objective of this paper is to investigate current successful modular and prefabricated residential projects in Ontario and analyze the key success drivers in these development projects in order to identify gaps in the affordable modular housing industry.

# 2   Modular Construction Methods

Modular construction is the process of constructing a building in pieces off-site and then assembling on-site to create the superstructure of the building [10]. The components of the building are manufactured in quality-controlled plant conditions and can be produced in the form of volumetric modules, flat panels, or prefabricated building elements. These building components are then transported and assembled

on-site once the foundation and substructure are complete. Modular construction can result in either temporary or permanent buildings, though this construction style is particularly well-suited for use in temporarily deployed buildings.

## 2.1 Types of Modularity

The implementation of modular construction methods can range from the use of individual prefabricated building elements up to the prefabrication of full building modules as shown in Fig. 1.

The types of modularity considered in this paper and what they entail are outlined below:

**Volumetric**: A volumetric modular approach is considered when three-dimensional units are manufactured off-site and simply placed or stacked on-site. This approach requires the least amount of work to be done on-site, but often results in a doubling-up of adjacent walls or floors and ceilings. The volumetric approach is seen in the popular steel shipping container modular construction method or the pre-cast concrete volumes of Habitat 67 (Montréal, Québec).

**Panelized**: A panelized modular approach is considered when panels (i.e., wall panels) are manufactured off-site and assembled on-site. This approach utilizes some level of pre-assembling panels off-site, for example, pre-built stud walls (wood or steel) or complete wall assemblies that include the structural member, insulation, cladding, etc. These can also include pre-installed electrical and plumbing systems. Structurally insulated panel (SIP) systems, freezer panel cladding systems, or pre-cast concrete insulated panels are all examples of panelized modular façades offering at least wind-bearing structural strength and thermal insulation, plus sometimes more enclosure functions.



Volumetric　　　Panelized　　　Prefabricated
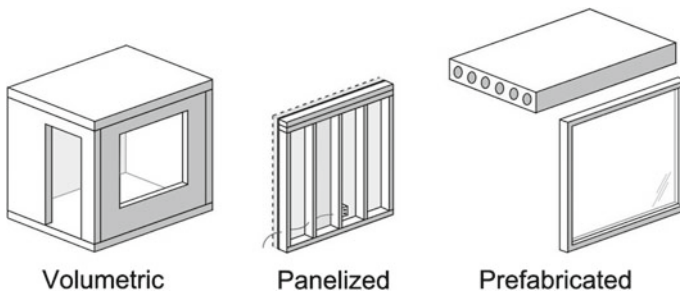
**Fig. 1** Levels of modularity

**Prefabricated (Individual) Units**: The prefabricated element approach is considered when structural elements, such as mass timber columns and beams, are manufactured off-site. CLT structural panels will also be considered individual prefabricated elements. Most modern mass timber construction can qualify as prefabricated modular construction, as well as construction using pre-cast concrete floor planks, bearing walls, or beams.

## 2.2 Materials and Structural Systems

Historically, modular construction has been achieved using concrete, steel, or timber structures. The use of steel in a modular project may range from individual hot-rolled I and H sections to volumetric steel-based modules manufactured off-site. Given its constructability and high strength, steel is traditionally used in large multi-story commercial projects. Modular approaches that utilize concrete may include pre-cast concrete panels (i.e., walls, floor, etc.) as well as pre-cast volumetric modules. With concrete's high resistance to damage, it is usually used in high security applications. In the residential modular sector, however, timber framing has been widely used to prefabricate panels and volumetric modules [11]

In recent years, the modular industry has gravitated toward more sustainable development thereby impacting the selection of structural system. This includes constructing multi-story buildings with timber-framed modules, converting retired shipping containers into insulated housing units, and more notably, implementing mass timber into larger scale projects. It should be noted that two or more primary construction methods are often seen in modular projects (e.g., concrete podium with wood volumetric units, cast-in-place concrete structure with aluminum panels). This recent sustainable progress made in the modular industry is explored in this paper through ten different case studies.

## 2.3 Advantages of Modular Construction

The implementation of any level of modularity in a project can provide several advantages over traditional construction methods:

- Reduced project timeline

Since the building elements are produced off-site, this process can begin before the site is fully prepared for construction reducing the overall project timeline. The project timeline can be established such that all modules or prefabricated elements are completed as soon as the site is prepared (i.e., foundations laid) and ready for assembly. This can reduce a project timeline by up to 50% [12].

- Quality Control

The off-site manufacturing method results in modular building components that are built in a controlled plant environment ensuring that strict quality control measures can be put in place as well as preventing materials from being exposed to outdoor conditions which might compromise the quality of the material.

- Less material waste

Materials are stored within the production plant and therefore cannot be damaged by outdoor conditions. Further, any unused materials are used for the next project being produced in the plant. Mass production of similar components can optimize material use by templating, material recycling, or secondary repurposing of offcuts.

- Standardized

Once the design for one module or building element is complete, the element can be reproduced without the need for additional complete design services. Climate and site-specific engineering is required, but engineering scope can be limited in subsequent developments. This is particularly beneficial in projects requiring a large quantity of identical modules (i.e., apartment buildings, hotels). The opportunity for reproduction for chain hotels or development of identical multi-story residential blocks makes standardization extremely attractive.

- Optimized working conditions

Module manufacturing is completed in a safe and controlled environment for workers resulting in a more efficient use of labor.

## 2.4 Disadvantages of Modular Construction

While modular construction methods bring the above advantages, among others, to a project, there are some disadvantages associated with these methods compared to traditional construction. These include:

- Negative perception of modular construction

The standardized nature of an efficiently modular construction method generates a repetitive and therefore more restrictive architectural style.

- Capital costs

Modular projects require a facility for the off-site construction as well as the equipment and skilled work force to produce the modules/panels/prefabricated elements.

- Upfront project costs

Modular projects come with higher upfront costs associated with the rigorous design phase required for the project to be successful.

- Lack of education

Contractors may lack installation training in the field, while architects and engineers may have limited knowledge or experience in modular construction.

- Non-economical designs

Volumetric modular projects are not particularly economical in their use of materials as when modules are stacked together, there are walls floor/ceilings doubled up. There is also a degree of structural over-design necessary to create fewer unique components in the building.

- Crane required

Volumetric modules typically require a crane to lift and place the modules onto the assembly. This, however, may be avoided by implementing a panelized or prefabricated approach (depending on the size and scale of the structure).

## 3 Current Residential Modular Construction in Ontario

Modular construction methods have been implemented in a range of residential projects throughout Ontario in recent years. The following sections will discuss some case studies of existing and upcoming residential modular projects. Table 1 presents a summary of the various case studies investigated by the authors by providing the name of the project, location, module type, primary structure material, whether it is temporary or permanent, and the number of units.

As per the City of Toronto's Housing to 2020–2030 Action Plan, the city committed to building 1000 modular homes as a rapid housing response for those experiencing homelessness [13]. The Modular Housing Initiative aims to create new homes by developing low-rise modular buildings on various sites around Toronto. Thus far, two developments have been completed (Phase I), both within 9 months of being approved by City Council; this accelerated timeline is likely the reason for which a modular approach was selected for the housing initiative. The two buildings have provided 100 new permanent homes with more to be provided by the three additional sites (Phase II) that are currently being developed [14].

**Table 1** Summary of Ontario residential modular case studies

| Project | City | Module type | Primary structure material | Temporary/ permanent | Number of units |
|---|---|---|---|---|---|
| City of Toronto Modular Housing Initiative | Toronto | Volumetric | Light-frame wood | Permanent | 100 so far |
| Waterloo Region Alternative Housing | Waterloo | Volumetric | Steel (shipping containers) | Permanent | 6 |
| Oshawa Micro-Housing Pilot Project | Oshawa | Volumetric | Light-frame wood | Temporary | 10 so far |
| JHS Supportive Housing (Carling Avenue) | Ottawa | Volumetric | Light-frame wood | Permanent | 40 |
| NRCan Rapidly Deployable House Prototype | – | Panelized | Structural Insulated Panels (SIPs) | Temporary | 1 |
| City of London Supportive Housing | London | Panelized | Steel frame | Permanent | 61 |
| JHS Supportive Housing (Lisgar Street) | Ottawa | Panelized | Cast-in-place concrete and steel frame | Permanent | 28 |
| YW of Kitchener-Waterloo Supportive Housing | Waterloo | Prefabricated | Mass timber | Permanent | 41 |
| R-Hauz V6 | Toronto | Prefabricated | Mass timber | Permanent | 10 |
| R-Hauz R-Suite | Toronto | Panelized | Light-frame wood | Permanent | 1 |

## 3.1 Volumetric Modular

### 3.1.1 City of Toronto Modular Housing Initiative

The volumetric units for the Modular Housing Initiative are manufactured by NRB Modular Solutions, in their facility in Grimsby, Ontario. The modules for the project were built using a light-wood-frame structure onto which the interior building enclosure layers were installed off-site and exterior cladding was installed on-site (i.e., post-assembly). The timeline for construction on the first two developments, including design, manufacturing, transport, and installation, was only 5 months, thus taking that a modular approach will ensure the success of remaining phases [15].

### 3.1.2 Waterloo Region Alternative Housing

In 2020, the Region of Waterloo proposed a pilot project for converting shipping containers into affordable housing as part of a larger plan to build more innovative affordable housing in the region [16]. The government-funded development will provide six new affordable housing units in the city of Cambridge. The project gained site approvals in October 2021, and as of December 2021, all modules have been assembled on-site. The project was set for completion and occupancy by early March 2022 [17].

As previously mentioned, the modules are converted shipping containers, and these therefore make up the structure of the module while the manufacturer completed the wall assembly, installed windows, doors, electrical, and plumbing off-site ensuring minimal time spent for on-site assembly. Once transported to site, the two levels of modules were assembled with a layer of concrete between the two levels for fire protection [9].

The manufacturer, Now Housing, was selected to build the modules for the project [17]. The manufacturing company in based in Cambridge indicated that costs would be kept relatively low for transporting the modules to site. However, given that the volumetric modular approach has been used, a crane was required for on-site assembly. Further, the assembly of the modules, including the concrete layer placed in between levels, makes for a permanent building meaning that the modules cannot be relocated and reused in the future.

### 3.1.3 City of Oshawa Micro-housing Pilot Project

As part of the Durham Region's commitment to creating 1000 new affordable rental units by 2024, the regional municipality has initiated the Oshawa Micro-housing Pilot Project. This project is aligned with the region's 10-year housing plan to end chronic homelessness [18]. The development of this micro-home community in central Oshawa will provide ten new affordable housing units. The pilot project began moving forward in April 2021, and as of January 2022, the manufacturing of modules was complete and site assembly was to begin [19]. The project is currently still in progress.

The 2.4 m × 12.2 m (8 ft × 40 ft) modules for this pilot project are being manufactured by NRB Modular Solutions, using light-wood-frame structures similar to the modules fabricated for the City of Toronto Modular Housing Initiative. The selected project site has been acquired by the region for a future road widening project meaning that the micro-home development will need to be relocated to a more permanent site [20].

### 3.1.4 John Howard Society (JHS) of Ottawa Supportive Housing (Carling Avenue)

The John Howard Society of Ottawa was awarded the bid to build permanent affordable housing for Ottawa's residents experiencing homelessness as part of the Rapid Housing Initiative in 2019. The Carling Avenue development will provide 40 new affordable housing units over four residential stories above a two-story concrete podium that will serve as the John Howard Society of Ottawa's main office [8, 21].

The project broke ground in September 2020 but has unfortunately faced significant delays due to rising construction prices, material and labor shortages, and COVID-19 pandemic protocols. The current anticipated completion date for the development is March 2022 [8, 21]. The volumetric modules for the development are prefabricated off-site using a light-wood-frame structure including interior partitions, electrical and mechanical rough-ins, as well as unfinished gypsum board assemblies. The remaining construction, including fire alarm systems and gas distribution, is to be completed on-site once the modules are lifted onto the concrete podium by crane.

## 3.2 Panelized

### 3.2.1 Rapidly Deployable Northern House Prototype

In 2016, researchers at the Natural Resources Canada Canmet Energy research center developed a prototype for a rapidly deployable flat-pack house for Northern Ontario. The prototype was developed in such a way that it can be assembled in under a week by hand; it does not require the use of a crane, tools, or fasteners and can fit entirely in a standard shipping container [22]. The prototype is a 7.3 m × 12.2 m (24 ft × 40 ft) free span structure with wall panels that can be placed anywhere within the structure. The roof and foundation systems are made up of light-weight steel trusses, while the exterior prefabricated wall panels are complete assemblies consisting of sheathing, vacuum insulation, and cladding, ensuring that minimal work needs to be done during on-site assembly [22].

### 3.2.2 City of London Affordable Housing (Baseline Road West)

The City of London along with the Housing Development Corporation, London (HDC), is moving forward on an affordable housing development at 122 Baseline Road West, London [7, 23]. The permanent four-story residential building will provide 61 new affordable housing units, including one, two, and three-bedroom units, for the city [7, 23].

The project received government funding from all levels including the CMHC RHI, provincial Social Services Relief Fund (SSRF), and municipal funding from the City of London and HDC [7, 23]. The project started in April 2021 and was

initially set for completion by the end of the year; however, the move-in date was extended to February 2022 due to delays due to weather, supply chain challenges, and completing inspections within COVID-19 protocols [24].

A panelized modular approach was used where prefabricated steel frame panels were transported and installed on-site. The panels were not complete wall assemblies (i.e., including insulation, cladding, electrical, etc.) and required on-site assembly to complete the construction. Although the panels were not complete wall assemblies and required on-site work, the modular-type build allowed the construction crews to overcome these challenges (i.e., weather, supply chain, pandemic) and minimize the delays [24].

### 3.2.3 John Howard Society of Ottawa Supportive Housing (Lisgar Street)

In addition to the Carling Avenue development, the John Howard Society of Ottawa is also building a four-story residence which will provide 28 new affordable units for women, with a focus on Indigenous women, experiencing homelessness [25]. This project is also funded by the Federal Government's Rapid Housing Initiative as it aims to create more affordable housing for vulnerable populations [25]. The project was set to break ground in mid-2021 and set for completion by March 2022 [25].

The four-story residence will be built out of cast-in-place concrete and use a panelized approach for the exterior walls to avoid congestion at the work site. The panels consist of a steel stud structure with an exterior sheathing and are manufactured off-site. Once ready, the panels are shipped and upon arrival to the site are immediately hoisted into place. The remainder of the construction including interior finishing as well as electrical and mechanical systems will be installed on-site.

## 3.3 Prefabricated

### 3.3.1 YW of Kitchener-Waterloo Supportive Housing

Motivated by the Rapid Housing Initiative, the YW of Kitchener-Waterloo assembled a team of designers to provide 41 units of affordable housing in Kitchener in 2021 [26]. The project is a permanent installation consisting of CLT panels, glulam columns, and panelized building enclosure modules. Modular construction was an obvious choice for the project since the funding source required accelerated construction times. The 27,000 $m^2$ complex was constructed using CLT and glulam components produced by Element5, a mass timber fabricator based in St. Thomas, Ontario [27]. The superstructure and modularized enclosure panels were assembled on a completed foundation to achieve an enclosed building in just 20 days [27].

### 3.3.2 R-Hauz V6, R-Town, and R-Suite Projects (Mass Timber Avenue Townhomes and Laneway Suites)

The suite of modular project ideas that have been produced by the Toronto-based R-Hauz group targets the "missing middle" size of housing developments in cities [28]. From laneway housing to mid-rise apartment blocks, the modular mass timber solutions bring more density to smaller neighborhoods in the city without introducing high-rises [29]. In 2021, the R-Hauz team completed their first constructed mid-rise project: a 2400 m², six-story mixed-use building in the neighborhood of Leslieville. The ground floor of the building offers two storefronts, while the upper levels are rented out as apartments. This pilot project dubbed "V6" was constructed in 9 months, but the development team believes that their subsequent projects will be able to cut this time to just 6 months [29]. The housing market in Toronto is experiencing a demand beyond what current construction methods can accommodate. These R-Hauz passivhaus-standard residential complexes come together in such a short time thanks to their modular construction techniques and offer a hope for supplying the units the city so desperately needs [28].

In 2018, the City of Toronto allowed for laneway housing development after years of lobbying from residents, planners, and architects [30]. Thus, in addition to their mass timber (prefabricated) projects, the R-Hauz team has applied light-frame wood panelized approach to this building type, dubbing them "R-Suites" with two-story prefabricated models ready to roll out [28]. The tight site constraints of laneway construction sites lend themselves to a panelized solution, which additionally helps reduce neighborhood disturbance, noise, and truck traffic due to shorter construction times. The R-Suite products are limited in their style variety, which means less uniqueness for an owner, but more rapid permitting times since the documentation is standardized and ready to file without modification [28]. As of January 2022, on-site assembly of the R-Suite pilot project began and was nearly complete within a day [28].

## 4 Discussion

The projects across Ontario discussed in this paper have been evaluated as to what project factors drove the success of the project as shown in Table 2. The factors considered are listed in the columns of Table 2.

When applying modularity to a project, one must consider transportation costs and efficiency. The timeline and cost of a project may be reduced when prefabricated building components require fewer or smaller vehicles to transport them to site. Panelized building components as well as prefabricated units can be transported as a "flat pack" of components, while volumetric building modules cannot be condensed for transportation. Whereas the case studies that employed volumetric units were successful, their proximity to the manufacturer was relatively close. However, for remote locations, it may not be economically feasible to employ volumetric modules.

**Table 2** Case study success drivers

| Project | Deployable | Flat-packable | Relocatable | Government funded |
|---|---|---|---|---|
| City of Toronto Modular Housing Initiative | ✓ | | | ✓ |
| Waterloo Region Alternative Housing | ✓ | | | ✓ |
| Oshawa Micro-housing Pilot Project | ✓ | | ✓ | ✓ |
| JHS Supportive Housing (Carling Avenue) | ✓ | | | ✓ |
| NRCan Rapidly Deployable House Prototype | ✓ | ✓ | ✓ | ✓ |
| City of London Supportive Housing | ✓ | ✓ | | ✓ |
| JHS Supportive Housing (Lisgar Street) | ✓ | ✓ | | ✓ |
| YW of Kitchener-Waterloo Supportive Housing | ✓ | ✓ | | ✓ |
| R-Hauz V6 | ✓ | ✓ | | |
| R-Hauz R-Suite | ✓ | ✓ | | |

Therefore, the ability to transport building components in flat-packs is considered to drive the success of a project.

The ability to relocate a modular structure is important when considering whether the structure is needed on a temporary or semi-permanent basis, so that when it is no longer needed, it may be relocated to another location where it can be reused. The majority of the projects discussed in this paper are permanent installations and cannot be relocated; while this makes sense for the types of buildings developed in these projects (i.e., providing permanent housing for people experiencing homelessness), there are benefits to developing housing that can be reused and relocated depending on how the demand for this housing type shifts over time.

A significant success driver for housing projects with any level of modularity is government funding. These types of projects require more upfront costs in the design stage, thus having stable government funding ensures that the project remains on track and meets timeline goals, for example, the 1-year timeline set out by the federal Rapid Housing Initiative.

As shown in Table 2, there is a clear lack of relocatable (temporary, or semi-permanent) modular housing projects being developed. Transportation efficiency is particularly important with temporary (relocatable) projects as the structure will be repeatedly packed up and transported. The ability to transport a structure as a "flat-pack" is a factor that seems to be lacking in studied developments; this is likely due to most buildings being permanent installations rather than temporary (where this factor is most relevant).

The CMHC announced a third round of funding for "*Northern Access: Supply Chain Solutions for Northern and Remote Housing*" with specific objectives of overcoming the barriers of: long distances to get supplies and, extended shipping timelines, harsh climate and short construction season, and high cost of materials and skilled labors [31] further emphasizing the importance of developing "flat-pack" modular options along the likes of the NRCan Rapidly Deployable House Prototype [22]. The current study has shown that light-frame and mass timber were good candidates for successful modular projects, and given the current climate change crisis, using sustainable and renewable materials such as wood is of the utmost importance. Whereas light-frame and mass timber have successfully been used in the current projects investigated, there are no real alternatives similar to the NRCan Rapidly Deployable House Prototype that can easily be assembled and disassembled [22].

For these types of projects (i.e., temporary or semi-permanent), it is important that the modular components are capable of withstanding loading associated with transportation and on-site assembly (i.e., lifting) more than once during their service life and to maintain structural integrity when re-assembled to resist standard gravity (e.g., dead, snow, live) and lateral (e.g., earthquake, wind) loads of the new site. While the projects investigated in the current paper have all been successful, they are for permanent housing and the type of connections used is most likely not adequate for disassembly and reassembly. Additional considerations to the type of material (e.g., light-frame wood, mass timber, steel) as well as systems (e.g., panels, volumetric) and their connections must be considered to improve the durability of temporary or semi-permanent housing. Although concrete would typically be considered due to its high-strength and damage-resistant capabilities, the self-weight of concrete makes it infeasible or unnecessary in smaller scale residential projects, particularly projects that require the transportation and assembly of pre-manufactured building elements. While steel would also be considered as the primary material for the walls and floors due to its durability and it being relatively lightweight, it does not directly align with the industry's move toward more sustainable construction. Wood is light and sustainable in addition to successfully being implemented in several modular projects for permanent housing however, further research on the durability of the system (e.g., light-frame wood panels vs. mass timber panels), and the connection system is required to develop a durable system that can be assembled and disassembled several times over its service life while maintaining structural integrity once reassembled.

The need for relocatable housing options stems from varying demand all over the province. Examples include temporary housing for remote communities in flood zones affected by climate change following an extreme weather (e.g., flood, hurricane, fire) or deliberated event (e.g., blast) or even as a temporary affordable housing option as an intermediate step to buying a standard detached home. These housing demands require structures that can be deployed and assembled on short notice and for a limited time span; however, a structure that is relocatable, and not a single-use temporary structure, can be disassembled and reused to accommodate for the inevitably ongoing temporary housing demand.

# 5   Conclusions

Based on the case studies discussed in this paper, a gap in the industry lies within relocatable housing. The need for the relocatable housing requires that the structures can be durable for assembly, reassembly, and transportation indicating that durable, but relatively light-weight materials should be used for the building components. Although wood is a light-weight material, further research is required to establish a preferred material type (light-frame wood vs. mass timber) and structural system with reusable connections. Further, transportation efficiency is key in ensuring the feasibility of a relocatable structure. A panelized modular approach provides the highest level of modularity, thus the least amount of on-site work without sacrificing the efficiency of transporting the structure, like a volumetric modular approach would.

Nearly all projects discussed are permanent builds that fall within Southern Ontario and are dedicated to serving the housing crisis in more urban settings. Considering that the housing crisis spans the entirety of the province, the industry specifically lacks housing that can be readily deployed to other regions of Ontario, in addition to densely populated areas. The lack of temporary housing in more remote areas often stems from the effects of climate change (i.e., flooding, forest fires, etc.) indicating a need for rapidly deployable and relocatable relief housing to be available for use and reuse based upon demand. In more remote areas in Ontario (e.g., Northern Communities), large cranes, tools, and skilled labor may not be readily available meaning that any deployed housing structure should be easily assembled with minimal tools required. Therefore, more research is needed in providing a sustainable modular housing solution that can easily be assembled and is readily deployable to any region in Ontario.

# References

1. Financial Post (2022) Ontario housing shortage is worst in the country and threatens to exacerbate affordability woes. https://financialpost.com/news/economy/ontario-alberta-and-manitoba-lead-the-provinces-in-canadas-chronic-housing-shortage-says-scotiabank
2. Canada Mortgage and Housing Corporation (CMHC) (2020) Canada to Rapidly Create Affordable Housing and Support the Homeless
3. Canada Mortgage and Housing Corporation (CMHC) (2022) Rapid Housing Initiative (RHI). https://www.cmhc-schl.gc.ca/en/media-newsroom/news-releases/2020/canada-rapidly-create-affordable-housing-support-homeless
4. Gibson C (2022) Renovations underway to convert 2 former Edmonton hotels into affordable housing units. CBC News
5. Price M (2022) Dartmouth hotel to be converted to housing units for Nova Scotians experiencing homelessness. CTV News
6. Pickel J (2022) Work is underway to turn a former Waterloo hotel into a homeless shelter. CTV News
7. City of London (2021) City of London partners with EllisDon to build affordable housing for Londoners. City of London. https://london.ca/newsroom/city-london-partners-ellisdon-build-affordable-housing-londoners-0
8. Porter K (2021) High construction costs hit Ottawa's affordable housing projects. CBC

9.  Engage Region of Waterloo (2021) The containers for the new Bechtel homes have arrived! https://www.engagewr.ca/affordable-housing-bechtel/news_feed/the-containers-for-the-new-bechtel-homes-have-arrived

10. Modular Building Institute (n.d.) The Voice of Commercial Modular Construction. https://www.modular.org/

11. Lawson M, Ogden R, Goodier C (2014) Design in modular construction. CRC Press, Boca Raton

12. Why Modular?—NRB Modular Solutions n.d. https://nrbmodular.com/why-modular/

13. Modular Housing Initiative—City of Toronto n.d. https://www.toronto.ca/community-people/housing-shelter/affordable-housing-developments/modular-housing-initiative/

14. City of Toronto announces the next two affordable supportive housing sites as part of Phase Two of its Modular Housing Initiative 2021

15. City of Toronto Supportive Housing, Toronto, ON—NRB Modular Solutions n.d. https://nrbmodular.com/what-we-do/projects/affordable-social-housing/city-of-toronto-supportive-housing-toronto-on/

16. Alternative Housing at Bechtel | EngageWR n.d. https://www.engagewr.ca/affordable-housing-bechtel

17. Thompson C (2022) Six seniors move March 1 into their new Cambridge apartments made from steel shipping containers. The Record 2022

18. Oshawa Micro-Housing Pilot Project is underway—Region of Durham n.d. https://www.durham.ca/en/news/oshawa-micro-housing-pilot-project-is-underway.aspx

19. McConnell L (2022) Micro-home project to temporarily house people experiencing homelessness begins installation in Oshawa. In Durham 2022

20. Regional Council recognizes the need for affordable housing to be expedited during COVID-19—Region of Durham n.d. https://www.durham.ca/en/news/regional-council-recognizes-the-need-for-affordable-housing-to-be-expedited-during-covid-19.aspx

21. Construction Daily; Excessive building prices hit Ottawa's reasonably priced housing initiatives. Construction Daily 2021

22. Haslip D, Sinha R (2016) Rapidly Deployable Northern House Prototype—Update for Parliament

23. Bogdan S (2021) Plans for 61-unit southwest London apartment building moving ahead—London. Global News

24. Juha J (2022) London's first rapid-build affordable housing project nears move-in date. The London Free Press

25. McGregor A (2021) Stability, community, connection for 28 women at new supportive residence on Lisgar Street. CentreTown Buzz

26. Kitchener YW (n.d.) Waterloo offers more housing options to single mothers. https://www-cbc-ca.cdn.ampproject.org/c/s/www.cbc.ca/amp/1.6303945

27. Four storeys in twenty days. Wood Industry n.d. https://woodindustry.ca/four-storeys-in-20-days/

28. R-Hauz n.d. https://r-hauz.ca/

29. Hanes T (2021) Debut of Toronto's 1st wooden midrise residential building. Toronto Star 2021. Debut of Toronto's 1st wooden midrise residential building | The Star

30. City of Toronto (n.d.) Changing lanes: laneway suites in the City of Toronto. https://www.toronto.ca/city-government/planning-development/planning-studies-initiatives/changing-lanes-the-city-of-torontos-review-of-laneway-suites/

31. Canadian Mortgage and Housing Corporation (CMHC) (n.d.) Canada invests $80M in third round of Housing Supply Challenge 2022. https://www.cmhc-schl.gc.ca/en/media-newsroom/news-releases/2022/canada-invests-third-round-housing-supply-challenge

# Low-Rise Modular Structure Wind Load Evaluation

**Mutaz Suleiman and Ahmed Elshaer**

**Abstract** Low-rise buildings represent the majority of commercial, residential, and industrial buildings. This raises the importance of accurately assessing the wind loads developed on their surfaces. Typical low-rise buildings can be designed using wind load obtained from methods provided by design codes. As for non-typical low-rise buildings, they require more sophisticated methods of wind load evaluation. In addition, with the increasing demand for healthcare space due to COVID-19, the urge to meet the space demand calls for immediate action to overcome this issue. When it comes to construction, the conventional method may not provide a prompt solution to the urgent need for healthcare space. This highlights the importance of utilizing advanced construction methods (e.g., modular construction) to respond to such problems. Modular construction relies on the use of prefabricated units that can be assembled on-site to form different types of structures. The application studied in this paper primarily focuses on the use of modularly constructed structures to provide healthcare space. Since modular buildings are typically of irregular layout low-rise buildings, wind load distribution can be complex compared with typical structures; thus, the expected wind load on different modules within the layout may vary. Accordingly, this paper demonstrates the non-typical wind distribution developed on a modularly constructed hospital. The computational fluid dynamics (CFD) method is utilized to evaluate wind loads developed on a non-typical layout. Based on the study results, critical forces developed on surfaces were found to be different depending on the module's location within the layout. Different corners, edges, and internal modules are examined in this study. The results of this study can be further used to design different grades of modules; thus, achieving better usability of materials.

**Keywords** Wind loading · Low-rise buildings · Modular structures

M. Suleiman (✉) · A. Elshaer
Department of Civil Engineering, Lakehead University, 955 Oliver Rd, Thunder Bay P7B 5E1, Canada
e-mail: masuleim@lakeheadu.ca

# 1 Introduction

Modular structures have been attracting significant attention from the construction industry. They provide many advantages over conventional structures due to their speedy delivery, safer construction process, less material wastage, and sustainability [10]. Modular construction is a technique that involves the prefabrication of major structural components in an off-site location, then transported and assembled on-site to form various types of structures. This helps improve the efficiency of the construction process and ensures the quality of structures [2, 6, 10, 15]. Different materials (i.e., steel, concrete, timber, and composite) can form different structures (i.e., low-rise, high-rise, and bridges), highlighting their adaptability to the project scope. When it comes to modular buildings, three different types can be utilized depending on the project, which are componentized, panelized, and volumetric modules. In general, all building projects are typically constrained by cost limitations, which is reflected in the decisions of designers and construction professionals. The cost has three main aspects, which are material, labour, and time, where prefabricated buildings provide reduction to all three. With the increasing demand for hospital beds due to COVID-19, modular buildings can be a suitable solution as they can be deployed rapidly and provide the healthcare system with the space needed to serve patients. A recent case where this technology has been adopted is Wuhan Thunder God Mountain hospital. Chen et al. [2] reviewed the accelerated design and construction methods utilized in the hospital's construction. The hospital consists of modular composite buildings finished product to reduce the workload of field operations and save time, which in turn provided a capacity of 1500 beds for COVID-19 patients, with the project taking a little more than ten days to complete. The project adopted a volumetric light steel structure skeleton and steel composite panels, with the mainframe beams and columns made of cold-formed steel welding. Many studies have focused on the structural aspect of modular buildings covering materials, connections (inter and intra), and types of modules. For instance, [9] performed numerical analyses of corner-supported modular buildings under wind actions using concrete-filled steel tubular columns, laminated double beams, and integrated concrete slabs in a 12-story modular building. The study determined that this type of composite modular building can effectively improve the structural performance of modular buildings with an average increase of 21% in elastic stiffness and 33% in the maximum capacity under lateral load compared with hollow steel sections. Another study conducted by Zhang et al. [14] focused on the mechanical property tests on full-scale assembled light steel modular buildings, consisting of the bottom frame and top frame connected with columns and high-strength bolts. In the vertical capacity test, the modular unit failed due to the excessive flexural–torsional buckling of the four columns, which is the typical primary buckling mode. As for the bottom frame, it remained in the elastic stage indicating good deformation capacity and weak rigidity. Another example is the study conducted by Wang et al. [13], which aimed to test the seismic performance of the assembled light steel modular building based on joint stiffness analysis. The study was carried out through quasi-static loading using the finite element to

perform stiffness analysis of the intra-modular and inter-modular connections. The study determined through the quasi-static test that the weld fractures at the connection between the ceiling beam and the corner fitting near the loading end decrease the bearing capacity, highlighting the importance of the connection quality. As for the ductility and energy dissipation for temporary buildings, capacity can be guaranteed; as for permanent modular structures, the performance is less. Gatheeshgar et al. [6] studied the development of affordable steel-framed modular units focusing on the enhancements of healthcare, structural, and fire performance. The study focused on weight optimization for cold-formed steel joists in varying shapes, with results showing weight per unit length reduction of up to 24% without compromising the structural capacity. As for their intra connection, a novel cut and bend method was introduced to improve the faster jointing method. Strap bracing is also used for lateral stability. As for healthcare performance improvement, modular breathing panels are utilized in the corner post modules as sidewalls to improve indoor air quality. As for the fire improvement, cold-formed steel joists can be utilized to control the heat transfer through the panels by increasing the heat insulation of the material. In another related aspect, a study conducted by Gbadamosi et al. [7] focused on isolation space creation for COVID-19 patients. Different spaces are analyzed in this case, including self-isolation at home, isolation at regular hospitals, epidemic hospitals, retrofitted buildings, temporary mobile cabins, and newly constructed temporary hospitals for COVID-19. The study is based on a mixed-method approach, which involves the analysis of secondary quantitative data and the qualitative review of literature on COVID-19. The study's outcome determined that the most effective methods of controlling the spread are through isolation at temporary mobile cabins or isolation at newbuild COVID-19 hospitals. Suleiman et al. [11, 12] conducted a study examining the propagation of mouth-generated aerosols within a modular room. It was determined that the main factors impacting the aerosols' final destination within a modular room are the air changes per hour rate and the flow path between the inlet and the outlet. Based on the literature, the main factors for designing modular buildings for COVID-19 patients are cost, efficiency, and structural performance. As for the cost, different modules grades can be proposed to reduce the cost and material usage through a multi-unit modular building. These grades can be categorized based on the location within the multi-unit layout of the structure, which will, in return, impact the developed load on the modules. The current study provides a detailed analysis of a multi-unit layout based on the forces developed on different modules surfaces due to wind loads. Peak forces are then compared, based on their location within the layout, to provide an understanding of how the location can impact the force development on the modules. The results can be further used to design different grades of modules, thus reducing the cost and materials used. Section 1 of this paper (this section) covered the literature review for the use of modular construction in various applications. In contrast, Sect. 2 covers the numerical model details, including the validation model's details concerning the geometry and physics adopted. The multi-modules layout is examined, and its geometrical details are presented in Sect. 3. Section 4 summarizes the results obtained after running the models highlighting the significant data, and finally, Sect. 5 concludes the summary of this paper.

## 2 Numerical Model Details

A study conducted by Ho et al. [8] involved a comprehensive quality check of data obtained through experimental wind-tunnel testing compared with full-scale models. Parameters such as roof slope, building height, and building plan dimension are examined for different wind angles of attack. Mean pressure coefficient and root mean square (RMS) pressure coefficient values obtained through wind-tunnel testing are then compared with the corresponding numerical models. A validation simulation of CFD techniques is performed to assess the fidelity and accuracy of the numerical technique covered in Sect. 2.2 of this paper. As for the procedure, it starts with extracting the force–time history for each module within the layout, then identifying the critical forces within each force–time history obtained, followed by picking the most critical force within different wind angles of attack, and categorizing modules based on the critical wind forces, as shown in Fig. 1.



**Fig. 1** Procedure of obtaining critical forces on modules
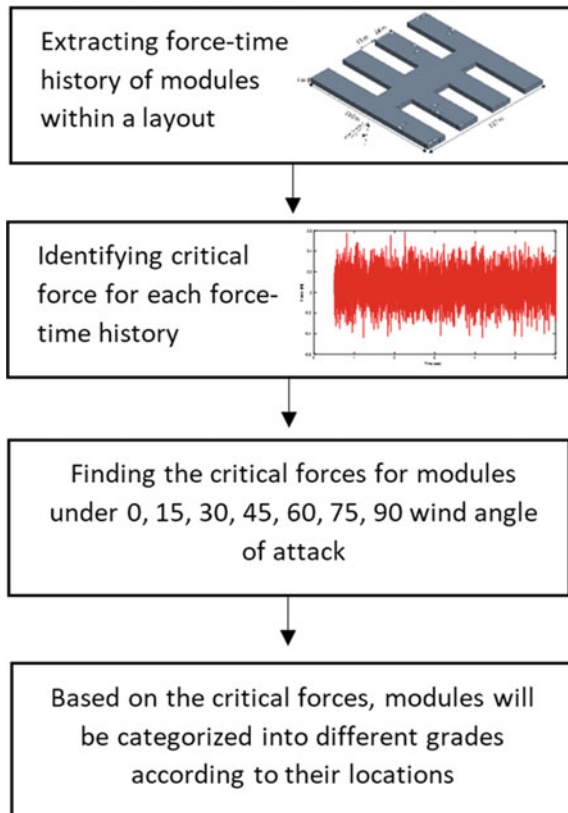
## 2.1 Building Geometry and Details Adopted in the Validation

A gable roof building with a roof slope of 1:12 and plan dimensions of 38.1 m × 24.4 m with a roof reference height of 7.32 m in full-scale using a wind angle of attack of 270° is used in the validation of the numerical model. As for the probes where the mean $C_p$ and RMS $C_p$ are collected, they are located across the roof, and they consist of 14 probes distributed on the roof surface, as shown in Fig. 2. The mean velocity and turbulence intensity profiles are generated to match an open-terrain exposure with a roughness height ($Z_o$) of 30 mm with a reference velocity of 37.6 m/s at the height of 10 m in full-scale. The wind-tunnel experimental study adopted a length-scale and time-scale of 1:100 and 1:25, respectively. The velocity and intensity profiles used in the case study matched with the wind-tunnel experiment using Eq. (1) for the mean wind velocity and Eq. (2) for the wind turbulence intensity in the longitudinal direction.

$$\overline{U}(z) = \overline{U}_{\text{ref}} \left( \frac{z}{z_{\text{ref}}} \right)^{1/\alpha} \tag{1}$$

$$I_u = c_u \left( \frac{z_{\text{ref}}}{z} \right)^{bu} \tag{2}$$

The constants of the equations are obtained through parameters optimization, where the value of $1/\alpha$ is determined to be 0.13, as for the $\overline{U}_{\text{ref}}$, it is obtained from [8], and it is 37.6 m/s in full-scale at reference height ($z_{\text{ref}}$) of 10 m. As for the intensity profile, a known intensity at a select height is used as a reference to obtain the values of $b_u$ and $c_u$, where the adjustment parameters are optimized to minimize the overall error in matching the target profile. The values obtained for the $c_u$ and $b_u$
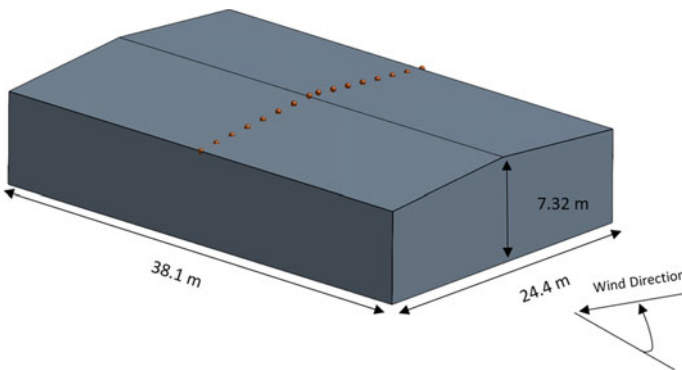


**Fig. 2** Full-scale geometric details of the validation model
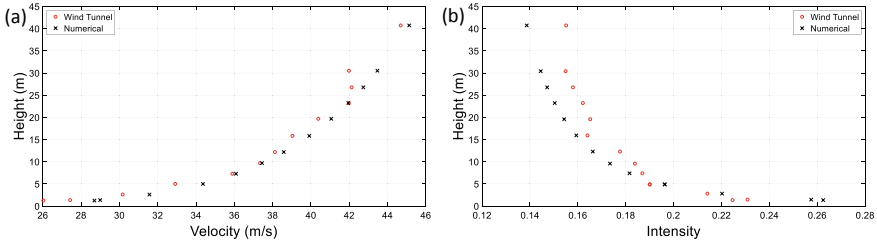
**Fig. 3** **a** Mean wind velocity profile adopted in the wind-tunnel experiment compared with numerical and **b** wind turbulence intensity profile adopted in wind-tunnel experiment compared with numerical

are 0.183 and 0.17, respectively, yielding an overall error of 3.64%. The profiles are matched as shown in Fig. 3a, b, respectively.

## 2.2 Numerical Details of the Validation Model

Based on the geometry explained in the previous section, STAR-CCM+2020.2 (15.04.008-R8) is used to perform a wind simulation following the large eddy simulation (LES) turbulence modeling. Consistent discrete random flow generation (CDRFG) [1] is used to generate the inflow turbulence following the procedure described in [4, 5]. A computational domain of dimensions of 2.1 m × 3.5 m × 0.5 m (in model scale) is used to perform the simulation, as shown in Fig. 4. The building is placed 0.6 m away from the inlet, and results collection started after 1000 time-steps to ensure the flow stabilization. As for the boundary conditions, the front wall is assigned as a velocity inlet, while the back wall is an outlet, sides and the roof of the computational domain are assigned as symmetry plane, while for the ground, it is set as a no-slip wall, as shown in Fig. 4a. The computational domain is discretized into two zones based on the hexahedral mesh cell. Zone 1 adopted a base mesh size of 15 mm, while zone 2 had dimensions of 0.5 m × 0.95 m × 0.25 m, adopted a mesh size of 7.5 mm yielding 1.36 M cells, as shown in Fig. 4b.

The simulation duration used is 10 s (in model scale) with a time-step of 0.5 milli-seconds with total time-steps of 20,000. The time-step is selected based on the velocity scale and the minimum cell size to satisfy the Courant-Friederichs-Lewy (CFL) number below unity to ensure the solution convergence [3]. As for the reference pressure used to calculate $C_p$, a pitot tube probe is placed in the domain at the midpoint of the inlet before the building at the height of 0.48 m. After running the validation model, the mean pressure coefficient ($C_p$) and RMS $C_p$ across the ridgeline are compared as shown in Fig. 5a, b, respectively. The validation model results show a good agreement between the reading of $C_p$ in the wind tunnel and the numerical method utilized in this paper. Mean $C_p$ results showed an error of 6.91%, as for the RMS $C_p$, it demonstrated an error of 17.32%.
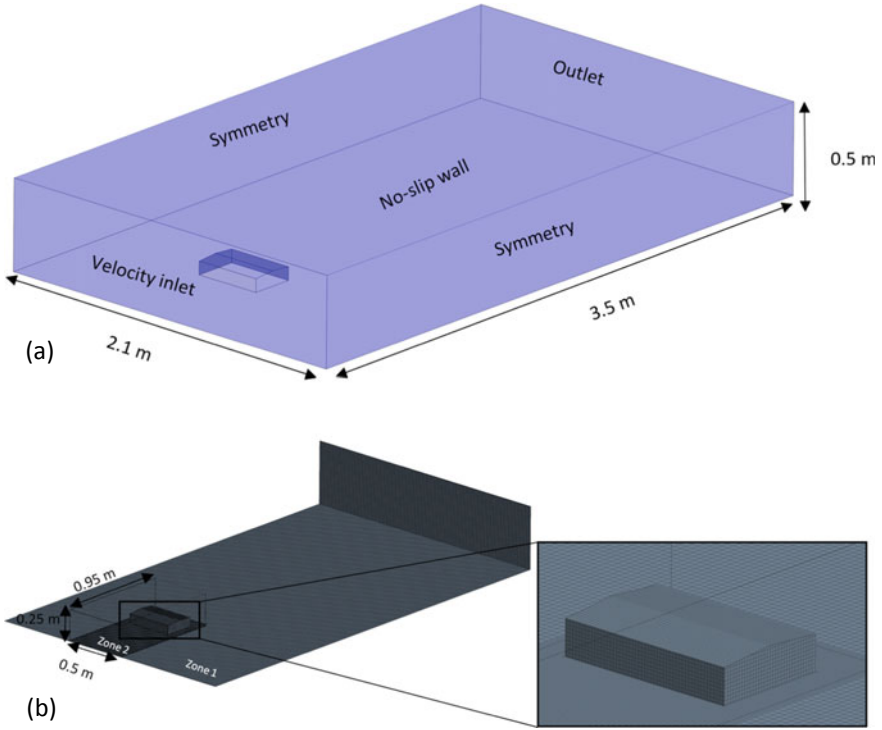
**Fig. 4 a** Computational domain and boundary conditions adopted in the validation and **b** mesh discretization of the validation model
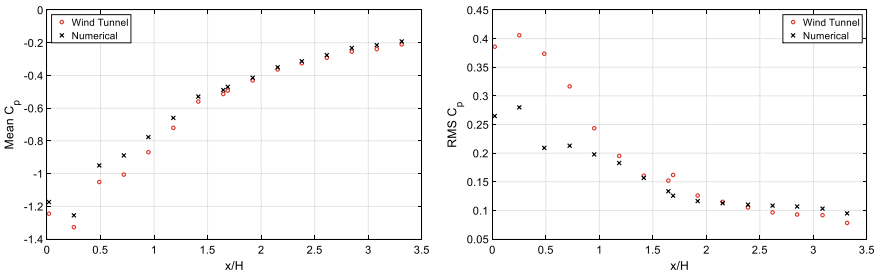


**Fig. 5** Comparison of **a** mean $C_p$, **b** RMS $C_p$ using CFD and wind-tunnel experimental testing

## 3 Case Study

This section utilizes the same physics adopted in the validation section to be used with a fishbone-like building layout of modular buildings adopted in Wuhan Thunder God Mountain hospital as discussed by Chen et al. [2] to obtain forces developed on their surfaces. Results can be further utilized to design different grades of modules

to be adopted in the locations tested. Seven wind angles of attack are considered, which are 0°, 15°, 30°, 45°, 60°, 75° and 90°. Since multi-modules building consists of single modules with a footprint of 3.0 m × 6.0 m with 4.0 m height as shown in Fig. 6a, a fishbone layout is to be examined in CFD to determine the wind forces developed on different surfaces distributed at select locations as shown in Fig. 6b. Four corner modules, four internal modules, and six edge modules are examined.

As for the computational domain for the multi-modules building adopted in the numerical model, a rectangular block of size 3 m × 5 m × 0.5 m is used to perform the simulation. The building is placed 0.8 m away from the inlet, and data collection starts after 2000 time-step to ensure flow stabilization. The front wall is assigned as a velocity inlet, while the back wall is an outlet, sides of the computational domain and the roof are assigned as symmetry plane, while for the ground, it is set as a no-slip wall as shown in Fig. 7.



(a)    (b)
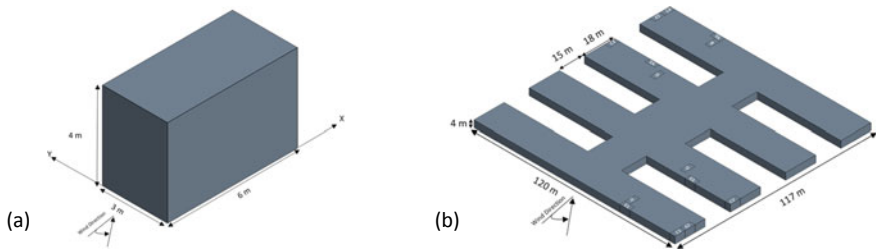
**Fig. 6** **a** Full-scale geometric details of a single module, **b** full-scale geometric details of multi-modules building
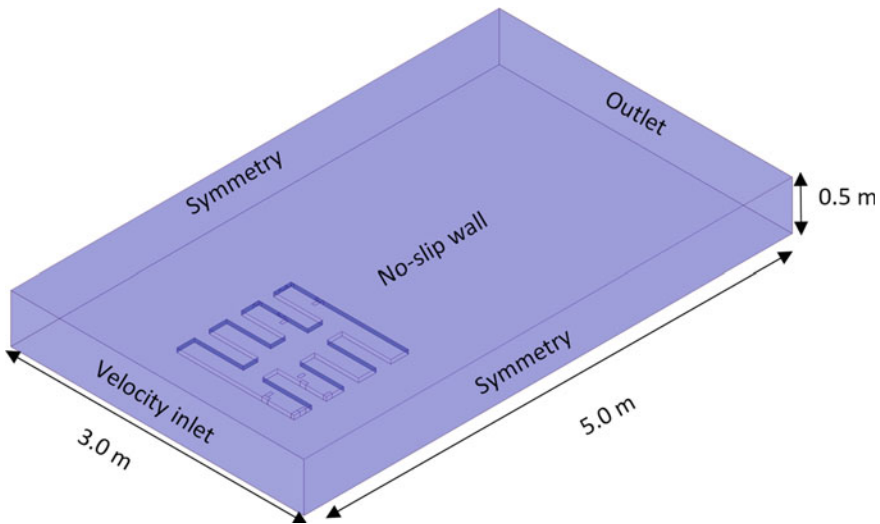


**Fig. 7** Computational domain and boundary conditions multi-modules building
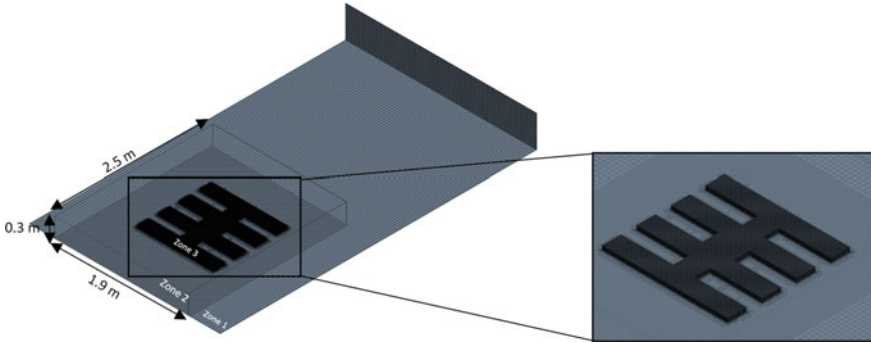
**Fig. 8** Mesh discretization of multi-modules buildings

The computational domain of the multi-modules building is discretized into three zones based on the hexahedral mesh cell. Zone 1 adopted a base mesh size of 50 mm, while zone 2, with dimensions of 1.9 m × 2.5 m × 0.3 m adopted a mesh size of 30 mm. Zone 3 consists of the building itself with a mesh size of 2.5 mm yielding 0.9 M cells, as shown in Fig. 8. The simulations duration is 6 s, with a time-step of 0.25 milli-second, with three inner-iterations, and a total of 24,000 time-steps. Data collection of forces starts after 2000 time-steps to establish flow stabilization. The time-step is selected based on the velocity scale and the minimum cell size to satisfy the Courant-Friederichs-Lewy (CFL) number below unity to ensure the solution convergence [3].

## 4   Results and Discussion

After running all the models, the force–time history of each module within the layout is extracted to find the critical forces developed on its surfaces. Since different wind angles of attacks are examined, the most critical force is selected as a peak design force for each direction (i.e., $X$, $Y$, and $Z$). The $X$-direction is chosen to be in the longer span direction, while the $Y$-direction is in the shorter direction as shown in Fig. 6a. As for the wind angle of attack 0° and 90°, the force values are the resultant on those surfaces, thus making them the values experienced by the modules. Unlike when the wind angle of attack is 15°, 30°, 45°, 60° and 75°, in these cases, the only force that can be utilized from the force–time history is the force in the $Z$-direction. As for the forces in the $X$-direction, and $Y$-direction, the resultant forces are found through resolving the forces reported in those directions. Force–time histories are reported in model-scale; to convert them to full-scale, forces are multiplied by a force scale of 160,000. Figure 9 shows a time history for module C4 in the $X$-direction from wind angle of attack of 30° from 0.5 to 6 s.

Since there are four corner modules, six edge modules, and four interior modules, the developed wind-induced loads are expected to be more critical in those corner
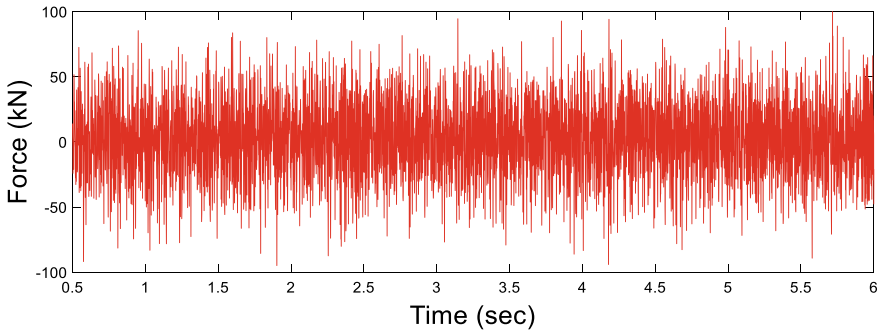
**Fig. 9** Force–time history of module C4 in the *X*-direction with a wind angle of attack of 30°

and edge modules. As for the internal modules, the critical forces are expected to occur in the *Z*-direction. The results summarized in Fig. 10 show the forces in *X*, *Y*, and *Z* directions. To categorize the grades of the modules, a comparison between the corner modules is conducted to determine the most critical to be used at corner locations. As for the edge modules, forces developed on them are compared with the corner ones. The critical loads can be used at all edge locations in the layout. As for the internal ones, the only comparison is in the *Z*-direction to the corner and edge modules since they experience little to no force in the *X* and *Y* wind directions. Based on the results, corner modules experience higher forces in *X* and *Y* wind directions. This can be attributed to the larger area of flow separation corner modules experience. For example, module C4 experienced the largest *X*-direction wind force of 100 kN compared with the corner modules under all different wind angles of attacks. As for the largest *Y*-direction wind force, it was developed on module C1 with a value of 103 kN. As for the *Z*-direction for the corner modules, the largest force was experienced by module C4 with a value of 74 kN, and this is the largest *Z*-direction force experienced by any modules tested. As for the edge modules, the module that experienced the largest force in the *X*-wind direction is module E2, with a value of 96 kN, which is 4% less than the largest force developed on corner modules. As for the *Y*-direction wind experienced by edge modules, the largest force developed on module E1 with a value of 93 kN, which is 10% less than the largest force developed on corner modules. Based on these findings, modules located at corners can be further reinforced against the straining actions caused by increased surface exposure, as they experience the most critical forces in the X-wind and the Y-wind directions. As for the edge modules, they tend to experience weaker forces than corner modules due to having less exposure to wind pressure. Thus, their design forces can be reduced to reduce the material used. As for internal modules, their design can be reduced further since they experience critical forces in Z-direction mainly. These observations can be further investigated by examining a single module under wind load to obtain forces developed on its surfaces. They can then be compared with the different module locations to determine the impact of the location on the module's design force.
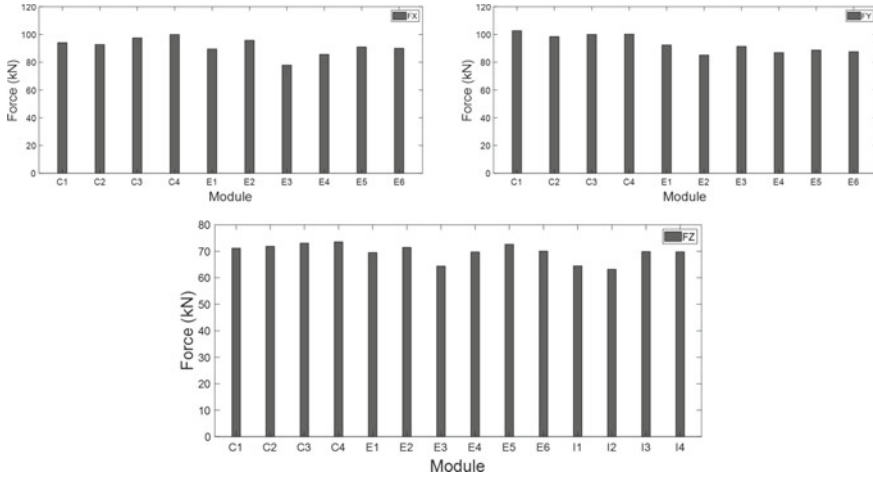
**Fig. 10** Forces developed on modules in a multi-module layout

## 5 Conclusion

The modular construction technique is an effective solution to the conventional construction challenges when it comes to healthcare space. There have been many studies concerning the structural optimization of the modular structure, but further studies are needed to investigate the impact of the lateral load (e.g., wind load) on modular structures. Based on the challenges proposed, a case study is conducted on a multi-modules building with a fishbone layout, including seven wind angles of attack, to obtain force–time history acting on the modules' surfaces. Peak forces developed on surfaces are extracted to get the design forces. Based on the results, it is determined that corner modules experienced the largest peak forces in all wind directions ($X$, $Y$, and $Z$). Edge modules experienced 5 and 10% less force than the corner module in the $X$ and $Y$ direction, respectively. The results highlight the importance of obtaining peak forces on modular buildings since the pressure distribution can be hard to predict, especially within complex layouts since they can consist of a large number of modules, thus highlighting the importance of categorizing the modules based on grades. The forces obtained can then be used to design modules with different grades based on the module location within the studied layout.

## References

1. Aboshosha H, Elshaer A, Bitsuamlak GT, el Damatty A (2015) Consistent inflow turbulence generator for LES evaluation of wind-induced responses for tall buildings. J Wind Eng Ind Aerodyn 142:198–216. https://doi.org/10.1016/j.jweia.2015.04.004

2. Chen LK, Yuan RP, Ji XJ, Lu XY, Xiao J, Tao JB, Kang X, Li X, He ZH, Quan S, Jiang LZ (2021) Modular composite building in urgent emergency engineering projects: a case study of accelerated design and construction of Wuhan Thunder God Mountain/Leishenshan hospital to COVID-19 pandemic. Autom Constr 124. https://doi.org/10.1016/j.autcon.2021.103555

3. Courant R, Friedrichs K, Lewy H (1928) Über die partiellen Differenzengleichungen der mathematischen Physik. Kurt Otto Friedrichs 53–95. https://doi.org/10.1007/978-1-4612-5385-3_7

4. Elshaer A, Aboshosha H, Bitsuamlak G, el Damatty A, Dagnew A (2016) LES evaluation of wind-induced responses for an isolated and a surrounded tall building. Eng Struct 115:179–195. https://doi.org/10.1016/j.engstruct.2016.02.026

5. Elshaer A, Gairola A, Adamek K, Bitsuamlak G (2017) Variations in wind load on tall buildings due to urban development. Sustain Cities Soc 34:264–277. https://doi.org/10.1016/j.scs.2017.06.008

6. Gatheeshgar P, Poologanathan K, Gunalan S, Shyha I, Sherlock P, Rajanayagam H, Nagaratnam B (2021) Development of affordable steel-framed modular buildings for emergency situations (Covid-19). Structures 31:862–875. https://doi.org/10.1016/j.istruc.2021.02.004

7. Gbadamosi AQ, Oyedele L, Olawale O, Abioye S (2020) Off-site construction for emergencies: a focus on isolation space creation (ISC) measures for the COVID-19 pandemic. Prog Disaster Sci 8. https://doi.org/10.1016/j.pdisas.2020.100130

8. Ho TCE, Surry D, Morrish D, Kopp GA (2005) The UWO contribution to the NIST aerodynamic database for wind loads on low buildings: Part 1. Archiving format and basic aerodynamic data. J Wind Eng Ind Aerodyn 93:1–30. https://doi.org/10.1016/j.jweia.2004.07.006

9. Peng J, Hou C, Shen L (2021) Numerical analysis of corner-supported composite modular buildings under wind actions. J Constr Steel Res 187. https://doi.org/10.1016/j.jcsr.2021.106942

10. Smith RE, Timberlake J, Smith F (2010) PREFAB ARCHITECTURE

11. Suleiman M, Elshaer A, Billah M (2021a) COVID-19 Modular Construction

12. Suleiman M, Elshaer A, Billah M, Bassuony M (2021b) Propagation of mouth-generated aerosols in a modularly constructed hospital room. Sustainability (Switzerland) 13. https://doi.org/10.3390/su132111968

13. Wang X, Su P, Liu J, Zhao S (2021) Seismic performance of ATLS modular house based on joint stiffness analysis. J Constr Steel Res 183. https://doi.org/10.1016/j.jcsr.2021.106770

14. Zhang JF, Zhao JJ, Yang DY, Deng EF, Wang H, Pang SY, Cai LM, Gao SC (2020) Mechanical-property tests on assembled-type light steel modular house. J Constr Steel Res 168. https://doi.org/10.1016/j.jcsr.2020.105981

15. Zhang Z, Pan W, Zheng Z (2020) Fighting Covid-19 through fast delivery of a modular quarantine camp with smart construction. Proc Inst Civ Eng Civ Eng 174:89–96. https://doi.org/10.1680/jcien.20.00025

# Transportation Specialty: Road Safety and Traffic Operations

# A Python Extension in Sumo for Simulating Traffic Incidents and Emergency Service Vehicles

**Tianxin Li, Wei Zhao, Carolina Baumanis, Jennifer Hall, and Randy Machemehl**

**Abstract**  Traffic signal retiming and coordination play a significant role in traffic management, especially when the traffic incidents disrupt the network. Many researchers have developed artificially intelligent (AI) traffic signal controllers based on goal-oriented machine learning frameworks to try and optimize network performance. However, previous efforts have lacked the means to evaluate these networks under traffic incident conditions. To make these AI traffic signal controllers more robust, current research needs to consider AI traffic controller performance under traffic incidents and accompanying emergency response. Obtaining field incident data and converting into inputs for simulation models to evaluate these machine learning models has been a huge hurdle because it is expensive, time-consuming, and sometimes even unfeasible. This paper provides an integrated traffic incident and response simulation tool for a grid network made in Simulation of Urban MObility (SUMO) to overcome this gap. The tool includes random traffic incident generation (location and duration), incident detection, random emergency vehicle generation, and emergency vehicle dispatching. With this tool, users can simulate a road network with traffic incidents and emergency vehicle response to produce substantial amounts of data for training robust reinforcement learning models. In addition, this tool will save future researchers and practitioners both time and effort in testing the impact of their proposed AI traffic control models and allow for a more complete evaluation of performance.

**Keywords**  Traffic incident simulation · SUMO

T. Li (✉)
Connecticut Transportation Institute, University of Connecticut, Storrs, CT, USA
e-mail: tianxin.li@uconn.edu

T. Li · C. Baumanis · J. Hall · R. Machemehl
Cockrell School of Engineering, Department of Civil, Architectural and Environmental Engineering, University of Texas, Austin, USA

W. Zhao
Department of Biological System Engineering, University of Wisconsin-Madison, Wisconsin-Madison, USA

# 1 Introduction

Traffic engineers primarily use simulation to establish confidence in innovative traffic signal timing concepts. Simulation establishes confidence by characterizing the field network, collecting traffic demand data, and testing potential signal retiming policies to analyze network performance (e.g., average vehicle delay). Traditionally, the person setting up the simulation must manually provide the potential signal timings for the time period(s) being considered in a simulation. However, reinforcement-based machine learning methods make it possible for the simulation (i.e., AI traffic controller) itself to analyze the traffic conditions at hand and pick an optimal signal timing to minimize delay, maximize flow, etc. Previous work has studied AI traffic signal controllers and a variety of control techniques have been tested through traffic simulations, but none have considered how their proposed AI traffic controllers function under traffic incidents and emergency response conditions.

At their core, reinforcement learning algorithms explore the relationship between an agent's actions (AI traffic controller) and its evolving environment (traffic conditions) by trial-and-error methods. Feedback from the environment measured by so-called rewards (delay, flow, etc.) can help the agent adjust its behavior to achieve more rewards in the future. The AI traffic controller can learn from its interaction with the environment, but an optimal response requires a large amount of experience that covers virtually all possible incident situations, so that AI controller has sufficient signal timing options to pick from. A field implementation of an AI traffic controller without sufficient experience would be disastrous. At the very least, an AI traffic controller should perform better than existing canned signal timing plans both with and without traffic incidents.

The next generation AI traffic signal control system are far from field application since many aspects, including traffic incidents, have not been tested thoroughly. One major reason AI traffic controllers have lacked testing under traffic incident conditions is that collecting field network data for validating proposed models is expensive and time-consuming. In general, most researchers cannot viably collect historical traffic incident and emergency vehicle response data. Therefore, we provide a Python extension for SUMO to allow microsimulation of an AI signal control system in a network experiencing incidents randomized in both time and space. This tool provides an inexpensive and practically feasible traffic simulation solution that allows the evaluation of an AI traffic controller under traffic incident and response conditions.

We begin by highlighting existing efforts in developing the next generation traffic signal control systems and available simulation software with traffic incident/response capabilities. Then, we describe the extraordinary features of SUMO and the framework we used to extend SUMO with a traffic incident/response module coded in Python. Lastly, we present the experiments conducted to show the use of the extended module.

## 2   Related Work

Traffic signal retiming plays a significant role in improving the network performance when traffic incidents occur. To maintain efficiency in operations, traffic simulations have been commonly adopted to test potential traffic signal timing policies before field implementation. Liu and Hall proposed a Windows operating system-based computer simulation software for simulating highway traffic incidents, as well as emergency vehicle dispatching [1]. The software only can consider traffic delay and cannot capture queue spill backs. While this software can help researchers and practitioners to broadly understand the impact of traffic incidents and determine the emergency dispatch strategies, it has several key limitations. This software only applies to highways, so users cannot simulate traffic signals contained within local networks.

Ozbay and Bartin developed a complete traffic incident simulation tool using the Siman language to generate incidents in the network and to send emergency vehicles to respond accordingly [2]. Their proposed simulation tool was tested with both real network and real-world data, and allows the user to evaluate various Traffic Incident Management (TIM) strategies to reduce the impact of traffic incidents in the network. However, the data scientist and machine learning modeling field rarely use the Siman programming language these days. Most of the advanced and latest machine learning methods are written in Python, which means the users who wish testing their advanced TIM strategies will know and prefer the Python over Siman.

Based on the cell transmission model, Ozbay proposed the Rutgers Incident Management System (RIMS) to simulate the traffic incidents and to test various incident response strategies [3]. The results indicate that implementing an Incident Management System could significantly reduce the traffic delay triggered by a traffic incident in the network. However, this tool lacks traffic signal timing because it is based on the cell transmission model, and therefore not appropriate for microsimulation.

A simulation-based method was proposed to test traffic incident management strategies in Visual Interactive System for Transport Algorithms (VISTA), a dynamic traffic assignment (DTA) embedded tool [4]. This DTA tool offers the opportunity for modelers to accurately estimate the impact of the traffic incidents by considering the dynamic change of road capacity and travel time, where static traffic assignment models fail to perform. The researchers extracted network and traffic demand data from the Chicago Area Transportation Study and various incidents in terms of locations and durations were simulated around I-94. Inside of the simulation, the researchers adjusted multiple surrounding traffic signals based on Webster's formula so that the green time would split to accommodate the change in traffic flow pattern once the incident occurs. The researchers analyzed the incident response actions, such as closure of a certain number of ramps upstream of the incident location, to find the best traffic delay alleviation strategies. The idea of this research is to preplan the traffic incident management strategies and take corresponding incident response actions once the incident occurs. This method might work fine when the incident

locations are fixed and traffic demand patterns are predictable. However, due to the complexity of the network and scale of inputs, including traffic demand, network characteristics, and existing traffic signal control methods, in reality it is hard to find the optimal traffic incident strategies within a short period of time with just human intervention.

The traffic signal control field has adopted reinforcement learning methods to improve signal retiming efforts. The main advantage of the reinforcement learning methods is the use of deep neural networks, to perform approximation of the inputs from the environment and estimate the cumulative long-term expected rewards with a model-free method. A model-free method does not know anything about the specific dynamics of the environment like a model-based method would, and evaluates actions through trial and error. To achieve accuracy in the high-level function approximation, the reinforcement learning method requires substantial amounts of data look back on and learn from.

Common limitations of existing traffic incident simulation tools are:

- Tools have not been maintained or published, making it difficult for other users to find and replicate the experiments or design new experiments to test traffic signal control strategies. The traffic control modeling field would benefit from a free and open-source simulation software.
- The existing tools cannot generate a test network and associated traffic demand, which would minimize the costs of preparing the base scenario.
- The scale of existing inputs is not enough to train machine learning models for field deployment. Most existing experiments use a single or multiple real data points to simulate the traffic incident environment.
- The functions in the existing tools are not comprehensive enough to test proposed strategies from different angles, including vehicle rerouting and traffic signal timing.
- The existing tools are not available for multi-cross platforms, preventing the use of high-performance computing advantages these days.
- The simulation environment is closed, meaning it is hard for the users to customize and extend it to other languages like Python.
- Measures of effectiveness (MOE) are limited and do not match up with the network performance measurements used nowadays, where consideration of vehicle emission and fuel consumption are required.
- Manually generating test networks, traffic demand, and incident occurrence are not efficient for training machine learning algorithms for traffic signal retiming.

To develop robust AI traffic control systems, we need a simulation testbed that incorporates traffic signal retiming and a traffic incidents/response system. The purpose of this work is to provide a highly automated process to generate random traffic incidents in a network, as well as the corresponding emergency service vehicles as an extension of the existing popular microscopic traffic simulation software called SUMO. Key components in the extension include random traffic incident generation, traffic incident detection, emergency service vehicle generation, and emergency service vehicle dispatching. By conducting simulations in this kind of

setting, researchers can test new traffic signal control methods, while considering the traffic incidents in the network and tune them for field application.

## 3 Traffic Incident/Response Module

SUMO is an open-source microscopic traffic simulator developed and maintained by the German Aerospace Center [5]. It is portable and works on various operating systems, including Windows, Linux, and MacOS. Since SUMO works with Linux systems, researchers can easily implement it using high-performance computing machines, which will significantly reduce simulation run time for a large-scale implementation.

SUMO provides a TCP/IP protocol method of retrieving and controlling the simulation by using the Traci library. The Traci library allows users to obtain real-time traffic information, such as vehicle location and speed, traffic signal phase and duration, network delay situation (e.g., queue length for a specific lane), etc. It also allows the user to offer input to change the parameters in the simulation, such as number of vehicles stopped. Traci allows users to implement traffic control algorithms via Python scripts, which greatly reduces the script preparation time and improves the efficiency of implementation. Users can easily choose the functions in Traci to realize the things they plan to test.

SUMO simulation requires at least two files, including network file and route file. The network file defines the road network, including intersections, edges, connection rules, and traffic signals. There are several common types of traffic signals provided in SUMO, including pretimed, actuated, adaptive, and other more advanced (self-organized traffic signals) control frameworks. The user can define detectors, including loop, area detector, etc. and customize the traffic control algorithms as needed, including the reinforcement learning traffic signal control methods.

### 3.1 Network Preparation

As another benefit, SUMO provides a network generation library (NETGENERATE) that allows users to easily build a grid-like network. With this library, users can determine the number of intersections in horizontal and vertical directions within the network. Users can also choose the number of lanes and length of each approach for each intersection. In addition, users can add pretimed traffic signals to the target intersections in the network. The tool provides a way to set up the cycle length, left turn protection phases, green split, yellow time, and all red time durations to mimic practical applications.

## 3.2   Demand Preparation

SUMO provides another important and useful Python script to prepare traffic demand randomly based on the developed network, which is especially users for circumstances where it is not possible to get real-life demand data. This way, users can focus on evaluating a more generalized traffic signal control algorithm and cannot worry about spending time collecting field data. The tool allows users to set the ratio of internal and external traffic demand. In this study, we assume that all traffic demand is external traffic by making the ratio between through and internal traffic demand an extremely large integer. This large integer effectively means that all the traffic is starting and ending from the fringe of the network. The trip table saves as an XML file so the user can easily repeat experiments.

SUMO is also commonly used to generate the traffic demand by dynamically adding vehicles to the system. However, the issue with this method is that SUMO also calculates the shortest path in the network dynamically, so traffic can easily adapt and detour around the incident location and the overall impact of the incident on the network might be underestimated. To isolate the effect of the traffic signal retiming provided by the AI traffic controller, we need to lock the traffic paths so that when there is a traffic incident in the system, the traffic does not automatically shift paths. While in reality travelers would shift routes to avoid being stuck in a long queue in the network, we assume that no travelers change paths for two reasons. First, the benefits of optimizing the signal plan based on the AI traffic signal controller need to be calculated. If the travelers are allowed to shift paths, the net benefits of signal plan optimization are difficult to quantify. The other reason is the ratio of travelers who shift paths and remain on original ones relate to the traffic demand pattern and characteristics of intersections, which are also hard to quantify for this particular research. Therefore, this effort uses the first method mentioned above and edits the original traffic demand file (XML format) to add traffic incidents, including incident locations, incident durations, and emergency vehicle response.

## 3.3   Incident Simulation in SUMO

SUMO provides three methods to simulate traffic incidents in the network: (1) Stop a car at a designated location for a specific period (2) Reduce the road capacity of associated lanes (3) Reduce the design speed of the associated road edges. In SUMO, there are several important concepts of network components. Edge defines the approach of the intersection, and an edge includes a certain number of lanes. The lanes are named based on the edgeID and lane index. The easiest and most realistic way to simulate traffic incidents is the first option. Option 1 will require editing the route file with one line of code to reflect the stop of an incident vehicle. Figure 1 shows the added traffic incident information in the route file. In this example, the

```
<vehicle color="1,0,0" depart="2.00" id="2">
    <route edges="right2C2 right2C2.100.00 C2C1 C2C1.100.00 C1C0 C1C0.100.00 C0right0"
    />
<stop duration="1500" endPos="20" lane="C2C1_1" parking="false" /></vehicle>
```

**Fig. 1** Settings of stopping vehicle in route file

vehicle with ID 2 will stop at Lane "C2C1_1" 20 m from the end of this lane for 1500 s.

## 3.4 Emergency Service Vehicles Simulation in SUMO

In addition to the incident vehicle generation, we also generate emergency service vehicles in the simulation once the traffic incident is detected. During normal traffic movement, no vehicle will stop at a location for a long period of time, which is a user-defined time threshold (e.g., 5 min). Once the system has detected that a vehicle is stuck in the network for more than a specific period of time, the emergency service vehicles are generated and dispatched to that location. Users can choose the number of emergency service vehicles to reflect real-life emergency response, such as multiple police cars and EMS vehicles.

When first dispatching emergency response vehicles, we realized that it is not always possible for all the vehicles to reach the incident location due to heavy traffic congestion. To overcome this issue, we decided to edit the emergency vehicle length to represent multiple emergency service vehicles being needed. The default length of per emergency service vehicle is 7.5 m, including 5 m for the vehicle length and 2.5 m for the clear space. For example, if 3 police cars and 1 EMS vehicle are required to deal with a traffic incident, a total of 4 emergency service vehicles, then a vehicle with length of 30 m will be generated and dispatched in the simulation. The extra long vehicle will block a total of 30 m in the incident lane to reflect the combination impact of multiple emergency services vehicles in practice.

The route of the emergency service vehicle is defined before it is dispatched into the network. To generalize the implementation of emergency vehicle response, we randomly select an origin for its route from the fringe of the network. The destination of the route is the incident edge. During the incident response service, the emergency vehicle will occupy the lane next to the incident vehicle. For example, if the incident vehicle stops at the middle lane of an edge and there are three lanes for this edge, the emergency service vehicle will randomly stop in either the first (straight and right turn lane) or the third lane (left turn lane in our experiment) of the same edge. The emergency vehicle will arrive at the incident location after the incident vehicle has been detected and then the emergency service vehicle will stay stopped for the same duration as the incident vehicle. Once the emergency service vehicle completes its service, it will finish its route and reach the intersection of the destination edge.

```
Step = 0
hasIncident = False
While numberOfVehicles() > 0:
        executeSimulation() # 1 step, e.g., 1 second per step
        If incident detected() and not hasIncident:
                getIncidentInformation() # including location and stopping duration
                generate emergency service vehicle() and dispatch()
                hasIncident = True # this will avoid generating emergency service vehicle
        multiple times
        Step += 1
```

**Fig. 2** Pseudocode for the simulation framework

In Traci, the function to generate a route based on the origin and destination edges is traci.simulation.findRoute(origin_edge, destination_edge). Once the two parameters are given, the function will find a feasible and the shortest route in the network. The route information can be called to show the edges used in this route by calling the route.edges property.

To dispatch the emergency service vehicle in the system, the function traci.route.add(routeID, route_edges) needs to be called to add the edges of the emergency service vehicle route into the route file. The emergency service vehicle then can be added to the route file by calling traci.vehicle.setStop(vehicle_id, route_edges, stop_lane_index, stop_duration). Users can customize the traffic signal to give emergency service vehicle priority, so that they can arrive at the incident location as quickly as possible.

For a two-lane edge, the whole edge will be blocked by both the incident car and emergency service vehicle, while for a three or more-lane edge, two lanes will be blocked and capacity will be reduced significantly. We examined the impact of only considering the incident vehicle without the emergency service vehicle in the system and the impact on delay is significantly different, showing that accounting for the emergency service vehicles in the system will produce a more realistic picture.

The pseudo code for the simulation is shown in Fig. 2 to show the simulation logic.

## 4   Simulation Procedure

Once the network and traffic demand are prepared, the customized incident Python script will read the route XML and randomly select a vehicle to generate a traffic incident. Then, the simulation starts and once the incident vehicle is detected in the network stopping for more than 5 min (or any user-defined threshold), emergency service vehicles will be generated by calling DISPATCH_EMERGENCY VEHICLE() function. Blue is the default color of the emergency vehicle and the total length is the number of emergency service vehicles needed to respond to the

incident multiplied by 7.5 m. Therefore, the incident vehicle will be shown in red and the emergency service vehicle will be shown in blue when viewing the animation of the simulation process.

In Fig. 3, a 4 × 4 grid network is shown as well as the incident vehicle and emergency service vehicle. Figure 4 shows a larger view of the incident vehicle (RED) and emergency service vehicle (BLUE).

The developed incident generation and emergency service vehicle response Python script is published in the following GitHub https://github.com/Flexing920/dissertation/tree/main/tests/tl/dissertation. The network directory includes a 4 × 4 grid network generated by calling the NETGENERATE command. The main functions for incident generation and emergency service vehicle response are in incidentRoute.py located in the root directory of this GitHub repository. The current Python script is for single traffic incident preparation. Users could extend it to include multiple incidents as needed.
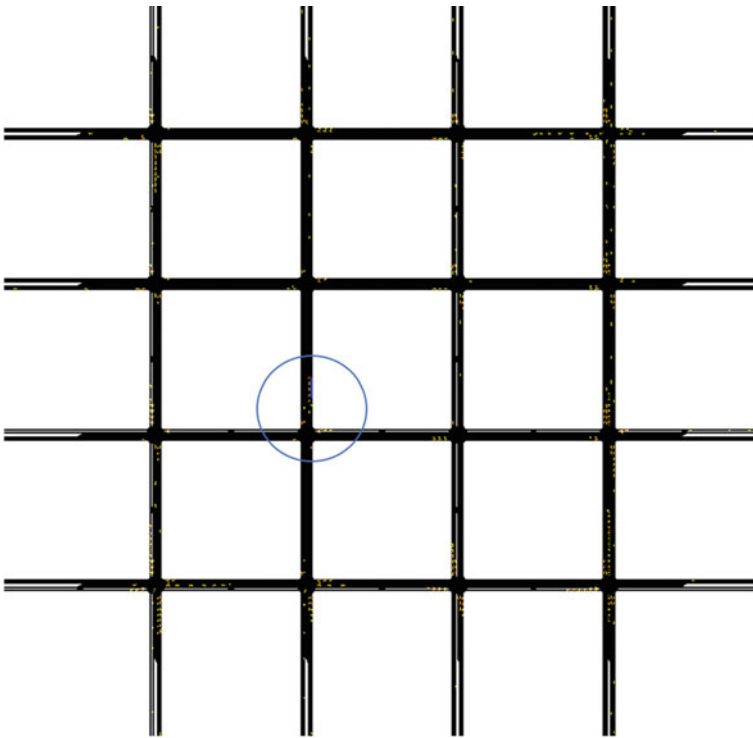


**Fig. 3** 4 × 4 grid network with traffic incident
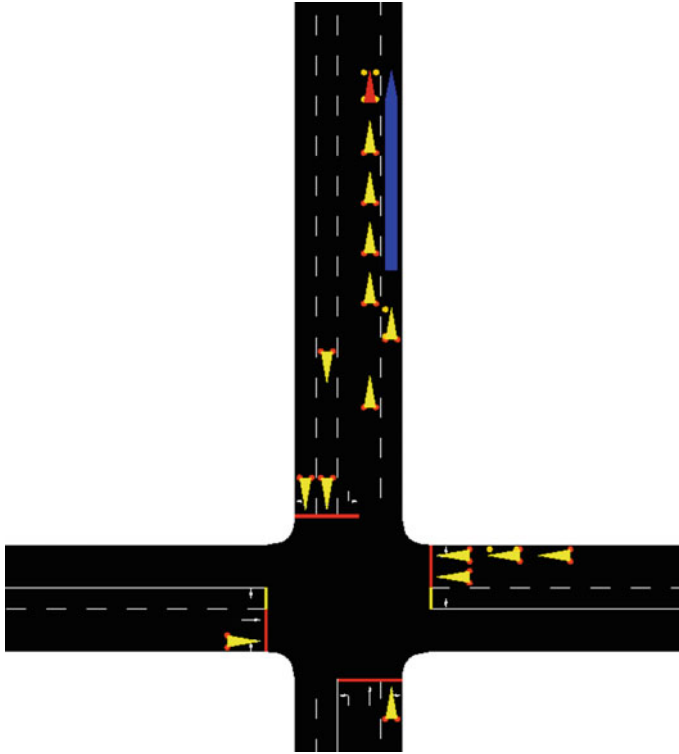
**Fig. 4** Example of the incident vehicle (red) and emergency service vehicles

## 5 Implementation

Running the NETGENERATE module provided by SUMO will generate a $4 \times 4$ grid network. All the parameters as well as their meaning can be found in Appendix 1. The user can prepare traffic demand for the $4 \times 4$ grid network by running the trip generating Python script in SUMO. Some of the key parameters that users can define include the ratio of internal and external trips, hourly traffic flow, and turning ratios. The commands used in this paper can be found in Appendix 2 as well as the explanation of the parameters.

For this study, traffic demands are all external traffic, meaning the origins and destinations of all trips are located at the network fringe. Intersections are all controlled by pretimed traffic signals with four phases, including east–west straight movement phase, east–west left turn phase, north–south straight movement phase, and north–south left turn movement phase. Right turn movement is allowed and included in the straight movement phases. Cycle time for every intersection is the same, 90 s. The cycle is split 50–50 between the east–west and north–south directions with the straight/right movement receiving 27 s and the left turn phase receiving 13 s with both

yellow clearance intervals 3 and 2 s all reds. More traffic signal setting information is located in the network file.

To add random incidents in the created network, the Python script must be called. Several inputs need to be defined before calling the extension, including the network XML file provided by the NETEDIT function, the traffic demand XML file produced by calling the randomTrip.py tool provided by SUMO, and the corresponding SUMO configuration file. The traffic incidents are generated before the simulation starts by randomly selecting a vehicle from the first third of the simulation period. The selected vehicle must have a route crossing the center of the network, otherwise the stopped lane will be located at the fringe of the network and prevent vehicles from entering the network. The traffic incident lasts for a random period of time anywhere from 15 to 30 min in 5 min increments. Once the vehicle reaches the incident location, it will fully stop and block the traffic behind. The traffic simulation system will record the stop duration for all vehicles in the network. Once the simulation detects that one vehicle stopped for more than 5 min, in the same location, it assumes a traffic incident exists and will dispatch emergency response.

Emergency medical service and police cars are generated as a single long length vehicle to represent their impact within the simulation. The origin of this emergency vehicle will be a random location along the network fringe and its destination is the incident location. The emergency vehicle will be stopped for the same amount of time as the incident vehicle. For a two-lane edge, the incident vehicle and emergency vehicle will fully block the road. The extension could be customized easily if multiple incidents are required for any scenario.

## 6  Conclusion

This research provides a convenient Python script for SUMO extension. Rather than only considering the traffic incident impact in the network, this research also provides a way to simulate emergency service vehicle impact in the network which is nontrivial. As shown in the experimental results, the combination impact of traffic incidents and corresponding emergency service vehicle response could cause significantly more delays than only considering the traffic incident itself in the network. This tool can help researchers to provide more realistic traffic incident management strategies to reduce the impact of traffic incidents and optimize the traffic management methods, including vehicle rerouting and traffic signal retiming, using a widely adopted programing language Python.

# Appendix

## *Appendix 1*

Below command was run for generating the $4 \times 4$ grid network illustrated in this paper.

netgenerate --grid --grid.number=4 --grid.length=200 --default.lanenumber=2 --default.speed=20 --no-turnarounds=true --turn-lanes=1 --turn-lanes.length=100 --default-junction-type=traffic_light --grid.attach-length=200 --tls.yellow.time=3 --tls.left-green.time=12 --tls.allred.time = 2 --output-file=net.net.xml

Network generating parameters and their meanings:

--grid: grid network will be generated. SUMO also provides other types of the network to be generated automatically, including spider and random networks.

--grid.length defines the length of each intersection leg in meters

--default.lanenumber defines the number of lanes for each approach

--default.speed defines the edge design speed in meters/second

--no-turnarounds defines whether to allow turn around for the left turn lane

--turn-lanes defines the number of left turn lanes

--turn-lanes.length defines the length of left turn lanes

--default-junction-type defines the intersections in the network are controlled by the pretimed traffic signals

--grid.attach-length defines the length of road attached to the fringe of intersections in the network

--tls.yellow.time defines the duration of yellow phase in seconds

--tls.left-green.time defines the protected left turn movement green time in seconds

--tls.allred.time defines the duration of all red phase in seconds

## *Appendix 2*

Traffic demand was prepared by calling python randomTrips.py -n net.net.xml -r random.rou.xml --fringe-factor=100000000 --period=0.5 -e 3600.

where randomTrips.py is a Python script tool provided by SUMO.

-n net.net.xml defines the location of the network file.

-r defines the name of the output route file.

--fringe-factor defines the ratios of through and internal traffic demand in the network. An extremely large number is used here to eliminate the internal traffic demand in the network.

--period defines the 1/number of vehicles generated per second. 0.5 used here means two vehicles will be generated per second in the network.

-e defines the end simulation step of generating trips, so here one hour traffic demand is generated.

## References

1. Liu H, Hall R (2000) INCISM: Users Manual
2. Ozbay K, Bartin B (2003) Incident management simulation. SIMULATION 79(2):69–82
3. Ozbay KM, Xiao W, Jaiswal G, Bartin B, Kachroo P, Baykal-Gursoy M (2009). Evaluation of incident management strategies and technologies using an integrated traffic/incident management simulation. World Rev Intermodal Transp Res 2(2–3):155–186
4. Wirtz JJ, Schofer JL, Schulz DF (2005) Using simulation to test traffic incident management strategies: the benefits of preplanning. Transp Res Rec 1923(1):82–90
5. Krajzewicz D, Erdmann J, Behrisch M, Bieker L (2012) Recent development and applications of SUMO-Simulation of Urban MObility. Int J Adv Syst Meas 5(3&4)

# Operating-Speed Models for Horizontal Curves on Two-Lane Rural Highways: Case Study in Nigeria

**Abayomi Afolayan, Oladapo Samson Abiola, Said M. Easa, Funmilayo Modupe Alayaki, and Olusegun Folorunso**

**Abstract** Geometric elements of highways play a significant role in accident occurrences on curves. Hence, curved sites and the corresponding transition sections represent the most critical locations when considering safety measures on rural highways. Excessive speeds may cause inconsistency in a horizontal alignment. Hence, attaining geometric consistency is vital in designing and redesigning two-lane rural highways. Operating speed models were developed to evaluate operating speed consistency on a two-lane rural highway in Nigeria using speed data for 111 horizontal curves. The test of significance on the vehicle speed in the different lanes and the consistency of speed measurements show no statistical difference between the speeds in both directions. Also, at the 5% significance level, there is no statistical significance between the speed data obtained using a stopwatch and an automatic counter. However, the automatic counter allows for more observations. Based on the different categories of curve radius (CR) considered in the model development, Model 1 with CR < 1200 m has a statistically significant and influential relationship. Thus, this model is highly recommended for operating speed prediction on horizontal curves in Nigeria.

**Keywords** Consistency · Roads · Two-lane · Rural · Operating speed · Models

A. Afolayan (✉) · O. S. Abiola · F. M. Alayaki
Department of Civil Engineering, Federal University of Agriculture, Abeokuta P.M.B 2240, Ogun State, Nigeria
e-mail: afolayan.abayomi@pg.funaab.edu.ng

S. M. Easa
Department of Civil Engineering, Ryerson University Toronto, Toronto M5B-2K3, ON, Canada

O. Folorunso
Department of Computer Science, Federal University of Agriculture, Abeokuta P.M.B 2240, Ogun State, Nigeria

# 1 Introduction

Yearly, an average of 500,000 persons are killed and about 10,000,000 persons sustain an injury in vehicle accidents globally, leading to annual financial losses that amount to several billions of dollars (Abiola et al. 2018; Popoola et al. 2017) [39]. In Nigeria, about 11,033 persons were involved in 2080 cases of traffic accidents in the 2nd quarter of the year 2020 alone [34]. More than half of all deaths that occurred on rural highways, as estimated, could be accredited to accidents that take place on horizontal curves (Popoola et al. 2018) [21]. Hence, horizontal-curved sites and the corresponding transition sections represent the most critical locations for safety precautions on rural highways. A lack of geometric design consistency, defined as the extent to which roadway elements are built and constructed to prevent emergent driving movements, can be one of the leading causes of accidents, resulting in unwarranted accident risk [4]. Furthermore, a consistent highway design allows conformance of a highway's geometry with driver expectancy, by ensuring that successive geometric elements coordinate to produce harmonized driver performance without unaticipated events. Enhancing the geometry of two-lane highways should be of paramount importance for highway practitioners as they are essential road elements [38].

The most frequent scenario of geometric inconsistency is a sharp horizontal curve after a long tangent highway section. Past studies show that majority of all accidents on two-lane rural highways may be associated with inappropriate speed variation [9, 11]. Inconsistency in horizontal alignment may result from most errors due to excessive speed. Hence, attaining geometric uniformity is vital in designing and redesigning two-lane rural highways. Assessing design consistency and establishing any inconsistencies during the design phase of a proposed highway can significantly enhance the safety of the highway network [14, 37].

Nicholson [35] also defined design consistency as the agreement of road geometry with drivers' anticipation. More so, a consistent design does not contradict the image that most drivers figure out in their minds of the approaching character of the roadway in front of them. Various methods that can be used for design consistency evaluation have been identified by Fitzpatrick et al. (2000a) and Gibreel et al. [12] some of which are: operating speed, vehicle stability, alignment indices, and driver workload. Operating speed has been identified as the most effective approach of these methods.

## 1.1 Design Consistency Measures

Recently, researchers on highway design have been studying creating tools and approaches to help highway designers design highways with the highest degree of safety accomplishment. Such contributions can be seen explicitly in research associated with the geometric design of highway (advancement with a necessary

consequence on accident occurrence). Applications of the concept of design consistency have been among the most promising approaches in this field. There are three major fields in which previous research work can be divided, namely: (1) speed factors, (2) safety factors, and (3) performance factors [12]. The impact of various design parameters on the estimation of operating speed is addressed in the speed factor. Furthermore, regarding operating speed, the assessment of design accuracy of different road elements has been discussed.

In the choice of transportation mode, speed is a crucial factor that is mainly considered. The road user weighs the attractiveness of different highways in terms of convenience, cost, and time. The speed factor entails operating speed prediction and consistency measures on single and successive elements. The actual operating speed is the speed chosen by highway users when other users are not present [i.e., in free-flow conditions [36]]. The 85th percentile speed is usually used to describe this. Several factors affect the prediction of operating speed. These include horizontal curve radius, horizontal curve length, side friction factor, superelevation, sight distance, and pavement conditions.

Following a study of existing design literature, the most popular measures that were considered helpful in determining the accuracy of geometric alignments were identified as operating speed, vehicle stability, alignment indices, and driver workload. These methods can be basically grouped into two different classes [10]: the non-speed-based and speed-based approaches. The non-speed-based approaches consist of vehicle stability, driver workload, and alignment indices, while the speed-based approaches include operating speed methods and speed distribution measures. The operating speed method is used to determine the variation and distribution of vehicular speeds, while the speed distribution measures entail the basic statistics of speed such as mean, standard deviation, variance, coefficient of variation, kurtosis, and skewness. Amidst the mentioned approaches, the operating speed method is commonly used in literature due to its simplicity and quantifiability.

### 1.1.1 Operating Speed

Various methods have been developed to forecast operating speed on two-lane rural roadways with a horizontal alignment [2, 27, 31, 33] (Zuriaga et al. 2010). The use of curvature change rate (CCR) to anticipate the operating speed and identify speed inconsistency on horizontal alignments was suggested by Lamm et al. (1986). The CCR is expressed as the total addition of the angular changes in a roadway section per unit length [12]. In a further study, Lamm et al. [24] examined the correlation between $V_{85}$ and horizontal curve features using data from 322 curve sections. It was affirmed that the critical parameter influencing operating speed was the curve radius (degree of curve). The speed conduct of drivers on horizontal alignments of two-lane rural highways in Greece was studied by Kanellaidis et al. [18]. Islam and Seneviratne [16] looked at the changes in operating speed on two-lane rural roadways in Northeastern Utah and discovered that is the most critical factor in predicting operating speed on horizontal curves It was also discovered that on the

same horizontal curve, there were significant differences in operating speed at the Point of Curve (PC), Point of Tangent (PT), and at the middle of the Curve (MC). Jaydip et al. [17] modeled operating speed by vehicle type for two-lane rural highway in Indian hilly terrain and concluded that curve length has a significant effect on all vehicle types considered. In the same vein, Krammes et al. [19, 20] established a speed profile model to estimate the consistency of horizontal alignment on two-lane rural highways. $V_{85}$ at various points along the horizontal curve were estimated by the model. Two design consistency models that are based on operating speed data from 78 curved sections were established by McFadden and Elefteriadou [30].

The most prevalent criterion for evaluating roadway design consistency is operating speed [12]. The geometric design consistency can be for a single geometric element or for successive geometric elements. Design consistency is assessed for a single geometric element by comparison of design speed ($V_d$) with $V_{85}$. While for successive geometric elements, it is based on the $V_{85}$ of the elements.

*Single Geometric Element*

A single highway element is one that contains an independent feature of the highway without reference to the other features. This includes the curve, either horizontal or vertical, and tangent. During free-flow situations, operating speed refers to the speed drivers are observed driving their cars. While design speed is chosen speed used to establish the different design elements of the roadway [1]. Various methods have been developed to estimate the design consistency on a single element based on the difference between $V_{85}$ and $V_d$. Different countries of the world have developed standards to assess the consistency of design on a single element. European countries standards for consistency between operating and design speeds were summarized by Brenac [7]. Based on average accident rates, the disparity between $V_{85}$ and $V_d$ was inferred as a criterion to determine consistency, as shown in Table 1. Criterion I [25].

Besides using $V_{85}$ as a guide for choosing $V_d$, the posted speed should also be chosen based on $V_{85}$. The relationship between operating speed, design speed, and posted speed on two-lane rural highways was studied by Fitzpatrick et al. [9]. $V_{85}$ on horizontal curves was discovered to be less than $V_d$ for all curves with $V_d > 70$ km/

**Table 1** Criteria for design consistency [25]

| Design evaluation | Criterion I | Criterion II | Recommendations |
|---|---|---|---|
| Good | $V_{85} - V_d \leq 10$ km/h | $\Delta V_{85} \leq 10$ km/h | Alignment corrections not required |
| Fair | $10$ km/h $< V_{85} - V_d \leq 20$ km/h | $10$ km/h $< \Delta V_{85} \leq 20$ km/h | Alignment corrections are required |
| Poor | $V_{85} - V_d > 20$ km/h | $\Delta V_{85} > 20$ km/h | Redesign of hazardous locations is required |

$\Delta V_{85} =$ speed differential

h. It was inferred that a speed inconsistency scenario would occur at this place if the operating speed is higher than the design speed.

*Successive Geometric Elements*

Diverse means have been put forward to ensure highway sections with varied elements are designed consistently, particularly those with two elements in a row. This development, as outlined by Lamm et al. (1986), includes: (1) Average curvature obtained by dividing the length of a roadway section by the sum of the central angles of horizontal curves in that section, (2) average hilliness, estimated as the total of the lengths between each crest vertical curve and the subsequent sag vertical curve on a specific highway stretch, divided by the section length, (3) the length ratio was defined as the sum of horizontal and vertical curve lengths in a particular highway section divided by the section length, (4) the average radius of a group of horizontal curves in a specific roadway stretch was defined as the average radius of those curves, and (5) design radius, which is the average radius divided by the minimum radius connected to the design speed on a specific highway stretch.

However, operating speed is the most frequent and easiest approach to determining design consistency on successive elements. Several different combinations of consecutive elements have been investigated, including: a long tangent followed by a horizontal curve and two horizontal curves in succession, with or without a short tangent. Different countries have established design standards for evaluating the design consistency of successive elements. Switzerland was the first country to incorporate this disparity into its design methodology as a consistency measure [19]. Kanellaidis et al. [18] evaluated $V_{85}$ on the tangent that is based on speed data and used the developed model to determine $V_{85}$ on successive horizontal curves. It was inferred that a good design could be accomplished when the difference between $V_{85}$ on the tangent and the succeeding curve is not greater than 10 km/h. Based on average accident rates, criterion to determine design consistency between a tangent and the succeeding curve was suggested by Lamm et al. [25], as shown in Table 1, Criterion II.

Al-Masaeid et al. [4] stated additional models developed to show the change in speed in terms of current serviceability rating, the distance between a tangent and the next curve as a function of geometric factors and pavement condition. As a result, three models of operating speed change between tangent and subsequent curves were developed.

The first is for a horizontal curve on a flat gradient, the second is for a specified gradient, and the third is for vertical curves.

Misaghi [28] pointed out the need for an adequate methodology to predict variation in speed (or speed differential) values at specific locations of highways. Due to the variation in speed with which drivers negotiate a particular highway location, a highway designer will be able to estimate the design consistency of the highway location with the application of related standards. The concern will be methodology and criteria to model speed or speed differential values at a specific highway location with a pretty high chance of speed variation [28].

Various researchers have studied the influence of different factors on collision rates. Wilson [40] inferred that the radius of curve is a very important feature in the safety of highways. He discovered that a curve with $R_C > 910$ m has less collision than that with $R_C < 170$ m. Statistical studies on accident rate have indicated that accident increases as radius decreases and decreases as radius increases [7, 41]. Divers criteria for site selection in operating speed model development especially related to radius, have been discovered in the literature. The Operating speed model was developed by Fitzpatrick et al. [10] for PC with a radius of curve between 110 to 3500 m considered one of the site selection criteria. Awatta [6], Misaghi and Hassan [29] also modeled operating speed and speed differential for curve radius less than 1200 m and total curve length greater than 100 m. Dwikat (2004) eliminated curve radius less than 100 m and considered those greater than 1000 m as tangents. The majority of the previous studies suffer from common pitfalls, some of which are considering a maximum curve radius of 3500 m. The majority of past studies were conducted in the United States and Europe. Thus, models reflecting Nigerian rural roads' particular condition (e.g. topography, geographical, and environmental) are limited. Considering, the aforementioned limitations, this study is conducted to consolidate the suitability of the operating speed prediction methodology. In this respect, the models were developed for various horizontal curve radii available within the study route.

## 2   Methodology

### 2.1   The Study Route

The methods of data collection used in past studies were reviewed, and scheme for data collection was established. The study route is Lokoja-Abuja-Kaduna highway, linking the Southwest to the North Central. It is a dual carriageway with an average traffic volume of 8514 vehicles per day. This was selected based on the accident records from FRSC. It is divided into four sections namely: Lokoja-Kotonkarifi (section I), Kotonkarifi-Abaji (section II), Abaji-Abuja (section III), and Abuja-Kaduna (section IV). A total of 111 horizontal curves with different geometric features like curve radius, curve length, tangent length, and superelevation, were selected for evaluation from section I-IV. The curve sites selection criteria include:

- Rural area: not close to developed areas.
- Not affected by intersections.
- Low traffic volume: average annual daily traffic (AADT) $\leq$ 10,000 vehicles/day.
- No physical features or activities adjacent to or in the roadway may create abnormal hazards such as narrow bridges, institutions, industries, etc.
- Roadways paved.
- The pavement must be smooth and in dry condition.

- The curve radius was categorized into three classes (curve radius < 1200 m; > 1200 m; and combined radius) and model developed based on each category.

This study focuses on developing operating speed models for passenger cars (PSC) and evaluating the geometric design consistency based on the operating speed. Speed data were collected at the middle of each curve with at least 100 observations using the stopwatch approach. The data were collected for 12 h (6:00 am–6:00 pm) during the dry season. The two directions of traffic were combined and taken as one site as the geometric and features of traffic in both ways do not significantly affect drivers' speed behaviour.

The effect of an automatic speed data recorder was verified on the drivers' behaviour by creating a small database using TRAX Apollyon automatic traffic data recorder to obtain speed data for 24 h in parallel with the manual data collection on five curves in the study area. Figure 1 shows some of the curve locations in the study area.
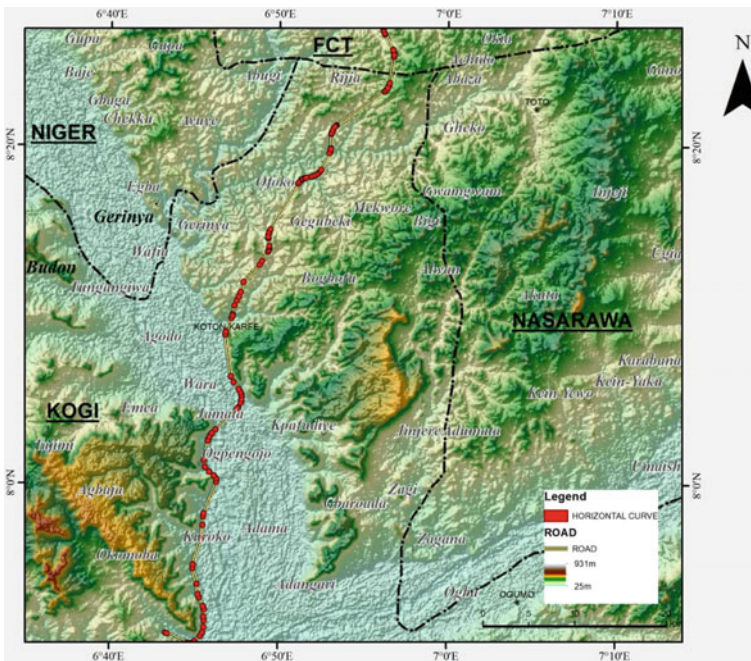


**Fig. 1** Horizontal curve locations

## 2.2 Data Preparation and Preliminary Analysis

### 2.2.1 Sorting of Raw Data

This step aimed at sorting and screening the data collected by the observers and the traffic counter to exclude data that could have been disturbed due to the presence of the observers during installation and counter retrieval. Due to this, the final and initial disturbances, non-free-flow traffic data, nighttime data, misses in sensor recording; wet pavement data, timing error, and vehicle classification were identified. There is likely tendency of drivers to associate the presence of observers and the counter tube to speed enforcement within the study area, thus reducing their speed when approaching the observers or the counter. The outliers were removed from the raw data based on non-free flow speed identified if the headway was greater than 5 s. Moreover, night times and wet pavement data recorded on the database were also screened out as this is beyond the scope of this study.

### 2.2.2 Vehicle Category

Based on the National Bureau of Statistics [34] report on road traffic crashes on Nigerian roads, out of the 3334 accident cases involving different categories of vehicles in the 2nd quarter of 2020, PSC was reported to have the highest frequency 3290. This necessitated the choice of vehicle considered in the model development.

An automatic counter was used for vehicle classification based on a number of axles and wheelbase as highlighted in AASHTO [1] and Hassan [15] criterion.

### 2.2.3 Tests of Significance

Basic statistical analysis of variance (ANOVA) was conducted before model development to compare the vehicle speed in the different lanes and to determine the consistency of speed measurement by the counter and manual approach. The results of the ANOVA indicated that, in most of the cases considered (93%), there was no statistically significant difference between the speed data obtained in both directions of traffic. Thus, the speed data on both travel directions were combined and taken as a single site as recommended by Misaghi and Hassan [29].

In addition, to determine the consistency of speed data obtained using manual and automatic counters, ANOVA was conducted to compare the first 100 speed data obtained by both the observers and the automatic counter. The results show that, in 68% of the cases, there were no statistical significances at a 5% level of significance between the speed obtained by the observers and counter. Consequently, it can be inferred that both methods of speed data collection were adequate.
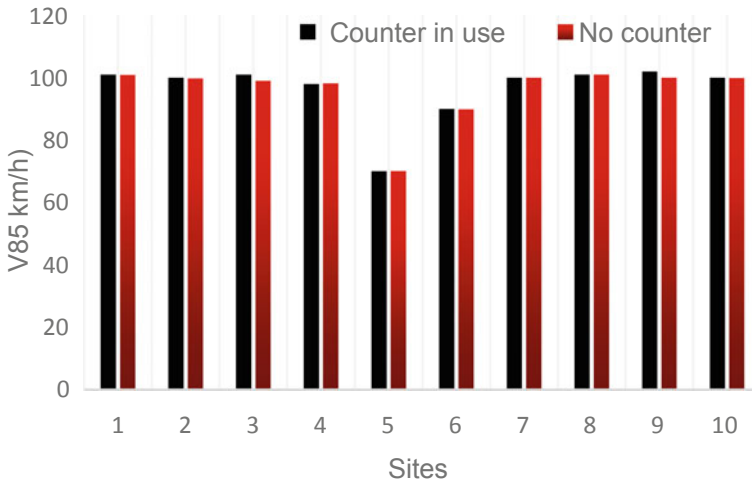
**Fig. 2** Effect of the use of counter on operating speed data collection

### 2.2.4 Effects of Automatic Traffic Counter

The effect of the used counter was examined by collecting speed data with the counter at 10 curve locations and simultaneously collecting speed data with a stopwatch at the same locations. The data obtained at these locations were separated from those collected with the stopwatch only. The speed data collected by the counter were divided into two samples representing "counter in use" and "no counter," respectively. As indicated in Fig. 2, from these 10 sites, $V_{85}$ of the first sample "counter in use" was almost the same as that of the second sample with 0.02 km/h difference. This difference in speed is negligible and not statistically significant at 5% level of significance based on the result of ANOVA. Hence, both instruments are adequate for speed data collection.

## 2.3 Preliminary Analysis

With the speed database prepared and required independent variables identified, a preliminary analysis was carried out before model development to obtain the descriptive statistics of the data, distribution of the speed data and correlation of the variables with the operating speed in SPSS (Statistical Package for Social Sciences).

# 3 Model Development

A total of 111 horizontal curves were used for the model development. The 85th percentile speed values were calculated for passenger car under free-flow conditions and dry pavement. With the 85th percentile values (dependent variable) calculated for each site. Each site's geometry and traffic attributes were prepared as independent variables. Some independent variables were derived from as-built drawings, while others were measured in the field and others were calculated as a function of other variables.

The independent variables included in the model development were: radius of curve ($R_C$), length of curve ($L_C$), lane width ($L_W$), shoulder width ($S_W$), longitudinal grade ($G$), superelevation rate ($e$), tangent length ($T_L$), deflection angle ($D_A$), preceding curve radius (pre_rad), succeeding curve radius (suc_rad), curve direction ($C_D$), degree of curvature ($D_C$), and average annual daily traffic (AADT). Besides the preceding independent variables, the following variable transformations were also considered in the model: $R_C^2$, $\sqrt{R_C}$, and $\frac{1}{R_C}$.

The above variables included nearly every independent variable used in the previous prediction of speed models. Among all the variables, $R_C$, $L_C$, $G$, $e$, $D_A$, $T_L$, pre_rad and suc_rad were obtained from the as-built drawings of the study area, $L_W$, $S_W$, and $C_D$ were measured in the field. While $D_C$ and AADT were estimated. The cumulative speed was obtained and plotted against the mid-speed for each curve to determine its 85th percentile speed. The dependent (85th percentile operating speed) and independent (geometric design and traffic parameters) variables were entered into SPSS 23 for regression analysis. The analysis was conducted in three stages:

Stage I: curves with radii less than 1200 m [28, 29]
Stage II: curves with radii greater than 1200 m [10].
Stage III: curves with radii in I and II combined.

## 3.1 Speed Prediction Model

The stepwise method was used to establish the relationship between the dependent and independent variables. Thus, independent variables that were not statistically significant at the 95% confidence level were automatically taken out of the model. The developed model was used to estimate each curve's operating speed. The differences between the operating and design speed for the curves were obtained and compared with the criterion proposed by Lamm et al. [25], to evaluate the consistency of the design of each horizontal curve.

# 4   Results and Discussion

Stage I

In this stage, curves with radii less than 1200 m were considered following previous studies by Misaghi [28] and Misaghi and Hassan [29]. The developed model for $R_C$ < 1200 m is shown in Table 2. Based on the model $\sqrt{R_C}$, $e$, and $T_L$ has a linear relationship with $V_{85}$. These variables can explain 84.1% of the variations in the operating speed of drivers on curves. This is consistent with the models developed by Andueza [5] and Gibreel et al. [13]. As the radius of the curves increases and the superelevation and tangent length decrease, drivers tend to increase their speed on the curves, thus increasing operating speed. The base model for curves with radii less than 1200 m is shown in Table 3.

Stage II

To further verify the effects of the radius selection criteria on the operating speed of drivers at the horizontal curves, stepwise regression was performed for radii greater than 1200 m. The result is presented in Table 4. A critical look at the model indicates that as the curve radius increases, $V_{85}$ also, increase. This should be expected as drivers driving on curves will need more speed adjustment on curves with large radius than small radii. Also, the smaller the AADT, the higher the speed with which drivers will move on the curve as there will be ease of maneuvering. The superelevation also has a direct impact on $V_{85}$ resulting in increased speed change on curves that have a higher superelevation. A large lane and shoulder width will allow drivers to drive

**Table 2**   Model for $R_C$ < 1200 m

| Model No | Model | $R$ | $R^2$ | Adjusted $R^2$ | SEE |
|---|---|---|---|---|---|
| 1 | $V_{85} = 46.028 + 2.255\sqrt{R_C} - 3.871e - 0.062T_L$ | 0.917 | 0.841 | 0.816 | 8.528 |

**Table 3**   Base model for $R_C$ < 1200 m

| Base model | Predictor variables | Coefficient | $t$ statistic | $p$ value | $R^2$ | Standard error of estimate |
|---|---|---|---|---|---|---|
| 1 | Constant | 19.347 | 1.514 | 0.145 | 0.521 | 14.091 |
| | $\sqrt{R_C}$ | 2.463 | 4.778 | 0.000 | | |
| 2 | Constant | 48.575 | 3.712 | 0.001 | 0.708 | 11.272 |
| | $\sqrt{R_C}$ | 1.885 | 4.254 | 0.000 | | |
| | $e$ | −3.648 | −3.580 | 0.002 | | |
| 3 | Constant | 46.028 | 4.640 | 0.000 | 0.841 | 8.528 |
| | $\sqrt{R_C}$ | 2.255 | 6.484 | 0.000 | | |
| | $e$ | −3.871 | −5.008 | 0.000 | | |
| | $T_L$ | −0.062 | −3.993 | 0.001 | | |

at high speed as sufficient allowance is available for maneuvering of their vehicles. The base model is shown in Table 5.

Stage III

The stepwise approach was used to figure out how the dependent and independent variables are related. The variables that are not statistically significant at the 95% confidence level were automatically excluded from the model.

The developed models for all radii obtained for the study area are presented in Table 6. As shown, the independent variables can account for 61% of the dependent variable. This implies that there is 78.2% linear relationship between operating speed and the independent variables ($D_C$, AADT, and $R_C$) involved in the model. The degree of curvature as a variable in the model is consistent with the model developed by Islam and Seneviratne [16] and Morrall and Talarico [32]. With a coefficient of determination of 61% and at the 5% level of significance, all of the independent variables have been statistically significant. The model is highly recommended. Since it is possible that many of the predictor variables may not be easily obtainable in evaluating the operating speed, the root models that characterized the various procedures in the stepwise regression for this model are presented in Table 7.

A close look at the model indicates that as the curve radius and AADT increase, the degree of curvature decreases, increasing the operating speed. It is reasonable to anticipate such a tendency as drivers tend to increase their speed on the curve with a flat radius. As the traffic decreases, drivers tend to move at high speed as the difficulty of maneuvering and obstructions from other vehicles will not be encountered. This is consistent with the findings of Misaghi [28]. The operation speed of vehicles on curves with $R > 1200$ m is slightly lower than that at the tangent section has vehicles are free from cornering effects on tangents, hence they move at higher speed on tangent compared to curves.

Based on the different categories considered, model No 1 consists of $R_C < 1200$ m gave $R^2$ of 84.1%, model No 2 comprising of $R_C > 1200$ m had $R^2$ of 71.3%, and model No 3 with different radii had $R^2$ of 61%. This implies that model No 1 with a high coefficient of determination can adequately explain the variations in the operating speed of drivers on the horizontal curves. Thus, model No 1 is highly recommended. This is in line with the finding of Misaghi and Hassan [29].

The validation of the developed model was carried out to confirm its predictability. In this respect, a chart indicating the operating speed as measured and expected for all sites is shown in Fig. 3. As noted, in most cases, the anticipated and observed $V_{85}$ values are in good agreement.

**Table 4** Model for $R > 1200$ m

| Model No | Model | $R$ | $R^2$ | Adjusted $R^2$ | SEE |
|---|---|---|---|---|---|
| 2 | $V_{85} = 166.855 - \frac{36443.882}{R_C} + 0.001 AADT + 1.306e - 18.346L_W - 1.063G + 4.270S_W$ | 0.845 | 0.713 | 0.692 | 6.791 |

**Table 5** Base model for $R > 1200$ m

| Base model | Predictor variables | Coefficient | $t$ statistic | $p$ value | $R^2$ | SEE |
|---|---|---|---|---|---|---|
| 1 | Constant | 123.045 | 35.075 | 0.000 | 0.435 | 9.251 |
| | $\frac{1}{R_C}$ | −47,962.265 | −8.145 | 0.000 | | |
| 2 | Constant | 109.874 | 27.300 | 0.000 | 0.568 | 8.142 |
| | $\frac{1}{R_C}$ | −43,472.269 | −8.269 | 0.000 | | |
| | $AADT$ | 0.002 | 5.102 | 0.000 | | |
| 3 | Constant | 103.258 | 24.277 | 0.000 | 0.621 | 7.669 |
| | $\frac{1}{R_C}$ | −38,179.630 | −7.361 | 0.000 | | |
| | $AADT$ | 0.002 | 5.452 | 0.000 | | |
| | $e$ | 1.168 | 3.432 | 0.000 | | |
| 4 | Constant | 174.809 | 7.976 | 0.000 | 0.665 | 7.249 |
| | $\frac{1}{R_C}$ | −36,821.792 | −7.485 | 0.000 | | |
| | $AADT$ | 0.001 | 3.456 | 0.001 | | |
| | $e$ | −1.423 | 4.303 | 0.000 | | |
| | $L_W$ | 18.515 | −3.321 | 0.001 | | |
| 5 | Constant | 181.922 | 8.628 | 0.000 | 0.698 | 6.929 |
| | $\frac{1}{R_C}$ | −35,920.746 | −7.624 | 0.000 | | |
| | $AADT$ | 0.001 | 2.602 | 0.011 | | |
| | $e$ | 1.331 | 4.193 | 0.000 | | |
| | $L_W$ | −19.597 | −3.669 | 0.000 | | |
| | $G$ | −1.132 | −2.976 | 0.004 | | |
| 6 | Constant | 166.855 | 7.624 | 0.000 | 0.713 | 6.791 |
| | $\frac{1}{R_C}$ | −36,443.882 | −7.880 | 0.000 | | |
| | $AADT$ | 0.001 | 2.860 | 0.005 | | |
| | $e$ | 1.306 | 4.195 | 0.000 | | |
| | $L_W$ | −18.346 | −3.482 | 0.001 | | |
| | $G$ | −1.063 | −2.842 | 0.006 | | |
| | $S_W$ | 4.270 | 2.091 | 0.040 | | |

**Table 6** Model for all radius sizes

| Model No | Model | $R$ | $R^2$ | Adjusted $R^2$ | SEE |
|---|---|---|---|---|---|
| 1 | $V_{85} = 63.803 - 0.848D_C + 0.002AADT + 0.547\sqrt{R_C} - 0.001R_C$ | 0.782 | 0.610 | 0.598 | 9.922 |

$R$ = regression coefficient, $R^2$ = coefficient of determination, SEE = Standard error of the estimate

**Table 7** Base models for model I

| Base model | Predictor variables | Coefficient | $t$ statistic | $p$ value | $R^2$ | Standard error of estimate |
|---|---|---|---|---|---|---|
| 1 | Constant | 100.034 | 64.513 | 0.000 | 0.366 | 12.515 |
| | $D_C$ | −1.516 | −7.926 | 0.000 | | |
| 2 | Constant | 87.846 | 28.278 | 0.000 | 0.463 | 11.569 |
| | $D_C$ | −1.515 | −8.565 | 0.000 | | |
| | $AADT$ | 0.002 | 4.423 | 0.000 | | |
| 3 | Constant | 84.624 | 27.423 | 0.000 | 0.520 | 10.988 |
| | $D_C$ | −1.391 | −8.107 | 0.000 | | |
| | $AADT$ | 0.002 | 4.583 | 0.000 | | |
| | $\sqrt{R_C}$ | 0.060 | 3.566 | 0.000 | | |
| 4 | Constant | 63.803 | 12.777 | 0.000 | 0.612 | 9.922 |
| | $D_C$ | −0.848 | −4.488 | 0.000 | | |
| | $AADT$ | 0.002 | 5.015 | 0.000 | | |
| | $\sqrt{R_C}$ | 0.547 | 5.579 | 0.000 | | |
| | $R_C$ | 0.001 | −5.025 | 0.000 | | |
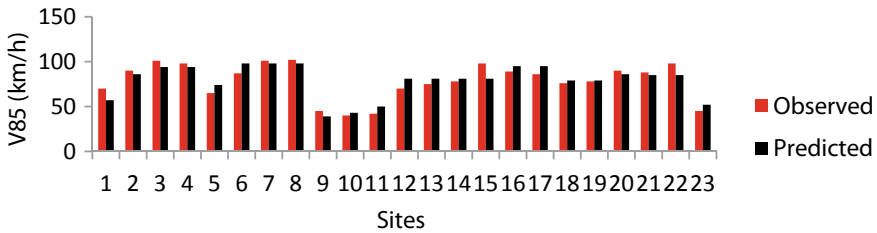


**Fig. 3** Comparison between observed and predicted values of $V_{85}$

## 5 Application: Design Consistency Evaluation

The values of operating speed predicted by Model No 1 were used for the consistency evaluation of the curves. There are 23 curves with $R < 1200$ m in the study route. The design speed for the route is 100 km/h. The discrepancy between the predicted and actual operating speeds is shown in Table 8. Based on the result obtained, all the curves are good design with no alignment corrections required.

**Table 8** Consistency evaluation based on Lamm et al. [25] criteria

| Sites | Radius (m) | $V_{85}$ predicted (km/h) | $V_{85}$ observed (km/h) | $V_{85ob} - V_{85pr}$ | Design speed, $V_d$ (km/h) | $V_{85} - V_d$ | Criteria | Remark |
|---|---|---|---|---|---|---|---|---|
| 1 | 346.70 | 57 | 70 | 13 | 100 | −43 | Good | Consistency exit |
| 2 | 986.70 | 86 | 90 | 4 | 100 | −14 | Good | |
| 3 | 1013.30 | 94 | 101 | 7 | 100 | −06 | Good | |
| 4 | 986.70 | 94 | 98 | 4 | 100 | −06 | Good | |
| 5 | 661.70 | 74 | 65 | −9 | 100 | −26 | Good | |
| 6 | 996.35 | 98 | 87 | −11 | 100 | −02 | Good | |
| 7 | 1003.65 | 98 | 101 | 3 | 100 | −02 | Good | |
| 8 | 1003.65 | 98 | 102 | 4 | 100 | −02 | Good | |
| 9 | 99.76 | 39 | 45 | 6 | 100 | −61 | Good | |
| 10 | 213.30 | 43 | 40 | −3 | 100 | −57 | Good | |
| 11 | 363.30 | 50 | 42 | −8 | 100 | −50 | Good | |
| 12 | 500.00 | 81 | 70 | −11 | 100 | −19 | Good | |
| 13 | 500.00 | 81 | 75 | −6 | 100 | −19 | Good | |
| 14 | 500.00 | 81 | 78 | −3 | 100 | −19 | Good | |
| 15 | 500.00 | 81 | 98 | 17 | 100 | −19 | Good | |
| 16 | 500.00 | 95 | 89 | −6 | 100 | −05 | Good | |
| 17 | 500.00 | 95 | 86 | −9 | 100 | −05 | Good | |
| 18 | 500.00 | 79 | 76 | −3 | 100 | −21 | Good | |
| 19 | 500.00 | 79 | 78 | −1 | 100 | −21 | Good | |
| 20 | 884.52 | 86 | 90 | 4 | 100 | −14 | Good | |
| 21 | 500.00 | 85 | 88 | 3 | 100 | −15 | Good | |
| 22 | 500.00 | 85 | 98 | 13 | 100 | −15 | Good | |
| 23 | 575.00 | 52 | 45 | −7 | 100 | −48 | Good | |

# 6　Conclusions

This study presents an experimental investigation of drivers' speed behaviour on horizontal curves of two-lane two-way rural highways in Nigeria. The research was patterned to prevent the shortcomings of previous speed modeling bids, including the site selection criteria regarding the radius of horizontal curves and equipment used for data collection. The primary findings of this study can be outlined as follows:

1. There was no significant difference between manual and automatic counting of vehicles along the sites selected.
2. The developed model for $R_C < 1200$ m shows that $\sqrt{R_C}$, $e$, and $T_L$ has a linear relationship with $V_{85}$. These variables can explain 84.1% of the variations in the operating speed of drivers on curves.

3. Model for $R_C > 1200$ m gave a coefficient of determination ($R^2$) of 71.3%, and the model with combined radii gave $R^2$ of 61%.
4. Based on the developed model, there is no difference between the operating and design speed for the curves when used to assess the design consistency of each horizontal curve.
5. The higher the number of sites and speed observations, the better the model. The 111 sites considered in this paper, gave models with strong relationships compared to a few sites in previous literature.
6. Models based on speed differential obtained by tracking each vehicle at various points on horizontal curves are strongly recommended for future study.

# References

1. AASHTO (2011) A policy on geometric design of highways and streets. American Association of State Highway and Transportation Officials, Washington D.C.
2. Abdul-Mawjoud AA, Sofia GG (2008) Development of models for predicting speed on horizontal curves for two-lane rural highways. Arab J Sci Eng 33(2B)
3. Afolayan A, Abiola OS, Easa S, Alayaki FM, Folorunso O (2021) Vehicle stability approach to roadway consistency evaluation: a practical application. In: Proceedings of the 2021 SEET annual conference. Held between 6th–8th October, 2021 at the T.I. Francis Auditorium, the Federal University of Technology, Akure, Ondo State, Nigeria, pp 530–540. Available at https://iaraseta.futajeet.com
4. Al-Masaeid HR, Hamed M, Ela MA, Ghannam AG (1995) Consistency of horizontal alignment for different vehicle classes. Transp Res Rec 1500. Transportation Research Board, Washington, D.C., pp 178–183.
5. Andueza PJ (2000) Mathematical models of vehicular speed on mountain roads. Transp Res Rec 1701: 104–110. Transportation Research Board, Washington, D.C.
6. Awatta M (2003) Highway design consistency and safety: individual and overall evaluation criteria. Master thesis of Applied Science in Civil Engineering, Department of Civil and Environmental Engineering, Carleton University Ottawa, Ontario Canada
7. Brenac T (1996) Safety at curves and road geometry standards in some European countries. Transp Res Rec 1523:99–106. Transportation Research Board, Washington, D.C.
8. Dwikat MG (2014) Modeling relationship between geometric design consistency and road safety for two-lane rural highways in the West Bank. Master thesis of Roads and Transportation Engineering, Faculty of Graduate Studies, An-Najah National University, Nablus-Palestine
9. Fitzpatrick K, Krammes RA, Fambro DB (1997) Design speed, operating speed, and posted speed relationships. J Inst Transp Eng 67(2):52–59
10. Fitzpatrick K, Wooldrige MD, Tsimhoni O, Collins JM, Green P, Bauer KM, Parma KD, Koppa R, Harwood DW, Anderson IB, Krammes R, Poggioli B (2000) Alternative design consistency rating methods for two-lane rural highways. Final report FHWA-RD-99-172, Mclean, VA
11. Gemechu SM, Tulu GS (2021) Safety effects of geometric design consistency on two-lane rural highways: the case of Ethiopia. Am J Traffic Transp Eng 6(4):107–115. https://doi.org/10.11648/j.ajtte.20210604.11
12. Gibreel GM, Easa SM, Hassan Y, El-Dimeery IA (1999) State of the art of highway geometric consistency. J Transp Eng 125:305–313
13. Gibreel G, Easa SM, Al-Dimeery IA (2001) Prediction of operating speed on three-dimensional highway alignments. J Transp Eng 127(1):21–30
14. Hassan Y, Sayed T, Tabernero V (2001) Establishing practical approach for design consistency evaluation. J Transp Eng 127(4):295–302

15. Hassan Y (2003) Traffic and speed characteristics on two-lane highways: field study. Can J Civ Eng 30(6):1042–1054
16. Islam MN, Seneviratne PN (1994) Evaluation of design consistency of two-lane highways. Inst Transp Eng J 64(2):28–31
17. Goyani J, Chaudhari P, Arkatkar S, Joshi G, Easa SM (2022) Operating-speed prediction models by vehicle type on two-lane rural highways in Indian Hilly Terrains. J Transp Eng Part A Syst 148(3). https://doi.org/10.1061/JTEPBS.0000644
18. Kanellaidis G, Golias J, Efstathiadis S (1990) Driver's speed behaviour on rural road curves. Traffic Eng Control 31(7/8):414–415 London
19. Krammes RA, Brackett RQ, Shafer MA, Ottesen JL, Anderson IB, Fink KL, Collins KM, Pendleton OJ, Messer CJ (1994) Horizontal alignment design consistency for rural two-lane highways. Rep. No. FHWA-RD-94-034, Federal Highway Administration, Washington, D.C.
20. Krammes RA, Rao KS, Oh H (1995) Highway geometric design consistency evaluation software. Transp Res Rec 1500:19–24. Transportation Research Board, Washington, D.C.
21. Lamm R, Choueiri EM, Mailaender T (1992) Traffic safety on two continents—a ten year analysis of human and vehicular involvements. In: Proceedings of strategic highway research program (SHRP) and traffic safety on two continents, pp 18–20
22. Lamm R, Psarianos B, Guenther AK (1994) Interrelationships between three safety criteria: modern highway geometric design, as well as high risk target locations and groups. In: Proceedings of the third international conference on safety and the environment in the 21st century, 7–10 November, Tel-Aviv, Israel. Tel-Aviv Israel Ministry of Transport, p 640
23. Lamm R, Psarianos B, Mailaender T (1999) Highway design and traffic safety engineering handbook. McGraw-Hill Companies, New York, US
24. Lamm R, Choueiri EM, Mailaender T (1990) Comparison of operating speed on dry and wet pavement of two lane rural highways. Transp Res Rec 1280:199–207. Transportation Research Board, Washington, D.C.
25. Lamm R, Guenther AK, Choueiri EM (1995) Safety module for highway geometric design. Transp Res Rec 1512:7–15. Transportation Research Board, Washington, D.C.
26. Lamm R, Choueiri E, Mailaender T (1991) Side friction demand versus side friction assumed for curve design on two-lane rural highways. Transp Res Rec 1303:11–21. Transportation Research Board, Washington, D.C.
27. McFadden J, Yang W, Durrans SR (2001) Application of artificial neural networks to predict speeds on two-lane rural highways. Transp Res Rec J Transp Res Board 1751:9–17. https://doi.org/10.3141/2F1751-02
28. Misaghi P (2003) Modeling operating speed and speed differential for design consistency evaluation. MSc thesis, Carleton Univ., Ottawa
29. Misaghi P, Hassan Y (2005) Modeling operating speed and speed differential on two-lane rural roads. J Transp Eng 131(6):408–418. https://doi.org/10.1061/(ASCE)0733-947X(2005)131:6(408)
30. McFadden J, Elefteriadou L (1997) Formulation and validation of operating speed-based models using bootstrapping. Transp Res Rec 1579:97–103. Transportation Research Board, Washington, D.C.
31. Montella A, Pariota L, Galante F, Imbriani L, Mauriello F (2014) Prediction of drivers' speed behavior on rural motorways based on an instrumented vehicle study. Transp Res Rec J Transp Res Board 2434:52–62. https://doi.org/10.3141/2434-07
32. Morrall J, Talarico RJ (1994) Side friction demanded and margins of safety on horizontal curves. Transp Res Record 1435:145–152. Transportation Research Board, Washington, D.C.
33. Morris CM, Donnell E (2014) Passenger car and truck operating speed models on multi-lane highways with combinations of horizontal curves and steep grades. J Transp Eng 140(11):04014058. https://doi.org/10.1061/(ASCE)TE.1943-5436.0000715
34. National Bureau of Statistics Q2 2020. Road transport data. https://www.nigerianstat.gov.ng. Assessed 12 Aug 2021

35. Nicholson A (1998) Superelevation, side friction, and roadway consistency. J Transp Eng ASCE 124(5):411–418
36. Poe CM, Tarris JP, Mason Jr JM (1996) Relationship of operating speed to roadway geometric design speed. Final Report No. FHWA-RD-96-024, Federal Highway Administration, Washington, D.C.
37. Arief R, Dixit V, Pande A, Junirman RA (2017) Predicting casualty-accident count by highway design standards compliance. Int J Transp Sci Technol 6:174–183. https://doi.org/10.1016/j.ijtst.2017.07.005
38. Shawky M, Hashim I (2010) Impact of horizontal alignment on traffic performance at rural two-lane highways. In: 4th international symposium on highway geometric design, Valencia
39. Terlow JC (1990) Transport safety: European co-operation for the 90s. Lecture on Traffic Safety, City of Westminster, London, England
40. Wilson TD (1968) Road safety by design. J Inst Highway Eng 15:23–33
41. Zegeer CV, Stewart JR, Council FM, Reinfurt DW, Hamilton E (1992) Safety effects of geometric improvements on horizontal curves. Transp Res Rec 1356: 11–19. TRB, National Research Council, Washington, D.C.

# Improving Safety of Rural Intersection with Approaching Reverse Curve

Devashree Rege, Dewmi Seneviratna, Tazrian Hassan,
Viththahan Puvanendran, Hamed Esmaeeli, Manny Rataul, Sulaf Alkarawi,
Arkatkar Shriniwas, and Said M. Easa

**Abstract** This paper exhibits the safety improvement study for the reverse curve and unsignalized stop-controlled intersection at Regional Road 14 and Young Street in the Niagara Region. Regional Road 14, also known as Thirty Road, is a major road running north/south in the Town of West Lincoln. Under current conditions, many collisions have been reported at the intersection of Thirty Road and Young Street and along the reverse curve portion of Thirty Road itself. With a projected annual growth rate of 5%, traffic volumes travelling in the direction of Smithville are expected to increase by 2041 drastically. This study aims to evaluate viable design alternatives and further develop the selected improvement that can safely accommodate the projected 2041 traffic volumes for Thirty Road at Young Street. Data provided by the Niagara Region for analysis includes existing geometric conditions, utility locates, 2019 collision data, 2011 baseline volumes, and forecasted volumes for the horizon year 2041. The alternatives presented are realignment of the reverse curve with a roundabout, signalized intersection, or all-way stop intersection. The evaluation criteria used in the analysis are as follows: safety, level of service, cost, and environmental impact. A ranked system in tandem with weighted criteria was used to assess the level of influence of the alternatives, with the results then weighted using the final evaluation model. The evaluation showed that the alternative with a roundabout was the best. Surrounding utilities and other constraints were considered when developing detailed designs of the improved realignment and intersection using AutoCAD Civil 3D.

**Keywords** Electrochemical technique · Reinforced concrete · Corrosion · Cementitious materials · Substrate

D. Rege · D. Seneviratna · T. Hassan (✉) · V. Puvanendran · S. M. Easa
Department of Civil Engineering, Ryerson University, Toronto, Canada
e-mail: tazrian.hassan@ryerson.ca

H. Esmaeeli · M. Rataul · S. Alkarawi
Transportation Planning, Regional Municipality of Niagara, Toronto, Canada

A. Shriniwas
Sardar Vallabhbhai National Institute of Technology (SVNIT), Surat, Gujarat, India

# 1 Introduction

Regional Road 14, also known as Thirty Road, is a major arterial located in the Town of West Lincoln, connecting the QEW to the community of Smithville. The north/south roadway has seen an increasing number of collisions at the intersection with Young Street. As population growth rises, traffic volumes will correspondingly increase in Smithville, creating an urgency for safety improvements. Based on collected collision data from the Niagara Region, most collisions occur at the current two-way stop-controlled intersection. Other collisions have occurred along the reverse curve during clear, daytime conditions. In addition, it was noted that many drivers stated that they "lost control." After further evaluation, the two main issues identified are the lack of intersection safety and geometric design flaws in the reverse curve approaching Young Street on Thirty Road. The proposed solution should be developed to address these issues while facilitating the projected 5% annual population growth.

This study aims to realign the identified section of Thirty Road to prevent such accidents from reoccurring in the future, while also accommodating the projected increase in traffic capacity. The study investigates various aspects of geometric road design to ensure safe passage for vehicles, while considering the surrounding area constraints to ensure minimal delays with increased demand at the study intersection. Based on these investigations, three alternatives were identified (1) road realignment with a signalized intersection, (2) road realignment with roundabout, and (3) road realignment with all-way stop control.

# 2 Data Collection and Preparation

To further understand the context and scope of the study, a data collection and preparation process was completed. Relevant topics, including the geometric design of horizontal curves and various intersections, the environmental assessment (EA) process, and case studies on similar projects were reviewed.

Both qualitative and quantitative data were primarily collected through a field investigation and reports of existing conditions. This data was obtained or confirmed through the Niagara Region. The collected information includes existing geometry, current traffic volumes, existing underground and overground utilities, and five-year collision data. Due to inconsistencies in provided measurements along the reverse curve section, maximum superelevation ($e_{Max}$) values of approximately 6% and 5% were used for the northern and southern curves, respectively. Based on the provided traffic volumes, the intersection peak hours are 7:30 to 8:30 AM and 3:30 to 4:30 PM.

Following the Niagara Region Transportation Master Plan (TMP), the existing data were used to project significant growth between the years 2016 to 2041. This was

achieved by calculating an annual growth rate to forecast safety and capacity requirements accurately. The projected data was then considered the basis for designing and evaluating alternatives.

## 3   Descriptions of Alternatives

The proposed solution consists of two parts: the realignment of Thirty Road and intersection improvement at Thirty Road and Young Street. Due to immediate safety concerns for the existing reverse curve, the implementation of road realignment was considered for all alternatives and did not undergo evaluation. A key constraint is the presence of recently constructed hydroelectric poles that are not relocatable along Thirty Road. This constraint results in approximately 350 m of the road being reconstructed on the north side of the hydro poles. The acquisition of roughly two acres of land from the neighbouring property is necessary to perform this reconstruction. Key benefits to this approach include more significant space to design the intersection, increased driver sight distance, and the removal of the existing skewed intersection.

### 3.1   All-Way Stop-Control (AWSC) Intersection

The development of the AWSC alternative consists of two stop signs placed in the northbound and southbound directions along Thirty Road at Young Street. The only requirement is signage installation. Thus, the implementation of the AWSC alternative is the most efficient. The key benefits include driver familiarity with the concept of an AWSC.

### 3.2   Roundabout Intersection

The design and construction of a single-lane roundabout is a significant upgrade to the current intersection. The roundabout was geometrically designed to have four approaches with one entry lane each and lane widths and a radius that are designed according to heavy vehicle requirements. This design is likely to require surrounding land acquisition, resulting in the need for a right-of-way assessment and increased construction costs. In addition, this design would require the completion of the roundabout screening form as provided by Niagara Region.

## 3.3 Signalized Intersection

The introduction of traffic signals for all four approaches along Thirty Road at Young Street would be a significant upgrade to the current intersection. The traffic signals would be designed to minimize travel delays by accommodating changes in off-peak and on-peak volumes. This design would require a traffic signal warrant and consideration of long-term maintenance costs. An initial estimate was conducted using the signal warrant spreadsheet provided by the Ontario Ministry of Transportation's Book 12.

## 4 Evaluation of Alternatives

A scoring system was developed to evaluate all alternatives based on safety, intersection operations, cost, and environmental impact. These criteria were selected through discussion with advisors and the Region. The following steps were taken to determine the final scores:

(1) Each alternative is evaluated based on the given criteria.
(2) Each alternative is ranked 1–3.
(3) First rank is given a score of 100, second rank a score of 75, and third rank a score of 50.
(4) All scores are added together and multiplied by predetermined weights.

The alternatives were evaluated based on each criterion, as further discussed below. Safety was considered the highest priority for the Region, hence being given the largest weight of 40%. The final evaluation function is as follows:

$$0.40\,\text{Safety} \times 0.20\,\text{LOS} \times 0.15\,\text{Delay} + 0.15\,\text{Cost} + 0.10\,\text{Environmental Impact} \tag{1}$$

## 4.1 Intersection Operations

Level of service (LOS) was used as an indicator of overall intersection performance. The LOS letter system goes from A to F, where A is the best and F is the worst. As per the Highway Capacity Manual, LOS is defined through various control delay values. As such, two different alternatives with the same LOS could potentially have different delays. To assist with ranking alternatives in such cases, intersection delays were included for evaluation as an added measure. The roundabout and traffic signal alternatives were prepared for LOS evaluation as follows:

**Table 1** Intersection delay and LOS ranking for all alternatives

| Alternative | Intersection delay | | | Intersection LOS | | |
|---|---|---|---|---|---|---|
| | Delay | Rank | Score | LOS | Rank | Score |
| All-way stop | 16.5 | 3 | 50 | C | 3 | 50 |
| Roundabout | 7.15 | 1 | 100 | A | 1 | 100 |
| Signalized | 8.25 | 2 | 75 | A | 1 | 100 |

(1) A diameter of approximately 130 ft and 1 lane with a 12 ft width were used for the roundabout design [5].

(2) The traffic signal was set to actuated-uncoordinated to facilitate detection [11]. Both the cycle lengths and splits were optimized, with manual adjustments for LOS improvement made to cycle lengths, as necessary. The intersection delay and LOS for each alternative are summarized in Table 1.

The roundabout can be identified with optimal performance levels in 2041, followed by the signalized alternative. On the other hand, the AWSC alternative would perform at acceptable levels in 2041.

## 4.2 Cost

The evaluation of proposed alternatives requires an economic appraisal to justify the countermeasures. The cost evaluation was broken down as follows: (1) Initial construction (2) Operating and maintenance (3) Road users (4) Collisions. The initial construction costs included equipment, material, and labour for constructing the alternative. In addition, an engineering fee of about 20% was applied to the roundabout and signalized intersection alternatives to cover the cost of planning and implementation. An equivalent annual cost was then calculated for each initial cost. Road user costs were generated by developing a relationship between congestion and fuel consumption. Specific stop-control alternatives result in increased time taken to traverse the intersection, thereby leading to increased delay. A minute of idling uses approximately 0.5 L of fuel for a vehicle (DHEC 2019), which correlates to roughly $0.04/min of idling. Lastly, the annual benefits of each safety improvement alternative were calculated by multiplying the predicted reduction in crashes of a given severity by the applicable societal cost. Using this number and the Societal Crash Cost Estimates by Crash Severity (HSM 2010), a monetary cost value was given to reduce collisions (Table 2).

**Table 2**  Summary of individual cost categories

| Element | All-way stop-control | Signalized | Roundabout |
|---|---|---|---|
| Construction | $47.05 | $9,679.06 | $14,492.04 |
| Operation/maintenance | $0 | $4000.00 | $1000 |
| Road user | $60,902.53 | $14,407.96 | $12,108.88 |
| Collision | $37,296.00 | $28,638.00 | $19,832 |
| Total annual cost | $98,246 | $56,725 | $47,433 |

**Table 3**  Summary of results

| Land usage | Rank | Score | Emissions | Score | Final score |
|---|---|---|---|---|---|
| 0 | 1 | 100.00 | 59,856.00 | 50 | 70 |
| 50 | 3 | 50.00 | 23,942.40 | 100 | 80 |
| 0 | 1 | 100.00 | 27,932.80 | 75 | 85 |

## *4.3  Environmental Impact*

The environmental impact was measured and ranked by considering both vehicle emissions and land usage with the following function:

$$0.60 \, \text{Emissions} \times 0.40 \, \text{Land Usage} \tag{2}$$

Emissions are calculated using a relationship between vehicle emissions and congestion. For every minute of idling, the average vehicle emits approximately 1.16 m$^3$ of $CO_2$ per minute (DHEC 2019). This unit value was multiplied to find the delay associated with each alternative. The land usage was determined by estimating the construction area. For the roundabout alternative, it was estimated that 50 m$^2$ of land is required for construction. Table 3 shows the final weighting and ranking system for both categories.

## *4.4  Safety*

Crash modification factors are used to predict the expected number of crashes after a countermeasure is implemented. In the case of this study, the following three different countermeasures are being implemented: (a) A TWSC converted into an AWSC, (b) A TWSC converted into a roundabout, and (c) A TWSC converted into a signalized intersection.

The Highway Safety Manual was used to find the CMF factors for each countermeasure. The CMF factors were then compared, where a smaller CMF factor

**Table 4** Safety evaluation of each alternative

| Alternative | Safety | | |
|---|---|---|---|
| | CMF | Rank | Score |
| All-way stop | 0.52 | 2 | 75 |
| Roundabout | 0.29 | 1 | 100 |
| Signalized | 0.56 | 3 | 50 |

indicated a safer countermeasure due to the larger reduction in collisions. Table 4 summarizes the CMF factors for each alternative and score.

In this case, the roundabout has the lowest CMF factor, meaning it has the most significant reduction in collision after implementation. Thus, the roundabout countermeasure is the highest-ranked option with a score of 100.

## 4.5 Selection of Best Alternative

Each alternative was evaluated based on the impact on the criterion to determine the best option. The chart below summarizes the results from the evaluation.

As seen in Fig. 1, the roundabout is the best alternative. The signalized alternative is the next best alternative, followed by all-way stop control coming last. The roundabout was found to have the most significant reduction of crashes, minimal delay, lowest average annual costs, and the highest environmental impact. After a sensitivity analysis was conducted, the roundabout alternative had a score that consistently stayed in the high 90 s. It is notable that the signalized intersection is close to the capacity of a roundabout but remains last in the safety criteria.
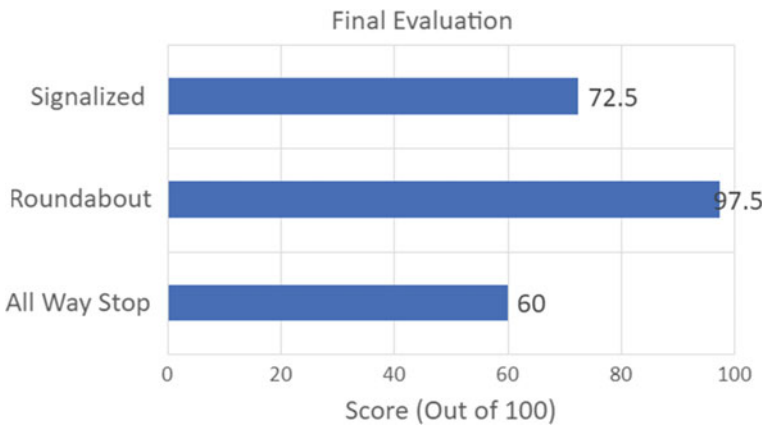


**Fig. 1** Summary of final evaluation

Despite the high impact on the environment, the roundabout alternative supports the safest and highest capacity alternative. Following the client's values, safety and capacity are the critical criteria.

## 5 Detailed Design

In recent years, the implementation of roundabouts has been widely seen all over southern Ontario and throughout the Niagara Region. The next phase of the project investigates the detailed design of the road realignment and roundabout. Manual calculations for design parameters were determined and modelled using Torus and AutoCAD Civil 3D software. The detailed design from an aerial view, profile view, and cross-section view was produced.

An iterative process was used to find an optimal roundabout solution. The iterations will explore minor changes to design parameters and the resulting impacts on movements. For this study, three iterations were developed using available resources. Typically, this process would be conducted using optimization software and mathematical models to evaluate many iterations. However, the use of this software is beyond this project's scope.

### 5.1 Design Constraints

Based on feedback from the Niagara Region, key design constraints include property acquisition, locations of hydroelectric poles, drainage, and environmental boundaries. To continue with the roundabout design, preliminary justifications have been considered as outlined below. It should be noted that these justifications are subject to change based on feedback and modelling results.

The roundabout design is likely to infringe on surrounding property, including private and town-owned property. In particular, the northeast quadrant of the intersection poses two key constraints. The first constraint is that the location of hydroelectric poles in this area cannot be changed. The second constraint is that this land quadrant is owned by the Town of Smithville and therefore cannot be considered in the final design. Both constraints are addressed by shifting the roundabout towards the west to accommodate the diameter if necessary. All other property acquisition requirements have been considered satisfied to proceed with the design.

When designing the realignment of the Thirty Road, a major spatial constraint is the presence of hydroelectric poles on the west side of the road. These hydroelectric poles are newly installed and expensive structures to relocate, making it ideal to leave them as is. However, to solve the issue of collisions, the radius of the reverse curve will need to be larger to prevent a skewed roundabout. This will require the road to be moved west of the hydroelectric poles. In addition, just north of the reverse curve

are protected fishery habitats that cannot be crossed. To allow for drainage, ditches were constructed on both sides of the road for stormwater drainage.

## *5.2 Geometric Design*

### 5.2.1 Roundabout

Preliminary design aspects such as the design vehicle, diameter, and speeds were selected based on primary usage and current data. Given projected AADT and left-turn-percentage values of 11,300 and 4.7%, respectively, it was concluded that a single-lane roundabout would provide sufficient operability. In addition, the traffic data and site visit observations indicate that a vast majority of vehicles traversing the roundabout are trucks. As such, the design vehicle was selected to be WB-67 to remain conservative in estimations. A typical single-lane roundabout with 90° angles will require a 40–55 m diameter (citation).

An initial 45 m diameter was assumed for preliminary calculations. In addition, a traversable apron surrounding the raised central island was considered to accommodate any large vehicles. Additional design considerations include the maximum entry, circulatory, and exit speeds. The maximum entry design speed was assumed to be 40 km/h. It should be noted that this entry speed requires significant deceleration in comparison with the current 60–80 km/h posted speeds on approach roads. The circulatory speed was then assumed to be 30 km/h.

Adequate visibility was considered for stopping and intersection sight distances. As a vehicle approaches the roundabout, the following three sight distances were considered, approach sight distance, circulatory sight distance, and crosswalk sight distance [2]. The intersection sight distance is the minimum distance needed for approaching vehicles to react to already circulating vehicles. This was expressed through two sight triangles, the length of the conflicting leg of the circulating vehicle and the length of the conflicting leg of the entering vehicle [1].

Since active transportation was a priority throughout the Region of Niagara by 2041 and beyond, pedestrian crossings were considered in the roundabout design. This consideration calls for splitter islands to be used on all four legs of the roundabout. The usage of splitter islands will serve multiple functions, including accommodating pedestrian crossing and traffic separation. Splitter islands were incorporated in future model iterations [13].

Figure 2 is a sample of the preliminary base roundabout modelled in AutoCAD. It should be noted that the above conclusions are subject to change depending on any updated data provided by the Region and subsequent modifications to calculations.
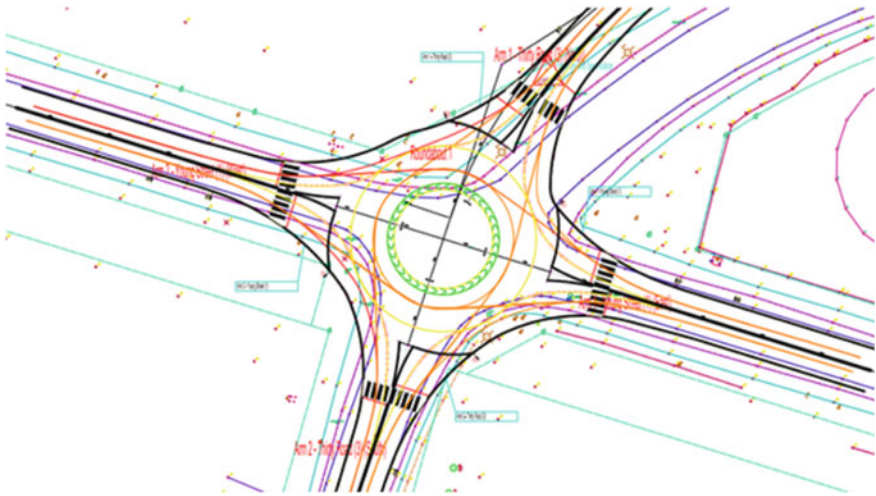
**Fig. 2** AutoCAD preliminary iteration model

### 5.2.2 Road Realignment

Preliminary calculations were completed to find the minimum stopping sight distance and minimum curve radii. With the design speed set to 60 km/h, the minimum stopping sight distance was calculated to be 85 m and minimum radii to be 130 m [13]. The road would maintain a similar superelevation of 6%. Using a recent topographic survey which was made available by Niagara Region, a preliminary alignment was created with the north approach being perpendicular to the east and west approaches. Adjustments were made to ensure adequate radii and stopping sight distances were maintained. The placement of the hydroelectric poles created a constraint in the realignment design as the road had to maintain a minimum clearance from them. Figure 3 shows the existing alignment and the proposed alignment.

## 5.3 Signage and Illumination

Correct traffic signs and signals, road improvement, and sufficient lighting all play an essential role in designing a safe operating system. The geometry of roundabouts results in reduced effectiveness of vehicle headlights on the curved radii. Thus, the reverse curve entering Young Street from Thirty Road requires additional lighting improvements to transition into the roundabout smoothly.

Perimeter lighting was implemented on the newly realigned Thirty Road to provide optimal visibility on collision locations, consistent visual guidance throughout the circulatory roadway, and clear visibility for road signs. As part of the design process, it is essential to recognize the disadvantages of perimeter

(a) Existing      (b) Proposed
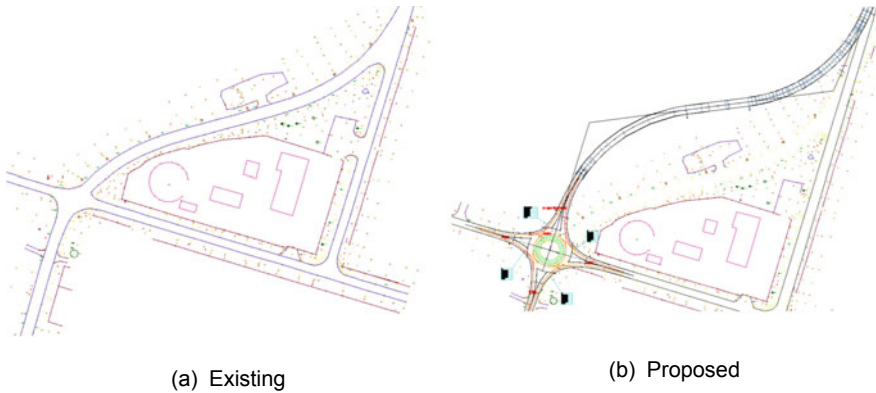
**Fig. 3** Comparison of existing and proposed road alignments

illumination. Disadvantages include the central island accommodating the weakest illumination and an increase in the number of equipment required.

Roundabout signage and reverse curve signage stem from general intersection signing. The following signs are required for the roundabout and reverse curve: speed advisory signs, chevron signs, yield signs, one-way signs, and guide signs. The following pavement markings were included in the roundabout design: Entry pavement markings consist of yield lines and zebra markings for pedestrians. As a vehicle nears the radius of the curve, the pavement markings will transition into solid lines, known as circulatory pavement markings. For the reverse curve, implementing a centreline and an edge line notifies the change in alignment and provides a smooth exit. To diminish the number of crashes due to road run-off, shoulder rumble strips along the reverse curve will give an audible vibration to warn the user. The strips were installed in the direction of travel along the horizontal curve to inform drivers of the alignment change and speed change.

## 5.4 Visibility

The predominant safety concern for the study area is the lack of visibility along the reverse curve and at the intersection. The approach sight distance and circulatory roadway sight distance were explored in the full capstone paper. Concerning the location of the roundabout conflicting with the various utilities in the area, emphasis is put on the intersection sight distance (ISD). To prevent sightlines conflicting with the existing hydroelectric poles, the ISD was analyzed. The intersection sight distance is the minimum distance needed for approaching vehicle to react to already circulating or entering vehicles. This is expressed through two sight triangles. The length of the conflicting legs of the circulating vehicle and the entering vehicles is calculated [1] and the length of the conflicting leg for the circulating vehicle is given by
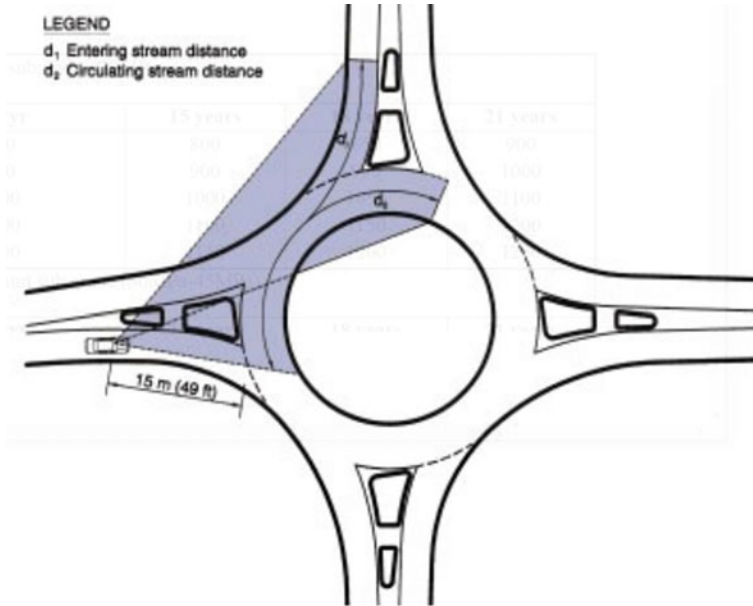
**Fig. 4** ISD sight triangle for a single approach

$$d_1 = 0.278\, t_c V_{\text{cir}} \tag{3}$$

where $T_c$ = the critical headway for entering a roundabout (5 s according to the guide), and $V_{\text{cir}}$ is the design speed of the conflicting circulating movement. The length of the conflicting leg for the entering vehicle is given by

$$d_2 = 0.278\, t_c (V_{\text{enter}} + V_{\text{cir}})/2 - d_{\text{cir}}(V_{\text{enter}} - V_{\text{cir}})/2V_{\text{cir}} \tag{4}$$

The entering speed is given by the conflicting entering movement. For example, on the south leg, the conflicting entering vehicle is the vehicle entering from the westbound direction. The circulating speed is given by the conflicting circulating movement. For the same example, the conflicting circulating movement is the vehicle travelling southbound. Lastly, the circulating distance is the distance from the centre island's centre to the circulating vehicle (Fig. 4).

## 5.5   Speed Control Strategies

A lower entry speed and circulation speed are key crucial attributes of roundabouts. This makes roundabouts highly adaptable to urban and suburban areas. However, speed control is necessary for high-speed settings. The required deceleration on
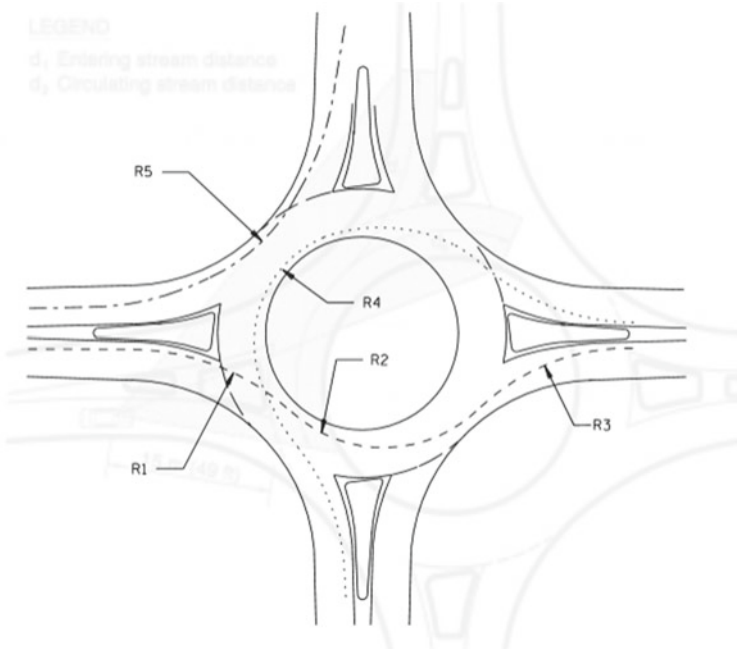
**Fig. 5** Fastest paths through a roundabout

the roundabout approaches is primarily accomplished through geometric design and traffic control devices. The fastest path analysis is used as a geometric check to ensure sufficient deceleration is met on the entry. The FHWA document Roundabouts: An Informational Guide states that the fastest path is determined by the speed relationships between $R_1$, $R_2$, and $R_3$ as well as between $R_1$ and $R_4$ as seen in Fig. 5 (FHWA 2010). The manual states the desired relationship is $R_1 \gg R_2 \ll R_3$, where $R_3$ should not be less than $R_1$ (FHWA 2010) and requires the left-turning path $R_1 \gg R_4$ (FHWA 2010). The difference in achieved design speed from $R_1$ to $R_2$ or $R_4$ should be with 10–15 km/h of the desired speed with 20 km/h maximum difference. Typical geometric treatments include the use of horizontal curvature and curbing on the splitter island to define the entry of roundabout. The reverse curve along Thirty Road, will be realigned with considering the necessary reduction of speed needed for the roundabout.

# 6 Conclusions

With the reported increase in collisions at Thirty Road and Young Street, it was determined the current road alignment and intersection would not satisfy the safety and service requirements to accommodate projected 2041 volumes. To improve

the current two-way, stop-controlled intersection, the following improvements were proposed: (1) an all-way stop, (2) roundabout, or (3) signalized intersection. Established evaluation criteria used to assess improvements were safety, level of service, delay, cost, and environmental impact. Following the evaluation, the roundabout alternative was found to have the greatest reduction of crashes, minimal delay, have the lowest average annual costs, and the highest environmental impact. With safety and capacity being the primary criteria of significance for the Region, the roundabout alternative was selected as the best alternative for detailed design. Preliminary calculations and AutoCAD models have been created for the roundabout and road geometry. The next steps for the design would be to develop an optimal solution through an iterative process using optimization models and Transportation Association of Canada (TAC) manual guidelines. Notable elements that will be produced are a detailed cost estimate and a construction schedule.

# References

1. Easa SM (2017) Design guidelines for symmetrical single-lane roundabouts based on intersection sight distance. J Transp Eng Part A Syst 143(10):04017052
2. Easa SM (2018) Modeling of unsymmetrical single-lane roundabouts based on stopping sight distance. KSCE J Civ Eng 23(2):800–809
3. Federal Highway Administration (2000) Roundabouts: an informational guide | FHWA SA-10-006. National Transportation Library
4. Federal Highway Administration (2015) Rumble strips and rumble stripes
5. Federal Highway Administration (2010) Roundabouts: a technical summary | FHWA SA-10-006. National Transportation Library
6. Highway Capacity Manual (2010) Volumes 1–4, including 2014 Errata-18. Signalized Intersections. Transportation Research Board
7. Highway Safety Manual (2010) C. Introduction and Applications Guidance, Introduction to the HSM Predictive Method. American Association of State Highway and Transportation Officials
8. Niagara Region (2014) Traffic Signal Standards, Niagara Region, Niagara, ON, Canada
9. Niagara Region (2016) Niagara Transportation Master Plan—Public Consultation, Niagara 2041
10. Idling Fact Sheet, 2019. | CR-010109. scdhec.gov. Department of Health and Environmental Control (DHEC). South Carolina, United States
11. Traffic Signal Timing Manual (2008) Chapter 5—Office of Operations. ops.fhwa.dot.gov
12. U.S. Department of Transportation
13. Transportation Association of Canada (2015) Geometric Design Guide for Canadian Roads—Intersections
14. Transportation Research Board (2016) Highway Capacity Manual—A Guide for Multimodal Mobility Analysis 6th ed., Transportation Research Board

# Redesigning an Urban Midblock Section to Improve Safety and Level of Service: Case Study in the Niagara Region

**Anish Nothoo, Zian Liu, Brahmjot Grewal, Sulaf Alkarawi, Manny Rataul, Hamed Esmaeeli, Essam Dabbour, and Said M. Easa**

**Abstract** Providing safe and complete streets that fit road users of All Ages and Abilities (AAA) with optimal traffic flow along urban built-up areas can often be challenging. Increased access points along midblock sections between busy intersections result in higher travel speeds, jaywalking, and delays. This paper evaluates a case in the Niagara Region, where the main corridor, Regional Road 20 (Lundy's Lane) between Montrose Road and Kalar Road, is being accessed for improvements. This corridor has many different factors, including multiple nursing homes, a secondary school, tourist accommodations, and local businesses. The alternative solutions included: implementing a road diet with a cyclist facility, two-way left-turn lanes, adding pedestrian crossing and numerous other minor improvements (Alternative 1); and implementing partial road expansions along the corridor to add in pedestrian refuge islands, partial channelized left-turn lanes, and additional minor improvements (Alternative 2). The best alternative was chosen through evaluation using four criteria: safety, traffic operations, cost, and environmental impacts. Each criterion was given a corresponding weight, and the best alternative was chosen through a weighted scoring method. Sensitivity analysis is also conducted for the weights and the proposed growth rate for the 2041 design year. In this regard, Alternative 1 showed the best fit with evaluation criteria. A detailed design of this alternative was created using AutoCAD, and PTV Vissim and Synchro were used to analyze the impact on traffic operations along the midblock section.

**Keywords** Fiber reinforced polymers · T-beams · Shear capacity · Ensemble machine learning · SHAP feature importance

A. Nothoo · Z. Liu · B. Grewal (✉) · E. Dabbour · S. M. Easa
Department of Civil Engineering, Ryerson University, Toronto, Canada
e-mail: brahmjot.grewal@ryerson.ca

S. Alkarawi · M. Rataul · H. Esmaeeli
Transportation Planning, Regional Municipality of Niagara, Ontario, Canada

573

# 1 Introduction

Urban roadways often have congestion issues for all road users, where optimal safety is not always achieved. In addition, areas with a high density of access ways create many conflict points between motorists, pedestrians, and cyclists. Collision reports indicate that 40% of accidents are reported in the study area as rear-end collisions. This situation poses a challenge for redesigning a safer and more efficient corridor to improve safety and mobility for all users. Multiple alternative solutions were proposed in this study to improve safety and capacity in the midblock section of Niagara Regional Road 20 (Lundy's Lane) between Montrose Road and Kalar Road. The alternatives were evaluated using weighted criteria to choose the best solution. The Niagara Region (The Region) predicts an annual population growth of 1.35% on Lundy's Lane for the horizon 2041. Many issues were identified through site observations, including long queues when vehicles are waiting for a safe gap to turn left, speeding, inadequate pedestrian crossing, inadequate cyclist facilities, poor level of service at intersections, and safety of all road users.

To address these issues, this study proposes two alternatives consisting of a set of solutions that, when implemented together can remedy significant problems in the corridor, improve the level of service, and improve safety for all users. These alternatives were evaluated based on safety, traffic operations, cost, and environmental impacts. Based on this evaluation, Alternative 1 was selected. A detailed design of this alternative was created in AutoCAD, PTV Vissim and Synchro were used to analyze the impact on traffic operations along the midblock section. The following diagram shows a high-level overview of the paper (Fig. 1).

# 2 Study Area

The study area is a midblock section of Regional Road 20 Lundy's Lane bounded by Regional Road 20 and Montrose Road to the east, and Regional Road 20 and Kalar Road to the west. The midblock section is a four-lane undivided major arterial roadway with a speed limit of 50 km/h spanning approximately 1 km in length. It experiences 5700 vehicles/h in the afternoon peak period and has an access point density of 87 access points/mile. The section is located in Niagara Falls and falls under the jurisdiction of Niagara Region. Along the built-up midblock section are many motels, a secondary school, two retirement homes, and many food establishments that thrive from the tourist activities in the area, shown in Fig. 2.
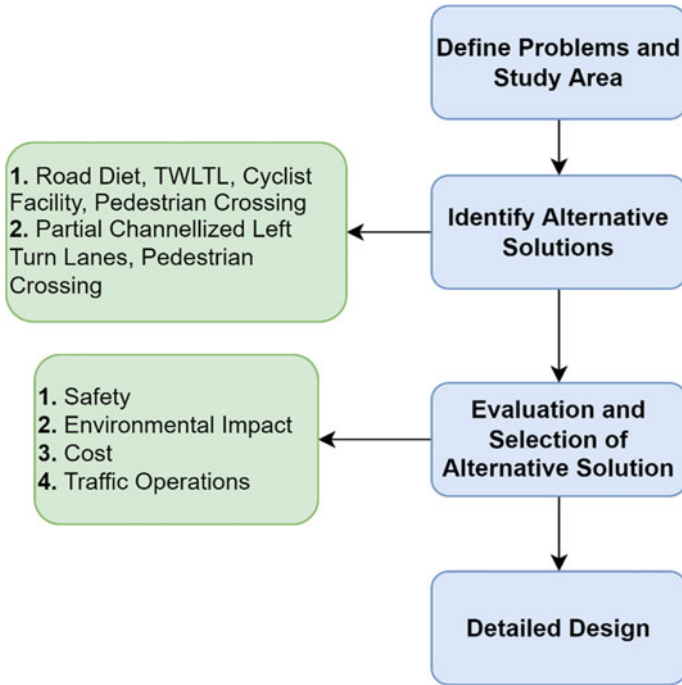
**Fig. 1** High-level overview of report contents
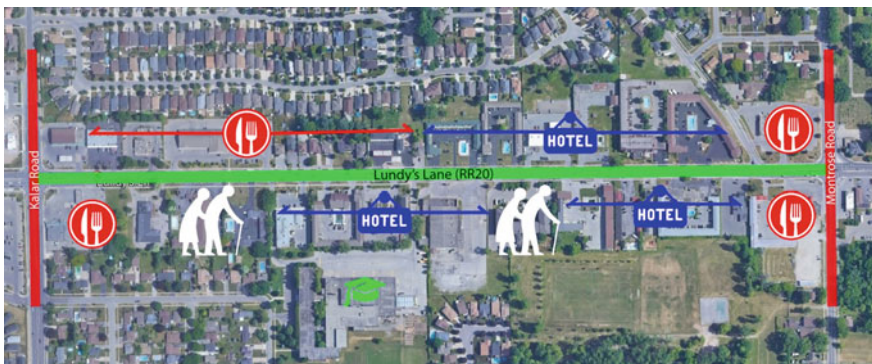


**Fig. 2** Google Earth image of the study area

## 3 Alternatives

Based on preliminary research, two alternatives to solve most of the issues along the corridor have been identified. The alternatives aim to solve the significant problems in the corridor, such as improving safety and the level of service (LOS) for all users.

## 3.1 Alternative 1

This alternative implements a road diet with a cyclist facility and a two-way left-turn (TWLT) lane, adding a pedestrian crossing at the midblock, along with other minor improvements. These include restricting left-turn movements of traffic coming from Beaverdams Road during the rush hour, optimizing signal timings at intersections and implementing speed cameras (Fig. 3).

According to the Federal Highway Association (FWHA), road diets are a roadway reconfiguration that can have many benefits, including enhancing safety, mobility, and accessibility for all road users. They have been deemed an effective way of reducing the crash frequencies on four-lane undivided roadways, especially as traffic volumes and turning movements increase over time. The two-way left-turn lane will help reduce the delay and queue along the roadway, when vehicles are waiting to turn left into an access point. The cycling facility will improve mobility for other transportation users.

Although there is an existing signalized pedestrian crossing close to the intersection of Kalar Road and Lundy's Lane, adding a pedestrian crossing would increase the mobility of pedestrians along the corridor. According to the Ontario Traffic Manual Book 15, a pedestrian crossover is warranted if it's not within 200 m of any other facility, deeming an additional pedestrian crossover feasible with space requirements.

Significant delays during the rush hour are observed at the unsignalized intersection of Beaverdams Road and Lundy's Lane, as the gaps in traffic to make a left turn onto the major street are infrequent. This results in larger vehicle queues along the minor approach, where drivers become impatient and turn left into an unsafe gap, causing collisions at this intersection. To reduce the delay and the collision rate, left-turn movements onto the major road during the rush hour can be restricted. Additionally, optimizing signal timings and adding speed cameras can increase safety along the corridor.



(a) Road before    (b) Road after

**Fig. 3** Road diet on Edgewater Drive in Orlando, Florida. *Source* Federal Highway Administration

## 3.2 Alternative 2

With this alternative, the right-of-way (ROW) is increased at certain locations along the corridor to add pedestrian refuge islands, partial channelized left-turn lanes, and other minor improvements. These include restricting left-turn movements of traffic coming from Beaverdams Road during the rush hour, removing objects close to the road to improve sight distances, optimizing signal timings at intersections, and implementing speed cameras (Fig. 4).

The addition of partial channelized left-turn lanes can aid in reducing long queues and delays when vehicles are waiting to turn left into an access way. A pedestrian crossing refuge island would also increase safety for pedestrians crossing the four-lane roadway. The need for another pedestrian crossing is justified as pedestrians have limited access to both sides of Lundy's Lane, with the existing crossing situated close to Lundy's Lane and Kalar Road.

Additional minor improvements include restricting left turns onto Lundy's Lane from Beaverdams Road during the rush hour, optimizing signal timings and implementing speed cameras. According to a study by Stevanovic and Kergaye, conflicts at signalized intersections can be reduced by increasing the intergreen time and optimizing green times depending on traffic volume. Along with this, speed cameras can be used to discourage drivers from speeding along the corridor. Sight distances can also be improved for road users by removing large objects close to the roadside.



**Fig. 4** Pedestrian crossing with a refuge island. *Source* Global Designing Cities Initiative

**Table 1** Traffic data collected during the site visit for Beaverdams Road

| Time frame | Traffic data collected during site visit | | East on RR20 | West on RR20 |
|---|---|---|---|---|
| | Beaverdams Rd | | East on RR20 | West on RR20 |
| | Left turn | Right turn | Left turn | Right turn |
| 15 min | 6 | 44 | 14 | 14 |
| Hourly | 24 | 176 | 56 | 56 |

## 4 Simulation of Alternatives

### 4.1 Data Collection and Analysis

From the turning movement reports, signal timing plans, and additional data provided by The Region of Niagara, the time frame selected for analysis was the PM peak rush hour as it had the highest hourly volume. However, the reports had no information about the signalized pedestrian crossing and traffic volume for the minor stop-controlled intersection of Beaverdams Road and Regional Road 20. During the site visit held on October 8th, 2021, the study team recorded a 15-min video to capture the traffic volume at this minor approach. This data was extrapolated and used in the traffic simulations. Table 1 summarizes the data collected.

To plan for the design year of 2041, Eq. 1 was applied to the given 2019 traffic volumes using two growth rate factors. The Niagara Transportation Masterplan expects the population to grow at a rate of 1.35% annually, and members of the Region of Niagara proposed using a 2.00% growth rate. For this reason, a sensitivity analysis was conducted in this study using both growth rate factors.

$$f(x) = a(1 + r)^n \tag{1}$$

where $f(x)$ = exponential growth function (future volume), $a$ = initial volume, $r$ = growth rate, and $n$ = time interval ($n = 22$ since the initial and planned volumes correspond to 2019 and 2041).

### 4.2 Model Simulation

Synchro 11 software was used to simulate traffic operations of both alternatives. Synchro 11 is a traffic analysis software developed by Trafficware that allows users to analyze signal timing and traffic flow for simulating multiple scenarios. Moreover, the software generates traffic reports that include key performance indicators for each approach and intersection. The alternatives were assessed objectively by using the generated reports. The most crucial feature of Synchro 11 is its SimTraffic tool which allows the user to run the traffic and signal timing inputs to visually assess the traffic

network and bottlenecks in the system. One major downside to using this software was its inability to properly model a midblock pedestrian crossing, lane markings, access points, bicycle lanes, and a partial channelized left-turn lane. To combat these, it was assumed that 10% of the traffic along the midblock section would be turning right and left into the access ways, allowing the model to simulate volumes from the two-way left-turn lane and partially channelized left-turn lanes.

The problems identified at the intersections and along the midblock section using the Synchro 11 Software include (1) heavy traffic in the southbound and eastbound approach at Montrose Road and Regional Road 20, and (2) a long queue of vehicles on the minor approach of Beaverdams Road. Along with this, accident reports provided by The Region were used to identify other significant issues and areas that have a substantial number of accidents.

## 5 Evaluation of Alternatives

### 5.1 Basic Evaluation

*Safety Evaluation*: Safety was analyzed in terms of lane dimensions along with conflict points with left and right turning vehicles. A point system was established for conflict points, where through traffic was awarded 2 points, 0.5 point to right turns, 1 point to pedestrians, and 1 point to cyclists. For a vehicle turning left into an access way, the respective conflicts include one opposing vehicle, a cyclist, a pedestrian, and a vehicle turning right into the access way. This gives a total score of 4.5. Following this process, Table 2 summarizes the conflict points for both alternatives (Fig. 5).

*Environmental Evaluation*: The second measure for evaluation was the environmental impact of each alternative. This can be determined by analyzing the output values of carbon emissions from the Synchro 11 software and qualitatively comparing the noise pollution that would come from implementing each alternative. The carbon emissions are 1418.5 g/h and 1438.8 g/h for Alternatives 1 and 2, respectively. A study by McAlexander et al. (2015) in New York City concluded that noise pollution at the street level could be directly associated with vehicular traffic density along a section. Therefore, out of a rank of 1–5, 1 being minimal noise pollution and 5 being

**Table 2** Summary of conflict points for the two alternatives

| Conflict point | Weight | Alternative 1 | Points | Alternative 2 | Points |
| --- | --- | --- | --- | --- | --- |
| Through traffic | 2 | 2 | 4 | 3 | 6 |
| Right turn traffic | 0.5 | 2 | 1 | 2 | 1 |
| Pedestrian | 1 | 4 | 4 | 4 | 4 |
| Cyclist | 1 | 4 | 4 | 4 | 4 |
| Total | | | 13 | | 15 |

(a) Alternative 1           (b) Alternative 2
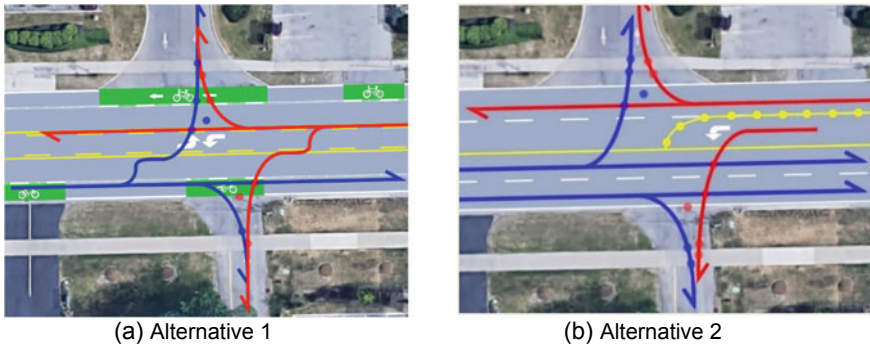
**Fig. 5** Render image of conflict points

excessive noise pollution, Alternative 1 was given a rank of 2.5 and Alternative 2 a rank of 3.5 due to the increased number of travel lanes for vehicles.

***Cost Evaluation***: The costs for both alternatives were calculated using estimated costs from similar municipalities surrounding the Greater Toronto Area. Each project has typical costs, including planning and design, construction, operation, and maintenance. The planning and design aspects of the cost are assumed to be undertaken by the Niagara Region. The construction costs are fixed costs, where Alternative 1 requires implementing a cycling lane, and Alternative 2 requires a road reconstruction. The operation and maintenance costs are variable costs, where Alternative 1 requires maintenance of the 2 cycling lanes with 3 vehicle traveling lanes, and Alternative 2 requires maintenance of 4 vehicle traveling lanes. Based on construction, operation, and maintenance costs, Alternative 1 is expected to have a net present cost of $3,778,553, and Alternative 2 is expected to have a net present cost of $5,186,370.

***Traffic Operation Evaluation***: For traffic operations, both alternatives were evaluated regarding their volume-to-capacity (v/c) ratio. This value was determined from the outputs of the Synchro 11 software after the simulation of the alternatives. Alternative 1 had a v/c ratio of 1.01, while Alternative 2 had a v/c ratio of 0.56.

## 5.2 Selection of Best Alternative

A weighted criterion method was used to evaluate the alternatives, where the better alternative will have a lower total alternative score. The original weights of each criterion are 40% for safety, 15% for environmental impact, 15% for cost, and 30% for traffic operations. These assigned weights are justified as our primary focus of the midblock improvements is to improve the safety and usability of the section.

Table 3 summarizes the scoring evaluation from all four categories, where Eq. 2 was used to calculate the total scores for each alternative. Based on this calculation,

**Table 3** Alternative scores of basic evaluation

| Alternative | Score | | | | |
|---|---|---|---|---|---|
| | Safety | Environmental | Cost (in hundred thousands) | Traffic operation | Total score |
| 1 | 13 | 2.5 | 2.29 | 1.01 | 6.22 |
| 2 | 15 | 3.5 | 8.85 | 0.56 | 8.02 |

**Table 4** Summary of sensitivity analysis

| Alternative | Total alternative score | | | |
|---|---|---|---|---|
| | Original | Increasing weight of safety | Increasing weight of environmental | Increasing weight of traffic operations |
| 1 | 6.22 | 7.28 | 5.77 | 5.56 |
| 2 | 8.02 | 8.90 | 7.59 | 6.88 |

alternative 1 is the optimal solution as it scores lower for cost and has a higher safety ranking with fewer conflict points than alternative 2.

$$S = 0.40\,x_s + 0.15\,x_{EI} + 0.15\,x_{CF} + 0.30\,x_{TO} \tag{2}$$

where $S$ = total score of alternative, $x_S$ = safety score, $x_{EI}$ = environmental impact score, $x_{CF}$ = cost score and $x_{TO}$ = traffic operations score.

A sensitivity analysis was also conducted for both alternatives, where the weights of each criterion were altered to see the effect it would have on the total score. The first case was to increase the weight of the safety score from 0.4 to 0.5 (or 40–50%). The second case was to increase the weight of the environmental score from 15 to 25%, and the final case was the increase of the weight of the traffic operations from 30 to 40%. Table 4 summarizes the results from all three cases explored. The results indicate that Alternative 1 would still be the most feasible solution as with each weight change, it still has an overall total score that is less than alternative 2.

## 6 Detailed Design

### 6.1 CAD—Design and Evaluation

The Niagara Region provided the digital version (in CAD) of the geometric design of Lundy's Lane and Kalar Rd and Lundy's Lane and Montrose Rd. The two intersection drawings were placed on top of a satellite Google image, where the midblock sections of Lundy's Lane was traced over. The measuring tool on Google maps was used to verify the accuracy, with road width dimensions as 13.75 m from curb to curb for the

midblock section of Lundy's Lane. According to OTM Book 18, physically separated bicycle lanes have requirements of 1.5 m in width and 0.3 m as buffers with flexible bollards. Wider cycling lanes would be desirable for cyclists' comfort. However, due to the road width constraints, this was not feasible. To further aid in the comfort and safety of the cyclists, flexible bollards would be placed in the middle of the buffer zone, spaced 6 m apart. The bollards would not be placed in areas where bus stops are located, or where access points are present. According to OTM Book 18, flexible bollards should be placed 6–12 m apart for urban areas and could be reduced to 3 m where motor vehicle encroachment is likely.

The Niagara Region follows MTO Geometric Design Standards and TAC Geometric Design Guides, which require lane widths of 3.3–3.7 m for urban arterial roads of design speeds of 60 km/h. To satisfy the constraint, the design allowed for lane widths of 3.3 m and two-way left-turn lane width of 3.55 m. The decision to have a wider two-way left-turn lane provides more comfortable left-turn movements into the high density of access points. In addition, it allows for a more comfortable merge into traffic when exiting the access points. Figure 6 represents the proposed road diet lane dimensions along the midblock section of Lundy's Lane in AutoCAD.

An additional pedestrian crossing will be implemented near Lundy's Manor Retirement Residence since the east midblock portion of Lundy's Lane does not have any safe crossing devices for pedestrians. The type of pedestrian crossing to be used will be a pedestrian hybrid beacon (PHB). Studies have shown that this type of crossing effectively increases safety and does not cause significant disruptions to traffic flow (federal highway administration). In addition, islands would be placed in the lane width of the two-way left-turn lanes. This will further protect pedestrians crossing the road and prevent vehicles from using the two-way left-turn lane to pass
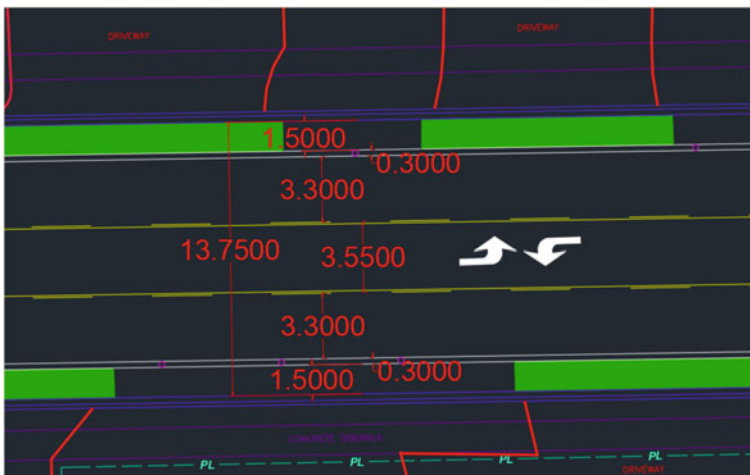


**Fig. 6** Lane width dimensions along midblock section of Lundy's Lane
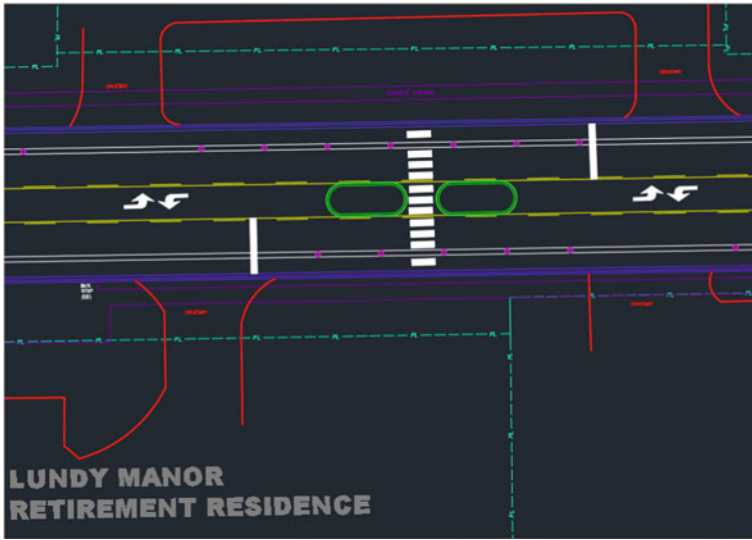
**Fig. 7** Pedestrian hybrid beacon with islands near Lundy's Manor Retirement Residence

slow-moving vehicles near the pedestrian crossing. Figure 7 represents the proposed pedestrian crossings along with the pedestrian refuge islands.

## 6.2 PTV VISSIM—Design and Evaluation

PTV VISSIM is the traffic simulation software that is used to evaluate the design of alternative 1. The evaluation will be broken down into two methods. First, the current road layout is modeled in the software, similar to Sect. 4.2. This layout has the geometric layout of the road and will not be enhanced aesthetically with road features such as medians, crosswalks, and sidewalks. The chosen alternative design was created in the software using the AutoCAD file for more accuracy, following this first layout design. The reason for recreating the current road layout is to have a fair comparison and evaluation of both designs in the same software instead of relying on the evaluation of Synchro 11 for the current layout.

Some challenges arose when designing the chosen alternative in the PTV VISSIM as some features were not available in the software. For example, the software is not able to properly model a two-way left-turn lane. Therefore, the solution was to identify the significant plazas within the midblock section and create dedicated left-turn lanes in the middle of the road. Since the traffic volumes entering and exiting the access points were not given, our team had to estimate these volumes based on the site visit we conducted. The base assumption was that 10% of the total volume along each direction would flow in and out of the access ways. This 10% was further

broken down into percentages for each major facilities access way. This was done by each team member independently choosing a percentage based on their experience from the site visit. This data is summarized in Table 5. For example, the traffic that will be entering Plaza #1, located across from Westlane Secondary school, would be 35% of the 10% of traffic turning right from the Westbound direction and 35% of the 10% of traffic turning left from the Eastbound direction, using the two-way left-turn lane. Additionally, the software did not have the ability to adequately model the pedestrian hybrid beacon (PHB) crossing. This crossing was replicated by selecting the signalized crossing type in the software and adjusting the signal timings to match the PHB signal type.

Furthermore, a topic that has been thoroughly researched in this study is the crash modification factors (CMF) associated with implementing a road diet, active transportation (bike lanes), and a signalized pedestrian crossing (i.e. PHB crossing). While the research shows that there should be a drastic reduction in collisions, this criterion was not effectively evaluated in the software. However, it is still crucial as safety is an important aspect of the midblock section.

Along with adjusting the traffic volumes for the proposed 2.0% annual growth rate, the change in traffic volumes due to the addition of a cyclists facility must also be considered. Since there is minimal data available regarding an increase in cyclists volume and a decrease in vehicular volume once a cyclist facility has been implemented, the cyclist volume was estimated. Using open-source data from the City of Toronto (City of Toronto, "Open Data Dataset"), similar midblock sections with characteristics such as being close to a major freeway, having a high volume of access points and being in the vicinity of a school were analyzed. Through this analysis, four intersections best fit the above criteria. Those intersections were Willowdale Ave and Finch Ave, Scarlett Rd and East Dr, Yonge St and St Clair Ave, and Danforth Ave and Broadview Ave. An example of a chosen intersection which was converted from a 4-lane highway to a 2-lane highway with a TWLTL can be seen in Fig. 8.

From the four intersections above, the data showed that there was a traffic reduction once the cycling infrastructure was implemented. The range of the reduction was anywhere from 2 to 56%, where the weighted average was approximately 25%. The major intersections were given more weight as the traffic volumes are higher. As well, there was an observed reduction in pedestrian traffic, varying from 8 to 48%,

**Table 5** Summary of volumes assumption for key access points (northbound)

| Volumes assumption north side Lundy's lane | | | | |
|---|---|---|---|---|
|  | Tim Horton's | Plaza #1 (Westlane) | Petro Canada Gas Station | Plaza #2 (Retirement home) |
| Anish | 30 | 40 | 20 | 10 |
| Zian | 10 | 40 | 10 | 40 |
| Brahmjot | 30 | 25 | 20 | 25 |
| Average | 23.33333333 | 35 | 16.66666667 | 25 |

| Before Cycling Lane Installation | After Cycling Lane Installation |
|---|---|
|  |  |
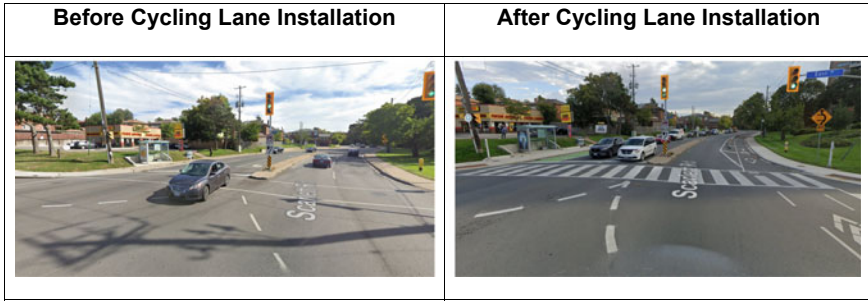
**Fig. 8** Example of intersection used to estimate new cyclist and vehicular volumes

with a weighted average of 20%. The cyclist volumes increased anywhere from 113 to 1600% with the weighted average being an increase of 250%.

Since the above analysis does not include a large sample of cycling facilities that match the stated criteria, the exact volume reduction percentages obtained above were not applied to our study area. However, a sensitivity analysis was conducted to show the effects of the traffic reduction. Three different percentages were used: 0, 5 and 10% as these are well below the weighted averages. The number of cyclists used in the simulation was 50% of the reduced traffic to see how much strain the system could handle, as an increase in cyclist volume should result in a slight delay when turning into access points.

To understand the impacts of this traffic reduction, the results in terms of Level of Service (LOS) were evaluated at five points across the midblock section as shown in Fig. 9. Point #1 is Lundy's Lane at Kalar Road, point #2 is the existing midblock crossing, point #3 is the newly implemented PHB crossing, point #4 is Lundy's Lane at Beaverdams Road, and point #5 is Lundy's Lane at Montrose Road. The growth rate of + 2.00% was used in the comparison.

Comparing the last two rows (5 and 10% traffic reduction) it can be observed that the LOS is improved. By reducing the traffic by 5 and 10% for the design year 2041 with a + 2.00% growth rate, this causes the effective growth rate to be + 1.76% and + 1.52%, respectively. Similar results were obtained for all four growth rates used (Table 6).

Another identified issue was the queue that formed from the left turning vehicles from Beaverdams Road onto Lundy's Lane. This was due to having inadequate gaps in the traffic on Lundy's Lane for vehicles to merge into. When the annual growth



**Fig. 9** Aerial view of midblock section with location IDs for evaluation. *Source* Google Maps

**Table 6**  Comparison summary of LOS results for + 2.00% growth

| + 2.00% growth rate results | | | | | |
|---|---|---|---|---|---|
| | #1 | #2 | #3 | #4 | #5 |
| Original layout | LOS C | LOS C | LOS F | LOS F | LOS F |
| Chosen alternative | LOS E | LOS C | LOS C | LOS D | LOS D |
| Optimized signal timing | LOS E | LOS C | LOS C | LOS D | LOS D |
| 5% traffic reduction | LOS D | LOS C | LOS C | LOS D | LOS D |
| 10% traffic reduction | LOS D | LOS B | LOS B | LOS D | LOS C |

rate factors were applied, the issue worsened. To remove this bottleneck from the system, left-turns from Beaverdams Road onto Lundy's Lane as well as left-turns onto Beaverdams Road will be restricted during the morning and afternoon peak hour periods. Figure 10 compares the vehicle delay, in seconds, at the intersection of Lundy's Lane and Beaverdams Road. The growth rate used is + 2.00% for all scenarios. As expected, once left turns are prohibited during the peak hour period, the vehicle delay is reduced and improved further once signal optimization is implemented. The signal timings are optimized by increasing the cycle time from 135 to 150 s, which provides more green time for the through and left-turning traffic along Lundy's Lane.

The results of the chosen alternative and the existing layout shows a significant reduction in vehicle delay, queue lengths and level of service. However, it is important to note that the improvement of the safety along the midblock section has not been factored in these numbers. A final summary of the results obtained from the simulation in PTV Vissim is given in Table 7, where four cases for improvements
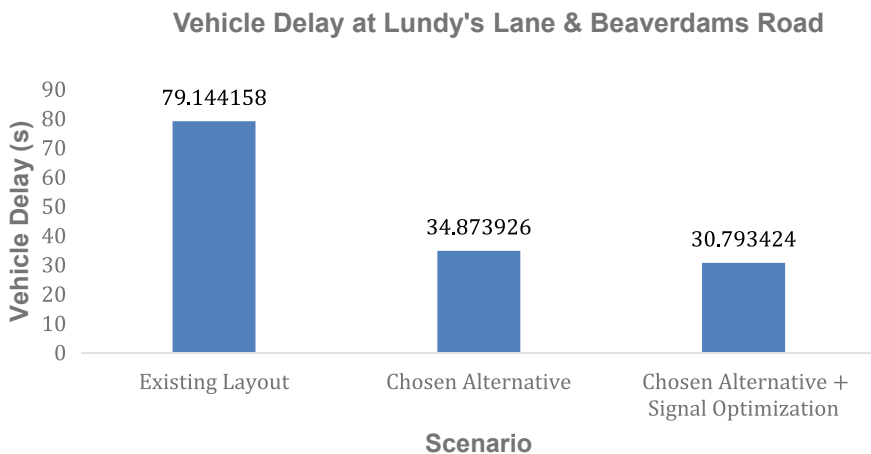


**Fig. 10**  Vehicle delay at Lundy's Lane and Beaverdams Road for three scenarios of + 2.00% growth rate

**Table 7** Multiple scenarios analysis for 2041 design year

| Scenario analysis | | | | | |
|---|---|---|---|---|---|
| | #1 | #2 | #3 | #4 | #5 |
| Do nothing alternative (+ 2.00%) | LOS C | LOS C | LOS F | LOS F | LOS F |
| Best case (+ 0.70% growth) | LOS D | LOS A | LOS A | LOS C | LOS D |
| Most likely (+ 2.00% growth) | LOS D | LOS C | LOS C | LOS D | LOS D |
| Worst case (+ 2.50% growth) | LOS E | LOS C | LOS C | LOS E | LOS E |

are summarized comparing their LOS. The 'Do Nothing' alternative assumes that the traffic volumes would grow at + 2.00% per year until 2041, and the current road layout would stay the same. The following three scenarios are all from the chosen alternative, using different growth rates and other minor factors. The 'best case' scenario assumes the lowest population growth rate with signal optimization performed and a traffic reduction of 10%. This would also mean that most people who are no longer driving would be using the bike lane. The 'most likely' case has been discussed in Sect. 6.2. The 'Worst Case' scenario assumes the highest population growth rate of + 2.50% and with no signal optimization and no traffic reduction even though the bike lanes have been installed. Even if the 'worst case' scenario was to occur, the overall level of service of the midblock section would still perform slightly better than the 'do nothing alternative', which had half of its location IDs perform at LOS F.

# 7 Future Research and Developments

Further developments can be done to assess the viability of the chosen design, ensuring that the safety is improved along with the level of service in the study area. Crash modification factors from similar studies can be analyzed in addition to the conducted conflict point analysis to improve the conducted safety evaluation. This can aid in verifying that the implementation of a road diet accompanied by a cyclists' facility increases the safety for all road users. To further verify that safety has been improved, an analysis of the pre and post-accident reports can be conducted once the alternative is implemented.

In addition, improvements to the study can be made if access to more data was available. Many assumptions were made with regards to the access point flow, the implementation of a cyclists' facility, and how that may alter the existing traffic volumes. Missing data that would have added to the study includes pedestrian and cyclists' volumes along the midblock section, specific locations where accidents occur, and an in-service road safety audit of the existing conditions.

# 8   Conclusion

In conclusion, the implementation of the chosen alternative showed an increase in safety along with an improvement in the level of service. The road diet with the two-way left-turn lane helped in reducing delays along the corridor and tackling the issue of speeding. The addition of a cyclist facility helps to promote active transportation usage, and through analysis of different models, has shown to decrease vehicular volumes by 5–10%. The additional pedestrian crossing will help increase mobility along the midblock section along with safety for pedestrians as a combination of a PHB and refuge island is used. As well, the optimization of signal timings further helps to improve the level of service. The restriction of left turns maneuvers during the rush hour periods at the stop-controlled intersection of Beaverdams Road and Regional Road 20 (Lundy's Lane) will create for less collisions and conflict points. Improving the safety level of service with redesigning this midblock section was achieved through our detailed design and simulation of this design.

# References

1. City of Toronto (2017) Cycling network map. City of Toronto Cycling Network Map
2. City of Toronto (2022) Open data dataset. City of Toronto's Open Data Portal
3. Federal Highway Administration (FHWA) (2021) 2009 Edition Chapter 4F. Pedestrian Hybrid Beacons. US Department of Transportation
4. Federal Highway Administration (FHWA) (2016) Safety—Road Diets (Roadway Reconfiguration). US Department of Transportation
5. Lyon C et al (2008) Safety evaluation of installing center two-way left-turn lanes on two-lane roads. Transp Res Rec 2075(1):34–41. https://doi.org/10.3141/2075-05
6. McAlexander TP et al (2015) Street-level noise in an urban setting: assessment and contribution to personal exposure. Environmental Health, BioMed Central, 28 Feb 2015
7. Niagara Region (2017) Niagara Region Transportation Master Plan Final Report. *Niagara Region*, Oct 2017, pp 1–113
8. Ontario Traffic Committee (2021) Ontario Traffic Manual Book 18—Cycling Facilities. Stinson, June 2021
9. Ontario Traffic Committee (2016) Ontario Traffic Manual Book 15—Pedestrian Crossing Treatments. Stinson, June 2016
10. Pedestrian Refuges (n.d.) Global Designing Cities Initiative
11. Stevanovic A, Stevanovic J, Kergaye C (2013) Optimization of traffic signal timings based on surrogate measures of safety. Transp Res Part C Emerg Technol 32:159–178

# Traffic Delay Analysis in Road Rehabilitation Projects: A Simulation Approach

**A. Sorour, A. Abdullah, Y. A. S. Essawy, and K. Nassar**

**Abstract** Population growth has put a great strain on our highway networks leading to an ever-greater need for road rehabilitation and reconstruction. Highway networks are overloaded with new commuters every day; leading to ever-increasing congestion levels. These congestion levels are exacerbated when there are construction activities, and a road cannot be rerouted. Consequently, user cost has become an essential part of the economic evaluation criteria for the decisions that go into planning road rehabilitation projects. The lost economic output due to the delay time incurred by road users forces governments to plan these projects on tight schedules and may even penalize the contractor for failing to finish on a certain date. Contractors engaged in road rehabilitation projects are continuously asked to work in expedited conditions to minimize the delay time incurred by road users. This makes the planning phase of any road rehabilitation project essential for successfully finishing the project on time. Simulation provides a capable tool for any contractor to aid in properly strategizing for road rehabilitation projects. From contractors' point of view, they can choose a strategy that satisfies the minimum delay versus project duration trade-off. This paper aims to allow the evaluation of the delay that is suffered by the users of

A. Sorour (✉)
The American University in Cairo (AUC), Cairo, Egypt
e-mail: asamir94@aucegypt.edu

A. Abdullah
Department of Architectural Engineering, Faculty of Engineering at Mataria, Helwan University, Helwan, Egypt
e-mail: abdelhamid.abdullah@m-eng.helwan.edu.eg; abdelhamid.abdullah@aucegypt.edu

A. Abdullah · Y. A. S. Essawy
Department of Construction Engineering, The American University in Cairo (AUC), Cairo, Egypt
e-mail: yasmeen.sherif@eng.asu.edu.eg; y_essawy@aucegypt.edu

Y. A. S. Essawy
Department of Structural Engineering, Ain Shams University (ASU), Cairo, Egypt

K. Nassar
Industrial Partnerships and Extended Education, Deparment of Construction Engineering, The American University in Cairo (AUC), Cairo, Egypt
e-mail: knassar@aucegypt.edu

590 A. Sorour et al.

four-lane freeways under different scenarios. The delays for the different number of lanes closed, working off-peak hours and different lengths of reconstruction area are evaluated using Anylogic simulation software. The results of this study should help contractors decide on the type of strategy to approach road rehabilitation projects based on delay time versus project duration trade-off.

**Keywords** Simulation · Anylogic · Road rehabilitation · Delay time

## 1 Introduction

The ever-growing number of vehicles coupled with road damage adversely impacts the flow of traffic causing traffic congestion, due to all vehicles reducing their speed at the same time. The road damage then requires some degree of road rehabilitation depending on its severity. During road rehabilitation, a special area called a work zone is needed to minimize the risk of workplace accidents both for road users and construction workers. The work zone denotes the area where road work takes place and the number of lanes available is reduced. The work zone for road rehabilitation causes speed delays and bottlenecks. In addition, it reduces the road capacity and the vehicle users must slow down their vehicle speed causing travel delays. On the other hand, contractors tasked with working on road rehabilitation projects are required to finish the work as fast as possible to minimize the delay time caused by the work zones. Contractors have to bear the responsibility, not only for the rehabilitation work but also for the state of the traffic on the road they are working on. That is why contractors should plan diligently before any such projects to meet the contractual obligations of project deadlines, delay time incurred by road users, and the trade-off between them. Simulation is one of the most powerful and effective tools that can help contractors decide on the kind of strategy that satisfies any particular project conditions. Simulation can aid in the prediction of road rehabilitation duration and the traffic delay caused by it. This study uses Anylogic software discrete event simulation on two separate models, a construction model and a traffic model. We tested the effect of a certain construction strategy on a certain road condition and see the delay time it causes to the road users. The traffic model and the construction model are both generic, which means that the user has the flexibility to enter the data that corresponds to the project under consideration. Finally, the study proposes a general guideline for what is an appropriate construction rehabilitation strategy that can minimize the delay time incurred by road users.
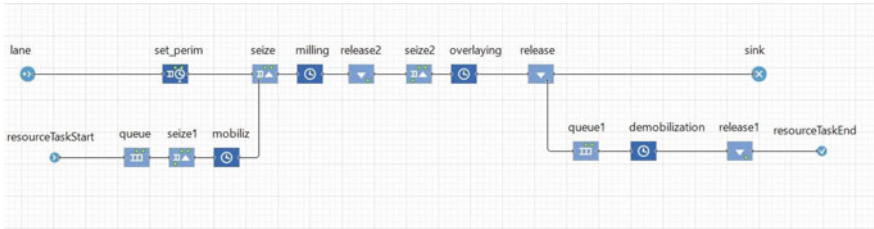
**Fig. 1** Construction model logic

## 2 Simulation Models

### 2.1 Construction Model

The construction model is a generic model that is made up of five activities. These activities are setting a perimeter, mobilization of workers and equipment, milling the damaged asphalt layer, overlaying the new asphalt layer, and finally demobilization of the worksite (Fig. 1).

The construction model uses four resource pools. These pools are trucks, a paver machine, road milling equipment, and foreman.

### 2.2 Traffic Model

The traffic model is a generic model that represents a stretch of road that is 1000 m long. The road is made up of four lanes, each lane is 3.5 m wide. The model allows the user to input the average daily traffic, road speed, the dimensions of the car, the type of car, and maximum and minimum deceleration. The traffic model assumes equal lane utilization for passing cars (Fig. 2).

Discrete event simulations are commonly used to analyze queuing problems by mimicking how real complex systems operate and includes variability, interactions,
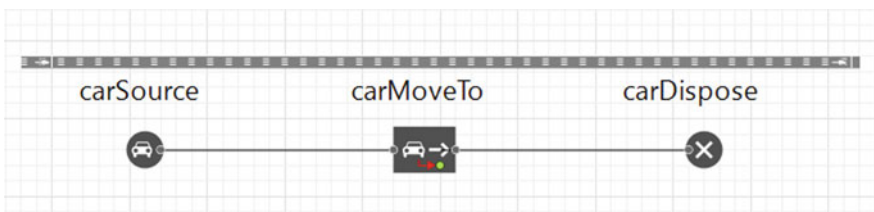


**Fig. 2** Traffic model logic

and dependencies of the real system. This type of simulation makes the process of modeling queues and related delays fairly easy.

## 3   Case Study

### 3.1   Scenario A

Scenario A represents the normal traffic conditions on a certain road. The data for this scenario is obtained from an actual road which is Interstate-66 in Fairfax County, Virginia, USA. The data for this road will be used as the baseline to compare the results of the different scenarios. The average daily traffic on the road is 90,000 cars. The traffic volumes of the model vary depending on the time of day representing peak hours and off-peak hours (Fig. 3).

The maximum speed in the model is 60 km/h, but depending on the time of day this speed limit may vary. During peak hours, the speed of road users starts to slow down due to road congestion. The speed of road users starts to pick up again during off-peak hours (Fig. 4).

It takes a car an average time of 73.89 s in the model to cross this road in normal traffic conditions. The data from this scenario (see Table 1) will be used as a baseline line against which the other scenarios will be compared, to determine the delay time for road users. The difference between the average time it took a car to pass the road at a given hour and the average time in normal traffic conditions is the delay time at this hour.
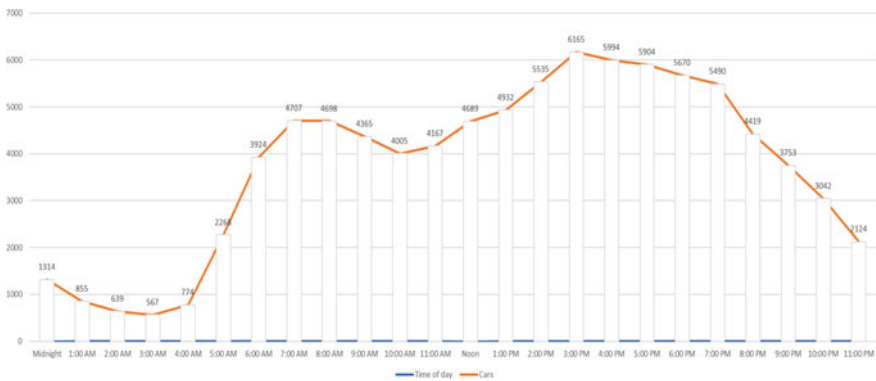


**Fig. 3**  Traffic distribution throughout the day
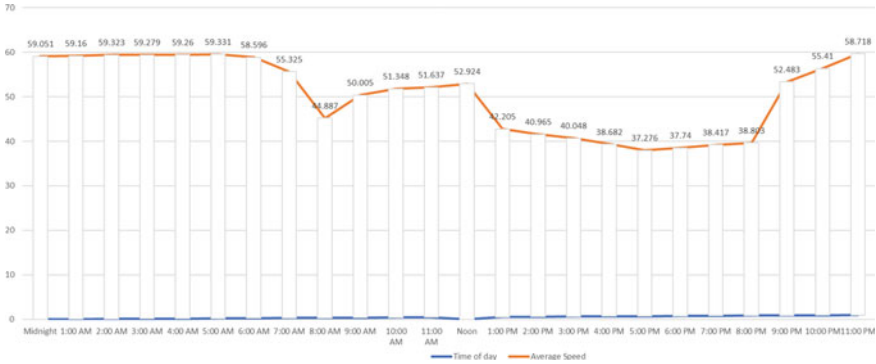
**Fig. 4** Average car speed distribution throughout the day

## 3.2 Scenario B

Scenario B represents a road rehabilitation project for a 380-m section of the road that covers the four lanes. The contractor may choose one of three strategies. The first strategy is to close off the entire length of the work zone for one lane and after finishing, move on to the other lane, and so on. The second str ategy is to close off two lanes of the road for the entire length of the work zone, finish them, and move on to the other two lanes. The third strategy is to close off three lanes for the entire length of the work zone, finish them, and move on to the last lane. It is assumed that the work is around the clock which means that the contractor is working 24 h till the project is completed (Figs. 5, 6 and 7).

The construction model is then run to get the project duration, in order to determine the simulation time for the traffic model. The durations for each activity and the number of resources are entered by the user and the model is left to run. The data used for the construction model are assumed. The traffic model is then left to run for the duration of each construction model to determine the traffic conditions in each scenario. The total project duration in Table 2 represents the time taken to finish the project in days using a certain strategy. The resources used for each construction model can be seen in Table 3.

After the runs are executed, we mainly get the average speeds of the passing cars throughout the day, the average times it takes a single car to pass the road throughout the day and the total delay incurred by the road user throughout the project. As we can see from Fig. 8, the average traffic speed falls precipitously for the 3-lane closure scenario followed by the 2-lane closure scenario and finally the 1-lane closure scenario. These trends continue throughout the total project duration, which gives a preliminary insight into the state of average traffic speed depending on the scenario. The average times that a car takes to cross the road is then obtained from the simulation runs and compared with the normal traffic conditions. The most delay happens in 3-lane closure scenario which suffers significantly from the suspension of 75% of the road capacity for a little over 5 days. The average daily delay for this

**Table 1** Time it takes to pass the road (seconds)

| Midnight 1:00 AM | 2:00 AM | 3:00 AM | 4:00 AM | 5:00 AM | 6:00 AM | 7:00 AM | 8:00 AM | 9:00 AM | 10:00 AM | 11:00 AM |
|---|---|---|---|---|---|---|---|---|---|---|
| 60.922 | 60.736 | 60.707 | 60.695 | 61.56 | 67.441 | 78.385 | 76.425 | 70.275 | 68.18 | 70.305 |
| Noon | 1:00 PM | 2:00 PM | 3:00 PM | 4:00 PM | 5:00 PM | 6:00 PM | 7:00 PM | 8:00 PM | 9:00 PM | 10:00 PM | 11:00 PM |
| 77.736 | 80.532 | 88.261 | 97.699 | 92.463 | 93.569 | 94.187 | 90.12 | 72.125 | 66.414 | 62.72 | 61.393 |

**Fig. 5** 1-lane closure



**Fig. 6** 2-lane closures



**Fig. 7** 3-lane closures

**Table 2** Activities durations (days)

| Activities | 1-lane closure | 2-lane closure | 3-lane closure + 1-lane closure | |
|---|---|---|---|---|
| Set perimeter | 0.15 | 0.3 | 0.5 | 0.1 |
| Mobilization | 0.3 | 0.5 | 0.7 | 0.1 |
| Milling | 1 | 1 | 1 | 1 |
| Overlaying | 1 | 2 | 2 | 1 |
| Demobilization | 0.4 | 0.6 | 0.8 | 0.5 |
| Total project duration | 7 | 8 | 8 | |

scenario is 9 min per car a day. The second most delay happens in the 2-lane closure scenario, where 50% of the road capacity is suspended for 4 days. The average daily delay for this scenario is 2.5 min per car a day. The scenario with least delay is 1-lane closure where only 25% of the road capacity is suspended for less than 2 days. The average daily delay for this scenario is less than a minute per car a day. The results for the delay are shown in Fig. 9.

Finally, from the obtained data we can determine the total delay time throughout the project duration. The results follow the same trends obtained from the previous metrics. The most delay occurs in the 3-lane closure scenario, followed by the 2-lane closure scenario, and finally, the least delay occurring in the 1-lane closure scenario.

**Table 3** Number of resources

| Resources | 1-lane closure | 2-lane closure | 3-lane closure + 1-lane closure | |
|---|---|---|---|---|
| Trucks | 4 | 6 | 8 | 3 |
| Paver | 1 | 2 | 3 | 1 |
| Milling machine | 1 | 2 | 3 | 2 |
| Foremen | 6 | 10 | 12 | 4 |
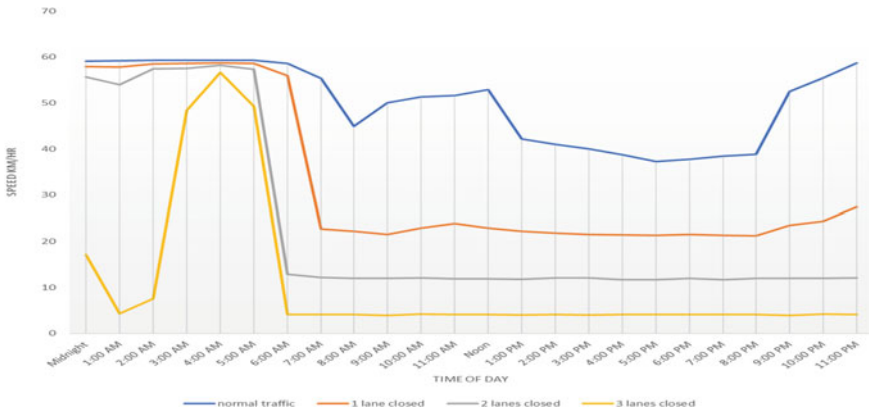
**Fig. 8** Average speed throughout the day
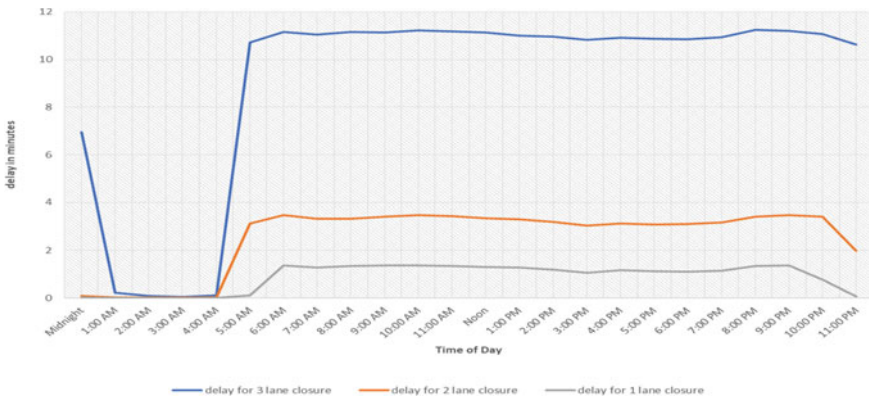


**Fig. 9** Average delay throughout the day

The results showing the cumulative delay time through the project duration are shown in Fig. 10.

We can see from Fig. 10 that the 3-lane closure scenario and 2-lane closure scenario take the same time. This is due to the longer time it takes to set the perimeter of a bigger work zone, and the longer time it takes to mobilize more resources for the 2-lane closure scenario compared with the 1-lane closure scenario. This leads to a longer duration in contrary to the common-sense assumption that the 2-lane closure scenario would finish earlier than the 3-lane closure scenario. The strategy chosen for such a project will depend on the nature of the road. If it is a critical road where there is heavy traffic and we do not want to cause a lot of disruption, it is best we choose either a 1-lane closure or 2-lane closure scenario. If the road is a non-critical road, we may choose either the 3-lane closure or the 2-lane closure scenario.
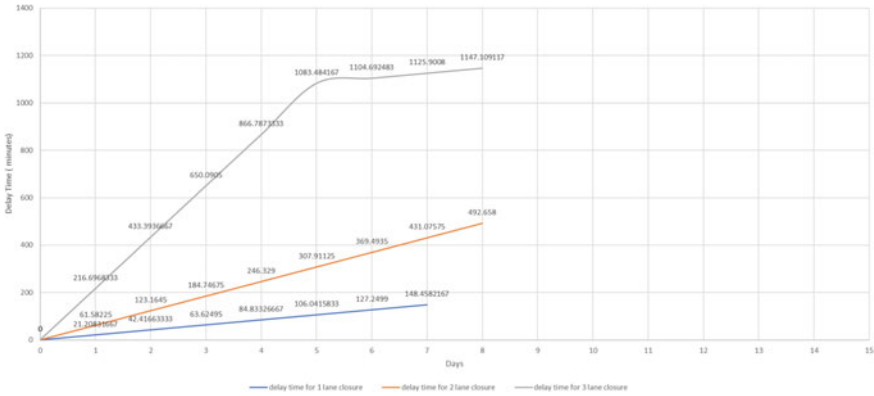
**Fig. 10** Delay time versus project duration

## 3.3 Scenario C

Scenario C represents a road rehabilitation project for a 380-m section of the road that covers 1-lane of a 4-lane road. The contractor may choose one of two strategies. The first strategy is to close off the entire length of the work zone for the lane or to divide the lane into four segments, each segment of length 95 m. It is assumed that the work is around the clock, which means that the contractor is working 24 h till the project is completed (Figs. 11 and 12).

The construction model is then run to get the project duration in order to determine the simulation time for the traffic model. The durations for each activity and the number of resources is entered by the user and the model is left to run. The data used for the 1-lane closure is the same as in Table 2. It took 3 days to finish the lane. The data used for the 1-segment closure construction model are assumed based on historical data for similar projects. The traffic model is then left to run for the duration of each construction model to determine the traffic conditions in each scenario. The total project duration in Table 4 represents the time taken to finish the project in hours using segmentation. The resources used for this method can be seen in Table 5.

It took the model 96 simulation run hours to finish the project which translates to 4 days of work. After the runs are executed, we obtained the average speeds of the passing cars throughout the day, the average time it takes a single car to pass the road throughout the day, and the total delay incurred by the road user throughout



**Fig. 11** 1-lane closure



**Fig. 12** 1-segment closure

**Table 4** Activities durations (hours)

| Activities | 1-segment closure |
|---|---|
| Set perimeter | 1 |
| Mobilization | 1 |
| Milling | 2.5 |
| Overlaying | 3 |
| Demobilization | 1 |
| Total project duration | 96 |

**Table 5** Number of resources

| Resources | 1-segment closure |
|---|---|
| Trucks paver | 3 |
| Milling machine | 1 |
| Foremen | 2 |
| Trucks paver | 4 |

the project. As we can see from Fig. 13, the average traffic speed fluctuates ever so slightly between the two scenarios. The only major change in average speed happens from 9 pm to midnight, where we see the traffic picking up speed again for the 1-segment scenario. This occurs due to lighter traffic flow in the later hours of the day. The delay times also do not differ significantly from each other. The average delay time for the 1-lane closure scenario is a little less than a minute while the 1-segment closure is a little over a minute. The results of the delay are shown in Fig. 14.
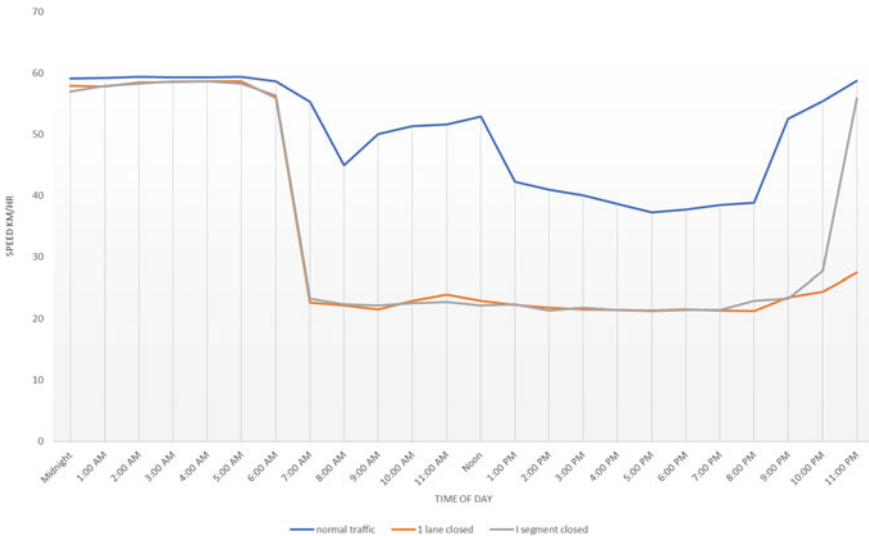


**Fig. 13** Average speed throughout the day
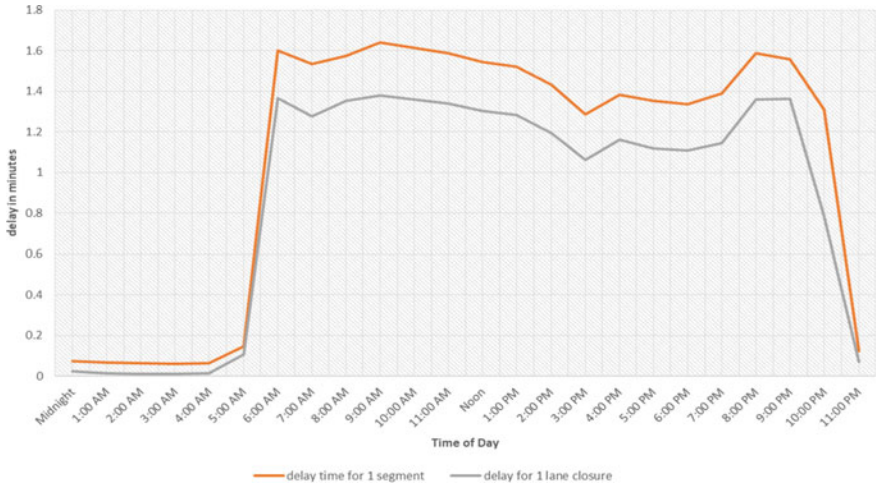
**Fig. 14** Average delay throughout the day

The results follow the same trends obtained from the previous metrics, where the most delay happens in the 1-segment closure scenario compared with the 1-lane closure scenario. The results showing the cumulative delay time through the project duration are shown in Fig. 15.

Because it takes the 1-segment scenario 1 day longer to finish the lane, the road user incurs an additional 25 min of delay, bringing the total delay 103.4 min for the entirety of the project. This is compared with only 63.62 min for closing the entire lane. The additional delay that happens in the 1-segment scenario compared with the 1-lane scenario is because of the constant moving of resources, setting a new work zone, and demobilizing from one segment to another.
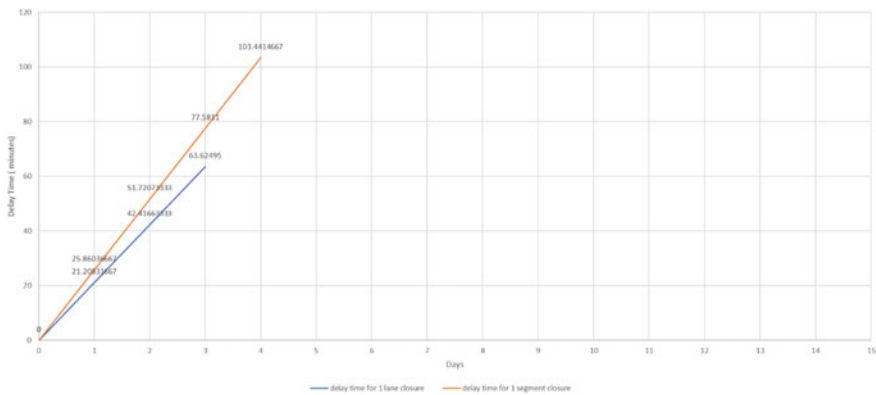


**Fig. 15** Delay time versus project duration

## 3.4 Scenario D

Scenario D represents a road rehabilitation project for a 380-m section of the road that covers 1-lane of a 4-lane road. The contractor may choose one of two strategies. The first strategy is to close off the entire length of the work zone for the lane where it is assumed that the contractor is working 24 h till the project is completed. The second strategy is to divide the lane into four segments, each length 95 m. The contractor then works on the segment during off-peak hours from 9 pm to 5 am. They employ more advanced equipment that gives them higher productivity rates, allowing them to finish the segment in 8 h. The road shape is the same as in Figs. 11 and 12. The duration of the 1-lane closure is 3 days, the same as in scenario C. The durations for each activity and the number of resources are entered by the user and the model is left to run. The data used for working off-peak hours' construction model are assumed based on historical data for similar projects. The traffic model is then left to run for the duration of each construction model to determine the traffic conditions in each scenario. The total project duration in Table 6 represents the time taken to finish the project working off-peak hours. The resources used for this method can be seen in Table 7.

It took the model 32 simulation run hours to finish the project. These 32 h are not continuous, meaning that each segment took approximately 8 h to finish, which translates to 4 days of work. After the runs are executed, we obtained the average speeds of the passing cars throughout the day, the average times it takes a single car to pass the road throughout the day and the total delay incurred by the road user throughout the project. As we can see from Fig. 16, the average traffic speed is practically the same as in normal traffic. It decreases starting at 9 pm when work commences and picks up after midnight as heavy traffic dissipates. Then it returns to

**Table 6** Activities duration (hours)

| Activities | 1-lane closure |
|---|---|
| Set perimeter | 1 |
| Mobilization | 1 |
| Milling | 2.5 |
| Overlaying | 3 |
| Demobilization | 1 |
| Total project duration (lane) | 32 |

**Table 7** Number of resources

| Resources | 1-segment closure |
|---|---|
| Trucks | 4 |
| Paver | 1 |
| Milling machine | 1 |
| Foremen | 5 |

the levels of the normal traffic speed after 5 am. The only major change in average speed happens from 9 pm to midnight. These average speeds are significantly better than the 1-lane closure scenario. The delay times also do not differ significantly from the normal traffic conditions. The average delay time for the 1-lane closure scenario is a little less than a minute while the off-peak hours' scenario is less than 10 s. The results of the delay are shown in Fig. 17.
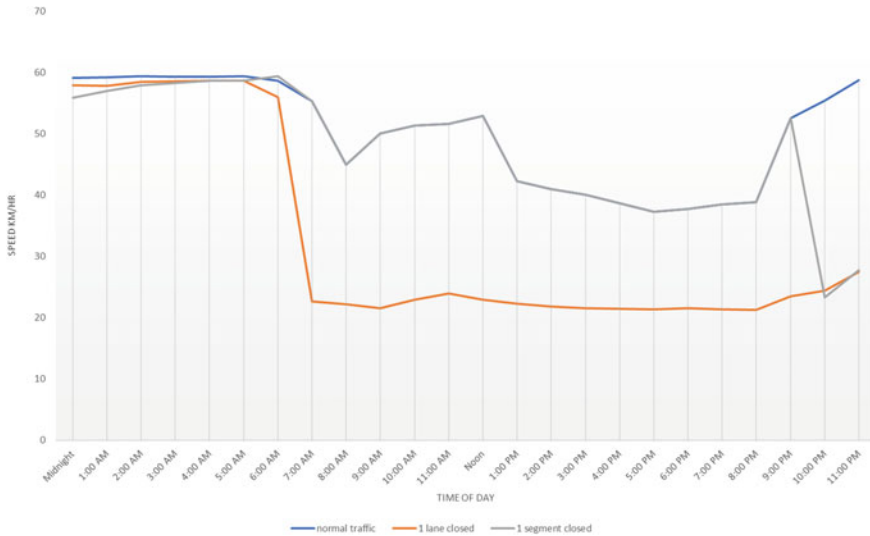


**Fig. 16** Average speed throughout the day
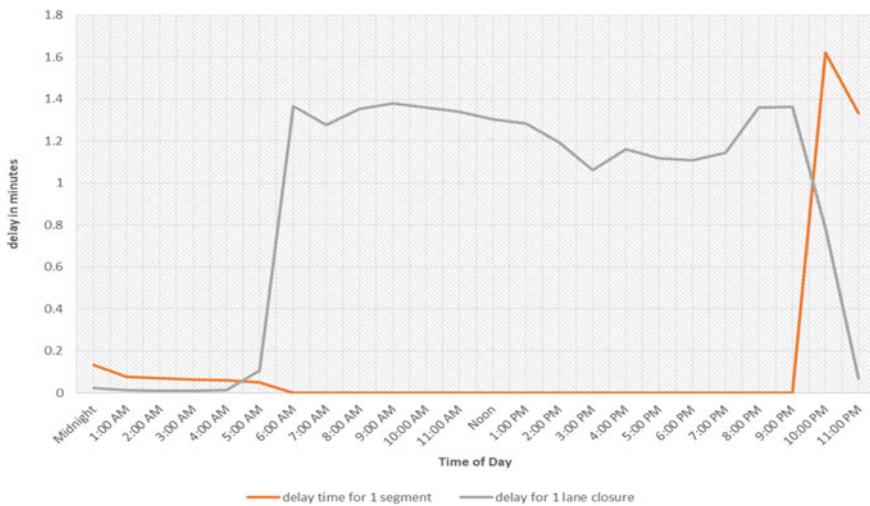


**Fig. 17** Average delay throughout the day
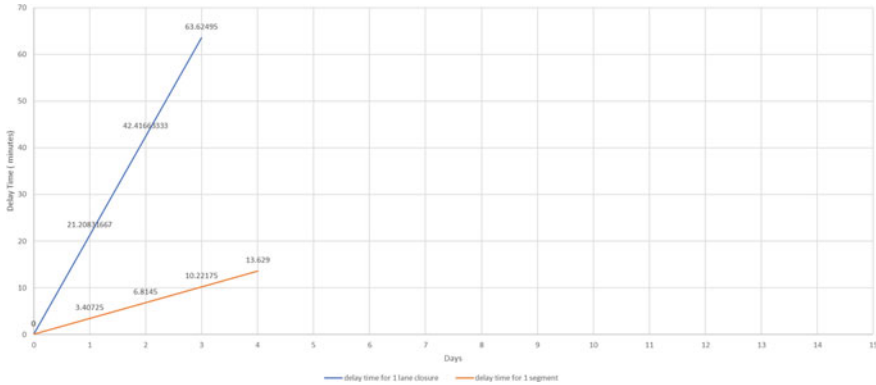
**Fig. 18** Delay time versus project duration

The results showing the cumulative delay time through the project duration are shown in Fig. 18.

These results show that even though the off-peak hours' approach took a day longer, the savings in delay time offsets the extra day. This approach would cost the contractors more money since they used more advanced and expensive equipment. This strategy would definitely be of benefit when a major road with high volumes of traffic needs rehabilitation with minimum disruption.

## 4 Conclusion

This study utilized a discrete event simulation approach to find the delay time caused by different road rehabilitation scenarios. The results obtained from the four scenarios are important in deciding the construction strategy for certain road rehabilitation projects, and how it affects road traffic. The traffic generic model is used to provide a great degree of flexibility to the user depending on the road conditions and the traffic characteristics of that road. The construction generic model logic can be modified to better resemble a certain constructing process. In addition, it allows the user to input the appropriate durations for the corresponding activities and the type and number of resources used.

This study can be improved for future work by, for example, better integrating the construction model and the traffic model. The construction model was run independently from the traffic model to determine the construction duration and then the traffic model was left to run for that duration to determine the traffic conditions for any given scenario. Also, the construction model looked into one type of rehabilitation that requires milling and overlying, future work should include an inspection activity that determines the type of damage and choose the appropriate way of dealing with it. Moreover, the study only looked at the delay time incurred by the road user; future

studies can also include the road user cost and lost economic output. In addition, the construction model only gave us the project duration; future studies can include the cost of the entire operation to give us a more holistic overview of a certain strategy. Furthermore, the traffic model characteristics can be expanded to include, for example, a two-way road, include different types of vehicles as opposed to only cars, and add intersections to the road.

Finally, this study provides a simple and straightforward approach to get the delay time caused by road rehabilitation projects, and how we can minimize it by choosing the appropriate construction strategy that satisfies the project conditions.

# References

1. Astarita V, Giofrè VP, Guido G, Festa DC (2014) Traffic delays estimation in two-lane highway reconstruction. Procedia Comput Sci 32:331–38. https://doi.org/10.1016/j.procs.2014.05.432
2. Dolama MG et al (2020) Probabilistic methodology to quantify user delay costs for urban arterial work zones. J Transp Eng Part A Syst 146(9):04020091. https://doi.org/10.1061/JTE PBS.0000424
3. Hassan MM, Gruber S (2008) Simulation of concrete paving operations on interstate-74. J Constr Eng Manage 134(1):2–9. https://doi.org/10.1061/(ASCE)0733-9364(2008)134:1(2)
4. Kalimanto D, Hadiwardoyo SP (2019) Impact of road rehabilitation zone on travel time to road user cost. IOP Conf Ser Mater Sci Eng 673(1):012114. https://doi.org/10.1088/1757-899X/673/1/012114
5. Lee E-B, Ibbs CW (2005) Computer simulation model: construction analysis for pavement rehabilitation strategies. J Constr Eng Manage 131(4):449–58. https://doi.org/10.1061/(ASCE)0733-9364(2005)131:4(449)
6. Lu M (2003) Simplified discrete-event simulation approach for construction simulation. J Constr Eng Manage 129(5):537–546. https://doi.org/10.1061/(ASCE)0733-9364(2003)129:5(537)
7. Orabi W, El-Rayes K (2012) Optimizing the rehabilitation efforts of aging transportation networks. J Constr Eng Manage 138(4):529–39. https://doi.org/10.1061/(ASCE)CO.1943-7862.0000445
8. Pasha A et al (2021) Evaluation of work zone road user cost of pavements based on rehabilitation strategy approach. J Transp Eng Part B Pavements 147(2):04021015. https://doi.org/10.1061/JPEODX.0000268
9. Zuniga-Garcia N et al (2021) Estimation of road user costs for work zones in data-limited or time-constrained environments. J Constr Eng Manage 147(3):04020182. https://doi.org/10.1061/(ASCE)CO.1943-7862.0001987
10. Work zone road user costs—concepts and applications: Chapter 5. Case studies—FHWA office of operations. Accessed 20 Dec 2021. https://ops.fhwa.dot.gov/wz/resources/publications/fhwahop12005/sec5.htm

# Performance Evaluation of Turbo and Double-Lane Roundabouts

**Roua Alkadi and Said M. Easa**

**Abstract** This paper aims to compare and evaluate turbo (TB) and double-lane (DL) roundabouts. The two types of roundabouts have many similarities and some differences. Thus, engineers are facing difficulty deciding which design is more effective. This paper evaluates both roundabouts regarding safety, performance, pollution, directional split, level of service, and capacity. The TB roundabout has fewer conflict points than the DL roundabout. The results show that the TB roundabout provides more capacity when the right-turn movement from the minor entries is high. Otherwise, DL and TB roundabouts perform similarly. The TB roundabout is the best design for reducing local pollution levels. However, if the aim is to reduce $CO_2$ and $NO_x$ specifically, the DL roundabout is better. Furthermore, there are various parameters to evaluate the effectiveness of DL and TB roundabout designs, such as stopping sight distance, intersection sight distance, and the fastest path. The approaching speed for DL and TB roundabouts is 25 mph (40 km/h) and 20 mph (32 km/h), respectively. The minimum sight distance to approach the crosswalk and stop safely for DL and TB roundabouts is 152 ft (46 m) and 112 ft (34 m), respectively, indicating that the TB roundabout is a safer design. Nonetheless, the minimum entering sight line distance is larger in TB than DL for intersection sight distance, 197.2 ft (60 m) and 151.7 ft (46 m), respectively.

**Keywords** Turbo-roundabout · Double-lane roundabout · Conflict points · Directional split performance · Safety · Pollution · Multi-objective model

R. Alkadi
Civil Engineering, Tetra Land Services, Houston, USA
e-mail: roualkadi0@gmail.com

S. M. Easa (✉)
Department of Civil Engineering, Toronto Metropolitan University, Toronto, Canada
e-mail: seasa@torontomu.ca

# 1  Introduction

Roundabouts are safer and reduce pollution, cost, and delay than a traffic signal. However, there are numerous roundabouts, such as single-lane, double-lane (DL), and turbo (TB) roundabouts. The traffic flow should be balanced to convert a traffic signal intersection into a roundabout, and site constraints permit the installation of roundabouts. Roundabouts have more advantages than traffic signals. In terms of safety, intersections converted to roundabouts showed a 39% reduction in overall vehicle crashes and a reduction in fatal collisions by 89% because roundabouts have fewer conflict points, and roundabouts eliminate cross-conflict points that cause the most dangerous collisions. Due to the fewer conflict points, roundabouts have higher safety performance [11]. For environmental benefit, roundabouts reduce carbon monoxide emission by 21–42%, fuel consumption by 30%, nitrous oxide by 6.36%, and hydrocarbons by 26.05%.

Regarding reducing delays during peak hours, roundabouts reduce the delay by 75% and vehicle stop by 52%. Lowering the cost of the design depends on the site. Still, usually, roundabouts reduce electricity costs by $3000 per year and maintenance by $13,000 compared with traffic intersections [2].

This paper focuses on the differences between DL and TB roundabout designs and specifies which cases TB roundabout would provide a more suitable design solution. DL and TB roundabouts are similar since the design of both roundabouts includes two entry lanes per approach, which offers more capacity and flexibility to the driver. The TB roundabout is safer than the DL roundabout since it directs the driver to the desired lane, which avoids weaving into traffic to switch lanes, and it does not confuse drivers who are less experienced. The operational performance between DL and TB roundabouts is based on the arrival of the circulating stream and entry capacity models. We can conclude that DL and TB roundabouts operate below capacity during all testing periods. Both roundabouts have many similarities since both have the same maximum travel time per vehicle, 36 s.

# 2  Comparing Operation and Efficiency

*Safety*: The TB roundabout has been designed to improve the DL roundabout in terms of safety without changing the level of efficiency [16]. Although entering flows must prioritize the circulating flows, the TB roundabout modifies the conflicting flow between entering and circulating flows [3]. It is recommended not to use lane marking because it is considered misleading and gives a "false sense of security" when circulating the roundabout. Therefore, TB roundabouts are safer than DL roundabouts because the raised splitters direct the drivers to the correct lane with a smaller radius and lower speed. Moreover, the curved paths force the drivers to merge into physically separated lanes. The TB roundabout has fewer conflicts than the DL roundabout due to the high angle between the entry and circulating paths [5]. The DL roundabout

(a) DL roundabout          (b) TB roundabout
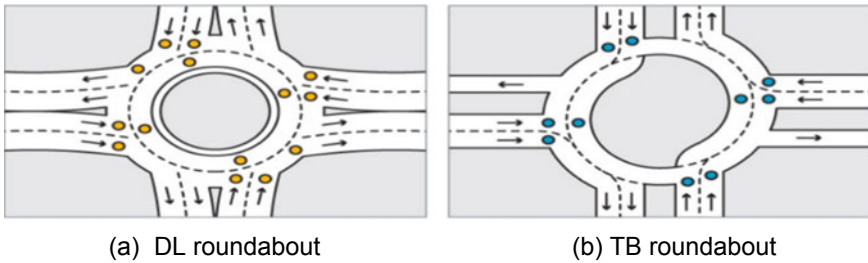
**Fig. 1** Conflict points in DL and TB roundabouts [6]

has 16 conflicts points, while the TB roundabout has 14 conflict points [1]. The safety performance calculations are related to the operating speed, which is affected by the geometry of the roundabout. Controlling the speed is a significant factor that affects safety, given that the average speed/approach is the average of the entry, circulating, and exit speeds [11].

Microsimulation models implementing VISSIM have been used to test the safety performance of the DL and TB roundabouts for the same site traffic operation in Bogota. Both models included the same traffic demand and conflicts, and surrogates were treated as clusters. The results demonstrated that the total number of conflicts in TB was 72% less than in the DL roundabout. The conflicts in the TB roundabout are grouped in a single cluster because they are related to a pattern of driving behavior. On the other hand, the DL roundabout has a massive scattering since conflicts can occur differently. Therefore, three-dimensional graphical analysis illustrated that TB is a safer design and reduces collisions by 80% [21]. Figure 1 compares the conflict points of DL and TB roundabouts.

*Pollution emission*: To reduce demand conditions, the TB roundabout leads to more decline in CO, $CO_2$, and PM (particle matter) emissions. However, suppose there is a high flow of right-turning movement, then the emission will increase. In that case, the TB roundabout tends to increase the emission of HC and $NO_x$ in comparison with the DL roundabout. If installing the TB roundabout is to reduce $CO_2$ and $NO_x$, the DL roundabout is a better choice. However, to reduce local pollution such as CO and HC, the TB roundabout offers a better solution [5].

*Performance*: Performance depends on flows at major and minor entries. Based on Fig. 2, legs 2 and 4 are significant entries, and legs 1 and 3 are minor entries [3]. TB roundabout provides more capacity when drivers turning right are above 60%. TB and DL roundabouts operate below capacity during all the testing periods because both have two entry lanes per approach, which offers more capacity and flexibility to the driver. Operation performance between the basic TB and DL roundabouts is based on the arrival of the circulating stream and entry capacity models [5].

*Level of Service*: The level of service (LOS) is estimated based on time delays in maneuvers, which occur when waiting phenomena happen to a non-prioritized traffic stream encountering a priority traffic stream. Thus, LOS depends on queue and delay evaluation. Heuristic models for time-dependent queues allow us to analyze different

(a) TB roundabout                                      (b) DL roundabout

**Fig. 2** TB and DL roundabouts [3]

situations, stationary and non-stationary, using coordinate transformation methods. Understanding capacity reflects on the queue discharge rate. Based on the entrance capacity, intersection performance, queue length, delays, and LOS are calculated [7]. The conversion between DL and TB roundabouts demonstrates a dramatic decrease in queue lengths. For the busiest peak-hour approach, the improvement in delay was 90%, while for the minor approaches, the improvement was 64%. In the case of unbalanced flow patterns, the TB roundabout provides the most suitable solution [22].

*Capacity*: According to [8], DL roundabout configuration suggested to use $ne = 1.14$; $T_f = 2.5$ s; $T_c = 4.3$ s and for a large DL roundabout to use: $ne = 1.6$; $T_f = 3$ s; $T_c = 4.1$ s. Vehicles coming from the right entry lane will only interact with outer circulating steam. But, entering vehicles coming from the left entry lane have to get into the inner circulating steam. Capacity at TB roundabout, based on [9], entry lane capacity is obtained as minor stream capacity. It will help evaluate both designs in terms of operational performance by comparing major entries and minor entries. According to [10], the gap acceptance values are taken from an existing turbo-roundabout design in the Netherland.

## 3   Comparing Directional Split Performance

Two traffic cases have been used to evaluate the directional split movement [3]. Each case has a balanced origin/destination matrix. The cases are:

Case (a): The DL roundabout performs better than the TB roundabout when entering flow from the major roads ranges from low to medium, and the entering flow from minor roads is high.

Case (b): The TB roundabout performs better than the DL roundabout when the left and right-turn movements from the minor to the major entries are prevailing from and to the minor entries. Thus, the TB roundabout operating advantages will shorter the delay.

Both DL and TB roundabouts perform similarly when traffic flow ranges from low–medium values.

The Hagring model allows the evaluation of entry capacity at the TB roundabout. It assumes a Cowan's M3 headway distribution in each conflicting stream along the circulating lanes where bunched vehicles can cause a drastic reduction in entry capacity when conflicting flow increases [3]. The TB roundabout can offer more capacity than the DL roundabout if the right-turn traffic from minor entries is high, which is not common. If right-turning traffic is usually less than left-turning traffic, then the DL roundabout will function with the same capacity as a TB roundabout. Therefore, installing a TB roundabout must be done only when there is a major increase in traffic flow or split. Otherwise, the same level of congestion will be maintained, and no major effect on the actual delays. DL roundabout is a necessary alternative for a single-lane roundabout. Unless a maximum output capacity is needed, then TB roundabouts operate at a higher capacity than DL roundabouts when the right-turning movement at minor entries is abnormally high (above 60%) [5].

- DL roundabout is the least safe layout based on the number and severity of conflicts points (weaving and cut-in conflicts). TB roundabout has the least conflict points. However, in comparison to single-lane roundabout, the conflict points at TB roundabout are more dangerous due to the increased angle between entry and circulating trajectories [3, 5] .
- To reduce $CO_2$ and $NO_x$, the two-lane roundabout is a better choice. The TB roundabout offers an advantage in lowering local pollution [5].

## 4   Comparing the Design Process

Determining whether to design a DL or TB roundabout depends on the objective of the design criteria, such as maximum operational performance and safety level. Depending on the purpose, the design engineer is required to optimize size, location, and other additional vital details. Therefore, roundabout design is an iterative process where the engineer cannot follow a specific template [11]. Using the iterative process, engineers must assume basic geometric parameters' initial values and then check the performance using specific software tools. Nowadays, using a multi-objective optimization model will help engineers to determine the global optimal roundabout design [4]. The multi-objective model provides more efficient results and requires less effort than the iterative process. The multi-objective model minimizes vehicle collision, total delay, and vehicle emissions.

### 4.1 Establishing Multi-objective Model

1. The user will *input data* or constraints such as the traffic data (average annual daily traffic and turning movement), limitations based on the design, and site conditions.
2. The user can determine the weights for each objective, or the model can determine the optimal weights.
3. The model will specify the output data: the optimal geometric dimensions, *decision variables* such as exit width, entry width, approach half-width, circulatory width, effective flare length, entry radius, entry angle, and circle diameter [4].

The methodology involves the following steps:

1. Modeling capacity predicted operating speed and speed profile because the geometric features of a roundabout are related to speed, safety, and mobility.
2. Measuring the objectives (collisions, delays, and emissions).
3. Using Solver software, the output data are calculated [4].

The *Solver* software is a Microsoft Excel add-in program to find the optimal maximum or minimum value for the objective cell (using a formula or a mathematical equation that contains decision variables). It is subjected to constraints on the worksheet to achieve the model's objective. Therefore, we need variable, constrain, and objective cells [12].

### 4.2 Size and Design Criteria

The size of the vehicles using the facility dictates the size of the roundabout. Most roundabouts feature truck aprons to accommodate an extra paved surface and keep the actual circulatory roadway width narrow to maintain speed control [11].

Torus 6, design software, uses the sub-path method to generate the roundabout geometry, which minimizes the iterative cycle in the design process. The design included crosswalks, pedestrians, splitting islands, splitting island envelopes, and an immediate path. Finally, to ensure the design effectiveness, Torus allows the evaluation of the fastest path, sightline analysis, and vehicle movement where truck apron has been added based on vehicle design Busyo-AASHTO2018 [20].

### 4.3 Evaluating Design Criteria Using Torus Software

To check the performance of any roundabout before finalizing the design, it is critical to test the following: path alignment, the fastest path, sight distance, and angles of visibility [11]. Table 1 shows the design criteria that have been used in Torus 6 software, and Fig. 3 shows the final designs of the TB and DL roundabouts.

**Table 1** Different design guidelines in designing DL and TB roundabouts

| General design details | DL roundabout | TB roundabout |
|---|---|---|
| Design guidelines | NCHRP Report 672 Double-Lane WB-62 | Turbo-roundabout (Transoft Vehicle Envelope) |
| Central island location $(x, y)$ | (635.73, 426.74) | (637.10, 4228.54) |
| Circle diameter (ft) | 150 | 125 |
| Truck apron (ft) | N/A | 8.19 |
| Vehicle design | AASHTO 2011 (US) Bus-40 | AASHTO 2011 (US) Bus-40 |
| Number of legs and bypass | 4 legs and 0 bypass | 4 legs and 0 bypass |
| Total number of sight lines | 21 | 21 |



(a) DL roundabout          (b) TB roundabout
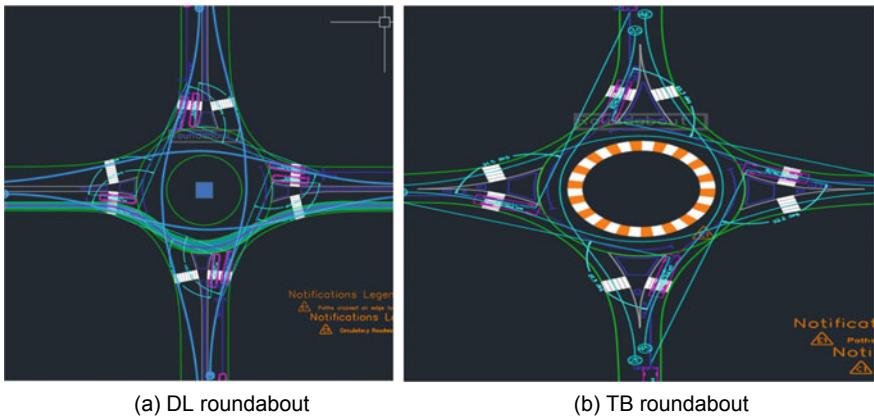
**Fig. 3** DL roundabout final designs of DL and TB roundabouts

*Path Alignment*: While drawing the natural vehicle path: [11]: (1) Drivers cannot change their direction or their direction instantaneously and (2) Consecutive curves should have a similar radius. Otherwise, the path must be adjusted if the radius of the second curve is smaller than the first curve. Using Torus, the approaching speed in a DL roundabout (14.58 mph) is lower than a TB roundabout (14.91 mph), with a minimum sight distance of 74.2 ft for both designs. Table 2 and Fig. 4 show a comparison of the path alignment radii of DL and TB roundabouts, where $R_1 =$ minimum radius on the fastest through the path, before the entrance line, $R_2 =$ minimum radius on the fastest through the path, $R_3 =$ minimum radius on the fastest through the path, into the exit line, $R_4 =$ minimum radius on the fastest through the path, on the conflicting left-turn movement, and $R_5 =$ minimum radius on the fastest through the path, on the right-turning vehicle movement.

*Fastest Path*: This is the fastest and smoothest path while ignoring lane marking and the absence of another traffic vehicle. To provide a safe speed through the natural path, we must ensure reasonable entry speeds [10]. The fastest path is influenced by

**Table 2** Path alignment evaluations (approach)

| Path alignment (ft) | Path description | DL roundabout | TB roundabout |
|---|---|---|---|
| $R_1$ | Entry path radius | 361.55 | 159.20 |
| $R_2$ | Circulating path radius | 164.91 | 80.54 |
| $R_3$ | Exit path radius | 537.33 | 185.33 |
| $R_4$ | Left-turn path radius | 46.48 | 49.20 |
| $R_5$ | Right-turn path radius | 157.01 | 139.69 |
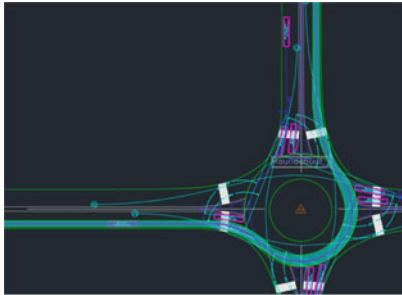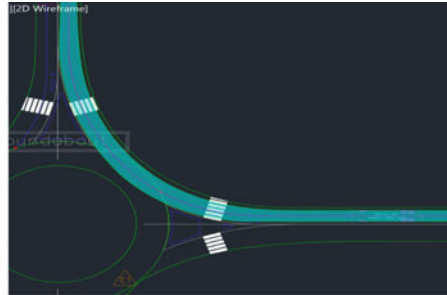


(c) DL roundabout          (d) TB roundabout

**Fig. 4** Path alignments for DL and TB roundabouts

multiple factors, such as each entry's geometry and approaching speed [11]. From Fig. 5 and Table 3, we can conclude that the TB roundabout speed is less than the DL roundabout, which shows that it is the safer design, especially on the main road the approaching speed on TB is lower than DL roundabout.

*Sight Distance*: Sight distance includes stopping sight distance and intersection sight distance, assuming that the driver's eye is 3.5 ft and object height is 2 ft [17]. *SSD* is the summation of two distances: the distance during perception and reaction time (2.5 s) and the distance to stop the vehicle [15]. *ISD* is the sight distance where the drivers need to visualize conflicting vehicles and safely have enough time to react to the acceptable gap [16]. It is achieved by establishing s*ight triangles* with legs that follow the curvature of the roadway [11]. From Tables 4 and 5, the stopping sight distance for TB is more minor than DL. The drivers have a higher probability of stopping safely. However, the minimum entering sightline and the minimum circulatory sight distances are larger in TB than in DL. Figure 6 illustrates the sight triangles used to establish ISD of both TB and DL designs.

*TB roundabout (ISD)*: Is calculated for a particularly critical time ($t_c$), which is the minimum time interval drivers in the approaching legs (minor road), and how ready to accept crossing or to enter the circulating traffic (major conflict zones) with an assumption of object height of 1.08 m. In both DL and TB roundabouts, the entering traffic yields for the circulating stream. Therefore, ISD is checked for conflicting circulating and entering vehicles to increase safety. However, providing extra ISD

(a) DL roundabout
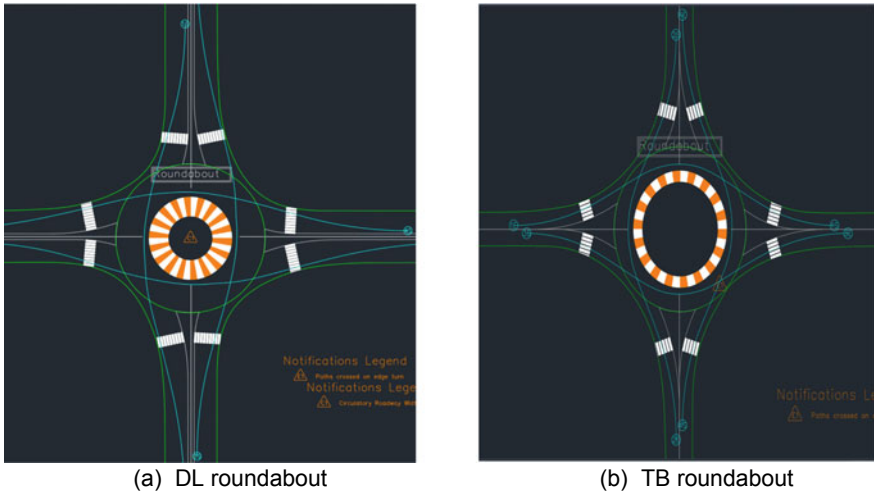
(b) TB roundabout

**Fig. 5** Fastest path alignment of DL and TB roundabouts

**Table 3** Fastest path results

| Approach 1 (mph) | DL roundabout | TB roundabout |
|---|---|---|
| $V_1$ | 33.44 | 24.59 |
| $V_{1o}$ | 30.50 | 26.13 |
| $V_2$ | 23.45 | 18.05 |
| $V_3$ | 38.66 | 26.03 |
| $V_{3o}$ | 34.82 | 30.28 |
| $V_4$ | 14.58 | 14.91 |
| $V_5$ | 24.47 | 23.45 |

**Table 4** Evaluating intersection sight distance of DL and TB roundabouts

| ISD | DL roundabout | TB roundabout |
|---|---|---|
| Distance to yield line (ft) | 50 | 49 |
| Critical gap (s) | 5.5 | 6.50 |
| Initial entering speed (mph) | 20.67 | 20.67 |
| Min entering sightline (ft) | 151.7 | 197.2 |
| Initial circulating speed (mph) | 15.37 | 15.77 |
| Min circulatory sight distance (ft) | 112.8 | 150.4 |

than the required value is not recommended because the drivers will increase their speed, automatically increasing the collision rate. Therefore, it is recommended to use landscaping techniques to restrict ISD to its required value [16].

**Table 5** Evaluating stopping sight distance of DL and TB roundabouts

| Element | DL roundabout | TB roundabout |
|---|---|---|
| *(a) SSD: approach to the crosswalk* | | |
| Approach speed (mph) | 25 | 20 |
| Min sight distance (ft) | 152.4 | 112.2 |
| *(b) SSD: yield line to the crosswalk* | | |
| Approach speed (mph) | 20.67 | 20.67 |
| Min sight distance (ft) | 117.3 | 117.3 |



(a) DL roundabout
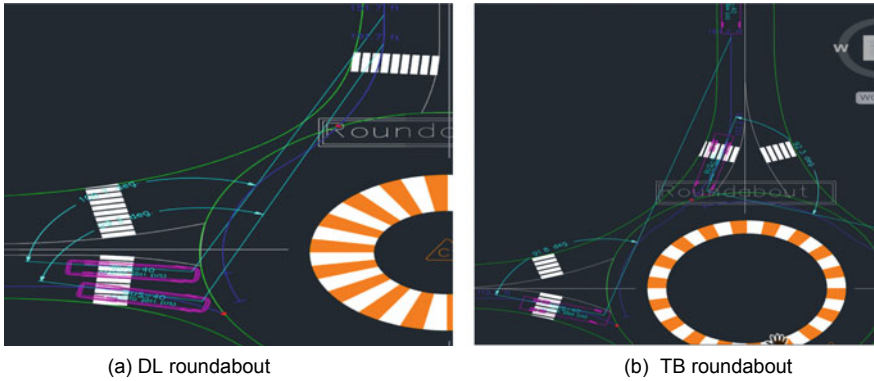
(b) TB roundabout

**Fig. 6** Intersection sight distance of DL and TB roundabout

*Angles of Visibility*: To allow drivers to turn their head to the left to view oncoming traffic from upstream; thus, the intersection angle between successive entries must be overly severe. Table 6 indicates that it is recommended to use 75° minimum intersection angle to accommodate old drivers and pedestrians (U.S. Dept. of Transportation, 2000).

**Table 6** Evaluating angles of visibility DL and TB roundabout

| Approach | Visibility angle (°) | |
|---|---|---|
| | DL roundabout | TB roundabout |
| 1 | 98.7 | 92.2 |
| 2 | 99.8 | 92.3 |
| 3 | 91.8 | 100.4 |
| 4 | 99.3 | 91.6 |

[*]Desired minimum angle of visibility: 75°

## 5 Discussion

In terms of safety, the TB roundabout is a safer design than the DL roundabout because the entering speed is lower, and it has less conflict points than DL. Moreover, DL is more confusing to new drivers because of the lane marking, while TB guides the drivers on which lane to use and eliminates cross-conflict points. Due to the severity of conflict points at DL such as weaving and cut-in conflict points, it is considered less safe than TB. Regarding pollution, the TB roundabout reduces local pollution emission when DL increases it. However, to decrease $CO_2$ and $NO_x$, the DL roundabout is the best alternative.

Both designs perform below capacity, but TB performs better when 60% of the split movement turns right. Therefore, TB provides more capacity when RT from minor turning traffic is high. Using Torus 6, it is more advisable to use a truck apron when designing the TB roundabout, especially if trucks or buses will be using the roundabout such as AASHTO 2011 (US) Bus-40. TB requires less stopping sight distance (SSD) than DL roundabout, especially when approaching the crosswalk. The minimum entering sight line distance is larger in TB than DL for intersection sight distance, 197.2 ft (60 m) and 151.7 ft (46 m), respectively. Therefore, we can conclude that TB is more suitable for a high volume of split traffic. Otherwise, both designs perform somehow similarly.

## 6 Overall Comparison

A summary of the overall performance of DL and TB roundabouts is presented in Table 7. The two roundabouts were compared concerning safety, pollution, operation, capacity, design guides, design vehicle, and sight distance in this table.

## 7 Conclusions

Roundabouts are safer than traffic signals since they have fewer conflict points. TB roundabout is safer than the DL roundabout because drivers are directed to the lane, avoiding weaving into traffic to cross from one street to another. However, when evaluating the performance of DL and TB roundabout, TB roundabout will provide an advantage when the flow of vehicles turning to the right is high. Otherwise, TB and DL roundabouts operate below capacity. Evaluating stopping sight distance, intersection sight distance, and fastest path using Torus 6 illustrates that a truck apron must be added if buses or trucks access TB roundabouts.

**Table 7** Overall performance comparison of DL and TB roundabouts

| Elements | DL roundabout | TB roundabout |
|---|---|---|
| Safety | • Lane marking confuses drivers<br>• Higher approaching speed and circulating radius<br>• Sixteen conflict points (more weaving and cut-in conflicts) | • Modifies the conflicting flow between entering and circulating streams<br>• Lower approaching speed and smaller circling radius<br>• Fourteen conflict points (avoids crossing conflicts) |
| Pollution emission | • Reduces $CO_2$ and $NO_x$ | • Declines CO, $CO_2$, and PM only when RT traffic is low<br>• Increases HC and $NO_x$ |
| Local pollution | • Increases CO, HC | • Reduces CO, HC |
| Operation | • Operates below capacity | • Operates below capacity<br>• 60% RT movement performs better |
| Capacity | • More capacity when RT traffic flow is less than LT traffic (standard case)<br>• Same level of congestion as TB when traffic split is medium–low<br>• Performs better when the O/D matrix is balanced | • More capacity when RT from minor turning traffic is abnormally high<br>• Actual delays significantly decrease when the traffic split increases<br>• Performs better when the O/D matrix is not balanced |
| Design guides | NCHRP Report 672 Double-Lane WB-62 | Turbo-roundabout (Transoft Vehicle Envelope) |
| Design vehicle | AASHTO 2011 (US) Bus-40 | AASHTO 2011 (US) Bus-40 |
| Truck apron (ft) | Not needed | 8.19 |
| Number of sightlines | 21 | 21 |
| Approaching speed | High approaching speed | Low approaching speed |
| ISD (ft): min entering sightline | 151.7 | 197.2 |
| min circulatory SD | 112.8 | 150.4 |
| SSD (ft): min distance to the approach crosswalk | 152.4 | 112.2 |
| Visibility angle (°) | 98.7 | 92.2 |

# References

1. Robinson BW, Rodegerdts L, Scarborough W, Kittelson W, Troutbeck R, Brilon W, Bondizo L, Courage K, Kyte M, Mason J, Flanney A, Myers E, Bunker J, Jacquemart G (2000) Roundabouts: an informational guide. FHWA. Publication No. FHWA-RD-00-067
2. Turner D (2011) Roundabouts: a literature review, Weblog. Rutgers University. 1–17. from: Daniel Turner | Urban Planning and Design | Online Portfolio (danielrturner.com). https://www.danielrturner.com/home/wp-content/uploads/2012/12/Roundabouts.pdf. Accessed on 9 Sept 2021

3. Giuffrè O, Granà A, Marino S (2012) Turbo-roundabouts vs roundabouts performance level. Procedia Soc Behav Sci 53:590–600
4. Ahmed H, Easa SM (2021) Multi-objective evaluation model of single-lane roundabouts. Transp Res Rec J Transp Res Board 2675(10):395–410
5. Vasconcelos L, Silva AB, Seco ÁM, Fernandes P, Coelho MC (2014) Turbo roundabouts. Transp Res Rec J Transp Res Board 2402(1):28–37
6. Kluiters J (2019) Turbo roundabout vs standard multi-lane roundabout. Transoft Solutions. https://www.transoftsolutions.com/emea/turbo-roundabout-vs-standard-multi-lane-roundabout/?setRegion=en. Accessed on 2 Dec 2022
7. San Mateo County (2005) Congestion Management Program, Traffic Level of service calculations, APPENDIX B. California. San Mateo. from http://ccag.ca.gov/programs/transportation-programs/congestion-management/. Accessed on 30 Jan 2022
8. Brilon W (2005) Roundabouts: a state of the art in Germany. In: Proceedings of the national roundabout conference. Vail, Colorado, US
9. Hagring O (1998) A further generalization of Tanner's formula. Transp Res Part B Methodol 32:423–429
10. Fortuijn LG (2009) Turbo roundabouts. Estimation of capacity. Transp Res Rec 2130:83–92
11. Colorado Department of Transportation (2018) Roadway to Design Guide. Chapter 19—Roundabout. From cdot-rdg-2018 (codot.gov). Accessed on 14 Feb 2022
12. Microsoft (2021) Define and solve a problem by using Solver. https://support.microsoft.com/en-us/office/define-and-solve-a-problem-by-using-solver-5d1a388f-079d-43ac-a7eb-f63e45925040#OfficeVersion=Windows. Accessed on 14 Oct 2021
15. Washington State Department of Transportation (2021) Design Manual WSDOT. Chapter 1260. http:// Design Manual | Manuals | WSDOT (wa.gov). Accessed on 19 Oct 2021
16. Salwan A, Easa SM, Raju N, Arkatkar S (2021) Intersection sight distance characteristics of turbo roundabouts. J Issue Cover. https://doi.org/10.3390/designs5010016
17. Rodegerdts L, Bansen J, Tiesler C, Myers E, Knudsen J (2012) NCHRP Report 672 Roundabouts. Transportation Research Board of the National Academies
18. U.S. Dept. of Transportation, Federal Highway Administration (2000) Geometric design. In: Roundabouts: an informational guide, pp 130–180
19. Brewer M, Chrysler S, Transportation Institute, T. A. M., Lindheimer T (2017) Strategies for effective roundabout approach speed reduction. Local Road Research Board, pp 1–100
20. Transoft Solutions (2020) Transoft Solutions. https://www.transoftsolutions.com/road-design/torus-roundabouts/. Accessed on 19 Feb 2022
21. Bulla-Cruz L, Barrera L (2016) Road safety assessment of a two-lane roundabout and a basic turbo-roundabout using microsimulation of traffic conflicts and analysis of surrogate measures by clusters and principal components. Research Gate. http://www.researchgate.net/publication/308982855_Road_safety_assessment_of_a_two-lane_roundabout_and_a_basic_turboroundabout_using_microsimulation_of_traffic_conflicts_and_analysis_of_surrogate_measures_by_clusters_and_principal_components
22. Gallelli V, Iuele T, Vaiana R (2014) Conversion of a semi-two lane roundabout into turbo roundabout: a safety analysis. ResearchGate, 1–9. https://www.researchgate.net/publication/266141762_Conversion_Of_A_Semi-Two_Lane_Roundabout_Into_Turbo_Roundabout_A_Safety_Analysis

# Transportation Specialty: Data, Analytics, and Technology

# Station Reallocation and Rebalancing Strategy for Bike-Sharing Systems: A Case Study of Washington DC

**Pedram Beigi, Michel Khoueiry, Mohammad Sadra Rajabi, and Samer Hamdar**

**Abstract** Bike-sharing is becoming increasingly popular as an urban traffic mode while increasing the affordability, flexibility, and reliability of interconnected public transportation systems (i.e., interconnected light rail, buses, micro-mobility, and ride-sharing modes of transportation). From the consumer's perspective, (1) finding a bike station in convenient locations where demand usually occurs and (2) the availability of bikes at rush hours with a lesser probability of encountering empty docks (for fixed-station bike-share systems) are two key concerns. Some stations are more likely to be empty or full, reflecting an imbalance in bike supply and demand. Accordingly, it is essential to understand a bike-share system's demand pattern to select the optimal locations and reallocate bikes to the right stations to increase the utilization rate and reduce the number of unserved customers (i.e., potential demand). The Capital Bikeshare in the Washington DC Metropolitan Area is one of the prominent bike-share systems in the USA—with more than 4300 bikes available at 654 stations across seven jurisdictions. This study provides a systematic analysis of a bike-sharing system's Capital Bikeshare system usage pattern. Our study intends to create an optimization strategy formulated as a deterministic integer programming for reallocating bike stations daily and rebalancing the bike supply system. From an operational perspective, such a strategy will allow overnight preparations to answer the rush-hour morning demand and during special events in Washington D.C.

**Keywords** Bike-sharing system · Rebalancing · Station reallocation · Optimization

P. Beigi (✉) · M. Khoueiry · M. S. Rajabi · S. Hamdar
Department of Civil and Environmental Engineering, The George Washington University, Washington, DC, USA
e-mail: beigi@gwu.edu

# 1 Introduction and Literature Review

Bicycling has had a revival as a popular form of transportation and pleasure due to the rising priority that modern society places on health and sustainability [7, 8]. Capital bike share is one of the prominent bike-sharing systems in the USA, with more than 4300 bikes available at 654 stations across seven jurisdictions.

When commuters face the usual last-mile difficulty, they confront when using just public transportation, they frequently opt for a motorized vehicle for the whole journey [1]. Bike-sharing systems (BSSs) are intended to solve the last-mile problem by encouraging people to take public transit rather than driving [18]. This should result in more people taking public transportation. At the same time, it allows individuals to opt to cycle during rush hour if buses and subways are crowded, so it can solve the overcapacity problem.

It has been shown that one of the keys to the success of bike-sharing programs is the location of bike stations and their relation to trip demand [12]. Todd et al. [20] described some of the variables that influence BSS usage and explained that the Number of Stations, Station Density, Station Capacity, and Distance to Station are the most important ones [9]. The placement of the station should be reliable and result in an acceptable total ride duration. Users prefer not to have to walk a long distance to drop off or pick up their bikes, but if there are too many stations close together, the cost of adding another station may outweigh the benefit of having that additional station [2]. Arriving at a station with no available bikes or docks is a vital concern to BSS implementers [13]. To better serve the users, policymakers should take note of this spatial mismatch trend and update the system setup accordingly [19]. The combination of station size and the defined maximum distance between stations and having a rebalancing strategy during day and night can reduce the likelihood of this issue [15].

Bryant [3] employed heuristic spatial analytic approaches to solve a modified version of the set coverage problem in the city of Richmond, Virginia, as the maximum covering location problem to find the best places for a BSS. The algorithm was used to find bike stations within a certain distance to cover the most high-demand sites on a transit network. Bryant's model employed an origin–destination analysis (based on Dijkstra's algorithm) to determine a suitable walking distance between stations after identifying all current bus stops as prospective station locations. In the end, around 400 m was decided.

Croci and Rossi [5] investigated the association between existing stations near points of interest and BSS usage, and they investigated the optimal relocation of present BSS stations in Milan using regression analysis results. Ma et al. [14] focused on the BSS's economic consequences based on station placements in Washington, D.C. [2] focus on maximizing the value of a BSS in the downtown Vancouver area by optimizing the placement of bike stations using data that provide pedestrian and bike traffic volumes and popular arrival and departure destinations.

Rybarczyk and Wu [17] and Larsen et al. [11] have utilized GIS-based multi-criteria analysis methods to assess bike infrastructure as well as estimate possible

demand distribution. García-Palomares et al. [8] have shown the possibilities for location-allocation models integrated with GIS and applied to bike-sharing stations in the city center of Madrid.

Kaviti et al. [10] studied the effect of price change and travel behavior, which led to the realization that some stations are overfitted while others are underfitted. They also found that when stations are at full capacity, users feel discomfort since they cannot safely park the bike, while if it is empty, users have to walk an additional distance in order to find a useable bike. Wergin and Buehler [21] were able to deduce that different stations act as both origins and destinations at different times of day, which led to the realization that bike stations cannot be modeled as static entities but as dynamic objects that have different aspects depending on the time of the day.

Generally, modeling the location-allocation problem for a BSS is done in two ways: either (a) determining which locations were the most acceptable based on the distribution of criteria such as population and public transit density or (b) creating a suitability map for locating the optimal locations utilizing optimization analyses such as asset or maximum covering problems. The first method aims to maximize the total number of people covered within a given radius by concentrating stations in areas with the highest potential demand. The second method allows station location to be maximized since it reduces the distance between supply and demand, resulting in a station distribution that is reasonably uniform over the whole area [8].

This study aims to identify a set of bike-share station locations that will maximize the value of a public bike-share system and solve an optimization problem for rebalancing strategy. A deterministic integer-programming model is utilized to identify an appropriate selection of station locations for a BSS. The model takes into account a variety of parameters, including demand, station size, as well as extra values for station sites in places with improved accessibility and convenience.

## 2 Methodology

### 2.1 Model Considerations

The Capital Bikeshare system in the DC region, which has 334 stations in 179 census tracts, is the subject of this study. Potential station locations must be selected as part of the data collection process. At this point, we assume that all the intersections in Washington, DC, are potential stations, and after finding optimal stations, we walk through the target area and manually classify the locations that could fit a bike-share station near that intersection. The present bike-sharing system's ridership was utilized as the demand of each census tract to add value to station sites. It is preferable to assign a demand based on pedestrian and bike data, which is not available for Washington DC.

Considering other indications like stations near cultural places, tourist attractions, parks, and city parks was also deemed desirable to fulfill the user. As a result, cycling

a) Demand Distribution          b) Net-drop-up Distribution          c) Net-pick-up Distribution
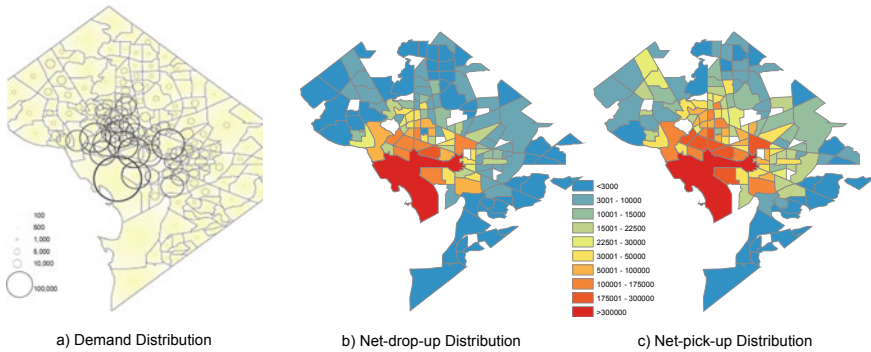
**Fig. 1** Bike demand distribution and balance distribution in District of Columbia

lanes, major tourism sites, popular locations, and subway stations were incorporated to better assess the value of each street for a potential BSS user. A station near bike lanes would be more valuable in terms of safety and convenience than a station on a typical street. Buck and Buehler [4] reveals a significant and positive relationship between bike lane supply near Capital Bikeshare stations and the number of trips originating from those stations.

The station density approach from previous successful studies such as New York City and Paris adheres to a density criterion of certain maximum and minimum distance between stations. Nair et al. [16] explain that Paris Vélib's docking stations are next to the Paris Metro stations and show most frequently utilized docking stations which are near transportation stops and services.

This model does not address station design and construction, bike-share equipment repair and maintenance, or determining bike rental pricing and payment methods. Our methodology focuses on identifying suitable station sites and their sizes. The tract demand distribution of the Capital Bikeshare system is presented in Fig. 1a, in which each dot represents bike where $D_j$ is defined as $\sum_{i \in j} \sum_k s_{pi} + s_{di}$, where $s_{pi}$ and $s_{di}$ represent the daily pick-up and drop-off frequency for station $i$ in tract $j$ in day $k$. Capital Bikeshare system, net drop-off/pick-up in each tract are presented in Figs. 1b and c, respectively.

## 2.2 Station Reallocation

The basic premise of our concept is that each potential station site has a corresponding value. The model sets a restricted number of stations to maximize the utility of the system, given specific limitations specifying where stations must or cannot be located (Table 1).

We assign location values by determining the demand and other relevant aspects of the target area. The features that we considered to add value to probable station

**Table 1** Parameters and variables

| Type | Name | Explanation |
|---|---|---|
| Binary variables | $x_i$ | Indicates whether a small-sized station is placed at location $i$ |
| Binary variables | $y_i$ | Indicates whether a medium-sized station is placed at location $i$ |
| Binary variables | $z_i$ | Indicates whether a large-sized station is placed at location $i$ |
| Sets | $P$ | Set of all potential locations |
| Sets | $F$ | Set of features that add value to locations |
| Variable | $N$ | Total number of stations to be placed |
| Variable | $M$ | Maximum number of medium stations |
| Variable | $L$ | Maximum number of large stations |

sites are included in list $F$. Each feature $f \in F$ has a value $v_f$ and is associated with a set of potential locations $P$. Demand distribution, bike lanes, protected bike lane, bike trail, bike shared lane, metro stations, and DC attractions are considered as features. Different size stations may be placed at each potential site in three sizes: small, medium, and large using three binary choice factors: $x_i$, $y_i$, and $z_i$. Furthermore, we verify that each potential site I has no more than one kind of station with $x_i + y_i + z_i \leq 1$ for potential locations $i$ and maximum number of stations has been considered as $\sum_{i \in P} x_i + y_i + z_i < N$, where $N$ is the maximum number of stations placed. The most convenient solution for bike-share users would be a bike station installed at every potential location. However, this is not economically feasible; thus, the total number of stations that may be installed is restricted.

There is a list of neighbors for each potential location $j$, $Dj$ contains all possible station locations within $m$ meters of j, and $\text{dist}(x_i, x_j) \geq \text{d}m$ guarantees that if a station is placed at j, the nearest station to $j$ is at least d$m$ away. Similarly, if a station is established at position $j$, we do not want another station to be placed close next to it. $\text{dist}(x_i, x_j) \leq \text{d}l$ replicates the reality that clustering many stations in a limited region would not compound value for bike-share users.

In order to give the model an incentive to place larger stations near high-value features, we multiply the value of a potential station location by $\alpha$ if a small station is used, by $\beta$ if a medium station is used, and by $\gamma$ if a large station is used, where $\alpha$, $\beta$, $\gamma$ represent the scale of stations with $\sum_{i \in P} z_i < L$ and $\sum_{i \in P} y_i < M$ that ensure the number of medium and large stations which are limited to $M$ and $L$. Therefore, our objective function is:

$$\text{Maximize} \sum_{i \in P} v_f (\alpha x_i + \beta y_i + \gamma z_i).$$

## 2.3 Rebalancing Strategy

This section aims to provide an optimization framework for the Capital Bikeshare Reorganizing System and to give the truck drivers an easy-to-follow schedule that outlines when and how to visit each station, as well as how many bikes they should pick up/deposit at each. We will do so while attempting to reduce operational costs, which mostly comprise petrol costs, which vary depending on the distance traveled. To put it another way, we want to reduce the truck's effective distance traveled while also reducing the number of times it visits each station. We are assuming a truck passes three times per day (11 AM to reset after morning rush and prepare for evening rush, 7 PM to reset after evening rush, and 3 AM to prepare for morning rush). On this basis, we divided our stations into two groups, one for Origins ($O$) and one for Destinations ($D$). The origin stations will be kept at 100% capacity in order to satisfy the biggest possible need, while the destination stations will be kept at 50% to accommodate for the small number of residents and miscellaneous trips while keeping empty docks so that people can safely deposit their bikes. The objective function is as follows while minimizing the total distance traveled:

$$\text{Minimize} \sum_{i,j} x_{ij} d_{ij},$$

where $dij$ represents the distance between origin station $i$ and destination station $j$. This distance is the Manhattan distance between stations $i$ and $j$. Constraints $\sum_i x_{ij} \leq 1$ and $\sum_j x_{ji} \leq 1$ ensure that at most one trip departs from a station and at most one trip arrives to it, where $x_{ij}$ is a binary selection variable indicates a trips from station $i$ to station $j$. $\sum_i x_{ii} = 0$ ensures that even though the distance from a station to itself is always the shortest, it cannot be selected.

Constraint $b_i - o_i \leq p_i \leq b_i$ and $o_i - b_i \leq q_i \leq c_i - b_i$ show how many bikes should be pick up/drop at every station, where $b_i$ represents the number of bikes at station $i$ before the truck arrives, $p_i$ is number of bikes picked up at station $i$, $q_i$ is number of bikes dropped at station $i$, parameter $o_i$ is the optimal number of bikes that should be available at station $i$ after the rebalancing process, and $c_i$ is the capacity of station $i$. If we need to pick up, $t_j = t_i - q_i + p_i$ and $t_i \leq B$ show that the number must be between the number of bikes in the station and the difference between this number and the optimal number of bikes in the station. If we need to drop bikes, the number must be between the difference of the current number of bikes in the station and the optimal number of bikes in the station and the difference between the number of bikes in the station and the maximum capacity of bikes, so we do not increase this number, where variable $B$ is the maximum number of bikes that we can fit on the truck and variable $t_i$ is the number of bikes on the truck before arriving to station $i$.

This specification can vary depending on the time of day, and we can get this feature by analyzing the data published on the Capital Bikeshare Website and check whether there are more departures or arrivals from the station in the desired time-frame. We can see the different number of trips departing and arriving on average in
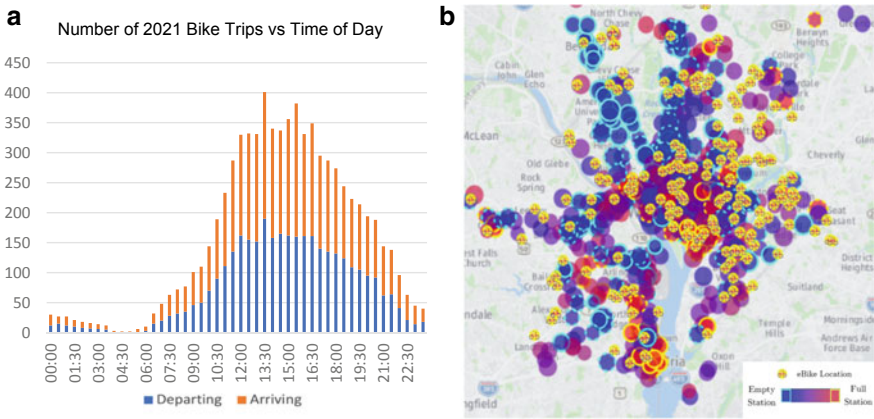
**Fig. 2** **a** Average number of trips during day. **b** Station type in DMV area

the year 2021. Figure 2a shows the average number of trips during day. Comparing these values station by station would lead to determining the status of the station. Figure 2b map shows the station type at a specific instant of time, with red signifying supply stations and blue demand stations.

## 3 Results and Discussion

We solved the model, considering our objective function and constraints and based on different number of $N$ and $m = 50, l = 50$, d$m = 300$, d$l = 1500$. Figure 3 illustrates the solution obtained. Decent set of bike station placements in the research region discovered which covered the study area, there are no isolated clusters of stations that are difficult to reach or depart from, and the city's most popular and valuable areas are easily accessible. Varying the total number of stations to be placed is an interesting problem by itself. The more stations we are allowed to place, the higher our objective function value will be. However, given that certain locations are more valuable than others, we expect that there will be diminishing returns. That is, if $N$ is small, then it is likely that there is another highly valued location that can still be used, and $N + 1$ will result in a significant rise in the objective function value. If $N$ is big, however, there are unlikely to be any more highly rated places to choose from, and so placing $N + 1$ stations will only result in a slightly higher objective function value.

We solve our model for $N$ values that steadily increase. Figure 4b shows a plot of the objective function value vs. number of stations, it indicates a falling rate of rise that virtually flattens out completely, as predicted. Because of the as-needed region restrictions, low values of $N$ are either infeasible or result in station placements that do not add much value to the objective function, and the above graph does not
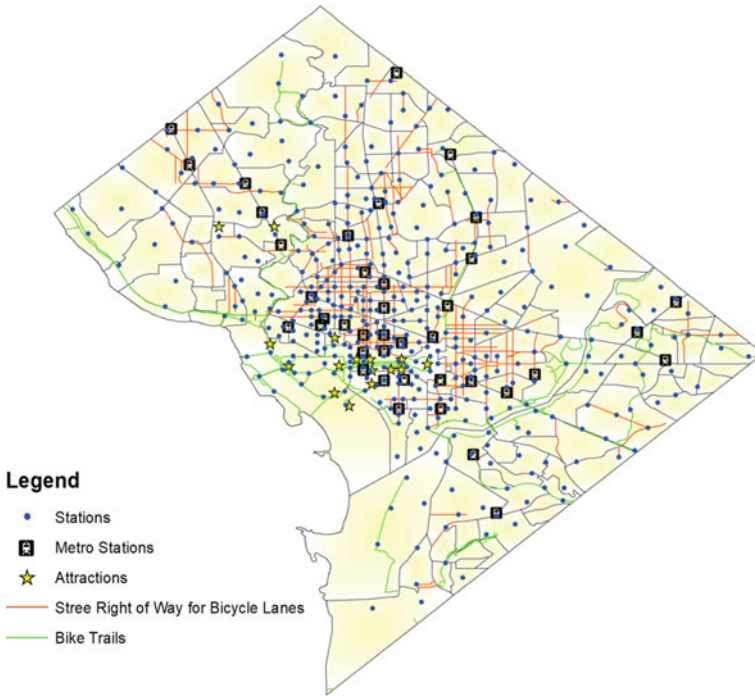
**Fig. 3** Station allocation result

consider small numbers of $N$. That is, before attempting to maximize the objective function, the model must first fulfill the constraints. This study supports the concept that $N = 400$ is a suitable choice if adequate resources are available.

We were also able to solve the rebalancing model. Figure 4a depicts the simple output that helps the driver visualize his tasks and itinerary for Foggy Bottom region,
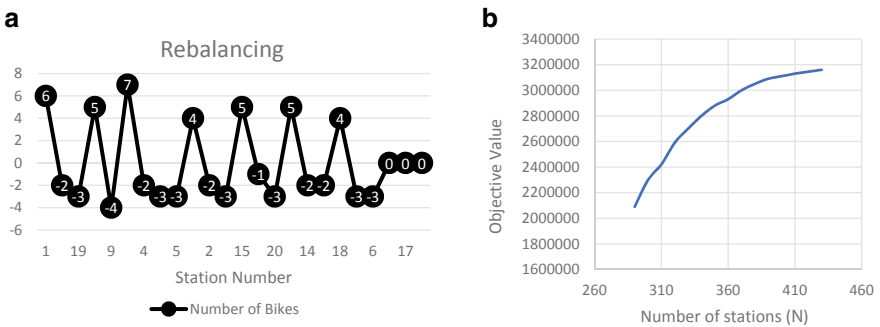


**Fig. 4 a** Visualization for rebalancing strategy. **b** Increase rate of objective value by increasing of $N$

which contains 22 stations. As can be seen, our algorithms aid the driver in determining the number of bikes to be picked up (positive) or dropped off (negative), with a 0 value for the station indicating that no rebalancing is required with showing order of stations to be reach. The optimal method would be to divide the DC region into multiple zones based on the number of trucks and apply the technique to each zone separately.

## 4 Conclusion

This study provided an optimization solution for a centralized bike-relocation system for Capital Bikeshare and developed a comprehensive bike station network optimization approach by selecting bike station locations with high value defining with features which led to improving the performance of the BSS. The models presented can be readily replicated to other data sources or regions, and it holds the potential to provide implications for transportation planning and policy making.

The placement of bike stations relationship with demand and the public transportation system are all important factors in the success of a BSS. Since all other infrastructures are linked to bicycles, new facilities are often developed for recreational cycling or keeping bicycles "out of the way" of motorized traffic in the absence of such a system for situating new facilities [8]. However, to best serve, methods should be developed to objectively determine how to optimally place a BSS [11]. Measuring the value of the objective function has made it possible to confirm that an increment in the number of stations logically leads to an increase in both the demand covered and the accessibility of stations to potential destinations but with diminishing returns. As [6] note, a large number of stations may result in an unreasonable rise in the system's cost without bringing about any significant improvements.

The present study has some limitations. The demand distribution will benefit from pedestrian and bike data and empty/full station patterns' analysis could benefit from a complete data set covering a more extended period. Due to data unavailability, the optimization analysis does not consider the dynamic demand in real-time but rather uses past trip records to approximate demand. In addition, the optimization analysis would become more practical if the costs of adding a station and shifting a dock between stations are available. A possible improvement to the model would be to include the BSS revenues and expenditures, which could help to optimize the results further. This issue would be addressed by requesting more data from the Capital Bikeshare System in future studies. Also, the connection of the installed stations is a potential improvement to our approach. While we ensure that each station is at most 300 m from another, that instance does not rule out the possibility of isolated clusters of stations apart from the main set. Another limitation is the presence of relatively isolated stations, particularly in the maximize-coverage model. However, these stations can easily be identified and eliminated after the accessibility analysis [8].

# References

1. Ahillen M, Mateo-Babiano D, Corcoran J (2016) Dynamics of bike sharing in Washington, DC and Brisbane, Australia: implications for policy and planning. Int J Sustain Transp 441–454
2. Beddis M, Mitrovic M, Sharma M (2015) Selection station locations for a public bike-share program: a case study for the City of Vancouver, BC. Analytics Now
3. James B (2013) Finding the optimal locations for bike sharing stations: a case study within the city of Richmond, Virginia
4. Buck D, Buehler R (2012) Bike lanes and other determinants of capital bikeshare trips. In: 91st Transportation research board annual meeting, pp 703–706
5. Croci E, Rossi D (2014) Optimizing the position of bike sharing stations. the milan case. CERE Working Paper 68
6. Chardon D, Medard C, Caruso G, Thomas I (2016) Bike-share rebalancing strategies, patterns, and purpose. J Transp Geogr 55:22–39
7. Erfani A, Tavakolan M, Mashhadi AH, Mohammadi P (2021) Heterogeneous or homogeneous? A modified decision-making approach in renewable energy investment projects. AIMS Energy 9:558–580
8. García-Palomares, Carlos J, Gutiérrez J, Latorre M (2012) Optimizing the location of stations in bike-sharing programs: a GIS approach. Appl Geogr 235–246
9. Hu Y, Zhang Y, Lamb D, Zhang M, Jia P (2019) Examining and optimizing the BCycle bike-sharing system—a pilot study in Colorado, US. Appl energy 1–12
10. Kaviti S, Venigalla MM, Lucas K (2019) Travel behavior and price preferences of bikesharing members and casual users: a Capital Bikeshare perspective. Travel Behav Soc 15:133–145
11. Larsen J, Patterson Z, El-Geneidy A (2013) Build it. But where? The use of geographic information systems in identifying locations for new cycling infrastructure. Int J Sustain Transp 299–317
12. Lin J-R, Yang T-H (2011) Strategic design of public bicycle sharing systems with service level constraints. Transp Res Part E: Logistics Transp Rev 284–294
13. Liu J, Li Q, Qu M, Chen W, Yang J, Xiong H, Zhong H, Fu Y (2015) Station site optimization in bike sharing systems. In: 2015 IEEE international conference on data mining. IEEE, pp 883–888
14. Ma T, Liu C, Erdoğan S (2015) Bicycle sharing and public transit: does capital bikeshare affect metrorail ridership in Washington, DC? Transp Res Rec 1–9
15. Mudiyanselage SE, Nguyen PHD, Rajabi MS, Akhavian R (2021) Automated workers' ergonomic risk assessment in manual material handling using sEMG wearable sensors and machine learning. Electronics 10:2558
16. Nair R, Miller-Hooks E, Hampshire RC, Bušić A (2013) Large-scale vehicle sharing systems: analysis of Vélib. Int J Sustain Transp 85–106
17. Rybarczyk G, Wu C (2010) Bicycle facility planning using GIS and multi-criteria decision analysis. Appl Geogr 282–293
18. Shakerian M, Rajabi MS, Tajik M, Taghaddos H (2022) Hybrid simulation-based resource planning and constructability analysis of RCC pavement projects. arXiv preprint arXiv:2204. 05659
19. Taghavi A, Khaleghparast S, Eshghi K (2021) Optimal agent framework: a novel, cost-effective model articulation to fill the integration gap between agent-based modeling and decision-making. Complexity
20. Todd J, O'Brien O, Cheshire J (2021) A global comparison of bicycle sharing systems. J Transp Geogr 103–119
21. Wergin J, Buehler R (2017) Where do bikeshare bikes actually go?: Analysis of capital bikeshare trips with GPS data. Transp Res Rec 2662:12–21

# Needs of Autonomous Vehicles for Safe Operation on Existing Highways

**Said M. Easa, Yang Ma, Azam Alaei, Harsheev Desai, and Lee Weissling**

**Abstract** Autonomous vehicles (AVs) will gradually supersede human-driven vehicles (HDVs) in the future. Unlike human drivers who perceive their surroundings with their eyes, AV senses the ambient environments based on sensor fusion. More specifically, light detection and ranging (Lidar) sensors, video cameras, and radars are combined to help AV understand their surroundings. Current highway geometric design elements are mainly based on human driver-related parameters, such as perception and reaction time (PRT). However, AV will mix with HDV on existing highway infrastructures during the transition period. This study focuses on the sight distance aspect of highway geometric design. It is unsafe if an AV cannot effectively detect the objects within its required sight distance using the fused sensing system. Therefore, determining the needed sensor configurations (e.g. height, effective range, and field of view) is necessary for safe AV operation. This study used a simulation approach to determine the needed sensor configurations. First, the required stopping, decision, and passing sight distances for AV were determined considering that AV has a much shorter PRT than HDV. Second, the automated driving toolbox of MATLAB was used to construct different scenarios, each involving the road, obstacles, and actors. The road models were created following current design guides. A virtual AV equipped with a Lidar, cameras, radars, and an impeding agent served as the main actors on each road model. Third, many simulations were conducted with different sensor configurations to determine the Lidar configuration that achieves 100% detection for the safe operation of AV on existing highways.

S. M. Easa (✉) · A. Alaei · H. Desai
Department of Civil Engineering, Toronto Metropolitan University, Toronto, ON M5B 2K3, Canada
e-mail: seasa@torontomu.ca

Y. Ma
School of Transportation, Southeast University, Nanjing, China

School of Automotive and Transportation Engineering, Hefei University of Technology, Hefei 230009, PR China

L. Weissling
Ontario Society of Professional Engineers, Toronto, ON M2N 6K, Canada

## 1 Introduction

Autonomous vehicles (AVs) will reduce human errors and are expected to lead to
significant benefits in safety, mobility, and sustainability [10, 11, 14]. The technical
feasibility of automated highways has been demonstrated in San Diego, California, in
1997 [13]. Autonomous vehicles have already started to appear on the roads across the
globe. As the AV market expands, transportation professionals and researchers must
address many challenges before AV soon becomes a reality. Several governments and
industries have deployed demonstrations and field tests of the technology. Centres
for testing and education, products, and standards for AV have also been established.

In the geometric design guides by the American Association of State Highways
and Transportation Officials (AASHTO) and Transportation Association of Canada
(TAC) [1, 12], the available sight distance (ASD) for human-driven vehicles (HDV) is
measured from the driver's eye height above the pavement surface. For autonomous
vehicles, the driver's 'eye' is the Lidar. The ability of the AV to 'see' ahead is critical
for safe and efficient operation. Sufficient sight distance must be provided to allow the
AV to stop, avoid obstacles on the roadway surface, overtake slow vehicles on two-
lane highways, and make safe turns/crossings at intersections. For HDV, the required
sight distance is based on the driver's perception-reaction time (PRT), vehicle speed,
and other factors. Regarding PRT, a value of 2.5 s is used for HDV, while 0.5 s has
been assumed for AV [5]. This smaller reaction time will result in shorter required
sight distances for AV.

Eliminating the driver will have direct effects on highway alignment design. Since
the AV response time is much less than the driver's PRT, the required SD for AV would
be much shorter than that for HDV. The impact of AV on highway geometric design
has been explored preliminarily by making simple assumptions regarding system
reaction time and Lidar field of view [5]. However, the ASD for AV is determined by
the Lidar sensors, which depends on the Lidar's technical performance. For instance,
the number of laser beams on an object is reduced along the direction away from
the AV. If fewer than two beams are on a target, the AV cannot perceive it in an
unconnected environment. In this case, it is necessary to examine the relationship
between ASD and the required SD for AV, considering the influence of Lidar sensors.

For autonomous vehicles, the Lidar and object heights influence the required SD
for the design of highway vertical, horizontal, and 3D alignments [3]. The Lidar
height above the pavement surface is critical in determining the ASD. Since the
required SD for AV is shorter for crest vertical curves, the Lidar height needed for
safe operation, $h_L$, would be somewhat less than the design driver's eye height, $h_1$.
Thus, by placing the Lidar at or above $h_L$, the AV can safely operate on existing
highways without the need for modifying their design. For a sag vertical curve with
an overpass, where the truck driver's eye height controls the traditional curve design,

the required Lidar height for the safe operation would be somewhat larger than the design driver's eye height. Thus, by placing the Lidar at or below $h_L$, the AV can safely operate on existing highways. The Lidar height is not important for detecting horizontal obstacles, except when cut slopes are present.

Even though AV will substantially affect the design and operation of highways, it is currently unknown how the AV can safely adapt to the existing highways without quantitatively modifying highway design. In addition, the revisions that can be made to the current design standard remain unclear for the highways with only AV in the future.

The objectives of this study are fourfold: (1) to establish revised values of stopping sight distance (SSD), decision sight distance (DSD), and passing sight distance (PSD) that are required for autonomous vehicles, (2) to analyse AV-related parameters that may affect highway design and propose a procedure that can simulate the Lidar sensors of AV (Lidar height, range, and field of view), and (3) to investigate the configuration of Lidar sensors that can guarantee the safe operation of AV on the existing highways without modifying current geometric design standards.

## 2 Required Sight Distance for AV

The driver's reaction time and eye height are the major factors that influence the sight distances for HDV. When considering AV, the reaction time is much shorter, which will significantly affect all the sight distances, including SSD, DSD, PSD, and intersection sight distance. A value of PRT of 0.5 s is widely accepted for AV, which is 2 s faster than human drivers. The 0.5 s was achieved after extensive machine simulations and computations [15]. Hence, the revised values for different sight distance can be built on the current AASHTO standards. Three basic types of sight distance (SD) for AV are defined, as described next.

### 2.1 Stopping Sight Distance

SSD is the distance travelled by the AV during system reaction time and the braking distance from the operating speed to stop. Due to the quick perception of the roadway and obstacles (moving or stationary) and the communication with other vehicles, SSD for AV should be smaller. Two distances comprise SSD: perception-reaction distance and braking distance [1]. Adding the perception-reaction distance and the braking distance as shown in the AASHTO green book, SSD was calculated for three different reaction times: 0.2 s (only AV), 0.5 s (AV in mixed traffic), and 2.5 s (HDV). Figure 1a shows a comparison of SSD for AV and DSD for flat grades.
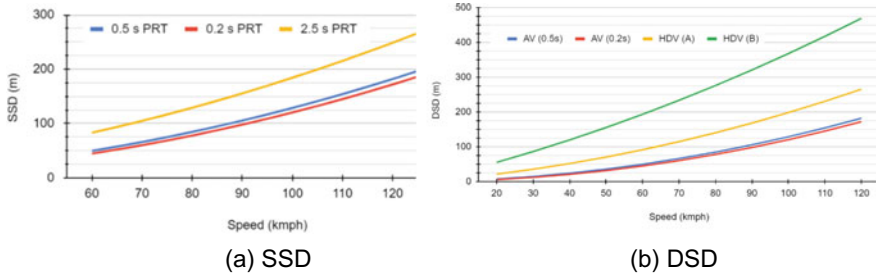
**Fig. 1** Comparison of SSD, DSD, and PSD for AV (0.5 s and 0.2 s) and HDV (2.5 s)

## 2.2 Decision Sight Distance

DSD is the distance that allows the AV to manoeuvre or change its operating speed or stop to avoid an obstacle on the roadway surface at complex locations. DSD ensures that a driver has enough distance to come to a stop or manoeuvre through difficult situations. AASHTO recognises five manoeuvres. Manoeuvres A and B are related to rural and urban roads, respectively. Manoeuvres C, D, and E are related to speed, path, or direction change on rural, suburban, and urban roads, respectively. DSD offers drivers sufficient SD to manoeuvre their vehicles at the same or reduced speed rather than to stop. Hence, the DSD values are substantially greater than the SSD values for HDV. However, since AV is equipped with Lidars, they require less manoeuvre times and a PRT of 0.5 s was used for Manoeuvres A and B. This means that the DSD values would be the same as the SSD values. According to AASHTO [1], a human driver requires 3 s for Manoeuvre A and 9.1 s for Manoeuvre B. A comparison of DSD for Manoeuvres A and B for AV and HDV is shown in Fig. 1b.

The SD values for AV are significantly smaller than HDV and would be even smaller for only-AV highways. There has not been much research covering Manoeuvres C, D, and E for AV as it includes pre-manoeuvre times, in addition to manoeuvre times, making it more complex. [6] established that drivers need to decide sight distances whenever there is a likelihood for error in either information reception, decision-making, or control actions. AV does not need this margin of error as computers are faster and much more accurate than human drivers. Likely, AV will not require higher reaction times for Manoeuvres C, D, and E, which involve changing speed, path, or direction. However, further research is needed to determine the time AV taken for these manoeuvres.

## 2.3 Passing Sight Distance

PSD is the distance, including system reaction time, required by the AV on rural two-lane roads to allow the vehicle to pass a slower vehicle by using the opposing

lane. PSD provides a driver with sufficient sight ahead and ensures that passing can be accomplished without interference from an oncoming vehicle. The critical sight distance by [4] was used to derive the PSD requirements for both HDV and AV. Their model was used here as, according to the model by [7], a safe passing manoeuvre may require a passing driver to abort the pass after being ahead of the vehicle, which is an impractical requirement to expect drivers to abide by. A difference of 19 km/h was assumed between the passing and passed vehicles, the deceleration rate in case of an aborted manoeuvre was 3.14 m/s$^2$, and the time headway between the vehicles was 1 s. The PRT for PSD was selected as 1 s for HDV [1] and 0.5 s for AV. Comparing the required SD for AV and HDV shows that AV needs about 20% less sight distance than HDV.

## 3   Methodology

The general workflow involves three main steps and is presented in Fig. 2. At Step 1, many 3D road models are built using MATLAB Driving Scenario Designer® ([9], hereinafter referred to as MDSD) based on the existing design policies. In this phase, roadside obstacles or overhanging obstacles are also set up to represent as-built road infrastructures. At Step 2, a virtual AV actor is created where different sensors, including Lidar, cameras, and radars, are added. At Step 3, a large number of test scenarios are designed. An actor is placed exactly at the required sight distance (RSD), measured along the lane centreline, in each test scenario away from the AV. Note that RSD here denotes the re-estimated sight distance requirements for AV (see Sect. 2). Then, simulations are conducted to examine whether the AV can effectively detect the actor ahead continuously. Each step is described in detail next.

**Fig. 2** Workflow of simulation
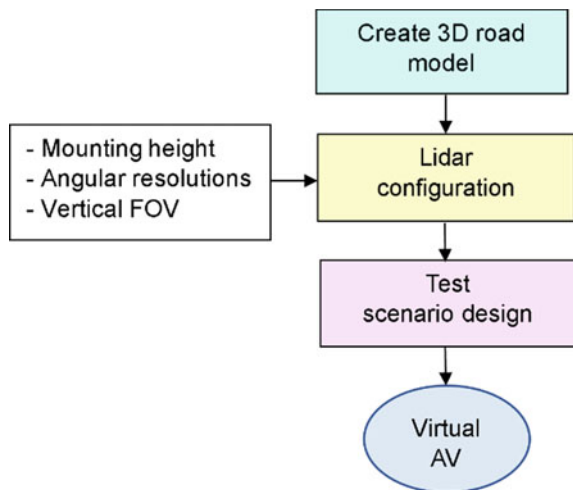
## 3.1  Virtual Road Environment

In this study, 3D road models are manually created according to the existing design policies. Users can first design their road alignment with some engineering software such as Civil3D. Then, the centreline coordinates can be imported into the MDSD app to build virtual road models. Alternatively, users may export extensible make-up language (XML) that contains road geometry information from the design software. Finally, the MDSD app can automatically create the road model using XML files as inputs.

As shown in Fig. 3, different road models of the combined alignments were created in the MDSD app. This study also considers obstacles that may significantly reduce an AV's sight distance to represent as-built highway infrastructures better. There are two main types of obstacles: continuous roadside obstacles and overhanging obstacles. Roadside obstacles may substantially affect an AV view on horizontal curves, while overhanging obstacles may cause significant occlusions (especially to trucks) on sag vertical curves.

The horizontal sightline offset (HSO) is commonly used to demarcate the boundaries of sight-clear zones to ensure that human drivers have adequate ASD on highways. As depicted in Fig. 4, roadside obstacles, in this case, are modelled by continuous concrete walls. The lateral distance from the inner-lane centreline to roadside obstacles is set to HSO. Note that roadside obstacles are high enough to block an AV's view adequately.

On sag curve road sections, overhanging objects serve as the primary sight obstacles for AV. An object overhanging the roadways can also be added when necessary. Note that the height from the road surface to the overhanging obstacle is adjustable to address different situations. The 3D road models and obstacles jointly depict the virtual road environment of as-built highways. Many virtual 3D road scenes can be created by changing geometric parameters (e.g. horizontal curve radius) or obstacle settings.



(a)  Crest vertical curve              (b)  Sag vertical curve
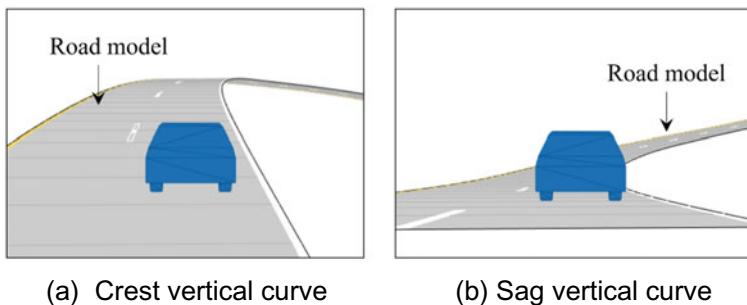
**Fig. 3**  Creation of road models
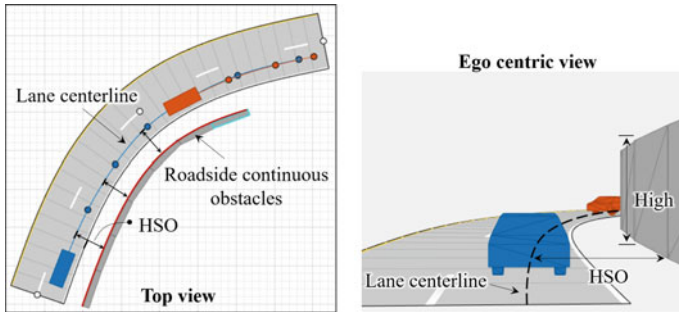
**Fig. 4** Roadside obstacles of virtual road environment

## 3.2 Actors and Sensors

Unlike human drivers who see the road environment using their eyes, AV perceives their ambient surroundings based on the fusion of Lidar, camera, and radar (Fig. 5). In terms of AV's sight distance, Lidar is the most critical sensor as it performs 3D detections of objects and can measure spatial distance accurately. Therefore, this study mainly focuses on Lidar as 'eyes' for AV, though radar and camera sensors are also implemented.

The MDSD app provides a flexible way of configuring Lidar sensors. Users can interactively adjust Lidar parameters to simulate different Lidar products. Generally, Lidars' detection performance is associated with several technical parameters: detection range, horizontal and vertical fields of view (FOV), horizontal and vertical angular resolutions. Besides, the placement of the Lidar sensor may also affect its detection results, especially on sag curves. Although many technical parameters may affect a Lidar sensor's detection performance, this study mainly focuses on vertical FOV, horizontal and vertical angular resolutions, and mounting height. The detection range of a Lidar sensor is determined based on the maximum RSD (200 m in this case) for AV. Regarding horizontal FOV, a typical value of 360° is used.

**Fig. 5** Sensor layout and output
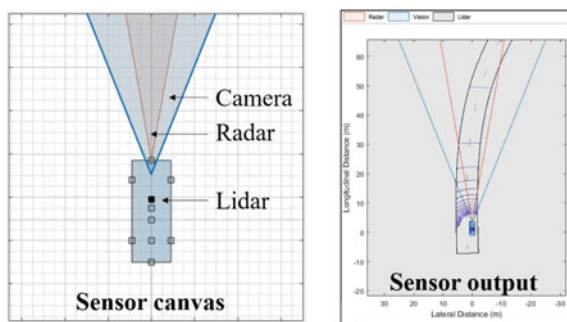


(a) Layout  (b) Output

## 3.3   Simulations

A typical test scenario is shown in Fig. 6. An AV equipped with multiple sensors and another actor (a car in this case) are placed on the road surface. Both the AV and the front actor travel at the same speed along the same path that overlaps with the lane centreline. As noted, the actor ahead is placed RSD away from the AV. The RSD here denotes the required sight distance for AV whose PRT is much less than human drivers. Note that the radar was not used in the simulations.

Waypoints are indispensable inputs that control the motion of both AV and the front actor. However, MDSD only provides a manual way of creating waypoints, making it complicated to initialise a test scenario efficiently, like Fig. 7. Therefore, this study developed a procedure to initialise the driving scenario automatically. The general workflow of the procedure is shown in Fig. 7. Consider the AV's waypoints for an illustration. First, the proposed procedure reads lane width and coordinates of points along the road axis from the scenario file. Second, the lane centreline points are acquired by offsetting the centreline points. Third, the natural cubic spline (NCS) is applied to fit the lane centreline points, and it is resampled into dense and uniformly spaced points [8]. In this way, it is easier to locate the RSD point away from the AV at which a front actor can be spawned. Regarding the offset-ting and resampling steps, let $P\{p_1, p_2 \ldots p_k \ldots p_n | 1 \leq k \leq n, k, n \in N^+\}$ and $A\{\alpha_1, \alpha_2 \ldots \alpha_k \ldots \alpha_n | 1 \leq k \leq n, k, n \in N^+\}$ be the centreline points and azimuth angles along the road axis, respectively. Consider $p_k$ for example, point $p_k'$ in the inner-lane centreline is given by

$$\begin{bmatrix} x_k' \\ y_k' \end{bmatrix} = \begin{bmatrix} x_k \\ y_k \end{bmatrix} + \frac{w}{2} \begin{bmatrix} \cos \alpha_k \\ -\sin \alpha_k \end{bmatrix} \tag{1}$$

where $(x_k, y_k)^T$ and $(x_k', y_k')^T$ = coordinates of $p_k$ and $p_k'$, respectively, and $w$ = lane width.

An NCS was fitted on the discrete points tracing the lane centreline. Using the method by [8], the fitted NCS is re-partitioned into dense and uniformly spaced



**Fig. 6** Illustration of test scenarios
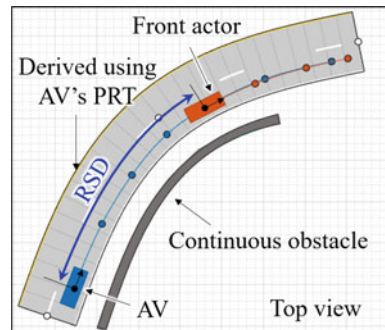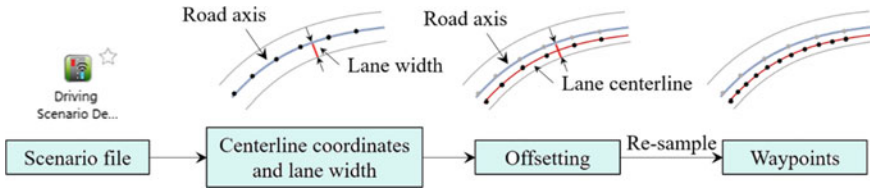
**Fig. 7** General workflow for creating waypoints for AV

points (the average gap is $\delta_d$). The distance between any two positions along the lane centreline is measurable. A critical condition is that the AV can effectively detect hazards within its RSD to guarantee that an AV can safely operate on existing highways designed for HDV. Once the simulation starts, the virtual sensors collect data and detect the front actor automatically. The sensor data and detection results were exported when a single simulation round was finished. If the AV cannot continuously detect the actor ahead, it is viewed as unsafe. In that case, the Lidar parameters were adjusted to ensure that the AV could effectively detect the front agent in all representative test scenarios.

## 4 Safe Lidar Configuration for AV

### 4.1 Three-Dimensional Curves

A total of 150 simulations were conducted using the MDSD app. The aim was to achieve 100 per cent object detection using the camera and Lidar configuration parameters. For the camera parameters, AV can use high-resolution digital camera images to perceive their surroundings, such as signs, traffic signals, and animals. The amount of light a camera uses to form an image is ultimately determined by the size of its sensor. Image sensors are made up of millions of light-sensitive patches (Photosites) that capture information about the objects viewed through the lens. To achieve optimal video and image resolutions, the camera configuration parameters were set as follows: maximum range (200 m), width (1280 p), height (720 p), and principal point (640, 360) [17]. The detection range was based on the revised SD for AV presented previously. However, considering the speed, the front vehicle was positioned by the RSD (200 m) from the AV in each simulation.

For the Lidar configuration parameters, the optimal values are shown in Table 1. According to existing Lidar in the market, for range accuracy, an accuracy of 0.03 m was selected in the simulations. A Lidar's FOV is a crucial parameter measured separately along the horizontal and vertical axes. Since the Lidar application requires hazard avoidance in an unconstrained space, a 360° horizontal FOV was used. After running many scenarios, a 40° vertical FOV was optimal for achieving 100 per cent object detection.

**Table 1** Lidar configuration for AV

| Max range | Range accuracy | Azimuthal resolution | Vertical resolution | Horizontal FOV | Vertical FOV | Lidar height |
|-----------|----------------|----------------------|---------------------|----------------|--------------|--------------|
| 200 m | 0.03 m | 0.16$^\circ$ | 0.5$^\circ$ | 360$^\circ$ | 40$^\circ$ | 1.6 m |

The angular resolution is a critical parameter when detecting objects in a scanning field. The captured points on a target are closer with a finer angular resolution, resulting in smaller objects being detected. As a result, the finer the angular resolution, the more Lidar beams will reflect off an oncoming object, and the higher spatial resolution. The angle at which the laser is emitted and recorded determines the azimuth angle, where the elevation angle of a laser emitter in a sensor remains constant. The optimal vertical and horizontal angular resolutions were found to be 0.5° and 0.16°, respectively. Different heights ranging (1.5–2.2 m) were tested using combinations of the Lidar configurations, and the Lidar height that achieved 100% object detection was 1.6 m.

## 4.2 Sag Vertical Curves with Overpasses

For sag vertical curves with overpasses, the line of sight may be obstructed by the overpass structure and limits the visibility. Therefore, it is essential to determine the sag curve length based on the required sight distance. The SD model proposed by [2] is based on mathematical optimization and offers more capabilities than the traditional AASHTO model. For HDV, the limiting vehicle would be a truck as it has a larger eye height. According to the Federal Highway Administration, trucks are about 4.11 m high. In addition, for autonomous vehicles, Lidar sensors are approximately 0.284 m long [16], bringing the Lidar height ($h_1$) to 4.394 m, and the height of the object ($h_2$) is considered as 0.6 m, which is the height of the tail lights for most vehicles [1]. Autonomous trucks will be more flexible as their Lidar sensor can be placed at any height. However, it is necessary to determine the optimal height to position the Lidar sensor. To achieve this, a road profile was created in MDSD to simulate conditions like an actual highway. Different Lidar configurations were used with the sensor placed at heights between 1 and 2 m. In addition, the scenarios have involved different curve lengths and grades. Since the sensor is small and compact, the sensor was placed in the front of the vehicle. The overpass was placed 4.5 m high from the road surface for each scenario, which is the standard vertical clearance. The results showed that the Lidar height that achieved 100% object detection was 1.6 m, identical to the optimal Lidar height for 3D alignments. This means that existing sage curves with overpasses would be pretty safe for autonomous trucks.

## 5 Conclusions

This paper has presented a methodology for determining the optimal Lidar configuration for AV to operate safely with human-driven vehicles. The revised sight distances for stopping, decision, and passing for AV were presented first and then used to inspect Lidar' height, effective range, and field of view using a simulation-based approach. The results show that AV requires SSD and PSD about 20% and 25% less than those needed for HDV. In addition, AV requires substantially less DSD than HDV for Manoeuvres A and B. Further research is required to determine Manoeuvres C, D, and E requirements for AV. The Lidar height is a critical parameter affecting AV object detection, including the vehicle ahead and other obstacles.

The results show that a Lidar height of 1.6 m will ensure AV safety when travelling alongside HDV on existing roadways. This optimal height was the same for 3D highway alignments and sag vertical curves with overpasses. This study has implemented a simulation-based approach for determining Lidar configuration. However, field testing of the optimal Lidar configuration should be undertaken to confirm the results presented in this paper.

## References

1. American Association of State Highway and Transportation Officials (2018) A policy on geometric design of highways and streets. AASHTO, Washington DC
2. Easa SM (2009) Improved sight distance model for sag vertical curves with overpasses. Transp Res Rec 2120:28–36
3. Easa SM, Ma Y, Elshorbagy A, Shaker A, Arkatkar S (2021) Visibility-based technologies and methodologies for autonomous driving. In: Gaiceanu M (ed) Self-driving vehicles and enabling technologies. IntechOpen Rijeka, UK
4. Hassan Y, Easa SM, Halim (1996) Passing sight distance on two-lane highways: review and revision. Transp Res 30A(6):453–467
5. Khoury J, Amine K, Abi Saad R (2019) An initial investigation of the effects of a fully automated vehicle fleet on geometric design. J Adv Transp 2019:6126408
6. King GF, Lunenfeld H (1971) Development of information requirements and transmission techniques for highway users. In: NCHRP report 123. Transportation Research Board, Washington, D.C
7. Glennon JC (1988) New and improved model of passing sight distance on two-lane highways. Transp Res Rec 1195(1988):132–137
8. Ma Y, Zheng Y, Easa SM, Hou M, Cheng J (2019) Automated method for detection of missing road point region in mobile laser scanning data. Int J Geo-Info 8(12):525
9. Matworks (2021) Driving scenario designer. Available at https://ww2.mathworks.cn/help/driving/ref/drivingscenariodesigner-app.html?searchHighlight=driving%20scenario%20designer&s_tid=srchtitle_driving%20scenario%20designer_1
10. Mohamed A, Ren J, El-Gindy M, Lang H, Ouda AN (2018) Literature survey for autonomous vehicles: Sensor fusion, computer vision, system identification and fault tolerance. Inter J Autom Control 12(4):555–581

11. National Cooperative Highway Research Program (2017) Connected and autonomous vehicles and transportation infrastructure readiness. Project 20–24(111), TRB, Washington, DC

12. Transportation Association of Canada (TAC) (2017) Geometric design guide for Canadian roads. TAC, Ottawa, Ontario

13. Shladover SE (2005) Automated vehicles for highway operations (automated highway systems). IME Proc, Part I: J Syst Control Eng 219(1):53–75

14. Shladover SE (2018) Connected and automated vehicle systems: introduction and overview. J Intell Transp Syst 22(3):190–200

15. Urmson C (2006) Driving beyond stopping distance constraints. In: IEEE/RSJ international conference on intelligent robots and systems. IEEE, pp 1189–1194

16. Velodyne (2017) User's manual and programming guide: high definition LiDAR sensor. HDL-64E S3, Available at: https://velodynelidar.com/products/hdl-32e/. Accessed on Oct 2021

17. XIMEA (2017) Case study: How XIMEA cameras power driverless cars. Available at https://www.ximea.com/en/corporate-news/gathering-data-driverless-roads-autonomoose. Accessed on Oct 2021

# Evaluation of Dynamic Incentive Pricing for Congestion Management in Transit System: An Agent-Based Simulation

**Yili Tang and Bingyu Zhao**

**Abstract** This paper analyzed the feasibility of a dynamic fare incentive strategy by characterizing commuters' travel patterns and the extent of their flexibility in departure times using multi-source data. In the proposed fare incentive, commuters incur a surcharge during the central peak period and obtain a monetary reward during the shoulder peak period. The fare incentive determines central period location and length, the value of reward and the reward ratio which is the ratio of the number of trips with reward to total number of trips. We proposed an agent-based simulation to evaluate the performance of the fare incentive inclusive of outlier analysis, travel pattern recognition, and crowdedness interpretations. The simulation and evaluation are applied to a metropolitan transit system using smartcard and operation data. Results reveal the practicality of the proposed fare incentive to reduce the congestion by affecting commuter departure time distribution while keeping the flexibility interval unchanged.

**Keywords** Agent-based models · Transit systems · Fare incentive analysis

## 1 Introduction

As the demand of public transportation grows faster than the transit capacity in metropolises, mass transit operators are facing significant challenges for finding feasible solutions to manage peak congestion and overcrowding. The capacity geared toward peak demand level is inefficiently utilized during off-peak periods; peak

Y. Tang
Faculty of Engineering and Applied Science, University of Regina, Regina, SK S4S0A2, Canada

B. Zhao (✉)
Department of Civil and Environmental Engineering, University of California, Berkeley, CA 94720, USA
e-mail: bz247@berkeley.edu

Institute of Transportation Science, Vienna University of Technology, 1040 Vienna, Austria

congestion also impacts the stability and reliability of transit services, therefore reduce user satisfaction. Generally, transit demand management strategies take two main forms: increasing service supply and reducing travel demand at peak times. It is not always feasible to increase service supply because transit lines with peak overcrowding usually operate at maximum capacity. Reducing peak demand is often done through fare differentials to spread demand. Temporally differential fares are easy to implement but politically unpopular: peak surcharges penalize peak hour commuters and off-peak fare discounts or rewards usually come at the expense of the government or transit operator.

To address these problems, it is critical to analyze traveler's behavior and the effects of fare strategies on transport system. Following some investigations of departure time [5, 13, 16, 17], various studies have incorporated departure time changes and flexibility of commuters to explore commuter travel behavior and manage peak period congestion. A few researchers discussed commuters' departure time switching decisions on day to day variations in laboratory experiments by using hypothetical data collected from commuters [8, 9]. Moreover, Mannering [10] utilized the commuter behavior survey in a congested Seattle metropolitan area and found that commuter's departure time changes are affected by the length of the travel time, work schedule flexibility, etc. Furthermore, Mannering et al. [11] showed that on both home-to-work and work-to-home, more than 60% of commuters have a lot or some flexibility in departure time. Particularly, the extensive diary survey of commuter behavior conducted in Dallas and Austin, US showed that the preferred time for commuters to arrive early is up to 15 min [4]. All of these suggest that commuters will respond differently to the demand management strategies according to their scheduling flexibility.

A number of researchers investigated the rewarding schemes and incentives to reduce congestion and queuing during the peak period. For instance, Daganzo and Garcia [2] proposed a pricing strategy that provides a proportion of users the exemptions from paying tolls. Rouwendal et al. [12] rewarded commuters at the two shoulders of the peak period. Moreover, Yang and Tang [18] proposed a fare-reward scheme that one assigned free trip is rewarded to commuters during the shoulder period after certain paid journeys within the peak period. Tang et al. [15] further incorporate commuter's scheduling flexibility and proposed a hybrid fare strategy to accommodate heterogeneous commuter scheduling patterns. While previous theoretical studies demonstrate the efficiency of rewarding schemes to reduce congestions in mass transit system, it is significant to explore the feasibility and practicality of such schemes for providing transport and behavior analysis with an informative and in-depth reference.

To improve the design of such fare incentives, this paper uses longitudinal smart card data to investigate the feasibility of the fare incentive and gain insights into commuters' travel patterns and the extent of their rigidity/flexibility in travel times. The features used to segment users' travel patterns include the following: how often passengers use the transit system in peak hours; the days and times of their typical trips (variability in departure time); the entry and exit stations they typically travel between. The analysis of commuter departure time patterns offer insights into

commuters' spatial and temporal use of the system and identify different levels of regularity among users [3, 6, 7].

This paper is organized as follows. Section 2 introduces design and regulation of the proposed individual-based fare incentive and develops the framework of feasibility analysis. Section 3 developed the agent-based simulations to capture individual patterns and trip activities and derive the in-vehicle and platform congestion and crowdedness. Section 4 compared the system performance before and after the fare incentive. Section 5 concluded the study and discussed future research.

## 2 The Fare Incentive and Implementation

### 2.1 The Surcharge-Reward Scheme

The fare incentive strategy proposed in this paper is the surcharge-reward scheme [14] which splits the peak period into one central period and two shoulder periods, as shown in Fig. 1. Commuters incur a surcharge $\Delta s$ for each trip by traveling in central period. The surcharges are reimbursed and cumulated in commuter's personal account and can be used during the shoulder periods. During the shoulder period, commuters are eligible to use a monetary discount $\Delta r$ for each trip from the account balance cumulated by previous surcharges. Commuters are not allowed to use the reward if the account balance is less than the value of the reward. Hence the transit operator (or policy makers) determines the central period location, duration and the values of surcharge and rewards.

Under the surcharge-reward scheme, commuters can be fully refunded by occasionally shifting to shoulder periods. We further define the reward ratio $\lambda$ as $\lambda = \frac{\Delta s/\Delta r}{1+\Delta s/\Delta r}$ to control the amount of the rewards, where $\Delta s/\Delta r$ represents the number of shoulder period trips required for one commuter to get fully refunded with one surcharge. If $\Delta s/\Delta r < 1$, it indicates that the value of one surcharge is less than one reward, hence a commuter can use one reward after several surcharged trips and in the meantime, he/she needs to take fewer trips during shoulder periods than central period to get fully refunded. If $\Delta s/\Delta r > 1$, it indicates that the value of one surcharge is greater than one reward, hence a commuter can use one reward after one surcharged trip and need to take more trips during shoulder periods than central period to get fully refunded. Therefore, the reward ratio can be regarded as
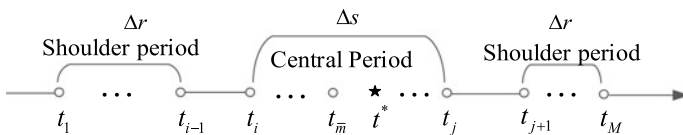


**Fig. 1** The surcharge-reward scheme

the ratio of the number of trips with reward to the total number of the trips for one commuter. Hereinafter, the reward ratio is used to represent the reward value $\Delta r$ where $\Delta r = \frac{(1-\lambda)\Delta s}{\lambda}$ and a higher value of the reward ratio indicates a lower value of the reward for a given surcharge.

## 2.2   A Framework of Fare Incentive Implementation

The surcharge-reward scheme aims at reducing congestion in mass transit system. As one of the demand management strategies, the rewarding scheme also leads to impacts on both individuals and transit systems. Based on this, a feasibility analysis of the surcharge-reward scheme is conducted with smartcard data and operation data from a metro line in Beijing Metro network. As shown in Fig. 2, with the available smartcard data and operation data, data cleaning and outlier analysis is carried out first. Passenger's departure time patterns are then determined, and individuals are assigned to each service runs. Meanwhile, several scenarios of surcharge-reward schemes are proposed in the system. The system effects of the surcharge-reward scheme are then recognized in both individual level and transit level in which the former one reflects the change of passenger's departure time pattern and inbound volume and the latter one demonstrates the change of the peak hour and queuing time. The surcharge-reward scheme as illustrated in above, introduces the central period location, duration, the reward ratio and the values of the rewards.
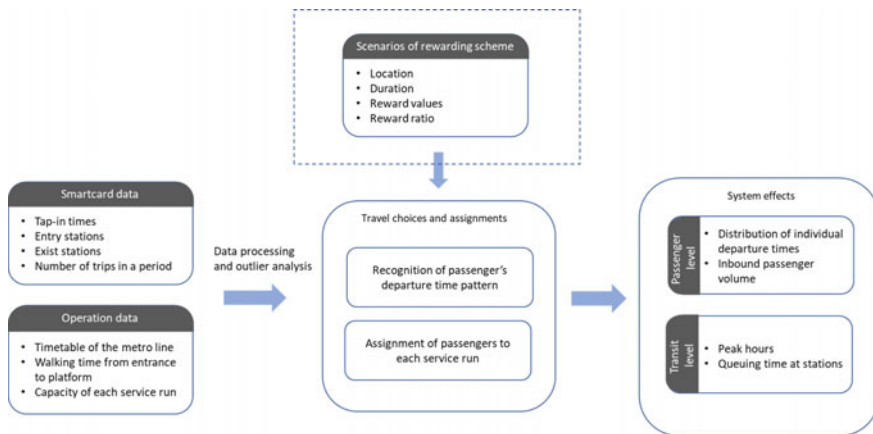


**Fig. 2**   The framework of feasibility analysis of surcharge-reward scheme

## 3   The Agent-Based Simulation

### 3.1   Data-Driven Behavioral Recognition

*Recognition of passengers' departure time patterns*

To explore the feasibility and practicality of the surcharge-reward scheme, passengers' departure time patterns are analyzed first. The surcharge-reward scheme has influences on both the departure time interval and the ratios within the interval. Therefore, passenger's departure time pattern is determined including the departure time flexibility interval (DTFI) and the departure time distribution within the DTFI. The former one is the time interval that a passenger is flexible to change their departure times while the latter one is the distribution of departure times over the period in the DTFI.

To recognize every passenger's departure time pattern, it is important to determine the earliest and latest departure time they usually choose to travel. Since our preliminary dataset consists of three-month of trip records, in some cases, a departure time in one day can be quite different from the departure times in the other days for one passenger due to a different purpose, such as a meeting trip instead of a commuting trip during the peak. To eliminate the effects of those occasional trips, the outlier analysis is conducted to improve the precision of the determination of departure time patterns. In the outlier analysis, a passenger $i$'s departure time distribution is fitted by a lognormal distribution with the mean value $\mu_i$ (departure time point) and the standard deviation $\sigma_i$. The $3\,\sigma$ criterion [1] is used to recognize the outlier, namely a departure time $t$ is defined as an outlier and will be excluded if

$$|\ln(t) - \mu_i| > 3\sigma_i \tag{1}$$

The remaining departure time records define the departure time pattern for passenger $i$, as shown in Fig. 3a. The DTFI is then determined by the earliest departure time and the latest departure time of each passenger, as shown in Fig. 3b.

*Changes of departure time pattern with different types of commuters*

The outlier analysis increases the precision of departure time pattern recognition. Since departure time pattern is analyzed by the long-period smart card records, it is assumed that it reflects passengers long-term travel behavior. The time interval can be categorized into three groups: shoulder DTFI, central DTFI, and the cross DTFI as shown in Fig. 4a. Our study does not consider passenger's socio-demographic attributes, it is thus assumed that passengers with shoulder and central DTFI will not be affected under the implementation of the rewarding schemes.

For the group of passengers with cross DTFI, the change of their departure time distribution is influenced by the determination of central peak period and the reward ratio. A peak demand ratio $\rho_i$ of a passenger $i$ is defined which is the cumulative distribution over the central peak period. If passenger $i$'s peak demand ratio is less
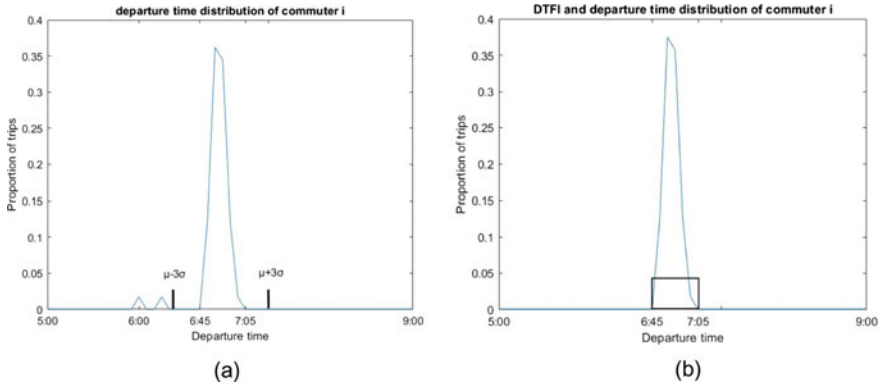
**Fig. 3** **a** Outlier detection, and **b** departure time pattern after outlier analysis
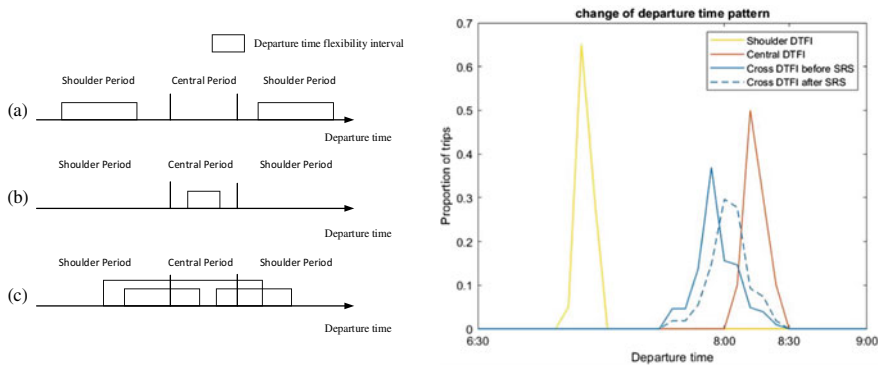


**Fig. 4** **a** Different departure time patterns. **b** Change of departure time distribution under the surcharge-reward scheme

than the reward ratio given by the surcharge-reward scheme, namely, $\rho_i \leq 1 - \lambda$, he or she can use up the amount of the surcharges with the existing departure time pattern hence the departure time distribution will not be affected. On the contrast, if $\rho_i > 1 - \lambda$, passenger $i$ has to take the extra trips in shoulder period in order to balance the surcharge, and under the assumption that demand is inelastic, the extra trips are assumed to be shifted from the central peak period. Therefore, the departure time distribution after the fare incentive for passenger $i$ is derived as

$$p_s = P'_s \cdot \frac{\lambda}{P'_s} \tag{2}$$

$$p_c = P'_c \cdot \frac{1 - \lambda}{1 - P'_s} \tag{3}$$

where $p'_s$ and $p_s$ are the departure time distributions in the shoulder period before and after the surcharge-reward scheme respectively, $P'_s$ is the cumulative distribution over the shoulder period. Similarly, $p'_c$ and $p_c$ are the departure time distributions in the shoulder period before and after the rewarding scheme respectively, $P'_c$ is the cumulative distribution over the shoulder period (hereinafter, '$s$' refers to the shoulder period case and '$c$' refers to the central peak period case).

Different types of passengers will response differently to the surcharge-reward scheme. For instance, suppose a surcharge-reward scheme where the surcharge period is from 8:00 am to 8:30 am and reward ratio is 0.6. Passengers with shoulder DTFI and central DTFI do not change their departure time distribution, as shown in Fig. 4. However, passengers with cross DTFI are incentivized to shift to the shoulder period in order to utilize the monetary reward. As shown in Fig. 4b, a passenger with cross DTFI shifts the departure times latter according to his or her original departure time pattern. Thus the distribution of departure times is changed corresponding to the reward ratio and the individual's peak demand ratio.

## 3.2 The Agent-Based Simulation

To capture individual's travel pattern and the dynamics in transit system, we developed an agent-based simulation where each passenger is regarded as an agent. The simulation integrated each agent's time-varying actions and transit operations in the transit systems to derive the crowding and congestion dynamics at the levels of individual, vehicle, platforms as well as the overall transit networks.

The inputs of the agent-based simulation include the network topology, transit schedules, and the origin–destination demand matrix. The simulation updates the status of transit vehicles and travelers at a given time step (e.g., every 20 s). The workflow of the simulation is shown in Fig. 5.

# 4 System Crowding and Congestion—Case Study of Beijing Metro Networks

## 4.1 The Preliminary Dataset and Statistics

We further conducted a case study using the smartcard data and operation data from Beijing Metro network. The smartcard data includes records of the passengers observed in stations in Changping rail line in Beijing subway system as shown in Fig. 6. Hereinafter, we selected Nanshao and Shahe stations as examples. The dataset recorded passengers' trips for 3 months from 5 to 10 am. The smartcard data contains the origin and destination stations, as well as the enter time and exit time of each transactions. The surcharge-reward scheme requires passengers to occasionally
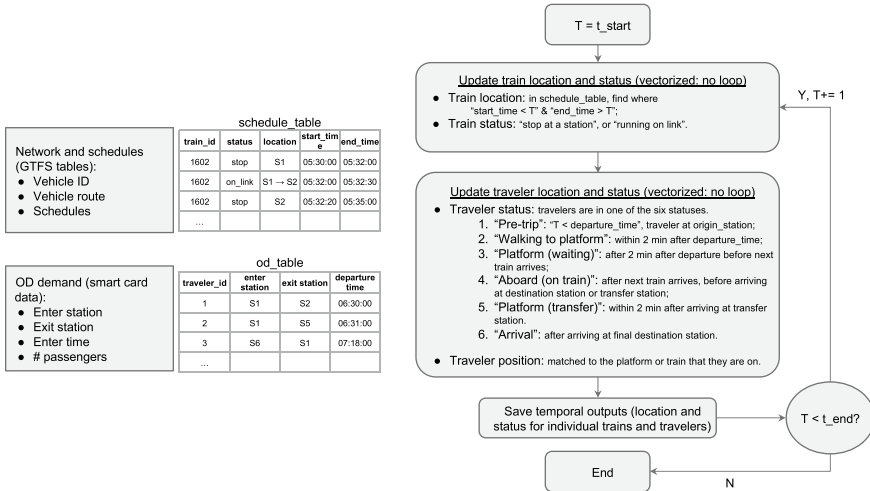
**Fig. 5** Workflow of the agent-based simulation

change their departure time in order to utilize the benefits of the monetary reward during the shoulder period. Therefore, we focus on target passengers who complete at least five weekday trips during the 3 months.

In the case study, the total inbound passenger volume from 5 to 10 am on an average workday for the two selected stations are 6890 and 24,724, as shown in Table 1. And the percentage of target passengers are 44.67% and 46.27%, respectively. This
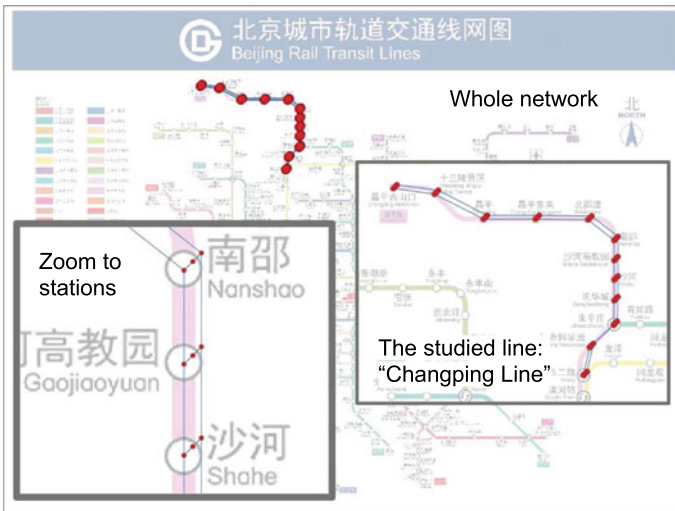


**Fig. 6** Network and stations

also indicates the target passengers carried approximately half of the trips during the morning period every day. On the other hand, the total outbound passenger volume is between 1651 and 2755. The excessive inbound demand and unbalanced outbound demand in the two stations indicates the potential of the fare incentive (e.g., surcharge-reward scheme) to relieve the congestion and crowding in the transit systems.

The individuals' trip patterns will affect the performance of the transit systems as indicated in Sect. 3.1. From the perspective of individual departure time patterns, as shown in Fig. 7, it is found that nearly 59.42% of target passengers in Changping line have a length of DTFI between 10 and 50 min which indicates the practicality to implement the surcharge-reward scheme by incentivizing passengers to change their departure time distribution without changing their DTFI.

**Table 1**  Characteristics of smartcard data with two selected stations

| Station | Total inbound volume | Percentage of inbound target passengers (%) | Total outbound volume |
|---------|---------------------|---------------------------------------------|----------------------|
| Nanshao | 6890 | 44.67 | 1651 |
| Shahe | 24,724 | 46.27 | 2755 |
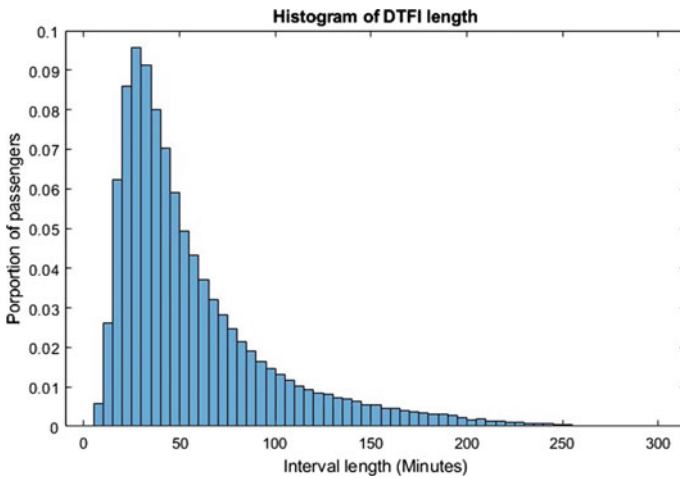


**Fig. 7**  Histogram of passenger's DTFI length in Changping line

## 4.2 The Baseline—System Performance Without Fare Incentives

The baseline of the system performance for the selected metro network is derived where there is no fare incentive implementation, i.e., the original case. From the perspective of platform performance, Fig. 8 depicted the platform crowdedness of the two selected stations (Nanshao and Shahe stations). The dotted lines are the cumulation of passengers on the platform while the vertical lines are the arrivals of the vehicles. As shown in the figure, there exists two peak crowding times at Shahe station in southbound during 7:00–8:00 am and during 8:00am to 9:00am, respectively, which are due to the increasing passenger flow. The platform crowdedness also increases after 10:00am with the extended headway which is different from the previous peak times. The passengers' inbound and outbound volumes from smartcard data reflect the average condition over the 3-month period, hence the agent-based simulation also reflects the average conditions that passengers wait for the service runs on the platform with possible boarding failure of the first arriving service run.

From the perspective of vehicle level crowdedness, Fig. 9 shows the capacity occupancy of two representative trains (train # 331029 and train #321047). The vertical lines are the stations along the rail line. Both trains are fully occupied when leaving Shahe station at 7:36 AM and at 9:00 AM, respectively, and maintained the full occupancy when leaving in the downstream station. Figure 10 further depicted the in-vehicle occupancy for all vehicles in Changping line in the morning hours where 30 out of 128 trains have reached capacity.
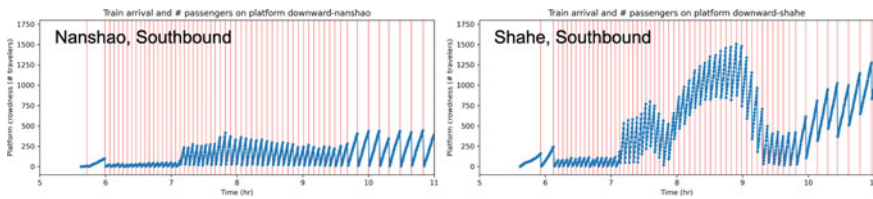


**Fig. 8** Platform crowdedness in two stations
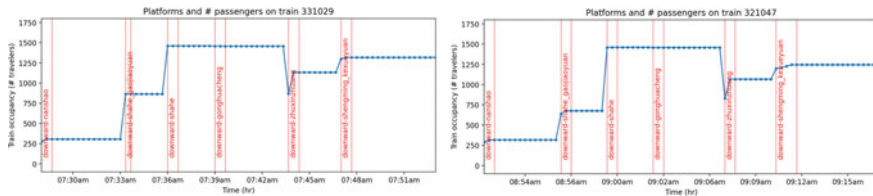


**Fig. 9** Vehicle crowdedness of selected trains
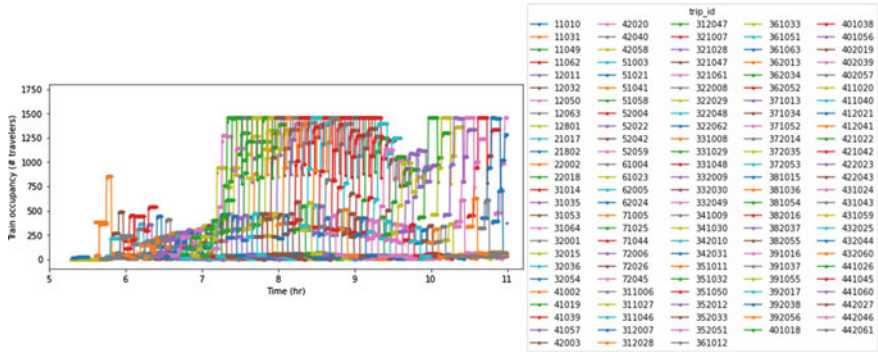
**Fig. 10** Overview of in-vehicle crowdedness for all service runs before fire incentive is introduced (baseline scenario)

## 4.3 Comparison of System Performance Before and After Fare Incentive

To evaluate the system performance of the proposed fare incentive, we first derive the individual travel patterns. As indicated in Sect. 3.1, the change of individual's departure time pattern depends on the original individual-based departure time pattern and the design of the surcharge-reward scheme. We proposed a scenario that the central peak period is defined from 8:00 to 8:30 am for all stations, namely, a passenger incurs a surcharge if he or she enters the station between 8:00 to 8:30 am and can use the rewards outside the central peak time window. The reward ratio is determined as 0.6. Based on the proposed scenario, the composition of different types of passengers is shown in Table 2 where 39.2% passengers' travel patterns are changed. Figure 11 further presents the differences of passengers' departures at stations before and after the fare incentive.

Figure 12 shows the platform crowdedness for Nanshao and Shahe stations before and after the fare incentive. It is noted that the Shahe station are able to be cleared for each service run after the fare incentive implementation while the other stations remain cleared. Figure 13 represents the in-vehicle crowdedness changes. After the fare incentive, the crowdedness of the selected service runs is relieved where the vehicle is no longer at full capacity during the peak periods which indicates all passengers are able to board on the first incoming vehicle. It is also noted that after the fare incentive, the majority of the service runs do not reach the full capacity

**Table 2** Percentage of different types of passengers under the six scenarios

| Type of passengers | Percentage (%) |
|---|---|
| Central DTFI (interval) | 1.89 |
| Shoulder DTFI | 59.10 |
| Cross DTFI | 39.02 |
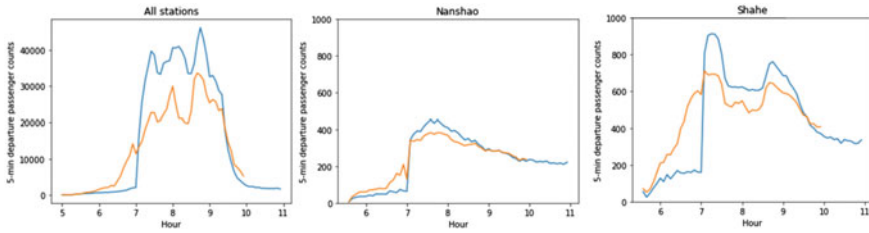
**Fig. 11** Passenger departure curves at stations before and after the fare incentive
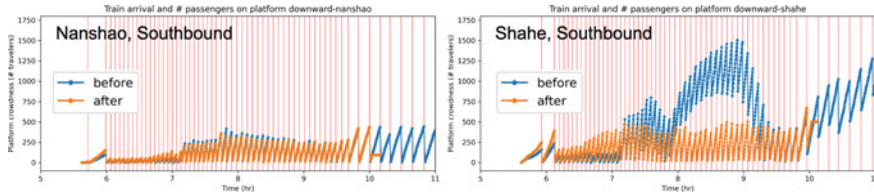


**Fig. 12** Platform crowdedness comparisons
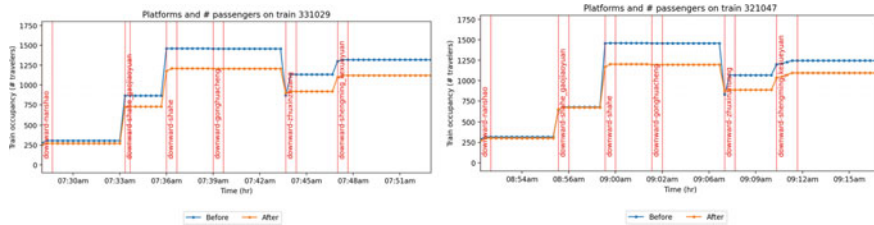


**Fig. 13** In-vehicle crowdedness comparisons

which indicates the potential of the fare incentive to reduce fleet sizes and operation costs for long-term operations as shown in Fig. 14.

We further analyzed the reduction of the travel times, crowdedness, and occupancy with the implementation of the fare incentives, as shown in Table 3. Results indicated that the capability of the incentive strategies to relieve the congestion at individual, train and platform levels.

## 5 Conclusions and Future Research

This paper proposed a framework of feasibility analysis with agent-based simulations and explores passenger's departure time pattern with multi-source data. Passenger's departure time pattern is determined as a departure time flexibility interval and a distribution within the interval. An outlier analysis is explored to detect the extreme
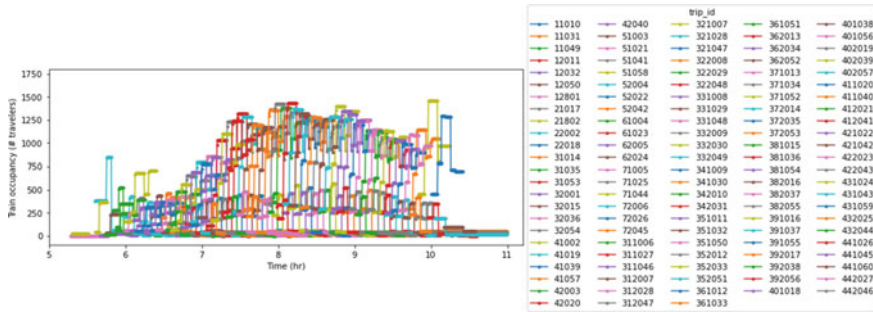
**Fig. 14** Overview of in-vehicle crowdedness for all service runs after fire incentive is introduced

**Table 3** Percentage reductions of waiting times, train occupancy and platform crowdedness

| Indicators | Percentage changes (%) |
|---|---|
| Average waiting time (minutes) | −14.6 |
| Time that train occupancy exceeds 90% of designed capacity (train-minutes exceeding 1300 passengers) | −67.9 |
| Average platform crowdedness (# passengers at any time per platform) | −23 |

value of departure times due to occasional trip purposes hence improve the precision of the departure time pattern determination. According to the design of the surcharge-reward scheme and the departure time patterns, passengers are recognized into three types, namely, cross DTFI, shoulder DTFI, and central DTFI. It is found that nearly 59.42% of target passengers have a length of departure time flexibility between 10 and 50 min in the selected station in Beijing Metro system which implies the practicality to implement the rewarding scheme by incentivizing passengers to change departure times within their flexibility interval.

We further developed an agent-based simulation to conduct the case study using the Beijing Metro network with three-month smartcard data and operation data for over 5 million trips. The scenario of the surcharge-reward scheme is proposed with setting for central period and reward ratio. Participation of different types of passengers is analyzed and the change of departure time pattern of each passenger is explored. The crowdedness at platform and service run levels are derived with the agent-based simulations by capturing the individual level trip activities.

Results reveal that the proposed surcharge-reward scheme is able to effectively reduce the peak hour congestion by changing passenger's departure time distribution while their flexibility interval is unchanged. This indicates the individual-based fare incentive may have higher practical acceptability than other pricing strategies or incentives as it considers passenger's tolerance of departure time switching. Future research may consider demand elasticity to understand the change of passenger's

flexibility interval with incentives. Optimization of the rewarding schemes in a large-scale mass transit network is also worthwhile to be explored for the potential benefits for passengers, transit operators as well as the system as a whole.

# References

1. Aggarwal CC (2015) Outlier analysis. In: Data mining. Springer, pp 237
2. Daganzo CF, Garcia RC (2000) A pareto improving strategy for the time-dependent morning commute problem. Transp Sci 34(3):303–311
3. Halvorsen A, Koutsopoulos HN, Lau S, Au T, Zhao J (2016) Reducing subway crowding: analysis of an off-peak discount experiment in Hong Kong. Transp Res Rec 2544(1):38–46
4. Jou R, Mahmassani H (1996) Comparability and transferability of commuter behavior characteristics between cities: departure time and route-switching decisions. Transp Res Rec: J Transp Res Board 1556:119–130
5. Lam WH, Zhang Y, Yin Y (1999) Time-dependent model for departure time and route choices in networks with queues. Transp Res Rec 1667(1):33–41
6. Langlois GG, Koutsopoulos HN, Zhao J (2016) Inferring patterns in the multi-week activity sequences of public transport users. Transp Res Part C: Emerg Technol 64:1–16
7. Ma X, Wu Y, Wang Y, Chen F, Liu J (2013) Mining smart card data for transit riders' travel patterns. Transp Res Part C: Emerg Technol 36:1–12
8. Mahmassani HS, Chang G (1986) Experiments with departure time choice dynamics of urban commuters. Transp Res Part B: Methodol 20(4):297–320
9. Mahmassani HS, Herman R (1990) Interactive experiments for the study of trip maker behaviour dynamics in congested commuting systems. In: Jones P (ed) Developments in dynamic and activity-based approaches to travel analysis. Avebury, Gower, Aldershot, England, pp 272–298
10. Mannering FL (1989) Poisson analysis of commuter flexibility in changing routes and departure times. Transp Res Part B: Methodol 23(1):53–60
11. Mannering F, Kim S, Barfield W, Ng L (1994) Statistical analysis of commuters' route, mode, and departure time flexibility. Transp Res Part C: Emerg Technol 2(1):35–47
12. Rouwendal J, Verhoef ET, Knockaert J (2012) Give or take? Rewards *versus* charges for a congested bottleneck. Reg Sci Urban Econ 42(1–2):166–176
13. Small KA (1982) The scheduling of consumer activities: work trips. Am Econ Rev 72(3):467–479
14. Tang Y, Jiang Y, Yang H, Nielsen OA (2020) Modeling and optimizing a fare incentive strategy to manage queuing and crowding in mass transit systems. Transp Res Part B: Methodol 138:247–267
15. Tang Y, Yang H, Wang B, Huang J, Bai Y (2019) A Pareto-improving and revenue-neutral scheme to manage mass transit congestion with heterogeneous commuters. Transp Res Part C: Emerg Technol
16. Vickrey WS (1969) Congestion theory and transport investment. Am Econ Rev 59(2):251–260
17. Xiong C, Zhang L (2013) Positive model of departure time choice under road pricing and uncertainty. Transp Res Rec 2345(1):117–125
18. Yang H, Tang Y (2018) Managing rail transit peak-hour congestion with a fare-reward scheme. Transp Res Part B: Methodol 110:122–136

# Hybrid Simulation-Based Resource Planning and Constructability Analysis of RCC Pavement Projects

**Mohammad Shakerian, Mohammad Sadra Rajabi, Mohammad Tajik, and Hosein Taghaddos**

**Abstract** One of the critical challenges in infrastructural constructions is designing and planning operations and their related resources. The complex interlinked composition of different factors and variables affecting resource productivity has made simulation a powerful approach for operational planning. The construction sector has recently seen a notable surge in applying various simulation tools to enhance further the quality of projects' planning, particularly in large-scale infrastructure developments (e.g., highway construction). Due to possible cost overruns in improper resource allocation, optimizing the design and construction planning stages of megaprojects such as massive pavement projects is essential. Recent studies aimed to build a simulation-based strategy in construction designing and planning by combining various simulation approaches (e.g., discrete-event simulation, system dynamics, agent-based simulation, and hybrid simulation) to enhance the planning phase. This paper introduces an evolving real-time hybrid simulation technique regarding the project's intrinsic time-varying inputs and factors to optimize the planning of Roller-Compacted Concrete (RCC) pavement projects. Several scenarios are investigated using various resource combinations to achieve the best execution method for delivering concrete to the project. An actual highway project case study validates the proposed model and its application for future projects. This study's findings exhibit the proficiencies of the simulation-based approach in resource planning of RCC pavement projects within the time and cost constraints and their related regulations.

**Keywords** Construction simulation · Hybrid simulation · Equipment planning · RCC pavement · System dynamics

M. Shakerian · M. Tajik · H. Taghaddos (✉)
School of Civil Engineering, College of Engineering, University of Tehran, Tehran, Iran
e-mail: htaghaddos@ut.ac.ir

M. S. Rajabi
Department of Civil and Environmental Engineering, The George Washington University, Washington, DC, USA

# 1 Introduction

The efficient scheduling and planning phase of a construction project significantly impacts its likelihood of success. However, such a significant step requires a considerable amount of work and resources due to the complexity of construction projects. A better understanding of construction operations is obtainable through visual modeling of construction activities.

Traditional planning and scheduling methods encounter many shortcomings when applied to complex construction projects. Pritsker [19] has presented some of these inadequacies. For instance, conventional planning approaches are limited due to their static and deterministic assumptions. Traditional techniques are more suitable for projects with fewer activities and fewer uncertainties. Critical Path Method (CPM), Line of Balance (LOB), and Program Evaluation and Review Techniques (PERT) are a few of these mentioned traditional scheduling methods [1].

Therefore, simulation modeling has been introduced to develop computer-based representations of construction systems to recognize their behavior to improve the efficiency in project management and even construction safety [2, 3]. In previous studies, mathematical modeling systems such as mathematical programming and queuing theory did not demonstrate suitable applications in large-scale and more complex construction projects [15]. To address these issues, computer simulation techniques were introduced as an effective tool to design and analyze construction procedures despite their complexity or size. Computer models can generate the proper solutions while considering the overall logic of various activities, the resources involved, and the environment under which the project is constructed [10]. Simulation models are entirely successful in embodying the process of building a facility and can be used to develop better strategies, optimize resource utilization, minimize costs or project duration, and improve overall construction project management [2].

Numerous simulation tools have been introduced in recent years in which: CYCLONE, STROBOSCOPE, Simphony.NET, and VitaScope are among the most recent ones [13, 14]. Sawhney et al. [21] describe the enhancements made to the CYCLONE modeling methodology to allow simultaneous simulation of processes involved in a construction project. These enhancements aim to develop individual components for all the processes that constitute a project and then link them to simulate them simultaneously using a shared resource pool. Although simulation modeling is focused on the planning stages, better decision-making requires modeling the project during the construction and planning phases [5].

Recent studies have employed discrete-event simulation (DES), Agent-based simulation, system dynamics (i.e., continuous simulation), or hybrid simulation integrating discrete-event simulation and system dynamics models to model construction environments [16]. In a hybrid simulation, feedback loops play a significant role in automating the process [20]. Such studies model a construction project from different perspectives, such as effective resource allocation, safety enhancement, and site layout planning [6, 12, 24, 25]. Similarly, various studies have analyzed different aspects of project management, such as risk evaluation, stochastic variants,

and decision-making strategies with the help of simulation tools and techniques [7, 11, 17].

The focus of this study is to employ hybrid simulation to enhance the supply chain management of RCC pavement projects. The most relevant study for this paper is [23], which introduces a simulation-based approach to model a significant milestone of the construction process in an RCC dam. Several what-if construction scenarios were analyzed for the milestone based on different combinations of the resources, and then a time–cost trade-off analysis was used to find the optimum construction scenario for the milestone. The proposed approach gives the managers a vision of the total time and cost of the project based on the different alternative scenarios.

However, the construction of RCC dams and RCC pavement has significant differences. RCC pavement is among the linear project, making supply chain management (i.e., concrete supply from batching plant to the paver) more challenging. The following chapter provides a brief background to RCC pavement projects.

The primary simulation software used in this research is Simphony.NET 4.6. Simphony was first developed in 1998 by Dr. Simaan AbouRizk and Dr. Danny Hajjar. Its successor, Simphony.NET, was developed by Dr. Abourizk and Stephen Hague and continues to be developed at the University of Alberta [4, 13].

## 1.1 RCC Pavements

Roller-compacted concrete (RCC) is a durable, economical, and low-maintenance material for low-speed heavy-duty paving applications, including industrial and transit pavements. Recently, there has been increasing interest in the use of RCC for public roadways. Its consistency is rigid enough that it can maintain its stability under the load of the roller compactor with vibration and, at the same time, allow a proper spreading of the concrete mixture without any separation. Similar to many other construction projects, pavement construction involves complex geometry and complicated processes [9]. RCC heavy-duty pavements may be constructed in single or multiple layers depending on the design capacity of the road [18]. Generally, roller-compacted concrete is spread by a modified asphalt paver and compacted by a steel drum roller, vibrating roller, and rubber wheel roller [8].

Figure 1 shows a visual sequence of activities that conclude an RCC pavement project. Dump trucks are usually used to haul the concrete mix to the paving front. Iranian concrete pavement guideline allows for a maximum elapsed time of 45 min after mixing has occurred. This factor is most dominant when the pavement site or work zone is far from the batching plant. Compaction of the placed RCC must follow instantly after its placement [18]. Curing and cutting wedges are another two primary operations.

A steady concrete supply to the paver machine must be maintained for civil code compliance and better surface quality. Planning of hauling machines gets more complicated when project geometry is constantly changing. In road projects, the
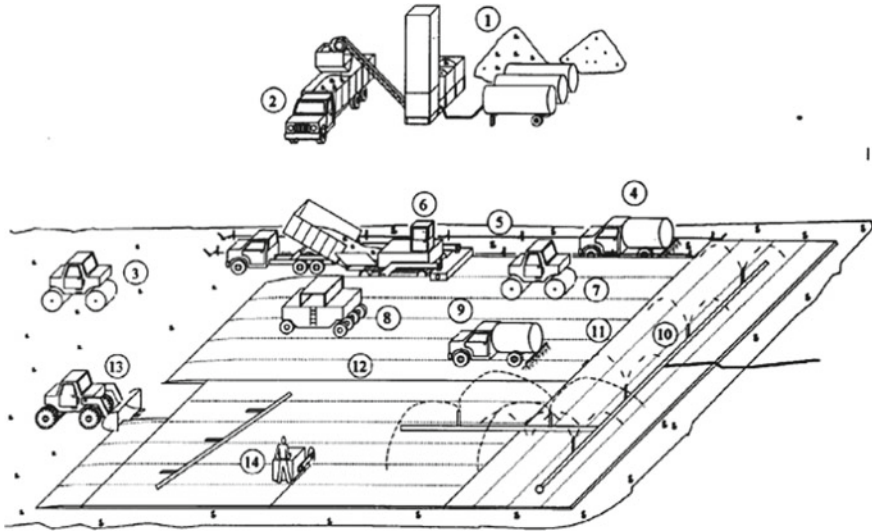
**Fig. 1** Schematic illustration of RCC pavement construction activities. Captured from Iranian guidelines for the construction of concrete roads (issue #733)

relative distance of resources is essential in decision-making. Also, few constraints for maintaining the quality of concrete affect planning and resource scheduling.

This paper proposes a simulation model to optimize resources for concrete supply to the paver using different capacity dump trucks while meeting all the constraints issued by concrete-based road guidelines. For better results, this study embeds a dynamic feedback system to allow automated alteration of resources regarding the state and progress of the project.

## 2 Overview of Case Study ("Shahrbabak-Harat" RCC Highway 2nd Lane)

"Shahrbabak" city is located on the "Tehran-Bandar Abbas" transit road, and the "Shahrbabak-Harat" transit road sits at the heart of Iran's east–west transport corridor. It is located on the Sassanid historic road and was built by the National Construction and Development of Transport Infrastructure Organization in 2016. The second lane of this highway, with a length of 44 km and a width of 11 m, is the subject of this study, used to develop an accurate model for future planning of the same type of project. In order to obtain a high-quality surface in the "Shahrbabak-Harat" project, according to the employer's recommendation, a paving machine with an 11 m width distribution capability was rented. Unlike conventional concrete paving, roller concrete paving is made without molds, dowels, or steel reinforcements. It is usually unnecessary to make a joint with a saw, but if required by the technical specifications, the distances of
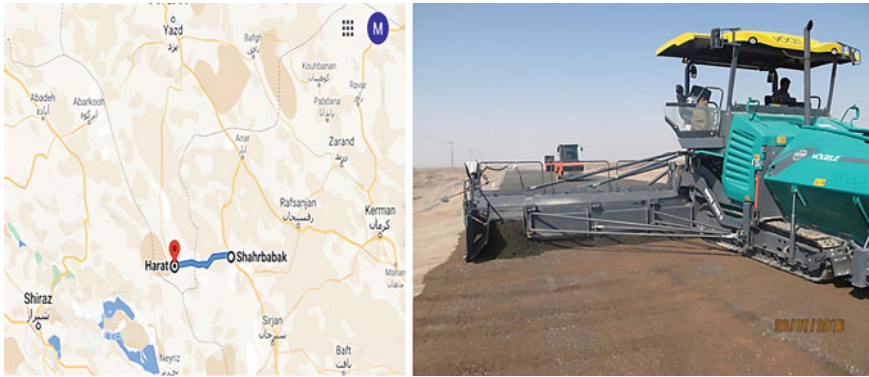
**Fig. 2** On the (left) Location and path of the studied pavement project On the (right) A picture of paving machinery used on the project in 2016

transverse joints are longer than concrete paving. The concrete plant sits at a distance of 25 km from the start point ("Shahrbabak" city) in the middle of the proposed road (Fig. 2).

## 3 Proposed Multi-Step Methodology

### 3.1 Modeling of the RCC Pavement Construction

As shown in Fig. 3, a linear RCC pavement project is modeled using Simphony.NET 4.6. Generally, linear construction projects are defined as projects in which most work consists of highly repetitive activities. These operations are repeated in each location for the entire road length. The flow of concrete from batching plant through dump trucks and into the paver must be modeled continually to control regulations and guidelines more effectively. Therefore, a combination of DES and continuous simulation has been applied. This model is also equipped with a system dynamic method with the same general premise as Fig. 4.

Due to the nature of road projects, equipment location and their relative distance are in constant change. Hence, behavior of activities follows functions related to the progress of simulation and the state of other operations. This model uses four feedback loops to allocate resources better as the project advances as its relative distances and durations change. This feature can help the process to adapt to the available resources at a given time. For example, similar to this case study, if the concrete plant is at the middle point of the road, as the project progresses, the pavement frontline gets closer to batching plant, and a smaller fleet of trucks is required to maintain a steady flow of concrete to the paver. After passing the middle point
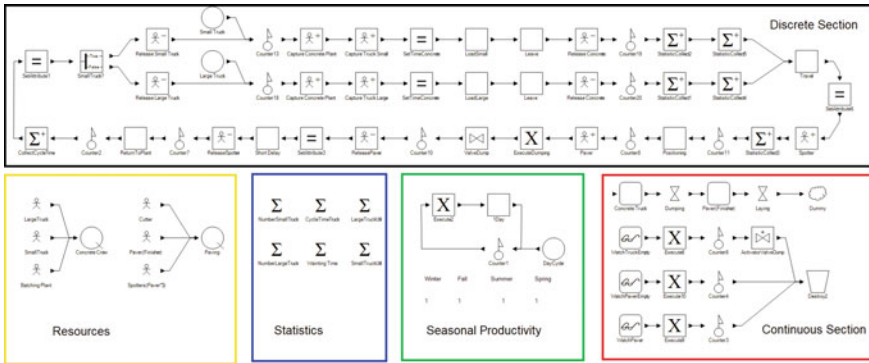
**Fig. 3** Developed model for RCC pavement construction in Simphony.NET 4.6
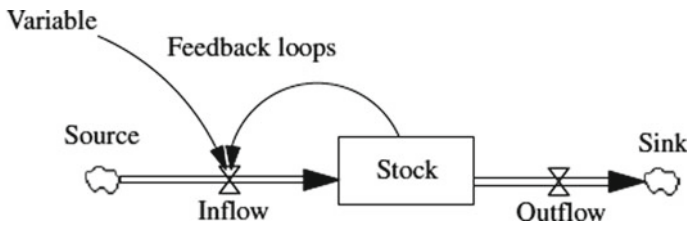


**Fig. 4** Simple diagram of a system dynamic model. Adapted from Sterman [22]

of the road, the relative distance to the concrete plant increases, and the number of required resources changes.

The proposed model in this study focuses on the supply chain of concrete to the paver, as these operations are affected the most by the project's geometry. For example, the number of required trucks would be much lower in the middle point of the construction rather than the start point since the work zone moves toward the batching plant. All project inputs, durations, and relative distances are user-defined. This ability enhances the model's customizability; therefore, it can be used for similar projects such as asphalt pavements without much effort in changing its components and inner properties. This study considers all the essential tasks in an actual RCC pavement project which correlate to the concrete supply resources.

## 3.2 Scenario Analysis for Various Combinations of Resources

Pavement construction is composed of many resources linked and reliant on each other. Table 1 shows the main activities in an RCC pavement project, its duration, and necessary resources. One of the primary resources and the object of this study is the dump trucks used to convey concrete to the paver on site. Dump trucks with different

capacities are often used concurrently in the same project. Large dump trucks can carry 7.5 cubic meters of concrete in this study, 50% more than small dump trucks. The main object of this scenario analysis is to find the optimum number of large and small dump trucks while satisfying the government's RCC regulations and those imposed by the owner. Two main constraints in this model are listed below.

1. Concrete must be placed and compacted within 45 min.
2. For a steady concreting process, dump trucks must maintain an interarrival time of less than 3 min.

All possible combinations must be modeled to find an optimum scenario with the highest utilization rate. These different scenarios must be filtered to satisfy the owner's constraints and mandatory regulations. The maximum number of large and small dump trucks is 10 and 5, respectively. In theory, 50 different scenarios must be checked to find the optimum dump truck combination for this project. Table 2 shows the accepted composition of dump trucks and the mean utilization of each type in every scenario. This table indicates that scenario #39 is the optimum resource grouping since it has a higher average utilization. Also, due to the limited capacity of the paver for laying concrete, increasing the number of dump trucks after a certain point will only result in higher waiting times and long queues.

**Table 1** Main activities and their required resources

| Activity* | Duration (minutes) | Resources |
|---|---|---|
| Loading small truck | 3 | Small truck, batching plant |
| Loading large truck | 4.5 | Large truck, batching plant |
| Travel to paver | Inconstant* | Small or large truck |
| Dumping | 2.5 (small truck) 3.75 (large truck) | Small or large truck, paver, spotters |
| Return to batching plant | Inconstant* | Small or large truck |

* Travel distances are continuously changing during the project

**Table 2** Accepted scenarios for dump trucks

| Scenario number | Number of large dump trucks | Number of small dump trucks | Mean utilization large dump truck (%) | Mean utilization small dump truck (%) | Total project duration (minutes) |
|---|---|---|---|---|---|
| #39 | 9 | 4 | 65.5 | 7.7 | 96,919 |
| #40 | 10 | 4 | 58.9 | 7.7 | 96,919 |
| #49 | 9 | 5 | 65.5 | 6.1 | 96,919 |
| #50 | 10 | 5 | 58.9 | 6.1 | 96,919 |

## 3.3 Enhancement of Resource Planning with System Dynamics

After finding the optimum scenario, this model is integrated with a system dynamic approach to obtain more detailed resource planning while the project progresses. Since road projects are constantly changing location, the number of required resources might need to update along the way. Feedback loops can change the number of resources while the simulation progresses. As the pavement advances, the frontline of work is getting closer to the batching plant in this study. Therefore, the number of dump trucks could be updated to maintain a high utilization.

Figure 5 shows the utilization of large dump trucks without any feedback loops during pavement construction based on the optimum scenario determined in the last step. The average utilization rate of large dump trucks is 65.5%. After finding the optimum resource combination for the dump trucks, the SD method, explained in the methodology, is enabled for detailed planning of the resources throughout the project's lifespan. Figure 6 shows the utilization of large dump trucks being constantly updated using feedback loops during the construction. The average utilization rate with this enhanced method is 89.9%. This figure also shows the effectiveness of the system dynamics method for yielding a more significant average utilization rate.

Figure 7 shows detailed resource planning as this study's main result and output for Babak-Herat RCC Road. A detailed resource allocation plan is presented for construction managers and industry practitioners. With this method, engineers will be able to reallocate these excess resources to other projects to reduce the total cost of projects.



**Fig. 5** Utilization rate of large dump trucks
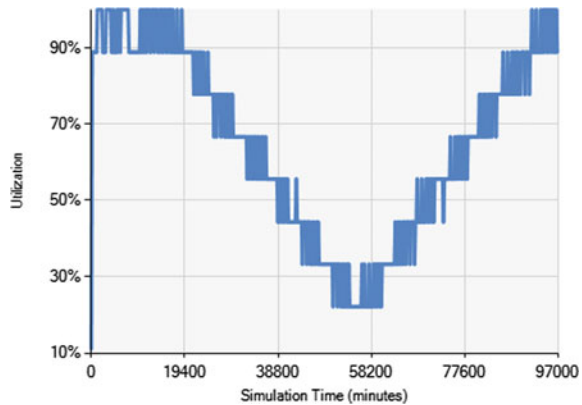
**Fig. 6** Enhanced utilization rate of large dump trucks
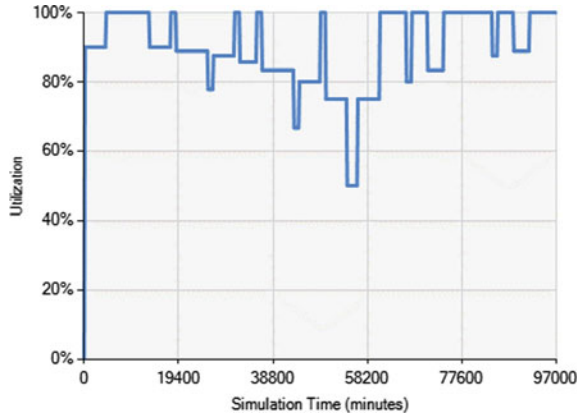


**Fig. 7** Final enhanced resource scheduling of large dump trucks
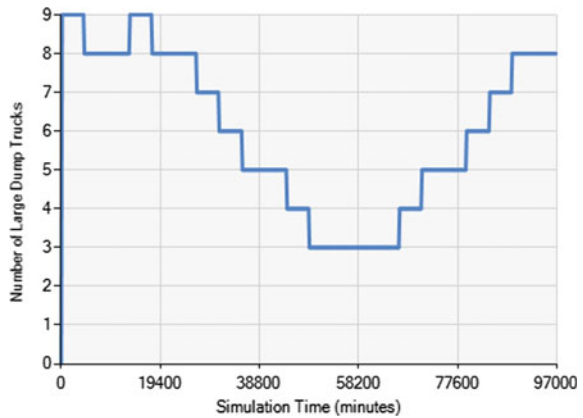


## 4 Limitations

The proposed model in this study is limited to RCC pavement but can be effortlessly extended to include other pavement materials such as hot mix asphalt (HMA). Optimization of resources unrelated to work zone geometry has been neglected for simplicity. Since these resources do not correlate with any variables in their behaviors, static and traditional planning methods were opted for based on experts' judgments. The main reason behind all the above limitations is that this study only includes the specific optimization and level of detail required by the project owner.

# 5   Conclusion

The primary purpose of this study was to find the optimum resource combination of different dump truck types that are mainly involved in the RCC supply chain to the paver at the frontline. All the possible combinations were tested concerning the government guidelines on concrete pavement construction. The optimum resource combination is then selected based on the higher utilization of resources. A case study of the RCC pavement project is also investigated using a hybrid model in Simphony.NET 4.6. The results illustrate the capabilities of the simulation-based approach in designing and planning pavement construction projects.

This paper proposes a dynamic hybrid simulation-based approach to find the optimum scenario based on the available resources and constraints in an actual RCC pavement construction project. It utilizes mathematical equations based on the continuously changing durations in a horizontal project to regulate and adapt to the new geometry.

To validate the proposed model's results, the optimum scenario was compared to those used by the contractor in the original "Shahrbabak-Harat" highway in 2016. The comparison showed a better utilization rate but close to the actual project. Hence, this dynamic model can be used in future projects for better resource allocation and planning.

This study acknowledges the importance and advantages of simulation-based modeling in construction projects' planning and scheduling phase. Due to construction projects' dynamic and complicated characteristics, simulation tools have been utilized to model construction processes in recent years. Simulation-based modeling is a powerful tool capable of visualizing and modeling construction activities. Road, pavement, and resurfacing projects are critical infrastructural developments due to their enormous budget and importance to the public. Therefore, having an optimum resource and execution plan which meets all the governmental policies ensures lower cost and better product quality.

The overall results of this study demonstrate the proficiencies of simulation tools in planning resources for pavement projects. Simulation models can be programmed to develop more detailed resource schedules, yielding higher utilizations.

# References

1. Abdallah M, Marzouk M (2013) Planning of tunneling projects using computer simulation and fuzzy decision making. J Civ Eng Manag 19(4):591–607
2. AbouRizk S (2010) Role of simulation in construction engineering and management. J Constr Eng Manag 136(10):1140–1153

3. AbouRizk S, Halpin D, Mohamed Y, Hermann U (2011) Research in modeling and simulation for improving construction engineering operations. J Constr Eng Manag 137(10):843–852

4. AbouRizk SM, Hague S (2009) An overview of the COSYE environment for construction simulation. In: Proceedings of the 2009 winter simulation conference (WSC). IEEE, pp 2624–2634

5. Adra H, Roeder TMK, Frazier PI, Szechtman R, Zhou E, Huschka T (2016) Realtime predictive and prescriptive analytics with real-time data and simulation. In: Proceedings of the 2016 winter simulation conference. Institute of Electrical and Electronics Engineers, Inc., pp 3646–3651

6. Alzraiee H, Zayed T, Moselhi O (2015) Dynamic planning of construction activities using hybrid simulation. Autom Constr 49:176–192

7. Beigi P, Khoueiry M, Rajabi MS, Hamdar S (2022) Station reallocation and rebalancing strategy for bike-sharing systems: a case study of Washington DC. arXiv preprint arXiv:2204.07875

8. Chhorn C, Hong SJ, Lee SW (2017) A study on performance of roller-compacted concrete for pavement. Constr Build Mater 153:535–543

9. Delatte N (2004) Simplified design of roller-compacted concrete composite pavement. Transp Res Rec 1896(1):57–65

10. Ekyalimpa R, AbouRizk S, Farrar J (2012) Effective strategies for simulating one-of-a-kind construction projects. In: Proceedings of the 2012 winter simulation conference (WSC). IEEE, pp 1–13

11. Erfani A, Tavakolan M (2020) Risk evaluation model of wind energy investment projects using modified fuzzy group decision-making and monte carlo simulation. Arthaniti: J Econ Theo Prac 0976747920963222

12. Goh YM, Ali MJA (2016) A hybrid simulation approach for integrating safety behavior into construction planning: an earthmoving case study. Accid Anal Prev 93:310–318

13. Hajjar D, AbouRizk S (1999) Simphony: an environment for building special purpose construction simulation tools. In: Proceedings of the 31st conference on Winter simulation: simulation—a bridge to the future, vol 2, pp 998–1006

14. Halpin DW (1977) CYCLONE–method for modeling job site processes. J Constr Div 103(3):489–499

15. Moeinifard P, Rajabi MS, Bitaraf M (2022) Lost vibration test data recovery using convolutional neural network: a case study. arXiv preprint arXiv:2204.05440

16. Moradi S, Nasirzadeh F, Golkhoo F (2015) A hybrid SD–DES simulation approach to model construction projects. Construct Innov

17. Mudiyanselage SE, Nguyen PHD, Rajabi MS, Akhavian R (2021) Automated workers' ergonomic risk assessment in manual material handling using sEMG wearable sensors and machine learning. Electronics 10(20):2558

18. Piggott RW (1986) Roller compacted concrete for heavy-duty pavements: past performance, recent projects, and recommended construction methods. Transp Res Rec 1062:7–12

19. Pritsker AAB (1989) Why simulation works. In: Proceedings of the 21st conference on Winter simulation, pp 1–9

20. Salloum Y, Jodehl A, Thewes M, König M (2020) From forecasting to real-time process controlling with continuous simulation model updates. In: Proceedings of the 37th international CIB W78 conference

21. Sawhney A, AbouRizk SM, Halpin DW (1998) Construction project simulation using CYCLONE. Can J Civ Eng 25(1):16–25

22. Sterman J (2010) Business dynamics. Irwin/McGraw-Hill c2000

23. Taghaddos H, Dashti MS (2017) Simulation-based constructability analysis of an RCC dam. In: Proceedings of the 6th CSCE/CRC international construction specialty conference. CSCE Vancouver, Canada

24. Taghaddos H, Hermann U, AbouRizk S, Mohamed Y (2014) Simulation-based multiagent approach for scheduling modular construction. J Comput Civ Eng 28(2):263–274

25. Taghaddos H, Heydari MH, Asgari A (2021) A hybrid simulation approach for site layout planning in construction projects. Construct Innov

# Comparative Analysis of Intersection Data Derived from INRIX and GRIDMART

**Maria Bassil, Natalia Ruiz Juri, and Randy Machemehl**

**Abstract** With an increase in transportation funding, the need arises to implement analytic tools to measure the effects of improvements and guide decisions regarding the effective planning and design, as well as the operation of streets. Recent advances in intelligent transportation systems (ITS) and data collection made available high volumes of data from multiple data sources. However, a significant challenge remains in digesting and understanding the large and complex data available. In the specific case of intersections, the estimation of performance metrics is challenging due to the presence of different traffic control systems, multiple data sources and multi-modal interaction. The principal objective of this research is to evaluate intersection performance metrics calculated using two different data sources and using Austin, Texas, as a case study. The evaluation is based on the fusion of INRIX data and GRIDSMART data. The main contributions include development of comparative intersection performance metrics combining two data sources, implementation of all required data workflows, and analysis of the fusion of GRIDSMART data and INRIX data. The analyses suggest that while total volume estimates provided by INRIX are not likely to be accurate, and discrepancies with GRIDSMART data are larger than 20% in most analyzed cases, differences in turning movement ratios yielded more promising results with differences between the two data sources generally less than 10%. Those results provide information that can help practitioners select an appropriate methodology for evaluating intersection performance.

M. Bassil (✉)
Department of Civil, Architectural, and Environmental Engineering, The University of Texas at Austin, Austin, TX, USA
e-mail: maria.bassil@utexas.edu

N. Ruiz Juri
Center of Transportation Research, The University of Texas at Austin, Austin, TX, USA

R. Machemehl
Nasser Al-Rashid Centennial Professor in Transportation Engineering, Department of Civil, Architectural, and Environmental Engineering, The University of Texas at Austin, Austin, TX, USA

## 1 Introduction

Signalized intersections are indispensable parts of urban traffic networks. Currently, over 300,000 traffic signals exist in the United States (U.S.), accounting for \$82.7 billion in public investments [8]. With two-thirds of urban vehicle miles traveled on signal-controlled roads [6], signalized intersections have often become hot-spots of traffic congestion, causing 295 million vehicle-hours of delay annually. Considering the number of traffic signals and their impact to the traffic network, it is critical to operate traffic signals efficiently [3].

Until recently, data collection required expensive infrastructure imposing many limitations on performance measures development. The development of the global positioning system (GPS) technology and intelligent transportation systems (ITS) has increased data availability as well as analysis capabilities [2]. Nevertheless, it remains challenging to understand, process, and interpret the large and complex volume of data available. In the specific case of corridor intersections, the estimation of performance metrics is challenging due to the presence of different traffic control systems, multiple data sources, and multimodal interaction [11].

This study aims to present an automated workflow to compare INRIX and GRIDS-MART data having different formats and labels. It is based on conducting a preliminary validation of new intersection performance metrics provided by INRIX by analyzing data at selected intersections, where GRIDSMART cameras are deployed. This analysis is focused on total intersection volume and average daily turning movement counts by approach. Since errors may be present in both data sources, this study also proposes simple quality control metrics to identify scenarios in which GRIDSMART data may not be reliable.

## 2 Background

Data collection has been used on roadway systems since as early as the 1930's and it has continued to evolve with technology [10]. The amount and quality of available data are key components for improving transportation systems safety and performance. The continuing challenge is gathering complete and accurate data and making it more accessible and easier-to-use for transportation leaders and decision-makers [5].

Traffic volume data serves multiple needs for transportation professionals and is vital to establishing the baseline conditions for roadways and intersections. Transportation planners rely on traffic counts to support traffic impact studies, long-range transportation plans, corridor studies, travel demand forecasting, and signal warrant

studies for municipal, agency, or institutional clients [1]. Additionally, traffic engineers leverage volume data to assess near real-time operating conditions on corridors and/or intersections. These assessments are critical to help identify operational constraints, assess safety conditions, and support the maintenance of these facilities [9].

Transportation-related probe data has evolved over the past decade. Available information from probe data sources has become functionally more complex as the saturation of data-providing devices and the speed at which this data is made available has greatly expanded, with a majority of these data sources now reporting latencies less than one minute or near real-time. Probe data generally has a capture rate of 10–25% of the total number of vehicles passing through an intersection depending on the nature of the surrounding area [9].

Similarly, intersection turning movements' counts are critical input data for traffic studies, analysis, and forecasting. These types of counts are often used to analyze operational performance of signalized intersections under different traffic conditions and peak hours [4].

This study consists of a comparative analysis that aims to address the on-going challenge of gathering complete and accurate data for intersections. This study's line of effort aims to bridge the gap between the data challenges and the development of intersections performance metrics.

## 3 Intersection Data Description

### 3.1 INRIX

#### 3.1.1 INRIX Traffic Counts Data

In January 2020, INRIX announced a signal analytics platform in collaboration with the Center for Advanced Transportation Technology (CATT Lab). This product ("Signal Analytics") is advertised as the industry's first signal analytics platform based exclusively on anonymous vehicle data. Signal Analytics provides signal performance metrics by intersection, movement, time of day, and day of week. The data is collected purely from probe vehicles, with no roadside infrastructure required. The platform provides also the top five intersections with worsened control delay [7]. Initial metrics available at all intersections include:

1. Arrival on green: Percent of vehicles without a stop recorded within the intersection crossing.
2. Stopped vehicles: Number of observed vehicles that stopped at the intersection.
3. Actual movements: Number of observed movements at the intersection for a chosen time period.
4. Travel time: Distribution of time for each movement sequence in the intersection.
5. Approach speed: Speed distribution of vehicles directly before the intersection.

6. Intersection delay: Observed vehicle delay at the intersection by movement.

Daily INRIX signal analytics data can be accessed through the INRIX IQ website, while historic data analyses and data downloads are available through the RITIS platform. The maximum allowed analysis period cannot exceed 30 days, and at most 400 intersections may be selected for a report (at the time of our study). Historic data is provided in JSON format and aggregated at the daily level (hourly or time of day aggregates are not available).

### 3.1.2   INRIX Turning Movements Data

INRIX provides aggregate reports for user-specified intersections and time periods. Intersections are selected manually on a map through their web interface for each analysis. Results represent an average for the analyzed time period (across days of the week and hours of the day). The reports are provided in JSON format (the structure of the file is described in documentation available from the vendor). Results include several types of metrics at the intersection, approach, and turning movement levels. In our analysis, we consider turning movement-level data by approach. Extracted fields include:

1. Intersection ID (INRIX_id): Unique ID of the intersection given by INRIX.
2. Latitude: Latitude of the intersection center point.
3. Longitude: Longitude of the intersection center point.
4. Location point: Geometric location of the intersection.
5. Name: Name of the intersection.
6. Inbound direction: Movement inbound direction as the vehicle approaches the intersection center.
7. Outbound direction: Movement outbound direction as the vehicle leaves the intersection center.
8. Direction: Direction of the movement.
9. Start date: Analyzes start date.
10. End date: Analyzes end date.
11. Turn percent: Turn percentage based on the total observed vehicle counts on this movement relative to the approach count.
12. Turn maneuver: A string describing the turn maneuver of the movement (e.g.,: left, right, through).
13. Control delay: The difference between the actual travel time for a vehicle to move through the intersection vs the reference travel time. The reference travel time is calculated as the fifth percentile of travel times for non-queued vehicle movements through the intersection, as per INRIX documentation.

## 3.2 GRIDSMART Data

### 3.2.1 GRIDSMART Traffic Counts Data

The City of Austin (CoA) operates 126 optical traffic detectors (GRIDSMART cameras), for which turning movement data and some performance metrics are posted online daily. The status of these detectors is also tracked on the CoA's Open Data Portal. At the time of this study, 42 GRIDSMART detectors were broken, 9 were removed, 4 needed verification and 2 were labeled as unknown. The GRIDSMART data includes the following fields:

1. Record ID: A unique ID for each row created as a hash of intersection name, time, truck status, direction, and movement.
2. ATD device ID: The ID of the device as noted in the "traffic detectors" table.
3. Read date: The start of the respective time interval used for aggregation, UTC.
4. Intersection name.
5. Direction: The travel direction of the approach toward the intersection.
6. Movement: The turning movement of respective traffic entering the intersection.
7. Heavy vehicle: A classifier for vehicles that are measured to be 17 feet or longer.
8. Volume: The number of vehicles traveling in the respective direction and making the respective turning movement throughout the 15-min interval.
9. Speed average (miles per hour): Average speed of vehicles that entered the intersection, including those that had started after the end of a red light.
10. Speed stddev: Standard deviation of all speed measurements, or 0 if volume is less than 2.
11. Seconds in zone average: Average amount of time that vehicles were in the measurement zone, including time that vehicles are stopped at a red light.
12. Seconds in zone stddev: Standard deviation of "seconds in zone".
13. Month The numeric month of the aggregation interval.
14. Day: The numeric day of the aggregation interval.
15. Year: The numeric year of the aggregation interval.
16. Hour: The numeric hour of the aggregation interval.
17. Minute: The numeric minute of the aggregation interval.
18. Day of week: Starting with Sunday is 0 and Monday is 1, and so on.
19. Bin Duration (seconds): Number of seconds for the aggregation interval: always 15 min.

The Open Data Portal notes that average speed measurements may not have been calibrated for all intersections, and that all measurements have been collected using automated machine vision processes and have not been validated.

### 3.2.2 GRIDSMART Turning Movement Data

GRIDSMART provides turning movement traffic volumes every 15 min. Our workflow computes a daily turning movement ratio by approach based on daily turning

movement volumes and averages it over the selected analysis period to produce a metric comparable with the INRIX data. Daily turning movement ratios are saved in a summary table which includes the following fields:

1. ATD device ID: The ID of the device as noted in the "traffic detectors" table.
2. Intersection name.
3. Direction: The travel direction of the approach toward the intersection.
4. Movement: The turning movement of respective traffic entering the intersection.
5. Month The numeric month of the aggregation interval.
6. Day: The numeric day of the aggregation interval.
7. Year: The numeric year of the aggregation interval.
8. Hour: The numeric hour of the aggregation interval.
9. Day of week: Starting with Sunday is 0 and Monday is 1, and so on.
10. Movement volume: Total volume of cars for a specific movement.
11. Approach movement (approach_mov): The turning movement of the specific approach.
12. Turning ratio (tm_ratio): Calculated by dividing the turning volume by the total volume of a specific approach.
13. Movement_INRIX: This column is added to map the GRIDSMART nomenclature for turning movements to INRIX's.
14. Dir_INRIX: This column is added to map the GRIDSMART nomenclature for incoming approach direction to INRIX's.

Tables 1 and 2 describe the mapping of GRIDSMART approach and movement nomenclature to the corresponding INRIX nomenclature.

The GRIDSMART turning ratios for each intersection are illustrated in Fig. 8 and the INRIX turning ratios for each intersection are illustrated in Fig. 9 of the Appendix.

**Table 1** Movements matching

| GRIDSMART movements | INRIX movements |
| --- | --- |
| Left turn | Left |
| Right turn | Right |
| Through | Through |
| U-turn | Not matched |

**Table 2** Directions matching

| GRIDSMART directions | INRIX directions |
| --- | --- |
| Eastbound | E |
| Westbound | W |
| Northbound | N |
| Southbound | S |

# 4 Proposed Methodology and Results

## 4.1 Traffic Counts Comparison

For the comparison of intersections traffic counts, the total volume by day was first plotted (as shown in Fig. 1) for the GRIDSMART data from December 2020 to 25 March 2021. Note that some of these intersections have broken, unknown, or unverified detectors as discussed earlier in Sect. 3.2.

Figure 1 shows that for some cameras/months daily patterns are somewhat erratic, which suggests that the corresponding data may not be reliable. Based on that, this study proposes the following metrics for a preliminary assessment of data quality:

- Standard deviation of average daily volumes by month and day of week (SD): The monthly ratio of SD to the corresponding mean value for each day of the week (R_DOW) are plotted (Fig. 10 of the appendix). An intersection is considered reliable on a particular month when R_DOW is lower than 35% for at least four days of the week, and lower than 50% on all days of the week.
- Availability of data: GRIDSMART cameras are expected to produce 96 data points per day, one every 15 min. If data points are missing, daily volumes are likely to be underestimated. This study proposes considering data at locations where at least 85% of expected data points are available. Figure 11 of the appendix presents data availability by month at all locations active as of March 2021.

After identifying intersections having reliable GRIDSMART data, the differences between INRIX daily traffic estimates and GRIDSMART counts were calculated. Table 3 compares data from both sources on a specific date, and Table 4 compares
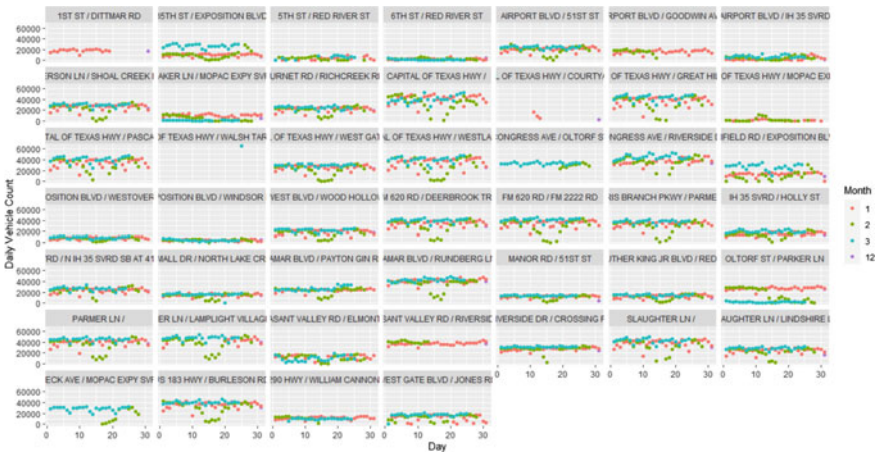


**Fig. 1** Average daily volume by month at available GRIDSMART locations (December 2020–March 2021)

**Table 3** Daily traffic counts at selected intersections for Thursday, March 25, 2021

| | INRIX | | GRIDSMART | Difference | Difference percentage |
|---|---|---|---|---|---|
| Intersection name | Observed counts | Scaled counts | Detectors counts | Scaled counts—detectors counts | $\frac{\text{Difference} \times 100}{\text{scaled counts}}$ (%) |
| West Gate Boulevard and Jones Road | 646 | 15,014 | 20,000 | −4986 | −33.21 |
| West Anderson Lane and Shoal Creek Boulevard | 1235 | 28,515 | 31,486 | −2971 | −10.42 |

one day of INRIX data to GRIDSMART's monthly average counts for a specific day of week. Observed differences range between −6097 and 18,354 vehicles, with negative values representing lower values in the INRIX dataset. Percent differences range between 10% points and 50% points.

Another comparison metric is the difference percentage (or error percentage) between GRIDSMART and INRIX traffic counts calculated as follows (Fig. 2):

$$\text{Error}(\%) = \frac{\text{INRIX traffic counts - GRIDMART traffic count}}{\text{GRIDSMART traffic count}}$$

The root mean squared error is 7693.57, with individual errors ranging between—21,191.8 and 8657.46. Negative values indicate that GRIDSMART traffic counts are higher than the INRIX traffic counts. Average volumes in February across valid GRIDSMART locations are 28,442.01 using GRIDSMART data, and 22,203.8 according to INRIX data.

## 4.2 Turning Ratios Comparison

### 4.2.1 Workflows for the Automated Analysis of Turning Movement Ratios

Our team at the center for transportation research (CTR) developed workflows to process INRIX reports, provided in JSON format, and extract turning movement-based metrics of performance. Workflows include steps to identify intersections in both datasets, and to match turning movements and approaches as defined in the INRIX data to the corresponding data when extracted from GRIDSMART cameras. The analysis process also involves computing average turning movement ratios by

**Table 4** INRIX daily traffic counts on Thursday, March 25, 2021 v. GRIDSMART average daily counts for Fridays at selected intersections

| | INRIX | | GRIDSMART | Difference | Difference percentage |
|---|---|---|---|---|---|
| Intersection name | Observed counts | Scaled counts | Average daily counts (March) | Scaled counts—Detectors counts | $\frac{\text{Difference} \times 100}{\text{scaled counts}}$ (%) |
| West Gate Boulevard and Jones Road | 663 | 15,014 | 19,558 | −4544 | −30.27 |
| West Anderson Lane and Shoal Creek Boulevard | 1225 | 28,515 | 32,435 | −3920 | −13.75 |
| Red River Street and East Martin Luther King Jr Boulevard | 868 | 35,595 | 17,241 | 18,354 | 51.56 |
| East 51st Street and Airport Boulevard | 778 | 21,308 | 27,405 | −6097 | −28.61 |
| Far West Boulevard and Wood Hollow Drive | 806 | 20,622 | 23,580 | −2958 | −14.34 |
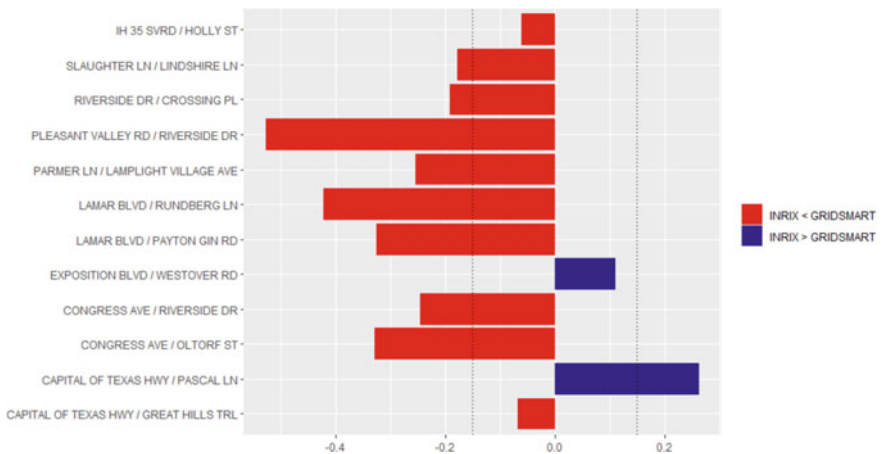


**Fig. 2** GRIDSMART and INRIX total vehicle count comparison for the month of February 2021

approach using the raw GRIDSMART data, in order to generate data comparable with that provided by INRIX. The following sections describe the compared turning movement datasets and proposed analysis workflows.

The analysis workflow involves three steps, all performed in a single query given the data schema proposed in Sect. 3.

- Identify intersections present in both data sources.
- Average GRIDSMART data for the analysis period specified in the INRIX data.
- Compute the difference in turning movement ratios across data sources.
- Analyze the differences using *R* (open-source statistical software).

This research's observations suggest that the data representation at complex inter-sections, such as those involving frontage roads, may differ between sources. There is often a single GRIDSMART camera location reported in these cases, while two INRIX data points are provided. Further analysis is needed to understand how to interpret and compare available data.

Using the approach/movement mapping proposed in Sect. 3, the analysis was performed for all intersections that were mapped geographically to the same loca-tion. GRIDSMART and INRIX turning movement ratios were compared at 28 inter-sections and 337 approaches. The difference (in percent points) between the turning ratios of the two data sources was computed for each available turning movement ratio as follows:

$$\text{Difference(pct)} = \text{INRIX Turning ratios}(\%) - \text{GRIDMART Turning ratios}(\%)$$

At the aggregate level, the average absolute difference by intersection is computed as the average of the absolute differences across all movements for which there is data as follows:

$$\text{Average Absolute Difference(pct)} = \frac{\sum_{\text{All Movements of intersection } x} |\text{Difference(pct)}|}{\text{Number of movements of intersection } x}$$

Observed differences range between 3.5% point and 57% points, with an average value of 18% points. Figure 3 shows average difference by intersection.

Figure 4 illustrates the average turning ratio difference (pct) per intersection; 67% of the intersections have a turning ratio difference of 20% points or less.

The calculated differences in turning ratios between INRIX data and GRIDS-MART data by approach and turn maneuver are illustrated in Fig. 5 for all analyzed intersections. The plots show that there are several intersections on which both data sources are very consistent, with small differences across approaches and move-ments. Large errors are observed at some locations, with left and right turns often exhibiting the larges differences. There is not an obvious pattern in the direction of the differences by movement.

Figure 6 shows the distribution of turning ratios differences (absolute value). The average absolute differences across all observed turning movements are 16.8% points,
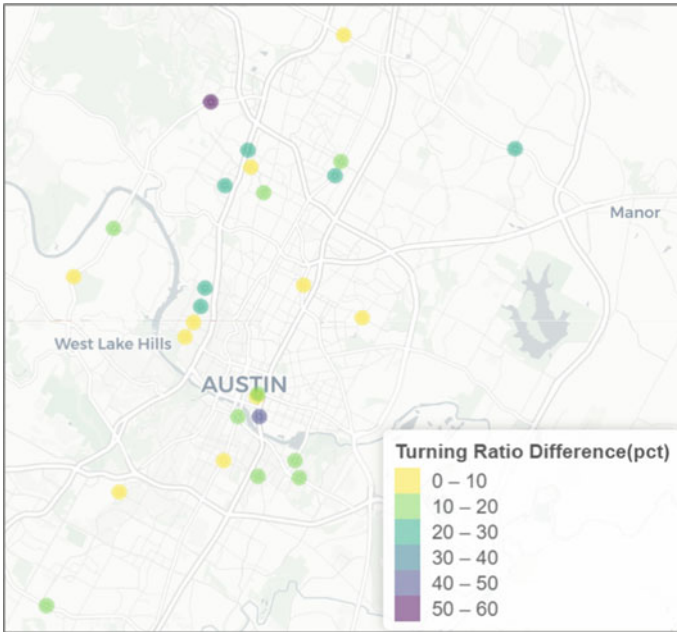
**Fig. 3** Map showing the turning ratio difference per intersection
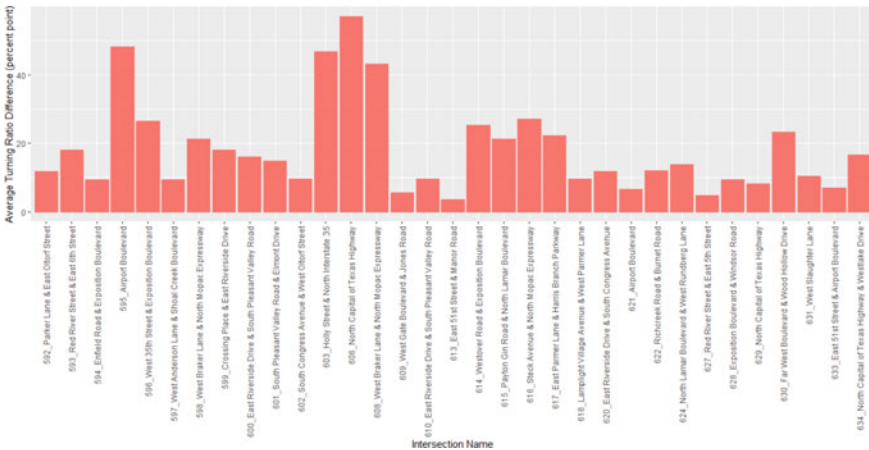


**Fig. 4** Average turning ratio difference aggregated by intersection name

with a root mean square error of 25.35% points. Almost half of the observed differences (47%) are below 10% points, and 80% of the observations exhibit differences lower than 25% points.
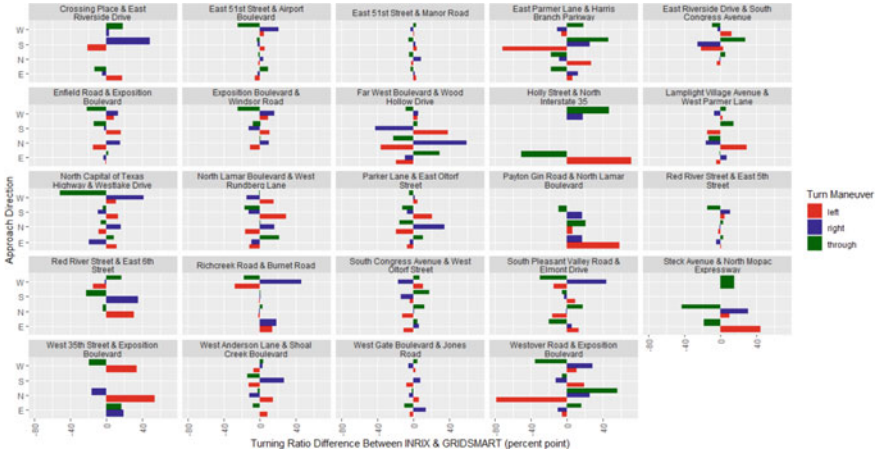
**Fig. 5** Turning ratios difference between INRIX and GRIDSMART data by intersection and approach
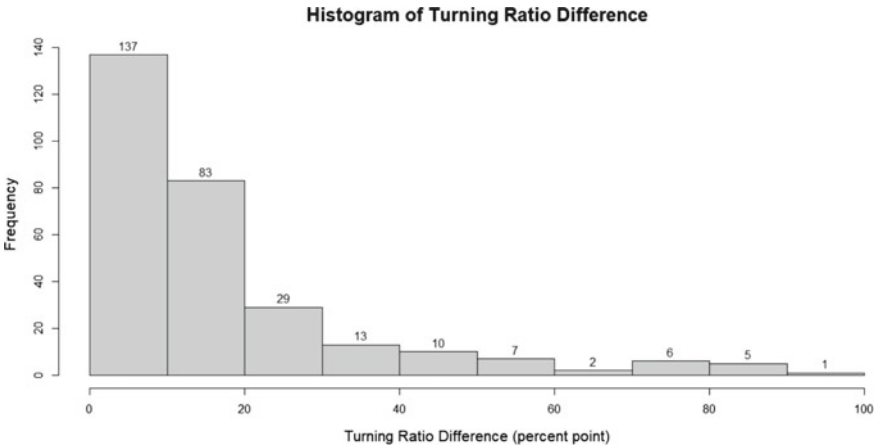


**Fig. 6** Distribution of turning ratios differences (movement-level data)

Figure 7 analyzes differences by turning movement type, while Table 5 gives the average absolute difference by turn maneuver. The largest observed difference is for left turns (23% points) and the smallest is for through traffic (16% points). Figure 7 suggests that the lower differences between data sources observed for through movements are likely to be statistically significant. Additionally, this figure suggests that INRIX data may tend to overestimate right turn movements and underestimate through movement (the difference in through movements is mostly negative indicating that the GRIDSMART through movement ratio is higher than the INRIX through movement ratio).
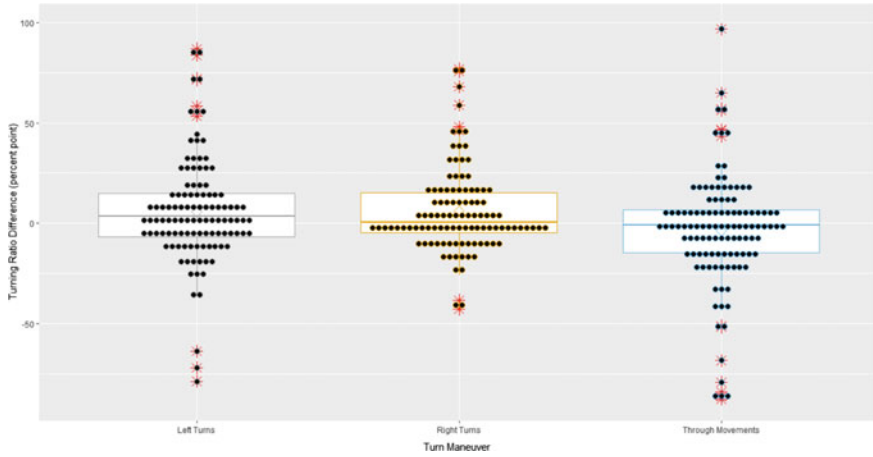
**Fig. 7** Box plots of the turning ratio difference by turn maneuver

**Table 5** Average of the difference absolute value per turn maneuver

| Turn maneuver | Average of the differences absolute value (percent point) |
| --- | --- |
| Left | 23.54 |
| Right | 20.59 |
| Through | 16.24 |

## 5 Discussion Summary and Conclusion

This study conducted a preliminary validation of new intersection performance metrics provided by INRIX by analyzing data at selected intersections where GRIDSMART cameras are deployed. Not all GRIDSMART data is directly comparable with the metrics performance provided by INRIX. Since errors may be present in both data sources, the methodology section proposes simple quality control metrics to identify scenarios in which GRIDSMART data may not be reliable (Fig. 1). The average daily volumes comparison by intersection was conducted at locations where INRIX and GRIDSMART data is available. The results in Fig. 2 illustrate that most differences were larger than 20%. While GRIDSMART data may contain errors, the observed differences suggest that INRIX estimates—which are an estimation based on extrapolating a relatively small sample—are not likely to be accurate and may not be suitable for applications that require accurate volume estimates.

To conduct the analyses presented in this paper, automated workflows were developed to process the INRIX reports, provided in. json format, and map them to GRIDSMART data. The processing includes geographic mapping to identify intersections where both data types are available, and the matching of approaches and corresponding turning movements between data sources. This study compares INRIX

and GRIDSMART average daily turning movement ratios by approach for February 2021. The findings (in Fig. 3 through Fig. 6) suggest that INRIX estimates are not far from GRIDSAMRT measurements, with almost half of the differences in turning movement ratios below 10% points in the analyzed dataset. The relative magnitude of each turning movement type by approach was also found to be very similar across data sources.

The results presented in this document are not final; more extensive tests and the use of a robust method to measure ground-truth conditions, such as manual traffic counts and advanced traffic signal performance metrics (ATSPM) computed using detector data, are desirable in order to assess the value of INRIX and GRIDSMART data for specific use cases. This study is considered a valuable step toward the development of a robust intersections' performance metrics framework. Future research can be built upon this study to provide information that can help practitioners select an appropriate methodology for evaluating intersection performance.

## Appendix

See Figs. 8, 9, 10 and 11.
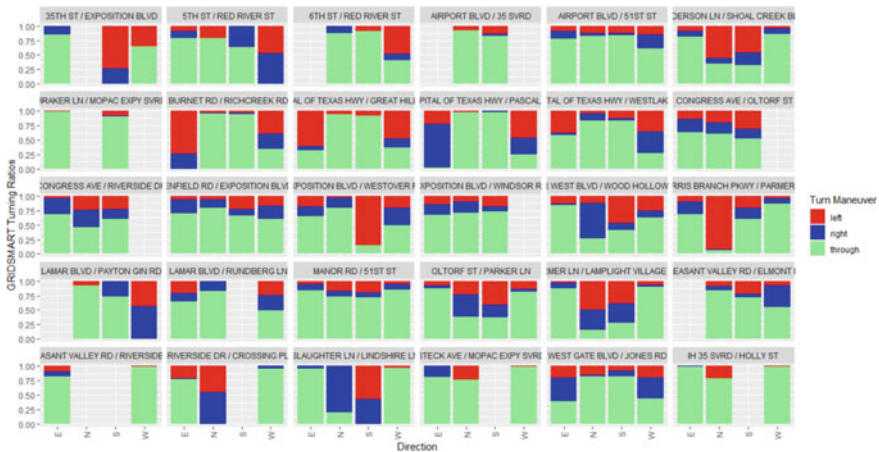


**Fig. 8** GRIDSMART turning ratios for each intersection
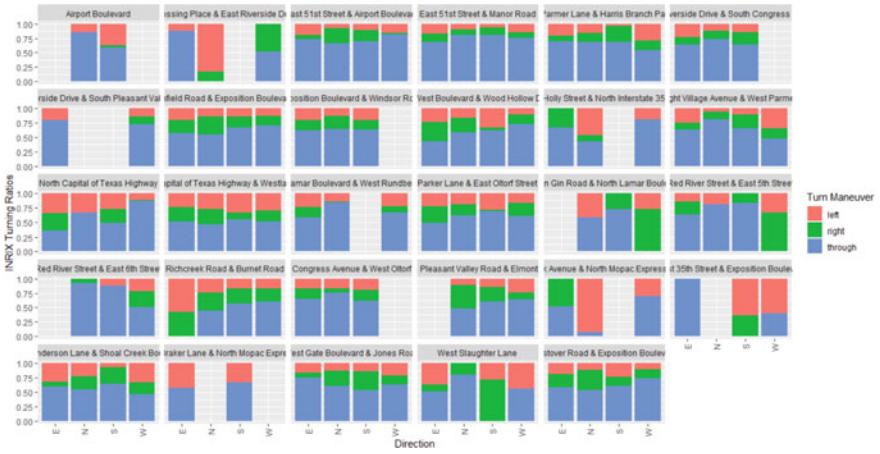
**Fig. 9** INRIX turning ratios for each intersection
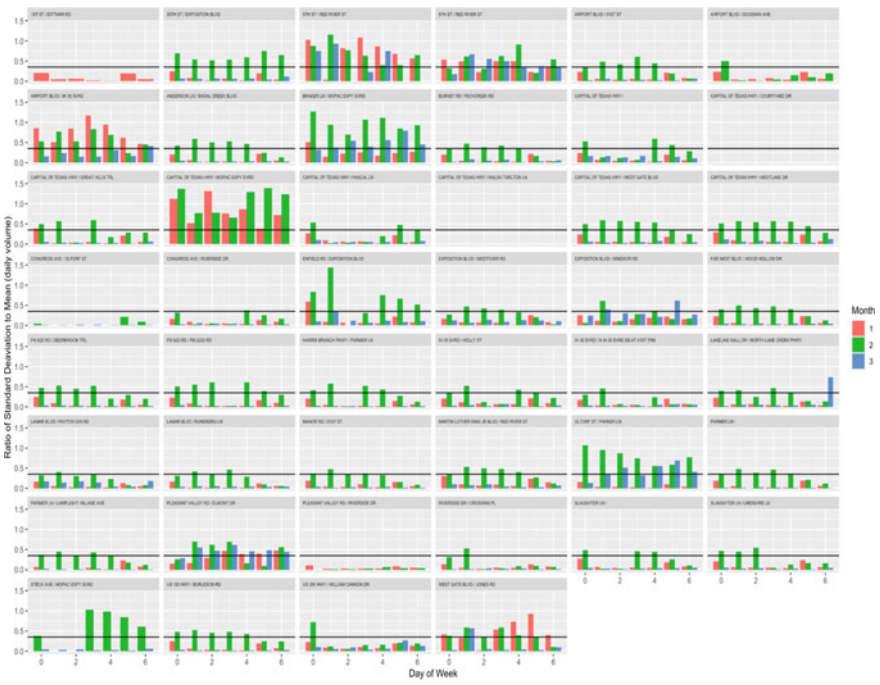


**Fig. 10** Ratio of the standard deviation of average daily volumes and the corresponding mean value for each intersection
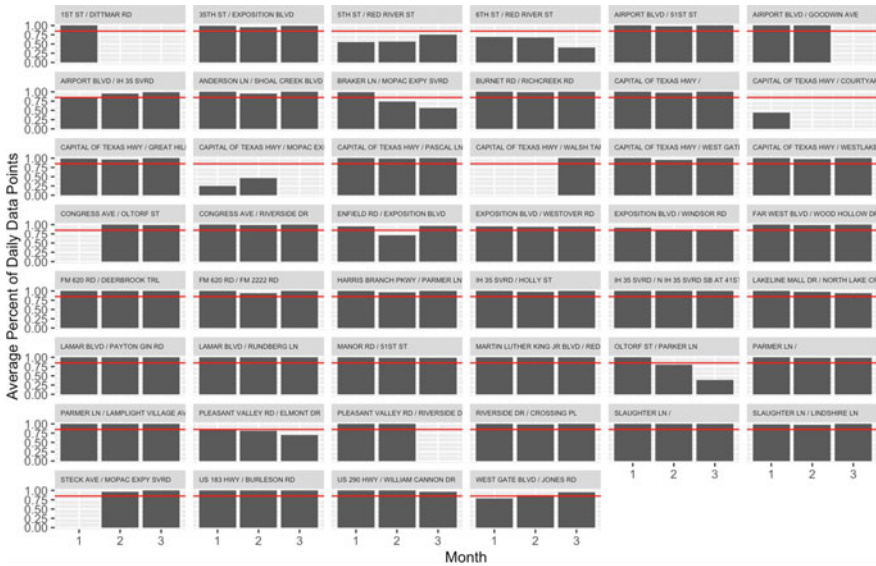
**Fig. 11** Average percentage of daily data points by month at all locations active as of March 2021

# References

1. Barry Barker J, Brown LL, Butler DH, Garber NJ, Kinnier HL, Hamiel JW, Helme EA, Rosser TL, Seltzer D, Stotlar DW (2010) NCHRP SYNTHESIS 409. Transp Res Board. http://www.national-academies.org/trb/bookstore
2. Carroll M, Ferrell CE, Levinson HS, Reinke D, Appleyard B, Dowling R, Cervero R, Ashiabor S, Deakin E (2011) Reinventing the urban interstate: a new paradigm for multimodal corridors. Reinventing the urban interstate: a new paradigm for multimodal corridors. National Academies Press. https://doi.org/10.17226/14579
3. FHWA (2021) Traffic signal timing manual. https://ops.fhwa.dot.gov/publications/fhwahop08024/chapter3.htm
4. Ghanim MS, Shaaban K (2019) Estimating turning movements at signalized intersections using artificial neural networks. IEEE Trans Intell Transp Syst 20(5):1828–1836. https://doi.org/10.1109/TITS.2018.2842147
5. Griffith MS, Hayden C, Kalla H (2003) Data is key to understanding and improving safety | FHWA. https://highways.dot.gov/public-roads/januaryfebruary-2003/data-key-understanding-and-improving-safety
6. McCracken J (1996) Demonstration project 93 - making the most of today's technology | FHWA. https://highways.dot.gov/public-roads/winter-1996/demonstration-project-93-making-most-todays-technology
7. Kirkland W (2021) INRIX expands signal analytics with systemwide dashboards and reporting to measure intersection performance without hardware - INRIX. https://inrix.com/press-releases/inrix-iq-signal-analytics/
8. NTOC (2012) 2012 national traffic signal report card | national operations center of excellence. https://transportationops.org/publications/2012-national-traffic-signal-report-card
9. Rizavi A (2021) Intersect—where data and results converge | new Hampshire municipal association. https://www.nhmunicipal.org/town-city-article/intersect%E2%80%94where-data-and-results-converge

10. Rowell S (2021) Radars: a cost effective, reliable source for traffic data collection - stinson ITS. https://stinsonits.ca/blog/radars/
11. Zuniga-Garcia N, Ross HW, Machemehl RB (2018) Multimodal level of service methodologies: evaluation of the multimodal performance of arterial corridors. Transp Res Rec 2672(15):142–154. https://doi.org/10.1177/0361198118776112

# A Study on the Mobility Pattern of Slum Dwellers in Dhaka, Bangladesh

**Ayesha Siddika, Kazi Ehsanul Bari, and Md. Musleh Uddin Hasan**

**Abstract** Dhaka is the capital and one of the oldest cities of Bangladesh, mostly renowned as the economic and business hub of the economy of the country. Transport studies on Dhaka, the capital and primate city of Bangladesh, do fairly reflect on the overall mobility scenario of the city. However, there is a paucity of literature on the subject for the four million people who live in slums. Furthermore, most of the extant gray literature contradicts itself, claiming that many slum people utilize rickshaws and other non-motorized vehicles. As a result, low-income people's mobility needs are frequently disregarded in transportation policies and programs. This study summarizes the findings of the movement pattern of inhabitants of four slums in Dhaka in order to make an empirical contribution in this area. The majority of slum inhabitants' routine excursions are for employment, with 58% taking place on foot, followed by rickshaws (12%), bicycles (6%), boats (7%), public buses (6%), and scooter/tempo (6%) (11%). Slum residents walk because they cannot afford to pay for transportation. They also visit their families on occasions, such as during festivals and other holidays. Gender differences in transport mode selection were observed. The most influential criteria for slum residents' mode choice behavior include household income, distance, trip cost, journey time, and so on.

**Keywords** Slum · Mobility · Vulnerability · Affordability · Mode Choice

A. Siddika (✉)
Department of Civil and Environmental Engineering, Natural Resources Engineering Facility, University of Alberta, 9211 116 St. NW, Edmonton, AB 01-070, Canada
e-mail: siddika@ualberta.ca

K. E. Bari
Dhaka School of Economics, University of Dhaka, Dhaka, Bangladesh

Md. M. U. Hasan
Department of Urban and Regional Planning, Bangladesh University of Engineering and Technology, Dhaka, Bangladesh

# 1 Introduction

Mobility for the poor and vulnerable groups is an essential precondition for achieving Sustainable Development Goals (SDG) in cities, especially in developing countries. A city with integrated modes of transportation is more likely to prosper as a center for trade, commerce, industry, education, tourism, and services. Most of the poor and low-income groups in society do not have adequate mobility options. In urban and transport planning and development, understanding and enhancing the mobility options of the poor are of significant importance. Asia has by far the highest number of city dwellers living in slums. South Asia faces the greatest problem, with half of the urban population living in slums [3]. This is no different for Dhaka, Bangladesh's capital. It is rare, if not nonexistent, to find studies addressing their mobility patterns. A few studies offer insight into low-income people's modal choice in general. Furthermore, several studies have shown that a large number of men in lower-income communities work as rickshaw pullers [2]. Based on such findings, some gray literature conceives that rickshaw is the main mode of transportation for the slum people—which is not only misleading but also contributes in targeting 'wrong' policy interventions for improving their mobility [8]. This study seeks to understand the mobility pattern—defined as accessibility to destination, reason and frequency of use, cost of using different modes, etc.—of the people living in slums in Dhaka. The study areas include four slums in four different parts of core Dhaka city, Dhaka North City Corporation (DNCC) and Dhaka South City Corporation (DSCC).

# 2 Literature Review

Dhaka, the capital of Bangladesh, is the largest city in the country. Contributing more than 30% of national GDP [1], Dhaka is unrivaled among Bangladeshi cities in terms of its economic, social, and political activities and opportunities. So, people migrate to Dhaka for better livelihood opportunities. Approximately 3.4 million people lived in five thousand slums of Dhaka city in 2005 [4]. These people constitute more than one-third of the total population and nearly all the low-income population of Dhaka.

As already stated, to the best of authors' knowledge, there is no literature on the mobility and modes used by these slum dwellers. Only few studies are found, which are on low-income people, in general. Fahmi et al. [5] studied the mobility of slum dwellers only in the case of their eviction from the slums, not in normal condition. They found that evicted slum dwellers most perform their outdoor activities by walking. Islam [7] and Nahiduzzaman [13] in their studies on the housing and integration of the slum dwellers have found that most of the inhabitants of slum and squatter settlements in the city prefer to go to their workplace on feet to save money. On the other hand, Mannan and Karim [11] found that people of low-income group of Dhaka city have higher propensity to choose bus to move around; as income level increases, people try to avoid bus and use rickshaw or tempo.

In contrast, JICA ([8], pp. 3–15 to 3–16) in the report on Dhaka Urban Transport Network Development Study shows that rickshaw is the most widely used transportation mode of the low-income households. This conclusion has also made the study 'biased' (as argued in Hasan and Davila 2018) toward investment intensive, heavy infrastructure requiring metro rail-based rapid transit solutions, but walking and non-motorized transport infrastructure development remained unduly addressed, if not overlooked. Gwilliam [6] and Mahendra [10] have also echoed similar concern in their studies on different other parts of the world. Unfortunately, empirical mobility studies focusing on the slum dwellers are also too few for other countries and context. In other parts of the world, mobility of slum dwellers is not in a very good condition. Several findings of different mobility-related studies of slum dwellers have been found in different secondary literatures.

Ram et al. [14] identified vans, cycles, metro cable, and BRT light as the main modes of transport of the slum dwellers of Delhi, India. The study has also suggested that mobility of slum dwellers should be considered while rehabilitating them. Salon and Gulyani [15] in their study have focused on the travel 'choices' of the urban poor who live in informal settlements in Nairobi, Kenya. This study has found that the slum residents walk practically everywhere they go and sometimes they cover a long distance by walking. The slums of Nairobi are relatively well connected by privately owned and operated transit vans and small buses called Matatus. The problem is not a lack of motorized transport options, and the slum residents are walking largely because they cannot afford the motorized options. Recently, the study of Kodransky and Lewenstein [9] has focused on the Rise of Shared Mobility in USA in order to increase the working efficiency of the low-income people.

## 3 Study Areas and Methodology

For selection of study areas, Dhaka city has been divided into four zones A, B, C, and D based on the density of slum clusters (Fig. 1). From each zone, a slum with sufficient number of population and household has been selected as study area. The slums selected from different zones are Kalshi slum, Mirpur (zone A), West Islambagh slum (zone B), Korail slum (zone C), and Sturapur slum (zone D). Table 1 shows the basic demographic and occupational profile of the people in the studied slums.

Out of the 27,000 households in the four slums, 384 were planned to be surveyed. However, during survey as 100 households had been surveyed at each slum, total sample size increased to 400. In this study, the information of all the household members was collected from the household head/representative. So the dataset represents the information of a total of 1382 slum dwellers.

A set of questions have been asked to determine the frequency of trips, duration of trip or travel time, modes of trip, travel cost of the respondents, presence of company during travel to ensure safety and comfort, spatial extent of mobility including influence zone and mode chain of slum dwellers, etc.
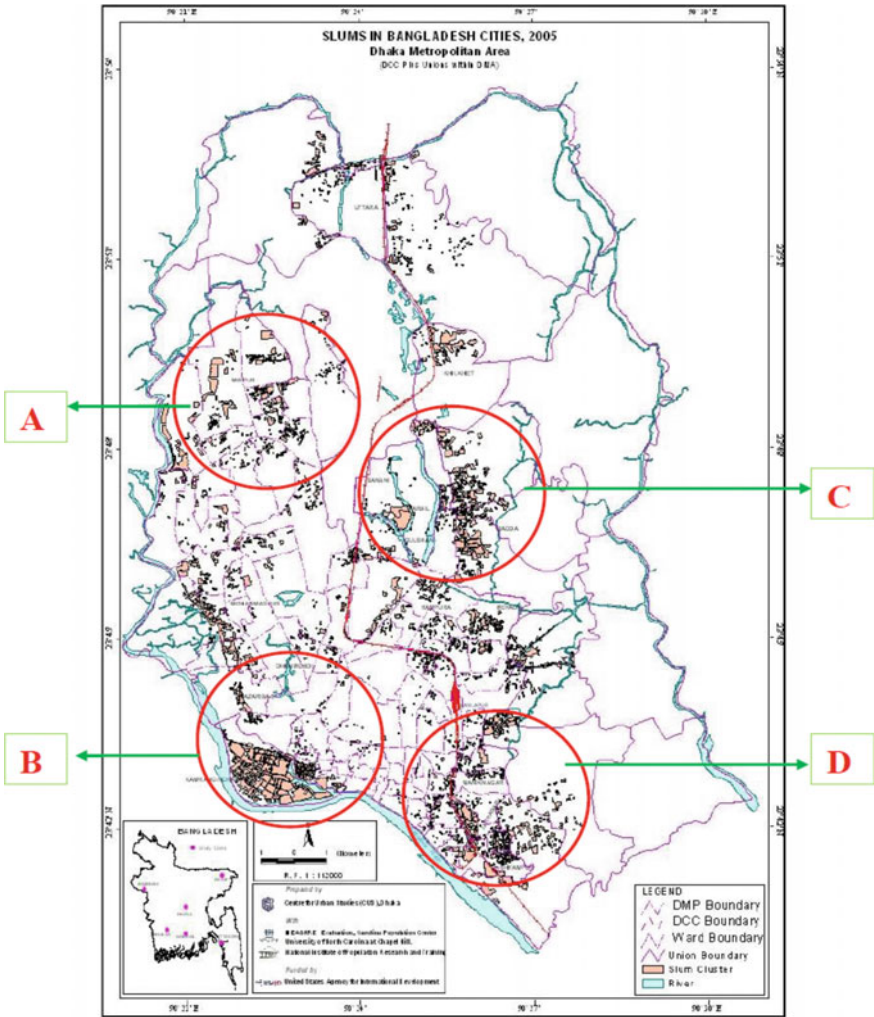
**Fig. 1** Location of study area

**Table 1** Demography of the study area

| Name of slum | Number of households* | Population* | Average monthly income (BDT)** | Occupation |
|---|---|---|---|---|
| Kalshi | 8500 | 42,500 | 5000–10,000 | 1.Rickshaw puller |
| West Islambagh | 3000 | 15,000 | 5000–10,000 | 2.Day laborer |
| Korail | 14,480 | 80,000 | 10,000–15,000 | 3.Small business 4.House maid |
| Sutrapur | 1800 | 9000 | 5000–10,000 | 5.Garments worker |

*Source* * CUS et al. [4], ** Field Survey

# 4    Case Study Analysis

The following sub-sections put light on the modes used for traveling; duration, extent, frequency, and cost of the regular trips made by the slum dwellers. There is also a separate sub-section on the occasional trips made by the slum people.

## 4.1    *Modal Share*

About 60% slum dwellers live within walkable distance to their regular travel destinations. Preference of non-motorized vehicle is quite common among the slum dwellers. About 83% respondents use non-motorized transport, including walking, as their prime category of mode of regular travel, whereas only about 17% use motorized vehicle. About 58% respondents of slums prefer walking. The other dominant mode of regular travel is rickshaw (12%), tempo (11%), public bus (6%), bicycle (6%), and boat (7%).

The survey has found that the mode choice of respondents of the two slums of Old Dhaka (Sutrapur and West Islambagh slums) differs from the other two slums (Korail and Kalshi slum) (Fig. 2). The respondents of slums of Old Dhaka prefer walking as their prime mode. The study has found that about 67% respondents of West Islambagh slum prefer walking which is highest among the four slums. About 61% respondents of Sutrapur slum prefer walking which is the second highest among the four slums. The major difference is that the dwellers of Sutrapur and West Islambagh slums use boat as their prime mode which is because of the locational distribution of the slums. The location of Sutrapur slum is about one and half kilometer and West Islambagh slum is about half kilometer distance from the Buriganga River which influences their mode choice behavior. Though the respondents of Korail slum have to use boat to cross the Gulshan Lake, it is not considered as the prime mode of the respondent.
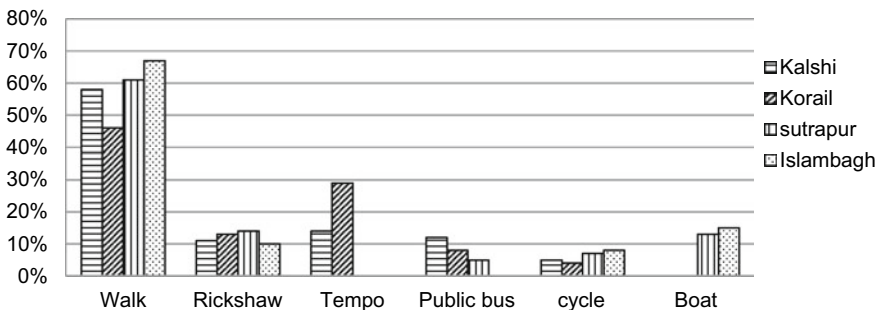


**Fig. 2**   Modal split of the slum dwellers of Dhaka city
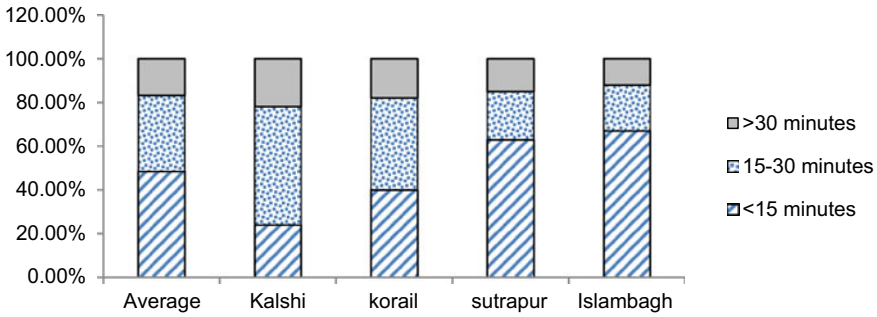
**Fig. 3** Average travel time of slum dwellers of Dhaka

Rickshaw is the second most dominantly used mode of the slum dwellers. Some of the dwellers have rickshaw of their own. Besides, the absence of public transport in Old Dhaka influences the use of rickshaw as a regular mode of transport. Cycle is another preferable non-motorized mode of regular transportation the slum dwellers.

Use of public bus and other motorized vehicles is most common in Korail and Kalshi slums which is rare in Sutrapur and West Islambagh slums. Rather, the dwellers of Sutrapur and West Islambagh slums prefer non-motorized vehicle as their prime mode of travel. Slum dwellers also use tempo (one kind of local vehicle run by petrol) due to its availability in their locality and its reasonable cost.

## 4.2 Travel Time

Almost 49% of dwellers travel less than 15 min, 34% dwellers travel 15–30 min and 17% dwellers travel more than 30 min to reach their workplace (Fig. 3). Most of the slum dwellers prefer to reside adjacent to their working place which is the important reason behind their low travel time (less than 30 min).

It has been found that low travel time is more dominant in Sutrapur and West Islambagh slums because of having working place adjacent to their locality. The respondents of Korail and Kashi slum have more travel distance to cover than the others.

## 4.3 Spatial Extent of Mobility

Figure 4 shows that among the dwellers of Kalshi slum, a small number of dwellers have working trip within half kilometer distance, 16% have working trip of one km, 9% dwellers have to travel about 2 km, and another 75% have to travel more than two kilometers to reach their work places. Their working places are located mainly

in Mirpur 10, Mirpur 11, and Mirpur 12, Rupnagar, Gabtoli, and Technical area. The presence of Tejgaon Cantonment at the Northeast side of the slum creates a mobility barrier of the slum people (Fig. 5).

The major destinations of the respondents of Korail slum are in Gulshan, Banani, Mohakhali, and Tejgaon. About 25% respondents travel less than one kilometer, 65% travel up to 1 km, and about 10% respondents travel more than 1 km regularly to reach their workplaces. The map also shows that the respondents of Korail slum do not have any mobility barrier to move to their destinations.

Figure 6 shows that among the dwellers of Sutrapur slum, 20% dwellers have working trip within half kilometer distance, about 19% have working trip of one km, 48% dwellers have to travel about 1.5–2 km, and another 13% have to travel more than two kilometers to reach their work places. Their working places are located mainly in Paltan, Motijheel, DholaiKhal, Sutrapur, Gendaria, and Jatra Bari area.

Figure 7 shows the major destinations of the respondents of West Islambagh slum areas in East Islambagh, Lalbagh, Azimpur, New Market, Chak Bazar, Sadarghat, and Kamrangir Char. About 33% respondents travel less than one kilometer, 25%
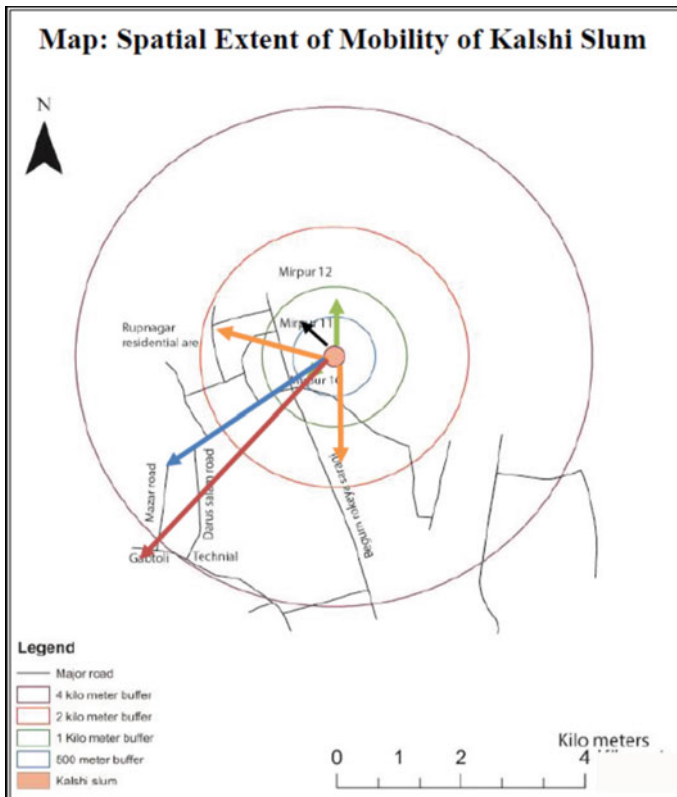


Fig. 4 Spatial extent of mobility (Kalshi slum)
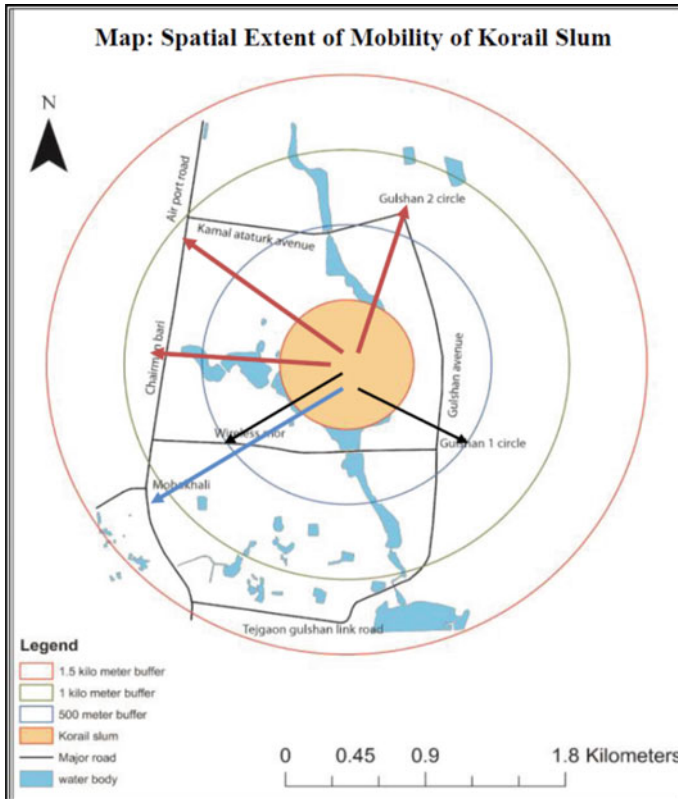
**Fig. 5** Spatial extent of mobility (Korail slum)

travel up to 1 km, and about 52% respondents travel more than one to two km regularly to reach their workplaces. The study also reveals that the respondents of West Islambagh slum do not have any mobility barrier to move to their destination.

## 4.4 Frequency of Trips

Frequency of trips is also related with the travel time and travel cost. Those who have to pay the least travel cost and spend least travel time make frequent travel. Trip frequency also determines the availability of the service. Generally, two trips are generated for one activity (starting trip and return trip). The study has found that, on an average, the slum dwellers have to make highest four regular trips (Fig. 8).
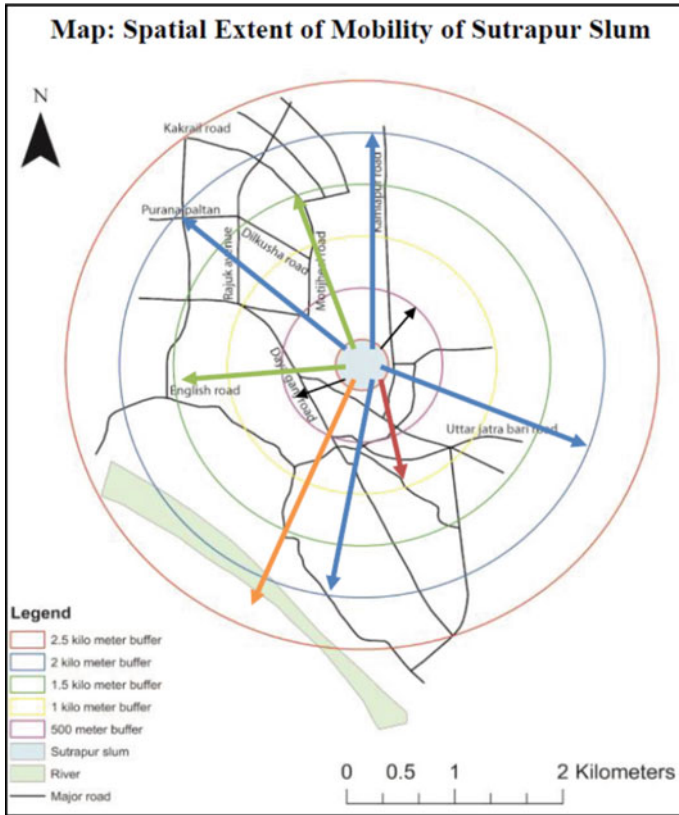
**Fig. 6** Spatial extent of mobility (Sutrapur slum)

## 4.5 Trip Cost

Daily travel cost is directly related with the modal share of the slum dwellers. The study has found that most of the slum people prefer walking as their prime mode which tends to the zero-cost travel of majority of slum dwellers. About 64% people of these slums do not have to pay any monetary value as their travel cost. The study has also revealed that about 26% costs less than 15 taka and about 10% costs 15–30 taka on an average.

Figure 9 shows the regular travel cost scenario of the respondents of the four slums of the study area. As the number of walking trip is highest in Sutrapur and West Islambagh slums, the concentration of zero-cost travel is larger than the other two slums (Kalshi and Korail slums).
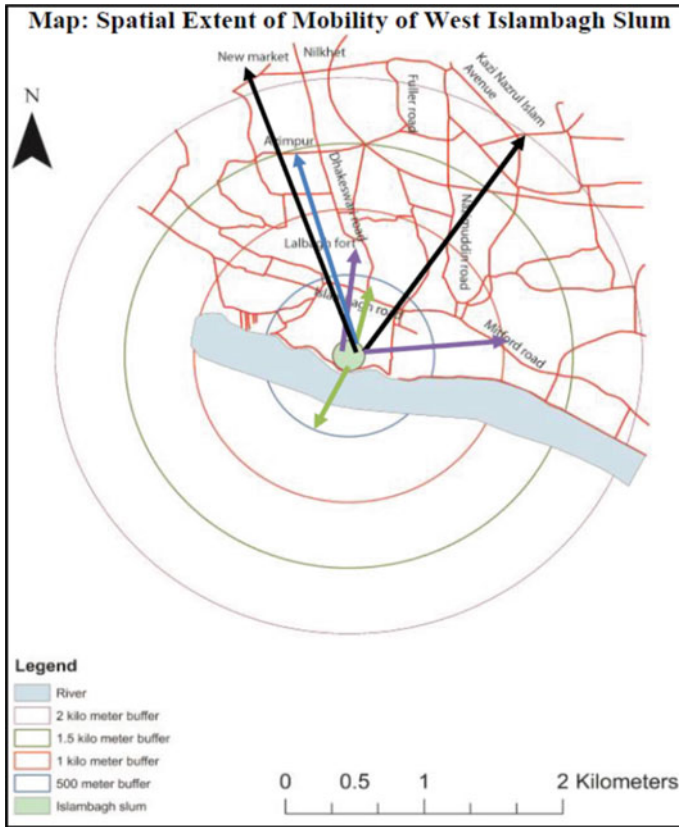
**Fig. 7** Spatial extent of mobility (West Islambagh slum)
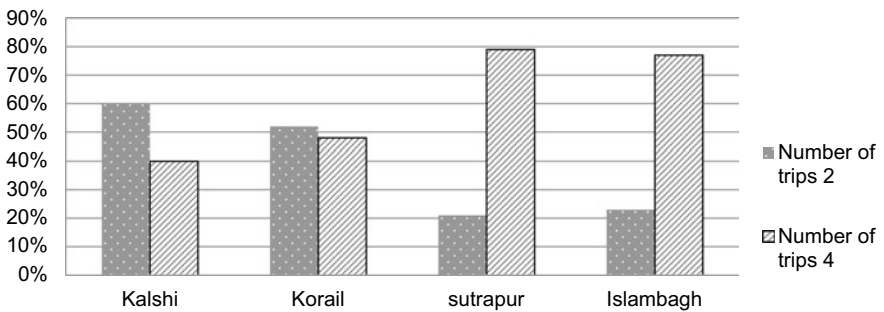


**Fig. 8** Regular frequency of trips of slum dwellers
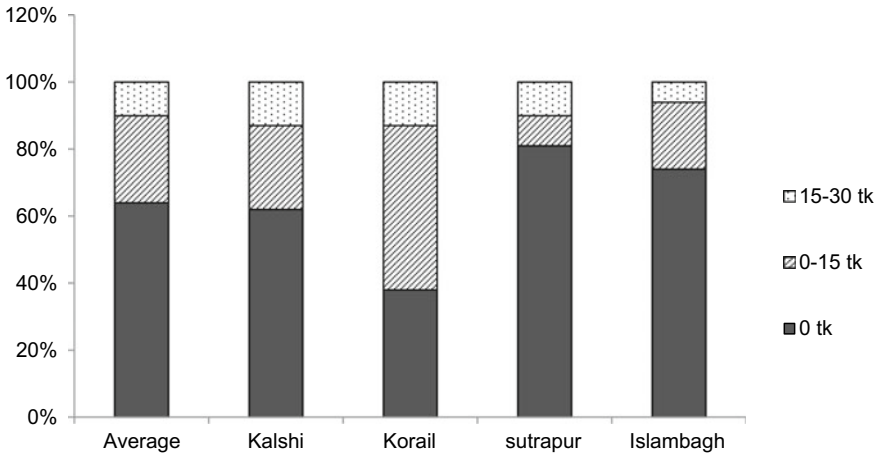
**Fig. 9**  Travel cost of slum dwellers of Dhaka city

## 4.6  Mode Chain and Number of Mode(s) per Trip

Mode chain has a relationship with travel cost. Travel cost increases with the increase in total number of mode present in the mode chain. Distance is also a dominant factor for increasing or decreasing number of mode chain. Long-distance travel has a longer mode chain than the short-distance travel (Fig. 10).

The figure above shows that the mode chain of respondents of Sutrapur and Kalshi slums lies between one and two modes, whereas some respondents of Korail and West Islambagh slums have three modes in their mode chain. As 23% respondents of Korail slum have three modes of their mode chain, the travel cost is comparatively high in case of this slum.
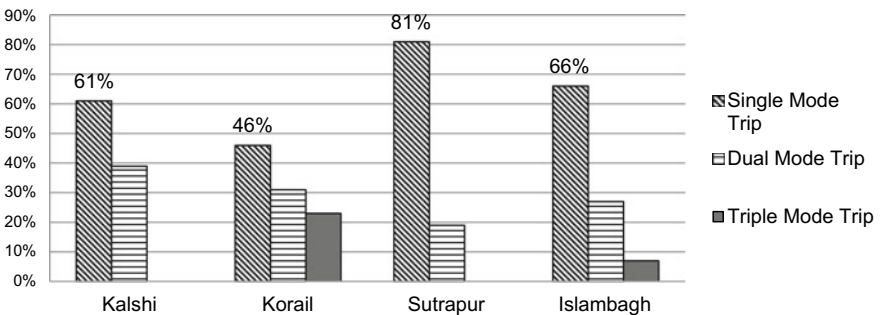


**Fig. 10**  Regular mode chain of slum dwellers of Dhaka city

## 4.7   Occasional Trip of the Slum Dwellers

It is found that the occasional trips are not only made for seasonal or temporary work but also for the purpose of visiting family members during religious festivals (i.e., Eid, Puja, Christmas etc.). The study has revealed that about 67% of the occasional trips are generated during yearly festivals like Eid Ul Fitr, Eid Ul Azha, Puja, etc. These yearly trips are made to go to villages to meet the near and dear ones during the festivals. These long-distant trips are made by bus, train, or launch. Among all the reasons, visiting family members is the second important reason. It is more dominant in case of the temporary migrants of slums. About 27% occasional trips of the slum dwellers are made for the reason of visiting family members who reside in their origin and other areas. The study has also found that about 6% slum dwellers of Dhaka city have made occasional trip for better earning opportunity. Availability of some seasonal employment opportunities outside the city encourages the slum dwellers to make occasional trip for additional earning. Better earning opportunities influence the slum dwellers to make occasional trip (Fig. 11).

About 64% respondents have occasional trip frequency of less than or equal to four, 24.5% respondents have occasional trip frequency of 4–8, 8.5% have occasional trip frequency of 8–12, and only 2% have occasional trip frequency of 12–16. The study has also revealed that 3% respondents of West Islambagh slum have occasional trip frequency in between 16 and 20. These respondents are mainly factory worker and they live in the slum without their family members. For that reason, they visit their family quite frequently.
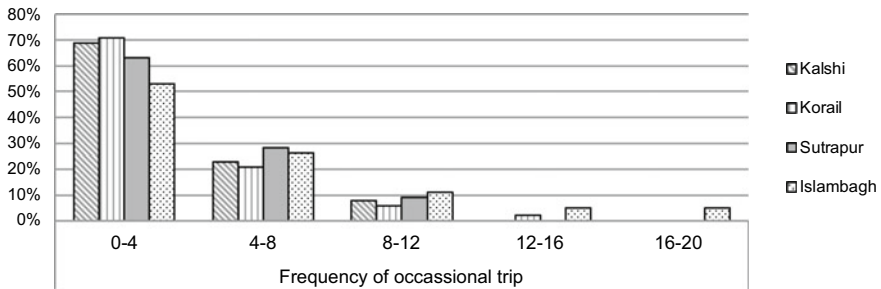


**Fig. 11**  Yearly frequency of occasional trip of slum dwellers

# 5 Major Findings and Conclusion

## 5.1 Results and Discussion

Mobility is a complex phenomenon and is influenced by a multitude of variables, including technology, spatial behavior, the configuration of networks, the emergence of policy organizations and institutions, regulatory systems, etc. The study on transport mobility of slum dwellers seeks to address the research gap and understand the mobility pattern of the slum dwellers in Dhaka city.

Majority of slum dwellers prefer walking (about 58%). Again about 60% respondents live within walkable distance. Most of the slum dwellers prefer to reside adjacent to their working place in order to save their travel time and travel cost. About 64% people of these slums do not have any travel cost. About 49% of respondent and their household members have travel time less than 15 min, and only 17% dwellers have to travel more than 30 min to reach their workplace. The mostly preferred mode of slum dwellers is walking (58%) and the second highest is rickshaw (12%).

Besides, mobility pattern is not always constant for all slums of Dhaka city due to locational distributions of the slums and availability of modes. Boat is considered as a prime mode for slum dwellers in Old Dhaka. Trip frequency of daily trip of the slum dwellers of Old Dhaka is also higher than the dwellers of Korail and Kalshi slums.

Mobility pattern also varies for men and women in the slums. Most of the women of the slums prefer walking and rickshaws as their prime mode of regular travel to their workplaces. For men, the two prime modes are walking and bus. Almost two-thirds of the females move in group—40% of them travel with their co-workers and rest with their neighbors and family members.

One of the major findings of the study is that the slum dwellers of the city do not have recreational trip, except the yearly long-distant trip to their villages to celebrate the biggest religious and social festivals. The study has found that the slum dwellers are more concerned with the monetary issue rather than safety issue. However, a few slum dwellers face problems of footpath: safety and comfort-related problems.

# 6 Conclusion

As is has been stated in the beginning that there is paucity of information regarding how really the slum dwellers move, where, how frequently, etc., measures to improve their mobility pattern are found either absent or targeted to a 'wrong' or least useful direction. This study has revealed that improvement of facilities and options for walking is fundamental for slum dwellers. Policies and legislations should encourage the factors those positively affect walking and should minimize the factors those affect negatively. Safety and comfort of travel should be ensured, particularly for women.

As regards issues for future research, it is felt that disaggregation of modal share by trip purpose, i.e., for work, education, health, and others will help to identify the preferable modes for various trip purposes and hence identify the areas where further intervention is required.

# References

1. Ahsan A (2019) Dhaka-centric growth: at what cost? In: Policy insights. Policy Research institute, Dhaka
2. Begum S, Sen B (2005) Pulling rickshaws in the City of Dhaka: a way out of poverty? Environ Urban 17(2):11–25
3. Bloom DE, Khanna T (2008) The urban revolution. Retrieved from https://perencanamuda.wordpress.com/2008/11/07/
4. CUS, NIPORT and MEASURE Evaluation (2006) Slums of urban Bangladesh, mapping and census, 2005, Center for Urban Studies (CUS), National Institute of Population Research and Trainaing (NIPORT) and MEASURE Evaluation, Dhaka, Bangladesh and Chapell Hill, USA
5. Fahmi SFK, Hossain MD, Abdullah AMM (2008) Mobility pattern of slum evicted people and socio economic impact of slum eviction (a case study of Mirpur and Tejgaon Slum). Bachelor thesis, submitted to the Department of Urban and Regional planning, Bangladesh University of Engineering and Technology (BUET), Dhaka, Bangladesh
6. Gwilliam K (2003) Urban transport in developing countries. Transp Rev 23(2):197–216
7. Islam MS (2012) Integrating the urban poor in Dhaka: review of development policies and strategies. Master's thesis, submitted to the Department of Urban and Regional planning, Bangladesh University of Engineering and Technology (BUET), Dhaka, Bangladesh
8. JICA (2010) Dhaka urban transport network development study (DHUTS)- Final report, submitted to Dhaka transport coordination board (DTCB). Ministry of Communication, Government of Bangladesh
9. Kodransky M, Lewenstein G (2014) Connecting low-income people to opportunity with shared mobility. institute of transportation and development policy. Retrieved from https://www.itdp.org/wp-content/uploads/2014/10/Shared-Mobility_Full-Report.pdf
10. Mahendra A (2008) Vehicle restrictions in four Latin American cities: is congestion pricing possible? Transp Rev 28(1):105–133
11. Mannan MSM, Karim MM (2001) Current state of the mobility of the urban dwellers in Greater Dhaka. Retrieved from http://www.eng-consult.com/pub/mobility-paper.PDF
12. Mattson J (2012) Travel behavior and mobility of transportation-disadvantaged populations: evidence from the national household travel survey. A research of Upper Great Plains Transportation Institute of North Dakota State University, Fargo, USA.
13. Nahiduzzaman KM (2006) Housing the urban poor: planning, business and politics a case study of Duaripara Slum, Dhaka city, Bangladesh. Retrieved from http://fpd-bd.com/wp-content/uploads/2013/04/FULLTEXT01.pdf

14. Ram S, Gupta S, Sudagani BG (n.d.) Transport systems for slum dwellers. Retrieved from http://www.urbanmobilityindia.in/Upload/Conference/6281d248-6be4-42bc-b1cc-1f4351a10c4b.pdf
15. Salon D, Gulyani S (2010) Mobility, poverty, and gender: travel 'choices' of slum residents in Nairobi, Kenya. Transp Rev 30(5):641–657

# Towards Data-Informed Sub-Models for Pedestrian Microsimulation of Transportation Terminals

**Timothy Young and John Gales**

**Abstract** Pedestrian microsimulation software is used to model and evaluate the circulation of pedestrians in transportation terminals. It can be used to determine potential travel times and visualize congestion during the design phase so that change and optimization can be made. Model parameters can also easily be changed to simulate a variety of scenarios, including peak travel times, events, and emergency evacuations. These models can be augmented and extended through the use of Software Development Kits (SDKs), including the introduction of new behaviours via modifications to the movement algorithm. However, these extended sub-models require validation. This presentation uses a study of a transportation terminal to demonstrate the evolution of a Pedestrian Microsimulation Sub-Model for group behaviour, the importance of real-world validation data, and potential data collection methodologies. Multiple versions of the group forces model are demonstrated as implemented within the pedestrian microsimulation software MassMotion, starting from initial concepts through to full implementations of potential group movement algorithms. Preliminary data collection efforts in an intercity transportation terminal are discussed, including the benefits and drawbacks of extracting movement and behavioural data from prerecorded video. New modifications to open-source motion tracking software will be demonstrated and compared with LIDAR and manual notetaking methods. Finally, a path forward will be discussed for employing video data analysis to assist with calibration, verification, and validation of Pedestrian Microsimulation Sub-Models. With further development, the use of data-informed sub-models has the potential to include more accurate movement and behaviours in pedestrian modelling and allow practitioners and engineers to design buildings, pedestrian spaces, and transportation terminals with higher confidence in pedestrian flow results.

**Keywords** Pedestrian modeling · Pedestrian tracking · Movement speeds · Data collection

T. Young (✉) · J. Gales
York University, Toronto, Canada
e-mail: timyoung@yorku.ca

# 1 Pedestrian Microsimulation Overview

Transportation terminals play an important role in a country's infrastructure, facilitating the movement of people as they board vehicles to travel across transportation networks. Ensuring the safe and efficient flow of passengers through these environments is of utmost importance, especially as these facilities may be required to serve thousands of people every day. The efficient, uncrowded flow of passengers contributes to a pleasant experience which may be helpful in encouraging passengers to continue to use the facility and infrastructure. Conversely, poor passenger flow and crowding may encourage passengers to seek other travel methods instead [20]. In extreme cases, crowding can lead to crowd crush or overcrowding conditions, resulting in injuries or death [20] [6]. Thus, engineers must design these spaces to ensure good, safe pedestrian flow which accounts for the behaviours of the occupants.

Pedestrian circulation engineering utilizes a concept called Level of Service (LOS) to quantify flow. LOS was primarily developed for highways for measuring and categorizing attributes such as travel speed and traffic signal delay on a scale from A (Freeflow conditions) to F (Highly congested, Complete breakdown in flow). In the pedestrian context, LOS is evaluated by measuring pedestrian density in persons per square metre, space per pedestrian, or pedestrian flow rate in pedestrians per minute per metre of width [12]. This has impacts on pedestrian walking speed, comfort, and safety. At low levels of service and high density, crowd crush and other safety concerns begin to mount. The different levels of service are illustrated in Fig. 1.

Different LOS measures, values, and acceptable limits may exist for different areas or pieces of infrastructure, such as platforms, waiting areas, queues, stairs, and concourses [12]. These spaces should be designed to meet or exceed the minimum level of service in various scenarios as set by the client. These scenarios are meant to simulate the operations of a terminal in peak demand conditions, but may also include additional situations such as off peak, events or emergencies [20, 22, 27].
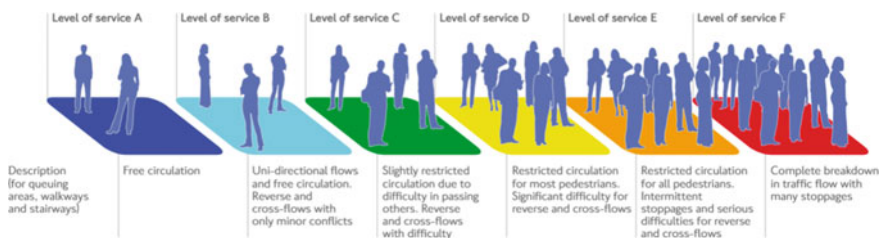


**Fig. 1** Fruin levels of Service [25]

## 1.1 Pedestrian Microsimulation and Modelling Tools

One tool involved in the design of these spaces is pedestrian modelling software, such as MassMotion. This allows designers and engineers to create 3D models of prospective facility designs, populate it with virtual 'agents' representing people, and then simulate their actions and movements. The results from the model allow engineers to spot potential problems in pedestrian flow such as congestion or crowding and make changes in the design stage to address these issues and assure compliance with building codes and regulations. MassMotion can also be used to estimate travel times within certain areas, or determine where people are likely to look for wayfinding sign placement [23]. This software has been used in the creation and renovation of complex buildings and infrastructure, including Toronto's Union Station [14]. The software is also used in fire and life safety design, ensuring that building occupants can egress safely in the event of a fire or other emergency [15, 29].

MassMotion is able to easily evaluate the level of service for entire structures while factoring in the differences in LOS calculations, allowing engineers to quickly pinpoint areas which do not meet client specifications or standards. This can be especially important for shopping centres, museums, and stadia [10, 11].

MassMotion can provide powerful insights which influence building and transportation terminal design. However, like all modelling software it relies on pedestrian motion models and input data. Moreover, the field of pedestrian modelling is still evolving and developing, thus current versions may not include parameters or effects to accommodate new or undiscovered human factors and resulting behaviours. Through Software Development Kits, data-driven modelling, and new data collection methodologies, pedestrian models can be improved and tailored to Canadian data and environments.

## 2 Software Development Kits and Sub-models

One feature of MassMotion is a Software Development Kit (SDK). This consists of additional commands which programmers and engineers can use to further extend the capabilities of the software. This may include automating simulation runs, dynamically adjusting parameters of simulations, or processing results. In some cases, the SDK allows for complete modification of the pedestrian motion model which is used to calculate the results. These are henceforth referred to as sub-models. Sub-models, when properly validated and verified, can be invoked in specific situations as needed to modify the simulated behaviour of agents well beyond the initial movement model. This could be location-specific, such as using a different model for pedestrians standing or overtaking on an escalator, or agent-specific, allowing certain agents to behave differently using a modified movement model. As an example, a previous attempt at modelling group behaviour by implementing group force algorithms is presented below as developed by the authors [28].

## 2.1  Sub-model Example: Development of a Group Behaviour Model

The Software Development Kit provided with MassMotion included multiple examples of potential SDK applications. One of these, of particular interest for this project, was a custom social forces model. The social forces model is the core movement algorithm of the software, which calculates the movement of each agent based on a sum of 'forces' which pull the agent towards their goal while pushing away from obstacles and other agents. This demonstration code suspended the traditional social forces model used by MassMotion, and applied a new, custom social forces model for agents to follow. One of these forces demonstrated in the custom model was an agent repulsion force, which calculated a vector between two agents. This vector was multiplied by a factor and added to the sum of forces, pushing the agents away from each other. The first version of the Group Forces Model, GFM 0.1, simply added a negative multiplication of the repulsion factor. As seen in Fig. 2, this was enough to pull agents within a certain radius together, forming 'groups'. These groups were very uncharacteristic of real-life groups, with agents merging into each other, popping out the other side of the group, and then turning around to do so again. The groups also grew extremely quickly, attracting other agents to form large clusters. Although this was somewhat unrealistic, it proved that making agents travel in groups was indeed possible.

In GFM 0.2, the code was heavily modified to consider group forces using a new social forces-based algorithm [21]. The parameters from Moussaïd's Group Forces Model were tested on a simple hallway environment, where agents walked from one end of the hallway to the other. This showed promising results consistent with the observations made by Moussaïd et al. for groups of 3 agents [21]. Larger groups did not precisely conform to the observations but did show a definite improvement over the default Social Forces Model for the simulation of groups. The visual results of the basic hallway tests are shown in Fig. 3.

As seen in the Fig. 3, the new group forces encourage agents to walk closer together and in formations which encourage conversation and social interaction. Of



**Fig. 2**  Group forces model 0.1 results. Note agent clusters on right half of image
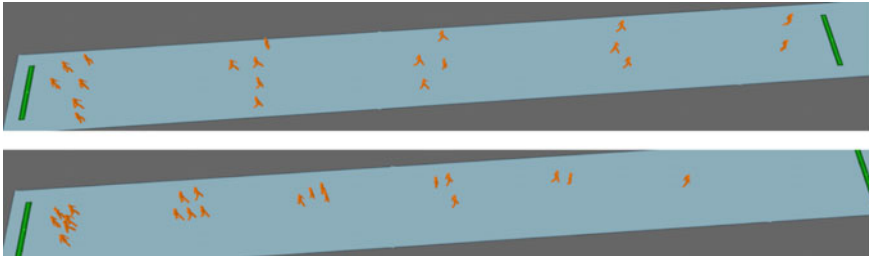
**Fig. 3** Default social forces model (upper) versus group forces model 0.2 (lower)
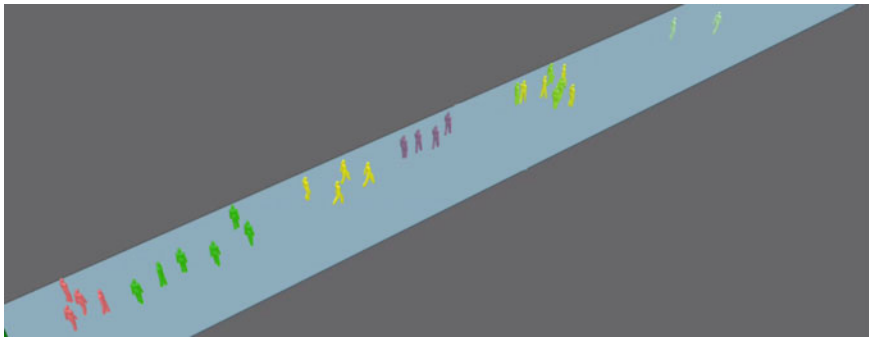


**Fig. 4** Group distinct coloration in group forces model 0.3

particular interest is the group of three agents, which forms the v shape as observed by Moussaïd, thus confirming that the social forces are working as intended. However, it is important to highlight that the current model suspends the social forces model which has been validated, leading to erratic movement.

Further improvements were made in GFM 0.3, with maximum group sizes being limited by a variable, paving the way for distribution-based group sizes. Grouping was still distance-based, but now each group was assigned a unique random colour to make members easier to track. The results are seen in Fig. 4.

## 2.2 Challenges with Calibration Validation of Sub-models

While the work done to create group simulations appeared promising, a new challenge quickly emerged; The new sub-models relied on specific input parameters to function, including walking speeds, distance between agents, and agent body diameters. The default social forces model was carefully balanced to reflect validation and verification tests performed by the developer, and altering these resulted in shakier movement. Even if resolved, the results of the model could not easily be compared with real-life examples. The changes made meant the model no longer complied

with the careful validation and verification of the original model. Hence, a method to quickly and easily validate pedestrian models is needed.

## 3   Data-Driven Models and Data Capture Methods

One potential way to resolve this is to move towards data-driven sub-models, which self-calibrate to input data using machine learning. In this case, the output would be the positions and densities of the walkways, and the given factors would include the geometries of the area and coordinates of the people walking. This has been successfully achieved by several researchers, especially with regards to groups. This initially started as an easy way to model crowds based on lab studies [17] but other researchers have also used public video of emergency situations to build their data-driven models [30].

While the methods shown demonstrate promise towards data-driven pedestrian models, many practical limitations of the methodology revolve around the enormous amount of position data and potential factors for the model to consider. These potential factors are vast, but may include elements such as group size, disabilities, environment, and local culture. In the previous works, these factors were not explicitly defined and were instead implied as part of the data-driven model. This may result in overfitting, where the data-driven model perfectly represents the precise situation observed, but cannot be applied to new situations with as much certainty. Each factor may be more specific to the local area or type of project being modelled, and should be parameterized so that practitioners can specify expected factors to tailor new models. As such, massive amounts of locally collected data in a variety of scenarios and environments is needed. However, this analysis generally requires a significant amount of time-consuming human input. Computer Vision technology makes it possible to automate this process [3], but fully autonomous methodologies generally are unable to distinguish between different human factors and details which may influence pedestrian behaviour.

One of the inputs for the model is a walking speed distribution which is meant to represent the population being modelled. Currently, modelling software includes default profiles which are based on past studies. However, walking speeds vary significantly due to a number of factors, including different locales and facility types [4]. Thus, these included profiles may not be fully representative of the populations and behaviours being modelled. While some agencies publish localized profiles for their engineers and consultants to use [22], this information is not easily found in Canada. One researcher noted that there is a significant lack of Canadian input data available while attempting to model Canadian subway stations [24].

The thought processes and actions may also vary between people. Pedestrian simulation software attempts to accommodate this by modelling the tasks conducted by people as they move through the environment. This could include the completion of different tasks in the terminal by visiting and dwelling in different locations, route selection to go from one place to the other, where to wait, where to queue, whether to

use stairs, escalators, or elevators, and more [23, 27]. This can be influenced by many factors, including mobility impairments or luggage. While it is possible to adjust the models to reflect these behaviours, it is highly difficult as behaviour can be highly variable depending on the situation and environment. Ultimately, pedestrian models make assumptions about behaviour which may differ from real-world results, and a much stronger database is needed to improve the reliability of pedestrian models [5].

## 3.1 Manual Tracking Methods

Manual tracking methods have historically been used to collect information such as movement speeds and details about people. This usually consists of timing a person as they travel a known distance between two points. While this can be done in field studies relatively easily, accurate timing is difficult. This becomes even more problematic in highly crowded areas. Playing back prerecorded video is possible, but time consuming. While it is possible to consider personal details, behaviours, and contexts using prerecorded video, it is not possible to collect precise position data. One method involved the use of cameras mounted high above the area to be analysed, which gave fairly effective results for pedestrian counting, but movement speed generation was limited to manually timing the movement of each track between two lines [19]. Manual tracking is best suited for linear pathways and simple trajectories. When there are multiple entrances and exits, the distances travelled must be determined for each pathway, which increases the processing time. In previous studies carried out, manual tracking could require several minutes per person tracked [10, 11]. Thus, manual tracking cannot scale to large crowds or congested areas.

## 3.2 Automated Tracking Methods

There have been several studies done in the past few years to collect pedestrian speeds and trajectories using a variety of techniques and technologies. A more recent study mounted cameras directly above the area to be analysed and could track pedestrians automatically if a marker was applied to the pedestrian's heads. Unfortunately, this method would be impractical for a study of the general public. Alternatively, stereo cameras were able to provide depth perception and thus could autonomously detect and track pedestrians without user input [3].

In Australia, a project called Dwell Track was undertaken in which 3D infrared cameras were used to monitor passenger numbers and track passenger movement on station platforms [26]. This automated process requires wired mounting and installation and does not provide demographics data. Although the anonymized data may pose some challenges for detailed data collection, this does allow Dwell Track to be used in locations with stricter privacy regulations.

A similar alternative is the use of LIDAR sensors to automatically track pedestrians, which generate point clouds showing the distances to surfaces and create live 3D point maps of the environment. Pedestrians can be identified from the background using software and software development kits, and tracking can be done on the identified persons [2]. Much like Dwell Track, the sensors cannot record faces or other personally identifying information, and thus could be used in more privacy-sensitive or restrictive environments.

While these methods can produce position data and can potentially operate in real-time, they lack the level of detail and context provided by manual methods and can be expensive to acquire and set up. While it is possible to both simultaneously, this is both time consuming and expensive. In order to generate the needed data for data-driven modelling, a low-cost method to collect fast and detailed data is needed.

### 3.3  Semiautomated Tracking

To address this missing combination of manual tracking and precise automatic video analysis, a new methodology was devised. The methodology allows for tracking to be done automatically using computer vision software, while incorporating manual tagging elements and has therefore been named Semiautomated Tracking.

Semiautomated Tracking makes use of an open-source kinematics analysis software called Kinovea [9]. The software is able to track the movement of selected points and make corrections for camera perspective angles and scaling to output distances and instantaneous speeds. As Kinovea tracks objects (or in this case people) frame-by-frame [8], it is useful in scenarios where people may not have a defined start and end point for tracking. The requirement for users to manually specify the point to track does open the door for manual tagging of details, which allows for more specific analysis.

Kinovea and other video tracking technologies brings some advantages to the level of detail that can be applied to an analysis. While LIDAR and infrared can be used in more restrictive environments, they may not capture finer details which may be useful for identifying demographics or other features such as disabilities, mobility devices, or luggage which may have an impact on a pedestrian's movement speeds, personal space, and/or decisions made. Kinovea's manual tagging and tracking means that this finer detail can be captured, and also does not have the marker or stereo camera requirement, making it possible to analyse footage taken from security cameras or other non-specialized cameras. Kinovea and the other softwares do not directly output statistical distributions of walking speeds, necessitating additional manual calculations and analysis. Each tracked pedestrian or object would need to be sorted or categorized if using a more detailed analysis method. In order to provide a faster method of analysis, additional software was developed to process the output data from Kinovea.

## 3.4 Profile Generator Development and Case Study

To increase the speed of processing pedestrian motion videos in Kinovea, two additional pieces of software were developed. The first was an automation script which was designed to help automate the input processes, whereas the second was a post-processing software used to generate the statistical distributions taken from Kinovea's outputs.

To expedite the creation of tags on tracked people and objects, a custom Auto-HotKey script was created. The script is used to automate keypresses and jump to relevant data entry fields, saving time by mimicking the inputs that a user would need to make, including several clicks and mouse movements. When this script is enabled, users are automatically prompted to enter a string of characters in the 'Name' field to represent the tags desired. The window automatically opens when a person is selected to end tracking, and the prompt window automatically closes and stops tracking once the tags are entered. The tagging window shows the person being tagged, but the user can also determine this while tracking is ongoing. The tags can be used to represent practically any attribute as specified by the user, as shown in Fig. 5.

Kinovea can output the raw x–y coordinates of each tracked object for each frame as a text file. Custom scripts have been coded to interpret these files and calculate movement speeds categorized by demographics tag. These scripts use the coordinate data and time between frames to calculate instantaneous and average walking speeds for each tracked person. Excel VBA has been employed to accomplish this in an iterative fashion which automatically scales with the number of frames and number of people tracked. The data is automatically separated and compiled according to each tag assigned in the tagging process. The script can also make adjustments for different camera frame rates, as well as detect and accommodate duplicated frames. The final output of the script is the average walking speeds and counts for each demographic analysed, as well as an overall total. The process is largely automated, with the user only needing to select the output.txt file generated by Kinovea.

In a case study of a Canadian passenger rail terminal, Semiautomated Tracking was able to find significant walking speed differences between passengers with and

**Fig. 5** Tagging window in Kinovea (tags l and s applied, indicating late passenger with suitcase)
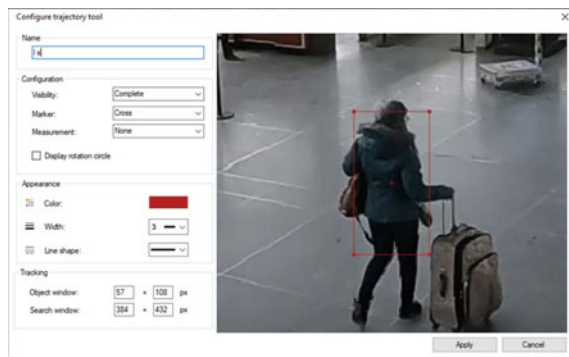
without luggage, passengers boarding right before departure versus those who arrived earlier and queued, along with many other differences with lower significance due to low sample size. The use of video footage and context knowledge also revealed specific behaviours, such as late passengers holding beverages from the in-station café, and boarding passengers running when observing a closing automatic door.

## 4   Comparison of Methods

Considering the novelty of Semiautomated Tracking, comparisons must be made against the other methodologies currently available to determine their benefits and drawbacks.

Prior to the enhancements of Semiautomated tracking, Larsson and Friholm of Lund University used Kinovea to track pedestrian motion, including walking speed and body movement in a lab environment [16]. Their results were compared to an automated motion tracking system which required the participants to wear tracking markers, to determine the effectiveness of each system for a detailed analysis of limb motion, walking speeds, and separation between pedestrians.

While the automated optical motion capture method demonstrated higher data accuracy, lower user dependency, and faster analysis, there were drawbacks identified which made the method less effective for crowd investigations. Equipment costs were significant and applying markers to a general crowd was unfeasible. Video tracking took longer but was less expensive and could be used in a realistic crowd investigation [16]. Their table has been adapted further to incorporate LIDAR, Manual Tracking, and updated capabilities of video analysis using Semiautomated Tracking (Table 1).

Kinovea, as with all line-of-sight methodologies suffer from challenges in occlusion when a person passes behind another person or object. Once line-of-sight is lost, it becomes very difficult or impossible for tracking to continue. Infrared and LIDAR cameras are particularly susceptible as even transparent obstructions such as glass walls or barriers will block the cameras. When examining large crowds, the same occlusion issues exist as infrared signatures start to blend and shadows are cast by the first object in the LIDAR's line-of-sight. Steep or near vertical camera angles may make it easier for individuals in denser crowds to be tracked, as shown by PeTrack's methodology [3]. One benefit of Semiautomated Tracking is that partial trajectories can be used, so if a person or object is partially occluded, tracking can be done during the non-occluded parts of the footage. Higher resolutions and frame rates also result in more detail which may improve tracking accuracy and abilities for denser crowds. In Kinovea, cameras are best set up with 4 measurable points visible in a rectangular shape, such as a floor tile pattern. This allows for calibration to correct viewing angles and distortion. The camera lens distortion must also be recorded and taken into effect using parameters set within Kinovea or through corrections applied to the raw video in video editing software.

**Table 1** Gales data capture methods comparison [16] (Modified from)

| Evaluation aspect | Video analysis (semiautomated tracking) | Optical motion capture | LIDAR | Manual tracking |
|---|---|---|---|---|
| User friendliness | High | High | Moderate | High |
| Economical aspects | Cheap even if hardware needs to be purchased | Expensive if hardware needed | Very expensive if hardware needed | Cheap, but costs increase with duration and size |
| Data accuracy | Moderate, depends on sampling rate | High, sampling rate is 100 measurements per second | High, sampling rate is up to 50 measurements per second | Low, only measures average speed |
| User dependency | High, many elements have user dependent aspects | Low, only preparation has user dependent aspects | Low, only preparation has user dependent aspects | Very high, everything has user dependent aspects |
| Can handle obstructed markers | Markers can be manually estimated or data cut short | Yes, but only if obstructions are for short periods of time | Yes, especially if multiple sensors used | Yes, as only start and endpoint are tracked |
| Can analyse without the use of markers | Yes, but accuracy will be lower | No | Yes, markers not required | Only unmarkered tracking possible |
| Time consuming: collection | Depends on number of participants and tests | Depends on number of participants and tests | Real-time data collection | Very high, depends on number of participants and tests |
| Time consuming: analysis | Moderate if analysis is automatic, high if tracking environment congested | None, analysis is completed during the experiment | None, analysis is completed during the experiment | Very high, automatic analysis not possible |
| Partial trajectories possible | Yes | Yes | Yes | No |
| Can be used for crowd investigation in public spaces | Yes, especially if cameras already exist | No, cannot place markers for tracking on general public | Yes, but requires mounting of custom LIDAR equipment | No, method does not scale well to very large crowds |

## 4.1 Verification of Profile Generator Output and Limitations of Data Collection Techniques

The outputs from Semiautomated Tracking are intended to act as the basis for future research. Thus, it is of high importance that the outputs of this new methodology are

validated against real-world observations to ensure that the newly generated data is reliable. To check this, old video footage and walking speed data was re-analysed under the new methodology to compare the two outputs. The old data comes from previous work analysing pedestrian motion at a Canadian passenger rail station. The validation focused on passengers entering the station concourse via an escalator and proceeding to the exit of the station using the Manual Tracking methodology.

This methodology has also been used for the collection of pedestrian speeds by previous researchers [1]. This older manual technique has a few distinct disadvantages; The distance travelled is only an estimate based on optimal linear distances although pedestrians may take less-than-optimal paths, the longer distances required manual tracking across multiple cameras, the final speed reported is an average over the entire distance which may be impacted by changes in walking speed, and finally some pedestrians took actions that disqualified them from manual tracking such as pausing to adjust bags, waiting for other group members, or visiting locations that were not the main exits. Of the 61 pedestrians on the route for this study, only 29 could be tracked using the manual methodology. In comparison, 53 of the 61 pedestrians were successfully tracked using the new semiautomated technique within a single video. The entry time and luggage carried by each pedestrian was used to determine which pedestrian was being tracked, as each pedestrian in the old data was assigned an agent number. This agent number was then applied to the tracked contour in Kinovea for direct comparisons between values. The statistical distribution for the pedestrian walking speeds is displayed in Table 2.

The new Profile Generator methodology produced walking speeds that were similar the manually tracked data, albeit slightly faster, with an average difference of + 0.11 m/s and a maximum difference of + 0.47 m/s which was noted for two pedestrians. In one case, the pedestrian slowed briefly to allow a group member to catch up but then resumed walking at a fast rate. Notably, the manual tracking method shows a 0.11 m/s difference in walking speeds between the two group members despite them walking side-by-side for the majority of their time in the concourse whereas the speeds generated by Semiautomated Tracking are nearly identical with only a 0.02 m/s difference. In another case the pedestrian took a longer path to avoid another pedestrian who had paused in the concourse to adjust luggage, thus travelling a greater distance than assumed by manual tracking. In both cases these may have played into error with the manual tracking resulting in a slower-than-reality walking

**Table 2** Profile generator verification test results

| Data source | Population tracked | Mean (m/s) | Median (m/s) | Standard deviation (m/s) |
|---|---|---|---|---|
| Manual tracking | 29 | 1.04 | 1.05 | 0.209 |
| Semiautomated tracking | 53 | 1.15 | 1.18 | 0.26 |
| Semiautomated tracking (direct comparison with manual tracking) | 27 | 1.15 | 1.11 | 0.27 |

speed in manual tracking, and thus the error lies within the manual tracking methodology. In most cases, the walking speed is lower than the speeds reported by Profile Generator. However, the manual methodology once again assumes the most direct, optimal path with no slowing down, speeding up, or pauses. Thus, profile generator may actually be reporting a closer result than manual tracking.

There are also challenges regarding the video data used for collection, which applies not only to the validation but also future analysis of these particular videos. As the recordings used were not intended for use in Kinovea and Profile Generator, a heavy fisheye lens distortion effect existed on the original video data. A checkerboard pattern captured with the same cameras, combined with video editing software was used in an attempt to significantly reduce the fisheye effect. Work has been done by several researchers to automate this process [18]. However, no freeware automated software was found that could generate acceptable results, thus this process was done manually. It is noted that this effect could not be fully eliminated, both here and in Lee et al. due to approximation errors. As the video recordings predate the development of Kinovea and the need for a calibration grid, the initial grid corner locations needed to be estimated. In this case, the roof support column bases combined with movable rope barrier stanchions as seen in the videos were used to generate the $x$–$y$ grid at approximately torso-height as seen in Fig. 6. These approximations may have had an impact on the distance interpreted by Kinovea and Profile Generator.

The challenge in doing this type of comparison is that each method may have their own disadvantages and errors which may have impacts on the data. Without knowing the real 'ground truth' movement speed to compare to, the utility of this exercise is limited to saying that the new methodology produces similar movement speeds to the old methodology and thus should be acceptable for the generation of speed data. However, this data should not be relied upon until comparisons can be made to a real 'ground truth'. While this was initially planned for this project, public health restrictions and challenges have relegated this validation experiment to future study. It is planned to run this study with multiple tracking technologies and with a speed sensor applied to people or tracked objects in a lab environment. By doing so, multiple technologies and methodologies can be evaluated simultaneously against known speed data.
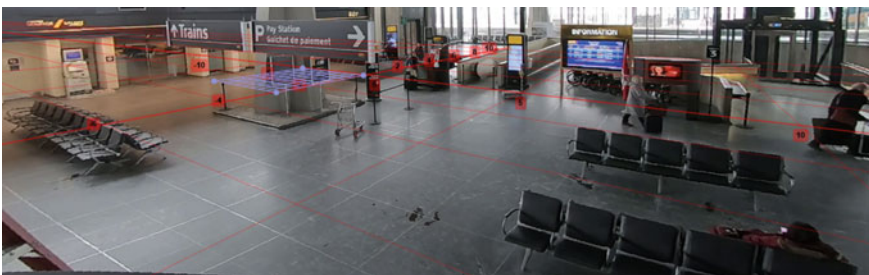


**Fig. 6** Calibration grid for validation testing

## 5    Future Research and Impacts

The future use cases for Semiautomated Tracking is vast, extending beyond transportation terminals and video footage. For industry and engineering applications, the methodology has significant potential to improve data collection and allow practitioners to easily produce movement speeds and data for their pedestrian models or to meet client needs in observing occupant behaviours. The methodology is highly accessible, considering that Kinovea is open-source and Profile Generator is designed to run within Excel. Furthermore, the use of inexpensive cameras and potentially preexisting CCTV systems minimizes equipment costs. Tracking and tagging processes within Kinovea are easy for new users and requires little to no knowledge of computer vision algorithms and techniques. Profile Generator is almost completely automated, requiring only the selection of the output.txt file to run. This should allow users to minimize training times and start using the methodology quickly. Finally, the time savings offered by Kinovea should minimize the number of working hours required to analyse acquired footage, reducing project costs or improving project results at minimal expense.

Ultimately, the use of Semiautomated Tracking may unlock a deeper level of analysis for security camera footage, provided that the camera quality is sufficient. This could spur on a new level of understanding for the field of pedestrian behaviour and microsimulation, as any building with a CCTV system could become an instant data collection site. Circulation within transportation facilities, shopping centres, stadiums, museums, and other buildings would become significantly easier to study without the need to set up additional equipment. However, the most significant use may be for fire safety, emergency, and other high-stress scenarios.

By having cameras at the right place at the right time, rare and useful observations can be captured. In the transportation terminal study, a snowstorm provided good conditions to observe high-stress situations. It was found that passengers in the high-stress situation of nearly missing their train resulted in faster walking speeds. With CCTV as a potential data source, the likelihood of having cameras at the right place and right time to capture rare scenarios such as fires, evacuations, and other emergencies increases significantly, enabling mass analysis of pedestrian behaviour in a variety of situations across the globe. This is exemplified further by a co-authored research project and publication which used CCTV footage in a museum to examine behaviour in fire drills and unplanned evacuations [7, 13].

Before Profile Generator can be used, additional testing and development is required. Future work is required to modify Profile Generator to improve its capabilities and reach its full potential. Additional validation testing of movement speeds and positioning is needed to determine best practices for using camera footage. This may include a list of best practices to yield the most accurate results. As calibration of the initial $x$–$y$ grid is critical to an accurate result, improvements to the calibration process would be beneficial. To assist in this, LIDAR pedestrian tracking is being used to generate the needed baseline for data collection.

Profile Generator can easily be modified to work with other text-based input formats. In the future, more options should be developed to allow for $x$–$y$ inputs from other video tracking software and hardware, including LIDAR and Stereo Cameras. This will allow Profile Generator to work with new potential video or data sources for further applications. Ultimately, any $x$–$y$ coordinate source should be usable with Profile Generator.

Using the data from these scenarios can help engineers and practitioners get a better sense of how people behave and move under complex and rare conditions. This ultimately could translate into a better understanding of human behaviour in emergencies and further the development and validation of new pedestrian movement models.

# 6    Conclusions

Pedestrian modelling software is an important tool for designing transportation terminals and pedestrian infrastructure. While extensions to the underlying model are possible to develop, these sub-models require calibration and validation using highly detailed data which is currently difficult to generate. Ultimately, mass-collection of detailed motion and contextual data is needed as the first step towards data-driven sub-models. A Semiautomated Tracking methodology can provide low-cost, high-detail data to fulfil this need by providing most of the benefits of both manual and automated tracking. The use of video footage and open-source software may allow for pre-existing security footage to be used, giving critical insight into rare and specific behaviours. The continued development of Semiautomated Tracking and similar technologies will pave the way forward for data-driven sub-models, allowing engineers to achieve more detailed and accurate results in their pedestrian simulations.

# References

1. Aucoin D (2019) The use of human behaviour to inform egress modeling in stadiums. York University, Toronto, ON
2. Benedek C (2014) 3D people surveillance on range data sequences of a rotating lidar. Pattern Recogn Lett 50:149–158
3. Boltes M, Seyfried A (2013) Collecting pedestrian trajectories. Neurocomputing 100:127–133
4. Bosina E, Weidmann U (2017) Estimating pedestrian speed using aggregated literature data. Physica A 468:1–29
5. Carattin E, Brannigan V (2014). Lost in abstraction: the complexity of real environments vs the assumptions of models. In: Fire and evacuation modeling technical conference 2014. Gaithersburg, MD
6. CBC News (2015) Union Station commuter dragged to death under train. (CBC News) Retrieved 20 May 2021, from https://www.cbc.ca/news/canada/toronto/union-station-commuter-dragged-to-death-under-train-1.3053644
7. Champagne R, Young T, Gales J, Kinsey M, Weckman B (2019) Fire evacuation and strategies for cultural centres. In: Interflam 2019: 15th international conference and exhibition on fire science and engineering. Windsor, UK
8. Charmant J (2011) Optimizing markers for tracking. (Kinovea Forums) Retrieved 18 Nov 2019, from https://www.kinovea.org/en/forum/viewtopic.php?id=404
9. Charmant J (n.d.) Kinovea. (Kinovea) Retrieved 2 Nov 2019, from https://www.kinovea.org/
10. Chin K, Young T, Chorlton B, Aucoin D, Gales J (2022) Crowd behaviour in Canadian football stadia - Part 1. Canadian J Civ Eng
11. Chin K, Young T, Chorlton B, Aucoin D, Gales J (2022) Crowd behaviour in Canadian football stadia - Part 2 - modelling. Canadian J Civ Eng
12. Fruin JJ (1970) Designing for pedestrians: a level of service concept. Polycechnic Insititute of Brooklyn, New York
13. Gales J, Champagne R, Harun G, Carton H, Kinsey M (2022) Fire evacuation and exit design in heritage cultural centres. Springer Briefs in Architectural Design and Technology
14. Hoy G, Morrow E, Shalaby A (2016) Use of agent-based crowd simulation to investigate the performance of large-scale intermodal facilities: case study of Union Station in Toronto, Ontario, Canada. Transp Res Rec 2540(1):20–29
15. Kinsey M (2015) The verification and validation of massmotion for evacuation modelling. ARUP, London, United Kingdom
16. Larsson G, Friholm J (2019) Evaluation of measurement methods for determining individual movement in crowds. Lund University, Lund
17. Lee KH, Choi MG, Hong Q, Lee J (2007) Group behavior from video: a data-driven approach to crowd simulation. In: Eurographics/ACM SIGGRAPH symposium on computer animation. Eurographics Association, San Diego, CA, pp 109–118
18. Lee S-H, Lee S-K, Choi J-S (2009) Correction of radial distortion using a planar checkerboard pattern and its image. IEEE Trans Consum Electron 55(1):27–33
19. Li S, Sayed T, Zaki MH, Mori G, Stefanus F, Khanloo B, Saunier N (2012) Automated collection of pedestrian data through computer vision techniques. Transp Res Rec 2299(1):121–127
20. Loukaitou-Sideris A, Taylor B, Voulgaris CT (2015) Passenger flows in underground railway stations and platforms. Mineta Transportation Insititute, San Jose, CA
21. Moussaid M, Perozo N, Garnier S, Helbing D, Theraulaz G (2010) The walking behaviour of pedestrian social groups and its impact on crowd dynamics. Plos One 5(4)
22. Rail N (2011) Metro station capacity assessment guidance. Network Rail, London
23. Oasys (2020) Mass motion help guide. Oasys
24. Srikukenthiran S (2015) Integrated microsimulation modelling of crowd and subway network dynamics for disruption management support. Graduate Department of Civil Engineering, University of Toronto, Toronto, Ontario
25. Transport For London (2012) Station planning standards and guidelines. Retrieved May 21, 2021, from https://docplayer.net/13988764-Station-planning-standards-and-guidelines.html

26. Virgona A, Kirchner N, Alempijevic A (2015) Sensing and perception technology to enable real time monitoring of passenger movement behaviours through congested rail stations. In: Australasian transport research forum 2015 proceedings. Sydney, Australia
27. Wong H, Clear C (2016) Station modelling with Legion spaceworks: best practice guide. Transport for London, London, UK
28. Young T (2019) Simulating group behaviour in passenger terminals. Carleton University, Ottawa, ON
29. Young T, Gales J, Kinsey M, Wong WC-K (2021) Variability in stadia evacuation under normal, high-motivation, and emergency egress. J Build Eng 40(1):102361
30. Zhang J, Liu H, Li Y, Qin X, Wang S (2018) Video-driven group behavior simulation based on social comparison theory. Physica A 620–634

# Transportation Specialty: Climate and Pandemic Resiliency

# Bike Share's Impact on COVID-19 Transmission and Bike Share's Responses to COVID-19: A Case Study of Washington DC

**Pedram Beigi, Mohaiminul Haque, Mohammad Sadra Rajabi, and Samer Hamdar**

**Abstract** Due to the wide-ranging travel restrictions and lockdowns applied to limit the diffusion of the SARS-CoV2 virus, the coronavirus disease of 2019 (COVID-19) pandemic has had an immediate and significant effect on human mobility at the global, national, and local levels. At the local level, bike-sharing played a significant role in urban transport during the pandemic since riders could travel outdoors with reduced infection risk. However, based on different data resources, this non-motorized mode of transportation was still negatively affected by the pandemic (i.e., relative reduction in ridership). This study has two objectives: (1) to investigate the impact of the COVID-19 pandemic on the numbers and duration of trips conducted through a bike-sharing system—the Capital Bikeshare in Washington, DC, USA, and (2) to explore whether land use and household income in the nation's capital influence the spatial variation of ridership during the pandemic. Toward realizing these objectives, this research looks at the relationship between bike-sharing and COVID-19 transmission as a two-directional relationship rather than a one-directional causal relationship. Accordingly, this study models (i) the impact of COVID-19 infection numbers and rates on the use of the Capital Bikeshare system and (ii) the risk of COVID-19 transmission among individual bike-sharing users. In other words, we examine (i) the cyclist's behavior as a function of the COVID-19 transmission evolution in an urban environment and (ii) the possible relationship between the bike-share usage and the COVID-19 transmission through adopting a probabilistic contagion model. The findings show the risk of using a bike-sharing system during the pandemic and whether bike-sharing remains a healthier alternative mode of transportation in terms of infection risk.

P. Beigi (✉) · M. Haque · M. S. Rajabi · S. Hamdar
Department of Civil and Environmental Engineering, The George Washington University, Washington DC, USA
e-mail: beigi@gwu.edu

## 1   Introduction and Literature Review

COVID-19 was firstly reported in Wuhan, Hubei, China, on March 11, and the World Health Organization (WHO) investigated and declared COVID-19 as a pandemic on March 11. By the end of October 2021, WHO had received reports of about 247,400,000 cases and 5,000,000 fatalities caused by COVID-19, most of which occurred in America and Europe [39]. Many nations employed various lockdowns to postpone the pandemic's peak and smooth the curve as early as the first months of the infection [22, 31]. Several studies have demonstrated that unrestricted mobility would have hastened the development of COVID-19 [33, 40], and those travel limitations, in general, tended to slow the disease's global growth [3, 13, 25, 30].

Corresponding travel restrictions and various lockdowns had a significant impact on the entire transportation system globally [21, 27, 34]. Tian [37] offered a different perspective on urban traffic and air pollution in sample Canadian cities affected by the outbreak. Sun et al. [36] used a network science technique to conduct a complete empirical investigation of the impact of the COVID-19 epidemic on air travel from a complex system standpoint. In another study, Aloi et al. [2] examined the influence of the quarantine imposed in Spain on March 15, 2020, on urban mobility in the northern city of Santander. They discovered a 76% drop in total mobility and a 93% drop in public transportation utilization in Santander, Spain. Gajendran [20] employed descriptive research approaches to analyze travel scenarios under the normal situation, pre-lockdown, and until the COVID-19 epidemic ends with understanding better the influence of coronavirus on Indian people's travel patterns. Moreover, in another study in the USA by Doucette et al. [17], the effect of the lockdown on daily vehicle miles traveled (VMT) and MVCs in Connecticut has been investigated. The results declare that in the post-stay-at-home timeframe of 2020, the mean daily vehicle miles traveled (VMT) declined by 43% [17].

In addition to the ephemeral alterations in urban mobility that occurred during lockdowns [16, 18], COVID-19 prompted permanent changes in transportation policy and practice [7, 8, 28]. Many megacities, as well as medium-sized cities throughout the world, have redistributed public space in favor of cycling and walking, imposed automobile traffic limits, and even provided financial assistance to inhabitants for the purchase of bicycles [1]. According to several experts [4, 15, 26], the pandemic will result in a long-term avoidance of public transportation, an increased bicycling and walking, and a reduced total trips due to greater teleworking. These projections are backed up by research that has already been published. According to a survey conducted in the Netherlands, individuals are now more favorable toward vehicles and more negative against public transportation [14]. According to the same survey, a high number of people who worked from home during the epidemic anticipate doing so more frequently in the future [14]. Another research based on data from Budapest,

Hungary, found an 80% decline in public transportation demand, but only a 23% fall in biking and a 2% reduction in bike-sharing [6]. In Beijing, China, the decline in bike-sharing utilization was even more pronounced, with 40% fewer rentals made compared to the same time in 2019 [11].

Bike-sharing systems have previously been shown to be effective in the face of unexpected events such as public transportation strikes [5, 32]. During the COVID-19 crisis, bike-sharing was likewise proven to be more resilient than a subway system in New York City, with a less-significant ridership drop. Although research on the influence of COVID-19 on passengers' views toward private automobiles, public transportation, bicycles, and walking has already been conducted, little research has been done to investigate the impact of COVID-19 on bike-sharing mobility systems. In particular, the pandemic's influence on bike-sharing in the Washington DC metropolitan area is of significant interest, and the exact correlations between COVID-19 infection rate and bike-sharing ridership are still unclear.

As a result, the present study will examine the impact of the COVID-19 pandemic and household property on bike-sharing ridership, as well as the impact of the bike-sharing system on COVID-19 spread and whether it should continue to operate in the event of a pandemic.

## 2  Methodology

The methodology for the analysis is based on (i) a numerical comparison with ordinary least square (OLS) regressions to assess the relation of COVID-19 cases and bike-sharing ridership and (ii) adapting contagion models generally used for buses and light rail into a contagion model for shared bike services. We began by employing a time series analysis to examine the bike-sharing system's weekly average ridership with OLS regression to explore their relationship with the number of COVID-19 cases. We utilize spatial analysis to look at the influence of household income, unemployment rate, and density of D.C. tracts on bike ridership in that tract to see how people deal with bicycles during the pandemic.

### 2.1  COVID-19's Impact on DC Public Transport

COVID-19's influence on the bike-sharing system was assessed using a statistical method. In this investigation, ordinary least square (OLS) regressions were used. Ordinary least square (OLS) regression is a method for analyzing the relationship between a dependent variable and one or more independent variables by minimizing the sum of squared residuals (the difference between the observed and predicted values) of the dependent variable, which is shaped like a straight line (linear relationship) [19]. The aim of the regression modeling is to determine the significance and effect of COVID-19 on the behavior of the bike-sharing system rather than to

produce a predictive application because there are so many exogenous elements at play. Figure 2 represents this variation and compares it with the reported number of daily new COVID-19 cases and its daily ridership. To investigate the impact of the COVID-19 pandemic on the D.C. bike-share, the after-pandemic ridership data (i.e., March 2020 to September 2021) are compared to the ridership of 2019. The statistical model of multivariate linear regression is as follows (Fig. 1):

$$Y = \beta_0 + \sum_{i=1}^{I} \beta_i X_i + \varepsilon \quad i \in I,$$

where $Y$ is the dependent variable, $X_i$ is the independent variables, $\beta_0$ is the model constant, $\beta_1$ is the model coefficients, $I$ is the number of independent variables, and $\varepsilon$ is the random error. Given the amount of skewness in Table 1, the variable of the COVID-19 case does not have a normal distribution. To solve this problem, we use
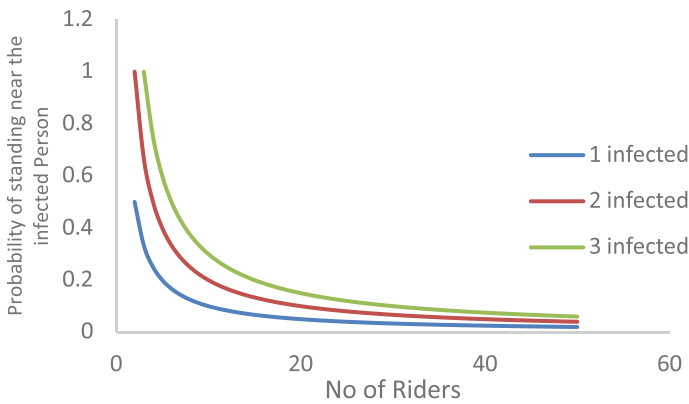


**Fig. 1** $P(B)$ for 1, 2, and 3 infected people
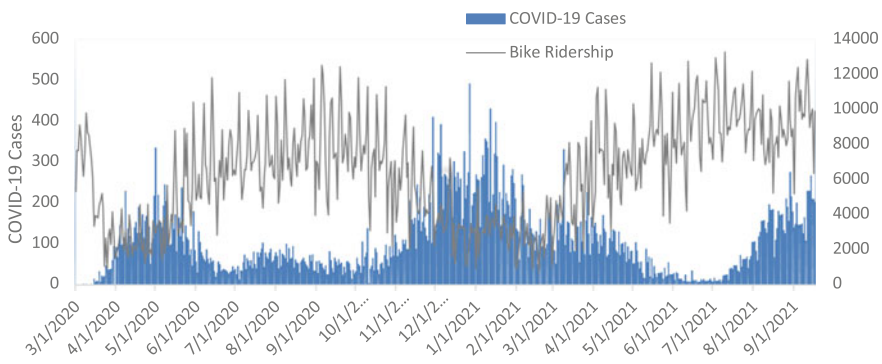


**Fig. 2** COVID-19 cases and bike-share ridership after the pandemic

the natural logarithm of variables. Therefore, the final model is as follows where BR is bike ridership, and CC is COVID-19 cases.

$$\ln(\text{BR}) = \beta_0 + \beta_1 \times \text{CC} + u.$$

The District of Columbia has 179 census tracts, 450 block groups, and 6507 census blocks. The average annual income, unemployment rate, and density of D.C.'s tracks were used for spatial analysis to observe how these characteristics of zones can impact the behavior of people using bikes during the pandemic. Figure 3 illustrates that changes in bike-share usage are influenced not just by COVID-19 but also by other factors such as the built environment. The use of the bicycle is affected by a combination of factors. We look at the influence of income, unemployment rate, and density in each tract as independent variables on the dependent variable, bike ridership. We compare each station's pre- and-post-COVID19 bike riding rates to get a more accurate comparison.

In overall, during the COVID-19, public bicycle utilization was 28% lower than before. If the ratio of COVID-19 to pre-COVID-19 public bicycle usage is nearly the same for each station, the shift in utilization is due to the epidemic and has nothing to do with other factors. Suppose this ratio varies substantially from station to station. In that case, it indicates that the change is influenced not just by the COVID-19 but also by the station's and surrounding area's features, such as the built environment and demography. Figure 4 depicts the spatial analysis of this ratio with respect to income, density, and unemployment rate.

**Table 1** Statistical summary of data

| Variable | Standard deviation | Average | Max | Third quarter | Second quarter | First quarter | Min | Skewness |
|---|---|---|---|---|---|---|---|---|
| Bike rides before COVID-19 | 3228.9 | 8897.1 | 14,831 | 11,871.5 | 9174 | 6296.5 | 626 | −0.35 |
| Bike rides after COVID-19 | 2911.6 | 6339.7 | 13,286 | 8511.2 | 6521.5 | 3711.7 | 730 | 0.1 |
| COVID-19 case | 82.03 | 104.5 | 492 | 148 | 83 | 43.75 | 0 | 1.24 |
| Density | 4734.9 | 7063.7 | 25,061.6 | 9685 | 5797 | 3653.0 | 9.17 | 1.23 |
| Income | 29,924.2 | 55,088.1 | 142,543 | 79,781 | 48,246.5 | 29,791.7 | 4183 | 0.54 |
| Unemployment rate | 6.02 | 7.43 | 34.2 | 9.8 | 5.5 | 3.5 | 0.2 | 1.8 |
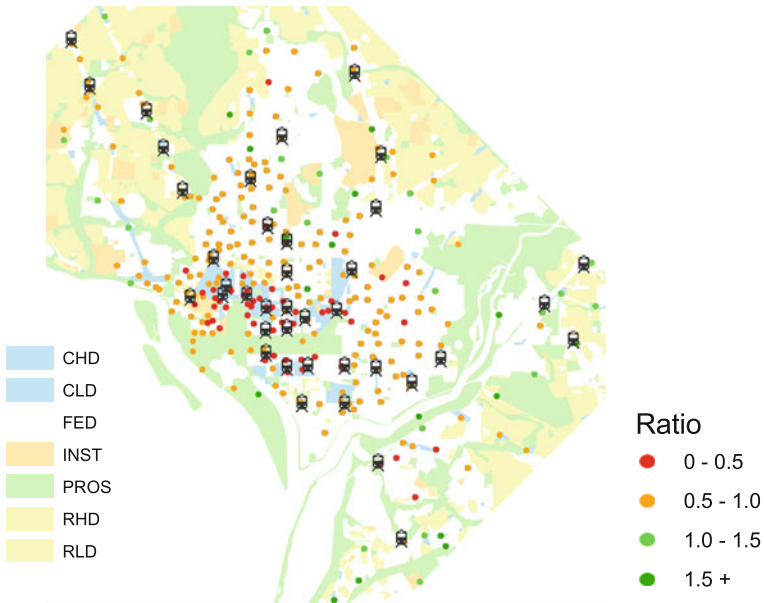
**Fig. 3** Ratio of bike-share ridership after and before pandemic with respect to land use



a)

b)
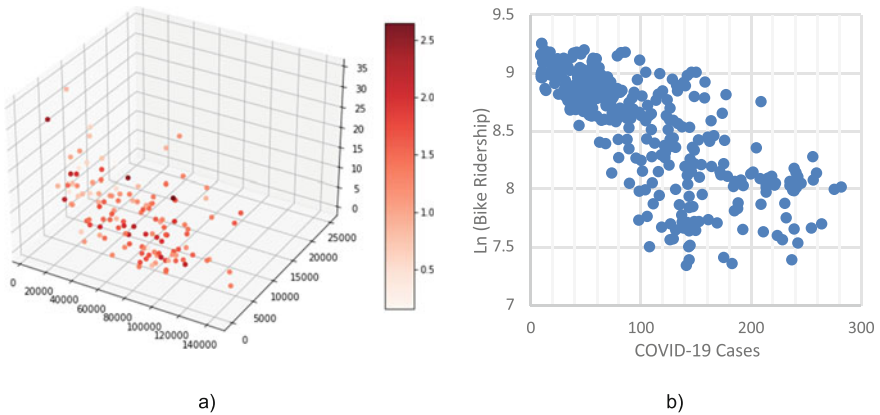
**Fig. 4** **a** Bike ridership usage ratio before and after pandemic in terms of *x*: income, *y*: density, and *z*: unemployment rate of tracts. **b** Natural logarithm of Bike ridership in terms of COVID-19 Cases

## 2.2 COVID-19 Transmission

COVID-19 can be transmitted directly via human-to-human contact/proximity due to droplet formation and movement. The droplets are forming at times of breathing, talking, sneezing, and coughing varies in both size and content. The size of the

droplets significantly depends on various environmental factors, such as gravity, the direction and strength of local airflows, temperature, and relative humidity. Droplets > 5 µm in diameter fall rapidly to the ground under gravity and therefore are transmitted only over a limited distance (e.g., ≤ 1 m). In contrast, if the nuclei of the droplets are ≤ 5 µm in diameter, they can remain suspended in the air for significant periods of time, allowing them to be transmitted over distances > 1 m. The term droplet is often taken to refer to droplets > 5 µm in diameter [12].

Therefore, in this study, we will suppose the droplets which have a diameter of roughly 5 µm and can spread throughout a 1.5-m-diameter circular region. Droplets of this size can stay in the air for 8–12 min, according to [35]. As a result, we will use airtime of 8, 10, and 12 min for the droplets while retaining the spread diameter at 1.5 m. Furthermore, we will assume that the probability of a person becoming infected as a result of being in close proximity to someone who is infected (P(A/ B)—which is dependent on crowding conditions and adherence to social distancing at the bike-share station) is equal to 1 if the relative distance between them is less than or equal to 1 m and 0 if the relative distance is greater than 1.5 m (five feet). The majority of D.C.'s bike-share stations have 15 bike docks with an average of 17 docks, each measuring 3 × 6 ft. Only ten cyclists should be allowed at any given time to maintain the 1 m social separation. For a 1.5 m separation barrier, only six cyclists should be permitted. The possibility of wearing masks (and the quality of the mask) or using cleaners/hand sanitizers are not taken into account in this contagion probability analysis.

Based on the above, the ratio between the number of infected riders at stations and the total number of riders in a given track segment or station defines the probability that a person is standing next to someone infected ($P(B)$), which is related to the number of people infected in the area. For the scenario where one, two, or three infected riders are present at a station, an illustration of this probability for different riders' numbers is presented below.

Given such reasoning, if it is assumed that the riders are exposed to the infected person either at the start or the end location (i.e., origin and destination—O.D.), the probability that each person's susceptibility can be calculated is as follows:

$$P_s = \left(1 - P\left(\frac{A}{B}\right)_{\text{start}} * P(B)_{\text{start}}\right) * \left(1 - P\left(\frac{A}{B}\right)_{\text{end}} * P(B)_{\text{end}}\right).$$

Here, the subscript start represents the starting station, and the subscript end represents the ending station of a given user's trip. The virus can also be transmitted via the human-to-surface-to-human path from one person to another. Droplets created by the infected person when talking, sneezing, and other activities will ultimately fall on nearby surfaces. Anyone who contacts that surface and subsequently touches his mouth, nose, or eye might become infected. This is a critical transmission mode in shared bikes since everyone who rides them will be in close contact with the bike's handles. The coronavirus can be stable for up to four hours on copper, up to 24 h on cardboard, and up to two to three days on plastic and stainless steel, according to the

National Institute of Health (NIH) [29, 38] investigated the survivability of SARS-CoV-1 and SARS-CoV-2 (COVID-19) on various surfaces in comparative research. Viruses were applied to copper, cardboard, stainless steel, and plastic for 7 days at a temperature of 21–23 °C and relative humidity of 40%. Their study shows that the virus lasted 15 h on copper, 24 h on cardboard, 76 h on stainless steel, and 76 h on plastic based on tissue-culture infectious dose (TCID50) per liter of collecting material. For this study, we will use a stable period of 1, 2, and 3 days. In other words, we will assume a person using the same bike as the infected user within the specific time period will get infected.

## 3  Data Analysis

The study area is Washington DC, with 179 census tracts. Washington DC's Capital Bikeshare, in August 2008, became the first city in North America to launch a bike-sharing system. Capital Bikeshare (CaBi) is metro D.C.'s bike-share system, with more than 4300 bikes available at 654 stations across seven jurisdictions. The variables used in this study include Bike ridership (BR), COVID-19 daily cases (CC), average annual household income per capita (AI), unemployment rate (UR), and density (DE) of D.C.'s tracks. The economic characteristics and population data for D.C. Census Tracts are publicly accessible, as well as data on Capital Bike-Share Ridership. This bike-share dataset comprises information on trip start and end times, the stations used at both the beginning and end of trips, and user categorization, distinguishing between annual members and casual users. Ridership data of CaBi were retrieved from January 2019 to September 2021. The number of COVID-19 cases is available in the Centers for Disease Control and Prevention (CDC) database. The statistical summary of data is shown in Table 1.

Some trips lasted a very short (or long) time, and those lasting more than four hours or less than one minute were excluded from the current study to increase accuracy. Short trips can be caused by various circumstances, such as when a user finds that the bike is in bad condition and returns to exchange it for a better one or when the bike is promptly locked before a user can take it out of the dock. Since then, it is true that the majority of these one-minute-or-less trips began and finished at the same stations. Similarly, we discovered several extremely lengthy trips. These long trips might be the result of the dock system failing to lock the bike upon return, which the users were unaware of this situation, sometimes because the station is offline, or the bike is lost or stolen after it was checked out.

## 4    Results and Discussion

### 4.1    COVID-19's Impact on DC Public Transport

Capital Bikeshare's trips duration was aggregated monthly to determine if and how this increase in the trip's duration is related to the coronavirus pandemic by comparing the monthly trip duration before and during the pandemic. The data reveal a continued growth in the average trip duration, from a 13-min daily average at the beginning of January 2019 to a 19-min average by the end of September 2021, translating into a 44% increase. From January 2019 to February 2020, the average monthly trip duration is 15.5 min, while after the pandemic from March 2020 to September 2021, the average monthly trip duration is 21 min. This could mean that people prefer short trips on foot. Only those who have always used a bicycle for daily commuting continue to use it. Since the average percentage of casual users before the pandemic is only 11% and after a pandemic is 43%, the average duration of trips for casual users is 35 min before and 30 min after the pandemic. This average for members is 13 min before and 14.5 after the pandemic. It is also important to note that tourists have made many trips, which have been drastically reduced due to COVID-19 restrictions.

Considering ridership, as shown in Fig. 4, the ridership fluctuated around 6300–11,900 before the COVID-19. After the COVID-19, it was followed by a quick decline from nearly 3700–8500. The potential daily average bike ridership of 2020 is 10560 trips [9] while 5834, meaning a 45% decrease in daily ridership.

Regression model results are shown in Table 2. Model (1) takes the natural logarithm of three days average ridership of Capital Bikeshare trips as the dependent variable and the average weekly number of new COVID-19 cases as the independent variable, Model (2) takes the ratio of average daily ridership of Capital Bikeshare stations trips in tracks before and after COVID-19 as the dependent variable and the census data of tracts as the independent variable.

In the estimated model, the coefficient is negative, which means a decrease in the bike ridership with increasing COVID-19 cases. These results seem to be in line with reality. In the fitted model, $\beta_0$ indicates the elasticity of the bike ridership relative to COVID-19 cases. As the COVID-19 cases increase, people reduce unnecessary trips, and society will feel more afraid of the pandemic and getting infected, which means that the bike-share ridership will decrease.

Figure 3 demonstrates that during the COVID-19, the ridership of most stations decreased while that of certain stations increased, with the ratio varying substantially. It demonstrates that before COVID-19, the stations with the lowest ridership ratio were focused around downtown D.C. The office employment density is a significant factor; it is usually negatively correlated with the ridership. It is most likely because the COVID-19 stay-at-home directive reduced the number of individuals working in offices, reducing the use of public bicycles in locations with a large concentration of office workers. As a result, the detrimental impact is readily apparent in the city center. While it is reasonable to assume that the highest strata of society use personal vehicles during the pandemic and that bicycle riding declines in these areas while

**Table 2** Regression results

| Model 1 | Coefficient | Std. err | P-value | 95% CI |
|---|---|---|---|---|
| Constant | 9.090033 | 0.030272 | 0 | 9.030494, 9.149573 |
| COVID-19 cases | −0.00534 | 0.00025 | 3.92E-65 | −0.00583, −0.00485 |
| Adj. $R2$ | **0.567325** | | | |
| N | 347 | | | |
| Model 2 | | | | |
| Constant | 1.281053985 | 0.19402709 | 1.1339E-09 | 0.89692618, 1.66518179 |
| Density | 2.82337E-06 | 1.9077E-06 | 0.014147 | −9.535E-07, 6.6002E-06 |
| Income | −6.76883E-06 | 9.1009E-06 | 0.045846 | −2.479E-05, 1.12489E-05 |
| Unemployment rate | −0.008492973 | 0.00933344 | 0.036465 | −0.026971, 0.009985039 |
| Adj. $R2$ | 0.050141912 | | | |
| N | 125 | | | |

the opposite is true in low-income communities, regression analysis shows that there is no significant relationship between wealth, population density, unemployment rate, and bicycle ridership before and after the pandemic. However, Fig. 3 shows bike-share reduced more significantly in commercial and office areas which are in downtown of D.C.

## 4.2 Impact of the Bike-Share Services in COVID-19 Transmission

Table 3 shows the average, 75 percentile, and maximum number of users during the peak hours at 8, 10, and 12-min intervals, which indicates that human–human transmission would be extremely unlikely. Two strangers at a station simultaneously are extremely unlikely to come into close proximity. And only 19% of time intervals contain two or more that people in a station. However, we consider the actual average, 50% capacity, and 100% capacity to investigate the different scenarios.

In Table 4, the number of infected persons using the contagion model is shown in the case of 1, 2, or 3 infected persons using a single bike-share station during a day while assuming that the aerosols stay in the air for a duration ranging between 8 and 12 min.

**Table 3** Average, 75 percentile, and maximum number of users at stations

|        | No. of users per 8-min interval | No. of users per 10-min interval | No. of users per 12-min interval |
|--------|--------|--------|--------|
| Mean   | 0.14   | 0.18   | 0.21   |
| 75%    | 4      | 5      | 6      |
| Max.   | 14     | 16     | 17     |

**Table 4** Infection from human-to-human transmission

|        | One infected people | | | Two infected people | | | Three infected people | | |
|--------|--------|--------|--------|--------|--------|--------|--------|--------|--------|
|        | 8 min  | 10 min | 12 min | 8 min  | 10 min | 12 min | 8 min  | 10 min | 12 min |
| Mean   | –      | –      | –      | –      | –      | –      | –      | –      | –      |
| 75%    | 1      | 1      | 1      | 2      | 2      | 3      | 2      | 3      | 3      |
| Max.   | 3      | 3      | 4      | 5      | 7      | 8      | 8      | 10     | 13     |

**Table 5** Infection from surface to human transmission

|        | 1 day | 2 days | 3 days |
|--------|-------|--------|--------|
| Mean   | 1     | 2      | 3      |
| 75%    | 2     | 4      | 5      |
| Max.   | 5     | 9      | 15     |

On the other hand, human–surface–human may be possible. The numbers of trips per bike per 1, 2, and 3 days are calculated from the data for the human-to-surface-to-human transmission. The number of persons infected via surface to human transmission is shown in Table 5.

In [23], the authors used a similar contagion model to study the transmission in D.C. Metro. The authors found that three infected persons can infect 20,000 people during a 3-day period. According to our study, during a 3-day period, three infected persons can infect 27 people while using the bike-share stations. In other words, comparing the D.C. Metro service to the bike-share service, biking remains a healthier transportation alternative in terms of infection risk.

Despite this finding, the use of bike-sharing systems may need to be regulated as the full capacity operation may still lead to a significant rate of infection and transmission. To see the impact of bike-share on virus transmission, we assume that the network of bike-share is connected, and the infected people are coming back to use the service every day and contribute to the transmission of the virus. We can make such an assumption because the users with membership are more likely to be using the services for their daily commute. According to [10, 24], the average incubation period seems to be around 5 days and 95% of the infected people recover after ten days. So, we will assume a 5-day incubation period and ten days' recovery period for the modeling. In other words, each person will transmit the virus between days 5 and
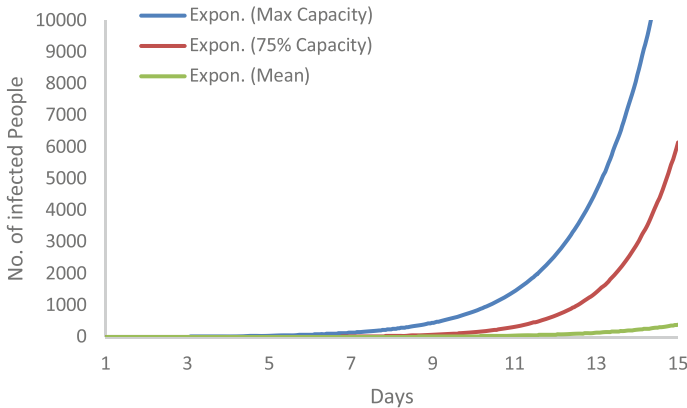
**Fig. 5** Predicted number of infected people from bike-share service

10 after getting infected. With such assumptions, Fig. 5 shows the impact of the bike-share services on the transmission of the virus with a different operating capacity of the bike stations when one infected person uses the service on day one. It takes 12 days to reach exponential contagion at full station operating capacity, 15 days for 75% station operating capacity. However, with a 50% operating capacity, the contagion does not reach exponential contagion within 27 days.

## 5    Conclusion

In this paper, the impact of COVID-19 on the D.C. bike-share system as well as the bike-share usage impact on disease transmission is explored D.C.'s Capital Bikeshare program lost around 10,000 daily users at the beginning of the pandemic in March of 2020. Later on, the ridership numbers increased, but the Capital Bikeshare services are still below their daily averages from earlier years by an estimated 9000 trips per day. The data reveal continued growth in the average trip duration from 13 to 19 min. This could mean that people prefer short trips on foot instead of cycling as before the pandemic. Moreover, the stations with the lowest ratio of ridership after to before the pandemic were focused around downtown D.C. The office employment density is a significant factor in bike ridership. While it is reasonable to assume that the upper class of the society uses personal vehicles during the COVID-19 and that bicycle riding declines in these areas, while the opposite is true in low-income communities, regression analysis shows that there is no significant relationship between wealth, population density, and bicycle ridership before and after the pandemic. However, it has been shown that land use plays an essential role in bike-sharing ridership, which it reduced more significantly in commercial and office areas in downtown D.C.

   With such usage, to analyze the impact of bike-sharing on the dynamics of the COVID-19 reported case, the transmission process is classified into two types: (i)

human-to-human transmission and (ii) human-to-surface-to-human transmission. A probabilistic contagion model is used to represent the first form of transmission. Transmission from one person to another would be infrequent. It is exceedingly improbable that two strangers at a station will come into close proximity at the same time. On the other hand, the second type is more likely to happen, and it will be anticipated using the average number of trips per bike throughout the study interval and the corresponding duration during which the virus remains stable on a given surface.

The numerical analysis indicated that one infected person could infect a maximum of five persons, and three infected persons can infect a maximum of 28 persons during a 3-day interval (ignoring the possible infections beyond the bikers' community). The peak value of the 7-day moving average of infected persons is 194.

The findings show that bike-sharing has a minor impact on the COVID-19 infection rate and that the government and decision-makers should consider it as a safe mode of transportation that should be maintained because it can encourage people to use it instead of the subway or bus. In comparison to other modes of public transit, bike-share remains a relatively healthier option.

The limitation is that there does not appear to be any real-world assessment of how bike-share users interact at stations. Also, for future studies, given the more specific datasets (i.e., the trip history dataset with a user identification number, socio-economic characteristics in a given location, datasets provided at this stage with routing information), the interaction of users at a station can be modeled much more realistic. Moreover, with the travel paths' data complemented by pedestrian density information along some routes, we can predict the total impact of bike-share services at the origins, destinations, and in between the origin-destination (O.D.) pairs.

# References

1. Ahangari S, Chavis C, Jeihani M (2020) Public transit ridership analysis during the COVID-19 pandemic. Medrxiv
2. Aloi A, Alonso B, Benavente J, Cordera R, Echániz E, González F, Ladisa C, Lezama-Romanelli R, López-Parra Á, Mazzei V (2020) Effects of the COVID-19 lockdown on urban mobility: Empirical evidence from the city of Santander (Spain). Sustainability 12
3. Anzai A, Kobayashi T, Linton NM, Kinoshita R, Hayashi K, Suzuki A, Yang Y, Jung S-M, Miyama T, Akhmetzhanov AR (2020) Assessing the impact of reduced travel on exportation dynamics of novel coronavirus infection (COVID-19). J Clin Med 9:601
4. Batty M (2020) The coronavirus crisis: what will the post-pandemic city look like? Environ Plan B: Urban Anal City Sci 47:547–552
5. Beigi P, Khoueiry M, Rajabi MS, Hamdar S (2022) Station reallocation and rebalancing strategy for bike-sharing systems: a case study of Washington DC. arXiv.2204.07875
6. Bucsky P (2020) Modal share changes due to COVID-19: the case of Budapest. Transp Res Interdiscip Perspect 8
7. Budd L, Ison S (2020) Responsible transport: A post-COVID agenda for transport policy and practice. Transp Res Interdiscip Perspect 6
8. Campisi T, Acampa G, Marino G, Tesoriere G (2020) Cycling master plans in Italy: the I-BIM feasibility tool for cost and safety assessments. Sustainability 12

9. CapitalBikeshare (2022) Capital bikeshare system data. https://capitalbikeshare.com/
10. CDC (n.d.) Ending isolation and precautions for people with COVID-19: interim guidance. https://www.cdc.gov/coronavirus/2019-ncov/hcp/duration-isolation.html. Accessed 2022
11. Chai X, Guo X, Xiao J, Jiang J (2020) Analysis of spatial-temporal behavior pattern of the share bike usage during COVID-19 pandemic in Beijing. arXiv preprint arXiv:2004.12340
12. Chartier Y, Pessoa-Silva CL (2009) Natural ventilation for infection control in health-care settings. World Health Organization
13. Chinazzi M, Davis JT, Ajelli M, Gioannini C, Litvinova M, Merler S, Piontti APV, Mu K, Rossi L, Sun K (2020) The effect of travel restrictions on the spread of the 2019 novel coronavirus (COVID-19) outbreak. Science 368:395–400
14. de Haas M, Faber R, Hamersma M (2020) How COVID-19 and the Dutch 'intelligent lockdown'change activities, work and travel behaviour: Evidence from longitudinal data in the Netherlands. Transp Res Interdiscip Perspect 6
15. De Vos J (2020) The effect of COVID-19 and subsequent social distancing on travel behavior. Transp Res Interdiscip Perspect 5
16. Dindar A, Ourang S, Ghadikola EG (2022) Development of a communication-assisted adaptive overcurrent protection scheme in smart distribution networks in presence of wind and solar generation. SSRN
17. Doucette ML, Tucker A, Auguste ME, Watkins A, Green C, Pereira FE, Borrup KT, Shapiro D, Lapidus G (2021) Initial impact of COVID-19's stay-at-home order on motor vehicle traffic and crash patterns in Connecticut: an interrupted time series analysis. In: Injury prevention, pp 3–9
18. Erfani A, Tavakolan M, Mashhadi AH, Mohammadi P (2021) Heterogeneous or homogeneous? A modified decision-making approach in renewable energy investment projects. AIMS Energy 9:558–580
19. Field A (2013) Discovering statistics using IBM SPSS statistics. Sage
20. Meena S (2020) Impact of novel coronavirus (COVID-19) pandemic on travel pattern: a case study of India. Indian Journal of Science and Technology 13(24): 2491–2501 https://doi.org/10.17485/IJST/v13i24.958
21. Huang J, Wang H, Fan M, Zhuo A, Sun Y, Li Y (2020) Understanding the impact of the COVID-19 pandemic on transportation-related behaviors with human mobility data. In: Proceedings of the 26th ACM SIGKDD international conference on knowledge discovery and data mining
22. Javadinasr M, Magassy TB, Rahimi E, Davatgari A, Salon D, Bhagat-Conway MW, Chauhan RS, Pendyala RM, Derrible S, Khoeini S (2021) The enduring effects of COVID-19 on travel behavior in the United States: a panel study on observed and expected changes in telecommuting, mode choice, online shopping and air travel. arXiv preprint arXiv:2109.07988
23. Krishnakumari P (2020) Virus spreading in public transport networks: the alarming consequences of the business as usual scenario
24. Lauer SA, Grantz KH, Bi Q, Jones FK, Zheng Q, Meredith HR, Azman AS, Reich NG, Lessler J (2020) The incubation period of coronavirus disease 2019 (COVID-19) from publicly reported confirmed cases: estimation and application. Ann Intern Med 172:577–582
25. Linka K, Peirlinck M, Costabal FS, Kuhl E (2020) Outbreak dynamics of COVID-19 in Europe and the effect of travel restrictions. Comput Meth Biomech Biomed Eng 23:710–717
26. Megahed NA, Ghoneim EM (2020) Antivirus-built environment: lessons learned from Covid-19 pandemic. Sustain Cities Soc 61
27. Mogaji E (2020) Impact of COVID-19 on transportation in Lagos, Nigeria. Transp Res Interdiscip Perspect 6
28. Musselwhite C, Avineri E, Susilo Y (2020) Editorial JTH 16—the coronavirus disease COVID-19 and implications for transport and health. J Transp Health 16
29. National Institutes of Health (2020) New coronavirus stable for hours on surfaces. URL: https://www.nih.gov/news-events/news-releases/new-coronavirus-stable-hours-surfaces. Access Date 23 Mar
30. Oztig LI, Askin OE (2020) Human mobility and coronavirus disease 2019 (COVID-19): a negative binomial regression analysis. Public Health 185:364–367

31. Razavi M, Alikhani H, Janfaza V, Sadeghi B, Alikhani E (2022) An automatic system to monitor the physical distance and face mask wearing of construction workers in covid-19 pandemic. SN Comput Sci 1:1–8
32. Saberi M, Ghamami M, Yi G, Shojaei MHS, Fishman E (2018) Understanding the impacts of a public transit disruption on bicycle sharing mobility patterns: a case of tube strike in London. J Transp Geogr 66:154–166
33. Shakerian M, Rajabi MS, Tajik M, Taghaddos H (2022) Hybrid simulation-based resource planning and constructability analysis of RCC pavement projects. arXiv preprint arXiv:2204.05659
34. Shang W-L, Chen J, Bi H, Sui Y, Chen Y, Yu H (2021) Impacts of COVID-19 pandemic on user behaviors and environmental benefits of bike sharing: a big-data analysis. Appl Energy 285
35. Stadnytskyi V, Bax CE, Bax A, Anfinrud P (2020) The airborne lifetime of small speech droplets and their potential importance in SARS-CoV-2 transmission. Proc Natl Acad Sci 117:11875–11877
36. Sun X, Wandelt S, Zhang A (2020) How did COVID-19 impact air transportation? a first peek through the lens of complex networks. J Air Transp Manag 89
37. Tian X, An C, Chen Z, Tian Z (2021) Assessing the impact of COVID-19 pandemic on urban transportation and air quality in Canada. Sci Total Environ 765
38. Doremalen V, Neeltje TB, Morris DH, Holbrook MG, Gamble A, Williamson BN, Tamin A, Harcourt JL, Thornburg NJ, Gerber SI (2020) Aerosol and surface stability of SARS-CoV-2 as compared with SARS-CoV-1. N Engl J Med 382:1564–1567
39. WHO, World Health Organization (2022) WHO coronavirus (COVID-19) dashboard. https://covid19.who.int/ Accessed 2022.
40. Zargari F, Aminpour N, Ahmadian MA, Samimi A, Saidi S (2022) Impact of mobility on COVID-19 spread—A time series analysis. Transp Res Interdiscip Perspect 13

# What Can We Learn from On-Demand Transit Services for Ridership? A Case Study at the City of Regina, Canada

Yili Tang, Duha Abdullah, Adesola Adewuyi, Nathan Luhning, and Satinder Bhalla

**Abstract** The urgent need to optimize operational efficiency, boost ridership, enlarge effective communication technologies, and improve customer convenience has led to the emergence of on-demand transit (ODT) services. ODT can be advantageous in several ways, including reliability, improving mobility, cost-effectiveness, and reducing the need for multi-transit services. This paper analyzed the trip patterns of on-demand services and the impacts on ridership by the difference-in-difference method. The pattern analyses showed that the origin–destination flow patterns are concentrated in large commercial and dense residential areas with significantly reduced travel times including the waiting times and in-vehicle times. Furthermore, the difference-in-difference model analyses yielded positive relations between the ridership and the on-demand transit services for the overall transit network while the effects vary with specific landuse zones. Results indicated the potential of on-demand transit services to benefit passengers and ridership recovery during the pandemic and post-pandemic.

**Keywords** On-demand transit · Ridership · Difference-in-difference model · Travel time · Passenger · Public transit

Y. Tang (✉) · D. Abdullah · A. Adewuyi
Faculty of Engineering and Applied Science, University of Regina, Regina, Canada
e-mail: ytang564@uwo.ca

Y. Tang
Department of Civil and Environmental Engineering, University of Western Ontario, London, Canada

Department of Electrical and Computer Engineering, University of Western Ontario, London, Canada

N. Luhning
Transit and Fleet Department, City of Regina, Regina, Canada

S. Bhalla
TransSIGHT LLC, California, USA

# 1 Introduction

Throughout the history of urban mobility, mass transit and private automobiles have served different purposes. While mass transit was conceived to provide a bulky, cut-price conveyance for passengers, cars existed for flexibility and independence. Yet neither is functioning productively in most cities as cities population is growing and the need for less pollution, congestion, and crowdedness have arisen [12, 14, 19, 23, 24]. Travel innovations, such as on-demand transit services, offer higher per-passenger benefits than those provided by comparable public services. In comparison with fixed-route mass transit, ODT offers greater flexibility and convenience. The service also renders less traffic and air pollution than solo travel modes. In addition, on-demand transits can serve as a practical, data-driven, and individual-centric solution for transportation issues.

Given the likelihood that the future presence of ODTs will convey critical transformations to the urban transportation system, exploring the implementation of this system has been the cornerstone of the transportation research community in recent years. Weinreich et al. [22] examined the fragmentation challenges and causes in app-based, on-demand services via surveying cities and transit agencies across Texas. A combination of archival research and interviews was employed as a basis for documenting the paper's findings: fixed-route services jurisdictional challenges. On the other hand, Hazan et al. [11] discussed the possibility of on-demand services to make significant changes to urban mobility. The study investigated the performance and quality, socioeconomic footprint, impact on congestion, and pollution of the on-demand transit experience. Furthermore, as part of the data analysis-based studies, two case studies were conducted concerning the ODT pilot project in Belleville, Canada, in Zhang et al. [25] and Sanaullah et al. [18]. Zhang et al. [25] present the promising benefits of ODT based on the results of user surveys and Sanaullah et al. [18] use the data gathered between September 2018 and May 2019 to profoundly analyze the level of service, spatiotemporal demand and supply, and origin and destination patterns of the users of Belleville ODT. Moreover, Bürstlein et al. [4] examine the first-mile commuting in Markham, a suburban community within the Greater Toronto Area, using a thorough different approach to data analysis. Analysis of operational systems is conducted using various on-demand solutions that can complement the current GO Transit commuter train system. Another study was conducted to understand passengers' preferences and willingness to pay for on-demand transportation, in which 3985 Australians were surveyed [20]. The study reflects promising results regarding expanding public transportation use and lowering solo automobility use. Furthermore, Haglund et al. [10] and Komanduri et al. [13] assess the degree to which on-demand services can boost ride-sharing platforms.

In terms of testing the efficiency of the ODT service, the MVMANT pilot project was launched in Dubai, UAE, Giuffrida et al. [9]. In order to determine a configuration that is most satisfactory to both community members and service operators, the program was tested in some low-demand areas using both a Geographic Information System (GIS) and an agent-based model. It has been observed that route choice

strategies can be crucial to locating a balance between users and operators in terms of costs.

Apart from empirical studies, a number of research developed various models to explore the performance of different on-demand services. For instance, in Wang et al. [21] an agent-based model was developed to assess the service performance for ODT operations delivered by a fleet of shared automated vehicles. Simulation of shared automated vehicles operating in parallel transit service and tailored time-varying transit service is performed using the model. Zhao et al. [26] present another example of ODT modeling, where machine learning is utilized to scrutinize travel behavior and, especially, modeling how individual travel pattern modifications are delivered with an on-demand mobility alternative. A simulation study was conducted by Archetti et al. [2] to assess the service's responsiveness, benefits, and scalability. The results indicate that a demand-driven system may be capable of accommodating a substantial share of user transportation demands and should therefore be implemented alongside conventional systems. Daoud et al. [5] develop analytical models to enhance the efficiency of the on-demand system, primarily taxi and carsharing. By optimizing fleet control and allocating resources through the models, profitability and a high level of service for the general public are assured. For the purpose of examining the relationship of the on-demand service with other smart transportation services, Daoud et al. [7] develop a generic and multi-agent model to explore the issues of having a joint system of ODT and autonomous vehicles and to assist scheduling and allocation in auto fleets, respectively. Likewise, Ronald et al. [16] explored the benefits of the engagement of ODT in transporting passengers and parcels, co-modality, where a simulation of shared ODT is developed and compared to the existing systems. It has been demonstrated that co-modality can enhance both the operator and the passenger experience, relying on the demand. Using Artificial Neural Networks, Deep Neural Networks, Bagging, and Random Forest methods, Alsaleh and Farooq [1] developed trip distribution and production models for on-demand transportation at dispersal areas. The analysis suggests that areas with industrial/commercial land use and residential land use experience higher trips distributions when compared with other dissemination areas.

Besides the analytical studies, a number of ODT studies have identified management, usefulness, regulations, and drawbacks of the services. Awareness, commuting considerations, and across-the-board frequency of usage of ODT were investigated via Devaraj et al. [8], where the three intention dimensions were correlated to work commute scatters and demographic characteristics. Results reveal that awareness does not directly correspond to usage frequency or considerations but that consideration and frequency of use are endogenous. On the other hand, Dablanc et al. [6] examine the effect of app-based transportation services, such as ODT, on business models, European public policies, freight trips and data, and labor legislation. Ruch et al. [17] modeled a framework for evaluating the advantages and disadvantages of ride-sharing on the transportation system. By integrating a dynamic-routing algorithm in an agent-based simulation of traffic, Navidi et al. [15] provide a comprehensive comparison between conventional public transportation and on-demand transit services. The study results indicate that replacing traditional public

transportation with on-demand ones will diminish travel time without any cost additions. Badia et al. [3] investigated the impact of developing a user-friendly bus network on ridership, using data from the first three phases of the Nova Xarxa, Barcelona, deployment program. It is found that the structure of bus networks influences demand significantly, and bus networks facilitated for enhancing transfers can promote demand.

While transit ridership has fallen during the COVID-19 pandemic, the on-demand transit services are growing rapidly worldwide for its merits in flexible options for travelers and predicable operations for transit agencies. However, existing studies cannot explain the demand responses of passengers, the effects on trip patterns, and the impacts on overall ridership in pandemic situations and for post-pandemic recovery. To this end, this paper examined the trip patterns of on-demand services and employs econometric methods to analyze the impacts of on-demand transit services on ridership by using the cases at the City of Regina.

The rest of the paper is organized as follows. Section 2 illustrated the on-demand transit services operations, areas, and collected datasets at the City of Regina. Section 3 analyzed the trip patterns with respect to origin–destination flow, in-vehicle and waiting times, and the demand variations. Section 4 introduced the difference-in-difference model to quantify the impacts on ridership in the overall transit network and for different landuse zones. Section 5 concludes the papers and discusses the limitations and future research of this study.

## 2   Study Area

The study is conducted on the on-demand transit pilot project executed in Regina, Saskatchewan province, in Canada. Regina transit initiated the on-demand transit service on August 31, 2020, where the service operates Monday through Saturday between 7 p.m. and 1 a.m. During the pilot period, bus route 10 served as a test run. That is, bus route 10 was switched to on-demand services in the evening. Customers may request a bus to pick them up and drop them off at the bus stop of their choice within the service area. The service areas include Normanview, Downtown, Warehouse, Cathedral Area, Northgate Mall, and Avonhurst Shopping Mall as shown in Fig. 1a covering all the transit stops within the area as shown in Fig. 1b. Bookings can be made through the on-demand transit app, website, or telephone.

### 2.1   Data Sources and Descriptions

The study included two data sources: the on-demand transit data (ODT data) and the transit stop-level ridership in the network (network data). The on-demand data have the following characteristics.

**Fig. 1** **a** Regina on-demand transit service area. **b** On-demand transit service stop locations

- *Order ID*: the unique identification for each trip requested for on-demand service.
- *Trip Service Date*: the date a trip request is sent.
- *Pickup Location*: the origin transit stop ID and name of a trip.
- *Pickup Location Geocode*: the latitude and longitude if the pickup transit stop.
- *Drop-off Location*: the destination transit stop ID and name of a trop.
- *Drop-off Location Geocode*: the latitude and longitude of the drop-off transit stop.
- *Requested Time*: the date and time a trip request is sent.
- *Passenger Count*: number of passengers for a trip.
- *Status*: the final status of the trip with values of "Cancelled", "Assigned", "In Active", "Not Assigned".
- *Arrival At Pickup Location*: the date and time of a transit vehicle arriving at the pickup location.
- *Arrival At Drop-off Location*: the date and time of a transit vehicle arriving at the drop-off location.

The network data are the aggregated ridership for each stop by hours which has the following characteristics.

- *Stop Description:* the stop ID and name.
- *Hour*: the hour of the day.
- *Month:* the month of the year.
- *Year:* calendar year.

Section 3 used the on-demand transit services data and Sect. 4 used both the on-demand transit service data and network data.

## 3 Trip Patterns Analysis for On-Demand Transit Service

To analyze trip patterns with on-demand transit services, we collected the data between September 2020 and September 2021.

### 3.1 The Origin and Destination Flow Patterns

The origin and destination flow patterns are concentrated in certain transit stops. Figure 2 shows the most frequently used transit stops considering both the pickups and drop-offs. The number in the bracket is the stop ID followed by the stop names. Among the most five frequently used transit tops, the stop [1545] and [110] are located in commercial areas with shopping centers and amenities, while the other three stops are located in residential areas. This indicates that the on-demand transit service has the potential to improve the convenience of travelers' daily routine.

Beside the aggregated frequency, Table 1 shows the top three frequencies of transit stops distinguished by the pickups, drop-offs, and the OD pairs. The first and third most frequently selected OD pairs are the routine operated by Bus Route #10 with fixed schedules. Travelers are continuing using the routine with on-demand transit service. The second most frequently selected OD pairs are the routine operated by other bus routes with fixed schedules and become available during the on-demand services' time. This indicates that the on-demand transit services have the potential to attract new ridership to the selected bus route while maintain the existing trip demand.

Furthermore, the waiting time ranges from 3 to 7 min which has greatly reduced given the 30-min headway of bus route #10 with fixed schedules. The in-vehicle times are similar to the fixed schedule services as the on-demand services did not change the vehicle route. Moreover, the on-demand services also tend to eliminate travelers' walking time by the door-to-door pickups and drop-offs. For instance, in the first OD pair, the stop "[875] 4TH AVE @ CAMPBELL ST (EB)" is not in the fixed schedules of bus route #10. Shifting to on-demand service saved 3–5 min of
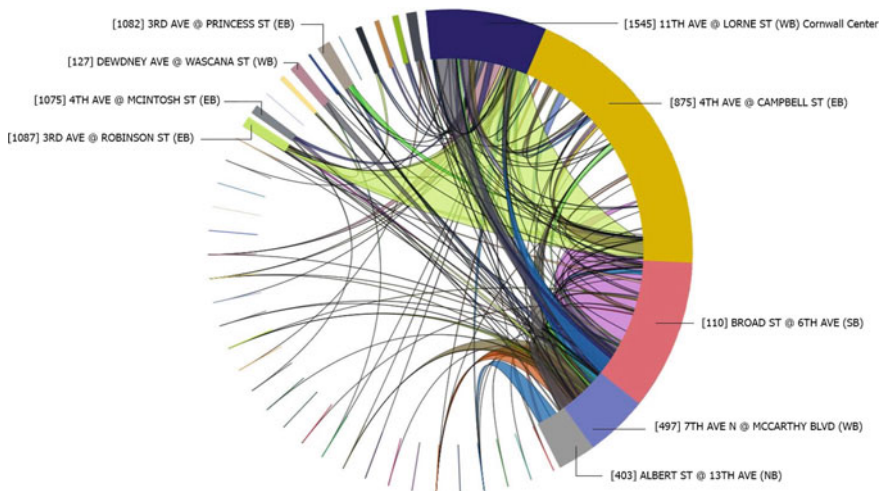


**Fig. 2** ODT origin–destination patterns (May 2021–August 2021)

**Table 1** Frequent origins, destinations, and OD pairs

| | Trip (%) | In-vehicle time (minutes) | Waiting time (minutes) | Walking time saving (minutes) |
|---|---|---|---|---|
| *Pickup locations* | | | | |
| [1545] 11TH AVE @ LORNE ST (WB) Cornwall Center | 16.31 | 9 | 3 | Na |
| [875] 4TH AVE @ CAMPBELL ST (EB) | 9.70 | 7 | 5 | 3–5 min |
| [110] BROAD ST @ 6TH AVE (SB) | 6.00 | 10 | 5 | Na |
| *Drop-off locations* | | | | |
| [1087] 3RD AVE @ ROBINSON ST (EB) | 9.94 | 7 | 5 | Na |
| [700] 13TH AVE @ PASQUA ST (WB) | 9.80 | 6 | 7 | Na |
| [978] 2ND AVE @ GREY ST (WB) | 8.78 | 11 | 4 | Na |
| *OD pairs* | | | | |
| Origin:[875] 4TH AVE @ CAMPBELL ST (EB) Destination: [1087] 3RD AVE @ ROBINSON ST (EB) | 9.61 | 7 | 5 | 3–5 min |
| Origin: [1545] 11TH AVE @ LORNE ST (WB) Cornwall Center Destination: [700] 13TH AVE @ PASQUA ST (WB) | 7.25 | 7 | 5 | Na |
| Origin: [110] BROAD ST @ 6TH AVE (SB) Destination: [136] DEWDNEY AVE @ GRACE ST (WB) | 4.62 | 15 | 5 | Na |

walking for travelers. The on-demand services have extend the bus stops from 11 to 164 stops which have greatly improved traveler's accessibility and reduced walking times.

## 3.2 In-Vehicle Time

Bus rides are known to be time-consuming because of the long headway and the stoppings along the trip. On-demand transit services allow passengers to bypass all of the stops made by public transportation, making it faster for them to reach the drop-off point.

From the perspective of in-vehicle time, most of the ridership in-vehicle time falls within 20 min (90.58% Fig. 3). The bypassing has reduced the in-vehicle travel times. For instance, the trip from "Broad St @ 6th Ave (SB)" to "13th Ave @ Albert
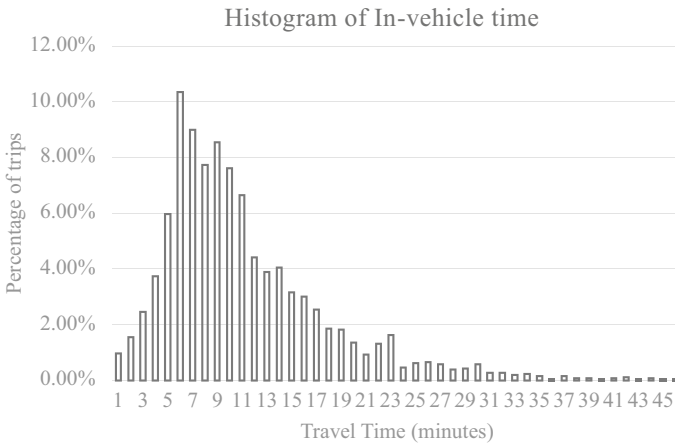
**Fig. 3** Regina on-demand transit service area

St (WB)" takes 6 min via on-demand transit services (Table 1) while 12 min using the fixed route #10 service during regular operating hours.

## 3.3 Waiting Time

On regular public buses, the arrival time at each stop within the city is predetermined, and passengers would have to adhere to the specified time frames. With the on-demand transit services, passengers can request buses according to their needs. The on-demand transit service is a convenient and time-saving option, provided that passengers do not have to wait for very long periods before their ride is available.

We further analyzed the waiting time as shown in Fig. 4. About 71% of trips experienced waiting times within 9 min, while 17% of the trips had the riders wait for 9–15 min as shown in Fig. 4a. This indicates the efficiency of on-demand transit service to reduce the waiting time given that the headway for fixed routes at the City of Regina is 15–40 min. Figure 4b depicts the relationship between the average waiting time and the monthly demand for trips. Approximately 60–70% of passengers have experienced a waiting time between 0 and 6 min in every month which indicates that the majority of the travelers are benefited from the reduced waiting times.

## 3.4 Demand over Service Hours and Months

The temporal trip distributions were also executed for on-demand transit services, which runs from 7:00 pm to 1:00 am, as shown in Fig. 5. Passengers tend to have
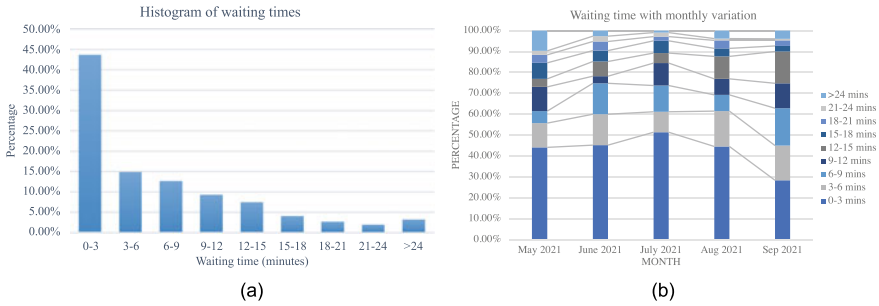
**Fig. 4** **a** Waiting time and trips percentages. **b** Waiting time with monthly variation
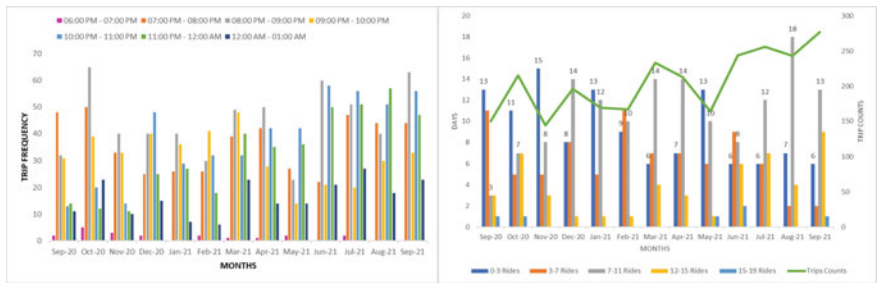


**Fig. 5** Variation of trips over service hours and months

higher demand during 8:00 PM–9:00 PM in cold months from September 2020 to March 2021. Most pickup locations are commercial in this timeframe, and their closing times coincide with the requested pickup time. Hence, these patterns may be attributed to work-to-home or shop-to-home trips. In warmer months from April to August in 2021, more trips are taken between 10 pm and 1 am. Figure 7 further presents the frequency of daily demand from September 2020 to September 2021. It is shown that the common frequency is 7–11 trips per day. The daily trips are increasing over the months indicating the trend of ridership increase for on-demand transit services.

## 3.5 Times versus Demand

In regular on-demand services, such as ride-sourcing or food delivery services, the times for users to get served are affected by the demand that requested the services. The demand is even more critical in on-demand transit services given that transit systems usually have fixed fleet size with capacity constraints. Figure 6 is depicted the relations between in-vehicle times and hourly demand and between average
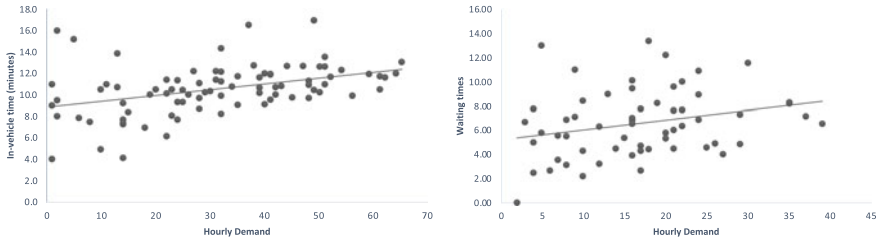
**Fig. 6** In-vehicle times and average waiting times with respect to hourly demand
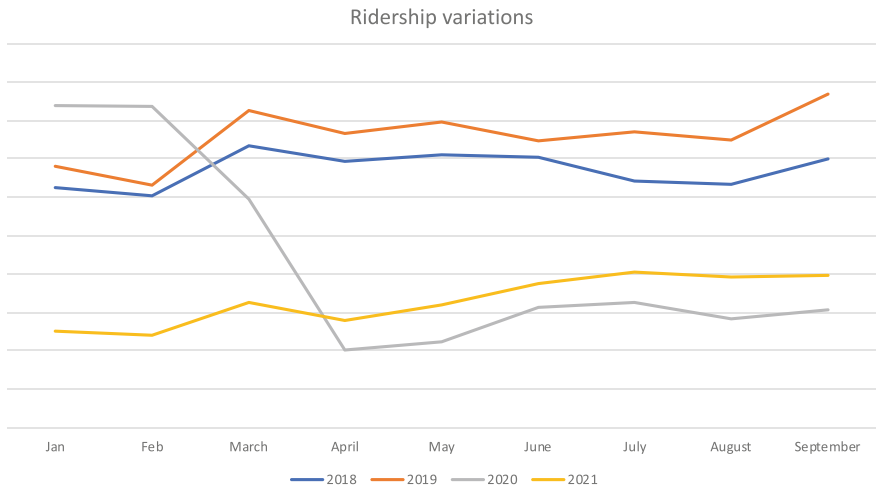


**Fig. 7** Monthly ridership from 2018 to 2021

waiting time and hourly demand during the service hours. It is shown that both in-vehicle times and waiting times have the trend to increase with the demand. This is because when they are multiple requests during a time period, the bus will need to pick up each individual travelers and also drop off them at designated locations. Therefore, the more requests for services, the longer in-vehicle and waiting times a traveler will experience for the bus vehicle to pick up and drop off other passengers.

## 4    On-Demand Service Impacts on Ridership

As shown in the above analysis, on-demand transit services are able to reduce travel time, increase accessibility, and provide more flexible travel options, which indicates its potential to attract more ridership. While transit usage has fallen during the COVID-19 pandemic, on-demand transit service becomes an emerging strategy in urban and metropolitan areas given its convenience for travelers and predicable

operations for transit agencies. This section quantified the impacts of on-demand services on ridership during the COVID-19 pandemic by using the difference-in-difference method and interpreted how the transit agencies can be benefited from the on-demand services for pandemic recovery and future ridership growth.

## 4.1 Overview of the Transit Network Ridership

We collected the monthly ridership from year 2018 to 2021 at the City of Regina. The ridership was affected significantly since April 2020. This is because various restrictions have been taken corresponding to the COVID-19 pandemic since that time. To ensure the consistency and eliminate the pre-COVID effects, we select the samples from May to September in year 2020 and 2021, in total 10 months for analysis where all samples are within the pandemic period with similar scale of ridership (Fig. 7).

## 4.2 Difference-In-Difference (DID) Method

We use the difference-in-difference method to quantify the impact of on-demand transit services on ridership. The DID method compares the observations from treatment and control groups to estimate a causal effect of a specific intervention or treatment at two or more different time periods. DID estimates the treatment effects based on the data from pre- and post-intervention. Specifically, the DID model compares the outcomes $Y_{it}$ for unit $i = (1, 2, \ldots, N)$ during the time periods $t = (1, 2, \ldots, T)$, with binary effects $d_i = \{0, 1\}$. $d_i = 0$ represents the unit in control group and $d_i = 1$ represents the unit in treatment group. In this paper, we established the DID model as follows:

$$Y_{it} = \beta_0 + \beta_1 \text{time} + \beta_2 \text{treat} + \beta_3 (\text{treat} \times \text{time}) + \lambda X_i + \varepsilon_{it},$$

where $i$ represent each transit stop, $t$ represent the months of the year as indicated in Sect. 5.1, $Y_{it}$ represents the monthly ridership between 7:00 pm and 1:00am for transit stop $i$ at month $t$, time is the dummy variable representing time periods that is equal to 1 if the observation is during the time periods where the on-demand service is implemented, namely, between May and September, 2021, $treat$ is the dummy variable that is equal to one if the transit stop is used for on-demand transit service and 0 otherwise, $X_i$ is the covariates of the transit stops including the landuse types, the number of amenities nearby the transit stops and the average distance of the amenities to the transit stop, and $\varepsilon_{it}$ is the residual term.

The average effects of the on-demand transit service on the ridership are represented by the coefficient value $\beta_3$. This can be explained by considering a simple case where $i = \{1(\text{treat}), 2(\text{control})\}$ and $t = \{1, 2\}$, $t = 1$ represent the pre-intervention

period and $t = 2$ represents the post-intervention period. Then, we have

$$\mathbb{E}[(y_{11} - y_{12}) - (y_{21} - y_{22})]$$
$$= [(\beta_0 + \beta_1(\text{time} = 0) + \beta_2(\text{treat} = 1) + \beta_3(\text{treat} \times \text{time} = 0) + \lambda X_i + \varepsilon_{11})$$
$$-(\beta_0 + \beta_1(\text{time} = 1) + \beta_2(\text{treat} = 1) + \beta_3(\text{treat} \times \text{time} = 1) + \lambda X_i + \varepsilon_{12})]$$
$$- [(\beta_0 + \beta_1(\text{time} = 0) + \beta_2(\text{treat} = 0) + \beta_3(\text{treat} \times \text{time} = 0) + \lambda X_i + \varepsilon_{11})$$
$$-(\beta_0 + \beta_1(\text{time} = 1) + \beta_2(\text{treat} = 0) + \beta_3(\text{treat} \times \text{time} = 0) + \lambda X_i + \varepsilon_{12})] = \beta_3$$

which can be interpreted that the treatment effect is indicated by $\beta_3$

### 4.3   Data and Statistics

To measure the effects of the on-demand transit services, we constructed the datasets comprising the stop-level ridership, the landuse characteristics, and the amenities characteristics for the transit stops. The stop-level ridership was collected from the City of Regina covering all the transit stops in the network on hourly bases from May to August in year 2020 and year 2021. The amenities' characteristics are numerical variables constructed with the number of buildings and distance for all commercial services, restaurant, stores, health services, school, transit stops, lodging services, and tourism places. The amenities data were collected through Google Map API. Table 2 is summarized the mean and standard deviation of the numerical variables.

The landuse characteristics are categorical variables including two levels. The first level captures the exact landuse type where the transit stop is located. Table 3 presents the sample size in different landuse zones. The second level of landuse characteristics captures the number of landuse types near the transit stop as shown in Table 2.

### 4.4   Effects of On-Demand Transit Service on Ridership

Table 4 presents the regression results of the DID models using ordinary least square method. It includes five sets of results. The first one estimated the on-demand service effects in the overall transit network, the rest of the four model estimated the effects in specific landuse zones.

The estimation of the Network model yields a positive coefficient for the transit stop ridership which indicates that the on-demand transit services have the positive impacts on ridership increases. The effects of the on-demand services vary with the different types of zones. The on-demand transit service in commercial zones and special zones has the positive impacts for ridership increase. This could be the reason that on-demand services provided more accessible transit stops, flexible travel options as well as short waiting times which encouraged travels in commercial

**Table 2** Descriptive statistics for explanatory variables

| Explanatory variables | Full sample | | Treatment group | | Control group | |
|---|---|---|---|---|---|---|
| | Mean | Standard deviation | Mean | Standard deviation | Mean | Standard deviation |
| nearby_residential_ zones | 1.35 | 0.97 | 1.28 | 0.99 | 1.36 | 0.96 |
| nearby_commercial_ zones | 0.48 | 0.75 | 0.77 | 0.81 | 0.41 | 0.72 |
| nearby_industrial_ zones | 0.10 | 0.35 | 0.10 | 0.33 | 0.10 | 0.36 |
| nearby_special_ Zones | 0.63 | 0.72 | 0.67 | 0.71 | 0.62 | 0.72 |
| all_number | 57.32 | 2.30 | 57.67 | 0.70 | 57.23 | 2.53 |
| all_distance | 537.56 | 105.07 | 524.40 | 85.93 | 540.66 | 108.89 |
| food_number | 15.04 | 13.60 | 15.13 | 15.54 | 15.02 | 13.10 |
| food_distance | 674.69 | 172.57 | 646.65 | 159.03 | 681.80 | 175.21 |
| school_number | 6.05 | 3.13 | 6.93 | 2.76 | 5.84 | 3.18 |
| school_distance | 642.64 | 132.37 | 654.87 | 114.48 | 639.73 | 136.18 |
| transit_number | 37.98 | 10.65 | 41.85 | 6.67 | 37.07 | 11.19 |
| transit_distance | 641.18 | 58.83 | 646.08 | 53.66 | 640.02 | 59.95 |
| health_number | 16.78 | 15.74 | 18.97 | 16.80 | 16.27 | 15.45 |
| health_distance | 660.45 | 169.46 | 625.68 | 139.68 | 668.84 | 174.93 |
| store_number | 4.64 | 6.03 | 5.90 | 8.08 | 4.32 | 5.36 |
| store_distance | 654.08 | 203.65 | 626.50 | 206.42 | 660.72 | 202.54 |
| tourism_number | 2.38 | 2.69 | 2.78 | 3.05 | 2.18 | 2.46 |
| tourism_distance | 690.04 | 193.99 | 649.99 | 199.27 | 714.27 | 187.01 |
| lodging_number | 2.11 | 2.35 | 2.13 | 2.63 | 2.11 | 2.27 |
| lodging_distance | 680.61 | 193.30 | 639.98 | 210.53 | 693.13 | 186.17 |

**Table 3** Sample size

| Sample group | Full sample (numbers) | Control Group | Treatment Group |
|---|---|---|---|
| Network | 10,040 | 8128 | 1912 |
| Residential zones | 5480 | 4664 | 816 |
| Commercial zones | 2112 | 1416 | 696 |
| Industrial zones | 560 | 480 | 80 |
| Special zones | 1648 | 1336 | 312 |

**Table 4** Estimation of difference-in-difference model

| | Network | Residential zones | Commercial zones | Industrial zones | Special zones |
|---|---|---|---|---|---|
| *Predictors* | *Estimates* | *Estimates* | *Estimates* | *Estimates* | *Estimates* |
| (intercept) | 13.57 | −232.67 | 453.12 | −608.48 | −88.32 |
| Treat time | 15.20 | −5.89 | 13.82 | −10.26 | 2.08 |
| Treat | 57.20 *** | −3.11 | 27.37 | 51.53 *** | 20.27 |
| Nearby Residential zones | −25.56 *** | 9.70 *** | −23.63 | 10.40 | 1.88 |
| Nearby commercial zones | 6.65 | 28.29 *** | −29.62 | 24.40 *** | 40.98 *** |
| Nearby industrial zones | −97.28 *** | 5.48 | −127.19 * | −18.88 *** | −35.10 |
| Nearby special Zones | −54.18 *** | −5.44 | −90.29 ** | −6.44 | 7.75 |
| All numbers | 8.65 *** | 7.32 ** | 24.27 *** | 13.06 * | 1.01 |
| All distances | −0.48 *** | −0.12 *** | −1.28 *** | −0.25 *** | −0.11 ** |
| Food numbers | 3.21 ** | 3.44 *** | −13.67 *** | −3.49 *** | 0.20 |
| Food distance | 0.01 | −0.00 | 0.89 *** | −0.01 | −0.02 |
| School numbers | −15.44 *** | 3.91 *** | −73.22 *** | 7.99 *** | 14.44 *** |
| School distance | −0.06 * | 0.01 | −0.87 *** | −0.00 | −0.01 |
| Transit numbers | 2.03 *** | 0.65 * | 12.73 *** | 1.63 * | 0.16 |
| Transit distance | 0.05 | −0.20 *** | 0.21 | −0.01 | 0.09 |
| Stores numbers | −2.09 ** | −2.07 *** | −0.48 | 2.37 *** | −0.11 |
| Stores distance | −0.18 *** | −0.03 * | −1.78 *** | −0.01 | 0.05 ** |
| Health numbers | 18.76 *** | 4.48 *** | 78.69 *** | 0.13 | −5.75 *** |
| Health distance | −0.04 * | −0.02 ** | −0.01 | −0.04 *** | −0.01 |
| Tourism numbers | 8.09 | −23.08 *** | −48.65 ** | −7.29 | 6.02 |
| Tourism distance | −0.09 *** | 0.03 ** | −0.08 | −0.01 | −0.01 |
| Lodging numbers | 23.05 *** | 5.06 * | 21.47 | 12.01 | −1.71 |
| Lodging distance | −0.08 *** | 0.01 | −0.12 | −0.05 ** | −0.01 |

(continued)

**Table 4** (continued)

|  | Network | Residential zones | Commercial zones | Industrial zones | Special zones |
|---|---|---|---|---|---|
| Observations | 10,040 | 5480 | 2112 | 560 | 1648 |
| $R^2/R^2$ adjusted | 0.165/0.163 | 0.102/0.098 | 0.257/0.248 | 0.295/0.260 | 0.160/0.146 |

*$p < 0.05$, **$p < 0.01$, ***$p < 0.001$

areas that are generally dispersed. Yet the coefficients do not yield strong statistical significance, which indicates that there exists weak significant linear relation between the on-demand service and the ridership. The weak significance may also come from unobserved factors. One possible reason could be passengers get used to the pandemic situations or the vaccination coverage which directly or indirectly encouraged more ridership.

On the contrary, the ridership decreases in residential zones and industrial zones with on-demand services. This could be the reason that the on-demand service is operated between 7 pm and 1 am in the case study which is mainly for back-home trips that generated from other areas such as commercial zones. Another reason could be that travelers have the on-demand services to go to more desirable places such as downtown shopping centers rather than the nearby services or amenities in home or workplaces as in residential and industrial zones. As a result, the ridership during the service hours was shifted from home and workplaces to commercial and downtown areas.

It is also noted that the ridership in special zones increases. The special zones in urban areas at the City of Regina are mainly for public services which includes the active and passive recreational places such as parks and community gardens. The positive coefficient indicates that the on-demand transit services also increased travelers' accessibility to essential services as well as their social activities.

## 5 Conclusion and Future Research

This paper analyzed the travel patterns and quantified the impacts of on-demand transit services on ridership during the COVID-19 pandemic. Results indicate that the origins and destinations are concentratedly selected, that are mainly located in large commercial areas and dense residential areas. The on-demand services are able to reduce significantly the waiting time with the majority trips waited less than 6 min. It also reduced the overall travel time by eliminating the walking distance and stopping during the fixed routes. However, the travel times tend to increase with the demand given the fixed fleet size of the transit systems. This indicates the necessity to optimize the bus fleet size and routine with large-scale on-demand transit service implementations.

Furthermore, the quantitative analyses have shown the positive impacts of on-demand transit services to increase the ridership, which indicate its capability to improve passengers' satisfaction and generating mobilities as a recovery strategy during the COVID-19 pandemic as well as post-pandemic.

The study limited the analyses in short-term periods and with static characteristics which can be improved for future research to analyze the temporal–spatial impacts. This paper also opens new avenues in on-demand transit services such as the optimization of operations and demand response modeling.

# References

1. Alsaleh N, Farooq B (2021) Interpretable data-driven demand modelling for on-demand transit services. Transp Res Part A: Policy Pract 154:1–22
2. Archetti C, Speranza MG, Weyland D (2018) A simulation study of an on-demand transportation system. Int Trans Oper Res 25(4):1137–1161
3. Badia H, Argote-Cabanero J, Daganzo CF (2017) How network structure can boost and shape the demand for bus transit. Transp Res Part A: Policy Pract 103:83–94
4. Bürstlein J, López D, Farooq B (2021) Exploring first-mile on-demand transit solutions for North American suburbia: A case study of Markham, Canada. Transp Res Part A: Policy and Pract 153:261–283
5. Cuevas V, Estrada M, Salanova JM (2016) Management of on-demand transport services in urban contexts. Barcelona case study. Transp Res Procedia 13:155–165
6. Dablanc L, Morganti E, Arvidsson N, Woxenius J, Browne M, Saidi N (2017) The rise of on-demand 'Instant deliveries' in European cities. Paper Presented Supply Chain Forum: Int J 18(4):203–217
7. Daoud A, Balbo F, Gianessi P, Picard G (2021) A generic multi-agent model for resource allocation strategies in online on-demand transport with autonomous vehicles. In: Paper presented at the proceedings of the 20th international conference on autonomous agents and multiagent systems (AAMAS 2021), vol 3
8. Devaraj A, Srinivasan KK, Basheer S (2020) Awareness, consideration and usage frequency of on-demand transport services in the Indian context. Transp Dev Econ 6(2):1–19
9. Giuffrida N, Le Pira M, Inturri G, Ignaccolo M, Calabrò G, Cuius B, Pluchino A (2020) On-demand flexible transit in fast-growing cities: the case of Dubai. Sustainability 12(11):4455
10. Haglund N, Mladenović MN, Kujala R, Weckström C, Saramäki J (2019) Where did kutsuplus drive us? ex post evaluation of on-demand micro-transit pilot in the helsinki capital region. Res Transp Bus Manag 32:100390
11. Hazan J, Lang N, Wegscheider AK, Fassenot B (2019) On-demand transit can unlock urban mobility. Boston Consulting Group
12. Javanmard ME, Tang Y, Wang Z, Tontiwachwuthikul P (2023) Forecast energy demand, CO2 emissions and energy resource impacts for the transportation sector. Appl Energy 338:120830
13. Komanduri A, Wafa Z, Proussaloglou K, Jacobs S (2018) Assessing the impact of app-based ride share systems in an urban context: findings from Austin. Transp Res Rec 2672(7):34–46

14. Liu Y, QI J, Yang H, Tang Y (2022) The passenger's willingness to wait with sunk waiting time: an empirical study in ride-sourcing market. Available at SSRN 4285203
15. Navidi Z, Ronald N, Winter S (2018) Comparison between ad-hoc demand responsive and conventional transit: a simulation study. Public Transp 10(1):147–167
16. Ronald N, Yang J, Thompson RG (2016) Exploring co-modality using on-demand transport systems. Transp Res Procedia 12:203–212
17. Ruch C, Lu C, Sieber L, Frazzoli E (2019) Quantifying the benefits of ride sharing
18. Sanaullah I, Alsaleh N, Djavadian S, Farooq B (2021) Spatio-temporal analysis of on-demand transit: a case study of Belleville, Canada. Transp Res Part A: Policy Pract 145:284–301
19. Tang Y, Jiang Y, Yang H, Nielsen OA (2020) Modeling and optimizing a fare incentive strategy to manage queuing and crowding in mass transit systems. Transp Res Part B: Methodological 138:247–267
20. Vij A, Ryan S, Sampson S, Harris S (2020) Consumer preferences for on-demand transport in australia. Transp Res Part A: Policy Pract 132:823–839
21. Wang S, Correia GHA, Lin HX (2019) Exploring the performance of different on-demand transit services provided by a fleet of shared automated vehicles: an agent-based model. J Adv Transp
22. Weinreich DP, Reeves SM, Sakalker A, Hamidi S (2020) Transit in flex: examining service fragmentation of app-based, on-demand transit services in Texas. Transp Res Interdiscip Perspect 5:100060
23. Xi H, Tang Y, Waller ST, Shalaby A (2023) Modeling, equilibrium, and demand management for mobility and delivery services in Mobility-as-a-Service ecosystems. Comput Aided Civ Infrastruct Eng 38(11):1403–1423
24. Yang H, Tang Y (2018) Managing rail transit peak-hour congestion with a fare-reward scheme. Transp Res Part B: Methodological 110:122–136
25. Zhang Y, Farber S, Young M (2020) The benefits of on-demand transit in Belleville: findings from A user survey. Retrieved from https://tspace.library.utoronto.ca/handle/1807/100570
26. Zhao X, Yan X, Van Hentenryck P (2019) Modeling heterogeneity in mode-switching behavior under a mobility-on-demand transit system: an interpretable machine learning approach. arXiv Preprint arXiv:1902.02904

# The Impact of Curfew on Transit Demand and In-Vehicle Density

**Haesung Ahn, Sungho Lim, and Yong Hoon Kim**

**Abstract**  Many countries have implemented a restriction on the operation hours of restaurants and bars at night during COVID-19 to curb the spread of the virus. In Canada, transit demand has plunged significantly during curfew hours. Seoul also implemented a similar type of restriction and cut the number of operating buses by 20% after 9 p.m. The impacts of the restrictions on transit demand and in-vehicle density varied according to transit mode, time, and location. This study aims to analyze the impacts of the restrictions using Seoul smart card data from August 24 to September 11, 2020. We observed several significant findings regarding changes in transit demand patterns. First, the demand from 9 p.m. to midnight shifted to alternative departure times. Second, there was a curfew rush hour at approximately 9 p.m., when many people rushed home simultaneously, increasing volumes by 34%, while transit demand after 9 p.m. plunged by 30% compared to before curfew periods. Third, passengers showed different sensitivity to their transit modes. This is because they understood the frequency of bus operations would be reduced as a part of the restriction. Fourth, the curfew rush hour demand emerged in high-density socializing establishments. Lastly, due to the curfew rush hour effect, in-vehicle density significantly increased on certain bus routes, potentially endangering passengers by spreading the virus. These findings provide insights for implementing restrictions on transit operation and pandemic preparedness planning.

**Keywords**  Curefew · Curfew rush hour · Smart cards · Passenger density in transit · COVID-19 · Transit user behaviour

H. Ahn · Y. H. Kim (✉)
Department of Civil and Environmental Engineering, University of Windsor, Windsor, Ontario N9B3P4, Canada
e-mail: kim523@uwindsor.ca

S. Lim
Department of Civil and Environmental Engineering, University of Michigan, Ann Arbor, Michigan 48109, United States

# 1  Introduction

COVID-19 outbreaks forced many countries to implement various restrictions to curb the spread of the virus. The limits have varied from scaling back hours of operation at social establishments to conducting area-wide curfews. Ontario and Quebec governments enforced robust restrictions: stay-at-home orders and curfews during the pandemic's peak. The Ontario government declared a state of emergency at the pandemic's beginning, but the situation was not alleviated quickly. The government issued a stay-at-home order in January 2021, enforcing that everyone must stay home except for the essential purposes of trips, such as picking up groceries or going to medical appointments [11]. The Quebec provincial government enforced curfews after 8 p.m. from January 6, 2021, to May 28, 2021 [8].

Noticeably, the fear of the virus and imposed restrictions affected transit demand. Figure 1 depicts the demand fluctuations over the restrictions [17]. In particular, the curfew affected transit demand during the restricted hours significantly. According to a real-time transit information provider's data, the transit demand in Montreal from 8 p.m. to 9 p.m. was reduced to half compared to before the curfew [20].

On the other side of the Pacific Ocean, South Korea also introduced similar restrictions that forced the owners of socializing establishments to close and banned in-person dining after 9 p.m. In addition, Seoul transit officials cut the frequency of bus services by 20% after 9 p.m. [2, 13]. The transit officials expected people to refrain from nightlife and return home early due to the restrictions. However, some people stayed at social establishments until around 9 p.m. and subsequently rushed home. Their responses could lead to an unexpected peak in transit. Further studies on how transit users responded to the restrictions are needed to understand their behavior and prepare for the next potential pandemic event.

This study aims to analyze transit users' behavior over time under COVID-19 restrictions. We estimated in-vehicle crowdedness by reconstructing in-vehicle passengers from Seoul transit smart card data. Many researchers have studied transit users' behavior based on smart cards, which are central to automated fare collection
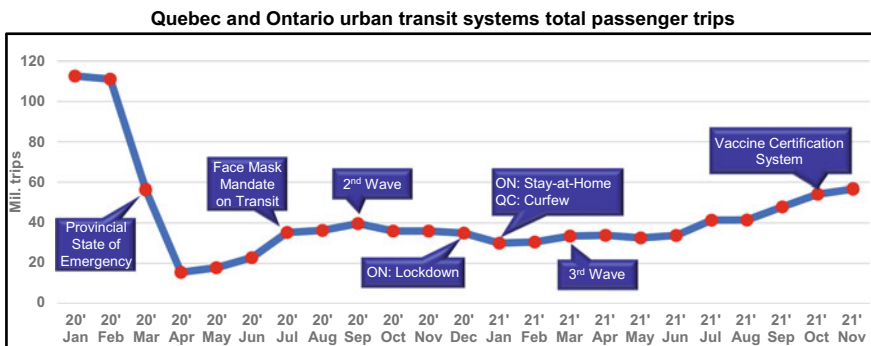


**Fig. 1** Total passenger trips both in Quebec and Ontario urban transit systems

(AFC) systems. This dataset contains information, such as card ID, trip data (trip mode, origin/destination, travel time, and fare), and personal identification data [5, 9, 21]. In particular, the Seoul smart card system collects almost all transit users' information: 100% of subway users and 99% of bus riders out of 13 million daily transit passengers [12]. It is also noted that the card data include multimodal transfers, so it allowed us to track a complete multimodal trip trajectory. Accordingly, this study can understand entire transit users' behaviors more comprehensively. This may overcome the issues of traditional travel surveys, census records or mobile app data. Thus, transit usage variability in response to external factors such as COVID-19 restrictions is examined using space and time data from individual trip information extracted from smart card data. The study team accessed these data sets from Seoul Big Data Campus [14]. We compare card data from before the restriction (August 24, 2020, Monday) to the end (Friday, September 11, 2020). Our study can provide insights to decision-makers in developing and determining the efficiency of pandemic-related transportation policies.

This paper is organized as follows. Section 2 introduces COVID-19 restrictions on operating social establishments and transit supply. Section 3 discusses transit users' demand changes in detail. Section 4 summarizes the main findings and future study directions.

## 2 COVID-19 Restrictions

### 2.1 Curfew Under COVID-19 Situation

Government officials have conducted various restrictions under the COVID-19 crisis: stay-at-home order, curfew, reduced hours of operation for social establishments such as restaurants and bars and reduced transit service frequency. This study focuses on the curfews imposed in Montreal and Seoul. Table 1 shows a summary of regulations in the two cities. Montreal conducted a curfew policy to curb the spread of the virus. The duration of the curfew was from January to May 2021, starting at 8 p.m. or 9:30 p.m. (red zones or orange zones) until 5 a.m. of the next day. All restaurants had to ban indoor dining, but delivery was available after 7:30 p.m. [16]. Seoul also restricted the hours of operation for in-person dining at restaurants and bars. Even though measures limiting the operational hours in Seoul were not identical to the curfews imposed in Montreal, both restrictions significantly led to travel demand declines. Hence, we regard the restrictions in Seoul as essentially a curfew. However, there is a difference between the two cities in the fines from the violation of the curfews. In Montreal, the curfew was fined, whereas citizens in Seoul were not the target by the fine, but the owners of the social establishments were imposed the legal duty.

**Table 1** Restrictions in Montreal and Seoul

| Restriction | Montreal | Seoul |
|---|---|---|
| Curfew | Red zones (from 8 p.m. to 5 a.m.) (January 6–March 16, April 11–May 2, 2021) | – |
| | Orange zones (from 9:30 p.m. to 5 a.m.) (March 17–April 10, May 3–May 28, 2021) | |
| Reduction of hours of operation | Restaurants can provide only a delivery service after 7:30 p.m. | Restaurants can only offer take-out and a delivery service after 9 p.m. (August 31–September 13, 2021) |
| Fine | To an individual who breaks the rule, in the range of $1000–$6000 | To restaurant owners, up to $3200 |

## 2.2 Reduction in Bus Supply

In Montreal, two transit providers, STM and Exo, maintained transit service without reducing supply during curfew [3, 18]. In contrast, transit officials in Seoul announced that they would reduce the frequency of bus service after 9 p.m. by 20% from August 31 to September 11, 2020. We analyzed all 325 bus routes from 9 p.m. to 1 a.m. from smart card data, and Fig. 2 shows the number of buses in operation during nighttime. The number of buses in service was reduced by 15%, from about 3,500 to 3,000, after the restriction. The reduced frequency of bus service could affect transit users' behavior. Whereas some users could avoid taking buses during restricted hours, the rest could maintain their usage. In the following section, we analyzed induced demand changed by the reduced frequency of bus service.

## 3 Analysis of Transit Demand Under Curfew

## 3.1 Trip Departure Time Change in Seoul

Table 2 shows the total number of transit passengers before curfew (August 28) and after curfew (September 11) from the card data. All-day demand showed a minor difference during the periods, increasing by 8 thousand trips out of 6 million with a 0% growth rate. In particular, the morning transit demand between 5 a.m. and 1 p.m. was reduced by a mere 2 hundred out of 2.5 million passengers. With the neglectable amount of increase, the curfew seemed not to affect all-day and morning demand. By contrast, the demand during curfew hours, from 9 p.m. to the end of the day, was
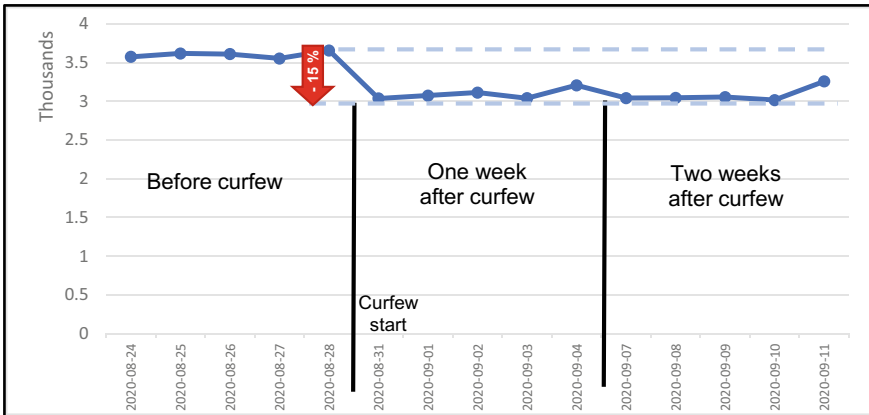
**Fig. 2** Decrease in bus supply under curfew for three weeks (9 p.m.–1 a.m.) in Seoul

**Table 2** Change of transit demand on Friday by different time slots in Seoul

| Time slots | | Total number of trips (bus + subway) | | | |
|---|---|---|---|---|---|
| | | Before curfew (August 28) | After curfew (September 11) | Difference | Growth rate (%) |
| All-day | | 6,012,670 | 6,020,707 | 8,037 | *0* |
| Before curfew hours | 5 a.m.–1 p.m. (morning) | 2,529,717 | 2,529,504 | *−213* | 0 |
| | 1 p.m.–9 p.m. (afternoon and evening) | 2,934,593 | 2,997,041 | *62,448* | 2 |
| During curfew hours (9 p.m.—end of the day) | | 548,360 | 494,162 | *−54,198* | −10 |

decreased significantly by 5.4 thousand passengers, or a drop of 10%. It seemed that people reduced nighttime demand due to curfew. We believe that the reduced demand during curfew hours shifted to other hours: afternoon and evening. This is because the demand for the hours, 1 p.m. to 9 p.m., was increased by 6.2 thousand, and this number is similar to the reduced demand during curfew hours. The data show that curfew affected late-night transit demand, and most of the demand shifted prior to the beginning of curfew.

## 3.2   Curfew Rush Hour in Seoul

We analyze smart card data to understand people's departure time changes in detail. Figure 3 presents transit users' departure time changes responding to curfew over

**Table 3** Proportion of app usage on Friday under different curfew levels in Montreal

| Time slots | | Proportion of app usage | | | |
|---|---|---|---|---|---|
| | | Before curfew (January 8) (%) | Red zone (January 15) (%) | Orange zone (March 19) (%) | Red zone (April 16) (%) |
| Before curfew hours | 5 a.m.–1 p.m. (morning) | 32.1 | 36.3 | 37.2 | 39.5 |
| | 1 p.m.–8 p.m. (afternoon and evening) | 49.1 | 53.4 | 50.1 | 51.4 |
| During **curfew hours** (8 p.m.—end of the day) | | *18.8* | *10.3* | *12.6* | 9.1 |

time. In general, trip demand reduces as time goes on at night, and there was a slight increase around 10 p.m. before COVID-19. This is because many social activities, such as nighttime work and studies at private academic institutes, finish around 10 p.m., so transit demand increases for a while. However, as shown in Fig. 3, people rushed to transit stations around 9 p.m. instead of 10 p.m. due to the curfew. We found an induced rush hour and an increased departure rate around the curfew hour.

Commuters who stayed in restaurants tried to maximize their time at these social establishments and headed home around the beginning of the restriction. In particular, from 9 p.m. to 9:20 p.m., the demand increased by 34%. We shall call the moment with sudden increased demand *Curfew rush hour* from 8:40 p.m. to 9:20 p.m. During the curfew rush hour, the demand surge might lead to a crowded in-vehicle density on buses. These crowded in-vehicle environments could make people feel uncomfortable and increase the probability of virus transmission in transit.

We can observe a similar phenomenon in drug market restrictions. The balloon effect is a negative consequence of an action taken against the drug market, similar to squeezing a latex balloon; one side will shrink, and another side will be swollen
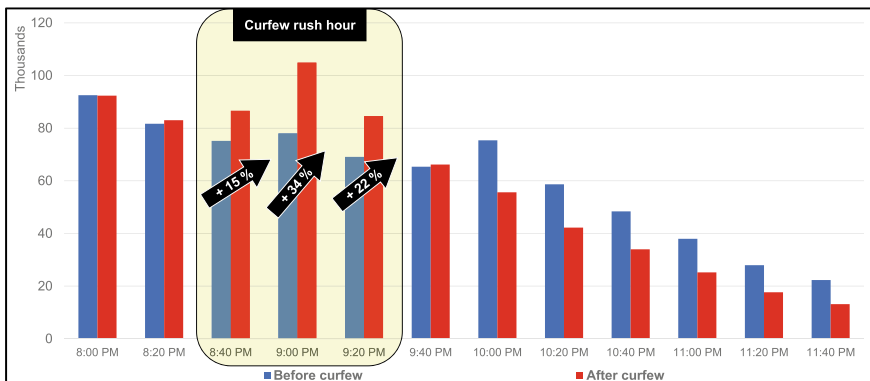


**Fig. 3** Number of boarding passengers on bus and subway by 20 min in Seoul
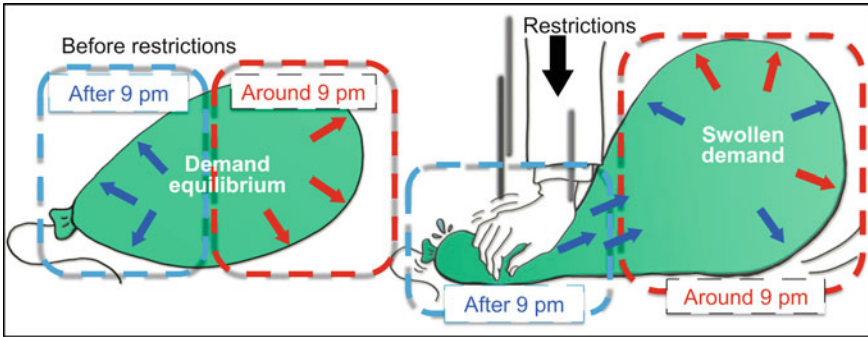
**Fig. 4** Concept of balloon effect in COVID-19 restriction affecting transit demand

[4]. As we observe in Fig. 3, the demand after 10 p.m. reduced considerably, and it seemed that the people who used transit after 10 p.m. moved to around 9 p.m. or earlier hours. We could say that the curfew induced people to run home and caused curfew rush hour simultaneously. This may lead to an increase in in-vehicle density. It is similar to the balloon effect of the drug market that demand can move to less restricted areas or hours to shun the restrictions, as shown in Fig. 4.

Therefore, it highlights that policymakers and transit operators need to carefully consider these users' behavior, including the balloon effect.

## 3.3 Transit Users' Reactions Based on Preannounced Information in Seoul

Authorities preannounced that frequency of bus services would be reduced by about 20% after 9 p.m. With the announcement, transit users could expect the in-vehicle density on buses to be crowded in advance. We believe that transit users would prefer the subway to the bus based on the expected in-vehicle density. We compared the mode shares before and after the bus frequency restriction by two time slots: daytime (from 5 a.m. to 8 p.m.) and nighttime (from 8 p.m. to 4 a.m.), as depicted in Fig. 5.

The change of transit mode shares before and after the bus restriction varies over time. During the daytime, the bus mode share before and after the restriction was changed from 51.1 to 51.8%, showing a minor change (0.7%). On the other hand, the bus share reduced by—2.3%, from 58.6 to 56.3% at nighttime. The reduced bus demand seems to have moved to the subway, which experienced a 2.3% increase. In a megacity such as Toronto or Seoul, increasing transit mode shares is challenging despite a 1% change, so the increase of 2.3% could reflect that many people chose the subway.

Therefore, we ascribe mode shares' change to the preannounced policy of reducing bus frequency. It seems that people who took the bus during the restricted hours
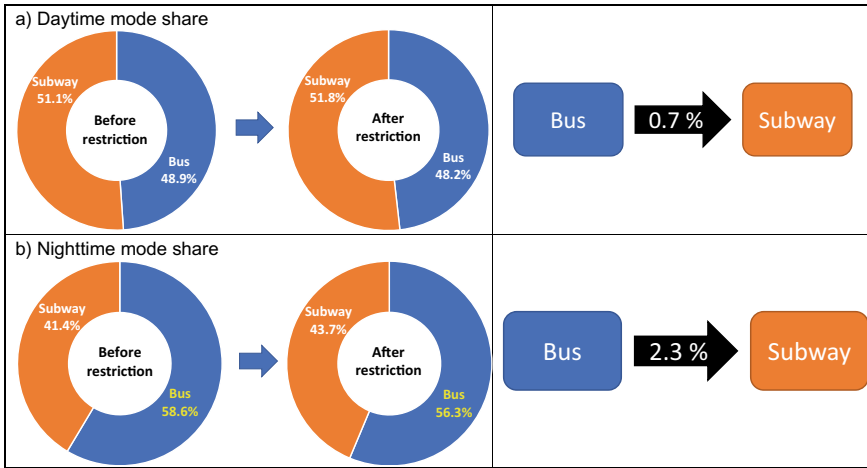
**Fig. 5** Change of transit mode shares before and after the bus frequency restriction in Seoul

changed their mode to the subway based on the prior information of reduced bus service.

## 3.4 Increased Bus Demand Due to Restrictions by Spatial Features in Seoul

Many researchers have investigated the relationship between landuse data associated with transit stops [1, 6, 10, 22]. We also consider spatial statistical data to understand the relationship between landuse and ridership change. We employ the unit number of social establishments, including restaurants, cafeterias, and bars per unit area of a community (per 1 km$^2$), based on open data source [15].

Figure 6 shows ridership in a heat map to depict ridership change by bus stops. It shows a meaningful change in the number of boarding passengers during curfew, especially from 9 p.m. to 9:20 p.m. As most social establishments were forced to close, many people headed for transit stations simultaneously. Accordingly, communities with more than 600 social establishments per 1 km$^2$, showed an abrupt increase in the number of boarding passengers. Most areas have a surge of transit demand that matches peripheral university areas or hot places.

From Fig. 6, we can deduce the curfew rush hour demand unexpectedly congregated in some specific areas with a high density of social establishments. The abrupt demand increase in the areas could cause a spike to in-vehicle density on the buses which pass the areas. In the following section, we can see the in-vehicle density situation from the surge of demand.
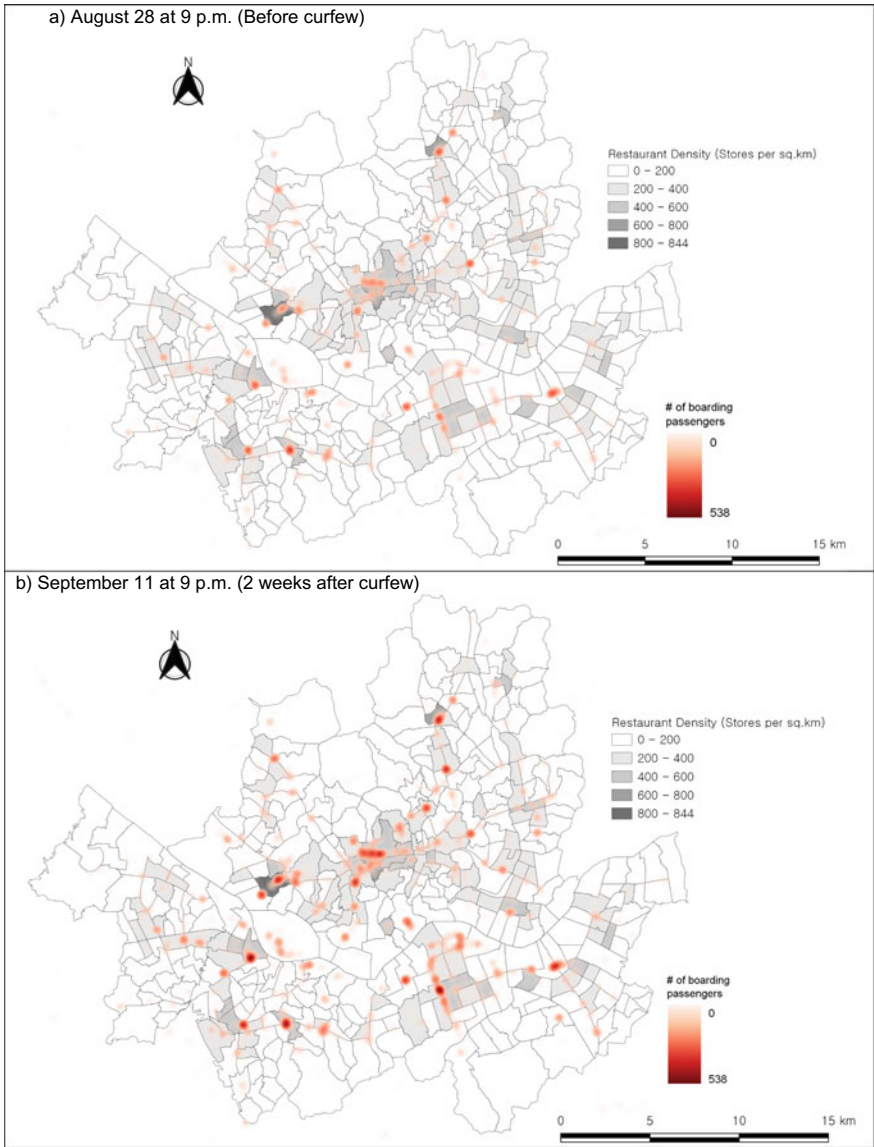
**Fig. 6** Heat map: number of boarding bus passengers in Seoul

## 3.5  Increased In-Vehicle Density on Buses by Spatial Features in Seoul

We estimated in-vehicle density to understand the risk of crowdedness on buses. Securing appropriate in-vehicle density in transit has become a critical social

distancing in the pandemic era. To estimate the in-vehicle density, we calculate every station's number of boarding and alighting passengers. In South Korea, almost all passengers tag their smart cards when they get off to obtain a fare discount while changing travel modes. We can measure the accurate onboard number of passengers from the tags. Most buses have 25 seats with 12 m in length, and 100% in-vehicle density means that all seats are occupied, and 25 people are standing. Kim's team surveyed bus users to understand the endurable level of in-vehicle density in South Korea. About 800 respondents responded that 50% is their endurable density in the bus and 60% for the subway [7].

We analyzed the in-vehicle density from 9 p.m. to 9:20 p.m. and displayed segments with greater than or equal to 50% of the density on the map. Figure 7 shows clearly that many segments with greater than 50% of the density are added after the restriction. In particular, Fig. 7b indicates that many condensed buses had to travel long distances along major roads. Given that the objective of the restriction is to refrain from gathering at night to reduce the probability of the spread of the virus, the condensed buses seem to bring about adverse results on the buses. Thus, policymakers should consider people's behaviors before imposing restrictions.

## 3.6   Transit Demand Change Under Curfew in Montreal

In Montreal, the curfew was conducted differently under the COVID-19 situation. The red zone means that the curfew started at 8 p.m. as a stricter control measure to lower the probability of virus transmission. During the orange zone period, the curfew started at 9:30 p.m. We analyzed the Transit app data, which measures demand for public transit based on millions of app opens [20]. In particular, we compared the proportion of app usage by time slots under the different curfew levels: the red or orange zones, to check whether the users changed their transit usage time. As discussed in Seoul's case, the curfew affected late-night transit usage, so the proportion of app usage during the curfew hours was reduced from about 19 to 10% (red zone) and 13% (orange zone), respectively.

Also, we analyzed weekly app usage proportions to find whether there was a curfew rush hour in Montreal. Figure 8 indicates the fluctuations of the app usage from 7 p.m. to 9 p.m. (before/after the curfew hour) under different curfew levels. On January 8 (before curfew), app usages for both hours were about 4.5%, respectively. However, during the red zone, the usage of the beginning of the curfew hour (8 p.m.–9 p.m.) was reduced by—2.5%, whereas before curfew hour (7 p.m.–8 p.m.) maintained the proportion for 3 weeks and increased gradually up to 5.8% on March 5. The difference in proportion for the two hours was diminished during the orange zone because 8 p.m.–9 p.m. was no longer affected by the curfew. We believe that a change in the app usage pattern could infer the transit user's demand change against the restriction. Further data collection would be needed to determine exactly how users responded to the curfew around 8 p.m., which was the very beginning moment of the restriction.
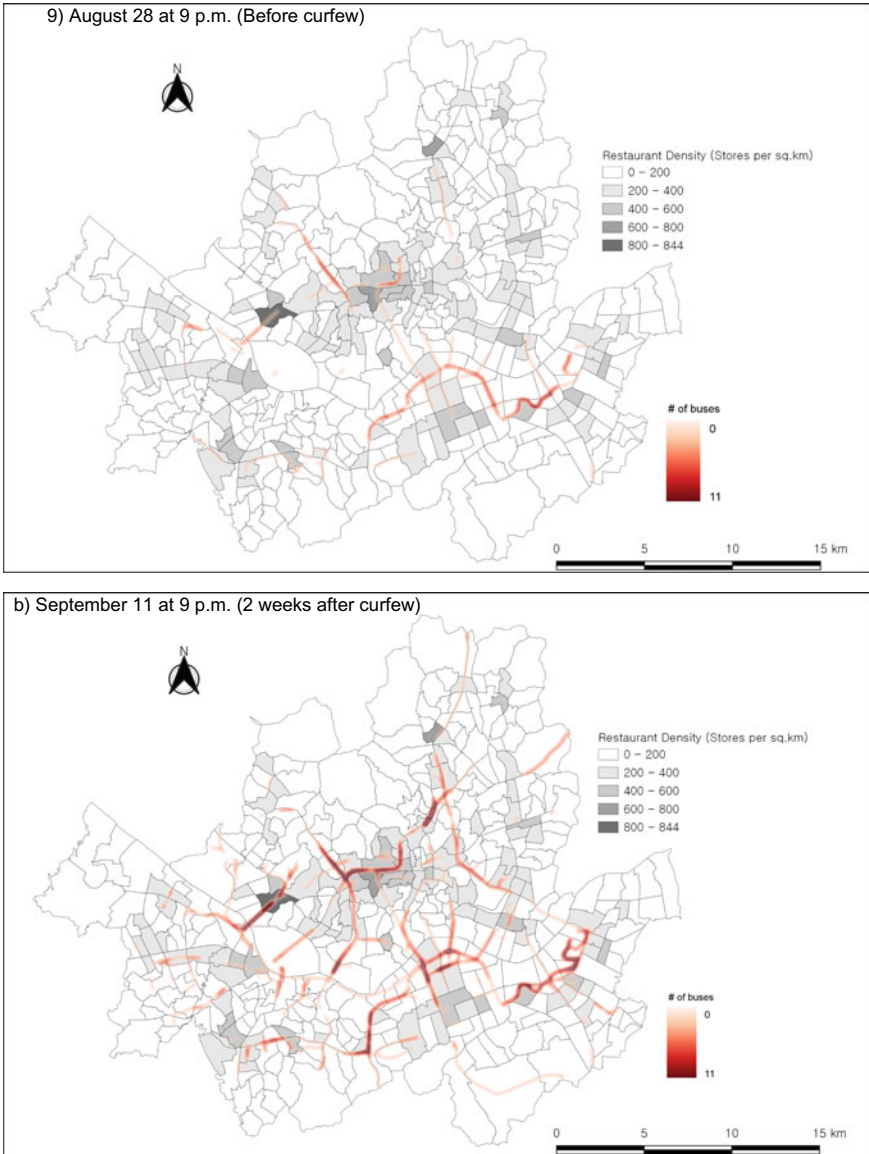
Fig. 7 Heat map: segments with greater than or equal to 25 passengers per bus in Seoul

## 4 Concluding Comments

Many governments have conducted various restriction policies depending on their own situation to prevent the spread of COVID-19. The curfew restriction policy may discourage people from gathering and induce them to go home early. We found
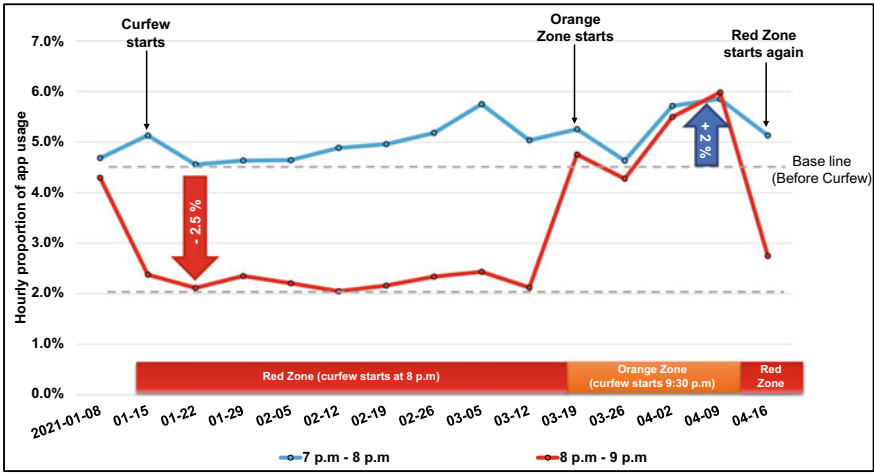
**Fig. 8** Fluctuation of an hourly proportion of app usage under curfew level in Montreal

five meaningful transit users' behavior against the restrictions from the smart card analysis.

First, curfew policies mainly impacted nighttime transit demand, and most of the demand shifted before the curfew hour. The demand for all-day and morning time, from 5 a.m. to 1 p.m., showed a slight change from the curfew. However, the demand during curfew hours was reduced, whereas the demand for afternoon and evening was increased significantly. The amount of reduced and increased demand was similar enough to cancel each other, and the all-day demand was not affected by the curfew. Thus, we believe that most of the demand during curfew hours moved prior to the beginning of the curfew.

Second, we found evidence of a curfew rush hour. People rushed to transit stations at the start of curfews due to the early closure of social establishments. It showed a sudden increase in demand (up to 30%) shifted from other hours. We call this *curfew rush hour*, and this sudden demand surge might lead to a more crowded in-vehicle density on buses. Government officials should consider the possibility of condensed transit demands during the hour prior before imposing any curfews in potentially new pandemic events.

Third, people chose transit modes differently based on the preannounced information. Due to the restriction on the frequency of bus services, subway mode shares increased by 2% compared to before restrictions.

On top of that, the high density of social establishments could bring about transit demand concentration. The abruptly increased curfew rush hour demand emerged near the hot places.

Lastly, concentrated transit demand in hot places caused crowded in-vehicle density on many buses, and the crowded conditions could endanger the passengers on buses. Accordingly, restrictions could exacerbate virus transmission contrary to

expectations. We believe the deteriorated in-vehicle density as a result of the curfew policy which created a paradoxical situation.

Our research suggests that policymakers and transit operators should take into account users' reactions to restrictions. People could react adversely to policymakers' expectations and sustain their nightlife until the beginning of restriction, even in the pandemic era. In particular, with those people's propensity for reaction to restriction, the supply of some transit lines which pass through highly dense social establishments should be maintained at a regular frequency. On the other hand, some areas with a low density of social establishments showed little transit demand during curfew rush hour. To provide additional service where needed, we could learn what TransLink did in 2020. TransLink reduced the service in the low-demand lines such as SeaBus and West Coast Express to increase the frequency of lines serving Downtown Vancouver based on continuous monitoring of ridership fluctuation [19]. For these reasons, transportation experts need to implement their policy regarding transit supply carefully and flexibly.

People's recognition of the threat of the virus could vary considerably by individual's propensity or amount of information. Transit users may spontaneously abide by restrictions when they fear the possibility of being infected by the COVID-19 virus and drastically cut nighttime activities. If the majority of people feel the prevailing fear of the virus, curfew and reducing transit frequency restrictions could be effective and practical measures. However, as we deduced in Seoul's case, people do not all consider the virus situation seriously and could be reluctant to reduce their nightlife. Future work will measure the fear index of the virus and establish optimal methods for operating transit to secure economic, flexible, and practical methods. Furthermore, this research could offer a better way of transit operations by considering the density of social establishments.

## References

1. Chakour V, Eluru N (2016) Examining the influence of stop level infrastructure and built environment on bus ridership in Montreal. J Transp Geogr 51:205–217. https://doi.org/10.1016/j.jtrangeo.2016.01.007
2. Choi J (2020) Night bus routes in seoul reduce operation by 20% until sept. 6 amid tighter social distancing. Arirang News, 31 Aug 2020. http://www.arirang.com/News/News_View.asp?nseq=264154. Accessed 11 Nov 2021
3. Haines BJ (2021) Quebec's Provincewide curfew will not affect montreal public transportation. Global NEWS https://globalnews.ca/news/7560843/quebec-provincewide-curfew-montreal-public-transportation/. Accessed 21 Dec 2021
4. IDPC (2022) Balloon Effect. International drug policy consortium (IDPC). https://idpc.net/publications/balloon-effect. Accessed 21 Dec 2021
5. Kim MK, Kim SP, Heo J, Sohn HG (2017) Ridership patterns at subway stations of seoul capital area and characteristics of station influence area. KSCE J Civ Eng 21(3):964–975. https://doi.org/10.1007/s12205-016-1099-8
6. Kim MK, Kim S, Sohn HG (2018) Relationship between spatio-temporal travel patterns derived from smart-card data and local environmental characteristics of Seoul, Korea. Sustainability (Switzerland) 10(3). https://doi.org/10.3390/su10030787

7. Kim SG, Ko J, Lee S, Jang JE, Jeong K (2013) Evaluation of the quality of public transport commuting in seoul. 2013-PR-33. Seoul

8. Laframboise K (2021) Here's how Quebec's latest lockdown rules and nightly curfew will work. Global NEWS. https://globalnews.ca/news/7560666/quebec-coronavirus-new-lockdown-curfew-rules-guide/. Accessed 21 Dec 2021

9. Ma X, Yao Jan W, Wang Y, Chen F, Liu J (2013) Mining smart card data for transit riders' travel patterns. Transp Res Part C: Emerg Technol 36:1–12. https://doi.org/10.1016/j.trc.2013.07.010

10. Ma X, Zhang J, Ding C, Wang Y (2018) A geographically and temporally weighted regression model to explore the spatiotemporal influence of built environment on transit ridership. Comput Environ Urban Syst 70(December 2017): 113–24. https://doi.org/10.1016/j.compenvurbsys.2018.03.001.

11. Rocca R (2021) Ontario declares 2nd state of emergency, issues stay-at-home order. Global NEWS. https://globalnews.ca/news/7571036/ontario-new-restrictions-lockdown-coronavirus/. Accessed 21 Dec 2021

12. Seoul Metropolitan Government (2017) Seoul life with transportation card big data. Seoul.go.kr. https://news.seoul.go.kr/traffic/archives/36011 (Website in Korean). Accessed 25 Nov 2021

13. Seoul Metropolitan Government (2021) Elevation of Social Distancing to Level 2 for the Seoul Metropolitan Area. Seoul.go.kr. http://english.seoul.go.kr/elevation-of-social-distancing-to-level-2-for-the-seoul-metropolitan-area/. Accessed 25 Nov 2021

14. Seoul Metropolitan Government Big Data Campus (2021) Seoul public transit and subway ridership data. https://bigdata.seoul.go.kr/data/selectSampleData.do?r_id=P213&sample_data_seq=13&tab_type=A&sch_cate=40&file_id=&sch_text=&sch_order=U&currentPage=2 (Website in Korean). Accessed 25 Oct 2021

15. Seoul Open Data (2021) Seoul population density (Dong). https://data.seoul.go.kr/dataList/10584/S/2/datasetView.do (Website in Korean). Accessed 25 Oct 2021; Seoul business distribution data (Dong). https://data.seoul.go.kr/dataList/10590/S/2/datasetView.do (Website in Korean). Accessed 25 Oct 2021

16. Silva V (2021) What the 'electroshock' lockdown means for restaurants in Quebec. EATER MONTREAL. https://montreal.eater.com/2021/1/7/22218475/curfew-lockdown-restaurants-quebec-montreal-takeout-delivery. Accessed 21 Dec 2021

17. Statistics Canada (2022) Table 23-10-0251-01 passenger bus and urban transit statistics, by the North American industry classification system (NAICS) (x 1,000,000). https://www150.statcan.gc.ca/t1/tbl1/en/tv.action?pid=2310025101&pickMembers%5B0%5D=2.1&cubeTimeFrame.startMonth=04&cubeTimeFrame.startYear=2019&cubeTimeFrame.endMonth=08&cubeTimeFrame.endYear=2020&referencePeriods=20190401%2C20200801. Accessed 25 Feb 2022

18. STM (2021) New lockdown measures – STM update. Societe de Transport de Montreal (STM). https://www.stm.info/en/press/press-releases/2021/new-lockdown-measures---stm-update. Accessed 25 Nov 2021

19. TransLink (2019) 2020 transit service performance review. https://public.tableau.com/app/profile/translink

20. Transit app (2021) How coronavirus is disrupting public transit. https://transitapp.com/coronavirus. Accessed 4 Nov 2021

21. Xu X, Xie L, Li H, Qin L (2018) Learning the route choice behavior of subway passengers from AFC data. Expert Syst Appl 95:324–332. https://doi.org/10.1016/j.eswa.2017.11.043

22. Zhao J, Deng W, Song Y, Zhu Y (2013) What influences metro station ridership in China? Insights from Nanjing. Cities 35:114–124. https://doi.org/10.1016/j.cities.2013.07.002

# A Review of the Application of Hybrid Models in Flood Risk Assessment Methods



**Aditya Rebally, Caterina Valeo, Jianxun (Jennifer) He, and Saeid Saidi**

**Abstract** Transportation networks, which are vital to society's function, are vulnerable to extreme events like floods. Under the influence of climate change, the intensity and the frequency of these food events are increasing globally at an alarming rate. These events result in a series of flood impacts and associated cascading effects, which reduce the overall resilience of the road network. Flood risk assessment methods, which are applied to analyze these impacts are almost always associated with hybrid methods/models, which improvise the overall assessment methodology and impact quantification. The present article is a short review of the hybrid models like GIS-based models, cellular automata, traffic simulation, and input–output models, which are the most applied in the flood assessment methods. Of these models, GIS-based models have wide range of applications and depict the impacts in spatial scale. The Calgary floods of 2013 is used to display the spatial impact and flood prone/risk areas.

**Keywords** Transportation · Flood impacts · Resilience · Flood assessment models

## 1 Introduction

It is acknowledged that hydrometeorological disasters like floods cause devastating effects on infrastructure, nature, and on lives [29]. Transportation infrastructure, which is one of the critical infrastructures necessary for the regular functioning of the current society is affected and is vulnerable to extreme flooding events [28]. Climate change combined with the rapid urbanization, global population growth, and exploitation of nature resulted in increased frequency and magnitude of these events in the last decade, and is predicted to increase further in the coming years,

A. Rebally (✉) · C. Valeo
Mechanical Engineering, University of Victoria, Victoria, Canada
e-mail: arebally@uvic.ca

J. (Jennifer) He · S. Saidi
Civil Engineering, Schulich School of Engineering, University of Calgary, Calgary, Canada
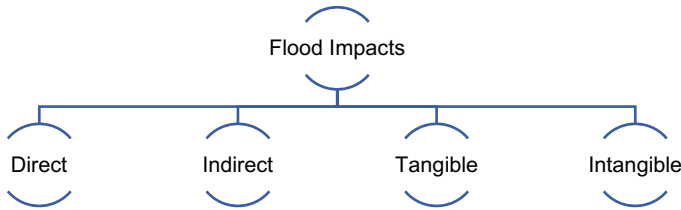
**Fig. 1** Flood impact classification [3]

with Intergovernmental Panel on Climate Change (IPCC) claiming that the human interference in nature resulted in these events being almost unstoppable [23]. The flooding events when occur leave multiple impacts along their path on the infrastructure. These impacts can be classified in terms of physical characteristics of flood water contact as direct and indirect impacts [3]. Direct impacts refer to the flood impacts resulting from the physical contact of flood waters and indirect impacts refers to the flood impacts on infrastructure without any physical contact with flood waters [3]. In economic terms, it can be divided into tangible and intangible, with tangible referring to the impacts which can be computed, and intangible impacts refer to the impacts which are difficult to compute and to define [3]. A general classification of flood impacts is shown in Fig. 1.

Apart from the physical and economic classification, flood impacts, which are dependent on spatio-temporal scale can also be defined in terms of spatial and temporal scales [22]. In general terms, flood impacts in temporal scale can be divided into short-term, medium-term, and long-term impacts. Short-term flood impacts refer to the impacts which occur during the flood period before the flood recovery phase and may occur with flood water contact. Medium-term impacts refer to the impacts which occur during the recovery phase, and with or without flood water contact. Long-term impacts refer to the impacts which occur post recovery phase with no flood water contact [5]. For these temporal scales, no specific timeline is defined, and the time scales are determined from case-to-case basis, based on the flood period and the recovery process. In spatial scale terms, the classification is carried out based on the scale of the flood impacts, i.e. community scale, urban scale, and regional scale [5]. With community scale referring to small-scale communities or specific areas with limited population, urban scale referring to an urban city with medium to large population densities, and regional scale refers to a state or a province and includes both the urban and community scale in it. A specific area is not assigned to the spatial scale as the area changes depending on space and time. A general schematic of the spatio-temporal classification is shown in Fig. 2.

These flood impacts are assessed through flood impact assessment methods which are classified primarily into probabilistic method, analytical method, fuzzy inference, graph theory, and empirical methods [8, 21]. A general schematic of flood assessment methods is shown in Fig. 3. Probabilistic method is applied to assess the performance of the transportation network by generating a probability density function through the application of historic climate data, transportation network data, etc. A probabilistic
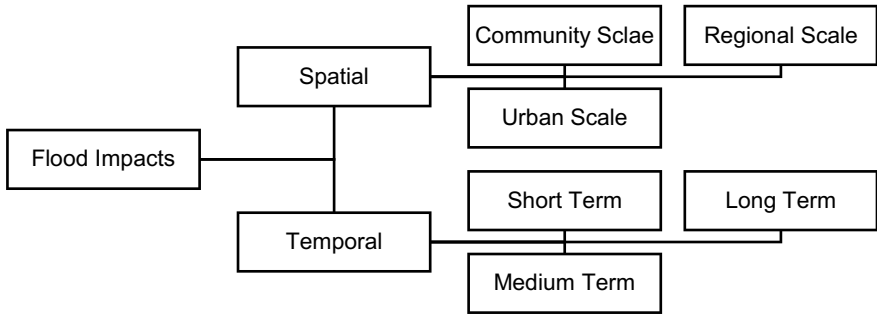
**Fig. 2** Flood impact classification in spatio-temporal scales

approach assesses the impact by generating multiple flood scenarios by incorporating uncertainties to the assessment [13].

Analytical methods are generally applied to assess the flood impacts in economic terms. It divides the system into multiple short or separate entities to analyze the flood
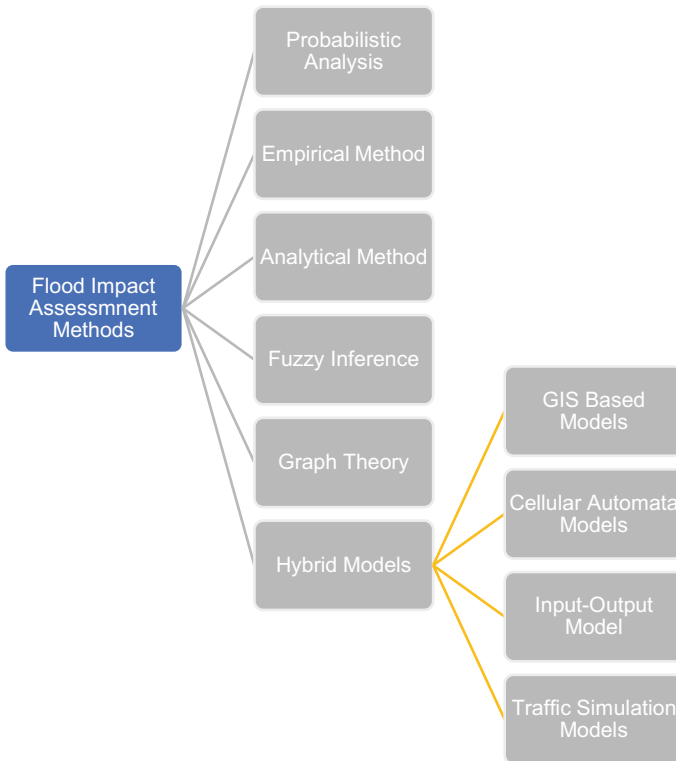


**Fig. 3** General classification of flood impact assessment methods [16, 17, 20]

impacts quantitatively. During the flood event, much of the data can be missing or misinterpreted [32]. Fuzzy inference, which is being applied frequently from the last decade incorporates the uncertainties from the vague data and uses the 'if-then' fuzzy rules, etc. to generate a crisp value or fuzzy set value to the impact. Although the application area is vast, the increase in rules might become complicated based on space and time [1, 19]. Graph theory, which represents the present transportation network can be depicted pictorially by dividing the network in the form of nodes and links, i.e. the junctions as nodes and the connecting roads or bridges as links. This allows for performing multitude of combinations for flood impacts thereby determining the resilience of infrastructure. But the interconnectivity of multiple infrastructures can be difficult to represent and analyze. Graph theory mostly uses statistical data of historical climate, road network, and/or digital terrain model information (DTM) [37]. Empirical methods are very much like probabilistic methods except in empirical, apart from the historical climate datasets, non-conventional datasets like surveys, interviews, etc. are also applied which may result in misrepresentation of the flood impacts [30].

Apart from the above-mentioned classification, there are multiple models like input–output model, traffic model, hydrological models, GIS-based models, etc., which although are not part of flood impact assessment methods, are applicable to almost every other known flood impact assessment method [2, 7]. Because of their representation of transportation networks, these models can be combinedly represented as hybrid methods.

These flood assessment methods are utilized to generate flood scenarios and provide an optimal form of results to increase the overall resilience of infrastructure and/or region. Resilience in terms of flood is defined as the ability of the infrastructure to retain its basic functionality during the extreme hazard event and return to its original functionality before the event with minimal external interference [3, 15]. In addition, these flood risk assessment methods can integrate multiple aspects of socio-economic, natural sciences, etc., to generate a complex decision-making process to increase the resilience, which can result in reduced flood impacts, deter the aftereffects of floods, etc. For this, flood modelling is one of the essential tools which helps in developing policies required for flood risk management and mitigation [31]. Hazard determination, vulnerability analysis, and risk determination are few of the basic steps carried out for a flood risk analysis [8]. A general flood risk assessment process is carried out in multiple steps, depicted as: event identification, assessment, impact estimation, risk evaluation, and flood risk assessment. A general flood risk assessment methodology needs to assess the flood impacts at multiple spatio-temporal scales.

The present article is a review of hybrid methods of the flood assessment methodology and provides an application of the applied model for the 2013 floods in the city of Calgary by using the existing GIS data and imagery from City of Calgary [9]. Section 2 provides a brief introduction to the hybrid models, followed by its application in the present flood assessment process. Section 3 provides a glimpse of the 2013 Calgary floods and the analysis done by using the hybrid models and a short discussion on how the direct and indirect impacts are classified.

## 2 Flood Impact Assessment Methods

Hybrid methods/models are a cluster of models which are applied as part of the flood assessment methodology to generate multiple scenarios to analyze the effects of the flood on the infrastructures. These hybrid models, which operate on mathematical complexities are referred to as simple models which can provide reasonable hypothesis/output with available data, with the results depending on the quality of data applied [27]. Based on this, multiple models have been built and applied to flood assessment methods. The most applied models in the hybrid methodology are GIS-based models, input–output models, cellular automata models, traffic simulation models, hydrological models, etc. These models, even with limited data available have been useful in mapping the flood impact models [12, 27]. The present section provides an introduction for these models.

### 2.1 Input–Output Model

Input–output models are one of the tools used for the economic footprint assessment following an extreme event like flood. It uses the statistical information of goods and services among multiple industries to generate an assessment, i.e. by utilization of the relations between consumers and producers [34, 36]. By using these relations, it can also assess the indirect economic impacts of the event. A general IO model can be divided into three sub steps: the input matrix which shows the cost of inputs, the output matrix which indicates and links the goods and services by each sector/industry, and finally the goods which are available for consumption which is represented as the final demand matrix [34, 36]. Regarding the application of IO model to transportation, it can be combined with the traffic scenarios to generate the start and end point of destination to assess the economic loss in terms of the time lost due to the interactions. These models can also be applicable for quantifying the cascading effects on the infrastructure/industry [17]. The IO model applied in Kinshasa to assess the flood effects on the urban transport and its accessibility can be a prime example for this case. The impacts are quantified by using the time lost during transit, traffic congestion, transit loss due to road conditions, etc. [10]

### 2.2 GIS-Based Models

Flood impact analysis developed by using the GIS models helps to visualize the flooding and its respective impacts on the infrastructures by using the available data sets like flood depth, climate change, elevation data, etc. [11]. GIS models also use ground surveys, aerial observation, etc. to generate the flood maps. The primary advantage of these GIS models is its ability to visualize the flooding extent

and generate a possible future flood scenario and the flood impacts on respective infrastructure [2]. GIS models in comparison with traditional mapping can merge multiple spatial datasets along with qualitative and quantitative assessment, based on which numerical assessments are carried out in a systematic way to generate the necessary flood maps. Apart from these, the flood risk maps generated through the GIS model can identify the links which are most vulnerable to the present and future flooding and can aid in the decision-making process to improve the resilience of the infrastructure [6, 38]. Although GIS models have wide applicability, the process can be time consuming, with increase in spatial context and with data limitations in those cases [14, 25].

An example for the GIS modelling approach can be the 2013 Calgary flood, which is one of the most devastating extreme events of the province which resulted in a net loss of $ 6 billion in the form of insurance, infrastructure damage, and repairs [18]. Multiple assessments were carried out for this flood, but almost every assessment carried out had a GIS model representation incorporated into it. Figure 4 provides a spatial scale representation of the flood affected areas and the potential flood zones. The spatial representation from the GIS mapping can potentially help in the flood risk management and the decision main process to increase the overall resilience of the vulnerable structures, herby decreasing the impacts from the future extreme events.

## 2.3    Traffic Simulation Model

A general evacuation strategy/route depends on multitude of factors like warning and response time, evacuation routes, traffic flow, and other external conditions [33]. Due to these multiple factors influencing the traffic flow, and with the added complexity of the flooding event and its aftermath, traffic simulation models can be said to be indispensable for the analysis and evacuation planning [4, 26]. Traffic simulation models are one of the primary tools w.r.t evacuation planning following an extreme vent like flood. It is generally applied with other flood assessment methods mentioned above to determine the congestion of the transportation network during the flood event, thereby assessing the flood impacts [4, 26]. These traffic simulation models can provide an insight into the possible time to start evacuation, and possible routes for emergency services during the flooding event [4, 33]. With increased demand for transportation combined with limited network capacity, the traffic simulation models need to be robust enough to accommodate and test multiple emergency situations, taking into consideration multiple modes of transport [4].

**Fig. 4** Spatial representation comparison map of 2013 Calgary flood and a one in eight-year return period flood extent in GIS modelling (Data retrieved from city of Calgary open data portal website [9, 24])

## 2.4   Cellular Automata Models

Cellular automata models are those where one can explore how local actions generate global actions through specific rules [12, 16]. These models divide the flood domain into finite number of grids, with each grid having a defined number of states. The evolution of flooding in spatio-temporal scale is translated into rules, which update the state of each cell based on the state of the surrounding neighbour cells and updating the cell continuously with each time step [12]. These CA models, which form an alternative grid-based simulation framework can express complex flow dynamics of spatial patterns, which are difficult to represent through mathematical terms [16]. These models generally use manning equation to calculate the intercellular flux rates with multiple time step variations which are comparatively faster than the urban inundation model used in flood assessment [35]. But the downsize of the models based on CA is that the time steps are dependent on the size of the cells. With smaller cell size, the time step needs to be reduced quadratically for numerical stability, which in turn decreases its computational resolution of the grids [12].

## 3   Discussion

One of the factors which should not be disregarded in flood model review is the formulations, which enhance the functionality of the flood model. An optimal flood model needs to represent the external spatial factors like slope, gravity, mass, momentum, etc., as a function of hydraulic processes with simplicity. But due to the limitations in data availability and the complexities involved in dynamic representation of multiple factors in the model, makes the applicability of these models in limited context. Among the flood models, the CA-based models, and GIS-based models are applied frequently in the urban flooding's due to its representation of the spatial context, but the accuracy is dependent on the quality of data available for the event. Even with these computational and data limitations, flood modelling is still the primary aspect of flood risk management. The data limitations may give rise to uncertainties or errors in the modelling, which can undermine or overestimate the expected results. These uncertainties, which account for variations in real world and model predictions are needed in assessing the level of reliability of the model.

In flood modelling, estimation of the uncertainties which arise from the model, input parameters and data, can be considered a crucial step in understanding the functionality of the flood modelling and their application in flood risk management. This may provide an estimation of up to what extent the models can be applied to other significant geographical locations with the same kind of data availability and scale. Apart from the uncertainty analysis carried out with flood modelling, the sensitivity analysis which helps in understanding the performance of the model can predict the effects of the input variables on the variations depicted in the model predictions and

the real scenarios. But limitations in the sensitivity analysis can lead to ambiguous results, which fail to reproduce the actual model behaviour [36].

The traffic simulation models, although can provide a near accurate assessment for the purpose of evacuation and emergency services during the flood and post-flood period, it suffers from data limitations as the data during the flood and post flood till the recovery phase may not be reliable or may even have gaps in them. Although multiple models and methods exist which incorporate multiple parameters in spatial scale, most of the models do not depict the temporal scale or the temporal parameters of the flood extent. This can also be viewed from the 2013 Calgary flood map in Fig. 4, where the map shows the flood extent with multiple return periods and the flood zone areas, but the depiction of the same flood maps with varying time post flood is complicated and cannot be achieved without the combination of other existing methods like graph theory, fuzzy logic, etc.

## 4   Conclusion

Flood, which have multiple effects on transportation in the form of physical and economic consequences are assessed by using the flood risk assessment methodologies. Among these methodologies, the hybrid methods which are a cluster of models form a core part of the flood risk assessment and management, and are applied to represent the flood effects by using the applicable data. These models predict the flood extent with near accuracy in spatial scale have uncertainties resulting from the data applicability. But the applicability and prediction capability of these models in spatial scale is limited and can only be achieved by combining these models with other applicable flood risk assessment methodologies.

## References

1. Ahmad SS, Simonovic SP (2013) Spatial and temporal analysis of urban flood risk assessment. Urban Water J 10(1):26–49. https://doi.org/10.1080/1573062X.2012.690437
2. Ali K, Bajracharya RM, Koirala HL (2016) A review of flood risk assessment. Int J Environ Agric Biotechnol 1(4):1065–1077. https://doi.org/10.22161/ijeab/1.4.62
3. Armaroli C, Duo E, Viavattene C (2019) From hazard to consequences: evaluation of direct and indirect impacts of flooding along the Emilia-Romagna coastline Italy. Front Earth Sci 7(August):1–20. https://doi.org/10.3389/feart.2019.00203
4. Balakrishna R, Wen Y, Ben-Akiva M, Antoniou C (2041) Simulation-based framework for transportation network management in emergencies. Transp Res Rec: J Transp Res Board, pp 80–88. https://doi.org/10.3141/2041-09
5. Bousquin J, Hychka K (2019) A geospatial assessment of flood vulnerability reduction by freshwater wetlands—a benefit indicators approach. Front Environ Sci 7(APR):1–14. https://doi.org/10.3389/fenvs.2019.00054
6. Correia FN, Castro Rego F, Da M, Saraiva G, Ramos I (1998) Coupling GIS with hydrologic and hydraulic flood modelling. Water Resour Manage 12:229–249

7. Darabi H, Choubin B, Rahmati O, Torabi Haghighi A, Pradhan B, Kløve B (2019) Urban flood risk mapping using the GARP and QUEST models: a comparative study of machine learning techniques. J Hydrol 569(December 2018):142–154. https://doi.org/10.1016/j.jhydrol.2018.12.002

8. Diez-Herrero A, Garrote J (2020) Flood risk analysis and assessment, applications and uncertainties: a bibliometric review. Water (Switz) 12(7). https://doi.org/10.3390/w12072050

9. Flood maps (n.d.) Retrieved 14 Mar 2022, from https://www.calgary.ca/pda/pd/calgary-land-use-bylaw-1p2007/floodway-flood-fringe-maps.html

10. He Y, Thies S, Avner P, Rentschler J (2020) The impact of flooding on urban transit and accessibility a case study of Kinshasa (Issue June). https://openknowledge.worldbank.org/handle/10986/34981

11. Introduction to Flood Impact Analysis—ArcGIS Solutions | Documentation (n.d.) Retrieved 1 Mar 2022, from https://doc.arcgis.com/en/arcgis-solutions/latest/reference/introduction-to-flood-impact-analysis.htm

12. Jamali B, Bach PM, Cunningham L, Deletic A (2019) A cellular automata fast flood evaluation (CA-ffé) model. Water Resour Res 55(6):4936–4953. https://doi.org/10.1029/2018WR023679

13. Kim BJ, Kim M, Hahm D, Han KY (2021) Probabilistic flood hazard assessment method considering local intense precipitation at NPP sites. J Hydrol 597(December 2020):126192. https://doi.org/10.1016/j.jhydrol.2021.126192

14. Kourgialas NN, Karatzas GP (2011) Flood management and a GIS modelling method to assess flood-hazard areas—a case study. 56(2):212–225. https://doi.org/10.1080/02626667.2011.555836

15. Lee RJ (2021) Vacant land, flood exposure, and urbanization: examining land cover change in the Dallas-Fort Worth metro area. Landsc Urban Plan 209(January):104047. https://doi.org/10.1016/j.landurbplan.2021.104047

16. Li Y, Gong J, Zhu J, Song Y, Hu Y, Ye L (2013) Spatiotemporal simulation and risk analysis of dam-break flooding based on cellular automata. 27(10):2043–2059. https://doi.org/10.1080/13658816.2013.786081

17. Mendoza-Tinoco D, Hu Y, Zeng Z, Chalvatzis KJ, Zhang N, Steenge AE, Guan D (2020) Flood footprint assessment: a multiregional case of 2009 central European floods. Risk Anal 40(8):1612–1631. https://doi.org/10.1111/risa.13497

18. Milrad SM, Gyakum JR, Atallah EH (2015) A meteorological analysis of the 2013 Alberta flood: antecedent large-scale flow pattern and synoptic-dynamic characteristics. Mon Weather Rev 143(7):2817–2841. https://doi.org/10.1175/MWR-D-14-00236.1

19. Mosavi A, Ozturk P, Chau KW, Review L (2018) Flood prediction using machine learning models: literature review. Water (Switz) 10(11):1–40. https://doi.org/10.3390/w10111536

20. Mouronte-López ML (2021) Analysing the vulnerability of public transport networks. J Adv Transp, vol 2021. https://doi.org/10.1155/2021/5513311

21. O'shea T, Bates P, Neal J (2020) Testing the impact of direct and indirect flood warnings on population behaviour using an agent-based model. Nat Hazard 20(8):2281–2305. https://doi.org/10.5194/nhess-20-2281-2020

22. Ogie RI, Holderness T, Dunn S, Turpin E (2016) Vulnerability analysis of hydrological infrastructure to flooding in coastal cities—a graph theory approach. In: Transforming the future of infrastructure through smarter information—proceedings of the international conference on smart infrastructure and construction, ICSIC 2016, pp 633–638. https://doi.org/10.1680/tfitsi.61279.633

23. Olsen JR, Lambert JH, Haimes YY (1998) Risk of extreme events under nonstationary conditions. Risk Anal 18(4):497–510. https://doi.org/10.1111/J.1539-6924.1998.TB00364.X

24. Open Calgary | Open Calgary (n.d.) Retrieved 14 Mar 2022, from https://data.calgary.ca/

25. Ouma YO, Tateishi R (2014) Urban flood vulnerability and risk mapping using integrated multi- parametric AHP and GIS: methodological overview and case study assessment. Water (Switz) 6(6):1515–1545. https://doi.org/10.3390/w6061515

26. Pel AJ, Bliemer MCJ, Hoogendoorn SP (2012) A review on travel behaviour modelling in dynamic traffic simulation models for evacuations. Transportation 39(1):97–123. https://doi.org/10.1007/S11116-011-9320-6/FIGURES/5

27. Rehman S, Sahana M, Hong H, Sajjad H, Ahmed BB (2019) A systematic review on approaches and methods used for flood vulnerability assessment: framework for future research. Nat Hazards 96(2):975–998. https://doi.org/10.1007/s11069-018-03567-z

28. Singh P, Sinha VSP, Vijhani A, Pahuja N (2018) Vulnerability assessment of urban road network from urban flood. Int J Disaster Risk Reduction 28(December 2017):237–250. https://doi.org/10.1016/j.ijdrr.2018.03.017

29. Tachaudomdach S, Upayokin A, Kronprasert N, Arunotayanun K (2021) Quantifying road-network robustness toward flood-resilient transportation systems. pp 1–16

30. Teng J, Jakeman AJJ, Vaze J, Croke BFWFW, Dutta D, Kim S (2017) Flood inundation modelling: a review of methods, recent advances and uncertainty analysis. Environ Model Softw 90:201–216. https://doi.org/10.1016/j.envsoft.2017.01.006

31. Tsang M, Scott DM (2020) An integrated approach to modeling the impact of floods on emergency services: a case study of Calgary, Alberta. J Transp Geogr 86(June):102774. https://doi.org/10.1016/j.jtrangeo.2020.102774

32. Usman Kaoje I, Abdul Rahman MZ, Idris NH, Razak KA, Wan Mohd Rani WNM, Tam TH, Mohd Salleh MR (2021) Physical flood vulnerability assessment using geospatial indicator-based approach and participatory analytical hierarchy process: a case study in Kota Bharu, Malaysia. Water (Switz) 13(13):1–22. https://doi.org/10.3390/w13131786

33. Wang W, Yang S, Gao J, Hu F, Zhao W, Stanley HE (2020) An integrated approach for assessing the impact of large-scale future floods on a highway transport system. Risk Anal 40(9):1780–1794. https://doi.org/10.1111/risa.13507

34. What are Input-Output Models?—Province of British Columbia (n.d.) Retrieved 1 Mar 2022, from https://www2.gov.bc.ca/gov/content/data/statistics/economy/input-output-model/what-are-input-output-models

35. Wijesekara GN, Gupta A, Valeo C, Hasbani JG, Qiao Y, Delaney P, Marceau DJ (2012) Assessing the impact of future land-use changes on hydrological processes in the Elbow River watershed in southern Alberta, Canada. J Hydrol 412–413:220–232. https://doi.org/10.1016/j.jhydrol.2011.04.018

36. Zeng Z, Guan D (2020) Methodology and application of flood footprint accounting in a hypothetical multiple two-flood event. Philos Trans Royal Soc A: Math Phys Eng Sci 378(2168). https://doi.org/10.1098/rsta.2019.0209

37. Zhang N, Alipour A (2019) Integrated framework for risk and resilience assessment of the road network under inland flooding. Transp Res Rec 2673(12):182–190. https://doi.org/10.1177/0361198119855975

38. Zhou Q, Su J, Arnbjerg-Nielsen K, Ren Y, Luo J, Ye Z, Feng J (2021) A GIS-based hydrological modeling approach for rapid urban flood hazard assessment. Water (Switz) 13(11):1–12. https://doi.org/10.3390/w13111483

# Assessing Risk of Climate Change on Existing Canadian Bridge Infrastructure: A Multidisciplinary Approach

**Shereen Altamimi, Lamya Amleh, and Liping Fang**

**Abstract**  Addressing the impact of climate change on transportation infrastructure is one of the global challenges of this century. The impacts of climate change are visible across the globe and have been growing progressively worse over the last 50 years. The climate in North America will continue changing during the twenty-first century; current predictive models indicate that the mean annual temperature will rise by between 1 and 5.5 °C. Annual precipitation is likely to increase by up to 5% in most Canadian regions, while the intensity of daily precipitation and the probability of extreme precipitation intensities may increase across the entire country. Mean annual and extreme wind speeds are expected to increase and the sea level in some areas is likely to rise by up to 0.9 m by the end of the century. These changes create an environment of uncertainty when assessing the risk of climate change on existing bridge structures. In collaboration with the National Research Council, this is ongoing research which requires much effort in assessing the risk and developing a tool for engineers to assess existing bridges. A risk assessment tool is developed to equip practicing engineers and decision-makers with the challenging task of evaluating bridges structurally while considering the impact on socioeconomics. The presented protocol incorporates projected temperature values based on representative concentration model 6.0 (RCP 6.0) as outlined by the Intergovernmental Panel on Climate Change (IPCC). The methodology developed evaluates the impact of projected temperature on a given bridge both structurally and socioeconomically. This tool allows decision-makers to evaluate a portfolio of bridges to determine the level of risk and provides input toward prioritization of intervention projects and, therefore, resource allocation. The methodology is a systematic multidisciplinary approach that can be applied to assess existing bridges considering climate change.

S. Altamimi (✉) · L. Fang
Department of Mechanical and Industrial Engineering, Ryerson University, Toronto, ON, Canada
e-mail: saltamim@ryerson.ca

L. Amleh
Department of Civil Engineering, Ryerson University, Toronto, ON, Canada

## 1  Introduction

In 2021, the Intergovernmental Panel for Climate Change (IPCC) published that we continue to experience unprecedented changes to Earth's climate in every region across all climatic systems and these changes have been visible across the globe and progressively worsened over the last 50 years [1]. These changes include rising sea levels and increasing global surface temperature. Current predictive models, including those by IPCC, indicate that the mean annual temperature will rise by between 1 and 5.5 °C along with increasing wind speeds and sea level. For some areas, the sea level is projected to rise by up to 0.9 m by the end of the century. For most Canadian regions, annual precipitation is forecasted to increase by up to 5%. Extreme precipitation is expected to be intensified. Recent news reports have highlighted many of these events such as flash floods, wildfires and other climatic disasters. Some have made major headlines and interrupted many facets of everyday essentials such as British Columbia's record rainfall in November 2021.

These extreme events created unknown level of risk and many challenges for practitioners assessing the health of bridge infrastructure [2]. These risks create challenges in managing the existing portfolio of bridge infrastructure and considering the impact when planning for future infrastructure. There is a need to create a protocol to determine the impact of projected climatic data, specifically temperature, on bridge structural integrity as well as the impact on socioeconomics factors. This paper presents a protocol that can be applied in practice by practitioners to evaluate the risk of projected temperature value of IPCC model, which then is applied through an interdisciplinary approach to assess the structural and socioeconomic impact of projected climate change temperatures. The protocol is applied to a case study in London, Ontario to demonstrate its application and usability.

## 2  Background

Infrastructure is vulnerable to the uncertainty of climate change. Palu and Mahmoud [3] found that there will be a continuous reduction in bridge capacity as the climate warms if no intervention is conducted. Thermal stresses are impacted by the projected increase in temperature, which, according to IPCC models, is determined to continue to increase at an unprecedented rate [4]. As stated by Croce et al. [5], "The frequency of extreme events is continuously evolving, and changes are likely to continue in the future." Climate change will continue to create extreme and frequent climatic events that will need to be considered when assessing the health and safety of existing infrastructure in general and bridges in specific.

The 2016 Canadian infrastructure report card (a report by Canadian construction associations and the Federation of Canadian Municipalities (FCM)) found that 26% of the Canadian bridge inventory was rated fair and less [6], and these are the rating of the current portfolio of bridges without the implication of projected climatic data. Bridges and highways are essential for infrastructural assets that connect communities and are critical to healthy economies. Bridges are particularly vulnerable to extreme climate changes.

A major challenge for policy and decision-makers in planning infrastructure programs is assessing and minimizing the risk and impacts of climate change. One effective way to do this is to ensure that climate change adaptation is considered part of standards, code specifications, existing management, and decision-making processes [7]. There are significant economic implications for bridge vulnerabilities due to climate change. Studies have shown that by the year 2100, it will be less expensive to improve the condition of bridges in early stages of design rather than to respond to a negative impact (or catastrophic event) on a bridge infrastructure [8]. Climate change has both direct and indirect effects on structural assets. It can also impact the socioeconomic health of any community or jurisdiction. Addressing the impact of climate change on bridge assets is critical to the sustainability of our economy, and therefore, creating a protocol to assess the risk due to projected temperature on existing bridge structure is important and a challenging task which this paper will propose a methodology to address.

## 3   Protocol

IPCC's sixth assessment report concluded a high degree possibility of increased global warming level of 1.5 °C over the next ten years. IPCC has developed four projections of climate change scenarios (representative concentration pathways, RCPs) ranging from a very high temperature increase (RCP 8.5) through to a very low increase (RCP 2.6): RCP 8.5, RCP 6.0, RCP 4.5 and RCP 2.6. The impact of these projected values on structural integrity is an important area of research that may change design code [9]. The impact of climate change is experienced significantly in higher-latitude jurisdictions such as Canada [10].

A risk assessment protocol was developed to evaluate the risk of climate change on the existing bridge structure considering projected RCP 6.0 temperature values. The protocol assesses the risk based on structural integrity, by evaluating utilization factor, and socioeconomic impact. The protocol provides an approach that practitioners can apply to identify risk factors and inform decision-makers on the next steps. Figure 1 shows a schematic diagram of the assessment protocol to conduct a risk assessment on an existing bridge structure considering projected temperature values. The protocol is applied to a case study presented in the next section.
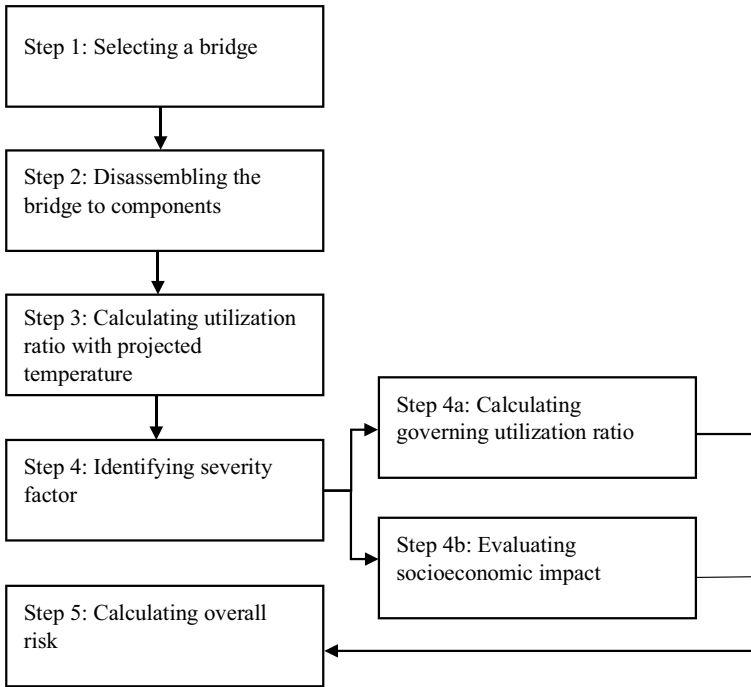
**Fig. 1**  Schematic of risk assessment protocol

## 4    Case Study

The described methodology was applied to a case study to determine the impact of
climate change, specifically temperature projections, on the structural integrity and
socioeconomic impact of an existing bridge.

### 4.1    Selecting a Bridge

The Westminster Drive Underpass, located in London, Ontario, as shown in Fig. 2,
was selected because of its age and condition. A case study by D'Andrea et al. [11]
described the Westminster Drive Underpass original bridge with a 28.8 m single-span
rigid frame bridge, constructed in 1959, comprising three variable depth reinforced
concrete box girders. This flyover structure merged two lanes of Westminster Drive
over four lanes of Highway 401 traffic. The abutments were situated adjacent to the
highway shoulders, within the clear zone, and would not allow for the widening of the
highway. D'Andrea et al. [11] further explained that the Ontario Ministry of Trans-
portation (MTO) identified approximately 40 bridges on Highway 401, primarily
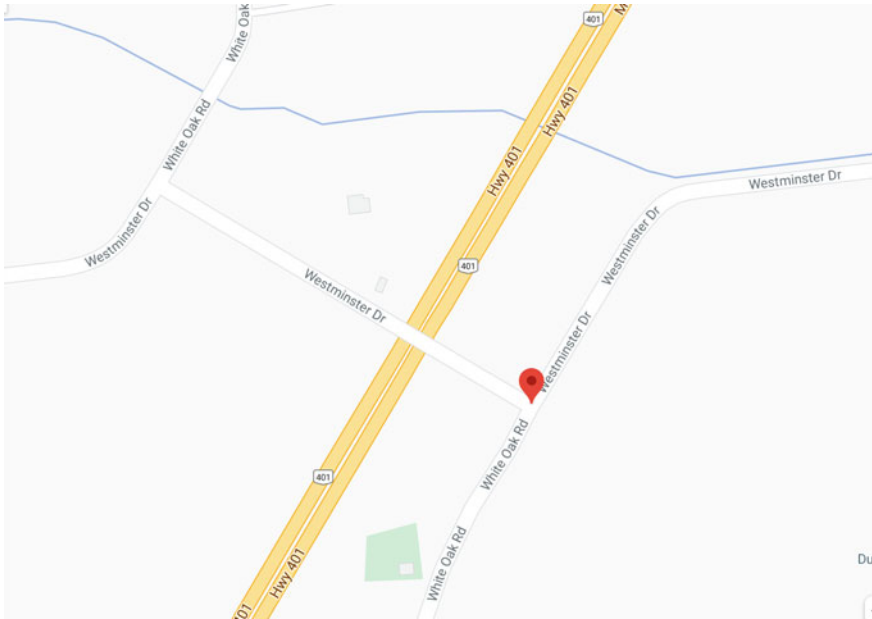
**Fig. 2** Westminster Drive underpass bridge [12]

underpasses, that needed to be replaced in the next 20 years to support the highway. Even though Westminster Drive itself might not have been critical to the surrounding area traffic flow, the underpass was critical to the function of Highway 401. The spans for the new structure will need to accommodate future highway widening by providing full clear zones for an ultimate 8-lane configuration of Highway 401 [11].

In the case study of D'Andrea et al. [11], the replacement was constructed using the get-in-get-out (GiGo) bridge concept. The new structure consisted of a two-span continuous integral abutment bridge with 29.8 m each. This configuration required the pier to be situated in the median. This reference bridge was selected to demonstrate the use of the protocol assessment model on the original bridge design and then again on the replacement structure.

## *4.2 Disassembling the Bridge to All Systems and Components*

Each of the London underpass bridge components is disassembled into its elements, and the impact of temperature on its functionality is identified, as illustrated in Table 1.

**Table 1** Disassembling of the bridge into components

| # | System | Sub-item # | Components | Critical to structure integrity? (Y/N) | Impacted by climate? (Y/N) |
|---|--------|-----------|-----------|---------------------------------------|---------------------------|
| 1 | Superstructure | 1.1 | Cast-in-place slab | Y | Y |
|   |                | 1.2 | Girders | Y | Y |
| 2 | Substructure | 2.1 | Abutment | N | N |
|   |              | 2.2 | Pier (Columns) In this case it is pile | Y | Y |
| 3 | Non-structure | 3.1 | Joints | N | N |
|   |               | 3.2 | Drainage system | N | Y—Indirect |

## *4.3 Calculating Utilization Ratio*

This step involves the calculation of the utilization factor (also known as utilization ratio, U/R) for each component based on design temperature (per code) and projected temperature (based on RCP 6.0). The utilization factor is the ratio between actual performance value and maximum allowable capacity. Therefore, it is:

- Utilization factor of a bridge = performance value/maximum allowable capacity,
- To calculate the bridge U/R, the U/R ratio of each component of the bridge must be calculated, and
- The governing U/R value is the highest across all the components, indicating the highest probability of failure.

The utilization factor for each component using the design temperature and projected temperature values considering climate change model RCP 6.0 is calculated. For the original London underpass reference bridge (one-span bridge), Table 2 shows the utilization factors calculated for the components [13].

**Table 2** Utilization factor of Westminster reference bridge* [13]

| Response | Capacity | Load combination | | | |
|----------|----------|------------------|------|------|------|
|          |          | 1 | | 2 | |
|          |          | UF | UF | UF | UF |
|          |          |    | DT | PT (2050) | PT (2100) |
| Girder positive moment | 13,740 kN·m | 0.77 | 0.837 | 0.85 | 0.86 |
| Girder shear | 4933 kN | 0.29 | 0.29 | 0.29 | 0.29 |
| Pile moment | 502 kN·m | 0.72 | 0.97 | 0.99 | 1 |
| Pile shear | 4800 kN | 0.075 | 0.1 | 0.11 | 0.12 |

*DT: design temperature; PT: projected temperature (based on RCP 6.0 models); and UF: Utilization factor

**Table 3** Utilization factor of Westminster reference bridge [13]

| # | System | Sub-item # | Components | Critical to structure integrity? (Y/N) | Impacted by climate? (Y/N) | Utilization factor |
|---|--------|-----------|------------|--------------------------------|---------------------------|-------------------|
| 1 | Superstructure | 1.1 | Cast-in-place slab | Y | Y | Non relevant |
|   |        | 1.2 | Girders | Y | Y | Moment: LC PT (2100): 0.86 Shear: LC PT (2100): 0.29 |
| 2 | Substructure | 2.1 | Abutment | N | N | Non relevant |
|   |        | 2.2 | Pier (Columns) In this case it is pile | Y | Y | Moment: LC PT (2100): 1.00 Shear: LC PT (2100): 0.12 |
| 3 | Non-structure | 3.1 | Joints | N | N | Non relevant UF as the impact is indirect |
|   |        | 3.2 | Drainage system | N | Y—Indirect | Non relevant UF as the impact is indirect |

The original Westminster Drive Underpass 1-span bridge (original bridge) capacity was calculated using the 300 MPa for steel yield strength and 20 MPa for concrete compressive strength. From Table 2, the load combination utilization factor is most relevant because of the impact of temperature factor based on design and projected climate change. More specifically, the projected temperature (PT) for the year 2100 will be used to determine the impact of climate change on the overall bridge infrastructure risk, as shown Table 3.

## 4.4 Identifying Severity Factor

The severity factor is calculated by determining (1) governing utilization factor and (2) socioeconomic impact. Once the severity factor is determined, the risk can be calculated.

### 4.4.1    Determining the Governing Utilization Factor

The governing utilization factor as an input to the assessment protocol is obtained from Table 3. The following utilization factors were calculated for the Westminster Drive Underpass original 1-span bridge. These results [13] were used to determine the maximum utilization factors:

- For the superstructure, the UF for the moment was 0.86, and the UF for the shear was 0.29. The higher utilization factor of 0.86 was used.
- For the substructure, the UF for the moment was 1.00, and the UF for the shear was 0.12. The higher utilization factor of 1.00 was used.
- For the non-structure, there was no UF calculated, and the impact was considered on an indirect basis only.

From the calculated utilization factors, the maximum utilization level is selected to be the overall governing utilization factor for the original 1-span Westminster Drive Underpass bridge. Therefore, the input to the protocol will be 1.00 calculated based on the projected temperature (in the year 2100) because of the impact on the flexure moment capacity on the substructure, i.e., UF PT(2100).

### 4.4.2    Assessing the Socioeconomic Impact

The assessment protocol outlines the following criteria:

- How long and how significant was the interruption to do the re-work? From the MTO reports, the work required complete rehabilitation and re-building of the underpass. This was a significant out-of-service-time for more than ten days. However, it was also clear that the underpass re-build was performed to support the future expansion of Highway 401. It was necessary to support the future needs of the surrounding community infrastructure; however, the rehabilitation re-work did not stop services and goods from reaching the area as there are alternate routes to access the community.
- How much impact did it have on the surrounding ecosystem? There were no reports of damage to the surrounding ecosystem, either temporarily or permanently.
- How significant was the interruption to do the re-work? Even though the re-build was done using the GiGo method, it did interrupt the current underpass; however, other alternative means of access were available to the community.

Therefore, based on the scoring criteria, summarized in Table 4, a score of 2 was achieved on the socioeconomic factor, resulting in a medium impact score. The factors that resulted in a score of 2 are:

- Time-out-of-service $\geq$ 10 days,
- Major interruption to service with high cost for the workaround,
- Alternative structures are available,
- Non-permanent damage to the surrounding ecosystem, and

- Partial re-build of structure is required.

Similarly, a score of 3 was achieved for the utilization factor, due to a U/R score of 1.00 calculated above, resulting in a high impact on this factor.

**Table 4** Severity factor

| Socioeconomic factor | Rating (A) | Utilization factor | Rating (B) |
|---|---|---|---|
| Complete termination of service for undefined time period<br>Time-out-of-service $\geq$ 10 days<br>Significant damage to surrounding ecosystem that have a permanent impact<br>Complete re-build of structure is required | High (3) | Totally and permanent damage to the system and fails to satisfy design limit<br>Utilization factor $\geq$ 100% | High (3) |
| Major interruption to service with significant cost for work around<br>Time-out-of-service < 10 days<br>Alternative structures are available<br>None-permanent damage to surrounding ecosystem<br>Partial re-build of structure is required | Medium (2) | Significantly reduces the effectiveness of the system such that it would fail to satisfy the design requirements. However, the system would still operate<br>90% $\leq$ Utilization factor < 100% | Medium (2) |
| Some interruption to service with workaround options available<br>Little damage to surrounding ecosystem that can be cleaned up<br>No re-build of structure is required<br>No Time-out-of-service | Low (1) | Reduces effectiveness, design requirements would still be satisfied<br>Utilization factor < 90% | Low (1) |

### *4.5   Calculating the Risk*

In this step, the overall risk due to climate change is calculated as follows:

$$\text{Risk} = \text{Severity Factor} \times \text{Occurrence of Failure} \tag{1}$$

Because the original Westminster Drive Underpass bridge was already determined to be replaced based on age and condition, the assessment would be a high score on the occurrence of failure. The completed assessment is shown in Table 5, which gives an overall rating of 8. This result confirms that the Westminster Drive Underpass is in the critical risk level category. This result was determined based on the projected temperature (2100) on load combination 2 of the original Westminster Drive Underpass bridge (1-span) on the substructure (pile).

### *4.6   Discussion on Case Study*

As the assessment protocol concluded a high-risk rating score of 8 for the original 1-span bridge, the Westminster Drive Underpass bridge would be classified as critical for re-building. Further analysis was conducted on the re-build of the 2-span underpass bridge, and the following utilization factors were determined, as shown in Table 6. The utilization factor decreased significantly on the pile moment from 1.00 to 0.8, which was used in the protocol for the 1-span bridge. When the new bridge was re-assessed using the presented protocol, the new 2-span bridge received a score of 6 (reduction of 2 points from the original 1-span bridge). This confirmed a lower risk level and ensured that the re-build of the bridge was effective. This further demonstrates that the model effectively predicted the need to intervene due to the critical level of integrity of the original 1-span bridge.

## 5   Summary

This paper presented a multidisciplinary approach to assessing climate change risk on existing bridge structures. The methodology is applied to a case study to demonstrate the application and ease of adaption in practice to provide a tool to practitioners. Further, in collaboration with the National Research Council of Canada, this methodology informs the impact of climate change on future design code requirements when considering projected climatic data as presented in RCP 6.0 models.

**Table 5** Risk evaluation

| # | Severity factor | | | | Occurrence of failure | | | Overall rating | |
|---|---|---|---|---|---|---|---|---|---|
| | Socioeconomic factor | Rating (A) | Utilization factor | Rating (B) | Definition | Probability | Rating (C) | Definition | Rating (A, B, C) |
| 1 | Termination of service for undefined time period Time-out-of-service ≥ 10 days Significant damage to surrounding ecosystem that have a permanent impact Complete re-build of structure is required | High (3) | Totally and permanent damage to the system and fails to satisfy design limit Utilization Factor ≥ 100% | High (3) | Highly likely for the severity to occur | Probability ≥ 65% | High (3) | Critical level of risk due to climate change Requires immediate intervention and significant resources | 6 < Rating ≤ 9 |
| 2 | Major interruption to service with significant cost for work around Time-out-of-service < 10 days Alternative structures are available None-permanent damage to surrounding ecosystem Partial re-build of structure is required | Medium (2) | Significantly reduces the effectiveness of the system such that it would fail to satisfy the design requirements. However, the system would still operate 90% ≤ Utilization Factor < 100% | Medium (2) | Likely/Possible for the severity to occur | 35% ≤ Probability < 65% | Medium (2) | Moderate level of risk due to climate change Requires planning for intervention | 3 < Rating ≤ 6 |

(continued)

**Table 5** (continued)

| # | Severity factor | | | Occurrence of failure | | | Overall rating | | |
|---|---|---|---|---|---|---|---|---|---|
| | Socioeconomic factor | Rating (A) | Utilization factor | Rating (B) | Definition | Probability | Rating (C) | Definition | Rating (A, B, C) |
| 3 | Some interruption to service with workaround options available Little damage to surrounding ecosystem that can be cleaned up No re-build of structure is required No time-out-of-service | Low (1) | Reduces effectiveness, design requirements would still be satisfied Utilization factor < 90% | Low (1) | Unlikely for the severity to occur | Probability < 35% | Low (1) | Insignificant level of risk, likely manageable through preventative maintenance programs | Rating ≤ 3 |

**Table 6** Utilization factor for 2-span bridge

| Response | Capacity | Load combination | | | |
|---|---|---|---|---|---|
| | | 1 | | 2 | |
| | | UF | UF | UF | UF |
| | | | DT | PT (2050) | PT (2100) |
| Girder positive moment | 17,950 kN·m | 0.28 | 0.42 | 0.43 | 0.44 |
| Girder negative moment | 13,420 kN·m | 0.56 | 0.67 | 0.7 | 0.72 |
| Girder shear | 5750 kN | 0.28 | 0.3 | 0.305 | 0.31 |
| Pile moment | 574 kN·m | 0.46 | 0.72 | 0.77 | 0.81 |
| Pile shear | 4800 kN | 0.06 | 0.12 | 0.125 | 0.13 |

[*]350 MPa for steel yield strength and 30 MPa for concrete compressive strength

# References

1. IPCC (2021) Climate change widespread, rapid, and intensifying. Intergovernmental Panel on Climate Change, 9 Aug 2021. Retrieved 15 Nov 2021, from https://www.ipcc.ch/reports/
2. Nasr A, Kjellström E, Björnsson I, Honfi D, Ivanov OL, Johansson J (2020) Bridges in a changing climate: a study of the potential impacts of climate change on bridges and their possible adaptations. Struct Infrastruct Eng 16(4):738–749. https://doi.org/10.1080/15732479.2019.1670215
3. Palu S, Mahmoud H (2019) Impact of climate change on the integrity of the superstructure of deteriorated U.S. bridges. PLoS One 14(10). https://doi.org/10.1371/journal.pone.0223307
4. Wu D, Deng X, Mao J, Mao W, Ye Y, Bi X (2007) Macro-and microstructures of heavy fogs and visibility in the Dayaoshan expressway. J Meteorol Res 21:342–352. https://doi.org/10.1007/s00376-018-8017-6
5. Croce P, Formichi P, Landi F (2019) Climate change: impacts on climatic actions and structural reliability. Appl Sci 9(24):5416. https://doi.org/10.3390/app9245416
6. Hajializadeh D, OBrien E, O'Connor A (2017) Virtual structural health monitoring and remaining life prediction of steel bridges. Can J Civ Eng 44(4):264–273. https://doi.org/10.1139/cjce-2016-0286
7. CSA Group (2018) Retrieved 15 Nov 2021, from Bridging the gap in climate policy. https://www.csagroup.org/article/bridging-the-gap-in-climate-policy/
8. Neumann JE, Price J, Chinowsky P, Wright L, Ludwig L, Richard S, Jones R, Smith J, Perkins W, Jantarasami L, Martinich J (2015) Climate change risks to US infrastructure: impacts on roads, bridges, coastal development, and urban drainage. Clim Change 131:97–109. https://doi.org/10.1007/s10584-013-1037-4
9. IPCC (2013) Climate change 2013: the physical science basis-contribution of Working Group I to the fifth assessment report of the Intergovernmental Panel on Climate Change. Cambridge and New York: Cambridge University Press. Retrieved 15 Nov 2021, from https://www.ipcc.ch/reports/
10. Larsen PH, Goldsmith S, Smith O, Wilson ML, Strzepek K, Chinowsky P, Saylor B (2008) Estimating future costs for Alaska public infrastructure at risk from climate change. Glob Environ Chang 18(3):442–457. https://doi.org/10.1016/j.gloenvcha.2008.03.005

11. D'Andrea M, Young W, Turnbull A (2016) Westminster Drive Underpass—accelerated bridge construction using GIGO (get in-get out) bridge concept. In: Resilient Infrastructure—Proceedings of the 2016 Canadian Society for Civil Engineering (CSCE) Annual Conference (CSCE 2016), STR-847-1 to STR-847-10
12. Google Maps (2021) Westminster Drive Underpass Bridge, Ontario, Canada. Accessed 15 Nov 2021
13. Amleh L, Husain L, Othman H, Altamimi S, Nassar M, Hassan M, Alfaseeh L (2021) Methodologies and guidelines for design and evaluation of highway bridges in a changing climate. Final technical report. National Research Council of Canada, Ottawa, Canada

# Materials Specialty: Advanced Composite Materials and Technology

# Rheological Properties of Geopolymer Mortars Incorporating Construction and Demolition Wastes-Based Binders and Aggregates

**Obaid Mahmoodi, Hocine Siad, Mohamed Lachemi, Sina Dadsetan, and Mustafa Sahmaran**

**Abstract** The re-utilization of construction and demolition wastes (CDWs) in the emerging geopolymer technology has been recognized as an environmentally friendly solution for tackling the ecological challenges caused by the increased landfilling of CDWs and sustainability issues of Portland Cement (PC) production. Geopolymers are synthesized as a result of intricate chemical interactions between aluminosilicate-based precursors and highly alkaline solutions resulting in the production of amorphous inorganic geopolymers possessing three-dimensional cross-linked networks of Si–O–Al and Si–O–Si bonds. The aim of this study is to investigate the effect of incorporating different types of aggregates including recycled concrete aggregates sand (RAS), silica sand (SS) and natural sand (NS) on the rheological properties of geopolymer mortars (GPM) prepared from CDW-materials comprising a combined powder mixture of recycled clay brick (RCB), recycled ceramic tile (RCT) and recycled concrete (RCW) wastes as silico-aluminate binders. Yield stress, viscosity and shear stress were tested at 100% of RAS, SS and NS contents in GPMs prepared with sodium silicate and sodium hydroxide solutions as alkaline reagents and predefined chemical design factors of $SiO_2/Al_2O_3$, $Na_2O/SiO_2$, $H_2O/Na_2O$ and water-to-binder (W/B) ratios. The correlation between the rheological properties of GPMs and the predefined design parameters was considered. The highest yield stress and viscosity were obtained at medium $SiO_2/Al_2O_3$ molar ratio of 5.6 for all three GPM systems, while further increase in silicate species caused reduced stresses and viscosities. Comparable shear thinning behavior, higher viscosity and accelerated polycondensation properties were observed with increased RAS amounts compared to SS and NS.

O. Mahmoodi (✉) · H. Siad · M. Lachemi · S. Dadsetan
Department of Civil Engineering, Toronto Metropolitan University, Toronto, ON M5B 2K3, Canada
e-mail: omahmoodi@torontomu.ca

M. Sahmaran
Department of Civil Engineering, Hacettepe University, Ankara, Turkey

## 1 Introduction

The generation of construction and demolition wastes (CDWs) has been steadily
increasing worldwide owing to intensified infrastructure activities and urbanization
as rural areas are increasingly integrated into urban zones. An estimated 7–10 billion
tons of CDWs are generated globally every year accounting for about one-third of
the total global solid waste streams [24]. CDWs in Canada constitute up to 40% of
solid waste streams, of which only 20% is recycled [28], though developing countries
recycle less than 5% of the produced CDWs; more than 85% of CDWs ends up in
landfills and unlicensed waste sites [25] causing substantial ecological, economic
and health concerns. Recycled clay brick (RCB), recycled ceramic tile (RCT) and
recycled concrete (RCW) wastes constitute more than 90% of CDWs [22]. RCW
is of greater importance, given the fact that it accounts for almost 40–50% of total
CDWs output [3, 17]. Meanwhile, the construction sector contributes significantly to
global warming and greenhouse gas (GHG) emissions; it also consumes substantial
amounts of natural resources, consuming approximately 9 billion tons of aggregates
and 5 billion tons of Portland Cement (PC) [20] amounting to 626 kg of PC per capita,
which is projected to increase by 4% annually accumulating to more than 200% by
2050 [16, 26]. PC production is an energy-intensive process, approximately 4 GJ of
energy and 1.5 tons of raw materials are consumed to produce 1 ton of PC, in fact
the PC industry is responsible for around 8–15% of global anthropogenic $CO_2$ emis-
sions [21]. In the coming years, the combined effects of increased PC production
and excess CDWs will exacerbate $CO_2$ emissions and global warming potential of
the concrete industry. Hence, recent efforts to reduce global warming emissions and
mitigate climate change are leading to innovative research trends that explore alterna-
tives to PC-based concrete and recycling of CDWs in circular economy. Geopolymers
have emerged as the most promising sustainable alternative to PC due to their low
$CO_2$ footprint and energy requirements. Geopolymer production can reduce $CO_2$
emissions by up to 80% while requiring 60% less energy than PC [16]. Geopoly-
mers or inorganic Polysialates are produced from aluminosilicate precursor mate-
rials possessing amorphous to semi-crystalline microstructures [7]. Silico-aluminates
from solid precursor sources chemically react with alkaline hydroxide and silicates
to form a three-dimensional (3D) alkali aluminosilicate network, in which silica and
alumina tetrahedrals are connected by covalent Al–O–Al, Si–O–Al and Si–O–Si
bonds.

Researchers have conducted extensive research on geopolymeric materials in
recent years, which has helped improve our understanding of the geopolymerization
process. Indeed, chemical parameters such as $SiO_2/Al_2O_3$, $Na_2O/SiO_2$ (or $Na_2O/Al_2O_3$), $SiO_2/Na_2O$, $H_2O/Na_2O$, $Na_2O\%$ and liquids-to-solids (W/B) ratios have
been employed for the design and optimization of mechanical and microstructural

properties of various types of geopolymeric materials [11–14, 16]. Nonetheless, the rheological properties of geopolymers incorporating CDWs both as binders and aggregates are rarely explored in the current literature, indeed research studies on the assessment of the influence of chemical parameters such as $SiO_2/Al_2O_3$, $Na_2O/SiO_2$, $SiO_2/Na_2O$, $H_2O/Na$ and W/B ratios on the rheological characteristics of CDW-based geopolymers are non-existent. Rheology can characterize the flow of freshly mixed materials including workability loss, pumpability and compaction under varying shear rates and stresses. Metakaolin-based geopolymer pastes have been characterized as Newtonian fluids, where viscosity is controlled by the suspending alkaline silicate solution, rather than by the direct colloidal contact between the precursor particles [9]. Yet, other researchers have demonstrated that geopolymers are in fact suspended liquid–solid dispersion systems and reported the influential effects of interparticle colloidal and inertial contacts as well as viscous interaction between particles and alkaline reagents on the rheological properties of geopolymers [4, 6]. Indeed, Sitarz et al. [23] showed that geopolymer mortars (GPMs) are non-Newtonian pseudoplastic suspension systems demonstrating shear thinning behavior. Thus, the composition of alkaline reagents as well as the solubility of the elemental oxides in precursors play a significant role in determining the rheological properties of fresh GPMs. Accordingly, investigation of the influence of chemical design parameters such as $SiO_2/Al_2O_3$, $Na_2O/SiO_2$, $SiO_2/Na_2O$, $H_2O/Na$ and W/B ratios could provide vital information about the rheological properties of CDW-based GPMs.

Therefore, this study investigated the correlation between predefined $SiO_2/Al_2O_3$, $Na_2O/SiO_2$, $H_2O/Na$ and W/B ratios and the type of fine aggregates on the fresh state rheological properties including plastic viscosity, shear stress, yield stress and stress–strain relationship of CDW-based GPMs. An algorithmic mixture design procedure of specific precursor percentages, $SiO_2/Al_2O_3$ and $Na_2O/SiO_2$ ratios was employed to develop geopolymer mortar systems comprised of recycled clay brick (RCB), recycled ceramic tile (RCT) and recycled concrete (RCW) wastes and metakaolin (MK) as silico-aluminate binders in binary, ternary and quaternary arrangements with 100% recycled aggregate sand (RAS), silica sand (SS) and natural sand (NS) as fine aggregates.

## 2  Experimental Work

### 2.1  Materials

CDW-based materials including recycled clay brick (RCB), recycled ceramic tile (RCT) and recycled concrete (RCW) wastes were used as silico-aluminate binders along with metakaolin (MK) as supplementary cementitious material (SCM) while recycled aggregate sand (RAS), silica sand and natural sand (NS) were used as fine aggregates. The CDW-based materials were obtained from a CDW sorting site in Toronto, Canada. The raw CDWs were crushed, pulverized and sieved on a 75 µm

sieve while RAS was obtained using a jaw crusher to conform to grading requirement of [2] while the median particle sizes for precursor powders were determined to be 19.9, 15.5, 15.1 and 4.5 $\mu$m, respectively, as shown in Fig. 1. The chemical compositions of RCB, RCT and RCW precursors as determined by X-ray fluorescence (XRF) are presented in Table 1. The specific gravities RCB, RCT, RCW and MK precursor powders were measured as 2.69, 2.87, 2.71 and 2.40 g/cm$^3$, respectively, conforming to [1]. The alkaline reagents utilized in this study were sodium silicate and sodium hydroxide. Sodium silicate was industrial grade reagent solution with 28.7 wt.% SiO$_2$ and 8.9 wt.% Na$_2$O and silica modulus of 3.22, while NaOH pellets were with 97% purity before being dissolved in distilled water. ViscoCrete 1000 was utilized as a high range water reducing admixture (HRWRA), a polycarboxylate-based SP produced by Sika with an approximate solid concentration of 40% and a specific gravity of 1.06 g/cm$^3$ to produce high plasticity and enhance slump retention.
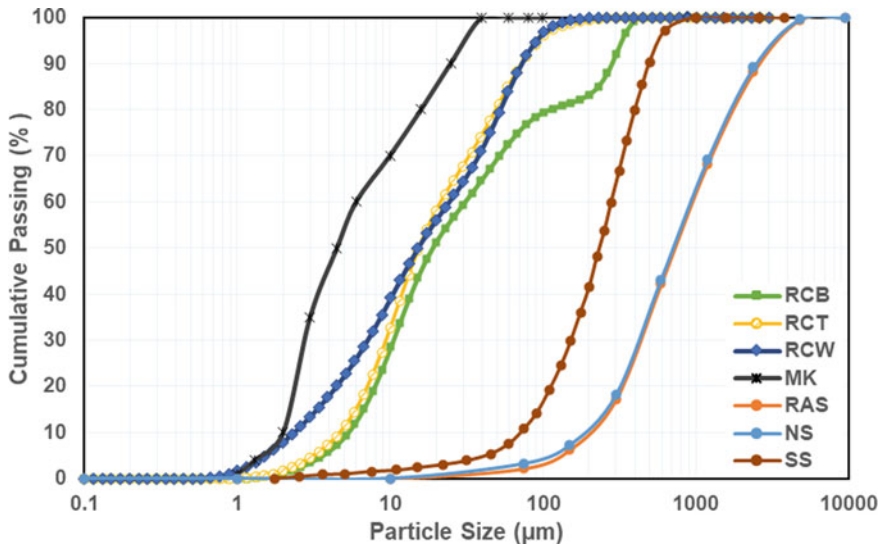


**Fig. 1** Particle size distributions of RCB, RCT, RCW and MK precursors and RAS, SS and NS fine aggregates

**Table 1** Elemental oxide compositions (wt.%) of RCB, RCT, RCW and MK by XRF analysis

| Chemical component | SiO$_2$ | Al$_2$O$_3$ | Fe$_2$O$_3$ | MgO | CaO | Na$_2$O | K$_2$O | Loss on ignition (LOI) | Specific gravity (g/cm$^3$) |
|---|---|---|---|---|---|---|---|---|---|
| RCB | 60.31 | 15.61 | 7.72 | 3.05 | 5.6 | 0.56 | 4.48 | 0.41 | 2.69 |
| RCT | 61.22 | 10.33 | 1.01 | 17.63 | 6.01 | 0.27 | 0.75 | 0.3 | 2.87 |
| RCW | 23.81 | 4.16 | 1.96 | 8.41 | 30.33 | 0.60 | 0.67 | 9.6 | 2.71 |
| MK | 55.74 | 38.07 | 1.84 | 0.03 | 0.18 | 0.02 | 0.27 | 1.17 | 2.40 |

## 2.2 Mixture Design Method and Composition of GPMs

The proportioning of CDW-based geopolymer mortars was initially based on calculating the $SiO_2/Al_2O_3$ and $Na_2O/SiO_2$ molar ratios in precursor powders determined by XRF analysis, followed by targeting specific chemical parameters in the total GPM system at a constant W/B ratio of 0.32. A similar binder to fine aggregate ratio of 1:2.50 was selected for all GPM systems when the desired fluidity was obtained based on a preliminary study where binder to aggregate ratios of 1:2.50, 1:2.75 and 1:30 (authors' preliminary research) were extensively investigated. The dosage of high range water reducing (HRWRA) superplasticizer (SP) manufactured by Sika (ViscoCrete 1000) was added at a constant 1% of the binder weight as higher SP content proved to negatively affect the mechanical properties of GPMs. A total of 9 compositions were synthesized in this study where RAS, SS and NS were used as fine aggregates for comparison purposes, having five compositions each with varying molar ratio of $SiO_2/Al_2O_3$ ranging from 5.3 to 5.7, while molar ratio of $Na_2O/SiO_2$ was kept constant at 0.18; the same ranges of $SiO_2/Al_2O_3$, $Na_2O/SiO_2$ and W/B were used for GPMs containing different fine aggregates. In Fig. 2, the sequential algorithmic mix design procedure used for estimating the amounts of different precursors, fine aggregates, alkaline solutions and water to reach the targeted $SiO_2/Al_2O_3$, $Na_2O/SiO_2$ and W/B is summarized. Table 2 presents the mixture proportions of GPM systems, where chemical factors of $SiO_2/Al_2O_3$ and $Na_2O/SiO_2$ are nominal molar ratios representing synthesis parameters of the whole GPM system rather than reactive components. In addition to the pre-targeted parameters, $H_2O/Na_2O$ and $Na_2O\%$ are also reported in Table 2. The synthesized GPMs were denoted based on the type of CDW precursor and values of $SiO_2/Al_2O_3$, $Na_2O/SiO_2$ and W/B ratios and type of incorporated fine aggregate. For example, BCMK-5.3-0.18-0.32-30MK-RAS denotes a GPM composition prepared with $SiO_2/Al_2O_3 = 5.3$, $Na_2O/SiO_2 = 0.18$, W/B $= 0.32$ containing 30% MK as precursor and 100% recycled aggregate sand as fine aggregate type.

## 2.3 Experimental Methodology and Rheological Characteristics

The geopolymer mortars were synthesized in a mixer with 10-L capacity. In the first step, the NaOH solid flakes were dissolved in distilled water and allowed to cool for 24 h to exhaust exothermic heat generated during dissolution of NaOH flakes followed by being mixed with the required $Na_2SiO_3$ solution and stirred for around 15 min and let cool for another 3 h before being mixed with dry precursors and fine aggregate. Dry precursors and fine aggregate were initially mixed at the lowest mixing speed for 1 min followed by being mixed with alkaline solution for another minute at the same speed, and the blending speed was steadily increased every 1 min until the completion of the mixing process at 5 min. The fresh GPMs were then tested for
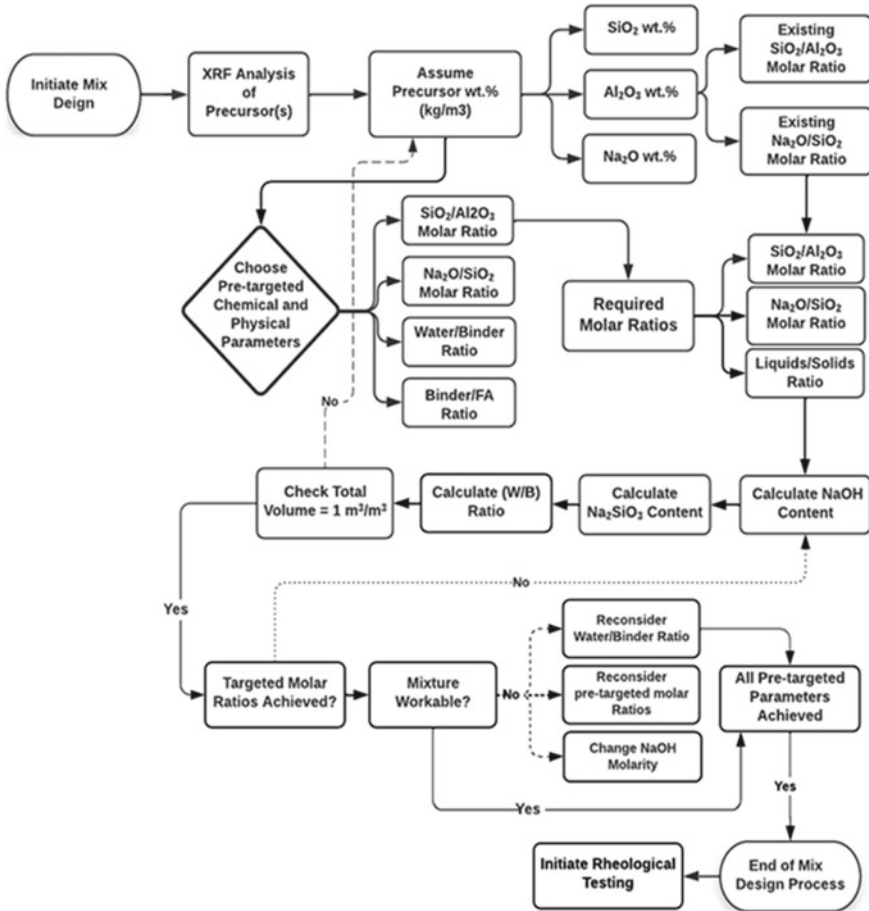
**Fig. 2** Flowchart and algorithmic mix design sequence

rheological characteristics including yield stress, plastic viscosity, stress–strain relations, and time-dependent viscosity were investigated using Brookfield's rotational DV3TRV rheometer. The yield test was conducted using V-73 vane spindle rotating at a speed of 3.5 RPM shear rate while viscosity measurements were made with RV-6 spindle with a hysteresis loop rotation where the rotation of the spindle was steadily increased from 0.5 to 200 RPMs in the up ramp phase and then steadily reduced from 200 to 0.5 RPMs in the down ramp phase, both spindles were immersed up to primary immersion mark in GPM located on the spindle shaft. The corresponding step-up method-based shear rates (sec$^{-1}$) program comprising ramp-up and ramp-down phases is shown in Fig. 3. The shear rate protocol employed in this study was similar to those described in earlier studies on geopolymeric materials, as these shear rates are proven to be suitable for precisely simulating gravity-induced flow of geopolymeric materials [6, 10]. For the assessment of time-dependent viscosity

**Table 2** Mixture proportions of geopolymer mortars (kg/m³)

| Matrix composition | | | | | | | | | | Fine aggregate | | | Na₂SiO₃ | NaOH | H₂O | SP | Synthesis parameters | | |
|---|---|---|---|---|---|---|---|---|---|---|---|---|---|---|---|---|---|---|---|
| Composition code | Precursor (%) | | | | Mix proportions (kg/m³) | | | | | | | | | | | | | | |
| | RCB | RCT | RCW | MK | RCB | RCT | RCW | MK | | RAS | SS | NS | | | | | $H_2O/Na_2O$ | $Na_2O\%$ | W/B |
| BCTMK-5.7-0.18-0.32-30MK-RAS | 10 | 30 | 30 | 30 | 49.40 | 148.20 | 148.20 | 148.20 | | 1236 | 0 | 0 | 153.70 | 116.36 | 99.00 | 4.94 | 17.99 | 5.25 | 0.32 |
| TCMK-5.6-0.18-0.32-30MK-RAS | 0 | 25 | 45 | 30 | 0.00 | 123.50 | 222.30 | 148.20 | | 1234 | 0 | 0 | 182.26 | 97.01 | 94.00 | 4.94 | 19.27 | 4.90 | 0.32 |
| BCMK-5.3-0.18-0.32-30MK-RAS | 25 | 0 | 45 | 30 | 123.25 | 0.00 | 221.85 | 147.90 | | 1232 | 0 | 0 | 192.34 | 93.87 | 89.00 | 4.93 | 19.11 | 4.94 | 0.32 |
| BCTMK-5.7-0.18-0.32-30MK-SS | 10 | 30 | 30 | 30 | 54.30 | 162.90 | 162.90 | 162.90 | | 0 | 1357 | 0 | 168.95 | 127.91 | 43.00 | 5.43 | 14.06 | 5.20 | 0.32 |
| TCMK-5.6-0.18-0.32-30MK-SS | 0 | 25 | 45 | 30 | 0.00 | 135.75 | 244.35 | 162.90 | | 0 | 1355 | 0 | 200.34 | 106.63 | 38.00 | 5.43 | 15.09 | 4.90 | 0.32 |
| BCMK-5.3-0.18-0.32-30MK-SS | 25 | 0 | 45 | 30 | 135.25 | 0.00 | 243.45 | 162.30 | | 0 | 1353 | 0 | 211.10 | 103.01 | 33.00 | 5.41 | 14.94 | 4.94 | 0.32 |
| BCTMK-5.7-0.18-0.32-30MK-NS | 10 | 30 | 30 | 30 | 54.15 | 162.45 | 162.45 | 162.45 | | 0 | 0 | 1353 | 168.48 | 127.55 | 51.00 | 5.42 | 15.55 | 5.14 | 0.32 |
| TCMK-5.6-0.18-0.32-30MK-NS | 0 | 25 | 45 | 30 | 0.00 | 135.00 | 243.00 | 162.00 | | 0 | 0 | 1350 | 199.23 | 106.04 | 49.00 | 5.40 | 15.81 | 4.90 | 0.32 |
| BCMK-5.3-0.18-0.32-30MK-NS | 25 | 0 | 45 | 30 | 134.00 | 0.00 | 242.10 | 161.40 | | 0 | 0 | 1345 | 209.89 | 102.44 | 44.00 | 5.38 | 15.70 | 4.94 | 0.32 |
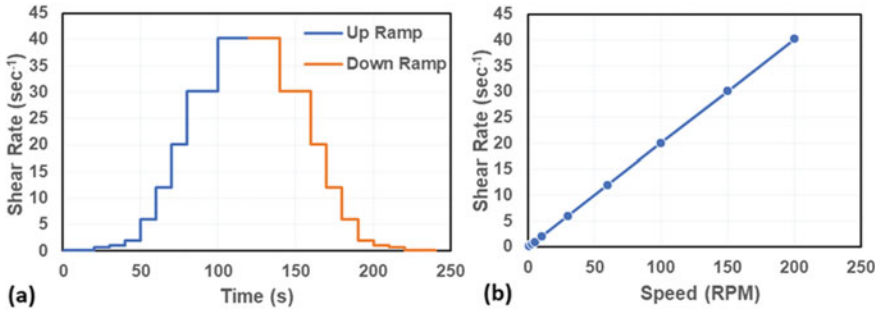
**Fig. 3** **a** Applied shear rate loop protocol and **b** shear rate versus speed relationship

behavior, the same step-up shear protocol was administered at 1 and 30 min. The rheometer data collection was set up as multipoint averaging form where data was collected every 5 s and averaged every 10 s. A modified Bingham mathematical model shown in Eq. (1) was used to analyze data and the relationship between shear rate, shear stress and viscosity values was calculated according to [18]. Meanwhile, in order to understand the influence of chemical factors and the effect of different precursors and fine aggregates on the fresh rheological properties of GPMs, the rheological data were fitted using modified Bingham model.

$$\tau = \tau_0 + \mu\dot{\gamma} + C\dot{\gamma}^2, \tag{1}$$

where $\tau$ is shear stress (Pa), $\tau_0$ is yield stress (Pa), $\mu$ is plastic viscosity (Pa s), $\dot{\gamma}$ is shear rate (1/s) and $C$ is a second order parameter (Pa s$^2$).

The shear stress was calculated according to Eq. (2) as follows:

$$\tau_i = k_{\alpha\tau}\alpha_i, \tag{2}$$

where $k_{\alpha\tau}$ is a torque conversion factor for spindle used in the test as provided in [18], $\alpha_i$ is the scale deflection on the torque dial.

The flow index ($n$) can be determined from the $\log \tau_i - \log N_i$ using power-law graphing tool, where $N_i$ is the rotational speed in RPM.

The corresponding shear rate $\gamma_i$ values can be calculated from Eq. (3) as follows:

$$\gamma_i = k_{N_\gamma}(n)Ni. \tag{3}$$

All rheological measurements were conducted with a delay of 1 min after completion of the mixing process. A standard 600 ml low-form Griffin graduated beaker was used for all rheological testing.

# 3  Results and Discussion

## 3.1  Viscosity and Shear Stress of GPMs

Shear stress versus shear rate and viscosity versus shear rate of GPMs containing 100% natural sand (NS), 100% silica sand (SS) and 100% recycled aggregate sand (RAS) as fine aggregates are shown in Figs. 4, 5 and 6, respectively. The applied share rate ranged from 0.1006 to 42.24 (sec$^{-1}$) characterizing a greater level of structural destruction of GPMs at the peak shear rate and preventing the structural molecules to assemble back together [6]. All compositions exhibited shear thinning behavior in which viscosity decreases with the increased applied shear rate as seen in Fig. 4c and d at 1 and 30 min after mixing, the same is true for SS (Fig. 5) and RAS-based (Fig. 6) GPMs at the same testing intervals. It was observed that the rheology of GPM mortars is highly influenced by the chemical design parameters employed in this study including $SiO_2/Al_2O_3$ and $Na_2O/SiO_2$ as well as $H_2O/Na_2O$. In addition, the concentrations of CDW-based precursors that directly correlates to the $SiO_2/Al_2O_3$ and $Na_2O/SiO_2$ molar ratios and the type of fine aggregate were influential in controlling the rheological behavior of GPMs.
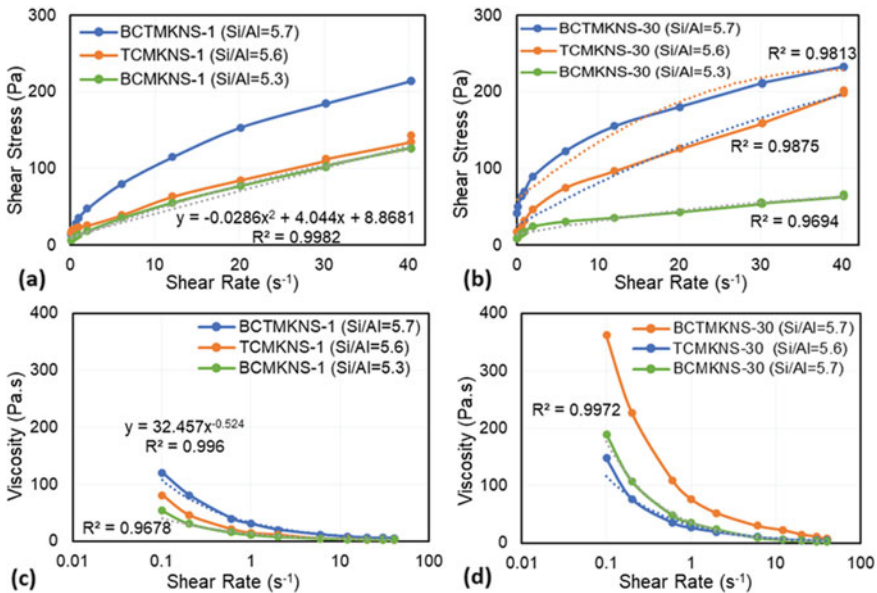


**Fig. 4** Shear stress and viscosity versus shear rate of GPM incorporating 100% natural sand **a** shear stress versus shear rate at 1 min **b** shear stress versus shear rate at 30 min **c** viscosity versus shear rate at 1 min and **d** viscosity versus shear rate at 30 min
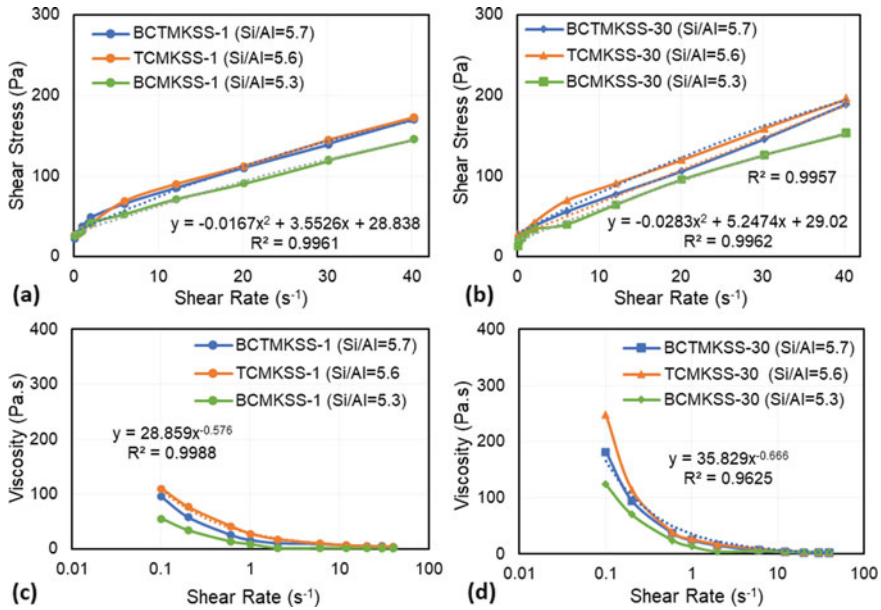
**Fig. 5** Shear stress and viscosity versus shear rate of GPM incorporating 100% silica sand **a** shear stress versus shear rate at 1 min **b** shear stress versus shear rate at 30 min **c** viscosity versus shear rate at 1 min and **d** viscosity versus shear rate at 30 min

### 3.1.1 GPMs Incorporating Natural Sand

As seen in Fig. 4, the increased shear rate resulted in decreased viscosity of 100% natural sand-based GPMs indicating a pseudoplastic or shear thinning behavior which signifies a higher fluidity or flow level at increased shear stresses. The chemical design parameters highly influenced the rheological behavior of the GPMs both at 1 and 30 min post mixing. At a constant $Na_2O/SiO_2 = 0.18$ and water-to-binder (W/B) ratio of 0.32, the viscosity increased with increasing $SiO_2/Al_2O_3$ molar ratio as seen in Fig. 4c and d, which indicates a reduced flow tendency at higher $SiO_2/Al_2O_3$ molar ratio. For example, 1 min after mixing, at a constant $Na_2O/SiO_2 = 0.18$ and at the same shear rate of $0.1 \, s^{-1}$, viscosity and shear stress increased from 54 to 120 Pa s and 19.30 to 47.70 (Pa), respectively, when $SiO_2/Al_2O_3$ molar ratio was increased from 5.3 to 5.7. The enhanced viscosity and shear stress can be ascribed to the increased silicate species at higher of $Na_2SiO_3$ alkaline solution content in the geopolymeric gel system [5, 16]. Meanwhile, higher silicate species in the GPM system could result in rapid oligomerization hence resulting in accelerated gelation and enhanced viscosity requiring increased stresses to shear the colloidal particles in the liquid–solid suspending colloidal GPM systems. Similar rheological patterns were also observed for GPM-NS at 30 min after mixing though with significantly higher shear stresses and viscosities indicating initiation and progressing of the geopolymerization
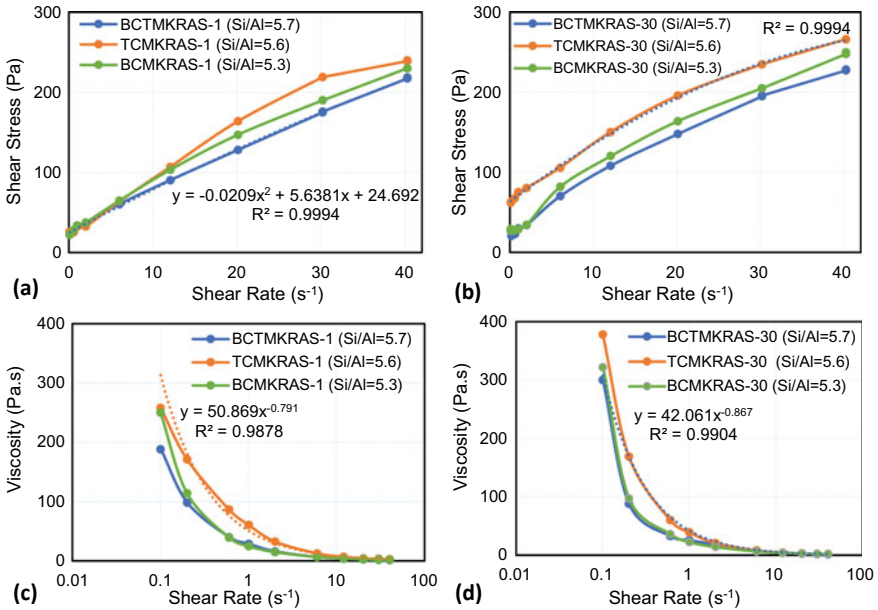
**Fig. 6** Shear stress and viscosity versus shear rate of GPM incorporating 100% recycled aggregate sand **a** shear stress versus shear rate at 1 min **b** shear stress versus shear rate at 30 min **c** viscosity versus shear rate at 1 min and **d** viscosity versus shear rate at 30 min

phases, especially polycondensation and its influence on the rheological properties of GPMs.

Furthermore, shear stress and viscosity enhanced as the NS-based GPMs aged from 1 to 30 min indicating polycondensation and agglomeration of geopolymeric materials. For instance, the shear rate and viscosity of BCTMKNS ($SiO_2/Al_2O_3 = 5.7$) augmented from 214 to 233 Pa and 120 to 148 Pa s, respectively, between 1 and 30 min. The same trend is true for other NS-based GPM compositions. However, composition TCMKNS ($SiO_2/Al_2O_3 = 5.6$) exhibited a rapid increase in viscosity between 1 and 30 min, which can be attributed to the threshold optimal $SiO_2/Al_2O_3$ ratio of 5.6 as well as ascribed to the physical properties of the composition as seen in Table 2, which contains 25% RCT, 45% RCW and 30% MK as precursors in its composition, both RCW and RCT have finer median particle sizes than RCB and thus higher specific surface areas of 1.281 and 1.181 $m^2$/g compared to 0.854 $m^2$/g of RCB. This likely resulted in greater consumption of readily available water and hence likely caused greater increase in viscosity for TCMKNS-based GPM compared to other GPMs at 30 min.

### 3.1.2  GPMs Incorporating Silica Sand

The rheological properties pf silica sand (SS)-based GPMs including viscosity and shear stress at varying shear rate and post mixing times are presented in Fig. 5. A similar trend for shear stress and viscosity of GPM-SS systems can be observed to that of NS-based GPMs, though with declined viscosities and shear stresses indicating an increased flow tendency with SS aggregates as well as the important effect of the fine aggregate type on the rheological properties of SS-based GPMs. For example, the shear stress for composition with $SiO_2/Al_2O_3 = 5.7$ at the maximum shear rate of $42.24 \, s^{-1}$ declined from 214.32 Pa for BCTMKNS to 172.83 Pa for BCTMKSS at 1 min testing age. Similarly, for the same composition, viscosity declined from 120 to 95 Pa s when silica sand replaced natural sand. The SS-GPM systems showed a slower increase in shear stresses and viscosities. For example, at 30 min, the maximum shear stress value declined from 233 to 196 Pa when natural sand was replaced by silica sand. A similar trend was observed for viscosity, where the maximum viscosity value declined from 362 to 248 Pa s when SS was added instead of NS at 30 min testing age. This suggests a slower consumption of water when SS is incorporated to GPMs due to its round particles shape despite having finer grains compared to both NS and RAS aggregates (Fig. 1). Nevertheless, an important observation that can be made from Fig. 5 is that higher viscosity and shear stress are shown by TCMKSS ($SiO_2/Al_2O_3 = 5.6$) both at 1 and 30 min compared to BCTMKSS and BCMKSS GPMs. The probable reason for the development of higher shea stresses and viscosity in TCMKSS ($SiO_2/Al_2O_3 = 5.6$) could be reaching a threshold level for SS-based GPMs as further increase in $SiO_2/Al_2O_3$ likely caused imbalanced silico-aluminate gel system causing rapid and substantially higher disintegration of geopolymeric bonds hence greater flow tendency and decline in viscosity when $SiO_2/Al_2O_3$ was enhanced to 5.7. Meanwhile, the fineness of the precursor particles can also affect the rheological properties of GPMs as TCMKSS contain higher amounts of particles with larger specific surface areas compared to the two other SS-GPM compositions thus likely increasing the water consumption causing increase viscosity [16, 27]. These observations confirm that the particle shape of both precursors and fine aggregates likely played an important role in influencing the viscosity and shear stresses of GPMs.

### 3.1.3  GPMs Incorporating Recycled Aggregate Sand

The viscosity and shear stress results of recycled aggregate sand-based GPMs are depicted in Fig. 6. The RAS-based GPM system showed shear thinning behavior of viscosity reduction with increased shear rate just like the previous NS and SS-based GPM systems. Yet, significant increases in viscosities were observed with the incorporation of RAS into GPM systems, while shear stress saw considerable enhancement compared to SS-GPMs and NS-GPMs. Like SS-GPM systems the increase in $SiO_2/Al_2O_3$ molar ratio from 5.3 to 5.6 resulted in maximum improvement in viscosity and shear stress. As an illustration, the shear stress for TCMKRAS ($SiO_2/Al_2O_3 = 5.6$)

enhanced from 172 to 239 Pa when SS was replaced by RAS for the 1 min testing regime. The rheological properties responded the same way at 30 min testing regime with improved shear stresses for all three RAS-based compositions. Similar to the rheological characteristics at 1 min testing age, the incorporation of RAS aggregates significantly enhanced the viscosity of all compositions compared SS and NS-based GPMs. For example, at 30 min post casting age, the viscosity of TCMKRAS ($SiO_2/Al_2O_3 = 5.6$) composition augmented from 248 to 378 Pa s when RAS replaced SS indicating a 130 Pa s or about 52% increase in viscosity. These findings reveal an increased consumption of water by RAS which may have contributed to the decline of fluids available in the mixture for lubrication and ease of movement resulting not only in increased torque and shear stresses but also viscosity as highly viscous solid phase of alkaline solution remain in the geopolymer system until the geopolymerization process takes place and consumes the available alkalis in the geopolymeric viscous gel system [9, 16]. Meanwhile, the threshold level for maximum shear stress and viscosity was reached at $SiO_2/Al_2O_3 = 5.6$ similar to SS-GPMs when optimal viscous silicate species were supplied. However, an enhancement in $SiO_2/Al_2O_3$ likely triggered greater flow tendency due to significant silicate species in the system while concentration of aluminate species declined hence resulting in an unbalanced silico-aluminate system initiating a reverse effect on the viscosity of the RAS-GPMs, hence resulting in reduced viscosity and shear stress [15].

## 3.2 Yield Stress of GPMs

The influence of predefined $SiO_2/Al_2O_3$ molar ratios and types of fine aggregates on the yield stress of GPMs is shown in Fig. 7. The relationship between the yield stress and $SiO_2/Al_2O_3$ parameter shows that the threshold level of silicates at the medium value of $SiO_2/Al_2O_3$ resulted in maximum yield stress corresponding to the maximum viscosity and shear stress results presented in the previous section. Evidently, at a constant $Na_2O/SiO_2$ ratio of 0.18, increasing $SiO_2/Al_2O_3$ from 5.3 to 5.6 resulted in enhanced yield stress; however, further increment to 5.7 led to reduced yield stress indicating the liquification of GPMs due abrupt disintegration of geopolymer gel system at excessive silicate level caused by higher $SiO_2/Al_2O_3$ molar ratio [6, 16]. The same trend was observed for GPMs incorporating the three different fine aggregate types including RAS. This increased liquification can be attributed to the enhanced solubility of precursors at higher $SiO_2/Al_2O_3$ molar ratios causing reduced interparticle interaction and forces [6, 8]. The considerably higher yield stress for TCMKRAS ($SiO_2/Al_2O_3 = 5.6$) indicates the possible rapid absorption of available water and formation of highly viscous residual paste around the recycled fine aggregate creating thin film of a new interfacial transition zone around RAS resulting in highly viscous GPM gel system, hence requiring higher shear stresses to initiate yielding of the geopolymer mortars.

Figure 8 illustrates the initial shear stress versus shear strain of GPMs before yielding. As seen, GPM systems with the medium level $SiO_2/Al_2O_3$ ratio of 5.6
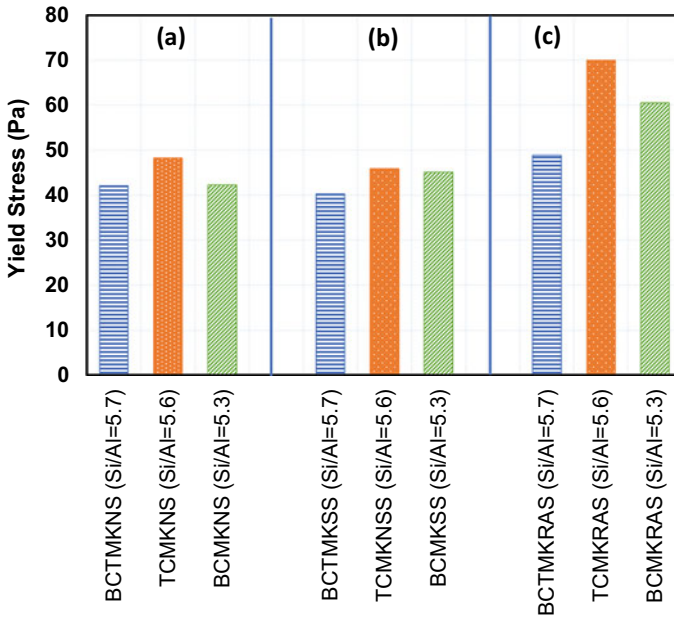
**Fig. 7** Yield stress versus SiO2/Al2O3 molar ratios for GPMs incorporating **a** 100% natural sand **b** 100% silica sand and **c** 100% recycled aggregate sand

exhibited higher yield stress levels indicating higher level of geopolymeric interactions due to the presence of optimal silicate species and more reactive precursors in the geopolymer system. Meanwhile, higher amounts of RCW precursor probably led to the increased formation of higher C–A–S–H/C–S–H geopolymeric gels leading to rapid polycondensation, thus leading to higher stress and viscosity [19]. However, as mentioned previously, with the incorporation of RAS, increased water absorption could also lead to equivalent and/or higher yield stresses. Furthermore, it can be clearly seen that more fluid systems such as silica sand-based GPMs lead to lower yield stresses, whereas the RAS incorporating GPMs lead to the rapid rise of shear stresses at relatively low shear strains when compared to SS or NS-based GPMs. For instance, for TCMKSS ($SiO_2/Al_2O_3 = 5.6$), the yield stress reached 45.9 Pa in about 0.18 microstrain, while the yield stress of 70 Pa for TCMKRAS ($SiO_2/Al_2O_3 = 5.6$) was reached in comparatively lower strain of 0.015 microstrain confirming the previous statement about rapid consumption of water and alkaline reagents in the system causing rapid rise of yield stresses. Furthermore, the increasing shear stress as the strain enhances confirms the previous statement about the shear thinning thixotropic behavior of GPMs indicating the breakage of chemically formed linkages between the geopolymeric gels and fine aggregates under increased shear strains.

The shear stress versus torque and strain versus torque envelopes prior to yielding of the GPMs are plotted in Fig. 9. Varying levels of torque (%) were required to reach
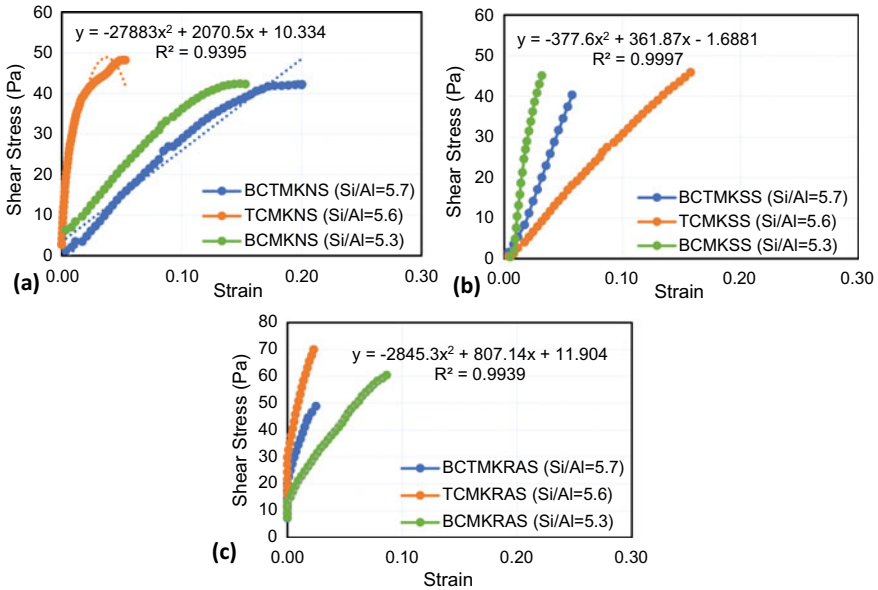
**Fig. 8** Shear stress versus shear strain for GPMs incorporating **a** 100% natural sand **b** 100% silica sand and **c** 100% recycled aggregate sand

yield stresses for different GPMS systems. Higher torque (%) and shear stresses were needed to initiate yielding of TCMK-based GPMs compared to BCTMK and BCMK geopolymers in all three different GPM systems. For instance, in NS-based GPMs, a maximum shear stress of 48.2 Pa was registered for TCMKNS ($SiO_2/Al_2O_3$ = 5.6) compared to 42.1 Pa for BCTMKNS ($SiO_2/Al_2O_3$ = 5.7). This confirms the previous statement about the formation of C–A–S–H/C–S–H gels causing accelerated geopolymerization and the importance of proper balancing of $SiO_2/Al_2O_3$ in the geopolymer gel system. Furthermore, a considerably higher torque was required to trigger the yielding of recycled aggregate-based GPMs compared to SS and NS-based GPM systems. As explained earlier, the addition of RAS likely resulted in increased consumption of liquids and alkaline gels due to the presence of residual pastes around their particles hence causing more viscous geopolymeric gel system. Therefore, a greater torque (%) was required to cause the breakage of chemically formed geopolymer linkages to initiate reversable structural breakdown.

## 4 Conclusions

This study investigated the influence of chemical parameters such as $SiO_2/Al_2O_3$ and $Na_2O/SiO_2$, as well the effects of precursor and fine aggregates type on the rheological characteristics of sustainable CDW-based geopolymer mortars incorporating RCB,
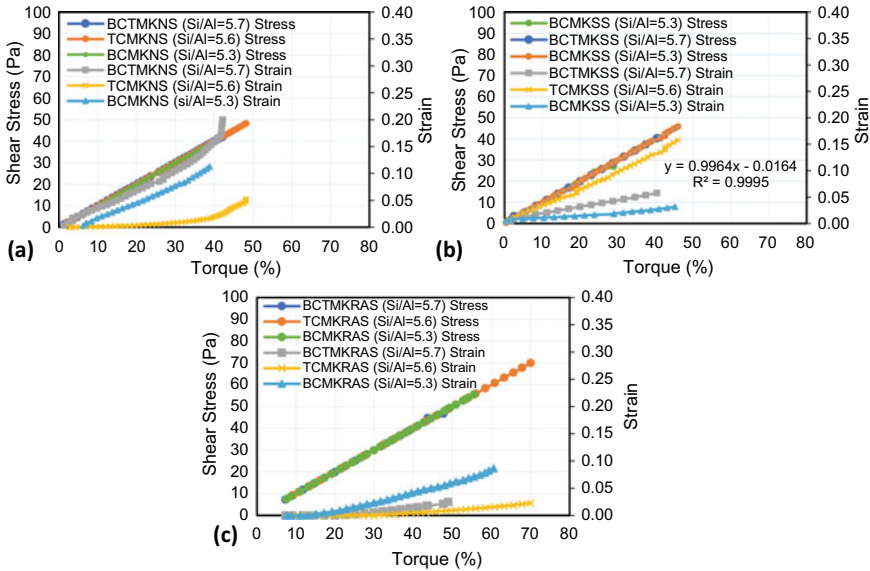
**Fig. 9** Shear stress and shear strain versus torque for GPMs incorporating **a** 100% natural sand **b** 100% silica sand and **c** 100% recycled aggregate sand

RCT and RCW along with MK as precursors. Recycled aggregate, silica and natural sands were utilized as fine aggregates for comparison purposes. Following main conclusion can be drawn from this study:

1. All geopolymer mortar systems exhibited shear thinning behavior under increasing shear rates when characterized by modified Bingham mathematical model.

2. The shear stress, viscosity and yield stress of GPMs increased as the $SiO_2/Al_2O_3$ were increased to a medium threshold level; however, excessive silicate led to enhanced flow tendency, except for BCTMKNS ($SiO_2/Al_2O_3$) GPM system which showed higher viscosity at 1-min post mixing age.

3. The presence of precursors with higher specific surface areas resulted in increased viscosity and greater formation of geopolymeric gels in the GPM systems, hence requiring higher yield and shear stresses to attain equivalent viscosity levels.

4. The incorporation of recycled aggregate sand led to likely absorption of water and alkaline solution leading to rapid rise in viscosity and thus abrupt enhancement of yield stresses.

5. The incorporation of RCW precursor likely led to generation of augmented C–A–S–H/C–S–H species resulting in higher viscosity and yield stresses as exhibited by TCMK-based systems.

# References

1. ASTM C188-17 (2020) Standard test method for density of hydraulic cement. pp 2–4. https://doi.org/10.1520/C0188-17.2
2. ASTM C33 (2018) Standard specification for concrete aggregates. ASTM Standards i (C), pp 1–8. https://doi.org/10.1520/C0033
3. Coelho A, de Brito J (2013) Preparation of concrete aggregates from construction and demolition waste (CDW). https://doi.org/10.1533/9780857096906.2.210
4. Dadsetan S, Siad H, Lachemi M, Mahmoodi O, Sahmaran M (2019) The effect of chemical factors and glass powder on the rheological properties of metakaolin based geopolymer pastes. In: CSCE annual conference, pp 1–11
5. Dadsetan S, Siad H, Lachemi M, Mahmoodi O, Sahmaran M (2022) Optimization and characterisation of geopolymer binders from ceramic waste, glass waste and sodium glass liquid. J Clean Prod 342(July 2021):130931. https://doi.org/10.1016/j.jclepro.2022.130931
6. Dadsetan S, Siad H, Lachemi M, Sahmaran M (2021) Extensive evaluation on the effect of glass powder on the rheology, strength, and microstructure of metakaolin-based geopolymer binders. Constr Build Mater 268:121168. https://doi.org/10.1016/j.conbuildmat.2020.121168
7. Davidovits J (1994) Geopolymers: man-made rock geosynthesis and the resulting development of very early high strength cement. Mater Educ 16(2–3):1–25
8. Fang G, Ho WK, Tu W, Zhang M (2018) Workability and mechanical properties of alkali-activated fly ash-slag concrete cured at ambient temperature. Constr Build Mater 172:476–87. https://doi.org/10.1016/j.conbuildmat.2018.04.008
9. Favier A, Hot J, Habert G, Roussel N, Lacaillerie JBDD (2014) Flow properties of MK-based geopolymer pastes. a comparative study with standard Portland cement pastes. Soft Matter 10(8):1134–1141. https://doi.org/10.1039/c3sm51889b
10. Han D, Yoon JY, Kim JH (2019) Control of viscosity of cementitious materials using waste limestone powder. Int J Concr Struct Mater 13(1). https://doi.org/10.1186/s40069-018-0325-9
11. Lahoti M, Narang P, Tan KH, Yang E-H (2017) Mix design factors and strength prediction of metakaolin-based geopolymer. Ceram Int 43:11433–11441. https://doi.org/10.1016/j.ceramint.2017.06.006
12. Mahmoodi O, Siad H, Lachemi M, Dadsetan S, Sahmaran M (2020) Development of ceramic tile waste geopolymer binders based on pre-targeted chemical ratios and ambient curing. Constr Build Mater 258:120297. https://doi.org/10.1016/j.conbuildmat.2020.120297
13. Mahmoodi O, Siad H, Lachemi M, Dadsetan S, Sahmaran M (2020) Optimization of brick waste-based geopolymer binders at ambient temperature and pre-targeted chemical parameters. J Clean Prod 268:122285. https://doi.org/10.1016/j.jclepro.2020.122285
14. Mahmoodi O, Siad H, Lachemi M, Dadsetan S, Sahmaran M (2020) Development of normal and very high strength geopolymer binders based on concrete waste at ambient environment. J Clean Prod 279(January):123436. https://doi.org/10.1016/j.jclepro.2020.123436
15. Mahmoodi O, Siad H, Lachemi M, Dadsetan S, Sahmaran M (2021) Development and characterization of binary recycled ceramic tile and brick wastes-based geopolymers at ambient and high temperatures. Constr Build Mater 301(February):124138. https://doi.org/10.1016/j.conbuildmat.2021.124138
16. Mahmoodi O, Siad H, Lachemi M, Dadsetan S, Şahmaran M (2022) Optimized application of ternary brick, ceramic and concrete wastes in sustainable high strength geopolymers. J Clean Prod 338:130650. https://doi.org/10.1016/j.jclepro.2022.130650
17. Mesgari S, Akbarnezhad A, Xiao JZ (2020) Recycled geopolymer aggregates as coarse aggregates for Portland cement concrete and geopolymer concrete: effects on mechanical properties. Constr Build Mater 236:117571. https://doi.org/10.1016/j.conbuildmat.2019.117571
18. Mitschka P (1982) Simple conversion of brookfield R.V.T. readings into viscosity functions. 209:207–209
19. Ren X, Zhang L (2019) Experimental study of geopolymer concrete produced from waste concrete. J Mater Civ Eng 31(7):1–14. https://doi.org/10.1061/(ASCE)MT.1943-5533.0002750

20. Robalo K, Costa H, Júlio E (2021) Experimental development of low cement content and recycled construction and demolition waste aggregates concrete. Constr Build Mater 273:121680. https://doi.org/10.1016/j.conbuildmat.2020.121680

21. Robayo-Salazar RA, Mejía-Arcila JM, de Gutiérrez RM (2017) Eco-efficient alkali-activated cement based on red clay brick wastes suitable for the manufacturing of building materials. J Clean Prod 166:242–52. https://doi.org/10.1016/j.jclepro.2017.07.243

22. Shaikh FUA (2016) Mechanical and durability properties of fly ash geopolymer concrete containing recycled coarse aggregates. Int J Sustain Built Environ 5(2):277–287. https://doi.org/10.1016/j.ijsbe.2016.05.009

23. Sitarz M, Urban M, Hager I (2020) Rheology and mechanical properties of fly ash-based geopolymer mortars with ground granulated blast furnace slag addition. Energies 13(10). https://doi.org/10.3390/en13102639

24. Soultana A, Valouma A, Bartzas G, Komnitsas K (2019) Properties of inorganic polymers produced from brick waste and metallurgical slag. Minerals 9(9):1–17. https://doi.org/10.3390/min9090551

25. Turkyilmaz A, Guney M, Karaca F, Bagdatkyzy Z, Sandybayeva A, Sirenova G (2019) A comprehensive construction and demolition waste management model using PESTEL and 3R for construction companies operating in Central Asia. Sustainability (Switz) 11(6). https://doi.org/10.3390/su11061593

26. Environment UN, Scrivener KL, John VM, Gartner EM (2018) Eco-efficient cements: potential economically viable solutions for a low-$CO_2$ cement-based materials industry. Cem Concr Res 114(June):2–26. https://doi.org/10.1016/j.cemconres.2018.03.015

27. Yaseri S, Hajiaghaei G, Mohammadi F, Mahdikhani M, Farokhzad R (2017) The role of synthesis parameters on the workability, setting and strength properties of binary binder based geopolymer paste. Constr Build Mater 157:534–545. https://doi.org/10.1016/j.conbuildmat.2017.09.102

28. Yeheyis M, Kasun M, Alam S, Eskicioglu C, Sadiq R (2013) An overview of construction and demolition waste management in Canada: a lifecycle analysis approach to sustainability. Clean Technol Environ Policy 15(1):81–91. https://doi.org/10.1007/s10098-012-0481-6

# Applications of Recycled Gypsum from Waste Drywalls in the Construction Industry: A Review

**Alireza Jafari and Pedram Sadeghian**

**Abstract** Reusing and recycling construction and demolition waste materials are one of the main approaches to reduce the environmental impacts of the construction industry. Waste gypsum drywalls from ever-growing renovation projects and scrap drywalls from new constructions have become a major issue for municipalities. Several researchers have studied the potential use of recycled gypsum from waste drywall as a second-raw construction material, especially for concrete construction. However, there is no comprehensive review study on the topic while it can identify research gaps and provide a direction for future studies. With this background, this review paper focuses on the applications of recycled gypsum drywall (RGD) in the construction industry and its environmental and economic benefits. Additionally, this paper proposes the best mixtures for the concrete containing RGD through the literature review. The cementitious composite of this mixture can be used in other introduced applications. To this end, applications of RGD in the construction industry were classified into seven groups, including supplementary materials in concrete materials, soil stabilization, ceramic industry, recycled aggregates, cement production, plaster, as well as blocks and walls, and new achievements in each group were discussed. Then, the most eco-friendly concrete mixture with acceptable mechanical strength was proposed, assisting researchers in future studies. The results illustrate that reusing RGD can significantly reduce the carbon dioxide emissions of the concrete and provide economic benefits. A combination of ordinary Portland cement, recycled gypsum, fly ash or perlite, and slag was proposed as the most appropriate cementitious concrete composite.

**Keywords** Recycled gypsum drywall · Construction industry · Cementitious composites · Environmental impact · Economic benefits · Recycling

A. Jafari (✉) · P. Sadeghian
Department of Civil and Resource Engineering, Dalhousie University, Halifax, NS B3H 4R2, Canada
e-mail: Alireza.Jafari@dal.ca

P. Sadeghian
e-mail: Pedram.Sadeghian@dal.ca

# 1   Introduction

Todays, reusing and recycling waste materials are well-known as one of the strategies to not only decrease the cost of produced materials but reduce the environmental impacts of industries and materials. Given these benefits and the critical situation of global climate-changing, which results from releasing a vast amount of greenhouse gases, many researchers have established their studies on reusing and recycling waste materials in industries.

One of the primary sources of waste materials that contributes to approximately 27% of total solid waste materials in Canada is the construction industry [56]. Meanwhile, many construction and demolition waste materials can be recycled and reused in the construction industry, significantly reducing the demand for landfill space and virgin and raw materials. Additionally, using recycled construction and demolition waste materials can noticeably decrease the carbon dioxide ($CO_2$) emissions of the construction industry. This reduction is also accentuated due to the 65% of the contribution of $CO_2$ in greenhouse gases effects and the critical situation of global climate-changing [20, 38].

Gypsum is one of the most common construction materials that have been used for hundreds of years due to its suitable characteristics. Currently, the majority of gypsum in the construction industry is used in manufacturing gypsum drywalls because of its heat and sound insulation characteristics, which increase the utilization of the walls in the construction industry. Regarding this increasing demand, drywall waste has also been raised to the extent that the gypsum drywalls contribute to about 9% of total construction and demolition waste in Canada, typically disposed of in the landfills [41]. Disposing of the gypsum drywall, however, has some environmental impacts not only on the landfill space but on the underground water sources since the gypsum can react with the rain and leachate and produce toxic liquids [41, 43]. On the other hand, previous studies indicated that gypsum has a close recycling loop and can be completely recycled at least three times [9, 10]. Therefore, studying the applications of recycled gypsum drywall (RGD) is necessary for protecting the planet.

Despite the above advantages of RGD, its utilization has been limited in the construction industry due to the sparse number of studies on its applications and benefits. Therefore, providing a review paper on the applications of RGD can indicate the research gaps and provide a direction for future studies.

Given this fact, the present paper aims to provide a comprehensive review of the applications of RGD in the construction industry to not only indicate its applications as well as environmental and economic benefits but also introduce the most appropriate mix for the cementitious composites containing RGD. To this end, earlier studies were classified into seven groups based on their proposed applications for RGD in the construction industry. Then, a brief comprehensive review of the applications was represented. Next, the environmental and economic benefits of using RGD were determined, and the most appropriate mix for the cementitious composites containing RGD was introduced. Finally, the research gaps were identified based on the literature, and several research directions were proposed for future studies.

## 2 Methodology

This study focuses on the English published papers between 2019 and 2021, which have one or any combination of recycled gypsum, gypsum, drywall, and wallboard words and are related to the applications in the construction industry on Google Scholar. The period includes studies that not only covered the past applications of RGD but introduced new applications of RGD in the construction industry, while the earlier studies than 2019 mainly focused on the applications of RGD as a soil amendment for agricultural purposes, animal bedding, and water treatment.

## 3 Paper Structure

The first section briefly introduces RGD's characteristics and recyclability. The second section indicates applications of recycled gypsum that have been studied during the determined years. The third section is allocated to the environmental benefits of using RGD in introduced applications, while the economic benefits of this utilization are discussed in the fourth section. The most appropriate mix for creating the most environmentally friendly cementitious composites is proposed through literature in the next section. Finally, the main research directions and gaps are identified based on the reviewed papers.

## 4 Recycled Gypsum Drywall

RGD is powder or aggregate forms of gypsum drywalls that are currently considered as construction waste materials. The powder form can be treated thermally at a temperature between 125 and 180 °C for around 24 h to increase its reactivity, which is called the calcination process [55]. However, according to the literature [55], thermal treatment can improve the reactions of the RGD, some researchers such as Hansen and Sadeghian [20] showed that RGD powder can be used as a supplementary material without any heat treatment, which can improve the sustainability index of reusing RGD as a cementitious material. These powders were typically used as supplementary cementitious materials or filler in soil stabilization [27, 52], manufacturing drywalls [19], concrete materials [14, 20, 39], plaster [34, 44], blocks [25], cement production [4], and ceramic industry [16]. The aggregate form has been generally employed as recycled aggregate in concrete and composite materials [18].

# 5   Applications

This section aims to briefly introduce the studied applications of RGD in the literature. The applications of RGD can be clustered as supplementary materials in concrete materials, soil stabilization, ceramic industry, recycled aggregate, cement production, plaster, and blocks and walls.

## 5.1   Supplementary Materials in Concrete Materials

Supplementary cementitious materials are materials used as a partial replacement for ordinary Portland cement (OPC) and contribute to the hardening and strengthening reactions of the concrete through hydraulic and pozzolanic activity. The substitution can significantly reduce the environmental impacts of cementitious composites since OPC is responsible for around 5–7% of $CO_2$ emissions of the construction industry and consumes a vast amount of energy while its production is also required a vast amount of raw materials that can deteriorate the environment [22, 54].

RGD is one of the supplementary cementitious materials that has been studied in the literature. Although utilizing the combination of RGD and OPC could significantly reduce the strength of concrete [20], recent studies approved that adding fly ash [20], mine waste such as perlite [14], and slag [39] could significantly enhance the compressive strength of concrete while substantially reducing the OPC demand and the harmful environmental impacts of cementitius composites. The recent studies also indicated that the RGD acted as an activator for alkali materials such as fly ash and slag and improved their participation in the concrete strengthening reactions [20, 23, 39]. Additionally, [23] also presented that employing RGD could improve the waterproof characteristics of concrete. In addition to the strength of concrete, an earlier study demonstrated that using the combination of OPC, RGD, and fly ash could significantly improve the water resistance and reduce the drying shrinkage of cementitious mortars and concrete [28]. Additionally, [53] denoted the potential of RGD in 3D-printed composite materials, which showed the efficiency of RGD as supplementary cementitious materials. Table 1 briefly shows the previous studies on using RGD as supplementary cementitious materials.

## 5.2   Soil Stabilization

Traditionally, gypsum was used for soil stabilization because of its appropriate characteristics and price. Recently, using RGD for soil stabilization has been frequently studied so that the topic is mentioned in a large number of published papers on applications of RGD. The majority of the articles were studied stabilizing expansive and

**Table 1** Recent studies on using RGD as supplementary cementitious materials

| Study | Materials | | | | | Objectives of study | | | |
|---|---|---|---|---|---|---|---|---|---|
| | OPC | RGD | Fly ash | Slag | Others | S | WR | D | Others |
| Hansen and Sadeghian [20] | √ | √ | √ | – | – | √ | – | – | – |
| Hansen [21] | √ | √ | √ | – | – | √ | – | √ | – |
| Chernyshova et al. [14] | √ | √ | – | – | Mine waste | √ | – | – | – |
| Hong et al. [23] | √ | √ | – | √ | – | √ | – | – | Electrical resistivity |
| Lu et al. [35] | √ | √ | √ | – | – | √ | √ | – | – |
| Nguyen et al. [39] | – | √ | – | √ | – | √ | – | – | Bending beam (fracture) |
| Mukhametrakhimov et al. [37] | √ | √ | – | – | Metakaolin | √ | – | – | – |
| Nguyen et al. [40] | – | √ | – | √ | – | √ | – | – | Effect of retarder |

S: Strength, WR: Water resistance, D:
Although recent studies indicated the potential of RDG as supplementary materials, one of the main adverse effects of utilizing RGD is that it significantly reduce setting time of the composite. Due to this adverse effect, some researchers, such as [40], examined the effect of retarders on the setting time and compressive strength of concrete containing RGD and slag. Their results represented that the citric acid retarder could significantly improve the compressive strength of the concrete while increasing the setting time of the fresh mix. However, they proposed an appropriate retarder; the effect of other retarders and superplasticizers on the properties of concrete containing RGD is still unknown. Additionally, the impact of adding RGD to concrete on its durability characteristics is undetermined.

clayey soils with a composite containing RGD for the structural foundation, back-fills, and road base and subbase [24, 30, 33]. In addition to using the RGD powder, some researchers utilized the RGD aggregates for soil stabilization. Their results illustrateed that the RGD aggregates could be used in road subbase and pipeline bedding [24]. Table 2 demonstrates the recently published papers on using RGD for soil stabilization and their research goal.

According to Table 2, most studies on stabilizing soils by using RGD only examined the unconfined compressive strength of their mixes, while one of the main points of reusing the RGD in the construction industry is the penetration of the leachate to groundwater and soil pollution. Therefore, although replacing OPC with RGD has some environmental benefits regarding $CO_2$ emission reduction, other environmental impacts of this replacement should be studied in the future. Additionally, there are spare numbers of studies on the durability of stabilized soil by recycled gypsum and the effect of the water on the mechanical and durability properties of the stabilized soil, which can be studied in future studies.

**Table 2** Recent studies on soil stabilization and their objectives

| Study | Materials | | | | Objectives |
|---|---|---|---|---|---|
| | RGD | Soil | OPC | Others | |
| Krishnaiah et al. [33] | √ | √ | – | – | Strength of expansive clay soil |
| Kamara et al. [29] | √ | √ | √ | Slag, Quarry waste dust, and asphalt filler | Strength, high-pressure flow, and freeze/thaw |
| Tan and Adajar [50] | √ | √ | – | Rice husk ash | Strength, Expansion index, and Atterberg's limits |
| Imteaz et al. [24] | √* | √ | – | – | Suitability of RGD in aggregate form for non-load bearing embankment |
| Maqsood et al. [36] | √ | √ | – | – | Strength, unconfined creep, and cyclic loading properties |
| Allah et al. [3] | √ | √ | – | – | Strength of unbounded paving materials |
| Janbaz et al. [27] | √ | √ | √ | – | Unconfined compressive strength |
| Cheng et al. [13] | √ | √ | √ | Fly ash, quicklime, and skeleton soil | Unconfined compressive strength |
| AL-Adili et al. [2] | √ | √ | – | – | Unconfined compressive strength |
| Apriyanti et al. [5] | √ | √ | – | – | Shear and unconfined compressive strength |
| Rustam et al. [48] | √ | √ | – | – | Shear and unconfined compressive strength |
| Thul et al. [52] | √ | √ | – | Tin tailing | Strength, Atterberg's limit, and free swell index |
| Bure and Kamara [11], Kamara et al. [30] | √ | √ | – | Reclaimed asphalt filler, medium hydrated tailing, slag, by-pass dust | Unconfined compressive strength |

*RGD used in aggregate form

## 5.3 Ceramic Industry

Utilizing RGD as a raw material in the ceramic industry is another application of RGD that has been studied in the reviewed papers. However, there is only one published article on this application among the reviewed papers, which examined the effect of temperature on the ceramic composites containing RGD [16]. The encouraged readers referred to the past reviewed paper on this topic [4].

## 5.4  Recycled Aggregates

One of the potential applications of RGD is its usage as recycled aggregate, which can reduce the required energy for grinding and extraction of aggregates while slowing down the natural source depletion [51]. Unfortunately, there is no study on using the RGD as recycled aggregate in concrete. Therefore, it can be a topic for future studies that reduce the environmental impacts of disposing of gypsum, the demand for natural aggregates, and the deterioration of the environment due to the extractions.

## 5.5  Cement Production

In addition to studies on using RGD as supplementary cementitious material, some researchers focused on utilizing RGD in cement production [31]. Although these studies were quite limited in recent years, their results showed the potential of RGD as a replacement for natural gypsum in cement clinker [31]. According to a study, replacing natural gypsum with RGD not only reduced the environmental impacts of extracting gypsum but also boosted the compressive strength of composites made of the cement. This outcome is completely aligned with the proposed close recycling loop of RGD in earlier studies [9].

## 5.6  Plaster

Utilizing the RGD as a partial or complete replacement of commercial gypsum in manufacturing plaster were studied in recent articles. The reviewed papers focused on not only the mechanical properties of plaster containing RGD [34] but the workability [45], sound absorption [42], and thermal properties [46] of the plaster as well. Additionally, an earlier study evaluated the effect of the heating process on the RGD plaster, which showed the effect of the thermal treatment on the RGD properties [46]. According to the articles, the plaster containing RGD plaster had the same mechanical, workability, and sound absorption as the commercial gypsum plaster. Pedreño-Rojas et al. [46] also demonstrated that the plaster with entirely replaced RGD could achieve the appropriate performance. Table 3 summarizes the reviewed articles on the partially and entirely RGD replaced plasters.

## 5.7  Blocks and Walls

The final studied application of the RGD in the literature is employing RGD in the manufacturing blocks, bricks, and drywalls [6, 7, 15]. According to [15], the RGD

**Table 3** Reviewed paper on using RGD in plaster

| Study | Type of replacement | | Results |
|---|---|---|---|
| | Partially | Entirely | |
| Pedreño-Rojas et al. [47] | – | √ | The RGD plaster achieved higher strength and thermal conductivity than the commercial gypsum plaster |
| Pedreño-Rojas et al. [45] | √ | √ | There was no difference between the microstructure of plasters made of heated and unheated RGD. Their results also demonstrated that the RGD plaster could achieve sufficient mechanical strengths and thermal conductivity compared to reference plaster |
| Cristina et al. [17] | – | √ | Heating treatment up to 150 °C efficiently increased the reactivity of the RGD by returning its microstructure to the commercial gypsum. Their tests also demonstrated that the RGD plaster obtained a higher setting time and compressive strength |
| Oliveira et al. [42] | – | √ | The sound absorption of RGD plaster was similar to the commercial plaster |
| Pedreño-Rojas et al. [46] | – | √ | Commercial gypsum could be completely replaced with the unheated RGD in the plaster based on the mechanical properties and thermal conductivity |
| Bartolomei et al. [8] | √ | – | Employing RGD could improve thermal stability and reduce the flammability of the composite |

could be efficiently used as a mineral foaming agent in manufacturing lightweight bricks, which improved the mechanical properties and thermal conductivity of the bricks. Additionally, using RGD is an efficient method to reduce the $CO_2$ emission of bricks [15]. A recent study also represented that the walls manufactured by RGD had superior mechanical performance compared to the conventional ones [7]. Iqbal et al. [25] also used the RGD for producing unfired mud blocks based on the fire resistance and inflammability of the RGD. In the end, Arumugam and Shaik [6] reported that the gypsum could activate the fly ash in the mud bricks and, therefore, act as a cementitious material in brick manufacturing.

# 6 Environment Benefits

This section examines the environmental benefits of using RGD as a supplementary cementitious material. One of the main environmental factors that was widely studied in the environmental evaluations of concrete materials is $CO_2$ emission since this gas is responsible for around 65% of greenhouse gases' effects [38]. Another factor that can be considered as an environmental benefit of employing RGD is the reduction of landfill pollution due to decreasing the amount of RGD by reusing the waste as secondary raw materials. The RGD contains nanometal particles that can pollute the landfill's soil and underground and surface water while reacting with rainwater and producing leachate [41, 43]. In addition, the reaction between RGD and rainwater releases hydrogen sulfide gas which is toxic, flammable, and dangerous for public health [41].

However, other parameters such as underground and surface water pollution are also important; this section mainly focuses on the effect of using RGD on the $CO_2$ emission of concrete. Additionally, due to the variability of the $CO_2$ emission of transportation, which is affected by the type of transporting vehicle and distance, this study only focused on the $CO_2$ emissions of the material production. The data on the $CO_2$ emissions of the materials and the mix design contents were also achieved through literature. The main property for mix design selection was the 90-day compressive strength of hardened concrete since this characteristic is one of the essential features of concrete.

Tables 4 and 5 show the estimated $CO_2$ emissions of materials and the mix designs used to calculate the $CO_2$ emissions of concrete mixtures with the 90-day compressive strength of 35 MPa. Additionally, since the previous article denoted that the RGD can be used as supplementary cementitious material without thermal treatment, this study ignores the $CO_2$ emissions from heating the RGD [20]. Table 6 indicates the estimated $CO_2$ emissions based on the mentioned data in Tables 4 and 5. Figure 1 also illustrates the estimated $CO_2$ emissions.

According to Table 6, using a combination of RGD, OPC, and fly ash could reduce the $CO_2$ emissions of the concrete with the compressive strength of 35 MPa up to 55.7%. It is worth mentioning that increasing the substitution rate by using slag could also reduce the $CO_2$ emissions of concrete more than the estimated amount; however, due to the lack of data on the compressive strength of concrete made of a combination of slag, OPC, RGD, and fly ash, this article could not estimate the reduction.

**Table 4** $CO_2$ emissions of mix design components

| Material | OPC | Fly ash | RGD | Slag | Fine aggregates | Coarse aggregates |
|---|---|---|---|---|---|---|
| $CO_2$ emissions (kg/kg) | 0.82[a] | 0.027[a] | 0.034[b] | 0.143[a] | 0.0139[a] | 0.0459[a] |

[a]Source [26]
[b]Source [55]

**Table 5** Weight of mix design components with the specified compressive strength of 35 MPa

| Materials | Weight of materials (kg/m$^3$) | | | | |
|---|---|---|---|---|---|
| | OPC | Fly ash | RGD | Fine aggregate | Coarse aggregate |
| Mix design 1[a] | 435 | – | – | 672 | 1093 |
| Mix design 2[b] | 138.32 | 197.6 | 59.28 | 574.6 | 1184.3 |

[a]ACI method (211.1-91)
[b][20]

**Table 6** Estimated $CO_2$ emissions of the mix designs

| Materials | $CO_2$ emission (kg) | | | | | |
|---|---|---|---|---|---|---|
| | OPC | Fly ash | RGD | Fine aggregate | Coarse aggregate | Total |
| Mix design 1 | 356.7 | – | – | 9.34 | 50.17 | 416.21 |
| Mix design 2 | 113.42 | 6.72 | 1.6 | 7.99 | 54.36 | 184.09 |



**Fig. 1** Estimated $CO_2$ emissions of the mix designs
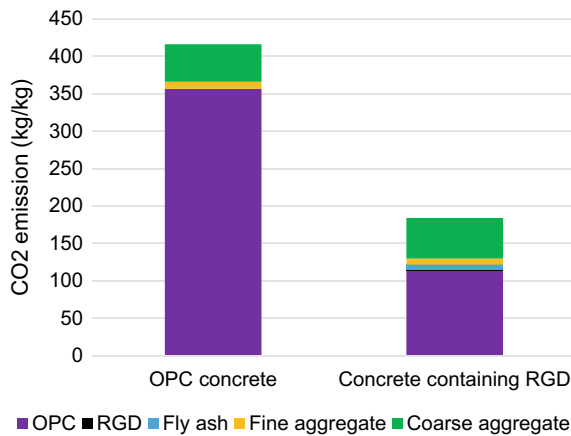
## 7 Economic Benefits

This section aims to introduce and evaluate the economic benefits of utilizing RGD based on the cost of materials. According to the last section, due to the variety of transporting types and distances, the cost of material transportation was ignored in this section. Tables 7 and 8 show the price of each material and the cost of mix designs determined in Table 5. The sources of unit prices were also mentioned in Table 7. Figure 2 also demonstrates the estimated cost of two mix designs schematically.

According to the estimated cost, 35 MPa-compressive strength concrete containing RGD, OPC, and fly ash is around 11.8% cheaper than pure OPC concrete. Additionally, it is anticipated that the estimated cost will decrease by increase the

**Table 7** Unit price of concrete mix design components

| Material | OPC | RGD | Fly ash | Fine aggregate | Coarse aggregate |
|---|---|---|---|---|---|
| Unit price (CAD/kg) | 0.24[a] | 0.25[b] | 0.21[a] | 0.021[a] | 0.013[a] |

[a]Ocean contractors: https://www.oceancontractors.ca
[b]*Source* www.usagypsum.com

**Table 8** Estimated cost of mix design

| Material | Cost of materials (CAD) | | | | | |
|---|---|---|---|---|---|---|
| | OPC | RGD | Fly ash | Fine aggregate | Coarse aggregate | Total |
| Mix design 1 | 104.4 | – | – | 14.11 | 14.21 | 132.72 |
| Mix design 2 | 33.2 | 14.82 | 41.5 | 12.07 | 15.4 | 117 |



**Fig. 2** Estimated cost of mix designs
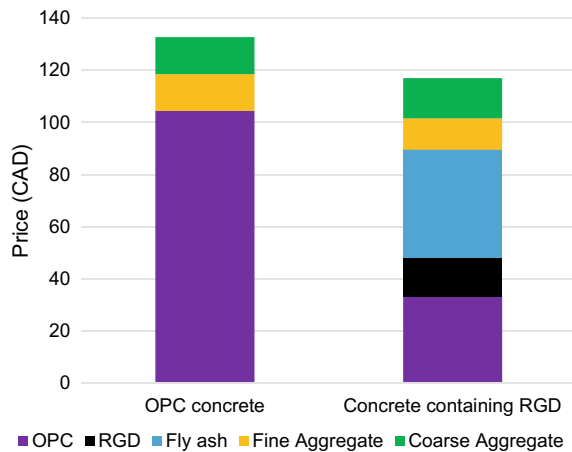
replacement rate and using slag as another cement alternative since the slag is a waste of steel production and is cheaper than OPC.

# 8 Discussion on the Most Appropriate Mixture

This section aims to discover the most appropriate mix for the composite containing gypsum. Based on the literature, the strength of gypsum products in contact with water reduced between 50 and 60% due to the dissolution of ettringite crystals, separation of structural elements due to the wedging action of water films, and recrystallization process [1, 12, 32, 49]. Given this strength reduction, [12] proposed a gypsum-ordinary Portland cement composite to reduce the effect of water on the strength reduction of the gypsum composite. Accordingly, many researchers studied

the gypsum composites containing slag [39], ordinary Portland cement [20], fly ash [20], pozzolana [37], and mine waste [14] to improve the strength of concrete containing gypsum.

According to [14], adding the perlite mine waste with a specific surface area of 600 m$^2$/kg could improve the compressive strength of gypsum composite, while the best chemical additive to the mixture is S-3. It is worth mentioning that the chemical compositions of the perlite was approximately similar to the fly ash. On the other hand, some researchers like [20] used the combination of ordinary Portland cement, fly ash, and RGD to manufacture the concrete specimens. Their findings illustrated that RGD could act as an activator for fly ash while the combination of gypsum and fly ash could reduce up to 50% of ordinary Portland cement demand, which significantly reduced the CO$_2$ emissions of the concrete industry. Additionally, recent studies approved that adding gypsum to the slag composite could improve the hydration reactions of slag while the dosage of gypsum was lower than 30% [39].

Based on the above mentioned and the similarity between the chemical compositions of slag and ordinary Portland cement, it is anticipated that the combination of recycled gypsum drywall, ordinary Portland cement, fly ash or perlite, and slag can result in concrete that can meet the concrete structural requirements while the RGD percentage is limited to 30% of cementitious materials in the mixture.

## 9    Main Insights and Research Directions

This section discusses valuable insights based on the literature review and provides research directions for future studies. It includes understanding the most promising research lines that can better contribute to dealing with the open and difficult research challenges of using RGD in the construction industry. The main insights and research directions of the literature review are:

- The majority of studies examined the mechanical strengths of mixtures containing RGD. However, these factors are the critical parameters for constructions; the durability parameters are also significant since they are used to evaluate the lifetime of buildings. Therefore, examining the durability parameters of the mixtures such as concrete containing RGD and the cement or plaster should be examined in future studies.
- In contrast to the effect of RGD dosage on the mechanical strength of the construction composites, its influence on the microstructure of the composites such as concrete was not fully determined. Thus, evaluating and surveying the effect of RGD on the chemical reactions and microstructure of the construction materials can be considered as one of the research fields in using RGD as the second-raw construction materials.
- Soil stabilization is one of the main applications of RGD. However, with regard to the reactions between RGD and rainwater, the environmental impacts of soil stabilization with RGD should be conclusively examined in the future.

- One of the applications of RGD that was rarely studied in the literature is using RGD as recycled aggregates, which can significantly reduce the demand for extracting the natural aggregates. Given the fact that the source of natural aggregates will be depleted by 2050, examining the effect of RGD as recycled aggregate can provide a new source of aggregates for concrete manufacturers.
- However, the previous studies indicated the applicability of RGD in the construction industry; the RGD cost can significantly limit its usage. Therefore, however, this research direction is not related to the utilization of RGD in the construction industry at first glance; investigating new approaches to minimize the production cost of RGD powder can significantly expand its applications in not only the construction industry but also other industries.

## 10 Conclusions

This paper reviewed the applications of recycled gypsum drywall (RGD) in the construction industry through the literature published between 2019 and 2021. Then, the environmental and economic benefits of using RGD as a supplementary cementitious material were determined, and the most appropriate mixture was proposed based on the reviewed articles. The main conclusions of this study are:

- RGD can be fully recycled based on the literature and used as supplementary cementitious material and aggregate in the construction industry.
- RGD can be used as supplementary cementitious material whether it is thermally treated or not.
- Utilizing the combination of RGD and fly ash as supplementary cementitious materials can reduce the $CO_2$ emissions of the concrete by at least 55.7%.
- Employing the combination of RGD and fly ash as supplementary cementitious materials can decrease the cost of concrete by at least 11.8%.
- The combination of RGD, OPC, fly ash or perlite, and slag as cementitious materials can result in economically eco-friendly concrete.
- Perlite mine waste can be used as a replacement for fly ash to reduce the cost of concrete containing RGD.
- Several insights and research directions were proposed for future studies.

## References

1. Ahmed A, Ugai K, Kamei T (2011) Investigation of recycled gypsum in conjunction with waste plastic trays for ground improvement. Constr Build Mater 25:208–217. https://doi.org/10.1016/j.conbuildmat.2010.06.036
2. AL-Adili A, Salim N, Al-Soudany KY (2019) Response of soft soil mixing with recycled gypsum (plasterboard) as stabilized agent for soil underneath oil tank as a case study. In: IOP

conference series materials science and engineering. https://doi.org/10.1088/1757-899X/579/1/012048

3. Allah RAF, Al-Busaltan S, Shaban AM (2020) Determining field bearing resistance of subgrade soils using physical characteristics. In: IOP conference series: materials science and engineering, vol 745. https://doi.org/10.1088/1757-899X/745/1/012143

4. Almeida KSD, Soares RAL, Matos JMED (2020) Effect of gypsum and granite residues on products from the red ceramic industry: literature review. Revista Materia, vol 25. https://doi.org/10.1590/s1517-707620200001.0893

5. Apriyanti Y, Fahriani F, Fauzan H (2019) Use of gypsum waste and tin tailings as stabilization materials for clay to improve quality of subgrade use of gypsum waste and tin tailings as stabilization materials for clay to improve quality of subgrade. In: IOP conference series: earth and environmental science, pp 1–6. https://doi.org/10.1088/1755-1315/353/1/012042

6. Arumugam C, Shaik S (2021) Transforming waste disposals into building materials to investigate energy savings and carbon emission mitigation potential. Environ Sci Pollut Res 28:15259–15273. https://doi.org/10.1007/s11356-020-11693-0

7. Assis FD, Neto M (2019) Recycled gypsum block: development and performance. https://doi.org/10.1590/s1678-86212019000200307

8. Bartolomei SS, Augusta E, Moura BD, Wiebeck H (2019) Recycled expanded polystyrene by biodegradable solvent—preparation and characterization. Springer International Publishing, pp 757–763. https://doi.org/10.1007/978-3-030-05749-7

9. Basile M, Conti S, Arfò S, Matarazzo A, Cirino E (2020) Gypsum as second raw material to be used endless times in green building. In: 24th International trade fair of material & energy recovery and sustainable development, pp 69–77

10. Boccarusso L, Durante M, Iucolano F, Langella A, Minutolo FMC, Mocerino D (2020) Recyclability process of standard and foamed gypsum. Procedia Manuf 47:743–748. https://doi.org/10.1016/j.promfg.2020.04.227

11. Bure K, Kamara B (2020) Making road base and foundation from secondary waste minerals and recycled aggregates

12. Carvalho MA, Calil C, Savastano Jr H, Tubino RMC, Carvalho MT (2008) Microstructure and mechanical properties of gypsum composites reinforced with recycled cellulose pulp. Mater Res 11:391–397. https://doi.org/10.1590/S1516-14392008000400002

13. Cheng X, Li B, Chen G, Gao S (2020) Solidification/stabilization of textile sludge as subgrade: usage of binders and skeleton material. Adv Civ Eng, vol 2020. https://doi.org/10.1155/2020/8873098

14. Chernyshova N, Lesovik V, Fediuk R, Timokhin R (2020) Enhancement of fresh properties and performances of the eco-friendly gypsum-cement composite (EGCC). Constr Build Mater 260:120462. https://doi.org/10.1016/j.conbuildmat.2020.120462

15. Chiang K, Yen H, Lu C (2018) Recycled gypsum board acted as a mineral swelling agent for improving thermal conductivity characteristics in manufacturing of green lightweight building brick

16. Cipriano PB, Galdino T, Sá C, Ferraz A (2020) Study of phases formed during sintering at different temperatures in ceramic composites containing gypsum waste. https://doi.org/10.21203/rs.3.rs-21149/v1

17. Cristina H, Cordon F, Carvalho F, Furlan F (2019) Comparison of physical and mechanical properties of civil construction plaster and recycled waste gypsum from São Paulo, Brazil. J Build Eng 22:504–512. https://doi.org/10.1016/j.jobe.2019.01.010

18. Diotti A, Galvin AP, Piccinali A, Plizzari G, Sorlini S (2020) Chemical and leaching behavior of construction and demolition wastes and recycled aggregates. Sustainability (Switz) 12:1–12. https://doi.org/10.3390/su122410326

19. Grasielly D, Assis FD, Neto M (2019) Recycled gypsum block: development and performance, pp 45–58

20. Hansen S, Sadeghian P (2020) Recycled gypsum powder from waste drywalls combined with fly ash for partial cement replacement in concrete. J Clean Prod 274:122785. https://doi.org/10.1016/j.jclepro.2020.122785

21. Hansen SKA (2020) Gypsum powder recycled from waste drywalls as a partial cement replacement in concrete
22. Hendriks CA, Worrell E, Price L, Martin N, Ozawa Meida L, de Jager D, Riemer P (1999) Emission reduction of greenhouse gases from the cement industry. In: Greenhouse gas control technologies, vol 4. Elsevier, pp 939–944. https://doi.org/10.1016/B978-008043018-8/50150-8
23. Hong SH, Yuan TF, Choi JS, Yoon YS (2020) Effects of steelmaking slag and moisture on electrical properties of concrete. Materials 13:1–14. https://doi.org/10.3390/ma13122675
24. Imteaz MA, Arulrajah A, Maghool F (2020) Environmental and geotechnical suitability of recycling waste materials from plasterboard manufacturing. Waste Manage Res 38:383–391. https://doi.org/10.1177/0734242X19881213
25. Iqbal K, Hussain S, Farooq A (2020) Influence of waste gypsum on the microstructural characteristics and strength behavior of unfired mud block. Arab J Sci Eng 45:8551–8560. https://doi.org/10.1007/s13369-020-04749-3
26. Islam A, Alengaram UJ, Jumaat MZ, Bashar II, Kabir SMA (2015) Engineering properties and carbon footprint of ground granulated blast-furnace slag-palm oil fuel ash-based structural geopolymer concrete. Constr Build Mater 101:503–521. https://doi.org/10.1016/j.conbuildmat.2015.10.026
27. Janbaz M, Iacobucci L, Francisco K, Miskewitz R, Kitazume M, Maher A (2021) Effect of gypsum and cement content on unconfined compressive strength of soft sediment. Int J Geotech Eng 15:373–378. https://doi.org/10.1080/19386362.2019.1573474
28. Jiang C, Wang Y, Huang S, Tao G (2018) Properties and microstructure of cementing material made with waste silty clay soil. Eur J Environ Civ Eng 8189:1–12. https://doi.org/10.1080/19648189.2018.1426499
29. Kamara KB, Ganjian E, Khorami M (2021) The effect of quarry waste dust and reclaimed asphalt filler in hydraulically bound mixtures containing plasterboard gypsum and GGBS. J Clean Prod, vol 279. https://doi.org/10.1016/j.jclepro.2020.123584
30. Kamara KBB, Ganjian E, Khorami M (2019) Optimisation of secondary waste gypsum for mechanical stability in road (base) and foundation. In: Fifth international conference on sustainable construction materials and technologies. https://doi.org/10.18552/2019/IDSCMT5100
31. Khudyakova TM, Kolesnikov AS, Zhakipbaev BE, Kenzhibaeva GS, Kutzhanova AN, Iztleuov GM, Zhanikulov NN, Kolesnikova OG, Mynbaeva E (2019) Optimization of raw material mixes in studying mixed cements and their physicomechanical properties. Refract Ind Ceram 60:76–81. https://doi.org/10.1007/s11148-019-00312-2
32. Kondratieva N, Barre M, Goutenoire F, Sanytsky M (2017) Study of modified gypsum binder. Constr Build Mater, vol 149, pp 535–542. https://doi.org/10.1016/j.conbuildmat.2017.05.140
33. Krishnaiah E, Kiran DN, Kumar GK (2020) Amelioration of expansive clay using recycled bassanite. In: Problematic soils and geoenvironmental concerns. https://doi.org/10.1007/978-981-15-6237-2_12
34. Li Z, Xu K, Peng J, Wang J, Ma X, Niu J (2019) Study on hydration and mechanical property of quicklime blended recycled plaster materials. Constr Build Mater 202:440–448. https://doi.org/10.1016/j.conbuildmat.2019.01.036
35. Lu W, Ma B, Su Y, He X, Jin Z, Qi H (2020) Low-energy consumption preparation of fine waterproof cementitious material with high-volume phosphogypsum. J Mater Civ Eng, vol 32. https://doi.org/10.1061/(ASCE)MT.1943-5533.0003423
36. Maqsood Z, Koseki J, Miyashita Y, Xie J, Kyokawa H (2020) Experimental study on the mechanical behaviour of bounded geomaterials under creep and cyclic loading considering effects of instantaneous strain rates. Eng Geol 276:105774. https://doi.org/10.1016/j.enggeo.2020.105774
37. Mukhametrakhimov RK, Galautdinov A, Gilmanshin I (2019) Modified gypsum-cement-pozzolanic composites reinforced with polypropylene fibers. In: IOP conference series: materials science and engineering. https://doi.org/10.1088/1757-899X/570/1/012068
38. Naik TR (2008) Sustainability of concrete construction. Pract Period Struct Des Constr 13:98–103. https://doi.org/10.1061/(ASCE)1084-0680(2008)13:2(98)

39. Nguyen H, Kinnunen P, Carvelli V, Mastali M, Illikainen M (2019) Strain hardening polypropylene fiber reinforced composite from hydrated ladle slag and gypsum. Compos B Eng 158:328–338. https://doi.org/10.1016/j.compositesb.2018.09.056

40. Nguyen H, Kinnunen P, Gijbels K, Carvelli V, Sreenivasan H (2019) Ettringite-based binder from ladle slag and gypsum—the effect of citric acid on fresh and hardened state properties. Cem Concr Res 123:105800. https://doi.org/10.1016/j.cemconres.2019.105800

41. Oh H (2019) Opportunities for promoting the recycling of gypsum board from construction, renovation, and demolition in Manitoba

42. Oliveira KAD, Barbosa JC, Christoforo AL, Molina JC (2020) Sound absorption of recycled gypsum matrix composites with residual cellulosic pulp and expanded polystyrene. https://doi.org/10.15376/biores.14.2.4806-4813

43. Oliveira M, Izquierdo M, Querol X, Lieberman RN, Binoy K, Silva LFO (2019) Nanoparticles from construction wastes: a problem to health and the environment. J Clean Prod. https://doi.org/10.1016/j.jclepro.2019.02.096

44. Papailiopoulou N (2018) Techno-economic impact assessment of recycled gypsum usage in plasterboard manufacturing

45. Pedreño-Rojas MA, de Brito J, Flores-Colen I, Pereira MFC, Rubio-de-Hita P (2020) Influence of gypsum wastes on the workability of plasters: heating process and microstructural analysis. J Build Eng 29:101143. https://doi.org/10.1016/j.jobe.2019.101143

46. Pedreño-Rojas MA, Flores-Colen I, De Brito J, Rodríguez-Liñán C (2019) Influence of the heating process on the use of gypsum wastes in plasters: mechanical, thermal and environmental analysis. J Clean Prod 215:444–457. https://doi.org/10.1016/j.jclepro.2019.01.053

47. Pedreño-Rojas MA, Rodríguez-Liñán C, Flores-Colen I, de Brito J (2020) Use of polycarbonate waste as aggregate in recycled gypsum plasters. Materials, vol 13. https://doi.org/10.3390/ma13143042

48. Rustam RK, Resti A, Purwanto H, Firdaus M (2019) The effect of gypsum plafond waste on shear strength of soft clay soil. In: IOP conference series: materials science and engineering paper. https://doi.org/10.1088/1757-899X/620/1/012039

49. Singh N, Middendorf B (2007) Calcium sulphate hemihydrate hydration leading to gypsum crystallization. Prog Cryst Growth Charact Mater 53:57–77. https://doi.org/10.1016/j.pcrysgrow.2007.01.002

50. Tan JF, Adajar MAQ (2020) Recycled gypsum and rice husk ash as additives in the recycled gypsum and rice husk ash as additives in the stabilization of expansive soil. Int J GEOMATE 18:197–202. https://doi.org/10.21660/2020.70.9201

51. Tazi N, Idir R, Ben Fraj A (2021) Towards achieving circularity in residential building materials: potential stock, locks and opportunities. J Clean Prod 281:124489. https://doi.org/10.1016/j.jclepro.2020.124489

52. Thul P, Raut T, Yadav K, Inamdar MM (2019) Stabilization of black cotton soil by using waste gypsum. Int J Res Eng Sci Manage 2:2–4

53. Timpano CS (2019) A review on manufacturing, machining, and recycling of 3D printed composite materials. pp 0–6. https://doi.org/10.1088/1757-899X/653/1/012024

54. Toufigh V, Jafari A (2021) Developing a comprehensive prediction model for compressive strength of fly ash-based geopolymer concrete (FAGC). Constr Build Mater 277:122241. https://doi.org/10.1016/j.conbuildmat.2021.122241

55. Weimann K, Adam C, Buchert M, Sutter J (2021) Environmental evaluation of gypsum plasterboard recycling. Minerals 11:1–13. https://doi.org/10.3390/min11020101

56. Yeheyis M, Hewage K, Alam MS, Eskicioglu C, Sadiq R (2012) An overview of construction and demolition waste management in Canada : a lifecycle analysis approach to sustainability. https://doi.org/10.1007/s10098-012-0481-6

# A Study on the Mechanical and Durability Properties of Rubberized Concrete

**Rubaiya Rumman, Salamah Meherier, Mohammad Tiznobaik, and M. Shahria Alam**

**Abstract** Even though concrete is a huge contributor to global greenhouse gas emissions, it has become an indispensable part of our everyday life. The use of recycled materials in concrete has the potential to provide an eco-friendly solution to concrete construction technology and reduce its carbon footprint to some extent. Research has been carried out for decades to make concrete an environmentally friendly material and the inclusion of rubber crumb as a replacement for aggregate is gaining popularity in recent times. This also solves the disposal problem of scrap rubber tires which is a serious concern considering the huge market of rubber tires all over the globe. Contrasting results are observed in previous research on the effect of crumb rubber in concrete. Moreover, a proper guideline is necessary for incorporating rubber crumb in concrete as its properties vary with the origin of the rubber scraps. To determine an optimum replacement level of crumb rubber in concrete, this study investigated the properties of cement concrete made with crumb rubber replacing particles at levels 10, 30, and 50% with fixed water-to-cement ratio of 0.31. Concrete properties that were examined in this comprehensive study include fresh property: slump and mechanical properties: compressive strength and failure pattern. It was observed that up to 10% replacement of sand with crumb rubber in concrete resulted in comparable mechanical properties.

**Keywords** Rubber crumb · Fine aggregate replacement · Mechanical property · Concrete durability

R. Rumman (✉) · S. Meherier · M. Tiznobaik · M. S. Alam
The University of British Columbia Okanagan, Kelowna, Canada
e-mail: rrumman@student.ubc.ca

R. Rumman
Bangladesh University of Engineering and Technology, Dhaka, Bangladesh

# 1   Introduction

Concrete, which is the second most-consumed material after water [40], is also a huge emitter of $CO_2$. The global availability of its constituents, low cost, and flexibility in forming various shapes makes concrete such a ubiquitous material. Unfortunately, concrete's main constituent, cement, is solely responsible for about 8% of the world's total greenhouse gas emission and 90% of the cement sector's emission occurs during the production of clinker [37]. Consequently, extensive research is being carried out to explore innovative ways of reducing concrete's environmental impact. Using waste and recycled materials as a replacement for one or more of the ingredients of concrete can be a probable solution in this regard. Like any other waste material, crumb rubber (CR) derived from recycled rubber waste has a great potential to be used in concrete and make it environment friendly by lowering GHG emissions [17].

Using waste rubber materials as aggregates of concrete not only provides an eco-friendly solution in concrete production but also solves the disposal problem of the huge amount of rubber discarded every year after the end of their life. It is estimated that one billion rubber tires reach their expiration date every year and hardly half of them are properly recycled [11, 38]. Utilizing this huge amount of discarded rubber waste in the construction sector in the form of CR is a sustainable solution to meet the environmental challenges [9]. Tire-derived aggregates and CR have been successfully used as coarse and fine aggregate replacements, respectively, in concrete [9, 19, 29].

However, significant compressive strength reduction in concrete using CR leads to limited structural applications as a construction material, mostly in non-structural forms [1, 11]. Contrastingly, rubberized concrete showed better performance in terms of strain development, energy absorption capacity, ductility, thermal, and durability aspects [17, 22, 27, 34, 36, 44, 49]. However, consistent results of rubber-based concrete are difficult to predict because of the variation of rubber's chemical composition with varying sources.

Rubber-based concrete showed varying results in previous studies. Increasing rubber content in the concrete mixture significantly decreases its workability [2, 21–23, 25, 30, 41, 45, 48]. The low slump value can attribute to the increase in inter-particle friction between CR and cement matrix and the entrapped air [42]. Furthermore, the mixing process and pre-treatment of CR could also influence its workability [47, 50].

Effect of using CR in concrete on its compressive strength has also been studied. Rubber used as coarse aggregate decreased concrete strength more than it being used as fine aggregate [30, 31, 46, 48]. Some other studies observed that coarse aggregate replaced with rubber performed better in terms of strength than fine aggregate replacement [3, 18]. Untreated CR unanimously reduced the compressive strength of concrete as observed by many researchers [29, 48, 50], while a few examples of strength improvement are also observed with NaOH-treated CR [47]. NaOH-treated CR has also been observed to provide satisfactory compressive and flexural strength in recycled aggregate concrete, although CR lowered the strength values [43]. Similar

to compressive strength in most of the research, the addition of rubber particles in the cement matrix reduces flexural and splitting tensile strength [26, 48, 50]. CR not only affects the strength of concrete but also impacts the toughness and elasticity of concrete. Modulus of elasticity was found to decrease with the reduction in compressive strength for rubberized concrete [26]. Moreover, increasing the rubber content would keep decreasing the modulus of elasticity [50].

The inconsistencies in fresh, durability, and mechanical properties of CR-replaced concrete observed in these previous studies give rise to the necessity of further research. In addition, there is no available guideline in the usage of rubber crumb waste in concrete, whereas these scraps can be an environment-friendly solution in the construction industry. Hence, to find a directive to the most suitable replacement level of CR and investigate the properties of concrete, this study was carried out. It investigates the fresh, mechanical, and durability properties of cement concrete made with CR replaced of sand particles at levels 10, 30, and 50% with fixed water-to-cement ratio (0.31). Since CR has a specific gravity lower than sand, a weight-based replacement was not possible, and a volumetric replacement method was considered. The mixtures used in this study targeted lower-strength concrete to be used in non-load-bearing masonry structures. Hence, untreated well-graded CR was used. Slump values of the concrete mixtures were determined as fresh property of concrete. Moreover, mechanical properties for instance compressive strength and failure pattern of rubber-based concrete were also observed and compared with control specimens. Rapid chloride permeability test and freeze-thaw were used as durability tests on concrete cylinders.

## 2 Experimental Program

### 2.1 Materials

Concrete mixtures of this study consisted of general use (GU) cement, sand and CR as fine aggregates, gravel as coarse aggregates, and water. The maximum nominal size of sand was 4.75 mm and gravel 20 mm. CR was produced by shredding waste rubber tire in a commercial manner. Sand was replaced by CR by volume at 10, 30, and 50% levels.

CSAA23.2-6A [15] and CSAA23.2-10A [12] standards were followed for determining water absorption and specific gravity of sand and gravel, respectively. CR floats on water instead of being submerged in it. This happens because the rubber crumb has a specific gravity like that of water. Hence, these physical properties of CR were determined using ethyl alcohol according to the standard FM 5-559 [20]. All the other properties except absorption capacity and specific gravity were determined using the same testing standard as sand. The sieve analysis and gradation of both sand and CR were carried out according to the specifications of CSAA23.2-2A [13]. The fineness modulus of sand was 2.24 which was lower than that of rubber
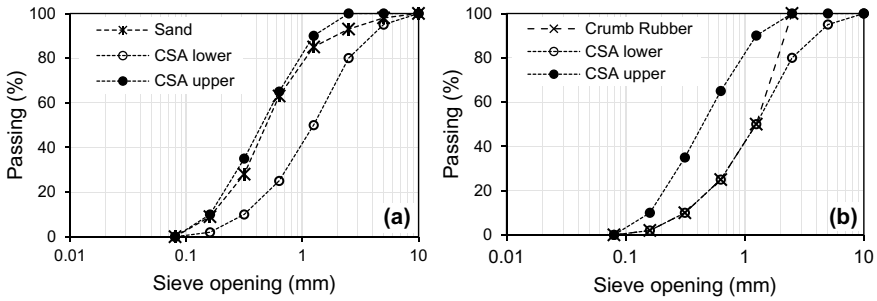
**Fig. 1** Gradation curve of **a** sand, **b** crumb rubber

**Table 1** Physical properties of aggregates

| Variables | Gravel | Sand | Crumb rubber |
|---|---|---|---|
| Bulk specific gravity (SSD) | 2.66 | 2.60 | 1.15 |
| Bulk specific gravity (dry) | 2.64 | 2.56 | |
| Apparent specific gravity | 2.71 | 2.67 | |
| Fineness modulus | – | 2.24 | 3.68 |
| Absorption capacity (%) | 0.98 | 1.52 | 1.20 |
| Bulk density (kg/m$^3$) | 1563 | – | – |

crumb, 3.85. This signifies that CR was coarser than sand particles. Figures 1a and b illustrate the gradation curves of sand and CR, respectively. The figures also show the upper and the lower limits of gradation according to CSA standard.

Figure 1 shows that both the sand and CR are well graded. They also are well within the range determined by CSA. However, CR particles were manually mixed to fit them within the CSA ranges since the CR originally supplied by a company was gap graded. The physical properties of the coarse and fine aggregates along with CR are shown in Table 1. Table 2 shows the chemical composition of CR.

## 2.2 SEM Images of Crumb Rubber

For viewing the morphological pattern of CR and cement paste at a microscopic level, Mira3 Tescan Scanning Electron Microscope (SEM) images of rubber crumb were observed. Three different magnifications of the particles were produced and are shown in Fig. 2. These SEM images can well distinguish probable air entrainment between the particles. In the SEM images of Fig. 2, the tire particles are seen as being fragmented into jagged shapes and there are irregular rough surfaces. These fragmented and rough surfaces of the particles let air be trapped between them during mixing. The hydrophobic nature of rubber also results in a high percentage of air entrainment in the samples [10, 35]. The deformation of CR under external

**Table 2** Chemical properties of crumb rubber

| Elements | Percentage |
|---|---|
| Carbon | 69.95 |
| Oxygen | 20.93 |
| Sodium | 0.38 |
| Magnesium | 0.23 |
| Aluminum | 0.71 |
| Silicon | 1.53 |
| Sulfur | 1.42 |
| Potassium | 0.12 |
| Calcium | 0.22 |
| Iron | 2.43 |
| Copper | 0.15 |
| Zinc | 1.91 |
| Total | 99.98 |
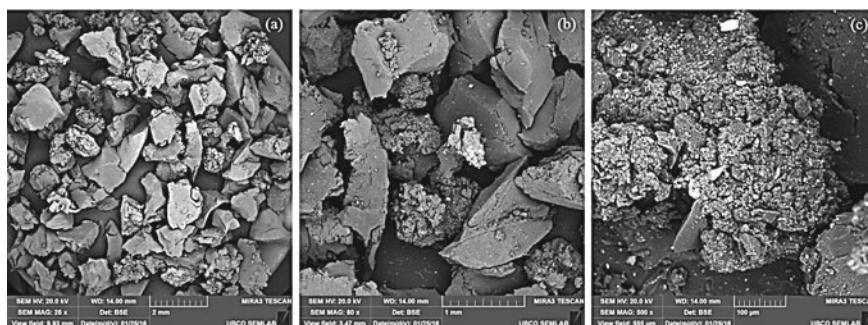


**Fig. 2** Crumb rubber particles at magnification levels of **a** 28x, **b** 80x, and **c** 500x using Scanning Electron Microscope (SEM)

load is much higher than the cement paste. This causes a weak Interfacial Transition zone (ITZ) compared to concrete with regular aggregates [28]. These are the reasons behind the feeble bonding of CR with cement paste, hence the lowering of compressive strength.

## 2.3 Mixture Design

In this study, four mixtures were cast and experimented where the water-to-cement (w/c) ratio was fixed as 0.31. CR was incorporated in the mixtures in a volumetric replacement of fine aggregate by 10, 30, and 50%. The control mixture and these

**Table 3** Mix details of the concrete cylinders (per m³)

| Batch code | Crumb rubber (%) | Water (kg) | Cement (kg) | Gravel (kg) | Sand (kg) | Crumb rubber (kg) | Air entraining admixture (ml) | Water reducer (ml) |
|---|---|---|---|---|---|---|---|---|
| R0 | 0 | 119 | 385 | 1142 | 633 | 0 | 192 | 3140 |
| R10 | 10 | 119 | 385 | 1142 | 570 | 29 | 192 | 3140 |
| R30 | 30 | 119 | 385 | 1142 | 443 | 86 | 192 | 3140 |
| R50 | 50 | 119 | 385 | 1142 | 317 | 143 | 192 | 3140 |

CR-replaced mixtures were denoted by R0, R10, R30, and R50, respectively. The target compressive strength was 35 MPa. Table 3 shows the mixture proportions of concrete that were used in this study.

# 3 Results and Discussion

## 3.1 Fresh Properties

Slump values of fresh concrete have been determined according to the specification of [14] and are presented in Fig. 3. It can be observed from the figure that slump value is decreasing with the increase in CR percentage in concrete. For instance, the control mix R0 showed the highest slump value among all the samples, which is 95 mm. On the other hand, the slump value was reduced by 5.3, 21.1, and 36.8% for the mixtures R10, R30, and R50, respectively. This reduction may attribute to the nature of CR to keep moisture away while attracting air on their rough surface [4].

**Fig. 3** Slump values of the concrete mixtures
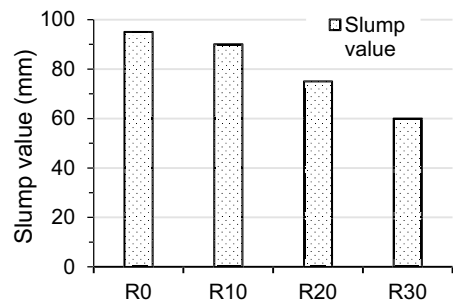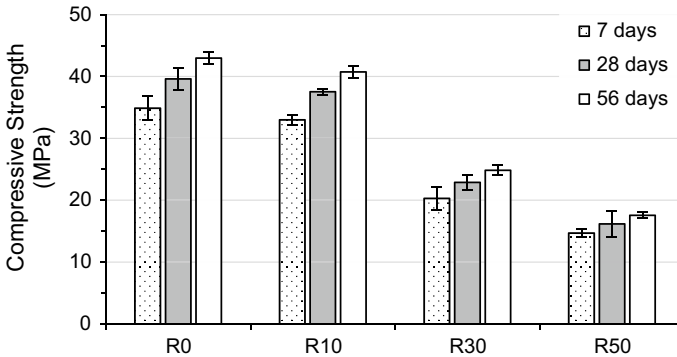
**Fig. 4** Compressive strength of concrete cylinders

## 3.2 Mechanical Properties

### 3.2.1 Compressive Strength

Compressive strength was carried out on concrete cylinders according to the specification of CSAA23.3-9C [16]. The results have been presented in Fig. 4. Concrete compressive strength has been determined for up to 56 days of curing age. From the graph in Fig. 4, it can be seen that the addition of CR decreases the compressive strength compared to the control concrete. The control mixture R0 resulted in the highest compressive strength, 39.6 MPa at 28 days and 45.2 MPa at 56 days. At 56 days of curing, the compressive strengths of R10, R30, and R50 were reduced by 8.2, 41.8, and 58.6%, respectively, compared to control mixture R0.

It can also be observed that the strength gain rate over the curing period of 56 days was the highest for R0 and it gradually decreased for R10, R30, and R50. Moreover, the target compressive strength of 35 MPa was only achieved by R0 and R10 at 28 days. For R30 and R50, the 28-day compressive strengths were 22.9 and 16.2 MPa, respectively. The reduction in strength with an increased percentage of CR can attribute to the weak bond between CR and cement particles.

### 3.2.2 Failure Pattern

Figure 5 illustrates the failure pattern of the concrete cylinders upon compressive load. Combined cone and shear failure occur for the control concrete R0 (Fig. 5a) which has no CR in it. However, the specimens with CR in them failed in a more gradual manner compared to the brittle failure characteristics of the control one. The failure pattern of concrete with 10% and 50% CR (Figs. 5b and d, respectively) showed a well-defined cone on both ends which are similar to the Type 1 failure mentioned in ASTM C39 [6]. Figure 5c shows the failure pattern of R30 concrete
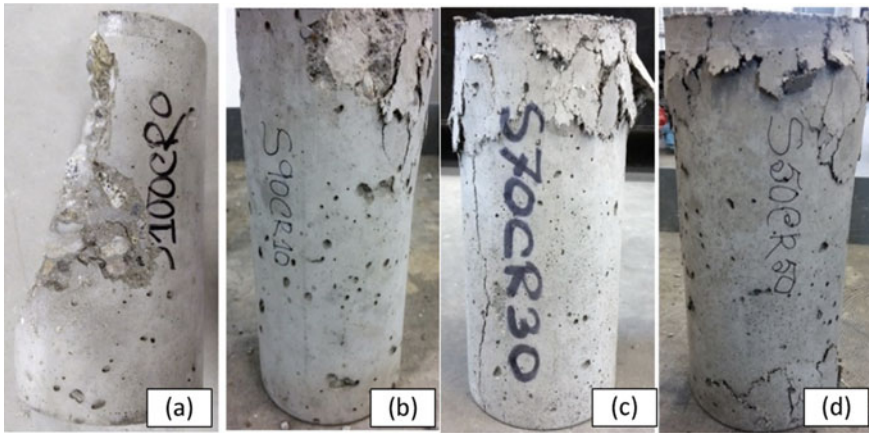
**Fig. 5**  Failure pattern concrete specimens upon compression; **a** R0, **b** R10, **c** R30, **d** R50

which is close to the Type 2 pattern, which is a cone on one end and a vertical crack running through the cylinder.

## 3.3   Durability Properties

### 3.3.1   Rapid Freeze-Thaw Durability Test

Procedure A of ASTM C666 [8] was followed in determining the freeze-thaw durability of the concrete prisms. In this test procedure, these prisms were moist cured for 14 days before starting the freeze-thaw test. Concrete samples underwent repeated freeze-thaw cycles and rapid deformation. Hence, concrete deteriorated because of the formation of cracks in it. As a result, a change in dynamic modulus of elasticity was evident during the 300 cycle periods. Dynamic modulus of elasticity is a property that denotes the concrete quality in terms of degradation due to cracks. The relative dynamic modulus of elasticity of concrete specimens is presented in Fig. 6.

By observing Fig. 6, it can be concluded that all the concrete samples showed a decrease in the relative dynamic modulus of elasticity with the increase in the number of freeze-thaw repetitions. Although all the specimens started showing a decline after the 72nd cycle, the least significant drop was observed for R50 samples, which is 3%. On the other hand, the control concrete prism showed the lowest drop at 72nd cycle, 91%. The values of relative dynamic modulus of elasticity kept decreasing and the declining rate was higher for the control specimens even at the 300$^{th}$ cycle. The reference mixture R0 showed the lowest value of dynamic modulus of elasticity which was 66%. R10 and R30 showed a gradual increase in the value of dynamic modulus of elasticity 70 and 73%, respectively. The value was at maximum for R50 which was 80%. The trend signifies that increasing CR content in concrete increases
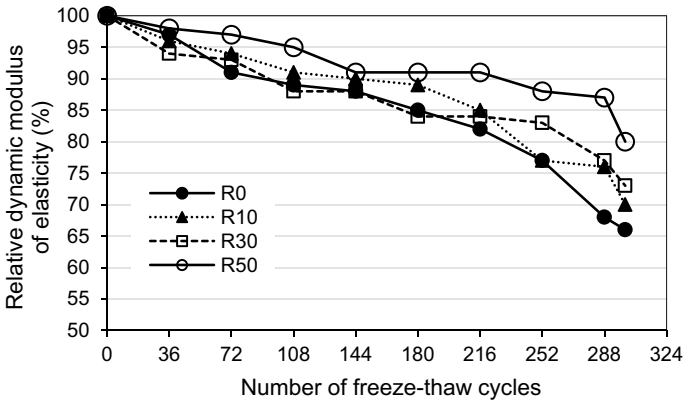
**Fig. 6** Relative dynamic modulus of elasticity of concrete prisms in freeze-thaw test

its freeze-thaw resistance. It should also be noted that all of the samples survived the freeze-thaw test up to the 300th cycle. All of them also followed the criteria of the value being at least 60% according to ASTM C666 [8] so that the test was not needed to terminate.

The hydrophobic nature of CR results in porous concrete upon their inclusion in the mixture. CR also creates air pockets as it repels moisture and attracts air to its surface. Crumb rubber creates porous concrete, thereby entrapping air in the voids. The water inside concrete creates internal stress after freezing occurs. This results in micro-cracks once the internal stress becomes greater than the tensile strength of concrete [39]. The energy dissipation and absorption capacity of CR make crumb rubber concrete perform better under frost conditions and hence freeze-thaw test [33].

Figure 7 illustrates the change in weight in percentages for the freeze-thaw cycles. All the mixtures show weight gain in the initial stages. This occurred due to the water absorption and continuous hydration of the mixtures [24]. After the initial stage, weight loss can be observed in the prisms. Weight loss in the freeze-thaw test signifies surface scaling or spalling at the concrete surface [32]. Both mechanisms continued to occur for the whole freeze-thaw duration over all 300 cycles. These changes indicate the damage process due to the freeze-thaw cycles on the prisms.

At the 300th cycle, control concrete R0 showed the highest weight change, 2.71%. On the other hand, R50 showed the lowest weight change which was 1.93%. Moreover, the weight change and loss of rubberized concrete remained constant throughout the whole process. This also signifies that CR resisted any micro-cracks occurring in the concrete because it was more deformable than control samples.
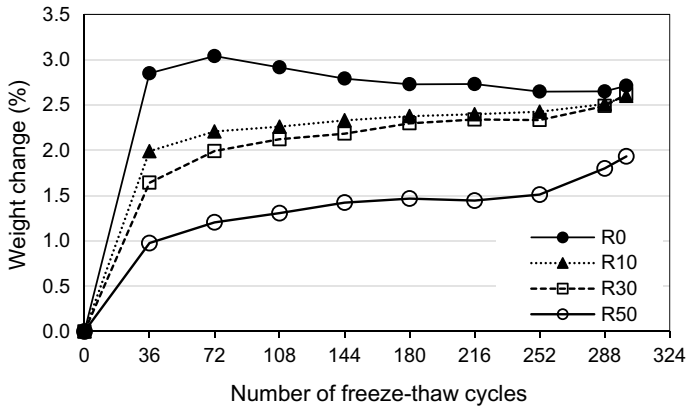
**Fig. 7** Weight change percentages of concrete prisms in the freeze-thaw test

### 3.3.2 Rapid Chloride Permeability Test

A rapid chloride permeability test was performed on all the concrete specimens according to the specification of ASTM C1202 [5]. A 2 inch slice of concrete was placed between two cells containing NaOH and NaCl solution. A potential of 60 V was maintained between the two cells, and the total passed charge was calculated over a period of 6 h. The more permeable the concrete is, the more charge it should let through. Hence, it is an indirect representation of concrete permeability.

Figure 8 represents the total charge passed in coulombs for the concrete mixtures from the RCPT test. From the graph, it can be observed that CR reduces the charge passed through the concrete specimens compared to the control concrete. The reduction in total charge was 41, 56, and 39% for R10, R30 and R50 samples compared to control, respectively. Moreover, where the control concrete stood in the moderate permeability range, all the three rubberized samples were in the low permeability range by the classification defined by ASTM C1202 [5]. However, although all the rubberized concrete hindered the passage of chloride ingress and reduced the overall charge passed, 50% CR inclusion increased the charge values slightly. Hence, CR inclusion of up to 30% of the fine aggregate in concrete lowered the coulomb value and showed better permeability. However, a higher percentage (50%) of CR inclusion resulted in more air void in the concrete, which eventually increased the coulomb value, although still lowers than control concrete.

**Fig. 8** RCPT test results of concrete
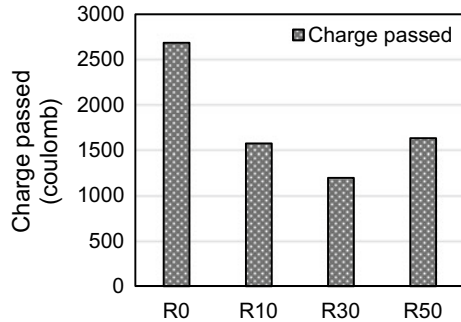


## 4 Conclusions

Various fresh, mechanical, and durability characteristics of concrete with incorporated rubber crumbs were observed and compared with concrete with no CR inclusion. The results can be summarized as follows:

1. CR inclusion in concrete reduces slump hence workability of the fresh concrete mixture. The highest reduction was observed for the highest percent replacement of CR in concrete, which was 36.8%. This reduction in a slump can be attributed to the hydrophobic nature of CR and eventual air void creation in the mixture.
2. CR reduced compressive strength of concrete. The reduction in strength is quite significant at 30% or higher percentages of fine aggregate replacement. However, the 10% replaced specimen provided comparable results with the control concrete, not lower than 35 MPa.
3. The failure pattern upon compression load of the specimens showed more gradual failure in the CR-replaced concrete compared to the reference sample which was more brittle.
4. CR significantly improved the durability of concrete, both in terms of freeze-thaw resistance and chloride permeability. Freeze-thaw resistance was gradually improved with the increase in CR content. However, chloride permeability decreased up to 30% of CR inclusion, and then, it increased at 50%.
5. Considering the compressive strength, durability, and failure pattern of all the four mixtures used in this study, it can be concluded that a 10% replacement of fine aggregate with CR is an optimum percentage for rubberized concrete.

# References

1. Abaza OA (2018) Flexural behavior of rubberized concrete for cold regions applications. In: International conference on transportation and development 2018. Selected papers from the international conference on transportation and development

2. Albano C, Camacho N, Reyes J, Feliu JL, Hernández M (2005) Influence of scrap rubber addition to Portland I concrete composites: destructive and non-destructive testing. Compos Struct 71(3–4):439–446. https://doi.org/10.1016/j.compstruct.2005.09.037

3. Ali N, Amos A, Roberts M (2000) Use of ground rubber tires in Portland cement concrete. In: Proceedings of the international conference on concrete, vol 390

4. Alsaif A, Bernal SA, Guadagnini M, Pilakoutas K (2019) Freeze-thaw resistance of steel fibre reinforced rubberised concrete. Constr Build Mater 195:450–458. https://doi.org/10.1016/j.conbuildmat.2018.11.103

5. ASTM C1202—19 (2019) Standard test method for electrical indication of concrete's ability to resist chloride ion penetration

6. ASTM C39/C39M—20 (2020) Standard test method for compressive strength of cylindrical concrete specimens. http://www.astm.org/cgi-bin/resolver.cgi?C39C39M-16a

7. ASTM C618—19 (2019) Standard specification for coal fly ash and raw or calcined natural pozzolan for use in concrete. https://www.astm.org/Standards/C1202

8. ASTM C666/C666M-15(2015) Standard test method for resistance of concrete to rapid freezing and thawing

9. Bala A, Gupta S (2021) Thermal resistivity, sound absorption and vibration damping of concrete composite doped with waste tire rubber: a review. Constr Build Mater, vol 299. https://doi.org/10.1016/j.conbuildmat.2021.123939

10. Benazzouk A, Queneudec M (2002) Durability of cement rubber-composites under freeze thaw cycles. In: International congress of sustainable concrete construction, pp 355–362. https://doi.org/10.1680/scc.31777.0036

11. Bisht K, Ramana PV (2019) Waste to resource conversion of crumb rubber for production of sulphuric acid resistant concrete. Constr Build Mater 194:276–286. https://doi.org/10.1016/j.conbuildmat.2018.11.040

12. CSAA23.2-10A (2019) Relative density and absorption of coarse aggregate

13. CSAA23.2-2A (2019) Sieve analysis of fine and coarse aggregate

14. CSAA23.2-5C (2019) Slump of concrete

15. CSAA23.2-6A (2019) Relative density and absorption of fine aggregate

16. CSAA23.2-9C (2019) Compressive strength of cylindrical concrete specimens

17. Dezhampanah S, Nikbin IM, Charkhtab S, Fakhimi F, Bazkiaei SM, Mohebbi R (2020) Environmental performance and durability of concrete incorporating waste tire rubber and steel fiber subjected to acid attack. J Clean Prod, vol 268. https://doi.org/10.1016/j.jclepro.2020.122216

18. Fattuhi N, Clark L (1996) Cement-based materials containing shredded scrap truck tyre rubber. Constr Build Mater 10(4):229–236

19. Feng LY, Chen AJ, Liu HD (2021) Effect of waste tire rubber particles on concrete abrasion resistance under high-speed water flow. Int J Concr Struct Mater 15(1). https://doi.org/10.1186/s40069-021-00475-8

20. FM, 5-559 (2011) Florida Method of test for testing of ground tire rubber. Florida Method

21. Gerges NN, Issa CA, Fawaz SA (2018) Rubber concrete: mechanical and dynamical properties. Case Stud Constr Mater 9:1–13. https://doi.org/10.1016/j.cscm.2018.e00184

22. Grinys A, Balamurugan M, Augonis A, Ivanauskas E (2021) Mechanical properties and durability of rubberized and glass powder modified rubberized concrete for whitetopping structures. Materials, 14(9). https://doi.org/10.3390/ma14092321

23. Gupta T, Chaudhary S, Sharma RK (2014) Assessment of mechanical and durability properties of concrete containing waste rubber tire as fine aggregate. Constr Build Mater 73:562–574. https://doi.org/10.1016/j.conbuildmat.2014.09.102

24. Hasnat A, Ghafoori N (2021) Freeze-thaw resistance of nonproprietary ultrahigh-performance concrete. J Cold Reg Eng 35(3):1–9. https://doi.org/10.1061/(asce)cr.1943-5495.0000255
25. Hossain FMZ, Shahjalal M, Islam K, Tiznobaik M, Alam MS (2019) Mechanical properties of recycled aggregate concrete containing crumb rubber and polypropylene fiber. Constr Build Mater 225:983–996. https://doi.org/10.1016/j.conbuildmat.2019.07.245
26. Irmawaty R, Parung H, Md Noor N (2020) Experimental study of rubber particles from recycle tires as concrete aggregates. IOP Conf Ser: Earth Environ Sci 473(1). https://doi.org/10.1088/1755-1315/473/1/012130
27. Kaloush K, Way G, Zhu H (2005) Properties of crumb rubber concrete. Transp Res Rec: J Transp Res Board 1914:8–14
28. Kara De Maeijer P, Craeye B, Blom J, Bervoets L (2021) Crumb rubber in concrete—the barriers for application in the construction industry. Infrastructures 6(8):1–20. https://doi.org/10.3390/infrastructures6080116
29. Kazmi SMS, Munir MJ, Wu YF (2021) Application of waste tire rubber and recycled aggregates in concrete products: a new compression casting approach. Resour Conserv Recycl 167(July 2020). https://doi.org/10.1016/j.resconrec.2020.105353
30. Khatib ZK, Bayomy FM (1999) Rubberized Portland cement concrete. J Mater Civ Eng 11(3):206–213. https://doi.org/10.1061/(asce)0899-1561(1999)11:3(206)
31. Khed VC, Mohammed BS, Nuruddin MF (2018) Effects of different crumb rubber sizes on the flowability and compressive strength of hybrid fibre reinforced ECC. IOP Conf Ser: Earth Environ Sci 140(1). https://doi.org/10.1088/1755-1315/140/1/012137
32. Kolay PK, Sulaiman SO, Kumar S (2018) Freeze-thaw durability of concrete with natural and recycled concrete aggregates using air-entraining admixture. Adv Civ Eng Mater 7(3). https://doi.org/10.1520/ACEM20170079
33. Li Q, Xu F, Zheng H, Shi J, Zhang J (2022) Experimental study on freeze-thaw effects on creep characteristics of rubber concrete
34. Li Z, Li F, Li J (1998) Properties of concrete incorporating rubber tire particles. Mag Concr Res 50(4):297–304
35. Olesen A (2018) Durability and mechanical properties of Portland cement concrete that utilizes crumb rubber as an alternative fine aggregat [MSc. Thesis, Lakehead University]. https://pdfs.semanticscholar.org/ee0c/0fb626455d8ccd8d87371ebda9409dd6218d.pdf
36. Richardson AE, Coventry KA, Ward G (2012) Freeze/thaw protection of concrete with optimum rubber crumb content. J Clean Prod 23:96–103. https://doi.org/10.1016/j.jclepro.2011.10.013
37. Rodgers L (2018) Climate change: the massive CO2 emitter you may not know about—BBC News. BBC News. https://www.bbc.com/news/science-environment-46455844
38. Roychand R, Gravina RJ, Zhuge Y, Ma X, Youssf O, Mills JE (2020) A comprehensive review on the mechanical properties of waste tire rubber concrete. Constr Build Mater, vol 237. https://doi.org/10.1016/j.conbuildmat.2019.117651
39. Safiuddin M, Kaish AA, Woon CO, Raman SN (2018) Early-age cracking in concrete: causes, consequences, remedial measures, and recommendations. Appl Sci (Switz) 8(10). https://doi.org/10.3390/app8101730
40. Sheheryar M, Rehan R, Nehdi ML (2021) Estimating $CO_2$ emission savings from ultrahigh performance concrete: a system dynamics approach. Materials 14(4):1–22. https://doi.org/10.3390/ma14040995
41. Sofi A (2018) Effect of waste tyre rubber on mechanical and durability properties of concrete—a review. Ain Shams Eng J 9(2018):2691–2700. https://doi.org/10.1016/j.asej.2017.08.007
42. Steyn ZC, Babafemi AJ, Fataar H, Combrinck R (2021) Concrete containing waste recycled glass, plastic and rubber as sand replacement. Constr Build Mater, vol 269. https://doi.org/10.1016/j.conbuildmat.2020.121242
43. Tamanna K, Tiznobaik M, Banthia N, Shahria Alam M (2020) Mechanical properties of rubberized concrete containing recycled concrete aggregate. ACI Mater J 117(3):169–180. https://doi.org/10.14359/51722409
44. Tantala MW, Lepore JA, Zandi I (1996) Quasi-elastic behavior of rubber included concrete (RIC) using waste rubber tires. In: Proceedings of international conference on solid waste technology and management, pp 391–399

45. Topçu İB, Demir A (2008) Durability of rubberized mortar and concrete. Transp Res Arena Europe 2008, 1561(February):454–461. https://doi.org/10.1061/(ASCE)0899-1561(2007)19
46. Topçu İB, Demir A (2007) Durability of rubberized mortar and concrete. J Mater Civ Eng 19(2):173–178. https://doi.org/10.1061/(asce)0899-1561(2007)19:2(173)
47. Tudin DZA, Rizalman AN (2020) Properties of cement mortar containing NaOH-treated crumb rubber as fine aggregate replacement. IOP Conf Ser: Earth Environ Sci 476(1). https://doi.org/10.1088/1755-1315/476/1/012030
48. Wanasingh D, Aslani F, Dai K (2021) Effect of age and waste crumb rubber aggregate proportions on flexural characteristics of self-compacting rubberized concrete. Struct Concr: J FIB. https://doi.org/10.1002/suco.202000597
49. Yi O, Mills JE, Zhuge Y, Ma X, Gravina RJ, Youssf O (2021) Performance of crumb rubber concrete composite-deck slabs in 4-point-bending. J Build Eng, 40(May). https://doi.org/10.1016/j.jobe.2021.102695
50. Youssf O, Mills JE, Benn T, Zhuge Y, Ma X, Roychand R, Gravina R (2020) Development of crumb rubber concrete for practical application in the residential construction sector—design and processing. Constr Build Mater, vol 260. https://doi.org/10.1016/j.conbuildmat.2020.119813

# Effect of Ultrafine Granulated Blast Furnace Slag on the Strength Development of Portland Cement Mortar

**Saeid Ghasemalizadeh and Rahil Khoshnazar**

**Abstract** The current study evaluated the effects of ultrafine granulated blast furnace slag (GBFS) on the compressive strength development of Portland cement mortar. The previous studies have investigated the effects of ultrafine slag (UFS) with sizes of around 3–5 $\mu$m on the concrete performance. Despite the great potential of smaller size GBFS particles to enhance the concrete performance, such effects are not clearly known. In this study, UFS particles with sizes of around 1 and 0.6 $\mu$m were prepared using a planetary ball mill. UFS was then used to replace Portland cement by 5, 10, and 15 wt.% in preparing mortar specimens. The compressive strength of the specimens was measured at different ages. Isothermal calorimetry was also used to provide insight into the strength development mechanisms of specimens. The results showed that UFS powders significantly increased the 1-d and 3-d compressive strength of mortar specimens by up to 46 and 52%, respectively. The compressive strength increase was proportional to the replacement level of Portland cement with UFS powders. Compared to the 1 $\mu$m UFS, only a minor enhancement in 1-day compressive strength of the specimens containing 0.6 $\mu$m UFS was observed. The 28-day compressive strength of all specimens was similar regardless of their UFS content. The isothermal calorimetry results showed that the UFS powders increased the early hydration rate of Portland cement. A preliminary analysis of energy consumption of UFS preparation showed that partial replacement of Portland cement with UFS could result in cementitious binders with less GHG emission.

**Keywords** Ultrafine granulated blast furnace slag · Portland cement · Compressive strength · Isothermal calorimetry

S. Ghasemalizadeh · R. Khoshnazar (✉)
University of Calgary, Calgary, Canada
e-mail: Rahil.khoshnazar@ucalgary.ca

847

# 1   Introduction

Portland cement concrete is the most widely used man-made product on the earth. About 30 billion tons of Portland cement concrete are produced globally per year [9]. This has made the concrete industry one of the largest consumers of natural resources and a major source of anthropogenic greenhouse gas (GHG) emissions. The production of Portland cement is the primary source of GHG emissions in the concrete production process. Considering the increasing demand for concrete due to population growth in urban areas and the need for concrete structures and infrastructure, the cement and concrete industry should pursue applicable strategies to satisfy both the increasing demand and the need for reducing the environmental impacts of the cement and concrete production.

One of the low-cost and practical methods of reducing the GHG emissions of the cement and concrete industry is the utilization of supplementary cementitious materials (SCMs) as Portland cement replacements in concrete manufacturing. The use of SCMs as partial substitutions for Portland cement can have economic and environmental advantages and benefit the concrete performance. However, due to the slower reactivity of most SCMs compared to the Portland cement at early ages, the early-age compressive strength of the cementitious materials with SCMs has mainly resulted from the hydration of Portland cement [15]. Hence, the appropriate replacement level of Portland cement with SCMs should be carefully determined. When a small or moderate amount of SCMs is used in the cementitious binder, SCMs can increase the hydration rate of the Portland cement because of the filler and nucleation effect at early ages. In addition, the later-age compressive strength of concrete will be further enhanced due to the pozzolanic and/or hydraulic reaction of SCMs. However, for the high replacement levels of Portland cement with SCMs, due to the lower reactivity of SCMs and lower Portland cement content, the obtained cementitious binder contains less hydration products at early ages. Therefore, the early-age compressive strength of the resulted concrete is typically low. That would be a limiting factor toward using large volumes of SCMs in many applications.

One of the methods for increasing the reactivity of SCMs is reducing their particle size through fine or ultrafine grinding of particles. Grinding of the particles produces powders with an increased surface area and reactivity. Nowadays, different types of milling with a high-energy efficiency have been invented to reduce the particle size of different materials into different ranges. The previous studies investigated the fine or ultrafine grinding of fly ash, granulated blast furnace slag (GBFS), and kaolinite clay [8, 10, 11, 16].

For the case of GBFS, Kumar et al. [8] used attrition milling to obtain ultrafine GBFS with a mean diameter of around 4 μm. The 28-d compressive strength of mortar samples containing 60 and 70 wt.% of ultrafine GBFS was approximately 15 and 36% higher than that of the sample with only Portland cement. Bouaziz et al. [5] used a high-energy planetary ball mill and obtained ultrafine GBFS with a mean diameter of 5 μm. The obtained particles were then used to replace 45 wt.% of Portland cement in preparing paste samples. Both short and long-term compressive strengths

of the samples containing ultrafine GBFS obtained from high-energy milling were improved by up to 10% compared to the reference Portland cement paste.

Sharmila and Dhinakaran [14] utilized ultrafine GBFS with a particle size of 5 µm to replace 5, 10, and 15 wt.% of Portland cement in preparing high-strength concrete. They observed that the ultrafine GBFS accelerated the compressive strength gain of concrete at the early ages. The 7-d compressive strength of concretes with 5, 10, and 15 wt.% of ultrafine GBFS was equal to 63%, 74%, and 60% of their 28-d compressive, respectively. Another study obtained GBFS particles with a mean diameter of 3 µm through a wet-grinding process using water as a wetting agent in a stirred media mill [16]. The obtained slurry was utilized to replace 50% of Portland cement in mortar specimens to measure the activity index of the obtained ultrafine GBFS. The results showed that the activity index of GBFS prior to the wet grinding was 90.8%, which increased to 126.5% for GBFS after 50 min of milling [16].

Most of the previous studies reduced the particle size of GBFS into the ranges of 3–5 µm. However, the effects of smaller size GBFS particles on the performance of cementitious systems are not clearly understood. The current study aims to fill this research gap by investigating the influence of ultrafine GBFS with a mean particle size of about 1 µm and smaller on the hydration and mechanical properties of cementitious mortar samples. Compressive strength measurements and isothermal microcalorimetry were conducted to investigate the strength development and hydration heat of samples. Finally, the energy efficiency, limitations, and advantages of grinding the GBFS particles were also discussed.

## 2 Materials and Method

### 2.1 Materials

Ordinary Portland cement type general use cement (GU/GUL cement, QUIKRETE) complying with the Canadian standard (CSA A3001) was used in this study. A commercial GBFS (Lafarge) was used for preparing the ultrafine slag (UFS) powders. In addition, a high-early strength Portland cement (HE cement) from Lafarge was utilized to compare the early-age strength development of the proposed mixtures with the HE cement. The oxide composition of the cementitious materials is presented in Table 1. A polycarboxylate-based superplasticizer (Glenium 3030, Master Builders Solutions) was also used in preparing the mortar samples incorporating UFS particles to keep the slump flow of the samples constant.

**Table 1** Oxide composition of the GU cement, GBFS, and HE cement (wt.%)

|  | SiO$_2$ | Al$_2$O$_3$ | Fe$_2$O$_3$ | CaO | MgO | SO$_3$ | K$_2$O | Na$_2$O | Others | LOI |
|---|---|---|---|---|---|---|---|---|---|---|
| GU cement | 18.29 | 3.79 | 3.32 | 60.15 | 4.53 | 3.29 | 0.39 | 0.12 | 6.12 | 5.89 |
| GBFS | 31.02 | 12.81 | 1.05 | 42.34 | 5.34 | 2.56 | 0.25 | 0.29 | 4.34 | 3.16 |
| HE cement | 18.71 | 4.71 | 3.07 | 60.05 | 4.10 | 3.09 | 0.27 | 0.10 | 5.9 | 5.85 |

## 2.2 Sample Preparation and Testing

The GBFS was ground to ultrafine powders with two different particles sizes (UFS1 and UFS2) using a laboratory-scale planetary ball mill (Restch PM 100 CM). The UFS particles were characterized by dynamic light scattering (DLS) and scanning electron microscopy coupled with energy dispersive X-ray spectroscopy (SEM/EDX).

Reference mortar samples were prepared according to the ASTM C109 (2021) for the compressive strength test. The obtained UFS powders were used to replace the GU cement at 5, 10, and 15 wt.%, as indicated in Table 2. The UFS powders were first shear-mixed in water containing the superplasticizer for preparing the samples. Then, the mixtures were mechanically mixed according to the ASTM C305 [3]. The mortars were cast in cubic molds with the dimension of 50 mm × 50 mm × 50 mm. The samples were de-molded after 24 h and were kept in a fog room until the specified testing age. The compressive strength tests were performed at ages of 1, 3, 7, and 28 d, according to the ASTM C109 [1].

Cement paste samples with a water to cementitious materials ratio of 0.42 were also prepared for the isothermal calorimetry test. The test was conducted using an isothermal microcalorimeter (TAM Air, TA instruments) according to the [2]. Quartz sand with the same thermal mass as the tested specimens was put in reference cells to measure the baseline of the experiments 24 h before the main experiments. Approximately 40 g of the cementitious pastes, according to the binder composition of Table 2, were prepared in a plastic container. Around 9–10 g of each paste were poured into a glass ampoule and then were placed in testing cells of the calorimeter

**Table 2** Binder composition for the paste and mortar samples (wt.%)

|  | GU | HE | UFS1 (1 μm) | UFS2 (0.6 μm) |
|---|---|---|---|---|
| R-GU | 100 |  | – | – |
| R-HE | – | 100 | – | – |
| UFS1-5 | 95 | – | 5 | – |
| UFS1-10 | 90 | – | 10 | – |
| UFS1-15 | 85 | – | 15 | – |
| UFS2-5 | 95 | – | – | 5 |
| UFS2-10 | 90 | – | – | 10 |
| UFS2-15 | 85 | – | – | 15 |

**Fig. 1** Particle size distribution of the UFS powders
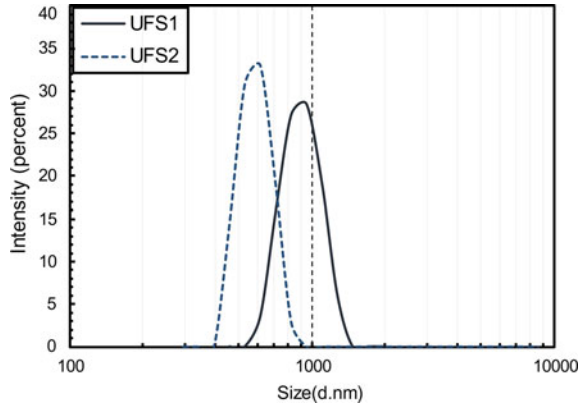


approximately 5 min after mixing the binders with water. The heat evolution of samples was recorded for 96 h.

# 3　Results and Discussion

## 3.1　Characteristics of the UFS Particles

The particle size of the UFS powders as determined by the DLS method is presented in Fig. 1. The results are the average of 3 measurements. The average particle size of the UFS powder was around 1.0 and 0.6 $\mu$m for UFS1 and UFS2, respectively.

Figure 2 shows the SEM images of UFS1 and UFS2 particles compared to the as-received GBFS. EDX analysis was also used to define the elemental composition of the powders. Before and after milling, the main elements detected for the obtained powders were Ca, Si, Al, and Mg. Possible iron and chromium contamination of the final powder by elements from balls and jars was not detected.

## 3.2　Compressive Strength of the Mortar Samples

Figure 3 shows the compressive strength of the mortar samples at the ages of 1, 3, 7, and 28 d. The compressive strength of the samples containing UFS particles was higher than that of the samples made with only GU cement at the early ages. The compressive strength increase was more pronounced at the higher replacement levels of the GU cement with the UFS particles. The average 1-d compressive strength of R-GU was 11.2 MPa, while the average 1-day compressive strength of UFS1-15 and UFS2-15 was 15.2 and 16.4 MPa, respectively. The average 3-d compressive strength of R-GU, UFS1-15, and UFS2-15 was 20.8, 31.9, and 32 MPa, which indicated an
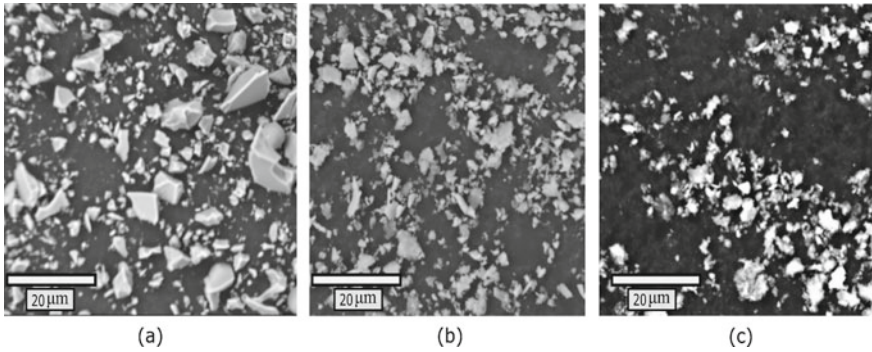
Fig. 2 SEM images: **a** as-received GBFS, **b** UFS1, **c** UFS2

approximately 52% increase due to the use of the UFS particles. Mortar samples containing 10 and 15 wt.% of UFS gained more than 70% of their 28-d compressive strength at the age of 3 d. The 1-d and 3-d compressive strength of R-GU samples were around 65% of the compressive strength of R-HE samples at a similar age. Replacing GU cement with 5, 10, and 15 wt.% of UFS increased the 1-d and 3-d compressive strength of samples to the level of around 75, 83, and 90% of the compressive strength of R-HE samples at similar ages.

Only minor enhancement in the 1-d compressive strength of the mixtures was observed for samples containing UFS2 compared to those containing UFS1. At 5, 10, and 15 wt.% replacement, the average 1-d compressive strength of samples with
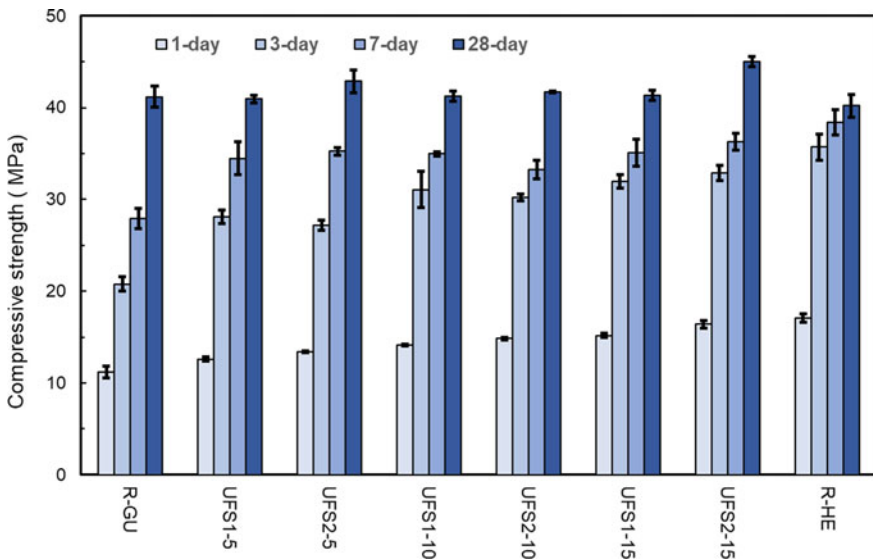


Fig. 3 Compressive strength of specimens at the ages of 1, 3, 7, and 28 days

UFS2 was only 6, 5, and 8% higher than those of the samples with UFS1, respectively. At later ages (3, 7 and 28 d), no significant difference was observed between samples containing UFS1 and UFS2.

The enhancing effect of UFS on the compressive strength of the samples was reduced at later ages. The average 7-d compressive strength of R-GU was 27.9 MPa, while for the mixtures containing UFS, the average 7-d compressive strength varied between 33.3 and 38.3 MPa. At the age of 28 days, all the samples indicated approximately a similar compressive strength value regardless of their UFS content and size, and the average compressive strength values varied between 41 and 45 MPa for different samples.

## 3.3 Heat Flow Measurements

Figure 4 shows the normalized heat flow and normalized cumulative heat based on the cement mass for different pastes for a period of 96 h. R-GU hydration heat curve included two peaks. The first peak indicated the formation of calcium-silicate-hydrate (C–S–H) due to the reaction of tri-calcium-silicate ($C_3S$). The second peak was related to ettringite formation due to the hydration of tri-calcium aluminate ($C_3A$) in the presence of gypsum [12].

When UFS1 and UFS2 were added to the mixtures, no significant change was observed in the initiation of the acceleration period. However, a considerable increase in the intensity of the first peak occurred. These changes were more pronounced by increasing the proportion of the UFS particles in the binders. The increased heat flow was likely due to the presence of extra nucleation sites provided by the UFS particles for the formation of C–S–H. In addition, the shearing rate possibly increased due to reduced inter-particle distance in systems containing UFS. The increase in shearing rates speeds up the ion dissolution from the cement grains and results in the enhanced formation of C–S–H [4]. The presence of UFS particles also altered the position of the first peak. In the pastes with UFS, the first peak occurred faster (shifting to the left), and the change was more evident by increasing the UFS content in the binder.

The incorporation of UFS into the cementitious systems also influenced the position and intensity of the second peak. The changes in the second peak were more pronounced by increasing the content of UFS powders in the binders. In UFS1-15 and UFS2-15 curves, the position of the first and second peaks is pretty close to each other. Zunino and Scrivener [18] stated that the sulfate ions are adsorbed on the surface of C–S–H formed from the hydration of $C_3S$. An increase in the rate of C–S–H formation increases the sulfate adsorption on the C–S–H surface; therefore, the depletion of gypsum occurs faster. After depletion of sulfate ions, sulfate is desorbed from the C–S–H and becomes available to react with $C_3A$ to form ettringite [18].

Figure 5 presents the heat flow per gram of cement for UFS1-15 and UFS2-15 and R-GU samples for a better comparison of the effect of the particles size of UFS powders on the heat flow curves. The heat flow and hydration peaks of UFS1-15 and UFS2-15 are generally similar. Finer particles of UFS2 had only a minor
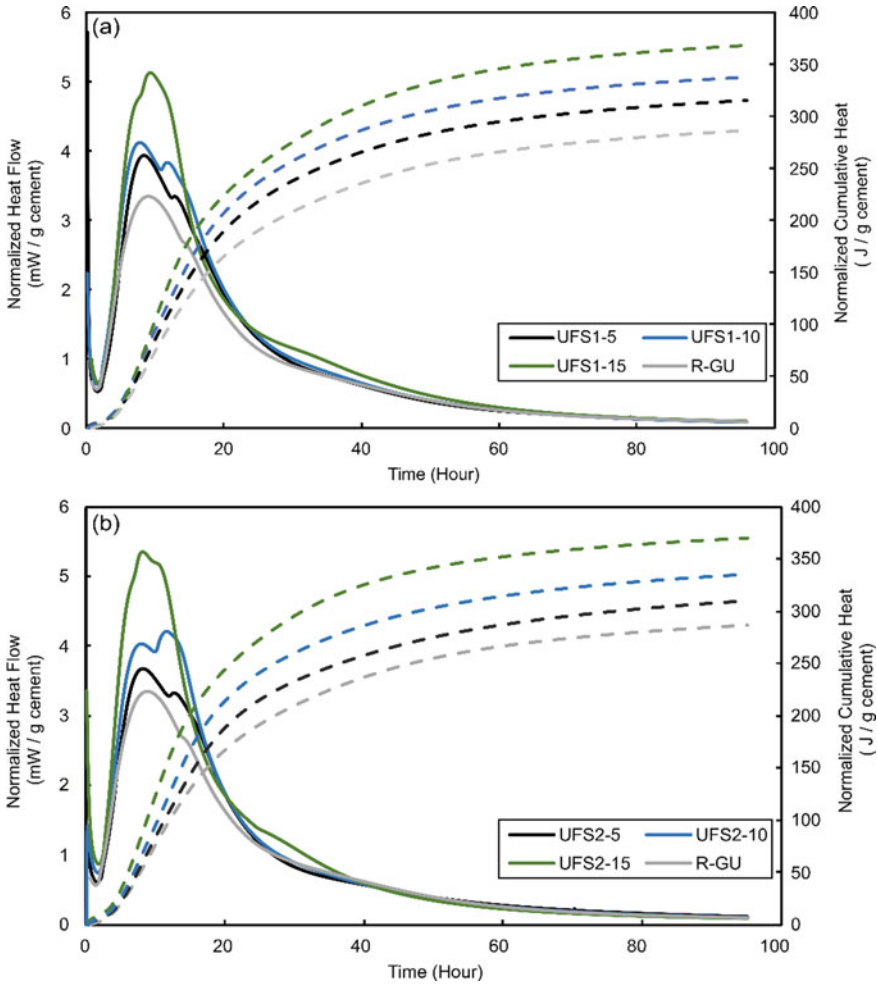
**Fig. 4** Normalized heat flow and normalized cumulative heat for different cementitious pastes containing **a** UFS1 and **b** UFS2

enhancing effect on the amount of first and second peaks compared to the UFS1 particles. However, the cumulative heat of these samples after 96 h of hydration is approximately the same and is about 30% higher than that of R-GU. The same trend was also observed for mixtures with 5 and 10% replacement of GU with UFS2 and UFS1. The cumulative heat of samples with 5 and 10% GU replacement with the UFS powders was about 7 and 15% higher than that of R-GU at a similar age.
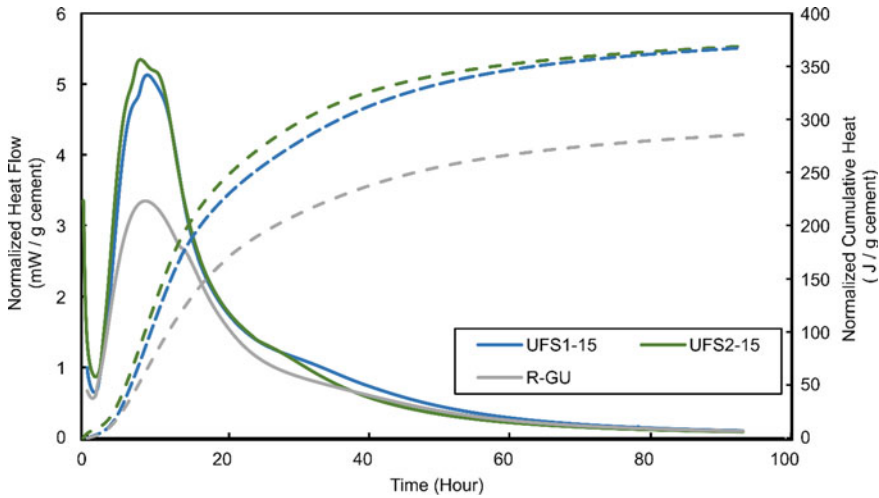
**Fig. 5** Normalized heat flow and cumulative heat for the hydration of UFS1-15, UFS2-15, and R-GU samples

## 4   Potential Environmental Advantages and Disadvantages of Using Ultrafine Slag

Reducing the particle size of GBFS to UFS needs extra energy consumption for grinding that produces additional GHG emissions. In most cases, electricity is used as energy for grinding. The extra electrical energy and GHG emissions should be considered to evaluate the environmental advantages and disadvantages of UFS utilization in concrete. The GHG emission of electricity generation and consumption varies between different regions. For example, in different regions of Canada, the GHG emission for 1 kWh electricity consumption varied between 0.0013 and 0.89 kg of $CO_2$-eq in 2019 [7]. The GHG emissions associated with electricity consumption are higher in regions where sources such as coal and natural gas are used for electricity generation. On the other hand, electricity generation by nuclear, hydro, wind, and solar sources in some areas results in less GHG emissions [7].

Few studies have reported the required electricity consumption for reducing the particle size of SCMs and, in particular, GBFS. Different types of mills with different energy efficiency have been used for the ultrafine grinding of SCMs [6, 8, 16]. The final particle size of the obtained ultrafine powders after grinding was larger than or equal to 2 $\mu$m in these studies. In one of the studies, Sebaibi and Boutouil [13] stated that increasing the Blaine specific surface area of each ton of GBFS from 4500 $\frac{cm^2}{g}$ (standard GBFS) to 9000 $\frac{cm^2}{g}$ (GBFS with the mean diameter of 2.5 $\mu$m) required 300 kWh more electrical energy. In another study, [6] used a supersonic steam jet mill to reduce the GBFS particle size and reported that 17 kWh electrical energy and

0.88 tons of steam were required to produce one ton of GBFS with a mean particle size of 2.25 μm.

In the current study, the UFS powders were obtained by a laboratory-scale planetary ball mill. The electricity consumption associated with the production of the UFS particles of our study can be different from, and likely higher than, that in bulk production of UFS. However, the electricity consumption analysis of this study showed that the GHG emission resulted from GBFS grinding to obtain 1 ton of UFS1 could range from approximately 11–7500 kg of $CO_2$-eq in different regions of Canada. The GHG emission of grinding will be the lowest in provinces such as Quebec and Manitoba. The GHG emission associated with the production of each ton of Portland cement is 700–900 kg of $CO_2$-eq [17]. Thus, partial replacement of Portland cement with UFS1, at least in provinces with a low GHG emission for electricity generation, results in cementitious binders with less GHG emission. The results presented in Sect. 3.2 also indicated that the use of 5–15 wt.% UFS with type GU Portland cement resulted in a higher early-age compressive strength of the Portland cement mortars. Hence, the utilization of UFS may allow a high replacement level of Portland cement with conventional SCMs in cementitious binders without compromising the early-age properties of the concrete mixtures. Moreover, the compressive strength results showed that the combination of UFS and type GU Portland cement could be considered an alternative for HE cement. Production of UFS2 required further grinding which results in higher electricity consumption and higher GHG emissions compared to the UFS1 production. The compressive strength measurements, however, showed that the enhancing effects of the UFS1 and UFS2 on the compressive strength of the mortars were relatively similar. Thus, a more comprehensive study on the effects of UFS2 particles on the engineering properties of concrete and its environmental impacts will be needed to determine the suitability of using UFS2 in concrete production.

It is also worth mentioning that partial replacement of Portland cement with GBFS also provides other benefits in addition to the potential carbon footprint reduction. The GBFS utilization in concrete avoids landfilling of slag. In addition, reducing the share of Portland cement in concrete preserves natural resources required for the production of Portland cement. Analyzing the effects of replacing type GU Portland cement with UFS on different environmental impacts through a comparative life cycle assessment (LCA), that considers the effects of regional availability of slag, energy use and efficiency of grinding facilities, and transportation of UFS, can provide more insights into the potential advantages and disadvantages of using UFS for different projects.

## 5   Conclusion

The current study assessed the effect of using UFS as partial Portland cement replacement on the compressive strength, heat flow, and environmental impacts of cementitious mixtures. Two different ultrafine slags with average particle sizes of around

1 (UFS1) and 0.6 $\mu$m (UFS2) were obtained by ultrafine grinding and used as 5–15 wt.% replacement of the Portland cement in cementitious mixtures. The main conclusions are summarized as follows:

- Substitution of type GU Portland cement with 5–15 wt.% UFS powders increased the compressive strength of mortar samples at early ages (1, 3, and 7 d). The improving effects of the UFS powders were more pronounced at 1 and 3 d. This resulted in mortar samples with superior compressive strength, comparable to that of mortars prepared with the HE cement at similar ages. The use of finer UFS2 powders slightly enhanced the 1-d compressive strength of the mortar samples compared to the UFS1 utilization. Its effects, however, were similar to those observed for the UFS1 powders at other testing ages.
- The calorimetry results indicated that the presence of UFS powders increased the heat evolution of the Portland cement systems. The increase in the heat flow was enhanced by increasing the replacement level of the GU cement with the UFS powders. However, there was only a slight difference in the heat flow curves of samples containing UFS1 and UFS2, and both samples resulted in a similar cumulative heat after 96 h of hydration.
- A preliminary analysis showed that depending on the source of electricity, obtaining the UFS1 powders could have lower GHG emissions than that required for the Portland cement production. Thus, replacing Portland cement with UFS1 can reduce the embodied GHG emissions of concrete mixtures in addition to enhancing their early-age properties. It will also have other environmental benefits such as landfill avoidance of slag and preservation of the natural resources used for the Portland cement production. Further grinding of UFS1 particles to achieve UFS2 might not be justified due to the small enhancing effects on the compressive strength of the mortar samples of this study. A more comprehensive analysis of the engineering and environmental performance of concrete mixtures incorporating UFS particles will be needed to determine the optimum particle size of the UFS for specific concrete applications.

# References

1. ASTM C109/109M-21 (2021) Standard test method for compressive strength of hydraulic cement mortars (Using 2-in. or cube specimens). ASTM International, West Conshohocken, PA, pp 1–10
2. ASTM C1702 (2017) Standard test method for measurement of heat of hydration of hydraulic cementitious materials using isothermal conduction calorimetry. ASTM International, West Conshohocken, PA

3.  ASTM C305-20 (2020) Standard practice for mechanical mixing of hydraulic cement pastes and mortars of plastic consistency. ASTM International, West Conshohocken, PA
4.  Berodier E, Scrivener K (2014) Understanding the filler effect on the nucleation and growth of C–S–H. J Am Ceram Soc 97(12):3764–3773
5.  Bouaziz A, Hamzaoui R, Guessasma S, Lakhal R, Achoura D, Leklou N (2017) Efficiency of high energy over conventional milling of granulated blast furnace slag powder to improve mechanical performance of slag cement paste. Powder Technol 308:37–46
6.  Duan S, Wu H, Liao H, Cheng F (2021) Design and experimental study of a blended cement containing high-volume solid waste activated ultrafine powder. Constr Build Mater 303:124504
7.  Environment and Climate Change Canada (2019) 2019 National Inventory Report (NIR)—Part 3
8.  Kumar S, Kumar R, Bandopadhyay A, Alex TC, Kumar BR, Das SK, Mehrotra SP (2008) Mechanical activation of granulated blast furnace slag and its effect on the properties and structure of Portland slag cement. Cem Concr Compos 30(8):679–685
9.  Monteiro PJM, Miller SA, Horvath A (2017) Towards sustainable concrete. Nat Mater 16(7):698–699
10. Norhasri MSM, Hamidah MS, Fadzil AM, Megawati O (2016) Inclusion of nano metakaolin as additive in ultra high performance concrete (UHPC). Constr Build Mater 127:167–175
11. Paul KT, Manna ÆSKSÆI, Nando KKCÆGB (2007) Preparation and characterization of nano structured materials from fly ash: a waste from thermal power stations, by high energy ball milling. Nanoscale Res Lett 2(8):397–404
12. Scrivener KL, Juilland P, Monteiro PJM (2015) Advances in understanding hydration of Portland cement. Cem Concr Res 78:38–56
13. Sebaibi N, Boutouil M (2020) Reducing energy consumption of prefabricated building elements and lowering the environmental impact of concrete. Eng Struct 213:110594
14. Sharmila P, Dhinakaran G (2016) Compressive strength, porosity and sorptivity of ultra fine slag based high strength concrete. Constr Build Mater 120:48–53
15. Skibsted J, Snellings R (2019) Reactivity of supplementary cementitious materials (SCMs) in cement blends. Cem Concr Res 124:105799
16. Wang Y, He X, Su Y, Yang J, Strnadel B, Wang X (2019) Efficiency of wet-grinding on the mechano-chemical activation of granulated blast furnace slag (GBFS). Constr Build Mater 199:185–193
17. WBCSD I (2009) Cement technology roadmap: carbon emissions reductions up to 2050. World business council for sustainable development and international energy agency
18. Zunino F, Scrivener K (2019) The influence of the filler effect on the sulfate requirement of blended cements. Cem Concr Res 126:105918

# Mechanical Performance of Concrete Incorporating Waste Glass Fiber-Reinforced Polymer Materials from Recycled Wind Turbine Blades

**Dmitry Baturkin, Ousman A. Hisseine, Radhouane Masmoudi, Arezki Tagnit-Hamou, Slimane Metiche, and Luc Massicotte**

**Abstract** This paper presents the results of an experimental study on the effects of the addition of waste glass fiber-reinforced polymer (GFRP) materials from wind turbine blades (WWTB)—designated as WWTB-GFRP—into concrete as fiber reinforcement. Compressive and flexural strength and flexural toughness of concrete cured in standard conditions for 28 days were investigated. Fiber addition rates of 1–1.75 vol. % have been used for two types of WWTB-GFRP: with wood component and after wood removal. According to the test results, the increase in the WWTB-GFRP fiber content leads to a slight to negligible decrease in compressive strength of 6% maximum (for 1.75% of fibers with wood added), an increase in flexural strength up to 22% (for 1.75% of fibers added after wood removal), and an increase in flexural toughness by more than 4 times (for the mixture with 1.75% of fibers without wooden content). Mixtures containing fibers without wood content demonstrated better results in all tests. In general, the results presented in this paper support the use of WWTB-GFRP material as fiber reinforcement in concrete.

**Keywords** Decommissionned wind turbine blades · Valorization of fiber-reinforced polymers (FRP) · Concrete mixture · FRP fibers percentage · Mechanical properties of concrete

D. Baturkin · O. A. Hisseine · R. Masmoudi (✉) · A. Tagnit-Hamou · S. Metiche
Department of Civil Engineering and Building Engineering, Université de Sherbrooke, Quebec, QC, Canada
e-mail: radhouane.masmoudi@usherbrooke.ca

L. Massicotte
Ecological-Industrial Advisor, Synergie Matanie, Matane, QC, Canada

# 1  Introduction

The wind power industry is gaining popularity in the last decades due to the increasing awareness of environmental matters [22]. Wind energy is expected to cover up to 15–18% of the global electricity demand by 2050 [19]. Up to 10.4% of the energy consumed in the European Union (EU) is produced by wind turbines in a normal wind year with approximately 77,000 turbines estimated [8]. The EU's future energy plans include reducing greenhouse gas emissions by 80–95% by 2050 and covering up to 27% of the energy consumption by renewable energy by 2030, which is unachievable without increasing the wind energy production [15]. In the United States of America (USA), wind energy is expected to fulfill up to 20% of the nation's electricity demand by 2030 and up to 35% by 2050 [16].

In Canada, more than 3 million households (6% of electricity demand) are supplied by wind energy with 295 wind farms operating on Canada's territory, including two of the three northern territories. The installed capacity of wind generation reached 12.239 MW in 2017 [31].

The project lifetime of a wind turbine is 20 years, and today older wind turbine structures are at the end of their lifecycle. A common practice is to recycle portions of a wind turbine that contain large quantities of steel, such as the tower, gearbox, and hub. Some researchers [1, 24, 28] investigated repurposing of decommissioned wind turbine blades in such structures as roofing, pedestrian bridges, and others. Around 80% of the total weight of a wind turbine can be also recycled, though no solution has been determined for the blades [30]. Some portion of the blade (mainly fiberglass composite materials) is potentially recyclable [23], yet the waste material from the blade is responsible for the major portion of the turbine to landfill [12].

One of the promising recycling solutions for the WWTB-GFRP is the extraction of discrete fibers to be used as a replacement of synthetic macrofibers in fiber-reinforced concrete. The results from [7] demonstrated positive effects for concrete with WWTB-GFRP fibers addition with the increase of flexural strength up to 15% for 1.75 vol. % fibers addition with the slight positive effect of wood removal on compressive and flexural strength.

Multiple studies were performed for recycled glass fiber-reinforced concrete in terms of compressive and flexural strength [11, 14, 26, 27] and durability of virgin fiber-reinforced concrete [9, 10, 13, 18, 21, 25, 29]. Correia et al. [11] used thermoset-based GFRP waste in the concrete mix. Reduced concrete performance in terms of mechanical and durability properties was reported; thus, the low dosage of GFRP was suggested for non-structural applications. However, under the pressure of the environmental issues, few extractions methods were identified and applied for glass fibers in the acrylic waste [14], but still, the results were not promising. Limited research evidence was found on the ecoefficiency of fibers extraction techniques and GFRP waste use as reinforcement in concrete. Patel et al. [27] used recycled glass fibers from acrylic waste obtained using a shredder and investigated its effects on the mechanical properties of concrete containing up to 0.3 vol. % of recycled glass fibers. The increase in compressive strength up to 21% and in tensile strength up to 28% was

observed. Oliveira et al. [26] used mechanically recycled (chipped) GFRP as fiber reinforcement in cement mortar ($42 \, \text{kg/m}^3$ for all mixtures). The highest compressive and flexural strengths of 47.3 MPa and 9.83 MPa, respectively, were achieved. The compressive strength was either increased up to 20% or decreased by 10% depending on fiber type. Flexural strength was increased up to 44% or decreased by 6%. The source of recycled material and non-uniformity of fibers had a big influence on the mechanical properties of mortar. The great number of fiber balls and particles of the sieved GFRP fiber cluster reduced the workability and compressive strength of mortar.

This paper presents the results of an experimental study on the effects of the addition of waste glass fiber-reinforced polymer (GFRP) materials from wind turbine blades (WWTB)—termed throughout this manuscript as WWTB-GFRP— into concrete as fiber reinforcement. Recycled fiber addition rates of 1–1.75 wt.% were investigated. The resulting concrete mixtures were characterized for their mechanical performance (compressive strength, flexural capacity, and flexural toughness at 28 days). Research outcomes are expected to contribute to the advancement of cleaner products for the cement and concrete industry while fostering sustainable development.

## 2 Experimental Program

### 2.1 Materials Properties

#### 2.1.1 Wind Turbine Blade Waste Material

The recycled WWTB-GFRP material used in the project was received from the Bouffard group (QC, Canada). The material is obtained from disassembled wind turbines at the end of their lifecycle (Fig. 1a). Part of the material was chipped using an industrial woodchipper of high processing capacity (Fig. 1b). For another part of the material, wood was manually separated (Fig. 1c) followed by chipping separated GFRP using an industrial woodchipper of high processing capacity. Fibers of length between 20 and 30 mm and the length-to-diameter ratio between 5 and 15 were obtained (Fig. 1d). Special measures of protection have been taken while working with glass fiber to avoid health hazards and protect the skin, eyes, and upper respiratory tract: protective clothes, gloves, safety glasses, and mask with respirator.

#### 2.1.2 Basic Concrete Constituents

Type General Use (GU) Portland Cement (CSA A3001) equivalent to Type I cement [5] was used. Natural river sand (nominal maximum size of 5 mm) with a specific gravity of 2.61 and water absorption of 0.91% was also used. Crushed limestone
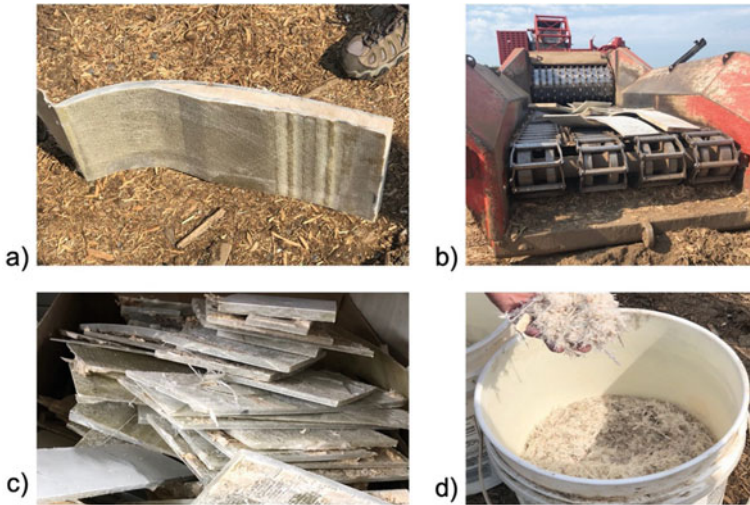
**Fig. 1** Waste wind turbine blades (WWTB) material processing: **a** piece of decommissioned turbine blade used for the project, **b** industrial woodchipper of high processing capacity, **c** WWTB with wood separated, and **d** fibers extracted

aggregates with nominal maximum sizes of 14 and 20 mm and a specific gravity of 2.7 were considered. Potable water from the laboratory was used for concrete mixing. The source of water is free from any form of contamination.

## 2.2 Mixture Proportions

To investigate the effect of GFRP-WWTB on concrete properties, two different forms of GFRP-WWTB were considered: (i) as received GFRP-WWTB after chipping, as well as (ii) chipped after manual removal of wooden content. GFRP-WWTB material was incorporated as a fiber reinforcement (at 0, 1, and 1.75 vol. %). Table 1 presents the proportions of concrete mixtures incorporating GFRP-WWTB after cutting and chipping as received and after wood removal. Mixture Ref is the reference mixture (plain concrete), for the mixtures containing fibers, the first number describes fiber addition rate (% wt.), and letters describe the type of fiber used (WW for fibers with wood, NW for fibers after wood removal).

**Table 1** Mixture proportions of GFRP-WWTB concrete (kg/m$^3$ of concrete)

| Mixture | Ref | 1%WW | 1.75%WW | 1%NW | 1.75%NW |
|---|---|---|---|---|---|
| W/B ratio | 0.48 | 0.48 | 0.48 | 0.48 | 0.48 |
| Cement | 410 | 410 | 410 | 410 | 410 |
| Water | 200 | 200 | 200 | 200 | 200 |
| Sand | 735 | 735 | 735 | 735 | 735 |
| 14 mm aggregates | 421 | 421 | 421 | 421 | 421 |
| 20 mm aggregates | 632 | 632 | 632 | 632 | 632 |
| GFRP-WWTB with wood | 0 | 18 | 30 | 0 | 0 |
| GFRP-WWTB no wood | 0 | 0 | 0 | 18 | 30 |

## 2.3 Specimen Preparation

Specimen preparation comprised two stages. The first concerns the preparation of GFRP-WWTB. The second concerns the preparation of concrete mixtures and casting specimens.

### 2.3.1 Waste Wind Turbine Blade Material Preparation

Woodchipper at the site of the industrial partner was used to prepare the fibers from GFRP-WWTB. The wooden part was separated manually, and then the GFRP polymer part was processed using the same woodchipper.

### 2.3.2 Specimen Preparation

Concrete batching was carried out using a 100 L capacity concrete mixer following the mixing procedure described in ASTM C192 [2]. In an attempt to enhance mixture homogeneity, GFRP-WWTB material was dry mixed with coarse aggregate for 10 min prior to adding to the final mixture.

After mixing, specimens were sampled for the different tests. Cylinders 150 × 300 mm were used for the compressive test; prisms 100 × 100 × 400mm were used for four-point bending test. After sampling, specimens were covered with plastic sheets and kept in a room with relative humidity (RH) and temperature of approximately 50% and 23 °C, respectively. After 24 ± 1 h, the specimens were unmolded and transferred for storage. Specimens were placed in a fog room at 100% RH and 22 °C temperature and were kept there until the age of testing. Three specimens for each test were prepared.

**Fig. 2** Four-point bending test: **a** tested specimen, **b** testing equipment

## 2.4 Test Procedure

The compressive strength was evaluated on $150 \times 300$ mm cylinders (three specimens for each mixture) following the guidelines of [4]. The flexural capacity was conducted on $100 \times 100 \times 400$ mm prisms on three specimens using a four-point bending configuration (Fig. 2) following the procedure described in ASTM C78 [3] with the loading rate of 0.075 mm/min. The four-point bending test was chosen over three point to avoid premature failure and due to the expected non-homogeneity of the specimens. Following the flexural capacity test, the flexural toughness was determined following the ASTMC1609 [6] approach, whereby the toughness is defined as the area under the flexural load–deflection curve immediately before failure. The flexural toughness of all mixtures was compared to the reference mix at 28 days (100%).

## 3 Analysis and Discussion of the Experimental Results

### 3.1 Mechanical Performance at 28 Days

The following sections describe and discuss the results of compressive and flexural tests performed on cylinders and prisms after 28 days curing in a fog room under uniaxial compression and the four-point bending test. The comparative results for all mixtures are presented in Fig. 3a for compressive strength, Fig. 3b for flexural strength, and Fig. 3c for flexural toughness.
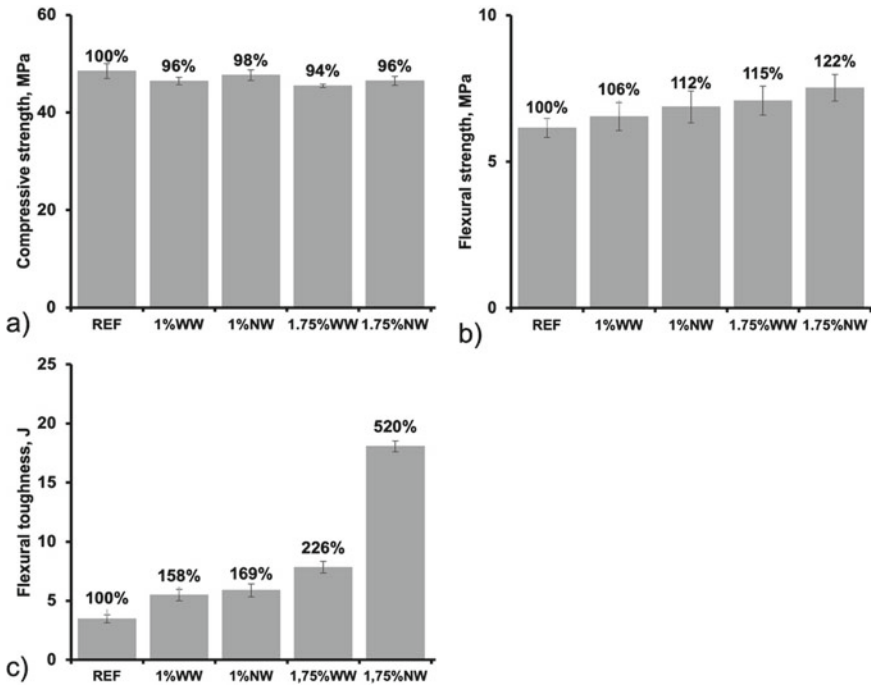
Fig. 3 Experimental results: **a** compressive strength; **b** flexural strength, and **c** flexural toughness. REF is used for reference mix, WW for the fibers with wood inclusions, and NW for the fibers after wood removal

## 3.2 Compressive Strength at 28 Days

The effects of WWTB-GFRP fibers on the compressive strength of concrete mixtures are presented in Fig. 3a. At 28-day age, the reference mixture (REF) achieved 48 MPa strength in compression. Mixtures 1%WW and 1.75%WW showed a slight decrease in compressive strength (4% and 6%, respectively). Mixtures 1%NW and 1.75%NW demonstrated a 2 and 4% decrease in compressive strength. As it can be concluded from the results, the elimination of the wood reduces the negative effect of fibers' addition on compressive strength. Obtained results are similar to those obtained in previous research for fibers including wood.

## 3.3 Flexural Capacity at 28 Days

The effects of WWTB-GFRP fibers on the flexural capacity of concrete mixtures are presented in Fig. 3b. The flexural strength–deflection curves are presented in Fig. 4a-e. At 28-day age, the reference mixture achieved 6 MPa in a four-point

bending test. Mixtures 1%WW and 1.75%WW showed a 6% and 15% increase in flexural strength, respectively. Mixtures 1%NW and 1.75%NW 12 and 22% increase in flexural strength. As can be seen from the results, the elimination of the wood increases the positive effect of fibers addition. Obtained results are similar to those obtained in previous research for fibers including wood. The increase in flexural strength for fibers without wood is similar though inferior to that observed for similar addition levels of virgin steel and glass fibers [6, 17, 20].

## 3.4   Flexural Toughness at 28 Days

The average flexural toughness of tested specimens at 28 days is depicted in Fig. 3c. With the increase of fiber content and decrease of wooden content, flexural toughness increased noticeably. For mixtures with 1% fiber addition with and without wood, the increase in flexural toughness reached 58% and 69%, respectively. The increase in flexural toughness for mixtures with 1.75% fibers addition is noticeably more pronounced for the mixture without wood reaching a 420% increase in flexural toughness, while the mixture with wood gained 126%.

## 3.5   Flexural Strength–Mid-Span Deflection Curve Analysis for the Four-Point Bending Test

The flexural strength–deflection curves for each mixture are presented in Fig. 4. Each graph represents the results of the four-point bending test for each mixture after curing 28 days in a fog room. In the name of specimens, the first letters define mixture tested, the following number represents the age at the day of testing (28 days), and the last number represents the number of the specimen (1, 2, 3). The four-point bending test for reference concrete mix exhibited a drastic decline in flexural strength after brittle failure for all curing conditions (Fig. 4a), often reported in the literature as a typical curve for plain concrete in four-point bending tests [6, 17, 20]. Four-point bending curves for mixtures with fibers addition are similar to the results of the [17] for polymeric fibers and [20] for steel fibers. Han et al. [20] defined three different behavioral types of the load–displacement curve of the steel fiber-reinforced concrete. First, the smaller the fiber content and the lower the tensile strength of the fiber, the wider and more drastic the load reduction appears in the section where the load reduces after the first peak load was reached (type A). Second, the greater the increase in the fiber content and the higher the tensile strength of the fiber, the longer the load–displacement curve increases over the first peak load after a slight load decline (type B). Finally, after the cracking of the concrete matrix, the load transfer to the fiber increases nonlinearly, without any load reduction (type C). In the case of WWTB-GFRP fibers, the mixture with 0.75% fibers with wood and without wood
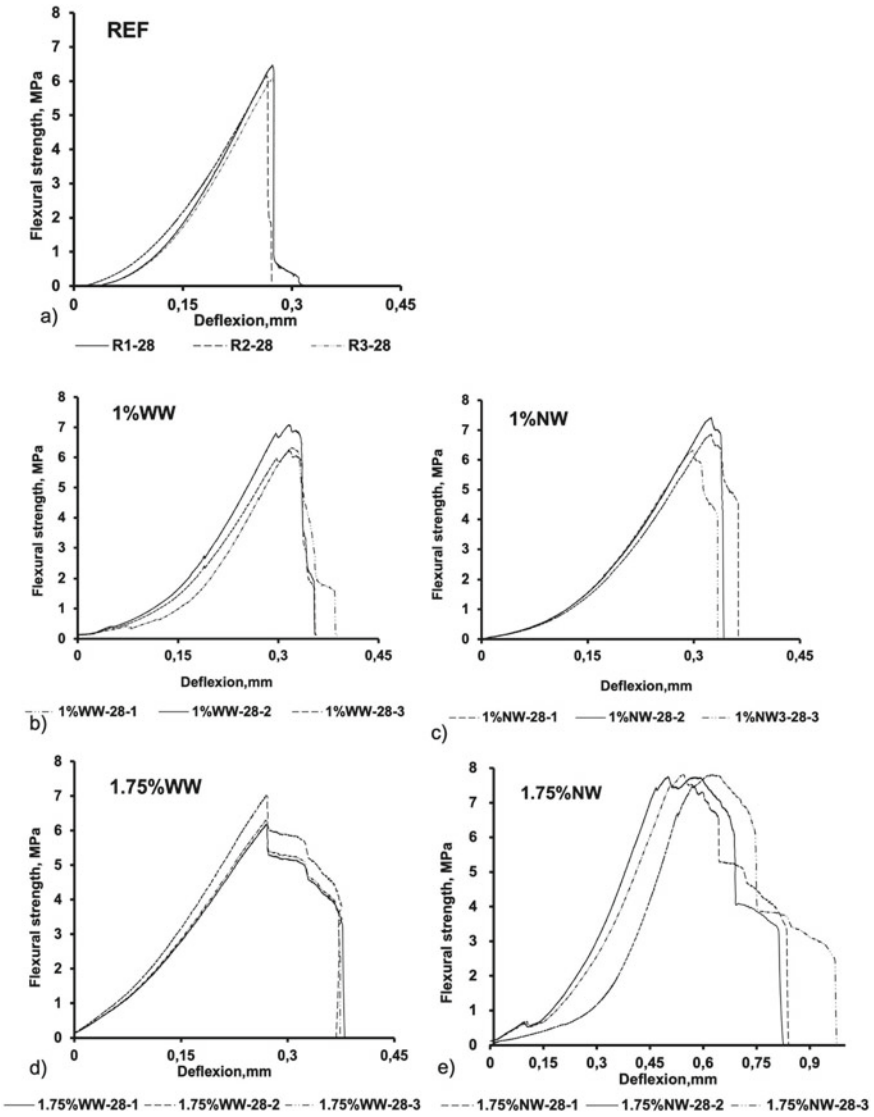
**Fig. 4** Flexural strength–mid-span deflection curve at 28 days: **a** reference mixture; **b** 1%WW mixture; **c** 1%NW mixture; **d** 1.75%WW mixture; **e** 1%NW mixture

shows a slightly smoother curve peak at the failure point similar to the results of [20] for mixture with 0.5% of hooked steel fibers (Type A), with noticeably shorter post-peak stage followed by the rapid load decrease. That type of curve can be explained by smaller fiber content and weak bond between fibers and concrete matrix compared to the hooked steel fibers at the post-peak stage, where the flexural behavior is generally driven by fibers tensile strength and slip bond resistance between fiber and

concrete matrix. Mixture without wood reaches a higher value of flexural strength due to the absence of negative effects of wooden content on concrete strength, but overall behavior is similar for both mixtures (0.75% with wood and without wood). Mixture with 1.75% of fibers with wood exhibits very pronounced peak with rapid load decrease after, followed by smooth decrease curve driven by fibers (Type A). The observed curve is similar to Specimen 2 for the mixture with 1% of hooked steel fibers added. The increase in fiber content increases post-peak curve length; the lower strength of added material (fibers and wood) determines the post-peak behavior according to the model proposed by [20]. The curve for 1.75% of fibers added without wood demonstrates a slight strength increase driven mainly by fibers, similarly to the Type C curve by [20]. At a 1.75% addition rate, the wood removal had a pronounced effect on fiber strength allowing the Type C flexural behavior.

## 4   Conclusion

In this study, the viability of valorizing WWTB-GFRP in concrete as fiber reinforcement was investigated. The addition rate of 1–1.75 vol. % into concrete for the fibers containing wood as received from the industrial partner, and after wood removal, was studied. Results indicate that WWTB-GFRP fibers addition slightly decreases compressive strength for all mixtures and increases flexural strength for all mixtures. Wood removal increases flexural strength gain and decreases compressive strength reduction for all mixtures. Quantity and type of fiber influence the failure mode and post-peak behavior, and the strength–displacement curves are similar to those for steel fiber-reinforced concrete. Specific findings are as follows:

- When WWTB-GFRP is incorporated in concrete as fiber reinforcement, an enhancement in flexural capacity of up to 22% was achieved.
- The flexural strength increases with the increase of fiber content and decrease of wooden content.
- A noticeable increase in flexural toughness with the increase in fiber content and decrease of wooden content is observed.
- The compressive strength decrease of up to 7% was observed for mixture with 1.75% of fibers with wood added.
- The compressive strength decreases with the increase of wooden content and with the increase of fiber content.
- Flexural strength–mid-span deflection curve shape varied depending on the fiber addition rate and type of the fiber added. A weaker fiber-concrete bond was observed resulting in a shorter post-peak stage and lower flexural toughness compared to virgin fiber-reinforced concretes.

Therefore, the WWTB-GFRP material can be valorized when it is added to concrete in the fiber form where the flexural capacity can be improved significantly. In general, this study supports the use of WWTB-GFRP in concrete as fiber reinforcement. The techniques of recycling fibers producing more homogeneous length

and width of fibers are to be found, and an explicit environmental analysis is needed to estimate the positive environmental effects of WWTB-GFRP recycling.

# References

1. Analysis and design of a pedestrian bridge with decommissioned FRP windblades and concrete (n.d.). https://www.researchgate.net/publication/333747778_Analysis_and_Design_of_a_Pedestrian_Bridge_with_Decommissioned_FRP_Windblades_and_Concrete. Accessed 9 Apr 2022
2. American Society for Testing and Materials. ASTM C192/C 192M (2016) Standard practice for making and curing concrete test specimens in the laboratory. ASTM International 2016, 04
3. American Society for Testing and Materials (ASTM) ASTM C78/C78M—02 (2002) Standard test method for flexural strength of concrete (using simple beam with third-point loading). ASTM International USA 2002. 04.02.
4. ASTM C39 (2016) ASTM Standard C39/C39M-16, standard test method for compressive strength of cylindrical concrete specimens
5. ASTM C1157/C1157M-20a (2020) Standard performance specification for hydraulic cement. ASTM International 2020, 2
6. ASTM C1609/C1609M-19a (2019) Standard test method for flexural performance of fiber-reinforced concrete (using beam with third-point loading). ASTM International
7. Baturkin D, Hisseine OA, Masmoudi R, Tagnit-Hamou A, Massicotte L (2021) Valorization of recycled FRP materials from wind turbine blades in concrete. Resour Conserv Recycl 174:105807. https://doi.org/10.1016/J.RESCONREC.2021.105807
8. Beauson J, Brøndsted P (2016) Wind turbine blades: an end of life perspective, pp 421–432. https://doi.org/10.1007/978-3-319-39095-6_23.
9. Beigi MH, Berenjian J, Lotfi Omran O, Sadeghi Nik A, Nikbin IM (2013) An experimental survey on combined effects of fibers and nanosilica on the mechanical, rheological, and durability properties of self-compacting concrete. Mater Des, vol 50. https://doi.org/10.1016/j.matdes.2013.03.046.
10. Çavdar A (2014) Investigation of freeze-thaw effects on mechanical properties of fiber reinforced cement mortars. Compos Part B: Eng, vol 58. https://doi.org/10.1016/j.compositesb.2013.11.013.
11. Correia JR, Almeida NM, Figueira JR (2011) Recycling of FRP composites: reusing fine GFRP waste in concrete mixtures. J Clean Prod 19:1745–1753. https://doi.org/10.1016/J.JCLEPRO.2011.05.018
12. D'Souza N, Gbegbaje-Das E, Shonfield P (2011) Life cycle assessment of electricity production from a V112 turbine wind plant. vol 21
13. Düzgün OA, Gül R, Aydin AC (2005) Effect of steel fibers on the mechanical properties of natural lightweight aggregate concrete. Mater Lett, vol 59. https://doi.org/10.1016/j.matlet.2005.05.071
14. Esmizadeh E, Khalili S, Vahidifar A, Naderi G, Dubois C (2019) Waste polymethyl methacrylate (PMMA): recycling and high-yield monomer recovery. Handb Ecomater 4:2977–3009. https://doi.org/10.1007/978-3-319-68255-6_164

15. European Council (2014) Conclusions on 2030 climate and energy policy framework. Zhurnal Eksperimental'noi i Teoreticheskoi Fiziki 2014
16. Fox T (2016) Recycling wind turbine blade composite material as aggregate in concrete. Graduate Theses and Dissertations. https://doi.org/10.31274/etd-180810-4761.
17. de Freitas I, Darwish F, Pereira MV, Allende K (2014) Fracture behavior of polymeric fiber reinforced lightweight structural concrete. Mater Res. vol 17. https://doi.org/10.1590/1516-1439.287314.
18. Giner VT, Baeza FJ, Ivorra S, Zornoza E, Galao Ó (2012) Effect of steel and carbon fiber additions on the dynamic properties of concrete containing silica fume. Mater Des, vol 34. https://doi.org/10.1016/j.matdes.2011.07.068.
19. GWEC (2015) Global wind report annual market update
20. Han YJ, Oh SK, Kim B (2017) Effect of load transfer section to toughness for steel fiber-reinforced concrete. Appl Sci (Switz), vol 7. https://doi.org/10.3390/app7060549
21. Keleştemur O, Yildiz S, Gökçer B, Arici E (2014) Statistical analysis for freeze-thaw resistance of cement mortars containing marble dust and glass fiber. Mater Des, vol 60. https://doi.org/10.1016/j.matdes.2014.04.013
22. Meyer C (1992) Concrete materials and sustainable development in the United States
23. Nagle AJ, Delaney EL, Bank LC, Leahy PG (2020) A comparative life cycle assessment between landfilling and co-processing of waste from decommissioned Irish wind turbine blades. J Clean Prod 277:123321. https://doi.org/10.1016/J.JCLEPRO.2020.123321
24. Nagle AJ, Mullally G, Leahy PG, Dunphy NP (2022) Life cycle assessment of the use of decommissioned wind blades in second life applications. J Environ Manage, vol 302. https://doi.org/10.1016/J.JENVMAN.2021.113994
25. Niu D, Jiang L, Bai M, Miao Y (2013) Study of the performance of steel fiber reinforced concrete to water and salt freezing condition. Mater Des, vol 44. https://doi.org/10.1016/j.matdes.2012.07.074
26. Oliveira PS, Antunes MLP, da Cruz NC, Rangel EC, de Azevedo ARG, Durrant SF (2020) Use of waste collected from wind turbine blade production as an eco-friendly ingredient in mortars for civil construction. J Clean Prod 274:122948. https://doi.org/10.1016/J.JCLEPRO.2020.122948
27. Patel K, Gupta R, Garg M, Wang B, Dave U (2019) Development of FRC materials with recycled glass fibers recovered from industrial GFRP-acrylic waste. Adv Mater Sci Eng, vol 2019. https://doi.org/10.1155/2019/4149708
28. Russell Gentry T, Al-Haddad T, Bank LC, Arias FR, Nagle A, Leahy P (2020) Structural analysis of a roof extracted from a wind turbine blade. https://doi.org/10.1061/(ASCE)AE.1943-5568.0000440
29. Tanyildizi H (2009) Statistical analysis for mechanical properties of polypropylene fiber reinforced lightweight concrete containing silica fume exposed to high temperature. Mater Des, vol 30. https://doi.org/10.1016/j.matdes.2008.11.032
30. Transportation costs take the "wind" out of clean energy (n.d.). https://www.reliableplant.com/Read/10090/transportation-costs-take-'wind'-out-of-clean-energy. Accessed 2 Oct 2021
31. Why Wind Works—Canadian Wind Energy Association (n.d.). https://canwea.ca/wind-facts/why-wind-works/. Accessed 2 Oct 2021

# Partial Cement Replacement in Concrete with Gypsum Powder Recycled from Waste Drywalls

**Kasra Takbiri and Pedram Sadeghian**

**Abstract** Construction industry is one of the most significant contributors to environmental issues in today's world. For this reason, sustainable approaches in building industry have always been sought by researchers in this domain. Cement manufacturing process, for example, emits considerable amounts of greenhouse gasses contributing to global warming. Replacing cement with other materials which have less environmental footprints has been considered a solution. Construction and demolition waste disposal, also, could cause environmental issues in landfills. Gypsum drywalls account for a considerable amount of construction waste which contains a noticeable amount of gypsum. Utilizing recycled gypsum from waste drywalls as a partial replacement for cement in concrete could address both problems regarding the impact of construction on the environment. In this study, recycled gypsum powder from waste drywall will be used as a partial replacement for cement in concrete. Five concrete mix designs which include 0, 10, and 20% of recycled fine gypsum powder and whole gypsum are considered for this study. Since it has been proven that gypsum does not function well as the only partial replacement of cement, 50% of each mix design is dedicated to fly ash. Three cylindrical (100 mm × 200 mm) specimens of each mix design are planned to be tested at 7, 28, and 90 days. This paper will introduce the combination of fly ash and recycled gypsum as a sustainable replacement for cement in concrete and suggest more environmentally friendly concrete for our infrastructure.

**Keywords** Cement replacement · Concrete · Gypsum · Recycling · Waste drywalls

K. Takbiri (✉) · P. Sadeghian
Civil and Resource Department, Dalhousie University, Halifax, Canada
e-mail: kasra.takbiri@dal.ca

# 1   Introduction

The negative impact of the construction industry on the natural environment is unde-batable. Hereby, two of the most noticeable topics are discussed. First, the cement manufacturing process could result in carbon dioxide ($CO_2$) production, thereby contributing to climate change and global warming. Second is the gypsum drywall disposal in landfills, which could result in soil degradation and the contamination of nearby water resources. Utilizing recycled gypsum as a partial replacement for cement in concrete structures could be considered as an approach to address both issues [1].

Cement manufacturing plants emit significant amounts of greenhouse gasses (GHG) into the atmosphere. The emissions resulting from the cement industry account for up to 10% of artificial GHG emissions in the world [1, 2]. Also, the cement industry alone is responsible for 7% of global $CO_2$ emissions [3]. Needless to say that $CO_2$ could have devastating impacts on the natural environment. Since it is the major contributor to air pollution and global warming [4]. Furthermore, the cement industry consumes a significant amount of energy annually for manufac-turing the product [2]. This could be an amplification for the production of GHGs resulting from cement manufacturing since a considerable amount of fossil fuels needs to be burned for sufficient energy to be provided for the cement manufacturing process every year [5]. Nearly 3.4 billion tons of cement are produced as the major raw material for concrete manufacturing [2]. The costs of cement production and the huge volume of cement that is produced annually convinced civil and environ-mental engineers to look for replacements for cement as the cementitious material in concrete.

Construction materials disposal at landfills is another noticeable issue in today's world. Each material could have different impacts on the natural environment depending on the material's chemical and mechanical properties. Gypsum wall-boards (also known as drywalls) account for a significant amount of residential construction waste (nearly 20%). As a result of drywall disposal, huge amounts of gypsum are accumulated in landfills, which will cause several environmental issues. Gypsum is capable of releasing hydrogen sulfide gasses which could result in soil degradation [6]. It is also a flammable gas that could be lethal in high concentrations [7, 8]. Hydrogen sulfide could also penetrate the soil and cause water contamina-tion in nearby areas [7]. Utilizing the accumulated gypsum resulting from drywall disposal is considered as an approach to address the issues resulting from cement manufacturing and gypsum drywall waste disposal [7].

Using recycled gypsum from waste drywalls as a partial replacement for cement in concrete could reduce the demand for cement production and as a result, fewer GHGs would be emitted to the atmosphere. Also, it could be a rational approach to eliminate gypsum from our landfills and turn it into a resource. Naik et al. [1] used the combination of recycled gypsum powder and fly ash class C as a partial replacement for cement in concrete. According to the results, between 30 and 60% of cement could be replaced by a gypsum-fly ash class C mixture. More importantly,

concrete specimens containing 10% gypsum as cementitious material are shown to have the same compressive strength as the conventional concrete after 28 days. Hansen and Sadeghian [7] attempted to replace a higher volume of cement with a gypsum-fly ash mixture (up to 70%). Gypsum could have negative impacts on the compressive strength of concrete in a short period after manufacturing. However, the concrete containing gypsum alongside fly ash and cement as the cementitious paste is proven to have higher compressive strength compared to the concrete mixture that has only cement and fly ash as the cementitious material [7]. Therefore, the application of recycled gypsum powder is acceptable, and utilizing this material in concrete manufacturing is feasible.

In a previous study by [7], only fine particles of the recycled gypsum from waste drywalls were used. To be more specific, the particles remaining on the sieve No 100, sieve no 200, and the pan during sieve analysis were separated and used in the concrete. This proportion accounts for only 38% of a certain sample of recycled gypsum. In other words, a considerable proportion of gypsum drywalls would remain as waste and would be dumped in the landfills again. Therefore, solutions are needed to be introduced in order to make this approach more sustainable. In this study, one more step has been taken in the domain of application of recycled gypsum in concrete, and the whole recycled gypsum is used as a replacement for cement in several concrete specimens. The main goal of this paper is to introduce an ultimate performance for the waste gypsum in our infrastructure.

## 2 Experimental Program

### 2.1 Test Matrix

Five total mix designs are considered for this study including one control batch, two batches that involve fine gypsum as a partial replacement for cement in different amounts (20 and 10%), and two batches that involve the whole gypsum as partial replacements for 10 and 20% of cement in the concrete. Fly ash accounts for half of the cementitious material mass in all the batches, and the other half is dedicated to cementing only for the control batch and the combination of cement and gypsum for other batches. The purpose of considering mixed designs with fine gypsum is to validate the results achieved by Hansen and Sadeghian [7] making an appropriate comparison with this study. The detail for mixtures is presented in Table 1. Also, the proportion of each component of cementitious materials is demonstrated in Table 2. The capital letter G stands for the mixtures that involve the whole gypsum, while FG stands for those in which only fine particles of gypsum are used. The letter C stands for control specimens. The number in front of each letter indicates the proportion of cement which is replaced by the corresponding gypsum (fine or whole amount). In order to make better comparisons considered that the mix design for this study is the same as Hansen and Sadeghian [7] (Figs. 1 and 2).

**Table 1** Mix design (the material quantities for 1 m³ of concrete)

| Material | Quantities |
|---|---|
| Water (kg) | 187.9 |
| Coarse aggregate (kg) | 1184.3 |
| Fine aggregate (kg) | 574.6 |
| Cementitious materials (kg) | 395.2 |
| Superplasticizer (L) | 0–1.6 |

**Table 2** Contribution of each component of cementitious material in

| Specimens ID | Cementitious material (%) | | |
|---|---|---|---|
| | Cement | Fly ash | Gypsum |
| C | 50 | 50 | 0 |
| G10 | 40 | 50 | 10 |
| G20 | 30 | 50 | 20 |
| FG10 | 40 | 50 | 10 |
| FG20 | 30 | 50 | 20 |

**Fig. 1** Fine aggregate particle size distribution
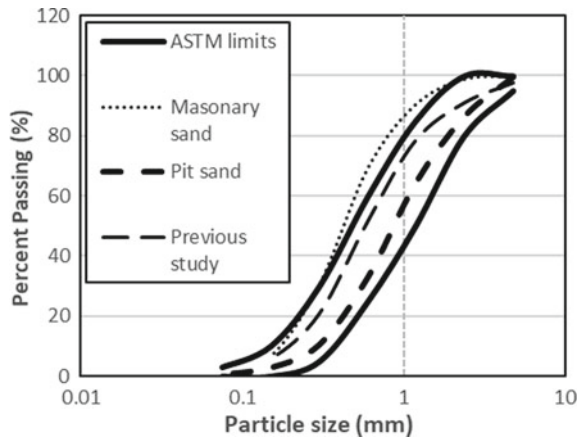


## 2.2 Material Properties

Overall, three types of sand were available for this study; masonry sand, sand donated by local sources (Casey Metro, Halifax, NS, Canada) in the previous years which was used by Hansen and Sadeghian, and sand donated by the same source recently. After sieve analysis, it was revealed that masonry sand is not falling into the ASTM parameters for making concrete. While both curves corresponding to the second and third sand are located between the ASTM top and bottom limit, they are not identical. The third type is decided to be used because of its availability for this study and later research related to this topic. The coarse aggregate donated by the same source is

**Fig. 2** Gypsum particle size distribution
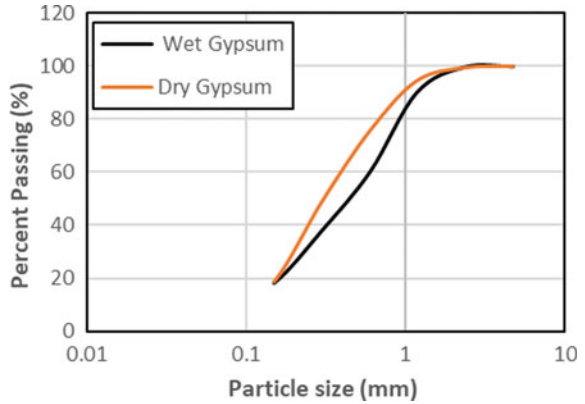
half-inch stone which is suitable for making concrete in terms of size distribution. The cement considered for this study is type GU Portland cement (CRH, Canada Group, ON, Canada). Fly ash used in the concrete was provided by local sources (Ocean Contractor Ltd, Dartmouth, NS, Canada). The recycled gypsum provided from waste gypsum drywalls was provided by USA Gypsum, Denver, PA, USA, which is the same gypsum used by Hansen and Sadeghian in the previous study. During Gypsum sieve analysis, the fiber-like particles which were many courses than normal gypsum particles were observed on most of the sieves (all sieves but sieve No. 200 and pan). For mix designs that contain fine gypsum (the ID starts with FG) only the gypsum retaining on sieve 200 and pan is used. For other mixes, the whole gypsum was used without removing fiber-like and coarser particles. Figure 3 demonstrates the fine gypsum and whole gypsum particles (Fig. 4).
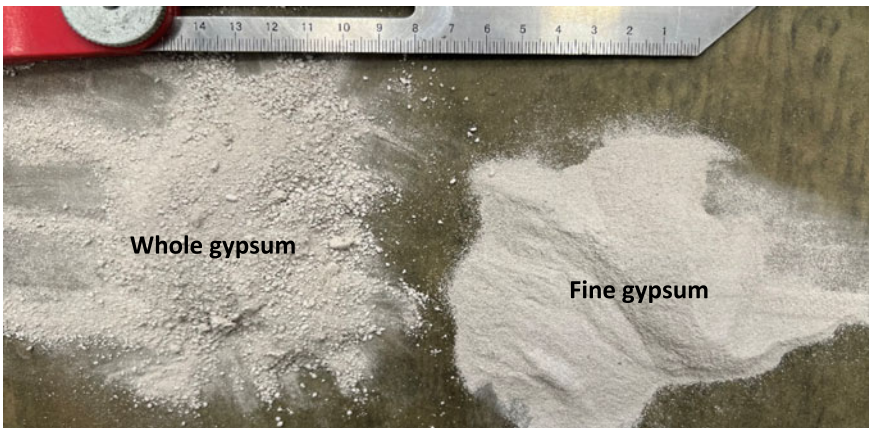


**Fig. 3** Fine gypsum and whole gypsum samples

**Fig. 4**  Gypsum concrete ingredients

After conducting sieve analysis on gypsum, some coarse fiber-like particles were witnessed on the sieve. These particles could be found on all the sieves except sieve No 200. In the previous research conducted by Hansen and Sadeghian, these particles did not show up on sieve No 100. The main suspect of this contradiction was the effect of humidity. To test this hypothesis, sieve analysis was conducted on dry gypsum as well. A specific proportion of gypsum was oven-dried for 24 h and afterward, and the sieve analysis was conducted on the dry sample. In this case, those fiber-like particles were no longer visible on sieve No 100. As can be seen in Figs. 2 and 5, there are significant differences between the particle size distribution of the two types of gypsum. It is worth mentioning that the moisture content of gypsum turned out to be more than 22%, measuring the weight of the dry sample. This proportion of moisture could affect the sieve analysis results.

## 2.3  Specimen Preparation

Five batches are considered for this study. Three batches including control specimens are considered to validate the previous studies regarding the impact of fine gypsum content as cementitious material on the compressive strength of concrete. The other two batches are considered to assess the impact of using the whole gypsum (fine particles and coarse particles) instead of fine gypsum in the concrete. A mini mixer was used for mixing all the ingredients of concrete. All the materials are added to the mixer in a certain order. The mixer was allowed to work until a homogenous mix is achieved. For those mix designs which involved gypsum, dehydration was witnessed
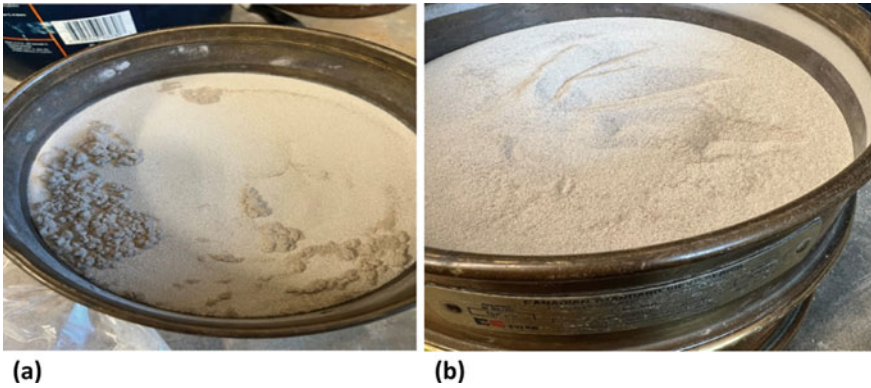
**Fig. 5** Retaining gypsum powder on sieve No.100 after shaking, **a** wet gypsum, **b** dry gypsum
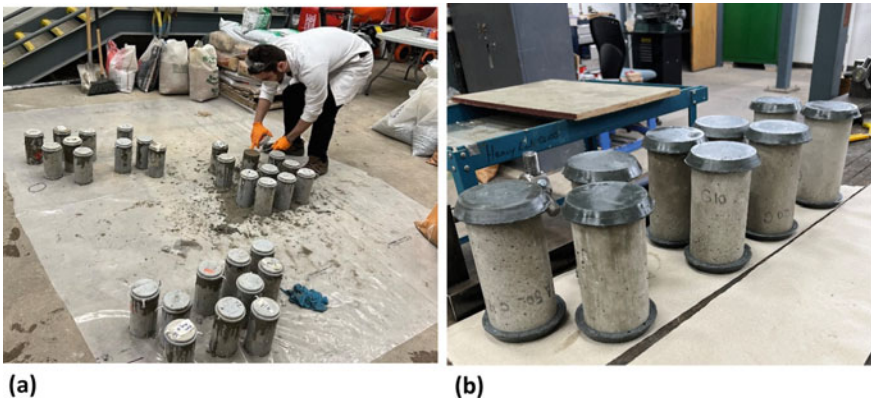


**Fig. 6** **a** Casting concrete in molds and preparing specimens. **b** Capped specimens

in the mix. For this reason, a superplasticizer is used to make the mix workable and hydrated. For each mix design, three 100 mm × 200 mm molds are considered which are tested on day 7, day 28, and day 90. All the specimens are cured in the moisture room after being demolded (Fig. 6).

## 2.4 Test Setup and Instrumentation

Specimens are removed from the moisture room and capped using sulfur compound after 24 h. After another 24 h, the capped specimens are tested at ages using the compressive test machine. The output is the maximum force that each specimen resists in pounds (lbs). After doing conversions and calculations, the compressive strength is calculated in Megapascal (MPa).

# 3 Results and Discussion

## 3.1 Compressive Test Results

Specimens were tested after 7, 28, and 90 days of curing in the moisture room. For each mix design, three specimens were tested on the testing day, and the average compressive strength was determined in MPa. The tested specimens and the compressive test results corresponding to day 7, 28, and 90 tests are demonstrated in Figs. 7, 8, and Table 3.



**Fig. 7** Specimens after compressive strength test



**Fig. 8** Compressive strength results
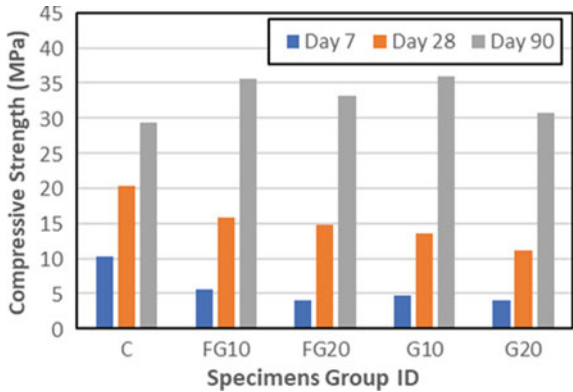
**Table 3** Average compressive strength of strength corresponding to each mix design

| Specimen ID | Compressive strength day 7 (MPa) | Standard deviation day 7 (MPa) | Compressive strength day 28 (MPa) | Standard deviation day 28 (MPa) | Compressive strength day 90 (MPa) | Standard deviation day 90 (MPa) |
|---|---|---|---|---|---|---|
| C | 10.2 | 0.49 | 20.4 | 1.98 | 29.4 | 3.1 |
| G10 | 4.7 | 0 | 13.5 | 1.14 | 36.0 | 0.1 |
| G20 | 4.1 | 0.43 | 11.1 | 0.71 | 30.8 | 1.99 |
| FG10 | 5.6 | 0.13 | 15.8 | 0.33 | 35.5 | 1.89 |
| FG20 | 4.0 | 0.25 | 14.7 | 0.85 | 33.2 | 3.4 |

**Table 4** Compressive strength reduction and increase compared to control specimens

| Specimen type | 10% gypsum (day 7) (%) | 20% gypsum (day 7) (%) | 10% gypsum (day 28) (%) | 20% gypsum (day 28) (%) | 10% gypsum (day 90) (%) | 20% gypsum (day 90) (%) |
|---|---|---|---|---|---|---|
| Whole gypsum | −53.9 | −59.8 | −33.8 | −45.6 | +22.4 | +4.8 |
| Fine gypsum | −45.1 | −60.8 | −22.5 | −27.9 | +20.7 | +12.9 |

## 3.2 The Impact of Using Fine Gypsum and Whole Gypsum

According to the compressive test results, the gypsum content could have a negative impact on the compressive strength of concrete. This strength reduction is more significant at early ages and became lower at later ages. In a longer period, however, the gypsum content had a positive impact on the compressive strength of concrete. Using fine gypsum could result in stronger concrete compared to the concrete which involves the whole gypsum in the mix design; however, according to the sieve analysis, almost 38% of the whole recycled gypsum would be used for making fine gypsum concrete. On the other hand, although the whole gypsum concrete is slightly weaker than fine gypsum concrete, the former is much more sustainable compared to the latter. Table 4 shows the comparison between whole gypsum, fine gypsum concrete, and control specimen in terms of compressive strength changes as a result of using gypsum in concrete.

## 3.3 Comparison of the Previous Studies

Hansen and Sadeghian [7] conducted a similar study in which fine gypsum concrete was evaluated. To make a better comparison, in this study, both fine gypsum and whole gypsum concrete are considered. According to Table 3, the compressive strength of

each mix design in this study is slightly different from that of the previous one although the same mix design and materials were used in both. Some parameters such as humidity, temperature, and the effect of superplasticizer could result in this difference. The impact of fine gypsum content followed a similar trend in both studies as can be seen in Table 4.

## 4 Conclusion and Recommendations

In this study, 5 batches with similar mix designs and different cementitious material compounds were considered. One control batch involved 50% cement and 50% fly ash as cementitious material, two batches with 10 and 20% of cement replaced with fine gypsum, and two batches in which 10 and 20% of cement were replaced with whole gypsum. To provide fine gypsum, only the retaining gypsum particles on sieve No. 200 and pan were used whereas for whole gypsum batches, specific proportions of gypsum were randomly added to the mix. 9 specimens were provided for each batch which are tested on day 7, day 28, and day 90. According to the tests on day 7 and day 28, the compressive strength of concrete reduces by increasing the proportion of gypsum by which cement is replaced. This strength reduction is more severe in early ages. The compressive strength even reduces to lower levels if the whole gypsum is used instead of fine gypsum as a replacement for cement. The promising point is that the strength reduction decreased significantly on the day 28 test. This could indicate that the negative impact of using gypsum in the concrete could become less noticeable or even negligible in the long-term period. According to day 90 test results, utilizing both fine and whole gypsum could increase the compressive strength of the concrete in the long-term period. Also, the slight difference between the compressive strength of whole gypsum concrete and fine gypsum concrete indicates that the whole gypsum concrete could be as practical in today's life as fine gypsum concrete with higher sustainability features. Some contradictions have been witnessed between this study and the previous studies in this domain, while similar mix designs were used in both. Some important factors could have contributed to this phenomenon including humidity rate, temperature, and the process of mixing materials and making specimens. It is highly recommended for further studies to consider the impact of gypsum content in concrete for a longer time period (more than 90 days). Furthermore, it is essential to seek solutions for addressing the issues regarding the lack of strength in the early ages of gypsum concrete. Also, it is worth mentioning that the durability of this type of concrete must be evaluated. For gypsum concrete to be fully functional in our infrastructure, it should be able to survive diverse environmental conditions.

# References

1. Naik TR, Kumar R, Chun YM, Kraus RN (2010) Utilization of powdered gypsum-wallboard in concrete. In: Proceedings of international conference on sustainable construction materials and technology
2. Nguyen L, Moseson AJ, Farnam Y, Spatari S (2018) Effects of composition and transportation logistics on environmental, energy and cost metrics for the production of alternative cementitious binders. J Clean Prod 185:628–645
3. Malhotra VM (1999) Role of supplementary cementing materials in reducing greenhouse gas emissions. In: Infrastructure regeneration and rehabilitation improving the quality of life through better construction: a vision for the next millennium, Sheffield, 28 June–2 July 1999, pp 27–42
4. Meyer C (2009) The greening of the concrete industry. Cem Concr Compos 31(8):601–605
5. Ke J, McNeil M, Price L, Khanna NZ, Zhou N (2013) Estimation of $CO_2$ emissions from China's cement production: methodologies and uncertainties. Energy Policy 57:172–181
6. Ahmed A, Ugai K, Kamei T (2011) Laboratory and field evaluations of recycled gypsum as a stabilizer agent in embankment construction. Soils Found 51(6):975–990
7. Hansen S, Sadeghian P (2020) Recycled gypsum powder from waste drywalls combined with fly ash for partial cement replacement in concrete. J Clean Prod 274:122785
8. Chandara C, Azizli KAM, Ahmad ZA, Sakai E (2009) Use of waste gypsum to replace natural gypsum as set retarders in Portland cement. Waste Manage 29(5):1675–1679

# Materials Specialty: Innovatinve and Emerging Materials

# Converting Other Flexible Plastic Packaging into Fiber Reinforcement for Concrete Structures

**Loveleen Sharma, Jaykumar Viradiya, Rishi Gupta, and Sam Baker**

**Abstract** Concrete is world's most common construction material owing to its unique formability where it is typically reinforced with steel rebars. Nevertheless, the high tensile strength of steel rebars is usually localized, and rebars are prone to corrosion creating deterioration of infrastructure costing billions of dollars for repairs. This has resulted in using fibers into concrete called fiber reinforced concrete (FRC). This replacement technology (i.e. FRC) not only improves the quality of concrete, but it is also environmentally friendly. Most commonly, steel, glass, synthetic cellulose, carbon, etc. are used as fiber for FRC. Aside from these, this research presents the use of other flexible plastic packaging (OFPP) as reinforcement in concrete. OFPP is one of the fastest growing types of packaging, which is not easily recyclable as it comprises multiple layers of different kinds of plastics. Examples of OFPP includes stand-up/zipper lock pouches, crinkly wrappers/bags, flexible packaging with plastic seal, non-food protective wrap, net bags for onions, avocados, etc. The major steps involved in this formulation include the sorting and cleaning of OFPP (as waste) to obtain clean and usable material, which is then shredded into fibers. Upon employing a patented coating technology developed at UVic, these shredded fibers are converted into green engineered surface-treated fibers (GESTF) for casting different concrete structures, *namely* FRC. In order to access the performance of FRC thus obtained, a set of mechanical testing is conducted according to ASTM/CSA test standards. On accomplishing the tests, a significant improvement in concrete structure is observed in terms of compression, uniaxial tension or indirect tension, flexure, and plastic shrinkage. This research will potentially open-up a new market and process for using OFPP for improving the mechanical and early-age shrinkage properties of concrete.

**Keywords** OFPP · GESTF · FRC · ASTM/CSA

L. Sharma · J. Viradiya · R. Gupta (✉)
Department of Civil Engineering, University of Victoria, Victoria, BC, Canada
e-mail: guptar@uvic.ca

S. Baker
Recycle BC, North Vancouver, BC, Canada

# 1   Introduction

There are almost 300 types of plastics, of which polypropylene (PP), polyethylene (PE), polyvinyl chloride (PVC), polyurethane (PU), polystyrene (PS), and phenolic resin [9, 11] are commonly used plastics in everyday products, mainly disposable plastic packaging. In order to meet day-to-day demand of plastic products, the production of plastic is continuing to rise. Globally, the plastic production has grown from 1.7 million metric tonnes in 1950 to ~ 360 million metric tonnes in 2018 [13]. By 2030, the amount of plastic in circulation is projected to increase to 417 million tonnes [16]. It is worth considering that with an increase in plastic production, it is becoming more crucial to find safe disposal methods for plastics to preserve the ecosystem. Canada recycles 9% of plastic waste each year, meaning the vast majority of plastics end up in landfills and about 29,000 tonnes finds its way into our natural environment (https://www.canada.ca/en/environment-climate-change/services/managing-reducing-waste/reduce-plastic-waste.html. Therefore, it is evocative to execute some discerning methods to recycle plastic waste as much as possible. By keeping this issue on the top of mind, Recycle BC has come up with some insightful measures to collect other flexible plastic packaging (OFPP). Recycle BC is responsible for residential packaging and paper recycling in British Columbia. Material is collected from residents by various means, including curbside collection, multi-family collection, and depot collection. Four types of material, due to their physical properties, are collected only in segregated streams at depots. These include non-deposit glass bottles and jars, plastic bags and overwrap, foam packaging, and other flexible plastic packaging (OFPP). While most plastic collected within the programme is recycled by their end market Merlin Plastics, some plastics, such as OFPP and films do not yet have a recycling solution. Examples of OFPP include: stand-up and zipper lock pouches, like pouches for granola, frozen berries, etc.; crinkly wrappers and bags, like coffee bags, or chip bags; flexible packaging with plastic seal, like packaging for fresh pasta or pre-packaged deli meats; non-food protective wrap like bubble wrap or plastic envelopes; and net bags for onions, avocados, lemons, etc. (https://recyclebc.ca/flexiblepackaging/). OFPP are types of film and flexible plastics that often include multiple layers of different types of plastic, making it more difficult to recycle. Therefore, OFPP is currently turned into engineered fuel. The idea is to find a higher end use for this material segment. This paper introduces the awareness of using OFPP as reinforcement for concrete by deploying experimental investigation.

Concrete is world's most common composite construction material due to its distinctive formability. However, concrete is brittle and prone to cracking under normal stresses and impact loads [1, 10, 14, 18]. In order to overcome this issue, concrete is strengthened with necessary reinforcement to resist stresses. Typically steel rebars are identified as reinforcement to provide high tensile strength, *acting locally*, to concrete. The reinforced concrete is less vulnerable to failure under applied load. At the same time, the steel rebars itself are prone to corrosion creating deterioration of infrastructure costing billions of dollars in repairs. This has resulted in a

multi-million dollar industry producing and marketing randomly distributed fibers to use in concrete. When fibers are added in concrete it is called fiber reinforced concrete (FRC) that provides improvement in properties such as non-magnetic, non-corrosive, easy to finish, reduced temperature causing shrinkages and expansions and alkali proof, etc. This replacement technology (i.e. FRC) not only improves the quality of concrete, but also results in reduced $CO_2$ emission, water usage, and fossil fuel consumption. Various types of fibers are used around the world including steel, glass, synthetic, cellulose, carbon, etc. The segment of synthetic fibers (example polypropylene, polyethylene, etc.) has a large share of the fiber industry owing to the inertness/durability of the fibers and their effectiveness in reducing cracking induced due to plastic shrinkage. However, most synthetic fibers like polypropylene, polyethylene, etc. are inherently smooth and have a weak bond with concrete. An invention by Dr. Gupta (filed in 2015, granted in 2018) allows coating of all reinforcement used in concrete including continuous rebar and randomly distributed discrete fibers with SCMs, resulting in "green engineered surface active" material. The fibers are called "green engineered surface-treated fibers" (GESTF) (https://patents.google.com/patent/US20150344367A1/en). This improves the bonding between engineered fibers and the surrounding matrix to enhance the reinforcement efficiency. Thus, herein an experimental study is delineated for converting OFPP to fibers to be used to create FRC.

## 2 Experimental

In order to understand the role of OFPP as fiber reinforcement in concrete, an experimental investigation was conducted. Mortar samples of different shapes were casted by using OFPP as reinforcement. The details of the material used, experimental conditions, and methodology are discussed in this section.

### 2.1 Materials

Type general use (GU) cement meeting the specifications of Canadian Standard Association (CSA), with specific gravity of the cement of 3.15 in accordance with ASTM C150 [5], was adopted as a binder (https://www.csagroup.org/store/product/CAN%25100CSA-A3000-13/). Locally available sand of grain size less than 4.75 mm was used as mixture to cement. The OFPP used for the experimentation was obtained from Recycle BC. However, the raw material (OFPP) obtained was first parted from other waste that came along with OFPP. The OFPP thus picked-up was washed and dried to remove left-over food or other taints of contaminated food stuff. On drying the washed OFPP, the sorting into six categories was accomplished as per the guidelines provided by Recycle BC and depicted in Fig. 1. To convert these OFPP into

monofilament fibres for using as a fibre reinforcement for concrete (FRC), plastics were shredded manually (by cutting blade equipment) to obtain an average size of 15 mm × 1 mm approximately. Figure 2 shows the prepared OFPP fibres for all six types. Once OFPP fibres were produced for desired dimensions, they were further converted into green engineered surface-treated fibers (GESTF) upon coating with supplementary cementing materials (SCMs) supplied by Kryton®. Thus, the shredded fibers were categorized into two parts, viz., uncoated OFPP and coated OFPP for casting different mortar samples, namely FRC. The uncoated fibres stands for virgin OFPP fibers, and coated fibres stands for OFPP coated with SCMs such as fly-ash, silica fume, etc. The purpose of coating the OFPP was to eliminate weak spots at the interface of the reinforcement and aggregate that causes cementitious particles to not pack densely, as plastic has very low surface energy that causes difficulty in adhesion with other surfaces/materials. Therefore, we used commercially available high strength adhesives for accomplishing coating of OFPP fibers. In order to attach silica fume on the surface of OFPP fibres following steps were followed:

(a)  Desired amount of each type of OFPP was weighed;



**1) Zipper Lock & Stand-Up Pouches:**
Including bags with a zip-seal top, like those for frozen fruit and stand-up pouches like those for oatmeal or quinoa.

**2) Crinkly Wrappers, Bags & Bars:**
This includes things such as bags for chips, energy bars, wrappers for cheese, etc..

**3) Flexible Packaging with Plastic Seal:**
Packaging for things like deli meat and cheeses, fresh pasta, etc.

**4) Woven & Net Plastic Bags:**
Such as netting for onions, avocados, oranges, and woven plastic bags like those for rice and dry goods.

**5) Non-Food Protective Packaging:**
Padded protective plastic such as shipping envelopes, air packets, bubble wrap, etc.

**6) Packaging Film:**
Thin includes thin plastic membranes such as films for separating area or volumes, to hold items, etc.

**Fig. 1** Categories of OFPP (https://recyclebc.ca/flexiblepackaging/)

**Fig. 2** Manually chopped OFFP fibers: **a** Woven and net bags; **b** Zipper lock and stand-up pouches; **c** Non-food protective packaging; **d** Crinkly wrappers, bags, and bars; **e** Flexible packaging with plastic seal; **f** Packaging Film

(b) The surface of sought-after OFPP was wetted by using commercially available adhesive for plastics, as shown in Fig. 3a;

(c) Silica fume is drenched on the wet surfaces of OFPP, as shown in Fig. 3b. In addition, little hand pressure was applied on adhesive contained OFPP, against silica, to ensure the desired coating;

(d) Lastly, kept silica fume coated fibres at a room temperature for one-two hour for curing purpose.
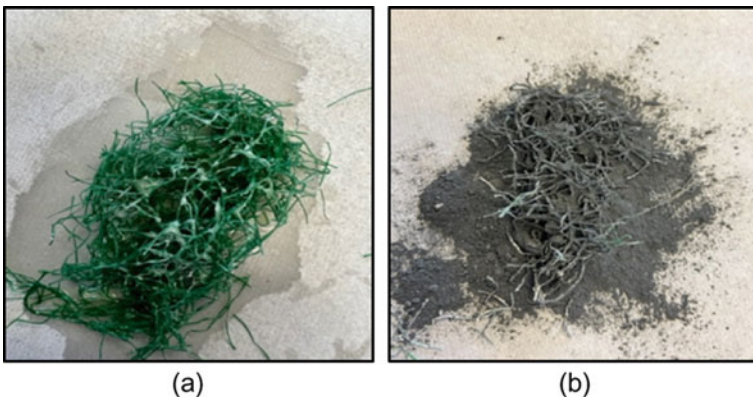


**Fig. 3** Surface coating procedure of fibres: **a** Wetted OFPP fibers with adhesive; **b** OFPP fibers drenched with silica fume

**Table 1** Properties of OFPP

| Type of OFPP | Physical properties | Constituents* | Density (kg/m$^3$) | Average length (mm) | Average width (mm) |
|---|---|---|---|---|---|
| Packaging film | Transparent and can be stretched | Polyethylene terephthalate Linear low-density polyethylene | $1250 \pm 7\%$ | 15 | 1 |
| Zipper lock and stand-up pouches | Bags with zip-seal top, and stand-up pouches | PET Linear low-density polyethylene (LLDPE) | $2000 \pm 12\%$ | 15 | 1 |
| Crinkly wrappers, bags and bars | Bags with metallic interior, including chip bags, energy bars | Biaxially oriented polypropylene (BOPP) Metallizing layer | $1600 \pm 8\%$ | 15 | 1 |
| Flexible packaging with plastic seal | Bags with very flexible film-like plastic, includes bags for deli meat and cheese | Polyvinyl chloride High-density co-ex blend polyethylene | $1333 \pm 5\%$ | 15 | 1 |
| Woven and net bags | Bags made of thin strings (looking like fish net) | Polypropylene | $1200 \pm 4\%$ | 15 | 1 |
| Non-food protective packaging | Padded protective plastic, including air packets and bubble wraps | Polyethylene terephthalate Linear low-density polyethylene opaque films | $1166 \pm 5\%$ | 15 | 1 |

*APC—Design Smart Material Guide—Flexible Plastic

On following the abovementioned steps, the desired quantity of coated OFPP fibers was achieved (Table 1).

## 2.2 Mix Design

Table 2 represents the details of the mix design used for castings of the mortar samples deployed in this study. Four shapes of mortar samples were casted, viz., cube samples (50 mm × 50 mm × 50 mm), dog bone samples (75 mm × 25 mm × 25 mm), beams samples (30 mm × 30 mm × 100 mm) and half dog bone samples

**Table 2** Mix design details

| Ingredients | Quantity (kg/m$^3$) |
|---|---|
| Cement | 662 |
| Sand | 1105 |
| Water | 331 |



**Fig. 4** Illustration for each type of OFPP fiber reinforced mortar sample, viz., cube, dog bone, beam, half dog bone

(37.5 mm × 25 mm × 25 mm). In order to cast the half dog bone specimen, a 3D printed piece of PLA slice was placed into the centre of the mould. Then, a plastic fibre was carefully inserted through the small hole of the 3D printed PLA slice with a specified embedded length equal to half the fibre length. Figure 4 presents the typical example for each type of sample. All six types of uncoated and coated OFPP were added as fibres for the amount of 1% by volume of cement in all mortar samples. Each type of casting repeated for three specimens along with control sample (without any OFPP fiber). Water cement ratio of 0.5 was adopted for obtaining a mortar of strength 25 MPa. On accomplishing the casting, the samples were cured for 28 days before conducting any measurement.

## 2.3 Testing Procedure and Equipment

Once the samples are cured, all four shapes (*namely, cubes, dog bones, beams, half dog bone*) casted by using coated and uncoated OFPP (*namely, zipper lock and stand-up pouches, crinkly wrappers and bags, flexible packaging with plastic seal, non-food protective packaging, woven and net plastic bags, packaging films*) were analyzed for crucial aspects to present the performance of OFPP as fiber reinforcement for concrete. Four types of testing were conducted subjected to each type of mortar sample, i.e. compressive strength (through cube samples analysis), tensile strength (through dog bone samples analysis), flexural strength (through beam samples analysis), and bond strength (through half dog bone samples analysis). For illustration, cubes were deployed for measuring compressive strength, dog bone samples were deployed for measuring tension strength, beam samples were deployed for measuring flexure strength, and half dog bone samples were deployed to conduct single fiber pull-out testing that measures the bond strength between single fiber and mortar sample.

Compressive strength test was performed on cube samples (50 mm × 50 mm × 50 mm) at 28-days age, in accordance with ASTM C109 [6] using FORNEY F-650 compression machine, as shown in Fig. 5a. The testing machine was equipped with the appropriate compression platens and the loading rate was 900–1800 N/s. For all six categories of OFPP fibre, three cube samples containing uncoated fibres and three cube samples containing coated fibres with silica fume were tested under compression.

Tensile strength test was performed according to ASTM C307 standard [3] on briquette samples/dog bone samples (width and depth at waistline of briquette was 25 mm and length is 75 mm) at 28 days of age. PASCO® Testing Machine (MTM) with 1 mm/min crosshead loading rate was used to carry out the tensile test, as shown in Fig. 5b. The MTM had a built-in load cell capable of measuring up to 7100 N of force and an optical encoder module that was able to measure the displacement of



**Fig. 5** Set-up for:
**a** Compression test,
**b** Tension test, **c** Flexural
test, **d** Pull-out test
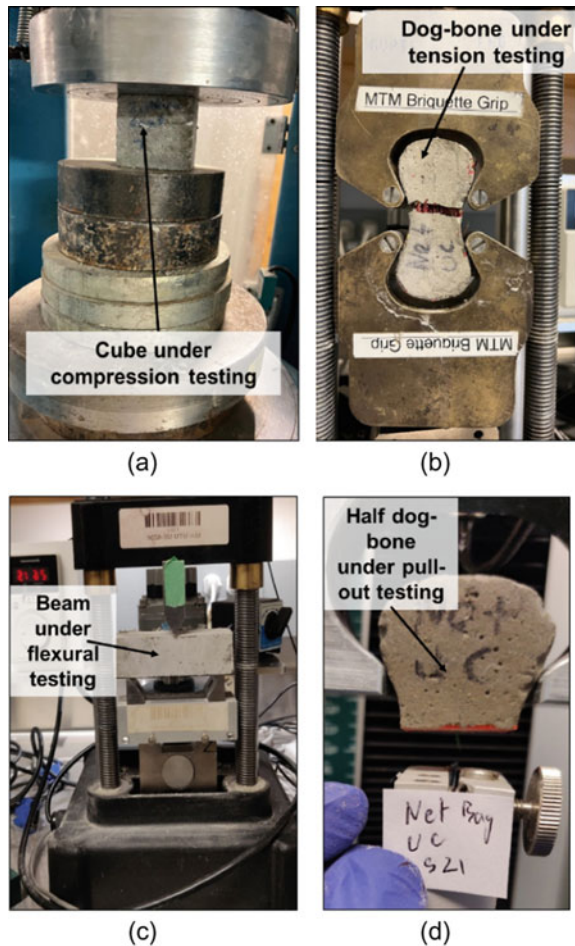
the load bar. MTM was coupled with PASCO® 550 Universal Interface to connect to the software. For each category of OFPP fibre, three dog bone samples containing uncoated fibres and three dog bone samples containing coated fibres with silica fume were tested under tension to measure tensile strength as explained by using Eq. (1).

$$TS = \frac{P}{bd} \tag{1}$$

where, TS is tensile strength (MPa); $P$ is ultimate load (N); $b$ is the width of the test specimens (mm), and $d$ is the depth of test specimens (mm)

Three-point flexural test was performed on prismatic samples with dimension (30 mm × 30 mm × 100 mm) at 28 days of curing according to ASTM C78 [4]. The load–deflection curve was obtained for each type of plastic fibre tested specimen. The deflection at the centre of the specimens was measured using linear variable differential transformers (LVDT), as shown in Fig. 5c. The load was applied by an MTM testing machine and the loading rate was set at 1 mm/min. A minimum of three specimens for each category of plastic mix was prepared for each test as mentioned above. The flexural strength or modulus of rupture (MOR) of beams subjected to centre-point bending test can be evaluated as follows by using Eq. (2).

$$MOR = \frac{3PL}{2bd^2} \tag{2}$$

where, MOR is the flexural strength (MPa); $P$ is the ultimate load (N); $L$ is the span of the test specimens (mm); $b$ is the width of the test specimens (mm), and $d$ is the height of the test specimens (mm).

Bond stress behaviour of individual plastic fibre to concrete substrate was tested for half dog bone samples (width and depth at waistline of briquette was 25 mm and length is 37.5 mm) at 28 days of age. Same PASCO® Testing Machine (MTM) with 1 mm/min crosshead loading rate which was used to carry out the tensile test was used for pull-out test, as shown in Fig. 5d. The bond strength for individual type of plastic fibre was calculated by using Eq. (3).

$$BS = \frac{P}{\pi dl} \tag{3}$$

where, BS is the bond strength (MPa); $P$ is the ultimate load (N); $d$ is the diameter of inserted fibre (mm), and $l$ is the embedded length of fibre in specimen (mm).

## 3 Results and Discussion

On taking the average of three testing conducted for one set of conditions, the final results are plotted and used to explain the findings. It is important to mention that the key words are used to explain the each types of uncoated and coated OFPP sample,

in the following discussion. For illustration, zipper lock and stand-up pouches are mentioned as *zip lock*; crinkly wrappers, bags and bars are mentioned as *crinkly*; flexible packaging with plastic seal is mentioned as *seal*; woven and net bags are mentioned as *net bags*; non-food protective packaging is mentioned as *non-food*; packaging film are mentioned as *film*.

## 3.1 Compressive Strength

Figure 6 shows the results of compressive strength of all samples after 28 days of curing, where uncoated net bags samples show competitively similar compressive strength to control samples. Moreover, the coated samples show better performance than uncoated samples with a few exceptions such as flexible packaging with plastic seal and net bags. This discrepancy can be attributed to coating mythology, where fibers were coated manually. The manual coating procedure causes fibers to agglomerate sometimes and thus forming weak sites. Although a careful procedure was followed, we considered such random behaviour from the results. Broadly, the reason for better performance of coated sample than uncoated samples is because of cessation of weak interfaces that exists between the reinforcement and concrete matrix by adding silica as coating for OFPP.

It is very important to consider that concrete is very strong in compression, but weak in tension owing to widening of existing micro cracks of concrete when subjected to tensile stress [15]. Therefore, the use of fiber reinforcement is mainly considered as a solution to arrest these micro crack and to improve the tensile and
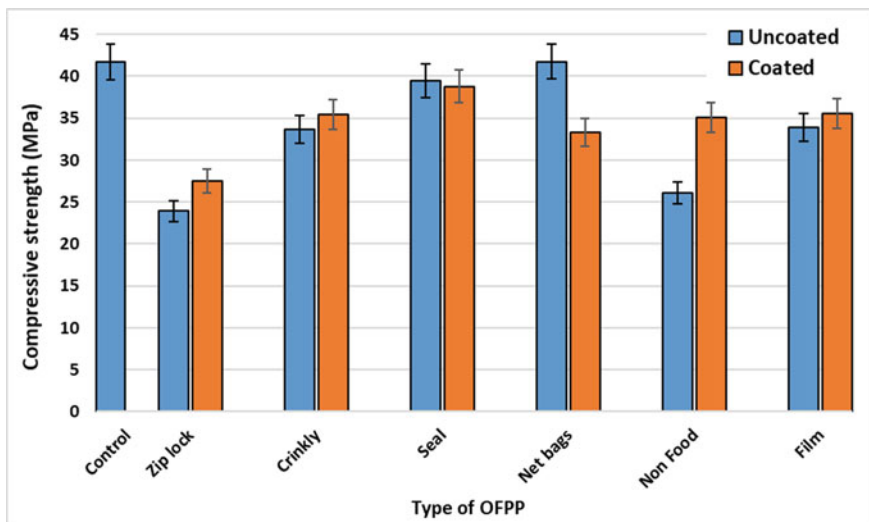


**Fig. 6** Compressive strength of samples after 28 days of curing

flexural strength of the concrete. Hence, it is very crucial to examine the tensile and flexural strength of each type of OFPP reinforced concrete.

## 3.2 Tensile Strength

The tensile strength of samples was examined upon analyzing the dog bone samples under tension and the results thus obtained are presented in Fig. 7. The coated OFPP fibers reinforced samples showed 2–25% increase in tensile strength, in contrast to control sample (without OFPP reinforcement) except zip lock samples. Even the uncoated net bag samples show 9% improvement in the tensile strength. Moreover, Fig. 8a-b shows the force ($N$)-displacement (mm) data for uncoated and coated samples of OFPP, respectively. From these figures, one can clearly observe post-crack behaviour in case of net bags where other OFPPs also didn't fail suddenly as happened in control sample. This proficiency of net bags is ascribed to characteristic fine assembly of net bag fibers (as shown in Fig. 2a). Or in other words, for identical dosage (1%) of fibers to concrete sample, more fibres for net bags were provided relative to all other types of OFPP. It is important to mention here that the idea of using fibers as reinforcement is to improve the performance of concrete by enriching tensile and flexural properties for regulating shrinkage and cracking. Thus, it can be stated through Fig. 7 that the coated OFPP fibers help in accomplishing the goal of this research by showing improvement in tensile strength relative to control sample.
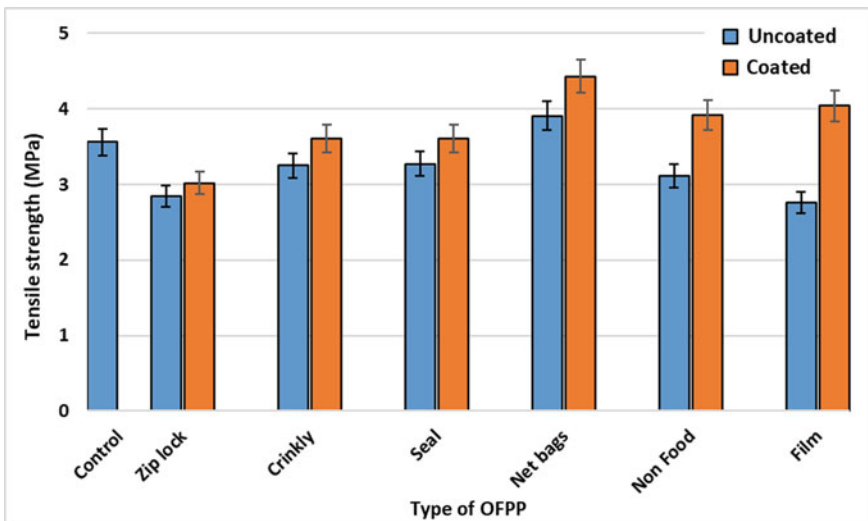


**Fig. 7** Tensile strength of samples after 28 days of curing
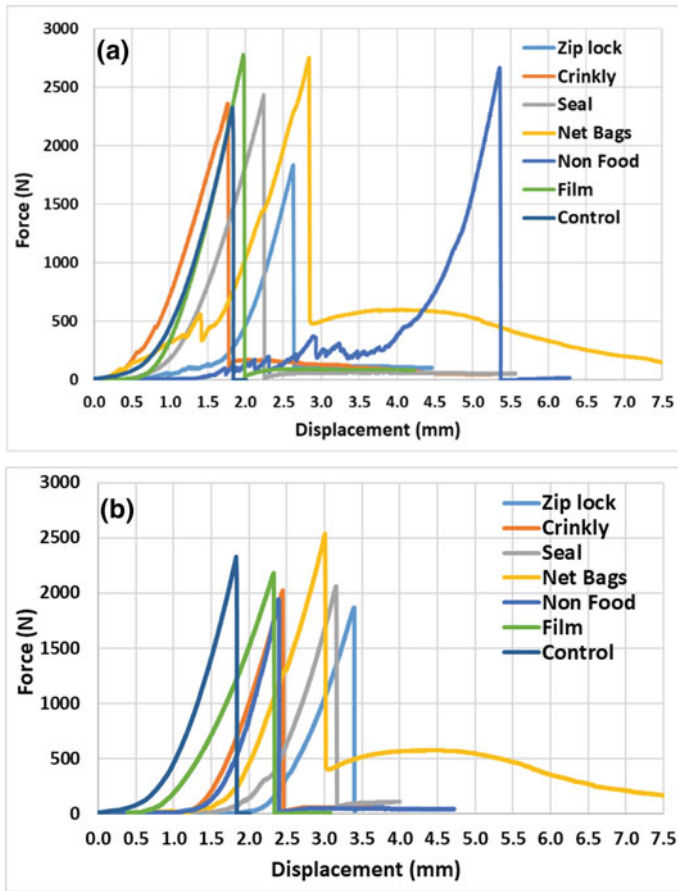
**Fig. 8** Force–displacement behaviour for samples under tensile test: **a** Uncoated OFPP, **b** Coated OFPP

## 3.3 Flexure Strength

A further check on the role of OFPP as reinforcement was made by conducting flexural testing, where an ability of samples to resist deflection and cracking was captured. Figure 9 shows the results for each type of OFPP for flexural strength. In broader sense, the results for coated fibers are furthered than the uncoated fibers for flexural strength. The important findings while flexural testing are shown in Fig. 10a-b, where force (*N*)-displacement (mm) data shows significant post-crack toughness. The performance of net bags for delaying the failure of samples is esteemed here as well. As stated earlier, the net bags provide more dosage per unit weight of mortar sample in comparison with all other types of OFPP to bring in the improvement in the performance of each type of structure.
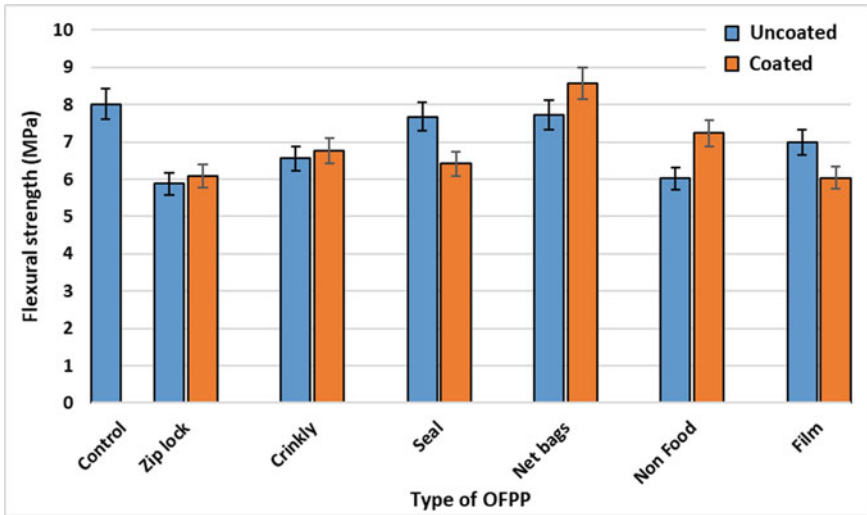
**Fig. 9** Flexural strength of samples after 28 days of curing

Moreover, it can be interpreted that the OFPP fibers (as reinforcement) helped in arresting fast crack proliferation and tried holding the structure together for longer than the control sample each time, viz., uncoated and coated. It can be measured that the post-crack strength of samples is nearly 10–90% of the peak load (or force ($N$)) and nearly 25–50% of peak load (or force ($N$)) for uncoated and coated samples respectively.

## 3.4 Bond Strength

In order to apprehend the reason for better performance of the coated fiber while each testing, pull-out tests for OFPP fibers embedded within the mortar samples were accomplished. In this way, the bond strength between the fiber and the mortar sample was calculated. Figure 10 shows the results for bond strength for each type of uncoated and coated OFPP fiber with mortar mixture. The data presented in Fig. 11 shows the existence of the better bonding of coated OFPP fibers with the mortar sample. This happens because of the elimination of weak spots at the interface that arises due to wall effect, where higher concentration of calcium hydroxide and water exists. SCMs provided through coating of OFPP react with calcium hydroxide to produce cementitious material, and hence improve the bonding between reinforcement and concrete matrix [17].
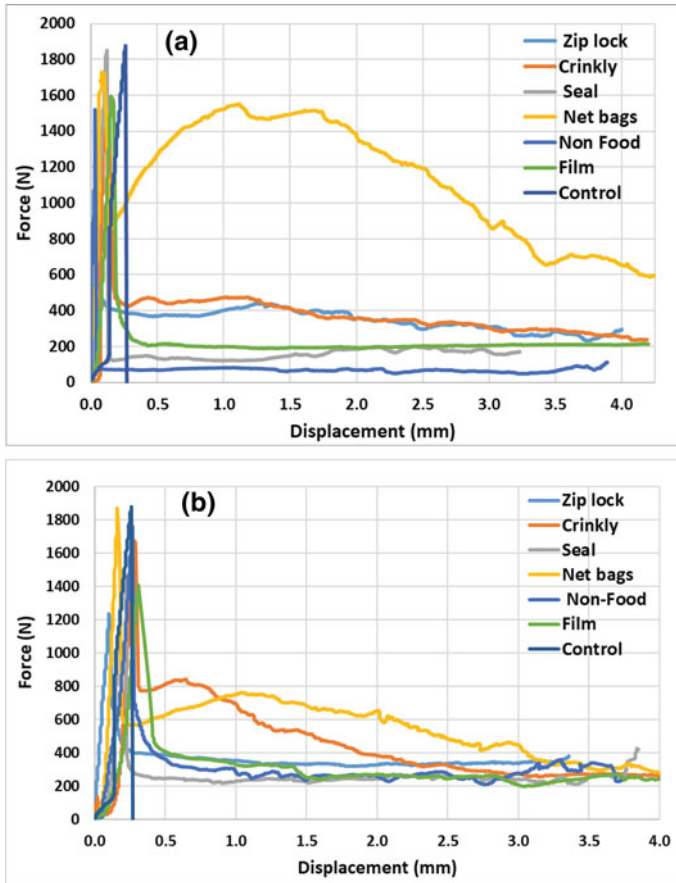
**Fig. 10** Force–displacement behaviour for samples under flexure test: **a** Uncoated OFPP, **b** Coated OFPP

## 4 Summary and Conclusions

Through this study, a higher end use of OFPP, as reinforcement for fiber reinforced concrete (FRC), is demonstrated through experimental analysis. The OFPP for this study was facilitated by Recycle BC, which is responsible for residential packaging and paper recycling in BC, Canada. Accordingly, the OFPP used for this study was collected within their programme in BC. On cleaning, sorting, and shredding of OFPP, it was converted into OFPP fibers. The part of OFPP fibers thus obtained were further coated with supplementary cementing materials (SCMs), i.e. silica fume. Hence, uncoated and coated OFPP fibers were used for casting different mortar samples, namely beams, cube, dog-bone, half dog bone. In order to elucidate the role of OFPP as reinforcement for FRC, a set of mechanical testing was conducted on these casted samples, in accordance to ASTM/CSA test standards. The cube samples were
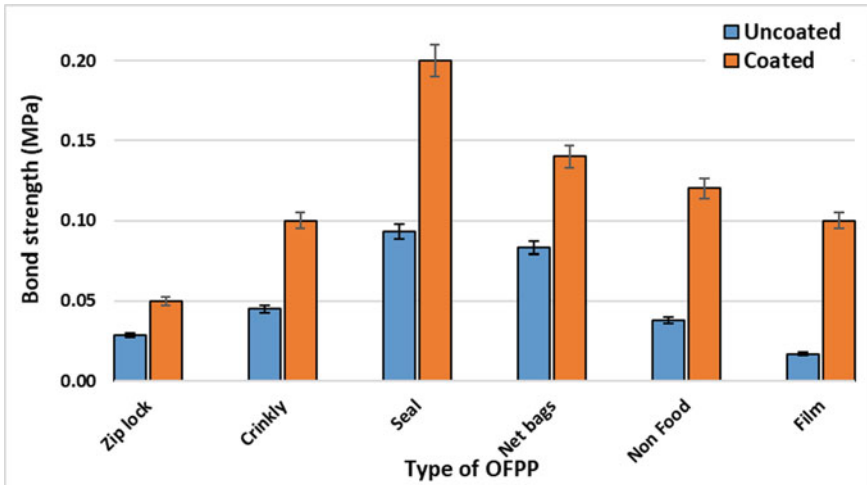
**Fig. 11** Bond strength of samples after 28 days of curing

investigated for compression, beam samples were investigated for flexure, dog bone samples were investigated for tension and half dog bone samples were investigated for pull-out strength.

All through the testing, the coated samples showed promising results relative to uncoated and control samples. The better performance of coated samples was brought-in by the reaction between SCM and calcium hydroxide that forms cementitious material to strengthen the bonding of reinforcement and cementitious structure. Furthermore, the force ($N$)-displacement (mm) curves from tensile and flexural testings exhibit the significant post-crack strength, which eliminate the rudimentary shortcomings of conventional concrete. Thus, the improvements offered by OFPP fibers in terms of compressive strength, tensile strength, and flexural strength allows the deployment of OFPP as reinforcement for FRC. For all cases, the net bags showed the superior results in comparison with all other types of OFPP, which is because of the higher number density of net bag fibers per unit weight relative to all other types of OFPP. Moreover, the surface of net bag fibers is corrugated, owing to weaving, that helps in altering surface energy for better coating of net bag fiber.

In summary, the usage of OFPP as fiber reinforcement will not only solve the inherent problems associated with concrete enactment, but will also bring the advantageous for the plastic waste management. The use of waste plastic, coated with industrial wastes like fly-ash and utilizing it to increase service life of concrete make this a truly green and sustainable project. The reuse of this material would divert it from its current energy application, thereby reducing GHG emissions emitted. This reuse application is also higher on the pollution prevention hierarchy than recycling, and avoids the energy requirements that would be required to remould this material into a recycled product.

# References

1. Ali B, Qureshi LA, Kurda R (2020) Environmental and economic benefits of steel, glass, and polypropylene fiber reinforced cement composite application in jointed plain concrete pavement. Compos Commun 22:100437
2. APC—Design smart material guide—Flexible plastic. (http://www.helenlewisresearch.com.au/wp-content/uploads/2014/03/Flexible_Plastic-DSMG-082013.pdf)
3. ASTM C307-03 (2012) Standard test method for tensile strength of chemical-resistant mortar, grouts and monolithic surfacing, Committee C-1 on Cement. American Society for Testing and Materials, West Conshohocken, PA, USA
4. ASTM C78/C78M (2010) Standard test method for flexural strength of concrete (using simple beam with third-point loading). American Society for Testing and Materials, West Conshohocken, PA, USA
5. ASTM. C150/C150M-17 (2017) Standard specification for Portland cement. American Society for Testing and Materials, West Conshohocken, PA, USA
6. ASTM (2013) Standard test method for compressive strength of hydraulic cement mortars (using 2-in. or [50-mm] cube specimens). American Society for Testing and Materials, West Conshohocken, PA, USA
7. Canadian Standards Association CSA A3000-13 Cementitious Materials Compendium (2013) Available online: https://www.csagroup.org/store/product/CAN%25100CSA-A3000-13/. Accessed on 14 Oct 2021
8. Environment and Climate Change Canada (2020). https://www.canada.ca/en/environment-climate-change/news/2020/10/canada-one-step-closer-to-zeroplastic-waste-by-2030.html
9. Giacovelli C, Zamparo A, Wehrli A, Alverson K (2018) In: Cannon T (ed) Single-use plastic: a roadmap for sustainability. UNEP. https://www.unenvironment.org/resources/report/single-use-plastics-roadmap-sustainability
10. Huang B-T, Yu J, Wu J-Q, Dai J-G, Leung CK (2020) Seawater sea-sand engineered cementitious composites (SS-ECC) for marine and coastal applications. Compos Commun 20(2020):100353
11. Kankanige D, Babel S (2020) Smaller-sized micro-plastics (MPs) contamination in single-use PET bottled water in Thailand. Sci Total Environ 717:137232
12. Other Flexible Plastic Packaging (2018). https://recyclebc.ca/flexiblepackaging/
13. Plastics Europe (2019) Plastics—the facts 2019: an analysis of European plastics production, demand and waste data (Plastics Europe 2018)
14. Qing L, Cheng Y, Mu R (2019) Toughness enhancement and equivalent initial fracture toughness of cementitious composite reinforced with aligned steel fibres. Fatigue Fract Eng Mater Struct 42(11):2533–2543
15. Romualdi JP, Batson GB (1963) Behavior of reinforced concrete beams with closely spaced reinforcement. J Proc 60:775–790
16. Schyns ZO, Shaver MP (2021) Mechanical recycling of packaging plastics: a review. Macromol Rapid Commun 42(3):2000415(1)–2000415(27)
17. U. S. Patent no. US 2015/0344367 A1, 3 Dec 2015. https://patents.google.com/patent/US20150344367A1/en

18. Yao X, Li L, Guan J, Zhang M, Liu Z, Han R, He S (2020) Initial cracking strength and initial fracture toughness from three-point bending and wedge splitting concrete specimens. Fatigue Fract Eng Mater Struct

# Novel Green Mortar Incorporating Crumb Rubber and Wood Fly Ash

**Samantha Krieg, Rubaiya Rumman, Meraj Rubayat Kamal, Ahmed Bediwy, Kishoare Tamanna, and M. Shahria Alam**

**Abstract**  Increased repercussions from climate change have popularized research into ways of mitigating the environmental impacts of construction processes. The production of building materials is a key concern, with the cement industry accounting for a considerable amount of global greenhouse gas emissions. Exploitative sand mining for use in infrastructure also has negative environmental impacts. The harmful effects of concrete would improve by reducing the cement and sand used in its production. Moreover, as coal plants become obsolete, coal fly ash will no longer be available and should be replaced. The purpose of this paper is to explore the behavior of mortar mixtures made with wood fly ash and crumb rubber as cement and sand replacements, respectively. The use of post-consumer waste tires as crumb rubber enhances the sustainability of these mortar mixtures by reducing the quantity of sand used. Furthermore, it eliminates the build-up of tires in landfills, which is a growing concern globally. In the samples cast, an aqueous sodium hydroxide solution-treated crumb rubber replaced 10 and 20% of the sand. Wood fly ash was used in conjunction with the crumb rubber. It substituted 15 and 30% of the cement used in the control mixture. Nine mortar mixtures were cast and tested under compression to demonstrate the effects of the combination of various materials and their failure patterns. Casting and compressive tests followed CSA standards. The microstructure of the samples was studied using scanning electron microscopy. The color of the mortar is of interest and has also been analyzed. Reducing the quantity of cement and sand used to produce mortar reduced their environmental impact. Results of the study show that incorporation of wood fly ash up to 30% can produce mortar with satisfactory strength. Although crumb rubber addition significantly reduces the mortar strength, it can still be used for constructing non-load-bearing structures. The use of wood fly ash and crumb rubber is a viable solution to the obsolescence of coal fly ash and increasing volume of tire wastes.

S. Krieg (✉) · R. Rumman · M. R. Kamal · A. Bediwy · K. Tamanna · M. S. Alam
The University of British Columbia, Kelowna, Okanagan, Canada
e-mail: skrieg@student.ubc.ca

R. Rumman
Bangladesh University of Engineering and Technology, Dhaka, Bangladesh

## 1 Introduction

As climate change worsens, it is vital to consider the environmental sustainability of infrastructure and building materials. Concrete and mortar are popular cement-based materials with diverse applications commonly used in construction. However, they have significant impacts on the environment. Ostovari et al. [20] found that the cement industry alone accounts for seven percent of global greenhouse gas (GHG) emissions. The majority of these GHG emissions are due to cement production [17]. Moreover, the exploitative mining of sand for use as fine aggregates in concrete and mortar presents serious environmental consequences [16]. As cities expand and urbanize, the demand for cement-based building materials will increase [17]. Therefore, it is vital to find ways to reduce the environmental burden of these construction materials while maintaining their efficacy.

Much of the negative environmental impact of building materials is attributed to cement [20]. Literature has established that the most effective way to reduce the GHG emissions of cement-based materials is by substituting the cement with admixtures [17, 22]. Historically, coal fly ash, a waste product from coal combustion for energy production, was commonly used as a replacement [17]. The use of coal fly ash in concrete and mortar became popular because of its efficacy as a cement supplement [14]. In recent years, coal power plants are becoming obsolete due to the focus on renewable energy reducing the availability of coal fly ash [14]. A potential replacement for coal fly ash as a cement supplement is wood fly ash (WFA), which is a by-product from energy production using wood waste [21]. The diversion of WFA from landfills has both economic and environmental benefits [22]. These materials have a high concentration of heavy metals and are very alkaline, making them difficult to dispose of [11, 22]. In Canada, nearly one million tons of wood ash waste are produced per year, of which the majority ends up in landfills [8]. The reuse of WFA in concrete and mortar is beneficial in diverting waste from landfills while supplementing traditional coal fly ash and cement.

There is significant interest in replacing fine aggregates with sustainable alternatives because of the devastating effects of sand mining [16]. Most notably, sand mining contributes to soil erosion, water pollution, and habitat loss [16]. The use of tire rubber as a fine aggregate replacement comes up frequently in literature. Rubber that is repurposed from post-consumer waste tires transformed into fine, uniform granules is termed crumb rubber (CR) [1]. The use of CR to substitute fine aggregates improves some mechanical properties of concrete and mortar, such as ductility and toughness [19, 23]. However, literature shows that as the amount of CR is increased, the compressive strength tends to decrease [1, 19, 23]. The successful redirection of waste tires into mortar and concrete would be beneficial in preventing their build-up in landfills, which is a growing concern globally [26]. Dabic-Miletic

et al. [10] reported that every year almost one billion tires are discarded globally, with half being sent directly to landfills. These tires present a significant environmental burden and contribute to soil, air, and water pollution [10]. Thus, replacing fine aggregates with CR from post-consumer waste tires has environmental benefits and can positively influence certain mechanical properties.

Extensive research has been conducted on various cement-based materials with fine aggregate replaced by CR [1, 19, 23, 25–27]. Additionally, concrete and mortar using WFA as a cement supplement have become popular topics in recent literature [6, 14, 15, 18, 21, 22]. To our knowledge, there has been no research on the use of CR and WFA in conjunction in mortar. This paper aims to investigate the behavior of a novel green mortar that incorporates both waste materials under compressive loading. An analysis of the microstructure of the novel mortar was performed using scanning electron microscopy for a better understanding of its properties. The successful combination of these materials in mortar would create significant environmental benefit due to the reduction in cement and sand used and the diversion of waste from landfills.

## 2   Methodology

### 2.1   Materials

#### 2.1.1   Cement and Wood Fly Ash

In this study, the mortar specimens were prepared using General Use (GU) cement. Wood fly ash supplied by Tolko, a local industry of forest products, was used to replace cement up to 30% by volume. Wood ash is a non-hazardous and alkaline waste material produced from the combustion of timber for energy or as a by-product of pulp and paper factories [7, 21]. Etiégni and Campbell [11] found that there are typically notable concentrations of heavy metals in wood ash, including silicon (Si), potassium (K), calcium (Ca), magnesium (Mg) and phosphorus (P). However, the chemical composition and therefore properties vary significantly based on timber species and regional environmental conditions [7, 9, 11]. Furthermore, these factors influence the alkalinity of the ash through fluctuations in bicarbonate, carbonate, and hydroxide content [9, 11].

Wood combustion for energy production produces two by-products, bottom ash, and fly ash [15]. Wood fly ash (WFA) can be categorized as fine or coarse [15]. It is possible to use all three forms of ash in concrete and mortar. Gabrijel et al. [15] established that fine fly ash has the greatest concentration of heavy metals and therefore has the highest environmental liability. Ukrainczyk et al. [24] found that the addition of fly ash into cement-based materials prevents them from transferring into their surroundings. Thus, the use of fine WFA in mortar is a promising means of repurposing it and mitigating its substantial environmental impact.

**Table 1** Chemical composition of wood fly ash from XRD analysis

| Mineral | Formula | Percentage |
|---------|---------|------------|
| Quartz | $SiO_2$ | 33.6 |
| Plagioclase | $NaAlSi_3O_8$—$CaAl_2Si_2O_8$ | 20.2 |
| K-feldspar | $KAlSi_3O_8$ | 10.7 |
| Calcite | $CaCO_3$ | 5.2 |
| Hematite | $\alpha$-$Fe_2O_3$ | 0.8 |
| Magnetite | $Fe^{2+}Fe^{3+}_2O_4$ | 0.5 |
| Akermanite | $Ca_2Mg(Si_2O_7)$ | 0.7 |
| Merwinite | $Ca_3Mg(SiO_4)_2$ | 0.9 |
| Amorphous | | 27.6 |
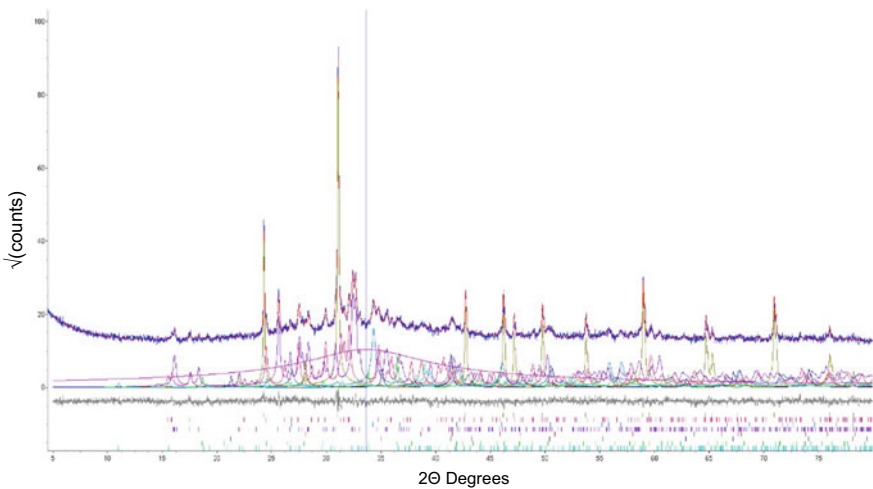


**Fig. 1** X-ray refinement plot of wood fly ash

The chemical composition of the wood ash used in the study is presented in Table 1 and was determined by X-ray diffraction (XRD). X-ray powder-diffraction data of the samples were refined using the Rietveld program Topas 4.2 (Bruker AXS). Figure 1 shows the X-ray diffractogram refinement plot of the wood ash used in this study. The properties of the wood fly ash are similar in characteristics with Class C fly ash according to the criteria established in ASTM C 618 [3].

### 2.1.2 Crumb Rubber and Sand

The mortar samples were prepared using locally sourced sand. CR replaced sand at 10 and 20% on a volumetric basis. Table 2 presents the material properties of sand and CR. The nominal maximum size of the sand and CR was 4.75 mm and

**Table 2** Material properties of sand and CR

| Aggregate | Specific gravity | Absorption capacity |
|-----------|------------------|---------------------|
| Sand | 2.60 | 1.52 |
| CR | 1.15 | 1.20 |

80 µm, respectively. The specific gravity of the CR was determined according to the specifications of FM, 5-559 [12, 13]. The properties of CR were determined using ethyl alcohol since CR cannot be fully submerged in water. The fineness modulus (FM) of sand and CR was calculated in compliance with [4] and was found to be 2.38 and 1.79, respectively. Figure 2 illustrates the gradation curves for the natural fine aggregates (NFA), sand, and CR. Additionally, the graph indicates the upper and lower limits of gradation specified by the CSA. Both sand and CR fall within these limits.

Before using the CR in the mortar mixtures, it was surface treated with an aqueous 20% sodium hydroxide (NaOH) solution. The CR was submerged in the solution for 30 min. It was then rinsed with tap water a total of three times until the pH reached seven on a Thermo Scientific Orian 5 Star pH meter. The treatment increased the roughness of the surface of the crumb rubber, improving the bonding between the rubber particles and the cement mortar.
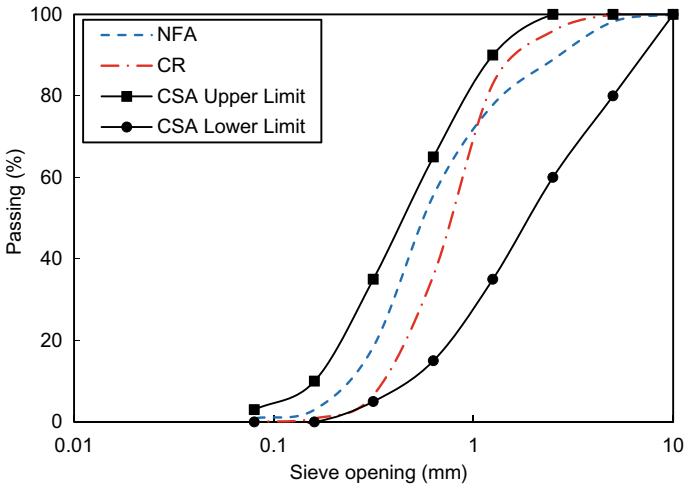


**Fig. 2** Gradation curves of sand and CR

**Table 3** Mix design matrix for mortar specimens

| Mix designation | Wood fly ash % | Crumb rubber % |
|---|---|---|
| $F_0CR_0$ | 0 | 0 |
| $F_0CR_{10}$ | | 10 |
| $F_0CR_{20}$ | | 20 |
| $F_{15}CR_0$ | 15 | 0 |
| $F_{15}CR_{10}$ | | 10 |
| $F_{15}CR_{20}$ | | 20 |
| $F_{30}CR_0$ | 30 | 0 |
| $F_{30}CR_{10}$ | | 10 |
| $F_{30}CR_{20}$ | | 20 |

## 2.2 Mortar Mix Design

About 50 mm mortar cubes were prepared according to the specification of [5]. Wood fly ash replaced GU cement in two ratios, 15 and 30%, and the control mixture was used for comparison. The water-to-cementitious ratio was fixed at 0.485 according to the specification. For each of these mortar mixtures, CR replaced the sand at two levels, 10 and 20%. Hence, there were nine mortar mixtures total, with nine samples cast for each. These specimens were tested for compressive strength and analyzed using SEM. Table 3 shows the mortar mixture matrix used in this study.

## 3 Results and Discussion

### 3.1 Compressive Strength

Figure 3 illustrates the compressive strength development with age for the nine mortar specimens. Three samples were tested for each mix design at 28, 56, and 91 days, and the average of the respective results obtained was used for analysis. Figure 4 shows the variation in compressive strength for different percentages of wood fly ash and CR. It is evident from Figs. 3 and 4 that the control mortar has the highest strength at all curing ages. However, the novel mortars containing fly ash provide sufficient compressive strength. $F_{15}CR_0$ achieves over 90% of the strength of the control mixture at 28 and 91 days. $F_{30}CR_0$ also reaches 83% and 87.5% strength of the control concrete at 28 days and 91 days, respectively.

The addition of CR reduces the strength significantly. Figure 4a shows that a 10% replacement of sand by CR in the samples without fly ash reduced the compressive strength by 70.5%. Furthermore, when 20% of the sand was replaced by CR, an 83.5% reduction in strength has occurred. A similar trend was observed for the mortars at 56 and 91 days. However, even the mixtures with the highest replacement of wood
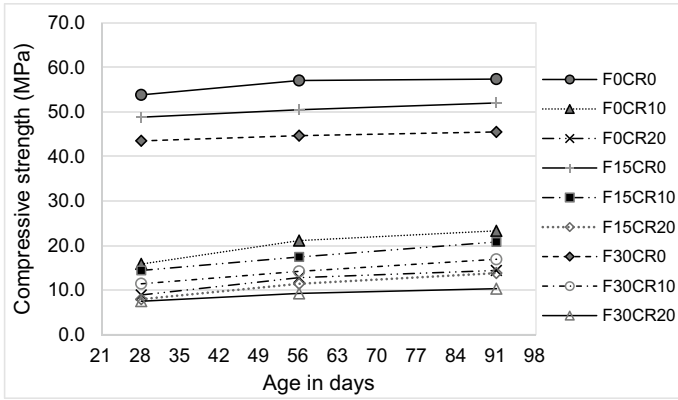
**Fig. 3** Compressive strength development of the mortar specimens at 28 days of curing age
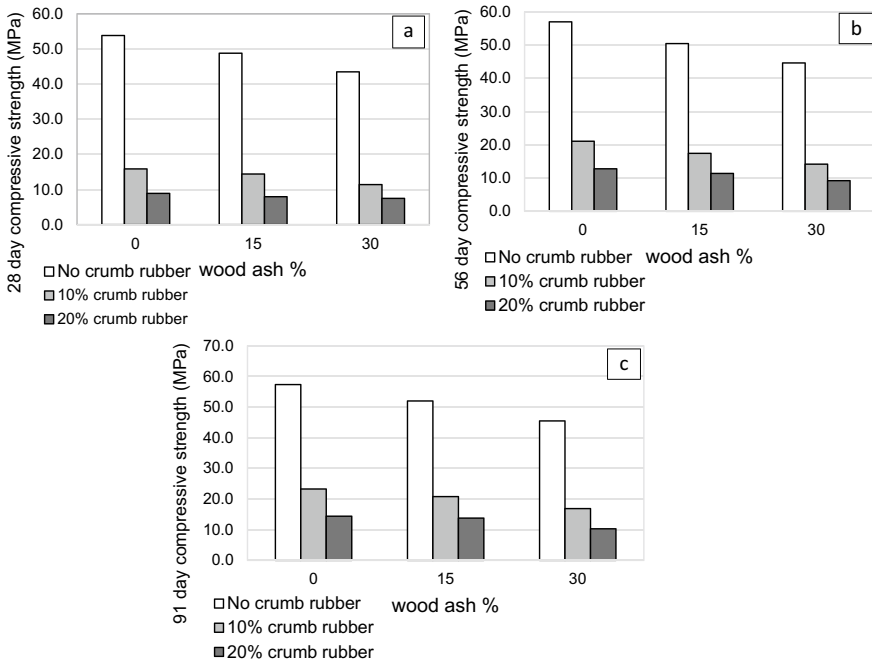


**Fig. 4** Compressive strength variation with various percentages of wood fly ash and CR at **a** 28 days, **b** 56 days, and **c** 91 days
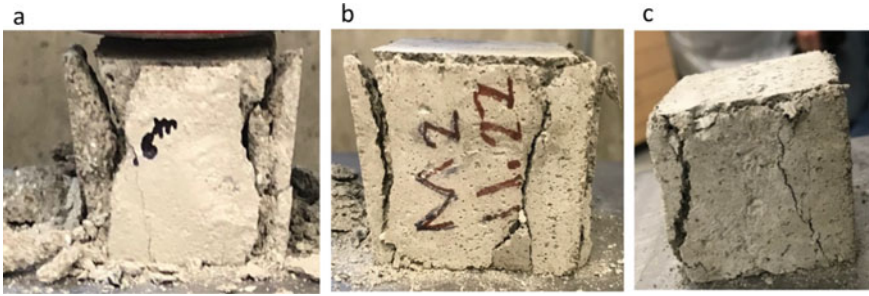
**Fig. 5** Failure pattern of **a** $F_0CR_0$ **b** $F_0CR_{10}$ and **c** $F_0CR_{20}$

fly ash and CR exceeded the minimum value of compressive strength required for non-load-bearing masonry structures [2].

## 3.2 Failure Pattern

Figure 5 shows the failure pattern of the mortar specimens at 28, 56, and 91 days of curing age for $F_0CR_0$, $F_0CR_{10}$, and $F_0CR_{20}$. With the increase of CR percentage in the mortar mixtures, the failure pattern was more gradual compared to the more brittle failure mode of the control mortar. This indicates the damage tolerance capacity of crumb rubber mortar. The similar trend was observed for other fly ash percentages with the increase of CR content.

## 3.3 Appearance

Figure 6 shows the appearance of the mortars with increasing proportions of both wood fly ash and CR. Figure 6 demonstrates that the color of the samples darkens with the addition of WFA and CR. The control concrete, $F_0CR_0$, had a lighter appearance when compared to the specimen containing the highest percentages of WFA and CR, $F_{30}CR_{20}$, which was the darkest. Therefore, the addition of these supplementary materials can be a cost-friendly alternative for producing dark concrete, which is desirable for landscaping or the construction of driveways, highways, and runways.
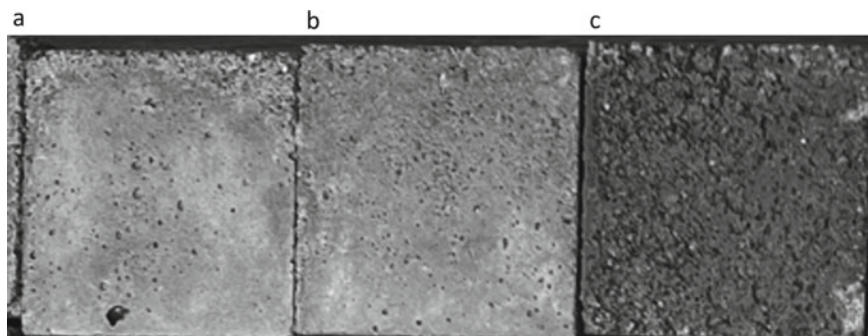
**Fig. 6** Appearance of **a** $F_0CR_0$ **b** $F_{15}CR_{10}$ and **c** $F_{30}CR_{20}$

## 3.4 Scanning Electron Microscopy (SEM) Analysis

The morphology and hydration of the mortar at a microscopic level were analyzed using Mira3 Tescan Backscattered Scanning Electron Microscope (BSEM) images. The chemical composition of the local area was determined from X-rays using energy-dispersive spectroscopy (EDS). Figure 7 presents the BSEM images of the mortar morphology of the sample with 20% of the sand replaced by CR. The morphology shows short and compact needles of ettringite and long needles of mono-sulfoaluminate forming. The reduced strength of the novel mortar can be attributed to the presence of the pores. The pores entrap a large amount of air because of the irregular shape of the rubber particles. All three mixtures show a reduced formation of C–S–H gel, which contributes to bonding between the particles and thus to the strength. Comparing the three mixtures, the quantity of C–S–H is the greatest in $F_0CR_{20}$, and therefore, it is the strongest.

The elemental composition of the paste shows that the addition of WFA decreases the hydratable component volume. The silicon content decreases, and the ratio of calcium to silicon increases as the quantity of wood fly ash used increases. These changes are detrimental to the mechanical performance of concrete.
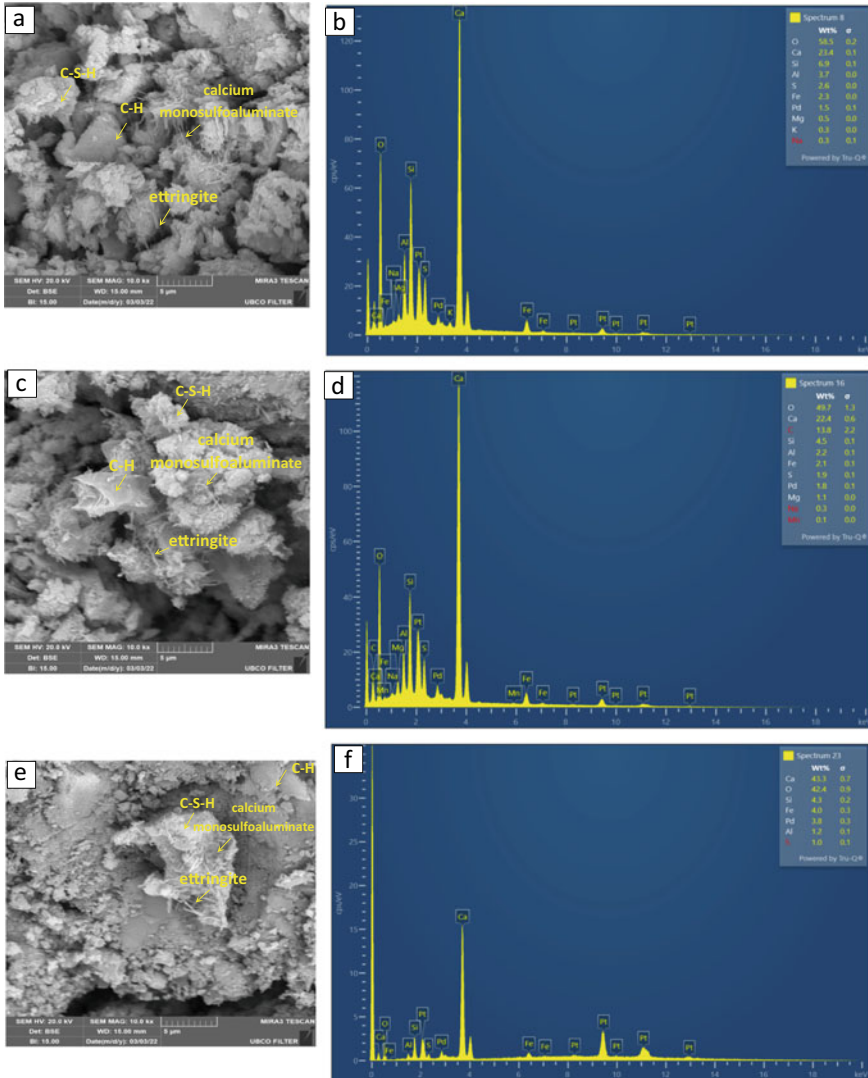
**Fig. 7** SEM images and spectrum showing elemental composition in mortar by EDS at 28 days of curing age for **a**, **b** $F_0CR_{20}$, **c**, **d** $F_{15}CR_{20}$, and **e**, **f** $F_{30}CR_{20}$

## 4  Conclusion

In this study, a novel green mortar was produced using wood fly ash and crumb rubber as cement and fine aggregate replacements, respectively. The successful use of this material has significant environmental benefits through reducing the GHG emissions associated with cement and the impact of sand mining. Furthermore, it diverts wood

fly ash and post-consumer waste tires from landfills, reducing their environmental burden. As the repercussions of climate change worsen and the demand for cement-based building materials increases with urbanization, it is vital to consider means of mitigating their environmental impact.

The results of the study on crumb rubber and wood fly ash can be summarized as follows:

1. The addition of wood fly ash decreased the compressive strength of mortar, although not significantly. Mortar with 30% of cement replaced by wood fly ash had compressive strength comparable to the control mixture. The addition of 30% wood fly ash with no CR resulted in a compressive strength of 43.5 MPa at 28 days, which is not significantly lower than the control mortar's compressive strength, 53.8 MPa.
2. Replacing sand with CR significantly reduced mortar compressive strength compared to control mortar. For instance, the addition of 20% CR resulted in an 83.5% reduction in compressive strength.
3. The failure pattern was more gradual with the addition of CR in mortar compared to the brittleness of control mortar failure.
4. All nine mixtures, even with the highest replacement level of CR and fly ash, achieved more than the minimum required strength, 3.5 MPa, of non-load-bearing masonry structures. Hence, rubberized mortar can be of use in this non-load-bearing masonry work.
5. CR addition resulted in a darker shade of gray in the mortar appearance. Making the color of mortar and concrete darker is expensive since it involves the addition of dyes. Hence, CR can be a good option in getting darker-colored concrete for non-load-bearing masonry units.

# References

1. Aman SS, Mohammed BS, Al-Fakih A (2021) Crumb rubber mortar and its properties: an overview. In: AIP conference proceedings, vol 2339, no 1. https://doi.org/10.1063/5.0044262
2. ASTM C129-17 (2017) Standard specification for nonloadbearing concrete masonry units. https://www.astm.org/Standards/C129
3. ASTM Standard C618-19 (2019) Standard specification for coal fly ash and raw or calcined natural pozzolan for use in concrete. ASTM International, West Conshohocken. https://www.astm.org/Standards/C1202
4. CSAA23.2-2A (2019) Sieve analysis of fine and coarse aggregate. Canadian Standards Association, Rexdale, Ontario, Canada
5. CSAA3004-C2 (2018) Test method for determination of compressive strengths of mortar. Canadian Standards Association, Rexdale, Ontario, Canada

6. Castrillón JJ, Gil H (2020) Mechanical properties of mortars modified with wood waste ash. J Indian Acad Wood Sci 17(1):90–99. https://doi.org/10.1007/s13196-020-00258-w
7. Cherian C, Siddiqua S (2020) Engineering and environmental evaluation for utilization of recycled pulp mill fly ash as binder in sustainable road construction. J Clean Prod, vol 298. https://doi.org/10.1016/j.jclepro.2021.126758
8. Cherian C, Siddiqua S (2019) Pulp and paper mill fly ash: a review. Sustain, Switz 11(16). https://doi.org/10.3390/su11164394
9. Chowdhury S, Mishra M, Suganya O (2015) The incorporation of wood waste ash as a partial cement replacement material for making structural grade concrete: an overview. Ain Shams Eng J 6(2):429–437. https://doi.org/10.1016/j.asej.2014.11.005
10. Dabic-Miletic S, Simic V, Karagoz S (2021) End-of-life tire management: a critical review. Environ Sci Pollut Res 29(7):68053–68070. https://doi.org/10.1007/s11356-021-16263-6/Published
11. Etitgni L, Campbell AG (1991) Physical and chemical characteristics of wood ash. Bioresour Technol, vol 37
12. Florida Test Method, FM 5-559 (2011) Testing of ground tire rubber. Florida Department of Rubber.
13. FM, 5-559 (2011) Florida method of test for testing of ground tire rubber. Florida Method
14. Fořt J, Šál J, Žák J, Černý R (2020) Assessment of wood-based fly ash as alternative cement replacement. Sustain, Switz 12(22):1–16. https://doi.org/10.3390/su12229580
15. Gabrijel I, Rukavina M, Štirmer N (2021) Influence of wood fly ash on concrete properties through filling effect mechanism. Materials 14(23):1764
16. Gavriletea DM (2017) Environmental impacts of sand exploitation: analysis of sand market. Sustain, Switz 9(7). https://doi.org/10.3390/su9071118
17. Habert G, Miller SA, John VM, Provis JL, Favier A, Horvath A, Scrivener KL (2020) Environmental impacts and decarbonization strategies in the cement and concrete industries. Nat Rev Earth Environ 1(11):559–573. https://doi.org/10.1038/s43017-020-0093-3
18. Ikotun BD, Raheem AA (2021) Characteristics of wood ash cement mortar incorporating green-synthesized nano-$TiO_2$. Int J Concr Struct Mater 15(1). https://doi.org/10.1186/s40069-021-00456-x
19. Liu F, Chen G, Li L, Guo Y (2012) Study of impact performance of rubber reinforced concrete. Constr Build Mater 36:604–616. https://doi.org/10.1016/j.conbuildmat.2012.06.014
20. Ostovari H, Müller L, Skocek J, and Bardow A (2021) From unavoidable CO2 source to CO2 sink? A cement industry based on CO2 mineralization. Environ Sci Technol 55(8):5212–5223. https://doi.org/10.1021/acs.est.0c07599
21. Teixeira ER, Camões A, Branco FG (2019) Valorisation of wood fly ash on concrete. Resour Conserv Recycl 145:292–310. https://doi.org/10.1016/j.resconrec.2019.02.028
22. Teixeira ER, Mateus R, Camões A, Branco FG (2019) Quality and durability properties and life-cycle assessment of high-volume biomass fly ash mortar. Constr Build Mater 197:195–207. https://doi.org/10.1016/j.conbuildmat.2018.11.173
23. Thomas BS, Gupta RC, Kalla P, Cseteneyi L (2014) Strength, abrasion, and permeation characteristics of cement concrete containing discarded rubber fine aggregates. Constr Build Mater 59:204–212. https://doi.org/10.1016/j.conbuildmat.2014.01.074
24. Ukrainczyk N, Vrbos N, Koenders EAB (2016) Reuse of woody biomass ash waste in cementitious materials. Chem Biochem Eng Q 30(2):137–148. https://doi.org/10.15255/CABEQ.2015.2231
25. Yang M, Guo Z, Zhang W, Chen G, Zhang L (2020) Static and dynamic compressive stress-strain behavior of recycled tire crumb rubber mortar. Front Mater, vol 7. https://doi.org/10.3389/fmats.2020.552043
26. Záleská M, Pavlík Z, Čítek D, Jankovský O, Pavlíková M (2019) Eco-friendly concrete with scrap-tyre-rubber-based aggregate: properties and thermal stability. Constr Build Mater 225:709–722. https://doi.org/10.1016/j.conbuildmat.2019.07.168
27. Zhu WX, Sun ZP, Shui LL, Chen KK, Li DY (2016) Research progress of crumb rubber mortar. KEM 680:451–4. https://doi.org/10.4028/www.scientific.net/kem.680.451

# Algorithmic Mix Design for 3D Printing Materials

**Vasileios Sergis and Claudiane Ouellet-Plamondon**

**Abstract** Additive manufacturing technology aims to revolutionize the construction sector. Researchers are looking for the optimum materials to use in mix design to control the fresh and final properties of the mix. Those properties are contradictory to each other, and finding the optimal mix design has always been a challenge. Developing an optimization tool that considers trade-offs among a variety of competing objectives can improve the mix design process. In this study, the mortars contained combinations of multiple factors, including the cement type, sand type, water content, and admixtures. Three properties investigated are flowability, buildability, and compressive strength. The buildability was assessed by measuring the shear stress with the direct shear apparatus based on the ASTM D3080. The workability was acquired by measuring the flow spread of the mortar mixes following the ASTM C1437, and the compressive strength following the ASTM C109. A multiobjective Pareto optimization method is used to improve the properties simultaneously. Feedforward neural networks were used to predict the properties of new mixes. The genetic algorithm was used to optimize the network parameters. This approach yields promising capability to improve the competing objectives of the mortar mixes by considerably reducing the time and the number of experiments.

**Keywords** 3D printing · Cement · Admixtures · Mix design · Optimization algorithms

## 1 Introduction

Developing cement-based materials for three-dimensional (3D) printing applications is a complicated process with many conflicting goals [11]. The necessity of recycling and reusing building materials adds to the complexity [22]. A mix design can be made by following a variety of techniques, such as modifying one factor at a time, or

V. Sergis · C. Ouellet-Plamondon (✉)
École de Technologie Supérieure, Université du Québec, Montreal, QC H3C 1K3, Canada
e-mail: Claudiane.Ouellet-Plamondon@etsmtl.ca

following a full-factorial design [2, 3, 5, 6, 10]. As the number of factors or their levels rise, the number of experiments can become an onerous task to fulfill [4, 9]. This study helps advance the development of a high-performance cement-based material for 3D printing applications. The proposed methodology gathers information on numerous factors in the mix design while using optimization algorithms and artificial intelligence. Many studies in civil engineering have used artificial intelligence [1, 12, 13]. While the final properties are always vital [7], the early age structural buildup throughout the dormant period and the flowability are equally important for 3D concrete printing [8, 14, 18–21]. The printed region and buildability of the mixtures are defined using slump and flow tests [19]. A smooth surface and great buildability are achieved, with mixtures having a slump flow value of 50–90% [19].

## 2 Materials, Testing Methods, and Methodology

### 2.1 Materials

Three types of cement, three types of sand, and five admixtures, including super-plasticizers, were chosen in total [16, 17]. The two admixtures were the biopolymer polysaccharide viscosity modifying agent (B) and the calcium silicate hydrate admixture (CSH-C). Two out of the three selected superplasticizers are based on synthetic organic polymers (PCE 1 & 2), whereas the third is sulfonated naphthalene polymer based. For cement, the three types are general use Portland cement, binary cement with silica fumes (GUbSF), and Portland cement with a high early strength (HE). All three sand types were fine aggregates with particle sizes below 2.5 mm including one being recycled sand. The three sands used in this study are shown in Fig. 1, and their particle distribution in Table 1.
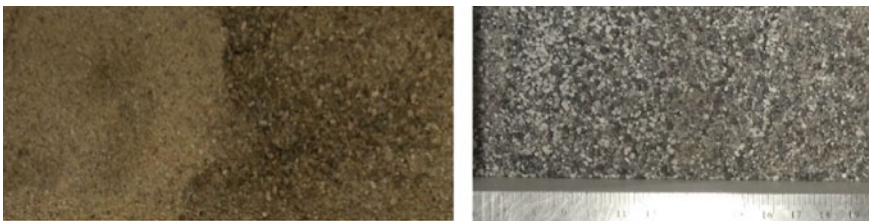


**Fig. 1** Three sands used in the study: fine, coarse, and recycled sand

**Table 1** Particle size distribution of the three types of sands

| Sieve size | Passing through (%) | | |
| --- | --- | --- | --- |
| | Fine sand | Coarse sand | Recycled sand |
| 2.5 mm | 100 | 100 | 100 |
| 1.25 mm | 90 | 96 | 83 |
| 630 µm | 78 | 67 | 66 |
| 315 µm | 57 | 24 | 34 |
| 160 µm | 20 | 4 | 12 |
| 80 µm | 3 | 3 | 5 |

## 2.2 Testing Methods

The flow test, direct shear test, and compressive strength test are the suggested testing procedures. The proposed tests allow to correlate the results with the flowability and buildability of the mixes in the fresh state and with their mechanical strength in the final state. Strength development of mortar during the dormant period can be seen in the ASTM D3080 direct shear test [20, 21]. Multiple direct shear tests were carried out in 90 min using a similar approach as in the reference study. Instead of developing a novel apparatus, the direct shear apparatus commonly used in soil mechanics was adapted. A shear box, a displacement sensor, a load sensor, and a linear displacement motor were all part of the redesigned apparatus. Figure 2a depicts the modified apparatus.

The spread of the mixes was assessed by using ASTM C1437 flow test, and the findings were linked to the mixes' pumpability. The tests were monitored from the side and the top view using two cameras (Fig. 2b). The target was set at a spread of at least 60% [19] five minutes following the mixing procedure, although multiple tests were performed within 90 min with a 15 min time interval. Finally, information on the mixtures' compressive strength was measured following the ASTM C109. Test cubes of 50 mm or two inches in diameter were formed and kept in a chamber with regulated humidity and temperature for up to 28 days. Tests were performed after 1, 7, and 28 days using a semiautomatic concrete compression machine.



**Fig. 2** Modified direct shear apparatus (**a**) and top view of the flow table (**b**)

## 2.3   Optimization Methodology

Optimization methods were used starting from the mix design. The D-optimal design was used to generate the optimum initial set of mixes, reducing the required number from ($3^6 = $) 729 to 18 mixes [17]. After the initial set, a multiobjective Pareto optimization algorithm guided the procedure. The objective functions were artificial neural networks that were trained using data from lab experiments. These networks were then used to predict the properties of the new mixtures proposed during Pareto optimization [16]. The best mixes were created and tested in the laboratory to acquire the real fresh and final properties of the mixes. The objectives were to increase simultaneously the buildability and the mechanical properties of the mixes, while acquiring an acceptable flowability.

## 3   Results

Twenty-one new mixes were introduced after five iterations of the Pareto optimization process. In total, 39 mixes were formed, including the initial set of mixes from the D-optimal design. The algorithm was able to determine which materials performed better and what was the optimum dosage for each one despite the high complexity of the mix design. The best materials were the HE and GUbSF cement types, the admixtures B, CSH-C and PCE-2 superplasticizer. Part of the results obtained are shown in Fig. 3 until Fig. 6. The results are grouped based on cement and sand type combinations. The initial mixes are represented with hollow markers, whereas the mixes proposed during the optimization process are shown with filled markers.

In Fig. 3, the *x*-axis is the shear stress at 90 min after the mixing process, and the *y*-axis is the compressive strength at 28 days. Aiming to improve both properties, the best mixes are located in the top right corner of the figure. All mixes in Fig. 3 include the GUbSF cement and the coarse sand. As it can be noticed, two mixes in the initial set were formed with this cement/sand combination and three more were generated
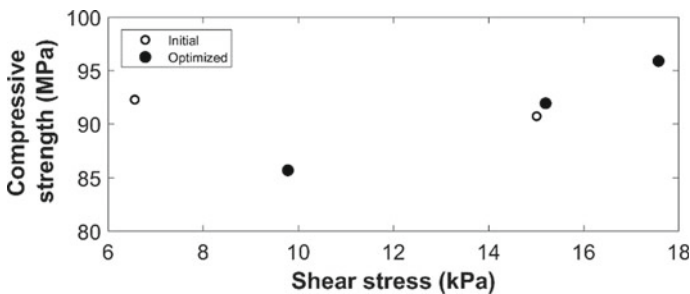


**Fig. 3**  Measured properties of mixes containing GUbSF cement and coarse sand proposed during the D-optimal design and the optimization process
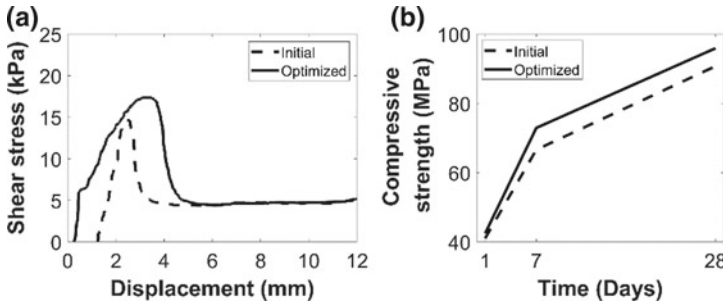
**Fig. 4** Comparison between the best initial and optimized mix containing GUbSF cement and coarse sand. The measured shear-displacement graph in 90 min after mixing (**a**) and the compressive strength after 28 days (**b**)

**Table 2** Mix proportions of the initial and optimized mix containing GUbSF cement and coarse sand

| Mixes | Cement | Sand | Water:binder | Sand:binder | Superplasticizer (Type A&F) | SP (%w/w) | B (%w/w) | CSH-C (%w/w) |
|---|---|---|---|---|---|---|---|---|
| Initial | GUbSF | Coarse | 0.345 | 2.3 | PCE-1 | 0.26 | – | 0.3 |
| Optimized | GUbSF | Coarse | 0.3 | 1.8 | PCE-2 | 0.26 | 0.018 | – |

from the optimization algorithm. The best mix of the initial set and the optimization set are compared in Fig. 4, and their mix proportions are presented in Table 2.

In Fig. 4, the mix from the initial set is shown with dashed line whereas the mixed proposed from the algorithm in solid line. Both properties were improved, where the shear stress was increased from 15 to 17.6 kPa and the compressive strength from 91 to 96 MPa. As in Fig. 3, the x-axis and the y-axis of Fig. 5 are the shear stress at 90 min after the mixing process and the compressive strength at 28 days, respectively. The best mixes are located in the top right corner of the figure. The mixes in Fig. 5 include the HE cement and the recycled sand. As it can be noticed, one mix in the initial set was formed with this cement/sand combination, and four more were proposed by the optimization algorithm. All of the proposed mixes performed better than the mix in the initial set. The mix from the initial set and the mix with the best performance from the optimization set are compared in Fig. 6, and their mix proportions are presented in Table 3.

Figure 6 presents the mix proposed from the algorithm in solid line, whereas the mix from the initial set is shown with dashed lines. Both properties were improved, where the compressive strength was increased from 81 to 88.5 MPa and the shear stress had a major increase from 12.5 to 19.6 kPa.
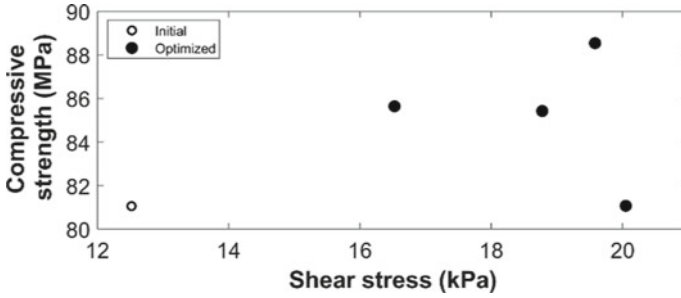
**Fig. 5** Measured properties of mixes containing HE cement and recycled sand proposed during the D-optimal design and the optimization process
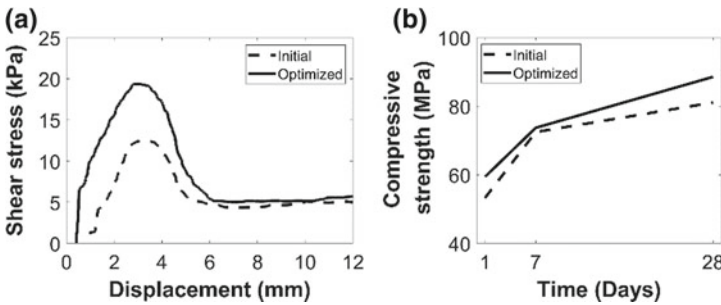


**Fig. 6** Comparison between the best initial and optimized mix containing HE cement and recycled sand. The measured shear-displacement graph in 90 min after mixing (**a**) and the compressive strength after 28 days (**b**)

**Table 3** Mix proportions of the initial and optimized mix containing HE cement and recycled sand

| Mixes | Cement | Sand | Water:binder | Sand:binder | Superplasticizer (Type A&F) | SP (%w/w) | B (%w/w) | CSH-C (%w/w) |
|---|---|---|---|---|---|---|---|---|
| Initial | HE | Recycled | 0.345 | 1.8 | PCE-1 | 0.26 | 0.013 | – |
| Optimized | HE | Recycled | 0.3 | 1.7 | PCE-2 | 0.28 | 0.013 | 0.11 |

## 4   Conclusion

The proposed methodology follows a multiobjective optimization trend. While making concessions, the conflicting objectives improved concurrently. The Pareto algorithm identified the important components and then excluded the less effective options while determining the preferred dosages. The neural networks assisted in visualizing the impact of each component. This approach yields promising capability to improve the competing objectives of the mortar mixes by considerably reducing the required workload.

# References

1. Ateş KT, Şahin C, Kuvvetli Y, Küren BA, Uysal A (2021) Sustainable production in cement via artificial intelligence based decision support system: case study. Case Stud Constr Mater 15. https://doi.org/10.1016/j.cscm.2021.e00628
2. Bos F, Wolfs R, Ahmed Z, Salet T (2016) Additive manufacturing of concrete in construction: potentials and challenges of 3D concrete printing. Virtual Phys Prototyping 11(3):209–225. https://doi.org/10.1080/17452759.2016.1209867
3. Buswell RA, Leal de Silva WR, Jones SZ, Dirrenberger J (2018) 3D printing using concrete extrusion: a roadmap for research. Cem Concr Res 112:37–49. https://doi.org/10.1016/j.cemconres.2018.05.006
4. Cavazzuti M (2012) Optimization methods: from theory to design scientific and technological aspects in mechanics, Springer Science & Business Media. 262p. https://doi.org/10.1007/978-3-642-31187-1
5. Charrier M, Ouellet-Plamondon CM (2022) Artificial neural network for the prediction of the fresh properties of cementitious materials. Cem Concr Res 156:106761. https://doi.org/10.1016/j.cemconres.2022.106761
6. Ding T, Xiao J, Zou S, Wang Y (2020) Hardened properties of layered 3D printed concrete with recycled sand. Cement Concr Compos 113. https://doi.org/10.1016/j.cemconcomp.2020.103724
7. Ghafor K, Mahmood W, Qadir W, Mohammed A (2020) Effect of particle size distribution of sand on mechanical properties of cement mortar modified with microsilica. ACI Mater J 117(1). https://doi.org/10.14359/51719070
8. Jayathilakage R, Sanjayan J, Rajeev P (2019) Direct shear test for the assessment of rheological parameters of concrete for 3D printing applications. Mater Struct 52(1). https://doi.org/10.1617/s11527-019-1322-4
9. Lawson J (2015) Design and analysis of experiments with R. CRC Press Taylor & Francis Group
10. Charrier M, Ouellet-Plamondon CM (2022) Artificial neural network for the prediction of the fresh properties of cementitious materials. Cement and Concrete Research 156:106761
11. Marchon D, Kawashima S, Bessaies-Bey H, Mantellato S, Ng S (2018) Hydration and rheology control of concrete for digital fabrication: potential admixtures and cement chemistry. Cem Concr Res 112:96–110. https://doi.org/10.1016/j.cemconres.2018.05.014
12. Pan Y, Zhang L (2021) Roles of artificial intelligence in construction engineering and management: a critical review and future trends. Autom Constr 122. https://doi.org/10.1016/j.autcon.2020.103517
13. Paul S, Panda B, Zhu H-H, Garg A (2019) An artificial intelligence model for computing optimum fly ash content for structural-grade concrete. ASTM Int 8:1–15. https://doi.org/10.1520/ACEM20180079
14. Rahul AV, Santhanam M, Meena H, Ghani Z (2019) 3D printable concrete: mixture design and test methods. Cement Concr Compos 97:13–23. https://doi.org/10.1016/j.cemconcomp.2018.12.014
15. Sergis V, Ouellet-Plamondon CM (2022) Fractional factorial design to study admixtures used for 3D concrete printing applications. Materials Letters 324(132697)
16. Sergis V, Ouellet-Plamondon CM (2022a) Automating mix design for 3D concrete printing using optimization methods. Digital Discov. https://doi.org/10.1039/D2DD00040G

17. Sergis V, Ouellet-Plamondon CM (2022b) D-optimal design of experiments applied to 3D high-performance concrete printing mix design. Mater Des 218:110681. https://doi.org/10.1016/j.matdes.2022.110681
18. Shakor P, Renneberg J, Nejadi S, Paul G (2017) Optimisation of different concrete mix designs for 3D printing by utilizing 6DOF industrial robot. Paper presented at the proceedings of the 34th international symposium on automation and robotics in construction (ISARC)
19. Tay YWD, Qian Y, Tan MJ (2019) Printability region for 3D concrete printing using slump and slump flow test. Compos Part B Eng 174. https://doi.org/10.1016/j.compositesb.2019.106968
20. Wolfs RJM, Bos FP, Salet TAM (2018) Early age mechanical behaviour of 3D printed concrete: numerical modelling and experimental testing. Cem Concr Res 106:103–116. https://doi.org/10.1016/j.cemconres.2018.02.001
21. Wolfs RJM, Bos FP, Salet TAM (2019) Triaxial compression testing on early age concrete for numerical analysis of 3D concrete printing. Cement Concr Compos 104. https://doi.org/10.1016/j.cemconcomp.2019.103344
22. Zou S, Xiao J, Ding T, Duan Z, Zhang Q (2021) Printability and advantages of 3D printing mortar with 100% recycled sand. Constr Build Mater 273:121699. https://doi.org/10.1016/j.conbuildmat.2020.121699

# Sustainability Analysis of Structural Materials Used in Multistoried Building Construction: A Cradle to Grave Approach

**Mohammad Masfiqul Alam Bhuiyan, Mohammad Rezaul Karim, and Ahmed Hammad**

**Abstract** Over time, the construction industry's development has been constantly questioned due to low productivity, high energy consumption, generation of wastes, and greenhouse gas emissions. According to a recent United Nations Environment Program report, building and construction account for 36% of global energy use and 39% of energy-related carbon dioxide ($CO_2$) and greenhouse gas emissions. Sustainable construction aims to minimize harm and maximize value by balancing social, economic, technical, and environmental aspects, commonly known as the pillars of sustainability. In general, concrete, timber, steel, masonry, etc., materials are used to construct multistoried buildings. Though technical and economic aspects are always considered while selecting the structural components, other elements like social and environmental are mostly ignored. A sustainable decision is always critical as it combines all technical, social, economic, and environmental factors in the decision-making process. On the contrary, though it seems crucial during the planning and conceptual development phase and costly while designing and construction, a sustainable choice is always more economical, eco-friendly, and convenient, considering the entire life cycle of any construction work. This paper analyzed the characteristics of commonly used structural materials from the sustainability point of view, considering the project's complete life cycle. We have followed a hybrid approach to analyze life cycle sustainability analysis by integrating the outcomes obtained through life cycle cost analysis, environmental life cycle analysis, and social life cycle analysis and taking the opinion of stakeholders. The outcome of the analysis is expected to enhance objectivity in the selection process of structural material by the decision-makers contributing to more sustainable building construction.

**Keywords** Building sustainability · Materials analysis · Multistoried Construction · LCA

M. M. A. Bhuiyan (✉) · M. R. Karim · A. Hammad
Department of Civil and Environmental Engineering, Construction Engineering and Management, University of Alberta, Edmonton, AB, Canada
e-mail: alambhui@ualberta.ca

# 1 Introduction

Sustainability entails addressing our own demands without jeopardizing future generations' ability to meet their own [20]. We require social and economic resources in addition to natural resources [2]. Environmentalism is not the only aspect of sustainability. Therefore, concerns for social equity and economic development are found in most definitions of sustainability [7]. Again, as the Brundtland Commission on Environment and Development recognized, economic progress at the expense of ecological health and social fairness did not lead to long-term success. It was evident that the world needed to find a method to balance environmental sustainability and economic growth. It defines sustainable development as "development that meets current demands without compromising future generations' ability to meet their own needs" [20]. Sustainability is a holistic strategy that considers the ecological, social, and economic components, realizing that all three must be regarded to achieve long-term prosperity [2].

Buildings or houses are one of the most necessities of human life. The building industry is an essential part of every economy. With the rapid rise of the population and hence fulfilling their requirements, the construction industry is now liable for significant environmental impact, currently accounting for 36% of global energy use and 39% of energy-related carbon dioxide ($CO_2$) emissions [21]. Building construction, fit-out, operation, and eventual demolition have a significant direct and indirect impact on the environment, both directly due to material and energy consumption and the resulting pollution and waste and indirectly through the effect of inefficient infrastructure. A reduction in the environmental impact of a building during its life cycle is, therefore, an essential target in terms of sustainable development [16]. In this context, there has been a considerable effort over the past few decades to investigate the life cycle energy use and impacts of buildings. However, the building sector is still primarily motivated by economic gain, particularly short-term gain [15]. Hence, to achieve sustainability, it is necessary to transform the practices on a large scale to focus on the environment and society, with the objective of sustainable practice being to have a beneficial influence effectively. It is necessary to encourage businesses to balance long-term benefits with instant returns to pursue inclusive and environmentally sound objectives. This encompasses a wide range of different practices. Cutting emissions, cutting energy consumption, obtaining items from fair-trade organizations, and ensuring their physical waste is disposed of appropriately and with as little carbon impact as possible would all qualify as steps toward sustainability while also lowering the price.

The speed with which steps toward sustainable application are done is determined by decisions made by a variety of participants in the building process, including owners, managers, designers, corporations, and others [4]. The sustainable selection of materials to be utilized in construction projects is a critical decision. The simplest method for designers to implement sustainable concepts in construction projects is to carefully select sustainable structural materials [14]. However, due to a lack of formal and available measuring criteria, the selection of construction materials is viewed as

a multi-criteria decision issue [10]. And it would be easier for the stakeholders to decide if numerical approaches can be developed in the life cycle assessment of the building keeping sustainability in mind.

Reinforced concrete is the most often used structural material for building construction. Concrete is a widely used material for a variety of construction applications due to its strength, durability, reflectivity, and adaptability [13]. These features make it a durable and long-lasting alternative for various residential and industrial building construction. However, ironically, concrete is one of the leading sources of environmental degradation and is harmful to our ecosystem and environment. Concrete manufacturing emits 2.8 billion tons of carbon dioxide, accounting for 4–8% of global greenhouse gas emissions [17]. Concrete consumes a tenth of all industrial water around the globe [9]. To achieve sustainability, it is required to look for alternatives in building construction. Steel may be used to replace concrete in structural construction due to its numerous advantages, including high strength, high tensile, ductile, flexible, and cost-effectiveness [12]. On the other hand, steel needs a lot of energy in its manufacturing process and might be expensive in some situations. Masonry is also a time-tested alternative to concrete construction, albeit burned bricks may emit significant levels of carbon during the manufacturing process, and masonry construction requires a substantial amount of cement [5]. So, in recent days, architects, builders, and sustainability advocates have been buzzing about timber, a building material that they believe has the potential to significantly reduce greenhouse gas (GHG) emissions in the building sector, as well as waste, pollution, and construction costs, while also creating a more physically, psychologically, and aesthetically healthy built environment [19]. A life cycle sustainability analysis using these materials in an example of multistory building structure may reveal a clear picture of the aspects influencing sustainability based on its four pillars: economic, social, technical, and environmental. The findings of the research will assist stakeholders in identifying viable materials for future building development from a sustainability standpoint.

## 2 Problem Statement

Traditionally, the structural materials for a building are based on the stakeholder's requirements or value demand. Here, the perspective is mainly influenced by experiences, local tradition, or understanding of construction materials. This is principally determined by affordability, cost–benefit analysis, and return on investment, among other factors, though it is true that while selecting materials, few consumers nowadays search for greenness or environmental issues. However, including the environment sustainability also involves a broader range of economic, technological, and social factors. Each of these four is given due weight in the study of sustainability. In many circumstances, the requirement of sustainability evolves apparently contradicting criteria such as being environmentally friendly while also being affordable or less expensive, having a better aesthetic perspective yet using local materials, having

a high efficiency while using less energy, and so on. As a result, focusing merely on the timeframe for constructing a facility may not necessarily provide a good picture of whether these parameters are met. Instead, it necessitates a comprehensive examination of the construction materials from conception to demolition or reuse, commonly referred to as a life cycle analysis (LCA), which can provide a more accurate picture of sustainability when choosing structural material for a building construction project.

## 3 Aim and Objective

This study aims to carry out a sustainability analysis balancing economic, environmental, technical, and social needs for a low to midrise multistoried building construction project with the following objectives:

- Based on the ground survey and literature reviews, select the alternative structural materials for low to midrise multistoried buildings.
- Conduct a sustainable life cycle analysis for each of the alternatives with the view that the building industry will enable identifying parameters and added values needed for an attractive and sustainable solution.
- Expert and stakeholder perspectives on material selection based on analytical results.

## 4 Methodologies

To undertake this study, the critical issue is: How can we ensure more sustainable structural materials for a construction project that can be implemented and considered in the decision-making process while considering all the pillars of sustainability? The authors followed the application of the life cycle perspective to the sustainability pillars, which can provide a method of incorporating sustainable development into decision-making processes. In this context, life cycle sustainability analysis refers to considering the environmental, technical, social, and economic implications of a building across its complete life cycle. The methodology is graphically explained in Fig. 1.

## 5 Selections of Alternative Structural Materials

For structural components of a house build, the construction industry employs several building materials. Architects engage structural engineers on the load-bearing capacities of the materials they design with, the most common of which are concrete, steel, wood, masonry, and stone. Each has its unique strength, weight, and durability,
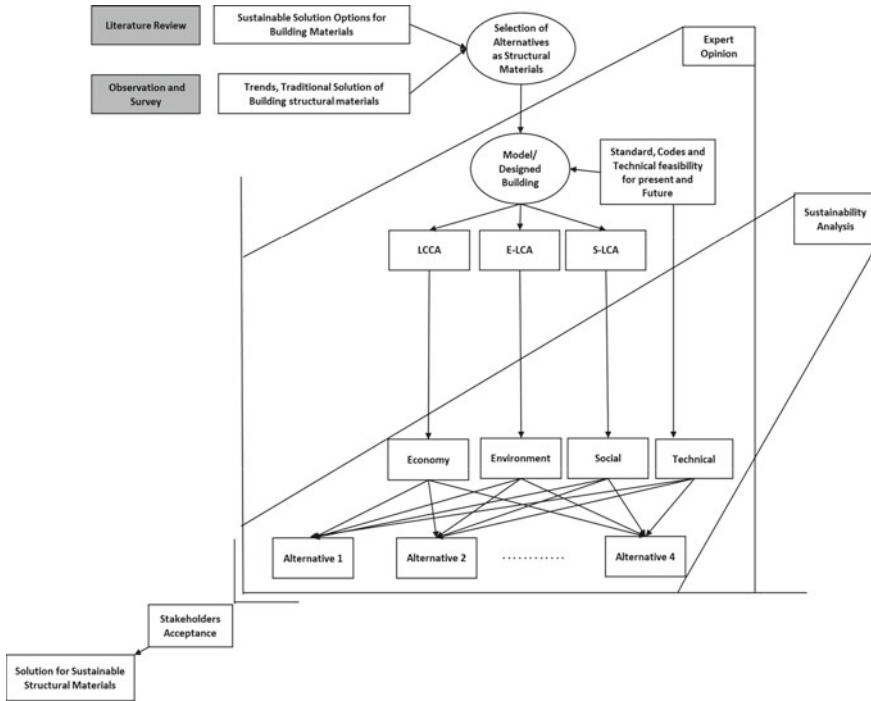
**Fig. 1** Research methodology

making it suited for a wide range of uses. National standards and testing processes control building materials used in the construction industry, so they can be relied on to ensure structural integrity. When selecting materials, architects consider both cost and appearance.

Owners are highly guided by different factors. Though most of them have shallow knowledge of the materials to be used for the building, traditionally it is driven by their experience, local practices, and affordability, with cost–benefit analysis. Other factors to consider include, if the material is long-lasting, reusable, less toxic, uses fewer resources, and is better for the environment, wildlife, and humans. So, choice of materials depends on the location, culture, material availability, materials price, weather susceptivity, etc.

Here, life cycle sustainability analysis (LCSA) is the sum of life cycle cost analysis (LCCA), environmental life cycle analysis (E-LCA), and social life cycle analysis (S-LCA).

$$LCSA = LCCA + E\text{-}LCA + S - LCA$$

**Table 1** Alternative building materials selected by researchers in sustainability or green building study

| References | Alternative materials selected for assessment |
| --- | --- |
| Gharehbaghi and Georgy [8] | Timber, concrete, steel for building construction |
| Abouhamad and Abu-Hamd [1] | Reinforced concrete framing (RC), steel framing (SS), and cold-formed steel framing (CFS) framework for the selection of construction systems of low and medium rise buildings |
| Davies et al. [6] | Concrete, steel, wood for life cycle analysis of building construction |

Several studies have been conducted in the past regarding alternative construction materials in the context of green building or sustainability. Table 1 contains a collection of instances.

## 6 Description of the Model/referenced Building

A three-story hypothetical building model exemplified as shown in the Fig. 2 was used as the case study building. The structure was inspired by New Zealand's new NMIT Arts and Media complex [6]. Each level of the building has a gross size of 500 sqm (5400 sqft) and a total height of 9.2 m (30 ft). There are 30 columns having a concrete column footing. Only the essential structural components, such as the foundation, column beam, floor slab, wall, and roof structure are considered while analyzing the building. Other elements are disregarded. The structure is then redesigned using reinforced concrete, masonry, and steel as primary structural materials. Except for masonry, all other scenarios require a concrete foundation. When utilizing concrete, the footing size increases significantly due to the increased self-weight of the structural components.



(a)    (b)    (c)
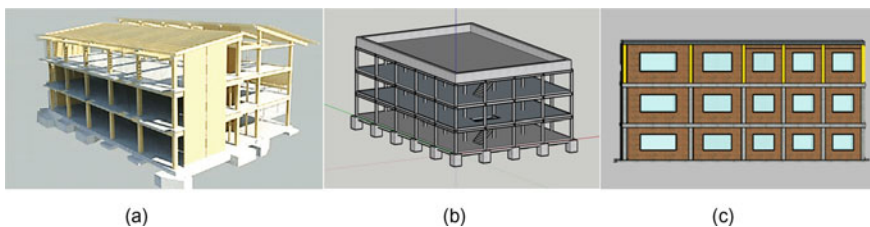
**Fig. 2** Three-story building design in timber, concrete, and masonry [6]

# 7 Life Cycle Sustainability Analysis (LCSA) of the Building

Life cycle sustainability assessment evaluates the negative environmental, social, and economic costs and advantages in decision-making processes toward more sustainable solutions throughout their life cycle (LCSA). An increased interest in developing methods to better understand and address the impacts of products throughout their life cycle has been sparked by a growing global awareness of the importance of environmental protection; an understanding of the risks of trade-offs between possible impacts associated with materials (both manufactured and consumed); and the necessity of taking climate change issues and biodiversity into account from a holistic perspective. LCSA of a building structure can be divided into three essential components, life cycle cost analysis (LCCA), environmental life cycle analysis (E-LCA), and social life cycle analysis (S-LCA). The model building is analyzed for its LCSA for a period of 60 years by using ATHENA [3]. ATHENA Impact Estimator for buildings, the first free software tool intended to analyze entire buildings and assemblies using internationally recognized life cycle assessment (LCA) methods. The Impact Estimator considers the environment with other more typical design elements at the conceptual stage of a project. The estimator considers all aspects of material production, including resource extraction and recycled content. It also considers related modes of transportation, variations in energy consumption, structure type and estimated lifespan, maintenance and replacement effects, disposal, demolition, etc.

## 7.1 Life Cycle Cost Analysis (LCCA)

The life cycle cost analysis (LCCA) approach is used to calculate the overall cost of facility ownership [18]. It considers the expenses associated with purchasing, owning, and disposing of a building or building system. LCCA is notably beneficial for comparing project options that meet the same performance criteria but differ in terms of initial and running costs to choose the one that optimizes net savings.

LCCA will assist in determining whether the inclusion of structural materials, which may increase initial costs but result in lower operating and maintenance expenses, is cost-effective. The lowest life cycle cost (LCC) is the most straightforward and simple economic assessment metric. Net savings, savings-to-investment ratio, internal rate of return, and payback period are more often used metrics [11]. They are compatible with the lowest LCC evaluation measure if the same parameters and research time are used. Building economists, certified value experts, cost engineers, architects, quantity surveyors, operations researchers, and others may employ one or more of these methods to assess a project. Whether it's termed cost estimates, value engineering, or economic analysis, the method to selecting cost-effective decisions for building-related projects can be relatively similar.

### 7.1.1 LCCA Method

The goal of an LCCA is to assess the total costs of project options and choose the design that assures the facility has the lowest overall cost of ownership while maintaining its quality and function [18]. To achieve a decrease in life cycle costs, the LCCA should be undertaken early in the design phase while there is still time to revise the design. The first and most difficult duty of an LCCA, or any economic evaluation approach, is to evaluate the economic consequences of various building and building system designs and quantify and represent these effects in monetary numbers.

### 7.1.2 LCCA Calculation

There are numerous costs related with operating, maintaining, and disposing of a building or building system. The general LCC formula for buildings summarizing all costs that occur from cradle to grave is given at Eq. 1 [18]:

$$LCC = I + Repl + E + W + EOL \qquad (1)$$

where

$I$ = investment costs,
Repl = replacement costs,
$E$ = operational energy costs,
$W$ = operational water costs,
and EOL = end-of-life costs.

However, to combine and compare cash flows incurred at different points over a project's life cycle, they must be made time equivalent. The LCC approach transforms cash flows to present values by discounting them to a single point in time, generally the base date, to make them time equivalent. The interest rate utilized for discounting is a rate that represents an investor's opportunity cost of money over time, which means that the investor wants to earn at least as much as her next best investment. As a result, the discount rate indicates the investor's acceptable minimum rate of return. The present value (PV) formula given at Eq. 2 was employed in the LCC calculation to discount future cash flows to current values [9]:

$$PV = F_t / \frac{1}{(1+d)^t} \qquad (2)$$

where

$PV$ = present value,
$t$ = time in unit of year,
$F_t$ = future cash amount that occurs in year $t$

$d$ = discount rate, which is used for discounting future amounts to the present value.

After identifying all costs by year, they are discounted to the present value, and added to arrive at the total LCC for each alternative, as shown in Table 2 and Fig. 3:

## 7.2 Environment Life Cycle Analysis (E-LCA)

E-LCA is a quantified evaluation approach for assessing environmental performance across the life cycle of a product or service. Throughout all stages, the extraction and consumption of resources (including energy) as well as emissions to air, water, and soil are measured. After that, their potential contribution to environmental impact categories is evaluated. Climate change, human and eco-toxicity, ionizing radiation, and resource base degradation are examples of these categories (e.g., water, non-renewable primary energy resources, land, etc.). The life cycle initiative was instrumental in developing the midpoint-damage framework for life cycle assessment, which conceptualizes the linkages between a product's environmental interventions and the ultimate damage caused to human health, resource depletion, and ecosystem quality—information that is critical for decision-makers. Three major indexes, total primary energy, $CO_2$ emission (global warming potential), and fossil fuel consumption are used to evaluate the influence of construction materials on the environment in this case. The ATHENA Impact Estimator for building software was used to calculate the amount, which is depicted in Fig. 4.

## 7.3 Social Life Cycle Analysis (S-LCA)

A social life cycle analysis (S-LCA) is a method for evaluating the social and sociological elements of goods and their existing and prospective positive and negative impacts throughout their life cycle. This covers raw material extraction and processing, production, distribution, usage, reuse, maintenance, recycling, and final disposal. S-LCA uses general and site-specific data, can be quantitative, semi-quantitative, or qualitative, and is used in conjunction with environmental LCA and LCC. It can be used independently or in combination with the other methods. The S-LCA material assessment presents an approach for developing life cycle inventories. A life cycle inventory is elaborated for indicators linked to impact categories which are related to five main stakeholder groups: worker, occupants, local community, society, and value chain actors. Here, the score of S-LCA is the sum of the positive and negative scores assigned to the indicators impacting the stakeholders' group. In comparison with the other three choices, timber has a higher social value, generates income for the community, connects people with nature, and reduces waste and pollution.

**Table 2** Comparative statement of the LCC of alternative structural materials [3]

| Stages and cost categories | | | Concrete | | Steel | | Timber | | Masonry | |
|---|---|---|---|---|---|---|---|---|---|---|
| | | | Actual | PV | Actual | PV | Actual | PV | Actual | PV |
| Production stage | Raw material supply (A1) | Construction cost | 900.5 | 900.5 | 1014.2 | 1014.2 | 973.2 | 973.2 | 880.2 | 880.2 |
| | Transport (A2) | | | | | | | | | |
| | Manufacturing (A3) | | | | | | | | | |
| Construction process stage | Transport to the building site(A4) | | | | | | | | | |
| | Installation into building (A5) | | | | | | | | | |
| Use stage (50 years) | Use/application (B1) | Maintenance cost | 83.2 | 50.7 | 149.6 | 91.2 | 79.9 | 48.7 | 24.4 | 14.9 |
| | Maintenance (B2) | | | | | | | | | |
| | Repair (B3) | | | | | | | | | |
| | Replacement (B4) | Replacement cost | 124.9 | 76.12 | 55.0 | 33.5 | 83.0 | 50.6 | 51.2 | 31.2 |
| | Refurbishment (B5) | | | | | | | | | |
| | Operational energy use (B6) | Operation energy cost | 23.1 | 14.1 | 30.8 | 18.8 | 16.6 | 10.1 | 10.8 | 6.6 |
| | Operational water use (B7) | Operation water cost | 17.2 | 10.5 | 14.6 | 8.9 | 13.0 | 7.9 | 28.2 | 17.2 |

(continued)

**Table 2** (continued)

| Stages and cost categories | | | Concrete | | Steel | | Timber | | Masonry | |
|---|---|---|---|---|---|---|---|---|---|---|
| | | | Actual | PV | Actual | PV | Actual | PV | Actual | PV |
| End-of-life stage (after 50 years) | Deconstruction/ Demolition (C1) | End-of-life cost | 272.7 | 101.3 | 34.3 | 20.8 | 42.9 | 26.1 | 158.8 | 59.0 |
| | Transport (C2) | | | | | | | | | |
| | Waste processing (C3) | | | | | | | | | |
| | Disposal and reuse (D1) | | | | | | | | | |
| Total | (Thousand USD) | | 1153.3 | | 1187.4 | | 1116.6 | | 1009.4 | |

*Note* Here, $d = 2\%$ and for PV of use stage $t = 25$ years (average of 50 years) is considered. All costs are in thousand USD.
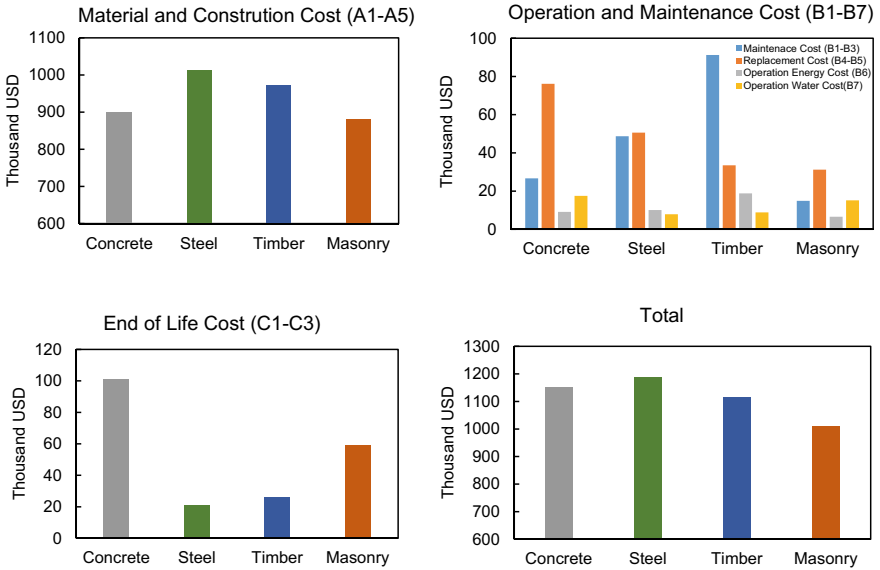
**Fig. 3** LCC of the building using different structural materials
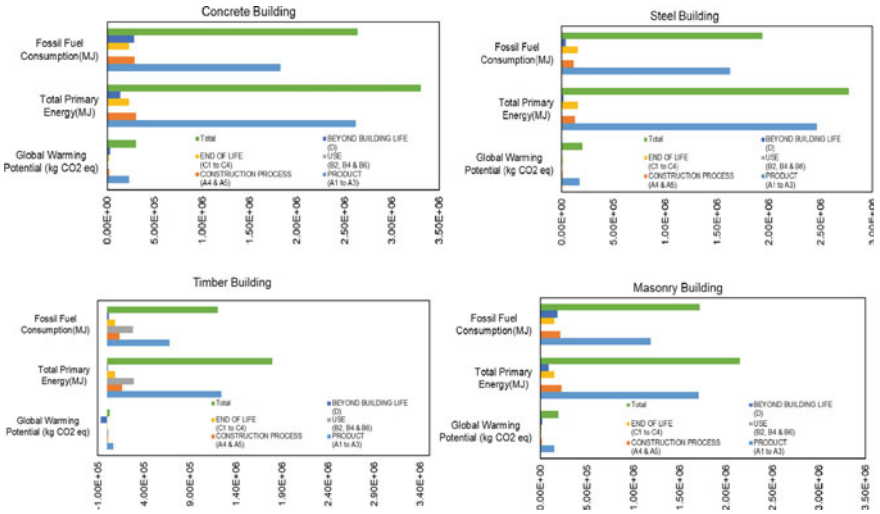


**Fig. 4** Impact of building materials on environmental index

# 8   Analysis Outcomes Based on the Expert Opinion

The statistics and analytical findings of the LCSA show that, despite having the greatest LCC, lumber may have a considerable positive impact on the environment. Although the overall LCC of timber building is just 10% higher than that of concrete, it decreases greenhouse emissions and energy use by nearly half. Masonry is also a more cost-effective option than concrete, and it emits less carbon. Steel is also a little more environmentally friendly and less costly than concrete throughout the course of its life cycle. The findings of this study's research will aid practitioners in organizing complex environmental, technological, economic, and social facts and data. It will assist in clarifying the trade-offs between the three sustainability pillars, life cycle phases and effects, products, and generations, by providing a complete perspective of the positive and negative implications along the product life cycle. It will show businesses how to take greater responsibility for their operations by taking into consideration the whole spectrum of effects associated with their goods and services. It will increase value chain players' understanding of sustainability problems, facilitate the discovery of defects, and enable future product life cycle improvements. It will help decision-makers prioritize resources and invest them where there is a higher possibility of positive results and a lower likelihood of harmful consequences and selecting sustainable technologies and materials. It can value compared to determine if things are more cost-effective, ecologically friendly, socially responsible, and more sustainable. Transparent LCSA information exchange promotes the development of trust among building construction businesses toward sustainability.

# 9   Conclusions

To achieve a sustainable building, it is critical to use sustainable materials. While quantifying all the economic, environmental, technical, and social ramifications of sustainability pillars is difficult, data and analysis of building materials allow for realistic comparisons between solutions based on specific criteria. Different materials can be employed as structural components in constructing a structure. Each of these materials has its sustainability characteristics; therefore, one may be cost-effective but more environmentally harmful or aesthetically incompatible with the environment. The requirement for multi-criteria decision-making is obvious, since several characteristics are beneficial in the end choice of selecting the most sustainable material. The LCSA has the potential to initiate interest in developing methods to understand better and address the impacts of building materials throughout their life cycle, as well as a growing global awareness of the importance of environmental protection; an understanding of the risks of trade-offs between potential infrastructure and its impacts on the environment and society; and the need to think about climate change and biodiversity holistically.

# References

1. Abouhamad M, Abu-Hamd M (2019) Framework for Construction System Selection Based on Life Cycle Cost and Sustainability Assessment. J Clean Prod 241(September):118397. https://doi.org/10.1016/j.jclepro.2019.118397
2. Akadiri PO, Olomolaiye PO (2012) Development of sustainable assessment criteria for building materials selection. Eng Constr Archit Manag 19(6):666–687. https://doi.org/10.1108/09699981211277568
3. ATHENA (2022) Impact estimator for buildings. Athena Institute
4. Bartlett E, Howard N (2000) Informing the decision makers on the cost and value of green building. Building Res Inform 28(5–6):315–24. https://doi.org/10.1080/096132100418474
5. Cowan HJ (1977) A history of masonry and concrete domes in building construction. Build Environ 12(1):1–24. https://doi.org/10.1016/0360-1323(77)90002-6
6. Davies D, Johnson L, Doepker B, Hedlund M (2018) Quantifying environmental impacts of structural material choices using life cycle assessment: a case study. In: Embodied carbon in buildings. Springer International Publishing
7. Doan DT, Ghaffarianhoseini A, Naismith N, Zhang T, Ghaffarianhoseini A, Tookey J (2017) A critical comparison of green building rating systems. Build Environ 123:243–260. https://doi.org/10.1016/j.buildenv.2017.07.007
8. Gharehbaghi K, Georgy M (2019) Sustainable construction by means of improved material selection process. Acad Res Commun Publ 3(February). https://doi.org/10.21625/archive.v3i1.433
9. Halloran D (2019) Life-cycle costing within the construction sector. Routledge, Cost and EU Public Procurement Law. https://doi.org/10.4324/9780429060045-8
10. Kovacic I, Zoller V (2015) building life cycle optimization tools for early design phases. Energy 92:409–419. https://doi.org/10.1016/j.energy.2015.03.027
11. Marszal AJ, Heiselberg P (2011) Life cycle cost analysis of a multi-storey residential net zero energy building in Denmark. Energy 36(9):5600–5609. https://doi.org/10.1016/j.energy.2011.07.010
12. Oldfield P (2019) The sustainable tall building. Routledge. https://doi.org/10.4324/9781315695686
13. Opon J, Henry M (2019) An indicator framework for quantifying the sustainability of concrete materials from the perspectives of global sustainable development. J Clean Prod 218:718–737. https://doi.org/10.1016/j.jclepro.2019.01.220
14. Pellegrini-Masini G, Bowles G, Peacock AD, Ahadzi M, Banfill PFG (2010) Whole life costing of domestic energy demand reduction technologies: householder perspectives. Constr Manag Econ 28(3):217–229. https://doi.org/10.1080/01446190903480027
15. Salvado F, Marques de Almeida N, Vale e Azevedo A (2018) Toward improved LCC-informed decisions in building management. Built Environ Project Asset Manage 8(2):114–33. https://doi.org/10.1108/bepam-07-2017-0042
16. Schmidt M, Crawford RH (2018) A framework for the integrated optimisation of the life cycle greenhouse gas emissions and cost of buildings. Energy Buildings 171:155–167. https://doi.org/10.1016/j.enbuild.2018.04.018
17. Stephan A, Stephan L (2016) Life cycle energy and cost analysis of embodied, operational and user-transport energy reduction measures for residential buildings. Appl Energy 161:445–464. https://doi.org/10.1016/j.apenergy.2015.10.023
18. Sterner E (2000) Life-cycle costing and its use in the Swedish building sector. Building Res Inform 28(5–6):387–393. https://doi.org/10.1080/096132100418537

19. Švajlenka J, Kozlovská M (2018) Houses based on wood as an ecological and sustainable housing alternative—case study. Sustainability 10(5):1502. https://doi.org/10.3390/su10051502
20. UN 2016 (2016) SDGs. https://sdgs.un.org/goals
21. Wallace D (2020) The UN regime and sustainable development: agenda 2030. In: Implementing sustainable development goals in Europe. Edward Elgar Publishing. https://doi.org/10.4337/9781789909975.00006

# Optimization of Pervious Concrete Mechanical Properties Through Incorporation of Fiber Reinforcement Schemes

**Adham Sherif, Ahmed Koura, Amir Ibrahim, Amr El Sayed, Aya El Kayyal, Donia ElDwib, Mayer Farag, and Mohamed Abou-Zeid**

**Abstract**  Portland Cement Pervious Concrete (PCPC) is a special high porosity concrete containing zero or minimal amount of fine aggregates. Such concrete endows the concrete to have significant voids allowing water to percolate; however, such an open void structure reduces the mechanical strength of the concrete considerably. It is recommended that chemical admixtures be added to the concrete to enhance its workability and other properties. The study aims to potentially enhance the properties of PCPC through the incorporation of various fiber reinforcement schemes. The fibers used in the scope of this study are hooked-end steel fiber, macro-polypropylene fiber, and glass fiber. To meet that objective, concrete mixes were prepared using varying fiber dosage rates and aggregate gradations. An experimental program was developed to test fresh concrete properties, hardened concrete properties, and durability. In order to gauge only the effectiveness of the aforementioned fiber, the PCPC mix design was standardized across the spectrum to eliminate such variables. It was evident that the glass fiber with Vf 0.17% (GF 2) enhanced mechanical properties with the most significant compressive strength increase, compared to the control sample, reaching 34 MPa. Moreover, (GF 2) has enhanced, compared to the control sample, the flexural and the splitting tensile strength with an increase of 93.7% and 161.9%, respectively. The outcome of the study is that the use of different fiber reinforcement schemes has managed to enhance the mechanical strength of PCPC while maintaining an adequate rate of infiltration that complies with ASTM standards. The research opens the door for further application of the proposed model in different contexts both regionally and internationally, thus playing a vital role in the concrete nexus.

**Keywords**  Pervious concrete · Porosity · Fiber reinforced pervious concrete · Mix design · Permeability

A. Sherif (✉) · A. Koura · A. Ibrahim · A. E. Sayed · A. E. Kayyal · D. ElDwib · M. Farag · M. Abou-Zeid
Department of Construction Engineering, The American University in Cairo, Cairo, Egypt
e-mail: adham-sherif@aucegypt.edu

939

# 1   Introduction

Regarded as best practice by the Environmental Protection Agency (EPA), pervious concrete is special given its open-pore structure allowing water to pass through. By rainwater collection, it provides multifarious benefits which include but are not limited to reducing stormwater runoff, recharging the groundwater table, and reducing the requirement for a stormwater management system. Enhancing the mechanical properties of the pervious concrete has become an ongoing research that aims to expand its applications. The current applications for the pervious concrete are using it in parking lots, walking pavements and decorative colored roads as it holds color pigments much better than normal concrete. In addition, it can be further used in gas stations as slab on grade and in rain trenches to collect water and reuse it. In this research, we chose to tackle the fiber reinforcement schemes and investigate its impact on the pervious concrete. Fiber reinforced pervious concrete is made primarily of cement, aggregates, and discrete reinforcing fibers. In this research, three fibers were investigated: steel fiber, polypropylene fiber, and glass fiber. Steel fiber reinforced concrete is a composite material having fibers as the additional ingredients, dispersed uniformly at random in small percentages by volume. On another hand, the polypropylene fibers can limit the width of plastic shrinkage cracks in the pervious concrete. The fiber also endows the concrete with some post-cracking ductility and increased strain capacity. For each fiber, three different dosages were investigated in order to be able to draw an analysis for the optimum dosage and to compare between each of them in terms of mechanical properties, infiltration rate, and durability.

# 2   Literature Review

Pervious concrete tends to have different properties from that of traditional impervious concrete. The fresh concrete properties vary in which pervious concrete is very stiff compared to the latter. According to Karthik [1], the slumps are very low with various mixtures having 0 mm slump, while others were able to reach as high as 50 mm. The following is dependent on the objective of the pervious concrete and its intended utilization [2]. It is imperative to mention that the slump has no correlation with workability and should not be added as an acceptance criterion. Furthermore, the typical densities and void ratio of pervious concrete range from (1600–2000) kg/m$^3$, while the latter ranges from 20 to 25%. Upon placement and compaction, the aggregates adhere to each other and exhibit the open-pore structure. It is important to note that following the open structure and its rough surface of concrete exposes an even greater surface of the cement to evaporation [3]. It is therefore of very high importance to ensure that the concrete is cured properly to ensure that the reaction is maintained. Curing the concrete properly tends to result in compressive strengths ranging from (3.5–28) MPa while having flexural strengths ranging from (1.8–3)

MPa. Seeing the following limitation of pervious concrete mechanical properties, the utilization of fibers has been studied to further enhance pervious concrete's purpose.

Regarding fibers, the following can be distinguished into two main types, metallic and non-metallic fiber. The first group is composed of steel fiber, while the latter category is composed of diverse classes of fibers. The following class of fibers include but are not limited to glass fiber, synthetic fiber, basalt fiber, carbon fiber, and natural fiber [4]. Many researchers believe that fibers enhance the properties of concrete favorably; however, there is an optimum design limit which compromises between workability and strength of the concrete mix. There are a lot of factors that tend to influence the impact of fibers on the concrete which include the fiber orientation, material, dimensions (aspect ratio, length, and diameter), water/binder ratio, type of cement, and supplementary cementitious material application [5]. Pertaining to steel fiber, there are various shapes that steel fiber tends to come in. There is an agreement that hooked-end steel fiber generates higher flexural strength and toughness than other shapes such as crimped and straight steel fiber. Furthermore, the steel fiber tends to play a vital role in crack propagation reduction [6]. It is best applied perpendicular to the crack in the direction of the stresses. The following could be problematic in pervious concrete given its open-pore structure. The typical dosage rates in concrete tend to range from (0.25–1.5) %, while the aspect ratio should be from 50 to 80 [4].

Steel fiber can positively impact concrete; however, they have a limitation given the nature of the open-pore structure of pervious concrete. The effects of the corrosive environment are negative for steel fiber; however, there is no impact on synthetic fibers which include but are not limited to glass fiber and polypropylene fiber [7]. On another hand, non-metallic fibers such as glass fiber are not effected by corrosion. Glass fiber tends to have an impact on the concrete properties in which they enhance durability, toughness, and explosive spalling resistance. It has been noted in the paper that the inclusion of 0.2% volume fraction of glass fiber resulted in an enhancement of up to 30% in tensile strength and up to 64% in flexural strength, citing the tendency of improved mechanical properties with the increase of fiber dosages until the optimal rate, with a gradual decrease after the optimal percentage [7].

Regarding polypropylene fiber, their influence on the mechanical properties, as well as abrasion resistance and freeze–thaw resistance relies heavily on the length of the fiber reinforcing the concrete. Accordingly, two main types of polypropylene fibers exist: macrofiber and microfiber. On one hand, the relevant type, used for structural purposes, is macrofiber, where the length varies between 30 and 50 mm, and on the other hand, microfiber, smaller in size, does not fulfill the load-bearing function for structures. In fact, it is worth mentioning as well that the optimal included quantity of polypropylene ranged from 0.15 to 0.5% in terms of enhancement of concrete's mechanical properties; however, the increase in fibers' dosages do not consequently guarantee the enhancement of the concrete due to random fiber distribution and potential workability deterioration [5].

On another note, pertaining to the pervious concrete mix design, it is important to understand that adding admixtures does favorably impact the concrete properties. PCPC often employs a variety of admixtures, including superplasticizers (SPs), viscosity modifying admixtures (VMA), and set-retarding admixtures (RE). These

chemical admixtures have a substantial impact on the paste component's flowability, film-forming ability, and film-drying time. As a result, the kind and amount of chemical admixture used has a significant impact on the workability of PCPC mixes. It has been indicated that the utilization of superplasticizers with (0.2–0.225) admixture dosage % by weight of cement does have positive properties on the pervious concrete's workability. [3].

## 3 Objective and Scope

The objective of this research was to potentially enhance the properties of pervious concrete through the incorporation of various fiber reinforcement schemes.

Accordingly, the primordial scope of work was to perform experimental work in which various concrete mixtures are prepared using various fiber reinforcement schemes in order to obtain adequate pervious concrete mix that yields optimal performance.

## 4 Experimental Work

### 4.1 Materials

1. **Coarse Aggregates:** Single-sized 12.5 and 9.5 mm coarse aggregates.
2. **Cement:** Type I Ordinary Portland Cement.
3. **Superplasticizer:** CMB Addicrete BVF1, high range water reducing, and superplasticizer concrete admixture.
4. **Water:** Ordinary tap water was used in the mix with a water cement ratio of 0.3.
5. **Glass Fiber:** Graded chopped fiber glass was used in the mix.
6. **Steel Fiber:** Hooked-end steel fiber was used with aspect ratio ($l/d$) 50.
7. **Polypropylene Fiber:** Macro-polypropylene fiber was used with length of 60 mm, and equivalent diameter 0.84 mm (Fig. 1).

### 4.2 Concrete Mix Design

The mix design was done while considering previous mix designs from the literature that would ensure adequate infiltration while also yielding acceptable ranges of mechanical properties [2]. Accordingly, a 1:5 ratio between the two sizes of aggregates was used where the single-sized 12.5 mm aggregates composes 80% of the coarse aggregate weight, while the remaining 20% are composed of the 9.5 mm single-sized aggregates (Table 1).

**Fig. 1** Sample of the fibers presented with glass fiber, steel fiber, and polypropylene fiber

**Table 1** Typical nomenclature

| Mix name | Mix code |
|---|---|
| Glass fiber dosage 1 | GF 1 |
| Glass fiber dosage 2 | GF 2 |
| Glass fiber dosage 3 | GF 3 |
| Steel fiber dosage 1 | SF 1 |
| Steel fiber dosage 2 | SF 2 |
| Steel fiber dosage 3 | SF 3 |
| Polypropylene fiber dosage 1 | PP 1 |
| Polypropylene fiber dosage 2 | PP 2 |
| Polypropylene fiber dosage 3 | PP3 |
| Control mix without superplasticizer | CC |
| Control mix with superplasticizer | CC-SP |

Moreover, by the end of the research, a control sample of 1:1 ratio of coarse aggregates was used to further investigate pervious concrete mechanical properties with respect to its serviceability property through abiding by the minimal infiltration rate. Accordingly, 7-day compressive strength and infiltration rate results were obtained for the new sample. These tests were conducted in order to potentially establish a correlation between the ratio of coarse aggregates mix and the infiltration rate, and that could be further investigated through incorporation of fibers in the future (Table 2).

## 4.3 Tests

### 4.3.1 Aggregate Tests

1. *Los Angeles Abrasion Test*: This test is done in order to determine the Los Angeles Abrasion number of concrete [8].

**Table 2** Mix design parameters

| Parameters (kg/m³) | CC | GF1 | GF2 | GF3 | SF1 | SF2 | SF3 | PP1 | PP2 | PP3 | CC-SP |
|---|---|---|---|---|---|---|---|---|---|---|---|
| Coarse Aggregates | 1500 | | | | | | | | | | |
| Water | 105 | | | | | | | | | | |
| Cement | 350 | | | | | | | | | | |
| Admixture | – | 6.75 | 6.75 | 6.75 | 6.75 | 6.75 | 6.75 | 6.75 | 6.75 | 6.75 | 6.75 |
| Fiber dosages[a] (Vf) | – | 0.1 | 0.17 | 0.25 | 0.3 | 0.4 | 0.5 | 0.1 | 0.25 | 0.5 | – |

[a]Vf is expressed as a percentage

2. *Density, Specific Gravity, and Absorption*: This test is done in order to determine the density, specific gravity and absorption of coarse aggregates [9].

### 4.3.2   Fresh Concrete Tests

1. *Temperature*: This test is done in order to determine the temperature of freshly mixed concrete [10].
2. *Slump*: This test is done in order to determine the workability of freshly mixed concrete [11].
3. *Density*: This test is done in order to determine the unit weight of freshly mixed concrete [12].
4. *Air Content*: This test is done in order to determine the air content of freshly mixed concrete [13].

### 4.3.3   Hardened Concrete Tests

1. *Compressive Strength*: This test is conducted in order to determine the 7-day and 28-day compressive strength of concrete cubes of dimensions 15 cm × 15 cm × 15 cm [14].
2. *Flexural Strength*: This test is conducted in order to determine the 28-day flexural strength of concrete beams of dimensions 75 cm × 15 cm × 15 cm [15].
3. *Splitting Tensile Strength*: This test is conducted in order to determine the 28-day splitting tensile strength of concrete cylinders of dimensions 30 cm × 15 cm [16]

### 4.3.4   Serviceability Tests

Standard Test Method for Infiltration Rate of Pervious Concrete: This test is conducted in order to determine the infiltration rate of pervious concrete [17].

• Samples with dimensions 40 cm × 40 cm × 10 cm were casted for each fiber type and cured for 7 days for this experiment.

### 4.3.5 Durability Tests

Standard Test for Horizontal Surface Abrasion: This test is conducted in order to determine the potential resistance to degradation of pervious concrete by impact and abrasion [18].

- Cylinders with dimensions 20 cm × 10 cm were casted and cured for 7 days before being placed in the LA Abrasion machine for 500 revolutions.

## 4.4  Results and Analysis

### 4.4.1  Aggregate Tests

**Density, Specific Gravity, and Absorption**

See Table 3.

**Los Angeles Abrasion**

See Table 4.

**Fresh Concrete Tests**

The fresh concrete results, obtained in Table 5, are acceptable as they are similar to the criteria found in the literature for pervious concrete. The obtained slump value was expected due to the very low workability of pervious concrete which justifies the use of the superplasticizer. Furthermore, the obtained density indicates that the concrete is lightweight as it is lower than the 2000 kg/m$^3$ threshold. Finally, the air content obtained indicates the high amount of voids which gives the concrete its permeable quality (Fig. 2).

**Table 3**  Coarse aggregate results

|  | Coarse aggregates (12.5 mm) | Coarse aggregates (9.5 mm) |
|---|---|---|
| Bulk specific gravity | 2.62 | 2.5 |
| Bulk specific gravity saturated surface dry | 2.66 | 2.51 |
| Apparent specific gravity | 2.73 | 2.54 |
| Absorption (%) | 1.61 | 0.75 |

**Table 4**  Los Angeles abrasion results

|  | Weight (g) |
|---|---|
| Initial weight | 5000 |
| Bulk specific gravity saturated surface dry | 3900 |
| Losses | 22% |

**Table 5** Fresh concrete results

| Parameter | Result |
|---|---|
| Slump (cm) | 0 |
| Air content (%) | 21 |
| Density (kg/m$^3$) | 1909 |
| Temperature (C) | 28.5 |

**Fig. 2** Image of fresh concrete



## Compressive Strength

The results in Table 6 and Fig. 3 show the 7-day and 28-day compressive strengths for each mix in which the second dosage for glass fiber (GF2) showed the highest results. The glass fiber and steel fiber results show that, within the chosen dosage range, the optimum mix was obtained. The same does not apply for the polypropylene fiber as the optimum dosage may not have been achieved within the chosen range as the trend shows a constant decrease in compressive strength as the dosage increases.

The aggregates' interlock in the mix affects the strength of hardened concrete which may indicate why the glass fiber exhibits the highest compressive strength.

**Table 6** Compressive strength results

| Mix | 7-Day compressive strength (MPa) | 28-Day compressive strength (MPa) |
|---|---|---|
| CC | 6.63 | 9.47 |
| CC-SP | 7.89 | 10.90 |
| GF 1 | 14.74 | 17.51 |
| GF 2 | 24.68 | 34.03 |
| GF 3 | 13.05 | 18.65 |
| SF 1 | 9.56 | 10.03 |
| SF 2 | 12.67 | 20.62 |
| SF 3 | 13.37 | 15.42 |
| PP 1 | 12.07 | 20.61 |
| PP 2 | 14.70 | 16.47 |
| PP 3 | 12.03 | 15.47 |
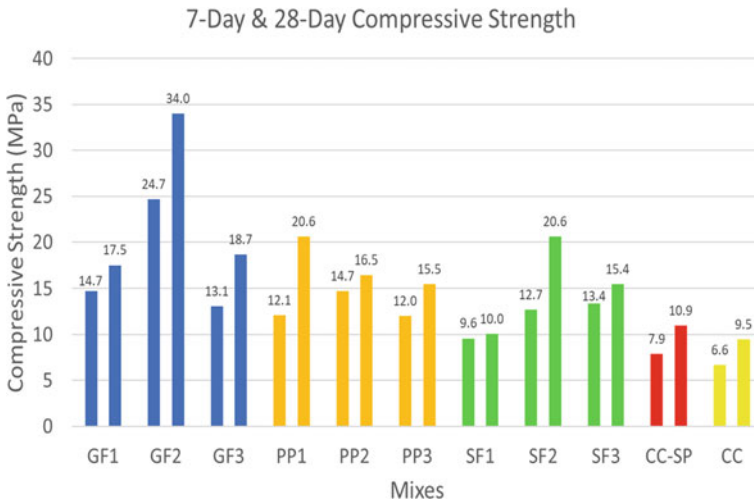
**Fig. 3** Chart of compressive strength results

The glass fiber is able to bond with the cement and aggregates due to its material texture and composition, as opposed to the steel fiber and polypropylene fiber, thus entailing a stronger interlock between the glass fiber and pervious concrete.

Furthermore, larger size aggregates exhibit lower compressive strength due to the lower surface area for cement paste to bond. In addition, the rough surface of pervious concrete with larger aggregate sizes has led to non-uniform load distribution as a result of the heterogeneity of the aggregates that were used in the mix. Accordingly, the 1:1 control sample yielded promising results with 17.6 MPa in 7-day compressive strength and provided a base for future investigation through incorporating the aforementioned fiber dosages and tests.

**Flexural Strength**

The 28-day flexural strength was tested on beams which were reinforced with GFRP rods using the one-point bending test. The flexural strength results follow a similar trend to the compressive strength as the glass fiber and steel fiber were optimized within the chosen range, whereas the polypropylene fiber was not. The GF2 mix exhibited the highest flexural strength, similar to the compressive strength. Furthermore, the results in Table 7 and Fig. 4 indicate a significant enhancement to the pervious concrete flexural strength found in the literature which had ranged between 1 MPa and 3.8 MPa.

### 4.4.2 Splitting Tensile Strength

The GF2 mix was consistent in all three mechanical properties tests as it exhibited the highest 28-day splitting tensile strength along with the compressive and flexural

**Table 7** Flexural strength results

| Mix | 28-Day flexural strength (MPa) |
|-----|-------------------------------|
| CC | – |
| CC-SP | 6.40 |
| GF 1 | 7.41 |
| GF 2 | 12.40 |
| GF 3 | 7.86 |
| SF 1 | 7.23 |
| SF 2 | 8.90 |
| SF 3 | 7.73 |
| PP 1 | 8.10 |
| PP 2 | 6.75 |
| PP 3 | 6.50 |
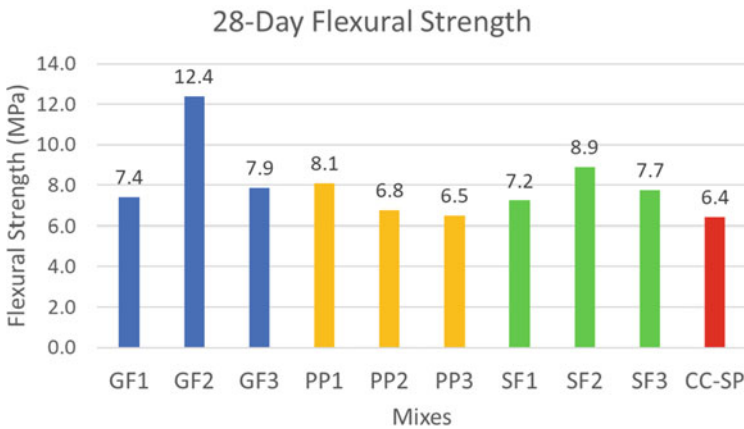


**Fig. 4** Chart of flexural strength results

strengths. The results for the tensile strength indicate a different trend for both the steel fiber and the polypropylene fiber as it shows that, within the indicated range, the polypropylene has been optimized at the second dosage, whereas the steel fiber may have yielded higher results using a larger dosage as shown by the constant increase. Finally, the literature presented a splitting tensile strength for pervious concrete ranging from 1 to 2 MPa which has been enhanced using the GF2 and PP2 mixes (Table 8; Figs. 5, 6 and 7).

**Table 8** Splitting tensile results

| Mix | 28-Day splitting tensile strength (MPa) |
|---|---|
| CC | – |
| CC-SP | 0.92 |
| GF 1 | 1.92 |
| GF 2 | 2.41 |
| GF 3 | 1.88 |
| SF 1 | 0.68 |
| SF 2 | 1.14 |
| SF 3 | 1.28 |
| PP 1 | 1.75 |
| PP 2 | 2.17 |
| PP 3 | 1.84 |



**Fig. 5** One-point bending test of pervious concrete beams

### 4.4.3 Serviceability Test

**Infiltration Rate Test**

According to the ASTM, the minimum infiltration rate accepted for pervious concrete is 200 inches per hour. The results in Table 9 indicate that all fibers have confidently surpassed the minimum requirement and achieved adequate infiltration rates.
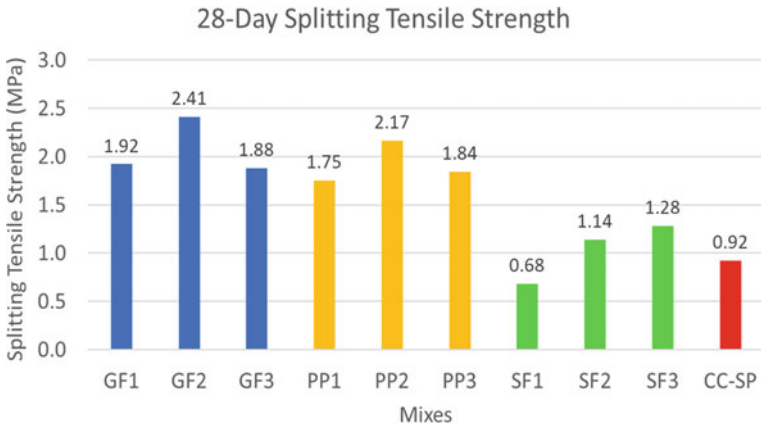
**Fig. 6** Chart of splitting tensile strength results



**Fig. 7** Examination of splitting tensile test specimen

**Table 9** Infiltration rate results

|  | CC (1:5) | GF3 | SF3 | PP3 | CC (1:1) |
|---|---|---|---|---|---|
| Time elapsed (s) | 21.71 | 22.27 | 24.33 | 37.14 | 119 |
| Infiltration Rate (in/h) | 1608.39 | 1567.95 | 1476.65 | 1286.59 | 293.34 |

The 1:1 control sample has also passed the test with an infiltration rate of 293.43 in/h. Accordingly, this infiltration rate can provide a base for future research with regard to this mix design in yielding higher mechanical properties for pervious concrete.

**Table 10** Durability test results

| Mix | CC-SP | GF1 | GF2 | GF3 | SF1 | SF2 | SF3 | PP1 | PP2 | PP3 |
|---|---|---|---|---|---|---|---|---|---|---|
| Losses (%) | 29.52 | 50.34 | 32.04 | 33.53 | 31.49 | 28.53 | 56.25 | 65.34 | 70.48 | 50.94 |

#### 4.4.4 Durability Test

The abrasion test demonstrated that some fiber dosages such as GF2, GF3, SF1, and SF2 did not negatively affect the losses in comparison with the control sample. However, the percentage of losses of the remaining dosages has increased which indicates that the remaining dosages have negatively affected the abrasion resistance of pervious concrete (Table 10).

## 5 Conclusion

The decisive outcome of this research is assimilated in the successful enhancement of pervious concrete through incorporation of fiber reinforcements without hindering its Infiltration properties.

On one hand, remarkable enhancement of pervious concrete's compressive and flexural strengths were secured through incorporation of SF2 (steel fiber, dosage 2: 0.4% Vf or 35 kg/m$^3$ of concrete), as well as PP1 (polypropylene fibers, dosage 1: 0.1% Vf or 0.9 kg/m$^3$ of concrete). On another hand, the most crucial and significant trend was acquired through incorporation of GF2 (glass fibers, dosage 2: 0.17% Vf or 3.5 kg/m$^3$ of concrete) since it yielded the highest compressive, flexural, and splitting tensile strengths. Consequently, it was apparent that the glass fiber reinforced pervious concrete has the highest homogeneity which is needed to overcome the absence of interlock between the aggregates because of the negligible amount of fines in all the concrete mixes. Accordingly, further uses of pervious concrete that possess enhanced qualities are encouraged in the construction industry.

## 6 Recommendations

Based on the outcomes of this research, it is crucial to recommend the following:

- Further enhance pervious concrete's mechanical properties while abiding by the minimal required infiltration rate (200 in/h), since reducing the infiltration rate entails better aggregates' interlock, and accordingly greater possibility for fibers' influence on the mechanical properties.
- Smoothen pervious concrete's surface to enhance its serviceability and durability.
- Ensure through experimental work pervious concrete's chemical resistance.
- Perform dynamic loading tests for roadway pavement applications.

- Validate the results and outcomes of the performed work through a larger scope of experimental work and field results.

Finally, it is vital to encourage the concrete industry to use fiber reinforced pervious concrete in adequate applications, where infiltration properties as well as strong mechanical properties are both needed.

# References

1. Karthik HO (2010) Review of pervious concrete—an overview. Indian Concr J 84(8):9–18
2. Arhin S, Madhi R, Khan W (2014) Optimal mix designs for pervious concrete for an urban area. Int J Eng Res V4(01):9–39
3. Jimma BE, Rangaraju PR (2015) Chemical admixtures dose optimization in pervious concrete paste selection – a statistical approach. Constr Build Mater 101(December):1047–1058
4. Xu BW, Shi HS (2009) Correlations among mechanical properties of steel fiber reinforced concrete. Constr Build Mater 23(12):3468–3474
5. Blazy J, Blazy R (2021) Polypropylene fiber reinforced concrete and its application in creating architectural forms of public spaces. Case Stud Constr Mater 14(June):e00549
6. Bayramov F, Taşdemir C, Taşdemir MA (2004) Optimisation of steel fibre reinforced concretes by means of statistical response surface method. Cement Concr Compos 26(6):665–675
7. Bolat H, Şimşek O, Çullu M, Durmuş G, Can Ö (2014) The effects of macro synthetic fiber reinforcement use on physical and mechanical properties of concrete. Compos B Eng 61(May):191–198
8. ASTM C131M-20 (2020) Standard test method for resistance to degradation of small-size coarse aggregate by abrasion and impact in the Los Angeles machine. ASTM International—Standards Worldwide
9. ASTM C127-15 (2016) Test method for relative density (specific gravity) and absorption of coarse aggregate. ASTM International—Standards Worldwide
10. ASTM C1064-M17 (2017) Standard test method for temperature of freshly mixed hydraulic-cement concrete. ASTM International—Standards Worldwide
11. ASTM C143M-20 (2020) Standard test method for slump of hydraulic-cement concrete. ASTM International—Standards Worldwide
12. ASTM C231M-17a (2017) Standard test method for air content of freshly mixed concrete by the pressure method. ASTM International—Standards Worldwide
13. ASTM C138M-17a (2017) Standard test method for density (unit weight), yield, and air content (gravimetric) of concrete. ASTM International—Standards Worldwide
14. BS 1881–119 (2011) Method for determination of compressive strength using portions of beams broken in flexure (equivalent cube method). British Standards Institution
15. ASTM C293M-16 (2016) Standard test method for flexural strength of concrete (using simple beam with center-point loading). ASTM International—Standards Worldwide
16. ASTM C496M-17 (2017) Standard test method for splitting tensile strength of cylindrical concrete specimens. ASTM International—Standards Worldwide
17. ASTM C1701M-17a (2020) Standard test method for infiltration rate of in place pervious concrete. ASTM International—Standards Worldwide
18. ASTM C1747M-13 (2013) Standard test method for determining potential resistance to degradation of pervious concrete by impact and abrasion. ASTM International—Standards Worldwide

# Materials Specialty: Cement and Concrete

# Chopped Fibre Dosage and Material Effects on the Fresh Properties of Normal Strength and Density Concrete

**Helmi Alguhi and Douglas Tomlinson**

**Abstract** Chopped fibre reinforced concrete (CFRC) is used in many applications, including shotcrete tunnel walls, bridge decks, pavements, and concrete slabs. Cracked concrete's service performance can be improved using chopped fibres. The influence of chopped fibre type and volume on fresh concrete properties and mixture design was investigated in this study. Trial mixtures were used to optimize a mixture initially developed using the American Concrete Institute's absolute volume method. Ten normal strength and density test mixtures were then prepared based on these optimized trial mixtures. Mixtures included one control (i.e. no fibres) and nine CFRC mixtures. Mixture parameters included chopped fibre type (steel, glass, and a combination of the two) and fibre dosage (0.5, 1.0, and 1.5%). The bulk fresh, one-day dry room temperature, and 28-day humidity room densities were obtained from 10 cylinders in each mixture. Workability was measured using both slump tests and Ve-Be time tests. Results show significant reductions in slump with increased fibre content, and glass fibre mixtures had less workability than steel fibre mixtures. The hybrid steel and glass fibre mixtures allowed for further study of each fibre's effect on workability. There was a good correlation between the slump and Ve-Be time results for mixtures with low fibre dosages, but Ve-Be time tests were found to be more appropriate to assess the workability of stiff concretes such as those with a high dosage of glass fibres. Both fresh and dry densities of CFRC cylinders increased due to adding steel fibres, and there was a minor reduction in these densities of glass fibre cylinders. Outcomes of this study will provide concrete mixture designers and structural engineers with additional guidance on mixture design and proportioning for CFRC to obtain desired fresh properties.

**Keywords** Fibre reinforced concrete · Workability · Steel fibre · Glass fibre

H. Alguhi · D. Tomlinson (✉)
University of Alberta, Edmonton, AB, Canada
e-mail: dtomlins@ualberta.ca

H. Alguhi
e-mail: alguhi@ualberta.ca

# 1  Introduction

Chopped fibre reinforced concrete (CFRC) acts as a structural reinforcement for concrete and is most often used in shotcrete tunnel walls, bridge decks, road pavements, and concrete slabs. Plain concrete has a low tensile strength compared to its compressive strength. The service life and post-cracking behaviour of concrete mixtures can be improved by adding chopped fibres. One of the main reasons for this growing use of chopped fibres is the possibility of replacing shear reinforcement with chopped fibres in structural applications [6, 12]. These chopped fibres can also improve ductility [1, 6], mitigate the size effect for shear [20], and can change failure modes from brittle shear failure to a more ductile flexural failure [1, 6, 11]. Even though there are various improvements in the mechanical properties of hardened concrete when using chopped fibres, the use of fibres reduces the flowability of fresh concrete [2, 3, 10, 13], which causes negative impact on concrete's workability. In particular, these effects may cause challenges with fresh concrete mixing, handling, pouring, compaction, and finishing.

Several researchers have studied the effect of chopped fibre on fresh concrete properties [2, 3, 10, 13]. However, there are limited studies that evaluate the performance of glass fibres and a combination of steel and glass fibres on fresh concrete properties. Glass fibre has a higher modulus of elasticity, tensile strength, weight and lower water absorption compared to synthetic and natural fibres [19]; these properties improve the mechanical behaviour of normal strength concrete (NSC). Glass fibres contribute more to the durability performance of high alkalinity concretes. Thus, this study evaluates the effect of dosage and materials of steel and glass fibres and a combination of these two chopped fibres on workability and densities for normal concrete strength (NSC).

# 2  Experimental Programme

For conventional concrete, workability is the main factor that determines the optimum upper limits of chopped fibre dosage. Fibre dosages that are too large are result in issues with the mechanical properties (such as workability) of fresh concrete mixtures. However, fibre dosages that lead to acceptable workability or consistency (excessive fluidity can cause concrete ingredient segregation) can enhance the mechanical properties of concrete mixtures. Sufficient density is required to sustain a particular loading and provide durable concrete. Larger density concretes are often stronger and more durable than lower density concretes since there are minimum voids and water absorption capacity.

**Fig. 1** Chopped fibres: **a** steel and **b** glass
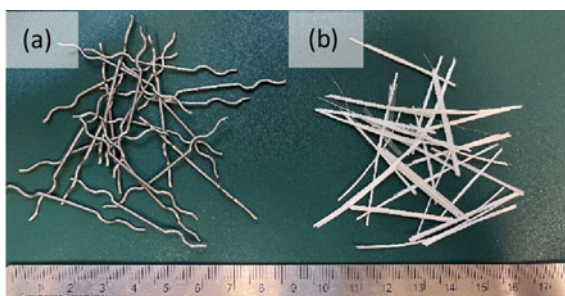
## 2.1 Materials

The main binder used is Type GU cement (70%), and the supplementary binder was fly ash (30%), which is a common ratio for concretes in Alberta. This ratio was selected to improve the concrete's long-term strength and durability [15], and the cement specifications are according to CSA A3000 and ASTM C150. Fly ash-type F was used to increase strength without reducing the workability of cementitious paste. Fly ash is one of the construction industry's most used pozzolans. Class F-fly ash is classified based on ASTM C618 and originates from anthracite and bituminous coals. A high range water reducer-HRWR Sika® ViscoCrete® 1000 was added into concrete mixtures to reduce water content and improve workability since adding more water to increase the workability (or slump) resulted in a weaker concrete.

Coarse and fine aggregates were selected to be typical aggregates used in normal strength-ready mix concrete in the Edmonton, Canada region. Pea gravel with a maximum size of 20 mm was used as the coarse aggregate in this study, and natural river sand with a maximum particle size of 4.75 mm was used as fine aggregate. The bulk specific gravity and water absorption of coarse and fine aggregates are (2.6 and 2.8) $g/cm^3$ and (1.32 and 1.43) %, respectively. Two different chopped fibres were used: hooked end steel fibres (SF) and AR-glass fibres (GF) as shown in Fig. 1; Table 1 gives the properties of the fibres obtained from their manufacturers. The hooked end steel fibres with high fibres lengths were used in this study, given that the slump of fresh SFRC mixture presents an increasing trend with steel fibre length increasing [14]. AR-glass fibres were used in this study for extra durability as well as their expected lower demand for water absorption and increased chemical resistance compared to other chopped fibres as steel and natural fibres.

## 2.2 Preparation

The ACI absolute volume method [4] was used to design trial concrete mixtures. This method is widely used in North America; it is generally accepted and convenient for normal concrete [4]. Ten mixtures were designed with a total volume of 0.08 $m^3$ per

**Table 1** Properties of steel and glass fibres

| Properties | SF | GF |
|---|---|---|
| Diameter (mm) | 0.92 | 0.54 |
| Length (mm) | 50 | 36 |
| Aspect ratio (length/diameter) | 54 | 67 |
| Tensile modulus of elasticity (GPa) | 200 | 72 |
| Tensile strength (MPa) | 1100–1500 | 1200–1800 |
| Specific gravity (g/cm$^3$) | 7.75 | 2.68 |

batch, one control mix and nine CFRC mixtures. These mixtures were developed after completing trial batches that are further described in Sect. 2.2.1. The CFRC mixtures were divided into those that used steel fibres (SF), those that used glass fibres (GF), and those that used a combination of steel and glass as a hybrid (H). Three different fibre contents (0.5, 1.0, and 1.5% volume fraction) were studied for both steel and glass fibres. For the hybrid mixtures, a constant fibre volume fraction of 1.0% was used with the three ratios of steel to glass fibres: 0.75% steel + 0.25% glass, 0.50% steel + 0.50% glass, and 0.25% steel + 0.75% glass, as given in Table 2. The optimum volumetric percentage of CFRC dosages should be in the range of between 0.5% and 1.5%. Dosages larger than 1.5% were not consider since there are physical difficulties in providing a homogenous CFRC leading to a decrease in compressive strength compared with plain concrete [7]. The addition of chopped fibres less than 0.5% will not affect concrete workability remarkably; however, this amount will not have a meaningful effect on the post-cracking behaviour of concrete [9] which is the main goal of this overall research programme.

A portable electrical drum mixer with a capacity of 155 L was used for CFRC mixing. The drum mixer was rinsed with water and completely drained before each batch was mixed. First, fine, and coarse aggregates were added and mixed for one minute. Then, the cementitious material (cement + fly ash) was added and mixed for 2 more minutes. After that, water was added gradually for 2–3 min. Then, the chopped fibres were added gradually for 3–4 min. Finally, the superplasticizer was added to the mixture. The total mixing time for each CFRC batch was about 8~10 min. The concrete was placed in the moulds in two layers and compacted by using a vibrating table with a frequency of 60 to 90 Hz. The specimens were demoulded 24 h after casting and placed in a laboratory room (temperature $25 \pm 2$ °C and relative humidity $35 \pm 5\%$) and then these samples were placed in a controlled humidity room (temperature $20 \pm 2$ °C and relative humidity $70 \pm 5\%$).

### 2.2.1 Trial Mixtures

Prior to batching the main mixtures, eleven trial mixtures were produced (Table 3) to optimize the mixture for CFRC. The target was compressive strengths between 35 and 55 MPa, which is within the range of compressive strength (25–55) MPa for NSC

**Table 2** Mixture components and material quantities

| TASK | Mix # | Mix ID | Fibre type and dosage | Batch vol. = 0.08 m³ | | Cement (kg) | Fly ash (kg) | Water* (kg) | CA (kg) | FA (kg) | Fibre (kg) | S.P (kg) |
|---|---|---|---|---|---|---|---|---|---|---|---|---|
| | | | | W/CM | Binder per m³ | | | | | | | |
| I | 1 | Control | No fibres | 0.35 | 400 | 22.40 | 9.60 | 13.30 | 91.72 | 61.15 | 0.00 | 0.16 |
| II | 2 | SF-0.5 | 0.5% SF | 0.35 | 400 | 22.40 | 9.60 | 13.29 | 91.08 | 60.72 | 3.00 | 0.16 |
| | 3 | SF-1.0 | 1.0% SF | | | 22.40 | 9.60 | 13.27 | 90.44 | 60.29 | 6.00 | 0.16 |
| | 4 | SF-1.5 | 1.5% SF | | | 22.40 | 9.60 | 13.26 | 89.79 | 59.86 | 9.00 | 0.16 |
| III | 5 | GF-0.5 | 0.5% GF | 0.35 | 400 | 22.40 | 9.60 | 13.29 | 91.08 | 60.72 | 1.03 | 0.16 |
| | 6 | GF-1.0 | 1.0% GF | | | 22.40 | 9.60 | 13.27 | 90.44 | 60.29 | 2.06 | 0.16 |
| | 7 | GF-1.5 | 1.5% GF | | | 22.40 | 9.60 | 13.26 | 89.79 | 59.86 | 3.10 | 0.16 |
| IV | 8 | H-1 | 1.0% (0.75%SF + 0.25%GF) | 0.35 | 400 | 22.40 | 9.60 | 13.27 | 91.08 | 60.29 | – | 0.16 |
| | 9 | H-2 | 1.0% (0.50%SF + 0.50%GF) | | | 22.40 | 9.60 | 13.27 | 90.44 | 60.29 | – | 0.16 |
| | 10 | H-3 | 1.0% (0.25%SF + 0.75%GF) | | | 22.40 | 9.60 | 13.27 | 89.79 | 60.29 | – | 0.16 |

SF steel fibre, GF glass fibre, H Hybrid, CM cementitious materials, CA coarse aggregate, FA fine aggregate, SP superplasticizer
*Including absorption

[21], and minimum slump of 150 mm for mixtures without fibres. Supplementary cementitious material (fly ash) was added to all trial mixes as 30% of the binder. Trial mixes T1 to T6 were prepared by hand to investigate concrete bleeding (a phenomenon in which free water in the mixture rises up to the surface) and mixture volume. The remaining mixtures (T7 to T11) were done using mini portable electrical drum mixer with a capacity of 50 L to simulate the large electrical drum mixer with a capacity of 155 L, which was used to mix large batches. The trial mixes T1 and T2 had the water to cementitious materials ratio w/cm of 0.45, and this results in both of them having concrete bleeding, as seen in Fig. 2a based on optical observations. The w/cm for T3 decreased to 0.35; this ratio leads to a decrease in the concrete bleeding and provides optimum volume (actual and measured cylinder volume are similar) as shown in Fig. 2b and obtained the estimated 28-day compressive strength of 44.9 MPa (see Table 3).

The cement and fly ash proportions for trial mixes T1, T2, and T3 were identical, but for T4, the cement quantity was larger compared to T1, T2, and T3. Trial mixes T5 and T6 were CFRC mixes with 1% of steel, and glass fibres, respectively. Trial mixes T9, T10, and T11 were CFRC mixes with 1.5% of fibre volume, and T9 and T10 were SFRC mixes, but for T10, the cement quantity was larger compared to T10.

To have reasonable workability of CFRC mixes, the slump of control mixes should not be less than 150 mm, to provide adequate workability after the addition of steel fibres (>50 mm) [8]; therefore, three trials of adding superplasticizer (0.4, 0.5, and 0.6%) by weight of the binder were performed, and from the trial mixes, it was observed that the best amount was 0.5% by weight of the binder to get the target slump test for the control mix.

From the trial mixes described in this section, one mix was selected to evaluate the mechanical properties of CFRC. The selected mixes included a maximum aggregate size of 20 mm and achieved the target strength and workability was T3.

## 2.3 Fresh Concrete and Densities Measurements

Workability was measured using slump tests according to ASTM C143/C143M-15 and Ve-Be time tests according to ASTM C1170/C1170M-14 of all mixtures (Fig. 3). Since adding chopped fibres to the concrete reduces workability [14, 18], a minimum slump of 150 mm for plain concrete was targeted to provide adequate workability after the addition of chopped fibres. Fresh, one-day dry at laboratory room and 28-day humidity room densities were obtained as per ASTM C138/C138M-17a.

**Table 3** Trial mixes for the NSC

| Hand mixing | | | | | | |
|---|---|---|---|---|---|---|
| Trial mixes | T1 | T2 | T3 | T4 | T5 | T6 |
| Target strength (MPa) | 35–55 | 35–55 | 35–55 | 35–55 | 35–55 | 35–55 |
| Max. agg. size (mm) | 20 | 20 | 20 | 20 | 20 | 20 |
| *Material proportions per 1 m³* | | | | | | |
| Cement-general use type (kg) | 280 | 280 | 280 | 315 | 280 | 280 |
| Fly ash-type F (kg) | 120 | 120 | 120 | 135 | 120 | 120 |
| w/cm ratio | 0.45 | 0.45 | 0.35 | 0.35 | 0.35 | 0.35 |
| Fine agg.—river sand (kg) | 651 | 721 | 764 | 729 | 754 | 754 |
| Coarse agg.—pea gravel (kg) | 977 | 1082 | 1147 | 1093 | 1130 | 1130 |
| Steel fibres (kg) | – | – | – | – | 75 | – |
| Glass fibres (kg) | – | – | – | – | – | 25.8 |
| 7-days water tank density (kg/m³) | * | * | 2440 | 2454 | 2477 | 2421 |
| 7-days water tank curing strength (MPa) | * | * | 29.4 | 32.5 | 26.2 | 25.6 |
| Estimated 28 days strength** (MPa) | * | * | 44.9 | 48.6 | 40.9 | 40.2 |

| Electric drum mixer | | | | | |
|---|---|---|---|---|---|
| Trial mixes | T7 | T8 | T9 | T10 | T11 |
| Target strength (MPa) | 35–55 | 35–55 | 35–55 | 35–55 | 35–55 |
| Max. agg. size (mm) | 20 | 20 | 20 | 20 | 20 |
| *Material proportions per 1 m³* | | | | | |
| Cement-general use type (kg) | 280 | 315 | 280 | 315 | 280 |
| Fly ash-type F (kg) | 120 | 135 | 120 | 135 | 120 |
| w/cm ratio | 0.35 | 0.35 | 0.35 | 0.35 | 0.35 |
| Fine agg.—river sand (kg) | 764 | 729 | 748 | 712 | 748 |
| Coarse agg.—pea gravel (kg) | 1147 | 1193 | 1122 | 1069 | 1122 |
| Steel fibres (kg) | – | – | 112.5 | 112.5 | – |
| Glass fibres (kg) | – | – | – | – | 38.7 |
| 7-days water tank density (kg/m³) | 2484 | 2656 | 2490 | 2608 | 2462 |
| 7-days water tank curing strength (MPa) | 38.6 | 40.8 | 33.7 | 37.6 | 29.1 |
| Estimated 28 days strength** (MPa) | 55.8 | 58.3 | 50.0 | 54.6 | 44.5 |

*Concrete bleeding occurs due to a high w/cm ratio

**Strength at 28 days estimated based on $f'_{c,28} = 3 \, (f'_{c,7})^{0.8}$ [17]

## 3 Results and Discussion

The results from these tests are summarized in Table 4.

As expected, and shown in Fig. 4a, there were meaningful reductions for all slump values with increased fibre content. The glass fibre mixtures had less workability than
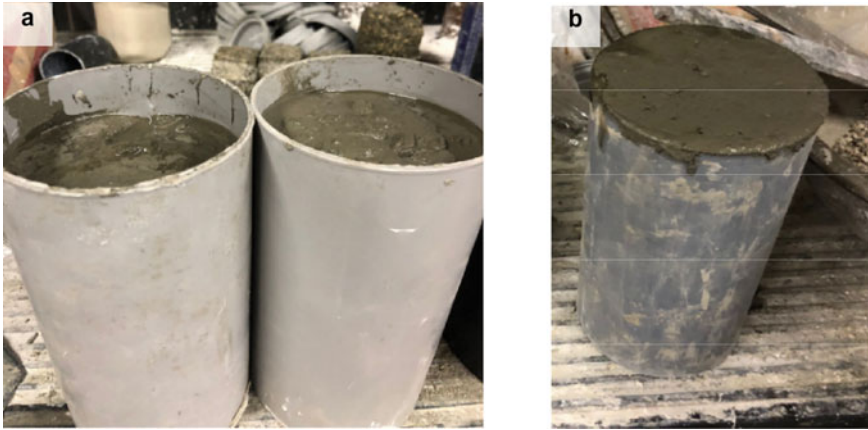
**Fig. 2** **a** Concrete bleeding and **b** optimum volume
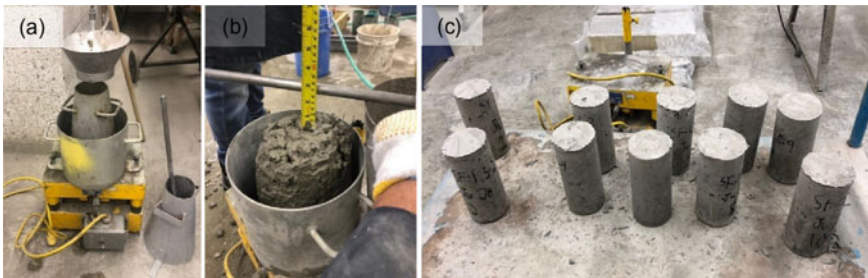


**Fig. 3** Fresh concrete and densities measurements: **a** Ve-Be time test, **b** Slump test, and **c** cylinders after one-day laboratory room temperature curing

**Table 4** Summary of test results

| Mix ID | Ve-Be time (seconds) | Slump (mm) | Density (kg/m³) | | |
|---|---|---|---|---|---|
| | | | Fresh | One-day dry at lab room | 28-day at humidity room |
| Control | 5.71 | 155 | 2523 ± 51 | 2500 ± 56 | 2456 ± 29 |
| SF-0.5 | 8.94 | 70 | 2651 ± 50 | 2623 ± 33 | 2586 ±30 |
| SF-1.0 | 12.92 | 65 | 2668 ± 35 | 2643 ± 33 | 2615 ± 27 |
| SF-1.5 | 16.70 | 45 | 2707 ± 41 | 2686 ± 36 | 2640 ± 33 |
| GF-0.5 | 9.36 | 65 | 2419 ± 18 | 2404 ± 11 | 2384 ± 19 |
| GF-1.0 | 14.82 | 50 | 2448 ± 13 | 2438 ± 11 | 2408 ± 09 |
| GF-1.5 | 17.69 | 35 | 2438 ± 20 | 2422 ± 18 | 2407 ± 15 |
| H-1 | 13.15 | 60 | 2481 ± 15 | 2454 ± 17 | 2446 ± 19 |
| H-2 | 13.95 | 55 | 2454 ± 16 | 2429 ± 14 | 2417 ± 07 |
| H-3 | 14.53 | 50 | 2441 ± 22 | 2417 ± 16 | 2406 ± 13 |

steel fibre mixtures. This is not only because glass fibres obstruct the mobility of the mixture's ingredients, but also these multifilament strands of glass fibre that are not intended to separate tend to do so and render the mixture unworkable because of their greatly increased surface area [16], which was also observed in the hybrid mixtures. For hybrid mixtures, the slump decreased as glass fibre content increased. The Ve-Be time results show a similar trend in terms of reducing the workability by adding chopped fibres, and the Ve-Be time increased as the fibre dosage increased. Glass fibre mixtures also had less workability compared to steel fibre mixtures; this is reflected in higher Ve-Be time results for glass fibre, and this is noticed in hybrid mixtures as the more the glass fibres, the higher the Ve-Be time results, as shown in Fig. 4b.

The effect of chopped fibres dosage and materials on workability measurements is shown in Fig. 5. The results show an inversely proportional relationship between slump results and increasing chopped fibre dosages, so there was a dramatic decrease in workability with increasing fibre content for both slump and Ve-Be time. The slump test is more effective in evaluating the influence of adding fibres, especially glass fibres. The Ve-Be time results also show an inversely proportional trend with increasing the chopped fibres dosages for glass and steel fibres, respectively.
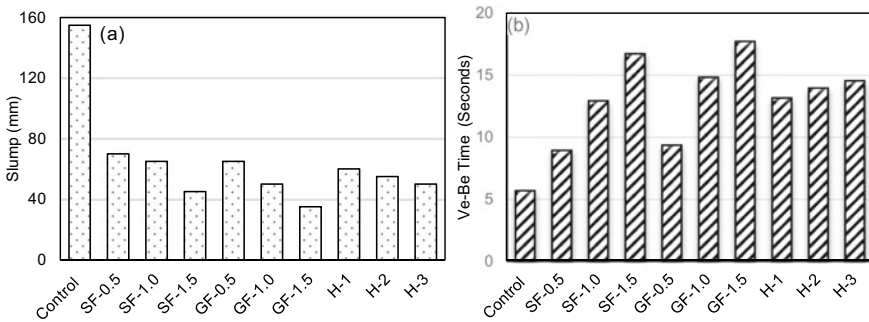


**Fig. 4** Workability results obtained in the **a** slump and **b** Ve-Be tests
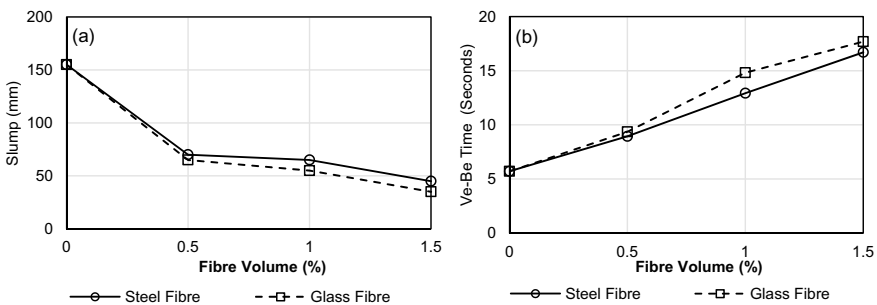


**Fig. 5** Effect of the chopped fibre material and dosages on **a** the slump and **b** Ve-Be time results of the CFRC

There was a good correlation between the slump and Ve-Be time results, as shown in Fig. 6. When slump is less than around 70 mm, the Ve-Be time increases more rapidly. There is almost no variation in the Ve-Be results when the slump value exceeds 70 mm regardless of fibre type and dosage. This demonstrates that the Ve-Be time test is more suitable for verifying the workability of stiff concretes. In other words, Ve-Be time results may be beneficial and confirm that the slump test has limited effect for evaluating CFRC because non-water-absorbent fibres reduce the stability or cohesion of the mixture under static conditions (the main factor evaluated in slump tests) of the mixture due to their needle-like shape and high specific surface area. The Ve-Be test can better evaluate how concrete behaves during compaction where this mechanized action allows fibres to rearrange, thus measuring workability from the perspective of concrete's mobility and compatibility for CFRC. However, the Ve-Be time test is less applicable for conditions in which the concrete is very plastic with slump results (125–190) mm [5].

Figure 7 shows the fresh, one-day dry, and 28-days at humidity room densities of CFRC cylinders. Adding steel fibres increases concrete densities due to steel's large specific gravity (7.75) $g/m^3$ of steel fibre, which is almost three times the replacement aggregate specific gravity (2.6–2.8) $g/m^3$ in the mixture. There was a minor reduction in the densities of glass fibre reinforced cylinders due to a slight decrease in the specific gravity of glass fibre (2.62) $g/m^3$ compared to the replacement aggregate specific gravity. This was also observed in the hybrid mixes where the increased ratio of glass fibres, the less the resulting densities. Table 4 shows the results summary of all cylinders.
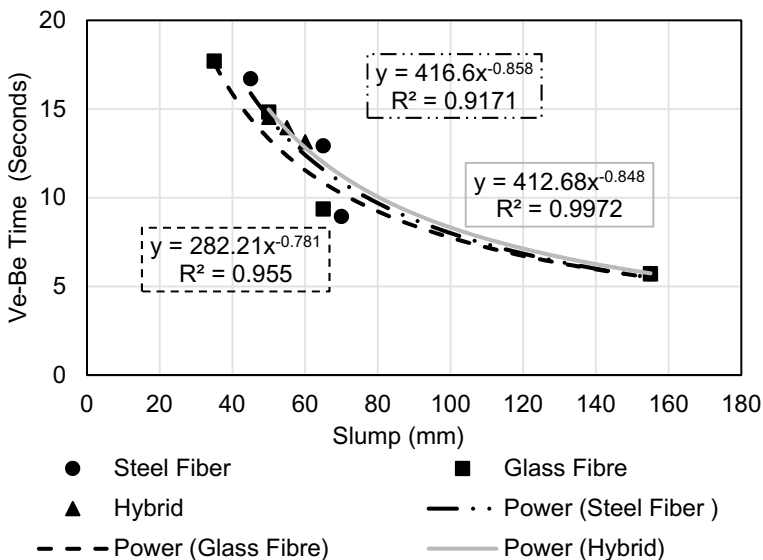


**Fig. 6** Correlation between all the slump values and the Ve-Be time
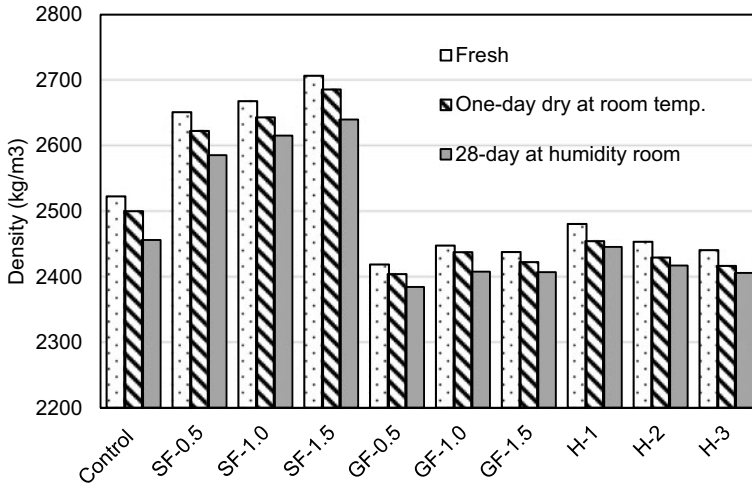
**Fig. 7** Fresh, one-day dry at laboratory room temp., and 28-day at humidity room densities of CFRC cylinders

## 4 Conclusions and Recommendations

Ten mixtures were prepared to investigate the effect of two fibre types (steel and glass) and a combination of them with volume fractions of 0.5, 1.0, and 1.5% on the fresh concrete's properties such as workability and densities. Workability was evaluated using both slump and Ve-Be time test. Three densities (fresh, one-day laboratory room and 28-day humidity room) of ten samples from each mix were measured. Based on the results reported in this paper, the following conclusions can be drawn:

1. Adding chopped fibres decrees workability remarkably, and there were considerable reductions for all slump values with increased fibre content, and glass fibre mixtures had less workability than steel fibre mixtures. This was further shown in the hybrid mixtures, where workability decreased as the dosage of glass fibres increased.
2. A good correlation between the obtained results between the slump and Ve-Be time can be seen based on this study's data.
3. The Ve-Be time test is more appropriate to evaluate the workability of stiff concretes such as CFRC because it gives an indication about the compatibility and the mobility aspect of freshly mixed concrete while slump tests evaluate mix response in static conditions.
4. The density of CFRC depends on specific gravity and dosage of chopped fibres so adding steel fibres increases concrete density. For this study, this increase ranged between 5.3 and 7.5% (after 28 days) which is enough of an increase that designers should consider the influence of steel fibres on self-weight of concrete elements. That said, there was a minor reduction in the densities of glass fibre

cylinders (< 3.0%) which indicates that their effect on member self-weight can be conservatively ignored. This was also shown in the hybrid mixtures, where density decreased as glass fibre dosage increased.

This study used gravel with a maximum size of 20 mm, so the maximum aggregate size and shape effects, which are essential factors that will play the key role in fresh concrete's properties and densities of CFRC should be investigated in future. Studying the influence of the geometric properties of chopped fibres such as aspect ratio and fibre profile (e.g. straight, hooked) as well as other fibre types (e.g. basalt, polypropylene) on concrete's fresh properties should be investigated further.

# References

1. Abbas AA, Syed Mohsin SM, Cotsovos DM, Ruiz-Teran AM (2014) Shear behaviour of steel-fibre-reinforced concrete simply supported beams. Proc Inst Civil Eng Struct Build 167(9):544–558
2. Abdelrazik AT, Khayat KH (2020) Effect of fiber characteristics on fresh properties of fiber-reinforced concrete with adapted rheology. Constr Build Mater 230:116852
3. Abousnina R, Premasiri S, Anise V, Lokuge W, Vimonsatit V, Ferdous W, Alajarmeh O (2021) Mechanical properties of macro polypropylene fibre-reinforced concrete. Polymers 13(23):4112
4. ACI 211.1-91 (1991) Standard practice for selecting proportions for normal, heavyweight, and mass concrete (ACI 211.1-91). American Concrete Institute
5. ACI 211.3R-02 (2002) Guide for selecting proportions for no-slump concrete reported by ACI Committee 211. American Concrete Institute, pp 1–26
6. Alguhi H, Tomlinson D (2019) Evaluation of proposed steel fibre reinforced concrete beams under ultimate and serviceability limit state. CSCE Annual Conference. Laval, Canada
7. Altun F, Haktanir T, Ari K (2007) Effects of steel fiber addition on mechanical properties of concrete and RC beams. Constr Build Mater 21(3):654–661
8. Bindiganavile V, Lubell AS, Shoaib A (2012) SER# 294: shear in steel fiber reinforced concrete without stirrups. University of Alberta. Edmonton, Canada
9. Branston J, Das S, Kenno SY, Taylor C (2016) Mechanical behaviour of basalt fibre reinforced concrete. Constr Build Mater 124:878–886
10. Carroll JC, Helminger N (2016) Fresh and hardened properties of fiber-reinforced rubber concrete. J Mater Civ Eng 28(7):04016027
11. Cucchiara C, La Mendola L, Papia M (2004) Effectiveness of stirrups and steel fibres as shear reinforcement. Cement Concr Compos 26(7):777–786
12. Ding Y, You Z, Jalali S (2011) The composite effect of steel fibres and stirrups on the shear behaviour of beams using self-consolidating concrete. Eng Struct 33(1):107–117
13. Gültekin A, Beycioğlu A, Arslan ME, Serdar AH, Dobiszewska M, Ramyar K (2022) Fresh properties and fracture energy of basalt and glass fiber-reinforced self-compacting concrete. J Mater Civ Eng 34(1):04021406
14. Han J, Zhao M, Chen J, Lan X (2019) Effects of steel fiber length and coarse aggregate maximum size on mechanical properties of steel fiber reinforced concrete. Constr Build Mater 209:577–591

15. Johnston CD (1996) Fly ash utilization bridge works. The University of Calgay.
16. Johnston CD (2014) Fiber-reinforced cements and concretes. CRC Press
17. Kabir A, Hasan M, Miah MK (2012) Predicting 28 days compressive strength of concrete from 7 days test result. In: Proceedings of the international conference on advances in design and construction of structures, Citeseer, pp 18–22
18. Liao L, Zhao J, Zhang F, Li S, Wang Z (2020) Experimental study on compressive properties of SFRC under high strain rate with different fiber content and aspect ratio. Constr Build Mater 261:119906
19. Madhkhan M, Katirai R (2019) Effect of pozzolanic materials on mechanical properties and aging of glass fiber reinforced concrete. Constr Build Mater 225:146–158
20. Minelli F, Conforti A, Cuenca E, Plizzari G (2014) Are steel fibres able to mitigate or eliminate size effect in shear? Mater Struct 47(3):459–473
21. Voort TV, Suleiman M, Sritharan S (2009) Characterization of precast UHPC pile drivability. Contemporary Topics in Deep Foundations, pp 303–310

# Fiber Effects on Phase Change Materials Concrete Properties

**Mahmoud Rady and Ahmed Soliman**

**Abstract** In the era of environmental concerns, the increase in the buildings' operating energy has necessitated the finding of efficient technology to reduce their energy losses. Incorporating phase change materials (PCMs) into building materials (i.e., concrete) had been adopted as a promising solution. However, adding PCM to concrete showed detrimental effects on its properties, mainly reduction in the mechanical properties. Hence, this study investigates the potential of overcoming this issue by adding fibers. Several types of fibers were added at rates 0.0, 0.5, and 1.0% by volume of the mixture and tested. Results showed that adding fiber to PCM-concrete had improved the mechanical properties, regardless of the fiber types and additional rates. The higher the fiber content, the higher the improvement in PCM-concrete properties. Also, the stiffness and geometry of the fiber had significant effects. Bridging voids induced by PCMs breakage and increasing tensile strength of the matrix enhanced the achieved strength. The findings of this study pave the way for higher PCMs incorporation leading to better thermal performance.

**Keywords** Phase change Materials · Cement · Flowability · Taguchi · Compressive strength

## 1 Introduction

Energy consumption in the building industry accounts for more than a third of energy consumption in the world. The use of sustainable approaches in today's building has become a goal of construction engineering. So, reducing energy consumption in buildings has become a target to achieve nowadays. Many ways have been suggested to reduce the building operating energy, and one of the most promising is the implementation of phase change materials into building materials [1]. PCMS can store and

M. Rady · A. Soliman (✉)

Department of Building, Civil and Environmental Engineering, Concordia University, Montreal, QC, Canada

e-mail: ahmed.soliman@concordia.ca

release energy at certain ranges of temperatures. Thus, adding PCM as an addition to concrete can help reduce the energy losses of concrete buildings. Because of their ability to absorb and release energy into the environment, phase change materials have the ability to lessen temperature variation. The PCM's functioning concept is to vary their status based on the temperature of the surrounding environment [2]. While the temperature rises, the PCMs absorb and store energy, changing from a solid to a liquid form. When the temperature drops, the material, on the other hand, has the potential to release previously stored energy, resulting in a transition from a liquid to a solid state [3].

The improvement of thermal properties of concrete containing PCM has been widely validated; however, there is a similar adverse effect on other properties such as fresh and mechanical properties. The compressive strength of concrete is one of its most important mechanical properties and is affected by the components of concrete. The incorporation of PCM into concrete and the increase in the amount of PCM presented a significant decrease in compressive strength [4].

Concrete has a very low tensile strength. Hence, cracks that propagate under loads will lead to a brittle fracture of concrete. The new technology of using fibers made the invention of fiber-reinforced concrete to overcome these problems associated with cement-based materials such as low tensile strength, poor fracture toughness, and brittleness of cementitious composites. This resulted in extensive use for various types of fibers like glass, steel, carbon, and polypropylene, etc. [5]. Hence, adding fiber to compensate for the reduction induced by PCMs addition can be a valid option. Fibers have grown into an efficient and well-recognized reinforcement approach for improving certain qualities, particularly brittle mediums [6]. The post-elastic characteristics of the matrices in which fibers are embedded are improved. The main rationale for incorporating fibers into a cement matrix is to improve the resultant composite's toughness and tensile strength and cracking deformation properties [7]. So, adding fiber to mixes with PCMs can help to improve their mechanical properties [8].

## 2 Experimental Program

### 2.1 Materials

In the grout mixtures, ordinary Portland cement (OPC) was employed. As a partial replacement for OPC, fly ash (FA) was used. Table 1 lists the physical and chemical parameters of the binders utilized (i.e., OPC and FA). Silica sand with a fineness modulus of 1.47 and a saturated surface dry specific gravity of 2.65 was used as a fine aggregate (Fig. 1), and polyvinyl alcohol (PVA) short fibers were utilized in reinforcing the mixtures. Table 2 illustrates the mechanical characteristics of the PVA fibers. Moreover, the Microencapsulated Phase Change Materials (MPCM) were provided by Microtek Laboratories Company (Fig. 2). The details related to

**Table 1** Properties of binders

|  | OPC | FA |
|---|---|---|
| $SiO_2(\%)$ | 19.60 | 43.39 |
| $Al_2O_3(\%)$ | 4.80 | 22.08 |
| CaO (%) | 61.50 | 15.63 |
| $Fe_2O_3(\%)$ | 3.30 | 7.74 |
| $SO_3(\%)$ | 3.50 | 1.72 |
| $Na_2O$ (%) | 0.70 | 1.01 |
| Loss on ignition (%) | 1.90 | 1.17 |
| Specific gravity | 3.15 | 2.50 |
| Surface area ($m^2$/kg) | 3.71 | 280 |

this material can be seen in Table 3. To use the PCM for the specific target of this study, the PCM with a melting point of 43 °C was chosen. In addition, based on previous studies on PCM application in the OPC mortar, it was added at rates of 5% and 10%.
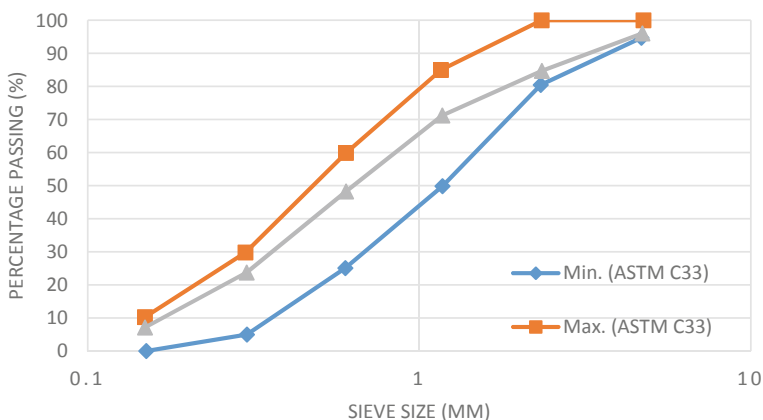


**Fig. 1** Sieve analysis of fine aggregate

**Table 2** Properties of PVA fibers

| Mechanical properties ultimate | Tensile strength (MPa) | Diameter (mm) | Length (mm) | Young's modulus (GPa) | Elongation (%) | Density (kg/m$^3$) |
|---|---|---|---|---|---|---|
| PVA | 1620 | 0.039 | 8 | 43 | 6 | 1300 |
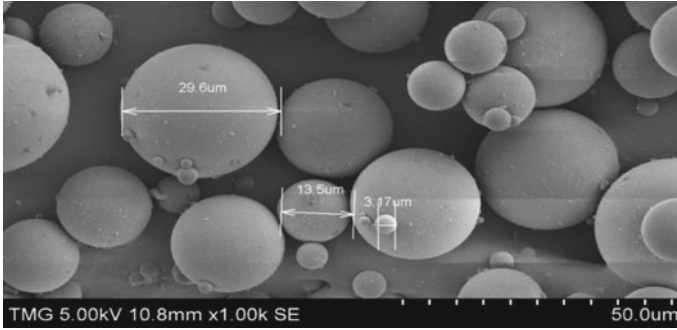
**Fig. 2** Particles size range for used MPCMs

**Table 3** Properties of PCM

| MPCM 43 | |
|---|---|
| Melting point (°C) | 43 |
| Latent heat capacity (J/g) | 175 |
| Moisture (%) | < 3% |
| Appearance | White to slightly off-white powder |

## 2.2 Mixture Proportions

To study the effect of adding PVA fibers and fly ash on the fresh and mechanical properties of cement mortar containing PCMs, with the use of the Taguchi method to study the effect of different three factors with three-level nine grout mixtures with three different percentages of PCMS (0, 5, and 10%) were prepared using different dosages of FA (0, 0.5, and 1%) and different dosages of PVA fibers (0, 0.5, and 1.0%) as given in Table 4. The sand-to-binder ratio ($s/b = 2.75$) and water-to-binder ratios ($w/b = 0.45$) were the same in all grout compositions. The quantity of the combination components utilized in this study is given in Table 5.

## 2.3 Experimental Procedures

Flowability was evaluated for all tested mixes using the flow table provided in Fig. 3 after combining all constituents. ASTM C230 is a standard that specifies how to make a product (Standard Specification for Flow Table for Use in Tests of Hydraulic Cement). On a drop table, a fresh mortar sample was deposited in the flow mold and stroked 25 times. The diameter of the crumbled mortar was then measured with a caliper at four different sites. The average of the four separate readings was used to get the flow reading. As shown in Fig. 4, the compressive strength of various combinations was determined using a 300 kN universal testing machine (UTM) in

**Table 4** Factors and levels in mix design

| Mix | PCM% | F% | FA% |
|---|---|---|---|
| 1 | 0 | 0 | 0 |
| 2 | 0 | 0.5 | 5 |
| 3 | 0 | 1 | 10 |
| 4 | 5 | 0 | 5 |
| 5 | 5 | 0.5 | 10 |
| 6 | 5 | 1 | 0 |
| 7 | 10 | 0 | 10 |
| 8 | 10 | 0.5 | 0 |
| 9 | 10 | 1 | 5 |

**Table 5** Mixes components ($kg/m^3$)

| Mixture no | Binder (kg/m$^3$) | | Sand (kg/m$^3$) | Water (kg/m$^3$) | PVA (kg/m$^3$) | PCM (kg/m$^3$) |
|---|---|---|---|---|---|---|
| | OPC | FA | | | | |
| 1 | 558 | 0 | 1533 | 251 | 0 | 0 |
| 2 | 528 | 28 | 1522 | 251 | 4 | 0 |
| 3 | 499 | 55 | 1511 | 251 | 7 | 0 |
| 4 | 528 | 28 | 1453 | 251 | 0 | 17 |
| 5 | 499 | 55 | 1442 | 251 | 4 | 17 |
| 6 | 558 | 0 | 1441 | 251 | 7 | 17 |
| 7 | 499 | 55 | 1374 | 251 | 0 | 34 |
| 8 | 558 | 0 | 1372 | 251 | 4 | 34 |
| 9 | 528 | 28 | 1361 | 251 | 7 | 34 |

accordance with ASTM C109 (Standard test technique for compressive strength of hydraulic cement mortars). For each mixture, cubic specimens of 50 mm × 50 mm × 50 mm were made and evaluated after 7 days.

## 3 Results and Discussion

### 3.1 Workability

Table 6 shows the flow table reading for all the tested mixtures. In addition, Fig. 5 shows the flowability and final diameter for the tested mixtures. Adding phase change materials had increased the flowability. This can be attributed to the circular shape for PCMs particles as illustrated in Fig. 2. As expected, adding PVA fibers decreases

**Fig. 3** Flow table test



**Fig. 4** Compressive machine



the flowability. The higher the fiber content, the lower the achieved flowability. This can be attributed to the interlocking and increase of the contact points. However, the addition of fly ash had improved the workability for both mixtures with and without fiber. This can be ascribed to the lubrication effect induced by the addition of fiber. Hence, it could be concluded that adding FA will help in compensating the effect of adding PVA on mixtures incorporating PCMs. The workability of the mixes having

**Table 6** Results for flow table test readings for the nine mixes

| Mix | D1 | D2 | D3 | D4 | Average |
|---|---|---|---|---|---|
| 1 | 15.5 | 16 | 16 | 15.5 | 15.75 |
| 2 | 16 | 16.5 | 16.5 | 15.5 | 16.125 |
| 3 | 13 | 12.5 | 13.5 | 12.5 | 12.875 |
| 4 | 18 | 19 | 18 | 19 | 18.5 |
| 5 | 17 | 16.5 | 17.5 | 17.5 | 17.125 |
| 6 | 12 | 11.5 | 11 | 11 | 11.375 |
| 7 | 20 | 20 | 20 | 20 | 20 |
| 8 | 14 | 14 | 15 | 15 | 14.5 |
| 9 | 14.5 | 14 | 14.5 | 14 | 14.25 |
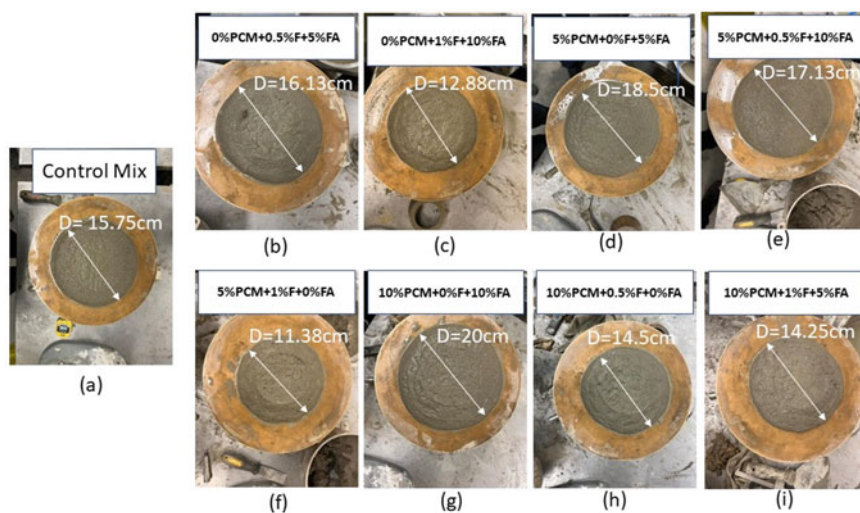


**Fig. 5** Flow table for the mixes

different % PVA fiber decreased due to increasing PCM content. This can be ascribed to the water absorption property of PCMs that led to harsh mix.

## 3.2 Compressive Strength Results

Figure 6 shows the compressive strength results for tested mixtures at age 7 days. As shown, adding fiber had increased the compressive strength slightly. This can be attributed to fiber's ability to bridge diagonal cracks and restrain their propagation.
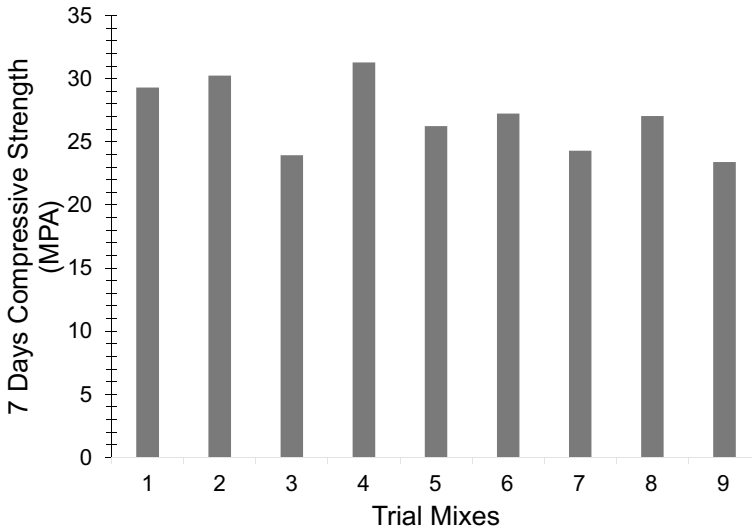
**Fig. 6** 7 days compressive strength for the mixes

Also, adding FA was found to reduce the strength. The higher the FA the lower the strength. This is ascribed to the fly ash's low reactivity at the early hydration period.

As expected, adding PCMs had reduced the strength. The reduction is mainly due to the breakage of PCMs particles leading to voids and releasing paraffin which will react with cement and delay hydration. Adding fiber did not improve the strength, which may be attributed to the poor compaction of the mixture.

## 3.3 Taguchi Mechanism

The Taguchi method uses a signal-to-noise (*S/N*) ratio to reduce unnecessary trials and helps to optimize the input parameters. The L9 orthogonal array requires only nine test runs, and the Taguchi method uses a signal-to-noise (*S/N*) ratio to reduce unnecessary trials and help to optimize the input parameters. The *S/N* ratio is useful for data analysis and predicting the best results. In practice, the orthogonal array generates a collection of well-balanced tests, with the *S/N* ratio serving as an optimization objective. The signal-to-noise ratio (SNR) is a measure of resilience. The analysis for the results is shown in Figs. 7 and 8, which agreed with the explanation for the flow table and compressive strength results.
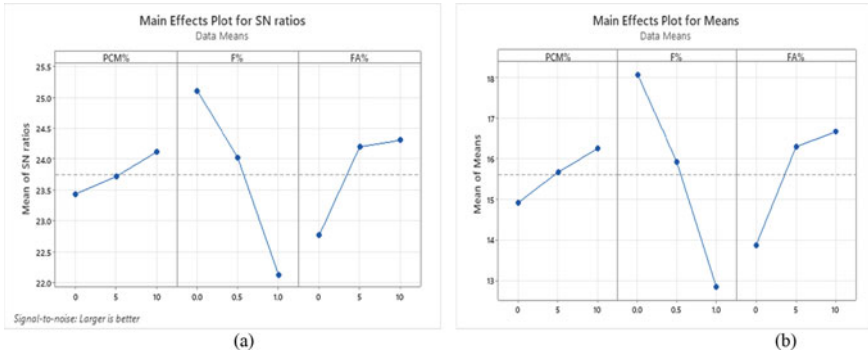
Fig. 7 Effect plots for **a** signal-to-noise ratio (larger is better) and **b** mean values for the flowability
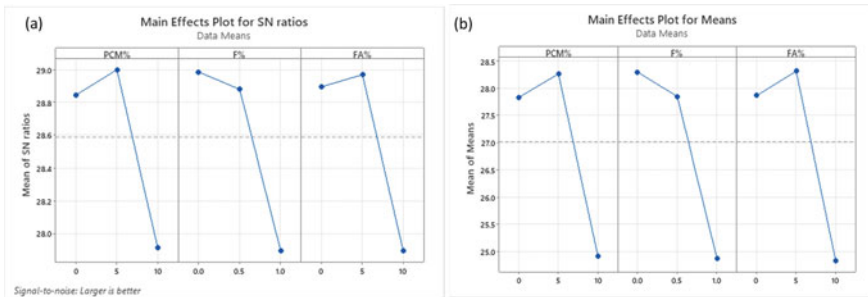


Fig. 8 **a** Main effects plot for *S/N* ratio (larger is better) and **b** main effect plot for mean for the compressive strength results

## 4 Conclusion

Adding fibers to mixtures incorporating PCMs will reduce workability. However, adding FA had overcome this negative impact on workability. Increasing the %PCMs content will decrease the workability in the mixes having different % PVA fiber, and it will increase the workability in the mixes having different % FA. On the other hand, higher compaction is needed for the fiber-reinforced mixture to densify the microstructure. However, this could lead to the breakage of PCMs. Hence, adding fiber did not enhance the strength of the mixture incorporating PCMs. Low compaction to protect PCMs led to higher voids and lower strength. High compaction led to more breakage for PCMs and more paraffin released, delaying cement hydration.

# References

1. Cunha S, Aguiar J, Pacheco-Torgal F (2015) Effect of temperature on mortars with incorporation of phase change materials. Constr Build Mater 98:89–101
2. Zhang Y, Zhou G, Lin K, Zhang Q, Di H (2007) Application of latent heat thermal energy storage in buildings: state-of-the-art and outlook. Build Environ 42(6):2197–2209
3. Zalba B, Marın JM, Cabeza LF, Mehling H (2003) Review on thermal energy storage with phase change: materials, heat transfer analysis and applications. Appl Therm Eng 23(3):251–283
4. Hunger M, Entrop AG, Mandilaras I, Brouwers HJH, Founti M (2009) The behavior of self-compacting concrete containing micro-encapsulated phase change materials. Cement Concr Compos 31(10):731–743
5. Brown R, Shukla A, Natarajan KR (2002) Fiber reinforcement of concrete structures. Report No. URITC FY99–02. University of Rhode Island, US
6. Shah AA, Ribakov Y (2011) Recent trends in steel fibered high-strength concrete. Mater Des 32(8–9):4122–4151
7. Johnston CD (2001) Fibre reinforced cements and concretes. J Adv Concr Technol 3:111–134
8. Panzera TH, Christoforo AL, Borges PR (2013) High performance fibre-reinforced concrete (FRC) for civil engineering applications. In: Advanced fibre-reinforced polymer (FRP) composites for structural applications. Woodhead Publishing, pp 552–581

# Analysis of a Corrosion Failure of Prestressed Concrete Cylinder Pipe: A Pilot Study

**Sara Hassi, Aadil Ejbouh, Bruce Menu, Mouhssine Galai, Adil Ech-chebab, Mohamed Ebn Touhami, and Hanane Benqlilou**

**Abstract**   This paper presents the findings of a pilot study designed to better understand the underlying causes of the high failure rates of the Prestressed Concrete Cylinder Pipe (PCCP) used in the semi-arid regions of Morocco. The study used mini-pipes (made of mortar coating and reinforcing steel) immersed in basins to simulate their performance in a near real-life service environment. Four basins were evaluated: Basin 1 (control basin) contained the control soil, whereas the other three basins contained chemically enriched soils (Basin 2 with sulfate solution; Basin 3 with chloride solution; and Basin 4 with combined chloride-sulfate solution). Each basin had four mini-pipes made from OPC mortars and a PCC mortar with 17% fly ash. In this paper, electrochemical impedance spectroscopy (EIS) technique was used to assess the corrosion process of the reinforcing steels specimen while a scanning electron microscopy with energy-dispersive X-ray spectroscopy (SEM/EDX) was used to study the steel-mortar interface. The preliminary results revealed, as expected, that the mini-pipes in Basin 4 had the highest corrosion rates. It was also found that the PCC mortar with 17% fly ash produced the best corrosion performance results in all four basins, implying that if used, can significantly improve the service life of pipes in semi-arid regions.

**Keywords**   PCCP · Mortar coating · Chloride · Sulfate · Fly ash · Electrochemical impedance spectroscopy · Corrosion

S. Hassi (✉) · A. Ejbouh · M. Galai · A. Ech-chebab · M. E. Touhami
Laboratoire des Matériaux Avancés et Génie des Procédés, Ibn Tofail University, Kenitra, Morocco
e-mail: hassi.saraa@gmail.com

B. Menu
Construction Daniel Dargis Inc., 5600 Hochelaga Est, #140, Montreal, QC H1N 3L7, Canada

H. Benqlilou
Institut International de l'Eau et de l'Assainissement (IEA), Office National de l'Electricité et de l'Eau Potable (ONEE), Rabat, Morocco

# 1   Introduction

Prestressed Concrete Cylinder Pipe (PCCP) is composed of core concrete, a steel cylinder, high-strength prestressing wires, and a mortar coating. The steel cylinder serves as a water barrier to seal water from leaking [3, 10, 11], while the high-strength prestressing wire which is wrapped to a certain prestress keeps the concrete core in compression [10]. The mortar coating on the other hand serves to protect the wire against corrosion by providing an alkaline environment [2].

PCCP has been extensively used in water and wastewater transmission lines worldwide by utilities for a long time because of its low cost, relatively good performance, and lower break rate compared with any other pipe materials [2, 9, 10, 11, 21]. In practice, however, it has been discovered that PCCP failure can occur suddenly with little warning that the pipe sections are at risk of failure [2, 10]. PCCP failures can be very catastrophic and cause severe damage due to the high pressure of water being released at failures [2, 9, 19]. Indeed, PCCP owners and users know that they have a potential problem since PCCP failures are caused by many factors, so the performance of PCCPs has been an item of interest to water utilities for a long time [20].

Some PCCP owners have devised strategies for obtaining condition data for their PCCP lines to make informed repair decisions. In the absence of such strategies, the Moroccan Water Authority (ONEE—Office National de l'Electricité et de l'Eau) decided in 2016 to conduct a large-scale survey to assess the condition of the PCCP lines used for water transmission in the country between 2007 and 2015. The general findings of the survey which have been reported in previous studies [12, 13, 14] indicated that there has been a major incidence of failures over the past few years and the rate of failures in each region is depended on the specific location the pipes were buried. The failures were particularly severe in the semi-arid region of the country.

Following the results of the study, a comprehensive research project on the performance of PCCP lines in Morocco was launched at the Laboratoire des Matériaux avancés et Génie des procédés, at Ibn Tofail University to investigate the main causes behind the severe deterioration of the PCCPs used in water transmission pipelines in *Northeastern Morocco, Tafilalet*, and *Greater Agadir* regions of Morocco. The results of these studies have been reported in previous studies [4, 12–16].

The purpose of this study is to develop a pilot project that simulates the influence of the key parameters influencing corrosion of PCCP lines as established in prior research under controlled conditions. These parameters included soil corrosivity, mortar coating quality, and cyclical variations in soil temperature and humidity. The ultimate goal is to determine the best conditions and mortar coating mixture for extending the service life of PCCP lines in the semi-arid region of the country. These studies are expected to contribute toward establishing proper guidelines for the design, manufacturing, bedding, and maintenance of PCCP pipelines in Morocco.

## 2   Experimental Program

This paper presents the results of a pilot study designed to better understand the underlying causes of the high failure rates of the Prestressed Concrete Cylinder Pipe (PCCP) used in the semi-arid regions of Morocco. The test program was carried out entirely at Laboratoire des Matériaux avancés et Génie des Procédés, Ibn Tofail University, Kenitra, Morocco. In the following sections, the detailed experimental program and the methods used are briefly described.

### 2.1   Materials and Mixture Proportion

A scale model PCCP was used in the present study (hereinafter referred to as mini-pipe). The mini-pipes were made with two types of cement: a CEM I cement, an ordinary Portland cement (OPC), and a CEM II cement, a Portland composite cement (PCC) optimized with fly ash (FA). The fly ash (FA) replacement level in the PCC cement is about 17% of the total cementitious materials by mass. The composition of the types of cement is given in Table 1. Overall, two standard mortar coating mixtures (OPC-38 and OPC-60) were designed using the CEM I cement, while one mortar coating mixture (PCC-60) was designed using the PCC cement. The same fine and coarse aggregate were used in all mixtures. The OPC-38 had a water-to-cementitious material (w/cm) ratio of 0.38, while the OPC-60 and PCC-60 mixtures had a w/cm ratio of 0.60. The mixture proportions of the mortars used in this study are presented in Table 2. It is worth noting that the OPC-38 mortar was used as the control mortar mixture in this study because it is currently used for spraying the PCCP mortar coating in Morocco.

The mini-pipes were made with the same reinforcing steel wire, with the following chemical composition by weight according on NF EN 10016-4: C 0.040%; Si 0.200%; Mn 0.420%; P 0.020%; S 0.025%; Cr 0.100%; Ni 0.100%; Mo 0.050%; Cu 0.150%; Al 0.010%; N 0.007%.

**Table 1** Chemical composition of cement (%)

| Chemical analysis % | CEM I | CEM II |
|---|---|---|
| Calcium oxide (CaO) | 58.42 | 52.81 |
| Silica ($SiO_2$) | 15.18 | 25.73 |
| Alumina ($Al_2O_3$) | 3.68 | 8.63 |
| Iron oxide ($Fe_2O_3$) | 2.36 | 3.72 |
| Magnesium oxide (MgO) | 2.55 | 2.18 |
| Sodium oxide ($Na_2O$) | 0.09 | 0.12 |
| Potassium oxide ($K_2O$) | 0.56 | 1.02 |
| Sulfur trioxide ($SO_2$) | 2.59 | 2.72 |
| Loss on ignition | 14.58 | 2.21 |

**Table 2** Proportioning of mortar coating mixtures

| Materials | OPC-38 | OPC-60 | PCC-60 |
|---|---|---|---|
| Cement, kg/m$^3$ | 450[a] | 300[a] | 300[b] |
| Water, l/m$^3$ | 172 | 179 | 179 |
| w/cm ratio | 0.38 | 0.60 | 0.60 |
| Sand dune, kg/m$^3$ | 536 | 536 | 536 |
| Aggregate, kg/m$^3$ | 1284 | 1284 | 1284 |
| G/S ratio | 2.39 | 2.39 | 2.39 |

[a]CEM I cement
[b]CEM II cement

## 2.2 Specimen Preparation

The mini-pipes used in the present study were made of a mortar coating and reinforcing rebar of 5 mm in diameter as shown in Fig. 1. The specimens were cast in a 100 × 400 mm PVC mold with an inside diameter of 40 mm (see Fig. 1a). For the OPC-38 and PCC-60 mortars, three specimens were cast and conventionally cured for 24 h at temperature of about 20 ± 2 °C and a relative humidity of 95 ± 5%, whereas six specimens were cast for the OPC-60 mortar (three conventionally cured and the other three heat-treated to accelerate the hardening of the mortar coating). These specimens will be called herein OPC-38-C, OPC-60-C, OPC-60-HT, and PCC-60-C. The last letter identifies the type of curing: conventionally cured (C) or heat treated (HT).

It should be noted that the accelerated hardening process of the OPC-60-HT specimens began about 2.5 h after mixing and lasted 34 h in total. It consists of 24 h of pretreatment (pre-setting at 20 ± 2 °C and relative humidity 95 ± 5%) a temperature-rise phase for about 3 h before isothermal bearing at 80 °C for 4 h, and finally a natural cooling phase for 3 h.

Twenty-four cubes (150 × 150 × 150 mm) were also cast for compressive strength testing. The compressive strength was tested 7 and 28 days after mixing with one day of curing in a standard room and 27 days of drying under conditions of 23 ±
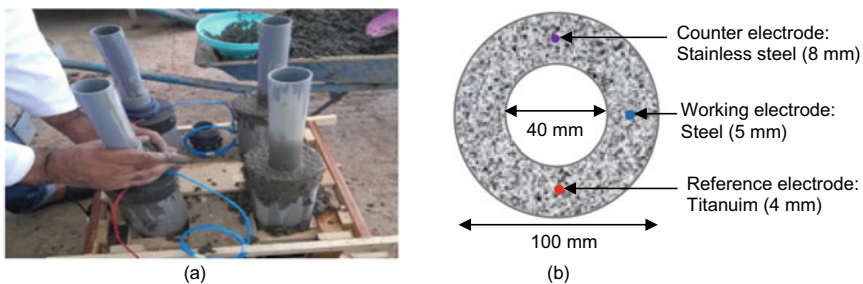


**Fig. 1** Mini-pipe: **a** Casting of the mini-pipes and **b** cross section of the mini-pipe

2 °C and relative humidity of $50 \pm 4\%$. Three samples were tested for each mortar, and the average value was reported.

The mixing was carried out in a 160-l mixer. The water used for the production was ordinary tap water from the Kenitra (Morocco) aqueduct system because its chemical composition is known and well regulated. The average temperature of the ingredient was about 22 °C.

## 2.3 Setup of the Pilot Project

The overall pilot setup was designed to simulate the effect of soil corrosivity, mortar coating quality, and cyclical variations in soil temperature and humidity on PCCP lines. A schematic representation of the pilot setup used is shown in Fig. 2a, while the final assembled setup is shown in Fig. 2b. The setup consisted of four basins: *Basin 1* (i.e., control basin) contained normal soil; *Basin 2* contained soil chemically enriched with sulfate solution; *Basin 3* contained soil chemically enriched with chloride solution; and *Basin 4* contained soil chemically enriched with a combined chloride-sulfate solution. Each basin had four mini-pipes: one made with the OPC-38 mortar (OPC-38-C), two made with the OPC-60 mortar (OPC-60-C and OPC-60-HT), and one made with the PCC-60 mortar (PCC-60-C). The basins were made of wood and measured 2 m in height, 3 m in width, and 1 m in length. It should be mentioned that the basins were waterproofed and protected by a thin layer of resin paint applied to the wood.

As illustrated in Fig. 2, a pump and a water tank were used to generate a constant pressure that mimics the pressure used to distribute drinking water into pipes in semi-arid regions. In each basin, a thermal resistance sensor was embedded in the soil and linked to a thermostat to regulate the temperature, allowing the soil to dry. These resistors operated during the day and shut down at night to simulate the daily temperature variation in semi-arid regions of Morocco. To ensure that the variation in soil humidification is consistent across all basins, an automatic soil watering
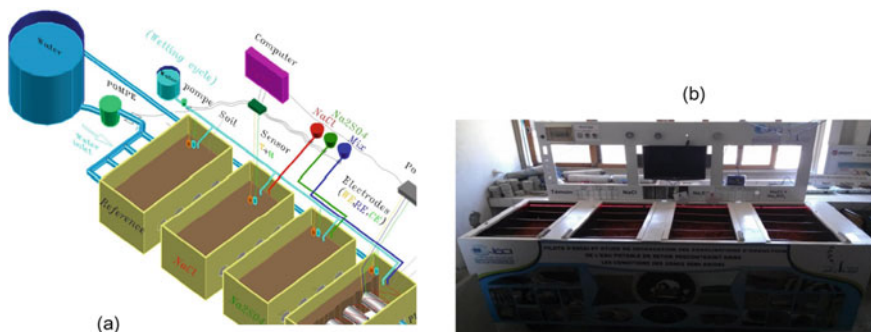


**Fig. 2** Pilot setup: **a** a schematic illustration of the pilot setup and **b** a picture of the final setup

system was also implemented using a soil moisture sensor. Indeed, the entire pilot system was automatic to also control all components including the electrochemical corrosion appliance sensors of each basin. The system was linked to the internet for remote access via an open-source platform. The temperature and humidity data were recorded at 15-min intervals.

## 2.4 EIS Test Procedure

The EIS measurements were performed using a three-electrode setup with reinforcing rebar soldered to a brazed copper wire connected to a potentiostat as a working electrode, stainless steel as a counter electrode, and titanium as a reference electrode as shown in Fig. 1b. The electrodes were positioned in the center of the mold to achieve a 15-mm-thick mortar coating (see Fig. 1b). Also, the rebar in contact with soil was coated with epoxy paint for protection against corrosion. After 28 days of moist curing, the specimens were placed in the basins for about 39 days with no conditions imposed (i.e., without simulating the climatic conditions). Afterward, the automatic pilot system's functions were fully operational (i.e., the climatic conditions were simulated). The impedance spectra of the samples were measured every week up to 475 days using an EIS machine. The experiment was carried out in a room with a temperature of $20 \pm 2°$ C. As previously mentioned, the temperature and humidity data were recorded at 15-min intervals.

### 2.4.1 Equivalent Circuit (EC) Modeling

One of the most difficult aspects of using equivalent circuits is deciding which specific equivalent circuit should be used out of the many possibilities [18]. In the present study, the Dong's EC model, $R_s(Q_1(R_{ct1}W_1))(Q_2(R_{ct2}W_2))$, was selected and used to fit the measured results to acquire transport properties such as the resistance to charge transfer of the electrochemical system during the chloride ion migration process of the specimens. The Dong's EC model was chosen because it had previously been successfully used to investigate the chloride ion migration of cement-based materials [5, 7, 15, 16]. The reader may refer to Dong et al. [5, 6, 7, 8] and Hassi et al. [15, 16] for a full description of the Dong's EC model, $R_s(Q_1(R_{ct1}W_1))(Q_2(R_{ct2}W_2))$, because this level of detail is not the scope of the present paper.

Selected data for the impedance spectra fittings (from Basin 3) at 200 days chloride penetration time is presented in Fig. 3. It can be observed from the figure that there is a good agreement the selected EC model and experimental results and thus suitable for studying the corrosion behavior of the mini-pipes. The model parameter $R_{ct1}$ (i.e., resistance to ion transfer process) was used to compare the resistance to ion migration of the mini-pipes in the different basins.
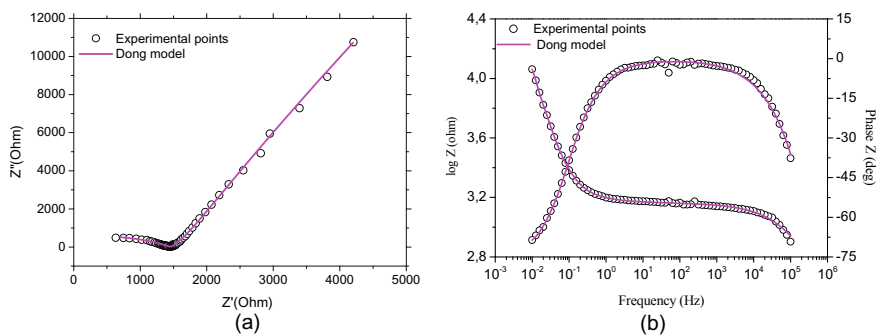
**Fig. 3** Impedance spectra fittings obtained for the PCC-60-C specimen in Basin 3 at 200 days chloride penetration time: **a** Nyquist curves and **b** bode and phase curves

## 3 Results and Analysis

The average compressive strength tests results at 28 days are 46 MPa, 31 MPa, 27 MPa, and 35 MPa, respectively, for OPC-38-C, OPC-60-C, OPC-60-HT, and PCC-60-C specimens. The overall trends observed are consistent with the current prevailing concepts that strength is a function mainly of the w/cm ratio [17]. It can also be seen that the long-term strength is reduced by increased temperatures when compared to concrete without heat treatment.

The Nyquist curves of the mini-pipes in the different basins after 39 days of immersion (i.e., without simulating climatic conditions) are shown in Fig. 4. Overall, two semicircles can be noticed on all the curves in the figures. In general, a second semicircle at intermediate frequencies is attributed to the formation of the corrosion products [18]. Thus, it can be inferred that no corrosion products have been formed after 39 days. It can also be seen that the diameter of the semicircle is affected by the quality of the soil. In essence, the charge transfer reaction is defined by the diameter of the high-frequency semicircle. Thus, an increase in this semicircle is associated with ionic system modification in the pore solution and change in physical pore structure in the cement paste [5, 7, 22].

It can be observed in the figures that the fly ash blended specimens had a larger semicircle diameter in the high-frequency zone of the Nyquist curve in all four basins. This indicates that fly ash incorporation can result in stronger ion migration resistance, as previously reported [5, 16]. This is attributed to the pozzolanic effect of fly ash (i.e., large specific surface area and filling of the voids between cement grains).

Regarding the OPC-based specimens, the control specimen (OPC-38-C) had larger semicircle diameters than the OPC-60-C and OPC-60-HT in Basins 1 to 3 (see Fig. 4a–c). This may be due to its lower w/cm ratio. In Basin 4, on the other hand, the semicircle diameter of the OPC-38-C specimen in the high-frequency zone was comparable to that of the OPC-60-HT but smaller than that of the OPC-60-C specimen (see Fig. 4d). The reason for this is not clear at this time, but the analysis
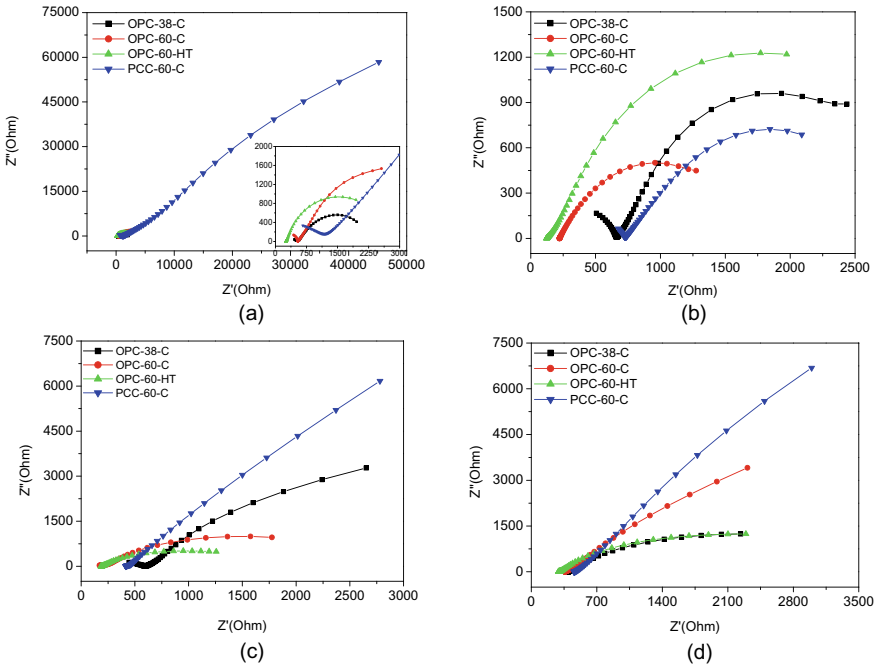
**Fig. 4** Nyquist curves of the mini-pipes mixtures at different basins at 24 h after immersion: **a** Basin 1, **b** Basin 2, **c** Basin 3, and **d** Basin 4

of the data is ongoing, and it is expected that the results after 475 days of migration will provide a clearer picture.

Also, in all Basins, except for Basin 2, the OPC-60-C specimen had larger semi-circle diameters in the high-frequency zone than the OPC-60-HT specimen. This implies that heat treatment of mortar coating is only beneficial under sulfate-only attack where climatic conditions are not in play.

The Nyquist curves of the mini-pipes in the different basins after 200 days of immersion coupled with climatic condition simulations are also present in Fig. 5. Again, two semicircles can be noticed on the curves in the figures. Globally, the results show that climatic conditions had a negative effect on all the mixtures due to the decrease in the diameter of the semicircles. In general, as the diameter of the semicircle decreases, the resistance to ion transport decreases, and the possibility for corrosion increases. Indeed, when studied visually and with a microscope at 475-day migration time, rust was discovered on the surface of some of the rebars.

The overall trends observed with regard to semicircle diameter in the high-frequency zone of the Nyquist curve in the basins are also different from that of the mortars in Fig. 4. In this case, the trends observed are consistent across all four basins. Thus, the fly ash blended specimen (PCC-60-C) had the highest resistance to ion migration followed by the OPC-38-C, OPC-60-C, and then the OPC-60-HT specimen. The lower resistance of the OPC-60 based specimens may be attributed
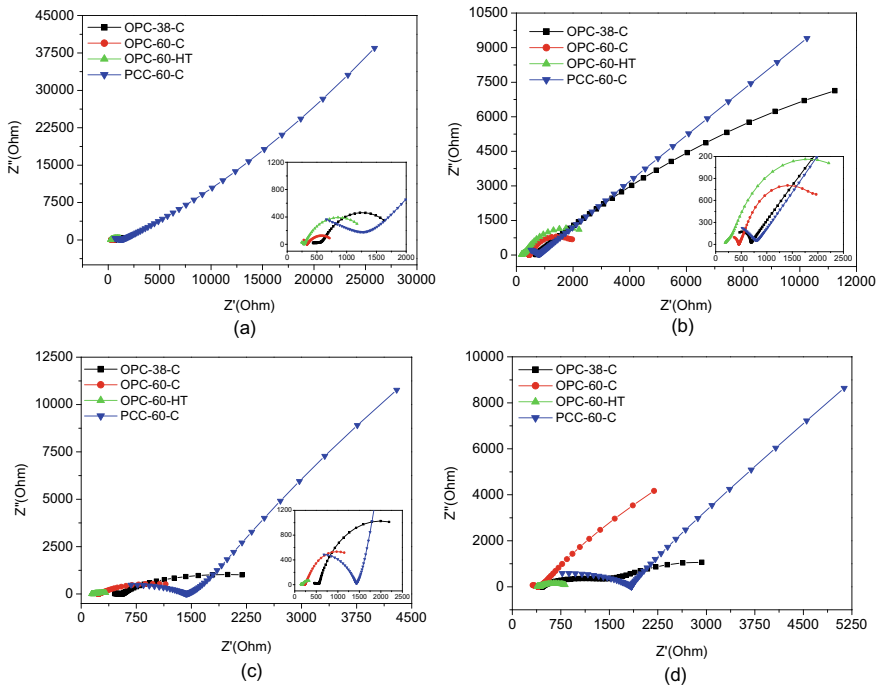
**Fig. 5** Nyquist curves of the mini-pipes mixtures at different basins at 200 days after the climatic condition: **a** Basin 1, **b** Basin 2, **c** Basin 3, and **d** Basin 4

to their higher w/cm ratio and thus higher porosity which in turn leads to a higher potential for ion migration. As previously explained, the higher resistance of the PCC-60-C specimen to the pozzolanic effect fly ash.

Overall, the findings show that fly ash can greatly improve the resistance to chloride ion migration and hence the service life of pipes in semi-arid environments. The result also shows that a higher w/cm ratio mortar without pozzolanic additive is not adequate for the environmental conditions in the semi-arid regions. Otherwise, heat treatment of mortar coating is also not beneficial to the performance of PCCP in a real-life service environment.

The resistance caused by ion transfer ($R_{ct1}R_{ct1}$) in the mortar samples due to chloride ion migration process obtained from the data fitting results is summarized in Table 3. Generally, the larger the diameter of the semicircle the higher the resistance to ion transfer is and the lower the corrosion rate [1, 18]. It was observed that all the specimens performed best when placed in Basin 1 (non-aggressive soil). This was expected and confirmed by inspecting the surface condition of the rebars with the naked eye and a microscope at 475-day migration time (see Fig. 6a). In the presence of soil enriched with sulfate (Basin 2), the resistance to ion transfer was reduced. This, however, did not affect the surface when inspected visually and with a microscope at 475-day migration time (see Fig. 6b).

**Table 3** Resistance to ion transfer, $R_{ct1}$

| Basins | OPC-38-C | OPC-60-C | OPC-60-HT | PCC-60-C |
|---|---|---|---|---|
| *Before simulating climatic conditions* | | | | |
| Basin 1 | 525.6 | 401.4 | 354.4 | 14,225.0 |
| Basin 2 | 403.5 | 343.2 | 320.5 | 1354.0 |
| Basin 3 | 366.0 | 200.8 | 198.3 | 632.7 |
| Basin 4 | 291.0 | 307.4 | 289.3 | 502.5 |
| *After simulating climatic conditions* | | | | |
| Basin 1 | 431.7 | 328.2 | 217.0 | 11,870.0 |
| Basin 2 | 301.0 | 242.0 | 192.5 | 975.5.0 |
| Basin 3 | 256.6 | 172.6 | 159.3 | 526.5 |
| Basin 4 | 215.1 | 134.7 | 118.0 | 452.7 |
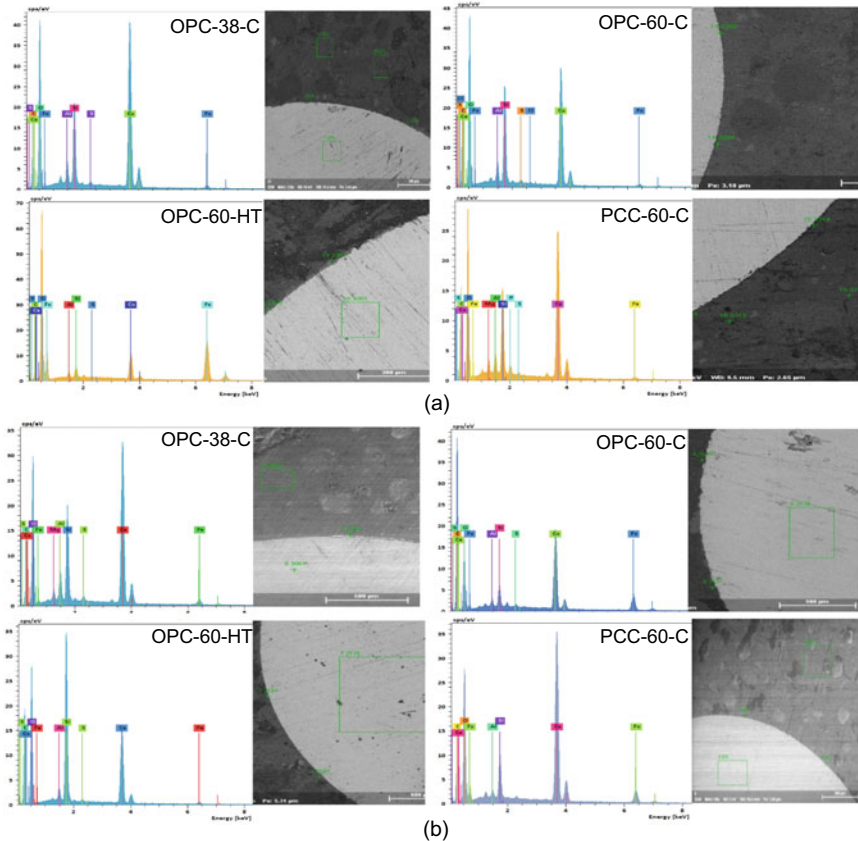


**Fig. 6** SEM and EDS analysis of the steel-mortar interface at 475-day migration time: **a** Basin 1 with control soil; **b** Basin 2 with soil enriched by sulfate; **c** Basin 3 with soil enriched by chloride; and **d** Basin 4 with soil enriched by chloride-sulfate

(c)



(d)
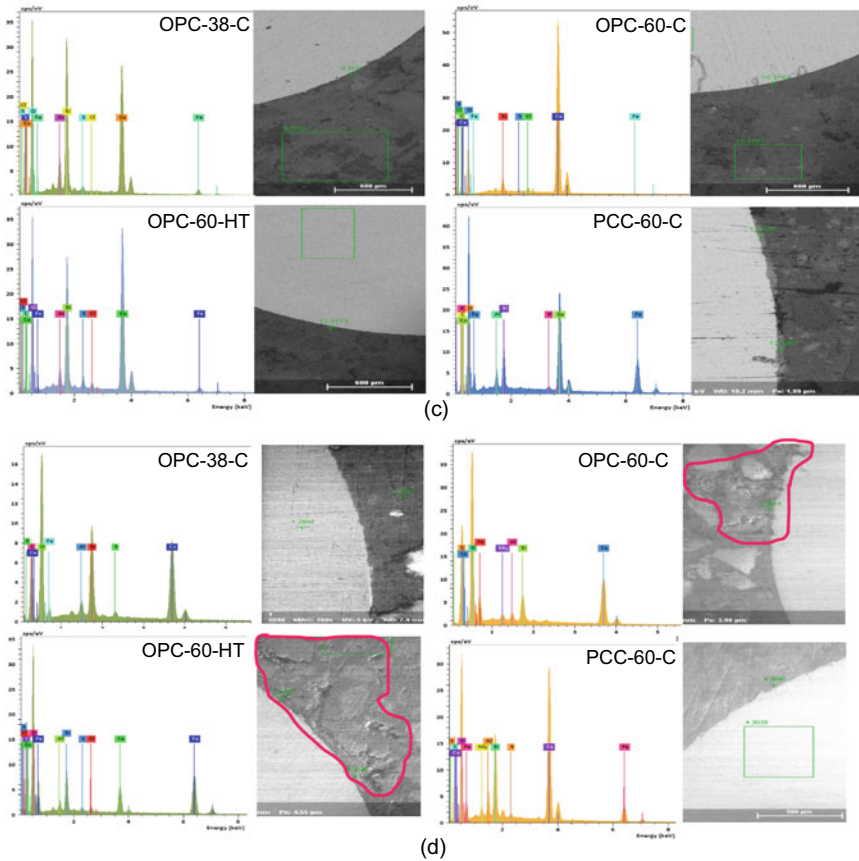
**Fig. 6** (continued)

The resistance to ion transfer was reduced even further in chloride-enriched soil (Basin 3). In this case, corrosion products were discovered on the surface of the rebars which was confirmed with SEM and EDS analysis at 475-day migration time (see Fig. 6c). In the presence of the combined chloride-sulfate (Basin 4), the resistance to ion transfer was the lowest, and rust was found on the surface of the rebars. This again was confirmed with SEM and EDS analysis at 475-day migration time (see Fig. 6d). It should be mentioned that the Nyquist curves and the corresponding resistance caused by ion transfer $(R_{ct1} R_{ct1})$ of that samples along with a technical paper dealing with all the data will be published shortly.

Globally, these results confirm previous observations that the chloride ions in mortar coatings are the main cause of corrosion of PCCP lines in semi-arid regions [12, 14]. The same studies also revealed that sulfate per se may not be the cause of the corrosion of the PCCPs in Morocco, but the co-existence of high sulfate and chloride ions may accelerate the corrosion process [12–14].

# 4   Conclusions

In the present study, a pilot study was designed to better understand the underlying causes of the high failure rates of the Prestressed Concrete Cylinder Pipe used in the semi-arid regions of Morocco. Based on the results and discussion presented, the following conclusions could be drawn:

- All specimens performed best when placed in non-aggressive soil (Basin 1);
- The presence of chloride in the soil is the main cause of corrosion of PCCP lines in semi-arid regions;
- Sulfate per se may not be the cause of the corrosion of the PCCPs in Morocco;
- The soil enriched with combined chloride-sulfate (Basin 4) demonstrated the highest corrosion rates, indicating that the co-existence of sulfate and chloride ions can accelerate the corrosion process;
- Fly ash produced the best corrosion performance results in all four basins, implying that if used, can significantly improve the service life of pipes in semi-arid regions.

# References

1. Aguilar A, Sagüés A, Powers RG (1990) Corrosion measurements of reinforcing steel in partially submerged concrete slabs. ASTM International
2. Al Wardany R (2008) Condition assessment of prestressed concrete cylindrical water pipes. In: 60th annual WCWWA conference and trade show, Western Canada Water and Wastewater Association (WCWWA), Regina, S.K., Canada, September 23–26
3. American Water Works Association (2014) Design prestressed concrete pressure pipe, steel cylinder type. ANSI/AWWA C301–14. Denver, CO: American Water Works Association
4. Berrami K, Ech-chebab A, Galai M, Ejbouh A, Hassi S, Benqlilou H, Ouaki B, Touhami ME (2021) Evaluation of fly ash effect on the durability of prestressed concrete cylindrical pipe in aggressive soil by electrochemical method. Chem Data Collect 32:100656
5. Dong B, Gu Z, Qiu Q, Liu Y, Ding W, Xing F, Hong S (2018) Electrochemical feature for chloride ion transportation in fly ash blended cementitious materials. Constr Build Mater 161:577–586
6. Dong B, Li G, Zhang J, Liu Y, Xing F, Hong S (2017) Non-destructive tracing on hydration feature of slag blended cement with electrochemical method. Constr Build Mater 149:467–473
7. Dong B, Wu Y, Teng X, Zhuang Z, Gu Z, Zhang J, Xing F, Hong S (2019) Investigation of the Cl—migration behavior of cement materials blended with fly ash or/and slag via the electrochemical impedance spectroscopy method. Constr Build Mater 211:261–270
8. Dong B-Q, Qiu Q-W, Xiang J-Q, Huang C-J, Xing F, Han N-X, Lu Y-Y (2014) Electrochemical impedance measurement and modeling analysis of the carbonation behavior for cementititous materials. Constr Build Mater 54:558–565

9. Ge S, Sinha S (2014) Failure analysis, condition assessment technologies, and performance prediction of prestressed-concrete cylinder pipe: state-of-the-art literature review. J Perform Constr Facil 28(3):618–628
10. Ge S, Sinha S (2015) Effect of various bedding conditions on structural integrity of prestressed concrete cylinder pipe. J Mater Sci Res 4(2):34
11. Ge S, Sinha S (2015) Effect of mortar coating's bond quality on the structural integrity of prestressed concrete cylinder pipe with broken wires. J Mater Sci Res 4(3):59
12. Hassi S, Ebn Touhami M, Ejbouh A, Berrami K, Boujad A, Ech-chebab A (2021) Case study of the performance of prestressed concrete cylinder pipes in the greater Agadir of Morocco. J Pipeline Syst Eng Pract 12(2):05021001
13. Hassi S, Ebn Touhami M, Menu B, Benqlilou H, Ejbouh A (2022) Case study of the performance of prestressed concrete cylinder pipes in northeastern Morocco. J Pipeline Syst Eng Pract 13(2):05022002
14. Hassi S, Ejbouh A, Ebn Touhami M, Berrami K, Ech-chebab A, Boujad A (2021) Performance of prestressed concrete cylinder pipe in North Africa: case study of the water transmission systems in the Tafilalet region of Morocco. J Pipeline Syst Eng Pract 12(2):05021002
15. Hassi S, Menu B, Ebn Touhami M (2022) The use of the electrochemical impedance technique to predict the resistance to chloride ingress in silica fume and fly ash-reinforced blended mortars exposed to chloride or chloride-sulfate solutions. J Bio Tribo Corr 8(1):1–14
16. Hassi S, Touhami ME, Boujad A, Benqlilou H (2020) Assessing the effect of mineral admixtures on the durability of Prestressed Concrete Cylinder Pipe (PCCP) by means of electrochemical impedance spectroscopy. Constr Build Mater 262:120925
17. Monteiro PJ, Helene PR, Kang S (1993) Designing concrete mixtures for strength, elastic modulus and fracture energy. Mater Struct 26(8):443–452
18. Ribeiro D, Abrantes J (2016) Application of electrochemical impedance spectroscopy (EIS) to monitor the corrosion of reinforced concrete: a new approach. Constr Build Mater 111:98–104
19. Romer AE, Bell GE (2001) Causes of external corrosion on buried water mains. In: Pipelines 2001: advances in pipelines engineering and construction, pp 1–9
20. Romer AE, Bell GE, Ellison RD (2007) Failure of prestressed concrete cylinder pipe. Pipelines 2007: advances and experiences with trenchless pipeline projects, 1–17
21. Xiong H, Li P, Li Q (2010) FE model for simulating wire-wrapping during prestressing of an embedded prestressed concrete cylinder pipe. Simul Model Pract Theory 18(5):624–636
22. Zhang J, Dong B, Hong S, Teng X, Li G, Li W, Tang L, Xing F (2019) Investigating the influence of fly ash on the hydration behavior of cement using an electrochemical method. Constr Build Mater 222:41–48

# Reducing Chloride Induced Corrosion Risk and Associated Life Cycle Cost of Marine RC Structure: Bangladesh Perspective

**Tanvir Manzur, Munaz A. Noor, and Tafannum Torsha**

**Abstract** Chloride induced corrosion poses significant threat to Reinforced Concrete (RC) structures in marine environment. Therefore, proper design of marine RC structures in terms of materials types, mix proportions, and concrete cover is prerequisite for ensuring adequate durability and sustainable construction practice. Inappropriate selection of mix proportions, mix constituents, and concrete cover can significantly hamper the expected service life of a marine RC structure and eventually, results in substantial repair costs. In this study, an attempt was made to investigate the effect of binder types on corrosion risk and corresponding life cycle cost of RC slab or wall made of locally used construction materials of Bangladesh under extreme marine conditions. Five different types of binder (combinations of ordinary Portland cement and 20%/40% replacement level of slag/fly ash) and two w/b (water to binder) ratios of 0.35 and 0.45 were used along with three concrete cover values of 19 mm, 25 mm, and 37.5 mm to perform the parametric study. The Life-365 environment was used to evaluate chloride induced corrosion risk and the associated life cycle cost of RC slab or wall structure made of considered concrete mixes for a design service period of 100 years. It was evident from the study that the type of binder, use of fly ash in particular, could have considerable impact on corrosion proneness of concrete mixes. The use of a typical cover value of 19 mm for RC slabs/walls was inadequate in providing satisfactory performance under extreme saline exposure even if a higher percentage replacement of fly ash is used. The benefit of using higher concrete cover and blended cement with a higher percentage of fly ash in a saline environment was also quantitatively apparent from this study in the context of Bangladesh. Moreover, life cycle costs of marine RC structure could be significantly reduced by utilizing higher cover values and blended cement with fly ash.

T. Manzur (✉) · M. A. Noor
Department of Civil Engineering, Bangladesh University of Engineering and Technology, Dhaka, Bangladesh
e-mail: tanvirmanzur@ce.buet.ac.bd

T. Torsha
Department of Building, Civil and Environmental Engineering, Concordia University, Montreal, QC, Canada

993

# 1  Introduction

Chloride induced corrosion of embedded reinforcement within reinforced concrete
(RC) is a major durability concern in coastal or marine environment [3, 5]. The
design service life of a marine RC structure can be significantly hampered due to
such corrosion caused by chloride ingress [2, 13, 15]. As a result, mix design of
concrete in marine environment must have appropriate emphasis on durability aspects
related to ingress of chloride ions along with strength requirements [9–11]. Type of
binder used in preparation of concrete and selection of design cover based on perfor-
mance requirements are two critical factors for safeguarding durability of marine
concrete. However, in Bangladesh, unavailability of durability focused local mix
design guidelines and use of deemed-to-satisfy criterion for concrete cover design
impose considerable safety risks to the RC structures in coastal environment. Conse-
quently, significantly high financial allowance may require for repair of degraded
RC structures in corrosion prone region at later stages of their service life [8, 16].
Therefore, it is of immense importance to enhance life cycle performance of marine
RC structures by ensuring appropriate mix design to prepare concrete and conducting
risk assessment due to chloride induced corrosion.

The primary objective of this study was to quantitatively assess the impact of
different binder types, i.e., typical Ordinary Portland Cement (OPC) and blended
cement (mixture of OPC and blast furnace slag/Class F fly ash) on corrosion suscepti-
bility of some common concrete mixes of Bangladesh under extreme marine exposure
considering three concrete cover values typically used for RC slab or wall construc-
tion. Such assessment of corrosion risk is imperative to develop performance-based
design guidelines for concrete mix design and concrete cover which is currently not
available in local codes. With this end in view, chloride induced corrosion risk of
RC slab or wall made from concrete having different mix variables was investigated
under extreme marine condition for three commonly used concrete covers in Life-
365 environment [6] in this study. The corrosion risk was assessed by generating
cumulative probability density function of chloride induced corrosion initiation for
all mixes up to design service period of 100 years. The variability of mixes included
five different binder types and two different w/b (water to binder) ratios. One binder
type consisted of Ordinary Portland Cement (OPC) and the other four were combi-
nations of OPC plus blast furnace slag/Class F fly ash with 20% and 40% replace-
ment level for each supplementary binder. The two different w/b ratios considered
were 0.35 and 0.45. Locally available commonly used aggregates (both fine and
coarse) were used to produce concrete. Therefore, the study considered a good range
of parameters to estimate the corrosion proneness of local concrete mixes under
extreme marine exposure. In addition, the life cycle cost (including repair required
for corrosion degradation) associated with the measured corrosion risk of RC slab/

wall due to chloride ingress was evaluated for 100 years of service life. The outcome of the study clearly exhibited the significance of using higher fraction of fly ash in blended cement to reduce corrosion susceptibility of concrete mixes in saline environment. The importance of providing higher design concrete cover to ensure adequate service life was also evident. Moreover, it was found that use of blended cement with higher percentage of fly ash in combination with relatively higher cover values could significantly reduce life cycle cost by delaying corrosion related degradation. Hence, it is apparent from the findings that this preliminary study has potential to aid in establishing performance-based guidelines within the local construction practice for ensuring adequate design service life of RC infrastructure system in severe marine environment.

## 2 Materials and Methods

This study was based on using chloride migration coefficients of concrete mixes (with different types of binders and w/b ratios) measured following Nordtest method NT BUILD 492 [12] and different covers (typically used) for evaluating design service life and corrosion probability of RC slab or wall in Life-365 environment [6] under extreme saline exposure. It is apparent that the two main variables considered were binder types and concrete covers since the nature of binder (whether has pozzolanic characteristic or not) directly impacts the permeability characteristics of resultant concrete and the cover value determines the traveling distance of chloride ions to reach to embedded reinforcement. The migration coefficients of the mixes were measured in previous studies [3, 4] and are given in Table 1. The concrete samples were prepared using Ordinary Portland Cement (OPC) and two percent replacements, i.e., 20% and 40% of OPC by Class F fly ash (FA20 and FA40, respectively) or blast furnace slag (S20 and S40, respectively) as supplementary cementitious material (SCM). Locally available 19 mm downgraded crushed stone chips were used as coarse aggregate and as fine aggregate, local sand with Fineness Modulus (FM) of 2.60 was used. The chemical composition of OPC and SCMs and different basic properties of both types of aggregates can be found in [3]. The concrete mixes were prepared with two w/b ratios of 0.35 and 0.45 following ACI Mix Design Manual [1] for target slump of 75–100 mm. The total amount of binder content for mixes with w/b ratio of 0.35 and 0.45 was about 605 kg/m$^3$ and 470 kg/m$^3$, respectively. Table 2 shows the approximate composition of different concrete mixes considered in the study [4]. Further details of the mix designs can be found in Baten et al. [3] and Baten [4]. Three typical concrete cover values of 19, 25, and 37.5 mm were used for determining chloride induced corrosion risk and associated service life of RC slab or wall made with mixes considered in the study. Cover values of higher than 37.5 mm was not considered since such larger cover would be less feasible (in terms of both cost and constructability) for construction of RC slab or wall. However, cover value larger than 37.5 mm should be provided in cases deemed necessary.

**Table 1** Migration coefficients of the concrete mixes measured following NT BUILD 492 [16] method

| Mix | w/b | Migration coefficient ($10^{-12}$ m$^2$/s) | Mix | w/b | Migration coefficient ($10^{-12}$ m$^2$/s) |
|-----|-----|---------------------------------------------|-----|-----|---------------------------------------------|
| OPC | 0.35 | 5.10 | OPC | 0.45 | 7.00 |
| S20 | | 3.54 | S20 | | 5.10 |
| S40 | | 2.47 | S40 | | 3.75 |
| FA20 | | 3.60 | FA20 | | 3.44 |
| FA40 | | 1.24 | FA40 | | 1.80 |

**Table 2** Composition of different concrete mixes considered in the study [4]

| Mix | w/b | Cement (kg/m$^3$) | Fly ash (kg/m$^3$) | Slag (kg/m$^3$) | Course aggregate (kg/m$^3$) | Fine aggregate (kg/m$^3$) |
|-----|-----|-------------------|---------------------|------------------|------------------------------|----------------------------|
| OPC 0.35 | 0.35 | 605 | - | - | 1110 | 667 |
| S20 0.35 | | 484 | - | 121 | 1110 | 737 |
| S40 0.35 | | 363 | - | 242 | 1110 | 702 |
| FA20 0.35 | | 484 | 121 | - | 1110 | 737 |
| FA40 0.35 | | 363 | 242 | - | 1110 | 702 |
| OPC 0.45 | 0.45 | 470 | - | - | 1110 | 628 |
| S20 0.45 | | 376 | - | 94 | 1110 | 706 |
| S40 0.45 | | 282 | - | 188 | 1110 | 667 |
| FA20 0.45 | | 376 | 94 | - | 1110 | 706 |
| FA40 0.45 | | 282 | 188 | - | 1110 | 667 |

As already mentioned, Life-365 [6] software was used to conduct life cycle analysis of RC slab or wall (made of selected concrete mixes of the study) exposed to corrosion due to chloride ingress. The Life-365 follows Fick's 2nd law to calculate chloride diffusion within concrete using the migration coefficient of any concrete mix. A decay index, m was used to account for time dependent changes in the migration coefficients of the mixes as per recommendation of the model [6]. The value of m depends on the fractions of fly ash and/or slag present in the binder with the maximum replacement level limit of 50% for fly ash and/or 70% for slag. The time dependent changes in migration coefficients of the mixes with w/b ratio of 0.45 (obtained from Life-365) are shown in Fig. 1 for 37.5 mm cover. Life-365 provides time dependent variations of coefficient values till the chloride ions travel the entire cover distance and reach to the embedded rebars. The marine spray zone was considered as exposure condition. Critical chloride content required to initiate corrosion in rebar and the maximum surface concentration of chloride on concrete were assumed as 0.05 and 1.0 wt.% of concrete, respectively. The buildup year for maximum surface chloride was taken as 10 years. The monthly variations in average temperature of Cox's bazaar
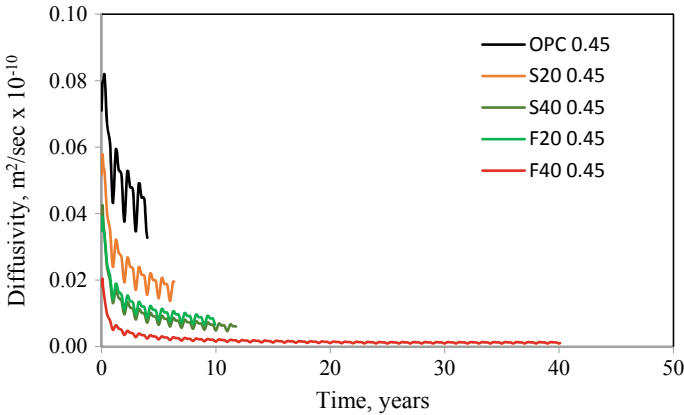
**Fig. 1** Diffusivity vs time of the mixes with 0.45 w/b ratio for 37.5 mm cover

area, a coastal city in Bangladesh, were used as exposure temperature of concrete. Service life of a RC structure due to chloride induced corrosion is usually taken as summation of time required for corrosion initiation and propagation. The propagation period is somewhat constant for a particular rebar type. Therefore, corrosion initiation period was considered in this study for comparison between service life values of various mixes.

The life cycle cost due to chloride induced corrosion was estimated in terms of cumulative present dollar (USD) value using the Life-365 software. The present dollar value includes the inflation rate in materials and labor cost as well as considers the discount rate [6]. The life cycle cost, in terms of cumulative present dollar value, is the summation of the above-mentioned cost. The cost of concrete and reinforcement was taken as USD 165/m$^3$ and USD 1.05/kg considering the current market price in Bangladesh. The approximate cost of repair was assumed as USD 190/m$^2$ of RC slab or wall. The repair cycle was considered as 5 years and at each cycle, the amount of repair area was assumed as 10%. The inflation rate and discount rate were approximated as 5% and 4%, respectively for this study in order to provide an idea about the impact of proper selection of binding material and concrete cover on life cycle cost of marine RC structure. However, the real values (based on comprehensive survey) of different rates, cost of materials, cost and cycle of repairs, amount of repair area, etc. should be used while determining life cycle cost of a particular RC element considering the time of evaluation and location of the structure. The life cycle cost was estimated for 100 years of service period with the base year taken as 2020.

# 3  Results and Discussion

The effect of different variables, primarily binder types and design cover, on corrosion initiation period and corrosion probability of different mixes for RC slab or wall construction are presented and discussed in this section. In addition, the life cycle costs in terms of cumulative present dollar are also compared and discussed for alternative binder options and different cover values.

## 3.1  Corrosion Initiation Period and Cumulative Corrosion Probability

Figure 2 shows the corrosion initiation period of different mixes for RC slab or wall construction in extreme marine exposure. It was evident that mixes with 40% fly ash experienced significantly higher corrosion initiation time as compared to their all other counterparts at larger cover values. Almost all mixes exhibited extremely reduced initiation period with concrete cover of 19 mm although mixes with 40% fly ash had relatively higher initiation period. No mixes were able to achieve corrosion initiation period of 20 years even with 37.5 mm cover except mixes having 40% fly ash with 37.5 mm cover (the mix with 40% fly ash and w/b ratio of 0.35 exhibited slightly higher corrosion initiation period of 20 year at cover of 25 mm). Such behavior of mixes with higher fly ash content was due to pozzolanic characteristic of active silica present in Class F fly ash. The active silica converts $CaOH_2$ (initial hydration products with less strength potential) in to more stable secondary CSH gel through pozzolanic reactions [7, 14]. Consequently, inter connectivity of pores reduces due to pore refinement resulting from formation of CSH at later ages. The relatively less effectiveness of fly ash mixes at lower cover was due to significantly reduced travel distance for chloride ions to reach to the embedded rebars.
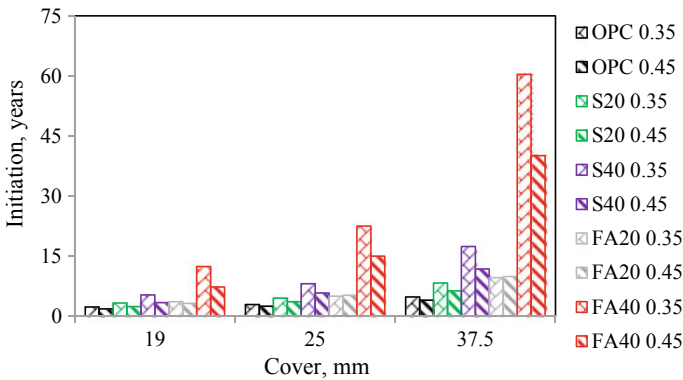


**Fig. 2**  Corrosion initiation period of different mixes for RC slab or wall construction
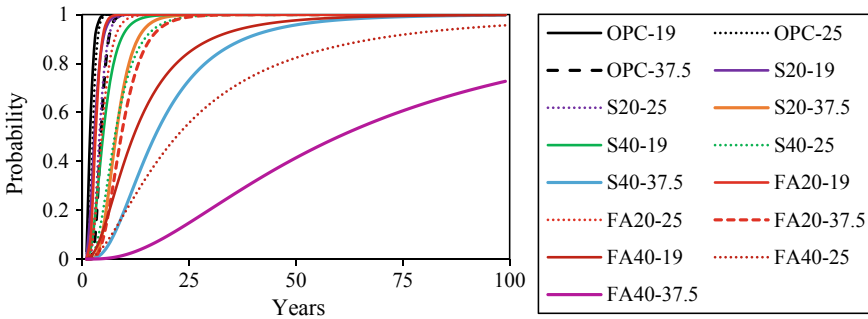
**Fig. 3** Cumulative probability of corrosion initiation periods of mixes with w/b ratio of 0.35

It was also observed that similar mixes with higher w/b ratio exhibited comparatively less corrosion initiation period than that of their lower w/b ratio counterparts. However, such differences in initiation period between similar mixes with lower and higher w/b ratio was prominent in case of 37.5 m cover since lesser covers could not provide sufficient travel distance for chloride ions. Lower initiation period in case of mixes with higher w/b ratio was due to formation of larger capillary pores within the concrete matrix resulting from evaporation of additional amount of water. The cumulative probability density functions of corrosion initiation period of all the mixes with w/b ratio of 0.35, presented in Fig. 3, also show the significant lower corrosion risk of 40% fly ash blended mixes due to chloride ingress at severe marine exposure.

## 3.2 Life Cycle Cost

The life cycle costs of the mixes for RC slab or wall construction with 37.5 mm cover are shown in Fig. 4 in terms of cumulative present value in USD for 100 years' service period under extreme marine exposure. The differences between life cycle costs for other two cover values were not significant since their corrosion initiation periods ranged within a close value as evident from Fig. 2. It is apparent from Fig. 4 that the present value costs remain constant for a significantly longer period for only 40% fly ash concrete (for w/b ratio of both 0.35 and 0.45) as compared to other mixes since these mixes had considerable higher initiation period. It was found that mixes with 40% fly ash would result in around 45% and 25% less life cycle cost per sqm for w/b ratio of 0.35 and 0.45, respectively for 37.5 mm cover and 100 years' service period for the assumed conditions considered in the study.
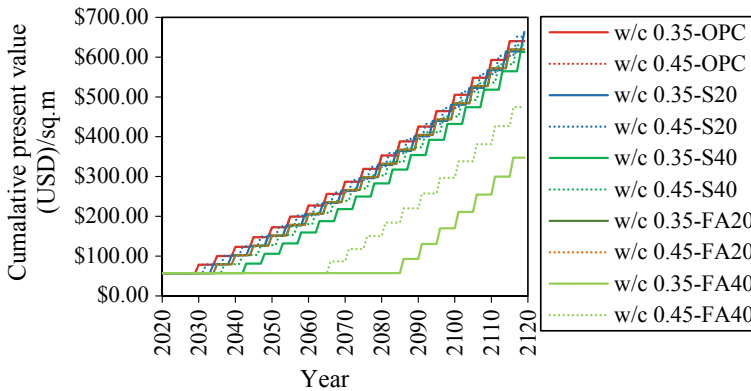
**Fig. 4** Life cycle cost in cumulative present value for 100 years' service period and 37.5 mm cover

## 4 Conclusions

The study showed the significance of using Class F fly ash in blended cement and providing higher concrete cover to ensure adequate service life and eventually, reduced life cycle cost for RC structure in extreme marine exposure. The use of lower w/b ratio could also have considerable positive impact on service life of RC structures in coastal regions if adequate cover and fly ash fractions are provided. However, the outcome of this article was based on very limited study performed and hence, further comprehensive research would be required for developing guidelines.

## References

1. ACI 211 (1991) Standard practice for selecting proportions for normal heavyweight, and mass concrete. American Concrete Institute, Michigan
2. Baten B, Manzur T, Torsha T, Alam S (2021) Parametric study with graphical approach for assessing corrosion vulnerability of concrete mixes in chloride environment. Construction and Building Materials, Elsevier, p 309
3. Baten B, Manzur T, Ahmed I (2020) Combined effect of binder type and target mix-design parameters in delaying corrosion initiation time of concrete. Construction and Building Materials, Elsevier, p 242
4. Baten B (2019) Effect of blended cement on service life enhancement of concrete structures in marine environment. M.Sc. Thesis, Department of Civil Engineering, Bangladesh University of Engineering and Technology, Dhaka, Bangladesh

5. Chidiac SE, Shafikhani M (2019) Phenomenological model for quantifying concrete chloride diffusion coefficient. Constr Building Mater Elsevier 224:773–784
6. Life-365 (2020) Service life prediction model and computer program for predicting the service life and life-cycle cost of reinforced concrete exposed to chlorides, version 2.2.3
7. Mahmud S, Manzur T, Samrose S, Torsha T (2021) Significance of properly proportioned fly ash based blended cement for sustainable concrete structures of tannery industry. Struct Elsevier 29:1898–1910
8. Mangat PS, Ojedokun OO, Lambert P (2021) Chloride-initiated corrosion in alkali activated reinforced concrete. Cement Concr Compos 115:103823
9. Manzur T, Hasan MJ, Baten B, Torsha T, Khan MFA, Hossain KMA (2019) Significance of service life based concrete mix design in marine environment. In: 7th international conference on engineering mechanics & materials by CSCE, Laval (Greater Montreal), Canada, June 12–15, 2019
10. Manzur T, Baten B, Hasan MJ, Bose B (2017) Application of corrosion potential as a tool to assess sustainability of indigenous concrete mixes in Bangladesh. In: International conference on sustainable infrastructure (ASCE) 2017, New York, USA. https://doi.org/10.1061/978078 4481219.010
11. Masum ATM, Manzur T (2019) Delaying time to corrosion initiation in concrete using brick aggregate as internal curing medium under adverse curing conditions. Constr Building Mater Elsevier 228:116772
12. NT BUILD 492 (1999) Concrete, mortar and cement based repair materials: chloride migration coefficient from non-steady state migration experiments. NORDTEST, Finland
13. Otieno M, Bauhausian H, Alexander M (2016) Chloride-induced corrosion of steel in cracked concrete—part I: experimental studies under accelerated and natural marine environments. Cement Concr Res Elsevier 79:373–385
14. Torsha T, Manzur T, Chowdhury NR, Hasan MJ (2022) Significance of integrating probabilistic performance-based cover design in local construction guidelines for adequate serviceability of coastal built environment: Bangladesh perspective. Nat Hazards 112:919–946
15. Torsha T, Khan MFA, Hasan MJ, Mutsuddy R, Manzur T (2019) Tentative design life of reinforced concrete structures: Bangladesh perspective. In: International conference on disaster risk management. Dhaka, Bangladesh, January 12–14, 2019
16. Vu KAT, Stewart MG (2000) Structural reliability of concrete bridges including improved chloride-induced corrosion models. Struct Safety Elsevier 22(4):313–333

# Microstructural Investigation of Coupled Sulfate and Freeze–Thaw Damage of Concrete Using Micro-Computed Tomography

**Mustafa Alhusain and Adil Al-Mayah**

**Abstract** Concrete structures in sub-zero temperatures can be severely damaged due to freeze–thaw cycles. The damage can be aggravated if the concrete is exposed to different sulfate environments. The damage is observed at a macroscale level; however, little attention has been paid to investigating the damage at the microscale level representing the early stage of damage. Therefore, the focus of this investigation is to study the microscale damage mechanisms of concrete subjected to up to 80 freeze–thaw cycles in different environments: water, potassium sulfate, and magnesium sulfate with 5 and 10% concentrations. It was observed that exposure to potassium sulfate significantly accelerated the frost damage leading to a complete disintegration of the samples, whereas the control specimen lost about 20% of its mass after 80 cycles. However, the typical mechanisms of frost damage were not altered, where the scaling damage started at the external surface and propagated toward its core. On the other hand, subjecting concrete to magnesium sulfate mitigated the severity of frost damage and changed its mechanisms, resulting in more expansion within the internal pores than the surface ones. Hence, the average mass loss of concrete after 80 freeze–thaw cycles in the magnesium sulfate environment was only 1.38%. Also, increasing the concentration of magnesium sulfate produced more frost damage.

**Keywords** Concrete damage · CT imaging · Freeze–thaw · Magnesium sulfate · Potassium sulfate

M. Alhusain (✉) · A. Al-Mayah
Mechanical and Mechatronics Engineering, University of Waterloo, Waterloo, ON, Canada
e-mail: malhusain@kfu.edu.sa; malhusain@uwaterloo.ca

A. Al-Mayah
Civil and Environmental Engineering, University of Waterloo, Waterloo, ON, Canada

M. Alhusain
Mechanical Engineering, College of Engineering, King Faisal University, Al Hofuf, Al-Ahsa, Saudi Arabia

# 1 Introduction

Exposure of concrete materials to severe environments, such as sulfate and frost environments, is one of the leading causes of concrete damage [1, 8]. As reported by the American Society of Civil Engineering (ASCE), damage to concrete infrastructure is anticipated to cost the United States about $2 trillion by 2025 [5]. Hence, the environmental degradation of concrete in sulfate and freeze–thaw environments has been extensively investigated. Prolonged exposure to sulfate salts, such as magnesium sulfate and potassium sulfate, can cause precipitation of expansive sulfate by-products (e.g., ettringite and gypsum) within the concrete capillaries, resulting in spalling damage, lower compressive strength and volume change [7, 9, 14, 15]. For example, exposing concrete to magnesium sulfate for five months decreased its compressive strength by over 80% [14]. Also, one year of immersion of a cement mortar bar ($25 \times 25 \times 150$ mm$^3$) into magnesium sulfate and potassium sulfate solutions increased its dimensions, such as the mortar's length which increased by 1.6% and 3.7%, respectively [9].

On the other hand, recurring exposure to cold environments can produce high internal expansive pressure by freezing the water retained with the capillaries of concrete, resulting in layer-by-layer scaling damage that increases the porosity and reduces the compressive strength [4, 6, 11]. For example, temperature fluctuation between cold (e.g., -20 °C) and warm (e.g., 20 °C) environments can induce thermal stress within the mortar-aggregate interface due to the variation of thermal expansion coefficients, leading to early cracking of the interfacial zone [12, 17]. Lu et al. [11] observed that subjecting concrete to 75 freeze–thaw cycles reduced its compressive strength from about 49.2 to 45.5 MPa. Also, exposing concrete to 40 freeze–thaw cycles increased its porosity from 3.3 to 4.55% [4].

Investigating the combined effects of sulfate and freeze–thaw on concrete is crucial since both factors can increase the porosity and permeability of concrete, degrading its resistance to further environmental damage [2, 4, 13, 16]. Xiao et al. [16] observed that concrete lost 1.7% of its mass and 29.5% of its compressive strength after being subjected to 300 freeze–thaw cycles in a sodium sulfate solution with a concentration of 5%. Similarly, Ren and Lai [13] reported 0.72% of mass loss and 56.3% of compressive strength reduction after exposing concrete to 300 freeze–thaw cycles in a 5% sodium sulfate solution.

Although the coupled sulfate and freeze–thaw damage was examined at the macroscale level, little research studied the microscale frost damage in magnesium sulfate and potassium sulfate solutions. The potassium sulfate salt was selected due to its high availability in soil and seawater, whereas the magnesium sulfate salt was used because it produces more severe sulfate damage. Thus, the main objective of this study is to investigate the microstructural coupled sulfate and freeze–thaw damage mechanisms by subjecting concrete to 80 freeze–thaw cycles in magnesium sulfate and potassium sulfate environments with 5 and 10% concentrations. A high-resolution micro-computed tomography (μCT) imaging system was used to obtain 3D images of the specimens before and after applying 40 and 80 frost cycles. The

severity of concrete damage was determined using mass loss and porosity expansion analysis. Also, the mechanisms of the coupled sulfate and frost damage were investigated by monitoring the progression of concrete damage throughout the applied freeze–thaw cycles.

## 2 Materials and Methodologies

### 2.1 Specimens

Five concrete specimens with a length of about 40 mm and a diameter of 14 mm were cast using water/cement (W/C), sand/cement (S/C), and aggregate/cement ratios of 0.5, 1, and 1.5, respectively, as shown in Fig. 1. The small size of the concrete elements was selected to maximize the resolution of CT imaging. The molds of the samples were removed about 24 h after casting, and the concrete elements were wet cured for 28 days at a temperature of about 20 °C and humidity of 60% before CT imaging and freeze–thaw testing in different sulfate environments. The sulfate solutions were prepared by dissolving the appropriate amounts of magnesium and potassium sulfate salts, made by Alpha Chemicals company, in tap water. The specimens (control, PS-5%, PS-10%, MS-5%, and MS-10%) were labeled according to the applied freeze–thaw environment. For example, sample PS-5% was exposed to potassium sulfate solution with a concentration of 5%, while specimen MS-10% was immersed in a magnesium sulfate solution with a concentration of 10%.
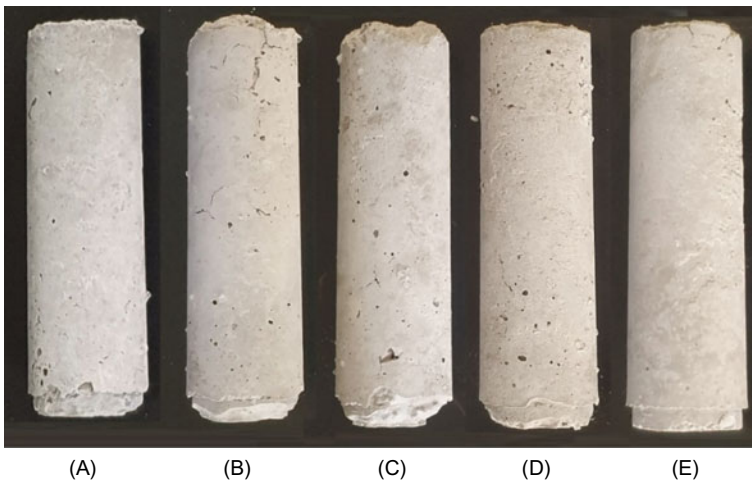


Fig. 1 **a** Control, **b** PS-5%, **c** PS-10%, **d** MS-5%, and **e** MS-10% concrete samples

## *2.2 Freeze–Thaw Cycles*

To investigate concrete's coupled sulfate and freeze–thaw damage, the samples were exposed to frost cycles in different solutions: water (control), potassium sulfate (PS-5% and PS-10%), and magnesium sulfate (MS-5% and MS-10%) with 5% and 10% concentrations, respectively, as listed in Table 1. The specimens were submerged into the mentioned solutions for at least 6 h to achieve full saturation before applying 80 freeze–thaw cycles. The specimens were subjected to 12.5 h of freezing and 11.5 h of melting in every cycle to simulate real frost environments, as demonstrated in Fig. 2. During each cycle, an average cooling rate of − 13.5 °C/h was applied to decrease the environment temperature from 11 to − 25 °C, after which the temperature was maintained between − 18 and − 25 °C for 7.2 h, followed by an average warming rate of 1.9 °C/h to increase the temperature back to about 11 °C.

**Table 1** Composition of immersion solution for freeze–thaw cycles

| Specimen | Solution |
|---|---|
| Control | Tap water |
| PS-5% | Tap water + 5 wt.% of $K_2SO_4$ |
| PS-10% | Tap water + 10 wt.% of $K_2SO_4$ |
| MS-5% | Tap water + 5 wt.% of $MgSO_4$ |
| MS-10% | Tap water + 10 wt.% of $MgSO_4$ |



**Fig. 2** Controlled environment temperature throughout each freeze–thaw cycle [4]
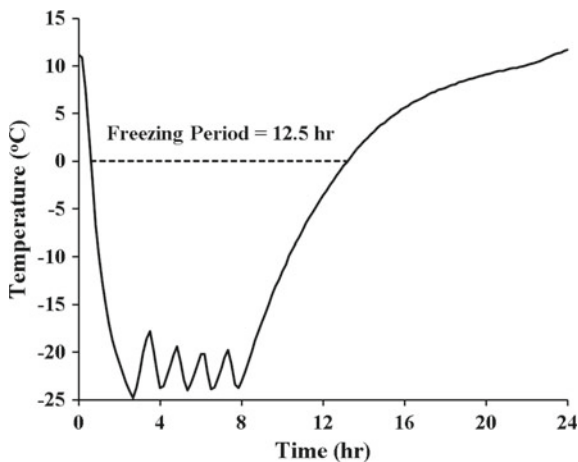
## 2.3   MCT Imaging and Post-processing

An industrial micro-computed tomography ($\mu$CT) imaging system, shown in Fig. 3a, was used to examine the internal microstructure of the concrete specimens before and after applying 40 and 80 freeze–thaw cycles. The CT scans were conducted using a tube voltage of 100 kV and a tube current of 80 $\mu$A, which were appropriate for capturing high-resolution images without degrading the image contrast or over-loading the imaging system [3]. One thousand X-ray images were collected with a resolution (voxel size) of 49.1 $\mu$m using an X-ray exposure period of 0.33 s per image. The captured CT images were then post-processed using VGStudio Max 2.2 software. Three-dimensional stacking of the CT images was performed, as illustrated in Fig. 3b, producing 3D models of the concrete elements. It is worth noting that only the 36 mm long midsection of the specimens was analyzed to reduce inconsistencies caused by the non-uniform top and bottom segments while obtaining higher resolution images, as highlighted in Fig. 3c. The CT imaging artifacts were reduced by applying a 3D median filtration, followed by material thresholding. Finally, three-dimensional detection of air voids was conducted, creating 3D reconstructions of the internal pore structures as demonstrated in Fig. 3d.

## 3   Results

## 3.1   General

The coupled sulfate and freeze–thaw damage was investigated by subjecting concrete specimens to distinct environments: water, potassium sulfate, and magnesium sulfate with 5% and 10% concentrations, respectively. The severity of frost damage was studied through mass measurement and porosity analysis, whereas the damage mechanisms were investigated using the post-processed CT images. It was observed that subjecting specimens PS-5% and PS-10% to potassium sulfate degraded the resistance to frost damage, resulting in higher mass loss and porosity expansion during the first 40 cycles and full disintegration by cycle 80. Although the potassium sulfate accelerated the concrete damage, it had little effect on the typical mechanisms of frost damage. On the contrary, exposure to magnesium sulfate mitigated the freeze–thaw damage and altered its mechanisms. Thus, it was noted that specimens MS-5% and MS-10% experienced the least mass loss and porosity expansion. Also, the frost damage of the two samples appeared mostly as considerable internal pore expansion followed by minor scaling damage. Notably, increasing the concentration of magnesium sulfate from 5% (e.g., MS-5%) to 10% (e.g., MS-10%) resulted in greater frost damage. However, the scaling damage of specimen MS-10% is substantially less severe and more uniform than the control sample.
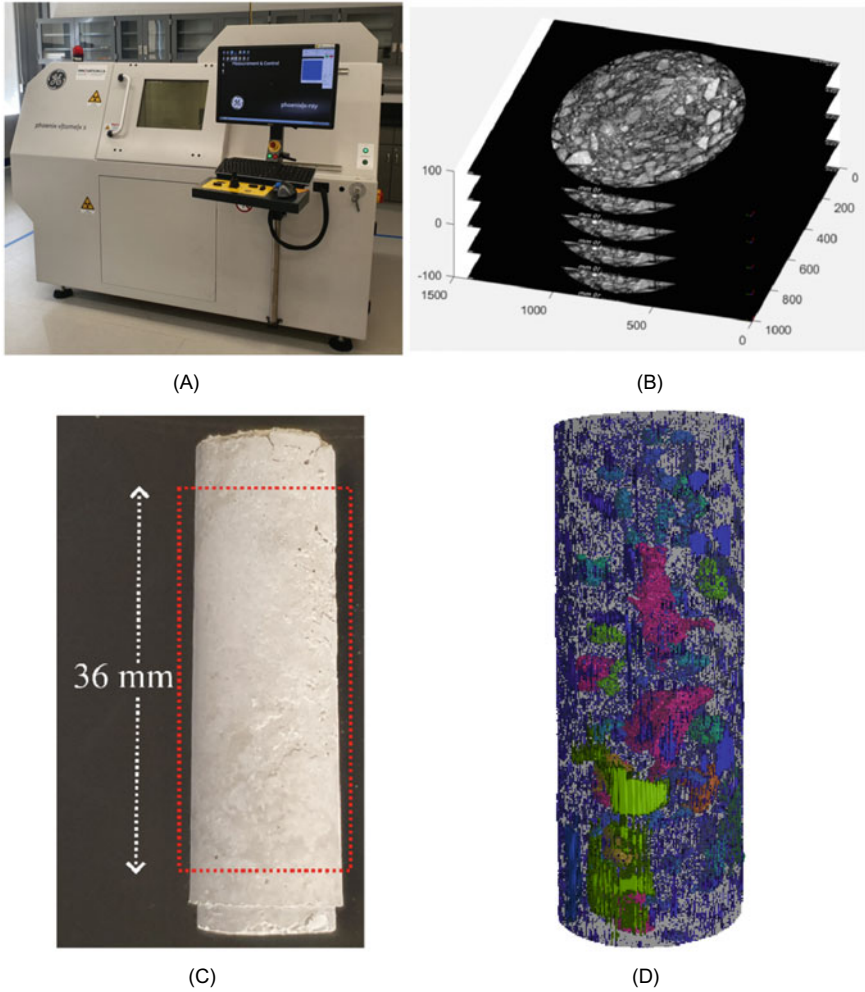
Fig. 3 **a** μCT imaging system, **b** 3D stacking of CT images [2], **c** Analyzed section of specimens, and **d** 3D reconstruction of internal pore structure [3]

## 3.2 Mass Measurement

The mass of the concrete specimens was measured before and after 40 and 80 freeze–thaw cycles using a high-precision scale ($\pm$ 0.01 g), as illustrated in Fig. 4. After applying 40 cycles, it was observed that the mass losses of the control, PS-5%, and PS-10% after 40 frost cycles were 4.35%, 5.06%, and 3.56%, respectively. On the other hand, specimens MS-5% and MS-10% experienced minor mass losses of about 0.78% and 0.95%, respectively. Thus, subjecting the concrete specimens to a potassium sulfate environment during the first 40 cycles had little effect on the
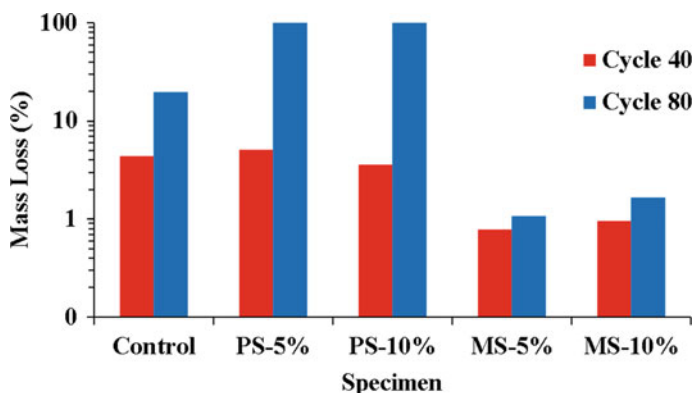
**Fig. 4** Frost-induced mass loss (%) of concrete specimens

frost damage, whereas the magnesium sulfate exposure mitigated the freeze–thaw damage. After 80 cycles, samples PS-5% and PS-10% were fully disintegrated, while the control specimen suffered a mass loss of 19.57%. In contrast, samples MS-5% and MS-10% experienced low mass losses of 1.08% and 1.67%, respectively, indicating an improved frost resistance. Therefore, it can be deduced that while subjecting concrete to potassium sulfate resulted in a delayed acceleration of frost damage, exposure to magnesium sulfate enhanced the concrete resistance to freeze–thaw damage, likely by reducing the concrete's permeability by filling its surface pores with sulfate by-products.

## 3.3 Porosity

The porosity of the concrete specimens was analyzed before and after applying the freeze–thaw cycles. It was found that the samples initially had comparable porosities with an average of 3.92% ($\pm$ 0.52%), as shown in Fig. 5. The porosities of samples PS-5%, PS-10%, and MS-10% increased to 5.29% (representing an increase of 0.89% from the initial porosity), 6.07% (an increase of + 1.48%), and 3.99% (an increase of + 0.77%), respectively, after 40 cycles. On the other hand, the control specimen and sample MS-5% experienced a comparable expansion of porosity with 4.22% (an increase of + 0.32%) and 3.86% (an increase of + 0.37%), respectively. After applying 80 freeze–thaw cycles, samples PS-5% and PS-10% were destroyed, while the porosities of specimens control, MS-5% and MS-10% increased to 13.89% (an increase of + 9.99%), 4.24% (an increase of + 0.75%), and 7.13% (an increase of + 3.91%), respectively. It is worth noting that the porosity expansion from cycle 40 to cycle 80 is much higher than the first 40 cycles because the freeze–thaw damage accelerates exponentially with more cycles [10]. Thus, subjecting concrete to potassium sulfate accelerated its frost damage even during the first 40 cycles,
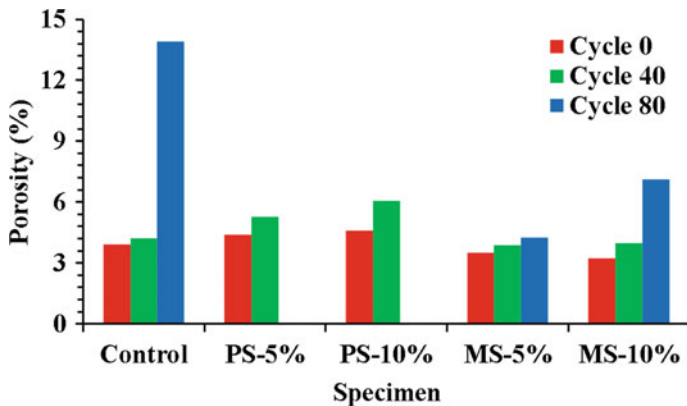
**Fig. 5** Concrete porosity before and after 40 and 80 freeze–thaw cycles

as indicated by the higher porosity expansion. In contrast, exposure to magnesium sulfate mitigated the freeze–thaw damage. Also, increasing the concentration of magnesium sulfate resulted in higher concrete damage.

## 3.4 Frost Damage Mechanisms

Specific two-dimensional sections of the concrete specimens were selected to monitor the mechanisms of the coupled sulfate and freeze–thaw damage throughout the applied freeze–thaw cycles, as demonstrated in Fig. 6. As illustrated, the concrete voids were colored based on the volume; thus, the largest and smallest pores were pink- and blue-colored, respectively. It was observed that the control specimen experienced minor pore expansion during the first 40 cycles and considerable scaling damage through the second 40 cycles, as indicated by the surrounding pink void in Fig. 6a. Also, samples PS-5% and PS-10% experienced similar damage mechanisms but at an accelerated rate, as shown in Fig. 6b and c. As a result, PS-5% and PS-10% suffered substantial scaling damage, represented by the pink-colored surface pores, within the first 40 cycles, and they were fully disintegrated as more cycles were applied. On the contrary, exposure to magnesium sulfate mitigated the frost damage and altered its typical mechanisms. Specimens MS-5% and MS-10% experienced considerable internal pore expansion in the first 40 cycles, after which minor scaling damage occurred in the following 40 cycles. It is worth noting that increasing the concentration of magnesium sulfate caused more frost damage, as demonstrated in Fig. 6d and e. Nonetheless, specimen MS-10% experienced minor and uniform scaling damage, unlike the control sample, which suffered harsh and localized damage. In conclusion, exposure to magnesium sulfate reduced the freeze–thaw damage and changed its mechanisms, whereas subjecting concrete to potassium sulfate accelerated the typical frost damage.
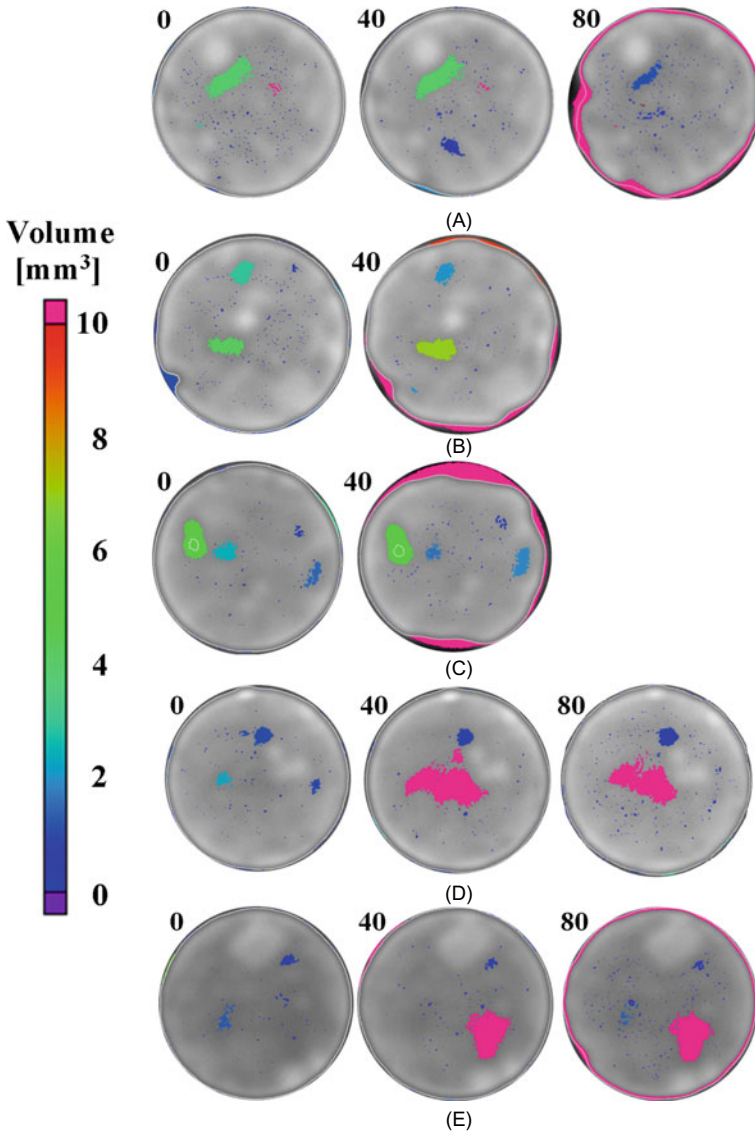
**Fig. 6** 2D sections of specimens **a** Control, **b** PS-5%, **c** PS-10%, **d** MS-5%, and **e** MS-10% before (left) and after 40 (middle) and 80 (right) frost cycles

## 4 Conclusions

Micro-computed tomography (μCT) was utilized to investigate the severity and mechanisms of the coupled sulfate and freeze–thaw damage of concrete, by analyzing its porosity expansion and monitoring the change of its internal microstructure

throughout the applied cycles. The mass loss data of the concrete specimens was also used to assess the severity of concrete damage, which matched well with the porosity expansion data. Based on the reported results, the following points were concluded.

- Micro-computed tomography ($\mu$CT) is a promising technology for investigating the microscale concrete damage and its mechanisms in a non-destructive manner.
- Subjecting concrete to potassium sulfate accelerated its frost damage without affecting its mechanisms, leading to severe scaling damage by cycle 40 and full disintegration by cycle 80.
- Exposure to magnesium sulfate substantially mitigated the freeze–thaw damage and altered its mechanisms, resulting in higher internal pore expansion and lower scaling damage.
- Higher concentrations of magnesium sulfate produced higher concrete damage. Nonetheless, the frost damage of the magnesium sulfate specimens was less severe and more uniform than the control sample.

# References

1. Adu-Amankwah S, Zajac M, Skoček J, Němeček J, Haha MB, Black L (2021) Combined influence of carbonation and leaching on freeze-thaw resistance of limestone ternary cement concrete. Constr Build Mater 307(November):125087. https://doi.org/10.1016/j.conbuildmat.2021.125087
2. Alhusain M, Al-Mayah A (2021) Three dimensional imaging of reinforcement corrosion using micro-computed tomography: literature review. Constr Build Mater 284(May):122813. https://doi.org/10.1016/j.conbuildmat.2021.122813
3. Alhusain M, Al-Mayah A (2022a) Three dimensional CT imaging analysis of concrete: effects of water and sand contents on pore characteristics. Springer.
4. Alhusain M (2022) Three-dimensional CT imaging and microstructural mechanical modeling of corrosion and freeze-thaw damage of concrete. UWSpace. https://hdl.handle.net/10012/18886
5. ASCE Infrastructure Report Card (2017) American Society of Civil Engineers (ASCE). https://www.infrastructurereportcard.org/wp-content/uploads/2016/10/2017-Infrastructure-Report-Card.pdf
6. Besheli E, Aref KS, Nejad FM, Darvishan E (2021) Improving concrete pavement performance in relation to combined effects of freeze-thaw cycles and de-icing salt. Constr Build Mater 277(March):122273. https://doi.org/10.1016/j.conbuildmat.2021.122273
7. Ince C, Shehata BMH, Derogar S, Ball RJ (2022) Towards the development of sustainable concrete incorporating waste tyre rubbers: a long-term study of physical, mechanical & durability properties and environmental impact. J Clean Prod 334(February):130223. https://doi.org/10.1016/j.jclepro.2021.130223

8. Jin S, Zheng G, Jing Y (2020) A micro freeze-thaw damage model of concrete with fractal dimension. Constr Build Mater 257(October):119434. https://doi.org/10.1016/j.conbuildmat.2020.119434

9. Kunther W, Lothenbach B, Scrivener K (2013) On the relevance of volume increase for the length changes of mortar bars in sulfate solutions. Cem Concr Res 46(April):23–29. https://doi.org/10.1016/j.cemconres.2013.01.002

10. Li Y, Li Y, Guan Z, Ding Q (2018) Elastic modulus damage model of cement mortar under salt freezing circumstance based on X-ray CT scanning. Constr Build Mater 191(December):1201–1209. https://doi.org/10.1016/j.conbuildmat.2018.10.097

11. Lu J, Zhu K, Tian L, Guo L (2017) Dynamic compressive strength of concrete damaged by fatigue loading and freeze-thaw cycling. Constr Build Mater 152(October):847–855. https://doi.org/10.1016/j.conbuildmat.2017.07.046

12. Maruyama I, Teramoto A (2011) Impact of time-dependant thermal expansion coefficient on the early-age volume changes in cement pastes. Cem Concr Res 41(4):380–391. https://doi.org/10.1016/j.cemconres.2011.01.003

13. Ren J, Lai Y (2021) Study on the durability and failure mechanism of concrete modified with nanoparticles and polypropylene fiber under freeze-thaw cycles and sulfate attack. Cold Reg Sci Technol 188(August):103301. https://doi.org/10.1016/j.coldregions.2021.103301

14. Sotiriadis K, Hlobil M, Viani A, Mácová P, Vopálenský M (2021) Physical-chemical-mechanical quantitative assessment of the microstructural evolution in portland-limestone cement pastes exposed to magnesium sulfate attack at low temperature. Cem Concr Res 149(November):106566. https://doi.org/10.1016/j.cemconres.2021.106566

15. Wu M, Zhang Y, Ji Y, She W, Yang L, Liu G (2020) A comparable study on the deterioration of limestone powder blended cement under sodium sulfate and magnesium sulfate attack at a low temperature. Constr Build Mater 243(May):118279. https://doi.org/10.1016/j.conbuildmat.2020.118279

16. Xiao QH, Cao ZY, Guan X, Li Q, Liu XL (2019) Damage to recycled concrete with different aggregate substitution rates from the coupled action of freeze-thaw cycles and sulfate attack. Constr Build Mater 221(October):74–83. https://doi.org/10.1016/j.conbuildmat.2019.06.060

17. Zeng Q, Li K, Fen-Chong T, Dangla P (2012) Effect of porosity on thermal expansion coefficient of cement pastes and mortars. Constr Build Mater 28(1):468–475. https://doi.org/10.1016/j.conbuildmat.2011.09.010

# Vacuum Mixed Concrete

**Mohamed Shahin, Omar Abdelmeguid, Ahmad El-Shantoury, Salma Ali, Hassan El Kassas, Reem Aboali, and Mohamed AbouZeid**

**Abstract** Vacuum mixing concrete results through the creation of a vacuum chamber by removing the air to introduce a vacuum medium through which concrete will be mixed. Mechanical and economic advantages as well as maintaining the well-being of the workers are amongst the advantages that can be expected from such concrete. In addition, this technique may reduce the mechanical effort needed to remove excessive bubbles within the concrete during the compaction stage. This may help in reducing resources and minimizing costs. The objective of this study is to explore the feasibility of producing vacuum mixed concrete by assessing its properties, and the environmental impact of its use in construction. To meet this objective, different concrete mixtures were produced using two w/c ratios: 0.40 and 0.55 while adjusting key parameters including the mixing time and the suction capacity. Fresh and hardened concrete tests as well as durability tests were introduced to evaluate the properties of the vacuum mixed concrete produced. Results reveal that vacuum mixed concrete can be produced using an adequate suction pump while adjusting parameters such as the pressure as well as the vacuum mixing time. Promising results in terms of enhancement of quality of such concrete are obtained which paves the floor for wider scale introduction for such concrete in concrete mixing plants and projects upon further validation and evaluation of these results.

## 1 Introduction

During the last few decades, the interest in high performance concrete has grown significantly where it is being used in a wide range of applications including high rise building, power plants, nuclear plants, etc. Therefore, in order to make a high-performance concrete, a good mixing procedure should be implemented. Thus, to obtain the desired properties of concrete, specific properties have to be monitored, such as mixing time, setting time, temperature, w/c ratio, viscosity. Moreover, the

M. Shahin (✉) · O. Abdelmeguid · A. El-Shantoury · S. Ali · H. El Kassas · R. Aboali · M. AbouZeid

Department of Construction Engineering, The American University in Cairo, New Cairo, Egypt
e-mail: Mohamed.yousri@aucegypt.edu

amount of entrapped air plays a vital role in the concrete's performance and monitoring the quality control of the concrete mix where fluctuations in the air content inside the concrete can affect the compressive strength as well as the workability of the concrete mix. In addition, if air bubbles accumulate on reinforcement bars, this can significantly affect the bond strength between the reinforcement and the surrounding concrete hence not having a strong passive layer, making the concrete less durable and more prone to corrosion attacks. Due to these undesirable effects, there have been several methods developed to reduce the amount of air bubbles, in which vacuum mixing concrete is one of them. Vacuum mixing concrete can be defined as the creation of a vacuum chamber by removing air to create a vacuum medium through which concrete will be mixed in. The vacuum mixing technology provides multiple advantages in the construction of any project. Vacuum mixing is considered a novel and significant process as it may enhance the mechanical properties as well as the durability of concrete without the addition of any supplementary admixtures. Mechanical and economic advantages as well as maintaining workers' well-being is amongst the advantages that can be obtained from vacuum mixing concrete. Amongst the advantages attained in the mechanical properties are: "an increase in compressive strength is measured. In addition, the bending tensile strength as well as splitting tensile strength increases. Furthermore, the modulus of elasticity improves" [1]. Also, this technique not only is predicted to enhance the concrete's mechanical properties, but also may save a lot of effort where it will not be necessary to compact the concrete as much on site since air bubbles will then be removed. This may help in reducing resources and minimizing costs. In addition, it reduces the curing time, making it very useful in fast-tracking projects. Besides this, it elevates the stiffness of concrete, hence, the removal of formwork may become much easier than that of the conventional concrete.

## 2 Literature Review

High-performance concrete has been one of the greatest evolutions in the construction industry in which conventional concrete is no longer common in today's industry. Furthermore, a lot of research and development has been performed in this field to explore the boundaries of new concrete types including steel fiber reinforced concrete, self-compacting concrete, self-cleaning concrete, etc. However, vacuum mixed concrete may be an alternative way for improving concrete's performance. Moreover, profound research is necessary in this area since little is known about this topic. Therefore, this study aims at testing this technique's influence on the concrete's mechanical properties, impacts related to workers' well-being, economic impacts, and environmental impacts. Regarding the mechanical properties, it is said that it is expected to have an increase in concrete's compressive strength, bending tensile strength, and splitting tensile strength [1]. For the workers well-being, it is known that cement comprises certain types of chemicals as well as lime and silica where excessive exposure to cement dust can cause respiratory disorders as well as pathogenesis, allergy, and different health complications [2]. According to a study

conducted by Rahmani et al., which assesses the health and well-being of workers exposed to cement dust for long times, it concluded that "long-term cement dust exposure and inhalation causes respiratory complications due to epithelial tissue damage and that can lead to secondary complications as well" [2]. Also, "workers lungs can be affected from the constant inhalation of cement dust. This can develop into a life-threatening problem such as lung cancer or silicosis" [3]. For the economic impacts, vacuum mixing concrete may reduce the need for more labors on site, require less supervision, and eliminate the need for using compactors compared to conventional concrete. For the environmental impacts, removing cement dust reduces the probability of workers and surrounding people from developing respiratory diseases, making it environmentally friendly as a whole [4]. Therefore, vacuum mixing concrete could potentially be one way to preserve and protect the worker's health and well-being. Some critiques might say that self-compacting concrete can do the same job that the vacuum mixing concrete can do if not better. However, if we look closely to the self-compacting concrete, its main disadvantages encountered are the following:

- "The mechanical properties (compressive strength, flexural tensile strength, dynamic modulus of elasticity) of the tested (self-compacted) concretes generally decreased with the rise in temperature" [5]. This is a problem that SCC has that is handled by the vacuum mixed concrete.
- Self-compacting concrete requires the use of both viscosity modifying admixtures (VMA) to be self-compacted and the use of mineral admixtures to be highly durable and impermeable which vacuum mixed concrete does not require.
- Self-compacting concrete is said to have increased formwork costs due to the higher formwork pressures, and also requires an increased technical expertise to develop and control the admixtures [6]. However, vacuum concrete achieves high strength, eliminates the use of admixtures and compactors, minimizes the need for experts and supervision, and does not require additional formwork costs.

In addition, as discussed previously, vacuum mixing technology sucks the cement dust, making it less harmful to the surrounding people and the environment as a whole. Finally, it is found that "plastic shrinkage crack may occur due to the low water cement ratio [concrete mixtures]"; however, this problem is resolved through curing. While in the vacuum mixing, curing time is also reduced. There are various challenges that are expected to be encountered. Even though concrete vacuum mixers are available worldwide, they are not available currently in Egypt. Therefore, our team is planning on crafting our own concrete vacuum mixer. Moreover, it will be challenging to place the concrete in a vacuumed medium for the vacuum mixing technique to work. Thus, the following are required to be procured in advance: a suction pump, tube to exhaust the air, a chamber to place the concrete mix in, and a gauge to determine the pressure inside the chamber. Moreover, to craft the mold in which the concrete will be mixed in that will be able to sustain the vacuum medium, a steel worker is required so that all openings in the mold are sealed through which air cannot enter and disturb the vacuum environment.

## 3    Objective and Scope

In this research, the main objective is to explore the feasibility of producing vacuum mixed concrete with local materials by assessing its properties, and its environmental impact when used in construction. The objective was obtained through producing several concrete mixes of different w/c ratios under different vacuum conditions, where the fresh and hardened concrete properties, durability, economic, and environmental impact were assessed.

## 4    Experimental Program

### 4.1    Material Properties

- Cement: Type I Ordinary Portland Cement and White Ordinary Portland Cement
- Fine Aggregates: Natural sand
- Coarse Aggregates: Well graded coarse aggregates
- Water: Ordinary tap water was utilized in the concrete mix and for curing the concrete.

### 4.2    Concrete Mix Design and Testing Parameters

Tests were conducted over ten samples. Mixes 1 and 2 are control mixes that were not subjected to any suction, whereas mixes 3–10 were mixed under vacuum conditions. The vacuum effect on concrete was tested on two water-to-cement ratios; the 0.55 w/c ratio being the common concrete mix in Egypt and 0.40 w/c ratio to investigate the vacuum effect on a dryer mix. In order to measure the effectiveness of the vacuum mixed concrete, different key parameters have to be examined, from which different vacuum mixes are deduced and will be tested accordingly. The key parameters are mixing time (how long we are going to mix the concrete for while vacuumed) and suction capacity. Regarding the mixing time, conventionally, concrete is mixed for around 5 mins. Based on that convention, the vacuum short time was defined to be 5 mins. Accordingly, the vacuum long time was defined to be double the short time to be around 10 mins. Moving on to our second key parameter, the suction capacity, some data were obtained prior to the pump suction capacity calculation. These data include the mixer volume which was equal to $1/6\,m^3$. Based on certain calculations, the final pump specifications were calculated as follows: Required pump capacity = 1 hp and Pump rotational speed = 3000 rpm. Based on the pump rotational speed, the equivalent inverter frequency 50 Hz. Using the same analogy implemented for the vacuum short and long time and based on experimentation on an empty mixer, high vacuum was defined to 50 Hz while low vacuum was defined to 35 Hz. Therefore,

**Table 1** Concrete mixes

| Mix | Type | w/c ratio | Suction capacity | Pressure (bar) | Mixing time (min) |
|---|---|---|---|---|---|
| 1 | Control | 0.40 | – | – | 5 |
| 2 | Control | 0.55 | – | – | 5 |
| 3 | Vacuum | 0.40 | High | − 0.78 | 5 |
| 4 | Vacuum | 0.40 | High | − 0.72 | 10 |
| 5 | Vacuum | 0.40 | Low | − 0.44 | 5 |
| 6 | Vacuum | 0.40 | Low | − 0.32 | 10 |
| 7 | Vacuum | 0.55 | High | − 0.44 | 5 |
| 8 | Vacuum | 0.55 | High | − 0.30 | 10 |
| 9 | Vacuum | 0.55 | Low | − 0.34 | 5 |
| 10 | Vacuum | 0.55 | Low | − 0.44 | 10 |

**Table 2** Concrete mix design

| w/c ratio | Cement ($kg/m^3$) | Coarse aggregate ($kg/m^3$) | Fine aggregate ($kg/m^3$) | Water ($kg/m^3$) |
|---|---|---|---|---|
| 0.40 | 438 | 1120 | 655 | 175 |
| 0.55 | 319 | 1120 | 752 | 175 |

after defining the different key parameters, the concrete mixes are determined to be as follows:

- For each type of concrete mix, both the vacuum mixed and conventional concrete, 0.40 and 0.55 w/c ratio mixes are to be tested.
- For each vacuum mix, whether 0.40 or 0.55, both a high vacuum and a low vacuum medium mix are to be tested.
- Coarse Aggregates: Well graded coarse aggregates.
- For each vacuum medium, whether high or low vacuum, both long time and short time vacuum mixes are to be tested.

See Table 1 for the concrete mixes to be tested and Table 2 for the concrete mix designs.

## 4.3 Tests

### 4.3.1 Fresh Concrete Tests

*Temperature*: This test is conducted to ensure the concrete's conformity with standard temperature specifications according to [ASTM C1064] [7].

*Slump*: This test is conducted to check the workability of the fresh concrete according to [ASTM C143-78] [8].

*Air Content*: This test is conducted to determine the air content of the concrete according to [ASTM C231] [9].

*Unit Weight*: This test is conducted to determine the unit weight of the concrete according to [ASTM C138] [10].

### 4.3.2 Hardened Concrete Tests

*Compressive Strength*: This test is conducted to evaluate the concrete's strength of a 150 mm * 150 mm * 150 mm cube at 3, 7 and 28 days according to the [ASTM C109] [11].

*Splitting Tensile Strength*: This test is conducted to evaluate the concrete's strength of a 300 mm * 150 mm cylinder at 28 days according to the [ASTM C496] [12].

*Microscopic Examination*: This test was used to examine the micro-structure of the concrete, highlighting the void size and number. The scanning electron microscope uses a beam of high-energy electrons emitted on a solid specimen, which helps display the structure using magnification with a range of 20X to 1000X [ASTM E986—SEM] [13].

### 4.3.3 Durability/Permeability

*Chemical Durability*: This test was done by immersing the concrete into a 10% concentration of sulfuric acid to assess the durability of concrete [ASTM C267-20] [14].

*Rapid Chloride Permeability*: This test was used to rapidly assess the durability of concrete, specifically its resistance against chloride ion penetrability [ASTM C1202] [15].

## 4.4 Results and Analysis

### 4.4.1 Fresh Concrete

*Temperature*: The obtained temperature results projected that the vacuum medium creation did not result in the increase/decrease of the temperature of the mixes. The concrete mix that experienced the highest temperature was found to be mix 7 while the concrete mix experiencing the lowest concrete temperature was found to be mix 4.

*Slump*: The slump range varied from 15 to 65 mm in the 0.40 w/c ratio mixes (low-acceptable workability), while the range varied from 35–85 mm in the 0.55 w/c ratio

**Table 3** Fresh concrete test results

| Mix | Slump (mm) | Air content (%) | Temperature (°C) | Unit weight (kg/m$^3$) |
|---|---|---|---|---|
| 1 | 20 | 5 | 28 | 2390 |
| 2 | 35 | 4 | 27.4 | 2237 |
| 3 | 5 | 1.5 | 27.6 | 2424 |
| 4 | 25 | 2.5 | 26.3 | 2420 |
| 5 | 65 | 3 | 27.2 | 2419 |
| 6 | 60 | 3 | 29.3 | 2433 |
| 7 | 70 | 2.5 | 29.5 | 2421 |
| 8 | 85 | 3.5 | 28.5 | 2421 |
| 9 | 70 | 3 | 28.5 | 2404 |
| 10 | 75 | 3 | 28 | 2390 |

mixes. (acceptable workability). The results illustrate that the mix with the highest workability was mix 8 while the mix with the lowest workability was found to be mix 3.

*Air Content*: All of the vacuum mixes recorded lower air content percentages than the control mixes which indicates a direct relation between applying vacuum conditions and the air content percentage in the concrete mixes. For the 0.40 w/c ratio mixes, the air content ranged from 1.5 to 5%, where the lowest air content percentage was recorded for mix 3. This corresponds to the highest negative pressure reached in this w/c ratio (− 0.78 bar). The highest air content percentage was recorded for mix 4 (2.5%) which corresponds to the lowest negative pressure reached in this mix design (− 0.32 bar). As for the 0.55 w/c ratio mixes, the air content ranged from 2.5 to 4% with mix 7 yielding the lowest air content percentage. This also corresponds to the lowest negative pressure reached in this mix design (− 0.44 bar). The highest air content percentage (3.5%) was recorded for mix 8 which corresponds to the lowest negative pressure reached (− 0.3 bar).

*Unit Weight*: The mix with the highest unit weight was found to be mix 6 with 2433 kg/m$^3$, while the mix with the lowest unit weight was found to be mix 2 with 2237 kg/m$^3$.

See Table 3 for the fresh concrete test results.

### 4.4.2 Hardened Concrete

*Compressive Strength*: The compressive strength test results are illustrated in Figs. 1 and 2. The compressive strength test was implemented to validate the hypothesis of the enhanced compressive strength of the concrete due to mixing the concrete in a vacuum medium. Regarding the 0.40 w/c ratio, the compressive strength at day 3

**(a)** Compressive Strength Results (0.40 w/c Mixes)          **(b)** Compressive Strength Results (0.55 w/c Mixes)
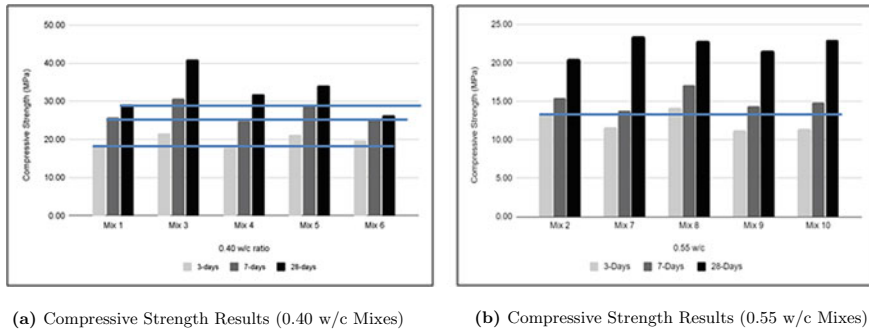
**Fig. 1** Two images that show the results of the compressive strength. **a** Shows the compressive strength results for 0.40 w/c mixes while, **b** shows the results of the compressive strength results for the 0.55 w/c mixes

for the vacuum mixes (mixes 3, 5, 6) exceeded the conventional mix which stands at 18.48 MPa except for mix 4 which fell short standing at 17.77 MPa. Furthermore, the compressive strength at day 7 had a similar behavior in which all vacuum mixes (mixes 3, 5, 6) exceeded the conventional mix which stands at 25.78 MPa except for mix 4 which fell short again standing at 24.86 MPa. Lastly, at day 28, the behavior of the compressive strengths took a slightly different turn where all vacuum mixes (3, 4, 5) exceeded the conventional mix standing at 29.17 MPa; however, mix 6, which was ahead at days 3 and 7, unexpectedly yielded compressive strength lower than conventional mix standing at 26.40 MPa. On the other hand, mix 4, which was slightly lower than the conventional mix at 3 and 7 days, surprisingly managed to overtake the conventional mix at day 28 with a compressive strength of 31.89 MPa. Overall, amongst the 0.40 w/c ratio mixes, mix 3 had the highest compressive strengths at days 3,7, and 28 while the mixes with the lowest compressive strengths at days 3,7, and 28 were mix 4, mix 4, and mix 6, respectively. Regarding the 0.55 w/c ratio, the compressive strength at 3 days for vacuum mix 8 was the only vacuum mix that was greater than the conventional mix standing at 13.44 MPa. In addition, the rest of the vacuum mixes (mixes 7, 9, 10) had a compressive strength lower than the conventional yielding 11.58, 11.15, and 11.32 MPa, respectively. Furthermore, the compressive strength at day 7 had a similar behavior in which all vacuum mixes (mixes 7, 9, 10) standing at 13.82, 14.41, and 14.92, respectively, were lower than the conventional mix which stands at 15.51 MPa with the exception of mix 8 which yielded a higher compressive strength than conventional at 17.15 MPa. Lastly, at day 28, unexpectedly, all vacuum mixes (mixes 7, 8, 9, 10) which yielded 23.36, 22.77, 21.5, and 23 MPa, respectively, including those that were lower than conventional at days 3 and 7, had a higher compressive strength than conventional standing at 20.43 MPa. Overall, amongst the 0.55 w/c ratio mixes, the mixes with the highest compressive strengths at days 3, 7, and 28 were mix 8, mix 8, and mix 7, respectively, while the mixes with the lowest compressive strengths at days 3,7, and 28 were mix 9, mix 7, and the conventional mix, respectively.

**(a)** Splitting Tensile Strength Results (0.40 w/c Mixes)

**(b)** Splitting Tensile Strength Results (0.55 w/c Mixes)
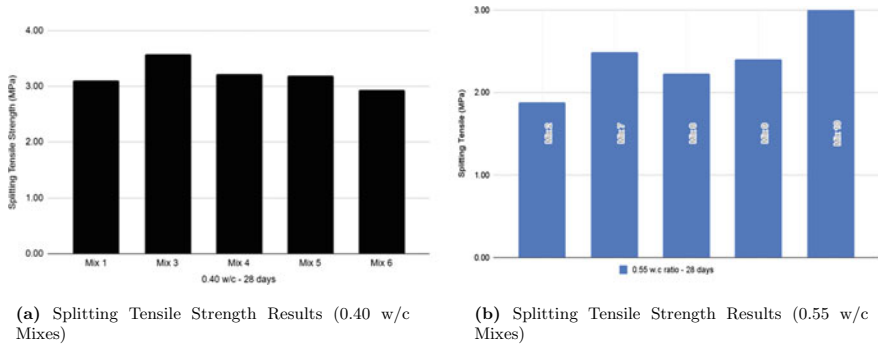
**Fig. 2** Two images that show the results of the splitting tensile strength results. **a** Shows the splitting tensile strength results for 0.40 w/c mixes while, **b** shows the results of the splitting tensile strength results for the 0.55 w/c mixes

See Fig. 1 for the compressive strength test results for the 0.40 w/c mixes and Fig. 2 for the compressive strength test results for the 0.55 w/c mixes.

*Splitting Tensile*: The splitting tensile strength was conducted at day 28 for all 10 mixes. Regarding the 0.40 w/c ratio mixes, it ranged from 2.93 to 3.58 MPa, where mix 3 recorded the highest value while mix 5 yielded the lowest value. All mixes yielded higher results than the control mix (mix 1) except for mix 5 as shown in Fig. 3. Regarding the 0.55 w/c ratio, all the vacuum mixes yielded higher splitting tensile strengths than the control mix (mix 2). Values for the vacuum mixes ranged from 2.22 to 3 MPa as shown in Fig. 4, where mix 10 recorded the highest value. It may be misperceived that mix 10 had the highest splitting tensile strength; however, this may be explained as it reached the highest negative pressure in the 0.55 w/c ratio category. Lastly, a relation can be drawn between the pressure and the splitting tensile strength.

See Fig. 2a for the splitting tensile strength test results for the 0.40 w/c mixes and Fig. 2b for the splitting tensile strength test results for the 0.55 w/c mixes.

*Microscopic Examination (SEM Test)*: Results show that the vacuum mixing technology has a direct effect on the average void size of all the mixes. This is clear as both conventional mixes had the highest average void sizes with 234.8 μm and 294 μm for mixes 1 and 2, respectively, whereas variation takes place in the average diameters of voids in vacuum mixes while maintaining much smaller values than the former ones. For the mixes with 0.40 w/c ratio, mix 5 had the lowest value, however, it was considered to be an outlier as it was out of range compared to the other mixes. Therefore, this sample was not considered in further analysis making Mix 3 the one with the lowest average void size. This corresponded to the highest vacuum pressure reached which was − 0.78 bars. In addition, mix 6 had the second lowest average void size of 92.46 μm which corresponds to the second highest negative pressure of − 0.72 bars. Both of these mixes were subjected to high vacuum conditions. For the 0.55 w/c ratio, mix 7 recorded the lowest average void size of 115.29 μm which

**Table 4** Hardened concrete test results (0.40 w/c)

| Mix | Compressive strength 3 days (MPa) | Compressive strength 7 days (MPa) | Compressive strength 28 days (MPa) | Splitting tensile strength 28 days (MPa) | Microscopic examination— average void size (μm) |
|---|---|---|---|---|---|
| 1 | 18.5 | 25.8 | 29.2 | 3.1 | 234.98 |
| 3 | 21.5 | 30.7 | 41.0 | 3.6 | 86.33 |
| 4 | 17.8 | 24.9 | 31.9 | 3.2 | 116.70 |
| 5 | 21.1 | 28.6 | 34.1 | 2.9 | 36.20 |
| 6 | 19.7 | 25.2 | 26.4 | 3.2 | 92.46 |

**Table 5** Hardened concrete test results (0.55 w/c)

| Mix | Compressive strength 3 days (MPa) | Compressive strength 7 days (MPa) | Compressive strength 28 days (MPa) | Splitting tensile strength 28 days (MPa) | Microscopic examination— average void size (μm) |
|---|---|---|---|---|---|
| 2 | 13.4 | 15.5 | 20.4 | 1.9 | 294.00 |
| 7 | 11.6 | 13.8 | 23.4 | 2.5 | 115.29 |
| 8 | 14.1 | 17.1 | 22.8 | 2.2 | 226.75 |
| 9 | 11.2 | 14.4 | 21.5 | 2.4 | 124.00 |
| 10 | 11.3 | 14.9 | 23.0 | 3.0 | 121.65 |

corresponds to a negative pressure of $-0.44$ bars. Mix 8, on the other hand, had the largest average void size in all the vacuum mixes with a value of 226.75 μm which corresponds to the lowest negative pressure attained which was $-0.3$ bars. From the data attained, it is clear that for both w/c ratios, the mixes which were subjected to high vacuum conditions for a shorter mixing time yielded the lowest values for average void size. Also, for mixes with the same w/c ratio and suction capacities, subjecting the mixes to longer mixing times resulted in attaining lower negative pressures as well as larger averages for void size.

See Table 4 for the hardened concrete test results for the 0.40 w/c mixes and Table 5 for the hardened concrete test results for the 0.55 w/c mixes.

### 4.4.3  Durability/Permeability

*RCPT*: As a general trend, it can be deduced that vacuum mixes are less permeable than the control mixes as they recorded lower numbers of coulombs passed. Regarding the 0.40 w/c ratio, mix 1 (control mix) passed the 5345 coulombs, which corresponds to a high permeability class. Mix 3 passed 1504 coulombs, which is the least of all. While, the other vacuum mixes were classified to be moderately permeable. Regarding the 0.55 w/c ratio, the control mix (mix 2) also recorded the highest

**Table 6** Chemical durability and permeability results (0.40 w/c ratio mixes)

| Mix | Chemical durability (sulfuric acid immersion 1 week)—% mass weight loss | Permeability (RCPT)—coulombs passed |
| --- | --- | --- |
| 1 | 10.7 | 5345 |
| 3 | 7.6 | 1504 |
| 4 | 8.5 | 2809 |
| 5 | 6.8 | 3122 |
| 6 | 7.2 | 3167 |

**Table 7** Chemical durability and permeability results (0.55 w/c ratio mixes)

| Mix | Chemical durability (sulfuric acid immersion 1 week)—% mass weight loss | Permeability (RCPT)—coulombs passed |
| --- | --- | --- |
| 2 | 22.6 | 5458 |
| 7 | 4.7 | 3342 |
| 8 | 5.6 | 4103 |
| 9 | 4.6 | 3504 |
| 10 | 9.7 | 4232 |

number of coulombs passed (5458 coulombs) which is classified as high permeability. On the other hand, the permeability classes of the vacuum mixes varied between moderate and high with mix 7 recording the lowest permeability in thus mix design (3342 coulombs passed). Lastly, these results can be correlated with the microscopic examination results as both the average void size and the permeability decrease.

*Durability*: The samples were immersed in a concentration of 10% sulfuric acid for one week. Generally, the vacuum mixed samples are more durable than the conjugate control samples for both w/c ratios. Regarding the 0.40 w/c ratio, the control sample experienced a mass loss of 10.7% while the vacuum mixes experienced a less percentage of mass loss, which ranged from 6.8 to 8.5%. Regarding the 0.55 w/c ratio, the control sample experienced a 22% mass loss while the vacuum mixes experienced a less percentage of mass loss ranging from 4.7 to 9.7%.

See Table 6 for the chemical durability and permeability results for the 0.40 w/c mixes and Table 7 for the chemical durability and permeability results for the 0.55 w/c mixes.

## 4.5  Analysis

*Strength Development Factor*: As mentioned previously in the compressive strength for 0.40 w/c ratio, mix 4 initially had a lower compressive strength compared to the conventional mix at days 3 and 7. After that, mix 4 at day 28 had a larger compressive strength than conventional mix at day 28. This sudden increase in strength was due to the increase in the development strength that can be best represented by the strength development factor shown below.

The strength development factor was simply calculated by taking the compressive strength at 28 days to be the reference in relation to the 3 and 7 days. In other words, the ratio was performed for the compressive strength at day 28 over day 7, and at day 28 over day 3. In addition, the compressive strength of 7 days relative to the 3 days was also calculated. Looking at the table above, the strength development factor for conventional concrete for 28/3 days was 1.58 and for 28/7 was 1.13. Looking at mix 4, for the 28/3 development factor, it was higher than the conventional mix (mix 1) where it yielded to be 1.79. Thus, it can be deduced that the strength development of mix 4 was higher from day 7 to day 28 leading mix 4 at day 28 to have a higher compressive strength compared to the conventional mix. However, regarding the strength development from day 3 to day 7, both mixes 1 and 4 had the same development factor which was 1.40. Thus, it can be deduced that the strength development of mix 4 was low from day 3 to day 7 leading mix 4 at day 7 to have a lower compressive strength compared to the conventional mix since both developed strength at the same rate while mix 4 had a compressive strength. Therefore, the following was deduced: for lower w/c ratio, mixes are much drier and hence have much lower moisture contents making the choice of the mixing times as well as the difference in intervals between the short mixing time and the long mixing time have a much higher impact on compressive strength compared to higher w/c ratios, which has a minimal effect on it.

Regarding the 0.55 w/c ratio mixes, as mentioned previously, mix 8 was the standout mix at days 3 and 7 where it was the only mix to exceed the compressive strength of the conventional mix. However, at day 28, all vacuum mixes, including those that were lower than conventional mix at days 3 and 7, had a higher compressive strength than conventional mix. This behavior can also be best interpreted due to the variant strength developments. For the 7/3 days, even though at days 3 and 7 all vacuum mixes had a lower compressive strength than the conventional, examining the behavior of how the compressive strength started at day 3 and how it ended up being at day 7 explains this irregularity. For instance, taking the example of mix 9, it started out at day 3 with a compressive strength of about 11.16 MPa compared to the conventional mix having 13.44 MPa (difference in strength is 2.28 MPa). However, looking at day 7, the compressive strength of mix 9 was 14.41 MPa (3.25 MPa gain in strength) whereas the compressive strength of the conventional mix was 15.51 MPa (difference in strength is 2.07 MPa which was less than 2.28 MPa of mix 9). Therefore, the gain in strength was higher in mix 9 than conventional mix; however, it was not enough to surpass the conventional mix's strength at day

**Table 8** Strength development factors (0.40 w/c ratio mixes)

| Mix | 28/7 days | 28/3 days |
|---|---|---|
| Mix 1 | 1.13 | 1.58 |
| Mix 3 | 1.33 | 1.91 |
| Mix 4 | 1.28 | 1.79 |
| Mix 5 | 1.19 | 1.61 |
| Mix 6 | 1.05 | 1.34 |

**Table 9** Strength development factors (0.55 w/c ratio mixes)

| Mix | 28/7 days | 28/3 days |
|---|---|---|
| Mix 2 | 1.32 | 1.52 |
| Mix 7 | 1.69 | 2.02 |
| Mix 8 | 1.33 | 1.62 |
| Mix 9 | 1.49 | 1.93 |
| Mix 10 | 1.54 | 2.03 |

7. The same was the case with all vacuum mixes except for mix 8 which surpassed the conventional mix at days 3,7, and 28. Delving more into the data, at day 28, the strength development of all vacuum mixes, mixes 7,8,9, and 10 being 2.02, 1.62, 1.93, and 2.03, respectively, was so much higher than the conventional concrete mix that the strength development factor 28/3 days for all vacuum mixes was higher by a good portion than conventional mix which was 1.52. This indicates that the strength development has somewhat accelerated for the vacuum mixes compared to the conventional concrete toward the end.

See Table 8 for the strength development factor for the 0.40 w/c mixes and Table 9 for the strength development factor for the 0.55 w/c mixes.

*Effect of w/c Ratio on Mixing Time*: As shown above, these are the parameters (i.e., compressive strength, splitting tensile, etc.) that were under scrutiny for the 0.40 w/c ratio as well as the 0.55 w/c ratio. For the 0.55 w/c ratio, closely examining mix 7 and mix 10, they yielded the same pressure and having almost the same results in all of the parameters even though mix 10 is exposed to the vacuum medium for a long time while mix 7 is exposed to the vacuum medium for a short time. On the other hand, regarding the 0.40 w/c ratio, closely monitoring mixes 3 and 4 which were in a similar situation to mixes 7 and 10 of 0.55 w/c ratio where they had almost the same results in all parameters with the exception that mix 4 which was exposed to the vacuum medium longer than mix 3. This resulted in a difference in compressive strength of about 9.1 MPa where mix 3 had a compressive strength of 41.0 MPa while mix 3 had a compressive strength of about 31.9 MPa. However, for mixes 7 and 10 of 0.55 w/c ratio, this was not the case as they had a difference in compressive strength of about 0.6 MPa where mix 7 yielded a compressive strength of about 23.4 MPa while mix 10 yielded a compressive strength of about 23 MPa. For the 0.40 w/c ratio,

which is considered a low w/c ratio, they take much less time to dry while mixing as they have lower water content compared to the 0.55 w/c ratio, which is considered a high w/c ratio, meaning that they take much longer time to dry while mixing as they have high-water content compared to the 0.4 w/c ratio. Therefore, since a small interval of time between the long and short time was chosen (5 mins for short and 10 mins for long) and knowing the nature of 0.40 w/c ratio having low water content and hence requiring much less time to dry up compared to the 0.55 w/c ratio, this difference in time interval was significant where mixing the 0.40 w/c ratio for a long time caused the mix to become drier in the mixer while under the vacuum medium hence leading to more air voids to be introduced, making the vacuum medium non-effective since air voids cannot be removed as it is no longer fresh leading to larger complications to be introduced to the mix such as honeycombing hence yielding a much lower compressive strength. On the other hand, for the 0.55 w/c ratio, since it is a high-water content mix and the mixing times, both long and short, are not that much to make the mix dry hence leading to having a non-dry mix in both cases and hence yielding a much lower negative impact on compressive strength. Therefore, it can be concluded that for lower w/c ratio, mixes are much drier and have much lower moisture contents hence the choice of the mixing times as well as the difference in intervals between the short mixing time and the long mixing time has a much higher impact on compressive strength compared to higher w/c ratios, which has a minimal effect on it.

## 5   Conclusion

In conclusion, it can be drawn that the optimum conditions of vacuum mixed concrete are reached in a short duration under high vacuum conditions; this is supported by mixes 3 and 7 which attained the highest pressure. In addition, these mixes had the lowest average void size, and consequently, the highest compressive strength. As the average void size decrease, the bond increases allowing the concrete to yield a higher compressive strength.

After experimentation, reporting, and analysis of the data at hand, the following conclusive remarks were deduced:

The trends discovered were as follows:

- Generally, the effect of the mixing concrete in a vacuum medium, regardless of the w/c ratio, resulted in improvement in concrete's mechanical properties.
- The best mix in terms of highest compressive strength, lowest air content, highest splitting tensile strength, and least permeable was found to be mix 3 (0.40 high vacuum short time).
- For concrete mixes mixed under vacuum medium, higher pressures yielded lower average voids sizes as well as lower air content percentages. In conclusion, the results and the analysis of the data in hand all point to the direction of having optimum mixing conditions of the highest pressure in the shortest mixing time

possible while considering the w/c ratio would yield the best concrete mix for a constant mixing capacity.

## 6 Recommendations

We recommend future work and research to include the following:

- Different w/c ratios.
- Different pump capacities.
- Different cement types.
- Dust quantification and reuse of dust in concrete.
- Examine a more detailed economic aspect with respect to conventional concrete technology.

We recommend future researchers to:

- Consider conducting a wider scale of work with this technology in the future.
- Attempt to combine different concreting technologies as well as the combination of different admixtures and see its impact on concrete.

If considered to be implemented on a large scale such as in batch plants, it is recommended to use a ready-made vacuum mixer with a concrete pump to pour the concrete.

## References

1. Dils J, Boel V, De Schutter G (2015) Vacuum mixing technology to improve the mechanical properties of ultra-high performance concrete. Mater Struct 48:3485–3501
2. Rahmani AH, Almatroudi A, Babiker AY, Khan AA, Alsahly MA (2018) Effect of exposure to cement dust among the workers: an evaluation of health related complications. Open Access Macedonian J Med Sci 6:1159–1162
3. Cutforth P (2012) Dangers of concrete mixing on building sites. Whitecard Australia 1
4. Sikra S (2017) How does construction impact the environment? Go Contractor 1
5. Benzaid M, Benmarce A (2017) Behaviour of self compacting concrete mixed with different additions at high-temperature. J Mater Environ Sci 8:3081–3092

6. Koehler EP, Fowler DW, Foley EH, Rogers GJ, Watanachet S, Jung M (2007) Self-consolidating concrete for precast structural applications: mixture proportions, workability, and early-age hardened properties
7. C1064, A (2017) Standard test method for temperature of freshly mixed hydraulic cement concrete. ASTM Int 1
8. C143-78, A (2017) Standard test method for slump of Portland cement concrete. ASTM Int 1
9. C231, A (2010) Standard test method for air content of freshly mixed concrete by the pressure method. ASTM Int 1
10. C138, A (2017) Standard test method for density (unit weight), yield, and air content (gravimetric) of concrete. ASTM Int 1
11. C109, A (2020) Standard test method for compressive strength of hydraulic cement mortars (using 2-in. or [50-mm] cube specimens). ASTM Int 1
12. C496, A (2017) Standard test method for splitting tensile strength of cylindrical concrete specimens. ASTM Int 1
13. SEM, A. E. (2017) Standard practice for scanning electron microscope beam size characterization. ASTM Int 1
14. C267-20, A (2020) Standard test methods for chemical resistance of mortars, grouts, and monolithic surfacings and polymer concretes. ASTM Int 1
15. C1202, A (2021) Standard test method for electrical indication of concrete's ability to resist chloride ion penetration. ASTM Int 1

# An Appraisal of Hydroplaning Pavement Surface Improvement Materials and Assessment Models

**Faria Raha, Armana Huq, and Zarrin Probha**

**Abstract** Wet pavement has always been a significant safety concern due to the rise in wet weather accidents. Each year, 70% of weather-related crashes happen on wet roads and 46% occur during precipitation. The reduced skid resistance and hydroplaning are two major challenges occurring in the wet pavement due to lack of surface friction. Curves, highways, intersections, single carriageway pathways, and four or higher-lane roads are more likely to experience hydroplaning and wet weather-related crashes. Previous studies suggest that the wet weather accident rate could be reduced by up to 70% by improving friction. This paper reviews the effectiveness of surface improvement materials, e.g., superhydrophobic materials, groove-filled pavement, etc. presented in recent papers to reduce the water film thickness and achieve suitable pavement friction properties. Previous review papers discuss the traditional empirical hydroplaning assessment models, such as the PAVDRN model, Gallaway model, etc., while few studies review the numerical models. In this paper, the traditional empirical and numerical models along with newly proposed hydroplaning models are discussed with references.

**Keywords** Pavement materials · Hydroplaning · Surface condition · Models · Safety

## 1 Introduction

Weather-related crashes refer to accidents that happen in inclement weather (such as rain, sleet, snow, fog, strong crosswinds, blowing snow, sand, or debris) or when the road surface is slippery (e.g., wet pavement, snowy pavement, or icy pavement). The 10-year averages from 2007 to 2016 of the NHTSA data revealed that there are typically more than 5,891,000 vehicle accidents annually. About 21% of these crashes are related to weather [6]. Every year, weather-related crashes result in more

F. Raha · A. Huq (✉) · Z. Probha
Bangladesh University of Engineering and Technology (BUET), Dhaka, Bangladesh
e-mail: ahuq002@fiu.edu

than 418,000 injuries and close to 5000 fatalities. 70% of these crashes happen on wet roads and 46% occur during precipitation [6]. The level of friction on the pavement is reduced in wet condition, and this can lead to skidding or hydroplaning. Wet weather crashes on highways caused by hydroplaning and reduced skid resistance have been a major concern of researchers.

Wet conditions reduce the degree of skid resistance and result in hydroplaning. A variety of materials are developed and being tested by researchers to improve the frictional characteristics of pavement surfaces. Retexturing and resurfacing the pavements with these materials can enhance the slip-resistance properties of the pavement. Asphalt concrete surface coatings by superhydrophobic materials are one of the popular methods. Researchers have also proposed surface treatment technology with groove-filled material, polymer-modified cement concrete (PCC), exposed aggregate concrete to increase hydroplaning speed [14].

Numerous studies have been conducted by the researchers to evaluate the hydroplaning condition of the pavement. Both empirical and numerical approaches have been explored to obtain the more accurate value of the hydroplaning speed (HPS). The underlying mechanisms causing hydroplaning or decreased skid resistance on wet pavements are not fully understood by the empirical relationships and theoretical study conducted thus far. Empirical models can provide an initial assumption of hydroplaning potentials. Nowadays, investigations on hydroplaning and pavement skid resistance are primarily analytical because of the complicated interactions between the tire, the fluid, and the pavement surface [23]. The validation of these computational models is mostly accomplished using the empirical models.

This study aims to systematically review the efficacy of some proposed surface improvement materials presented in recent papers. This paper also reviews the newly proposed hydroplaning models along with the empirical hydroplaning models in terms of variables and scopes with references. In Sect. 2, we discuss the different surface materials that have been proved to be useful for the regulation of skid resistance and reduction of the possibility of hydroplaning. Section 3 will discuss and compare the popular and effective models for estimating the HPS for a given vehicle, road, and weather condition.

## 2 Surface Improvement Materials

### 2.1 Superhydrophobic Materials

Various superhydrophobic materials have been introduced by different researchers as coatings on asphalt pavement. Table 1 provides some superhydrophobic materials' components with references. Zakerzadeh et al. mentioned the potential of these materials in increasing skid resistance in their paper. The HPS of the coated asphalt pavement has been found significantly higher than the uncoated one. It was observed that superhydrophobic material has desirable performance in road sections

**Table 1** A summary of the well-known superhydrophobic materials

| References | Material | Component |
|---|---|---|
| Rith et al. [28] | TiO$_2$-OA material | TiO$_2$-octadecanoic acid coating material |
| Arabzadeh et al. [2] | Polytetrafluoroethylene coating (PTFE) | Layer-by-layer method was used to create an asphalt concrete surface coating |
| Gao et al. [10] | Superhydrophobic and luminescent cement pavement materials (SLCPM) | Mechanical performance of SLCPM was improved with the addition of luminescent powder |
| Peng et al. [25] | Acrylic superhydrophobic coating (ASC) | Prepared from uncured acrylic acid and carbon nanotubes |
| Peng et al. [26] | Superhydrophobic coating (SC) | Room-temperature vulcanized silicone rubber (RTV) is the main component of the SC. The micro-/nano-SiO$_2$ particles modified by a silane coupling agent were sprayed on the RTV surfaces to prepare the SC |
| Li et al. [18] | Nano-TiO$_2$ superhydrophobic coating | Prepared from waterborne polyurethane and nano-TiO$_2$ modified by stearic acid |

with sharp slopes and areas with the greatest rainfall intensity. It may also have a notable effect on asphalt pavements with a greater mean texture depth. The factors that influence surface hydrophobicity are the amount of sprayed material and curing angle. Zakerzadeh et al. mentioned the significance of the optimum quantity of the materials. More research is required to find the optimum consumption rate to reduce the application cost of this treatment.

## 2.2 Groove-Filled Asphalt Pavement Materials

A pavement surface treatment technology of groove-filled polyurethane rubber particle elastomer (PRPE) was proposed by Yao et al. [29]. The groove-filled asphalt pavement has demonstrated the best skid resistance performance among various types of pavements verified under dry, wet, and icing conditions. They found that the skid resistance performance of groove-filled pavement has been increased by 4.5%, 10.8%, and 24.6% respectively under dry, wet, and icing conditions compared with the common asphalt mixture. Some characteristics of groove-filled PRPE asphalt pavement have been verified in their paper, however, the durability of PRPE itself after aging, the wear resistance of groove-filled asphalt pavement, and the determination of groove parameters still need to be further studied.

## *2.3  Rubberized Chip Seal Pavement Materials*

Gheni et al. [11] mentioned an environment-friendly material to improve the skid resistance of pavement in their paper. The eco-friendly rubberized chip seal has shown an enhanced drainage capability compared with conventional chip seal, especially on low slopes, because of the hydrophobic nature of crumb rubber versus the hydrophilic character of mineral aggregates. This material does not have a detrimental effect on environmental in terms of heavy metal leaching. The crumb rubber that comes from scrap tires is used as a substitute for mineral aggregate in chip seal pavement. The toxic heavy metals leached from the recycled rubber or rubberized chip seal are below Environmental Protection Agency (EPA) drinking water standards. Therefore, the research indicates that this material might not cause contamination of drinking water.

## *2.4  Polymer-Modified Cement Concrete Pavement Materials*

Fang et al. [5] proposed polymer-modified cement concrete pavement materials to ensure the safety and comfort of driving. Traditional grooved cement concrete pavement was shown to have a high initial skid resistance level, however, this level quickly fell after being exposed to traffic. Compared to conventional pavement, polymer-modified cement concrete demonstrated a durable performance.

## *2.5  Exposed Concrete Pavement Materials*

Rith et al. [28] studied the characteristic of long-term skid resistance of exposed aggregate concrete pavement (EACP). They showed that the reduction rate of skid resistance in transverse and longitudinal tinning was more rapid than that in exposed aggregate concrete texture under traffic load. This indicated that EACP not only provides sufficient skid resistance at an early age but also well maintained the high surface durability against wearing and stabilizes its adequacy for long-term performance. A summary of discussed materials is presented in Table 2.

## 3  Hydroplaning Models

Hydroplaning speed modeling can be classified into empirical and numerical approaches that involve generating relationships to relate hydroplaning speed with different parameters. Numerous studies have been conducted to determine methods to improve the threshold of hydroplaning. We have summarized the major models

**Table 2** A summary of discussed surface improvement materials

| References | Pavement types | Materials | Component |
|---|---|---|---|
| Zakerzadeh | Asphalt pavement | Mentioned in Table 1 | (1) Higher HPS<br>(2) Desirable performance with sharp slopes and areas<br>(3) Great performance in high rainfall intensity |
| Yao et al. [29] | Groove-filled asphalt pavement | Polyurethane rubber particle elastomer (PRPE): 40 mesh rubber particles, 60% polyurethane binder content, 3% catalyst, and 5% diluent | (1) Ice breaking quality<br>(2) Higher skid resistance<br>(3) Durable PRPE bonds |
| Gheni et al. [11] | Rubberized Chip Seal Pavement | Two types of recycled rubber, ambient, and cryogenic | (1) Eco-friendly<br>(2) Skid resistance under ambient and elevated temperature |
| Fang et al. [5] | Polymer-modified cement concrete pavement | Exposed concrete pavement (EACCP) and (polymer-modified cement concrete pavement (PCC) | (1) Reduces the noise between the pavement and tires<br>(2) Higher sliding resistance of the pavement<br>(3) More durable skid resistance than traditional grooved pavement |
| Rith et al. [28] | Exposed concrete pavement | Exposed aggregate concrete pavement (EACP) | (1) Provides adequate skid resistance at early stage<br>(2) High surface durability against wearing and stabilizing its adequacy for long-term performance |

derived from different experimental and numerical studies in Tables 3 and 4, respectively.

**Table 3** A summary of the empirical methods and their scopes

| References | Empirical models | Parameters | Scope |
|---|---|---|---|
| Horne | Nasa hydroplaning equation | Tire inflation pressure ($P$) | (1) Used for validation for other models<br>(2) Does not consider other necessary variables such as tire footprint ratio, WFT<br>(3) Does not account WFD > 4.8 mm<br>(4) Overestimates truck hydroplaning |
| Gallaway et al. [9] | Gallaway hydroplaning model | Tread depth (TD), pavement macrotexture depth (TXD), water depth (WD), tire pressure ($p$), spin down percent (SD) | (1) Considers WFT, tire inflation pressure, and the pavement texture characteristics<br>(2) Validated for high-speed values<br>(3) Not accurate for highly textured surfaces<br>(4) Based on specific tire profiles<br>(5) Incorrect inputs built-in for spin down and tire tread depth |
| Huebner et al. [15] | PAVDRN hydroplaning model | Water depth (WD), pavement macrotexture depth (TXD), tire pressure ($p$) | (1) Can analyze flow over four different kinds of pavements<br>(2) Relatively unreliable for predicting hydroplaning in the inner lanes<br>(3) Provide incorrect results for highly texture surfaces and high rainfall intensities |
| Gunaratne et al. [12] | USF model | Wheel load (WL), tire pressure (Pt), water film thickness (WFT) | (1) Based on Ong and Fwa's comprehensive numerical prediction<br>(2) Can predict HPS for different light vehicles |
| Lee et al. [16, 17] | Florida enhanced hydroplaning model | Parameter used in Gallaway, PAVDRN, and USF models | (1) Offers different analysis<br>(2) Identifies high-risk location<br>(3) Limited number of variables<br>(4) Incapable of differentiating between upward and downward traveling vehicles |

**Table 4** A summary of the numerical methods and their scopes

| References | Modeling Features | Scope |
|---|---|---|
| Ong and Fwa [23] | Tire—FEM Pavement surface—FEM Fluid flow—contact algorithm Tire–fluid contact—ALE | (1) Able to take varying speed, WFT, locked wheel sliding speed<br>(2) Provides information on the relative contribution of traction and fluid drag to skid resistance<br>(3) Provides information on the changes in the area of tire pavement contact zone |
| Zhu et al. [30] | Tire—FEM Pavement surface—FEM Fluid flow—contact algorithm Tire–fluid contact—ALE | (1) Provides good accuracy due to due to choosing a shear stress transport model<br>(2) Predicts HPS on different asphalt pavement |
| Ding and Wang [4] | Tire—FEM Tire–fluid contact—CEL | (1) A 3D grooved tire–water–pavement interaction model<br>(2) Mentions effectiveness of Permeable friction course for reducing HP |
| Nazari et al. [22] | Tire—FEM Tire–fluid contact—CFD model using star-CCM+ | (1) Improves the prediction due to the two-phase flow of water and air<br>(2) The volume fraction of other fluids can be captured which can be used to study tire tread design |
| Fourey et al. [7] | Tire—FEM Tire–fluid contact—CPS algorithm for SPH–FE coupling | (1) Reduces the final algorithmic complexity and provides better computational efficiency<br>(2) Compressible feature of SPH<br>(3) Allows larger time steps |

## 3.1 Empirical Models

### 3.1.1 NASA Hydroplaning Equation

In 1962, the NASA Langley Research Center developed the NASA hydroplaning equation, which is still commonly used in tire, aviation, and automobile industries, and the highway and airport authorities [3]. This formula was extended and adapted to passenger cars in 1968 by Horne. Equation 1 describes the relationship between tire inflation pressure ($P$) and hydroplaning speed ($V_p$). This equation is used for the validation of different numerical models by researchers.

$$V_p = 6.35\sqrt{P} \tag{1}$$

However, the NASA equation cannot predict the hydroplaning speed correctly due to not considering other necessary variables such as tire footprint ratio, and water film thickness [23]. This equation does not consider water film depth greater than 4.8 mm and overestimates truck hydroplaning [24].

### 3.1.2 Gallaway Model

The Gallaway model is one of the commonly used empirical models which relates hydroplaning speed ($V_p$) to parameters such as water film thickness, tire inflation pressure, pavement texture characteristics [9]. The terms of Eqs. 2 and 3 are defined in Table 3.

$$V_p = (\text{SD})^{0.04}(P)^{0.3}(\text{TD} + 1)^{0.06}A \tag{2}$$

$$A = \max\{(10.409/\text{WD}^{0.06} + 3.507),\ (28.952/\text{WD}^{0.06} - 7.718)T \times D^{0.14}\} \tag{3}$$

The Gallaway model was validated for high-speed values. Some drawbacks of this model are mentioned by different researchers in their papers. This formula is not accurate for highly textured surfaces [27]. The Gallaway equations are based on specific tire profiles so they cannot predict hydroplaning situations for other tire profiles [9]. Besides, the equations have incorrect inputs built-in for spin down and tire tread depth [16].

### 3.1.3 PAVDRN Hydroplaning Model

Huebner et al. [15] introduced a computer model named PAVDRN for predicting water film thickness and potential for hydroplaning on new and reconditioned pavements in 1997 [15]. The model is based on the work of Gallaway et al. [9]. PAVDRN can predict hydroplaning potential on four pavement types, Portland cement concrete, grooved Portland cement concrete, dense-graded asphalt concrete, and open-graded asphalt concrete [1].

The PAVDRN model for $V_p$ is provided for two levels of water film thickness (WFT).

$$V_p = 26.04\,\text{WD}^{-0.259}, \quad \text{for WFT} < 2.4\,\text{mm} \tag{4}$$

$$V_p = 3.09\,A, \quad \text{for WFT} \geq 2.4\,\text{mm} \tag{5}$$

A is defined in Eq. 3 and WD is the water depth. PAVDRN is seen to be more reliable in predicting hydroplaning incidents on outer lanes including those of wider road sections and relatively unreliable in the inner lanes [12]. The model does not provide accurate results for highly textured surfaces as the Gallaway model. For higher rainfall intensities, the WFT values have been found underestimated [27].

### 3.1.4  The University of South Florida (USF) Model

The USF model is an analytical hydroplaning prediction (HP) model developed at the University of South Florida. The USF model was developed by Gunaratne et al. in 2012 by fitting an empirical equation to the finite element (FE) simulation results provided by Ong and Fwa [12]. The USF model can be used to predict the hydroplaning speeds for different light vehicles that employ tires compatible with the locked wheel tester tires [19].

$$V_p = \mathrm{WL}^{0.2}\, p_t^{0.5}\big((0.82/\mathrm{WFT}^{0.06}) + 0.49\big) \tag{6}$$

### 3.1.5  Florida Enhanced Hydroplaning Model

An HP tool has been developed by Lee et al. [16] of the Florida Department of Transportation (FDOT) for predicting the traveling speed at which a vehicle would start hydroplaning. A total of four Empirical WFT models namely, Gallaway model, U.K. Road Research Laboratory (RRL) model, New Zealand (NZ) Modified model, PAVDRN model, and three HPS models, PAVDRN model, USF model, and Gallaway model were implemented in the tool. The tool was implemented in a macro-enabled Excel spreadsheet environment. It comprises macros or code written in Visual Basic for Application (VBA) language, primarily for the user to navigate through the spreadsheet, run advanced analysis, and generate output tables and plots as appropriate. The program provides a variety of analysis options, including deterministic, sensitivity, and risk analyses. The primary use of the new HP tool is for checking the final geometric roadway design parameters for hydroplaning potential. In addition, this tool can also be used for identifying specific locations with a greater potential for hydroplaning. The main limitation of this tool is the use of a limited number of variables available in the empirical equations of WFT and HPS. Besides, this tool cannot differentiate the hydroplaning potential of a vehicle traveling downwards from that of a vehicle traveling upwards.

## 3.2  Numerical Models

Researchers have developed many numerical models based on soil mechanics, fluid mechanics, and fluid–structure interaction (FSI) to simulate the hydroplaning phenomenon. The FSI simulation is a very challenging and complex problem. Many researchers are exploring new methods for solving FSI. Using the Arbitrary Euler Lagrangian (ALE), Coupled Euler Lagrangian (CEL), or other fluid–structure interaction formulations, hydroplaning can be simulated by assigning different frames to the tire and the fluid domain [20].

Ong and Fwa [23] proposed a numerical model to simulate the hydroplaning of a locked wheel slide on the wet pavement. In this model, fluid flow modeling is achieved by modeling the behavior of fluid flow near the tire pavement contact patch using the complete set of Navier–Stokes equations using ALE formulation. The model is able to take varying speed, water film thickness and locked wheel sliding speed and provide information on the relative contributions of traction and fluid drag to skid resistance and the changes in the area of tire pavement contact zone. They discovered that HPS increased with decreasing water film thickness and increasing tire load pressure [8]. Zhu et al. [30] established a finite element model (FEM) of tire–fluid–pavement in ABAQUS, composed of a 225-40-R18 radial tire and three types of asphalt pavement covered with a water film. Water film in the numerical hydroplaning model was approximated as a Newtonian fluid, which obeyed the conservation of mass, momentum, and energy. The model provided good accuracy due to choosing a shear stress transport model. The results could be applied to predict HPS on different asphalt pavements and improve pavement skid resistance design. A 3D grooved tire–water–pavement interaction model was proposed by Ding and Wang [4] in their paper. In the study, the CEL method is used to capture the hydroplaning phenomenon.

Nazari et al. [22] mentioned the drawback associated with the CEL method in their recent paper. The CEL method does not account for the transport of the turbulent shear stress and assumes laminar fluid flow therefore this can affect results due to overprediction of the eddy-viscosity. They proposed a computational fluid dynamics (CFD) fluid–structure interaction model in their paper. The commercial software STAR-CCM+ was employed for the CFD work. It provides the advantage for FSI with the capability to couple with ABAQUS for the FE modeling. For the fluid flow, the Navier–Stokes equations were applied coupled with turbulence and multiphase flow models. The model utilizes the shear stress transport k–ω model and the two-phase flow of water and air that improves the predictions with real hydroplaning scenarios. The problems associated with this model are large computation time and memory [21].

Fourey et al. [7] utilized a cost-reducing Conventional Parallel Staggered (CPS) algorithm for fluid–structure coupling which can provide better computational efficiency. They presented a new Smoothed Particle Hydrodynamics (SPH) and finite element model for hydroplaning stimulation. Their suggested algorithm is dedicated to SPH–FE coupling strategies. This feature significantly reduces the final algorithmic complexity. Another advantage of SPH resides in its compressible feature, allowing for considering actual compressible effects when needed and permitting the incompressible fluid assumption. It allows larger time steps due to the absence of a prohibitive CFL condition [13].

## 4 Conclusion

Hydroplaning is a concerning phenomenon that may cause minor to fatal vehicle crashes. In this paper, we have summarized five recently proposed hydroplaning surface improvement materials and ten hydroplaning models. Superhydrophobic coating material has a high potential to increase the skid resistance of pavement surfaces because of its high efficiency and low environmental impact. Curing angle and sprayed material quantity can influence hydrophobicity and need to be further studied. Groove-filled pavement has demonstrated better skid resistance performance compared with the common asphalt mixture. The eco-friendly rubberized chip seal can be an effective alternative to the conventional chip seal due to its enhanced drainage capability, especially on low slopes, because of the hydrophobic nature of crumb rubber versus the hydrophilic character of mineral aggregates. Exposed aggregate cement concrete pavement (EACCP) and polymer-modified cement concrete pavement (PCC) can be used to improve ordinary traditional grooved pavement. They can provide adequate skid resistance with high surface durability against wearing. Other important characteristics of these materials, such as maintenance cost and longevity need to be explored in the future.

Hydroplaning estimation can be done by empirical and numerical approaches. Empirical tools can be used for an initial assumption of hydroplaning potentials. But these empirical models may not include all the relevant parameters in some cases. Numerical models can input varying speed, water film thickness, vehicle tire, and pavement surface parameters. Therefore, it can provide better results than empirical models. However, some parts of the numerical modeling are more complex than usual, e.g., FSI simulation, and they require a separate discussion on how to solve them. We have discussed various models that address and solve the problem. The Arbitrary Euler Lagrangian (ALE) and Coupled Euler Lagrangian (CEL) fluid–structure interaction formulations are mostly used in different numerical models. The drawback of these formulations is that they consider water flow as laminar and do not account for shear stress, whereas a recently proposed CFD-FSI simulation can solve this problem but requires more computation time and memory. Another approach, the Conventional Parallel Staggered (CPS) algorithm can be a cost-reducing approach for fluid–structure coupling but a huge computational time is required to stimulate the whole wheel with fine spatial tire resolution. There are scopes to improve the numerical models in the future by designing a more robust tire–fluid interaction model for better computational efficiency.

# References

1. Anderson DA, Huebner RS, Reed JR, Warner JC, Henry JJ (1998) Improved surface drainage of pavements, TRB, Project 1–29, Contractor Final Report
2. Arabzadeh A, Ceylan H, Kim S, Gopalakrishnan K, Sassani A (2016) Superhydrophobic coatings on asphalt concrete surfaces: toward smart solutions for winter pavement maintenance. Transp Res Rec 2551(1):10–17
3. Comfort G (2001) Wet runway friction: literature and information review
4. Ding Y, Wang H (2018) Evaluation of hydroplaning risk on permeable friction course using tire–water–pavement interaction model. Transp Res Rec 2672(40):408–417
5. Fang J, Tu J, Wu K (2020) Analysis of skid resistance and noise characteristics for varieties of concrete pavement. Adv Mater Sci Eng, Volume 2020, Article ID 7427314. https://doi.org/10.1155/2020/7427314
6. Federal Highway Administration (FHWA) (2018) How do weather impact roads? U.S. department of Transportation Federal Highway Administration. https://ops.fhwa.dot.gov/weather/q1_roadimpact.htm
7. Fourey G, Hermange C, Le Touzé D, Oger G (2017) An efficient FSI coupling strategy between smoothed particle hydrodynamics and finite element methods. Comput Phys Commun 217:66–81
8. Fwa TF, Ong GP (2008) Wet-pavement hydroplaning risk and skid resistance: analysis. J Transp Eng 134(5):182–190
9. Gallaway BM, Ivey DL, Hayes G, Ledbetter WB, Olson RM, Woods DL, Schiller Jr RF (1979) Pavement and geometric design criteria for minimizing hydroplaning, FHWA-RD-79–31 Final Report
10. Gao Y, He B, Xiao M, Fang Z, Dai K (2018) Study on properties and mechanisms of luminescent cement-based pavement materials with super-hydrophobic function. Constr Build Mater 165:548–559
11. Gheni A, Liu X, ElGawady MA, Shi H, Wang J (2018) Leaching assessment of eco-friendly rubberized chip seal pavement. Transp Res Rec 2672(52):67–77
12. Gunaratne M, Lu Q, Yang J, Metz J, Jayasooriya W, Yassin M, Amarasiri S (2012) Hydroplaning on multi lane facilities. Univ. South Florida, Tampa, Report, Issue No 201311
13. Hermange C, Oger G, Le Chenadec Y, Le Touzé D (2019) A 3D SPH–FE coupling for FSI problems and its application to tire hydroplaning simulations on rough ground. Comput Methods Appl Mech Eng 355:558–590
14. Huang K, Liu J, Wang J, Shi X (2021) Characterization and mechanism of a new superhydrophobic deicing coating used for road pavement. Crystals 11(11):1304
15. Huebner RS, Anderson DA, Warner JC, Reed JR (1997) PAVDRN: Computer model for predicting water film thickness and potential for hydroplaning on new and reconditioned pavements. Transp Res Rec 1599(1):128–131
16. Lee HS, Carvajal M, Holzschuher C, Choubane B (2021) Florida department of transportation's enhanced hydroplaning prediction tool. Transp Res Rec 2675(10):340–352
17. Lee HS, Ayyala D (2020) Enhanced hydroplaning prediction tool. Applied Research Associates, Inc., Report number: BE570
18. Li H, Lin X, Wang H (2021) Fabrication and evaluation of nano-TiO2 superhydrophobic coating on asphalt pavement. Materials 14(1):211
19. Luo W (2015) Pavement hydroplaning risk evaluation with inertial measurement unit (IMU) and 1mm 3D texture data. Doctoral dissertation, Oklahoma State University
20. Mahadevan S, Taheri S (2017) Review of vehicle hydroplaning and tire-pavement interactions. SAE Int J Passeng Cars—Electron Electri Sys
21. Nazari A, Chen L, Battaglia F, Ferris JB, Flintsch G, Taheri S (2020) Prediction of hydroplaning potential using fully coupled finite element-computational fluid dynamics tire models. J Fluids Eng 142(10):101202(11 p). https://doi.org/10.1115/1.4047393

22. Nazari A, Chen L, Battaglia F, Taheri S (2018) Developing an advance tire hydroplaning model using co-simulation of fully coupled FEM and CFD codes to estimate cornering force. In: ASME international mechanical engineering congress and exposition, vol 52033. American Society of Mechanical Engineers, p V04AT06A040
23. Ong GP, Fwa TF (2007) Wet-pavement hydroplaning risk and skid resistance: modeling. J Transp Eng 133(10):590–598
24. Ong GP, Fwa TF (2008) Modeling and analysis of truck hydroplaning on highways. Transp Res Rec 2068(1):99–108
25. Peng C, Hu X, You Z, Xu F, Jiang G, Ouyang H, Chong G, Hongchao M, Li L, Dai J (2020) Investigation of anti-icing, anti-skid, and water impermeability performances of an acrylic superhydrophobic coating on asphalt pavement. Constr Build Mater 264:120702
26. Peng C, Chen P, You Z, Lv S, Xu F, Zhang W, Jianying Y, Zhang H (2018) The anti-icing and mechanical properties of a superhydrophobic coating on asphalt pavement. Constr Build Mater 190:83–94
27. Pourhassan A, Gheni AA, ElGawady MA (2021) Water film depth prediction model for highly textured pavement surface drainage. Transp Res Record 03611981211036349
28. Rith M, Kim YK, Lee SW (2020) Characterization of long-term skid resistance in exposed aggregate concrete pavement. Constr Build Mater 256:119423
29. Yao T, Han S, Men C, Zhang J, Luo J, Li Y (2021) Performance evaluation of asphalt pavement groove-filled with polyurethane-rubber particle elastomer. Constr Build Mater 292:123434
30. Zhu S, Liu X, Cao Q, Huang X (2017) Numerical study of tire hydroplaning based on power spectrum of asphalt pavement and kinetic friction coefficient. Adv Mater Sci Eng. https://doi.org/10.1155/2017/5843061

# Materials Specialty: Materials and Structures I

# Design Methodology and Properties of Concrete Mixes Developed for an Underwater Repair Application

**Sudip Talukdar, Negar Roghanian, Roland Heere, and Neil McAskill**

**Abstract** Designing a concrete mix which can be easily placed for underwater construction and repair of marine structures, while meeting strength and durability requirements can be an engineering challenge. This paper presents the design methodology and properties of a concrete mix used for an underwater repair project at a hydropower dam spillway repair located in Western Canada. Small-scale lab trials of different design mixes were initially batched to screen potential mix designs, according to properties including compressive strength, visual index, flow characteristics, and washout resistance. Based on the results, these trials were followed by larger scale mockup trials. These served not only to verify properties determined during the initial lab trials, but also to determine additional properties like abrasion resistance and capacity to bond to the substrate. Thereafter, a design was finalized to be used for on-site repairs. As per lab and mockup test results and observations, it was found that well-graded aggregates, higher paste contents, and optimal use of supplementary cementitious materials, such as silica fume and fly ash lead to high flow and ease of placement. Optimum amounts of high-range superplasticizing admixtures can also enhance the flowability, but excessive amount of superplasticizer can significantly increase bleeding. To enhance the washout resistance, use of an anti-washout admixture (water-soluble polymers with strong absorption capacity) and silica fume is also generally recommended. The type of aggregates used can also affect bleeding and flowability.

**Keywords** Underwater · Concrete · Bond · Admixtures · Durability · Abrasion

S. Talukdar (✉)
Department of Civil Engineering, British Columbia Institute of Technology, Burnaby, BC, Canada
e-mail: stalukdar1@bcit.ca

N. Roghanian · R. Heere · N. McAskill
Metro Testing and Engineering Ltd., Burnaby, BC, Canada

# 1 Introduction

Underwater concrete (UWC) is a highly flowable concrete that can spread into place under its own weight and achieve good compaction in the absence of vibration, without exhibiting defects due to segregation and bleeding. Underwater concrete technology has developed dramatically in recent years. It is now possible to proportion mixes with high fluidity as well as high resistance to washout and segregation [1]. However, designing UWC mixes remains challenging, as specific rheological properties are desired in order to achieve sufficient flowablility to enable the mix to be pumped and placed underwater without segregating or washout. Moreover, at the same time, strength and durability criteria for the mix must also be met.

Underwater concrete washout resistance has been studied by many researchers. Over the past decades, underwater casting of concrete has been carried out by mixing fresh concrete with high-range water-reducing agents and anti-washout admixtures (AWAs), which are water-soluble polymers with a chain shape and high absorption capacity [2]. AWAs impact the concrete's rheology by increasing the flowability resistance and plastic viscosity, and reducing dilution by water. It has been reported by several authors that increasing AWA dosage reduces the slump and may increase segregation which can be compensated by increasing cement and content and fine aggregate ratio. Sonebi and Khayat evaluated the effects of the dosage and type of AWA, w/cm ratio, the advantages of incorporating silica fume on wash-out resistance and strength of highly flowable concrete [3]. According to their findings, the reduction of w/cm and increase of AWA (with the use of high-range water-reducing agent to maintain a given consistency) can increase the wash-out resistance of high flowable concrete [4]. In addition, the incorporation of silica fume into UWC mixtures improves their anti-washout properties and consistencies [5].

The abrasion resistance of ordinary concrete is proportional to the amount and hardness of the aggregates used. However, in the case of underwater concrete, researchers reported that the resistance to abrasion is mainly dependant on the hardness of the cement matrix, which is linked to the washout resistance of matrix components. Research shows that the addition of fly ash and silica fume increases the abrasion resistance of UWC and decreases the risk of cracking [6].

The effectiveness and long-term durability of the underwater repair are also strongly dependent on the bond between the repair and the substrate which consisted of mechanical interlocking and chemical adhesion. Appropriate roughness of the surface results in better mechanical interlocking and interfacial bond strength. Brzozowski et al. investigated the effect of surface preparation on the adhesion of UWC containing anti-washout admixture and superplasticizer. Researchers confirmed the correlation between increased hydrostatic pressure and the adhesion of the underwater repair to the horizontal substrates, hammered or sandblasted [7].

## 2 Research Significance

This paper presents the mix design methodology, tests selection and results, lessons learnt, and recommendations associated with the design of a UWC mix for a hydropower dam spillway repair project in Western Canada. Three stages of engineering work are presented, initial small-scale testing of mixes in the laboratory, further laboratory testing of larger scale batches, followed by testing of the final selected mix in a series of field mockups. The findings should be useful to engineers considering the use of concrete in underwater repair, requiring high flow characteristics to secure adequate mechanical properties and durability.

## 3 Design Criteria

The mix to be designed is for an underwater concrete placement to repair sections of a hydroelectric dam spillway in Western Canada. The concrete would be placed at a water depth of approximately 30 m. The mix was to be self-consolidating concrete (SCC), with a minimal loss of cohesion when placed under water. The specified minimum compressive strength of the mix was 31 MPa at 28 days. Furthermore, mix specifications called for the mix to contain between 20 and 40% fly ash by weight of cementitious materials, a w/cm ratio of less than 0.45, and conformance to the CSA A23.1:19 exposure classification F-1. For reference, a single original concrete core from the area to be repaired was provided for further analysis. The core compressive strength, tested as per CSA A23.2-14C in a wet condition, was 48 MPa. Finally, the mix design was to contain Hard Cem, manufactured by Kryton, to improve abrasion resistance of the mix.

The maximum allowable washout of the mix was limited to 8% when tested as per US Army Corp of Engineers Specification CRD C61. Explicit slump flow specifications were not provided by the client. Concrete and aggregate were to be provided by a local supplier, and the maximum nominal size of aggregate was limited to not more than 10 mm for ease of placement.

The typical characteristic of a good UWC mix design is that it should flow easily into place. To aid ease of placement, the mix should require minimal to no consolidation when it is being placed underwater. Therefore, a high flow or SCC mix was preferred. At the same time, the mix must be cohesive enough to minimize washout during underwater placement. Therefore, the mix was designed towards maximum slump flow, while maintaining enough cohesion to minimize washout. A consequence of this is that the T50 flow time for the mix is higher than that of a usual SCC mix.

After reviewing the available literature, specifications, and test results, we attempted to design an SCC mix with a maximum washout value of 8% (as per CRD C61), meeting exposure class F1, and having a target compressive strength of minimum 45–50 MPa, such as to match the compressive strength of the provided test core and enhance compatibility with the substrate concrete. Flowability is aided

by use of a dense aggregate gradation (well-graded aggregate), higher paste contents of the mix, liberal use of supplementary cementitious materials such as silica fume and fly ash, and use of high-range superplasticizing admixtures. In order to aid in washout resistance, we anticipated using an anti-washout admixture (AWA). By contrast, air entraining admixture is usually not required, as it would serve little purpose in underwater mixes.

## 4   Mixture Proportioning and Test Programme

**Phase 1: Small-scale Laboratory Testing.**

A series of 14 different initial trials were conducted on samples batched in the laboratory, each having a volume of 2 L. The purpose of the tests was to determine the optimal mix designs for the next phase of testing which involved batching larger volumes (20–25 L) of material. Each mix was visually examined as it was being batched, and its flow characteristics were assessed. For the purpose of initial testing only, washout was estimated by modifying the CRD C61 washout test. Rather than dropping the sample three times into a plastic tube filled with 1700 mm of water, the sample was dropped 10 times into a barrel filled with 510 mm water of water, followed by measuring mass loss and washout. The following materials were used in the different mix designs:

- Type GU Portland cement
- 10 mm coarse aggregate (CA)
- Fine aggregate (FA)
- Potable tap water
- Type F fly ash
- Silica fume
- Master matrix UW 450: A liquid cellulose-based anti-washout admixture, manufactured by Master Builders Solutions
- ADVA Cast 575: A polycarboxylate-based high-range water reducer, manufactured by GCP
- Hard Cem: An integral hardening admixture used to increase abrasion and erosion resistance of concrete, manufactured by Kryton
- Xanthan gum: A polysaccharide powder commonly used as a food additive. It has also been shown to enhance stability and cohesion of concrete mixes. A literature review indicated that concentrations of Xanthan gum should be limited to not more than 0.6% by mass of cementitious material. At values greater than 0.6%, 28-day compressive strengths may be adversely affected [8].

For this phase of the project, w/cm ratios ranging from 0.41 to 0.47 were tested. Ratios of fine aggregate to coarse aggregate (FA:CA) varied between 55:45 and 60:40. Paste fractions ranged between 32 and 37% by volume. Based on the initial trials, three mixes were selected for further testing in the next phase where batch

sizes were scaled up to 20–25 L volumes. Details of selected mixes are provided in Sect. 4. Through successive iterations, some general observations are noted and listed below:

- As it was also reported by other researchers, there is an inverse relationship between the amount of AWA used and the flowability of a mix. As the amount of AWA increases, the likely slump flow and T50, values decrease. Therefore, there is a trade-off between washout resistance and flowability of a mix.
- Increasing the silica fume content of a mix improves mix cohesion, reduces washout, and aids in slump flow of a mix by allowing for higher amounts of superplasticizer in the mix without the risk of segregation.
- Slump flow of mixes can be improved by increasing the sand content, and increasing the volume fraction of paste in the mix.
- UWC mix designs tend to flow more slowly compared with true SCC mixes, as a result of the presence of AWAs.

**Phase 2: Large-scale Laboratory Testing**

As it was described in phase 1, three mixes were selected for testing in 20–25 L batches (Tables 1, 2 and 3). It was recognized that the fly ash percentage used for all three mixes was less than the 20% specified, but as the rheology and flow characteristics of the mixes were important, that deviation from the specifications was accepted by the client. A brief description of each mix is as follows:

> **Mix A**—High AWA: A higher dosage of UW450 AWA was used in this mix to minimize washout. Washout, slump flow and T50 values are lower for this mix.

**Table 1** Mix A—high AWA

|  | Quantity | Density (kg/m$^3$) | Volume (m$^3$) |
|---|---|---|---|
| Type GU cement (kg) | 324 | 3150 | 0.103 |
| Silica fume (kg) | 66 | 2200 | 0.030 |
| Fly ash (kg) | 81 | 2010 | 0.040 |
| Water (kg) | 210 | 1000 | 0.210 |
| 10 mm coarse aggregate (SSD) (kg) | 650 | 2600 | 0.250 |
| Fine aggregate (SSD) (kg) | 945 | 2600 | 0.363 |
| ADVA cast 575 (L) | 6 | 1070 | 0.011 |
| UW 450 (L) | 6 | 1200 | 0.005 |
| Xanthan gum (kg) | – | 1500 | 0.000 |
| Hard Cem (kg) | 40 | 1650 | 0.024 |
| Air (L) | – | – | 0.010 |
|  |  |  | 1.047 |

**Table 2** Mix B—low AWA

|  | Quantity | Density (kg/m$^3$) | Volume (m$^3$) |
|---|---|---|---|
| Type GU cement (kg) | 324 | 3150 | 0.103 |
| Silica fume (kg) | 66 | 2200 | 0.030 |
| Fly ash (kg) | 81 | 2010 | 0.040 |
| Water (kg) | 207.5 | 1000 | 0.208 |
| 10 mm coarse aggregate (SSD) (kg) | 650 | 2600 | 0.250 |
| Fine aggregate (SSD) (kg) | 945 | 2600 | 0.363 |
| ADVA cast 575 (L) | 6 | 1070 | 0.011 |
| UW 450 (L) | 2.5 | 1200 | 0.002 |
| Xanthan gum (kg) | – | 1500 | 0.000 |
| Hard Cem (kg) | 40 | 1650 | 0.024 |
| Air (L) | – | – | 0.010 |
|  |  |  | 1.042 |

**Table 3** Mix C—Xanthan gum

|  | Quantity | Density (kg/m$^3$) | Volume (m$^3$) |
|---|---|---|---|
| Type GU cement (kg) | 324 | 3150 | 0.103 |
| Silica fume (kg) | 66 | 2200 | 0.030 |
| Fly ash (kg) | 81 | 2010 | 0.040 |
| Water (kg) | 207.5 | 1000 | 0.208 |
| 10 mm coarse aggregate (SSD) (kg) | 650 | 2600 | 0.250 |
| Fine aggregate (SSD) (kg) | 945 | 2600 | 0.363 |
| ADVA cast 575 (L) | 6 | 1070 | 0.011 |
| UW 450 (L) | – | 1200 | 0.000 |
| Xanthan gum (kg) | 1.5 | 1500 | 0.001 |
| Hard Cem (kg) | 40 | 1650 | 0.024 |
| Air (L) | – | – | 0.010 |
|  |  |  | 1.041 |

*Note* The Xanthan gum concentration by weight of cementitious materials is 0.32%.

**Mix B—Low AWA**: A lower dosage of UW450 AWA was used in this mix to maximize flowability. The washout value was higher for this mix, but the mix had better flow characteristics.

**Mix C—Xanthan gum**: Similar to mix B, but UW450 AWA was replaced with an appropriate dose of Xanthan gum to provide a mix with characteristics comparable with mix B.

The batching sequence consisted of mixing the sand and cementitious materials in a drum mixer, then adding two-third of the mixing water followed by the admixtures

**Table 4** Fresh concrete tests [9, 10]

| Test name | Applicable test standard |
|---|---|
| Slump Flow/T50 | CSA A23.2-5C |
| Air content | CSA A23.2-4C |
| Temperature | CSA A23.2-17C |
| Plastic density | CSA A23.2-6C |
| Washout | CRD C61 |

and the rest of the water. The concrete was mixed for 3 min, rested for 1 min, followed by a further 2 min of mixing. The ambient temperature during concrete preparation and sampling was approximately 20 °C. Table 4 presents the plastic concrete tests conducted on the three mixes batched. Test results are summarized in Tables 5 and 6.

The consistency of the mixes was evaluated by the slump flow test (see Fig. 1). Additionally, cylinders were cast for compressive strength testing at 7, 28, and 56 days. Table 7 and Fig. 2 present the results.

The presence of Xanthan gum in mix C was able to generate a mix which had acceptable rheological properties. However, even at 0.32% concentration its presence clearly affected the compressive strength of the mix. As it was desirable to produce a stable mix with as much slump flow as possible, it was decided to proceed to the field mockup phase with mix B.

**Table 5** Mix design parameters

| | Mix A | Mix B | Mix C |
|---|---|---|---|
| Paste fraction (by vol) | 0.37 | 0.37 | 0.37 |
| Silica fume of CM% | 14.0 | 14.0 | 14.0 |
| Fly ash of CM% | 17.2 | 17.2 | 17.2 |
| w/cm | 0.45 | 0.44 | 0.44 |
| FA:CA (by mass) | 60:40 | 60:40 | 60:40 |

*CM* cementitious materials

**Table 6** Mix performance

| | Mix A | Mix B | Mix C |
|---|---|---|---|
| Slump flow (mm) | 575 | 725 | 700 |
| T50 (s) | > 10 | 6 | 6 |
| Air content (%) | 1 | 1.5 | 1.3 |
| Temperature (°C) | 26 | 25 | 24 |
| Plastic density (kg/m$^3$) | 2346.6 | 2349 | 2367 |
| Washout (%) | 4 | 7.8 | 9.3 |

**Fig. 1** Slump flow results (L–R)—Mix A, Mix B, Mix C

**Table 7** Average compressive strength test results

|  | Test age (days) | Average compressive strength (MPa) |
|---|---|---|
| Mix A | 7 | 37.0 |
|  | 28 | 64.1 |
|  | 56 | 68.0 |
| Mix B | 7 | 38.1 |
|  | 28 | 62.3 |
|  | 56 | 67.8 |
| Mix C | 7 | 18.9 |
|  | 28 | 28.4 |
|  | 56 | 33.5 |
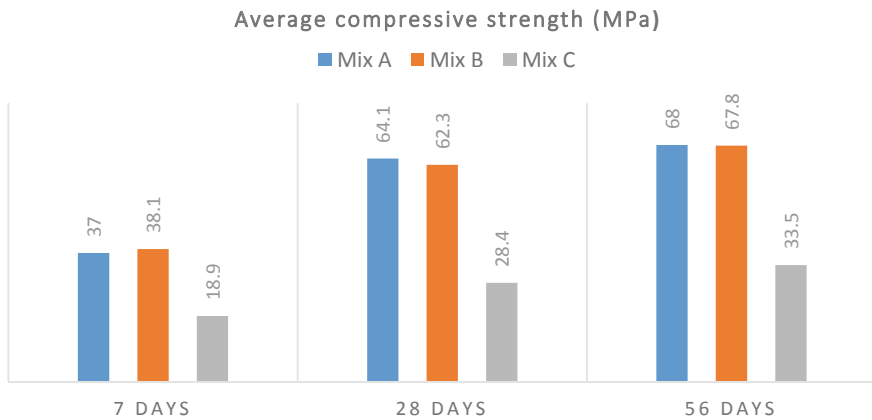


**Fig. 2** Average compressive strength test results

**Phase 3: Mockups/Field Trials**

A series of three field trials were held at the placement contractor's facility. Our objectives were:

- To evaluate the performance of the selected repair mix in the field.
- To ensure correct selection of placing equipment for the mix.
- To develop competency for the placement crew in working with the mix and placing it underwater.
- To evaluate the bond characteristics of the mix with the repair substrate.
- To evaluate abrasion resistance of the repair mix as per ASTM C1138 [11].

Mockups were carried out by casting concrete blocks which were placed into a water tank at the contractor's facility. Concrete was placed by pumping it into forms, which had been bolted onto prepared 'repair areas' on each of the block surfaces. Repairs were carried out in an inclined position as well as a vertical position. Figure 3 shows the dimensions (ft) of the concrete blocks:

Figure 4 shows the blocks prior and after being immersed in the water tank. Figure 5 shows the placement process in the tank. For each mockup, the dimensions
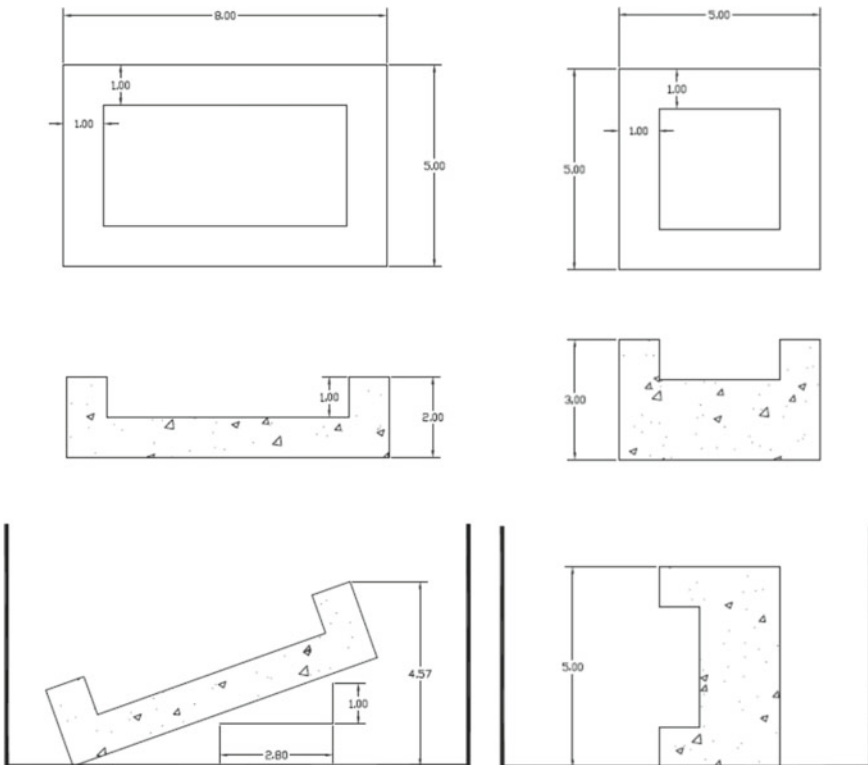


**Fig. 3** Repair block dimensions (L—inclined, R—vertical). Dimensions in feet

**Fig. 4** Concrete blocks prior and after immersion in the water tank

**Fig. 5** Placement of UWC
repair mix
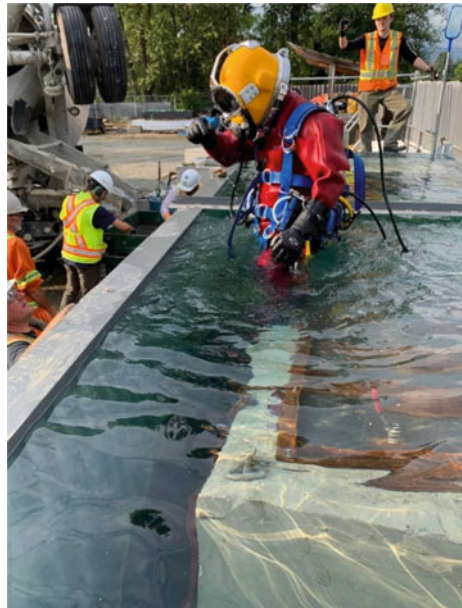


and orientation of the blocks were not varied, therefore, essentially, the process was repeated three times.

## 5 Discussion of Results

The concrete repair mix performed as expected in its plastic state. Test results of the fresh properties of the mix, as well as the strength development are summarized in Table 8 and Fig. 7:

**Table 8** Fresh concrete test results of mockup 2

| Slump flow (mm) | 725 |
|---|---|
| Air content (%) | 1.4 |
| Density (kg/m$^3$) | 2328 |
| Temperature (°C) | 29 |



**Average Compressive Strength (MPa)**

- 7 DAYS: 33.3
- 28 DAYS: 47.4
- 56 DAYS: 64.1
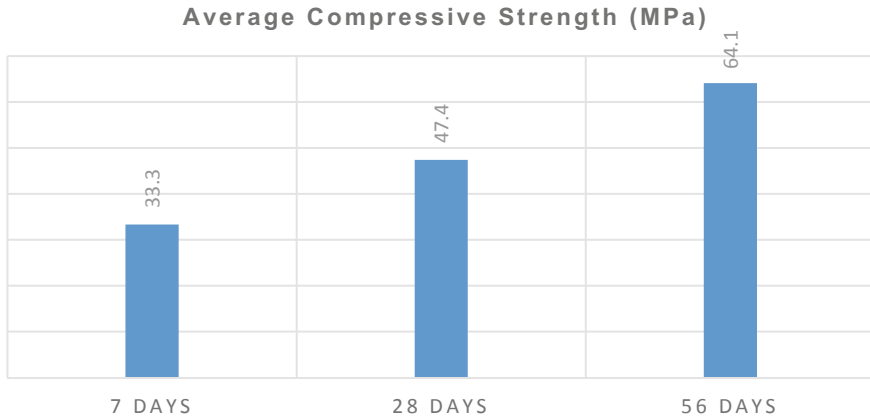
**Fig. 7** Average compressive strength test results, mockup 2

The repairs from mockup 1 were visually inspected after the formwork was removed. The repairs appeared to have been cast in an acceptable manner, based on visual observation. The panel which had been cast in a diagonal position exhibited air pockets, likely due to bubbles which had formed at the interface between the form and the top of the repair surface. The cause of the bubbles is unknown. The panel which had been cast in a vertical position showed no such air bubble formation. Therefore, it is possible that the placement orientation may have an effect on formation of surface imperfections such as air bubbles on the repair surface. This is a matter which may need to be researched further.

Under the impact of flowing water, hydraulic structures and repairs will inevitably be subjected to abrasive forces. Therefore, a sample was cast to evaluate the abrasion resistance of the mix as per ASTM C1138-19. Test results are provided in Table 9, and a picture of the surface of the specimen after testing is provided in Fig. 8. Strength and abrasion test results indicated the mix would likely exceed minimum strength criteria and would have a good durability while in service.

A good quality repair however, is not simply achieved by placement of the repair material. If there is inadequate bonding between the repair and the substrate, the repair

**Table 9** Abrasion test results, mockup 2

| Height (mm) | Diameter (mm) | Mass loss (g) | Mass loss (%) |
|---|---|---|---|
| 105 | 279 | 63 | 0.4 |

**Fig. 8** Abrasion test
specimen at end of test



becomes effectively useless. Bond strength can be influenced by different factors, including the presence of contaminants on the substrate surface, substrate surface roughness, and the presence of surface micro-cracks. To verify bond strength and to evaluate the adequacy of the surface preparation procedures, cores were extracted from the repaired mockup concrete blocks to test the bond strength as per CSA A23.2-6B (see Fig. 9). The test results from the first two mockups were alarming, as the majority of the cores failed due to bond delamination during the coring process itself, indicating a very poor bond (see Table 10).

The tensile bond test results from the first two mockups were communicated to the placement contractor, and the surface preparation methods used for these two mockups were reviewed. For the third mockup, extra care was paid to surface

**Fig. 9** Tensile bond test
set-up



Round steel plate
glued to end of
core sample

Bond interface

Round steel plate
glued to end of
core sample
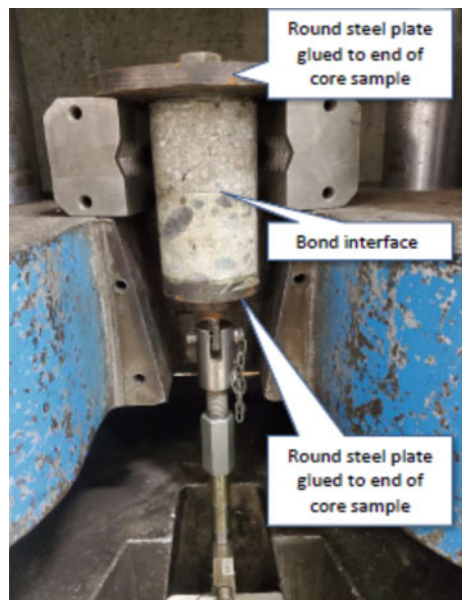
**Table 10** Tensile bond strength test results

| Mockup 1 | Core 1 | Bond failure during coring | Average = 0.23 MPa |
|---|---|---|---|
|  | Core 2 | Bond failure during coring |  |
|  | Core 3 | 0.7 MPa |  |
| Mockup 2 | Core 1 | Bond failure during coring | Average = 0.30 MPa |
|  | Core 2 | Bond failure during coring |  |
|  | Core 3 | 0.9 MPa |  |
| Mockup 3 | Core 1 | 0.9 MPa | Average = 1.07 MPa |
|  | Core 2 | 0.9 MPa |  |
|  | Core 3 | 1.4 MPa |  |

preparation. The surface was pressure washed to ensure a clean substrate, free of deleterious materials with surface texture of at least ICRI CSP 6. The increased emphasis on surface preparation appeared to work, as the test results from mockup 3 were significantly improved. All three cores were extracted with the bond intact. All tensile bond strengths were $\geq$ 0.9 MPa. Overall, the repair mix performed well and could be pumped and placed fairly easily in the field.

Field trials allow for verification of the performance requirements of the repair mix, and they give the placement crew an opportunity to work with and familiarize themselves with the repair mix. They allow for proper selection and testing of the equipment which will be used to place the mix (i.e. pumps, hoses, etc.), and prepare in advance for potential issues on-site, such as the ones experienced in this project regarding substrate preparation.

## 6 Conclusion and Recommendations

A number of important lessons were learnt which other practitioners involved in design of placement of UWC mixes may find useful:

- Based on visual observations in phase 1 of this study, the variations of washout and slump flow is highly affected by the w/cm ratio, the use of supplementary cementitious materials such as silica fume and fly ash, as well as the concentration of AWA.
- As the amount of AWA increases, slump flow decreases and T50 value increases (Table 6).
- Based on visual observations in phase 1 of this study, for a given fluidity, regardless of AWA content, increasing the silica fume content of the mix improves mix cohesion and washout resistance.
- Based on visual observations in phase 1 of this study the slump flow of the mixes can be improved by increasing the volume fraction of paste in the mix.

- Xanthan gum appears to have an adverse effect on strength development of UWC mixes.
- The field trial/mockup process is a necessary stage and should be encouraged prior to actual placement of UWC for a repair project.
- Substrate preparation is essential to ensuring a durable repair. Improper surface preparation may result in premature debonding of the repair material.
- Placement orientation may have an effect on the formation of minor surface imperfections on the repair concrete.

# References

1. Al-Tamimi AK (2008) Developments in the formulation and reinforcement of concrete
2. Nasr AA, Songgui C, Feng J (2021) Washout resistance of self-protected underwater concrete in freshwater and seawater. Constr Build Mater 289:123186
3. Khayat KH, Sonebi M (2001) Effect of mixture composition on washout resistance of highly flowable underwater concrete. Mater J 98(4):289–295
4. Heniegal AM (2012) Behaviour of underwater self compacting concrete. JES J Eng Sci 40(4):1005–1023
5. McLeish A (ed) (1994) Underwater concreting and repair. Halsted Press
6. Horszczaruk E, Brzozowski P (2017) Effects of fluidal fly ash on abrasion resistance of underwater repair concrete. Wear 376:15–21
7. Brzozowski P, Horszczaruk E (2021) Influence of surface preparation on adhesion of underwater repair concretes under hydrostatic pressure. Constr Build Mater 310:125153
8. Sikandar MA et al (2020) Effect of various anti-washout admixtures on the properties of non-dispersible underwater concrete. Constr Build Mater 245(2020):118469
9. CSA A23.2:19 (2019) Concrete materials and methods of concrete construction/test methods and standard practices for concrete. Canadian Standard Association
10. CRD-C 61-89A (1989) Test method for determining the resistance of freshly mixed concrete to washing out in water
11. ASTM C1138-19 (2019) Standard Method for abrasion resistance of concrete (underwater method). ASTM International, West Conshohocken

# Interfacial Bonding of Nano-modified Cementitious Composites Incorporating Basalt Pellets to Normal Concrete

**Elhadary Riham and Bassuoni Mohamed**

**Abstract** Interfacial bonding between precast normal concrete (NC) and cast-in-place high-performance fiber-reinforced cementitious composites (HPFRCC) has received significant attention in recent years, for applications such shear key fillers in bridge deck joints. Novel HPFRCC has been recently developed at the University of Manitoba. These composites include various constituents (cement, slag, nano-silica) and reinforced with fiber systems (single and hybrid) including polyvinyl alcohol (micro-PVA) and basalt fiber pellets (macro-BFP). BFP is a novel class of basalt fibers, where basalt fiber strands are coated by a polymeric resin with textured surface micro-grooves. In this study, the interfacial shear bond adhesion and coefficient of friction between the NC and HPFRCC were evaluated using bi-shear test and slant shear test, with an inclination angle of 33.7º with the vertical. The results showed that nano-silica had a significant effect at improving the interfacial bonding strength and coefficient of friction with NC. The addition of 1% micro-PVA fibers to macro-BFP (hybrid system) in the nano-modified composites led to a noticeable improvement in their interfacial bonding and coefficient of friction with NC, which suggests their promising use for future field applications.

**Keywords** Nano-silica · Slag · Cement · Polyvinyl alcohol fibers · Basalt fiber pellets · Slant shear · Bonding

## 1 Introduction

The use of cementitious composites in precast concrete (e.g., bridges) segmental methods is popular due to their high performance and excellent quality [1–4]. The precast segments are sequentially assembled with jointing [shear key joints]. These joints ensure the continuity and shear load transfer between the segments during service and under extreme loads. Numerous experimental and theoretical studies

E. Riham · B. Mohamed (✉)

Civil Engineering, University of Manitoba, Winnipeg, MB R3T 5V6, Canada

e-mail: Mohamed.Bassuoni@umanitoba.ca

have focused on the shear behavior of shear key joints with different types of filler materials to predict the shear bond capacity [5–9]. However, poor compatibility with the existing concrete segments, cracking behavior, premature deterioration due to water infiltration and chemical agents, corrosion of reinforcing steel and reduction in the monolithic behavior of the segments [10] remain challenging issues for these types of connections.

A viable way to impede the deterioration effects (cracking, poor bonding, delamination signs) between precast concrete segments is to fill the joints with high-performance materials that are able to control the initiation, coalescence, and propagation of cracks (e.g., [11–13]). High-performance fiber-reinforced cementitious composites (HPFRCC) can be adopted as a new filler material, owing to its balanced performance in terms of mechanical and durability properties [14–17]. Moreover, HPFRCC has gained increased attention from engineers and researchers due to its high ductility under flexural, tension, and impact loading configurations, depending on key mixture design parameters. Different types of binder (General Use cement [GU], slag, fly ash, etc. and a range [0.25 to 0.35] of water-to-binder [w/b] ratios) have been utilized in HPFRCC with various types and geometry of fibers (e.g., polyvinyl alcohol [PVA], steel) (e.g., [18, 19]). Different types of ultrafine nanoparticles (e.g., nano-silica) have been incorporated in HPFRCC to modify the microstructure and enhance hardened properties. For instance, the addition of 6% nano-silica by mass to cement-based binders without/with supplementary cementitious materials creates additional nucleation sites for precipitation of hydration products [20, 21], accelerates the pozzolanic reactivity [20, 22], and enhances particle packing (filler effect) in the hardened paste. Also, it reduces w/b in the paste due to water absorption into its ultrahigh surface porosity.

The behavior of hybrid fiber systems exceeds that of the single fibers utilized in HPFRCC (e.g., [4, 17, 23, 24]). For example, in binary-scale fiber systems, micro-fibers impede the coalescence of micro-cracks, and macro-fibers restrain the growth of macro-cracks. Hence, various types and sizes of metallic, synthetic, and natural fibers have been used to improve the plastic and hardened properties of HPFRCC. For instance, PVA macro-fibers have a tensile capacity up to 1600 MPa, with a reasonable modulus of elasticity (up to 66 GPa) [25]. The hydrophilic nature of PVA improves the potential for impeding the nucleation of micro-cracks [26]; the typical dosage of PVA micro-fibers is 2% by volume of the composite to yield a strain hardening behavior [25, 27]. For example, Wagner et al. [28] investigated the performance of interfacial bond stress by incorporating 0.5% and 1% PVA micro-fibers of length 8 mm and 12 mm into repair materials. It was reported that 1% of 12 mm PVA micro-fibers were able to deviate the interfacial micro-crakes outside the interface as well as impede the nucleation of micro-cracks at the interfacial bond zone.

Macro-basalt fibers have emerged in concrete research due to their mechanical properties (modulus of elasticity up to 110 GPa and high tensile strength up to 4000 MPa), thermal resistance, non-corrosive nature, and lower cost compared with other alternative fibers such as glass and carbon fibers [29–32]. However, basalt fiber initially has an excellent bond with the cementitious matrix, but this bond losses with time (approximately 90 days) due to alkali-silica reactions between the silicate

component of basalt and pore solution. Subsequently, basalt fiber pellets (BFP) have been produced, where basalt strands are encapsulated with a polymeric resin (e.g., polyamide [33]) for protection against alkaline media. However, there is still death of information on the use HPFRCC reinforced with a hybrid system (macro-BFP with micro-PVA) in various applications (e.g., shear key joints), particularly the interfacial bond shear stress between HPFRCC and normal concrete (NC), hence the motive for the current study.

## 1.1  Research Significance

The constant demand for HPFRCC in various structural applications prompts continual research on resilient composites exploiting recent of progress in materials manufacturing. Ongoing studies at the University of Manitoba led to developing HPFRCC composites comprising cement, high-volume slag, nano-silica and reinforced with BFP [14, 15, 33], or hybrid BFP/PVA systems [17]. Yet, focused research is still needed on aspects such as exploring the compatibility between precast NC concrete and HPFRCC under shear loading configurations. Such data is crucial to identify the functionality of these composites for resilient use as a filler/joint material. Hence, the primary objective of the current study was to evaluate the shear bond stress of HPFRCC composites comprising high-volume slag with/without nano-silica and reinforced with single BFP or hybrid BFP/PVA systems.

# 2  Experimental Program

## 2.1  Materials and Mixtures

General Use cement (GU) and grade 100 slag meeting CSA-A3001 (2018) requirements were used as the main components of the base binder 700 kg/m$^2$. A constant dosage 6% of nano-silica solution (NS) was used as an additive material; this solution comprises 50% $SiO_2$ particles dispersed in an aqueous solution with mean particle size of 35 nm, and its density, specific surface area, viscosity, and pH values are 1.1 g/cm3, 80,000 m$^2$/kg, 8 cP, and 9.5, respectively. A fine aggregate was used in the mixtures with the continuous gradation of 0 to 600 μm, and its specific gravity, absorption, and fineness modulus are, 1.5%, 2.6, and 2.9. A high-range water reducer (HRWR), poly-carboxylic acid-based complying with ASTM C494 Type F (2017), was added to improve the workability of the mixtures. Two different fiber types were used to reinforce the mixtures: BFP macro-fibers and PVA micro-fibers (Fig. 1). Table 1 shows the geometry, dosages, and properties of two different fibers.

**Fig. 1** Fiber type: **a** PVA and **b** BFP

**Table 1** Properties of fibers

| Property | PVA | BFP |
|---|---|---|
| Length (mm) | 12 | 36 |
| Diameter/width (mm) | $38 \times 10^{-3}$ | 1.8 |
| Aspect ratio | 315 | 20 |
| Specific gravity | 1.3 | 1.7 |
| Tensile strength (MPa) | 1600 | 2300 |
| Elastic modulus (GPa) | 66 | 65 |
| Volume fraction [$V_f$] (%)[*] | 1 | 2.5 |

[*] PVA and BFP are expressed by volume of composite

Three mixtures comprising 50% GU cement and 50% slag by mass of the base binder (700 kg/m³) with 0.3 *w/b* were prepared, meeting the requirement for high-volume supplementary cementitious materials (HVSCM-1) concrete, according to Annex K in CSA 23.1 [2019]. About 6% of nano-silica by mass of the binder (42 kg/m³) was added to two mixtures (i.e., ternary binder content of 742 kg/m³), as this dosage led to marked improvement of mechanical properties as reported in previous studies at the University of Manitoba (e.g., [14, 22]). All mixtures were reinforced with either single dosage of macro-BFP or hybrid BPF/PVA fibers. Mixtures reinforced with single fibers comprised 2.5% BFP, while the mixtures reinforced with hybrid fibers included 2.5% BFP combined with 1% PVA. The proportions of all mixtures are listed in Table 2. For the mixtures' ID, the letters G, N, B, and V refer to slag, nano-silica, BFP, and PVA, respectively, while the numbers indicate the dosage of fibers. The mixing protocols introduced by Elhadary and Bassuoni [17] were followed herein, whereas the dry ingredients were added first, followed by gradually addition of liquid phases, and subsequently fibers were added. After casting the mortar in molds, all specimens were compacted using a vibrating table. Polyethylene sheets were then used to cover the surface of the specimens for 24 h. The specimens were then demolded and cured in a standard curing room (maintained at a 22 ± 2 °C and relative humidity of more than 95%) until testing.

**Table 2** Mixtures proportions per cubic meter

| Mixture ID | Cement (kg) | Slag (kg) | Water* (kg) | NS (kg) | Fine aggregate (kg) | PVA | BFP | Compressive stress of HPFRCC (MPa) |
|---|---|---|---|---|---|---|---|---|
| G-B2.5 | 350 | 350 | 210 | – | 1288 | – | 43.3 | 79 |
| G-N-B2.5 | 350 | 350 | 180 | 84 | 1167 | – | 43.3 | 83 |
| G-N-B2.5-V1 | 350 | 350 | 180 | 84 | 1142 | 13 | 43.3 | 85 |

## *2.2　Tests*

The compressive strength of full cylinder HPFRCC specimens was determined by testing triplicate cylinders (100 diameter and 200 mm height) at 56 days according to ASTM C39 [2018]. To study the bond strength between NC and HFRCC materials, the slant shear test with a combination of compressive and shear stress on the interface plane and bi-shear test with a pure shear stress at the interface plane were applied. According to AASHTO LRFD Bridge Construction Specification [2020], the NC mix design (400 kg/m$^3$ GU cement with 15% fly ash replacement and 0.4 *w/b)* for both slant and bi-shear tests was the one typically used in the composite deck slab in Manitoba bridges' superstructure; its compressive strength was 45 MPa at 28 days. The NC specimens/substrate were cured in a standard curing room (maintained at a $22 \pm 2$ °C and a relative humidity of more than 95%) for 28 days. Subsequently, the NC surface was wire brushed, cleaned, and misted to act as a substrate layer surface.

In the slant shear test, three triplicate cylinders of dimension 100*200 mm were tested at 56 days following the general guidelines of ASTM C39 [2018] and ASTM C882/C882M [2020]. The NC concrete was casted in the inclined wooden form to fill half of the cylinder at 33.7º with the vertical (Fig. 2), and then the HPFRCC was placed to fill the other half of the mold after 28 days. This inclination angle represents the critical theoretical inclination angle for a combination of shear and normal stresses at the interface plane. Thereafter, the specimens were cured in a standard curing room until testing. Figure 3a shows the specimen set-up and the linear variable differential transducers (LVDTs) to measure the resultant of displacement at the interface (i.e., perpendicular and parallel) during loading. The adhesion and coefficient of friction can be expressed using Mohr circle Eqs.1–3, where: $\tau_n$ and $\sigma_n$ are the shear and normal (positive for compression) stresses acting on the bond interface, c is adhesion strength (the pure shear strength), $\mu =$tan( $\phi$) is the coefficient of friction, $\phi$ is the internal friction angle, $\sigma o$ is the shear bond stress at the interface, and $\alpha$ is the angle of inclination with vertical.

$$\tau_n = c + \mu\,\sigma_n \tag{1}$$

$$\tau_n = 0.5\sigma o\,\sin(2\alpha) \tag{2}$$

$$\sigma_n = \sigma o \; \sin^2(\alpha) \tag{3}$$

In bi-shear test, three triplicate concrete cubes of dimensions 150 mm were tested at 56 days under pure shear load at the interface, following the loading rate guideline of ASTM C39 [2018]. A wooden form of dimension 150 * 150 * 50 mm was inserted on the cube framework of dimension 150 mm to control the dimension of NC concrete (150 * 150 * 100 mm) during casting. After curing and preparing the NC surface, the HPFRCC was casted side-by-side to NC to fill the other rest part of the cube of dimensions 150*150*50 mm. Thereafter, the specimens were cured in a standard
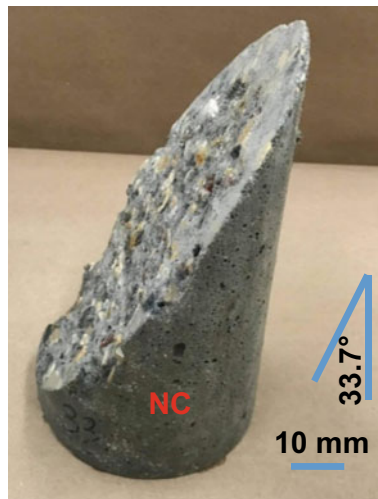


**Fig. 2** Slant shear inclination angle with vertical at 33.7°
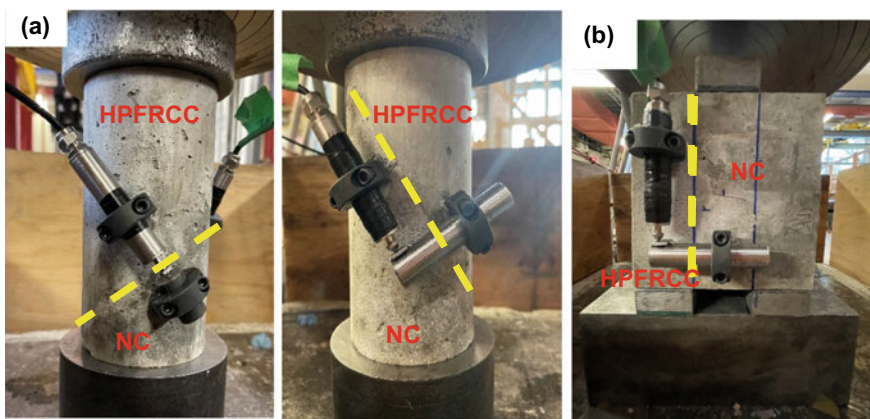


**Fig. 3** Test set-up: **a** slant shear test and **b** bi-shear test

curing room until testing. Figure 3b shows the specimen set-up. The concrete cube block was supported at the outside edge by using two steel plates, while the loading plates were rested on the NC side at the interface between HPFRCC and NC materials. Moreover, the interface slip was measured by attaching LVDT at the interface during loading. The adhesion bond stress was calculated by Eq. 4, where: $\tau$ = interfacial shear bond strength, $P$ = maximum applied load, and $A$ = Area of the interface.

$$\tau = P/2A \qquad (4)$$

In addition, mercury intrusion porosimetry (MIP) were determined for different matrices G, G-N, and G-N-V1 to identify the pore structure at 56 days. Two concrete cylinders were casted for each mixture to extract the small pea-sized chunks as test samples. Each sample was dried on oven at $50 \pm 2$ °C associated with silica gel till attainment of constant mass. The pressure of apparatus ranges from sub-ambient to 228 MPa. By assuming a cylindrical geometry of pores and surface tension of 485 dynes/cm with 130° of mercury contact angle, the high-pressure limit (228 MPa) yields a pore radius of about 3 nm, implying intrusion of all capillary pores. Besides, thermal test was also performed to corroborate the trends from the bulk tests. At constant heating rate 10 °C/min, the thermogravimetric analysis (TGA) was assessed on powder samples extracted from the triplicate cylinders used in compressive strength (pulverized by a mechanical grinder and passing sieve #200 [75 $\mu$m]), to predict the content of calcium hydroxide CH in the matrix.

## 3 Results and Discussion

### 3.1 Compressive Strength and Hydration Development

Table 2 lists the compressive strength of the full cylinders made from HPFRCC, which ranged from 79 to 85 MPa at 56 days. Inclusion of 6% NS in the slag-based binder improved the compressive strength of composites. This trend can be explained by alteration of the pore features in the G-N matrix (Table 3: reduction in porosity and threshold pore diameter: 10% and 0.08 $\mu$m, respectively, and increase in micropores proportion: 58%). In addition, the thermal analysis (Fig. 4) showed that the normalized CH content in the G-N binder relative to that in the reference G binder continuously decreased from 0.82 at one day to 0.33 at 90 days. This improvement can be ascribed to the ultrahigh specific surface of NS (80,000 m²/kg), which acts as additional nucleation sites for precipitation of hydration products [20]. This process is coupled with vigorous pozzolanic reactivity (consumption of CH with time to precipitate additional/secondary C-S–H), as indicated by the TG trends]. This was associated with particle packing/filling effect of nano-silica which densified the microstructure.

**Table 3** Summary of MIP test results at 56 days

| Mixture ID | Apparent total porosity (%) | Threshold pore diameter (μm) | Proportion of micro-pores (<0.1 μm) |
|---|---|---|---|
| G | 11.6 | 0.11 | 44 |
| G-N | 10.3 | 0.08 | 58 |
| G-N-V1 | 10.4 | 0.07 | 64 |



| Normalized Calcium Hydroxide Content | Time (days) | | | | | |
|---|---|---|---|---|---|---|
| | 1 | 3 | 7 | 28 | 56 | 90 |
| G-N/G | 0.82 | 0.64 | 0.52 | 0.34 | 0.31 | 0.33 |
| G-N-V1/G-N | 1.02 | 1.02 | 1.02 | 1.01 | 1.01 | 1.01 |
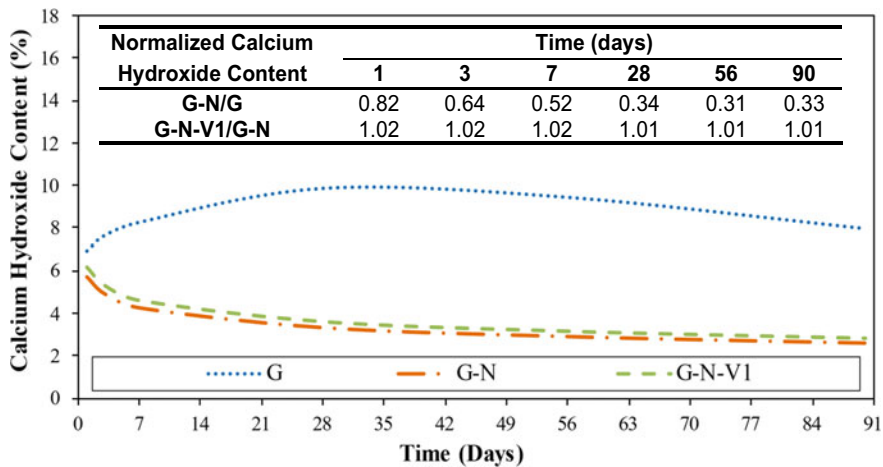
**Fig. 4** TGA results for the CH contents (at a temperature range of 400–450 °C) in the mixtures

Regarding the hybrid system, 1% micro-PVA fibers in combination with macro-BFP fibers (G-N-B2.5-V1) increased the compressive strength of composites compared with that of the corresponding mixture without PVA fibers (G-N-B2.5). Moreover, inclusion of the PVA micro-fibers changed the mode of failure from abrupt crushing of the matrix to gradual evolution of multiple cracking, where the matrix remained intact after reaching its capacity (Fig. 5a vs. Fig. 5b). This trend can be explained by the microstructural refinement induced by addition of PVA micro-fibers. The MIP results (Table 3) showed that the addition of 1% PVA to mixture G-N to produce mixture G-N-V1 densified the pore structure as the proportion of micro-pores increased to 64% due to interrupting the continuity of capillary pores. In addition, the hydrophilic effect of PVA led to reduction of *w/b* and thus enhancing the ITZ with the matrix [26]. Also, the synergetic interaction between PVA micro-fibers and BFP macro-fibers led to impeding the nucleation of micro-cracks and controlling or the propagation of macro-cracks in the matrix and thus enhanced the matrix integrity.
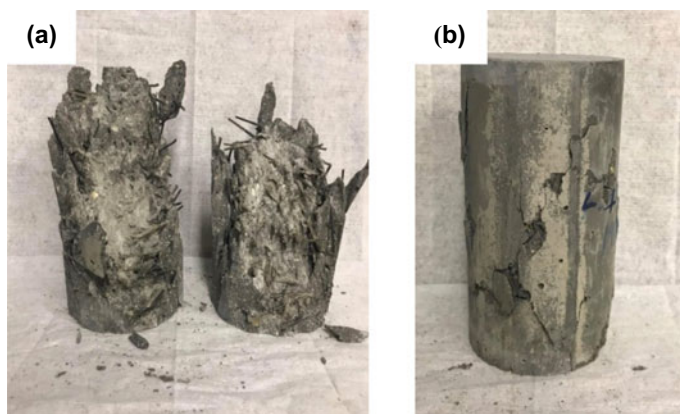
**Fig. 5** Exemplar mode of failure of specimens after the compressive strength test at 56 days: **a** G-N-B2.5 and **b** G-N-B2.5-V1

## 3.2 Shear Bond Mechanism Evaluation

### 3.2.1 Slant Shear Stress

Figure 6 shows representative load–displacement curves for all specimens cast with HPFRCC at 33.7º with the normal strength concrete (NC) substrate. The slant bond stress ($\sigma_o$) was calculated from Eq. 1, and it was in the range from 16.4 to 28.5 MPa for all specimens. On the other hand, the de-bonding energy from the slant shear tests was calculated as the area under the load–displacement curve. The bond stress and de-bonding energy improved with increasing the compressive capacity of the HPFRCC mixture (Table 2), which was associated with a directly proportional load–displacement relationship up to a slippage of approximately 1.3 mm. For example, the slant bond stress and de-bonding energy for the composite specimens G-N-B2.5 were 27% and 42% higher than that of the G-B2.5 specimens, which were 16.4 MPa and 9.9 J, respectively. The mode of failure for all specimens cast with G-B2.5 and G-N-B2.5 assemblies displayed interface failure, indicating the dominance of slant shear stresses over the normal stress component. However, the nano-modified matrix achieved higher normal and shear stress properties by 27% (Table 4). This improvement could be attributed to the effective pozzolanic reactivity of NS (consumption of CH content (5.4%) in the NC surface), resulting in precipitation of additional/secondary C-S–H at the interface, which led to improving the adhesion behavior through filling the gaps/voids at the interface between NC and HPFRCC.

The addition of 1% PVA micro-fibers to 2.5% BFP macro-fibers forming a hybrid system significantly affected the interfacial bonding parameters. The slant bond stress and de-bonding energy of composite G-N-B2.5-V1 specimens were 37% and 114% higher than that of the G-N-B2.5 specimens, which were 20.9 MPa and 14.1 J, respectively (Table 4). The composite comprising PVA promoted deviation of the

| Mixture ID | Slant Bond Stress σo (MPa) | De-bonding Energy (J) | Mode of Failure |
|---|---|---|---|
| G-B2.5 | 16.4 (0.7) | 9.9 (0.4) | Interface |
| G-N-B2.5 | 20.9 (0.8) | 14.1 (0.6) | Interface |
| G-N-B2.5-V1 | 28.5 (1.4) | 30.1 (1.9) | NC+ Interface |
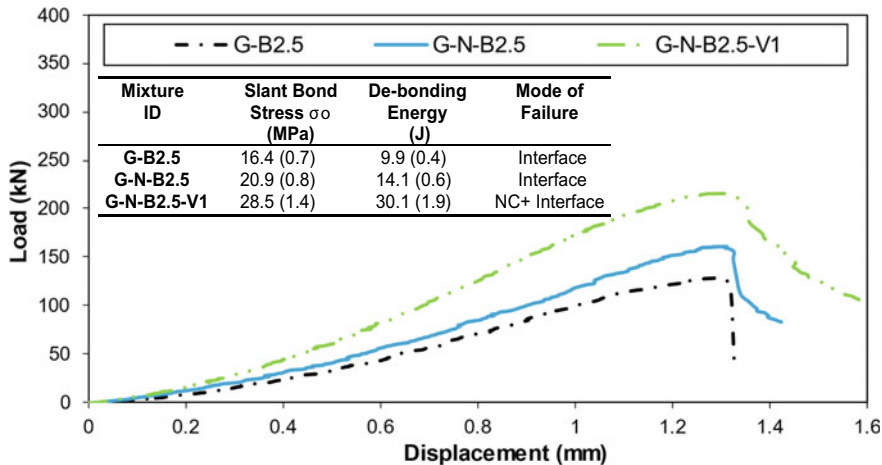
**Fig. 6** Load–displacement relationships from the slant shear test specimens at 56 days

**Table 4** Slant shear test results

| Mixture ID | Normal stress $\sigma_n$ (MPa) | Shear stress $\tau_n$ (MPa) | Coefficient of friction ($\mu$) |
|---|---|---|---|
| G-B2.5 | 5.1 (0.7) | 7.6 (0.7) | 0.8 |
| G-N-B2.5 | 6.5 (0.8) | 9.6 (0.8) | 0.86 |
| G-N-B2.5-V1 | 8.8 (1.4) | 13.1 (1.4) | 0.96 |

[*] Values in parentheses represent standard deviations

fracture plane from interface failure only to localized interfacial bond followed by cracking of NC substrate. This trend might be linked to the hydroxyl groups ($OH^-$) functionality on the PVA surface, which enhanced the interaction with cement paste forming hydrogen bond between the HPFRCC and NC surfaces (chemical effect). The coexistence of PVA micro-fibers with BFP macro-fibers contributed to micro-crack deviation and blunting at the interface, which bonding of the two layers.

### 3.2.2 Bi-shear Stress

Figure 7 shows the load–displacement for all specimens cast with HPFRCC side-by-side with NC under the direct shear load. The pure shear bond stress ($\tau$) represents the adhesion (c) in Eq. 1 and was calculated from Eq. 4. On the other hand, the de-bonding energy from the bi-shear test was calculated as the area under the load–displacement curve. A directly proportional load–displacement relationship up to a maximum slippage of approximately 1.6 mm was observed. Complying with the slant shear results, the incorporation of 6% NS into the cementitious matrix led to marked improvement in the interfacial adhesion between HPFRCC/NC layers. For example,

| Mixture ID | Pure Shear Stress $\tau$ (MPa) | De-bonding Energy (J) | Mode of Failure |
|---|---|---|---|
| G-B2.5 | 2.5 (0.3) | 14.9 (0.9) | Interface |
| G-N-B2.5 | 3.9 (0.3) | 20.9 (1.2) | Interface |
| G-N-B2.5-V1 | 6.0 (0.4) | 26.1 (1.5) | NC+ Interface |
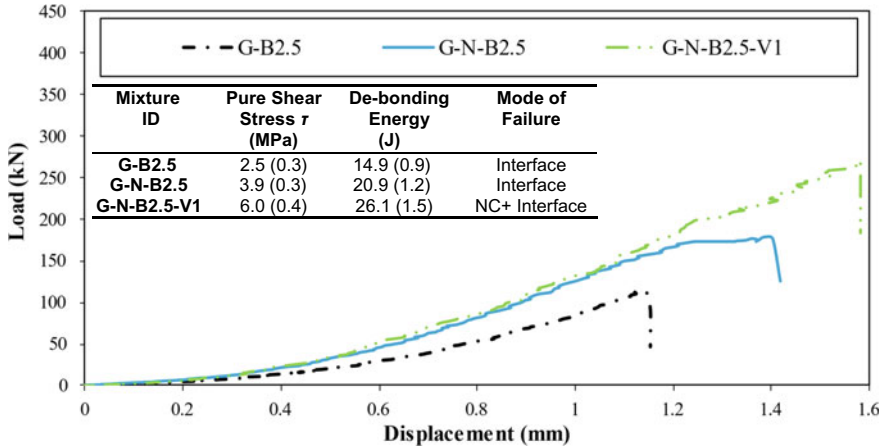
**Fig. 7** Load–displacement relationships from the bi-shear test specimens at 56 days

the pure shear bond stress and the de-bonding energy for mixtures G-N-B2.5 were 56% and 40% higher than that of the G-B2.5 specimens, which were 2.5 MPa and 14.9 J, respectively, owing to the functionality of nano-silica explained earlier.

The addition of 1% PVA micro-fibers to 2.5% BFP macro-fibers had a significant effect at improving the adhesive capacity of the composite specimens. The pure shear bond stress and de-bonding energy for the G-N-B2.5-V1 composite specimens were 52% and 25%, respectively, higher than that of G-N-B2.5 specimens, which were 3.9 MPa and 20.9 J. Moreover, 1% PVA fibers promoted deviation of the fracture plane from interface failure only to localized interfacial cracking and crushing of NC layer, due to the role of PVA in improving the bond with the matrix, creation of higher contact surface between the HPFRCC and NC and increasing surface roughness and interlocking at this zone. This was reflected by the larger displacement (1.6 mm) at failure and de-bonding energy (26.1 J).

### 3.2.3 Coefficient of Friction and Adhesion

Table 4 lists the slant shear bond stress parameters (normal stress $\sigma_n$ and shear stress $\tau_n$) at the interface between HPFRCC and NC. The normal and shear stress were calculated using Eqs. 2 and 3, respectively. The ratio between the shear and normal stresses ($\tau_n/\sigma_n$) for all specimens was approximately 1.5. The coefficient of friction ($\mu$) and adhesion ($c$) are important design parameters in several design codes. For example, AASHTO LRFD Bridge Design Specifications [2020] indicate that the applied shear displacement along the interface between two contact concrete is resisted by two components: interface friction and adhesion. In order to determine the coefficient of friction ($\mu$), a combination of bi-shear and slant shear results should be available. The coefficient of friction ranged from 0.80 to 0.96 amplitude (Table 4),
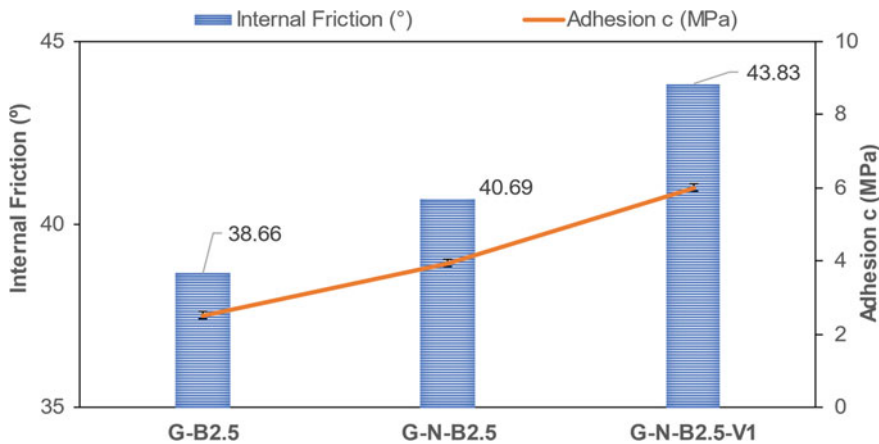
**Fig. 8** Repaired specimens versus internal friction (°) and adhesion ($c$)

while the friction angle, which was calculated as $\tan^{-1}(\mu)$, ranged between 38.66° and 43.83° (Fig. 8). Indeed, the internal friction angle increased with the adhesion capacity (due to the inclusion of nano-silica and PVA, as explained earlier) between the HPFRCC and NC.

## 4 Conclusions

Based on the variables and tests implemented in this study, the following conclusions can be drawn:

- The synergistic effects of nano-silica, cement, and slag enhanced the degree of binder maturity and produced dense microstructure, leading to improvement in the compressive strength of the composites.
- The incorporation of 6% NS (i.e., G-N-B2.5) had a noticeable improvement in terms of bonding stress, de-bonding energy, and coefficient of friction. This was attributed to the nucleation, pozzolanic reactivity, and filling effects of NS, resulting in extensive participation of additional cementitious gel/products at the contact surface area and consequently the enhancement of adhesion behavior at the interface between HPFRCC and NC.
- The hydroxyl groups (OH⁻) and crack bridging effects of PVA micro-fibers offered a marked improvement in compressive strength and adhesive behavior between HPFRCC and NC, in terms of bond stress, de-bonding energy, and coefficient of friction. Moreover, the coexistence of PVA micro-fibers with BFP macro-fibers contributed to micro-crack deviation and blunting at the interface and enhanced matrix integrity. Hence, mixture G-N-B2.5-V1 may have promising

potential in field applications such shear key and precast concrete fillers/joints in bridges.

# References

1. Jia J, Zhang K, Saiidi MS, Guo Y, Wu S, Bi K, Du X (2020) Seismic evaluation of precast bridge columns with built-in elastomeric pads. Soil Dyn Earthq Eng 128:105868
2. Jiang H, Chen L, Ma ZJ, Feng W (2015) Shear behavior of dry joints with castellated keys in precast concrete segmental bridges. J Bridg Eng 20(2):04014062
3. Li C, Bi K, Hao H, Zhang X, Van Tin D (2019) Cyclic test and numerical study of precast segmental concrete columns with BFRP and TEED. Bull Earthq Eng 17(6):3475–3494
4. Wang Q, Yi Y, Ma G, Luo H (2019) Hybrid effects of steel fibers, basalt fibers and calcium sulfate on mechanical performance of PVA-ECC containing high-volume fly ash. Cement Concr Compos 97:357–368
5. James PH (2012) Finite element modeling of full depth precast concrete bridge deck connections in bending and shear (Doctoral dissertation, Utah State University)
6. Julander JL (2009) Finite element modeling of full depth precast concrete transverse bridge deck connections. Graduate Theses Dissertations, p 469
7. Ma ZJ, Cao Q, Chapman CE, Burdette EG, French CE (2012) Longitudinal joint details with tight bend diameter U-bars. ACI Struct J 109(6)
8. Porter SD (2009) Laboratory testing of precast bridge deck panel transverse connections for use in accelerated bridge construction. Utah State University
9. Weber ED, Pantelides CP, Reaveley LD (2015) Performance of CFRP posttensioned transverse grouted joints for full-depth precast concrete panels. PCI J Art Res
10. Russell HG (2011) Adjacent precast concrete box-beam bridges: State of the practice. PCI J Article Res 56(1)
11. Bandelt MJ, Billington SL (2016) Impact of reinforcement ratio and loading type on the deformation capacity of high-performance fiber-reinforced cementitious composites reinforced with mild steel. J Struct 142(10):04016084–04016114
12. Ranade R, Li VC, Stults MD, Rushing TS, Roth J, Heard WF (2013) Micromechanics of high-strength, high-ductility concrete. ACI Mater J 110(4):375–384
13. Yang IH, Joh C, Kim BS (2010) Structural behavior of ultra-high performance concrete beams subjected to bending. Eng Struct 32(11):3478–3487
14. Azzam A, Bassuoni MT, Shalaby A (2019) Properties of high-volume fly ash and slag cementitious composites incorporating nanosilica and basalt fiber pellets. Adv Civ Eng Mater 8(3):255–274
15. Azzam A, Bassuoni MT, Shalaby A (2021) Nanomodified Cementitious Composites Incorporating Basalt Fiber Pellets under Tensile and Impact Loads. J Mater Civ Eng 33(10):04021260–04021314
16. Azzam A, Bassuoni MT, Shalaby A (2022) Flexural performance of nano-modified cementitious composites with BFP as a bonded overlay. J Mater Civ Eng (Accepted; in press)
17. Elhadary R, Bassuoni MT (2021) Mechanical properties of nano-modified cementitious composites reinforced with single and hybrid fibers. Transp Res Rec 2675(9):56–64

18. Meng D, Huang T, Zhang YX, Lee CK (2017) Mechanical behaviour of a polyvinyl alcohol fibre reinforced engineered cementitious composite (PVA-ECC) using local ingredients. Constr Build Mater 141:259–270
19. Pan Z, Wu C, Liu J, Wang W, Liu J (2015) Study on mechanical properties of cost-effective polyvinyl alcohol engineered cementitious composites (PVA-ECC). Constr Build Mater 78:397–404
20. Kong D, Du X, Wei S, Zhang H, Yang Y, Shah SP (2012) Influence of nano-silica agglomeration on microstructure and properties of the hardened cement-based materials. Constr Build Mater 37:707–715
21. Said AM, Zeidan MS, Bassuoni MT, Tian Y (2012) Properties of concrete incorporating nano-silica. Constr Build Mater 36:838–844
22. Ghazy A, Bassuoni MT, Shalaby A (2016) Nano-modified fly ash concrete: a repair option for concrete pavements. ACI Mater J 113(2):231–242
23. Özkan Ş, Demir F (2020) The hybrid effects of PVA fiber and basalt fiber on mechanical performance of cost-effective hybrid cementitious composites. Constr Build Mater 263:120564–120616
24. Özkan Ş, Çoban Ö (2021) The hybrid effects of basalt and PVA fiber on properties of a cementitious composite: physical properties and non-destructive tests. Constr Build Mater 312:125292–125317
25. Li VC, Wang S, Wu C (2001) Tensile strain-hardening behavior of polyvinyl alcohol engineered cementitious composite (PVA-ECC). ACI Mater J 98(6):483–492
26. Liu SG, He C, Yan CW, Zhao XM (2011) Water permeability of polyvinyl alcohol (PVA) fiber reinforced cementitious composites. Adv Mater Res 150:1009–1012
27. Zanotti C, Rostagno G, Tingley B (2018) Further evidence of interfacial adhesive bond strength enhancement through fiber reinforcement in repairs. Constr Build Mater 160:775–785
28. Wagner C, Bretschneider N, Slowik V (2013) Characterization of the interface between strain hardening cementitious repair layers and concrete subgrade. FraMCoS-8, Toledo (Spain)
29. Ayub T, Shafiq N, Nuruddin MF (2014) Mechanical properties of high-performance concrete reinforced with basalt fibers. Procedia Eng 77:131–139
30. Arslan ME (2016) Effects of basalt and glass chopped fibers addition on fracture energy and mechanical properties of ordinary concrete: CMOD measurement. Constr Build Mater 114:383–391
31. Ghazy A, Bassuoni MT, Maguire E, O'Loan M (2016) Properties of fiber-reinforced mortars incorporating nano-silica. Fibers 4(1):1–16
32. Iyer P, Kenno SY, Das S (2016) Performance of fiber-reinforced concrete made with basalt-bundled fibers. Adv Civ Eng Mater 5(1):107–123
33. Mahmoud K, Ghazy A, Bassuoni MT, El-Salakawy E (2017) Properties of nanomodified fiber-reinforced cementitious composites. J Mater Civ Eng 29(10):04017173–04017212
34. AASHTO American Association of State Highway and Transportation Officials (2020) LRFD bridge design specifications (8th ed). Washington, DC
35. ASTM C39/C39M-18 (2018) Standard test method for compressive strength of cylindrical concrete specimens. ASTM International, West Conshohocken (PA)
36. ASTM (American Society for Testing and Materials) (2017) Standard specification for chemical admixtures for concrete. ASTM C494/C494M-17, West Conshohocken, PA, USA
37. ASTM C882/C882M-20 (2020) Standard test method for bond strength of epoxy resin concrete by slant shear. ASTM International, West Conshohocken, PA
38. Austin S, Robins P, Pan Y (1999) Shear bond testing of concrete repairs. Cem Concr Res 29(7):1067–1076
39. Al-Mahmoud F, Castel A, François R, Tourneur C (2007) Effect of surface preconditioning on bond of carbon fibre reinforced polymer rods to concrete. Cement Concr Compos 29(9):677–689
40. CSA (Canadian Standards Association) (2018) Cementitious materials for use in concrete. CSA-A3001–18, Canadian Standards Association, Mississauga, ON, Canada

41. CSA (Canadian Standards Association) (2019) Concrete materials and methods of concrete construction/test methods and standard practices for concrete. CSA A23.1/A23.2, Canadian Standards Association, Mississauga, Ontario, Canada
42. CW (2015) Portland cement concrete pavement works. CW3310-R17, City of Winnipeg Specification, Winnipeg, Manitoba, Canada
43. Cosenza E, Manfredi G, Realfonzo R (1997) Behaviour and modelling of bond of FRP rebars to concrete. J Compos Constr ASCE 1(2):40–51
44. Gomaa E, Gheni A, ElGawady MA (2020) Repair of ordinary Portland cement concrete using ambient-cured alkali-activated concrete: interfacial behavior. Cem Concr Res 129:105968
45. Malhotra VM, Zhang MH, Read PH, Ryell J (2000) Long-term mechanical properties and durability characteristics of high strength/high-performance concrete incorporating supplementary cementing materials under outdoor exposure conditions. Mater J 97(5):518–525
46. Nanni A, Bakis CE, Boothby TE (1995) Test methods for FRP–concrete systems subjected to mechanical loads: state of the art review. J Reinf Plast Compos 14(6):524–558
47. Wang Z, Li T, Qu H, Wei H, Li Y (2019) Seismic performance of precast bridge columns with socket and pocket connections based on quasi-static cyclic tests: experimental and numerical study. J Bridg Eng 24(11):04019105

# Monotonic and Cyclic Pullout Performance of Hooked-End Super Elastic Shape Memory Alloy Fibers and Steel Fibers Embedded into Concrete

**Demewoz W. Menna, Aikaterini S. Genikomsou, and Mark F. Green**

**Abstract** The bond characteristics between concrete and reinforcing fiber play a significant role in the performance of fiber reinforced concrete (FRC) under various loading conditions. The present work experimentally examined the pullout resistance of double hooked-end NiTi and steel fiber from 35 MPa (NS–Normal strength) and 60 MPa (HP–high-performance) concrete under monotonic and cyclic loading to assess the potential application of NiTi fiber in concrete. A novel SMA fiber fabrication method that starts with heavy cold-working the wire, then bending to the desired shape and followed by heat treatment at 350 °C was used. The heat treatment enabled higher strain recovery, shorter stresses plateau length and higher energy dissipation under cyclic loading. Individual fibers were embedded into concrete matrix with an embedment length of 30 mm. Comparison between steel and NiTi fibers on the maximum load, average and equivalent bond strength, and cyclic energy dissipation were studied. The results showed that the unique super elastic property of the NiTi shape memory fiber can be utilized by providing 5D anchorage that could be used to produce FRC with significant crack closing and energy dissipation capacity. The SMA fibers showed lower average bond strength and slightly higher equivalent bond strength than the steel counterparts. The SMA fibers outperformed the steel fibers on re-centering and energy dissipation under hysteretic pullout loading.

**Keywords** SMA fiber · Steel fiber · Hooked-end · Concrete · Bond · Pullout energy · Re-centering

## 1 Introduction

Addition of fibers improves the post cracking tensile strength, ductility, flexural strength, and energy absorption capacity of concrete [1, 2]. Fibers main contributions initiates after the concrete cracks, as the fibers transfer stress across cracks. Interfacial

D. W. Menna (✉) · A. S. Genikomsou · M. F. Green
Department of Civil Engineering, Queen's University, Kingston, Canada
e-mail: 18dwm@queensu.ca

bond strength between fiber and matrix plays a significant role on the stress transferring capacity of fibers [3]. Pullout behavior of fibers is governed by the mechanical anchorage and tensile properties of the fibers and transverse tensile strength of the matrix [4]. In cracked FRC, the fiber matrix bond strength weakens due to either time-dependent monotonic loading or cyclic-dependent repeated loading [5].

Steel fibers are the most commonly used type of fibers and other types include synthetic (polymer, polypropylene), natural, glass, and carbon fibers. Under repeated loading, hooked-end steel fiber reinforced concrete absorbs applied energy through deformation (hook straining) and yielding of fibers [6]. However, after the steel fibers yield they do not return to their original position and further energy could not be dissipated. In addition, this plastic deformation of steel fibers leads to crack widening, which allows corrosive chemicals to enter the FRC [7].

Shape memory alloys (SMAs) have recently been introduced as fiber materials for their remarkable recovery from significant deformation. Shape memory alloys recover from 8% strain either by heating (called shape memory effect) or when the stress is removed (called super elastic effect) [8]. These alloys have two internal crystal arrangement phases: the martensite and the austenite. Internal crystal shear lattice distortion exited reversable phase transformation from austenite to martensite (or vice versa) is responsible for super elastic and shape memory characteristics of SMAs [9]. A typical tensile stress–strain relationship of super elastic SMA is shown in Fig. 1. The stress grows linearly up to the forward transformation stress during the initial loading period, then gradually develops a stress plateau, which is referred to as the loading plateau. Further increase of the stress, leads to a rise in slope due to strain hardening. The unloading path starts with liner response until reverse transformation occurs, followed by the unloading plateau, and finally unloads to a smaller or zero residual strain [8]. This difference in loading and unloading paths enables super elastic SMAs to dissipate significant energy. The unique spontaneous strain recovery made super elastic SMAs a potential material for FRC with self-centering and crack closing capacities [7, 10]. Cement mortar beams with hooked-end super elastic SMA fibers placed above notch showed considerable re-centering and crack closing capabilities after large deformations [11]. Sherif et al. [7] investigated the cyclic flexural behavior of concrete prisms reinforced with randomly distributed straight super elastic fibers. They concluded that the contribution of the super elastic fibers to re-centering capacity was limited due to the poor pullout resistance of the fibers and recommended hooked-end fibers.

To exploit the re-centering capacity and dissipate significant energy, the super elastic SMA fiber's pullout resistance must be greater than the loading plateau stress of the SMA [10]. Various efforts have been made to improve the pullout resistance of super elastic SMAs. Choi et al. [12] compared the bond slip characteristics of L-shaped, N-shaped, and crimped end SMA embedded in mortar matrix and found that crimped fibers showed better anchorage and re-centering capacity under cyclic loading than L-shaped and N-shaped end fibers. The L-shaped and N-shaped end fibers suffer from excessive pullout under lower load and re-centering was not attained. Choi et al. [10] suggested spearhead-end super elastic fibers fabricated by pressing the end parts of straight fibers. The pullout resistance of single and

**Fig. 1** Typical stress strain response under cyclic loading
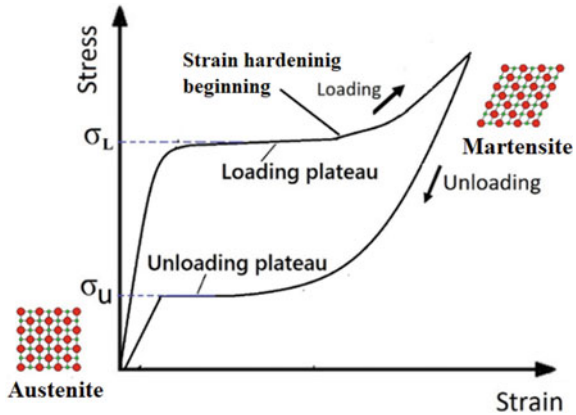


multi-hooked-end (3D, 4D, and 5D) super elastic fibers embedded in concrete were investigated by Dehghani and Aslani [13] and the results were compared with steel fibers with similar geometry. The number preceding "D" in the geometry designation stands for the number of segments in the hook, including the straight part. For example, 5D represents a hook with 5 segments, as shown in Fig. 3: the straight part plus the four segments with lengths ranging from L1 to L4. They reported that although adding the number of end hooks increased the pullout resistance of SMA fibers, SMA fibers were found to have significantly lower bond strength than similar geometry steel fibers. This difference in bond slip property between steel and SMA fibers attributed to the difference in the deformation process and mechanical properties of the materials. Further experimental study that could enhance the bond slip properties of super elastic SMA fibers is necessary [13]. This paper aims on improving the pullout resistance of multi-hooked-end (5D) super elastic SMA fibers using an innovative fiber manufacturing technique.

## 2 Experimental Program

### 2.1 Super Elastic SMA Fiber Production

Setting the desired end-hook shape of super elastic SMA requires post processing technique due to the spring back to its original shape. Usually, the end-hook shape setting of fibers is done by firmly constraining a straight wire in a mold and performing heat treatment while the fiber is pressed in the mold. The typical shape setting heat treatment for super elastic SMA wire is in the range of 500 °C and these treatments alter the mechanical properties of the wire [14]. Among the properties affected by the heat treatment is the tensile stress–strain response. It is well established that for hooked-end fibers embedded in cementitious matrix, the pullout resistance due

to both friction and mechanical anchorage are significantly affected by the tensile properties of the fiber [15]. Thus, heat treatments impact the bond slip characteristics of the super elastic SMAs.

The present work follows a novel approach on fabricating hooked-end super elastic SMA fibers with the aim of improving the pullout resistance of the fibers. The approach involves heavily cold-working prior to end-hook formation and heat treatment. Cold-working refers to gradually straining the wire to produce a longer and reduced cross-sectional area. It also increases the modulus of elasticity of the wire and decreases the super elastic property that allows shaping the fiber end-hooks by pressing in a mold, without requiring heat treatment while the fibers are in the mold. This method of producing desired shape form cold-worked wires followed by heat treating to regain superplastic property is common in medical and orthodontics applications [16, 17]. The proposed method is expected to produce super elastic fibers with better pullout resistance (by improving tensile property of SMA) and simplify the fiber fabrication process, by avoiding heat treating the fiber while it was in the mold.

The super elastic fibers in this research were made from 48% cold-worked (the initial strain reduced the cross-sectional area by 48%), NiTi SMA. The wire was commercially supplied by Memry corporation (Bethel, United States) and had 1 mm diameter after cold-work. After the hooks were bent, heat treatment at 350 °C for 40 min was conducted to regain the super elastic property. Heat treatment at 350 °C produces a shorter stress plateau length leading to strain hardening at relatively lower strain than heat treatment at higher temperature [18]. The 350 °C temperature was determined after evaluating the results of multiple heat treatment temperatures; the analysis results are beyond the scope of this paper and will be available in the authors' future papers. The term stress plateau length is used to refer to the range of the strain from the beginning of phase transformation to the start of the strain hardening. The stress plateau length was determined by subtracting the strain at the beginning of stress plateau from the strain at the end of stress plateau (Fig. 2). The austenite start ($A_S$) and austenite finish ($A_f$) temperatures of the super elastic wire were −15 °C and −6 °C, respectively. Thus, the wire shows super elastic behavior above −6 °C. The tensile stress–strain relationship of the 48% cold-worked wire and heat-treated super elastic SMA wire are shown in Fig. 2. The heat-treated wire's loading plateau stress was 625 MPa, the strain at the start of the plateau was 1.74%, strain hardening began at 4.78% strain, and thus the stress plateau length was 3.04%. The common super elastic fibers used in previous research had a strain hardening at 8–10% strain with a stress plateau length of 6.5–8% [12, 13]. The early strain hardening (short stress plateau length) gained in the present work is expected to increase the pullout resistance of the fibers, by increasing mechanical anchorage straightening resistance. The premise of this study is to achieve a pullout fiber stress higher than the loading plateau stress and initiate strain hardening so that a better crack closing capacity could be generated by SMA fibers in concrete. The pullout resistance of the produced SMA fibers was compared with one of the steel fibers.

Figure 3 presents the geometries of the SMA and the steel fibers investigated in this paper. Both the SMA and the steel fibers had multi-hooked-end (5D) mechanical
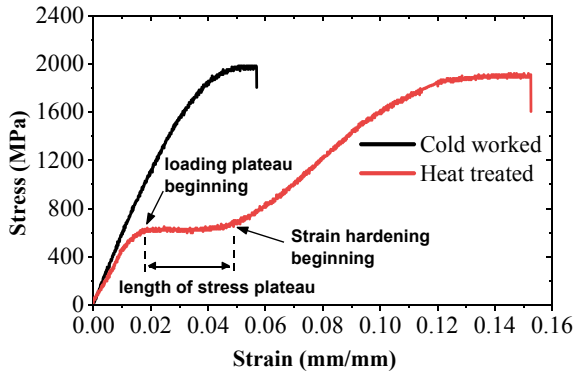
**Fig. 2** Tensile stress strain relationship of cold-worked and heat-treated super elastic SMA wire
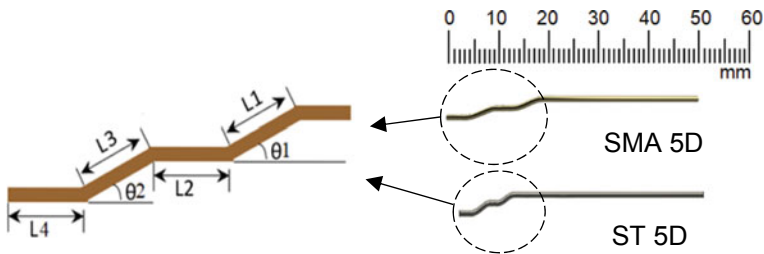


**Fig. 3** Geometry of the shape memory alloy (SMA 5D) and the steel fibers (ST 5D)

anchorage, with dimensions shown in Table 1. The fibers were embedded in concrete at the hooked-end with an embedment length of 30 mm. A 20 mm straight end was used to grip the fibers during the pullout test. The steel fibers used in this study were high strength 0.9 mm diameter Dramix[R] hooked-end fibers.

Figure 4 shows direct tensile test comparison between the steel and super elastic SMA. The tensile stress strain plot of the steel fiber was obtained from the manufacturer, Dramix[R]. The austenite Young's modulus of the SMA fibers was 44.2 MPa, and the loading plateau stress was 625 MPa. The steel fiber had a Young's modulus of 210 GPa and a yield stress of 2300 MPa. It is worth noting that the pullout tests were

**Table 1** Dimensions of the SMA and the steel fibers

| Fiber material | Geometry | Hook length (mm) | | | | Hook angle (°) | | $D_f$ (mm) | $f_U$ (MPa) |
|---|---|---|---|---|---|---|---|---|---|
| | | L1 | L2 | L3 | L4 | θ1 | θ2 | | |
| SMA | 5D | 4.5 | 4.5 | 4.5 | 4.0 | 22 | 24 | 1.0 | 625[a], 1900[b] |
| Steel | 5D | 2.6 | 2.4 | 2.6 | 2.6 | 28 | 31 | 0.9 | 2300 |

[a] Loading plateau, [b] Ultimate tensile strength

**Fig. 4** Tensile stress strain relationship of super elastic SMA and steel fibers
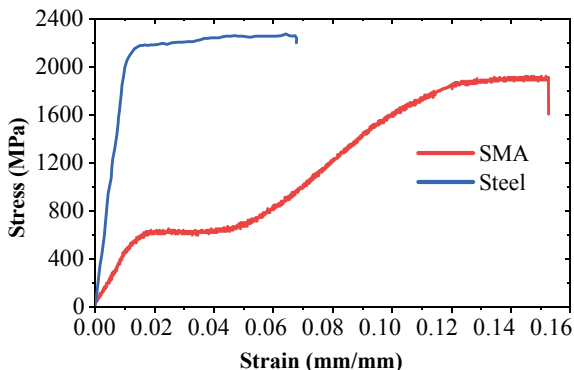


run at a round 23 °C, which is greater than the austenite finish temperature of the SMA fiber. Thus, the SMA fibers underwent stress-induced martensite hardening/transformation during the test.

## 2.2 Mixture Preparation

Two different types of concrete, normal strength (NS) and high-performance (HP) mixtures were used. For the normal strength concrete general use Portland-Limestone (GUL) type cement with water to cement ratio equal to 0.5 was considered. The aggregates in NS included natural coarse aggregates with a maximum size of 6 mm and natural sand fine aggregate. The mixture composition of NS concrete was 456 kg/m$^3$ cement, 228 kg/m$^3$ gravel, and 891.3 kg/m$^3$ sand. The NS concrete had 35 MPa compressive strength at 28-day age. The high-performance concrete was HP-S6, a commercially available pre-blended package supplied by King package materials. The HP concrete contained Portland cement, silica fume, air-entraining admixture, and aggregate with maximum nominal size of 6 mm. The HP concrete had a specified compressive strength of 60 MPa.

## 2.3 Sample Preparation

Single fiber pullout specimens were prepared using a 76 × 76 × 76 mm concrete cubes with a fiber embedment length of 30 mm. A steel molds with cubic opening at the top and bottom was carefully placed on the wood formwork with the fiber at the center of the formwork. Then the prepared concrete mixtures were slowly poured into the form ensuring the fibers alignment was maintained straight. Following vibration, the specimens were covered by a plastic sheet and left for 24 h at room temperature before removing the molds. Three 100 mm diameter cylindrical specimens were cast

to determine the compressive strength of each mixture. Then the specimens were further cured for 27 days in a laboratory at a temperature of $22 + -3$ °C. All the pullout and the compressive strength tests were conducted at 28–30 days age.

## 2.4 Experimental Setup

The pullout tests were conducted under monotonic and cyclic loading protocols using a testing setup shown in Fig. 5. The tests were conducted using a Zwick/Roell testing machine with 20 kN maximum capacity. A steel frame with two plates (one attached to the machine base and the other at the top of specimens) was used to hold the concrete cubes. A grab screw fiber griping system connected to the load cell was used to grip and pull the embedded fibers. Two linear potentiometers measured the slip. The monotonic pullout tests were run at a displacement-controlled loading rate of 1 mm/min. The cyclic pullout tests had 30 cycles starting at 1 mm slip to a maximum of 30 mm with an incremental increase of 1 mm. A constant 0.017 Hz frequency is used for all cycles. The cyclic tests are reported only for specimens imbedded in high-performance (HP) concrete. While the monotonic pullout results for SMA and steel fibers imbedded in NS and HP concrete are reported.

## 3 Results and Discussion

The pullout performance of the fibers was evaluated using the average bond strength $\tau_{av}$ and equivalent bond strength $\tau_{eq}$ parameters. $\tau_{av}$ and $\tau_{eq}$ are calculated using Eqs. 1 and 2 [13]. In Eq. 1 and 2; $P_{max}$, $d_f$, and $L_{em}$ represent the peak pullout load, diameter, and embedment length of the fiber, respectively. The total pullout energy



**Fig. 5** Experimental test setup
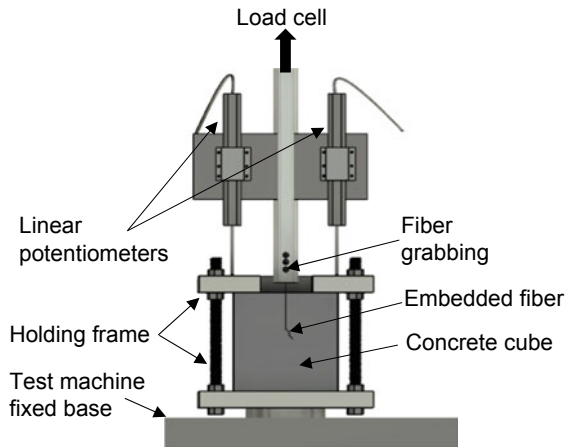
Ep is determined by calculating the area under the load slip curve. The equivalent bond strength has a good correlation with the tensile properties of high-performance fiber reinforced concrete [13].

$$\tau_{av} = \frac{P_{max}}{\pi d_f L_{em}} \qquad (1)$$

$$\tau_{eq} = \frac{8E_P}{\pi d_f L_{em}^2} \qquad (2)$$

### 3.1 Monotonic Pullout Response

The monotonic pullout-slip curves of the SMA and the steel fibers are presented in Fig. 6. Fiber rapture was not observed, and all the fibers pulled out completely from the concrete at the end of the tests. Both the fibers pullout response exhibited strong dependency on the concrete compressive strength. SMA and steel fibers imbedded in higher strength concrete showed higher pullout resistance. Similar behavior was also observed in previous research [4].

The SMA and the steel fibers' average peak pullout load raised by around 33% and 59%, respectively, as the concrete strength increased from NS (35 MPa) to HP (60 MPa). Similarly, the pullout energy increased by 48% and 35% for SMA and steel fibers, respectively, with the increase in matrix strength from NS to HP. Summary of peak pullout load, maximum tensile stress in the fiber, pullout energy, average, and equivalent bond strength results are shown in Table 2. The maximum tensile stress ($\sigma_{max}$) in the SMA fiber was significantly higher than the SMA loading plateau stress (625 MPa) which indicates that the proposed fiber geometry and the fabrication method resulted to adequate bond strength that can produce fibers with significant re-centering and energy dissipating capacity [10].

It should be noted that with increasing matrix strength, although the percentage increase in peak pullout load of steel fibers is higher than that of SMA fibers, the percentage increase in the pullout energy for SMA fibers is significantly higher. This attributed to the more ductile deformation of the SMA fibers after the stress in the fiber exceeded the loading plateau stress. Figure 7 compares the average pullout response of the SMA and the steel fibers normalized by dividing the pullout fiber stress to the yield stress. The pullout fiber stress was determined by dividing the pullout load ($P$) to the cross-sectional area of the fiber ($A_f$). The loading plateau stress of the super elastic SMA fiber was taken as the yield stress. The super elastic fibers showed significantly higher efficiency than the steel fibers. Figure 7 shows the pullout stress exceeded transformation stress of the SMA causing stress-induced martensite transformation that reflected on the hardening response in the pullout curve. The transformation resulted in a significantly higher deformation of the SMA that led to a higher slip (slip + deformation) at peak pullout load than the steel fiber.
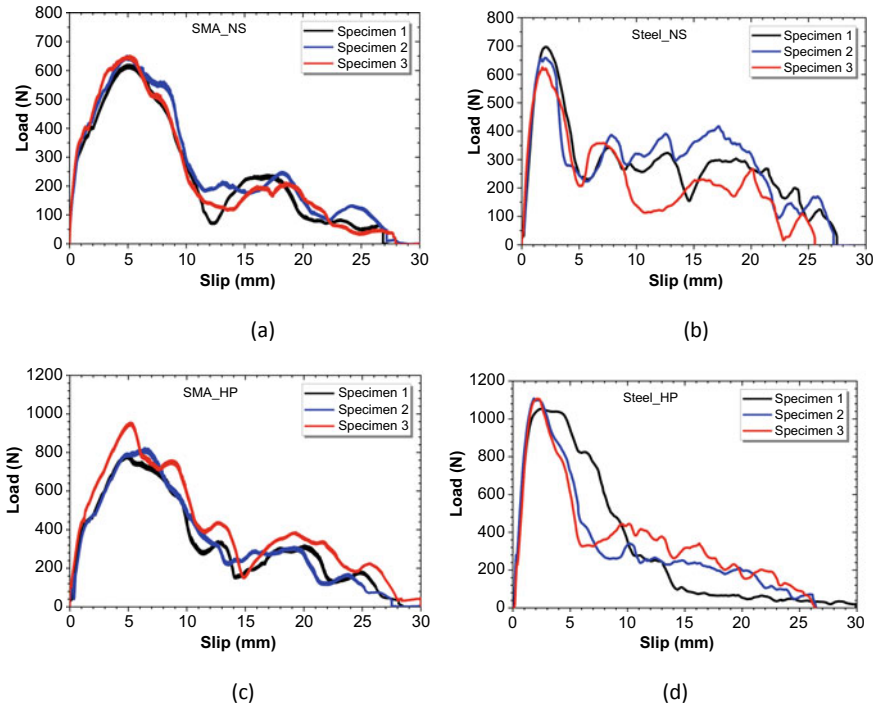
Fig. 6 Pullout behavior of samples for **a** SMA_NS, **b** Steel_NS, **c** SMA_HP, **d** Steel_HP

Table 2 Peak pullout load, maximum tensile stress in the fiber, pullout energy, average, and equivalent bond strength

| Fiber material | Concrete strength | $P_{max}$ (N) | $\sigma_{max}$ (MPa) | $E_P$ (Nmm) | $\tau_{av}$ (MPa) | $\tau_{eq}$ (MPa) |
|---|---|---|---|---|---|---|
| SMA | NS | 640.5 (18.3) | 815.5 (23.3) | 7258 (470) | 6.8 (0.2) | 20.5 (1.3) |
| | HP | 854.9 (88.8) | 1088.5 (113) | 10,753 (1388) | 9.1 (0.9) | 30.4 (3.9) |
| Steel | NS | 685.9 (35.9) | 1078.1 (56.4) | 7066 (1169) | 8.1 (0.4) | 22.2 (3.7) |
| | HP | 1089.4 (31.2) | 1712.4 (49) | 9525 (373) | 12.8 (0.4) | 29.9 (1.2) |

The numbers in bracket indicate standard deviation values

Figure 8 compares the average and equivalent bond strength results for SMA and steel fibers. Compared to 5D steel fiber, the 5D SMA fibers showed 16 and 30% less average bond strength with NS and HP concrete, respectively. However, the SMA fibers showed comparable pullout energy and equivalent bond strength with the steel fibers. The equivalent bond strength of the SMA fibers with NS concrete

**Fig. 7** Normalized average pullout behavior of samples for SMA and steel fibers
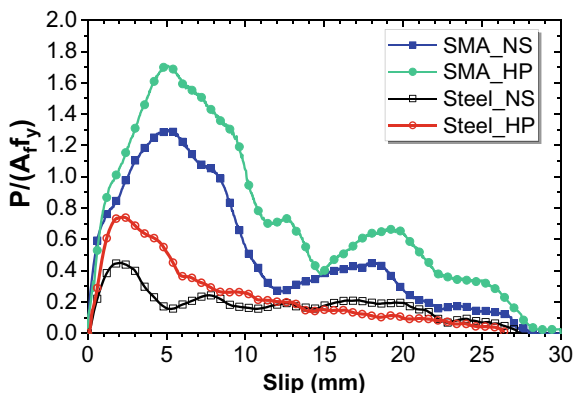


were 7.5% less than that of the steel counterparts. Although the SMA fibers exhibited less peak pullout load, SMA fibers extracted from HP concrete showed 1.6% higher equivalent bond strength than steel fibers. This higher equivalent bond strength of the SMA attributed to the more ductile response of the SMA fibers at peak load. As can be seen in Fig. 6b and d the steel fiber showed linear response up to peak load. While the SMA fibers showed a linear response up to around 400 N then flattens for a short slip and then follows a relatively gentle slope up to peak load. In the SMA fibers the peak load was recorded at around 5 mm slip while in the steel fibers the maximum load corresponds to around 2 mm slip. Thus, the SMA fibers could produce a more ductile fiber reinforced concrete than the steel fibers do. This variation in response is attributed to the stress plateau formation followed by strain hardening (shown in Fig. 2) of the heat-treated SMA. Although there are differences in concrete type, the SMA fiber average and the equivalent bond strength results from the present work were significantly higher than the SMA fibers with similar anchorage reported from previous research [13]. This improvement in pullout resistance is attributed to a shorter stress plateau length and higher strain hardening slope achieved through the proposed fiber fabrication process.

## 3.2 Cyclic Pullout Response

The cyclic pullout tests for SMA and steel fibers were evaluated for specimens embedded in HP concrete. Figure 9 compares the cyclic pullout load slip plots of SMA and steel fibers. The loading and unloading paths of the steel fibers had slight difference while the paths are completely different for the SMA fibers. It can be seen in the Fig. 9b that the SMA fibers showed a flag-shaped response during loading and unloading with high re-centering capacity. This flag-shaped response shows that adequate anchorage was provided by the 5D geometry and upper plateau stress of SMA was reached that led to a higher energy dissipation and deformation recovery.
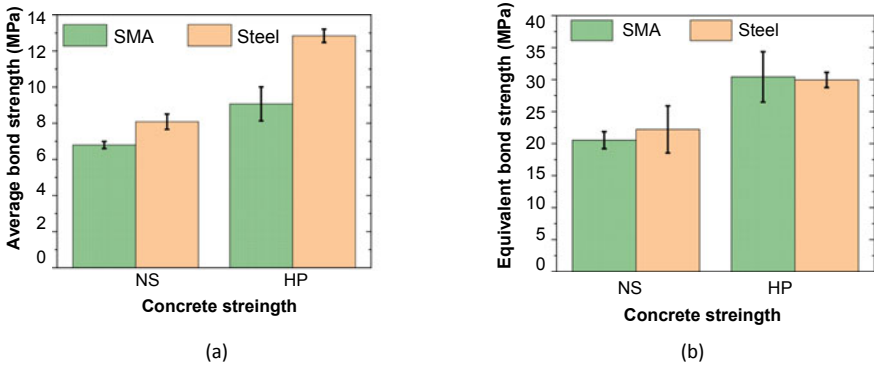
**Fig. 8** Pullout responses of SMA and steel fibers. **a** average and **b** equivalent bond strength

It is worth noting that the recorded pullout displacement was a combination of slip and deformation. For the SMA fibers during the first ten cycles, the fiber tensile stress was significantly higher than the loading plateau stress (transformation stress) this led to stress-induced martensite transformation, more energy was dissipated, and higher deformation was recovered. At subsequent cycles the tensile stress in the fiber decreases and relatively lower energy was dissipated, and higher portion of the pullout displacement accounts for the slip than deformation. It is worth mentioning that the cyclic tests were conducted at a frequency of 0.017 Hz and strain rate has an effect on the shape of the super elastic loop, strain localization and the dissipated energy [9, 19]. The commutative pullout energy of the SMA and steel fibers is shown in Fig. 10. At the initial cycles the steel fibers dissipate more energy than the SMA counterparts due to a steel fibers' higher pullout load at a lower slip. However, after the eighth cycle the SMA fibers start to outperform the steel fibers and at the end of the 30 cycles the total pullout energy of the SMA fibers was 25% higher than that of the steel fibers. It is well established that only structures that can disperse the energy exerted by the dynamic loads can withstand cyclic loads like earthquake [20]. Thus, the higher energy dissipation capacity and re-centering behavior of the SMA fibers favors a more ductile and dynamic load resistant fiber reinforced concrete.
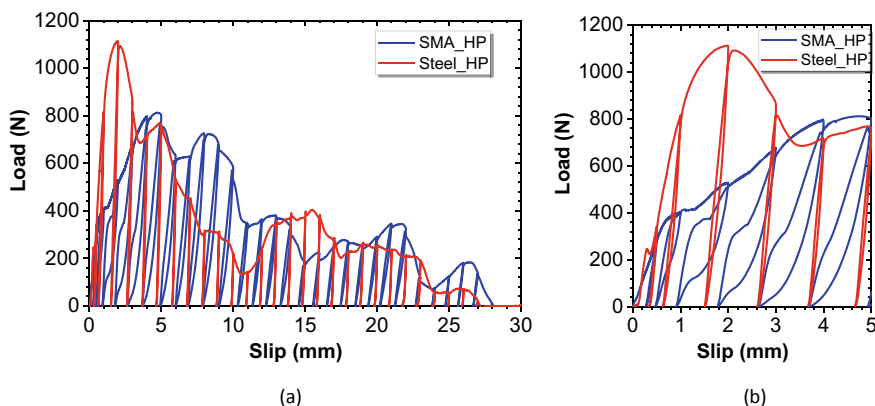
**Fig. 9** Cyclic pullout load versus slip for SMA and steel fibers **a** full response and **b** initial cycles
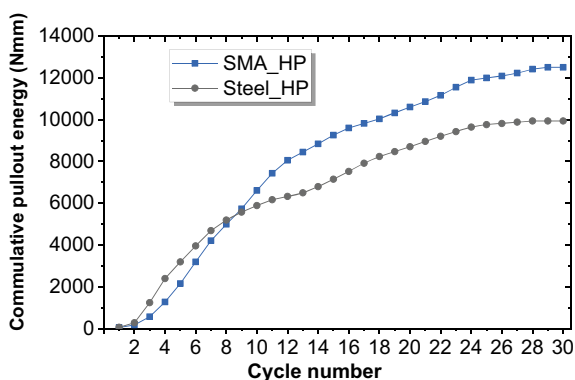


**Fig. 10** Cumulative pullout energy of SMA and steel fibers under cyclic loading

## 4 Conclusion

Single fiber pullout tests for super elastic SMA and steel fibers were conducted and the following conclusion can be drawn from the experimental results:

- The proposed fiber fabrication method: shaping the heavily cold-worked (48% cold worked) NiTi wires to the desired end-hook geometry followed by heat treatment at 350 °C could improve the anchorage property of the super elastic fibers. The improvement attributed to the short stress plateau length and strain hardening at relatively lower strain.
- Combining the proposed SMA fiber fabrication strategy and 5D geometry provided sufficient anchorage that the stress in the fiber exceeded the material's upper plateau stress. This sufficient bond led to a higher energy dissipation and deformation recovery during cyclic loading.

- SMA and steel fibers imbedded in higher strength concrete showed higher pullout strength.
- The SMA fibers showed a lower average bond strength than the steel counterparts. However, the SMA fibers showed comparable equivalent bond strength and significantly higher pullout energy than the steel fibers.

# References

1. Menna DW, Genikomsou AS, Green MF (2020) Flexural performance of double hooked end steel fibre reinforced concrete beams under cyclic loading. Paper presented at the XI International Conference on Structural Dynamics Athens, Greece
2. Zollo RF (1997) Fiber-reinforced concrete: an overview after 30 years of development. Cem Concr Compos 19(2):107–122
3. Robins P, Austin S, Jones P (2002) Pull-out behaviour of hooked steel fibres. Mater Struct 35(7):434–442
4. Abdallah S, Fan M (2017) Anchorage mechanisms of novel geometrical hooked-end steel fibres. Mater Struct 50(2):1–11
5. Lee S-C, Shin K-J, Oh B-H (2011) Cyclic pull-out test of single PVA fibers in cementitious matrix. J Compos Mater 45(26):2765–2772
6. Boulekbache B, Hamrat M, Chemrouk M, Amziane S (2016) Flexural behaviour of steel fibre-reinforced concrete under cyclic loading. Constr Build Mater 126:253–262
7. Sherif MM, Khakimova EM, Tanks J, Ozbulut OE (2018) Cyclic flexural behavior of hybrid SMA/steel fiber reinforced concrete analyzed by optical and acoustic techniques. Compos Struct 201:248–260
8. Lagoudas DC (2008) Shape memory alloys: modeling and engineering applications. Springer Science & Business Media
9. Suhail R, Chen JF, Amato G, McCrum D (2020) Mechanical behaviour of NiTiNb shape memory alloy wires–strain localisation and effect of strain rate. Mech Mater 144:103346
10. Choi E, Kim D, Lee J-H, Ryu G-S (2017) Monotonic and hysteretic pullout behavior of superelastic SMA fibers with different anchorages. Compos B Eng 108:232–242
11. Shajil N, Srinivasan S, Santhanam M (2013) Self-centering of shape memory alloy fiber reinforced cement mortar members subjected to strong cyclic loading. Mater struct 46(4):651–661
12. Choi E, Mohammadzadeh B, Hwang J-H, Kim WJJC (2018) Pullout behavior of superelastic SMA fibers with various end-shapes embedded in cement mortar. Constr Build Mater 167:605–616
13. Dehghani A, Aslani F (2021) Effect of 3D, 4D, and 5D hooked-end type and loading rate on the pull-out performance of shape memory alloy fibres embedded in cementitious composites. Constr Build Mater 273:121742
14. Sharma N, Kumar K, Kumar V (2018) Post-processing of NiTi alloys: issues and challenges. Powder Metall Met Ceram 56(9):599–609
15. Feng J, Sun W, Wang X, Shi X (2014) Mechanical analyses of hooked fiber pullout performance in ultra-high-performance concrete. Constr Build Mater 69:403–410
16. Liu X, Wang Y, Yang D, Qi M (2008) The effect of ageing treatment on shape-setting and superelasticity of a nitinol stent. Mater Charact 59(4):402–406

17. Noonai N, Khantachawana A, Kaewtatip P, Kajornchaiyakul J (2012) Improvement of mechanical properties and transformation behavior of NiTi drawn wires for orthodontics applications. Paper presented at the Advanced Materials Research
18. Sadiq H, Wong M-B, Al-Mahaidi R, Zhao X (2010) The effects of heat treatment on the recovery stresses of shape memory alloys. Smart Mater Struct 19(3):035021
19. Nemat-Nasser S, Guo W-G (2006) Superelastic and cyclic response of NiTi SMA at various strain rates and temperatures. Mech Mater 38(5–6):463–474
20. Ganesan N, Indira P, Sabeena M (2014) Behaviour of hybrid fibre reinforced concrete beam–column joints under reverse cyclic loads. Mater Des 54:686–693

# Elastostatics of Spherical Capsules in Self-healing Cement Matrix

**Shannon Guo and Samir E. Chidiac**

**Abstract** A rigorous solution for a liquid-filled spherical capsule in self-healing cement matrix with remote uniform strain or stress is presented. The capsule shell is considered as an elastic material, and the interface between the capsule and cement is simulated as imperfect elastic spring-type interface. The healing agent enclosed in the capsule is considered as incompressible fluid. The state of strain/stress in the capsule and on the capsule–cement interface are derived. Consequently, the failure modes of the capsule, being rupture or debonding on the interface, are determined. Numerical results demonstrate the significance of capsule design and imperfect interface on the failure modes of capsules. The model can be used to assess capsule properties, including shell thickness, diameter, and material properties, in the design of self-healing system.

**Keywords** On-demand transit · Ridership · Difference-in-difference model · Travel time · Passenger · Public transit

## 1 Introduction

The success of a capsule-based self-healing system is determined by the number of capsules hit by the cracks and the sealing of these cracks by the encapsulated healing agent [1]. If the crack induces debonding of the capsule from the cement, the encapsulated sealing agent will not be released, and the crack propagation will not be stopped. Therefore, it is important to determine the stresses developed in the capsule and at the interface zone between the cement and the capsule by studying the interaction between the crack and the capsule ([2, 3], Reda et al. 2022).

Cracking of early age concrete may be induced by shrinkage of different mechanisms: plastic shrinkage, autogenous shrinkage, drying shrinkage, and carbonation

S. Guo (✉) · S. E. Chidiac
Department of Civil Engineering, McMaster University, Hamilton, ON, Canada
e-mail: guoxs@mcmaster.ca

shrinkage. Depending on the concrete mixture design, curing regime, and environmental exposure conditions, one or more shrinkage mechanism can occur resulting in cracks developing in the concrete core and/or surface. This study examines the interaction between a shrinkage crack and a capsule containing a healing agent by assuming that the representative medium is composed of a composite matrix and a multi-phase composite sphere. The composite matrix represents cement containing distributed microcapsules and shrinkage cracks, while the composite sphere is composed of capsule shell encapsulating the healing agent in liquid form.

## 2   Statement of the Problem and Methodology

Figure 1 illustrates a representative volume element (RVE) with randomly distributed capsules containing self-healing agent. An imperfect interface is assumed between the capsule and cement matrix, which implies that sliding or debonding may take place on the interface. It is assumed that the liquid agent is incompressible, and the capsule shell response is elastic before rupture. The imperfect interface is simulated as a thin layer of weak, elasto-perfect plastic material, which allows sliding in the tangential direction and separation in the radial direction. The normal and tangential stiffness (as illustrated by the springs in Fig. 1b) can be determined using the elastic and shear moduli when given the thickness of the weak layer. In doing so, the capsule is considered equivalent to a three-phase composite sphere, or more generally, as a n-phase composite sphere.

The approach to determine the stresses and strains in each phase of the composite sphere consists of three steps, as illustrated in Fig. 1. By considering the RVE in Fig. 1a as a composite material consisting of randomly distributed, dispersed capsules, the cement is homogenized as an equivalent homogeneous matrix (Step 2). To achieve this goal, an equivalent homogeneous sphere is first obtained to replace the composite sphere (Step 1). The interaction between a capsule and cement is then simplified as an analysis for a single composite sphere in a homogeneous matrix subjected to far-field tensile stress (Step 3). For simplicity, only mono-sized spherical capsules are considered. The tasks in these steps are summarized as follows:

- Step 1: Micro-mechanical analysis to determine the effective elastic properties of a homogeneous sphere equivalent to the hollow sphere containing fluid.
- Step 2: Homogenization of cement matrix with distributed hollow spheres, or the equivalent homogeneous sphere and microcracks when necessary, to obtain the effective properties of the equivalent homogeneous matrix.
- Step 3: Determination of stresses in the multi-layered sphere and the stresses on its interface with the equivalent matrix.

Details about the individual steps are presented in the following sections.
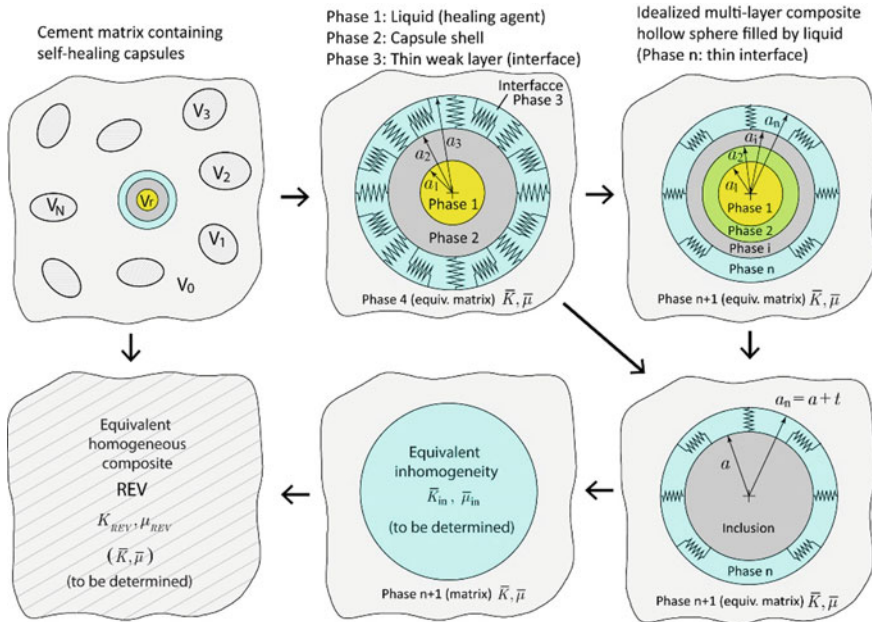
**Fig. 1** Liquid-filled hollow sphere having imperfect interface with cement matrix

# 3 A Multi-scale Model to Determine Stresses in a Composite Sphere

## 3.1 Equivalent Homogeneous Sphere

Figure 2 illustrates an inhomogeneity as a multi-phase composite sphere. Following the work by Goodier [4], a spherical inhomogeneity is defined by the elastic properties, elastic modulus $K_i$ and shear modulus $\mu_i$, the inner radius $R_{i-1}$, and the outer radius $R_i$ of each phase ($i \in [1, n + 1]$, $R_{n+1} \to \infty$). The system consists of an $n$-layer composite sphere where the outmost phase $n + 1$ is the matrix.

### 3.1.1 Stresses and Strain in Each Phase

Following [4], the spherical inhomogeneity problem can be described as a question of how to find the solution of an axisymmetric problem in a polar coordinate system. Let the multi-layered spherical inhomogeneity embedded in an equivalent homogenized bulk material inhomogeneity with elastic properties being $(\overline{K}, \overline{\mu})$. The remote displacement field is $u^{(\infty)}(x) = \varepsilon_{ij}^{(\infty)} x_j$, $r \to \infty$. The displacement field can be split as
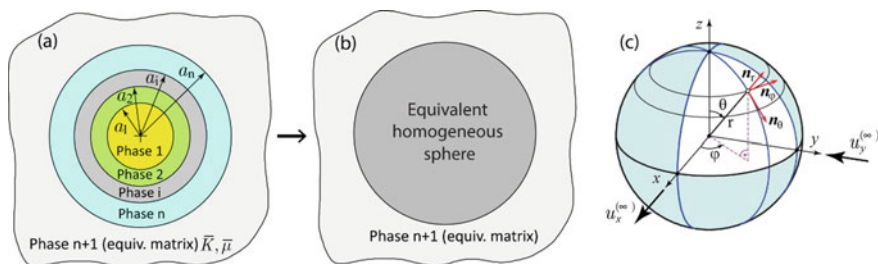
**Fig. 2** Composite sphere of multiple phases, with polar coordinate system

$$u^{(\infty)}(x) = u^{(\infty)}_{\text{spherical}}(x) + u^{(\infty)}_{\text{axisym}}(x) = \underbrace{\varepsilon^{(\infty)}_0 x_i}_{\text{spherical}} + \underbrace{e^{(\infty)}_{ij} x_j}_{\text{axisymmetric}}, \tag{1}$$

which corresponds to a uniform strain $\varepsilon^{(\infty)}$ at the far-field $\varepsilon^{(\infty)}_{ij} = \varepsilon^{(\infty)}_v \delta_{ij}/3 + e^{(\infty)}_{ij}$, with $\varepsilon^{(\infty)}_v = 3\varepsilon^{(\infty)}_0$ corresponding to the volumetric strain and $e^{(\infty)}_{ij}$ the deviatoric strain tensor. Similarly, the displacement and strains in the $i$th phase can be expressed as $u^{(i)}_k = u^{(i)}_k|_{\text{spherical}} + u^{(i)}_k|_{\text{axisym}}$ and $\varepsilon^{(i)}_{kl} = \varepsilon^{(i)}_v \delta_{kl}/3 + e^{(i)}_{kl}$. The stresses can be determined from the elastic stress–strain relationship $\sigma_{ij} = \lambda u_{k,k} \delta_{ij} + \mu(u_{i,j} + u_{j,i})$ or for the stress invariants

$$\begin{Bmatrix} p \\ q \end{Bmatrix} = \begin{bmatrix} K & 0 \\ 0 & 3\mu \end{bmatrix} \begin{Bmatrix} \varepsilon_v \\ \varepsilon_q \end{Bmatrix}, \tag{2}$$

in which $p = \sigma_{kk}/3$, $q = \sqrt{3J_2} = \sqrt{(3/2)s_{ij}s_{ij}}$, $\varepsilon_q = 2\sqrt{J_{2\varepsilon}/3} = \sqrt{(2/3)e_{ij}e_{ij}}$.

As a special case, axisymmetric purely deviatoric far-field strains can be expressed as $\varepsilon^{(\infty)}_{xx} = \varepsilon^{(\infty)}_{yy} = -\varepsilon^{(\infty)}_A$, $\varepsilon^{(\infty)}_{zz} = 2\varepsilon^{(\infty)}_A$, with $\varepsilon_q = \sqrt{(2/3)e_{ij}e_{ij}} = 2\varepsilon^{(\infty)}_A$. In the polar coordinates, the overall displacements can be expressed as [5–7]

$$\frac{u^{(i)}_r(\xi, \theta)}{r} = \left[ 12v_i \mathcal{A}_i \xi^2 + 2\mathcal{B}_i + 2(5 - 4v_i)\frac{\mathcal{C}_i}{\xi^3} - 3\frac{\mathcal{D}_i}{\xi^5} \right] \mathcal{P}_2(\cos\theta)$$

$$\frac{u^{(i)}_\theta(\xi, \theta)}{r} = \left[ (7 - 4v_i)\mathcal{A}_i \xi^2 + \mathcal{B}_i + 2(1 - 2v_i)\frac{\mathcal{C}_i}{\xi^3} + \frac{\mathcal{D}_i}{\xi^5} \right] \frac{d\mathcal{P}_2(\cos\theta)}{d\theta}$$

$$u^{(i)}_\phi(\xi, \theta) = 0, \tag{3}$$

in which $\mathcal{P}_2$ is the Legendre polynomial of order 2, $\xi$ is the dimensionless radius defined as $\xi = r/c$ with c being a characteristic radius. For convenience, let $c = a_1$. By applying the stress–strain relationship, the stresses in each phase are determined as

$$\frac{\sigma^{(i)}_{rr}}{2\mu_i} = \left( \mathcal{F}_i \frac{1 + v_i}{1 - 2v_i} - 2\frac{\mathcal{G}_i}{\xi^3} \right) + \left[ -6v_i \mathcal{A}_i \xi^2 + 2\mathcal{B}_i - 4(5 - v_i)\frac{\mathcal{C}_i}{\xi^3} + 12\frac{\mathcal{D}_i}{\xi^5} \right] \mathcal{P}_2(\cos\theta)$$

$$\frac{\sigma_{r\theta}^{(i)}}{2\mu_i} = \left[(7 + 2v_i)\mathcal{A}_i\xi^2 + \mathcal{B}_i + 2(1 + v_i)\frac{\mathcal{C}_i}{\xi^3} - 4\frac{\mathcal{D}_i}{\xi^5}\right]\frac{d\mathcal{P}_2(\cos\theta)}{d\theta}$$

$$\frac{\sigma_{\theta\theta}^{(i)}}{2\mu_i} = \left(\mathcal{F}_i\frac{1 + v_i}{1 - 2v_i} + \frac{\mathcal{G}_i}{\xi^3}\right) + 3(7 + v_i)\mathcal{A}_i\xi^2 + 2\mathcal{B}_i + (1 - 2v_i)\frac{\mathcal{C}_i}{\xi^3} + \frac{9}{2}\frac{\mathcal{D}_i}{\xi^5}$$

$$+ (3\cos^2\theta)\left[-7(2 + v_i)\mathcal{A}_i\xi - \mathcal{B}_i + (1 + 2v_i)\frac{\mathcal{C}_i}{\xi^3} - \frac{11}{2}\frac{\mathcal{D}_i}{\xi^5}\right]$$

$$\frac{\sigma_{\phi\phi}^{(i)}}{2\mu_i} = \left(\mathcal{F}_i\frac{1 + v_i}{1 - 2v_i} + \frac{\mathcal{G}_i}{\xi^3}\right) + 15v_i\mathcal{A}_i\xi^2 - \mathcal{B}_i - 5(1 - 2v_i)\frac{\mathcal{C}_i}{\xi^3} + \frac{3}{2}\frac{\mathcal{D}_i}{\xi^5}$$

$$+ (3\cos^2\theta)\left[-2(11 + 2v_i)\mathcal{A}_i\xi^2 + 3(1 - 2v_i)\frac{\mathcal{C}_i}{\xi^3} - \frac{5}{2}\frac{\mathcal{D}_i}{\xi^5}\right]. \tag{4}$$

The far-field boundary condition at $r \to \infty$ and the non-singularity of stress at $r = 0$ requires $\mathcal{C}_1 = \mathcal{D}_1 = 0$ and $\mathcal{A}_{n+1} = 0$ and $\mathcal{B}_{n+1} = \varepsilon_A^{(\infty)}$. Enforcing the continuity of displacement and traction on the interface between Layer $m - 1$ and Layer $m$ yields

$$\left[S_{m-1}^{(m,m-1)}\right]\{\tilde{\mathcal{A}}_{m-1}\} = \left[S_m^{(m,m-1)}\right]\{\tilde{\mathcal{A}}_m\}, \tag{5}$$

in which $\{\tilde{\mathcal{A}}_m\} = [\mathcal{A}_m\ \mathcal{B}_m\ \mathcal{C}_m\ \mathcal{D}_m]^T$ and

$$\left[S_{j=k+1}^{(k+1)k}\right] = \left[S_{j=k}^{(k+1)k}\right] = \begin{bmatrix} 12v_j\rho_{k1}^2 & 2 & 2(5 - 4v_j)\rho_{k1}^{-3} & -3\rho_{k1}^{-5} \\ (7 - 4v_j)\rho_{k1}^2 & 1 & 2(1 - 2v_j)\rho_{k1}^{-3} & \rho_{k1}^{-5} \\ -3v_j\mu_j\rho_{k1}^{22} & \mu_j & -2(5 - v_j)\mu_j\rho_{k1}^{-3} & 6\mu_j\rho_{k1}^{-5} \\ (7 + 2v_j)\mu_j\rho_{k1}^2 & \mu_j & 2(1 + v_j)\mu_j\rho_{k1}^{-3} & -4\mu_j\rho_{k1}^{-5} \end{bmatrix}. \tag{6}$$

The coefficients $\{\tilde{\mathcal{A}}_m\}$ in the displacement function for the $m$th layer can be obtained by solving the above equation progressively.

For deformation of spherical symmetry, the far-field displacement (Phase $n + 1$) in spherical coordinates is $u_r^{(\infty)}(r, \theta, \phi) = \varepsilon^{(\infty)}r$, $u_\theta^{(\infty)}(r, \theta, \phi) = u_\phi^{(\infty)}(r, \theta, \phi) = 0$ at $r \to \infty$. The displacement in the ith phase is

$$\frac{u_r^{(i)}(\xi, \theta)}{r} = \mathcal{F}_i + \frac{\mathcal{G}_i}{\xi^3}, \quad u_\theta^{(i)}(\xi, \theta, \varphi) = u_\varphi^{(i)}(\xi, \theta, \varphi) = 0, \tag{7}$$

in which $\mathcal{F}_{n+1} = \varepsilon_0^{(\infty)}$ is determined from the far-field boundary condition at $r \to \infty$. The incompressibility of the liquid requires $\mathcal{F}_1 = \mathcal{G}_1 = 0$. The continuity of displacement and traction on the interface provide the relation between two adjacent solid phases:

$$\left[R_{m-1}^{(m,m-1)}\right]\{\tilde{\mathcal{F}}_{m-1}\} = \left[R_m^{(m,m-1)}\right]\{\tilde{\mathcal{F}}_m\} \tag{8}$$

where $\{\tilde{\mathcal{F}}_m\} = [\mathcal{F}_m \ \mathcal{G}_m]^T$ and

$$[S_{j=k+1}^{(k+1)k)}] = [S_{j=k}^{(k+1)k)}] = \begin{bmatrix} 1 & \rho_{k1}^{-3} \\ 3K_j & -4\mu_j\rho_{k1}^{-3} \end{bmatrix}. \tag{9}$$

For hollow composite sphere filled by incompressible liquid (Phase 1 in Fig. 1), the traction condition on the interface of Phase 1 and Phase 2 is $\sigma_{rr}^{(1)} = \sigma_{\theta\theta}^{(1)} = -p$ and $\sigma_{r\theta}^{(1)} = 0$ with $p$ being the hydrostatic stress tensor in the liquid region, thus Eq. 4a can be simplified to

$$\frac{\sigma_{rr}^{(2)}(\xi = 1, \theta)}{2\mu_2} = \mathcal{F}_2\frac{1 + v_2}{1 - 2v_2} - 2\mathcal{G}_2 = -p. \tag{10}$$

On the inner surface of the capsule where $\xi = 1$, the incompressibility of liquid also requires the following condition to be satisfied [6]:

$$\int_{S_{int}} \mathbf{u} \cdot \mathbf{n} dS = \int_{S_{int}} u_r^{(2)}(a_1, \theta)c^2 \sin\theta d\theta d\varphi = a_1^3(\mathcal{F}_2 + \mathcal{G}_2) = 0 \tag{11}$$

where $S_{int}$ denotes the liquid/matrix interface at $\xi_1 = 1$. As such, $\mathcal{F}_2$ and $\mathcal{G}_2$ are then set as

$$\mathcal{F}_2 = -p\frac{1 - 2v_2}{3(1 - v_2)}, \quad \mathcal{G}_2 = -\mathcal{F}_2. \tag{12}$$

All other coefficients in the displacement function $u_r^{(i)}(\xi, \theta)$ can be determined from Eq. (5).

### 3.1.2 Local Average Stresses and Strains

The effective properties of the composite sphere, the local stresses, and strains in each phase are first determined for the cases where the sphere is subjected to pure shear and deformation of spherical symmetry.

**Pure shear**

The far-field boundary displacements under pure shear in the form of $u_1^{(\infty)} = \varepsilon_0 x_1$, $u_2^{(\infty)} = -\varepsilon_0 x_2$ and $u_3^{(\infty)} = 0$ are expressed as [5, 8, 9]

$$u_r^{(\infty)} = \varepsilon_0 r \sin^2\theta \cos 2\phi, \ u_\theta^{(\infty)} = \varepsilon_0 r \sin\theta \cos\theta \cos 2\phi, \ u_\phi^{(\infty)} = -\varepsilon_0 r \sin\theta \sin 2\phi. \tag{13}$$

The corresponding far-field tractions are

$$T_r^{(\infty)} = \sigma_0 \sin^2\theta \cos 2\phi, \ T_\theta^{(\infty)} = \sigma_0 \sin\theta \cos\theta \cos 2\phi, \ T_\phi^{(\infty)} = \sigma_0 \sin\theta \sin 2\phi. \tag{14}$$

In phase $(i)$, the displacement field $\mathbf{u}^{(i)}$ can be expressed as $\mathbf{u}^{(i)} = u_r^{(i)}\mathbf{n}_r + u_\theta^{(i)}\mathbf{n}_\theta + u_\phi^{(i)}\mathbf{n}_\varphi$ with

$$u_r^{(i)} = U_r^{(i)}(r)\sin^2\theta\cos 2\phi, \ u_\theta^{(i)} = U_\theta^{(i)}(r)\sin\theta\cos\theta\cos 2\phi, \ u_\phi^{(i)} = U_\phi^{(i)}(r)\sin\theta\sin 2\phi, \tag{15}$$

where $U_r^{(i)}, U_\theta^{(i)}, U_\phi^{(i)}$ are functions of $r$ only and can be generally expressed as

$$U_r^{(i)} = A_i r - 6\frac{v_i}{1 - 2v_i}B_i r^3 + 3\frac{C_i}{r^4} + \frac{5 - 4v_i}{1 - 2v_i}\frac{D_i}{r^2}$$

$$U_\theta^{(i)} = A_i r - \frac{7 - 4v_i}{1 - 2v_i}B_i r^3 - 2\frac{C_i}{r^4} + 2\frac{D_i}{r^2}, \ U_\phi^{(i)} = -U_\theta^{(i)}. \tag{16}$$

The boundary conditions at $r \to \infty$ requires $A_{n+1} = \varepsilon_0$ and $B_{n+1} = 0$. The strain and stresses in each phase can be determined subsequently.

The average strains in each phase are determined through local volume averaging:

$$\overline{\varepsilon}^{(i)} = \frac{1}{V_i}\int_{V_i}\varepsilon^{(i)}\mathrm{d}V = \frac{1}{V_i}\left[\int_{S_i}(\mathbf{u}^{(i)} \otimes \mathbf{n}_r)^s\mathrm{d}S - \int_{S_{i-1}}(\mathbf{u}^{(i)} \otimes \mathbf{n}_r)^s\mathrm{d}S\right] \tag{17}$$

where $\mathbf{n}_r$ denotes the unit outward normal to surface $S$, where $dS = r^2\sin\theta\mathrm{d}\theta\mathrm{d}\varphi$, $\theta \in [0, \pi]$, $\varphi \in [-\pi, \pi]$. After some algebraic manipulations, Eq. (17) can be expressed as

$$\overline{\varepsilon}^{(i)} = \frac{1}{V_i}\int_{V_i}\varepsilon^{(i)}\mathrm{d}V = \frac{3}{5A_{n+1}}\left(\frac{5}{3}A_i - \frac{7(R_i^5 - R_{i-1}^5)}{(1 - 2v_i)(R_i^3 - R_{i-1}^3)}B_i\right)\varepsilon^{(\infty)}. \tag{18}$$

The average strain in the whole n-layered composite sphere is calculated as

$$\overline{\varepsilon} = \frac{3}{4\pi R_n^3}\int_{S_n}(\mathbf{u}^{(i)} \otimes \mathbf{n})^s\mathrm{d}S = \left(1 - \frac{3}{5}\frac{7}{1 - 2v_{n+1}}\frac{B_{n+1}}{A_{n+1}}R_n^2 + \frac{4}{5}\frac{4 - 5v_{n+1}}{1 - 2v_{n+1}}\frac{D_{n+1}}{A_{n+1}R_n^3}\right)\varepsilon^{(\infty)} \tag{19}$$

To ensure limited values of $\overline{\varepsilon}$, $C_1 = D_1 = 0$ and $B_{n+1} = 0$ must hold true. It follows that

$$\overline{\varepsilon} = \frac{3}{4\pi R_n^3}\int_{S_n}(\mathbf{u}^{(i)} \otimes \mathbf{n})^s\mathrm{d}S = \left(1 + \frac{4}{5}\frac{4 - 5v_{n+1}}{1 - 2v_{n+1}}\frac{D_{n+1}}{A_{n+1}R_n^3}\right)\varepsilon^{(\infty)} \tag{20}$$

By considering the stress distribution, the average deviatoric stress in the whole n-layered inclusion is determined as

$$\bar{\mathbf{s}} = \left(1 - \frac{2}{5}\frac{7 - 5v_{n+1}}{1 - 2v_{n+1}}\frac{D_{n+1}}{A_{n+1}R_n^3}\right)\mathbf{s}_0 \tag{21}$$

$D_{n+1} = 0$ is the requirement of strain energy equivalence between the two systems including the original composite sphere and the equivalent homogeneous sphere.

**Spherical symmetry**

Following the same procedure as that in the analysis for pure shear deformation, local average strain in the $i$th phase under deformation in spherical symmetry is determined as $\bar{\varepsilon}_v^{(i)} = \mathcal{F}_i/\mathcal{F}_{n+1}$ . The average volumetric strain and the average mean stress in the whole n-layered sphere subjected to deformation of spherical symmetry are.

$$\bar{\varepsilon}_v = \left(1 + \frac{\mathcal{G}_{n+1}}{\mathcal{F}_{n+1}R_n^3}\right)\varepsilon_{v0}, \quad \bar{p} = \frac{1}{3}\left(1 - \frac{4\mu_{n+1}\mathcal{G}_{n+1}}{3k_{n+1}\mathcal{F}_{n+1}R_n^3}\right)\sigma_0, \tag{22}$$

where $\mathcal{F}_i$ and $\mathcal{G}_i$ have been determined previously. It should be noted that the far-field stress and strain can be related via

$$\varepsilon_0 = \frac{\sigma_0}{E_{n+1}} + v_{n+1}\frac{\sigma_0}{E_{n+1}} = \frac{\sigma_0}{2\mu_{n+1}}.$$

Alternatively, if we introduce strain concentration coefficients $T_d^{(i)}$ and $T_v^{(i)}$ for pure shear and deformation spherical symmetry, the local average strain of $i$th phase are expressed as [9]

$$\bar{\varepsilon}_v^{(i)} = T_v^{(i)}\varepsilon_v^{(\infty)}, \bar{\mathbf{e}}^{(i)} = T_d^{(i)}\mathbf{e}^{(\infty)} \tag{23}$$

$$T_v^{(i)} = \mathcal{F}_i/\mathcal{F}_{n+1}, \quad T_d^{(i)} = \frac{1}{A_{n+1}}\left(A_i - \frac{21}{5}\frac{R_i^5 - R_{i-1}^5}{(1 - 2v_i)(R_i^3 - R_{i-1}^3)}B_i\right). \tag{24}$$

It can be observed that $T_d^{(i)}$ and $T_v^{(i)}$ are functions of elastic and geometric properties of each phase of the multi-layered inhomogeneity and the effective elastic properties of the composite material.

## 3.2 *Effective Moduli of* **n**-*layer Composite Sphere*

The effective elastic properties of the equivalent homogeneous sphere for the layer composite sphere are determined using the Eshelby's strain energy equivalence

method. For the pure shear stress condition, the average spherical stress $\overline{p}^{(i)}$ and deviatoric stress $\overline{\sigma}_d^{(i)}$, which is defined as $\overline{\sigma}_d^{(i)} = (\overline{\sigma}_1^{(i)} - \overline{\sigma}_2^{(i)})/2$ with the deviatoric strain being $\overline{\varepsilon}_d^{(i)} = (\overline{\varepsilon}_1^{(i)} - \overline{\varepsilon}_2^{(i)})/2$, in the $i$th phase are calculated as

$$\overline{p}^{(i)} = K_i \overline{\varepsilon}_v^{(i)} = K_i T_v^{(i)} \varepsilon_v^{(\infty)}, \quad \overline{\sigma}_d^{(i)} = 2\mu_i \overline{\varepsilon}_d^{(i)} = 2\mu_i T_d^{(i)} \varepsilon_d^{(\infty)}, \tag{25}$$

where $K_i$ and $\mu_i$ are the bulk and shear moduli of the $i$th phase, respectively. The overall average strain and stress fields in the multi-layered inhomogeneity are calculated by volume averaging operations, as follows:

$$\overline{\varepsilon}_v^{in} = \sum_{i=1}^{n} \phi_i T_v^{(i)} \varepsilon_v^{(\infty)}, \quad \overline{\varepsilon}_d^{in} = \sum_{i=1}^{n} \phi_i T_d^{(i)} \varepsilon_d^{(\infty)}$$

$$\overline{\sigma}_m^{in} = \sum_{i=1}^{n} 3\phi_i K_i T_v^{(i)} \varepsilon_v^{(\infty)}, \quad \overline{\sigma}_d^{in} = \sum_{i=1}^{n} 2\phi_i \mu_i T_d^{(i)} \varepsilon_d^{(\infty)}, \tag{26}$$

where $\phi_i$ is the volume fraction of the $i$th phase in the multi-layered inhomogeneity.

To replace the multi-layered sphere with an equivalent homogeneous sphere, from the overall average strain and stress fields, the elastic properties of the equivalent homogeneous sphere are calculated as

$$\overline{K}_{in} = \frac{\overline{\sigma}_m^{in}}{3\overline{\varepsilon}_v^{in}} = \frac{\sum_{i=1}^{n} \phi_i K_i T_v^{(i)}}{\sum_{i=1}^{n} \phi_i T_v^{(i)}}, \quad \overline{\mu}_{in} = \frac{\overline{\sigma}_d^{in}}{2\overline{\varepsilon}_d^{in}} = \frac{\sum_{i=1}^{n} \phi_i \mu_i T_d^{(i)}}{\sum_{i=1}^{n} \phi_i T_d^{(i)}} \tag{27}$$

which are obtained by making the strain energy stored and the average strain (under the same applied displacement boundary condition) in both systems equal:

$$U_{in} = U_{eq}; \quad U_{eq} = \tfrac{1}{2} V_{in} \varepsilon^{(eq)} \sigma^{(eq)} = \tfrac{1}{2} V_{in} \varepsilon^{(eq)} L_{eq} \varepsilon^{eq}, \tag{28}$$

where $L_{ijkl} = \lambda \delta_{ij} \delta_{kl} + G(\delta_{ik} \delta_{jl} + \delta_{il} \delta_{jk})$ or alternatively $L_{eq} = 3\overline{K}_{in} I_m + 2\overline{\mu}_{in} I_d$. $I_m$ and $I_d$ are the hydrostatic and deviatoric parts of fourth-order unit tensor, respectively; $\overline{K}_{in}$ and $\overline{\mu}_{in}$ are the average values of bulk and shear moduli. The mean stress and deviatoric stress are related to the average volumetric and deviatoric strain via $\overline{\sigma}_m^{in} = \overline{K}_{in} \overline{\varepsilon}_v^{in}$ and $\overline{\sigma}_d^{in} = 2\overline{\mu}_{in} \overline{\varepsilon}_d^{in}$, respectively.

The average stress tensor $\overline{\sigma}^{in}$ for the multi-layer inhomogeneity is calculated by taking a volume average over all phases of the inhomogeneity.

$$\overline{\boldsymbol{\sigma}}^{in} = \sum_{i=1}^{n} \phi_i \overline{\sigma}^i = \sum_{i=1}^{n} \phi_i \overline{\mathbf{L}}_i \overline{\varepsilon}^i = \sum_{i=1}^{n} \phi_i \mathbf{L}_i \mathbf{T}^{(i)} \varepsilon^{(\infty)} \tag{29}$$

It follows that

$$\overline{\sigma}_m^{in} = \sum_{i=1}^{n} \phi_i K_i T_v^{(i)} \varepsilon_v^{(\infty)}, \quad \overline{\sigma}_d^{in} = \sum_{i=1}^{n} 2\phi_i \mu_i T_d^{(i)} \varepsilon_d^{(\infty)}. \qquad (30)$$

Similarly the average strains of the inhomogeneity are

$$\overline{\varepsilon}_v^{in} = \sum_{i=1}^{n} \phi_i T_v^{(i)} \varepsilon_v^{(\infty)}, \quad \overline{\varepsilon}_d^{in} = \sum_{i=1}^{n} \phi_i T_d^{(i)} \varepsilon_d^{(\infty)}. \qquad (31)$$

For hollow composite sphere filled by incompressible liquid-spherical symmetry, the determination of $\overline{\varepsilon}_v^{in}$ and $\overline{p}^{in}$ are modified as

$$\overline{\varepsilon}_v^{in} = \sum_{i=2}^{n} \phi_i T_v^{(i)} \varepsilon_v^{(\infty)}, \quad \overline{\sigma}_m^{in} = -\phi_1 p + \sum_{i=2}^{n} \phi_i K_i T_v^{(i)} \varepsilon_v^{(\infty)}. \qquad (32)$$

Consequently, the effective elastic properties of the equivalent homogeneous sphere for a liquid-filled composite sphere are calculated as

$$\overline{K}_{in} = \frac{\overline{\sigma}_m^{in}}{3\overline{\varepsilon}_v^{in}} = \frac{-\phi_1 p + \sum_{i=2}^{n} \phi_i K_i T_v^{(i)} \varepsilon_v^{(\infty)}}{\sum_{i=2}^{n} \phi_i T_v^{(i)} \varepsilon_v^{(\infty)}}, \quad \overline{\mu}_{in} = \frac{\overline{\sigma}_d^{in}}{2\overline{\varepsilon}_d^{in}} = \frac{\sum_{i=1}^{n} \phi_i \mu_i T_d^{(i)}}{\sum_{i=1}^{n} \phi_i T_d^{(i)}}. \qquad (33)$$

### 3.3 Effective Elastic Properties of Composite Containing n-layer Spheres

The $(n + 1)$-phase model by Herve and Zaoui [9] considers a n-phase composite sphere as an inclusion in a matrix that is considered as the $(n + 1)$-phase. To determine the effective moduli of the $(n + 1)$-phase system, [9] assumed that the average strain of the n-layered composite sphere is the same as the macroscopic strain imposed at infinity. This is similarly assumed in [8] and [10]. It should be noted that this is the solution for a medium containing composite spheres, not for the composite sphere itself.

Figure 1 illustrates the procedure to determine the effective properties of composite containing n-layer spheres. In this method, each multi-layered inhomogeneity is replaced by equivalent homogeneous solid spheres. The effective bulk and

shear moduli of the equivalent homogeneous solid sphere have been determined in previous sections. The procedure of this method is summarized as follows [11]:

1. Assume elastic properties $(\overline{K}, \overline{\mu})$ of the infinite homogenized medium containing spheres of different sizes. For applied far-field boundary displacement condition $\mathbf{u}^{(\infty)}$, determine effective elastic properties of the equivalent homogeneous sphere $\overline{K}_{in} = \overline{K}_{in}(\overline{K}, \overline{\mu})$ and $\overline{\mu}_{in} = \overline{\mu}_{in}(\overline{K}, \overline{\mu})$ for each inhomogeneity in the composite, since $A_{n+1} = \varepsilon_0 = \sigma_0/(2\mu_{n+1})$, $B_{n+1} = 0$ and $F_{n+1} = p_0/(3K_{n+1}) = \varepsilon_v/3$.
2. For a RVE of the composite material in which each multi-layered composite sphere has been replaced by the corresponding equivalent homogeneous material in the first step. The effective properties of the RVE $(\overline{K}_{REV}, \overline{\mu}_{REV})$ will be determined based on $(\overline{K}_{in}, \overline{\mu}_{in})$ using the Mori–Tanaka method [12].
3. Solve $\overline{K} = \overline{K}_{REV}$ and $\overline{\mu} = \overline{\mu}_{REV}$ to determine $\overline{K}$ and $\overline{\mu}$.

Following the three steps, for the n-phase composite sphere embedded in a homogeneous phase $(n + 1)$, as shown Fig. 2, the effective modulus of the n-phase sphere coincides that of the RVE of the composite containing many of the sphere. The effective bulk modulus $\overline{K}_{REV} = \overline{K}_n$ can be explicitly expressed as

$$\overline{K}_n = K_n + \frac{\left(R_{n-1}^3/R_n^3\right)\left(\overline{K}_{n-1} - K_n\right)(3K_n + 4\mu_n)}{3K_n + 4\mu_n + 3\left(1 - R_{n-1}^3/R_n^3\right)\left(\overline{K}_{n-1} - K_n\right)}, \quad n \geq 2, \qquad (34)$$

$$K = K_{(n)}^{\text{eff}} = K_n + \frac{R_{n-1}^3/R_n^3}{\frac{1}{K_{(n-1)}^{\text{eff}} - K_n} + \frac{3(R_n^3 - R_{n-1}^3)}{R_n^3}\frac{1}{3K_n + 4\mu_n}}, \quad n \geq 2, \qquad (35)$$

where $R_n$ and $R_{n+1}$ are the radii of phase $n$ and $(n\text{-}1)$, $K_n$ and $\mu_n$ are the bulk and shear moduli of phase n, and $\overline{K}_{n-1}$ is the effective bulk modulus of the $(n\text{-}1)$-coated inclusion. The above equation provides a recursive relationship to compute the effective bulk modulus. No explicit expression for $\overline{\mu}_{REV}$ is obtained from this approach.

As an example, the effective bulk modulus of a three-phase composite sphere (see Fig. 1b) can be expressed as

$$\overline{K}_3^{\text{eff}} = K_3 + \frac{\left(R_2^3/R_3^3\right)\left(\overline{K}_2 - K_3\right)(3K_3 + 4\mu_3)}{3K_3 + 4\mu_3 + 3\left(1 - R_2^3/R_3^3\right)\left(\overline{K}_2 - K_3\right)}, \qquad (36)$$

with

$$\overline{K}_2 = K_2 + \frac{\left(R_1^3/R_2^3\right)(K_1 - K_2)(3K_2 + 4\mu_2)}{3K_2 + 4\mu_2 + 3\left(1 - R_1^3/R_2^3\right)(K_1 - K_2)}, \qquad (37)$$

being the effective modulus of a spherical core with a single coating layer. As a result,

$\overline{K}_{(3)}^{\text{eff}}$

$$= K_3 + \frac{(3K_3 + 4\mu_3)R_2^3\left((K_1 - K_2)R_1^3(3K_3 + 4\mu_2) + (K_2 - K_3)R_2^3(3K_1 + 4\mu_2)\right)}{3(K_2 - K_1)R_1^3\left(R_2^3(3K_3 + 4\mu_2) + 4R_3^3(\mu_3 - \mu_2)\right) + (3K_1 + 4\mu_2)R_2^3\left(3R_2^3(K_3 - K_2) + R_3^3(3K_2 + 4\mu_3)\right)}. \tag{38}$$

It should be noted that other methods can also be used to estimate $(\overline{K}_{\text{REV}}, \overline{\mu}_{\text{REV}})$ after the composite sphere's effective properties $(\overline{K}_{in}, \overline{\mu}_{in})$ being determined. More specifically, the system is simplified as a composite containing many homogeneous spheres of different sizes. For example, the average strain $\overline{\varepsilon}^{(j)}$ and stress $\overline{\sigma}^{(j)}$ in the jth homogeneous sphere can be related to the average strain $\overline{\varepsilon}^{(0)}$ in the matrix and the far-field stress $\overline{\sigma}^{(0)}$ via $\overline{\varepsilon}^{(j)} = G^{(j)}\overline{\varepsilon}^{(0)}$, $\overline{\sigma}^{(j)} = H^{(j)}\overline{\sigma}^{(0)}$, in which the local strain concentration tensor $G^{(j)}$ and stress concentration tensor $H^{(j)}$ using the Mori–Tanaka method [12, 13]. Eshelby method (Eshelby 1957) is an alternate to determine the strain concentration tensor $G^{(j)}$ as $G^{(j)} = [I + S^{(j)}L_0^{-1}(L^{(j)} - L_0)]^{-1}$ in which $S^{(j)}$ is the Eshelby's tensor for the jth equivalent homogeneous inclusion. Knowing the strain concentration tensor, the values of effective elastic properties of the RVE are given by $\overline{\mathbf{L}} = \sum_{j=0}^{N} \eta^{(j)}\mathbf{L}^{(j)}G^{(j)}\left[\sum_{n=0}^{N} \eta^{(n)}G^{(n)}\right]^{-1}$ [11, 12] or explicitly

$$K^{\text{RVE}} = \frac{\sum_{j=0}^{N} \eta_j \overline{K}_j G_v^j}{\sum_{j=0}^{N} \eta_j G_v^j}; \quad \mu^{\text{RVE}} = \frac{\sum_{j=0}^{N} \eta_j \overline{\mu}_j G_d^j}{\sum_{j=0}^{N} \eta_j G_d^j},$$

where $\eta_j$, $\overline{K}_j$, and $\overline{\mu}_j$ are the volume fraction, equivalent bulk, and shear modulus of the jth homogeneous sphere, respectively.

## 4  Treatment of Imperfect Interface

In general, linear spring model is used to describe the relation between the tractions and the displacement discontinuities across the interface. Consider a spherical inclusion (Material 1 or inclusion) embedded in unbounded elastic isotropic matrix (matrix or phase $n + 1$ in Fig. 1) with a thin interphase layer ($i$) between the inclusion and matrix. In a polar coordinate system, the components of the traction on an interface $r = a$ are proportional to the displacement jumps:

$$\begin{aligned}
\sigma_{rr}^{(inc)}(a, \theta, \varphi) &= \sigma_{rr}^{(m)}(a, \theta, \varphi) = k_n[u_r] \\
\sigma_{r\theta}^{(inc)}(a, \theta, \varphi) &= \sigma_{r\theta}^{(m)}(a, \theta, \varphi) = k_t[u_\theta] \\
\sigma_{r\varphi}^{(inc)}(a, \theta, \varphi) &= \sigma_{r\varphi}^{(m)}(a, \theta, \varphi) = k_t[u_\varphi],
\end{aligned} \tag{39}$$

where $[u_r]$ and $k_n$ are the displacement jump at the interface in the $r$-direction and the normal stiffness, respectively, while $[u_\theta]$, $[u_\varphi]$ and $k_t$ are the tangential displacement jumps and the tangential stiffness.

In this study, the effect of interface is approximated by a thin flexible elastic layer, such as in [7] and [5]. Assuming the thickness $t$, elastic properties $\mu_i$ and $v_i$ of the interphase layer, the distribution of displacements and stresses in different material layers (including the interface layer, as shown in Fig. 1) can be determined using the method developed in the previous sections. The displacement jumps, $[u_r]$ induced by deformation of spherical symmetry and $[u_\theta]$ under axisymmetric deformation across an interface at $r = a$, are

$$[u_r] = u_r(a+t) - u_r(a) \approx \left.\frac{\partial u_r}{\partial r}\right|_{r=a} t, \ [u_\theta] = u_\theta(a+t) - u_\theta(a) \approx \left.\frac{\partial u_\theta}{\partial r}\right|_{r=a} t,$$

(40)

where

$$\frac{\partial u_r}{\partial r} = \left(\mathcal{F}_i - 2\frac{\mathcal{G}_i}{\xi^3}\right), \ \frac{\partial u_\theta}{\partial r} = \left[3(7 - 4v_i)\mathcal{A}_i\xi^2 + \mathcal{B}_i - 4(1-2v_i)\frac{\mathcal{C}_i}{\xi^3} - 4\frac{\mathcal{D}_i}{\xi^5}\right]\frac{d\mathcal{P}_2(\cos\theta)}{d\theta}$$

(41)

are determined using the displacement functions $\mathbf{u}(r, \theta, \varphi)$ given in Eqs. (3) and (7). The corresponding interface tractions in the jth phase being

$$\sigma_{rr}^{(j)} = 2\mu_j\left(\mathcal{F}_j\frac{1+v_j}{1-2v_j} - 2\frac{\mathcal{G}_j}{\xi^3}\right), \ \frac{\sigma_{r\theta}^{(j)}}{2\mu_j}$$

$$= \left[(7 + 2v_j)\mathcal{A}_j\xi^2 + \mathcal{B}_j + 2(1+v_j)\frac{\mathcal{C}_j}{\xi^3} - 4\frac{\mathcal{D}_j}{\xi^5}\right]\frac{d\mathcal{P}_2(\cos\theta)}{d\theta},$$

(42)

where $\xi = r/a$. The tractions $\sigma_{ij}^{(inc)}$ and $\sigma_{ij}^{(m)}$ correspond to $\xi = 1$ and $\xi = 1 + t/a$ with $a$ being the radius of the equivalent homogeneous sphere (See Fig. 1). After some algebraic manipulations, one has

$$k_n = \frac{\sigma_{rr}^{(i)}(a)}{[u_r]} = \frac{K_i + 4\mu_i/3}{\left(1 - \frac{K_i}{K_{inc}}\frac{2v_i}{1+v_i}\right)t}, \quad k_t = \frac{\sigma_{r\theta}^{(i)}(a)}{[u_\theta]}.$$

(43)

When $\mu_i \ll \mu_{inc}$, and $K_i \ll K_{inc}$ (i.e., $v_i < 0.5$ for compressible coating layer), the above relation can be approximated to

$$k_n = \frac{K_i + 4\mu_i/3}{t}, \quad k_t = \frac{\mu_i}{t}.$$

(44)

When the normal and tangential stiffness of the interface are estimated, the above relations can be used to select the thickness and the elastic properties ($\mu_i$ and $v_i$) of the interphase layer. Subsequently, the stresses and strains in each phase (including the interphase layer mimicking the interface) can be determined. When the composite sphere simulates a spherical capsule filled with healing agent, the failure mode of the capsule either shell rupture or interfacial debonding can be determined.

## 5 Numerical Examples

The numerical examples are limited to uniformly dispersed spherical capsules in an equivalent matrix with its effective properties being determined in Step 1. The interaction between a single capsule with the surrounding matrix is examined to determine the stresses and deformation of the capsule. Figure 3a shows a spherical capsule in a homogeneous isotropic matrix with far-field uniaxial tensile stress $\sigma_0$, as well as the local and global coordinates (Fig. 3b).

The material properties used in the simulations are

- Cement: $E_0 = 30$ GPa, $\nu_0 = 0.2$
- Shell material: $E_{cap} = 2 - 6$ GPa, $\nu_{cap} = 0.3$
- Capsule: diameter 200 μm, shell thickness $t_{shell} = (5 - 10)$ μm.

The case of a hollow spherical capsule with $E_{cap} = 2$ GPa, shell thickness $t_{shell} = 5$ μm, and a flexible interphase layer thickness $t_{int} = 5$ μm with elastic modulus $E_{int} = E_{cap}/10$ is used as a reference for comparison. Figure 4 compares the distribution of $\sigma_{r\theta}$, $\sigma_{rr}$, and $\sigma_{\theta\theta}$ at points on the interface obtained from (1) the reference case, (2) the shell thickness is increased to 10 μm, and (3) the stiffness of the interface is reduced by 50% when the capsules are assumed to be hollow. When the shell thickness increases, as one may expect, the increased shell thickness results in higher equivalent elastic modulus of the capsule, which corresponds to smaller deformation of the capsule. As a result, the maximum tensile stress $\sigma_{\theta\theta} @ \theta = 90°$ decreases, but the maximum tangential stress $\sigma_{r\theta} @ \theta = 45°$ increases. The maximum radial stresses $\sigma_{rr}$, tensile at $\theta = 90°$, and compressive at $\theta = 0°$, both increase. This implies that, as the shell thickness increases, the probability of capsule rupture decreases, while probability of sliding and debonding along the interface increases.

When the interface becomes more flexible by reducing the stiffness of the interface in Case (3), the magnitudes of $\sigma_{r\theta}$, $\sigma_{rr}$, and $\sigma_{\theta\theta}$ decrease. This clearly shows that the probability of capsule rupture decreases. When considering the decrease of bonding strength and sliding resistance of the interface for poor bonding, which tend to be more significant than the small reduction in the magnitudes of $\sigma_{r\theta}$ and $\sigma_{rr}$ shown in Fig. 4, it is expected that more debonding will occur on the capsule–cement interface.

**Fig. 3** composite sphere of multiple phases and the polar coordinate system
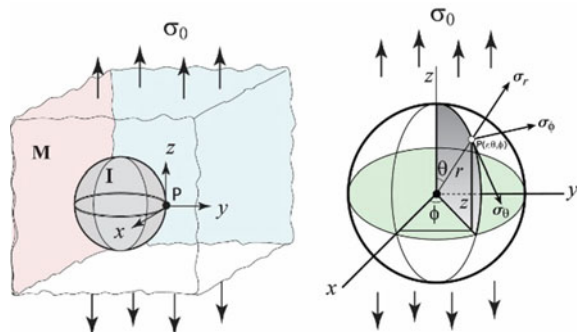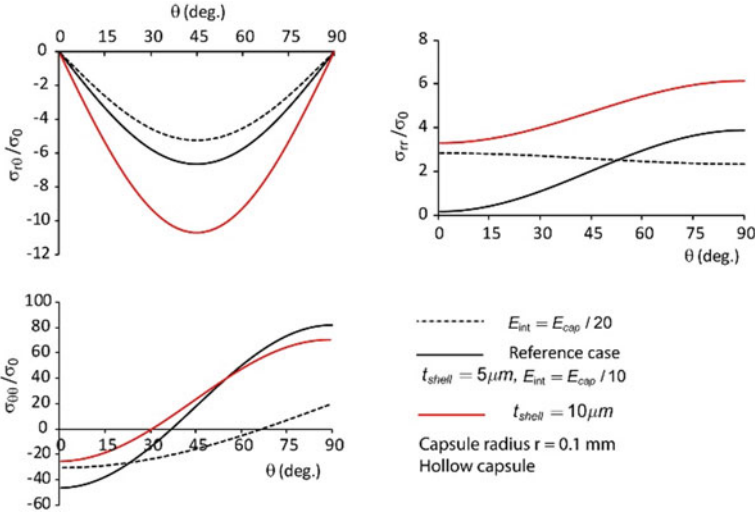
**Fig. 4** Distributions of different stresses for a hollow spherical capsule under uniaxial tension

However, more investigation is required to adequately capture the interface strength characteristics.

Figure 5 shows the distributions of $\sigma_{r\theta}$, $\sigma_{rr}$, and $\sigma_{\theta\theta}$ along the interface when the spherical capsule is filled by incompressible self-healing agent. It should be noted that healing agent is incompressible under hydrostatic pressure but can deform when subjected to shear. One observes that the hoop stress $\sigma_{\theta\theta}$ in the capsule shell and the interface tangential shear stress are not significantly affected by the encapsulated healing agent. The radial stress on the outer surface of the liquid-filled capsule is much higher than that for the hollow capsule. A weak contact surface reduces the magnitudes of $\sigma_{r\theta}$, $\sigma_{rr}$, and $\sigma_{\theta\theta}$. Similar to hollow sphere, the interface tangential shear stress on the liquid-filled capsule increases with increasing shell thickness.

## 6 Conclusions

Theoretical analysis is performed to determine the stresses in a single liquid-filled spherical capsule embedded in a matrix. A multi-scale method is proposed, with micro-mechanical analysis for the stresses in the capsule and homogenization method is used to determine the effective elastic properties of the composite sphere and the concrete cement with dispersely distributed capsules. The influence of imperfect bonding between the capsule and the matrix is taken into account. Numerical examples are presented to illustrate the proposed approach as well as the influence of capsule material properties and interface stiffness on the distribution of stresses within the capsules and that on the interface. The developed approach still needs to
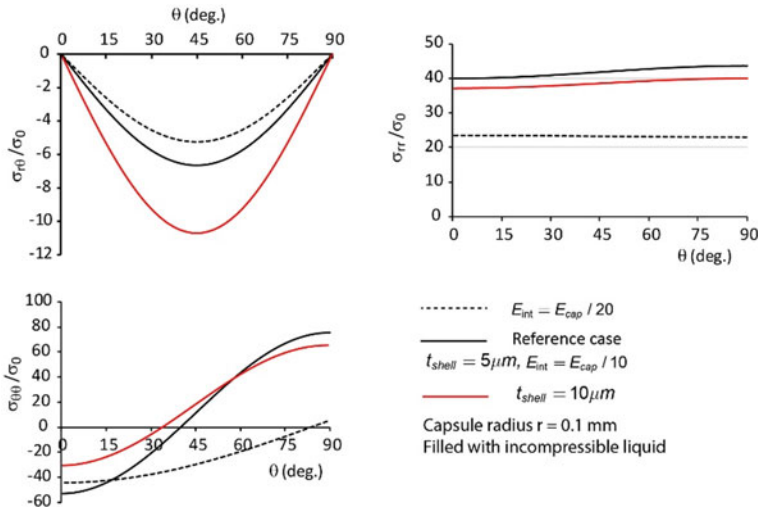
**Fig. 5** Distributions of different stresses for an incompressible liquid-filled spherical capsule under uniaxial tension

be validated using numerical or analytical methods before it can be implemented for the analysis of more complex capsule-crack interaction in self-healing concrete.

# References

1. Guo S, Chidiac SE (2019) Self-healing concrete: a critical review. CSCE Annual Conference, MAT152-1
2. Gilabert FA, Garoz D, Van Paepegem W (2015) Stress concentrations and bonding strength in encapsulation-based self-healing materials. Mater Des 67:28–41
3. Guo S, Reda MA, Chidiac SE (2020) Fracture of cementitious material containing spherical microcapsules. In: Maddalena R, Wright-Syed M, (RM4L eds) Proceedings resilient materials 4 life 2020 (RM4L2020), pp 197–202
4. Goodier JN (1933) Concentration of stress around spherical and cylindrical inclusions and flaws. ASME J Appl Mechanics 55(7):39–44
5. Hashin Z (1991) The spherical inclusion with imperfect interface. J Appl Mech 58:444–449
6. Mancarella F, Style RW, Wettlaufer JS (2016) Interfacial tension and a three-phase generalized self-consistent theory of non-dilute soft composite solids. Soft Matter 12:2744–2750
7. Marur PR (2014) Analysis of an Imperfectly Bonded Hollow Inclusion in an Infinite Medium. J Nanomechanics Micromech 4(4):A4013013, 1–10
8. Christensen RM (1979) Mechanics of composite materials. Dover, New York
9. Herve E, Zaoui A (1993) n-Layered inclusion-based micromechanical modelling. Int J Eng Sci 31(1):1–10

10. Christensen RM, Lo KH (1979) Solutions for effective shear properties in three phase and cylinder models. J Mech Phys Solids 27:315–330
11. Beniwal S, Sharma M, Bishnoi S (2019) Mechanical property evaluation of composites based on n+1 phase model and mori–Tanaka theory. J Eng Mech 145(3):04018139, 1–12
12. Mori T, Tanaka K (1973) Average stresses in the matrix and average elastic energy of materials with misfitting inclusions. Acta Metall 21(5):571–574
13. Qu J, Cherkaoui M (2006) Fundamentals of micromechanics of solids. Wiley, Hoboken
14. Bardella L, Genna F (2001) On the elastic behaviour of syntactic foams. Int J Solids Struct 38(40–41):7235–7260
15. Luo HA, Weng GJ (1987) On Eshelby's inclusion problem in a three-phase spherically concentric solid, and a modification of mori-tanaka's method. Mech Mater 6:347–361
16. Porfiri M, Gupta N (2009) Effect of volume fraction and wall thickness on the elastic properties of hollow particle filled composites. Compos B Eng 40(2):166–173
17. Reda MA, Guo S, Chidiac SE (2020) Challenges of self-healing concrete application. In: Maddalena R, Wright-Syed M, (RM4L eds) Proceedings resilient materials 4 life 2020 (RM4L2020), pp 130–135
18. Shen L, Li J (2005) Homogenization of a fibre/sphere with an inhomogeneous interphase for the effective elastic moduli of composites. Proc Roy Soc 461(2057):1475–1504
19. Shen Z, Zhou H (2020) Predicting effective thermal and elastic properties of cementitious composites containing polydispersed hollow and core-shell micro-particles. Cem Concr Compos 105:103439
20. Shi C, Tu Q, Fan H (2016) Interphase models for nanoparticle-polymer composites. J Nanomechanics Micromech 6(2):04016003

# Shear Behaviour of Concrete Beams Retrofitted with Anchored CFRP Wraps at Elevated Temperatures

**M. F. Qureshi and S. A. Sheikh**

**Abstract** Different anchoring techniques such as metal plates and bolts, U-shaped FRP jackets, FRP anchors have been used to delay the premature debonding of the FRP sheets in strengthened concrete structures. Among these, FRP anchors are more suitable since they can be applied simultaneously with the FRP sheets and are corrosion resistant. Anchored FRP sheets have shown promising results for both shear and flexure strengthened RC structures under room conditions. Due to the changing climate, structures are now exposed to higher than usual temperatures, so it is important to understand the behaviour of these anchored FRP sheets under elevated temperatures. The current study examined the thermal behaviour of four large-scale shear-critical steel-reinforced concrete beams, one unwrapped and three strengthened with a single layer of CFRP sheet and CFRP anchors. The beams tested at room conditions were monotonically loaded to failure, while beams tested at elevated temperatures (40 and 60 °C) were first subjected to a combined sustained load and elevated temperature during the 24 h conditioning period and then monotonically loaded to failure at that temperature. The tests showed the failure of the unwrapped beam by the rupture of a steel stirrup leg and that of the strengthened beams by pull-out of anchors accompanied by debonding of FRP sheet. A single layer of anchored CFRP wrap improved the beam strength by about 96% at room conditions, 101% at a temperature of 40 °C, and 88% at 60 °C. The midspan displacement also increased by 133% as a result of FRP wrapping at room conditions while exposure to 60 °C reduced this improvement to only 68%. A comparative study was also carried out to evaluate equations available in different FRP standards for shear strength predictions.

**Keywords** Fibre-reinforced polymers · CFRP · U-wrap · CFRP anchors · Reinforced concrete · Beam · Shear · Temperature

M. F. Qureshi (✉) · S. A. Sheikh
University of Toronto, Toronto, Canada
e-mail: faizan.qureshi@mail.utoronto.ca

# 1  Introduction

Over the past thirty years, fibre-reinforced polymer (FRP) composites have gained popularity as external reinforcement for strengthening and rehabilitation of rein-forced concrete (RC) structures. FRP offers several advantages over conventional materials such as higher strength to weight ratio, lesser installation time, corro-sion resistance. A large number of bridge girders have been strengthened in shear using FRP sheets. The field application of the FRP sheets is generally in the form of U-wraps due to the geometrical obstructions like the presence of a slab on the top side of the girder. This limits development of full capacity of the FRP sheet because of its premature debonding. Several anchoring techniques such as mechan-ical anchors, U-shaped FRP jackets, FRP anchors have been suggested by researchers to delay the premature debonding. Among the available techniques, FRP anchors are preferred because they are non-corrosive and can be applied simultaneously with the FRP sheets. Anchored FRP sheets can effectively strengthen concrete structures; however, limited information is available on the behaviour of anchored FRP sheets under elevated temperatures which is the need of the hour due to changing climate.

A few studies have reported the effects of high temperatures on the behaviour of concrete structures strengthened with FRP. Different temperature conditions have been examined such as the residual effect of elevated temperature (RT), sustained temperature (ST), freeze–thaw (FT) cycle, and sustained load with increasing temper-ature (SL) condition or fire scenario. Tan and Zhou [1] evaluated the residual effect of elevated temperatures on twenty-three small-scale flexural-critical beams. Seven un-strengthened beams, two beams strengthened with uninsulated GFRP, nine beams strengthened with insulated GFRP, and five beams strengthened with uninsulated BFRP were tested in this program. The beams were exposed to temperatures ranging between 28 and 1035 °C and then cooled overnight before testing under three-point loading. Un-strengthened beams tested at high temperatures showed a reduction in failure load and stiffness compared to control beams tested under room conditions. At elevated temperatures, beams strengthened with uninsulated GFRP sheets showed similar reductions as un-strengthened beams tested under the same conditions. On the other hand, beams strengthened with insulated GFRP sheets showed an insignifi-cant effect of temperature up to 500 °C. Beyond 500 °C, damage to the fibres caused about a 33% reduction in the failure load and beam stiffness compared to the values for the ambient GFRP strengthened beams. Test results from unprotected BFRP strengthened specimens showed better behaviour compared to uninsulated GFRP strengthened beams under the same conditions.

Tetta and Bournas [2] conducted a thermal study on medium-scale rectangular beams (series A) and full-scale T-beams (series B) in a temperature range of 20–250 °C. Series A comprised of 28 beams retrofitted with textile-reinforced mortar (TRM) and FRP sheets in three configurations: side bonding (SB), U-wrap (UW), and full wrap (FW). In series B, beams strengthened with non-anchored and anchored TRM sheets were assessed at elevated temperatures. Test results from series A showed better behaviour of TRM than FRP sheets at elevated temperatures. Moreover, beams

with FW performed the best followed by UW and SB at all temperatures for both types of strengthening. In series B, the anchored TRM beams improved strength by 64% at room conditions compared to ambient unanchored TRM beams. The effectiveness of anchors reduced at 150 °C with anchored TRM strengthened beams showing only a 28% increase over non-anchored TRM beams. All strengthened specimens failed in shear under room conditions except the fully wrapped specimens which demonstrated flexural failure.

Green et al. [3] tested twenty-seven small-scale beams strengthened in flexure using FRP. The test program included five plain concrete (PC) beams, eight reinforced concrete (RC) beams, seven RC beams strengthened with GFRP sheets, and seven RC beams strengthened with CFRP sheets. The beams were exposed to up to 200 freeze–thaw (FT) cycles and later tested under four-point bending under room conditions. One FT cycle was performed each day with a temperature ranging between −18 °C and +15 °C. The PC beams showed brittle failure with little change in flexural capacity due to FT conditioning. The test findings of the conditioned RC beams showed a small decrease in their flexural capacity than the control RC beam. The RC beams failed by concrete crushing after flexural steel yielding. On the other hand, beams strengthened with CFRP and GFRP sheets showed a slight improvement in the load capacity on exposure to FT cycles. The failure of these beams was due to flexural yielding followed by FRP sheet rupture.

In summary, all the temperature conditioning tested were found to be detrimental to the effectiveness of the FRP sheets except the FT cycling. This thermal deterioration is expected to increase when combined with a sustained load which simulates the real field conditions. To the best of the authors' knowledge, no study has been done to assess the beams strengthened with anchored FRP sheets under the dual effects of temperature and loading. Therefore, this study was designed to study the combined effect of temperature and sustained loading on the beams strengthened with anchored FRP sheets.

## 2 Experimental Program

This experimental program was aimed to investigate the effectiveness of CFRP anchors at high environmental temperatures. Four large-scale shear-critical RC beams were strengthened in shear with anchored CFRP sheets. The beams tested in this study were rectangular in section, 400 mm wide, 650 mm high, and 3600 mm in length. The beams reinforced with eight 30 M steel bars as tensile reinforcement, three 30 M steel bars as compression reinforcement, eight closed steel stirrups constructed from U.S. #3 bars spaced at 500 mm c/c, and had a flat metal plate welded at the ends of tensile reinforcement to provide extra anchorage. The flexural reinforcement was chosen to ensure shear failure. The schematic of the beam specimen is illustrated in Fig. 1, and the details of the experimental program are outlined in Table 1. A naming convention "BY-Z" was used for the beams, where B stands for beam specimen; Y corresponds to the type of strengthening: U for unwrapped
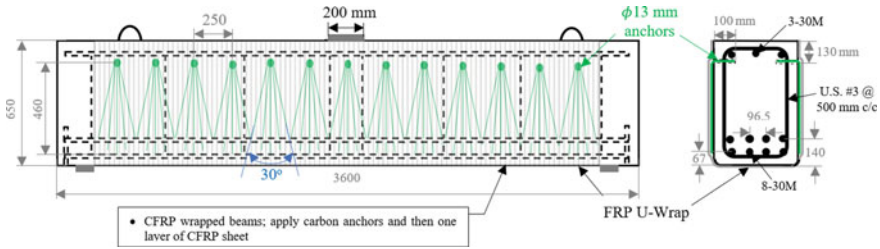
**Fig. 1** Schematic of beam strengthened with anchored CFRP sheet

**Table 1** Experimental program

| Specimen ID | Test temperature (°C) | Conditioning duration (Hr) | Sustained load[a] (%) | FRP strengthening |
|---|---|---|---|---|
| BU-A | 22 | – | – | – |
| BC-A | 22 | – | – | Anchored CFRP sheet |
| BC-40 | 40 | 24 | 30 | Anchored CFRP sheet |
| BC-60 | 60 | 24 | 30 | Anchored CFRP sheet |

[a] Sustained load is the percentage of the ambient strength of the unwrapped beam

beams and C for beams wrapped with anchored CFRP sheets; Z represents the test temperature: A for ambient conditions, 40 for 40 °C and 60 for 60 °C.

## 2.1 Material Properties

The mechanical properties of the steel bars and FRP materials used in the construction and strengthening of the beams are listed in Table 2. Commercially available unidirectional CFRP sheets and CFRP anchors were used in this test program. A two-component epoxy comprising resin (A) and hardener (B) was used as a polymer matrix in this study. Parts A and B were mixed in a volumetric ratio of 100:42 until uniform consistency. Additionally, thickened epoxy was prepared to assist in the anchor's application, and it is a combination of two-part epoxy and fumed silica. Fumed silica is added as a thickening agent to the epoxy to reduce its viscosity; about 300 g of fumed silica was added in 5 L of epoxy as per the supplier's recommendations. The casting of the beams was done in a wooden formwork using a ready-mix concrete (class C-1) designed following the CSA A23.2-19 code specifications [7]. The average 28-day nominal compressive strength of the concrete was about 37.0 MPa which increased to 37.2 at the test age of about 2 months.

**Table 2** Mechanical properties of FRP materials and steel bars

| Property | Units | 30 M bar | U.S. #3 bar | Carbon fibre | CFRP sheet | Epoxy |
|---|---|---|---|---|---|---|
| Ultimate tensile strength | MPa | 404 | 540 | 4300 | 986 | 72.4 |
| Yield strain | % | 0.22 | 0.25 | – | – | – |
| Tensile modulus | GPa | 184 | 210 | 250 | 95.8 | 3.18 |
| Rupture strain | % | 16.6 | 11.0 | 1.7 | 1.0 | 5 |
| Nominal thickness of the fabric | mm | – | – | 1.0 | – | – |

## 2.2 Beam Strengthening

The beam strengthening involved five steps: (1) preparing anchor holes of about 18 mm in diameter and depth of 100 mm, (2) chamfering the holes' edges to prevent stress concentrations in the CFRP anchors at the edge; (3) grinding of bottom corners of the beam to remove irregularities formed during casting; (4) concrete surface preparation using an ultra-high pressure water jet to improve bonding between the FRP sheet and the concrete; (5) application of CFRP anchors and CFRP sheets. For CFRP sheet application, the dry carbon fabric was first cut to the desired size followed by the preparation of two types of resins, the two-component epoxy and the thickened epoxy. Anchor holes were then filled with thickened epoxy, and carbon anchors saturated with two-component epoxy were applied by pushing the dowel region of the anchors through the hole using a metal rod. The fibres at the front end of anchors were fanned out as illustrated in Fig. 1. Finally, the carbon fibre sheets coated with epoxy were applied as U-wrap on top of the anchors and saturated with two-component epoxy using a paint roller. After completely saturating the FRP sheets, a plastic trowel was used to remove air voids and excess epoxy from the FRP sheets. Figure 2 displays the beam strengthened with anchored CFRP sheets. The beam was placed upside down for easier application of CFRP sheets.

## 2.3 Instrumentation and Test Setup

All FRP-wrapped beams were instrumented with a number of strain gauges and linear variable differential transformers (LVDTs) to capture the specimen behaviour. The instrumentation included strain gauges on longitudinal steel bars, steel stirrups, and FRP sheets. A total of eight strain gauges with a gauge length of 5 mm were installed on two tension bars and one compression bar. The location of longitudinal strain gauges is illustrated in Fig. 3a. Steel stirrups were instrumented with strain gauges with a gauge length of 5 mm. The strain gauges were applied at quarter heights and mid-height of the stirrups, i.e. 143 mm (top), 286 mm (middle), and 429 mm (bottom) measured vertically from the top horizontal leg of the steel stirrup as displayed in

**Fig. 2** Beam strengthened with anchored CFRP sheets

Fig. 3a. Strain gauges with 60 mm gauge length were also applied on FRP at the same vertical locations as for the steel stirrup strain gauges. Additionally, LVDTs were mounted on the fixtures attached to FRP sheets. Eleven LVDTs were installed on each beam to measure vertical displacements, horizontal deformations, and shear deformations during the test as shown in Fig. 3b. Out of the eleven LVDTs, two were placed at supports to measure support settlements, two at quarter points of the beam, and one at midspan to measure beam displacements. Two horizontal LVDTs were used to determine the longitudinal strains at the midspan of the beam. The two sets of diagonal LVDTs were used to monitor shear deformations. Both horizontal and diagonal LVDTs were attached to the front face of the beams.

The beam tests were carried out in a 5400-kN capacity Universal Testing Machine under three-point loading. After installation of the specimen in the machine, the ambient condition beams were monotonically loaded to failure, while the elevated temperature beams were first loaded to 220 kN, which corresponded to about 30% of the strength of the unwrapped beam at room conditions. Then, the chamber was brought in, and conditioning was done at the desired temperature. The beams were exposed to sustained temperature and sustained loading for at least 24 h following which monotonic loading was applied until failure of the beam. Figure 3b shows the schematic of the test setup.

## 3 Results and Discussion

A summary of results including beam failure modes, predicted and recorded peak loads, strength gain, associated midspan displacements, and maximum strains recorded at failure are provided in Table 3. The predicted peak loads for unwrapped and wrapped beams were calculated using CSA S806-17 standards [6]. The CSA standards do not provide any recommendations for FRP-wrapped specimens exposed to elevated temperatures, so peak load was not predicted for specimens tested at

**Fig. 3** Schematic of the beam
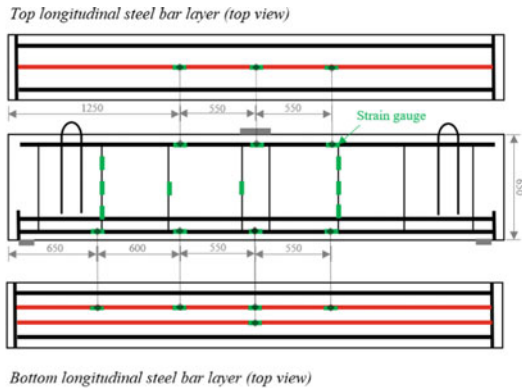


(a) Location of strain gauges
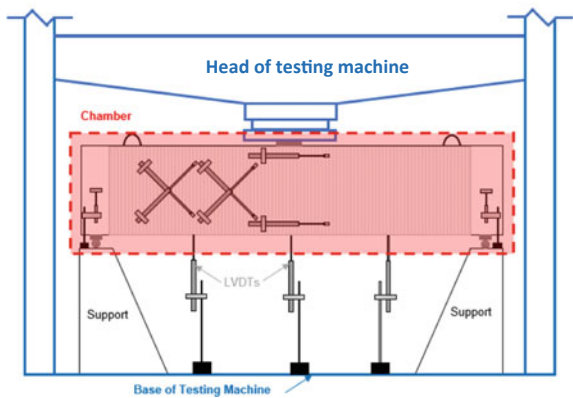


(b) Test setup

elevated temperatures using code equations. The experimental values of the peak load were recorded from the machine load cell. The strength gain provided by the anchored CFRP sheets was calculated as a percentage of the unwrapped strength. The maximum strains presented in the table were recorded at failure in the bottom tensile bars, stirrups, and FRP wraps using the strain gauges.

The visual observations from testing of the reference beam showed shear failure due to rupture of the steel stirrup leg at the primary shear crack location. The beams strengthened with anchored CFRP sheets showed the pull-out failure of the FRP anchors along with debonding of the FRP sheet. The pull-out failure of the FRP anchors was due to the failure of the concrete surrounding the FRP anchors, and this failure mode is known as a concrete cone failure. The debonded CFRP sheets had a layer of concrete attached to it varying in thickness between 5 and 15 mm showing good bond between the concrete surface and the CFRP sheets. All CFRP-wrapped beams regardless of the test temperature failed in shear as designed due to pull-out

**Table 3** Test results from the thermal study of beams strengthened with anchored CFRP sheets

| Sr # | Specimen ID | Concrete strength | Test temperature | Failure Mode | Predicted load CSA | Peak load | Strength gain | Midspan displacement at failure | Maximum strains at failure from strain gauges | | |
|------|-------------|-------------------|------------------|--------------|--------------------|-----------|---------------|---------------------------------|-----------------------------------------------|---|---|
| | | | | | | | | | Bottom long. steel | Stirrup | FRP |
| | | (MPa) | (°C) | | (kN) | (kN) | (%) | (mm) | (%) | (%) | (%) |
| 1 | BU-A | 37.2 | 22 | Stirrup rupture | 688 | 732 | – | 11.1 | 0.11 | 2.01 | – |
| 2 | BC-A | 37.2 | 22 | Anchors pull-out | 1611 | 1434 | 96 | 25.9 | 0.44 | 1.59 | 0.27 |
| 3 | BC-40 | 37.2 | 40 | | – | 1473 | 101 | 27.5 | 0.35 | 1.30 | 0.22 |
| 4 | BC-60 | 37.2 | 60 | | – | 1377 | 88 | 18.6 | 0.26 | 0.50 | 0.19 |

**Fig. 4** Specimen BC-40 at failure
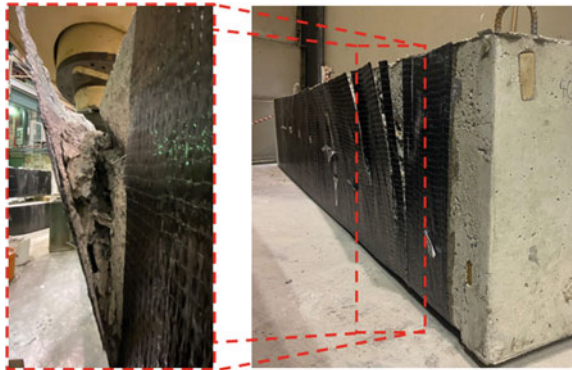


of FRP anchors and debonding of FRP sheets. Figure 4 presents the pull-out failure of beam BC-40 after the termination of the test.

## 3.1 Load–displacement Response

The load–displacement curves of the tested beams are defined by three branches; (1) uncracked, (2) during flexural cracking, (3) during shear cracking followed by rupture of the stirrup in unwrapped beam or failure of FRP anchors in the wrapped beams. The slopes of the first and second branches of the load–displacement plots were near linear and almost the same for all the tested beams due to similar concrete properties. The first flexural crack occurred around an applied load of 240 kN in all the beams. The slope of the third branch was nonlinear for the reference beam due to the propagation of shear cracks, while FRP-wrapped beams showed an almost linear slope after initiation of shear cracking owing to the presence of anchored FRP wraps.

The reference beam failed at a load of 732 kN and a corresponding midspan displacement of 11.1 mm. The load–displacement plot of the unwrapped beam is displayed in Fig. 5 showing linear slopes of the first and second branches followed by a nonlinear slope of the third branch due to the formation of shear cracks. With a further increase of displacement, a significant load drop was observed around 600–700 kN due to the widening of shear cracks. Shortly after the cracks widened, the yielding of stirrups was observed, and finally, the beam failed due to the rupture of a stirrup leg as illustrated in Fig. 6a. A residual load of about 300 kN was observed due primarily to the dowel action of the longitudinal steel bars.

Figure 5 also presents the load–displacement plots of the wrapped beams and compares these plots with the reference beam. The ambient CFRP-wrapped beam showed about 96% higher strength than the reference beam. The wrapped beam behaved similarly to the unwrapped beam specimen until rapid propagation of the shear cracks when a divergence was observed at a load of about 600 kN. The wrapped beams showed almost linear slopes after divergence until a plateau was observed in
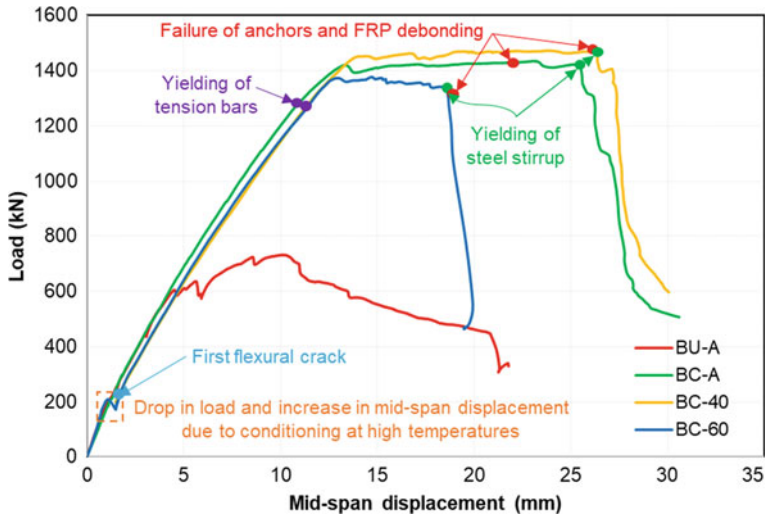
**Fig. 5** Load–displacement plots of the tested beams



a) Rupture of steel stirrup in unwrapped beams

b) Concrete cone failure in the wrapped beams

c) Combined concrete cone and dowel pull-out failure
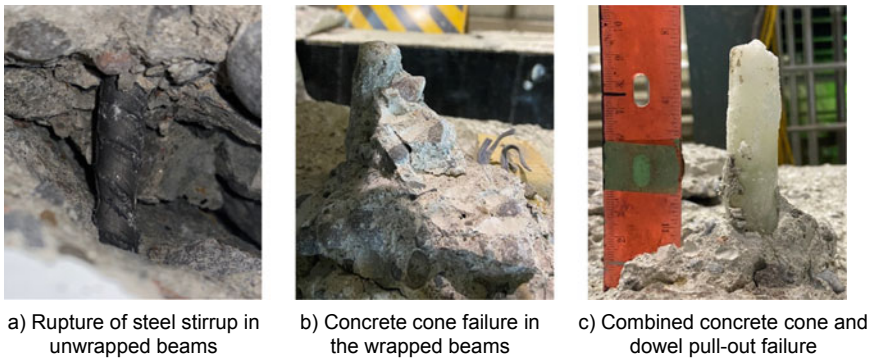
**Fig. 6** Failure modes of the tested beams

the load–displacement plots due to the flexural steel yielding. The final failure of the ambient wrapped beam occurred at a midspan displacement of 25.9 mm. The beam carried a residual load of about 550 kN due to the contribution of the steel stirrups and the dowel action of the longitudinal steel bars. The CFRP-wrapped specimen exposed to 40 °C showed similar behaviour and failure mode as the ambient wrapped beam, but the load capacity and the corresponding midspan deflection were slightly larger. At 60 °C, strength enhancement with respect to ambient strength due to the CFRP wraps dropped to 88% and midspan displacement reduced to 18.6 mm. The reduction in strength enhancement was due to the reduced mechanical properties of FRP sheets and reduced anchorage at high temperatures. This resulted in flexural yielding at a lower load and lower midspan displacement at ultimate. The weaker

anchorage caused by higher temperature resulted in early pull-out of the anchors and also shifted the failure mode from a concrete cone to a combined concrete cone and dowel pull-out failure. Figures 6b and c present the failure modes of the wrapped beams.

## 3.2 Strain Behaviour

Longitudinal strain versus load responses for the unwrapped and wrapped beams are compared in Fig. 7. The strains were measured at midspan in the top compression bars and the bottom tension bars. The strain responses were near linear until the beams almost reached failure states. The tensile strain in the reference beam was much lower than yield strain at failure, while in all the beams strengthened with FRP wraps, the measured tensile strains were greater than yield strain at failure. CFRP wraps were able to suppress the shear failure before flexural yielding in all the beams regardless of the exposure temperatures. Specimen BC-A failed at a tensile bar strain of 0.44% which reduced to 0.26% on exposure to an elevated temperature of 60 °C. In all the tested beams, compressive strains were smaller than 0.1% indicating that concrete crushing did not occur. The strain values calculated from horizontal LVDTs were found to be similar to the strains recorded from the strain gauges until initiation of flexural yielding. After that, a large variation was observed between the strains from the two sources with strain gauges showing larger strains.

The steel stirrups were instrumented with three strain gauges, two at quarter heights and one at mid-height to monitor strain variations with the applied load. The stirrups located at a distance of 500 mm or 1000 mm away from the support measured the highest strain readings in all the tested beams. Figure 8 presents the
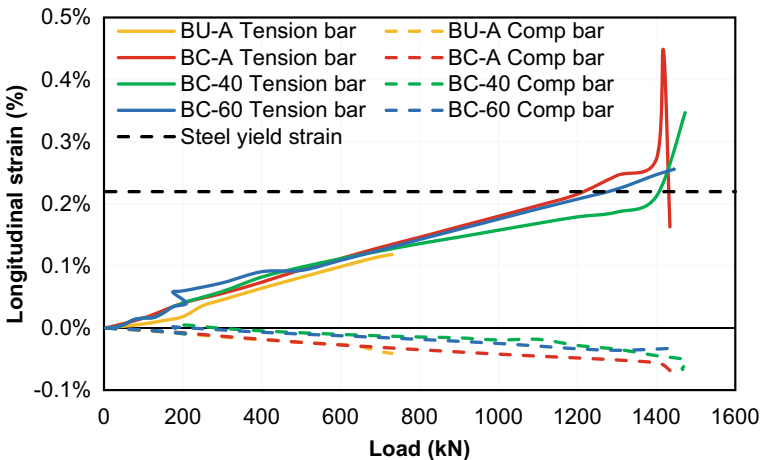


**Fig. 7** Longitudinal strain profiles of the tested beams
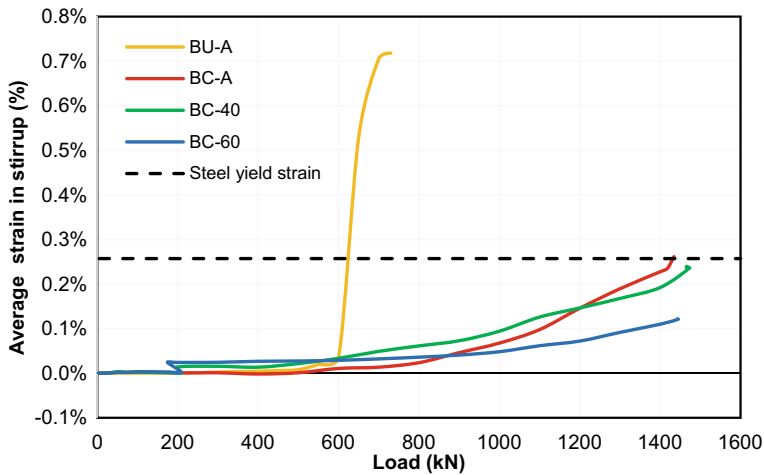
**Fig. 8** Steel stirrup strain profiles of the tested beams

average stirrup strain vs load plots. The strain values shown in Fig. 8 were obtained by averaging three strain gauge readings at a particular section. The measured strains in the unwrapped beam specimen showed insignificant straining up to an applied load of about 600 kN when a sudden increase in the stirrup strain was recorded with the increase in load. This was followed by beam failure due to stirrup rupture. The average stirrup strain variations in the specimen BC-A also showed minimal average strain up to an applied load of about 600 kN beyond which, the strain increased at a much higher rate up to failure. Variation of stirrup strain in specimens BC-40 and BC-60 was more uniform and did not show a sudden increase at any particular load level. A small kink was observed at a load of 220 kN likely due to the thermal expansion of the materials at elevated temperatures.

The average FRP strain variations with increasing load are presented in Fig. 9. As for strain in stirrups, largest FRP strains were recorded at a distance of 500 mm or 1000 mm away from the support. Insignificant FRP strains were recorded up to an applied load of about 600 kN in all the wrapped beams. Further increase in load resulted in a gradual increase in the strain until failure. The specimens BC-40 and BC-60 also showed similar strain behaviour with an additional kink at 220 kN due to conditioning at high temperatures. The comparison of beam tests revealed that the measured FRP strain, at a particular load level, was lower for higher temperature specimens which was also observed during tensile testing of FRP sheets [4]. In all cases, the measured strain at failure was significantly lower than the tensile rupture strain of the CFRP under ambient conditions, i.e. 1%. However, it is possible that larger strains occurred at non-instrumented locations.

The horizontal and diagonal strain values recorded during the beam tests were analysed to determine the state of average strain at a particular section. The horizontal strains ($\varepsilon_x$) were recorded from the strain gauges, and the diagonal strains, elongation
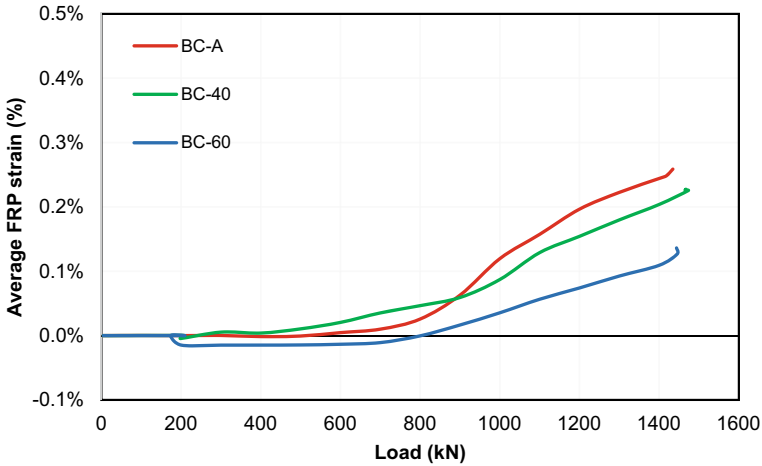
**Fig. 9** FRP strain profiles of the tested beams

($\varepsilon_b$), and shortening ($\varepsilon_c$) in the region of shear cracks were measured using two sets of diagonal LVDTs. Equations 1 to 3 were then used to calculate the ultimate transverse strain value, ultimate shear strain value, and angle of principal compressive strain at failure.

$$\varepsilon_y = \varepsilon_b + \varepsilon_c - \varepsilon_x \tag{1}$$

$$\gamma_{xy} = \varepsilon_b - \varepsilon_c \tag{2}$$

$$\theta = \frac{1}{2}\tan^{-1}\left(\frac{\gamma_{xy}}{\varepsilon_y - \varepsilon_x}\right) \tag{3}$$

The angle of principal compressive strain was also compared with CSA A23.3-19 [8] predictions as given by Eq. 4.

$$\theta = 29 + 7000\varepsilon_x \tag{4}$$

Table 4 presents the ultimate values for strain and angle of the principal compressive strain of the tested beams at the primary shear crack location. An examination of ultimate transverse and ultimate shear strains revealed higher strain values for the unwrapped beams than wrapped beams. The exposure to elevated temperatures decreased the average axial and transverse strain values at failure due to the reduced effectiveness of the FRP wraps. In contrast, the ultimate shear strains increased due to the reduced contribution of FRP sheets at high temperatures. At failure, the inclination of principal compressive strains calculated from the experimental data was larger

**Table 4** Summary of strains and angle of inclination at failure

| Specimen ID | Load (kN) | $\varepsilon_x$ (με) | $\varepsilon_y$ (με) | $\gamma_{xy}$ (με) | $\theta$ (Eq. 3) (Degrees) | $\theta$ (Eq. 4) (Degrees) |
|---|---|---|---|---|---|---|
| BU-A | 732 | 803 | 7853 | 8769 | 26 | 35 |
| BC-A | 1417 | 1165 | 1653 | 3593 | 41 | 37 |
| BC-40 | 1394 | 1180 | 1340 | 3444 | 44 | 37 |
| BC-60 | 1376 | 945 | 1092 | 3709 | 44 | 36 |

for beams tested at elevated temperatures than ambient wrapped beams. A comparison of angle of inclination from the tests with that calculated using CSA A23.3–19 equation [8] showed that for beams tested at ambient conditions, the CSA-predicted angle is 9° steeper. For beams under elevated temperatures, the reverse is true with the difference between the two angles as large as 8°.

### 3.3 Comparative Study of Available Codes and Standards

A comparative study of the available codes and standards was carried out to evaluate the shear capacity of the anchored FRP-wrapped beams. The shear capacities predicted using ACI 440.2R-17 [5], CSA S6-19 [9], CSA S806-R17 [6], and fib B14 [10] are presented in Table 5. The predicted failure load to experimental failure load ratios is also presented in Table 5. None of the available codes provide guidelines for the calculations of FRP shear contribution at elevated temperatures. Therefore, reduction factors were suggested to modify FRP shear contribution based on the limited test data. It can be inferred from the test results that no reduction factor is needed for temperatures up to about 0.7 $T_g$; however, a reduction factor of 0.85 is suggested for a temperature range of 0.7 $T_g$ to $T_g$. These factors have been used herein with code equations for shear capacity predictions of beams exposed to 40 °C and 60 °C. Overall, the predictions from the ACI 440.2R [5] and CSA S6-19 [9] were conservative for both unwrapped and wrapped beams. CSA S806-R17 [6] predictions were conservative for unwrapped beam and unconservative for wrapped beams. The fib B14 [10] predicted reasonably accurate shear capacities for both wrapped and unwrapped beams.

## 4  Conclusions

To understand the effects of climate change on the effectiveness of anchored FRP wraps, four shear-critical RC beams (one unwrapped and three CFRP wrapped) were tested under ambient conditions and elevated temperatures. A single layer of CFRP was used to wrap the specimens with CFRP anchors. The elevated temperature beams

**Table 5** Comparison of experimental and code predicted capacities

| Reference | BU-A | | BC-A | | BC-40 | | BC-60 | |
|---|---|---|---|---|---|---|---|---|
| | kN | PL/EL[a] | kN | PL/EL[a] | kN | PL/EL[a] | kN | PL/EL[a] |
| Experimental | 732 | | 1434 | | 1473 | | 1377 | |
| ACI 440.2R-17 [5] | 578 | 0.79 | 1363 | 0.95 | 1363 | 0.93 | 1246 | 0.90 |
| CSA S6-19 [9] | 688 | 0.94 | 1385 | 0.97 | 1385 | 0.94 | 1327 | 0.96 |
| CSA S806-R17 [6] | 688 | 0.94 | 1611 | 1.12 | 1611 | 1.09 | 1530 | 1.11 |
| fib B14 [10] | 681 | 0.93 | 1467 | 1.02 | 1467 | 1.00 | 1349 | 0.98 |

[a] PL/EL = predicted ultimate load to experimental ultimate load ratio

were subjected to a sustained loading and conditioned at elevated temperatures for 24 h before testing to failure under monotonic loading. The beams were subjected to temperatures of 40 and 60 °C. This study was conducted with two objectives: understand the shear behaviour of RC beams strengthened with anchored FRP sheets and evaluate their performance under elevated temperatures. The following conclusions can be drawn from the study.

1. A single-layered anchored CFRP U-wraps enhanced RC beam strength by 96% at room conditions, which increased to 101% at 40 °C and reduced to 88% on exposure to temperatures greater than $T_g$ (60 °C). The midspan displacement also improved by 133% at room conditions, 148% at 40 °C, and 68% at 60 °C due to CFRP wraps.
2. The presence of anchored FRP sheets reduced the straining rate of the steel stirrups and delayed their yielding.
3. The wrapped beams tested at room conditions experienced larger FRP strains than those tested at high temperatures. The ambient wrapped beam showed a maximum measured FRP strain at failure of around 0.27% which reduced to 0.19% at 60 °C. The rupture strain of CFRP at room temperature was about 1.0%.
4. The anchored FRP beams showed concrete cone failure around anchors which shifted to concrete cone and dowel pull-out failure at higher temperatures. This transition was due to the reduced effectiveness of CFRP anchors likely caused by the decrease in bond strength between the anchor and surrounding concrete.
5. The available codes and standards do not provide recommendations for the shear strength contribution of FRP wrap at elevated temperatures. Based on the limited test data, a shear strength reduction factor of 0.85 is recommended for a temperature range of 0.7 $T_g$ to $T_g$.

# References

1. Tan KH, Zhou Y (2011) Performance of FRP-strengthened beams subjected to elevated temperatures. J Compos Constr 15(3):304–311
2. Tetta ZC, Bournas DA (2016) TRM versus FRP jacketing in shear strengthening of concrete members subjected to high temperatures. Compos B 106:190–205
3. Green MF, Dent AJS, Bisby L (2003) Effect of freeze-thaw cycling on the behaviour of reinforced concrete beams strengthened in flexure with fibre reinforced polymer sheets. Can J Civ Eng 30:1081–1088
4. Qureshi MF, Sheikh SA, Almansour H (2022) Temperature effects on the mechanical properties of the GFRP sheets. In: 10th international conference on FRP composites in civil engineering (CICE2020/2021), Istanbul, Turkey
5. ACI 440.2R-17 (2017) Guide for the design and construction of externally bonded FRP systems for strengthening concrete structures. American Concrete Institute Committee, Farmington Hills
6. CSA S806-12 (reaffirmed 2017) (2017) Design and construction of building structures with fiber-reinforced polymers. Canadian Standards Association, Mississauga, Ontario
7. CSA-A23.2-19 (2019) Concrete materials and methods of concrete construction/test methods and standard practices for concrete. Canadian Standards Association, Rexdale, Ontario
8. CSA-A23.3-14 (2014) Design of concrete structures, Canadian Standards Association. Rexdale, Ontario
9. CSA-S6-19 (2019) Canadian highway bridge design code. Canadian Standards Association, Rexdale, Ontario
10. Fib Bulletin 14 (2001) Externally bonded FRP reinforcement for RC structures. Technical Report, Federation Internationale du Beton Task Group 9.3, CEB-FIP, Lausanne

# Use of Electrochemical NDT Tests for Evaluating the Effectiveness of Cementitious Materials for Corrosion Repair of RC

**Perla Rodulfo and Rishi Gupta**

**Abstract** For many years, electrochemical nondestructive testing (NDT) techniques have been utilized in the construction sector to examine the structural soundness and safety of many kinds of buildings. Half-cell potential, macrocell current, and linear polarization resistance are three distinct kinds of electrochemical NDT techniques described in this work to test RC resistance to chloride attack and to help develop solutions to improve the durability and hence the service life of RC structures. The effectiveness of these three kinds of NDT procedures is discussed, as well as the electrochemical processes that occur when three distinct types of cementitious repair materials are subjected to sodium chloride. The findings of this experimental investigation reveal that the three distinct forms of NDTs used to measure the performance of three different types of cementitious material restoration have a close connection in terms of outcomes. After monitoring corrosion of repair materials exposed to chloride attack using HCP for the duration of the testing period, it was discovered that there is a greater than 90% chance that no corrosion is occurring for Mix F. Similarly, during monitoring corrosion activity using the macrocell corrosion method, it was discovered that Mix F has the least amount of corrosion conductivity with a value of less than 5 Coulombs. Mix F had the lowest corrosion rate density utilizing LPR NDT, with a value of less than 1 $\mu A/cm^2$. Using these three types of NDT techniques, the differences in performance among three different kinds of cementitious materials while in contact with a concrete substrate and subjected to sodium chloride were also observed. Other NDT approaches will need to be investigated further in order to elucidate the chemical composition of more efficient cementitious repair materials subjected to sodium chloride.

**Keywords** Electrochemical technique · Reinforced concrete · Corrosion · Cementitious materials · Substrate

P. Rodulfo (✉) · R. Gupta
Department of Civil Engineering, Facility for Innovative Materials, and Infrastructure Monitoring (FIMIM), University of Victoria, 3800 Finnerty Road, Victoria, BC V8W 2Y2, Canada
e-mail: rodulfop@uvic.ca

R. Gupta
e-mail: guptar@uvic.ca

# 1 Introduction

Reinforced concrete is a flexible and widely used building material. It may be shaped into a variety of forms and has a variety of surface finishes. Although RC infrastructure is generally durable and capable of withstanding harsh exposure conditions for the duration of its service life, it can deteriorate due to environmental factors, loads, rebar corrosion, sub-zero temperatures, concrete resistance to volume changes, or chemical actions [1, 2]. Corrosion occurs in the concrete matrix and at the rebar. It may happen in any weather condition.

Corrosion products may precipitate, causing tensile tension and cracking. Such cracks may shorten the life of RC constructions [1, 3–5]. Extreme structural loads, climate, and weather conditions may all reduce an RC structure's service life. Consequences can include failure of bridges or buildings, even to the point of collapse.

Due to the economic difficulty of replacing many damaged buildings, restoring a deteriorating structure using sustainable and cost-effective materials is becoming an appealing alternative in the construction industry and a topic of research. Every year, new repair materials are suggested, tested, and created for different purposes [6]. Repair materials can be categorized as cement-based, polymer-modified cement-based materials, or epoxy resin materials [7].

The use of electrochemical NDT tests to assess the efficacy of cement-based or polymer-modified cement-based mortars as repair materials is the subject of this research. They are used to remediate corrosion caused by chloride exposure. Such exposure commonly occurs in marine environments or where de-icing salt is used [6, 8].

RC structures located in a marine environment are clear examples of structures affected by chloride attack [9, 10]. The corrosion process and physical characteristics of steel embedded in concrete have been discussed in much literature [11–13], and it continues to be an important area of ongoing research.

A basic background will be described to provide a better understanding of corrosion detection and protection methods in later sections. The chemical reactions and electrical current flow are present when rebar rusts have specific characteristics.

The following are the major components of a corrosion cell:

- Anode
- Cathode
- The electrolyte composition.

Figure 1 illustrates the interactions between the components of a corrosion cell and the electrochemical process of corrosion of embedded rebar in concrete.

The corrosion process has two half-cell reactions, oxidation, or anodic reaction and cathodic or reduction reaction. During this process, electron release occurs in the oxidation reaction, Eq. (1), whereas the reduction reaction produces electron consumption, Eq. (2) [1].
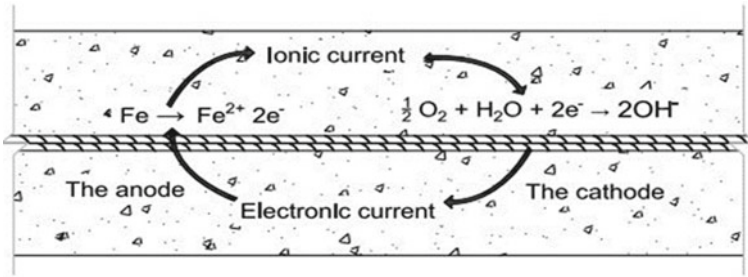
**Fig. 1** Corrosion process of embedded steel through anodic, cathodic, oxidation, and hydration reaction [1]

$$Fe \rightarrow Fe^{2+} + 4e \qquad (1)$$

Anodic or Oxidation reaction (dissolution of irons)

$$2e^- + H_2O + 1/2\,O_2 \rightarrow 2OH^- \qquad (2)$$

Cathodic or reduction reaction (oxygen reduction).

The anodic and cathodic reactions start the rusting process, and corrosion requires the presence of both water and oxygen.

Anodes are the active sites of reinforcement corrosion. When iron atoms lose electrons, ferrous ions travel to the concrete matrix Eq. (1).

Electrons in the rebar continue to migrate to cathode locations. The electrons mix with water and oxygen in the cathode reduction process Eq. (2).

As this electrochemical process progresses, the ferrous ions migrate through the water in the porous concrete matrix, ending up at the cathode sites. Ferrous hydroxide tends to react further with oxygen present in the environment surrounding the embedded reinforcing steel.

Equations 3, 4, and 5 show ferrous hydroxide becoming ferric hydroxide and then ferric oxide or rust.

$$Fe^{2+} + 2OH^- \rightarrow Fe(OH)2 \qquad (3)$$
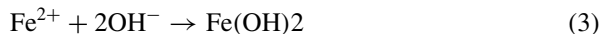
Ferrous hydroxide Eq. (3)

$$4Fe(OH)^2 + O_2 + 2H_2O \rightarrow 4Fe(OH)3 \qquad (4)$$
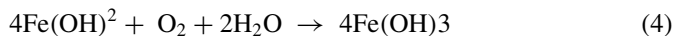
Ferric hydroxide Eq. (4)

$$2Fe(OH)_3 \rightarrow Fe_2O_3 \cdot H_2O + 2H_2O \qquad (5)$$
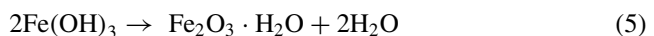
Hydrated ferric oxide (rust) Eq. (5)

The corrosion resistance of concrete repair mortars was studied by Velu Saraswathy et al. [7].

Their results showed that modified mortar systems treated with fly ash and micro silica have lesser permeable voids because of the smaller size of the micro silica particles compared to normal cement particles. Less permeable gaps and less water absorption occurred from the cement matrix's denser packing.

D. D. L. Chung et al. studied the corrosion resistance of cement-based materials incorporating silica fume content and found that SF improves a broad range of essential features, including steel corrosion resistance in comparison with polymer-modified mortars.

Desi Wang investigated the long-term durability of concrete in freezing and sulfate-rich environments. Both FA and SF were proven to increase concrete resistance, agreeing with the findings of D. D. L. Chung. According to Desi Wang's research, SF outlasted FA in terms of endurance.

Mailvaganam, N. P. and Taylor, D. A. studied the compatibility of repair systems for concrete structures [14]. It was shown that existing concrete and repair must be seen as components of a larger system. Even though materials vary, the objective must be to improve physical and chemical property compatibility.

The evaluation of cementitious-based materials for RC corrosion repair can be better understood and assessed by using several electrochemical NDT methods [15–17].

Several electrochemical NDT techniques may be used to better understand and analyze the assessment of cementitious-based materials for RC corrosion repair. Test methods to monitor corrosion initiation and diffusion can be destructive or nondestructive.

In destructive testing, a sample of the rebar is retrieved by taking a core from a structure and determining the rebar's loss in weight and hence the corrosion rate. In nondestructive testing, many electrochemical methods are available in the market. Destructive methods carry limitations in terms of disturbing the integrity of the structure and the repairs that need to be done afterward [18].

In this study, three NDT methods including half-cell potential method (HCP) [19], linear polarization resistance (LPR) [20], and macrocell current [21] were used to assess the corrosion development on RC repaired specimens. The half-cell potential uses a reliable reference electrode that may offer corrosion potential data for rebar in concrete. The potential for reinforcing corrosion in concrete or cement mortar is shown by a range of voltage values measured against the reference electrode. The major issue of this test is that it only gives an indication of the likelihood of corrosion, and it does not give any indication of the rate of the chemical reactions [19, 22, 23].

NDT linear polarization resistance provides data on the rate of metal corrosion. LPR provides a more accurate and quicker method to measure the corrosion rate of rebar. Saraswathy Velu et al. reported that LPR serves as a rapid and non-intrusive, corrosion monitoring technique that gives immediate data related to the current rebar corrosion rate. This test is more informative than corrosion potential testing [24–26].

Macrocell current method measures the current passing through a net of connected rebars. Observations made by Sarawasthy et al. [7] indicate that macrocell current

results measured for different corrosion repair mortars can be greater than 100%, depending on the chemical constituents and compatibility of the repair materials.

Three electrochemical NDT techniques are proposed for monitoring the corrosion rate, corrosion potential, and macrocell current of three repair materials in this research.

Results will help with the development of better choices for repair materials of RC structures exposed to marine environments.

The working procedure for each of the NDT methods used will be presented in the following section.

## 2 Experimental Investigations

### 2.1 Materials

Four types of materials were prepared: a normal concrete mix and three types of cement-based repair materials. The preparation of the concrete mix material was done with the purpose of it serving as the substrate receiving the cement-based materials. The design for the concrete mix proportions is given in Table 1; Quikrete Portland cement GU with a $w/c = 0.40$ was used for the concrete mix in accordance with ASTM C150 [27]. Tap water was introduced as the mixing water. Fine aggregate was used, meeting the ASTM C33 [28] requirement. Fine and coarse aggregates have fineness modulus values of 2.85 and 6.48, respectively. Air entraining agent (AEA) meeting ASTM C260 and a high-range reducing agent (HWRA) (as per ASTM C494) were used.

The other three commercially available mixes are termed as Mix M, P, and F. Table 2 shows the water-to-material (w/m) ratio as recommended by each manufacturer.

**Table 1** Control mix design

| Sample ID | Portland cement (kg/m$^3$) | Coarse aggregates (kg/m$^3$) | Sand (kg/m$^3$) | Water (kg/m$^3$) | HWA (kg/m$^3$) | AEA (kg/m$^3$) |
|---|---|---|---|---|---|---|
| Control | 180 | 450 | 1053 | 762 | 2.25 | 2.25 |

**Table 2** Mix design of cementitious—repair material

| Sample ID | Cement repair (kg/m$^3$) | Water (kg/m$^3$) |
|---|---|---|
| Mix M | 1562 | 118.75 |
| Mix P | 1250 | 137.5 |
| Mix F | 1746 | 291 |

**Table 3** Repair and substrate mix properties

| Category | Mix | Slump (mm) | Air content (%) |
|---|---|---|---|
| Substrate | S | 70 | 7 |
| Repair | M | 60 | 5.5 |
| Repair | P | 20 | 5 |
| Repair | F | 80 | 6 |

**Table 4** Steel reinforcement

| Steel reinforcement | Diameter (mm) | Modulus of elasticity (MPa) | Tensile strength (Fy) | Grade of steel (W) |
|---|---|---|---|---|
| Carbon steel | 11.3 | 200,000 | 400 MPa | 400 |

The cementitious material repair used in this research, mixes M, P, and F, can be classified as cementitious mortar, polymer-modified cement mortar, and cementitious concrete repair, respectively. Table 3 shows the fresh properties of all the mixes. Air content and slump were assessed following ASTM standards: ASTM 231 and ASTM C143.

Table 4 shows the properties of carbon steel, which is the reinforcement used in this study.

ASTM C192 determined mixture casting.

## 2.2 Cementitious/RC Material Preparation for Corrosion Repair

Eight RC beams measuring 530 × 150 × 150 mm (length × height × width) were constructed according to ASTM G109. See Figs. 2 and 3.

Specimen preparation of the RC beams:

(i) Three (3) 11.3-mm longitudinal carbon steel rebars of length 660.4 mm were put inside a steel form mold.

(ii) The rebars were wire power brushed and rinsed using deionized water to remove any contaminants or rust. This was performed with the purpose of facilitating the uniform formation of rebar surface's passive film.

(iii) Each rebar had stainless steel screws installed and welded in place.

(iv) Epoxy was used for sealing, and vinyl tubing was used for electrical insulation.

(v) For the preparation of the concrete corrosion repair, an area of 250 mm × 100 × 50 mm (length, width, height) was reserved along the top surface of the RC beam. This was the active area of experimentation.

(vi) Each fresh concrete mixture was poured and vibrated for 10 s for consistency.

(vii) Steel molds were covered by plastic sheets for 24 h.
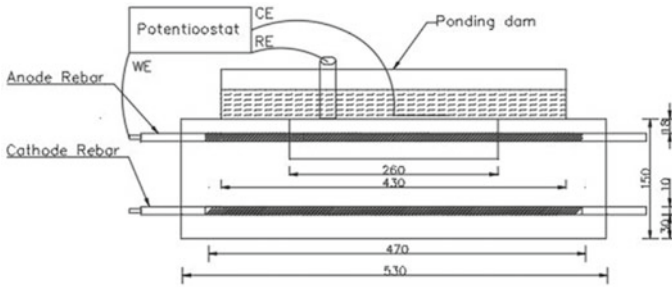
(a)
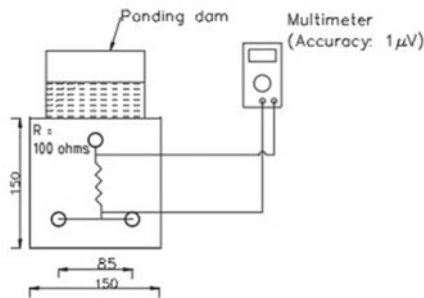


(b)

**Fig. 2**  **a** Longitudinal section view of beam specimen used for electrochemical measurement: LPR and HCP. **b** Cross section view of beam specimen showing macrocell current measurement

(viii)   Ambient conditions were (18 ± 2° C). Mixes M, P, and F were applied to the indentations on the top surfaces of the beams.

 (ix)   Burlap covering ensured moist curing for 28 days in an ambient temperature of (18 ± 2 °C).

  (x)   Four concrete control-beam specimens with cavities were also constructed and were left as no-ponding control beams, one for each admix and one for a regular concrete mix.

 (xi)   The bottom and top surfaces were unsealed. The sides were sealed with epoxy.

(xii)   3-mm Plexiglas was used for a salt solution ponding dam with dimensions of 431.7 × 114.4 × 76.2 mm, which was epoxied to the top surface of the eight beam specimens.

(xiii)   Specimens were placed onto insulated supports of at least 13 mm (0.5 inch) thick. This ensured adequate air flow during testing.

(xiv)   To retain moisture, a plastic loose fitting was placed on top of the ponding dam.

(a)



Top view

(b)
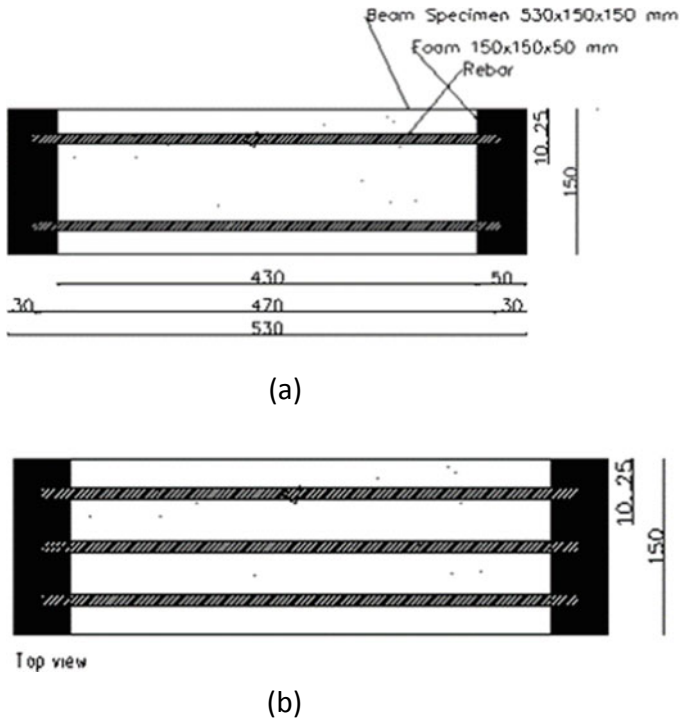
**Fig. 3** Specimen preparation. **a** side view, **b** top view

## 2.3 Experimental Setup

In Fig. 2, it is shown that the top rebar (anode) undergoes oxidation, and the bottom rebars (cathodes) undergo reduction.

After curing, wet and dry cycles (as per ASTMG 109) were conducted. In this experiment, this process simulates a high moisture and chloride environment such as the concrete in marine infrastructures.

The wetting cycles were two weeks, followed by two weeks of drying. NaCl solution was 3% by weight and 99% pure.

After the second wetting cycle, the NaCl solution was increased to 5% by weight.

Corrosion data was collected using a multimeter and a potentiostat. Measurements were taken using a three-electrode setup.

## 3 Methods Implemented and Equipment Used

### 3.1 Ponding Test Wet/Dry

A high impedance potentiostat and a multimeter with 1 μV resolution were used for testing, following ASTM G109. In this work after four cycles (16 weeks) of wet/dry cycles, NDT methods were used for obtaining values for corrosion potential, corrosion rate, and macrocell current of the repaired specimens.

### 3.2 Electrochemical Nondestructive Test (NDT) Methods

Half-cell potential, linear polarization resistance, and macrocell current NDTs were used to assess corrosion in the repaired specimens.

#### 3.2.1 Half-Cell Potential

HCP data was taken at the end of the wetting cycle in all the specimens using a commercially available nondestructive Gamry 600 + potentiostat equipment. A sulfate calomel electrode was used as a reference electrode, and the reinforcement embedded inside the concrete was used as a working electrode. ASTM C0876-15 was used to interpret corrosion activity results in terms of corrosion potential. As stated previously, HCP is a useful tool for monitoring the probability of corrosion.

#### 3.2.2 Linear Polarization Resistance

The corrosion rate (CR) was measured at different times of exposure using the linear polarization method (LPR) as described in ASTM G59. For all specimens, a high impedance voltmeter built in a commercially available nondestructive Gamry 600 + potentiostat was used. Studies show that LPR is a reliable NDT for corrosion measurement [29]. The steel rebar was polarized for a fixed duration of 270 s.

The resultant resistance polarization Rp (expressed in Ohms) was obtained.

$$R_p = ( \partial \Delta E / \partial i )_{i = 0, \, dE/dt \to 0;} \tag{6}$$

$R_p$ values were obtained to determine the corrosion current and density,

where $\Delta E = E - E$ corr. Icorr (in Amperes) was determined from the Stern-Geary equation formula [30] and ASTM G59.

$$I \, \mathrm{corr} = B/R_p; \tag{7}$$

$R_p$ is polarization resistance (in Ohms). $B$ is the Stern-Geary constant ($V$), given as:

$$B = \beta a \beta c / 2.303 \, (\beta a + \beta c), \tag{8}$$

where $\beta a$ is the (anode) Tafel constant and $\beta c$ is the (cathode) Tafel constant.

As per Andrade et al., and by RILEM direction, $B$ was assumed equal to 26 mV. $i$ corr (corrosion current density) was determined by:

$$i \, \text{corr} = I \, \text{corr}/As; \tag{9}$$

icorr is in $\mu A/cm^2$ and As is the area of exposed steel in $cm^2$. In this study, rebar surface corrosion was assumed to be uniform.

Corrosion penetration rate ($\mu m/year$) was calculated according to Faraday's law:

$$CR = Kaw/nF\delta \, i \, \text{corr} = \alpha \, i \, \text{corr}; \tag{10}$$

$K = 315,360$ (a unit's conversion factor); $F$ is the Faraday constant. ($F = 96,485 \, Cmol^{-1}$), n (number of moles of transferred electrons), aw (the atomic weight in grams), $\delta$ (density of the metal in $g/cm^3$), and icorr (the corrosion current density) in $\mu A/cm^2$ [31].

### 3.2.3 Macrocell Corrosion Rate

The macrocell current was measured once every twenty-eight days at the end of the wetting cycle, as per ASTM G109.

Also, as per ASTM G109, voltage was measured using a multimeter with an accuracy within 1 $\mu V$.

In the case of this study, the specimens setup resembles the macrocell corrosion mechanism.

Using Ohm's law, the macrocell corrosion current is found by measured voltage/ resistance value (100 ohms). Sample testing duration was 16 weeks.

## 4 Experimental Results and Discussion

## 4.1 Steel Reinforcement Corrosion

### 4.1.1 Visual Observation

Specimens were inspected after vacuuming the sodium chloride solution at the end of the last wet/dry cycle.
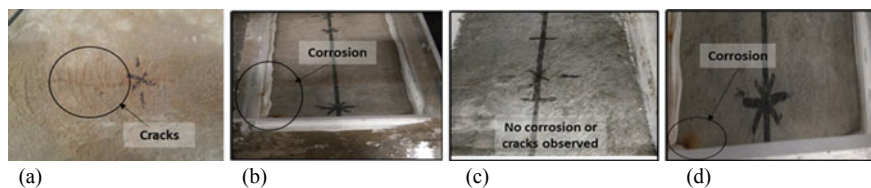
**Fig. 4** Visual observation of repair mixes and control. **a** Mix *M*, (cracks can be observed); **b** Mix *P*, (corrosion stains on surface; **c** Mix *F*, (no cracks or corrosion stains can be observed); **d** mix control, (corrosion stains on surface)

Small cracks were clearly observed on one out of three specimens where Mix M repair cementitious material had been tested and after completing 16 weeks of exposure to the salt solution. See Fig. 4.

On Fig. 4, signs of rust are clearly noticeable on the substrate concrete of Mix *P*. Signs of rust are clearly noticeable on two out of two of the control Mix. No signs of corrosion, cracks, or staining were observed on Mix *F*.

Corrosion potential, macrocell corrosion, and corrosion current density and rate results on all the specimens confirm the possibility of some cementitious materials being more vulnerable than others when exposed to a chloride attack or corrosive environment.

### 4.1.2　Half-Cell Potential (HCP) Results

As per ASTM C876, top (anode) rebars were monitored for the variations of HCP.

**Repair material plus substrate exposed to chloride**

At the beginning of the first cycle, the potential corrosion on repair cementitious material + substrate interface, Mix *P*, *F*, and control values ranged between −50 and −130 mV. Mix *M*, however, shows a range of −350 mV at the end of the first cycle.

At the end of the 16 weeks of exposure cycles, Mix *F* and control are in the range of −60 to −100 mV, while Mix *M* and *P* reached a potential corrosion value between −250 and −350.

Figure 5 indicates potential readings for Mix *F*, and the control specimens also show a probability of corrosion of less than 10%. However, potential corrosion for Mix *M* and *F* indicates corrosion activity to be uncertain.

The difference in potential values among the three different mixes can be explained by the potentially denser microstructure of Mix F and control compared to mixes *M* and *P* [22, 32]. Chlorides are transported into concrete with a lower resistivity or a more open pore structure (Fig. 6).
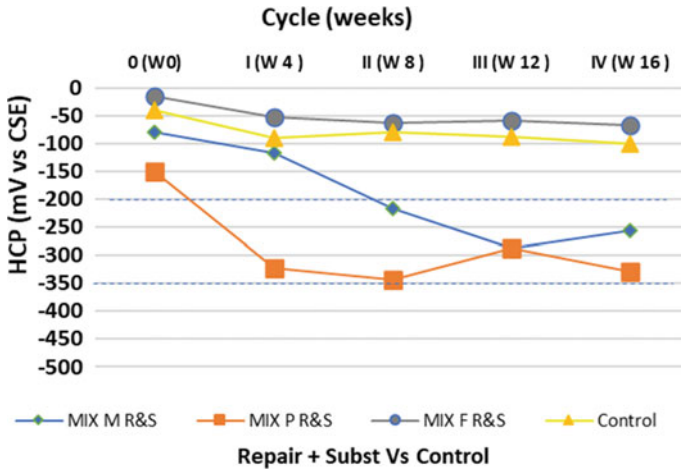
**Fig. 5** Half-cell potential. Repair materials + substrate versus control
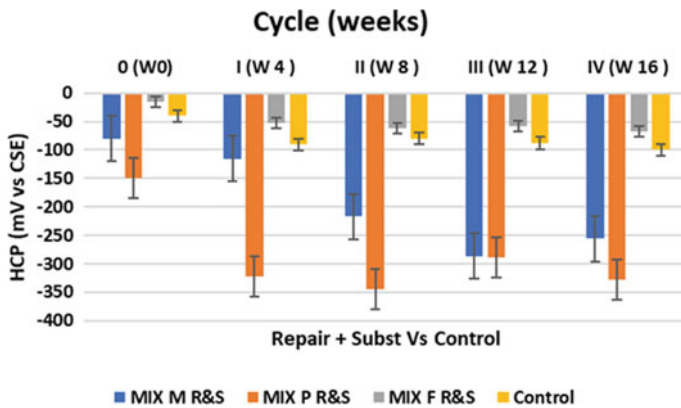


**Fig. 6** Half-cell potential std. deviation. Repair materials + substrate versus control

### 4.1.3 Macrocell Corrosion Results

Also, as per ASTM G109, for this test, the total charge between the reinforcement layers was monitored for 16 weeks.

Figure 7 presents the total charge for samples with repair cementitious materials plus substrate versus control (Fig. 8).

It can be observed that samples with Mix *M* and *P* present the highest value of charge passed with time, which indicates less resistance to chloride exposure during the testing period for repairs M and P compared to Mix *F*.

The data analysis revealed that Mix *M* and *P* had the highest rate of macrocell corrosion. This can be explained by the effect of the interface between the repair
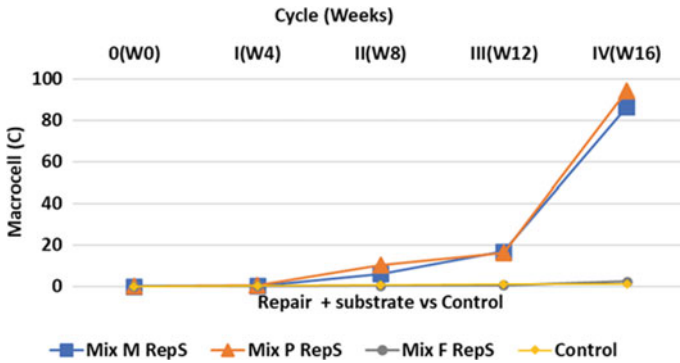
**Fig. 7** Macrocell corrosion. Repair materials + substrate versus control
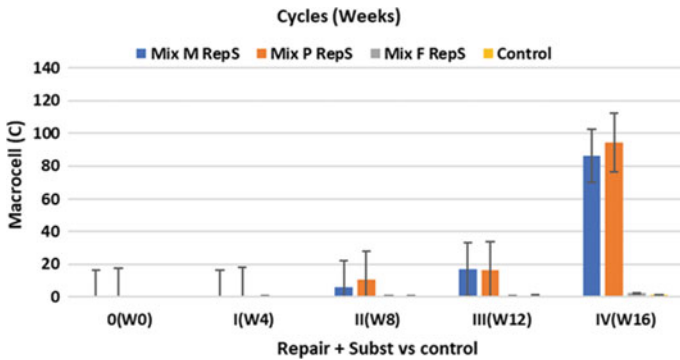


**Fig. 8** Macrocell corrosion. Std. deviation. Repair materials + substrate versus control

materials and substrates not being electrochemically compatible [7, 33, 34]. Cusson et al. [35] learned that after 3 years of corrosion repair performance assessment, the potential electrical difference between the patch and the substrate can worsen with time due to physical and chemical incompatibilities. Values of 100 to 150 mV were common in their study. Also, Pruckner and Gjørv [36] found that the potential difference between the substrate and repair can be as high as 500 mV.

Of all the mixes tested in this study, Mix *F* shows the lowest charge passed.

### 4.1.4 Linear Polarization Resistance—Corrosion Current Density Rate

After performing the biweekly linear polarization tests on the NaCl—exposed specimens, the following results were observed:

For repair material plus substrate exposed to chloride and considering the state of corrosion of the steel in the specimen, it was observed that mixes *M*, *P*, *F,* and control were in the range of negligible corrosion at 16 weeks of exposure.

However, the corrosion current density and rate result of each of the repair admixes indicate different results. Mix *F* presents the lowest corrosion rate results during the 16 weeks of exposure. The repair material identified as Mix *P* showed the highest corrosion rate result, during the 16 weeks of exposure.

Figures 9 and 11 show the values of corrosion current rate and corrosion density respectively. Figures 10 and 12 shows the standard deviation of the Figs. 9 and 11.
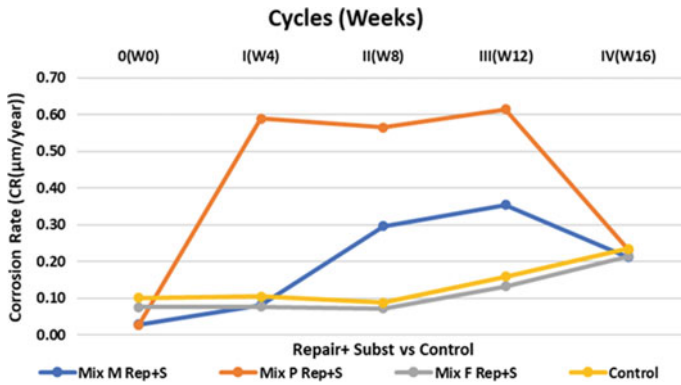


**Fig. 9** Corrosion current rate. Std. deviation. Repair materials + substrate versus control
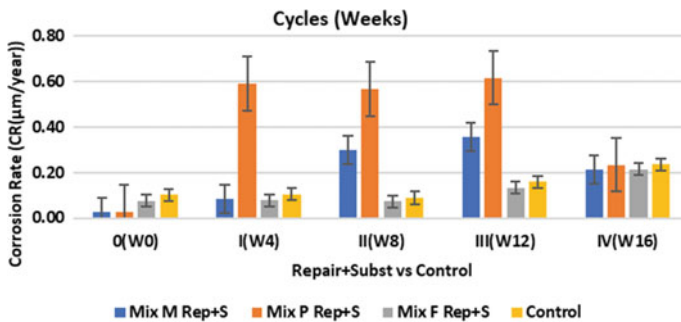


**Fig. 10** Corrosion current rate. Std. deviation. Repair materials + substrate versus control
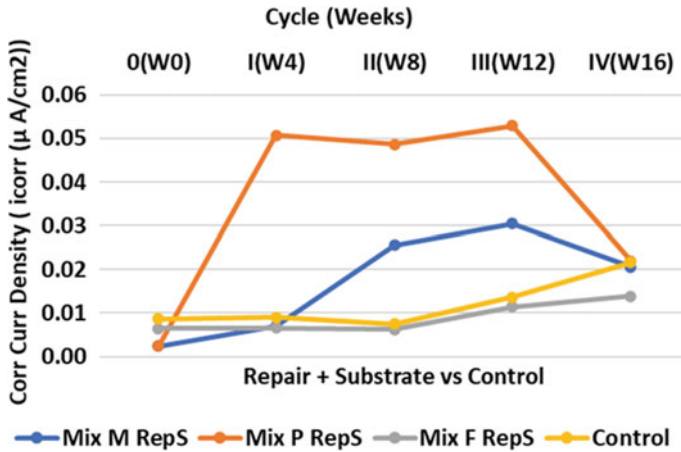
**Fig. 11** Corrosion current density. Std. deviation. Repair materials + substrate versus control
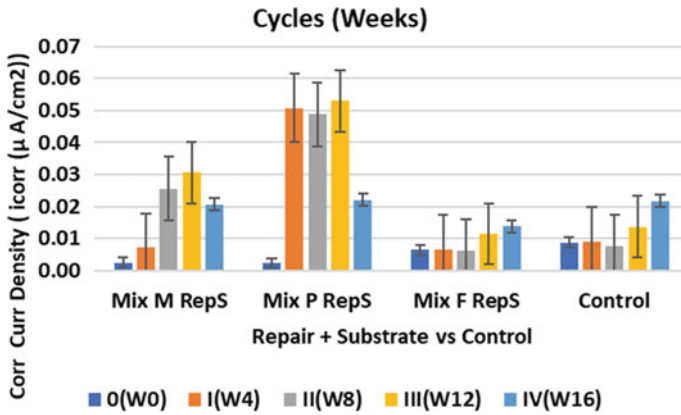


**Fig. 12** Corrosion current rate. Std. deviation. Repair materials + substrate versus control

## 5 Experimental Results and Discussion

### 5.1 Electrochemical Techniques

After performing HCP, macrocell, and LPR electrochemical tests on three different types of cementitious repair material, under chloride exposure, it is observed that all the results from the NDTs in terms of corrosion activity are correlated. Cementitious concrete (Mix F) presented the best performance in terms of lowest corrosion potential, corrosion rate, corrosion density, and corrosion current results at 16 weeks

of wet/dry sodium chloride exposure compared to cementitious mortar (Mix *M*) and polymer-modified cementitious mortar (Mix *P*).

Raghav et al. [34] reported that some chemical components present in some cement-based materials like silica fume (SF) can react in concrete leading to a physical contribution. Physically, silica fume fills the interface spaces, which reduces porosity.

The effectiveness of repair cementitious materials to delay/retard corrosion in RC exposed to high-chloride environments is highly dependent on how the repair and substrate materials react as a system to sodium chloride attack.

The evaluation of different repair cementitious materials was assessed by using three different electrochemical NDT methods: HCP, macrocell, and LPR. Results led to a correlation finding among these three methods.

## 6 Conclusion

Results of the experimental study of using electrochemical methods to assess the effectiveness of repair cementitious materials for corrosion repair can be summarized as follows:

1. The usage of electrochemical techniques to measure corrosion potential, HCP, macrocell corrosion, and linear polarization performed in this study showed a correlation regarding the behavior/effect of three different types of cementitious repair materials under chloride exposure.
2. The chemical components contained in Mix *F* (silica fume) make it a more desirable repair due to its higher surface area and electrochemical compatibility with the substrate when exposed to sodium chloride. Experimental results for Mix *F* show a lower corrosion potential, corrosion rate, and macrocell corrosion compared to repair Mix *M* and Mix *P* when exposed to sodium chloride.
3. Further NDT examination like the usage of SEM images will provide more information about the morphology and porosity network of these three different admixes after being exposed to chlorides.
4. The need for better physical and chemical compatibility between substrate and repair materials will continue to be a driver for research, experimentation, and modeling. Exposure environments, especially those with high sodium chloride content, are an important consideration when predicting and monitoring the service life of steel-reinforced concrete.

# References

1. Broomfield JP (2007) Corrosion of steel in concrete: understanding, investigation and repair, 2nd edn. Taylor & Francis, London
2. Hobbs DW (2001) Concrete deterioration: causes, diagnosis, and minimising risk. Int Mater Rev 46(3):117–144. https://doi.org/10.1179/095066001101528420
3. Ahmad S (2003) Reinforcement corrosion in concrete structures, its monitoring and service life prediction—a review. Cement Concr Compos 25(4):459–471. https://doi.org/10.1016/S0958-9465(02)00086-0
4. Bertolini L, Elsener B, Pedeferri P, Redaelli E, Polder RB (2013) Corrosion of steel in concrete: prevention, diagnosis, repair. Wiley
5. Francois R, Laurens S, Deby F (2018) Corrosion and its consequences for reinforced concrete structures. Elsevier
6. Panjehpour M, Abdullah A, Ali A, Demirboga R (2011) A review for characterization of silica fume and its effects on concrete properties. Int J Sustain Constr Eng Technol 2
7. Velu S, Song H-W (2007) Evaluation of cementitious repair mortars for corrosion resistance. Port Electrochim Acta 26:417–432. https://doi.org/10.4152/pea.200805417
8. Cusson D, Mailvaganam NP (n.d.) Durability of repair materials 8
9. American Concrete Institute (ed) (2014) Guide to materials selection for concrete repair. American Concrete Institute, Farmington Hills, Mich
10. Mangat PS, Limbachiya M (1995) Repair material properties which influence long-term performance of concrete structures. Constr Build Mater 9:81–90. https://doi.org/10.1016/0950-0618(94)00003-K
11. Gartner TK, Legat (2020) Monitoring the corrosion of steel in concrete exposed to a marine environment. Materials 13:407. https://doi.org/10.3390/ma13020407
12. Hunkeler F (2005) Corrosion in reinforced concrete: processes and mechanisms. Corros Reinf Concr Struct 1–45. https://doi.org/10.1533/9781845690434.1
13. Montemor MF, Simões AMP, Ferreira MGS (2003) Chloride-induced corrosion on reinforcing steel: from the fundamentals to the monitoring techniques. Cement Concr Compos 25(4):491–502. https://doi.org/10.1016/S0958-9465(02)00089-6
14. Mailvaganam NP, Taylor DA (n.d.) Compatibility of repair systems for concrete structures 23
15. Büyüköztürk O, Taşdemir MA (2013) Nondestructive testing of materials and structures. In: Güneş O, Akkaya Y (eds) Vol. 6. Springer Netherlands, Dordrecht
16. Karla H, Danner T, Geiker M (2020) Non-destructive test methods for corrosion detection in reinforced concrete structures. Nord Concr Res 62:41–61. https://doi.org/10.2478/ncr-2019-0005
17. Rehman KU, Sardar ZI, Memon SA, Jameel M (2016) Nondestructive test methods for concrete bridges: a review. Constr Build Mater 107:58–86. https://doi.org/10.1016/j.conbuildmat.2015.12.011
18. Asi M, Omar SB, Al-Amoudl (n.d.) IN-SITU testing of concrete 17
19. Satish VL (n.d.) Half cell potential studies for durability studies of concrete structures in coastal environment 11
20. Grantham MG, Herts B, Broomfield J (1997) The use of linear Polarisation corrosion rate measurements in aiding rehabilitation options for the deck slabs of a reinforced concrete underground car park. Constr Build Mater 11(4):215–224. https://doi.org/10.1016/S0950-0618(97)00040-8
21. Trejo D, Halmen C (n.d.) Corrosion performance tests for reinforcing steel in concrete: technical report 252
22. Elsener B, Andrade C, Gulikers J, Polder R, Raupach M (2003) Half-cell potential measurements—potential mapping on reinforced concrete structures. Mater Struct 36(7):461–471. https://doi.org/10.1007/BF02481526
23. Pour-Ghaz M, Isgor O, Ghods P (2009) Quantitative interpretation of half-cell potential measurements in concrete structures. J Mater Civ Eng 21.https://doi.org/10.1061/(ASCE)0899-1561(2009)21:9(467)

24. Rodrigues R, Gaboreau S, Gance J, Ignatiadis I, Betelu S (2021) Reinforced concrete structures: a review of corrosion mechanisms and advances in electrical methods for corrosion monitoring. Constr Build Mater 269:121240. https://doi.org/10.1016/j.conbuildmat.2020.121240
25. Velu S (2007) Corrosion monitoring of reinforced concrete structures—a review. Int J Electrochem Sci
26. Verma SK, Bhadauria SS, Akhtar S (2014) Monitoring corrosion of steel bars in reinforced concrete structures. Sci World J 2014:e957904. https://doi.org/10.1155/2014/957904
27. C01 Committee (n.d.) Specification for Portland cement. ASTM International. https://doi.org/10.1520/C0150_C0150M-20
28. C09 Committee (n.d.) Specification for concrete aggregates. ASTM International. https://doi.org/10.1520/C0033_C0033M-18.
29. Song HH, Yalagandula P (2007) Real-time end-to-end network monitoring in large distributed systems. In: 2007 2nd international conference on communication systems software and middleware, pp 1–10
30. Geary AL (1957) Electrochemical polarization. J Electrochem Soc 9
31. Azarsa P, Gupta R, Azarsa P, Biparva A (2021) Durability and self-sealing examination of concretes modified with crystalline waterproofing admixtures. Materials 14. https://doi.org/10.3390/ma14216508
32. Poursaee A, Hansson CM (2009) Potential pitfalls in assessing chloride-induced corrosion of steel in concrete. Cem Concr Res 39(5):391–400. https://doi.org/10.1016/j.cemconres.2009.01.015
33. Logeswaran V (2020) A study on compatibility of concrete repair materials 21
34. Raghav M, Park T, Yang H, Lee S-Y, Subbiah K, Lee H-S (2021) Review of the effects of supplementary cementitious materials and chemical additives on the physical, mechanical and durability properties of hydraulic concrete. Materials 14:7270. https://doi.org/10.3390/ma14237270
35. Cusson D, Qian S, Hoogeveen T (2006) Field performance of concrete repair systems on highway bridge. ACI Mater J 103
36. Pruckner F, Gjørv O (2002) Patch repair and macrocell activity in concrete structures. ACI Mater J 99:143–148

# Temperature Control and Crack Prevention Scheme for Tail Floor of Large Hydropower Stations in High-Altitude Regions

**Qiaorong Sun, Bingyong Ding, Zaixin Zheng, Running Du, and Sheng Qiang**

**Abstract** Temperature control and crack prevention for the tail floor of a large hydropower station are difficult in high-altitude regions. Therefore, research on fine temperature control and crack prevention according to climatic characteristics is necessary. Temperature stress and temperature control measures for the tail structure of a hydropower station in a high-altitude region are studied based on the three-dimensional finite element method, considering the climate characteristics in high-altitude regions and the limitation of conventional temperature control and crack prevention measures. The results show that the conventional pouring temperature control measures, water cooling measures, and surface insulation measures are unable to control the temperature stress of concrete within the safe range. The reasonable block-divided pouring measures (to avoid long pouring interval), reasonable post-pouring belt measures, and strong heat preservation measures are crucial to effectively control the thermal stress and ensure the structural safety. Based on the research and practice of concrete crack prevention in hydropower stations, during construction in high-altitude regions, the temperature and spatial distribution of concrete temperature stress, and a set of comprehensive crack prevention measures suitable for high-altitude climate conditions, construction conditions and structural characteristics of powerhouse are summarized and have reference significance for similar projects.

**Keywords** Mass concrete · Temperature control · Crack prevention · Optimal measures · High-altitude regions

Q. Sun · S. Qiang (✉)
College of Water Conservancy and Hydropower, Hohai University, Nanjing 210098, China
e-mail: sqiang2118@163.com

B. Ding · Z. Zheng · R. Du
Huadong Engineering Corporation, Hangzhou 310014, China

# 1   Background

With the development of hydropower, the focus of water resources development has gradually shifted from mild climates to high-altitude regions. However, the climate and environmental conditions in high-altitude regions are harsh, which is detrimental to concrete crack prevention. It is particularly difficult to perform the numerical simulation of complex concrete structures, temperature control designs, and construction schemes.

Hydraulic mass concrete structures include dams, hydropower stations, and aqueducts. Currently, the temperature control and crack prevention of concrete dams in low-altitude regions already have a relatively complete system. For example, the small temperature difference, early cooling, and slow cooling [1] proposed by Zhu Bofang have been widely used in the Jinping, Baihetan, and Wudongde projects, with good results [2–7]. Preliminary results have also been provided for the temperature control and crack prevention of dams and hydropower stations in high-altitude regions. For example, Wang Zhenhong summed up the climate characteristics in high-altitude regions and proposed reasonable temperature control indexes and suggestions to optimize temperature control measures for a concrete dam in Tibet [8–10]. Ouyang Haijun pointed out that the surface protection measures for concrete in high-altitude regions are extremely effective in reducing the internal and external temperature difference and reducing the risk of surface cracking, while strictly controlling the temperature stress of early concrete [11]. The allowable temperature difference in the foundation was simulated, and a reasonable temperature control guidance scheme for the pouring of concrete silos in high-altitude regions was provided by Huang [12]. A study was conducted on the pouring season of strong restrained zones for a high-altitude dam by Zhu et al. [13]. Zhu Kang et al. pointed out that the tensile stress of exposed concrete surfaces in high-altitude regions occurs easily, and the temperature control standards need to be strictly controlled [14]. The difficulties and related technical problems in the construction of RCC (roller-compacted concrete dam) dams in severe cold regions are analyzed and discussed by Deng [15]. Du Wei et al. perfected the application of thermodynamic theory in the field of concrete temperature control in severe cold regions [16]. Ruan Xinmin et al. worked out temperature control standards and optimized temperature control measures around the variation characteristics of the thermodynamic parameters of concrete under special thermal insulation conditions, the cold shock effect of temperature drops (cold wave) on concrete, overwintering temperature control, heat preservation material selection, and so on [17, 18]. In view of the key technologies such as dam structure design, concrete mix proportion, temperature control, and heat preservation in high-altitude regions, some researchers conducted a series of theoretical research studies and technological innovations, and some valuable research results have been obtained [19–23]. However, the anti-cracking technology of mass concrete, especially structural concrete in high-altitude regions, is not mature enough and can continue to be perfected.

For large hydropower stations, it is difficult to control temperature and optimize schemes for the bottom plate of the draft tube structure. In high-altitude regions, there is no space to control pouring temperature because the monthly average temperature is much lower than in mild climates, especially in winter. Moreover, the bottom plate is strongly restrained by relatively complete bedrock where elastic modulus is large. Complicated constrained structure also adds the difficulty. Finally, different locations of the hydropower stations need different standards and requirements, such as the function of impact and wear-resistant, antifreeze, anti-corrosion, impermeability, and so on, and need different kinds of concretes. The thermal and mechanical parameters (especially, the adiabatic temperature rise) of different kinds of concrete are very different from each other. Thus, concrete structures with different kinds of concrete may be constrained by each other and produce temperature stress after concrete pouring. In summary, more reasonable research and harsh measures are needed to conduct for large hydropower stations in high-altitude regions.

The conventional methods of mass concrete temperature control are reducing the pouring temperature, adopting the pipe cooling and surface protection measures, but these research studies are primarily aimed at dam mass concrete in mild areas. The climate in high-altitude regions is harsh, which is reflected in the large temperature difference between day and night, the strong solar radiation, dry climate, and low annual temperature. The climatic characteristics in high-altitude regions lead to stricter temperature control and crack prevention measures. The concrete of the draft tube structure belongs to high-grade concrete and has the characteristics of temperature insulation and fast heating. The temperature control measures for high-grade concrete structures in mild areas have been relatively strict. For example, a low heat cement concrete, the analysis and optimization of the mix proportion of the concrete, pipe cooling, constant surface running water maintenance, and other measures are adopted synthetically in the discharge caverns of Change Hydropower Station to reduce the internal hydration heat and cracking risk of high-grade concrete [24]. In high-altitude regions, the difficulty of temperature control and crack prevention increases and needs to be researched more in detail.

Based on the above discussion and the structure of hydropower stations in high-altitude regions, the temperature control and crack prevention of the hydropower station are studied under the climatic conditions and the limitations of conventional temperature control and crack prevention measures. A set of comprehensive anti-crack measures suitable for the cold weather conditions, construction conditions, and powerhouse structure features are determined, which is of great significance for similar projects.

## 2  Simulating Calculation Principle

### 2.1  Calculation Principle of the Temperature Field

At any point within concrete computational domain $R$, unstable temperature field $T(x, y, z, \text{and } t)$ should satisfy the heat conduction continuity equation [25]:

$$\frac{\partial T}{\partial t} = a\left(\frac{\partial^2 T}{\partial x^2} + \frac{\partial^2 T}{\partial y^2} + \frac{\partial^2 T}{\partial z^2}\right) + \frac{\partial \theta}{\partial \tau} \quad (\nabla(x, y, z) \in R), \tag{1}$$

where $T$ is the concrete temperature (°C), $a$ is the thermal diffusivity (m$^2$/h), $\theta$ is the adiabatic temperature rise (°C), $\tau$ is the age ($d$), and $t$ is the time ($d$).

### 2.2  Calculation Principle of the Stress Field

The strain increment of the concrete under a comprehensive stress state contains an elastic strain increment, creep strain increment, temperature strain increment, dry shrinkage strain increment, and autogenic volume strain increment. Thus,

$$\{\Delta\varepsilon_n\} = \{\Delta\varepsilon_n^e\} + \{\Delta\varepsilon_n^c\} + \{\Delta\varepsilon_n^T\} + \{\Delta\varepsilon_n^s\} + \{\varepsilon_n^0\}, \tag{2}$$

where $\{\Delta\varepsilon_n^e\}$ is the elastic strain increment, $\{\Delta\varepsilon_n^c\}$ is the creep strain increment, $\{\Delta\varepsilon_n^T\}$ is the temperature strain increment, $\{\Delta\varepsilon_n^s\}$ is the dry shrinkage strain increment, and $\{\Delta\varepsilon_n^0\}$ is the autogenic volume strain increment.

### 2.3  Equivalent Equation of the Conduction of Heat in Mass Concrete Considering the Effect of Pipe Cooling

In general, the average temperature of concrete is calculated according to the following formula, where the initial temperature of concrete is $T0$, the adiabatic temperature rise is $\theta0$, and the inlet water temperature is $Tw$[25].

$$T_1(t) = T_w + (T_0 - T_w)\phi(t) + \theta_0\varphi(t). \tag{3}$$

# 3   Simulation Calculation

## 3.1   Project Overview

The Hydropower Station in this study is primarily designed for power generation. In the upstream side of the dam site, the catchment area is 157,407 km$^2$. The standard impound level of the dam is 3374 m, and the corresponding storage capacity is 552.8 million m$^3$.

The powerhouse of the hydropower station is a post-dam powerhouse, which is arranged on the right side of the main riverbed. A total of four single-machine 165 MW hydrogenerator sets are installed in the station, with a total installed capacity of 660 MW. The length of the main powerhouse is 106 m, the height is 63.50 m, the upper width is 29.00 m, and the unit spacing is 25.00 m.

A unit at the side of the powerhouse was picked as an object in this research. The sizes of it are as follows: The length of the side unit is 48.5 m, the height is 27.7 m, and the upper width is 31.0 m. The floor of the draft tube structure is shown in Figs. 1 and 2. The length is 42.95 m, and the width is 31.0 m. The height of floor of elbow section is 4.7 m and the height of floor of linear progressive segment is 2.8 m. The sizes of the research objects are shown in Table 1.

Cracks often occur in parts of the changed structure including orifices and folding angles. The high-precision simulation of these details necessitates higher requirements for fine modeling, but there are a significant number of holes in the caverns of the powerhouse structure, and the fine simulation of the draft tube structure is especially difficult, so it is necessary to combine fine modeling technology to improve the simulation accuracy.

Explanatory notes: The sizes of original designed blocks are shown in Fig. 1. The sizes of optimized designed blocks are shown in Fig. 2. The detailed sizes of the floor of the draft tube structure are shown in Table 1.

## 3.2   The Finite Element Model

In the simulation calculations, the inlet section, the main powerhouse section, and the exit section of the side unit are taken as the calculation model. The 3D finite element computational model is shown in Figs. 3, 4, and 5. There are 350,879 elements and 378,403 nodes of the total model and 253,573 elements and 277,875 nodes of concrete model.

In the simulation calculation, the coordinate origin of the calculation model is located on the center bottom surface of the bottom floor, and the actual elevation is 3341.90 m. The Z-axis is vertical, the X-axis is upstream, and the Y-axis is perpendicular to the direction of water flow according to the right-hand spiral rule, pointing to the right bank. XOZ plane ($Y = 0$ m) is the central section of the side unit, and

**Table 1** Sizes of the floor of the draft tube structure

| Original designed blocks | A1:15.427 m × 19.5 m | | A2:15.573 m × 19.5 m | B1:12.25 m × 23.15 m | | B2:18.75 m × 23.15 m |
|---|---|---|---|---|---|---|
| Optimized designed blocks | A1:9.523 m × 19.5 m | A2:9.333 m × 19.5 m | A3:9.815 m × 19.5 m | B1:9.523 m × 23.15 m | B2:9.576 m × 23.15 m | B3:9.815 m × 23.15 m |

(a) View 1



(b) View 2
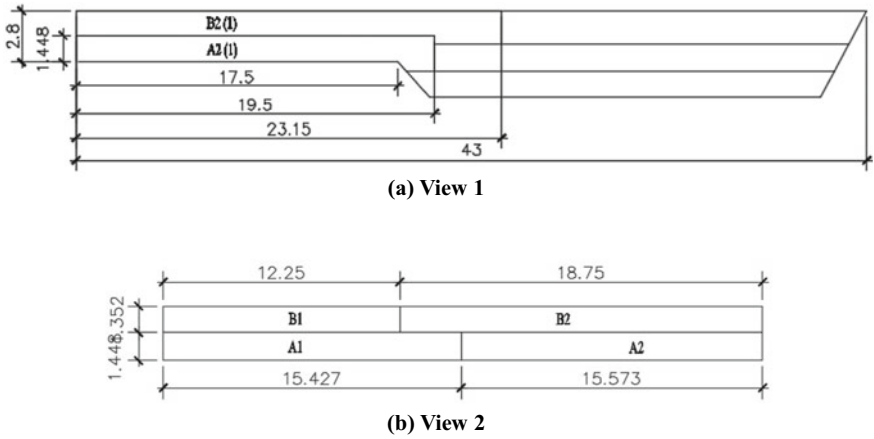
Fig. 1 Sides view of original designed blocks for the draft tube structure (m)
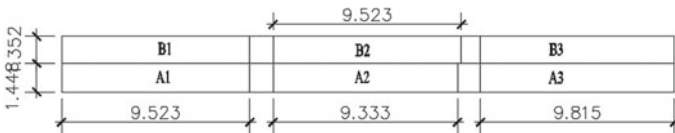


Fig. 2 Sides view of optimized designed blocks for the draft tube structure (m)
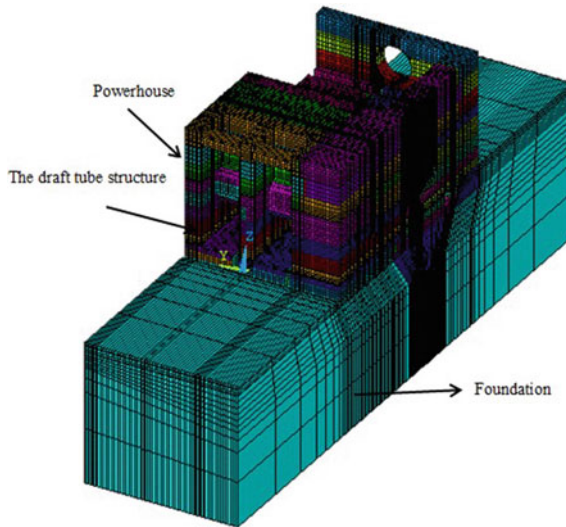


Fig. 3 Three-dimensional finite element computational model
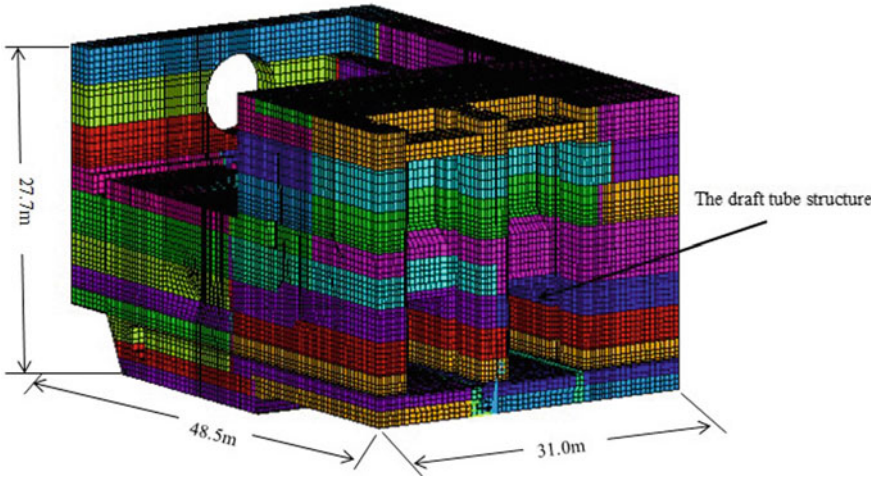
**Fig. 4** Three-dimensional finite element computational model of the entire concrete structure
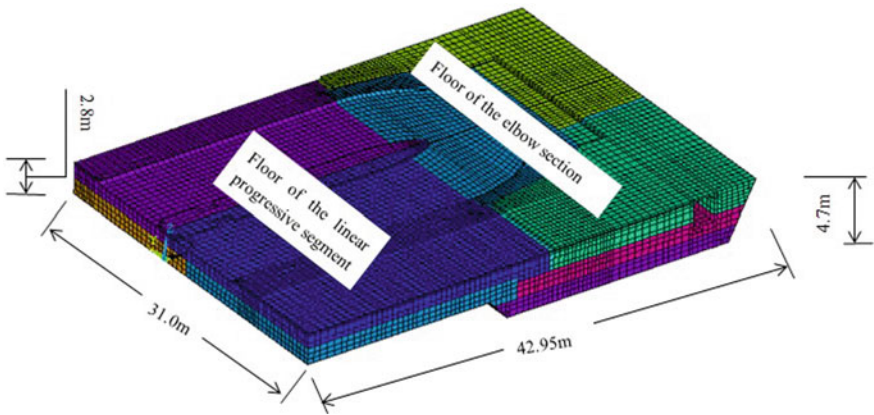


**Fig. 5** Three-dimensional finite element model of the floor

the pile number is $0 + 15.5$ m on the right. The finite element model of the bottom plate of the tailrace structure of the plant is depicted in Fig. 5.

### 3.3 Research Ideas

#### 3.3.1 Brief Introduction of Finite Element Calculation Process

The simulation calculation process is as follows: Firstly, a finite element model is established for the research object (side unit), and the mesh size is controlled to meet the calculation accuracy requirements, especially the mesh of the draft tube structure and its floor. Secondly, according to the local climate conditions and rock properties, the corresponding calculation parameters are obtained, and the mechanical and thermal parameters of concrete are obtained by the related experiment. Thirdly, based on the finite element simulation calculation program developed by our research team, the simulation calculation results are obtained by inputting the corresponding calculation parameters and setting reasonable boundary conditions.

#### 3.3.2 Brief Introduction to Optimization Method of Temperature Control Measures

The conventional temperature control measures of mass concrete are simulated, such as controlling concrete pouring temperature, strengthening concrete surface insulation, and burying cooling water pipes inside the concrete. According to the calculation results of the simulation of conventional temperature control measures, additional optimization temperature control measures of mass concrete should be taken to let the maximum tensile stress be less than the allowable value. The additional temperature control measures should be as simple, economic, and effective as possible. The additional temperature control measures proposed include optimization of pouring block sequence at key locations, adding post-pouring belts at appropriate locations, and covering the surface of the concrete with strong thermal insulation materials. The calculation model is optimized by adjusting the pouring sequence of concrete blocks at key locations, adding post-pouring belts at appropriate locations, and covering the surface of the concrete with strong thermal insulation materials to meet the concrete index standards. The flowchart of the simulation calculation is shown in the figure below:

The flowchart of this research is shown in Fig. 6.

### 3.4 Reliability of Simulation Calculation

The precision of temperature control and crack prevention calculation for mass concrete and the optimization of temperature control measures depend on several factors. These include the accuracy of the calculation program, the precision
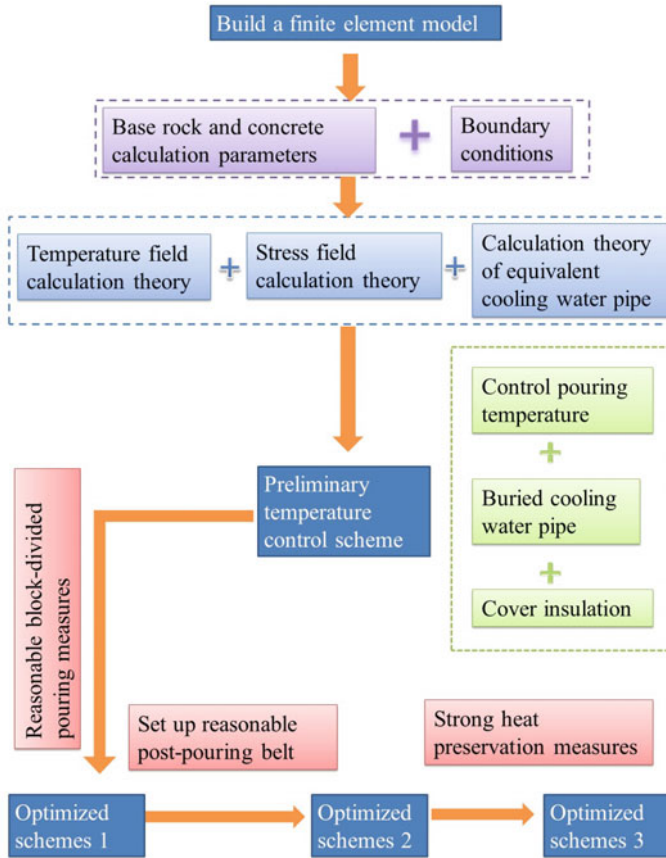
**Fig. 6** Flowchart of the simulation calculation

of boundary conditions, models, materials, and the feasibility of the temperature control measures implemented during the optimization process. The following aspects discuss the correctness of the simulation results in this paper:

(1) The research group of our research institute has carried out in-depth research on crack prevention of mass concrete and has carried out a lot of cutting-edge scientific research work [6-8, 27-29]. Many of them rely on or refer to this program for engineering and scientific research. Therefore, the correctness of this procedure can be guaranteed.

(2) The material data and boundary condition data in this paper are obtained from laboratory and field data, which are suitable for the research of this project.

(3) The research results of this paper have been approved by a design corporation. The design corporation has rich experience in hydropower station design. Therefore, the rationality of the temperature control measures can be guaranteed.

# 4 Difficulties and Optimization Schemes for the Floors of the Draft Tube Structure

## 4.1 Difficulties in Temperature Control and Crack Prevention in the Draft Tube Structure Floor of Large Power Stations in High-Altitude Regions

(1) The climatic conditions of high-altitude regions make it difficult to effectively restrain the tensile stress of structural concrete during overwintering by controlling the pouring temperature. Considering the environmental conditions of the hydropower station studied in this paper, the monthly average temperature is only 1.1 °C in January, and the thickness of the floor is approximately 3 m. The internal temperature of the floor is low in the overwintering season. Adopting a very low pouring temperature is necessary to control the concrete stress in the floor. The temperature in summer is high, and the solar radiation is strong in the region where the project is located, so it is necessary to take aggregate air-cooling measures to effectively control the pouring temperature. When air-cooling measures are taken to control the pouring temperature, the temperature of the concrete outlet is generally not less than 7 °C. Considering the recovery of the concrete temperature in the process of transportation and pouring, the pouring temperature of concrete in high-temperature seasons is difficult to control within 10 °C, and there is no great difference in pouring temperatures in mild areas. The above factors make it difficult to restrain the tensile stress of the floor in the overwintering season by controlling the pouring temperature. Table 2 shows the monthly average temperature of the project site over many years.

(2) A large-scale powerhouse needs to be built in relatively less weathered rock. Excavation is often deep, and the lithology is relatively complete. Therefore, the elastic modulus of bedrock is large, and the bedrock strongly restrains the bottom plate. The monthly average temperature varies greatly in high-altitude regions. In addition, the long interval can easily lead to a large temperature difference between the upper and lower layers. The structure and blocks of a hydropower station are complicated; moreover, the changeable layered structure can easily lead to the mutual constraint of different floors. The above reasons lead to unreasonable segmentation, which can easily lead to greater stress in different blocks of concrete. The thermal and mechanical calculation parameters of the bedrock are presented in Table 3.

(3) The concrete division of the hydropower station is complicated, and the concrete grades of different zones are different. Impact and wear-resistant concrete of label $C_{28}30$ is used in the draft tube structure and in the water-retaining side wall of the hydropower station. The rest of the draft pipe mass concrete is mainly composed of grade three, and the concrete label is $C_{90}30$. The structure of the diffusion section of the hydropower station is weak, and the crack resistance is

**Table 2** Average monthly temperatures from June 2011 to May 2013

| | January | February | March | April | May | June | July | August | September | October | November | December | Year |
|---|---|---|---|---|---|---|---|---|---|---|---|---|---|
| Mean annual temperature (°C) | 1.1 | 5.2 | 7.5 | 10.9 | 14.6 | 17.5 | 16.9 | 17.0 | 15.7 | 12.0 | 5.7 | 6.0 | 10.8 |
| Extreme max. temperature (°C) | 15.9 | 18.3 | 21.8 | 24.8 | 28.9 | 30.0 | 27.7 | 29.4 | 29.7 | 32.7 | 20.3 | 27.6 | 32.7 |
| Extreme min. temperature (°C) | −10.3 | −6.4 | −1.8 | 2.0 | 3.4 | 8.8 | 9.9 | 9.6 | 7.7 | −0.2 | −4.2 | −8.1 | −10.3 |

**Table 3** Thermal and mechanical parameters of the basement

| Basement | Thermal conductivity (kJ/ m h °C) | Specific heat (kJ/(kg °C)) | Coefficient of linear expansion ($10^{-5}$/°C) | Temperature conductivity ($m^2$/h) | Final elastic modulus (GPa) | Poisson's ratio | Density (kg/ $m^3$) |
|---|---|---|---|---|---|---|---|
| Granite III | 10.505 | 0.716 | 0.70 | 0.00560 | 20.8 | 0.23 | 2630 |

poor. The above reasons can lead to inconsistency in the shrinkage and deformation of the concrete and increase the risk of temperature stress cracks. The thermal characteristics of each concrete grade are presented in Table 4, and the zoning diagrams of different materials in the hydropower station are illustrated in Fig. 7. Concrete grades and division of the hydropower station are shown in Table 5.

Table 4 Thermal parameters of concrete

| Grade of concrete | Temperature conductivity (m$^2$/h) | Thermal conductivity (kJ/m h °C) | Specific heat (kJ/ kg °C) | Coefficient of linear expansion ($10^{-6}$/°C) | Adiabatic temperature rise final value (°C) |
|---|---|---|---|---|---|
| C$_{90}$30W8F200 | 0.00453 | 9.720 | 0.886 | 8.655 | 24.43 |
| C30W8F200 | 0.00427 | 9.364 | 0.920 | 9.364 | 41.52 |
| C30W4F150 | 0.00427 | 9.364 | 0.920 | 9.364 | 41.52 |
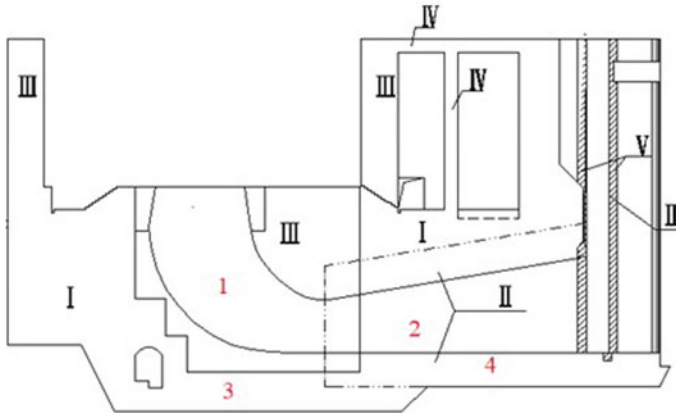


Fig. 7 Material zoning diagram. Structures 1 and 2 in the figure constitute a draft tube structure. The meanings of 1 ~ 4 are as follows: 1—elbow section; 2—linear progressive segment; 3—the floor of the elbow section; and 4—the floor of the linear progressive segment.

Table 5 Concrete grades and division of hydropower station

| Partition number | Grade index | Gradation | Application area |
|---|---|---|---|
| I | C$_{90}$30 W8 F200 | Third grade | Mass concrete for the draft tube |
| II | C$_{28}$30 W8 F200 | Second grade | Tailrace structure, retaining wall |
| III | C$_{28}$30 W4 F150 | Second grade | Wall below the generator |
| IV | C$_{28}$30 W4 F150 | Second grade | Wall above the generator |

## *4.2  Temperature Control Optimization Measures*

Currently, the conventional temperature control measures for impact- and wear-resistant concrete in mild regions can fulfill the needs of temperature control and crack prevention of the draft tube structure floors. However, there is little room for further tightening the temperature control and crack prevention measures. Temperature control and crack prevention in high-altitude regions are obviously more difficult than that in mild regions. Optimizing temperature control measures to meet the requirements of temperature control and crack prevention is necessary. Based on the engineering experience in high-altitude regions, this study optimizes the temperature control measures according to the following ideas:

(1) The conventional temperature control measures proposed by the preliminary temperature control scheme are simulated and analyzed. Moreover, the position and stress of the draft tube structure of the hydropower station are analyzed according to the calculation results.

(2) Conventional temperature control measures are considered according to the characteristics of concrete structures in high-altitude regions. Therefore, reasonable block-divided pouring measures (to avoid long pouring interval), post-pouring belt measures, and strong heat preservation measures are simulated and the control effects of various measures on stress are obtained. Reasonable temperature control and crack prevention measures are proposed accordingly.

## 5  Preliminary and Optimized Temperature Control Measures

Based on the experience of temperature control and crack prevention of concrete structures of powerhouses, a set of temperature control and crack prevention schemes for the hydropower station in a high-altitude region are formulated in this study. The schemes mainly consist of two parts. The preliminary scheme is a conventional temperature control scheme for the entire hydropower station. The optimized schemes are developed based on the calculation results of the conventional temperature control scheme. This development involves an analysis of the distribution of the temperature field, temperature stress field, and the measures for controlling temperature stress.

## *5.1  Preliminary Temperature Control Scheme*

The conventional temperature control measures are pouring temperature measures, surface heat preservation measures, and pipe cooling measures, the purpose of which is to reduce the basic temperature difference and the internal and external temperature

difference to control the temperature stress. The zoning of pouring blocks and the pouring time according to the preliminary temperature control scheme are presented in Table 6. The thickness of the insulation materials can be set as follows: Expandable Polyethylene (EPE) coil or polyethylene benzene plate with thickness 4 cm can be used on the facade; a layer of plastic film (for moisturizing and wind proofing) can cover the silo surface after a summer silo opening; a layer of plastic film 2-cm-thick EPE insulation quilt can cover the warehouse surface after the silo is closed in autumn or spring, and a layer of plastic film 4-cm-thick EPE insulation quilt can cover the warehouse surface after the warehouse is closed in winter.

### 5.1.1 Temperature Control Measures for the Floor

The pouring zones of the bottom plate at the diffusion section of the draft tube in the preliminary scheme are displayed in Fig. 8.

In the preliminary scheme, the pouring time of each partition is shown as follows: Region A1: 30 April; region A2: 10 April; region B1: 10 June; region B2: 20 May.

### 5.1.2 Analysis of Calculation Results

The temperature control and crack prevention calculation of the draft tube structure of the hydropower station is carried out according to the preliminary temperature control measures. The maximum temperature and tensile stress are exhibited in Fig. 9. The characteristic section position of the temperature and stress in the analysis structure is illustrated in Fig. 9b. The maximum temperature and maximum stress envelope diagrams of the structural surface are given in Figs. 9a and b. Figures 9c and d depict the maximum temperature and maximum stress envelope diagrams of the characteristic section. According to the calculation results, the stress in the plate of the diffusion section exceeds the standard and should be closely analyzed.

**Temperature analysis of the bottom plate of the draft tube structure**. As shown in Fig. 8, the pouring zone of the floor (region A1, A2, B1, and B2) and pouring time are analyzed. Because the external temperature in regions A1 and A2 is lower than that in regions B1 and B2, the highest temperature in region A1 and region A2 is lower than that in regions B1 and B2. According to the calculation results shown in Figs. 9c and d, the highest temperature in region A1 is 24.21 °C, 23.32 °C in region A2, 30.84 °C in region B1, and 29.9 °C in region B2.

**Temperature stress analysis of the bottom floor of the draft tube structure**. Because the external temperature in regions A1 and A2 is low, the pouring temperature is low. In addition, the constraint of the foundation and the temperature stress is small. The pouring temperature in regions B1 and B2 is higher, and the temperature stress in regions B1 and B2 is larger because of the long interval period between the pouring of B1 and B2 and the bottom concrete (the interval time is as long as 40 days), which leads to the high elastic modulus and low temperature of the old concrete at

**Table 6** Preliminary temperature control scheme

| Pouring temperature (°C) | | | | Surface insulation of floor | Water pipe cooling | | | | |
|---|---|---|---|---|---|---|---|---|---|
| Winter | Other seasons | | | Equivalent exothermic coefficient KJ/(m² · d · °C) | Temperature of inlet pipe(°C) | Flow of water (m³/h) | | Spacing between water pipes (m) | |
| | Strong restrained zone | Weak restrained zone | Free zone | | | 0~6 d | 6~20 d | Below 3355.00 m | Below 3344.40 m |
| ≥ 6 | ≤ 12 | ≤ 14 | ≤ 16 | 84 | 10 | 1.5 | 0.75 | 1.5 | 1.0 |

**Fig. 8** Designed pouring partitions of floor



**(a) Envelope diagrams of the surface maximum temperature**

**(b) Envelope diagrams of the maximum surface thermal stress**

**(c) Envelope diagrams of the typical section maximum temperature**

**(d) Envelope diagrams of the typical section maximum thermal stress**
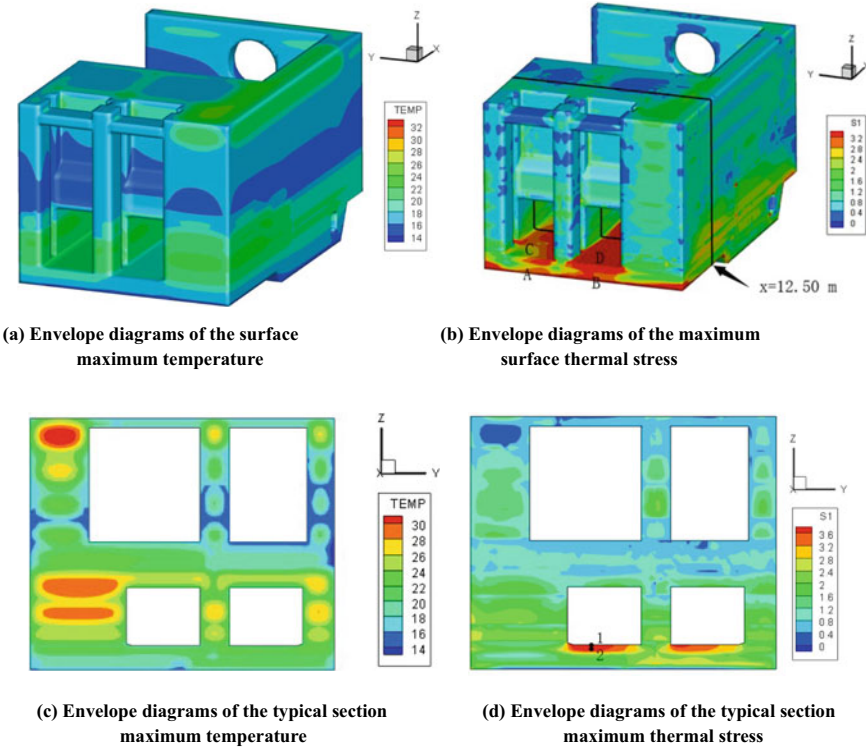
**Fig. 9** Envelope diagrams of the concrete (preliminary temperature control measures)

**(a) Temperature duration curves**          **(b) Stress duration curves**
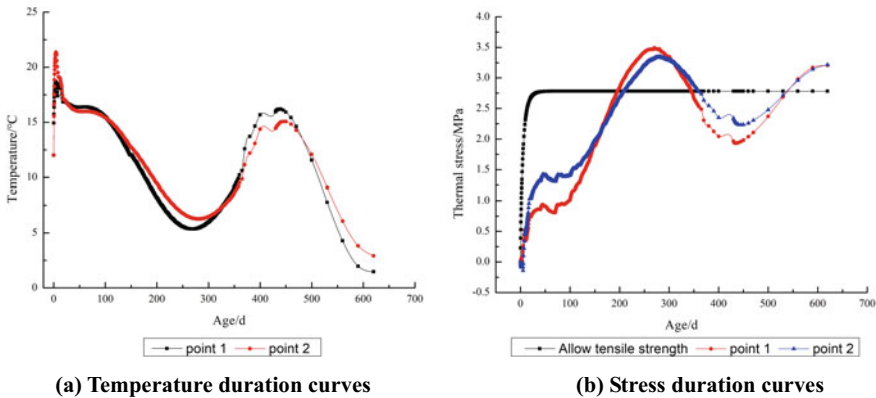
**Fig. 10** Temperature/stress time curves of typical characteristic points (preliminary temperature control measures)

the bottom. The tensile stress of the concrete near the gate pier is obviously larger because it is constrained by the gate pier.

**Analysis of the stress/process time curves of typical characteristic points**. The locations of the typical characteristic points are at 1 and 2 as shown in Fig. 9d. Analysis of the temperature and temperature–stress time curves of the surface and internal typical characteristic points of region B2, shown in Fig. 10, reveals that the highest temperature of the internal point is 21.35 °C, the maximum tensile stress is 3.35 MPa; the highest temperature of the surface point is 18.69 °C, and the maximum tensile stress is 3.49 MPa, which exceeds the allowable tensile strength for C30. The adoption of optimized temperature control schemes is essential to control the temperature stress.

According to the calculation results of the preliminary temperature control measures, it is necessary to adopt the optimized temperature control schemes to ensure the safety of dangerous parts such as the pier and diffusion section.

(1) Based on the preliminary temperature control scheme, reasonable block-divided pouring measures (to avoid long pouring interval) shall be taken for the base plate of the diffusion section with a high risk of cracking, to reduce the constraints on the new concrete from the old concrete.
(2) It is necessary to take the measure of the post-pouring belt to reduce the constraint of the pier on the bottom plate of the diffusion section.
(3) Since the first winter is dangerous to temperature control and crack prevention, the temperature stress can be reduced by strong heat preservation without passing the water at this time.

## 5.2   Optimized Schemes of Temperature Control

### 5.2.1   Optimized Schemes

According to the calculation results of the conventional temperature control measures, the following schemes are set up to optimize the temperature control measures.

(1) Optimized scheme 1: Reasonable block-divided pouring measures (to avoid long pouring interval) of the floor pouring block in the diffusion section should be adopted. In this scheme, the pouring time of each block in Fig. 8 is as follows: region A1: 30 May; region A2: 10 June; region B1: 10 June; region B2: 10 May. In the concrete pouring schedule arrangement, as far as possible, the thin layer, short interval, and uniform rise should be avoided. In the temperature drop stage, the new concrete in the upper layer cracks easily under the restriction of the old concrete, especially when the new concrete in the upper layer is thinner. Therefore, the pouring interval between the upper and lower layers of the bottom plate in the strong restraint zone should be shortened, and the 40 days in the original construction plan are changed to 10 days in this scheme.

(2) Optimized scheme 2: The pouring belt along the water flow direction of the bottom plate of the hydropower station is set as shown in Fig. 11. The size of the pouring block has an important influence on the temperature stress. The larger the size of the pouring block, the greater the temperature stress, and the easier it is to produce cracks. Therefore, the reasonable split seam block is of great significance in preventing cracks. To improve the crack resistance safety of the bottom plate of the diffusion section, a wide channel along the river direction is reserved in the position of the bottom plate of the diffusion section near the side pier and the middle pier. The width of the slot is approximately 1.2 m, and the micro expansive concrete is backfilled in the wide slot in the winter of that year.

(3) Optimized scheme 3: Basis on the conventional temperature control measures, the maximum tensile stress in the floor is significantly reduced, but the maximum tensile stress still cannot meet the tensile strength of C30 concrete even after measures are taken to shorten the pouring interval and set the post-pouring belt with a large tensile stress for the strong constraint zone of the floor. Therefore, strong heat preservation measures for the strong constraint zone are necessary, especially in winter, when the temperature is low. In optimized scheme 3, the bare silo surface of the draft tube floor is covered with a layer of plastic film 6-cm-thick EPE coil or polyethylene benzene board in winter and removed in the following spring. After the silo is closed in the spring and autumn, a layer of plastic film 3-cm-thick EPE coil or polyethylene benzene board covers the silo surface.

**The post-pouring belt**
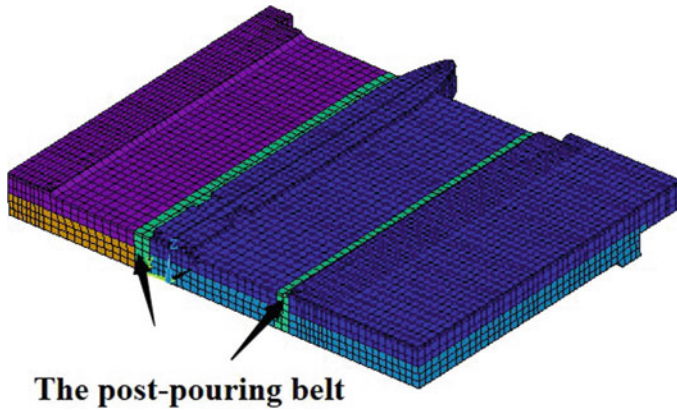
**Fig. 11** Schematic diagram of the post-pouring belt of the bottom plate in the diffusion section

### 5.2.2 Analysis of Calculation Results of Optimized Schemes

(1) Results of optimized scheme 1

The calculation results of optimized scheme 1 are displayed in Fig. 12. The diagram of the typical section maximum temperature stress illustrates that after reasonable block-divided pouring measures (to avoid long pouring interval) between the upper and lower blocks, the new concrete in the upper layer is constrained by the old concrete, and the maximum tensile stress is reduced from 3.9 to 3.2 MPa under the initial scheme. This shows that the tensile stress of the thin-layer pouring block can be effectively reduced by adjusting the construction pouring plan. After adjusting the interval period of floor pouring, the maximum tensile stress of the upper floor decreases, but the maximum tensile stress of the bottom plate located in the lower part of the gate pier increases. The maximum tensile stress reaches 3.33 MPa, which is beyond the tensile strength range of C30 concrete, and the cracking risk is high.

(2) Results of optimized scheme 2

The calculation results of optimized scheme 2 are displayed in Fig. 13. The diagram of the typical section maximum temperature stress illustrates that because the size of the transverse river direction of the bottom plate of the draft tube reduces, the constraint of the transverse river direction also reduces, and the maximum reduction is greater than 1.1 MPa. The maximum tensile stress of the upper floor of the draft pipe is reduced from 3.65 to 2.93 MPa, and the maximum tensile stress of the lower part of the pier is reduced from 3.33 to 2.07 MPa, which satisfies the tensile strength of C30 concrete. It can be seen that the tensile stress caused by strong constraint can be effectively reduced by setting the post-pouring belt in the strong constraint area of the structure. A good crack prevention effect has been achieved by this measure.

**(a) Envelope diagrams of the typical section maximum temperature**

**(b) Envelope diagrams of the typical section maximum temperature stress**

**Fig. 12** Envelope diagrams of the concrete (optimized scheme 1)



**(a) Envelope diagrams of the typical section maximum temperature**

**(b) Envelope diagrams of the typical section maximum temperature stress**
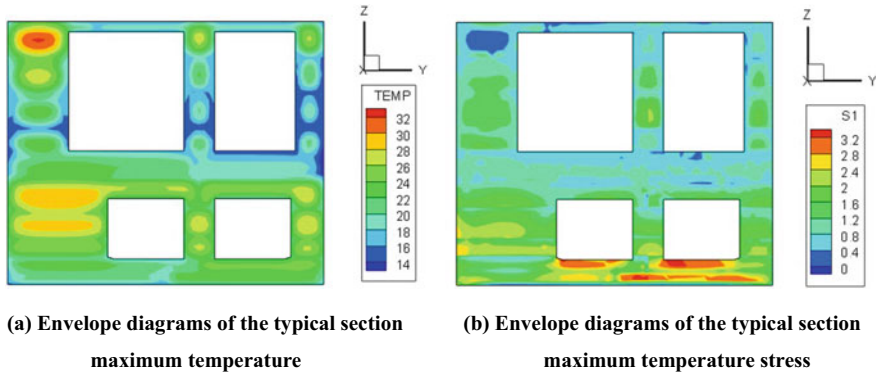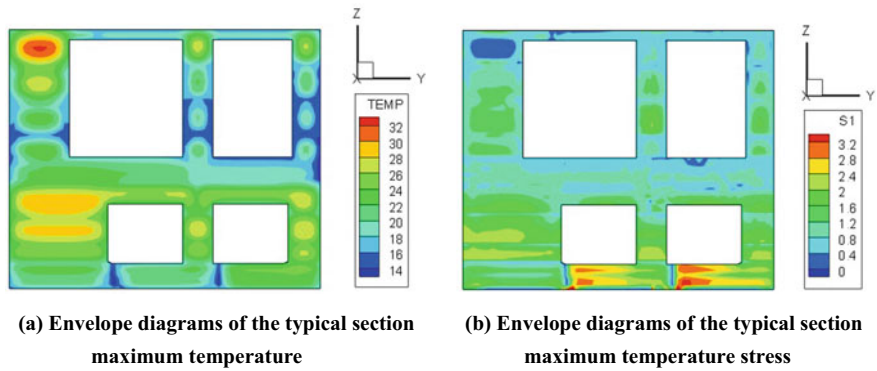
**Fig. 13** Envelope diagrams of the concrete (optimized scheme 2)

(3)   Results of optimized scheme 3

The calculation results of optimized scheme 3 are displayed in Fig. 14. The diagram of the typical section maximum temperature stress illustrates that the minimum temperature is increased in the first winter after the surface heat preservation of the strong constraint area, which reduces the foundation temperature difference of the draft tube floor. The maximum tensile stress of the center of the bottom plate is reduced from 2.78 to 2.48 MPa. It can be seen that in a low temperature season, the temperature difference in the foundation can be reduced by covering it with thicker heat preservation materials, so as to reduce tensile stress. If the maximum tensile stress in the strong constraint zone is completely controlled within the tensile strength range of C30 concrete, the thickness of the thermal insulation material can be further increased. When the heat preservation measures for the concrete surface of the floor concrete are strengthened, both the internal–external temperature difference and stress are reduced.

(a) Envelope diagrams of the typical section
maximum temperature

(b) Envelope diagrams of the typical section
maximum temperature stress
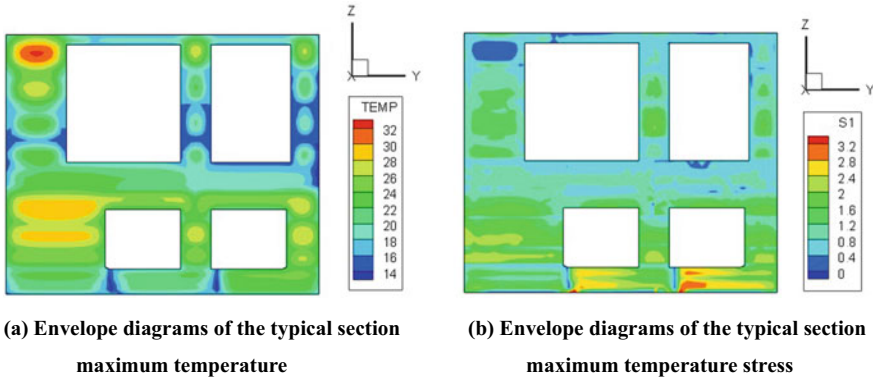
**Fig. 14** Envelope diagrams of the concrete (optimized scheme3)

# 6　Conclusions

This paper details the difficulties of temperature control and crack prevention for a large hydropower station constructed in a high-altitude region, as well as the stress generation mechanism of its floor.

The calculations and analysis exhibit that the conventional temperature control crack prevention measures have difficulty controlling the temperature stress of the floor in the safe range. According to the mechanism of stress generation, the temperature control measures suitable for hydropower stations in high-altitude regions are put forward.

(1) The results show that shortening the intermittent pouring period of new and old concrete can reduce the upper- and lower-layer constraints, which has a significant effect on improving the tensile stress of the floor.
(2) The calculation results show that for a floor that is greatly affected by the environment and strongly constrained by the gate pier, the measures of adding a post-pouring belt in the appropriate position and a reasonable block can effectively reduce the cracking risk of concrete.
(3) When strict temperature control measures cannot ensure the safety of concrete that is exposed and constrained by the structure itself, strong thermal insulation measures can be taken to control the temperature difference between inside and outside of the dangerous parts, and the crack resistance safety of concrete can be improved.

After taking the above measures, except for some stress concentration area, the tensile stress of the structure can be controlled within the allowable tensile strength based on the conventional temperature control measures. The cracks in the concrete can be effectively prevented according to the analysis of the calculation and results.

# References

1. Zhu BF (2009) Pipe cooling of concrete dam from earlier age with smaller temperature difference and longer time. Water Resour Hydropower Eng 40(1):44–50
2. Fan WY, Liang RQ, Chen H et al (2014) Concrete temperature control design for double-curved arch dam of Wudongde Hydropower Station. Yangtze River 45(20):80–84
3. Wang JM, Duan SH, Hu SH et al (2013) Practice and technology of temperature control and anti-cracking for super-high arch dam of Jinping I Hydropower Station. Water Resour Hydropower Eng 44(12):41–46
4. Zhang DR, Liu Y (2009) Features analysis and countermeasures for concrete temperature control in Jinping-I high arch dam. J China Inst Water Resour Hydropower Res 7(4):270–274
5. Zhao XL, Wan XB, Fang D et al (2018) Calculation and analysis of the underground powerhouse spiral case concrete temperature control for baihetan hydropower project. YunNan Water Power 34(6):84–88
6. Wang ZY, Li TC (2015) Key technologies in the construction of Jinping I High Arch Dam. Water Power 41(1):53–56
7. Qiang S, Zhu YM, Wu SY et al (2007) Temperature field and stress field simulation analysis for Jinping-1 high Arch Dam. Water Resour Power 25(2):50–52
8. Wang ZH, Li T, Liu Y et al (2018) Temperature control measures and temperature stress of mass concrete during construction period in high- altitude regions. Adv Civ Eng 12, Article ID 9249382
9. Wang ZH, Liu Y, Zhang GX et al (2015) Sensitivity analysis of temperature control parameters and study of the simultaneous cooling zone during dam construction in high-altitude regions. Math Probl Eng 12. Article ID 528589
10. Li BQ, Wang ZH, Jiang YH et al (2018) Temperature control and crack prevention during construction in steep slope dams and stilling basins in high-altitude areas. Adv Mech Eng 10(1):1–15
11. Ouyang HJ, Qin PX, Hu P et al (2015) Research on the temperature control and cracking prevention of concrete dams at high altitude and its application. J China Inst Water Resour Hydropower Res 12(1):22–29, 41
12. Huang DH, Jin YM, Zhang RX (2013) Simulation calculation of allowable range of temperature for mass concrete foundation base under strong constraint in paramos. Water Resour Power 31(3):103–105, 44
13. Shao ZT, Zhu YM, Qiang S et al (2008) Study on temperature control and crack prevention of concrete gravity dam in the Alpine region. J Three Gorges Univ 30(1):6–8
14. Zhu K, Chu DD, Zhou HY et al (2015) Study of thermal stress simulation analysis on mass concrete in high altitude area. J Qinghai Univ (Nat Sci Ed) 33(3):19–23
15. Deng MJ (2016) RCC dam building technology for extreme cold regions and engineering practices. J Hydroelectric Eng 35(9):111–120
16. Du W, Zhou FQ, Wu Y (2009) Inversion analysis on change law on heat preservation concrete internal temperature field in cold area. Water Power 35(6):32–34
17. Ruan XM, Xia SF, Lu YH et al (2009) Application and effect evaluation for the heat preservation measures of a RCC gravity dam in cold region. South-to-North Water Transfers Water Sci Technol 7(3):27–30
18. Ma XQ (2006) Technical characteristics of water conservancy and hydropower construction in high-altitude regions. Water Resour Hydropower Eng 37(7):45–49
19. Liu LX (2005) Study on high-performance concrete and its technologies in high-altitude and alpine regions. Constr Technol 34(S2):99–101
20. Deng T, Zhan DM, Wang YH (2005) Application of concrete construction technologies for Tibet straight-hole hydropower station in the alpine region at the low-temperature season. Water Resour Hydropower Eng 36(7):106–108
21. An K (2008) Influence of temperature on cracks during the concrete construction in high altitude region. Sci Technol Inf 27:642–743

22. Wang J, Jin YM, Zhu QL et al (2013) Discussion on concrete temperature control standard for foundation restraint area in alpine region. Water Resour Hydropower Eng 44(6):82–85
23. Xu BL, Lian D, Huang YY et al (2014) Research on mass concrete temperature control measures based on the basic allowable temperature difference in Paramos. China Rural Water Hydropower 4:129–136
24. Gan WZ, Zhang Z, Wang YF (2016) Temperature control and construction technologies of high-grade abrasion-resistant silica fume concrete for spillway tunnels of Changheba hydropower station. Water Power 42(10):83–86
25. Zhu BF (1998) Thermal stresses and temperature control of mass concrete. China Electric Power Press, Beijing

# Study on Variability of Mechanical Properties of Steel Rebars

**B. Huda Sumaiya, Sisay Tadele, Saif Aldabagh, and M. Shahria Alam**

**Abstract** Steel rebars are widely used in construction as reinforcement in reinforced concrete elements and for prestressing applications. The actual mechanical properties of steel bars might deviate from the specified values for a number of reasons. This deviation in mechanical properties increases the effect of material strength variability on the uncertainty associated with structural design. In this study, a statistical approach is undertaken for the variability analysis of Grade 60 steel rebars using 200 test data of different bar sizes. Beta and normal are employed to represent the variation in the in the yield strength, ultimate strength, bar diameter, and elongation. The Kolmogorov–Smirnov and Anderson darling goodness-of-fit test is carried out to identify the most suitable distribution for the considered properties.

**Keywords** Fiber reinforced polymers · T-beams · Shear capacity · Ensemble machine learning

## 1 Introduction

Material strength variability can increase the uncertainty of structural design which could cause a premature failure, failure without warning, and over strengthening of structural elements. Analyzing uncertainty and its causes is important aspect of structural design. For this reason, design codes adopted adjustment factors which account for the uncertainties from different sources. The need to minimize uncertainty is important, and studying the causes of uncertainty is the first step. If material properties of the reinforcing steel bars are considerably higher than the design value, the member may behave in a different way rather than planned response. For example, an over-reinforced flexural member experiences severe catastrophic effect if the member is overloaded. Overloaded over-reinforced members cause brittle failure as the concrete crushes before the steel yields.

B. H. Sumaiya · S. Tadele (✉) · S. Aldabagh · M. S. Alam
School of Engineering, The University of British Columbia, Vancouver, Canada
e-mail: sis21kah@mail.ubc.ca

Material strength variability which includes mechanical properties of bars is one of the prime causes for the uncertainty. Actual material properties of steel rebars often show deviation from the specified values which affect the structural capacity and performance. Those deviations emanate from several factors including variations in heat source, variation in alloying techniques and heat treatment, variation in bar size, and weight.

## 1.1 Literature Review

Previous studies on variability of mechanical properties were done including those by Alen ([4], Mirza and Macgregor [1], Nowak and Szerszen [2], and Darwin et al. [3]. Alen [4] studied variability of mechanical properties of steel bars on test data obtained from Canadian manufacturing plant consisting of total 132 bars and 102 tested by the National Research Council (NRC). The study indicated that the coefficient of variation of yield strength of Grade 40 steel bars was 0.5–3% for individual sizes and 4.1% for overall bar sizes collected from same source. Alen [4] found that data samples from the same heat sources and rebar group showed lower coefficient of variation (COV) values when compared to data samples from the whole plant and different rebar groups. A study by Mirza and Macgregor [1] investigated variability of yield strength, tensile strength, and modules elasticity of steel bars using 3947 data samples obtained from 13 published and unpublished sources. Several factors were considered in their study including manufacturing sources, cross-sectional area, and loading rates. They also developed a probability distribution function (PDF) to represent the yield and tensile strength data. Data samples were in found to be in good agreement with the normal distributions on 5th to 95th percentile. Beta PDF showed better representation of the data samples mainly at the upper and lower tails of the distributions. Nowak and Szerszen [2] developed a cumulative density function for yield strength of Grade 60 steel bars using 416 data samples. Their study included bar sizes ranging from No. 3 to No. 11. They found that normal distribution has good representation of the data samples for all the bar sizes. A study by Darwin et al. [3] conducted statistical analysis on data samples obtained from 33 mills. They studied variation of mechanical properties among different mills and compared them to the ASTM standard as well. They also developed beta and normal PDFs to represent the data samples. Beta function was found to show good agreement with the data distribution.

## 2 Methodology

To study the variability of mechanical properties of steel rebars, more than 200 tensile test data of Grade 60 steel rebar were analyzed. Those experimental test results are from different steel manufacturing organizations located in Bangladesh. The data

set included tensile test results for bar sizes of No. 3, No. 4, No. 5, No. 6, No. 8, and No. 10. This study focused on analyzing the variability of mechanical properties by investigating the variations in physical and mechanical properties of reinforcing steel from their nominal value and to analyzing the level which is maintained by the manufactures to satisfy requirements of ASTM. Mechanical properties of yield strength, tensile strength, elongation fracture, and bar size were investigated in this study. The statistical distribution of the bar diameter, yield strength, ultimate strength, and elongation before failure of Grade 60 are examined and expressed using beta and normal distribution and also presented as a suitable cumulative density function (CDF) to represent the variation in yield strength, ultimate strength, bar diameter, and elongation before failure.

## 3    Statistical Distribution and Tests for Goodness-of-Fit

A goodness-of-fit approach was used to develop a probability distribution function (PDF) for mechanical properties yield strength, tensile strength, elongation fracture, and bar size. The PDF function represents the likelihood occurrence of a value of mechanical property from a given data sample. Literature review showed normal and beta PDFs have better representation of the mechanical properties of steel rebars. These PDFs were thus adopted and used to represent the distributions of the data samples considered in this study. The values for the parameters of beta function are determined using the maximum likelihood approach. The effectiveness of the PDFs at representing the data samples is measured using a measure of goodness-of-fit. Goodness-of-fit checks if a given statistical distribution fits a given data sample within a limit of significance value known as p-value. A significance level of 5% and 2% is used in this study to evaluate the effectiveness of the statistical distributions at representing the data sample.

Goodness-of-fit measures known as chi-squared test and Kolmogorov–Smirnov test. Chi-squared test is one of the most commonly used goodness-of-fit test. According to Snedecor and Cochran [5], it is used to verify data set resulting from definite distribution. One of the shortcoming associated with chi-squared test is that it only applies to large amount of data sample. Another measure of goodness-of-fit is the Kolmogorov–Smirnov test. In this test, the empirical cumulative distribution function (CDF) is compared with an assumed theoretical model's CDF. One of the benefits of this test is that it is not influenced by the underlying CDF being tested. It is also more accurate in comparison with chi-squared test. The Kolmogorov–Smirnov (K–S) "$D$" test statistics is established based on maximum, single vertical offset between the empirical density function (EDF) and CDF over the range of data set. The maximum offset will always occur just to the left or right of an observation point on the EDF. Equation 1 can be used to calculate the "$D$" value. Once the value of D is computed, the critical D value used to measure the effectiveness of the distribution ($D_{critical}$) must be identified. Once $D_{critical}$ is known, it is compared against $D_{st}$ which is defined as $P[D_{st} \leq D_{critical}] = 1 - \alpha$. The assumed theoretical model is acceptable

only if the obtained $D_{st}$ value is less than $D_{critical}$ value at considered significance level $\alpha$.

$$D = \max\left(\left|F(x_i) - \frac{i-1}{n}\right|, \left|F(x_i) - \frac{i}{n}\right|\right). \tag{1}$$

Another measure of goodness-of-fit used in this study is Anderson darling test. It measures whether a given data sample taken from a larger data set follows a specific distribution. Andersen darling test gives more weight to the tails of the distribution. In this study, Anderson darling test is used together with Kolmogorov–Smirnov test to select the best distribution for the data samples.

In this study, two significance levels (2% and 5%) are used for calculating the value of $D_{st}$. Then, the observed value of $D_{st}$ is compared with the critical value $D_{critical}$. If the observed $D_{st}$ is less than the critical value $D_{critical}$, the assumed theoretical model is acceptable at the specified significance level. It should be mentioned that both the Anderson darling and Kolmogorov–Smirnov tests are independent of bin size.

## 4 Results

### 4.1 Yield Strength Variability

Yield strength is a characteristic of steel rebar which defines the strength within which steel rebars are in their elastic range. Variability in yield strength is associated with several factors including manufacturing techniques, quantity and type of alloys added, and difference in heat treatments. The tensile test data used for analysis in this study is obtained from several sources. Therefore, the variability is expected to be higher for yield strength data.

The coefficient of variation (COV) for yield strength given in Table 1 lies on a range of 5–13.36% for the different bar sizes. The coefficient of variation obtained are high, and they indicate significant variability of yield strength data. The high COV values are associated with the fact that the data samples are obtained from different sources. Mirza and Macgregor [1] also found similar results where data taken from many sources showed increased COV values comparing to data samples from same source. Similarly, Alen [4] found that data samples from the same heat sources and rebar group showed lower coefficient of variation (COV) values comparing to data samples from the whole plant. The deviation of the PDF of the yield strength from normal distribution measured by the skewness is presented in Table 1 above. Bar No. 3 is observed to have a smallest skewness which indicate a yield strength PDF close to normal distribution.

The yield strength data is also represented using the normal and beta PDFs. The accuracy of the fit of the distributions with yield strength data is measured by plotting the cumulative distribution function of the distributions. Once the CDF plots are

**Table 1** Summary of statistical parameters for yield strength for Grade 60

| Bar size (Imperial) | #3 | #4 | #5 | #6 | #8 | #10 |
|---|---|---|---|---|---|---|
| Mean (ksi) | 64.36 | 68.15 | 67.15 | 63.33 | 64.85 | 69.56 |
| Minimum (ksi) | 50.41 | 59.69 | 50.69 | 53.96 | 53.36 | 60.35 |
| Maximum (ksi) | 75.26 | 80.23 | 95.14 | 73.13 | 71 | 93.01 |
| Coefficient of variation (%) | 9.93 | 8.56 | 13.36 | 7.16 | 5 | 9.07 |
| Skewness | −0.21 | 0.61 | 0.71 | −0.38 | −0.32 | 2.05 |

developed, the PDF of the functions and data samples are plotted to represent the yield strength data for Grade 60. The beta distributions for yield strength representing Grade 60 rebar provided good representations for the distribution of individual bar sizes, with the exception of No. 4 and #No.10 bar, which exhibit slight difference in the distribution pattern. Normal distribution on the other hand is observed to deviate highly from the yield strength data as can be observed from Fig. 1. The K–S and Anderson darling goodness-of-fit tests were performed for each distribution with the measured yield strength. The results show that the distributions have good agreement with the yield strength data. Both tests indicate that the beta distribution gave the best fit except for No. 8 bar size because normal distribution fitted best.

## 4.2 Tensile Strength Variability

Tensile strength is another important mechanical property of steel rebar which indicates the maximum strength the bar can sustain before failure. Tensile strength determines the strength of the steel rebar after yielding. The influencing factors for the variation of the ultimate are also related to variation in production techniques, alloy additions, and heat treatments. Analysis of tensile strength for the different bar sizes shows bar size No. 4 has maximum COV equal to 17.19% and bar size No. 10 has a minimum COV value of 5.67%. The overall COV for the tensile strength data was 11.99% (Table 2).

A PDF distribution is also developed to represent the tensile strength data. CDF plots actual data plotted with normal and beta CDFs are presented in Fig. 2. The CDF plots indicate the accuracy of the fitted statistical distributions at representing the tensile strength data. The cumulative distributions for tensile strength indicate that beta has good representation of the data in comparison with normal distribution. The measures of goodness-of-fit K–S and Anderson darling are also used to evaluate if the statistical distributions fit the tensile strength data within a significance level of 2% and 5%. Both measures of test indicate beta distribution as best fit to the tensile strength data.

**Fig. 1** Cumulative density function for yield strength of Grade 60 bar sizes **a** No. 3, **b** No. 4, **c** No. 5, **d** No. 6, **e** No. 8, and **f** No. 10

**Table 2** Summary of statistical parameters for ultimate strength for Grade 60

| Bar size (Imperial) | #3 | #4 | #5 | #6 | #8 | #10 |
|---|---|---|---|---|---|---|
| Mean (ksi) | 93.85 | 100.37 | 100.88 | 99.69 | 100.52 | 111.84 |
| Minimum (ksi) | 66.74 | 89.41 | 67.59 | 78.81 | 89.46 | 101.53 |
| Maximum (ksi) | 120.70 | 125.67 | 141.29 | 114.31 | 114.31 | 124.25 |
| Coefficient of variation (%) | 13.85 | 17.19 | 13.7 | 8.28 | 6.31 | 5.67 |
| Skewness | −0.21 | −1.26 | 0.006 | −0.37 | 0.47 | 0.49 |

## 4.3 Bar Size Variability

Steel bars are produced in different sizes which give designers a material choice and design options. This variation in bar size is studied on the obtained data samples to see how bar size varies within the steel rebars obtained from several sources. The analysis indicates a bar size No. 10 and bar size No. 4 have a coefficient of variance equal to 1.13% and 2.06%, respectively. The COV for bar size of the remaining bar sizes is within the above the range of 1.13–2.06% (Table 3).

**Fig. 2** Cumulative density function for ultimate strength of Grade 60 of bar sizes **a** No. 3, **b** No. 4, **c** No. 5, d No. 6, **e** No. 8, and **f** No. 10

**Table 3** Summary of statistical parameters for bar diameter for Grade 60

| Bar size (Imperial) | #3 | #4 | #5 | #6 | #8 | #10 |
|---|---|---|---|---|---|---|
| Mean (in.) | 0.39 | 0.47 | 0.63 | 0.78 | 0.98 | 1.25 |
| Minimum (in.) | 0.38 | 0.45 | 0.61 | 0.75 | 0.96 | 1.22 |
| Maximum (in.) | 0.41 | 0.5 | 0.65 | 0.80 | 1 | 1.3 |
| Coefficient of variation (%) | 2.03 | 2.06 | 1.4 | 1.35 | 1.13 | 1.46 |
| Skewness | 0.19 | 0.75 | 0.26 | −0.39 | 0.60 | 0.16 |

A probability distribution plots are also developed for the bar size data sets. Beta and normal statistical distributions were used to represent distribution of the bar size data samples. The actual CDF of the bar size distribution is plotted together with CDF for beta and normal functions and the accuracy of fit of the distributions is analyzed. Beta distribution has better fit to the bar size distributions especially for bar size No. 3 and No. 10 where the bar size distribution is in good agreement with the beta functions. K–S and Anderson goodness-of-fit tests also indicate beta function as a better fit to the bar size distribution. The statistical distribution for bar sizes is also

positively skewed for most of bar sizes. PDF for No. 6 is the only distribution which is negatively skewed from normal distribution.

### 4.4  Elongation Fracture Variability

Elongation fracture refers to the maximum strain recorded just before the material fails. This mechanical property is good measure of ductility and strain hardening of steel rebars. The elongation fracture of the tensile test data is analyzed using similar statistical techniques to understand how elongation fracture variability looks. A higher coefficient of variance is observed for the variability of elongation fracture for the different bar sizes in comparison with the above mechanical properties. The COV values range between 12.1% which minimum recorded COV for bar size No. 8 and 37.15% which the maximum recorded COV corresponding to bar size No. 10.

The elongation fracture data is also represented using beta and normal distribution functions. The CDF plots indicate that those distributions can be used to represent the elongation fracture data. A better fit of beta function is also observed in comparison with normal distribution as can be observed from the CDF plots in Fig. 3. The measures of goodness-of-fit that is K–S and Anderson darling also show beta distribution as the most suitable function for representing the elongation fracture of Grade 60 steel rebar. The skewness which is measure of the deviation of the data distribution from normal given in Table 4 indicates that both negative and positive values are measured for elongation fracture. Bar size No. 8 is closer to normal distribution (Fig. 4).

## 5  Conclusions and Recommendations

This study aimed at investigating the variability of yield strength, ultimate strength, bar diameter, and elongation fracture of steel rebars. Standard statistical parameters such as mean, maximum, COV, and skewness were used to assess the variability of the mechanical properties. In addition, beta and normal PDFs are used to represent the distribution of the mechanical properties. The tensile test data were characterized by high coefficient of variation in comparison with previous works on statistical analysis of mechanical properties. The high value of COV for the mechanical properties indicated high data variability. Beta PDF is found to better represent most of the mechanical properties than normal PDF. Those results agree with previous findings. Therefore, beta PDF can represent the distribution data of Grade 60 steel rebars.

This study mainly focused on analyzing the effect of physical and mechanical parameters on the variability of mechanical properties of steel rebars. However, the chemical composition of steel rebars is also expected to cause variability in mechanical properties. Therefore, a statistical analysis which considers the effect of chemical composition should be considered. Besides, models that show variability
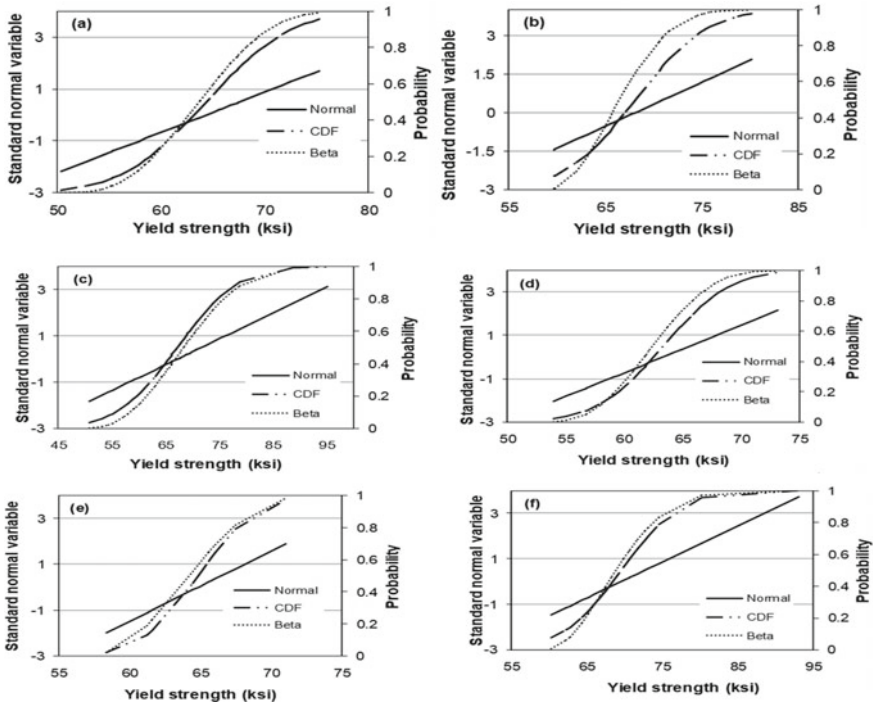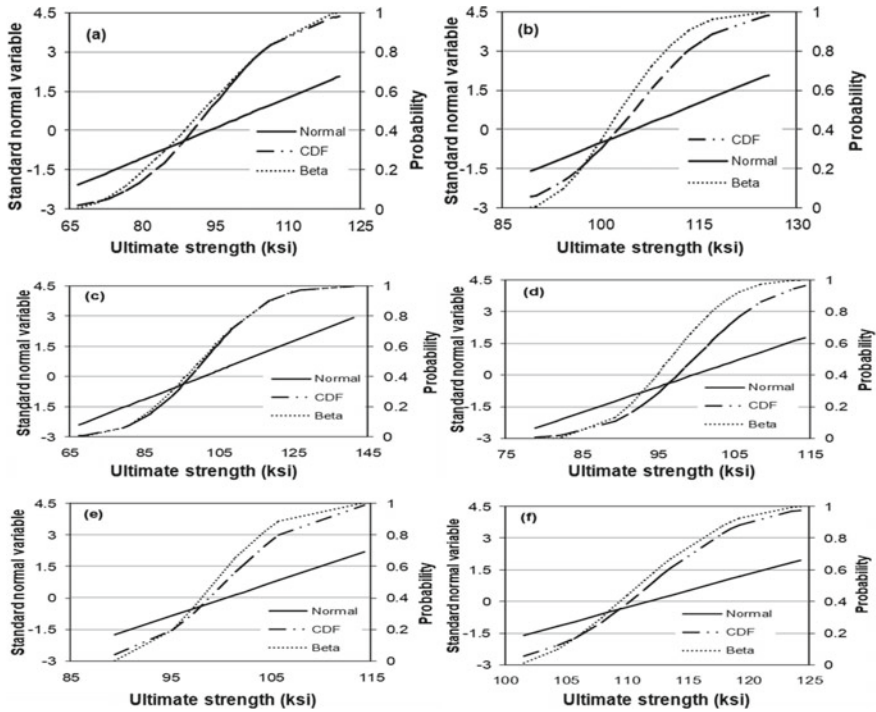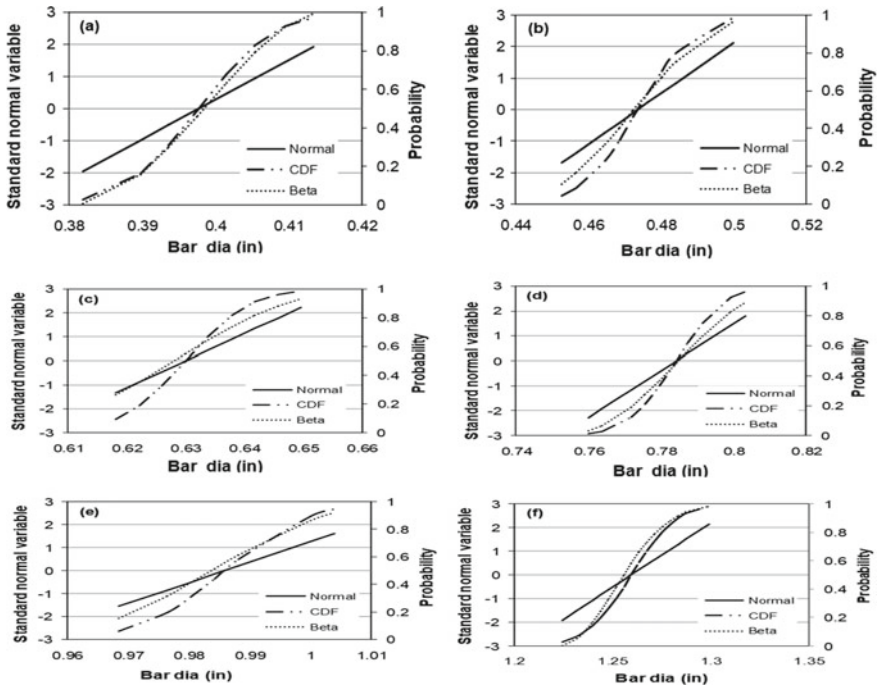
**Fig. 3** Cumulative density function for bar diameter of Grade 60 of bar sizes **a** No. 3, **b** No. 4, **c** No. 5, **d** No. 6, **e** No. 8, and **f** No. 10

**Table 4** Summary of statistical parameters for elongation before failure of Grade 60

| Bar size (Imperial) | #3 | #4 | #5 | #6 | #8 | #10 |
|---|---|---|---|---|---|---|
| Mean (%) | 17.57 | 19.69 | 17.6 | 18.12 | 20.67 | 13.19 |
| Minimum (%) | 12 | 11 | 1 | 6 | 16 | 5 |
| Maximum (%) | 25 | 26 | 25 | 26 | 24 | 23 |
| Coefficient of variation (%) | 19.19 | 21.54 | 25.39 | 20.87 | 12.1 | 37.51 |
| Skewness | 0.59 | 0.7997 | −2.13 | −0.8723 | −0.0915 | 0.2346 |

of mechanical properties might also be developed to incorporate the variability of steel rebars for different grades in building codes which could help structural design.
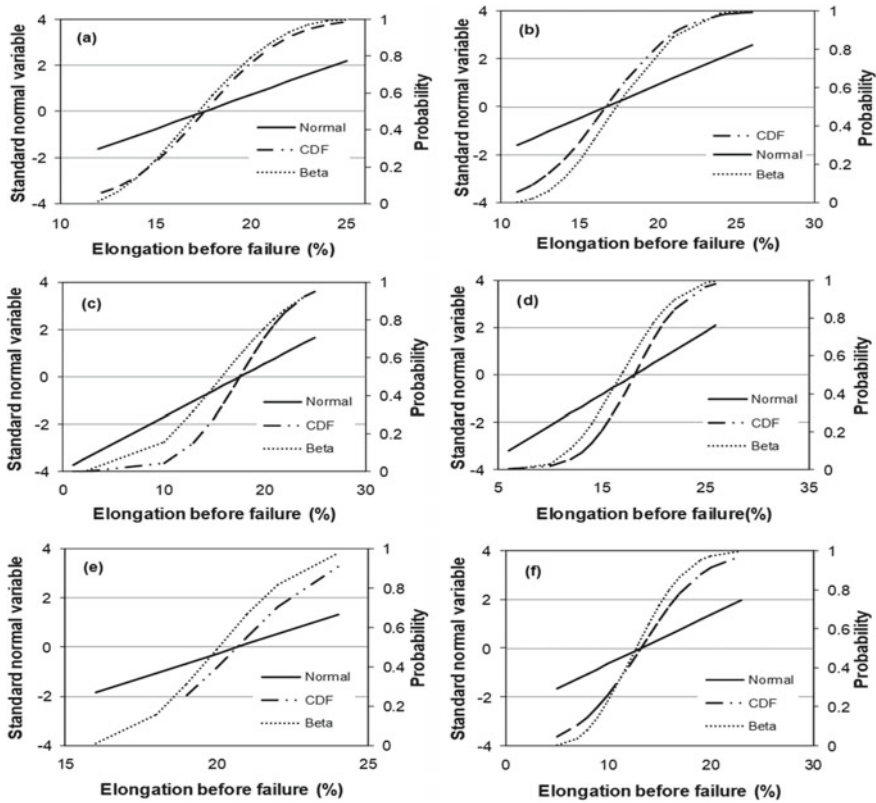
**Fig. 4** Cumulative density function for elongation before failure of Grade 60 of bar sizes **a** No. 3, **b** No. 4, **c** No. 5, **d** No. 6, **e** No. 8, and **f** No. 10

# References

1. Mirza SA, McGregor JG (1979) Variability of mechanical properties of reinforcing bars. J Struct Div ASCE 105:921–937
2. Nowak AS, Szerszen M (2003) Calibration of design code for building. J Struct Div ACI 100(3):377–382
3. Darwin D (2014) Statistical analysis of the mechanical properties and weight of reinforcing bars. Struct Eng Mater Lab SL R 04–1:198
4. Allen DE (1972) Statistical study of the mechanical properties of reinforcing bars. Building Research No. 85, National Research Council, Ottawa, Canada
5. Snedecor WG, Cochran WG (1989) Statistical methods 8th ed. Iowa State University Press
6. ASTM A 996-01 (2001) Standard specification for rail-steel and axle-steel deformed bars for concrete reinforcement. J Struct Div. West Conshohocken, Pennsylvania, PA, USA

7. Easy fit distribution fitting software (2011). http://www.mathwave.com/en/home.html
8. Microsoft (2007) Microsoft excel [computer software]. Microsoft, Redmond, Washington
9. Mood MA, Graybill FA, Boes DC (1974) Introduction to the theory of statistics 3rd ed. McGraw-Hill Companies, New York
10. Stephens MA (2003) EDF statistics for goodness of fit and some comparisons. J Am Stat Assoc 197(69):730–737

# Materials Specialty: Alkali-Silica Reaction and Alkali-Activated Concrete

# The Use of Self-Healing Technology to Mitigate the Alkali–Silica Reaction Distress in Concrete

**De Souza, Diego Jesus, Leandro Sanchez, and Alireza Biparva**

**Abstract** Alkali–Silica Reaction (ASR) is one of the most harmful distress mechanisms affecting the durability and serviceability of concrete infrastructure worldwide. ASR-induced deterioration leads to micro-cracking, loss of material integrity and functionality, significantly impacting the stiffness, tensile, shear, and compressive strength of affected concrete. Over the past decades, studies have demonstrated that the partial replacement of Portland cement by supplementary cementing materials or the addition of lithium-based admixtures (e.g., lithium nitrate, etc.) is effective preventive measures against ASR. Yet, new studies are now finding that the deterioration is only delayed and not entirely prevented. In this context, it has been verified that some products, such as crystalline admixtures, could enhance concrete's healing properties, thus presenting an interesting solution to reduce water ingress and recover damaged concrete elements. However, the potential of these materials to suppress durability-related distress due to ASR has not been assessed. This paper aims to evaluate different concrete mixes presenting two different types/nature of highly reactive aggregates (i.e., coarse vs. fine aggregates), incorporating a GU-type cement, lithium nitrate, a hydrophilic crystalline waterproofing material (CW), and two modified versions (CW-mod). The samples were fabricated, exposed to ASR development, and monitored over two years. Mechanical (i.e., compressive and shear strength, modulus of elasticity, and stiffness damage test) and microscopic (i.e., Damage Rating Index) techniques were selected to further analyze the distinct mixtures' appraised performance. The results show that the addition of CWs' agents in concrete minimized ASR development. In general, the mixtures not only delayed the development of inner damage but significantly lowered the compressive strength loss and slowed the crack propagation in the cement paste at equivalent expansion

D. Souza (✉) · D. Jesus
DTU Sustain, Technical University of Denmark, Kongens Lyngby, Denmark
e-mail: dsouz025@uottawa.ca

L. Sanchez
University of Ottawa, Ottawa, Canada

A. Biparva
Technical Director, Kryton International Inc., Vancouver, Canada

amplitudes than control specimens. Finally, comparisons among the results found are made, and further discussions and recommendations on the reliability of adopting self-healing products to suppress ASR are conducted.

**Keywords** Alkali-silica reaction · Durability of concrete · Self-healing · Crystalline waterproofing admixtures

## 1 Introduction

Alkali–Silica Reaction (ASR) is one of the most harmful distress mechanisms affecting the durability and serviceability of concrete infrastructure worldwide. ASR is conventionally defined as a chemical reaction between the alkali hydroxides (i.e., $Na^+$, $K^+$ and $OH^-$) dissolved in the concrete pore solution and some reactive mineral phases containing reactive silica forms present in the aggregates used in the mixture [1–5]. It generates a secondary product, the so-called alkali–silica gel, that induces expansive pressure within the reacting aggregate material and adjacent cement paste upon moisture uptake, leading to micro-cracking, loss of material's integrity, and functionality of the affected structure [1, 3, 5, 6]. ASR damage degree and features depend upon the type (i.e., fine and coarse aggregate) and reactivity of the aggregates used, the amount of alkalis of the concrete, the temperature and relative humidity of the environment [4, 7–12].

Over the years, several approaches and recommendations, including a comprehensive variety of laboratory test procedures, have been developed around the world to assess the potential alkali reactivity of concrete aggregates and the efficiency of preventive measures (i.e., control of the cement and concrete alkali content, use of supplementary cementing materials—SCMs, etc.) [5, 13]. Although numerous studies have found that ASR-induced expansion and distress may be prevented by the appropriate use of SCMs [1, 14, 15], recent studies are now finding that the deterioration is actually "only" delayed and not entirely suppressed [16]. Moreover, once ASR starts in the field, onerous (and often inefficient) human intervention becomes necessary.

In this context, numerous artificially triggering healing agents have been studied in the past years [17–20], and one of the smartest materials used is the so-called crystalline waterproofing materials (CW), a permeability-reducing admixture with hydrophilic nature [21], which when added to concrete, chemically reacts with water and un-hydrated cement particles to form insoluble needle-shaped crystals that fill capillary pores and micro-cracks in the concrete and block the pathways for water and waterborne contaminants, enhancing the resistant against aggressive substances [22–25]. However, although promising results have been demonstrated in the literature, indicating that CW-concrete significantly decreases water penetration depth [26, 27], enhances the resistance to chloride penetration [23, 26, 28], and almost fully recovers mechanical properties [24, 29, 30], its behavior under critical development of physicochemical mechanism such as ASR is quite unknown. Thus, this

study aims to appraise the impact of using engineered self-healing waterproofing technology to avoid and/or mitigate ASR-induced expansion and deterioration in concrete incorporating coarse and fine highly reactive aggregates.

## 2　Background

Crystalline admixtures are based on reactive, hydrophilic chemicals that react with water and cementitious materials to create a dense matrix and to precipitate crystalline pore-blocking deposits throughout the concrete [31]. Crystalline admixtures are used as permeability-reducing admixtures for hydrostatic conditions, which are sometimes informally referred to as "waterproofing admixtures". One of the pioneering research regarding the use of CW, Sisomphon and co-workers [32] demonstrated that adding 1.5% and 4% (by PC mass) of CW in cement paste mixtures induced cracks with a width of 250–400 $\mu$m were completed closed due to the healing activity of the CW. Moreover, once CWs offer other advantages such as permeability reduction and reducing shrinkage of the cementing materials, the healed paste samples showed zero permeability after 28 days of pre-cracking, and calcium carbonate was the major product found in the sealed cracks [32]. Combining 0.3% of CW, expansive additive (sulfate-based), and PVA fibers fully recovers the mechanical properties loss of strain-hardening cementitious composites measured by flexural strength, stiffness, and deflection capacity [33]. On the other hand, air-cured samples contributed with no visible healing phenomenon and very low mechanical recovery [33]. Yet, results demonstrate that air exposure specimens placed in R.H.-controlled rooms made of cement and crystalline admixtures (1% by cement weight) were highly effective in fully recovering concrete bending stiffness, load-bearing capacity, and visually closing cracks [29]. Likewise, healing ratios of 0.98 for cracks up to 400 $\mu$m were obtained after 42 days of healing by adding 4% CW (by PC mass) [25]; complete sealing of crack with widths below 300 $\mu$m [23]; 95% of strength regaining capacity [24]; and 50% lower water penetration, 30% lower chloride diffusivity, and healing ratios close to 1.0 [26].

It has been recently demonstrated that the combination of CW and SCMs (Blast Furnace Slag [34], Fly Ash [17, 22, 25, 30], and silica fume [20]) can even reach higher values of self-healing ratios, overall, efficiency between 90 to 105%, yet, depending on the exposure condition [30]. It is worth mentioning that there is a relative agreement in the literature in which cementitious composites soaked in water solution trend to achieve higher self-healing ratios and faster healing rates, followed by wet/dry cycles, water contact, and air exposure, respectively [20, 23, 25, 26, 29–31, 35]. Recent studies suggest that CW-made mortar bars may mitigate ASR expansion development by about 70%, likely due to the lower permeability of the exposed mortar bars, delaying the diffusion of alkali ions from the external solution. However, these findings still need further validation, particularly for concrete specimens exposed to ASR-induced development.

## 3    Scope of Work

As stated above, a number of techniques, supplementary cementing materials, and chemical admixtures have been used in the past, aiming to assess and mitigate the initiation and development of ASR in the field. However, there is very few research (if any) on the use of engineered self-healing products to mitigate ASR in concrete, thus leaving room for major developments in this area. This study aims to appraise the impact of using engineered self-healing waterproofing technology to avoid and/or mitigate ASR-induced expansion and deterioration in concrete incorporating coarse and fine highly reactive aggregates. The specimens were continuously monitored over time and at selected exposure periods (i.e., 90, 180, and 360 days), microscopic (i.e., Damage Rating Index) and mechanical (i.e., stiffness damage test, modulus of elasticity, compressive and shear strengths) were conducted and a comprehensive evaluation of the impact of CW on ASR-induced expansion and deterioration was performed.

## 4    Experimental Program

Ten different concrete mixtures incorporating two distinct highly reactive aggregate types and natures were fabricated and three different admixtures (i.e., lithium nitrate and two commercially available hydrophilic permeability-reducing so-called crystalline waterproofing materials—CWs) were selected for the research. Moreover, it was not used any type of superplasticizer in this research. It is worth mentioning that lithium compounds are commonly shown in the literature as a good alternative in modifying the reaction kinetics, yet they are quite expansive and impractical to be applied in different scenarios. Regardless that, lithium nitrate was selected is this study to be used as a second control mixture known to displayed acceptable results on ASR development. The coarse aggregates ranged from 5 to 20 mm in size. Non-reactive fine (NF) and coarse (NC) aggregates were also used in combination with two reactive aggregates (SPH and Tx) for concrete manufacturing. Table 1 provides information on the different aggregates used in this study, while Table 2 provides information about the chemical composition of the different binder materials used in this study. All ten concrete mixtures were mix-proportioned as per ASTM C1293 to present the same water-to-binder ratio (w/b of 0.45) and amount of binder materials ($420 + 10$ kg/m$^3$), as displayed in Table 3.

### 4.1    Manufacture of the Concrete Specimens

Thirty-six cylinders, $100 \times 200$ mm in size, were fabricated for each of the sixteen concrete mixtures in the laboratory. After 24 h, the samples were demolded and

**Table 1** Reactive (R) and non-reactive (NR) aggregates used in the research

| Aggregate | | Reactivity | Rock type | Specific gravity | Absorption (%) | AMBT[a] (%) |
|---|---|---|---|---|---|---|
| Coarse | NC | NR | Limestone | 2.79 | 0.42 | 0.00 |
| | SPH | R | Graywacke | 2.73 | 0.71 | 0.33 |
| Fine | NF | NR | Natural derived from granite | 2.67 | 0.82 | 0.08 |
| | Tx | R | Natural derived from granite | 2.63 | 0.91 | 0.86 |

[a] Results at 14 days of curing of the accelerated mortar bar testing (ASTM C 1260) carried out on the aggregates selected

**Table 2** Chemical composition of the cement

| | CaO | $SiO_2$ | $Al_2O_3$ | $Fe_2O_3$ | $SO_3$ | MgO | $Na_2O_{eq}$ | LOI |
|---|---|---|---|---|---|---|---|---|
| GU-cement | 61.93 | 20.1 | 5.02 | 3.80 | 4.38 | 2.42 | 0.91 | 2.91 |

**Table 3** Concrete mixtures cast with different aggregates using the same volumetric amount of reactive aggregates

| Mixture | w/cm = 0.45 | | Aggregates (kg/m$^3$) | | | | Admixtures (kg/m$^3$) | |
|---|---|---|---|---|---|---|---|---|
| | Water (kg/m$^3$) | Cement (kg/m$^3$) | NF | Tx | NC | SPH | CW1 | CW2 |
| SPH control | 189 | 420 | 836 | – | – | 938 | – | – |
| SPH LTM[a)] | 189 | 420 | 836 | – | – | 938 | – | – |
| SPH-CW1 | 189 | 420 | 836 | – | – | 938 | 8 | – |
| SPH-CW2[b)] | 189 | 420 | 836 | – | – | 938 | – | 8 |
| SPH-CW3[c)] | 189 | 420 | 836 | – | – | 938 | 4 | 4 |
| Tx control | 189 | 420 | – | 765 | 1019 | – | – | – |
| Tx LTM* | 189 | 420 | – | 765 | 1019 | – | – | – |
| Tx CW1 | 189 | 420 | – | 765 | 1019 | – | 8 | – |
| Tx CW2 | 189 | 420 | – | 765 | 1019 | – | – | 8 |
| Tx CW3 | 189 | 420 | – | 765 | 1019 | – | 4 | 4 |

[a] LTM—lithium nitrate ($LiNO_3$) admixture—the ratio Li/Na was kept constant as 0.74
[b] CW2—commercially available mortar admixture combined with hydrophilic crystalline admixture
[c] CW3—combination of 50% of CW1 + 50% of CW2

stored in a moist-curing room for another 24 h. Then, small holes (5 mm in diameter by 15 mm deep) were drilled at the two flat ends of the samples, in which steel gauge studs were glued in place with a fast-setting cement slurry, for longitudinal expansion measurements. Afterward, the samples were taken for the zero reading, being finally

placed in sealed plastic buckets lined with a damp cloth and stored at 38 °C and 100% RH. The ASR-affected cylinders were monitored for length changes over time for a total period of two years. As per ASTM C1293, the buckets were cooled to 23 °C for $16 \pm 4$ h before the periodic measurements.

## 4.2 Assessment of the ASR Development in the Concrete

### 4.2.1 Damage Rating Index (DRI)

A semi-quantitative petrographic analysis, using the DRI, was performed on one specimen from each concrete mixture after 90, 180, and 360 of exposure, according to the method described by Sanchez [3, 36]. The samples were cut in half axially and polished using a standard polishing device which uses diamond impregnated rubber disks (No 50 [coarse], 100, 400, 800, 1500, 3000 [very fine]); this device was found most suitable for the work, as it does not lose abrasive powders that can fill up cracks or voids in concrete, and high-quality polishing is obtained with minimal water supply so that AAR-gel leaching is avoided. Afterward, 1 cm$^2$ grids were drawn on the surface of the polished sections, and the DRI was performed as per Sanchez et al. [36]. The DRI final number presented in this work is the normalized 100 cm$^2$ value.

### 4.2.2 Compressive Strength Test

Compressive strength was measured through two different approaches with different and specific goals. First, to characterize all mixtures at 28 days compressive strength, samples were wrapped and placed at 12 °C, since some of the specimens contained highly reactive aggregates and ASTM C 39 method could not be followed as they could develop some ASR. Then, the cylinders were maintained at 12 °C for a 47-day period, according to the maturity concept as per ASTM C 1074. The second compressive strength measurements were carried out on three cylinders used for stiffness damage test, with the aim of verifying the compressive strength loss of the material as a function of AAR development. This procedure was adopted and considered valid after Sanchez et al. [3, 36] confirmed the largely non-destructive character of the SDT.

### 4.2.3 Stiffness Damage Test (SDT)

Three cylinders of each concrete mixture at 90, 180, and 360 days of exposure were subjected to five cycles of loading/unloading at a controlled loading rate of 0.10 MPa/s. The SDT procedure was performed following Sanchez et al. publications [3, 10, 37], i.e., using a loading level corresponding to 40% of the 28-day concrete

strength. Moreover, it is worth highlighting that the 28 days compressive strength of all mixtures was obtained using the maturity concept as per ASTM C 1074 to reach their mechanical capacity values.

### 4.2.4   Direct Shear Test

The direct shear test was performed according to the method and setup proposed by Barr and Hasso [38] and adapted by De Souza et al. [39]. The same approach considering the maturity concept was used to characterize the "zero" reading for all concrete mixtures at the equivalent 28 days. At 90 days of exposure, three samples of each concrete mixture were selected for analysis; however, differently from the compressive strength tests, the SDT was not performed on the samples prior to the shear test. Before testing, all samples were carefully ground so that a circumferential notch was created [38, 39]. The notch depth was adopted as about 20 mm ± 3 mm to ensure a shear-type failure without leaving a too-small area of the sample to be tested.

## 5   Results

### 5.1   ASR Kinetics

In this section, ASR expansion kinetics and amplitude results are presented for all sixteen mixtures fabricated in the laboratory, and Fig. 1 illustrates the average expansion values of each of them over time. A wide range of expansion kinetics and amplitudes were obtained as a function of the mixtures tested. In general, the mixtures containing the reactive Tx sand presented faster reactivity than those incorporating reactive SPH coarse aggregates. Disregarding the control groups (SPH and Tx—which displayed the greatest expansions, 0.45% and 0.81% at 360 days, respectively), the groups containing CWs presented faster reactivity than LTM mixtures, reaching 0.27% (CW1), 0.37% (CW2), and 0.32% (CW3) for mixtures containing the reactive SPH. Moreover, involving the extremely reactive TX, it was found that CW1 achieved 0.41% of expansion at 360 days of exposure, while the expansion values obtained for CW2 and CW3 mixtures were equal to 0.59% and 0.49%, respectively. After 360 days of ASR development, the lowest expansion values were obtained by mixtures containing lithium nitrate in the concrete, which decreased the expansion amplitude to 0.07% (SPH-LTM) and 0.10% (TX-LTM).
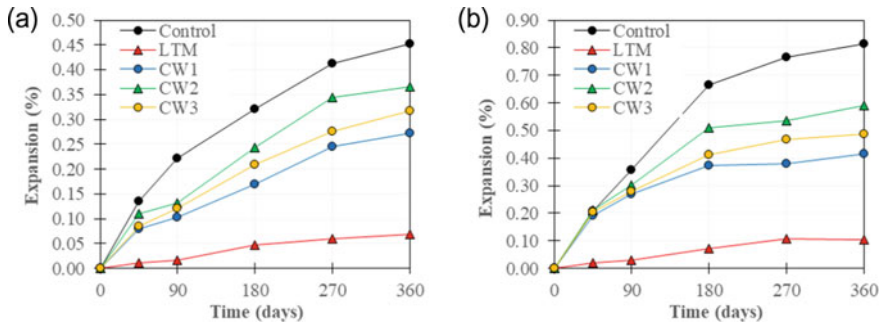
**Fig. 1** Expansion of the ASR-affected concrete specimens: **a** incorporating SPH reactive coarse, and **b** TX reactive fine aggregates

## 5.2 Microscopic Assessment

Figure 2 presents the microscopic damage features and DRI numbers obtained from the ASR-affected concrete specimens. Globally, it is possible to see that all the DRI numbers obtained for the different mixtures and aggregate types increase as a function of the specimens' expansions. Moreover, at equivalent expansion levels, the overall behavior of the different aggregates is somewhat similar, although TX mixtures reached higher values. Greater DRI numbers were found in control specimens (1088 for Tx control and 1019 for SPH control) followed by CW2 for both aggregates (859 for TX and 792 for SPH). Interestingly, CW1 made of SPH displayed a higher DRI number than CW3 (656 and 629, respectively), even achieving lower expansion amplitude after 360 of ASR development. On the other hand, for TX-made concrete mixtures, CW1 and CW3 followed closely the expansion obtained, and the DRI number was 672 (SPH-CW1) and 765 (TX-CW3). The lowest DRI numbers found after 360 days of testing were 331 (SPH-LTM) and 546 (TX-LTM).



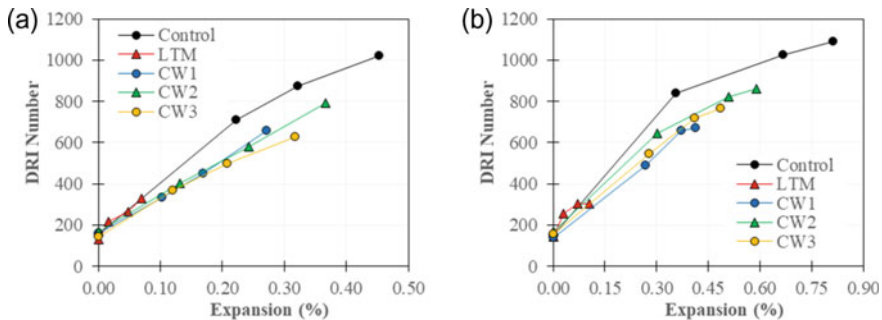**Fig. 2** DRI number in function of the expansion amplitudes for concrete specimens incorporating **a** SPH reactive coarse, and **b** TX reactive fine aggregates

## 5.3 Mechanical Properties Assessment

This section evaluates the compressive strength loss (CS), stiffness damage index (SDI), and losses in modulus of elasticity (ME) and shear strength (SS) of the various concrete mixtures investigated in this work. The data presented here are the variation ratio of values obtained at each selected "free" expansion level against the values obtained on sound concrete specimens. Moreover, one may notice that the mentioned mechanical ratios are displayed as a function of their respective expansion amplitudes to better visualize the binder compositions' mitigative behavior after ASR has already started. In general, compressive strength (CS) decreased in the function of the expansion amplitude; the higher the expansion level, the higher CS losses (Fig. 3). At each period of evaluation, SPH control reached 0.22%, 0.32%, and 0.45% of expansion resulting in 22%, 28%, and 35.1% of CS loss. Moreover, the faster ASR kinetics of TX attained to higher expansion values (i.e., 0.36%, 0.67%, and 0.81%); thus, the losses in CS were proportionally higher (i.e., 28%, 36%, and 40%). Curiously, the mixtures containing CWs lowered CS losses for comparable expansion levels than control specimens for both reactive aggregates. At 360 days of exposure, the compressive strength loss of CW1, CW2, and CW3 was 12%, 20%, and 18% for SPH-made concrete and 22%, 25%, and 20% for TX. The CS of lithium-made samples, also with low expansion levels, was found as 9% (TX-LTM) and 12% (TX-LTM).

Figure 4 illustrates the outcomes (i.e., SDI and ME) obtained through the stiffness damage test, as per Sanchez et al. [3, 10, 37]. The SDI results (Fig. 4a and b) were found to range from about 0.06 (LTM with 0.00% of expansion) to 0.39 (control with 0.45% of expansion) for SPH reactive coarse aggregate and from about 0.05 (lithium with 0.03% of expansion) to 0.47 (control with 0.81% of expansion) for Tx reactive fine aggregate. In general, SDI followed the development of expansion closely. Moreover, mixtures containing CWs tend to display overall lower SDI values than control specimens for similar expansion levels.
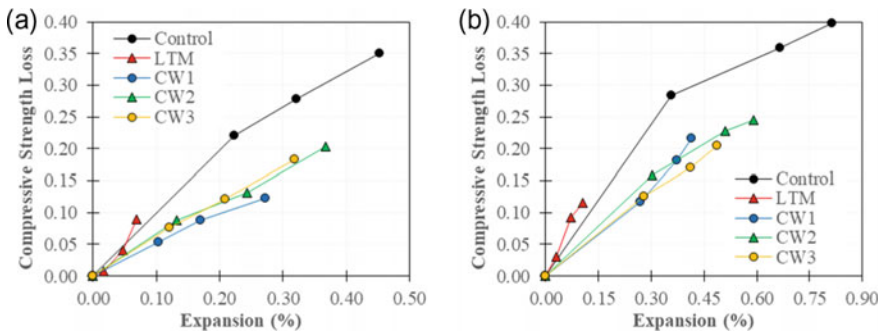


**Fig. 3** Compressive strength loss in function of the expansion amplitudes for concrete specimens incorporating **a** SPH reactive coarse, and **b** TX reactive fine aggregates
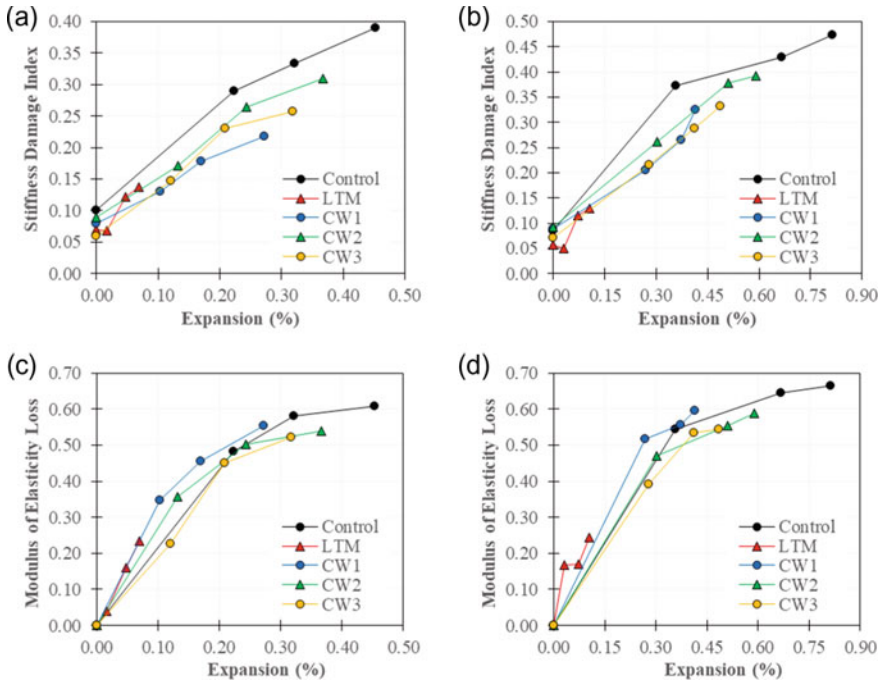
**Fig. 4** Stiffness damage test outcomes: stiffness damage index (SDI) of concrete made of **a** SPH reactive coarse, and **b** TX reactive fine aggregates; and modulus of elasticity loss (ME) of concrete made of **c** SPH reactive coarse, and **d** TX reactive fine aggregates

The ME losses (Figs. 4c and d) presented an increase as a function of time (i.e., decrease in modulus of elasticity) for all mixtures. Even though the different mixtures gathered a wide range of ME losses, the values indicated in both plots a concave trend toward ASR development. Globally, at equivalent expansion levels, regardless of the binder composition of the concrete mixtures, the loss in ME was somewhat similar. Furthermore, Tx mixtures, the control, CW1, CW2, and CW3 displayed the highest ME losses (i.e., 67%, 59%, 59%, and 55%, respectively), while the mixture incorporating LTM yielded 26% of ME loss at 360 days. On the other hand, SPH mixtures yielded similar, yet slightly lower, ME losses than TX at 360 days for all mixtures: control (61%), CW1 (55%), CW2 (54%), CW3 (52%), and LTM (22%).

The shear strength loss (SS) results (Figs. 5a and b) show similarities with the variations in the modulus of elasticity. However, the losses in SS were somewhat lower than in ME (i.e., control, CW1, CW2, CW3, and LTM). The SPH control samples displayed 61% of SS loss for 0.32% of expansion (at 180 days of testing), which was the higher value obtained among all mixtures. Yet, CW1, CW2, and CW3 incorporating SPH presented comparable losses in SS as the control specimen (51%, 57%, and 56%, respectively). One may notice that both control mixtures (i.e., SPH and TX) demonstrated a slight decrease in SS loss at 360 days, as for SPH, the higher

**Fig. 5** Sear Strength Loss in function of the expansion amplitudes for concrete specimens incorporating **a** SPH reactive coarse, and **b** TX reactive fine aggregates
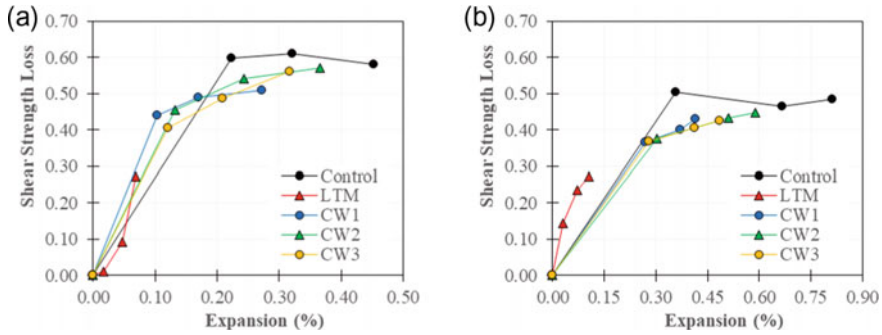
SS loss was not obtained at the end of the exposure period, but earlier, for TX the greater value was found at 90 days of ASR-induced development, i.e., 50%. The mixtures incorporating LTM, once again, showed the lowest losses, 27%, for both SPH and TX-made concrete specimens.

## 6 Discussion

### 6.1 ASR Kinetics

ASR damage development is often directly correlated to the level of expansion triggered by the concrete under this physicochemical mechanism. The results displayed a clear trend that concrete mixtures made of TX fine aggregate had faster ASR kinetics; this material has a generally smaller particle size, increasing the surface contact area between the reactive particles and the alkali solution. In general, the SPH control and TX control specimens showed that the rate of expansion decreased after about 180 days of curing. Likewise, similar behavior can be observed in all concrete mixtures, indicating different expansion amplitudes at the end of 360 days.

Lithium nitrate is a powerful mixture to mitigate ASR in concrete (especially, in the recommended ratio of 0.74 of Li/Na$_{eq}$). However, although both SPH-LTM and TX-LTM exhibit expressively lower ASR-induced expansion than control mixtures over the evaluation period, they could not maintain the expansion below 0.04% at 2 years of curing as per [40]. However, it is worth mentioning that both SPH and TX are classified as extremely ASR reactive aggregates.

The use of crystalline waterproofing materials (CWs) to enhance the healing properties has been demonstrated in the literature [17, 22, 25, 30, 41]. However, its behavior under the development of ASR in concrete specimens has not been explored. The results presented in this study showed promising evidence that, besides the CWs' mixtures displayed expansion values between 0.27% and 0.59% (considering both

reactive aggregates) after 360 days of ASR-induced development, they significantly modified the kinetics of the reaction. On average, CW mixtures lessened in 33% the expansion for concrete made of SPH and 28% for TX over all evaluation periods. Among the CWs' mixtures, CW1 lowered in 40% the expansion, while CW2 in 20% and CW3, 32% over the 360 days of evaluation compared to SPH and TX control. As demonstrated by De Souza and Sanchez [41], either autonomous or autogenous healing processes could partially self-heal cracks and recover the mechanical properties, yet the behavior was studied mainly in cracks formed in the paste matrix. Moreover, pre-existent and generated cracks within the aggregates' particles were not even partially healed [41]. In other words, these materials may create a physical barrier delaying the continuous cracking development through the paste matrix and further ASR-gel deposition, which can explain the change in the reaction kinetics. Moreover, it is clear that the bigger impact in the expansion amplitudes occurs mainly after about 0.07–0.10% of expansion (when crack generated by ASR would start to reach the paste matrix [4, 9]). Finally, the results above emphasize that the reactive behavior of mixtures made of CWs may depend on the aggregate type and nature (i.e., five vs. coarse, lithotype, reactivity degree, etc.) since the performance of CWs changed while the use of distinct aggregates (SPH-CWs displayed "efficiency" 18% higher than TX-CWs).

## 6.2   *Microscopic and Mechanical Evaluation*

Mechanical and microscopic analyses were performed to assess the extension of damage of the ASR-affected mixtures. ASR distress development has been widely studied and described by Sanchez et al. [9, 36]. At the beginning of the physico-chemical reaction, cracks are formed within the aggregate particles; as the ASR-induced damage raises, new cracks are still developed within the aggregate particles, yet the pre-existing cracks keep increasing in width and length, reaching the cement paste. At higher levels of expansion, the cracks keep propagating through the aggregate particles and cement paste, and due to the "minimum energy law", they start to connect to one another, forming a high crack networking compromising the mechanical properties of the affected concrete [9, 36]. The crack development following the "minimum energy law" is restricted to cracks formed by ASR and through pre-existing cracks within the particles generated over crushing/weathering processes. Moreover, the higher the expansion level, the higher the DRI number for all mixtures; consequently, the different kinetics of the aggregates and influence of the mixtures on it displayed an important role in the crack progress over 360 days of ASR-induced development. However, at equivalent expansion amplitudes, both aggregates displayed somewhat close DRI numbers. Considering only the control and LTM mixtures' results, SPH concrete specimens exhibit 10% higher values than TX. Moreover, the propagation of cracks due to ASR development was modified by the CWs (Figs. 6a and b), thus impacting not only the total amount of cracks and crack patterns but also the mechanical properties' losses.
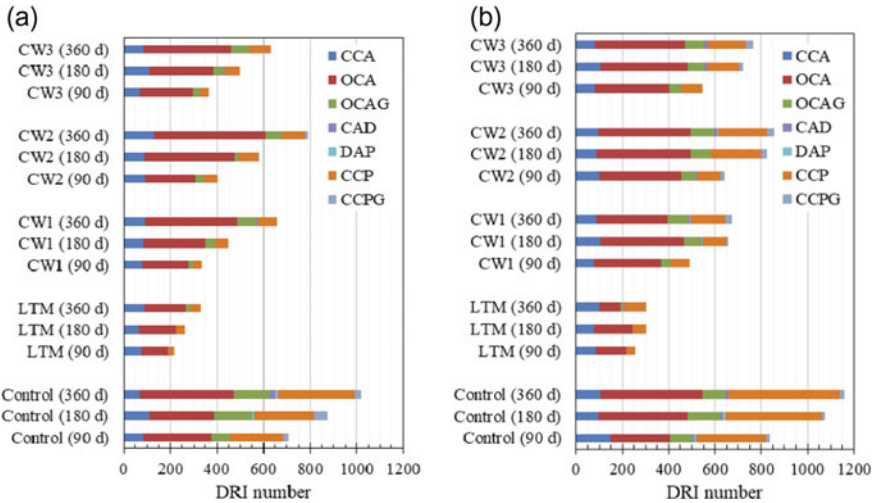
**Fig. 6** Microscopic features of concrete specimens incorporating **a** SPH reactive coarse, and **b** TX reactive fine aggregates

As discussed in the literature (Figs. 1a and b), in affected samples at low expansion levels (e.g., 0.05–0.07%), cracks can be mainly found inside the aggregate particles, and it is unlikely to find cracks in the cement paste extending from the aggregates. Moreover, until the point that the internal crack of the aggregates reaches the cement paste, it is unlike that CWs' admixtures start healing those cracks. In other words, a minimum influence on ASR-induced kinetics is observed. However, at moderate expansion levels (e.g., 0.10–0.12%), the cracks keep growing within the aggregates (in length and width) and extend to the cement paste. Therefore, crystalline admixtures (CW1, CW2 and their combination, CW3) can minimize the moisture and start healing the formed cracks in the cement paste, which may be responsible for the changes in the kinetics observed in Fig. 1. Indeed, Figs. 6a and b illustrate the microscopic features of the DRI analysis, and it is clear that CWs-made concrete mixtures lessened the number of cracks in the cement paste (i.e., CCP and CCPG). For instance, after 90 days of ASR-induced development, SPH control achieved 0.22% of expansion and total DRI number of 708, at close expansion amplitudes, SHP-CW2 and SPH-CW3 (i.e., 0.24% and 0.21% at 180 days, respectively) demonstrated 18% and 30% lower total DRI number. Furthermore, it is worth noticing that the DRI number of cracks found within the aggregate particles (i.e., CCA, OCA, OCAG, and CAD) and in the cement paste (i.e., CCP and CCPG) separately, and the influence of DWs is even clearer. Comparing SPH control (90 days), CW2 (180 days), and CW3 (180 days) with expansion around 0.22%, the sum of CCA, OCA, OCAG, and CAD are is similar among the distinct concrete mixtures' specimens (459, 493, and 435, respectively). However, the sum of CCP and CCPG, on the other hand, was 249, 88, and 61 for control, CW2, and CW3. Overall, CWs lowered the number of

cracks in the cement paste at equivalent expansion amplitudes in about 68% for SPH-made concrete, while 43% for TX. This can be explained by the faster kinetics and crack development of this highly reactive aggregate, which decreases the self-healing efficiency of the concrete. Among the different CWs-made mixtures, it is worth highlighting that CW1 demonstrated the best efficiency to decrease the number of cracks in the cement paste, 70% for SPH and 52% for TX-concrete. These promising results show evidence that these materials (i.e., CWs) can create a physical barrier delaying the continuous cracking development through the paste matrix and further ASR-gel deposition.

The influence mentioned above of the crystalline waterproofing materials in the development mechanism of ASR is supported by the mechanical properties analysis. For instance, the compressive strength of conventional concrete is a mechanical property known to be governed by the cement paste (CP) properties. Thus, any concrete mixture able to delay the damage development in the CP can also modify the rate of CS loss. Moreover, although CW mixtures exhibit relatively high expansion amplitudes and expressive CS losses, comparing the CWs results with control mixtures, they significantly decreased the CS losses at similar expansion levels (Fig. 3). On average, considering the data from both types of reactive aggregates and all CWs mixtures, incorporating 1.91% of CWs (by mass of PC) in the concrete could reduce CS losses by 47% over the 360 days of curing. Likewise, by adding crystalline waterproofing admixtures on concrete drops, SDI results in 14% over ASR development (Figs. 4a and b). The development of cracks within the aggregate particles and the propagation through the cement paste leads to an extension of inner damage in the affected concrete. Therefore, while being closed over a compressive and cyclic test of SDT, these cracks release a significant amount of energy, which results in the fast SDI values rise. Moreover, mixtures incorporating TX were found to dissipate more energy, since those samples have presented up to the date the highest expansion levels. Additionally, CWs seem to improve the quality of the microstructure (e.g., initially formed cracks, ITZ, etc.), thus, reducing SDI values, comparing the same expansion levels reached by CWs sample with those observed by Sanchez et al. [4] and obtained with non-CWs systems.

On the other hand, CWs-made concrete mixtures influenced less the modulus of elasticity and shear strength losses for unrestrained ASR development (Figs. 4c, d, and Fig. 5). This behavior was quite expected though since aggregates have more influence on the concrete's stiffness or modulus of elasticity and shear strength. While the modulus of elasticity of ordinary concrete is largely governed by the mechanical properties of the aggregates [42], the shear reduction is expected to take place due to "shear friction or aggregate interlock loss" caused by ASR-induced development. Therefore, the DRI results presented in Fig. 6 evidence that the use of CWs did not modify the overall amounts of cracks found within the aggregate particles. This pattern explains the similar losses of ME and SS of CWs, control, and LTM mixtures obtained.

# 7 Conclusions

The primary objective of this research program was to appraise the impact of using engineered self-healing (hydrophilic) waterproofing technology to avoid and/or mitigate ASR-induced expansion and deterioration in concrete incorporating coarse and fine highly reactive aggregates. From the results obtained in this study (after 360 days of evaluation), the following conclusions may be drawn:

- At least for the time-based evaluations, it seems that ASR kinetics, mechanical properties, and microscopic changes are dependent on the aggregate's type (i.e., fine vs. coarse aggregate). Samples incorporating the highly reactive TX sand were slightly more damaged after 360 days of curing than SPH samples. Moreover, samples containing TX have developed faster ASR kinetics and more cracks in the cement paste in shorter periods of time due to their faster ASR-induced kinetics;
- The use of hydrophilic crystalline waterproofing materials (CWs) was able to change the kinetics and distress caused by ASR, for both reactive aggregates used. It is believed that the CWs mainly start healing ASR deterioration when the cracks reach the cement paste. This interesting behavior can be drawn due to the significative change on ASR-induced kinetics after the point where cracks are expected to reach the cement paste;
- The most effective crystalline waterproofing admixtures in decrease the number of cracks in the cement paste of the affected concrete specimens was CW1 (commercially available crystalline waterproofing material);
- Although the CWs were not able to mitigate down ASR development to "safe" levels as recommended in different standards (i.e., 0.04% of expansion after 2 years of ASR-induced development), this material can be an important tool to modify ASR kinetics once the reaction starts to damage the paste matrix, delaying the deterioration and giving extra time to intervene and reinforce affected structures.

Finally, further development is being made by the authors to also understand the influence of supplementary cementing materials when used in combination with crystalline waterproofing admixtures and exposed to ASR-induced development. Larger number of samples are being tested and future publications will address those new results.

# References

1. Lindgård J, Andiç-Çakir Ö, Fernandes I, Rønning TF, Thomas MDA (2012) Alkali-silica reactions (ASR): literature review on parameters influencing laboratory performance testing. Cem Concr Res 42:223–243. https://doi.org/10.1016/j.cemconres.2011.10.004
2. Rashidi M, Knapp MCL, Hashemi A, Kim JY, Donnell KM, Zoughi R, Jacobs LJ, Kurtis KE (2016) Detecting alkali-silica reaction: a multi-physics approach. Cem Concr Compos 73:123–135. https://doi.org/10.1016/j.cemconcomp.2016.07.001
3. Sanchez (LFM) (2014) Contribution to the assessment of damage in aging concrete infrastructures affected by alkali-aggregate reaction 341
4. Sanchez LFM, Fournier B, Jolin M, Mitchell D, Bastien J (2017) Overall assessment of Alkali-Aggregate Reaction (AAR) in concretes presenting different strengths and incorporating a wide range of reactive aggregate types and natures. Cem Concr Res 93:17–31. https://doi.org/10.1016/j.cemconres.2016.12.001
5. Fournier B, Bérubé M-A (2000) Alkali-aggregate reaction in concrete: a review of basic concepts and engineering implications. Can J Civ Eng 27:167–191. https://doi.org/10.1139/cjce-27-2-167
6. Katayama T (2010) The so-called alkali-carbonate reaction (ACR) - Its mineralogical and geochemical details, with special reference to ASR. Cem Concr Res 40:643–675. https://doi.org/10.1016/j.cemconres.2009.09.020
7. Smaoui N, Bérubé M-A, Fournier B, Bissonnette B, Durand B (2004) Evaluation of the expansion attained to date by concrete affected by alkali–silica reaction. Part I: Experimental study, Can J Civ Eng 31:826–845. https://doi.org/10.1139/l04-051
8. Sanchez LFM, Fournier B, Jolin M, Bastien J (2014) Evaluation of the stiffness damage test (SDT) as a tool for assessing damage in concrete due to ASR: test loading and output responses for concretes incorporating fine or coarse reactive aggregates. Cem Concr Res 56:213–229. https://doi.org/10.1016/j.cemconres.2013.11.003
9. Sanchez LFM, Fournier B, Jolin M, Duchesne J (2015) Reliable quantification of AAR damage through assessment of the Damage Rating Index (DRI). Cem Concr Res 67:74–92. https://doi.org/10.1016/j.cemconres.2014.08.002
10. Sanchez LFM, Drimalas T, Fournier B, Mitchell D, Bastien J (2018) Comprehensive damage assessment in concrete affected by different internal swelling reaction (ISR) mechanisms. Cem Concr Res 107:284–303. https://doi.org/10.1016/j.cemconres.2018.02.017
11. Poyet S, Sellier A, Capra B, Foray G, Torrenti JM, Cognon H, Bourdarot E (2007) Chemical modelling of Alkali Silica reaction: influence of the reactive aggregate size distribution. Mater Struct Constr 40:229–239. https://doi.org/10.1617/s11527-006-9139-3
12. LFM (2014) Sanchez, Contribution to the assessment of damage in aging concrete infrastructures affected by alkali-aggregate reaction, 2014
13. Sanchez L (2014) Contribution to the assessment of damage in aging concrete infrastructures affected by alkali-aggregate reaction. UNIVERSITE LAVAL
14. Wei J, Gencturk B, Jain A, Hanifehzadeh M (2019) Mitigating alkali-silica reaction induced concrete degradation through cement substitution by metakaolin and bentonite. Appl Clay Sci 182:105257. https://doi.org/10.1016/j.clay.2019.105257
15. Thomas M (2011) The effect of supplementary cementing materials on alkali-silica reaction: a review. Cem Concr Res 41:1224–1231. https://doi.org/10.1016/j.cemconres.2010.11.003
16. Fournier B, Chevrier R, Bilodeau A, Nkinamubanzi PPC, Bouzoubaa N, Chevrier R (2016) Comparative field and laboratory investigations on the use of supplementary cementing materials (SCMs) to control alkali-silica reaction (ASR) in concrete. In: 15th International Conference Alkali-Aggregate Reaction. Bernardes, H.M & Hasparyk, N.P., São Paulo
17. Park B, Choi YC (2018) Self-healing capability of cementitious materials with crystalline admixtures and super absorbent polymers (SAPs). Constr Build Mater 189:1054–1066. https://doi.org/10.1016/j.conbuildmat.2018.09.061

18. Huang H, Ye G, Qian C, Schlangen E (2016) Self-healing in cementitious materials: materials, methods and service conditions. Mater Des 92:499–511. https://doi.org/10.1016/j.matdes.2015.12.091
19. Escoffres P, Desmettre C, Charron JP (2018) Effect of a crystalline admixture on the self-healing capability of high-performance fiber reinforced concretes in service conditions. Constr Build Mater 173:763–774. https://doi.org/10.1016/j.conbuildmat.2018.04.003
20. Reddy TCS, Ravitheja A, Sashidhar C (2020) Micromechanical properties of self-healing concrete with crystalline admixture and Silica fume. ACI Mater J 117:63–74. https://doi.org/10.14359/51722395
21. ACI 212.3R (2015) ACI 212. 3R-10 Report on Chemical Admixtures for Concrete, American Concrete Institute
22. Chandra Sekhara Reddy T, Ravitheja A (2019) Macro mechanical properties of self healing concrete with crystalline admixture under different environments. Ain Shams Eng J 10:23–32. https://doi.org/10.1016/j.asej.2018.01.005
23. Cuenca E, Tejedor A, Ferrara L (2018) A methodology to assess crack-sealing effectiveness of crystalline admixtures under repeated cracking-healing cycles. Constr Build Mater 179:619–632. https://doi.org/10.1016/j.conbuildmat.2018.05.261
24. Reddy TCS, Ravitheja A (2019) Macro mechanical properties of self healing concrete with crystalline admixture under different environments. Ain Shams Eng J 10:23–32. https://doi.org/10.1016/j.asej.2018.01.005
25. Roig-Flores M, Pirritano F, Serna P, Ferrara L (2016) Effect of crystalline admixtures on the self-healing capability of early-age concrete studied by means of permeability and crack closing tests. Constr Build Mater 114:447–457. https://doi.org/10.1016/j.conbuildmat.2016.03.196
26. Azarsa P, Gupta R, Biparva A (2019) Assessment of self-healing and durability parameters of concretes incorporating crystalline admixtures and Portland Limestone Cement. Cem Concr Compos 99:17–31. https://doi.org/10.1016/j.cemconcomp.2019.02.017
27. Ma H, Qian S, Zhang Z (2014) Effect of self-healing on water permeability and mechanical property of medium-early-strength engineered cementitious composites. Constr Build Mater 68:92–101. https://doi.org/10.1016/j.conbuildmat.2014.05.065
28. Liu H, Zhang Q, Gu C, Su H, Li V (2017) Self-healing of microcracks in engineered cementitious composites under sulfate and chloride environment. Constr Build Mater 153:948–956. https://doi.org/10.1016/j.conbuildmat.2017.07.126
29. Ferrara L, Krelani V, Carsana M (2014) A "fracture testing" based approach to assess crack healing of concrete with and without crystalline admixtures. Constr Build Mater 68:535–551. https://doi.org/10.1016/j.conbuildmat.2014.07.008
30. Reddy TCSR, Theja AR, Sashidhar C (2018) Self-healing ability of high-strength fibre-reinforced concrete with fly ash and crystalline admixture. Civ Eng J 4:971. https://doi.org/10.28991/cej-0309149
31. Biparva A, Gupta R (2015) Quantifying effect of integral crystalline waterproofing admixture on self-sealing property. In: 5th International conference on sustainable construction materials performance, innovation structure implicit. Whistler, Canada
32. Sisomphon K, Copuroglu O, Koenders EAB (2012) Self-healing of surface cracks in mortars with expansive additive and crystalline additive. Cem Concr Compos 34:566–574. https://doi.org/10.1016/j.cemconcomp.2012.01.005
33. Sisomphon K, Copuroglu O, Koenders EAB (2013) Effect of exposure conditions on self healing behavior of strain hardening cementitious composites incorporating various cementitious materials. Constr Build Mater 42:217–224. https://doi.org/10.1016/j.conbuildmat.2013.01.012
34. Li G, Liu S, Niu M, Liu Q, Yang X, Deng M (2020) Effect of granulated blast furnace slag on the self-healing capability of mortar incorporating crystalline admixture. Constr Build Mater 239:117818. https://doi.org/10.1016/j.conbuildmat.2019.117818
35. Guzlena S, Sakale G (2019) Self-healing concrete with crystalline admixture—a review. In: IOP conference series: Materials science and engineering 660. https://doi.org/10.1088/1757-899X/660/1/012057

36. Sanchez LFM, Fournier B, Jolin M, Bedoya MAB, Bastien J, Duchesne J (2016) Use of damage rating index to quantify alkali-silica reaction damage in concrete: fine versus coarse aggregate. ACI Mater J 113:395–407. https://doi.org/10.14359/51688983
37. Sanchez LFM, Fournier B, Jolin M, Bastien J (2015) Evaluation of the Stiffness Damage Test (SDT) as a tool for assessing damage in concrete due to alkali-silica reaction (ASR): Input parameters and variability of the test responses. Constr Build Mater 77:20–32. https://doi.org/10.1016/j.conbuildmat.2014.11.071
38. Barr B, Hasso EBD (1986) Development of a compact cylindrical shear test specimen. J Mater Sci Lett 5:1305–1308
39. De Souza DJ, Sanchez LFM, De Grazia MT (2019) Evaluation of a direct shear test setup to quantify AAR-induced expansion and damage in concrete. Constr Build Mater 229. https://doi.org/10.1016/j.conbuildmat.2019.116806
40. CSA A23.2-28A (2009) Standard practice for laboratory testing to demonstrate the effectiveness of supplementary cementing materials and chemical admixtures to prevent ASR in Concrete. Can Stand Assoc
41. De Souza DJ, Sanchez LFM (2021) Multi-level assessment of physical and mechanical properties recovery of self-healed concrete. Under Publication
42. Mehta PK, Monteiro PJM (2013) Concrete: microstructure, properties, and materials, 3rd Ed. https://doi.org/10.1036/0071462899

# Alkali-Activated Concrete Workability and Effect of Various Admixtures: A Review

**Nourhan Elsayed and Ahmed Soliman**

**Abstract** Alkali-activated concrete (AAC) is getting popular as a sustainable alternative for ordinary Portland cement concrete. Hence, questions regarding potential adaptation for existing concrete technologies to deal with performance issues of the new concrete type were raised. On top of these technologies, the efficiency of various admixtures and their interactions with the AAC's ingredients, hydration products, and microstructure development represent a knowledge gap. This paper reviews the workability requirements for AAC and the efficiency of various admixtures to achieve the targeted performance. The stability of admixtures in the alkaline medium, optimum dosages, and interaction with the activation process was highlighted. The reported data are anticipated to guide engineers in selecting suitable admixtures to achieve the desired workability while maintaining adequate performance.

**Keywords** Concrete · Alkali-activated materials · Workability · Admixtures · Hydration products

## 1 Introduction

Alkali-activated materials (AAMs) have been approved as an efficient, sustainable, eco-friendly alternative to ordinary Portland cementitious materials (PC) [1–3]. AAMs can be produced by activating a reactive solid aluminosilicate like blast furnace slag (BFS), fly ash (FA), metakaolin (MK), red mud, and other precursors using an alkaline activator such as alkali hydroxide, silicate, or carbonate in both liquid and solid forms [4–9]. The microstructure of AAMs is denser than conventional PC, leading to superior properties [10, 11]. Besides, the AAMs manufacturing process consumes lower energy and results in less $CO_2$ emission (*Egyptian Standards, E.S., "Cement-Physical and Mechanical Tests", ES 2421/2005*, n.d.; [3, 12].

N. Elsayed · A. Soliman (✉)
Concordia University, Montreal, Canada
e-mail: ahmed.soliman@concordia.ca

1201

However, achieving adequate workability is one of the main challenges for AAMs. This is ascribed to the inconsistency of raw materials and used activators [11, 13, 14]. Moreover, most commercial chemical admixtures, successfully used with PC, were reported incompatible in high alkali environment of AAMs [13–15]. Hence, the rheological properties of AAMs must be comprehensively studied, and basic factors controlling control their workability need to be investigated. This paper reviewed the effects of the nature and dosage of activators and precursors on the rheology of AAMs. The reported data are expected to guide engineers in understanding the workability and rheology of AAMs; hence, they can select suitable admixtures according to the desired workability. The various ingredients' effect on the rheology performance of AAMs is shown in the upcoming sections.

## 2  Alkaline Activators Types and Dosages

Activator is a crucial composition controlling the rheological behavior of AAMs. The most widely activators with a reasonable cost are sodium-based activators, such as sodium metasilicate ($Na_2O \cdot MSiO_2$), sodium carbonate ($Na_2CO_3$), sodium sulfate ($Na_2SO_4$) sodium hydroxide, or a mixture of two or more of them. In addition, some potassium-based activators have been used in laboratory studies. However, published literature showed that AAMs activated by NaOH solution usually exhibit higher yield stress and plastic viscosity than that activated by $KOH^-$ based [16]. This was attributed to the lower charge density of $K^+$, leading to lower ion–dipole forces and solution viscosity [17]. Similarly, the zeta potential value of the $KOH^-$ activated slag system is higher than that of the NaOH-based system, regardless of the used activator dosage. This is ascribed to the lower concentration of $Na^+$ cations adsorbed on the surface of the negatively charged particle. More adsorption of $K^+$ cations might reduce the van der Waals forces and increase the repulsive force of the double-layer between charged particles, thus contributing to a decrease in yield stress. By contrast, $Na^+$ cations would combine with water and consume more free water.

Activator concentration is another critical factor that affects the rheological behavior of AAMs. For instance, high NaOH concentration lowers the yield stress and plastic viscosity; thus, the fluidity of AAMs increases. Table 1 summarizes some reported results emphasizing the role of NaOH concentration. Changing NaOH concentration will affect the dissolution process and formation of products. At early stages, hydration products formed will have different abilities to bind water, leading to a variation in the amount of free water in the mixture. For instance, sodium aluminosilicate hydrate (N-A-S-H) (the main hydration product from activated fly ash precursor) will have a weaker ability to bind water compared to the hydration product from slag which is calcium aluminosilicate hydrate (C-A-S–H) [18]. However, the reported zeta potential results indicated that the electrostatic repulsion would dominate the behavior. Hence, there are contradictory data in the literature for various NaOH concentration ranges as shown in Fig. 1 [18–20]. Hence, attention must also

**Table 1** Yield stress and plastic viscosity for various concentrations of NaOH (modified of [20])

| Precursors | Alkali activator to precursor ratio (%) | Yield stress (Pa) | Plastic viscosity (pa*s) |
|---|---|---|---|
| Fresh fly ash blended pastes | 0 | 0.75 | 0.4 |
| | 2 | 2.4 | 1.3 |
| | 4 | 2.25 | 1 |
| | 6 | 1.8 | 1 |
| | 8 | 1.5 | 0.95 |
| | 10 | 1.4 | 0.9 |
| | 12 | 1.2 | 0.9 |

**Fig. 1** Reported trend for $\tau_0$ and $\mu$ with NaOH concentration
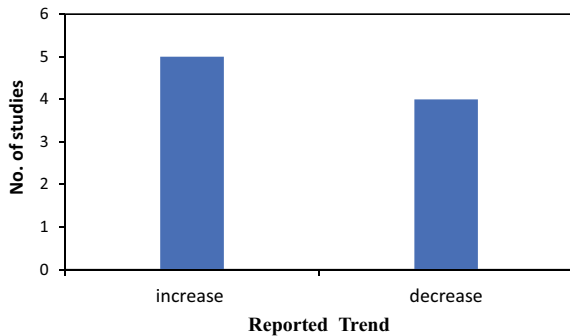


be given to the used precursor and the water-to-binder ratio (w/b) while selecting the suitable NaOH concentration.

Another important factor is the silica modulus (Ms), which is the $SiO_2/Na_2O$ molar ratio. Ms has a significant effect on the distribution of different ions in the solution and thus the rheological properties of AAM suspensions. Adjusting the Ms will directly affect the polymerization degree of silicate oligomers and their adsorption on the particle surface on the rheological properties. Recent studies reported that increasing the Ms increased the apparent viscosity and yield stress of AAMs [21]. However, in the high-ionized zone (the Ms < 1.8), the viscosity of suspensions showed insignificant responses to modulus variation.

**Hydration Products** The AAMs hydration process varied based on the precursors and was divided into three categories. First, the low-calcium system is generated from precursors with less than 10% calcium oxides (CaO), such as MK and FA-Class F. The main hydration product is highly cross-linked aluminosilicate geopolymeric gels known as N-A-S-H. The second category is a high-calcium system based on calcium-rich precursors with greater than 10% CaO, such as blast furnace slag. The formed product is tobermorite-like C-A-S-H. Finally, the third category blends the first two categories [22]. The AAMs' rheological behavior and parameters are substantially different when different precursors are used.

Usually, the third category is used to compensate for the drawbacks associated with the first and second categories. For instance, the high-calcium content for high-calcium precursors leads to changes in the precipitated gel systems, affecting yield stress. It was reported that the replacement of slag with fly ash reduced the yield stress [23]. However, increasing the replacement level of slag to 70 with respect to the weight of fly ash adversely affects the yield stress and consistency coefficient. This is attributed to reduced flocculation caused by fine FA particles and a faster dissolution of slag, resulting in low solid content [23]. Moreover, finer fly ash than slag enhanced attractive inter-particle forces. Conversely, it must be considered that the introduction of more slag means faster dissolution, higher structure buildup rate, and formation of more early C-A-S-H gels, with shorter percolation time, faster storage modulus growth, and flow loss [24, 25]. Another important aspect is the precursor's content, as this will reflect the packing and filler effects on the workability. Also, it will depend on the precursor's particle sizes, shapes, and amount of fines. The viscosity and yield stress of suspensions increase as the solid content increases. The following two aspects can explain it: (1) More solid particles will induce the particles-cluster effect; (2) less water added would increase the solids concentration, the inter-particle friction, and thereby the mortar is more reluctant to flow as given in Table 2 [26].

## 3  Various Used Chemical Admixtures

High-range water-reducing admixtures (HRWRA) are widely used to improve the rheology and workability of PC. There are many types of HRWRA including lignosulfonate-based, naphthalene-based, aminosulfonate-based, melamine-based, and polycarboxylate-based. Their working mechanisms and compatibility with ordinary Portland cement (OPC) have been well investigated **such** as inter-particle electrostatic repulsion and steric hindrance induced by the effective adsorption of admixtures on cement particles' surfaces. However, much research is still going to capture their mechanisms with AAM as no full understanding of their effects. Generally, it will be affected by the nature of the AAMs ingredients (i.e., activator pH and type, precursor). For instance, it was reported that only the naphthalene-based water-reducing admixture could lower the yield stress for alkali-activated slag mixtures. This was ascribed to its chemical stability in the alkaline environment. However, the polycarboxylate-based, melamine-based, and vinyl copolymer water-reducing admixture will have lower molecular weight fragments, which can still be adsorbed on the particles' surface, but the steric effect will be minimal [28]. However, it was reported that polycarboxylate superplasticizers were effective in alkali-activated fly ash mixtures, among other types of water-reducing agents [29]. In general, the interactions between most third-generation HRWRA admixtures and AAM will depend on the amount of dissolved $Ca^{2+}$, which directly affects the steric effect [30, 31].

Another set of admixtures that can affect AAMs' workability and rheological properties include shrinkage-reducing admixtures (SRA), retarders, and deflocculants. Previous study by Palacios and Puertas [32] showed that SRA addition

**Table 2** Yield stress (**a**) and plastic viscosity (**b**) of alkali-activated fly ash-silica fume blended grouts prepared by various water-to-binder ratios (modified of [27])

| W/b | Silica fume content (%) | Yield stress (Pa) | Plastic viscosity (Pa*s) |
|-----|-----|-----|-----|
| 0.75 | 0 | 0 | 0 |
| | 20 | 5 | 0.02 |
| | 40 | 10 | 0.75 |
| | 60 | 35 | 0.2 |
| 1 | 0 | 0 | 0 |
| | 20 | 0 | 0 |
| | 40 | 0 | 0 |
| | 60 | 15 | 0.1 |
| | 80 | 50 | 0.15 |
| | 100 | 60 | 0.3 |
| 1.25 | 0 | 0 | 0 |
| | 20 | 0 | 0 |
| | 40 | 0 | 0.25 |
| | 60 | 5 | 0.05 |
| | 80 | 20 | 0.75 |
| | 100 | 40 | 0.2 |
| 1.5 | 0 | 0 | 0 |
| | 20 | 0 | 0 |
| | 40 | 1 | 0 |
| | 60 | 1 | 0 |
| | 80 | 5 | 0.75 |
| | 100 | 10 | 0.125 |

did not improve the fluidity of alkali-activated slag paste and even increased the yield stress. Generally, the effect on fluidity will vary depending on the used dosages and the molecular weight of used shrinkage-reducing admixture such as polypropylene glycol (PG), as shown in Fig. 2 [33]. On the other hand, citric acid as a setting retarder admixture was found to increase AAMs fluidity.

## 4   Other Adding Ingredients

Adding inert mineral additions (e.g., limestone powder) is known to improve rheological properties due to optimizing the particle packing and freeing more water for lubrication. Adding up to 20 with respect-to-weight limestone powder in sodium silicate-activated slag-fly ash grout reduced yield stress and plastic viscosity [34]. On the other hand, it was reported that AAM is more sensitive to changes in liquid/solid ratio than ordinary OPC concrete [35]. This will also be affected by the nature
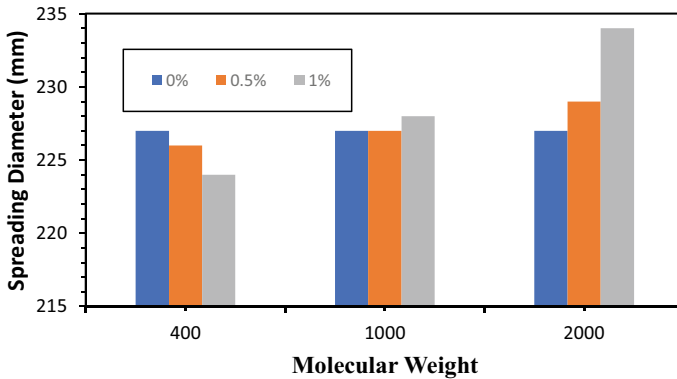
**Fig. 2** Fluidity of the AAS pastes with different molecular weights after adding different dosages of polypropylene glycol (PG)-based shrinkage-reducing agent

**Table 3** Flowability of fresh AAM based with different aspect ratios of straight steel fibers

| Aspect ratio of steel fibers | Volume fraction (%) | Flowability (mm) |
|---|---|---|
| 6/0.12 | 1 | 252 |
| | 2 | 248 |
| | 3 | 242 |
| 8/0.12 | 1 | 250 |
| | 2 | 245 |
| | 3 | 228 |
| 13/0.12 | 1 | 255 |
| | 2 | 248 |
| | 3 | 230 |
| 13/0.20 | 1 | 255 |
| | 2 | 247 |
| | 3 | 240 |

of aggregate and the amount of fine aggregate, as increasing fine aggregate will result in a higher surface area. Adding fiber to AAM to increase tensile strength and reduce potential cracking has become a common practice. Results reported by Liu et al. [36] showed that the aspect ratio and shape of the used fiber and contents are the most dominating factors for the mixture fluidity, as given in Table 3. However, its shape will have a negligible effect on the low fiber content. Also, changing the type of fiber (i.e., steel or polyvinyl alcohol (PA) will have a significant effect. Increasing PA fiber volume raised the viscosity and yield stress of the AAS composite due to its poor dispersibility [37]. However, producing PA fiber-reinforced AAS with high ductility, low plastic viscosity, and yield stress was still possible.

## 5　Various Rheological Models

Two critical values that control the flowability of any material are plastic viscosity and yield stress. Plastic viscosity reflects a material resistance to flow after the material begins to flow. Yield stress indicates the shear stress required to initiate flow. The relationships between shear stress and shear strain rate of fresh PC have been developed. The Bingham model modified Bingham model and Herschel–Bulkley (H–B) model are the most widely accepted for describing the rheological behavior of PC [38]. Adding admixtures in PC leads to the deviation of a linear relationship between shear stress and shear rate, which the modified Bingham model captures was proposed (Eq. 1) [26]:

$$\tau = \tau_0 + \dot{\mu}\gamma + \dot{c}\gamma^2, \tag{1}$$

where $\tau_0$ is the yield stress (Pa), $\mu$ is the plastic viscosity (Pa·s), and c is a pseudoplastic constant.

Published literature revealed that the Bingham model, modified Bingham model, and H–B model are empirically suitable for describing the rheological behavior of AAMs too. Generally, the Bingham model is recommended for NaOH-activated pastes [18], while the H–B model better suits the sodium silicate-activated pastes [28]. Both the Bingham model and the H–B model [39] were used in the systems activated by $Na_2CO_3$ (single or mixed with other activators). The modified Bingham model describes the nonlinear behavior deviating from Bingham fluid and avoids a variable dimension parameter like in the H–B model without mathematical limitation in the low shear rate region [40]. However, it is rarely used to describe AAMs' rheological behavior [20]. The applicability of the modified Bingham model in different AAM systems needs further study.

On the other hand, the composition of the aluminosilicates also has a significant impact on rheological behavior. Alkali-activated metakaolin systems generally exhibit higher viscosity and apparent yield stress due to their plate-like particles and large specific surface area [41], which means that suitable activators and adequate water are needed to ensure good workability [42]. As reported, alkali-activated fly ash pastes behaved like a Bingham fluid [29], while the rheological behavior of the fly ash-slag blended systems was more consistent with the H–B model [23]. These rheological behaviors could not be separated from the differences in particle size, dissolution behavior, the reactivity of different precursor particles, and the initially precipitated gels.

# 6   Conclusion

This study demonstrates that the rheological properties of AAMs are highly sensitive to use chemical admixtures which will vary based on the used activator (type and concentration), precursor, and other ingredients such as mineral additives. The following conclusions can be drawn from this review:

- There are contradictory data for the NaOH concentration effects on yield stress and plastic viscosity of AAMs. Attention must be given to the used precursor and the w/b while selecting the suitable NaOH concentration.
- The AAMs' rheological behavior and parameters are substantially different when different precursors types and dosages are used.
- The amount of dissolved $Ca^{2+}$ is the main factor that controls the interactions between HRWRA admixtures and AAM.
- The Bingham model is the most representative model for the performance of AAMs.

# References

1. Davidovits J (1994) Properties of geopolymer cements. In: First international conference on alkaline cements and concretes, pp 131–149
2. Provis JL (2018) Alkali-activated materials. Cem Concr Res 114:40–48. https://doi.org/10.1016/j.cemconres.2017.02.009
3. Yang KH, Song JK, Song KI (2013) Assessment of $CO_2$ reduction of alkali-activated concrete. J Clean Prod 39:265–272. https://doi.org/10.1016/j.jclepro.2012.08.001
4. Chindaprasirt P, Chareerat T, Sirivivatnanon V (2007) Workability and strength of coarse high calcium fly ash geopolymer. Cement Concr Compos 29(3):224–229. https://doi.org/10.1016/j.cemconcomp.2006.11.002
5. Kong DLY, Sanjayan JG, Sagoe-Crentsil K (2007) Comparative performance of geopolymers made with metakaolin and fly ash after exposure to elevated temperatures. Cem Concr Res 37(12):1583–1589. https://doi.org/10.1016/j.cemconres.2007.08.021
6. Provis JL, Duxson P, van Deventer JSJ, Lukey GC (2005) The role of mathematical modelling and gel chemistry in advancing geopolymer technology. Chem Eng Res Des 83(7 A):853–860. https://doi.org/10.1205/cherd.04329
7. Shi C (2002) Characteristics and cementitious properties of ladle slag fines from steel production. Cem Concr Res 32(3):459–462. https://doi.org/10.1016/S0008-8846(01)00707-4
8. Sun B, Ye G, de Schutter G (2022) A review: reaction mechanism and strength of slag and fly ash-based alkali-activated materials. Constr Build Mater 326(February):126843. https://doi.org/10.1016/j.conbuildmat.2022.126843
9. Zhang Z, Zhu Y, Yang T, Li L, Zhu H, Wang H (2017) Conversion of local industrial wastes into greener cement through geopolymer technology: a case study of high-magnesium nickel slag. J Clean Prod 141:463–471. https://doi.org/10.1016/j.jclepro.2016.09.147
10. Roy DM, Jiang W, Silsbee MR (2000) Chloride diffusion in ordinary, blended, and alkali-activated cement pastes and its relation to other properties. Cem Concr Res 30(12):1879–1884. https://doi.org/10.1016/S0008-8846(00)00406-3
11. Hammad N, El-Nemr A, El-Deen Hasan H (2021) The performance of fiber GGBS based alkali-activated concrete. J Build Eng 42(April):102464. https://doi.org/10.1016/j.jobe.2021.102464

12. McLellan BC, Williams RP, Lay J, Van Riessen A, Corder GD (2011) Costs and carbon emissions for geopolymer pastes in comparison to ordinary portland cement. J Clean Prod 19(9–10):1080–1090. https://doi.org/10.1016/j.jclepro.2011.02.010

13. Phoo-ngernkham T, Chindaprasirt P, Sata V, Hanjitsuwan S, Hatanaka S (2014) The effect of adding nano-SiO2 and nano-$Al_2O_3$ on properties of high calcium fly ash geopolymer cured at ambient temperature. Mater Des 55:58–65. https://doi.org/10.1016/j.matdes.2013.09.049

14. Rakngan W, Williamson T, Ferron RD, Sant G, Juenger MCG (2018) Controlling workability in alkali-activated class C fly ash. Constr Build Mater 183:226–233. https://doi.org/10.1016/j.conbuildmat.2018.06.174

15. Li H, Wang Z, Zhang Y, Zhang G, Zhu H (2021) Composite application of naphthalene and melamine-based superplasticizers in alkali activated fly ash (AAFA). Constr Build Mater 297:123651. https://doi.org/10.1016/j.conbuildmat.2021.123651

16. Kashani A, Provis JL, Qiao GG, Van Deventer JSJ (2014) The interrelationship between surface chemistry and rheology in alkali activated slag paste. Constr Build Mater 65:583–591. https://doi.org/10.1016/j.conbuildmat.2014.04.127

17. Poulesquen A, Frizon F, Lambertin D (2011) Rheological behavior of alkali-activated metakaolin during geopolymerization. J Non-Cryst Solids 357(21):3565–3571. https://doi.org/10.1016/j.jnoncrysol.2011.07.013

18. Zhang DW, Zhao KF, Xie FZ, Li H, Wang DM (2020) Effect of water-binding ability of amorphous gel on the rheology of geopolymer fresh pastes with the different NaOH content at the early age. Constr Build Mater 261:120529. https://doi.org/10.1016/j.conbuildmat.2020.120529

19. Rifaai Y, Yahia A, Mostafa A, Aggoun S, Kadri EH (2019) Rheology of fly ash-based geopolymer: effect of NaOH concentration. Constr Build Mater 223:583–594. https://doi.org/10.1016/j.conbuildmat.2019.07.028

20. Zhang DW, Wang DM, Lin XQ, Zhang T (2018) The study of the structure rebuilding and yield stress of 3D printing geopolymer pastes. Constr Build Mater 184:575–580. https://doi.org/10.1016/j.conbuildmat.2018.06.233

21. Hasnaoui A, Ghorbel E, Wardeh G (2019) Optimization approach of granulated blast furnace slag and metakaolin based geopolymer mortars. Constr Build Mater 198:10–26. https://doi.org/10.1016/j.conbuildmat.2018.11.251

22. Gartner EM, MacPhee DE (2011) A physico-chemical basis for novel cementitious binders. Cem Concr Res 41(7):736–749. https://doi.org/10.1016/j.cemconres.2011.03.006

23. Dai X, Aydın S, Yardımcı MY, Lesage K, De Schutter G (2020) Effects of activator properties and GGBFS/FA ratio on the structural build-up and rheology of AAC. Cem Concr Res 138(October):106253. https://doi.org/10.1016/j.cemconres.2020.106253

24. Jang JG, Lee NK, Lee HK (2014) Fresh and hardened properties of alkali-activated fly ash/slag pastes with superplasticizers. Constr Build Mater 50:169–176. https://doi.org/10.1016/j.conbuildmat.2013.09.048

25. Palacios M, Gismera S, Alonso MM, d'Espinose de Lacaillerie JB, Lothenbach B, Favier A, Brumaud C, Puertas F (2021) Early reactivity of sodium silicate-activated slag pastes and its impact on rheological properties. Cem Concr Res 140(October 2020):106302. https://doi.org/10.1016/j.cemconres.2020.106302

26. Yahia A, Khayat KH (2001) Analytical models for estimating yield stress of high-performance pseudoplastic grout. Cem Concr Res 31(5):731–738. https://doi.org/10.1016/S0008-8846(01)00476-8

27. Lu C, Zhang Z, Shi C, Li N, Jiao D, Yuan Q (2021) Rheology of alkali-activated materials: a review. Cem Concr Compos 121(April):104061. https://doi.org/10.1016/j.cemconcomp.2021.104061

28. Palacios M, Banfill PFG, Puertas F (2008) Rheology and setting of alkali-activated slag pastes and mortars: effect if organic admixture. ACI Mater J 105(2):140–148. https://doi.org/10.14359/19754

29. Criado M, Palomo A, Fernández-Jiménez A, Banfill PFG (2009) Alkali activated fly ash: effect of admixtures on paste rheology. Rheol Acta 48(4):447–455. https://doi.org/10.1007/s00397-008-0345-5

30. Uchikawa H, Sawaki D, Hanehara S (1995) Influence of kind and added timing of organic admixture on the composition, structure and property of fresh cement paste. Cem Concr Res 25(2):353–364. https://doi.org/10.1016/0008-8846(95)00021-6

31. Xie J, Kayali O (2016) Effect of superplasticiser on workability enhancement of class F and class C fly ash-based geopolymers. Constr Build Mater 122:36–42. https://doi.org/10.1016/j.conbuildmat.2016.06.067

32. Palacios M, Puertas F (2005) Effect of superplasticizer and shrinkage-reducing admixtures on alkali-activated slag pastes and mortars. Cem Concr Res 35(7):1358–1367. https://doi.org/10.1016/j.cemconres.2004.10.014

33. Ye H, Fu C, Lei A (2020) Mitigating shrinkage of alkali-activated slag by polypropylene glycol with different molecular weights. Constr Build Mater 245:118478. https://doi.org/10.1016/j.conbuildmat.2020.118478

34. Xiang J, Liu L, Cui X, He Y, Zheng G, Shi C (2018) Effect of limestone on rheological, shrinkage and mechanical properties of alkali—activated slag/fly ash grouting materials. Constr Build Mater 191:1285–1292. https://doi.org/10.1016/j.conbuildmat.2018.09.209

35. Alonso MM, Gismera S, Blanco MT, Lanzón M, Puertas F (2017) Alkali-activated mortars: workability and rheological behaviour. Constr Build Mater 145:576–587. https://doi.org/10.1016/j.conbuildmat.2017.04.020

36. Liu Y, Zhang Z, Shi C, Zhu D, Li N, Deng Y (2020) Development of ultra-high performance geopolymer concrete (UHPGC): influence of steel fiber on mechanical properties. Cem Concr Compos 112(November 2019). https://doi.org/10.1016/j.cemconcomp.2020.103670

37. Choi SJ, Choi JI, Song JK, Lee BY (2015) Rheological and mechanical properties of fiber-reinforced alkali-activated composite. Constr Build Mater 96:112–118. https://doi.org/10.1016/j.conbuildmat.2015.07.182

38. Jiao D, Shi C, Yuan Q, An X, Liu Y, Li H (2017) Effect of constituents on rheological properties of fresh concrete-a review. Cem Concr Compos 83:146–159. https://doi.org/10.1016/j.cemconcomp.2017.07.016

39. Torres-Carrasco M, Rodríguez-Puertas C, Del Mar Alonso M, Puertas F (2015) Alkali activated slag cements using waste glass as alternative activators. Rheological behaviour. Bol Soc Espanola Ceram Vidrio 54(2):45–57. https://doi.org/10.1016/j.bsecv.2015.03.004

40. Li L, Lu JX, Zhang B, Poon CS (2020) Rheology behavior of one-part alkali activated slag/glass powder (AASG) pastes. Constr Build Mater 258:120381. https://doi.org/10.1016/j.conbuildmat.2020.120381

41. Rovnaník P, Rovnaníková P, Vyšvařil M, Grzeszczyk S, Janowska-Renkas E (2018) Rheological properties and microstructure of binary waste red brick powder/metakaolin geopolymer. Constr Build Mater 188:924–933. https://doi.org/10.1016/j.conbuildmat.2018.08.150

42. Aboulayt A, Jaafri R, Samouh H, Cherki El Idrissi A, Roziere E, Moussa R, Loukili A (2018) Stability of a new geopolymer grout: Rheological and mechanical performances of metakaolin-fly ash binary mixtures. Constr Build Mater 181:420–436. https://doi.org/10.1016/j.conbuildmat.2018.06.025

# Utilizing Alkali-Activated Materials for Repair Applications: A Review

**Ahmed Khaled and Ahmed Soliman**

**Abstract** Alkali-activated materials are gaining attention as an alternative to cement-based materials. The high early strength and higher durability performance had promoted its use as a repair material for several structures. This review paper highlights the successful repair applications of alkali-activated materials. The selection criteria for the alkali-activated material mixtures meeting repair requirements are reviewed. The performance of the repaired elements, including mechanical and durability, is reviewed, highlighting the role of various alkali-activated materials properties. Based on the reviewed cases, recommendations for the utilization process for alkali-activated materials will be provided.

**Keywords** Alkali-activated materials · Repair · Durability · Damaged structure

## 1 Introduction

The deterioration of concrete structures has significantly increased due to severe climate conditions and environmental issues. Moreover, functional, structural, and aesthetic problems can be attributed to the little attention given to the durability issues when designing and building concrete structures. So, infrastructure rehabilitation has become a necessity as an economical alternative to the new reconstruction processes. Accordingly, repair techniques have been widely used to restore the integrity and the original conditions of different concrete structures. Recent research has considerably deduced that AAMs have the potential to be used as a repairing material. In addition to its advantageous characteristics as a friendly-environmental material, AAMs' fresh and mechanical properties have significantly fulfilled the requirements of repair applications [1].

A. Khaled · A. Soliman (✉)

Department of Building, Civil and Environmental Engineering, Concordia University, Montreal, Canada

e-mail: ahmed.soliman@concordia.ca

Furthermore, utilizing AAMs as repairing materials regarding the durability approach has been demonstrated to assure post-repair sustainable products. Compatibility with the existing concrete substrate and the post-repair structural compatibility are the major factors in considering the repair materials. Mechanical properties, compressive strength, flexural strength, modulus of elasticity, poisson's ratio, and the thermal expansion coefficient for the repair material must be compatible with the deteriorated existing substrate to maintain the long-term adhesion. Consequently, Table 1 indicates the specific requirements that must be fulfilled in repairing mortars.

Some procedures must be considerably assured to ensure the adhesion between the repairing material and the existing substrate. Firstly, cleaning the surface from all debris and small particles to maintain the bond along the repair surface. Moreover, it is necessary to rough the surface before applying the repair material as the roughness of the existing substrate affects the performance of repair mortars [2]. Besides the structural recovery and integrity enhancement for the concrete elements after repair, the durability approach must be considered. Consequently, three major factors significantly affect the durability of concrete-based structures. Firstly, microclimate is represented in water and aggressive agents inside the concrete and temperature with the pressure applied to the concrete substrate. Secondly, the concrete quality can be attributed to the type of cement affecting the pore connectivity binding, water/binder ratio affecting the porosity, and the curing scheme affecting the degree of hydration. Eventually, transport mechanisms control the internal movement of water and aggressive agents inside concrete either by diffusion, capillary suction, or permeability. Furthermore, Fig. 1 indicates the factors that also affect the durability of concrete repair [2].

**Table 1** Structural compatibility–general requirements for repair mortars

| Properties | Relation between the repair mortar and the concrete substrate |
|---|---|
| Compressive, Tensile, and Flexural strengths | Repair mortar > = Concrete substrate |
| Modulus in compression, tension, and flexure | Repair mortar = Concrete substrate |
| Poisson's ratio | Dependent on modulus and type of repair |
| Thermal expansion coefficient | Repair mortar = Concrete substrate |
| Curing and long-term shrinkage | Repair mortar > = Concrete substrate |
| Tension and Shear adhesion | Repair mortar > = Concrete substrate |
| Fatigue performance | Repair mortar > = Concrete substrate |
| Creep | Dependent on desirable or undesirable effects might be caused by Creep |
| Strain capacity | Repair mortar > = Concrete substrate |

[After Pacheco-Torgal, F, Z Abdollahnejad, S Miraldo, S Baklouti, and Y Ding. 2012. "An Overview on the Potential of Geopolymers for Concrete Infrastructure Rehabilitation." Construction and Building Materials 36: 1053–58.]
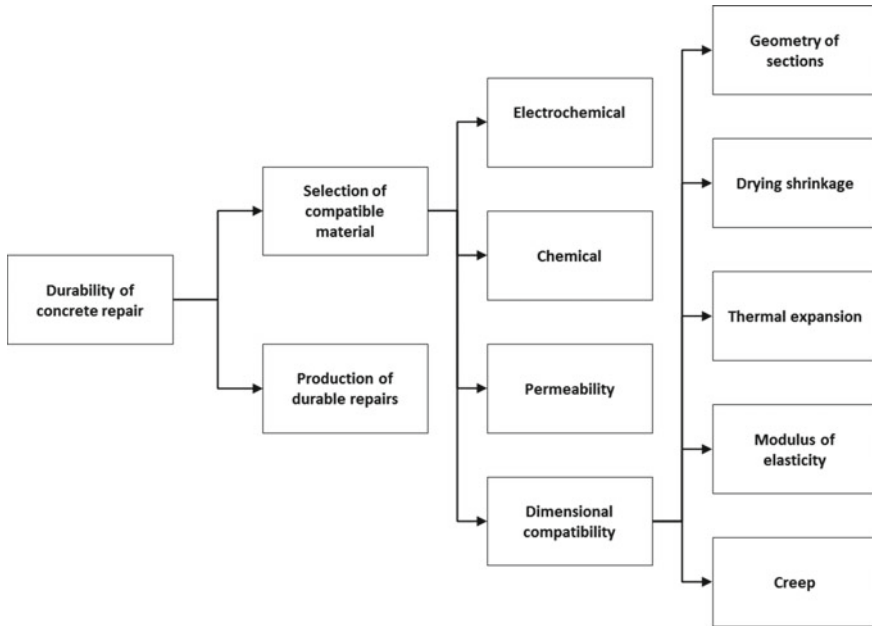
**Fig. 1** Factors that affect the durability of repair materials

## 2 Repair Application Using AAMs

Kramar et al. [3] investigated the suitability of AAMs for concrete repair based on three precursors (ground granulated blast furnace slag, fly ash, and metakaolin). Repair mortars must meet the requisites of the EN 1504 series before being used in practice. As a result of this experiment, the slag mortar was unsuitable for repair applications as it delaminated from the substrate during testing procedures. On the other hand, fly ash and metakaolin precursors exhibited good mechanical properties and adhesion. The bond strength of the fly ash and metakaolin mortars ranged from 1.8 to 2.3 N/mm$^2$ and thus met these criteria for both non-structural and structural repair mortars. The capillary absorption was too high in all three mixtures to be used in the structural repair regarding the criteria of EN 1504-3.

Moreover, metakaolin and fly ash mixtures have the potential to be used for non-structural repair works. Nevertheless, the problem of efflorescence was also assessed in all three mixtures. On vertical surfaces, difficulties were met when applying the FA and MK mortars. As shown in Fig. 2, these two mortars tended to sag down the surface. On the other hand, the S mortar was easier to apply as it was stiffer than the other two precursors. That can be attributed to the flowability and the setting time properties of the three tested mortars, whereas the flowability of S mortars decreases in a short time, unlike the two other mortars, FA and MK.
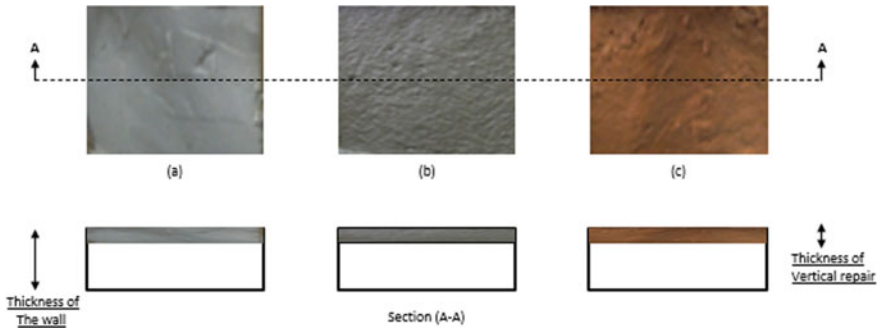
**Fig. 2** Application of the alkali-activated repair mortars to a vertical concrete surface. **a** the S mortar, **b** the FA mortar, and **c** the MK mortar

Fresh properties for the three mixtures, flowability, air content, bulk density, and setting time, were tested, and results were illustrated as follow; after 10 min, the flow value was the highest for the S mortar (180 mm), whereas the lowest value was obtained for the FA mortar (152 mm). The high flowability of the S mortar could be attributed to the low percentage of water glass in the mixture, as the flowability of AAMs depends mainly on the viscosity of the binder matrix, and silica dissolved in the water glass has a vital role in improving the viscous properties [4]. On the other hand, the flowability of S mortar after 30 min decreased remarkably (from 180 to 159 mm), whereas the flow value in the two other mixtures, FA and Metakaolin, remained relatively constant. Deb et al. [5] deduced that flowability decreased in the case of using ground granulated blast furnace slag as a precursor due to the angular shape of the slag particles and the accelerated reaction of calcium coming out of slag.

The bulk densities in the three different mortars ranged from 2187 to 2248 kg/ $m^3$. There were no specified differences between the three investigated AAMs for the air content value. The air content ranges from 4.1 to 5.2%, which generally ranges from 3 to 10% in cement-based mortars. Initial and final setting times were significantly different in the three alkali-activated mortars. Whereas the initial setting time of the FA mortar had the most extended amount of 2515 min, then MK mortar came next with 450 min, and S mortar was relatively the shortest with an amount equal to 60 min. Similarly, the final setting time of the FA mortar was the longest with an amount of 2910 min, followed by MK mortar with 505 min, and S mortar was also the shortest with an amount equal to 90 min. In general, using fly ash in AAMs decreases the rate of hydration reaction with low heat of hydration which results eventually in significant long setting time with low early strength, whereas the setting time decreases significantly with the higher percentage of slag content [4, 6, 7].

Compressive, flexural, bond strengths, bulk density, and modulus of elasticity were also illustrated in Table 2. After 7 days, the compressive strength of the three alkali-activated mortars had a range from 13.8 to 67.6 N/mm$^2$. The FA mortar had

**Table 2** Mechanical properties of AACs based on the three different precursors

| Mechanical properties | 7 days | 28 days | 56 days |
|---|---|---|---|
| *Compressive strength (N/mm$^2$)* | | | |
| Metakaolin | 67.6 | 71.2 | 71.5 |
| Slag | 32.4 | 52.2 | 61.0 |
| Fly ash | 13.8 | 51.1 | 76.5 |
| *Flexural strength (N/mm$^2$)* | | | |
| Metakaolin | 8.8 | 7.3 | 9.7 |
| Slag | 6.5 | 11.4 | 14.4 |
| Fly ash | 3.1 | 5.5 | 8.5 |
| Bond strength (N/mm$^2$) | Metakaolin | Slag | Fly ash |
| Vertical surface | 2 | N/A | 2.3 |
| Horizontal surface | 2 | N/A | 1.8 |

the lowest compressive strength; then, the S mortar achieved higher strength; eventually, the MK mortar attained the highest compressive strength. After 56 days, there were no remarkable differences between the MK and FA mortars, whereas the S mortar achieved the lowest compressive strength. FA achieved the slowest rate in compressive strength development, as the compressive strength increased from 13.8 to 76.5 N/mm$^2$ in 7 days and 56 days, respectively. This slow gaining of strength can be attributed to the low hydration reaction rate with low hydration heat and low early strength of fly ash. On the other hand, MK achieved the most rapid rate in compressive strength development, as the compressive strength increased from 67.6 to 71.5 N/mm$^2$ in 7 days and 56 days, respectively. MK's high specific surface area resulting in high reactivity is the main reason for the quick gain of compressive strength. Generally, the compressive strength of the three investigated mortars was approximately within a close range (60.0–76.5) N/mm$^2$ after 56 days [3].

Regarding the flexural strength, after 7 days, the tested mortars ranged from 3.1 to 8.8 N/mm$^2$, being lowest in the case of using the FA precursor and highest in the case of the MK mortars. Eventually, the S mortar reached the highest flexural strength among the three mortars after 56 days (14.4 N/mm$^2$), whereas the MK mortar (9.7 N/mm$^2$) achieved a value close to the FA mortar (8.5 N/mm$^2$). The amount of the precursor could be the factor that affected the flexural strength as the aggregate to solid binder ratio was approximately the same for the three tested mortars.

For the bond strength, as shown in the Table, it was not applicable to determine the value of bond strength in both vertical and horizontal surfaces in the case of using S mortars, as it delaminated before running the test, whereas the bond strength of the FA and MK mortars, had the range from 1.8 to 2.3 N/mm$^2$.

High early strength is one of the most important properties for any repair material. Abideng et al. evaluated the performance and the development of geopolymers, in road repair applications, based on the early strength characteristics. They used the metakaolin as a precursor, mixed with parawood ash (rubberwood ash) or oil palm ash as a binder agent, as shown in Fig. 3. The experimental work was performed

based on the hot mixes process with variant heat curing times (1, 2 and 4 h). As a result, very high early strength, low drying shrinkage, high compressive strengths, and very significant bond strength enhancement were considerably observed [8]. Figure 4. indicated that the percentage of metakaolin replacement with ashes would have a remarkable effect on the bond strength. Moreover, the greater the heat curing time, the higher the bond strength exhibited along the repair surface.

Evaluating durability parameters for geopolymer concrete made from fly ash activated with sodium hydroxide and sodium silicate is necessary for utilizing alkali-activated mortars in repair applications. David et al. studied the long-term durability Properties of geopolymer concrete; chloride diffusion and rapid chloride permeability, carbonation, water sorptivity, compressive strength, and workability have been investigated, as shown in Figs. 5, 6, and 7. Scanning Electron Microscopy
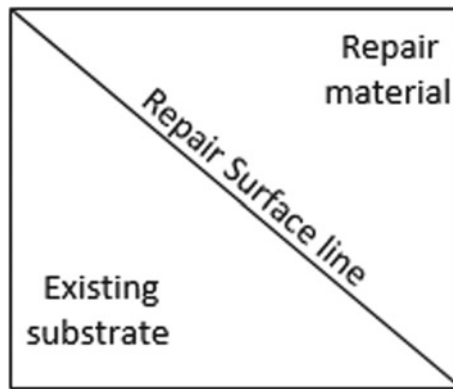


**Fig. 3** Schematic cross-section of geopolymer repair mortars bonded to OPC
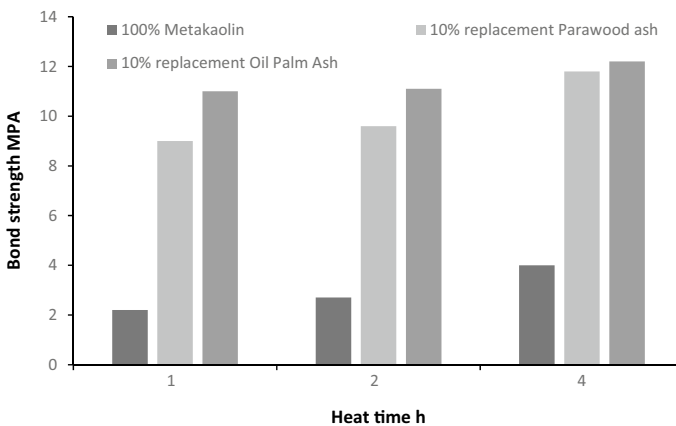


**Fig. 4** Bond strength (Geopolymer and OPC), measured using Slant Shear Test
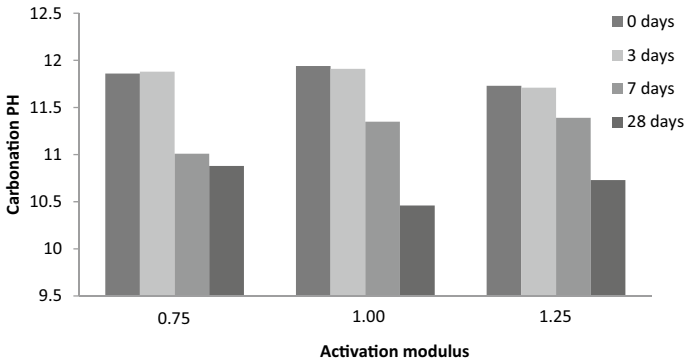
**Fig. 5** Carbonation data for geopolymer mortar specimens, PH
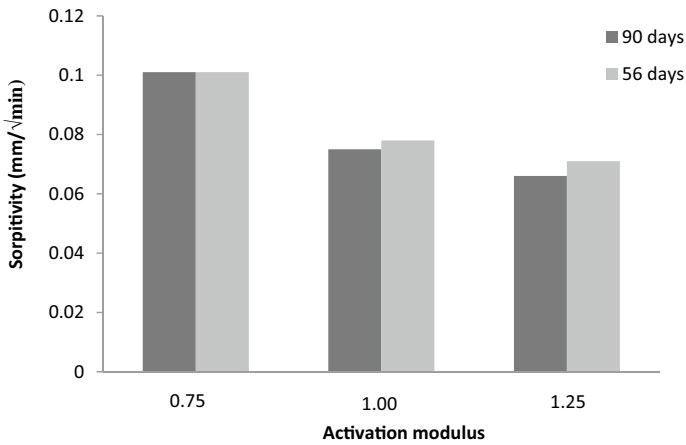


**Fig. 6** Water sorptivity @ 56 and 90 days

(SEM) and X-Ray Diffraction (XRD) were used to study the microstructures. As a result, both geopolymers with 1.00 and 1.25 activator modulus gave durability parameters comparable to OPC concretes, while the geopolymer with an activator modulus of 0.75 exhibited lower durability performance. However, due to the long-term chloride diffusion coefficient as shown in Table 3 and the initial pH of geopolymers with 1.00 and 1.25 activator modulus, there may be a concern to the long-term durability performance when considering chloride-induced corrosion of reinforcing steel [9].
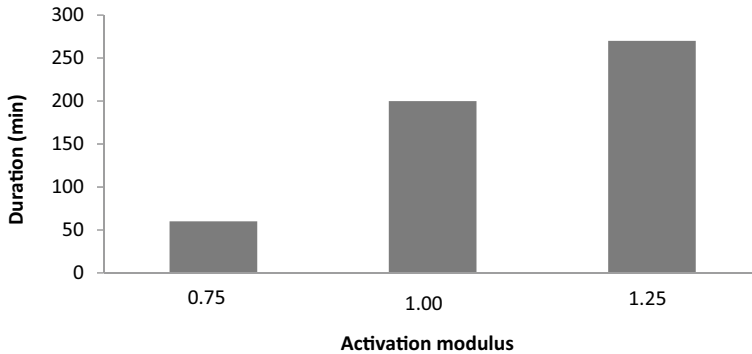
**Fig. 7** Rapid chloride permeability test data

**Table 3** The apparent chloride diffusion coefficient and surface chloride value

| Activation modulus | Cs (%) | $D^a \times 10^{-11}$ m$^2$/s |
|---|---|---|
| 0.75 | 0.16 | 3.1 |
| 1.00 | 017 | 3.1 |
| 1.25 | 0.14 | 3.7 |

# 3  Conclusion

Alkali-activated materials have the potential to be used in repair applications. AAMs' fresh, mechanical properties, and durability parameters exhibited a comparable result to OPC concretes. The repair mortars based on fly ash, metakaolin, and ground granulated blast furnace slag as precursors had appropriate flowability properties. However, the flow rate of slag mortars decreased within 30 min significantly, so further investigations will be mandatory to overcome the slag flowability defect. Also, the initial and final setting time for the slag repair applications still needs more investigation as the setting time will not be enough for the practical work applications, although it might be an advantageous characteristic in some particular cases.

# References

1. Nunes VA, Borges PHR, Zanotti C (2019) Mechanical compatibility and adhesion between alkali-activated repair mortars and Portland cement concrete substrate. Constr Build Mater 215:569–581. https://doi.org/10.1016/j.conbuildmat.2019.04.189
2. Pacheco-Torgal F, Abdollahnejad Z, Miraldo S, Baklouti S, Ding Y (2012) An overview on the potential of geopolymers for concrete infrastructure rehabilitation. Constr Build Mater 36:1053–1058. https://doi.org/10.1016/j.conbuildmat.2012.07.003
3. Kramar S, Šajna A, Ducman V (2016) Assessment of Alkali activated mortars based on different precursors with regard to their suitability for concrete repair. Constr Build Mater 124:937–944. https://doi.org/10.1016/j.conbuildmat.2016.08.018

4. Kumar S, Kumar R, Mehrotra SP (2010) Influence of granulated blast furnace slag on the reaction, structure and properties of fly ash based geopolymer. J Mater Sci 45:607–615
5. Deb PS, Nath P, Sarker PK (2014) The effects of ground granulated blast-furnace slag blending with fly-ash and activator content on the workability and strength properties of geopolymer concrete cured at ambient temperature. Mater Des 62:32–39
6. Nath P, Sarker PK (2014) Effect of GGBFS on setting workability and early strength properties of fly-ash geopolymer concrete cured in ambient condition. Constr Build Mater 66:163–171
7. Fernández-Jiménez AM, Palomo A, López-Hombradoc C (2006) Engineering properties of alkali-activated fly ash concrete. ACI Mater J 103:106–112
8. Hawa A, Prachasaree W, Taneerananon P, Tonnayopas D (2013) Development and performance evaluation of very-high early strength geopolymer for rapid road repair. Adv Mater Sci Eng 2013. https://doi.org/10.1155/2013/764180
9. Law DW, Adam AA, Molyneaux TK, Patnaikuni I, Wardhono A (2015) Long term durability properties of class F Fly Ash geopolymer concrete. Mater Struct 48(3):721–731. https://doi.org/10.1617/s11527-014-0268-9

# Evaluating the Performance of Phase Change Materials in Alkali-Activated Materials

Farshad Meftahi and Ahmed Soliman

**Abstract** The high energy consumption for buildings pursues researchers to examine various potentials to improve energy efficiency for construction materials. Among various potentials, the use of phase change materials (PCMs) demonstrated a high ability to modulate the inside temperature of the buildings. These materials can absorb and release the heat in a specific temperature range regulating thermal performance for mortars and concrete. However, the performance of PCMs, including stability and heat storage efficiency in non-cementitious mixtures such as alkali-activated materials (AAMs), is still questionable. Hence, this study evaluates the performance of micro-encapsulated paraffin, as an organic phase change material, in alkali-activated materials through various tests. Results showed that the high alkalinity of the used alkali activator did not significantly affect the performance and the stability of the micro-encapsulated PCMs. A slight reduction in the mechanical performance of the alkali-activated materials due to the addition of PCMs compared to cement-based mixtures was reported. This study can help the in situ engineers choose the proper mixture for environmental and mechanical performance.

**Keywords** Phase change materials · Alkali-activated materials · Mechanical performance · Durability · Heat of hydration

## 1 Introduction

Energy, environment, and sustainable development are important issues currently being faced by humankind. One of the most used materials in the current century can be named concrete, whose production grows yearly due to its low cost and severe demand. In this respect, it can be mentioned that concrete production is responsible for almost 8% of global anthropogenic GHG emissions and 3% of global energy

F. Meftahi · A. Soliman (✉)
Department of Building, Civil and Environmental Engineering, Concordia University, Montreal, QC, Canada
e-mail: ahmed.soliman@concordia.ca

demand, which evaluating proposed mitigation strategies in the sector is indispensable in the development of low- or zero-carbon emissions pathways [1, 2]. Cement, water, aggregates, and admixtures are the components of Ordinary Portland Cement (OPC) Concrete. As time is one of the greatest factors in the construction industry, the demand for shorter concrete preparation increased significantly, referring to this fact, steam curing was introduced. The steam curing method is the most used in precast concrete elements, which are regarded as an appealing solution to be considered in a various range of construction projects. This method provides many benefits such as reducing construction time, greater control and final quality of the elements, desirable cost-benefit relations, workforce, and less environmental impact compared to conventional concrete preparation [3]. However, a huge amount of energy for heating is used for its production. [4–6]. Abdullah M. Zeyad et al. reviewed the behavior of concrete in steam curing condition. According to their findings, stream curing can lead to increase in mechanical strength of concrete in short time, but it is along with negative effects on microstructure and other properties of concrete samples at later ages [7]. Shi et al. studied on the heat damages caused by steam curing of OPC and confirmed these facts [8].

As previously mentioned, a large portion of the current construction worldwide is made of OPC-based concrete, releasing a large quantity of carbon dioxide into the atmosphere. Approximately 1 tonne of carbon dioxide emissions for each ton of OPC produced, corresponding to more than 5% of greenhouse gas emissions worldwide and some of the recent studies on its heat curing procedures mentioned previously. Considering these facts, the study of alternative solutions, such as eco-efficient binders which can be named as alkali-activated binders, and the application of smart materials in the production of these materials is quite necessary. According to the study of M. L. Nehdi on AAMs, the possibility of lower carbon footprint, lower cost, saving natural resources by using by-products can be achieved when utilizing AAM binders [9]. In general, to produce alkali-activated materials (AAMs), any raw material with reactive silica and alumina in its chemical composition (entirely made of industrial wastes), such as fly ash (FA) or blast furnace slag, can be used together with an alkaline activator such as Sodium Hydroxide (NaOH) and thermal curing allows binding material with good mechanical properties to be obtained. According to the recent studies on the AAMs, it was observed that the compressive strength of these materials is influenced by many factors such as temperature, curing time, alkali-activated molarity (Sodium Hydroxide), and Sodium Silicate content used in the mix. As the curing time and temperature increase, the compressive strength of these materials increases proportionally [10]. According to the studies of Palomo et al. [11], the rising activator concentration can increase the PH of the mixture to increase the reactions inside the samples, which induce an increase in the compressive strength and density of the samples which eventually create a more durable sample. All these facts related to the preparation of these materials can enlighten the use of these materials as the perfect candidate for replacing the precast OPC materials with precast AAMs in the industry but yet the energy consumption of this system is questionable.

On the other hand, development in material technology in the last couple of decades demonstrated that the incorporation of phase change materials (PCMs) into the most used building material in the world (i.e., concrete) is an intelligence method to reduce the building energy assumption problem [12]. Application of PCMs in the mentioned materials may be a potential method for improving the above problems caused by steam curing. The ability to incorporate different materials inside the concrete mixtures nominate them as a proper host for PCMs.

PCMs are a kind of heat storage materials that are used in this field with a special capability called Thermal Energy Storage (TES), which is an important element in respect to energy. This capability can be used to store energy within the particles and use this energy later on with a specific target. In Fig. 1, the heat storage and latent heat composition in the used micro-encapsulated phase change materials can be seen. Kuznik et al. [14] define the phase change theory for the pure ideal body as an area in the space of the thermodynamic parameters (temperature, pressure, and volume) of the system composed uniquely of the pure body, in which the free energy is an analytical function. When heat exchange happens, PCMs pass by the solidification or fusion process, where materials transform from liquid to solid or solid to liquid. According to the recent studies on the application of PCM in the concrete mixtures, it was found that the interaction between PCM and cementitious materials is an issue of concern. Due to this matter, different techniques of PCM inclusion in building materials were introduced and tested (alveolar bricks, hollow bricks, and CSM panels). According to a recent study on the application of PCMs in cementitious materials [15], it has been found that the application of PCMs in the precast OPC materials can inhibit thermal cracking, enhance the capillary water absorption resistance, and improve early volume stability and freeze–thaw resistance of cement-based materials.

It should be noted that there are very few studies on the application of these materials in the concrete mixtures especially the on the green binders such as alkali-activated materials to see the properties of the final product. In this research, there has been a vast study on the application of micro-encapsulated PCMs and their impact
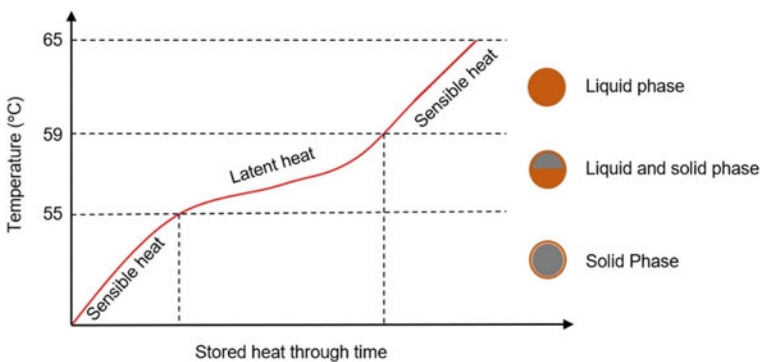


**Fig. 1** Heat storage as sensible heat and latent heat for MPCM 57 (after [13])

on various properties such as stability and mechanical performance, along with a proposal for shortening the time and reducing energy consumption in the production of precast OPC and AAMs.

## 2 Experimental Program

### 2.1 Materials

This study is based on two different construction materials containing MPCMs, including OPC and AAM mixtures. For the OPC mixtures, general use (GU) hydraulic cement, according to the ASTM C150, was used as the binding material (Table 1). The water-to-cement ratio was chosen 0.5, and the cement to the sand ratio of 1:2.75 was chosen to have the proper flowability [16]. Moreover, based on ASTM C136 for the sieve analysis, the sand used was within the range suggested by the standard [17]. The AAMs are composed of Ground Blast Furnace Slag (GBFS) (Table 1), which is an industrial by-product commonly used in AAM mixture design with the use of Sodium Hydroxide (NaOH) with 6 molarity, slag to the sand ratio of 1:2.25, and liquid-to-solid ratio of 0.55 as the optimum for maintaining flowability and strength was chosen.

The details related to the MPCM used in this research can be seen in Table 2. To use the PCM for the specific target of this study, which is heat curing, the PCM with

**Table 1** Chemical and physical properties of cement and GBFS

|  | Cement | GBFS |
|---|---|---|
| $SiO_2$ (%) | 19.80 | 32.97 |
| $Al_2O_3$ (%) | 4.90 | 17.97 |
| CaO (%) | 62.30 | 35.08 |
| $Fe_2O_3$ (%) | 2.30 | 0.72 |
| $SO_3$ (%) | 3.70 | 0.72 |
| $Na_2O$ (%) | 0.34 | – |
| MgO (%) | 2.80 | 10.31 |
| $C_3S$ (%) | 57.00 | – |
| $C_2S$ (%) | 14.00 | – |
| $C_3A$ (%) | 9.00 | – |
| $C_4AF$ (%) | 7.00 | – |
| $Na_2Oeq$ (%) | 0.87 | – |
| Loss on ignition (%) | 1.90 | 0.58 |
| Specific gravity | 3.15 | 2.88 |
| Major crystalline phases | – | Gehlenite |
| Specific Surface Area ($m^2$/g) | – | 3.15 |

**Table 2** Properties of the PCM 57 used in this study

| Product name | MPCM 57D |
|---|---|
| Classification | Organic mixture |
| Appearance | White, dry powder |
| Solubility | Insoluble |
| Melting point (°C) | 55–59 |
| Moisture (%) | $\leq 3$ |
| Paraffin Wax (%) | 79.6 |
| Melamine Resin (%) | 17.4 |
| Heat of fusion (J/g) | 172 |
| Mean particle size ($\mu$m) | 30.7 |
| Solid content (%) | 98.1 |

the melting point of 57°C was chosen. In addition, based on previous studies on PCM application in the OPC mortar, to have an optimum ratio between the mechanical performance and heat storage capacity of the samples, application of 6% PCM as an addition to the mixture was chosen.

## 2.2 Testing and Specimen Preparation

MPCM 57 was added to the mixture by 6% addition by the sand weight. In Fig. 2, the SEM analysis of the MPCMs used in this experiment can be observed. The MPCMs are made of fine spherical particles. The stability of the MPCM in NaOH solution of molarity 6 and 12 under ambient and heating up for 80 degrees and more were tested. Moreover, the MPCMs were tested during different heating cycles in environmental chamber machines with the help of thermocouples to determine their performance and stability.

The preparation of the AAM samples included the following steps: (a) preparation of alkaline activator solution (water and NaOH) and letting it cool down to room temperature, (b) two minutes mixing the sand with GBFS (dry mixing), (c) adding alkaline activator solution and continue mixing for two more minutes, (d) adding MPCM to the mixer and continue mixing for one minute. Moreover, the samples were prepared at room temperature (23 $\pm$ 2°C). Flowability was evaluated for all tested mixtures using the flow table according to ASTM C230, which is the standard specification for flow table for use in tests of hydraulic cement mortar [18].

Moreover, compressive strength testing was carried out according to ASTM C109, the standard test method for compressive strength of hydraulic cement mortars [19] using a 300 KN universal testing machine (UTM). Cubic specimens 50 × 50 × 50 mm were prepared for each mixture and tested at different ages of 1 day, 7 days, and 28 days. In addition, the mixing process, the weight of the cube samples after curing was recorded. The mortar samples during the casting process were connected to a data
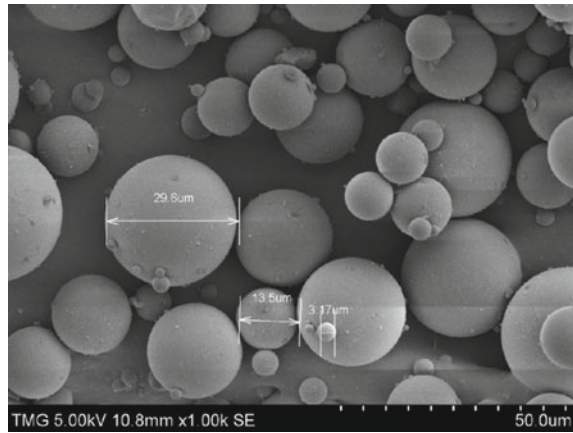
logger with thermocouples for measuring their internal temperature for the whole cycle (before and after heat cycles). According to the studies and standards about the heat curing regimes which some of them were mentioned previously and considering the material of the encapsulated PCMs, which is melamine resin (Table 2), the highest temperature was selected to be at 60°C and the heating rate and cooling rate of 20 and 15°C, respectively. The humidity of the environmental chamber was set to be 95% all time. The total duration of curing time considering the pre-set period was 17 h. The pre-set period was chosen to be 3 h for all the samples (Fig. 3).
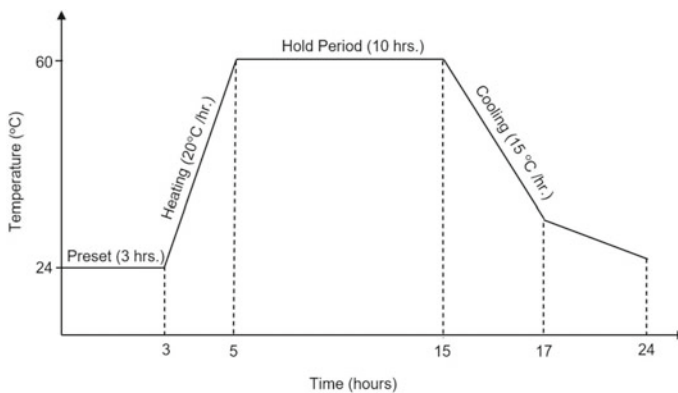


**Fig. 3** Different stages for heat curing regime

# 3　Results and Discussion

## 3.1　Stability of MPCMs

Stability is the most important factor when MPCMs are applied to the concrete mixtures. This fact arises a need to identify their behavior in different heat curing regimes, determine their performance within the OPC and AAMs mixtures, and the effect of the alkaline solution on them when MPCMs are applied in AAMs mixtures. The MPCMs are made of a shell or encapsulated with melamine resin which has limited mechanical performance in keeping the paraffin inside.

When MPCMs are applied in mixtures, a limitation due to the breakage of these materials during mixing will be added, which leads us to add them at the end of the mixture for a short period. This breakage can cause the release of paraffin into the mixture and affect the chemical composition of the mixture and increase the flowability as the first sign, and in continue, this fact can reduce the sample's heat capacity and significantly reduce the mechanical strength. Moreover, for identifying the real heat storage of the MPCM during the heat curing regimes, these materials were tested inside the environmental chamber through various heat cycles to confirm their change in phase for melting and solidification. Two samples of MPCMs instrumented with thermocouples are shown in Fig. 4.

According to the data gathered from monitoring the temperature changes of the MPCMs particles in different heat cycles and periods, no significant change in the heat storage of the particles was found after various cycles. Moreover, during the testing, the sensible heat of the particles was seen when a sudden temperature change happened before each phase change of liquid to solid and solid to the liquid phase. Based on the temperature recordings, a specific time is needed for the MPCMs to change their phase and to be able to use their full heat storage capacity. This fact also is related to the temperature variation and amount of material used as well. For



**Fig. 4** MPCM 57 inside the environmental chamber attached with thermocouples

**Fig. 5** Stability of the
MPCMs in alkaline solution
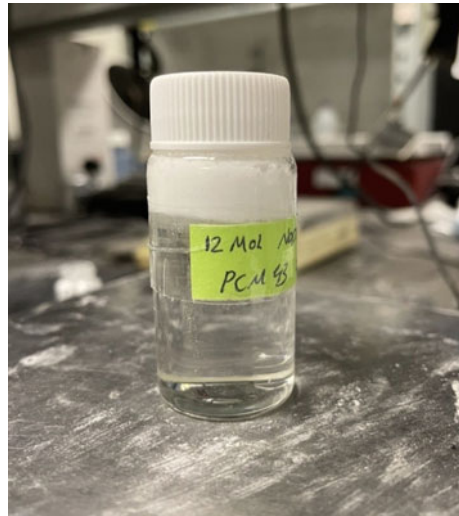


instance, in a temperature difference of 14 degrees, these materials needed at least
two hours to change their phase. In addition, it was observed that MPCMs tend to
move forward to the solid phase more than the liquid phase. Furthermore, the MPCMs
were tested in the alkaline solution made of Sodium Hydroxide (NaOH) with the
6 and 12 molarity to ensure their high alkalinity performance. Moreover, samples
were subjected to heat to identify their limitation in terms of their encapsulating
shell, which is made of melamine resin. Based on the observation and reviewing the
datasheet of this product, the MPCMs' particles are very fine, and the density of
these materials is much lower than the water or alkaline solution, which causes them
to stay above these materials (Fig. 5).

Apart from this fact, in ambient temperature in high alkalinity as 12 mol NaOH, the
MPCMs were stable. However, findings were questioned through the high tempera-
ture such as 80°C for the same period of precast concrete development in the same
solution with an environmental chamber. It was found that temperature above 80°C
could result in a change in the chemical composition of the MPCM shell and deform
them which causes some defects. This effect can be observed in Fig. 6 when the
sample was subjected to 12 molars NaOH, 80°C for a period of 10 h. The decompo-
sition of the MPCM shell can be seen clearly from this figure. This can be attributed to
the change in the chemical composition of the shell and releasing the inside materials
out. Based on this experiment, it is not suggested to increase the heat by more than
80°C when using MPCMs in AAMs samples. This can cause permanent deformation
and loss of its ability to perform as heat storage material.

**Fig. 6** Stability of the MPCMs in 12 Molar NaOH alkaline solution subjected to 80°C for 10 h
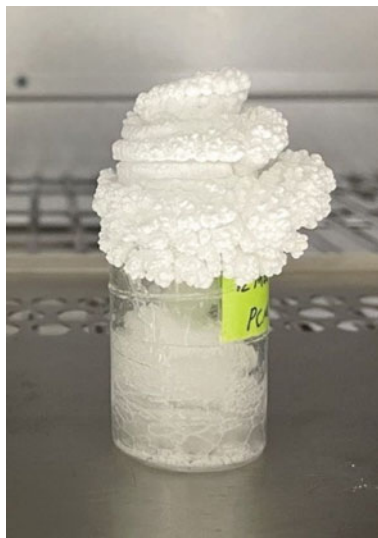


## 3.2 Flowability

The flow table was used to test out the flowability of the OPC and AAMs mortars containing MPCM. This test was carried out before and after adding MPCMs to mixtures to evaluate effects on the flowability. As it was mentioned in the datasheet of the MPCMs, these materials are hydrophilic and can absorb water. Moreover, these materials are very fine and spherical, filling the pores inside the samples. Based on the results, although the shape of these materials is spherical and should improve the flowability, they reduce the flowability significantly due to their water absorption. This fact in mortars made of OPC and AAMs reduces flowability respectively 20 and 22%. The results of flowability are provided in Fig. 7.

## 3.3 Temperature Variation Analysis Through Heat Curing

The mortar samples were monitored during the steam curing with the thermocouples connected to the datalogger. The whole heat curing process lasted 17 h. In the environmental chamber, including the pre-set period. The graph-related graph about this experiment can be seen below. As it can be observed from the graph, the max temperature was chosen 60°C concerning the previous studies and to maintain the stability of the MPCM shell. The inside temperature of the OPC and AAMs samples were elevated with the same slope of the temperature inside the chamber (blue curve) until it hit the melting point of the PCMs, which previously was discussed and determined the exact behavior of MPCM particles. The temperature slope was changed after

**Fig. 7** Flow table result before and after addition of MPCMs to the mixture of OPC and AAMs samples
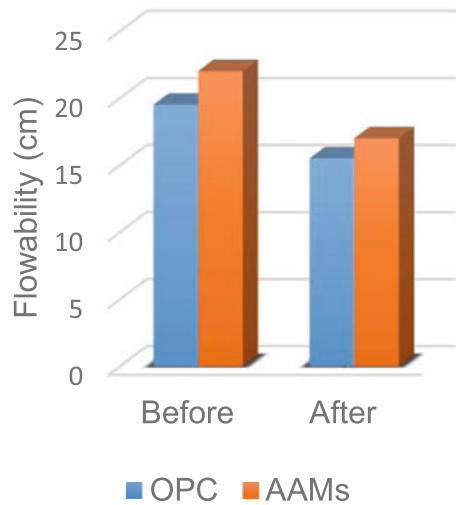
entering the 55°C zones slightly. The particles started to absorb heat and maintained the inside temperature of the samples at the same level for some time. This fact can be beneficial in terms of heat damages when in situations where sudden elevation in temperature can be seen.

This fact can prevent crack development inside the samples due to heat damage. After the completion of heat storage at 58–59°C, the slope tends to behave similar to the environmental chamber and reach 60°C. In following, after the holding period of 10 h. in the cooling period, as the temperature of the chamber drops, the MPCM particles start to release heat to prevent the sudden change of the inside temperature of the samples. This fact is beneficial in terms of the prevention of heat damages and inducing cracks in the microstructure of the sample. The particles continue to release heat until the full capacity is released, and they change their phase from liquid to solid at almost 55°C. It can be observed from Fig. 8 that the heating period can be extended with the help of these fine materials. This enlightens the fact that these materials can be used as heat storage during the precast process of concrete to absorb heat and release later to save energy and also modulate the temperature inside the samples for increasing the durability of the samples. Moreover, as it was mentioned, these materials are very fine, which can help to reduce the pore size of the sample for reducing the water absorption and increasing the durability of the samples. Moreover, the temperature inside the chamber is shown with the blue curve, OPC and AMMs samples are shown respectively with orange and gray color. Based on the observations, there is a slight difference between the temperature elevation of AAMs and OPC mortars which can be related to the particle size difference of the materials and chemical reactions inside the samples which are different. The AAMs tend to react to the temperature with a slight delay due to the mentioned reasons.
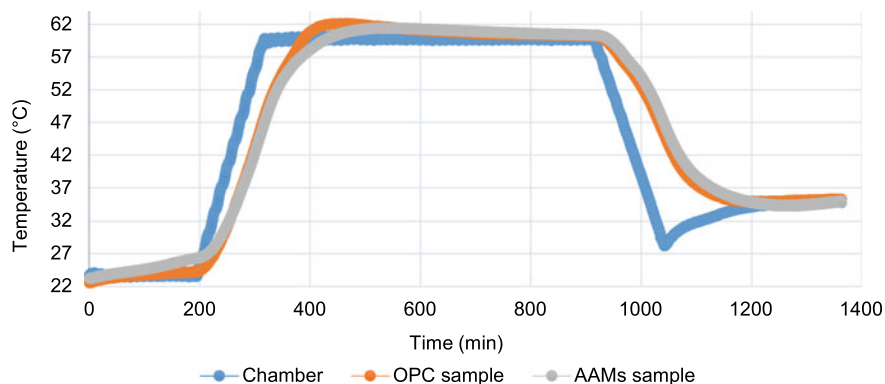
**Fig. 8** Steam curing regime of OPC and AAMs sample containing MPCM 57 (Maximum temperature 60°C, total period 17 h.)

## 3.4   Mechanical Performance

The compressive strength of the samples was tested in different periods, but the most important testing day was the 1-day testing to see the quick response of the samples to this curing regime. Generally, all samples' mechanical performance increased with age and adding MPCMs reduced the mechanical properties of the samples, which were seen through the compressive strength test. This drop was nearly 22% for the OPC samples in 1-day testing. Although this amount was significant, in the 7 days of testing, the samples' compressive strength was in the acceptable range and were higher than 19 MPa. The related information about the compressive strength of the samples can be observed in Fig. 9. Based on the findings, the AAMs containing MPCM has almost 40% higher compressive strength in 1-day testing. Moreover, the amount of compressive strength of 1-day heat curing AAMs is in the same level of AAMs cured at ambient temperature but in 7 days, demonstrating the effect of heat curing on the samples. The reason behind the drop in the compressive strength when using the MPCM can be attributed to the low mechanical performance of the MPCM shell and the leakage of the paraffin due to the breakage of the MPCM shell during the mix, which cause chemical reactions in the mix is effective in this respect.

## 4   Conclusions

This study evaluated the performance of OPC and alkali-activated mortar samples containing MPCMs with a melting point of 57°C during steam curing and after on. Moreover, the stability of the MPCM was monitored through different heat profiles and inside the alkaline solutions subjected to heat. Some of the findings of this study are mentioned below.
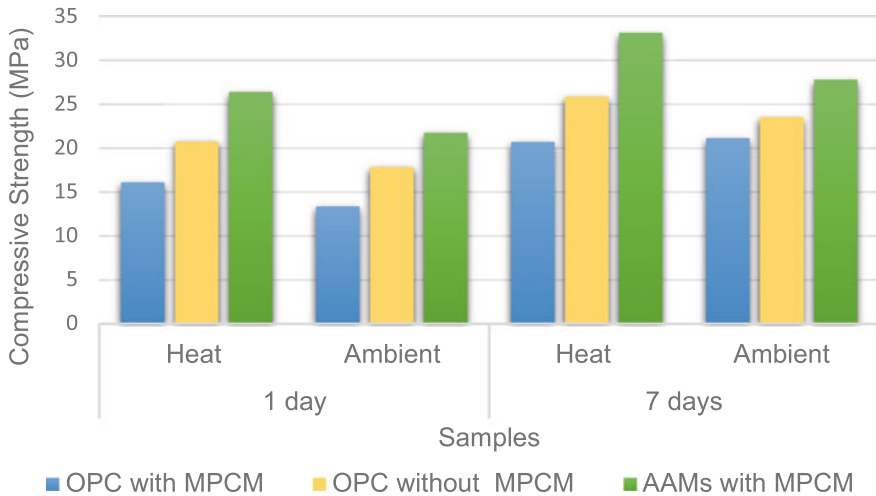
**Fig. 9** Compressive strength of OPC and AAMs samples with and without MPCM at different ages and different curing conditions

- The stability of the MPCMs was maintained through different heat cycles, but they were tended to move to the solid phase more than liquid phase. Their phase has changed from 55°C until 59°C where they absorbed and released heat.
- It was found that MPCMs lost their stability, and their shell deformed at temperatures above 80°C inside the high alkaline environments.
- MPCMs used in this experiment were hydrophilic and absorbed a significant amount of water during the mix which led to a 20% reduction in the flowability.
- The addition of the MPCMs to the mixture of OPC and AAMs can lead to a slight drop in the mechanical performance of the samples which can be attributed to the low strength shell of the MPCMs and breakage of their shell during the mix which can results in chemical reactions of paraffin with the ingredients.
- According to the monitoring of samples' heat profiles, MPCMs can modulate the temperature inside the samples and reduce the heat damages caused by the steam curing on the samples which can increase the durability of the samples by reducing the micro-cracks inside them.
- The energy absorbed by the MPCMs can be used for reducing the energy usage during the steam curing by maintaining heat over time.

## References

1. Miller SA, Horvath A, Monteiro PJM (2016) Readily implementable techniques can cut annual $CO_2$ emissions from the production of concrete by over 20%. Environ Res Lett 11(074029):1–7

2. Monteiro PJM, Miller SA, Horvath A (2017) Towards sustainable concrete. Nat Mater 16:698–699
3. Mostafavi SA, Joneidi Z (2022) Thermal model of precast concrete curing process: minimizing energy consumption. Math Comput Simul 191:82–94
4. Choi H-K, Choi Y-C, Choi C-S (2013) Development and testing of precast concrete beam-to-column connections. Eng Struct 56:1820–1835
5. Maya LF, Zanuy C, Albajar L, Lopez C, Portabella J (2013) Experimental assessment of connections for precast concrete frames using ultra high performance fibre reinforced concrete. Constr Build Mater 48:173–186
6. Wang Q, Li M, Zhang B (2014) Influence of pre-curing time on the hydration of binder and the properties of concrete under steam curing condition. J Therm Anal Calorim 118:1505–1512
7. Zeyad AM, Tayeh BA, Adesina A, de Azevedo ARG, Amin M, Hadzima-Nyarko M, Agwa IS (2022) Review on effect of steam curing on behavior of concrete. Cleaner Mater 3:100042
8. Shi J, Liu B, Zhou F, Shen S, Dai J, Ji R, Tan J (2020) Heat damage of concrete surfaces under steam curing and improvement measures. Constr Build Mater 252:119104
9. Gökçe HS, Tuyan M, Nehdi ML (2021) Alkali-activated and geopolymer materials developed using innovative manufacturing techniques: a critical review. Constr Build Mater 303:124483
10. Davidovits J (1989) Geopolymers and geopolymeric materials. J Therm Anal 35:429–441
11. Palomo A, Grutzeck MW, Blanco MT (1999) Alkali-activated fly ashes: a cement for the future. Cem Concr Res 29(8):1323–1329
12. Adesina A (2019) Use of phase change materials in concrete: current challenges. Renew Energy Environ Sustain 4(9):1–6
13. Yang H-B, Liu TC, Chern J-C, Lee M-H (2016) Mechanical properties of concrete containing phase-change material. J Chin Inst Eng 39(5):521–530
14. Kuznik F, David D, Johannes K, Roux J-J (2011) A review on phase change materials integrated in building walls. Renew Sustain Energy Rev 15(1):379–391
15. Al-Shdaifat M (2019) Smart construction materials incorporating microencapsulated phase change materials. Masters thesis, Concordia University
16. ASTM (2012) C150-07: standard specification for Portland cement. ASTM International, USA
17. ASTM (2015) C136-06: standard test method for sieve analysis of fine and coarse aggregates. ASTM International, USA
18. ASTM (2014) C230/C230M-14: standard specification for flow table for use in tests of hydraulic cement. ASTM International, West Conshohocken, USA, pp 1–6
19. ASTM (2021) C109/C109M-21: standard test method for compressive strength of hydraulic cement mortars. ASTM International, USA

# Mechanical and Durability Properties of Alkali Activated Concrete Incorporating Recycled Aggregates

**Bhavya Patel, Sonal Thakkar, and Urmil Dave**

**Abstract** Buildings made of concrete have been proven to be safe and durable. Concerns over global warming and carbon emissions have grown in recent years. The construction sector, particularly cement manufacturing, accounts for a significant portion of worldwide $CO_2$ emissions. Cement manufacturing is said to be responsible for 5–8 per cent of global $CO_2$ emissions. It is observed that alkali activated concrete has good strength and chemical resistance. As we know that aggregates occupy 60–75% of the volume in concrete, so to overcome this problem, recycled aggregate can be used by improving its essential properties. Recycled aggregates are produced from processing previously used building materials such as construction and demolition of building waste. This study was undertaken to compare M30 grade alkali activated concrete (AAC) and ordinary concrete (OC). Exploratory experiments were conducted incorporating recycled aggregate (RA) to replace coarse aggregate with 10, 20, 30, and 40% in concrete. Mechanical properties including compressive strength, split tensile strength, flexural strength, modulus for elasticity, and durability properties such as sulphate attack, chloride attack, water impermeability, and RCPT after 28 days of curing has been compared. Mechanical properties of both concrete decrease as the proportion of recycled aggregate increases. Comparison of AAC and OC shows that at 40% replacement of natural aggregate with RA, there is marginal change in compressive strength at 28 days. However there is sharp decrease in flexural strength, in AAC compared to OC at all levels of replacement. Decrease in split tensile strength and modulus of elasticity is not more when OC and AAC are compared. AAC offers poor durability, such as high water absorption because of more voids present in it, surface cracking, and high chloride penetration compared to OC when incorporated with RA. Hence AAC with RA can be used for non-structural work like paver blocks or road furniture which is not subjected to aggressive environments but can be produced on mass scale. As AAC utilises industrial waste it is environment friendly and also less costly compared to OC.

B. Patel (✉) · S. Thakkar · U. Dave
Institute of Technology, Nirma University, Ahmedabad, India
e-mail: 20mclc09@nirmauni.ac.in

S. Thakkar
e-mail: sonal.thakkar@nirmauni.ac.in

1235

## 1 Introduction

Sustainable construction and development have become a global goal of humanity in present times. Alkali activated concrete (AAC) appears as a novel construction material and seems to be in harmony with nature. Alkali activated concrete is defined as a class of concrete without cement different from Portland cement concrete (PCC). In AAC, cement is replaced by other additives such as ground granulated blast furnace slag (GBBS) or fly ash (FA) and alkaline activator. Sodium hydroxide and sodium silicate activated concrete based on slag and fly ash can exhibit high strength and good chemical resistance. It gains popularity due to its low energy costs, high strength, and durability compared to conventional Portland cement. Recycling is the act of converting recycled materials into materials to create a new product. In order to reduce the use of natural compounds, recycled compounds can be used as alternatives. The recycled aggregate is made up of finely ground, finely ground particles prepared from materials that have been used in the construction and disposal of waste. These are often the result of buildings, roads, bridges, and sometimes even disasters, such as wars and earthquakes. The use of recycled amount in construction sites is plentiful and has long been used. Rapid advances in research into the use of reconstructed concrete for new concrete have also led to the production of high-strength concrete and high performance.

Another topic that has recently piqued the interest of researchers is the use of recycled aggregates to substitute natural aggregates in alkali activated concrete [1–3], Thunuguntla and Rao 2018, [4] and Limeira [5]. The results conducted by [3] with the use of recycled aggregates, it was determined that the strength was reduced. However, when compared to regular concrete, the decrease was marginal (i.e. 8.6%) for 25% replacement, significantly higher (i.e. 36.9%) for 50% replacement and extremely high (i.e. 78.5%) for 75% replacement with recycled aggregates, respectively. The incorporation of concrete waste aggregate (CWA) and brick waste aggregate contributed to the poor compressive strength of recycled alkali activated concrete mixtures.

# 2 Materials and Method

## 2.1 Materials and Mixture

### 2.1.1 Properties of Raw Material

Recycled aggregates were made by crushing the previously tested concrete cubes into a fully mechanised crusher in 20 mm down and 10 mm down recycled aggregates. According to the test results, the compressive strength of locally accessible materials such as bricks was between 5 and 7.5 MPa, and the concrete compressive strength was between 25 and 30 MPa. Figure 1 shows the processed concrete and brick waste aggregate. RA consisted a combination of brick waste and waste from recycling of concrete (Tables 1 and 2).



(a)                                                          (b)

**Fig. 1** Concrete and brick waste aggregate

**Table 1** Physical and chemical properties of FA and GGBS

| Material | Specific gravity | Specific surface area (m$^2$/kg) | SiO$_2$ (%) | Al$_2$O$_3$ (%) | Fe$_2$O$_3$ (%) | CaO (%) |
|---|---|---|---|---|---|---|
| FA | 2.61 | 332.94 | 61.4 | 19.53 | 13.42 | 7.91 |
| GGBS | 2.79 | 379 | 36.8 | 17.12 | 0.92 | 31.4 |

**Table 2** Physical properties of NA and RA

| Properties | Bulk density (kg/m$^3$) | Specific gravity | Water absorption (%) | LA abrasion value (%) | Fineness modulus |
|---|---|---|---|---|---|
| NA | 1428 | 2.77 | 1.28 | 27 | 5.18 |
| RA | 1120 | 2.48 | 5.23 | 42 | 7.37 |

**Table 3** Details of mix proportion evaluated for ordinary concrete as per IS: 10262 [9]

| Mix type | RA (% mass) | Mixture quantity (kg/m³) | | | | | |
|----------|-------------|--------|------|------|------|-------|--------------------|
| | | Cement | F.A | C.A | RA | Water | Chemical admixture |
| OCRA0 | 0 | 380 | 790 | 1197 | – | 152 | 3.8 |
| OCRA10 | 10 | 380 | 790 | 1077 | 120 | 152 | 3.8 |
| OCRA20 | 20 | 380 | 790 | 957 | 240 | 152 | 3.8 |
| OCRA30 | 30 | 380 | 790 | 838 | 359 | 152 | 3.8 |
| OCRA40 | 40 | 380 | 790 | 718 | 479 | 152 | 3.8 |

**Table 4** Details of mix proportion evaluated for alkali activated concrete

| Mix type | RA (% mass) | Mixture quantity (kg/m³) | | | | | | | | |
|----------|-------------|---------|------|-----|------|------|-----------|------|-------------|---------------------|
| | | Fly ash | SLAG | F.A | C.A | NaOH | $Na_2SiO_3$ | R.A | Total water | Chemical admixture |
| AACRA0 | 0 | 202 | 202 | 790 | 1197 | 40.5 | 101.25 | 0 | 108.35 | 3.8 |
| AACRA10 | 10 | 202 | 202 | 790 | 1077 | 40.5 | 101.25 | 120 | 108.35 | 3.8 |
| AACRA20 | 20 | 202 | 202 | 790 | 957 | 40.5 | 101.25 | 240 | 108.35 | 3.8 |
| AACRA30 | 30 | 202 | 202 | 790 | 838 | 40.5 | 101.25 | 359 | 108.35 | 3.8 |
| AACRA40 | 40 | 202 | 202 | 790 | 718 | 40.5 | 101.25 | 479 | 108.35 | 3.8 |

### 2.1.2 Mixture Proportioning

The ratios of ordinary concrete and alkali activated concrete were evaluated to see whether RA (which includes both brick and concrete waste) could be used to replace natural aggregate (NA) in both concretes. So in mix design all important parameter is remain constant except RA because of replacement in concrete. An important parameter is selected from literature study and codal provision. Cement, fine aggregates and coarse aggregates confirmed to Indian standards [6–9]. The details of mix design is shown in Tables 3 and 4. OCRA10 represent 10% replacement by mass of natural aggregate by recycled aggregate in ordinary concrete similarly AACRA20 represent 20% replacement by mass of natural aggregate by recycled aggregate in alkali activated concrete. BASF Master-Glenium SKY 8549 is used as chemical admixture to enhance workability of concrete.

### 2.1.3 Specimen Preparation

AAC and OC specimens were cast in cubes of 150 mm × 150 mm × 150 mm mould size. The mould and steel base plates to be used were cleaned, fitted, and coated with a thin layer of oil. For AAC, alkaline activators in form of sodium hydroxide (NaOH) and sodium silicate ($Na_2SiO_3$) were used. NaOH was made by dissolving sodium flakes in tap water. The mass of NaOH solids in a solution varies based on

Fig. 2 Mixing of AAC and preparing specimens **a** dry mixing **b** solution **c** specimen **d** curing

the solution's concentration, represented in molar M. For instance, NaOH solution with a concentration of 14 M consisted of $14 \times 40 = 560$ g of NaOH solids (in flake form) per litre of the solution, where 40 is a molecular weight of NaOH. NaOH was left for 24 h. to cool down after that $Na_2SiO_3$ was added as per the ratio of sodium silicate to sodium hydroxide considered in the mix design. The mixing procedure for AAC is quite similar to that of conventional concrete. All of the components were mixed at room temperature in the laboratory. The fly ash, GGBS and the aggregate were first dry mixed in a pan mixture as shown in Fig. 2a. Dry mixing was allowed to be continued for about 3 to 4 min. The alkaline solution which was prepared one day before was added with additional water in the pan mixture and mixing was continued for 3 to 4 min. The fresh AAC was cast into the moulds immediately after mixing in three layers. For compaction of the specimens, each layer was given 25 to 35 manual strokes using a 20 mm rod. After the casting, the specimens have been kept at room temperature as per the designated rest period. Generally, two types of curing, i.e. ambient curing and oven curing have been used for preparing the AAC by various researchers. In the present investigation, ambient curing was used for AAC. In ambient curing, the specimens were left in an open atmosphere till curing time. Specimens placed on the terrace for curing are shown in Fig. 2d.

## 2.2 Experimental Methods

### 2.2.1 Strength

The compressive strength of concrete was determined as per the method given in IS 516–1959 [10]. Compression test of a cube having size 150 mm × 150 mm × 150 mm was done in compression testing machine as shown in Fig. 3a. Testing of cubes was done at age of 7, 14, and 28 days. Split tensile strength of concrete was carried out as per specifications of IS 5816–1999 [11]. The setup for the test is shown in Fig. 3b on 100 mm × 300 mm cylindrical specimens. A split tensile strength test was carried out after 28 days of curing. Flexural strength test was determined as per method given IS 516–1959 [10]. The test setup is shown in Fig. 3c. Specimen
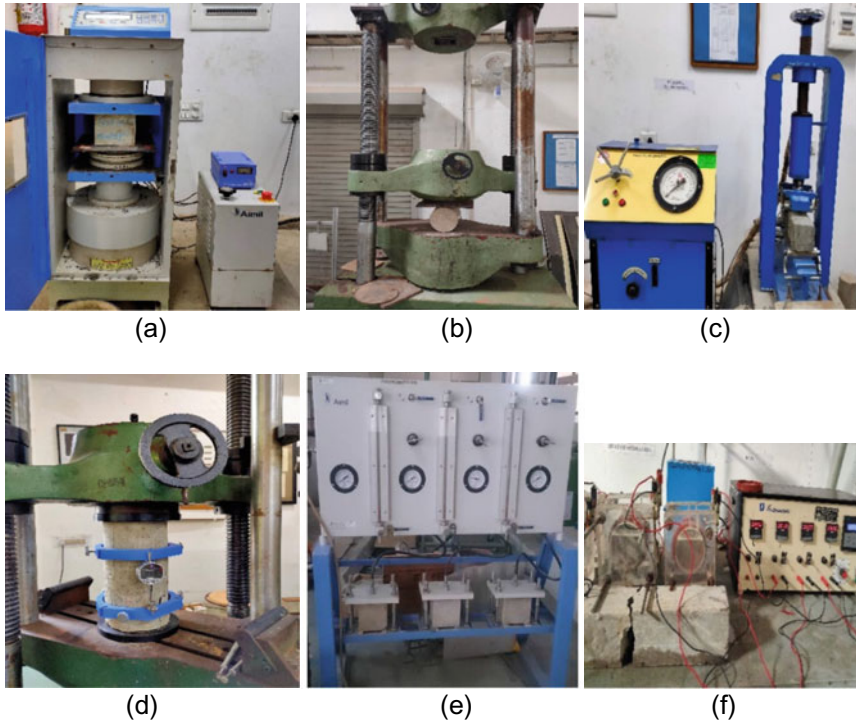
**Fig. 3** Laboratory instrument **a** CTM **b** UTM **c** Flexural **d** UTM **e** Water impermeability **f** RCPT

of 100 mm × 100 mm × 500 mm were cast for the flexural test. A flexural testing machine was used for the testing after 28 days of curing.

### 2.2.2 Modulus of Elasticity

Extensometer was used to estimate the modulus of elasticity of concrete specimens, as illustrated in Fig. 3d. The modulus of elasticity of concrete is measured using a cylinder specimen with a diameter of 150 mm and a height of 300 mm, as described in IS: 516–1959 [10]. Extensometers and recording points are attached at the same end. At equal load intervals, displacement is measured. From the foregoing findings, a plot of stress versus strain is generated. The tangent modulus offers the modulus of elasticity of the concrete specimen based on the slope of the supplied plot.

### 2.2.3 Sulphate and Chloride Attack

For determining the weight loss and change in compressive strength of concrete in sulphate solution, the cubes of size 150 mm × 150 mm × 150 mm were submerged

in 5% of sodium sulphate ($Na_2SO_4$) solution for 30 days. Chloride attack was carried out on the cubes of size 150 mm × 150 mm × 150 mm which were submerged in 5% of sodium chloride (NaCl) solution for 30 days. The weight loss and change in compressive strength in AAC were found out and compared with the initial weight and compressive strength prior to sulphate exposure and chloride exposure.

### 2.2.4　Water Impermeability

Impermeability test is performed as per German standard DIN-1048 part-5. A concrete cube of size 150 mm × 150 mm × 150 mm was used for testing and was done at the age of 28 days. Water is filled up to 75% of the total water capacity level through inlets in impermeability apparatus. Concrete cubes are placed in moulds such that the surface is perpendicular to the test surface. Screws are tightened to provide a tight fit on the specimen as shown in Fig. 3e. Valve is then opened to permit the flow of water. Water pressure is set to 5 kg/cm$^2$ using a pressure regulator through an air compressor. This pressure is maintained for 3 days with the help of a pressure adjusting machine. After 3 days water pressure is released and then the specimens are removed. Cubes are split into two parts and depth of water penetration was measured on both sides with the help of Vernier callipers. The final depth of penetration was calculated by taking an average of depth measured at the left, centre and right sides of the concrete specimen. Test setup for water impermeability is shown in Fig. 3e.

### 2.2.5　RCPT

The RCPT test was carried out in accordance with the specification of ASTM 1202C. After 28 days of water curing, three concrete cylinders with a diameter of 100 mm and a height of 50 mm were stored in a humidity chamber for two hours at 95% humidity. Each cylindrical specimen is held between two symmetric (polymethyl methacrylate) chambers in an Applied Voltage Cell (Two symmetric polymethyl methacrylate) chambers as illustrated in Fig. 3f. Electrically conductive mesh and external connections were included in each chamber. To prevent leakage, a sealant is put between the specimen and the voltage cell. The side of the cell that contains the specimen's top surface is filled with a 3.0% NaCl solution. The negative terminal of the power supply is linked to the said side of the cell. The opposite side of the cell is filled with 0.3 N NaOH solution and connected to the positive terminal of the power source.
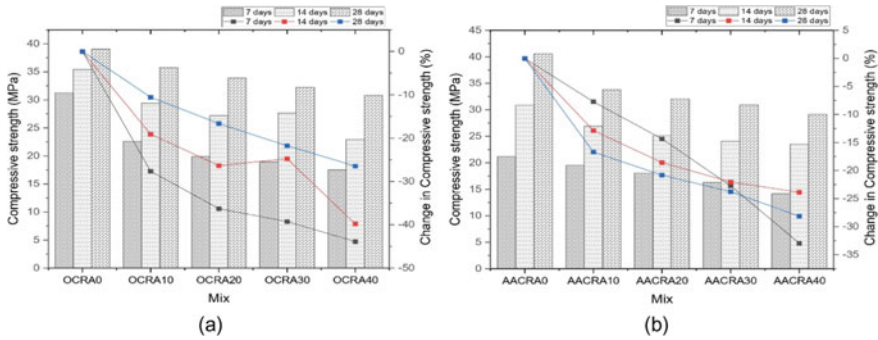
**Fig. 4** Compressive strength results of OC and AAC with different % of RA

## 3   Result and Discussion

### 3.1   Mechanical Properties

#### 3.1.1   Compressive Strength

The compressive strength at the age duration of 7, 14, and 28 days was evaluated for different concrete mixtures. Figure 4a and b is a graphical representation of the test results for the percentage decrease in compressive strength of recycled aggregate concrete with respect to the control concrete of M30 grade. It was observed that AAC compressive strength is lower at age of 7, 14, and 28 days due to ambient curing. But, the addition of fly ash and slag helps to improve the strength of recycled aggregate concrete at a later age. In addition, concrete strength has been observed to be reduced as a result of the presence of crushed clay bricks, as well as the weakness of old mortar in contrast to aggregate and newly produced paste.

#### 3.1.2   Split Tensile Strength

The splitting tensile strength for all concrete are measured at the age of 28 days. The results of split tensile strength are presented in Fig. 5. Average results of three specimens are taken as the final result. Mix of recycled aggregate concrete having 10, 20, 30, and 40% RCA has lower split tensile strength as compared to control concrete. Figure 5 shows the % decrement in split tensile strength in mix RA10, RA20, RA30, and RA40 with respect to control concrete. For AACRA mixes, the drop in average split tensile strength ranged from 15 to 16% of compressive strength, with the exception of AACRA40, which exhibited a larger compressive strength reduction.
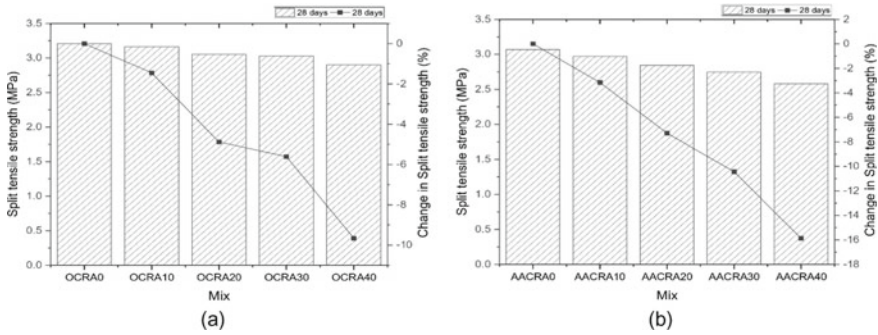
**Fig. 5** Split tensile strength results
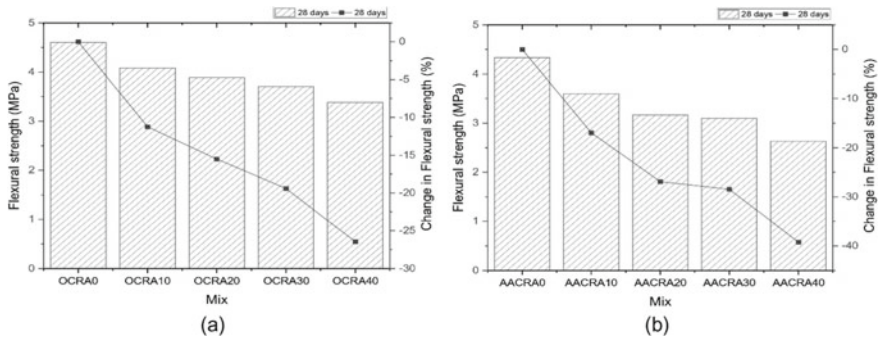


**Fig. 6** Flexural strength results

### 3.1.3 Flexural Strength

The flexure test for both concrete was measured at the age of 28 days. The results of flexure strength are presented in Fig. 6. Average results of three specimens was taken as the final result. A mix of recycled aggregate concrete has lower flexure strength as compared to control concrete. Figure 6 shows the % decrement in flexure strength in mix RA10, RA20, RA30, and RAC40 as compared to control concrete. Figure 6 shows the tested specimens of the flexure test.

### 3.1.4 Modulus of Elasticity

The modulus of elasticity test for three concrete mixes was carried out at the age of 28 days and the results are presented in Fig. 7. MOE values were calculated from the stress versus strain relationship using the tangent modulus method. Figure 7 represents the percentage change in modulus of elasticity of recycled aggregate concrete w.r.t. control concrete for M30 grade of concrete. It was observed that 28 days MOE
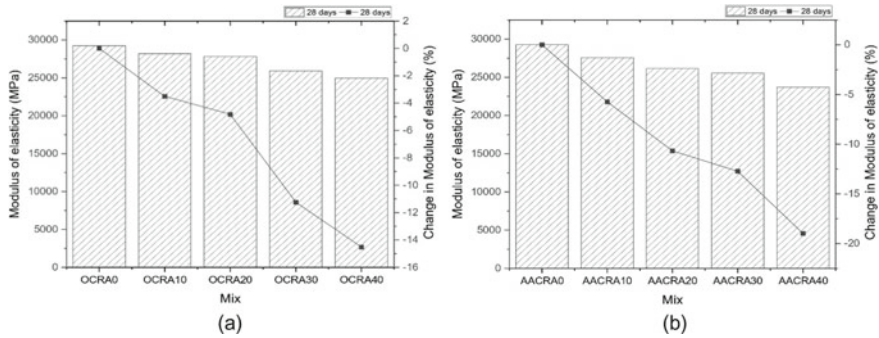
**Fig. 7** MOE test results

results were lower for recycled aggregate concrete as compared to control concrete of M30 grade. Temperature curing may improve the mechanical characteristics of AACWA. In addition to fly ash and GGBS contains $SiO_2$ and $Al_2O_3$, which can participate in the alkaline-activation process to produce Si–O-Al bonds.

## 3.2 Durability Properties

### 3.2.1 Sulphate Attack

The weight of specimens was measured after 28 days of water curing and then submerged into sulphate solution. After completion of 28 days of exposure time weight of specimens and change in compressive strength were measured again to calculate weight loss and change in compressive strength. Figure 8a represent the percentage change in compressive strength after sulphate exposure. Maximum reduction in strength shows in concrete having 40% replacement of recycled aggregate.

### 3.2.2 Chloride Attack

Weight of specimens were measured after 28 days of water curing and then submerged into chloride solution. After completion of 28 days of exposure time weight of specimens and change in compressive strength were measured again to calculate weight loss and change in compressive strength. Figure 8b represent percentage change in compressive strength after chloride exposure. Maximum reduction in strength shows in concrete having 40% replacement of recycled aggregate. The % weight loss increases with time for all of the mix types, but it is particularly high for AACRA40. The leaching of unreacted sodium occurs when acid enters the matrix via the
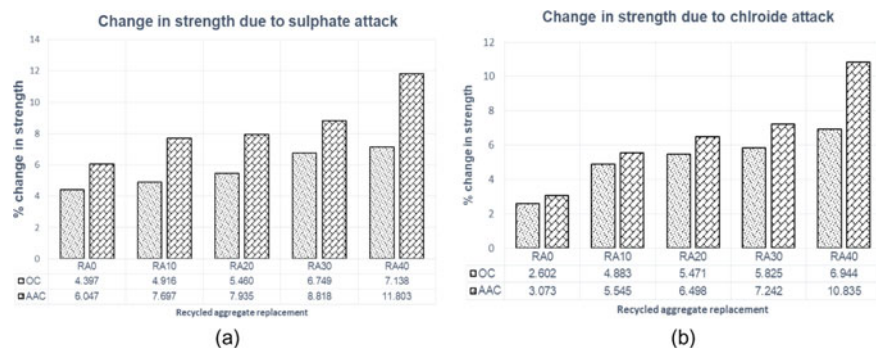
Fig. 8 Change in compressive strength due to **a** sulphate attack **b** chloride attack

porous media of AACRA mixtures. Furthermore, RA includes calcium hydroxide-containing cement mortar, and sulfuric acid combines with calcium hydroxide to cause weight loss.

### 3.2.3 Water Impermeability

After 28 days of water curing, specimens were tested for water impermeability. Because water evaporates in a matter of minutes, the water penetration depth is measured immediately after the cube was split. Water penetration depth is measured on three sides of a cube, left, centre, and right, for both split sides, and the average value is used to determine water penetration depth. Table 5 represents water penetration depth results of different concrete mixes. For example, the water penetration depth values of AACRA40 were 1.3 times greater on average than those of AACRA0.

The greater absorptive nature of concrete and brick waster aggregate may be ascribed to the enhanced water penetration for specimens containing waste aggregates. These results are also confirmed for AACRA40, which indicates that the hardened matrix is less dense and open, resulting in reduced compressive strength. RA also has associated mortar that is permeable by nature. Water may easily travel through the hardened matrix due to the porous mortar in RA, affecting water absorption and permeable void volume.

Table 5 Water penetration depth results

| Mix | Penetration depth (mm) | Mix | Penetration depth (mm) |
| --- | --- | --- | --- |
| OCRA0 | 23.3 | AACRA0 | 27.9 |
| OCRA10 | 24.2 | AACRA10 | 29.8 |
| OCRA20 | 26.1 | AACRA20 | 32.4 |
| OCRA30 | 28.1 | AACRA30 | 35.4 |
| OCRA40 | 30.3 | AACRA40 | 36.2 |

### 3.2.4   RCPT

RCPT test is done after 28 days curing of specimen having 100 diameter and 50 mm height cylinder. At 15-min intervals, the current for concrete mixes is recorded. Concrete mixtures have a poorer current passing ability up to the first 60 min, as can be shown. The present measurements in recycled aggregate concrete are greater than in control concrete. Because of the porous nature of AAC concrete or the greater number of voids contained in it, it has a higher current reading.

$$Q = 900 \times (I_0 + 2I_{30} + 2I_{60} + \ldots + 2I_{300} + 2I_{330} + 2I_{360})$$

where

$Q$ = charge passed (Coulombs),

$I_0$ = instantaneous current (Ampere) after voltage is supplied,

$I_t$ = current (Ampere) after voltage is applied at $t$ minutes.

From Fig. 9 it can be concluded that ordinary concrete have total charged passed of 2196 $Q$ which shows it has moderate chloride ion permeability. While all mixes of AAC concrete shows value higher than 4000 $Q$ which represents higher chloride ion permeability. Similarly, OCRA40 shows 2430 $Q$ and AACRA40 shows 8019 $Q$. So it can be concluded that alkali activated concrete shows higher chloride ion permeability compare to ordinary concrete because of more number of voids present in concrete.
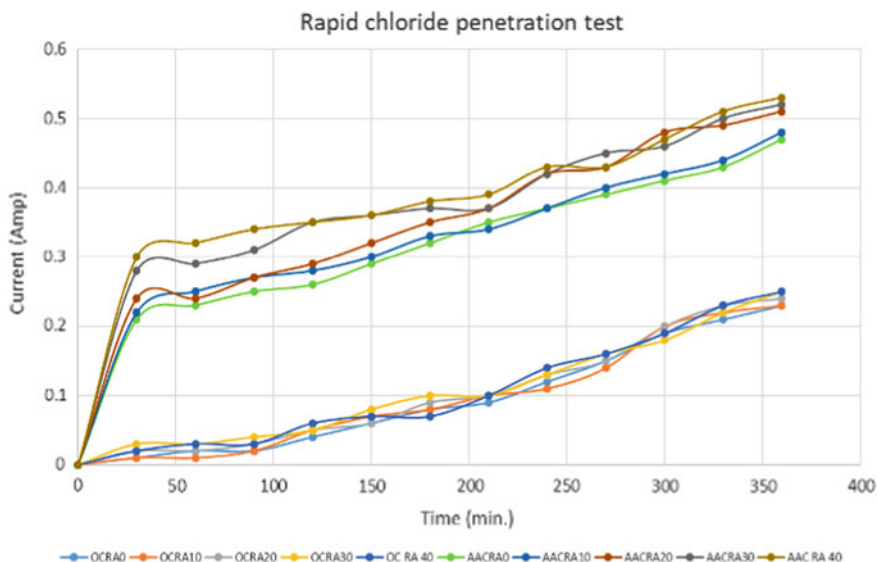


**Fig. 9**  RCPT test results

## 3.3  Benefits of AAC

The carbon emissions contributions from particular raw materials used in concrete manufacturing are shown in Fig. 10. Ordinary concrete and AACRA30 had total carbon emissions of 371.41 and 218.9 $kgCO_2$-eq/m$^3$, respectively. When compared to ordinary concrete, the AACRA30 concretes reduced carbon emissions by 41 per cent due to the use of recycled aggregate. Though the use of commercially made alkali activators provided 129.41 $kgCO_2$-eq/m$^3$ of $CO_2$ emissions to AAC concretes, which is a considerable contribution. The addition of slag and recycled coarse aggregate to the concrete, contributed 14.98 and 3.9 $kgCO_2$-eq/m$^3$, respectively, reducing carbon emissions. The results emphasise the need of focusing on mix designs with a low alkali activator component, which may help reduce carbon emissions even further.

An economic analysis of the suggested concrete mix was conducted to better understand the benefits of AACRA. In terms of cost, AACRA was compared to conventional concrete. The mix proportions are detailed in the Table 6 as are material prices based on current market value, excluding shipping, and other non-essential expenditures. As can be seen, the cost of AACRA30 is 10% cheaper than the cost of regular cement concrete, indicating that AACRA mixes are somewhat less costly



**Fig. 10** Pollution comparison of ordinary concrete and alkali activated concrete

| | OC | AACRA30 |
|---|---|---|
| Slag | 0 | 14.948 |
| Fly ash | 0 | 18.18 |
| Na2Sio3 | 0 | 78.975 |
| NaOH | 0 | 57.7125 |
| RA | 0 | 3.9131 |
| NA | 48.8376 | 34.1904 |
| sand | 10.981 | 10.981 |
| Cemet | 311.6 | 0 |

**Table 6** Cost comparison of ordinary concrete and alkali activated concrete in RS

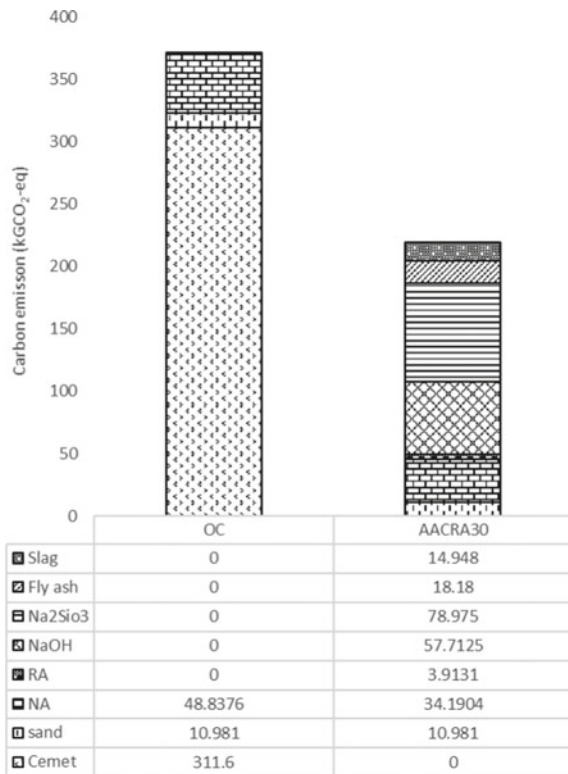| Ordinary concrete | | | | AACRA30 | | | |
|---|---|---|---|---|---|---|---|
| Material | Quantity (kG/m$^3$) | Unit cost (rs/kG) | Total cost (rs/m$^3$) | Material | Quantity (kG/m$^3$) | Unit cost (rs/kG) | Total cost (rs/m$^3$) |
| Cement | 380 | 7 | 2660 | Fly ash | 202 | 0.9 | 181.8 |
| Water | 152 | 0.25 | 38 | GGBS | 202 | 2 | 404 |
| NFA | 790 | 0.9 | 711 | NaOH | 40.5 | 25 | 1012.5 |
| NCA | 1197 | 0.9 | 1077.3 | Na$_2$SiO$_3$ | 101.25 | 10 | 1012.5 |
| Super plasticizer | 3.8 | 100 | 380 | NFA | 790 | 0.9 | 711 |
| | | | | NCA | 838 | 0.9 | 754.2 |
| | | | | RA | 359 | 0.3 | 107.7 |
| | | | | Water | 108.35 | 0.25 | 27.08 |
| | | | | Super plasticizer | 3.8 | 100 | 380 |
| Total | | | 4866.3 | Total | | | 4590.8 |

to produce than standard cement concrete mixes. Water shortage is another ongoing worry in India, affecting many lives each year. As a consequence, the Indian government has made water conservation a top priority. The usage of AACWA in the precast sector (for example, paver block production) may drastically cut water use. The amount of water required for M30 cement concrete, for example, is 152 kg/m$^3$ (as seen in Table 6). The amount of water needed to make AACRA is determined by the total amount of alkaline solution utilised. The maximum amount of water needed to make NaOH solution was 40.5 kg/m$^3$, whereas the maximum amount of water needed to make Na$_2$SiO$_3$ solution was 108.35 kg/m$^3$. As a result, AACRA will use 30% less water as a result of this. Furthermore, additional water is used for cement concrete curing, which is not required with AACRA. So, the cost comparison of ordinary concrete and AAC is shown in Table 6.

## 4 Conclusion

In the current study, the effect of recycled aggregate in ordinary concrete and alkali activated concrete was evaluated. Alkali activated concrete prepared with fly ash, GGBS, sodium hydroxide, and sodium silicate solution incorporating recycled aggregate. Mechanical and durability properties was determined using various methods. The following conclusions were assessed based on the experimental investigation.

- It has been seen that recycled aggregate has lower density and high water absorption as compared to natural aggregate due to old concrete mortar on the aggregates. It has been seen that the compressive strength decreases with the increase of recycled aggregate. This is because the density of recycled aggregate is lower and

there is a weaker bond between fresh mortar and old mortar. Also, a reduction in compressive strength can be due to the poor quality of recycled aggregate.

- There was a major decrease in compressive strength due to the incorporation of recycled aggregate in both, AAC and OC. However, compared to ordinary concrete, the decrease in compressive strength in AAC was lesser at 28 days.
- Flexural strength of AAC when compared with OC decreases by 12, 19, 16, and 22% when replacement of RA is 10, 20, 30, and 40% of natural aggregate.
- Split tensile strength of AAC decreases by 6, 7, 9, and 11% compared with OC at 10, 20, 30, and 40% of natural aggregate with RA, respectively. Modulus of Elasticity in AAC decreases by 2, 6, 2, and 5% compared with OC at 10, 20, 30, and 40% of natural aggregate with RA, respectively.
- AAC with RA exhibited poor durability compared to OC at same percentage replacement of RA due to of more voids and surface cracks.
- When 40% of replacement of RA is carried out in AAC, 30 MPa compressive strength is still obtained at ambient curing at 28 days. So for non-structural concrete AAC with 40% replacement can be recommended as it will be environment friendly and economical.

# References

1. Li Z et al (2021) A comparative study on the mechanical properties, autogenous shrinkage and cracking proneness of alkali-activated concrete and ordinary Portland cement concrete. Constr Build Mater 292:123418
2. Nanayakkara O et al (2021) Alkali activated slag concrete incorporating recycled aggregate concrete: long term performance and sustainability aspect. Constr Build Mater 271:121512
3. Mebanteiskhem P et al (2021) Properties of alkali-activated concrete (AAC) incorporating demolished building waste (DBW) as aggregates. Cogent Eng 8(1):1870791
4. Wang A et al (2020) The durability of alkali-activated materials in comparison with ordinary Portland cements and concretes: a review. Engineering 6(6):695–706
5. Limeira J, Agullo L, Etxeberria M (2010) Dredged marine sand in concrete: an experimental section of a harbor pavement. Constr Build Mater 24(6):863–870
6. IS: 12269: 1987 (1987) Specification for 53 grade ordinary Portland cement. In: Bureau of Indian Standards, New Delhi, India
7. IS: 383: 2016 (2016) Indian standard: coarse and fine aggregate for concrete- specification. In: Bureau of Indian Standards, New Delhi, India, pp 1–21
8. IS: 2386 (Part I): 1963 (1963) Method of test for aggregate for concrete. Part I—particle size and shape. In: Indian Standards (Reaffirmed 2002)
9. IS 10262: (2019) Bureau of Indian Standards (BIS), Concrete mix proportioning—guidelines. In: Bureau of Indian Standards (BIS)

10. IS 516: 1959 (2004) Method of tests for strength of concrete. IS: 516 1959 (Reaffirmed 2004), New Delhi, India
11. IS 5816: 1999 (1999) Indian standard: splitting tensile strength of concrete- method of test (First Revision). In: Bureau of Indian Standards, New Delhi (reaffirmed, pp 1–14)

# Materials Specialty: Recycled Materials

# Developing Predictive Equations for the Self-Centering Response of Beam-Column Connections with Steel Angles and Shape Memory Alloy Bolts

**Saber Moradi and Majid Mohammadi Nia**

**Abstract** This paper presents the development of predictive equations for the self-centering response of moment-resisting connections equipped with Shape Memory Alloy (SMA) bolts and steel angles. First, three-dimensional finite element models are developed in ANSYS. The analysis is validated using experimental results for seven beam-column connections. Using a design of experiments approach, a statistical sensitivity analysis of the cyclic response is performed to identify factors with significant effects. Next, a response surface study is presented to develop predictive equations for characterizing the cyclic response of steel beam-column connections with SMA bolts and steel angles. A confirmation study indicates acceptable accuracy of the developed equations for predicting the cyclic response of the SMA-based connections. The predictive equations can be used for developing computationally efficient models in the analysis and design of SMA-based connections and moment frames. This study also highlights the promising self-centering response of the newly developed SMA-based connections. Based on the results, deep beams should not be used to avoid possible early bolt fracture.

**Keywords** Shape memory alloys (SMAs) · Self-centering beam-column connection · Finite element modeling · Self-centering · Sensitivity · Response surface method

S. Moradi (✉) · M. M. Nia
Department of Civil Engineering, Toronto Metropolitan University, Toronto, ON M5B 2M2, Canada
e-mail: s.moradi@torontomu.ca

# 1 Introduction

The conventional design of earthquake-resistant steel structures relies on the ductility of steel. While providing life safety, this design approach is not intended to prevent structural damage. In moderate and severe earthquakes, structures experience widespread damage as they are designed to undergo large inelastic deformations. Consequently, costly repair and demolition of damaged structures are needed. This vulnerability can cause losses of billions of dollars, as experienced in past earthquakes, such as the Kobe and Northridge earthquakes [3, 4].

Recognizing the importance of mitigating damage and residual deformations in structures, researchers have developed self-centering systems that enable the structure to return to its plumb position following earthquakes. This self-centering is primarily achieved by using post-tensioned cables (for example, see [13, 17] or smart materials, shape memory alloys (SMAs) (for example, see [6, 8, 10]).

SMAs are a class of metallic alloys that can recover their original shape after experiencing large deformations (up to 10% strain for NiTi) [7]. This recentering capability is attributed to phase transformations in SMAs. These transformations occur upon mechanical unloading or heating. The former, known as superelasticity, occurs when SMA is at its austenitic phase. The latter, known as shape memory effect, occurs when SMA is at its martensitic phase [15]. In developing self-centering systems for building structures, superelastic SMAs have found several innovative applications, such as dampers [20], base isolators [19], and bracing systems [16], as well as new applications in steel connections [5]. SMAs possess several advantages that make them ideal for seismic applications. In addition to their inherent self-centering characteristics, SMAs offer supplemental damping and cyclic repeatability while being corrosion-resistant and requiring minimum or no maintenance.

Several early experiments have evaluated the idea of using SMAs in the form of tendons [8], bars [14], and fasteners [1] in steel beam-column connections. A feasible application of SMA bolts in endplate connections was later proposed [9]. Through experimental testing and numerical modeling [6], it was confirmed that SMA bolts could effectively prevent damage in beams while providing excellent self-centering and moderate energy dissipation compared to counterpart connections with high-strength steel bolts. Extended endplate connections with SMA bolts [6, 9] have the advantage of easy installation without the floor-slab interference in other SMA applications in steel connections [21]. More recently, self-centering beam-to-column connections with combined superelastic SMA bolts and steel angles were experimentally tested [22]. In these self-centering moment connections, SMA bolts provide self-centering while steel angles are utilized to yield and dissipate energy. The main structural members, including the beam and column, remain essentially elastic. Figure 1 shows a schematic view of a beam-to-column connection specimen equipped with SMA bolts and steel angles.

Although promising results were reported from the experimental testing of connections with SMA bolts and steel angles [22], high-fidelity finite element models

**Fig. 1** The self-centering connection with SMA bolts and steel angles
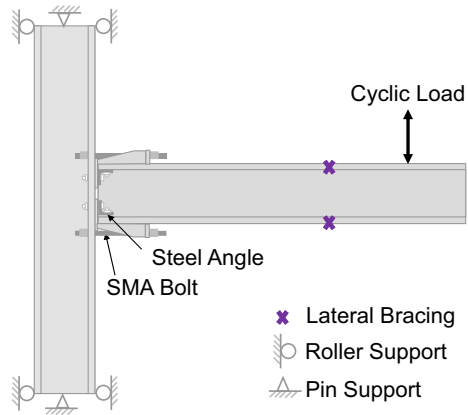
[18] are needed to expand on the test results. Moreover, the ductility of SMA connections is affected by the connection design. Since the past study [22] considered limited parameters, further research is necessary to determine how the response and damage behavior of the connections with SMA bolts change with variations in different design factors, including the material and geometry related factors. A parametric study [23] based on changing one factor at a time does not include factor interactions; therefore, it may not lead to reliable and general results. For this purpose, statistical Design of Experiments (DOE) [12] should be used for conducting comprehensive sensitivity studies.

In this paper, continuum finite element models were developed and experimentally validated for the newly developed connections with SMA bolts and steel angles. Cyclic response sensitivity analyses were performed in a DOE framework to identify the most influential factors. Next, simple equations were developed and verified to predict the SMA-based connections' self-centering response.

## 2 Finite Element Modeling and Validation

For seven experimentally tested specimens [22], high-fidelity finite element models were developed and analyzed using ANSYS Mechanical APDL [2]. Three-dimensional eight-node homogeneous elements, *SOLID185*, were used to mesh different components of the connection, including the column, beam, angles, SMA bolts, steel angles, washers, bolt heads and nuts, stiffeners, shim plates, shear tabs, and continuity plates. The SMA material properties used in the finite element modeling are listed in Table 1. Modulus of elasticity for steel, $E_{steel}$, was taken as 210 GPa. While using the experimental data, the steel and SMA materials were modeled by a bilinear stress–strain relationship and superelastic behavior, respectively. Contact and target elements were also defined to allow for contact and sliding behavior with a friction coefficient of 0.3 [18]. The SMA bolt pre-straining, connection details, and

**Table 1** SMA material properties used in the validation study

| Material Property | Value |
|---|---|
| Martensite start stress, $\sigma_{Ms}$ | 250 MPa |
| Martensite finish stress, $\sigma_{Mf}$ | 638 MPa |
| Austenite start stress, $\sigma_{As}$ | 170 MPa |
| Austenite finish stress, $\sigma_{Af}$ | 50 MPa |
| Modulus of elasticity for SMA, $E_{SMA}$ | 45 GPa |
| Maximum transformation strain, $\varepsilon_L$ | 5.2% |

boundary conditions reported in the reference experiment [22] were considered in the analysis. The developed finite element model for specimen Out-P125-L6, as an example, is shown in Fig. 2. Nonlinear static analyses were performed with the full Newton–Raphson method and large deformation option. The experimental results reported in [22] were used to validate the finite element analysis results for the specimens under cyclic loading. As shown in Fig. 3, the moment-rotation response from the analysis compares well with the experimental results. A detailed comparison between the simulation and experimental results is presented elsewhere (Sabouri [18].

**Fig. 2** The developed finite element model for connection specimen Out-P125-L6
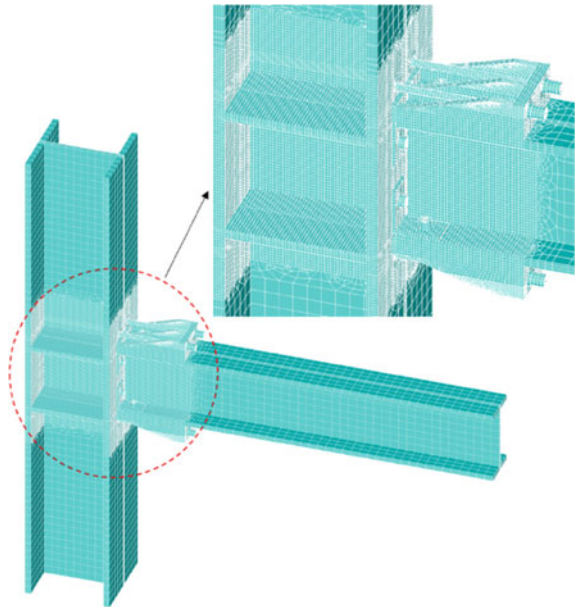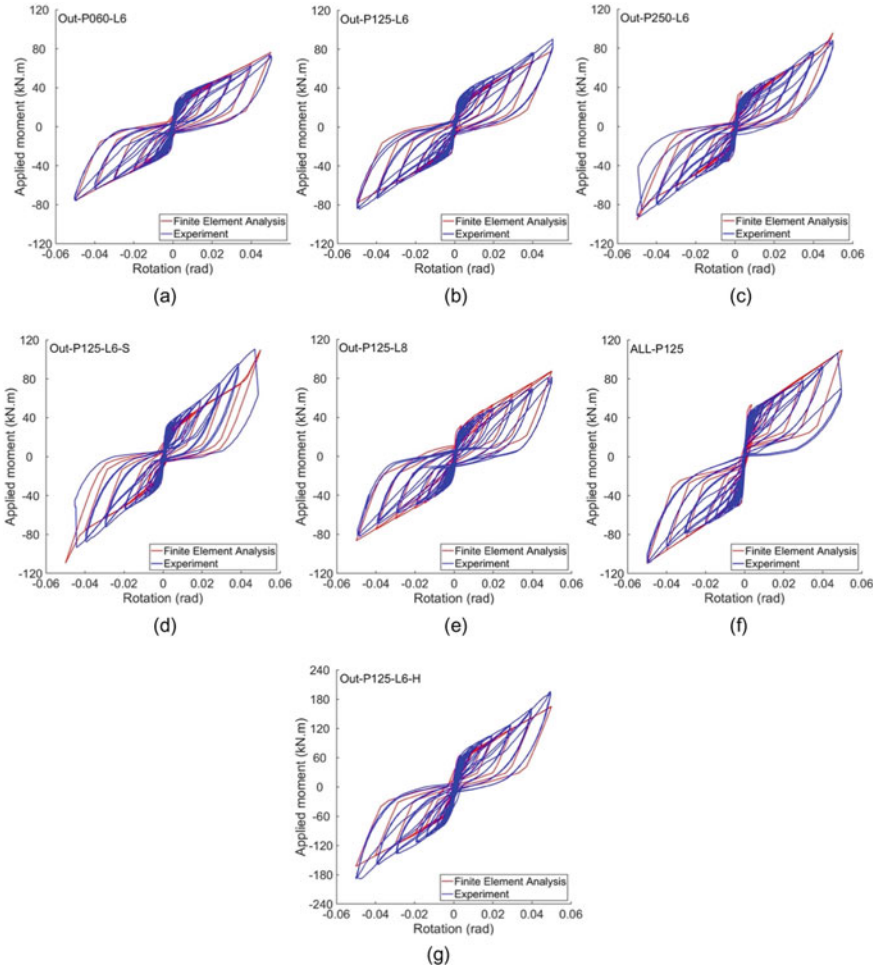
**Fig. 3** The finite element validation using experimental results for specimens: **a** Out-P060-L6, **b** Out-P125-L6, **c** Out-P250-L6, **d** Out-P125-L6-S, **e** Out-P125-L8, **f** All-P125, and **g** Out-P125-L6-H

## 3 Sensitivity Analysis

The self-centering response can be idealized using seven response variables, including initial rotational stiffness, $K_i$, rotation $\theta_B$, moment capacity, $M_{max}$, secondary rotational stiffness, $K_t$, returning path stiffness values, $K_{r1}$ and $K_{r2}$, and returning path moment, $M_D$. Figure 4 presents the idealized self-centering response curve for the SMA-based beam-column connections.

A two-level fractional factorial design was created for sixteen factors (including seven geometry related and nine material related factors). This design required

**Fig. 4** Idealized
self-centering response of
the SMA-based
beam-to-column connection
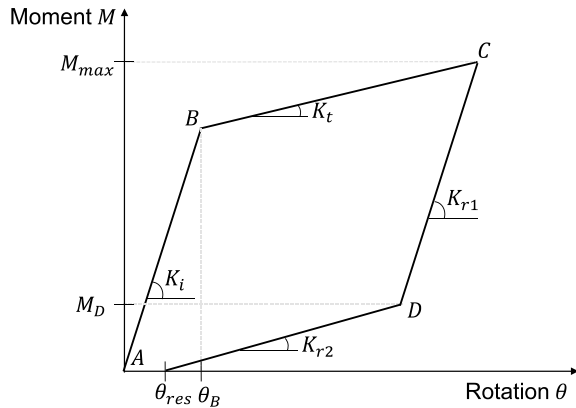


running cyclic analyses on thirty-two ($2^{16-11}$) connection models. Table 2 lists these factors and their corresponding ranges in the sensitivity analysis. Significant factors are identified by performing the analysis of variance on the data for six cyclic response characteristics, including residual rotation, stiffness values ($K_i$ and $K_{r2}$), moment capacity, SMA peak strain, and hysteretic energy dissipation. The sensitivity analysis results show that the beam web slenderness ratio influences all the response variables. The SMA bolt diameter and angle thickness affect five responses. The next significant factors affecting three response variables are the SMA bolt length and maximum transformation strain. The angle width, angle yield stress, and beam flange slenderness ratio are insignificant. Other factors are influential on one or two responses.

## 4  Developing Predictive Equations

An I-optimal design was next adopted to develop surrogate models for predicting the cyclic response of beam-column connections with SMA bolts (used outside the beam flange) and steel angles. Predictive equations were developed for seven response variables with the ten significant factors found in the sensitivity analysis [18]. Sixty-one factor combinations were generated. ANSYS was used to develop a finite element model for each factor combination or connection detail. But for each factor combination, two finite element analyses were performed. The connection was loaded up to a 4% drift in the first finite element analysis unless a complete phase transformation occurred in SMA. In the second finite element analysis, the connection was loaded until the SMA tensile strain reached $\varepsilon_L + (\sigma_{\mathrm{Mf}}/E_{\mathrm{SMA}})$ or until a connection rotation of 4%, whichever occurred first. Then, the connection was unloaded to record the self-centering response. By defining $\varepsilon_L + (\sigma_{\mathrm{Mf}}/E_{\mathrm{SMA}})$ as the endpoint for loading, it is assumed that SMA bolts fracture as the phase transformation is complete at the stress level of $\sigma_{\mathrm{Mf}}$ [11].

**Table 2** Factors and their corresponding ranges in the sensitivity analysis

| Factor | Symbol | Low level (−) | High level (+) | Unit |
|---|---|---|---|---|
| SMA bolt diameter to $D_3$ ratio | $D_{SMA}$ | 0.44 | 1 | – |
| SMA bolt prestrain | $\varepsilon_{pre}$ | 0.2 | 0.56 | % |
| Angle thickness | $T$ | 4 | 12 | mm |
| Angle width to column flange width ratio | $w_a$ | 0.14 | 0.2 | – |
| Angle yield strength | $f_y$ | 236 | 396 | MPa |
| Modulus of elasticity of steel | $E$ | 190,000 | 215,000 | MPa |
| Gage length | $G$ | 50 | 70 | mm |
| Maximum transformation strain | $\varepsilon_L$ | 0.05 | 0.135 | – |
| Martensite start stress | $\sigma_{Ms}$ | 280 | 380 | MPa |
| Martensite finish stress | $\sigma_{Mf}$ | 410 | 590 | MPa |
| Austenite start stress | $\sigma_{As}$ | 170 | 250 | MPa |
| Austenite finish stress | $\sigma_{Af}$ | 70 | 138 | MPa |
| SMA modulus of elasticity | $E_{SMA}$ | 27 | 50 | GPa |
| SMA bolt length (shank length) | $L_{sh}$ | 185 | 350 | mm |
| Beam web slenderness ratio ($h_{bw}/t_{bw}$) | $\lambda_{bw}$ | 22.1 | 43.6 | – |
| Beam flange slenderness ratio ($b_{bf}/2t_{bf}$) | $\lambda_{bf}$ | 4.7 | 5.6 | – |

The developed predictive equations are presented as Eqs. 1–7, which are two-factor interaction polynomial relationships between each response variable and the input factors. A natural logarithm transformation was applied to the $K_t$ and $K_{r2}$ responses to improve the prediction accuracy. Figure 5 compares the responses from predictive equations versus those from finite element analysis. The coefficient of determination, $R^2$, for each response ranges from 0.90 to 0.99. *Adjusted-$R^2$* values are also greater than 0.89. These results indicate acceptable (high) prediction accuracy.

A deformation recovery ratio, *DRR*, defined as the ratio of the recovered-to-maximum drift, was employed to quantify the self-centering capability of the connection models. The mean, median, and standard deviation of the *DRR* were 88%, 93%, and 12%, respectively. The maximum and minimum residual rotations were obtained for the connection models with deep and short beams, respectively. This finding is expected as deeper beams result in greater moment capacity, resulting in greater yielding in the angles and thus higher residual rotations. The results also found that 66% of the analyzed connections reached 4% rotation without experiencing any fracture. Additionally, a residual rotation of less than 0.2% is recorded for 46% of the connections.

$$K_i = (18814.8) - (54.1)\, d_b - (2185.9)\, d_{SMA} + (348.2)\, t - (57417.1)\, \varepsilon_{pre}$$
$$+ (7.5)\, d_b.d_{SMA} + (80.4)\, d_b.\varepsilon_{pre} + (4359.1)\, d_{SMA}.\varepsilon_{pre}$$
$$R^2 = 0.99 \tag{1}$$
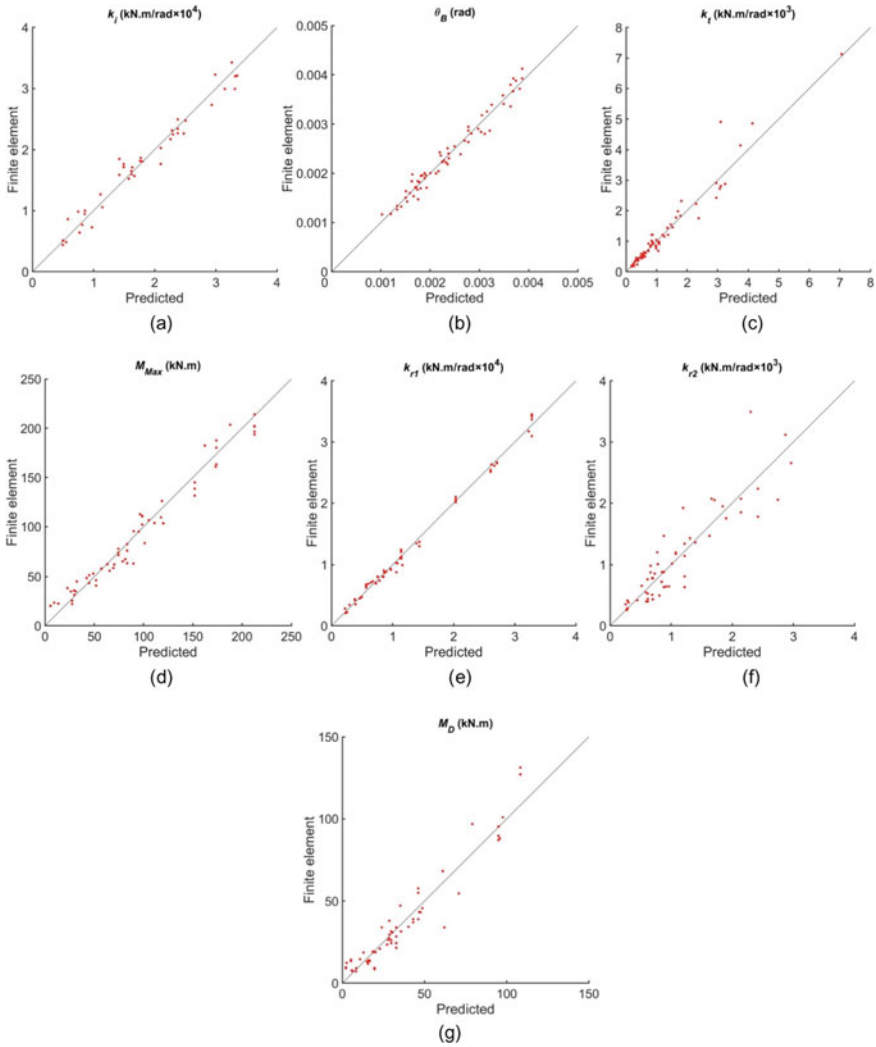
**Fig. 5** Comparison of the results from finite element analysis and predictive equations for: **a** $K_i$, **b** $\theta_b$, **c** $K_t$, **d** $M_{\max}$, **e** $K_{r1}$, **f** $K_{r2}$, and **g** $M_D$

$$\theta_B = -\left(1.8 \times 10^{-5}\right) - \left(3.3 \times 10^{-6}\right)d_b + \left(8.5 \times 10^{-5}\right)d_{\text{SMA}} + \left(6 \times 10^{-5}\right)\text{t}$$
$$- \left(2.22 \times 10^{-4}\right)\varepsilon_{\text{pre}} + \left(1.1 \times 10^{-5}\right)\sigma_{\text{Ms}} + \left(4.8 \times 10^{-6}\right)d_b.\varepsilon_{\text{pre}}$$
$$- \left(9.8 \times 10^{-5}\right)d_{\text{SMA}}.\varepsilon_{\text{pre}} - \left(1.3 \times 10^{-5}\right)\varepsilon_{\text{pre}}.\sigma_{\text{Ms}}$$
$$R^2 = 0.97 \tag{2}$$

$$K_t = \exp\left((4.07) + \left(3.1 \times 10^{-3}\right)d_b + \left(8.43 \times 10^{-2}\right)d_{\text{SMA}} + \left(9.8 \times 10^{-2}\right)t\right.$$

$$-\left(1.5 \times 10^{-3}\right)L_{\text{sh}} - (6.27)\varepsilon_L - \left(3.4 \times 10^{-3}\right)\sigma_{\text{Ms}} + \left(3 \times 10^{-3}\right)\sigma_{\text{Mf}}$$
$$R^2 = 0.96 \tag{3}$$

$$M_{\max} = -(61.4) - (0.163)d_b + (0.7)d_{\text{SMA}}$$
$$- (1.66)t + (0.12)\sigma_{\text{Mf}} + (0.02)d_b.d_{\text{SMA}} + (0.015)d_b.t$$
$$R^2 = 0.96 \tag{4}$$

$$K_{r1} = -(6890) - (3.28)d_b + (25.1)d_{\text{SMA}} - (332.2)t$$
$$+ (37.71)L_{\text{sh}} + (3.66)d_b.d_{\text{SMA}} + (1.7)d_b.t$$
$$- (0.062)d_b.L_{\text{sh}} - (2.25)d_{\text{SMA}}.L_{\text{sh}}$$
$$R^2 = 0.99 \tag{5}$$

$$M_D = (22.16) - (0.1196)d_b - (3.076)d_{\text{SMA}} - (7.298)t + (0.167)\sigma_{\text{As}}$$
$$+ \left(7.225 \times 10^{-3}\right)d_b.d_{\text{SMA}} + (0.01197)d_b.t + (0.432)d_{\text{SMA}}.t$$
$$R^2 = 0.92 \tag{6}$$

$$K_{r2} = \exp\left(\begin{array}{l}(2.95) + \left(4.9 \times 10^{-3}\right)d_b + (0.101)\,d_{\text{SMA}} \\ +(0.111)\,t + (5.758)\,\varepsilon_L - (0.023)\,d_b.\varepsilon_L\end{array}\right)$$
$$R^2 = 0.90 \tag{7}$$

## 5 Confirmation Study and Illustrative Design Example

Additional ANSYS models were analyzed for ten connections with randomly chosen details. By comparing the finite element results with those from using the predictive equations, the accuracy of the developed predictive equations is assessed. The predicted-to-finite element response ratios (Pred/FE) for these connection models are listed in Table 3. The close-to-one Pred/FE ratios confirm the accuracy of the developed predictive equations. Further details and an illustrative design example for using the predictive equations are presented elsewhere [18].

**Table 3** Confirmation of the predictive equations' accuracy

| Model nNo. | $K_i$ ratio [Pred/FE] | $\theta_B$ ratio [Pred/FE] | $K_t$ ratio [Pred/FE] | $M_{max}$ ratio [Pred/FE] | $K_{r1}$ ratio [Pred/FE] | $M_D$ ratio [Pred/FE] | $K_{r2}$ ratio [Pred/FE] |
|---|---|---|---|---|---|---|---|
| 1 | 1.00 | 0.95 | 1.10 | 1.11 | 1.04 | 0.76 | 1.10 |
| 2 | 1.06 | 1.14 | 0.90 | 1.04 | 1.18 | 0.97 | 1.16 |
| 3 | 1.03 | 0.89 | 0.89 | 1.08 | 1.01 | 1.14 | 0.94 |
| 4 | 1.04 | 1.13 | 0.93 | 1.16 | 1.19 | 1.16 | 1.23 |
| 5 | 1.00 | 1.10 | 0.89 | 0.97 | 1.05 | 0.90 | 1.01 |
| 6 | 1.05 | 1.08 | 1.09 | 1.07 | 1.08 | 1.19 | 1.16 |
| 7 | 0.97 | 0.89 | 1.06 | 1.03 | 1.05 | 1.16 | 1.01 |
| 8 | 1.00 | 0.97 | 1.04 | 1.17 | 1.14 | 1.18 | 0.95 |
| 9 | 1.01 | 1.08 | 0.97 | 1.13 | 1.06 | 1.09 | 1.15 |
| 10 | 1.07 | 1.01 | 1.11 | 1.19 | 1.06 | 1.09 | 0.80 |

## 6 Summary and Conclusions

This paper presented the development of predictive equations for the self-centering response of beam-column connections with combined Shape Memory Alloy (SMA) bolts and steel angles. Three-dimensional finite element models were first developed and analyzed in ANSYS. The finite element analysis results were validated using experimental data for seven connection specimens. By performing a statistical sensitivity analysis, significant factors influencing the self-centering response were identified. The self-centering response of SMA-based connections was characterized by seven response variables. Predictive equations were developed for these response variables using an I-optimal design in the context of the design of experiments. Finally, the accuracy of the developed predictive equations was confirmed using additional connection models with randomly generated factor combinations. Based on the results, the following main conclusions can be summarized:

- The self-centering behavior of the newly developed connections with SMA bolts and steel angles was confirmed. As expected, the damage was confined to the steel angles while beams and columns remained essentially elastic.
- The cyclic response of SMA connections was most sensitive to the beam web slenderness ratio, SMA bolt diameter, and angle thickness. The SMA bolt length and maximum transformation strain were influential on three response variables. The response was not sensitive to the angle width, angle yield strength, and beam flange slenderness ratio.
- Connections with beams of smaller depth and SMA bolts of larger diameter experienced lower residual rotations.

The developed predictive equations can be used for the analysis and design of SMA-based connections. The equations eliminate the need for detailed finite element

modeling and thereby can be used for developing computationally efficient frame models with SMA-based connections.

# References

1. Abolmaali A, Treadway J, Aswath P, Lu FK, McCarthy E (2006) Hysteresis behavior of t-stub connections with superelastic shape memory fasteners. J Constr Steel Res 62(8):831–838
2. ANSYS (2020) Mechanical APDL (release 2020 R1). ANSYS Inc., Canonsburg (PA)
3. Chung R (1996) January 17, 1995 Hyogoken-Nanbu (Kobe) earthquake: performance of structures, lifelines, and fire protection systems (NIST SP 901). NIST special publication; 901
4. Eguchi RT, Goltz JD, Taylor CE, Chang SE, Flores PJ, Johnson LA, Seligson HA, Blais NC (1998) Direct economic losses in the Northridge Earthquake: a three-year post-event perspective. Earthquake Spectra 14(2):245–264. Earthquake Engineering Research Institute
5. Fang C, Yam MCH, Chan TM, Wang W, Yang X, Lin X (2018) A study of hybrid self-centring connections equipped with shape memory alloy washers and bolts. Eng Struct 164:155–168. Elsevier
6. Fang C, Yam MCH, Lam ACC, Xie L (2014) Cyclic performance of extended end-plate connections equipped with shape memory alloy bolts. J Constr Steel Res 94:122–136
7. Lagoudas D (2008) Shape memory alloys: modeling and engineering applications. Springer, New York
8. Leon RT, DesRoches R, Ocel J, Hess G (2001) Innovative beam column connections using shape memory alloys. In: Liu S-C (ed) SPIE 8th annual international symposium on smart structures and materials, pp 227–237
9. Ma H, Wilkinson T, Cho C (2007) Feasibility study on a self-centering beam-to-column connection by using the superelastic behavior of SMAs. Smart Mater Struct 16(5):1555–1563
10. Mohammadi Nia M, Moradi S (2020) Limit state behavior and response sensitivity analysis of endplate steel connections with shape memory alloy bolts. J Intell Mater Syst Struct 31(18):2071–2087
11. Mohammadi Nia M, Moradi S (2021) Surrogate models for endplate beam-column connections with shape memory alloy bolts. J Constr Steel Res 187:106929. Elsevier
12. Montgomery DC (2013) Design and analysis of experiments. John Wiley & Sons Inc.
13. Moradi S, Alam MS (2017) Lateral load-drift response and limit states of posttensioned steel beam-column connections: parametric study. J Struct Eng (United States) 143(7)
14. Ocel J, DesRoches R, Leon RT, Hess WG, Krumme R, Hayes JR, Sweeney S (2004) Steel beam-column connections using shape memory alloys. J Struct Eng 130(5):732–740
15. Ozbulut OE, Hurlebaus S, Desroches R (2011) Seismic response control using shape memory alloys: a review. J Intell Mater Syst Struct 22(14):1531–1549
16. Qiu C, Zhu S (2017) Shake table test and numerical study of self-centering steel frame with SMA braces. Earthq Eng Struct Dyn 46(1):117–137. John Wiley & Sons, Ltd
17. Ricles JM, Sause R, Garlock MM, Zhao C (2001) Posttensioned seismic-resistant connections for steel frames. J Struct Eng 127(2):113–121
18. Sabouri Ghannad MM, Mohammadi Nia M, Moradi S (2021) Predictive equations and continuum FE models for self-centering response of SMA-based steel beam-column connections with steel angles. J Build Eng 43:102859. Elsevier

19. Shinozuka M, Chaudhuri SR, Mishra SK (2015) Shape-memory-alloy supplemented lead rubber bearing (SMA-LRB) for seismic isolation. Probab Eng Mech 41:34–45
20. Silwal B, Michael RJ, Ozbulut OE (2015) A superelastic viscous damper for enhanced seismic performance of steel moment frames. Eng Struct 105:152–164. Elsevier
21. Speicher MS, DesRoches R, Leon RT (2011) Experimental results of a NiTi shape memory alloy (SMA)-based recentering beam-column connection. Eng Struct 33(9):2448–2457
22. Wang W, Fang C, Liu J (2017) Self-centering beam-to-column connections with combined superelastic SMA bolts and steel angles. J Struct Eng 143(2):04016175
23. Yam MCH, Fang C, Lam ACC, Zhang Y (2015) Numerical study and practical design of beam-to-column connections with shape memory alloys. J Constr Steel Res 104:177–192. Elsevier

# Interpretable Ensemble Machine Learning Models for Shear Strength Prediction of Reinforced Concrete Beams Externally Bonded with FRP

**Jesika Rahman and A. H. M. Muntasir Billah**

**Abstract** Shear strengthening is a complex phenomenon that garnered significant attention in the structural engineering community. Due to the catastrophic nature of shear failures, several attempts have been made in retrofitting reinforced concrete (RC) beams out of which the incorporation of externally bonded fiber reinforced polymer (FRP) layers offer a remarkably fast, economical, and reliable solution. This paper presents an approach to predict the shear capacity of FRP strengthened RC T-beams using interpretable ensemble machine learning models. The study covers a comprehensive databank comprising a wide array of parameters including concrete design, FRP composition as well as beam cross sections. The efficiency of the developed models in predicting the shear capacity of FRP retrofitted RC T-beams is evaluated by comparing the results with several design guidelines. It is observed that the random forest and CatBoost models provide the most precise shear capacity estimations of the FRP retrofitted RC T-beams. The $R^2$ and MAE values obtained from the random forest model were 0.897 and 0.128 kN, respectively, whereas those by the CatBoost model were 0.899 and 0.127 kN, respectively. The best performing model CatBoost is made interpretable using the Shapley Additive exPlanations which reveal that the most important input parameter contributing to shear capacity of the FRP strengthened RC T-beams is the height of the FRP layers used in the retrofit process. The proposed ensemble models presented in this paper are proved to be superior to the existing mechanics-driven models currently being used for design practices.

**Keywords** Fiber reinforced polymers · T-beams · Shear capacity · Ensemble machine learning · SHAP feature importance

J. Rahman · A. H. M. Muntasir Billah (✉)
 Department of Civil Engineering, University of Calgary, Calgary, Canada
e-mail: muntasir.billah@ucalgary.ca

# 1 Introduction

Existing reinforced concrete (RC) structures are constructed following the old design guidelines where the design demand on the structure was evaluated based on mostly gravity loads. Such structures are highly vulnerable to deterioration due to accidental damage, earthquakes, poor maintenance, and corrosion. It is essential to adopt a retrofitting technique to avoid demolition and disruption to typical daily services. About 28% of the local road bridges and 25% of rural highway bridges in Canada were built more than 50 years ago, and approximately 15% of these bridges were found to be in the worst condition [19]. The fiber reinforced polymer (FRP) has gained popularity due to its favorable properties: lightweight, high strength, durable, non-corrosive, and easier installation [10]. FRP has made its way into the shear strengthening of structures and is being studied for further improvements in its serviceability.

Compared to rectangular beams, T-beams have higher resistance to shear cracks [16]. As the main objective of beam shear strengthening is to bridge the cracks, FRPs are one of the most effective strengthening solutions. The typical wrapping schemes observed in externally bonded FRP retrofitted beams are u-wrap, closed wrap, and side bonded wrap. Although termed as the best option, the closed wrap is mostly avoided as it is difficult to wire the FRP laminates up to the flange in T-beams. A reliable design method is necessary to increase the longevity of the retrofitted beams and utilize most of the properties of FRP laminates. Several experimental studies are available in the literature focusing on the shear strengthening of RC beams using externally bonded FRP layers [7, 8, 11]. Design codes and guidelines, namely ACI 440.2R-17 [1], CSA S6:19 [2] and CSA S806 [3], are widely followed in designing such retrofitting systems. However, the precision obtained from the design guidelines is inadequate and the design equations rely heavily on several parameters calculation of which is often tedious. Furthermore, a number of studies developed semi-empirical equations for the shear strength determination of externally bonded FRP retrofitted beams [2, 6, 15]. Various prediction models have also been developed in the past by researchers to identify the shear capacity of the beams [14, 20, 21]. The prediction models, however, lack accuracy when applied to factors outside the range of the data that were used to develop the models. A more comprehensive database is thus required to develop a high accuracy prediction model for the shear capacity of RC T-beams strengthened with FRP.

The application of artificial intelligence (AI) in structural engineering has allowed the community to attain reliable predictions models. The machine learning (ML) algorithms developed are able to estimate the shear capacity of structural components with satisfactory accuracy [5]. The ensemble learning models, namely random forest (RF), XGBoost (XGB), CatBoost (CB), and AdaBoost (AB) are found to be excellent tools to provide estimations with high precision. [17] studied the shear capacity estimation of steel fiber reinforced concrete beams using ML models and identified that the XGB gave the best results with the highest accuracy. This paper aims to develop an interpretable ML model using the ensemble learning models (RF, XGB,

CB, and AB) to estimate the shear strength of externally bonded FRP retrofitted RC T-beams. To evaluate the accuracy, the results are compared with the equations provided by design guidelines as well as the empirical studies done in the past. The study is unique in the sense that it covers the largest data of T-beams and therefore can be used to increase the accuracy of the prediction model.

## 2 Database Collection

A total of 302 data are collected for RC T-beams from experimental studies conducted between 1997 and 2021. The data includes details of cross-sectional dimensions: width ($b$) and effective depth ($d$), shear span to effective depth ratio ($a/d$), transverse steel ratio ($A_{sv}$), concrete compressive strength ($f_c'$), types of fiber, the total thickness of FRP ($n*t_f$), width of FRP strips ($W_f$), elastic modulus of FRP ($E_f$), ultimate strain of FRP ($\varepsilon_{frp,u}$), tensile strength of FRP ($f_{frp,u}$), and shear capacity contribution by FRP ($V_f$) along with the total experimental shear capacity ($V_{exp}$). The types of wrapping included in the database are U-wrap ($UW$), side bonded ($SB$) and closed wrap ($CW$). Correspondingly, the types of fibers in the database are carbon (CFRP), aramid (AFRP), basalt (BFRP), and glass fiber (GFRP). Figure 1 shows the schematic representation of an externally bonded FRP strengthened RC T-beam.

The statistical properties of the database are summarized in Table 1. The distribution of the database collected from literature in terms of the type of fiber and wrapping scheme is presented in Fig. 2. From Fig. 2, it can be seen that CFRP and UW are the most common type of fiber and wrapping scheme, respectively. The shear contribution by FRP is calculated by deducting the shear strength of RC T-beam without FRP (control specimen) from the total shear strength of the FRP retrofitted T-beams.
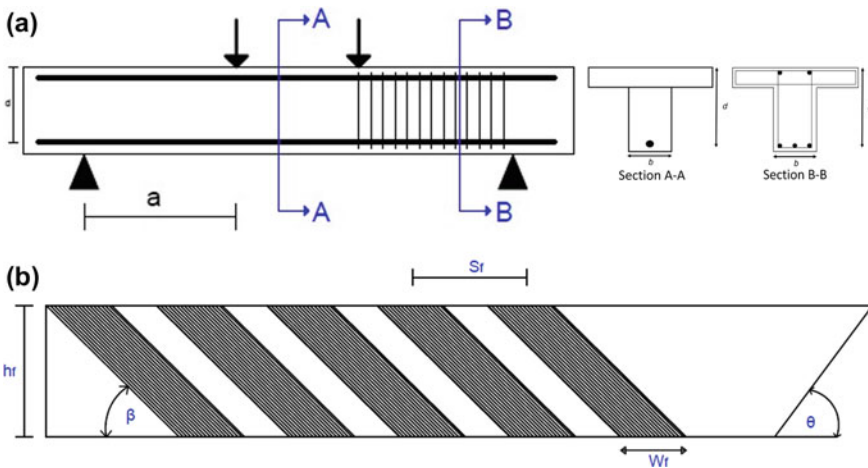


Fig. 1 a Typical T-beam under study and b orientation of FRP laminates

**Table 1** Statistical measures of input parameters

| Parameters | Min | Max | Mean | SD |
|---|---|---|---|---|
| Concrete strength, $f_c'$ (MPa) | 12.40 | 60 | 32.22 | 9.889 |
| FRP thickness, $n*t_f$ (mm) | 0.055 | 3.00 | 0.781 | 1.833 |
| FRP elastic modulus, $E_f$ (GPa) | 6.80 | 640 | 154.10 | 95.82 |
| FRP strength, $f_{frp,u}$ (MPa) | 13 | 4361 | 2295 | 1488 |
| FRP strain, $\varepsilon_{frp,u}$ | 0.004 | 0.047 | 0.015 | 0.005 |
| Beam width, $b$ (mm) | 64 | 457 | 162.25 | 83.52 |
| Beam effective depth, $d$ (mm) | 140 | 1092 | 365 | 186 |
| Shear span to effective depth ratio, $a/d$ | 1.20 | 5.00 | 2.77 | 0.68 |
| Transverse steel ratio, $A_{sv}$ (%) | 0.00 | 0.98 | 0.18 | 0.18 |

*Note Min = minimum, Max = maximum, SD = standard deviation of the data
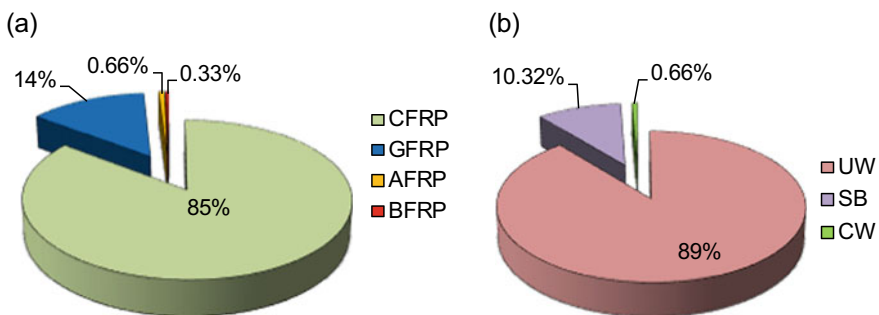


**Fig. 2** Distribution of data with respect to **a** type of fiber and **b** wrapping schemes

## 3 Selection of Input Features

For a satisfactory model performance, the selection of proper input features is very important. The input parameters chosen for this study in ML model development are based on the guidelines CSA S6:19 [4] and ACI 440.2R [1] as well as from empirical equations developed in earlier studies [2, 6]. The parameters considered as input include width of beam ($b$; effective depth of the beam ($d$); shear span to effective depth ratio ($a/d$); height of FRP strips ($h_f$); modulus of elasticity of FRP material ($E_f$); ultimate strain of FRP ($\varepsilon_{frp,u}$); ratio of transverse reinforcement ($A_{sv}$); concrete compressive strength ($f_c'$); total thickness of FRP layers ($n*t_f$); ultimate strength of FRP ($f_{frp,u}$); type of wrapping scheme and type of fiber. The variation in total experimental shear capacity of T-beam specimens retrofitted with the externally bonded FRP laminates ($V_{exp}$) with respect to $a/d$ ratio, $f_c'$, $n*t_f$ and $f_{frp,u}$ is illustrated in Fig. 3. Figure 3 also includes the variation in experimental shear contribution by FRP ($V_{fexp}$) with respect to $A_{sv}$.
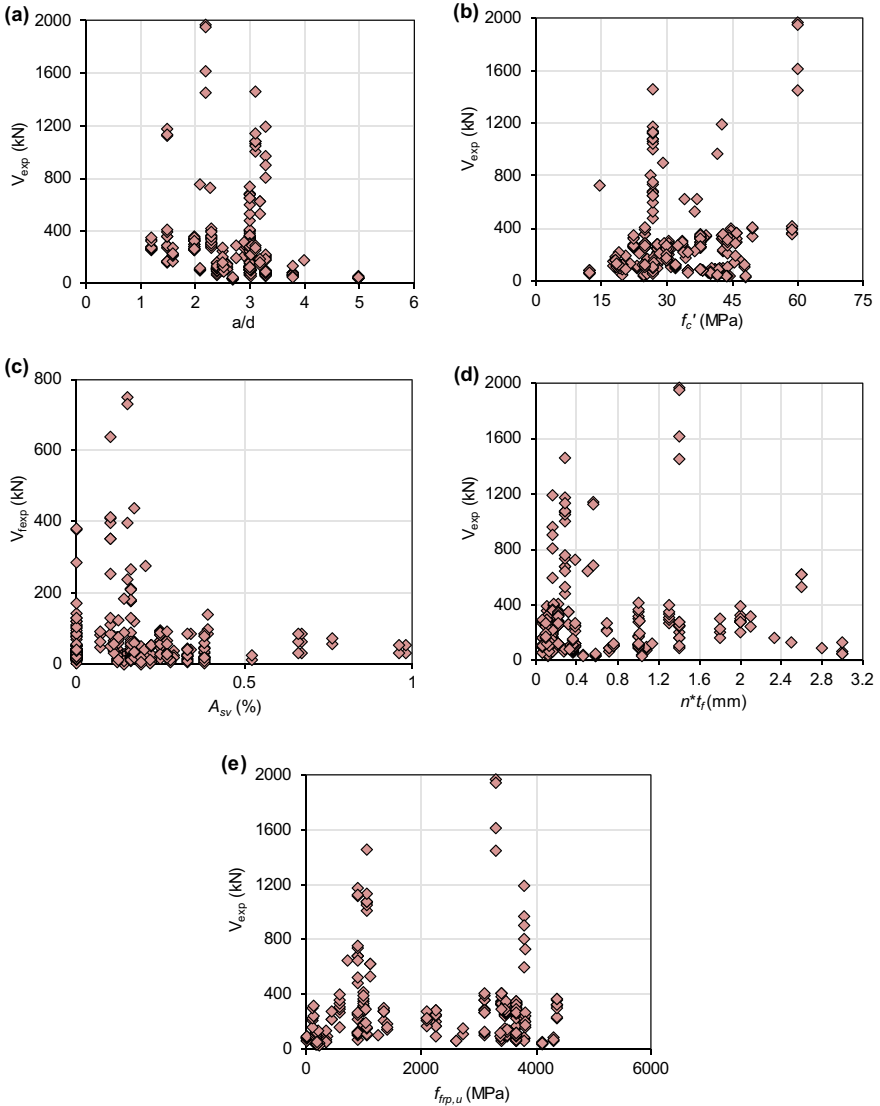
Fig. 3 Variation in shear capacity with respect to selected material parameters

From Fig. 3, it is seen that the total shear strength increased as *a/d* ratio increased up to 2.3 and then began to decrease as the ratio increased. At *a/d* ratio less than 2.0 the angle between the principal direction of fiber and critical shear crack is typically observed to be larger, thereby reducing the tensile stress in the fibers and consequently lower shear strength of the specimen [13]. The bond between FRP and concrete is vital in shear strengthening mechanism. It is observed in Fig. 3b that as

the $f_c'$ increased, the shear capacity of the beams increased as well. On the other hand, it is seen that as $A_{sv}$ increased, $V_{fexp}$ decreased. According to [12], the reason for such behavior could be that both transverse steel stirrups and FRP share the shear force. When there is lower transverse steel, FRP contributes most to the shear resistance in the beams [9]. In Fig. 3d, it is observed that as the total thickness of FRP increased the shear capacity also increased up to a thickness of 1.4 mm. The shear strength, however, remained constant beyond 1.4 mm thickness. No particular trend is observed in variation of $V_{exp}$ with respect to $f_{frp,u}$ (Fig. 3e) although the beams are found to have the highest capacity when the $f_{frp,u}$ is between 3000 and 4300 MPa.

# 4    Ensemble Machine Learning Model Overview and SHAP Feature

This section provides a brief introduction to models generated in this paper including a description of the SHapley Additive exPlanations (SHAP) for identifying the feature importance. The *k-fold* cross-validation technique is applied for all the models analyzed in order to improve the model performance, details of which is described in the next section.

The RF is a supervised ensemble learning algorithm that combines multiple decision trees in order to learn the mapping between input and output. The decision tree is a supervised learning algorithm that utilizes a chart-like tree to predict target variables from the training data. In RF, a random selection of training dataset and feature subset is made for each decision tree to avoid overfitting of data in the individual decision trees. Eq. 1 shows how the input variable ($x$) is mapped to the output where $y_n$ denotes the number of individual decision tree, $X'$ as random selection of features, and N as the total number of decision trees.

$$\hat{y} = \frac{1}{N} \sum_{i=1}^{M} y_n(X')$$
(1)

The XGB is called a gradient boosting algorithm which works on the decision tree as well. The gradient boosting feature minimizes the model error by using a gradient descent algorithm. An optimized technique for obtaining superior performance with diverse datasets is done in the XGB model. On the other hand, the CB algorithm works by combining the "Category" and "Boosting" features where the gradient boosting grows oblivious trees. All the nodes are maintained at the same level, and the predictions are done within the same conditions. Without extensive hyper tuning and data training, the CB yields a state-of-the-art performance. Adaptive Boosting technique is used in the AB algorithms where the weak learning algorithms are combined to improve the overall model performance.

The SHAP is used to explain the prediction of an outcome by computing the importance of each feature for the target prediction. The concept of SHAP is based

on the game theoretic approach of SHAP values, where each feature of the instance is considered as "player" and the output prediction as "payout." The technique indicates how the payouts are distributed among the features. The "summary.plot" from SHAP has been used in this study to explain the feature importance of the best prediction model.

## 5   Results and Discussion

The dataset is divided into training and testing sets with 80% as the training set chosen randomly to obtain the initial model hyperparameters. The remaining set is used as the testing data for model performance evaluation. A tenfold cross-validation technique is applied where the dataset is divided equally into 10 subsets with 1 being used as the validation and the remaining 9 sets for model training. The cross-validation technique is repeated 10 times with each of the subsets being used as validation data and average considered as the final output.

### 5.1   Cross-Validation and Hyperparameter Tuning

The results of cross-validation accuracy are shown in Fig. 4 where the interquartile range is presented by the box and the median value with a straight line in the middle of the box. The whiskers represent data exceeding 1.5 times the difference between the first and third quartiles, respectively. The median cross-validation accuracy of the ML models developed in this study ranged from 75% (AB) to 86% (RF). The median accuracy by CB is also close to that of RF (85.5%). Moreover, the interquartile range in RF is seen to be the smallest out of the four models showing less variation among data. The interquartile ranges of AB and XGB are similar with the lowest accuracy shown by AB. Therefore, it is understood that the best performing models out of the ones developed in this study are RF and CB.

Table 2 summarizes the optimized model hyperparameters used in this study. Table 3 presents the coefficient of determination ($R^2$), root mean square error (*RMSE*), and mean absolute error (*MAE*) values obtained from the models developed. The ensemble models RF and CB outperformed XGB and AB as evident by the highest $R^2$ (0.897 and 0.899, respectively) and relatively lower *MAE* values (0.128kN and 0.127kN, respectively). Table 4 presents the equations used to calculate the statistical measures used in monitoring the model performances.
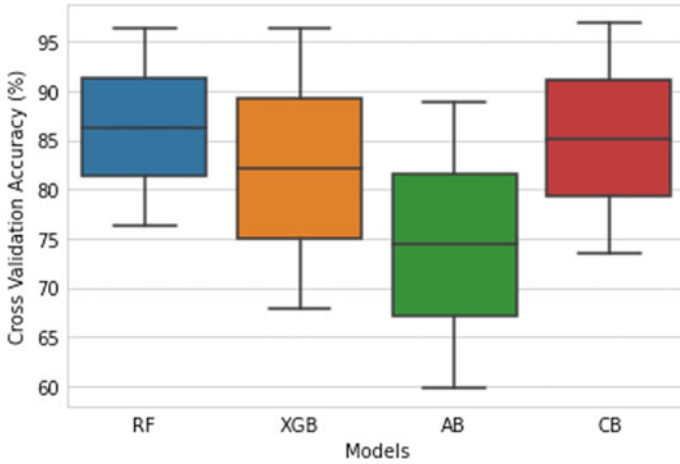
**Fig. 4** Cross-validation results

**Table 2** List of optimized hyperparameters

| Model | Hyperparameters | Value |
|---|---|---|
| RF | a. Random state | 500 |
| | b. Number of estimators | 400 |
| XGB | a. Number of estimators | 100 |
| | b. Learning rate | 0.1 |
| | c. Gamma | 0 |
| | d. Subsample | 0.75 |
| | e. Col_Sample by tree | 1 |
| | f. Max_depth | 3 |
| AB | a. Random state | 30 |
| | b. Number of Estimators | 50 |
| CB | a. Iterations | 700 |
| | b. Learning rate | 0.02 |
| | c. Depth | 5 |
| | d. Eval_metric | RMSE |
| | e. Random_seed | 23 |
| | f. Bagging_temperature | 0.2 |
| | g. od_type | Iter |
| | h. metric_period | 75 |
| | i. od_wait | 100 |

**Table 3** Performance measures of the developed ML models

| Model | Training data (80%) | | | | Testing data (20%) | | | | 10-fold cross-validation |
|---|---|---|---|---|---|---|---|---|---|
| | RMSE (kN) | $R^2$ | Adjusted $R^2$ | MAE (kN) | RMSE (kN) | $R^2$ | Adjusted $R^2$ | MAE (kN) | Mean $R^2$ |
| RF | 0.089 | 0.987 | 0.987 | 0.061 | 0.184 | 0.963 | 0.955 | 0.128 | 0.897 |
| XGB | 0.111 | 0.980 | 0.979 | 0.082 | 0.165 | 0.971 | 0.964 | 0.108 | 0.894 |
| AB | 0.259 | 0.890 | 0.885 | 0.216 | 0.285 | 0.912 | 0.892 | 0.243 | 0.805 |
| CB | 0.107 | 0.981 | 0.980 | 0.082 | 0.181 | 0.964 | 0.956 | 0.127 | 0.899 |

**Table 4** Formula to calculate the model performance measures

| Name of performance measure | Notation | Formula |
|---|---|---|
| Coefficient of determination | $R^2$ | $R^2 = 1 - \frac{\sum_{i=1}^{m}(P_i - A_i)^2}{\sum_{i=1}^{m}(P_i - \overline{A})^2}$ |
| Root-mean-squared error | RMSE | $RMSE = \sqrt{\frac{\sum_{i=1}^{m}(P_i - A_i)^2}{m}}$ |
| Mean absolute error | MAE | $MAE = \frac{\sum_{i=1}^{m}|P_i - A_i|}{m}$ |

* *Note* $A_i$ represents actual data and $P_i$ the predicted; $\overline{A}$ denotes the average value of actual data; $i = 1, 2, 3,…, m$ indicates the number of samples

## 5.2 *Interpreting Model Results Using SHAP*

The effect of input features on the CB model for the FRP wrapped T-beams is presented in Fig. 5. The importance of each feature is ranked from low to high, where the higher SHAP value indicates higher importance of the feature and vice versa. The y-axis presents the order of features in terms of lowest to highest importance and each point on the plot horizontally along the individual feature indicate the high impact (red) and low impact (blue) conditions. It can be seen that the height of the FRP layer ($h_f$) plays the most important part in predicting the shear capacity for models developed for the T-beams where the associated SHAP value increased with $h_f$ values. The *a/d* ratio is at the mid-rank in importance which shows that at low *a/d* values the SHAP values are higher, thereby implying that for lower values of *a/d*, the impact of *a/d* ratio is high in shear strength prediction. The least important parameter is observed to be the type of fibers.
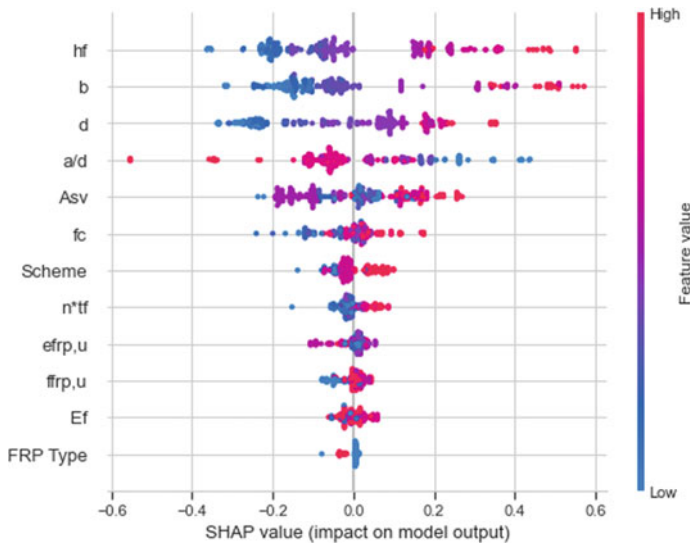
**Fig. 5** Feature importance explanation using SHAP

## 6   Comparison with Design Code and Empirical Equations

In order to identify the accuracy of the design guidelines and empirical equations proposed in literature, the results by these equations are compared with the experimental data collected in this study. One of the common approaches in calculating the total shear capacity ($V_{total}$) of FRP retrofitted RC beams is the summation of shear contribution by transverse steel ($V_s$), concrete ($V_c$), and FRP ($V_f$) as shown in Eq. 2.

$$V_c + V_s + V_f = V_{total} \tag{2}$$

Deducting the shear contributions by transverse stirrups and concrete to find out FRP contribution does not provide accurate information as identified by Rousakis et al. [18]. Following such observation, the total shear capacity of externally bonded FRP strengthened RC T-beams is considered for comparison purposes in this study. A total of three design guidelines and three empirical equations are used to calculate the shear contribution by FRP in the T-beams. The shear crack inclination is an important factor in shear calculation and determining the angle of inclination ($\theta$) is difficult. The ACI 440.2R [1] guideline considered the value of $\theta$ to be 45°, whereas CSA S6:19 [4] suggested its value as 42°. This paper considers a 45° angle of shear crack inclination in the subsequent calculations.

In order to monitor the efficiency of the chosen guidelines for comparison study, the experimental shear capacity is plotted against predicted shear capacity by the equations with a 45° line to identify the conservativeness of the formulations (Fig. 6). For instance, the points below the line indicate that the prediction is safe/conservative

to use whereas those above the line represent unsafe/unconservative prediction by the equations. In Fig. 6, it is seen that the CSA S6:19 showed the most conservative predictions with approximately 30% data above the line. Among the empirical equations, it is seen that D'Antino and Triantafillou [6] provided the least unsafe data. Most of the data points are above the 45° line in case of the Mofidi and Challaal (2014) equation implying its poor performance. It can also be noted that, except for CSA S6:19, the trend in all the results in Fig. 6 diverges significantly from the diagonal line. A comparison of the best models developed in this paper is also included where it is seen that the data points are close to the 1:1 diagonal line for the best and second-best performing models in terms of the tenfold cross-validation results (CB and RF, respectively).

The distribution of predicted to experimental ratio with respect to *a/d* of all the equations chosen for this study is illustrated in Fig. 7. It is seen that the CSA S806 [3] shows results with fairly conservative estimation and the lowest standard deviation (SD). Among the empirical equations, the worst prediction is observed from Mofidi and Challaal [15] where the mean is at 1.372 and the SD is at 0.87, thereby showing the high dispersion in data. The high scattered nature of data points is prevalent in all the formulas adopted for comparison up to an *a/d* ratio of 3.40. It can be observed
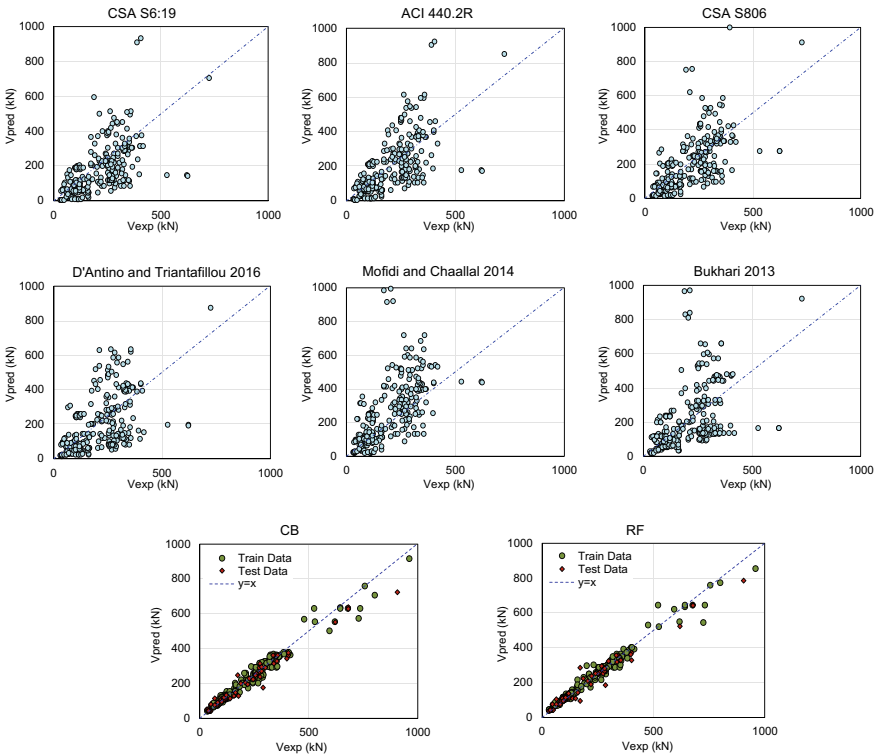


**Fig. 6** Comparison of the design code and empirical equations with the experimental results
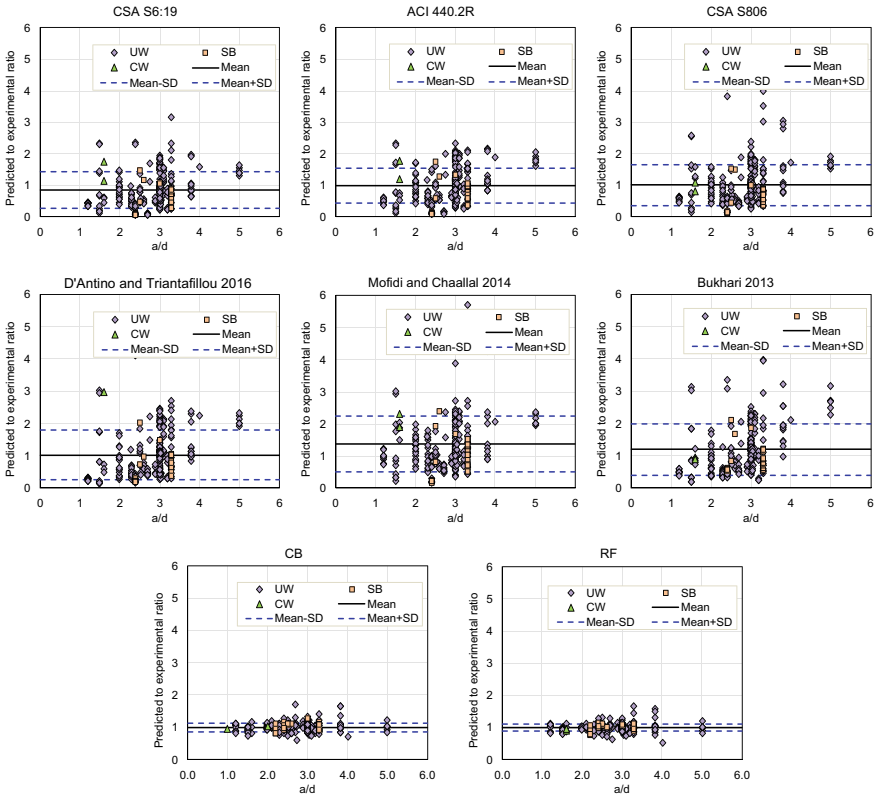
**Fig. 7** Variation in predicted to experimental ratio with respect to *a/d*

that the models CB and RF outperformed the rest chosen for comparison with a mean predicted to experimental results ratio of 1.00 and relatively low SD values of 0.13 and 0.12, respectively.

It is evident from the above speculations that the models developed in the current study are superior in prediction accuracy and can be applied to a wide range of data. It can also be noted that the equations chosen for comparison do not show a particular trend in terms of the performance measures analyzed in this study. For instance, from Fig. 6 it is seen that the code CSA S6:19 [4] shows the best performance with respect to the least data points in the unsafe zone. On the other hand, the results in Fig. 7 imply that the code CSA S806 [3] performs the best with low SD values and mean closest to 1.00. The models CB and RF, identified as the best and second-best models in this paper, are the only models that show consistent performance in all measures analyzed. Therefore, it is safe to say that the ensemble models CB and RF outperformed the XGB and AB in estimating the shear capacity of FRP strengthen T-beams.

# 7    Conclusions

This study is based on an extensive database regarding shear strengthening of reinforced concrete T-beams with externally bonded FRP layers. The database collected is then used to develop four ensemble learning models and identify the best models to generate an estimation method with higher accuracy and lower computational efforts that can be applied easily in the practical field. The effect of concrete and FRP properties and beam cross section details on the shear strength of the specimens is studied. SHapley Additive exPlanation is used to interpret the importance of input features of the models. Finally, a comparison of the data with those predicted with formulations used widely in research and practical designs is done to verify the accuracy of the guidelines. The following conclusions can be drawn from the study:

1. The shear capacity increased with increase in *a/d* ratio to a point beyond which the capacity decreased with increasing *a/d* values. The highest shear contribution by FRP is observed in specimens with no transverse reinforcement. Moreover, no particular trend is observed in shear capacity due to changes in FRP tensile strength.
2. From the tenfold cross-validation, the coefficient of determination obtained from RF and CB models were very close to 1.00 and the mean absolute error was found to be less than 0.25 kN.
3. The most important feature as explained by SHAP is the height of FRP layers. On the contrary, the least important feature is the type of fiber. It was also noted that lower *a/d* ratio has greater impact on the prediction of shear strength.
4. The design guidelines and empirical equations do not perform satisfactorily when applied to data outside the range considered in developing the corresponding equations.
5. The prediction data points obtained from CB and RF are seen to have low scatter and cluster at the 1:1 line when plotted against the experimental capacity.
6. The mean of predicted to experimental ratio results from CB and RF models is seen to be very close to 1.00 with standard deviations of only 0.12 and 0.13, respectively.

The results summarized above identify the fact that CB and RF models perform with satisfactory accuracy in shear strength estimation of externally bonded FRP retrofitted RC T-beams. The models developed can be implemented in design and strengthening solutions in practical field application.

# References

1. ACI 440.2R-17 (2017) Guide for the design and construction of externally bonded FRP systems for strengthening concrete structures. American Concrete Institute, Farmington Hills, MI
2. Bukhari IA, Vollum R, Ahmad S, Sagaseta J (2013) Shear strengthening of short span reinforced concrete beams with CFRP sheets. Arab J Sci Eng 38(3):523–536
3. Canadian Standard Association (2012) Design and construction of building structures with fibre reinforced polymers (CSA S806-12) (R2017). Mississauga, Ontario, Canada
4. Canadian Standards Association (2019) Canadian highway bridge design code. CAN/CSA S6:19. Mississauga, ON. CSA Group
5. Chaabene WB, Nehdi ML (2020) Novel soft computing hybrid model for predicting shear strength and failure mode of SFRC beams with superior accuracy. Compos Part C Open Access 3:100070
6. D'Antino T, Triantafillou TC (2016) Accuracy of design-oriented formulations for evaluating the flexural and shear capacities of FRP-strengthened RC beams. Struct Concr 17(3):425–442
7. Diab HM, Sayed AM (2020) An anchorage technique for shear strengthening of RC T-beams using NSM-BFRP bars and BFRP sheet. Int J Concr Struct Mater 14(1):1–16
8. El-Saikaly G, Godat A, Chaallal O (2015) New anchorage technique for FRP shear-strengthened RC T-beams using CFRP rope. J Compos Constr 19(4):04014064
9. Godat A, Chaallal O (2013) Strut-and-tie method for externally bonded FRP shear-strengthened large-scale RC beams. Compos Struct 99:327–338
10. Hollaway LC, Teng J-G (2008) Strengthening and rehabilitation of civil infrastructures using fibre-reinforced polymer (FRP) composites. Elsevier
11. Jayaprakash J, Samad AAA, Abbasvoch AA (2010) Investigation on effects of variables on shear capacity of precracked RC T-beams with externally bonded bi-directional CFRP discrete strips. J Compos Mater 44(2):241–261
12. Kim Y, Ghannoum WM, Jirsa JO (2015) Shear behavior of full-scale reinforced concrete T-beams strengthened with CFRP strips and anchors. Constr Build Mater 94:1–9
13. Li W, Leung CK (2017) Effect of shear span-depth ratio on mechanical performance of RC beams strengthened in shear with U-wrapping FRP strips. Compos Struct 177:141–157
14. Mofidi A, Chaallal O (2011) Shear strengthening of RC beams with EB FRP: Influencing factors and conceptual debonding model. J Compos Constr 15(1):62–74
15. Mofidi A, Chaallal O (2014) Tests and design provisions for reinforced-concrete beams strengthened in shear using FRP sheets and strips. Int J Concr Struct Mater 8(2):117–128
16. Pansuk W, Sato Y (2007) Shear mechanism of reinforced concrete T-beams with stirrups. J Adv Concr Technol 5(3):395–408
17. Rahman J, Ahmed KS, Khan NI, Islam K, Mangalathu S (2021) Data-driven shear strength prediction of steel fiber reinforced concrete beams using machine learning approach. Eng Struct 233:111743
18. Rousakis TC, Saridaki ME, Mavrothalassitou SA, Hui D (2016) Utilization of hybrid approach towards advanced database of concrete beams strengthened in shear with FRPs. Compos B Eng 85:315–335
19. Statistics Canada (2018) Canada's core public infrastructure survey: Roads, bridges and tunnels. Available from: https://www150.statcan.gc.ca/n1/daily-uotidien/201026/dq201026a-eng.htm. Accessed 12 August 2021
20. Triantafillou TC (1998) Shear strengthening of reinforced concrete beams using epoxy-bonded FRP composites. ACI Struct J 95:107–115
21. Zhou Y, Zhang J, Li W, Hu B, Huang X (2020) Reliability-based design analysis of FRP shear strengthened reinforced concrete beams considering different FRP configurations. Compos Struct 237:111957

# Evaluation of Concrete Characteristics Using Smart Machine Learning Techniques—A Review

**Chinmay Kapoor, Navneet Kaur Popli, Ashutosh Sharma, and Rishi Gupta**

**Abstract** Concrete is one of the most commonly used materials for a wide range of construction across the world. The heterogeneity of concrete results in wide variation in its properties. How different ingredients are mixed, determines the performance of concrete, especially its compressive strength. Hence, rigorous testing of concrete in the laboratories before it is finally selected to be used for a specific type of construction is required. This process of testing requires large quantities of material, time and money. The advent of machine learning and artificial intelligence appears to be promising and significant work has been done in this field for the development of high-performance concrete. Traditional curve fitting models provide the ability to interpolate data, however, this paper evaluates the efficacy of machine learning models and different types of neural networks that have been specifically utilized to predict in terms of various factors, the compressive strength of concrete. Various algorithms like group method of data handling (GMDH) type neural networks, adaptive neuro-fuzzy inference system (ANFIS), hybrid modified firefly algorithm with artificial neural networks (MFA-ANN) and other hybrid ANN algorithms have been used to perform a comparatively analyzed review.

Keywords · Artificial Neural Networks (ANN) · Fuzzy Logic (FL) · Ordinary Portland Cement (OPC)

## 1 Introduction

The continuous rise in the demand of new construction leads to an increase in the production of concrete. The production of cement, which involves calcination of limestone and high consumption of energy during manufacturing of products and raw materials, produces a very huge amount of $CO_2$. Given this scenario, there arises the need for production of materials which could be used either as a supplementary

C. Kapoor · N. K. Popli · A. Sharma · R. Gupta (✉)
Faculty of Engineering and Computer Science, University of Victoria, Victoria, BC, Canada
e-mail: guptar@uvic.ca

product or altogether as an alternative to cement, since cement production is one of the largest generators of carbon footprint in the world [1]. In order to do so, a huge number of chemical lab tests are done and conclusions are reached.

There have been various researches done in the same field using machine learning and neural networks, and the main goal of this paper is to review different researches based on predicting the strength of concrete and its different types. The conventional models which have been used for predicting various physicochemical properties of concrete mainly provided with pragmatic relationships developed using data modelling and statistical analysis of first-hand experimental observations where rudimentary machine learning models like regression have been developed. Although these models are quite productive and efficient in terms of time consumed, they lack the accuracy and better predicting efficiency of dealing with complex scenarios. When it comes to dealing with problems where huge amounts of factors are being considered, such in the case of dealing with multiple types of concrete mixtures, more complex machine learning and artificial neural network models are used.

There has been countless research that has taken place using higher performing models such as hybrid ANN-FL model (ANFIS), basic backpropagation neural networks (BPNN), etc. and thorough review of the literature has been done for the purpose of this survey. All the information which was either irrelevant, incomplete or repetitive has not been considered and a general review has been prepared. The paper has been divided into sections, keeping in mind the ease of understanding as Sect. 2, containing a basic overview of some of the most common types of concrete/concrete admixtures used in the construction industry and how they have evolved over the years in terms of mixing of minerals and ratios of materials used. Section 3 defines the different kinds of ML and ANN models which have been used and developed to estimate the values of the compressive strength of concrete and contains a critical review and performance analysis of all the models used. Section 4 concludes the review along with a few knowledge gaps explained simultaneously.

## 1.1 Concrete and Its Types

Concrete is a composite material made with cement, aggregates, admixtures and water [2]. There are several individual compounds like tricalcium silicate, dicalcium silicate, etc. which are used to form cement (Portland cement). Cement is the active constituent of concrete, which influences most properties like durability, strength, etc. of concrete. Concrete is the most widely and commonly used construction material [3] with its demand still rising as developing countries continue to improve their infrastructure.

This brings in the need for materials which can be used to reduce the production of cement and work as materials, which can be used as mixtures replacing cement or reducing the ratio of cement used per unit by using more of these supplementing materials.

## 2 Mineral Admixtures with Cement

Many materials are used and added to cement paste in order to increase the compressive strength and other physicochemical properties of concrete [4]. Many industries like agricultural industry produce waste products which can be used in place of either aggregates or cement to reduce cost or to increase the strength or durability of the concrete. This is one of the best ways to reduce the carbon induced by cement production. The use of such materials, not only serves as a less costly method but also as an eco-friendly method too. As an effect these methods bring about multiple variations in the durability and mechanical properties of concrete.

(A) **Fly ash**

Fly ash is obtained as a bi-product formed by the combustion of coal, at power-plants. It contains many minerals and oxides like calcium oxide, silica, etc. [5]. There are two kinds of fly ash, C-type and F-type. Both are different in terms of the content of calcium and only C-type has cementation properties.

(B) **Silica fume**

Silica fume is a waste bi-product, formed during the production of silicon. This is obtained by quartz reduction of coal in the electric arc furnace [6]. The major component of silica fume is silicon dioxide ($SiO_2$). Silica fume is used in order to prevent the corrosion of steel in coastal regions.

(C) **Rice husk ash**

Rice husk, which is also called as rice hull, is obtained from the milling of the paddy and is used as a fuel. When burnt, it leaves ashes, again rich in silica (more than 80%) [7]. Because of that, it too has the permeability properties and hence it's also used in coastal areas mainly to increase the strength and durability of the concrete.

(D) **Ground granulated blast furnace slag**

GGBS is an extracted product from the steam obtained inside the blast furnace. It can also be obtained from the molten slag which is dampened inside water. From all the different types of GGBS found, granulated slag is the most prominently used one. GGBS helps in increasing the compressive strength of the concrete [8].

(E) **Palm oil fuel ash**

POFA is a natural agricultural waste, generated during the burning of leftovers of palm kernels in chimneys. They are burnt to a temperature of 842 F. The ratio of palm oil produced to the ratio of dry-mass is said to be 1:4. The incorrect disposal of palm oil leads to many environmental issues and those are reduced with the usage of POFA in concrete. POFA is used in many structures requiring strong holders and tall skyscrapers [9].

(F) **Metakaolin**

Metakaolin is a material which has a particle size smaller than that of cement. This is obtained by calcination of kaolinite and is also known as calcined clay. Although it is obtained in a process similar to cement, it is obtained at a temperature range from 700 to 900 °C while cement requires nearly double. The pozzolanic quality of metakaolin is very good and due to that it helps in increasing the strength of cement.

(G) **Geopolymer concrete with mineral admixtures**

Geopolymer cement is an alternative binder used instead of OPC in some places and it is considered to be better for the environment, since it relies on products and materials which are minimally processed and hence reduce the carbon footprint [10]. Geopolymer is also a much stronger and more durable option but it also is more difficult to work with, given its property of fast setting.

Geopolymer concrete mixtures are formed with fly ash, rock-based geopolymers, etc.

## 3 Models Used

There have been various researches in similar fields using chemical lab tests or machine learning and neural networks. For this review, most of the research focussed on are the technically advanced machine learning and neural network derived experiments. Researchers have used basic machine learning algorithms like univariate and multivariate linear regressions, random forest and basic cross-validation techniques to train their models [11–17]. These basic machine learning algorithms have some limitations and that's where the need arises for models which are more advanced and can be used to solve complex problems with larger datasets. In such cases, we use neural networks and different modifications are done in order to fine-tune a solution [18–47, 80–84].

### 3.1 Machine Learning

Machine learning refers to the study of algorithms and tendency of a system to learn from experience and data and improve the decision-making capability automatically as it trains the model. This is derived from basic statistical analysis to find patterns in a set of massive data. Machine learning algorithms like linear regression, statistical analysis, SVM, random forest, etc. have been exceedingly used for the last so many years in various industries including construction industry. Koya et al. [11] in their research compared the performance of multivariate linear regression, SVM, decision tree, etc. in terms of predicting compressive strength and other mechanical properties of concrete while Nilsen et al. [12] in their research compared MVLR with random

**Fig. 1** (**a**) Linear regression (**b**) Support vector machines



(a) (b)
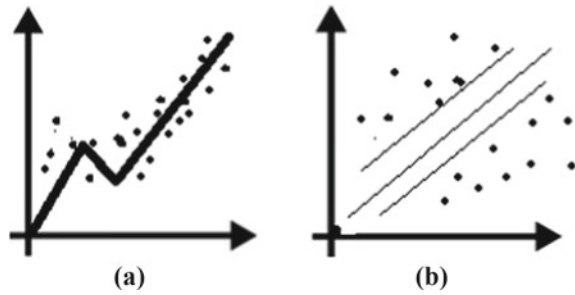
forest, worked in the same direction and got similar results that even though MVLR gave respectable predictions, it was still behind SVM, random forest, etc. in terms of the RMSE values, and hence lesser efficient. Mahamat et al. [15] in their research on the compressive strength of termite mound soil (TMS) put emphasis on the fact that ML techniques have helped in predicting outputs with the input, without knowing other correlations with high accuracy.

1. **Linear Regression**: This method, as the name suggests provides a linear relation between two (regular linear regression) or more (multiple linear regression) giving out a scalar value or multiple co-related variable values (multivariate linear regression). The main objective of this method is to provide a specific numerical output for variables which may or may not be dependent. The hypothesis of such a model revolves around one or more linear equations (See Fig. 1a).

2. **Support Vector Machines:** Support vector machine method is used for both regression and classification problems. This method works on the basis of maximizing the margin between the support vectors and the hyperplane. It also works well when a linear hyperplane is not possible.

## 3.2 Neural Networks

Neural networks are a subclass of ML and are used to solve complex problems with larger datasets. They are in some scenarios better than ML algorithms since they can make intelligent decisions on their own, while in ML decisions are made based on what it has learned only. Neural networks are composed of nodes and different hidden layers [18] ANN provides better output efficiency when compared with regression models since changing the weight in regression does not impact inputs of other functions, while in ANN the output from one layer is passed on as input to another and hence it brings about a lot of effect [21]. Moradi et al. used ANFIS, FL and MVLR in their research to compare the effect of Metakaolin as supplementary cementitious material (SCM) where they compared the 7-day compressive strength model with the 28-day compressive strength model. They also concluded that ANN with group

**Fig. 2** ANN

Functioning of Neural Network
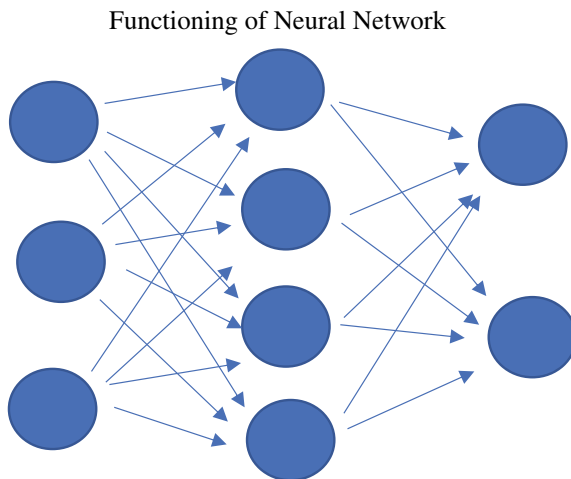


method of data handling (GMDH) model gave a higher accuracy and worked well with the complex system.

3. **ANN**: Artificial neural networks are the methods of classification derived from the biological concept of neural networks, connected with each other in various layers of a network. ANN offers features like parallel processing, data storage, memory distribution, etc. There are different types like feedforward, back propagation, etc., which are used (See Fig. 2a).

Backpropagation neural network (BPNN) was employed for instance to forecast the compressive strength of high-performance concrete (HPC) [36–38]. Referring to Table 1, we can see that most of the studies that have taken place in the past have used or concluded in their results, that ANN or hybrid models of ANN like ANFIS have been more efficient in terms of prediction accuracy and have shown similar results over generalized datasets too.

In their approach, Kasperkiewicz et al. [48] concluded that their model can be used to optimize the properties of design mixes. This could also help in keeping in control the lines of produce at factories continuously manufacturing cement. Pala et al. [49] in their research provided results proving that neural networks can be used to predict the long-term effects of supplementary cementitious products on CS of concrete. In their combined research about SCC and HPC's compressive strength, Prasad et al. [50] used the same dataset used to train an ANN model for SCC in training HPC as well, to reduce computational effort. This is still provided with a decently efficient prediction model for both, since the main components that influence the compressive strength of concrete are water/cement, cement ratio, water/powder ratio and not the other admixtures.

**Table 1** Research analysis: performance of various machine learning/neural network models

| S. no | Model used | Concrete, Pozzolan | Brief conclusion | References |
|---|---|---|---|---|
| 1 | ANN (BPNN), fuzzy logic (ARTMAP) | High-performance concrete (HPC), silica fume | ARTMAP performed better than BPNN | [48] |
| 2 | ANN | HPC, fly ash and GGBS | Even though ANN is time consuming, it depicts promising results | [44] |
| 3 | Linear model, ANN | Fly ash | Application of ANN brings out better performance than traditional linear model due to complex relations b/w variables | [51] |
| 4 | ANN | Low and high strength concrete, fly ash | ANN works well in discovering the effect of different factors and their interactions | [52] |
| 5 | ANN (BPNN, MLP) | Fly ash, silica fume | Long-term effect of cementitious materials on the compressive strength of cement can be evaluated | [49] |
| 6 | ANN, fuzzy logic | Fly ash | Showed the practicality of using ANN, FL instead of lab experiments, with small amount of time and error rates | [53] |
| 7 | ANN | Self compacting concrete (SCC), HPC, fly ash | Using data available for low volume fly ash SCC, an efficient generalized model was prepared for high volume SCC and HPC | [50] |
| 8 | ANN (BPNN), linear model, BFGS, one step secant backpropagation (OSS) | Ground granulated blast furnace slag (GGBS) | Models can be used to predict the compressive strength of GGBS, with a constant workability | [54] |
| 9 | ANN (BPNN), fuzzy logic | Ground granulated blast furnace slag (GGBS) | By using AI models, the researchers cut back on significant cost to design and predict effective ways to reduce carbon footprint | [55] |
| 10 | Regression, ANN, adaptive network-based fuzzy inference systems (ANFIS) | No slump concrete (NSC), | Satisfactory performance shown by all ANFIS models, with ANM4 (with gaussian membership) showing the best performance | [56] |
| 11 | ANN | Conventional concrete, SCC, fly ash | ANN showed great prediction capabilities of SCC with high correlation coefficient | [57] |

**Table 1** (continued)

| S. no | Model used | Concrete, Pozzolan | Brief conclusion | References |
|-------|------------|--------------------|------------------|------------|
| 12 | ANN, Regression, support vector machine (SVM), multiple additive regression trees (MART) | HPC | Out of all algorithms used MART showed best accuracy with R2 and RMSE methods. MART offered the most efficient predictive results | [58] |
| 13 | ANN (BPNN), cross validation | SCC, bottom ash, fly ash | Neural networks can be relied upon when deviation in the dataset can be expected | [59] |
| 14 | Fuzzy logic, SVM, fast messy genetic algorithms (fmGA), evolutionary fuzzy support vector machine inference model for time series data (EFSIMT), ANN(BPNN) | HPC | In SVM vs EFSIMT, the latter performed significantly better than the other. BPNN and EFSIMT performed well in the training dataset, but during testing, EFSIMT raced ahead | [5] |
| 15 | ANN radial bias function (RBF) | HPC, silica fume, pulverized fuel ash (PFA) | ANN developed could be retrained on a different dataset to be used for another problem | [60] |
| 16 | Non-linear Autoregressive model with exogenous inputs (NARX), ANN (RBF) | HPC, fly ash, slag, silica fume | Material ratios can be predicted using ANN but some trail mixes are important for material variability sometimes | [61] |
| 17 | Support vector regression (SVR), particle swarm optimization (PSO), ANFIS | Metakaolin, OPC (Portland cement) | SVR-PSO outperforms ANFIS in terms of robustness | [62] |
| 18 | K-nearest neighbour (K-NN), generalized regression neural network (GRNN) | Concrete | Model with the best attribute weighing outperforms other models, which is KNNA5 | [63] |

<div align="right">(continued)</div>

**Table 1** (continued)

| S. no | Model used | Concrete, Pozzolan | Brief conclusion | References |
|---|---|---|---|---|
| 19 | Fuzzy logic, ANN | High strength concrete (HSC), coarse aggregate | Fuzzy approach works much better than the ANN, in terms of RMSE and MAE. ANN showed a significant variation in terms of predicted values, while FL results were in a defined range | [64] |
| 20 | Decision tree, ensemble learning, stochastic gradient descent | HPC, fly ash, blast furnace slag | Ensemble models with decision tree as base predictors, performed better than DT alone | [65] |
| 21 | ANN, ensemble NN(BANN), | HPC, fly ash | ANN and ensemble methods combined with ANN (gradient boosting, etc.) are very efficient methods for prediction | [66] |
| 22 | MLP, SVM, classification and regression tree (CART) | HPC | Mixed results with mostly ensemble learning methods with MLP as base method provided respectable predictions. SVM was used as second-level model | [67] |
| 23 | ANN, group method of data handling (GMDH) | Metakaolin | Both models gave promising results over similar datasets | [21] |
| 24 | ANN | Fly ash | ANN model was able to give generalized outputs. When results were simulated, they were dispersed around the bisector | [68] |
| 25 | ANN, ANFIS, multiple nonlinear regression, linear regression | Rice husk ash | ANFIS and ANN exhibited a better result capability than other regression models. (ANN > ANFIS > MNLR > LR, in terms of accuracy) | [69] |
| 26 | ANN(BPNN) | SCC, silica fume | ANN combined with BPNN is found to be more productive than any other ANN algorithm | [70] |
| 27 | ANN, multi-objective salp swarm algorithm (MOSSA) | GGBS, OPC | The accuracy increases with the number of links. M5P model has an error rate double to that of ANN model used | [38] |

(continued)

**Table 1** (continued)

| S. no | Model used | Concrete, Pozzolan | Brief conclusion | References |
|-------|-----------|-------------------|------------------|-----------|
| 28 | ANN | Preformed-foam cellular concrete | ANN model developed provides a powerful tool to predict the performance and can therefore assist contractors in meeting the real-world expectations | [71] |
| 29 | ANN, regression | SCC, fly ash, silica fume, limestone powder | The results illustrated the possibility to use ANN and ML to evaluate variable values for best results | [72] |
| 30 | ANN, ANFIS, grey wolf optimizer (GWO) | Normal concrete (NC), HPC | Hybridization of ANN and ANFIS with GWO enhanced the predictive capabilities of the individual models | [35] |
| 31 | Linear and nonlinear SVM | SCC, fly ash | The importance of using the correct features and parameters was examined. Nonlinear SVM using RBF kernel was seen to be very efficient | [73] |
| 32 | ANN (BPNN) | Construction and demolition waste (CDW) | A relation between input parameters and response variable was formed. PCA helped in finding the accurate parameters for the model | [74] |
| 33 | ANN (BPNN), multiple regression, | GGBS, fly ash | ANN had better performance than MRA | [75] |
| 34 | ANN (GA-BPNN), ANFIS | Fly ash, GGBS | ANFIS performed very well and gave outputs, confirming it can be used without dealing complex calculations | [6] |
| 35 | Extreme learning machine (ELM), single layer feed-forward network (SLFN), MARS, M5 Tree | Lightweight foamed concrete | ELM gives the best predictive accuracy among the four models compared. Since the tool used is flexible, it makes it a great candidate for real-world use for engineers in construction world | [76] |
| 36 | ANFIS, ANN (BPNN) | Geopolymer concrete (GPC) | Both ANFIS and ANN-BPNN gave compelling results with little or no variation in the statistical comparison with the performance of the two models | [32] |

(continued)

**Table 1** (continued)

| S. no | Model used | Concrete, Pozzolan | Brief conclusion | References |
|---|---|---|---|---|
| 37 | ANN (BPNN), MP5, MLP, LR | HPC, GGBS, fly ash | The results show that although all models performed decently, M5P performed the best and gave an output that was flexible and accurate. (Trend-line analysis, RMSE, etc. were used) | [77] |
| 38 | MRA-(BPNN), LR, ANN | HPC, fly ash | ANN models perform better than LR. ANN models exhibit very low RMSE and MAP values. LR can be used for preliminary mix design calculations but ANN must be used for complex operations | [78] |
| 39 | MVLR, ANN, fuzzy logic, ANFIS | Normal concrete | ANN and ANFIS performed better than the simple LR and among all the algorithms, ANN performed the best. The sensitivity analysis also displayed the importance of input variables in terms of finding the right CS. Higher number of input parameters ~ higher accuracy | [79] |

## 4 Conclusion

In this paper, a critical review of previous experiments, where machine learning or advanced neural networks have been used for predicting compressive strength of concrete formed by using different materials other than cement has been done. This review has been done in order to focus on the impacts of computing compressive strength of concrete using software-oriented techniques that don't involve performing physical experiments, which save lots of time and resources.

Most of the reviewed studies have had a similar conclusion about using ML and ANN or hybrid ANN models for predicting compressive strength of concrete when used along several other materials supplementing or replacing some ratio of cement content in concrete structures, i.e. machine learning algorithms provide quick and efficient prediction models, but they work well with simple problem statements with relatively small or non-complex datasets. The problem arises here when more parameters are being considered or multi-feature dependent models are required, and traditional machine learning models are unable to cope up with the complexity of the datasets. There arises the need for hybrid machine learning algorithms (e.g. MART), ensemble learning methods and advanced neural networks. Chou et al. [58] in their research concluded that ML algorithms are outperformed by ensemble

learning models in most cases in terms of prediction accuracy. Basic ML algorithms take less time to extrapolate information from data but they only work well on some scenarios. As and when the complexity of the dataset increases, more hidden layers are added to the neural network to increase prediction accuracy [38]. After critical review of the RMSE, MAPE and $R^2$ values of different models on different datasets, most of the studies highlight the importance of hybridization of traditional models and forming of ensemble learning models for acquiring a higher prediction accuracy. Golafshani et al. [35] developed six hybrid ANN models using three different training algorithms (i.e. GD with Momentum and ALR (GDMALR), CG Fletcher-Reeves (CGFR), Levenberg–Marquardt (LM)) while using GWO over it for optimization which helped in increasing the efficiency of predicting compressive strength of the concrete over the traditional models. Their research highlighted the importance of meta-heuristic algorithms for better optimization in the training phase of neural network models which gives more reliable results.

Over time a lot of research has taken place and many knowledge gaps from the above reviewed research papers have been covered, which shows the rise in influence of software techniques in the construction industry. Still, there is not one best method to compute the compressive strength of concrete, because each problem statement requires a different approach for solution. For predicting the compressive strength of concrete formed by using materials that have been previously experimented on or materials with similar chemical properties, we can use software techniques like machine learning and neural networks. But there are still a few materials which require more experiments to take place in labs, so that more data can be collected and used for training prediction models.

# References

1. Turner LK, Collins FG (2013) Carbon dioxide equivalent ($CO_2$-e) emissions: a comparison between geopolymer and OPC cement concrete. Constr Build Mater 43:125–130
2. Ramachandran VS, Feldman RF (1996) Concrete science. In Concrete admixtures handbook. William Andrew Publishing, pp 1–66
3. Shah MI, Memon SA, Niazi KMS, Amin MN, Aslam F, Javed MF (2021) Machine learning-based modeling with optimization algorithm for predicting mechanical properties of sustainable concrete. Adv Civil Eng
4. Sabater C, Calvete-Torre I, Villamiel M, Moreno FJ, Margolles A, Ruiz L (2021) Vegetable waste and by-products to feed a healthy gut microbiota: current evidence, machine learning and computational tools to design novel microbiome-targeted foods. Trends Food Sci Technol 118:399–417
5. Cheng MY, Chou JS, Roy AF, Wu YW (2012) High-performance concrete compressive strength prediction using time-weighted evolutionary fuzzy support vector machines inference model. Autom Constr 28:106–115
6. Yuan Z, Wang LN, Ji X (2014) Prediction of concrete compressive strength: research on hybrid models genetic based algorithms and ANFIS. Adv Eng Softw 67:156–163
7. Khoso S, Keerio AM, Ansari AA, Khan JS, Bangwar KD (2017) Effect of rice husk ash and recycled aggregates on mechanical properties of concrete. Int J Sci Eng Res 8:1832–1835

8. Jagtap SA, Shirsath MN, Karpe SL (2017) Effect of metakaolin on the properties of concrete. Int Res J Eng Tech 4(7):643–645

9. Raju OHR, Singam PSR, Raju OHR (2017) An experimental investigation on partial replacement of cement with metakaolin and fine aggregate with robo sand. Int Res J Eng Technol 4(4):1169–1173

10. Hasnaoui A, Ghorbel E, Wardeh G (2019) Comparison between Portland cement concrete and geopolymer concrete based on metakaolin and granulated blast furnace slag with the same binder volume. Acad J Civil Eng 37(2):127–132

11. Koya BP, Aneja S, Gupta R, Valeo C (2021) Comparative analysis of different machine learning algorithms to predict mechanical properties of concrete. Mech Adv Mat Struct, 1–18

12. Nilsen V, Pham LT, Hibbard M, Klager A, Cramer SM, Morgan D (2019) Prediction of concrete coefficient of thermal expansion and other properties using machine learning. Constr Build Mater 220:587–595

13. Bonifácio AL, Mendes JC, Farage MC, Barbosa FS, Barbosa CB, Beaucour AL (2019) Application of support vector machine and finite element method to predict the mechanical properties of concrete. Latin Am J Solid Struct, 16

14. Bonifácio AL, Mendes JC, Farage MCR, Barbosa FDS, Beaucour AL (2020) Predicting the mechanical properties of lightweight aggregate concrete using finite element methods. Revista IBRACON de Estruturas e Materiais, 13

15. Mahamat AA, Boukar MM, Ibrahim NM, Stanislas TT, Linda Bih N, Obianyo II, Savastano H (2021) Machine learning approaches for prediction of the compressive strength of alkali activated termite mound soil. Appl Sci 11(11):4754

16. Bayar G, Bilir T (2019) A novel study for the estimation of crack propagation in concrete using machine learning algorithms. Constr Build Mater 215:670–685

17. Koya BP (2021) Comparison of different machine learning algorithms to predict mechanical properties of concrete

18. Paji MK, Gordan B, Biklaryan M, Armaghani DJ, Zhou J, Jamshidi M (2021) Neuro-swarm and neuro-imperialism techniques to investigate the compressive strength of concrete constructed by freshwater and magnetic salty water. Measurement, 109720

19. Chen X, Gruyaert E, Li J (2021) Modelling the effect of coarse recycled concrete aggregate on compressive strength of Portland cement concrete using volume fraction-based approach. Constr Build Mater 309:125159

20. Nunez I, Marani A, Flah M, Nehdi ML (2021) Estimating compressive strength of modern concrete mixtures using computational intelligence: a systematic review. Constr Build Mater 310:125279

21. Moradi MJ, Khaleghi M, Salimi J, Farhangi V, Ramezanianpour AM (2021) Predicting the compressive strength of concrete containing metakaolin with different properties using ANN. Measurement 183:109790

22. Murad Y (2021) Compressive strength prediction for concrete modified with nanomaterials. Case Stud Const Mat 15:e00660

23. Asteris PG, Skentou AD, Bardhan A, Samui P, Lourenço PB (2021) Soft computing techniques for the prediction of concrete compressive strength using Non-Destructive tests. Constr Build Mater 303:124450

24. Zhao K, Zhao L, Hou J, Zhang X, Feng Z, Yang S (2021) Effect of vibratory mixing on the slump, compressive strength, and density of concrete with the different mix proportions. J Market Res 15:4208–4219

25. Aryal R, Mishra AK (2020) In-situ compressive strength assessment of concrete in under-construction residential buildings at Gaindakot municipality. Mat Today: Proceed

26. Orouji M, Zahrai SM, Najaf E (2021) Effect of glass powder & polypropylene fibers on compressive and flexural strengths, toughness and ductility of concrete: an environmental approach. In Structures. Elsevier, vol 33, pp 4616–4628

27. Shen W, Wu M, Zhang B, Xu G, Cai J, Xiong X, Zhao D (2021) Coarse aggregate effectiveness in concrete: quantitative models study on paste thickness, mortar thickness and compressive strength. Constr Build Mater 289:123171

28. Zhang X, Akber MZ, Zheng W (2021) Prediction of seven-day compressive strength of field concrete. Constr Build Mater 305:124604
29. Gupta M, Raj R, Sahu AK (2021) Effect of rice husk ash, silica fume & GGBFS on compressive strength of performance-based concrete. Mat Today: Proceed
30. Ly HB, Nguyen TA, Tran VQ (2021) Development of deep neural network model to predict the compressive strength of rubber concrete. Constr Build Mater 301:124081
31. Duan J, Asteris PG, Nguyen H, Bui XN, Moayedi H (2021) A novel artificial intelligence technique to predict compressive strength of recycled aggregate concrete using ICA-XGBoost model. Eng Comp 37(4):3329–3346
32. Dao DV, Ly HB, Trinh SH, Le TT, Pham BT (2019) Artificial intelligence approaches for prediction of compressive strength of geopolymer concrete. Materials 12(6):983
33. Dao DV, Trinh SH, Ly HB, Pham BT (2019) Prediction of compressive strength of geopolymer concrete using entirely steel slag aggregates: novel hybrid artificial intelligence approaches. Appl Sci 9(6):1113
34. Song H, Ahmad A, Farooq F, Ostrowski KA, Maślak M, Czarnecki S, Aslam F (2021) Predicting the compressive strength of concrete with fly ash admixture using machine learning algorithms. Constr Build Mater 308:125021
35. Golafshani EM, Behnood A, Arashpour M (2020) Predicting the compressive strength of normal and high-performance concretes using ANN and ANFIS hybridized with grey wolf optimizer. Constr Build Mater 232:117266
36. Feng DC, Liu ZT, Wang XD, Chen Y, Chang JQ, Wei DF, Jiang ZM (2020) Machine learning-based compressive strength prediction for concrete: an adaptive boosting approach. Constr Build Mater 230:117000
37. Dao DV, Ly HB, Vu HLT, Le TT, Pham BT (2020) Investigation and optimization of the C-ANN structure in predicting the compressive strength of foamed concrete. Materials 13(5):1072
38. Kandiri A, Golafshani EM, Behnood A (2020) Estimation of the compressive strength of concrete containing ground granulated blast furnace slag using hybridized multi-objective ANN and salp swarm algorithm. Constr Build Mater 248:118676
39. Han IJ, Yuan TF, Lee JY, Yoon YS, Kim JH (2019) Learned prediction of compressive strength of GGBFS concrete using hybrid artificial neural network models. Materials 12(22):3708
40. Ngo HTT, Pham TA, Vu HLT, Giap LV (2021) Application of artificial intelligence to determined unconfined compressive strength of cement-stabilized soil in Vietnam. Appl Sci 11(4):1949
41. Dao DV, Adeli H, Ly HB, Le LM, Le VM, Le TT, Pham BT (2020) A sensitivity and robustness analysis of GPR and ANN for high-performance concrete compressive strength prediction using a Monte Carlo simulation. Sustainability 12(3):830
42. Setiawan AA, Soegiarso R, Hardjasaputra LH, State of the art of deep learning method to predict the compressive strength of concrete
43. Duan ZH, Kou SC, Poon CS (2013) Prediction of compressive strength of recycled aggregate concrete using artificial neural networks. Constr Build Mater 40:1200–1206
44. Yeh IC (1998) Modeling concrete strength with augment-neuron networks. J Mater Civ Eng 10(4):263–268
45. Moreno T, Pintó RM, Bosch A, Moreno N, Alastuey A, Minguillón MC et al (2021) Tracing surface and airborne SARS-CoV-2 RNA inside public buses and subway trains. Environ Int 147:106326
46. Chouhan P, Jamle S, Verma MP (2017) Experimental investigation on silica fume as partial replacement of cement for M-25 grade concrete. Int J Sci Adv Res Technol 3(5):714–717
47. Talsania S, Pitroda J, Vyas CM (2015) Effect of rice husk ash on properties of pervious concrete. Int J Adv Eng Res Studies/IV/II 296:299
48. Kasperkiewicz J, Racz J, Dubrawski A (1995) HPC strength prediction using artificial neural networks. J Comput Civ Eng 9(4):279–284
49. Pala M, Özbay E, Öztaş A, Yuce MI (2007) Appraisal of long-term effects of fly ash and silica fume on compressive strength of concrete by neural networks. Constr Build Mater 21(2):384–394

50. Prasad BR, Eskandari H, Reddy BV (2009) Prediction of compressive strength of SCC and HPC with high volume fly ash using ANN. Constr Build Mater 23(1):117–128
51. Sebastiá M, Olmo IF, Irabien A (2003) Neural network prediction of unconfined compressive strength of coal fly ash–cement mixtures. Cem Concr Res 33(8):1137–1146
52. Yeh IC (2006) Analysis of strength of concrete using design of experiments and neural networks. J Mater Civ Eng 18(4):597–604
53. Topcu IB, Sarıdemir M (2008) Prediction of compressive strength of concrete containing fly ash using artificial neural networks and fuzzy logic. Comput Mater Sci 41(3):305–311
54. Bilim C, Atiş CD, Tanyildizi H, Karahan O (2009) Predicting the compressive strength of ground granulated blast furnace slag concrete using artificial neural network. Adv Eng Softw 40(5):334–340
55. Sarıdemir M, Topçu İB, Özcan F, Severcan MH (2009) Prediction of long-term effects of GGBFS on compressive strength of concrete by artificial neural networks and fuzzy logic. Constr Build Mater 23(3):1279–1286
56. Sobhani J, Najimi M, Pourkhorshidi AR, Parhizkar T (2010) Prediction of the compressive strength of no-slump concrete: a comparative study of regression, neural network and ANFIS models. Constr Build Mater 24(5):709–718
57. Uysal M, Tanyildizi H (2011) Predicting the core compressive strength of self-compacting concrete (SCC) mixtures with mineral additives using artificial neural networks. Constr Build Mater 25(11):4105–4111
58. Chou JS, Chiu CK, Farfoura M, Al-Taharwa I (2011) Optimizing the prediction accuracy of concrete compressive strength based on a comparison of data-mining techniques. J Comput Civ Eng 25(3):242–253
59. Siddique R, Aggarwal P, Aggarwal Y (2011) Prediction of compressive strength of self-compacting concrete containing bottom ash using artificial neural networks. Adv Eng Softw 42(10):780–786
60. Khan MI (2012) Predicting properties of High-Performance Concrete containing composite cementitious materials using Artificial Neural Networks. Autom Constr 22:516–524
61. Khan MI (2012) Mix proportions for HPC incorporating multi-cementitious composites using artificial neural networks. Constr Build Mater 28(1):14–20
62. Gilan SS, Jovein HB, Ramezanianpour AA (2012) Hybrid support vector regression–particle swarm optimization for prediction of compressive strength and RCPT of concretes containing metakaolin. Constr Build Mater 34:321–329
63. Ahmadi-Nedushan B (2012) An optimized instance based learning algorithm for estimation of compressive strength of concrete. Eng Appl Artif Intell 25(5):1073–1081
64. Aggarwal P, Aggarwal Y, Siddique R, Gupta S, Garg H (2013) Fuzzy logic modeling of compressive strength of high-strength concrete (HSC) with supplementary cementitious material. J Sustain Cement-Based Mat 2(2):128–143
65. Erdal HI (2013) Two-level and hybrid ensembles of decision trees for high performance concrete compressive strength prediction. Eng Appl Artif Intell 26(7):1689–1697
66. Erdal HI, Karakurt O, Namli E (2013) High performance concrete compressive strength forecasting using ensemble models based on discrete wavelet transform. Eng Appl Artif Intell 26(4):1246–1254
67. Chou JS, Tsai CF, Pham AD, Lu YH (2014) Machine learning in concrete strength simulations: multi-nation data analytics. Constr Build Mater 73:771–780
68. Roshani MM, Kargar SH, Farhangi V, Karakouzian M (2021) Predicting the effect of fly ash on concrete's mechanical properties by ann. Sustainability 13(3):1469
69. Iqtidar A, Bahadur Khan N, Kashif-ur-Rehman S, Faisal Javed M, Aslam F, Alyousef R et al (2021) Prediction of compressive strength of rice husk ash concrete through different machine learning processes. Crystals 11(4):352
70. Serraye M, Kenai S, Boukhatem B (2021) Prediction of compressive strength of self-compacting concrete (SCC) with silica fume using neural networks models. Civil Eng J 7(1):118–139

71. Nehdi M, Djebbar Y, Khan A (2001) Neural network model for preformed-foam cellular concrete. Mat J 98(5):402–409
72. Elemam WE, Abdelraheem AH, Mahdy MG, Tahwia AM (2020) Optimizing fresh properties and compressive strength of self-consolidating concrete. Constr Build Mater 249:118781
73. Azimi-Pour M, Eskandari-Naddaf H, Pakzad A (2020) Linear and non-linear SVM prediction for fresh properties and compressive strength of high volume fly ash self-compacting concrete. Constr Build Mater 230:117021
74. Dantas ATA, Leite MB, de Jesus Nagahama K (2013) Prediction of compressive strength of concrete containing construction and demolition waste using artificial neural networks. Constr Build Mater 38:717–722
75. Atici U (2011) Prediction of the strength of mineral admixture concrete using multivariable regression analysis and an artificial neural network. Expert Syst Appl 38(8):9609–9618
76. Yaseen ZM, Deo RC, Hilal A, Abd AM, Bueno LC, Salcedo-Sanz S, Nehdi ML (2018) Predicting compressive strength of lightweight foamed concrete using extreme learning machine model. Adv Eng Softw 115:112–125
77. Deepa C, SathiyaKumari K, Sudha VP (2010) Prediction of the compressive strength of high-performance concrete mix using tree based modeling. Int J Comp Appl 6(5):18–24
78. Chithra S, Kumar SS, Chinnaraju K, Ashmita FA (2016) A comparative study on the compressive strength prediction models for high performance concrete containing nano silica and copper slag using regression analysis and Artificial Neural Networks. Constr Build Mater 114:528–535
79. Khademi F, Akbari M, Jamal SM, Nikoo M (2017) Multiple linear regression, artificial neural network, and fuzzy logic prediction of 28 days compressive strength of concrete. Front Struct Civ Eng 11(1):90–99
80. Chaabene WB, Flah M, Nehdi ML (2020) Machine learning prediction of mechanical properties of concrete: critical review. Const Building Mat 260:119889.ces
81. Kosmatka SH, Kerkhoff B, Panarese WC (2002) Design and control of concrete mixtures. Portland Cement Association, Skokie, IL, Vol 5420, pp 60077–1083
82. Kanamarlapudi L, Jonalagadda KB, Jagarapu DCK, Eluru A (2020) Different mineral admixtures in concrete: a review. SN Appl Sci 2(4):1–10
83. Uysal M, Tanyildizi H (2012) Estimation of compressive strength of self-compacting concrete containing polypropylene fiber and mineral additives exposed to high temperature using artificial neural network. Constr Build Mater 27(1):404–414
84. Yeh IC (1998) Modeling of strength of high-performance concrete using artificial neural networks. Cem Concr Res 28(12):1797–1808

# On a Universal Failure Criterion for Brittle Materials

**Ahmed Ahmed, George Iskander, and Nigel Shrive**

**Abstract**  To date, there is no universally accepted comprehensive explanation of brittle fracture in compressive stress fields. Researchers have developed many theories for brittle fracture, each of which is only applicable to particular materials and stress states. Additionally, some of these theories are based on questionable assumptions. A generalized fracture-based criterion should rationally explain brittle material behaviour across all stress states, providing unity in a poorly understood field. Visible crack formation implies the existence of tension to separate the surfaces. In the literature, there is no consensus on the source of these tensile stresses in compressive stress fields. Various sources of tensile stresses in compression are surveyed, with voids being found to be the most critical. Having identified the key source of tension, a way of predicting crack propagation is sought. Previously unsuccessful treatments of void-induced compressive fracture are examined, then a highly simplified way of quantifying the stress intensity factor ($K_I$) in compressive fracture is proposed. The simplification is validated against numerically calculated $K_I$ values for circular and rhomboidal voids of different sizes. In addition to the numerical efficiency of the simplified calculation, the simplification defines a function $\sigma(a)$ which can be used to explain and predict various compressive fracture phenomena which are counter-intuitive from a typical Griffith-type explanation.

**Keywords**  Failure criterion · Masonry · Compressive fracture

## 1 Contemporary Treatment of Brittle Material Behaviour in Compression—The Need for a Unified Approach

Full, general characterization of the behaviour of brittle materials under compression has eluded the scientific community. For example, the broad diversity of failure theories for masonry under different loads illustrates this situation well. Hilsdorf [1]

A. Ahmed (✉) · G. Iskander · N. Shrive
Department of Civil Engineering, University of Calgary, Calgary, AB, Canada
e-mail: ahmed.ahmed1@ucalgary.ca

and Khoo [2] provide failure criteria based on the idea that in brickwork compressed uniaxially normal to the bedding plane, the bricks are under compression-biaxial tension since they confine the lateral expansion of the softer mortar. Completely independently of Hilsdorf and Khoo's ideas, Mann and Muller [3] instead propose a Mohr–Coulomb type failure criterion for brickwork under combined compression and shear, such as would be present in a shear wall. On yet another isolated trail of thought, Baker [4] provides a principal stress failure criterion for load cases involving compression and biaxial moment. Such a diversity of concepts should not exist for the same material.

On a more general note, tensile testing in concrete lacks unity. Direct tension tests are practically difficult, strain gradient effects cloud the values obtained from Modulus of Rupture tests, and Brazilian tests are unique in their boundary conditions and induced stresses. It is surprising that there is no standardized way to obtain a "true" or "representative" tensile strength of concrete.

The current state of affairs appears quite illogical when there is a clear, common physical reality observed in the failures of all brittle materials: the formation of cracks. Near-identical crack patterns are observed in different brittle materials when load type, boundary conditions, and geometry are kept constant. Shrive and El-Rahman [5] noted that uniaxially compressed cylinders of similar aspect ratios made of glass, sulphur mortar, and concrete had similar crack patterns; they also note that, under similar loading, the crack patterns for masonry noted by Page are similar to those for plain concrete of similar dimensions reported by Vile. They further note that, under triaxial compression, rock and plain concrete behave similarly, according to reports by Bridgman and Akroyd, respectively. These similarities strongly point to a more fundamental underlying phenomenon that begs characterization.

There is clear consensus on the fact that "failure" of brittle materials is characterized by the common phenomenon of the formation and propagation of cracks. Investigation of the physical requirements of crack initiation and propagation seems a reasonable step towards a unified understanding of brittle material failure in compressive stress states.

## 2 Cracking Fundamentals and Requirements for Compressive Failure Criteria

### 2.1 Fracture Fundamentals—The Need for Tension and Griffith's Criteria

The very formation of a visible crack reveals a fundamental truth. For a crack to be visible, the two surfaces must have separated. Put simply: the formation of a visible crack implies the presence of tensile stress at the location of the crack, regardless of the macroscopically applied stress. The crack surfaces may additionally displace in a shearing mode, but the visibility of the crack produced by normal displacement

**Fig. 1** The bond force vs. interatomic spacing curve. Bond force has no maximum value in compression—tension is necessary to break interatomic bonds
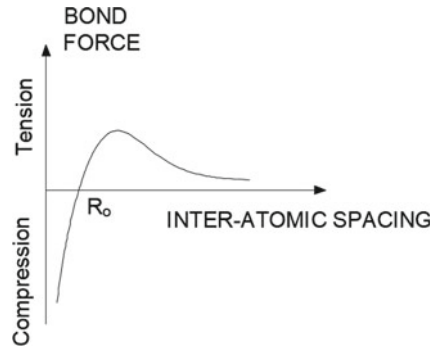


guarantees the presence of tensile stress that pulled the surfaces apart. That tension is necessary to cause cracks is, again, a proposition worth emphasizing: consideration of the interatomic bond force vs. separation curve [6] shown in Fig. 1, shows it is impossible to break a bond via compression—only tension can break the bond. This condition is empirically exemplified by the "plastic flow" observed in brittle materials when subjected to high hydrostatic pressure [7].

Griffith [8] investigated the development of cracks in brittle materials subjected to a macroscopically uniaxial tensile stress field. He proposed that tensile stresses magnified by flaws in materials drove fracture, overcoming interatomic bond strengths.

Further, Griffith [8] proposed cracks would form and propagate when two criteria were simultaneously met:

1. **Stress criterion**: The tensile stress at the location in question must be high enough to break the interatomic bonds of the material, which we will denote as $\sigma_{cr}$.
2. **Energy criterion**: The overall rate of change of energy ("energy release rate") caused by crack extension is zero—in other words, upon incremental crack extension, the strain energy released can satisfy the energy demands of crack growth. The threshold energy for incremental crack growth will be denoted as $G_{cr}$.

## 2.2 Application of Fracture Fundamentals in Uniaxial Compression

Griffith's principles have been thoroughly fleshed out in cases of uniaxial tension. However, many of these developments cannot be directly translated to the case of uniaxial compression. Two factors complicate the application of these principles in compression: the need for a more rigorous treatment of flaw geometry, and ambiguities in determining tensile stresses.

Assumptions of flaw orientation and dimension typical in uniaxial tensile formulations based on Griffith's ideas are incongruent with uniaxial compressive requirements [7]. In uniaxial tension, a flaw can be modelled as a one-dimensional crack

**Fig. 2** Stress contours
sketched in the case of (i) a
one-dimensional crack
perpendicular to a field of
uniaxial tension, and (ii) a
one-dimensional crack
parallel to a field of uniaxial
compression
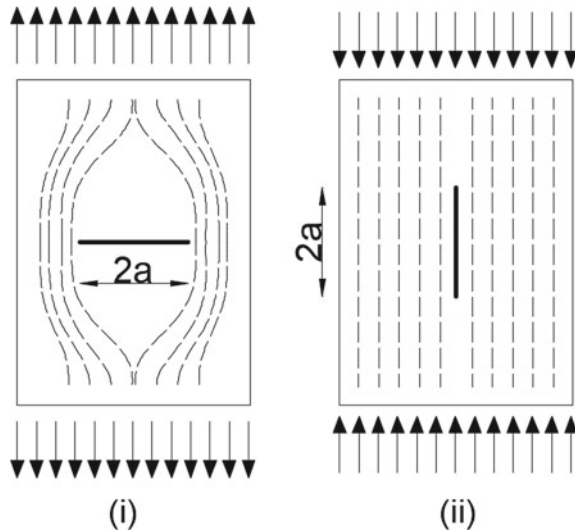


normal to the direction of applied stress: stresses at crack tips approach infinity (automatically satisfying the stress criterion), and an energy release rate can be calculated on the basis of the propagation of such a crack. However, in compression, observed cracks are not orthogonal to the applied stress—rather, they are in line with the applied stress. To make matters worse, propagation of an infinitely thin line crack in a continuum subject to uniaxial compression cannot result in the release of strain energy (as shown by the crude stress contours in Fig. 2); analysis of a one-dimensional crack thus precludes satisfaction of the energy criterion. A crack must be at least two-dimensional to induce strain energy release in compression. Naturally, this affects stress and energy criteria calculations.

A more fundamental issue is the presence of tension in the stress field itself. Where does tension arise from in a uniaxially compressive stress field?

## 2.3 Sources of Tension

Sources of tension generated in a uniaxial compressive stress field can be considered to fall in two categories:

1. **Universal sources**: Universal sources are ones which are understood to produce tensile stresses in all materials. For example, ellipsoidal voids, which are known to exist in virtually all brittle materials [9], have analytically [10] [11] and numerically [7, 12] been shown to produce tensile stresses in compressive stress states.
2. **Particular sources**: Particular sources are ones which cannot be generalized among all materials—they are a function of the brittle material's unique features

and composition. For example, Hilsdorf [1] notes that as a composite of relatively stiff bricks and relatively flexible mortar, in a compression test the bricks in masonry prisms are under compression and biaxial tension, whereas the mortar is subject to a state of triaxial compression.

In the most general sense, we may now say the following: brittle failure in any macroscopic stress state is caused by the development of tensile stresses, which may arise from particular or universal sources. Determination of the relative contribution of particular and universal sources to developed tensile stresses is, no doubt, vital to an accurate assessment of a given scenario.

## 3 Assessing Contributions of Tensile Stress Sources in Concrete and Masonry

### 3.1 Universal Sources—Voids

Voids are the only universal source considered in this paper. The presence of voids is well-known in concrete in particular and in brittle materials in general [9]; as previously discussed, voids/flaws disturb stress fields and can potentially produce tension. The consideration of the influence of voids is itself not straightforward. Meaningful analytic quantification of the extent to which singular voids and systems of voids disturb an arbitrary macroscopic stress field has proven complex and assumption-dependent. Consideration of a single void reduces mathematical complexity and is likely sufficient to reveal key influencing variables, but the utility of this solution to fully capture the disturbed stress field depends on the likelihood of void interaction. Void interaction is neglected in this work.

#### 3.1.1 Ellipsoidal Voids and General Solution Characteristics

An ellipsoid has been chosen as the basic void shape in many studies, noting that the axes of an ellipsoid can be modified to make a wide variety of shapes, improving the general applicability of the solution. Authors have typically relied on solutions rooted in linear elasticity. Noting that the constituents of concrete are essentially linear elastic until first cracking and that macro-scale nonlinearity in concrete is caused by crack initiation [13], use of solutions rooted in linear elasticity is easily justified.

#### 3.1.2 Analytical Stress Solution Around Individual 3D Voids

Wang and Shrive [9] used the Sadowsky and Sternberg solution [11] for the stresses around a single triaxial ellipsoidal void in an infinite elastic medium to investigate the

potential stress field disturbances caused by voids in concrete. The principal axes of the stress state are in line with the axes of the ellipsoid, as shown in Fig. 3. Sadowsky and Sternberg's solution, in ellipsoidal coordinates $\alpha_i$, provides the disturbed stress tensor $(\sigma_{ij}^c)$ as the sum of the macroscopic stress tensor $(\sigma_{ij}^\infty)$ and five component solutions, in which the coefficients $A_N$ can be determined from the boundary conditions (see [11] for details):

$$\sigma_{ij}^c = \sigma_{ij}^\infty + \sum_{N=1}^{5} A_N (\sigma_{ij})_N \tag{1}$$

Wang and Shrive noted that the magnitude of the disturbed stress depends on the macroscopic stress state, Poisson's ratio, and shape of the void (i.e. the ratio of the various radii of the ellipse to one another), but not the absolute size of the void itself.

Wang and Shrive applied a uniaxial compressive macroscopic load ($\sigma_y^\infty = -1$, $\sigma_x^\infty = \sigma_z^\infty = 0$) and sought the maximum tensile stresses induced on the surface of the ellipsoidal void, modifying the other two variables (Poisson's ratio and void shape). In uniaxial compression, the maximum tensile stress is tangent to the top of the void (i.e. at the point $P$ in Fig. 3).

The important characteristics of this solution are as follows:

1. For spheres, the peak tensile stress generated around a void ranges from 0.6 to 0.75 times the distant applied compressive stress, depending on Poisson ratio values; for ellipses with a broad range of aspect ratios, the peak tensile stress generated around the void ranges from 0.6 to 1.0 times the distant applied compressive stress.
2. In more spheroidal cases, Poisson's ratio more strongly influences the results. Further, in the 2D case, the influence of Poisson's ratio disappears. 2D solutions for stresses around ellipses do not account for Poisson effects—this can result in substantial variation between the 2D and 3D cases.



**Fig. 3** The ellipsoid of radii a, b, and c, as well as the axis system, used by Wang and Shrive [9] in their analysis of the stresses around an ellipsoidal void
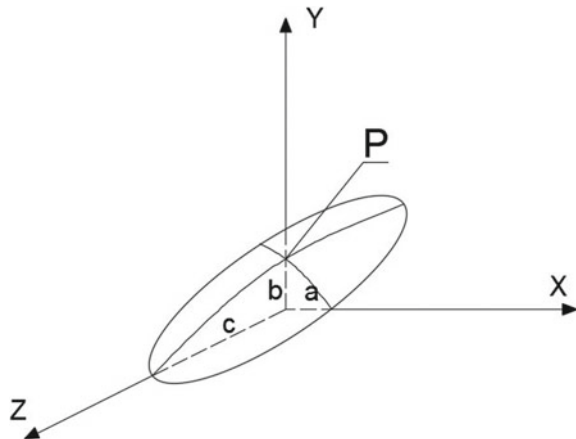
## *3.2 Particular Sources*

### 3.2.1 Solid Inclusions

An inclusion refers to an enclosed region within a continuum within which the material properties differ from those of the surrounding matrix [14]. The material incompatibility imposed by inclusions is well-understood to disturb stress fields and is a potential source of tensile stress. Solid inclusions are inclusions for which the material properties of the enclosed region are non-zero values (i.e. the inclusions considered here are different materials, not air pockets). Two types of solid inclusions can be easily identified in concrete and masonry: aggregates and reinforcing bars.

To estimate the effect of aggregate particles on the local stress field, Shrive [15] used Goodier's [10] solution for a spherical inclusion in an infinite, isotropic medium. Shrive plotted the results of this solution under uniaxial compressive stress for selected values of Poisson's ratio and varying $E_{agg}/E_{matrix}$. He included the useful limiting values when $E_{agg}$ approaches zero, allowing for comparison to Wang's solution for further verification.

Shrive found that Goodier's solution agreed well with that of Sadowsky and Sternberg. For reasonable values of $E_{agg}/E_{matrix}$, he found the maximum tensile stress generated at the surface of a spherical aggregate particle to range between 5 and 10% of the distant applied compressive stress. This figure pales in comparison to the maximum tensile stress produced by a spherical void (ranging between 60 and 75% of the applied compressive stress). Given a constant shape, the effects of voids significantly outweigh those of aggregate.

One may argue that an angular aggregate shape may have a far more severe impact on the solution than a spherical aggregate. However, Wang and Shrive's analysis of ellipsoidal voids [9] shows that a fairly distorted ellipsoid ($a/c = 10, b/c = 1$) produced a tensile stress about 25% higher than that of the sphere with Poisson's ratio held constant (0.95 vs. 0.75 normalized stress units). Even if the maximum tensile stress around an aggregate is increased by this amount, the tensile stresses surrounding an aggregate are negligible compared to those around a spherical void. This is not to mention that non-spherical voids may also present themselves in dry concrete mixes, such as those used in the production of concrete block [16].

### 3.2.2 Strain Incompatibilities (Masonry)

In the case of masonry, the differences in material properties of bricks and mortar may also induce tensile stresses. Hilsdorf [1] noted this when he proposed his "lateral tensile splitting" theory for masonry loaded in axial compression. Noting that mortar is more flexible than units, under compression he explained that the bricks would restrain the lateral expansion of the mortar, resulting in a state of triaxial compression in the mortar and a state of compression-biaxial tension in the bricks. Hilsdorf thought

the tensile forces arising due to this effect drove the failure of axially compressed masonry prisms.

Khoo [2] further extended Hilsdorf's concept of failure by tensile stresses caused by brick/mortar confinement effects. He postulated that bricks and mortar would have to simultaneously fail, found failure envelopes for bricks in compression-biaxial tension as well as mortar in triaxial compression, and sought to find if such simultaneous failure occurred. While he asserts that brick and mortar simultaneously fail due to the lateral straining effect in his paper, examination of his material stress–strain curves reveals that mortar would need to strain well past its ultimate limit in order to fail at the same stress–strain point as the bricks he tested.

Assuming positive directions in line with the standard right-hand positive Cartesian system, isotropy within each material, uniform stress distributions within each material, linear behaviour, and fully bedded mortar joints, one can straightforwardly derive an expression for the lateral tensile stress in the brick as a result of axial compression:

$$\sigma_{xb} = \frac{[\nu_b - \beta \nu_m]\sigma_y}{1 - \nu_b - \alpha\beta + \alpha\beta\nu_m} \tag{2}$$

where $t_b$ and $t_m$ are the thicknesses of block and mortar, respectively and $\alpha \underset{=}{\mathrm{def}} \frac{t_b}{t_m}$, $\beta \underset{=}{\mathrm{def}} \frac{E_b}{E_m}$.

The assumption of isotropy can be easily relaxed. Shrive and Jessop [17] assumed anisotropy in all three directions and produced the consequent equations. Solving for the lateral stresses using experimental values, they found lateral tensile forces amounting to 2% of the axial compressive stress. Shrive [18] reports that Stafford-Smith and Carter and Thomas and Turkstra performed similar analyses, finding, at most, lateral tensile stresses equal to 3% of the axial compressive stress. Further, Shrive [19] created a finite-element model of a four-unit high, fully bedded brick and mortar prism subjected to axial compressive load (symmetry conditions were applied and only one-eighth of the prism was explicitly modelled). This more detailed analysis (relaxing the assumption that the stresses are constant in each material) permits higher peak tensile stress values; even in this analysis, tensile stresses range between 3 and 4% of the macroscopic compressive stress. Needless to say, these values are clearly negligible when compared to the lateral stresses arising around voids.

## 3.3 Relative Impact of Tensile Stress Sources in Concrete and Masonry

The peak tensile stresses generated from all the tensile stress sources discussed above, based on linear elastic analyses prior to cracking, are plotted in Fig. 4. Voids are the dominant tensile stress source by a significant margin, despite the plotted values representing conservative values of void contribution. This numerical observation
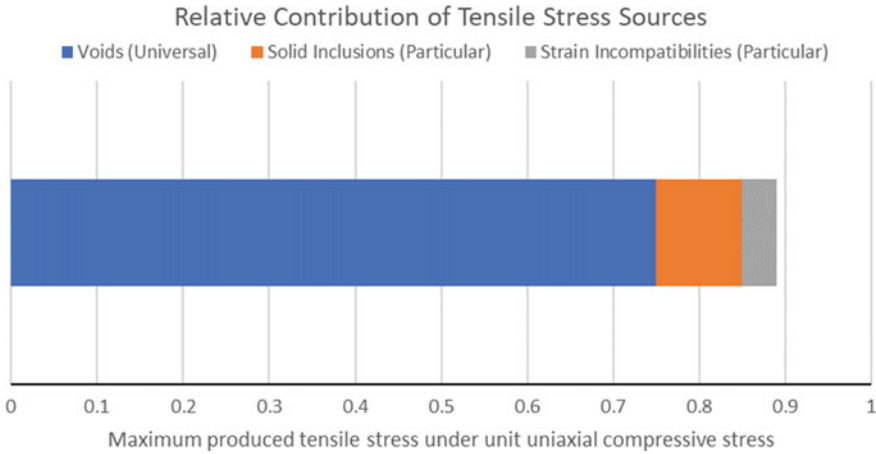
**Fig. 4** Contribution of each aforementioned source of tension to the global tensile stress state in uniaxially compressed concrete/masonry

supports the empirical observation that various brittle materials crack in similar ways.

### 3.3.1 Corollary Regarding Hilsdorf and Khoo's Lateral Tensile Splitting Theory

Clearly, any theoretical treatment of the fracture and failure of concrete and masonry in a globally compressive stress field ought to be considered to be governed by voids. Assertions that other sources of tension (e.g. the strain incompatibilities cited by Khoo and Hilsdorf in their lateral tensile splitting approach) are critical in a globally compressive stress field clearly misrepresent the problem. That such a key theory of failure in the masonry community is so poorly rooted in rudimentary stress analysis and physical reality is concerning.

## 4 Applying Griffith's Criteria in Compression—Crack Propagation and $K_I$

### 4.1 Brief Summary of Griffith's Criteria Applied in Uniaxial Tension

Having clarified the major source of tensile stresses in uniaxial compression (voids), the next step is to investigate the possibility of applying Griffith's criteria in the analysis of compressive fracture. A basic review of the application of Griffith's

criteria in the tensile fracture of brittle materials will elucidate the differences between the tensile and compressive case and provide guidance on a way forward.

Consider the most fundamental case—the tensile fracture of a brittle material in uniaxial tension with a notch-shaped crack. As previously mentioned, the stress at the tip of such a crack approaches infinity, so Griffith's stress criterion is easily satisfied. The energy criterion, however, is not satisfied, so the crack will not propagate. The crack will propagate if the release of strain energy by incremental crack growth is equal to the energy demands of that incremental crack growth. In the case of a brittle material, the energy demands are associated with the surface energy of the exposed surfaces. Equating the strain energy release rate and the energy demands produces the following equality, where σ is the distant tensile stress, a is the notch crack semi-length (Fig. 2), $E$ is Young's modulus, and $\gamma$ is the brittle material's surface energy:

$$\sigma = \sqrt{\frac{2\gamma E}{\pi a}} \tag{3}$$

Irwin [20] generalized this approach by defining this condition in terms of the stress intensity factor, $K_I$, and critical energy release rate, $G$:

$$\frac{K_I^2}{E} = G_{\mathrm{cr}} \tag{4}$$

In the straightforward case presented, the quantities $K_I$ and $G$ can be related to the previous equation as follows:

$$K_I = \sigma\sqrt{\pi a}, G_{cr} = 2\gamma \tag{5}$$

In the more general case, $G$ may primarily depend on demands other than surface energy. $K_I$ can be defined as follows for a notch crack in uniaxial tension, where $F$ is a term related to the geometry of the problem at hand:

$$K_I = F\sigma\sqrt{\pi a} \tag{6}$$

For an arbitrarily shaped crack $K_I$ can be defined as the following limit, where the stress state surrounding the crack is defined by polar coordinates at the crack tip:

$$K_I = \lim_{r\to 0}\sqrt{2\pi r}\sigma_{yy}(r,0) \tag{7}$$

Contemporary design procedures for tensile fracture are built on finding critical values for $K_I$ (denoted as $K_{\mathrm{IC}}$) after which the energy criterion and unbounded crack propagation ensues (i.e. crack propagation occurs when $K_I > K_{\mathrm{IC}}$). Note that, inherently, for $K_I$ to be a quantity of any value, the stress state at the crack tip must approach infinity, otherwise the limit evaluates to zero.

The formulations above were developed assuming the faces of the crack separated normally as the crack extended—this corresponds to what is known as "Mode I" failure. The crack surfaces could also shear in and out of plane relative to one another, known as "Mode II" and "Mode III" failure, respectively.

## 4.2 Previous Crack Geometry Assumptions in Compression

Attempting to apply a similar procedure in compression requires some thought and assumptions. To begin with, what approach will be taken to model the geometry of a crack in uniaxial compression, noting that voids are the sources of tensile stress in this case?

An admittedly crude means of conceptualizing crack growth originating from voids is to simply consider a crack growing from the top of a void to extend one of the ellipse's axes—a 2D sketch of the concept is shown in Fig. 5. Wang and Shrive [9] employed this approach when investigating energy release rate variation with crack extension; Yuan et al. [21] also investigated fracture nucleation in compression from this perspective.

The clear advantage of this approach is that it permits the use of the Sadowsky and Sternberg stress and associated displacement solutions to investigate the variation of stress and strain energy release with the extension of the idealized crack. Geometrically, this approach may provide broad characteristics of the global stress distribution and strain energy release as the nucleated crack reaches longer lengths—however, at shorter crack lengths the assumed geometry does not appear to be an ideal representation (see Fig. 5). In addition to the geometric shortcomings, $K_I$ cannot be utilized in this framework, preventing harmonization with tensile design procedures. The calculation of $K_I$ requires a stress field approaching infinity at the crack tip, so modelling a propagating crack as an ellipse (which produces a bounded tensile stress) negates the use of the $K_I$ concept. Yuan et al. [21] presented a $K_I$ formulation within this framework but it did not achieve internal dimensional consistency.



**Fig. 5** Observed and idealized crack propagation geometry as per Wang and Shrive [9] when investigating energy release rate
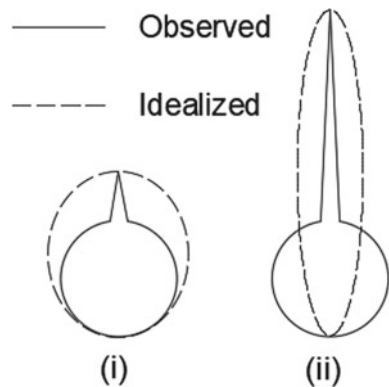
Nevertheless, this conception of crack propagation may give useful insight on strain energy release rate (as that depends less on local phenomena like the crack tip stress state), especially at later stages when the geometry of this approach more closely approaches expected observations.

## *4.3 New Crack Geometry Assumptions in Compression*

Since the largest tensile stresses in uniaxial compression were found by far and away to occur at the surface of ellipsoidal voids (specifically, at $P$ as labelled in Fig. 3), cracks ought to be considered to nucleate from the surfaces of these voids. Compression-parallel crack extension originating from ellipsoidal voids appears to take the form of planar cracks of negligible width propagating from a void, as shown in Fig. 6. To permit crack propagation along any radial line from the void, notches ought to be assumed to be radially distributed along the perimeter of a given void. A crack will propagate when the tensile stress at a radial position on the void surface satisfies energy requirements.

This distribution of notch flaws around the perimeter of the void is crucial if application of the concepts from tension is sought. Note that $K_I$ as a metric will only work if the stress state at the tip of the flaw tends to infinity. At an ellipsoidal void, stresses do not tend to infinity—the tensile stresses in this case were evaluated to lie between 0.6 and 1 times the distant compressive stress [9]. The distribution of notched cracks around the perimeter of a void permits the use of $K_I$ and associated approaches developed for tensile fracture.

Further, while we note three modes of crack extension can occur, it will be assumed that for crack extension within uniaxial compression, Mode I is the only relevant mode.

This conception of crack propagation in uniaxial compression matches experimental observations. Two particularly notable observations in the literature encourage the proposed idealization. Firstly, in typical compression cylinder testing of plain concrete, crack faces appear to separate only normally, not transversely. Secondly, Iskander and Shrive [22] tested a concrete specimen with a circular void cored through the depth, and obtained a planar crack originating from the top of the

**Fig. 6** Idealization of crack propagation in uniaxial compression. In subsequent analysis, crack length, a, will be defined as shown in (ii)

Radially distributed notches (i)

Propagated crack geometry (ii)
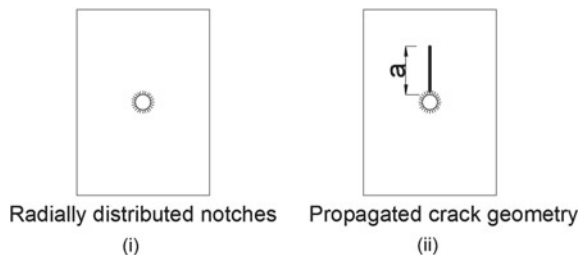
circle, matching the proposed idealization. These observations would suggest that Mode I separation is indeed the dominant mode.

While this idealization matches observation, at first sight it does not lend itself to well-understood analytical solutions. Simplification of the stress field evolution with crack growth and determination of $K_I$ would greatly benefit attempts to apply fracture mechanics principles to cases of uniaxial compression.

## 4.4 Determining $K_I$ vs. Crack Length in Uniaxial Compression

Iskander and Shrive [12] used the Cornell Fracture Group's FRANC2D to create a 2D, linear elastic, plane-strain finite-element model to investigate the evolution of stresses in the case where a line crack propagates from a 2D void in a field of uniaxial compression. A notch crack was explicitly seeded at the position of expected crack nucleation and propagation. A variety of shapes (circles, ellipses, and rhombuses of various sizes) were modelled. $K_I$ values were numerically determined as the hairline crack was propagated, and $K_I$ vs. crack length curves were plotted. Their results produced two particularly notable points:

1. As shown in Fig. 7, the numerically computed $K_I$ values did not monotonically increase with crack length—in tension, $K_I$ increases monotonically with crack length (as evident from $K_I = \sigma\sqrt{\pi a}$). This finding explains the possibility for stable crack propagation in compression as well as the unstable crack propagation observed in tension. In tension, reaching $K_{IC}$ for a particular applied stress guarantees $K_I > K_{IC}$ for all further crack lengths—in compression, $K_I > K_{IC}$ only over a finite range, after which the stress must be increased to make $K_I > K_{IC}$.
2. The influence of size and shape on $K_I$ values was initially counter-intuitive. The $K_I$ vs. crack length curve under constant applied stress looked similar for almost all void shapes. However, peak $K_I$ values depended on the absolute size of the source void. Having noted earlier that the maximum tensile stress generated by a void is independent of absolute size [9], this relationship requires further explanation. Further, applying Griffith-type a priori reasoning to determine critical void shapes yielded inaccurate results. Consider the two ellipses in Fig. 8. A Griffith-type explanation would suggest ellipse (ii) would be critical, as the sharper end is oriented along the direction of expected crack propagation. However, ellipse (i) produced higher peak $K_I$ values.

The authors postulated that these facts could be reconciled by considering $K_I$ to primarily depend on the tensile stresses along the line of expected crack propagation. To test this concept, a 2D plane-strain finite-element model with boundary conditions, material properties, and loading identical to that of Iskander and Shrive [12] was developed in Abaqus. However, no notch cracks were included in the geometry. This model was used to perform a stress analysis on four of the voids included in their
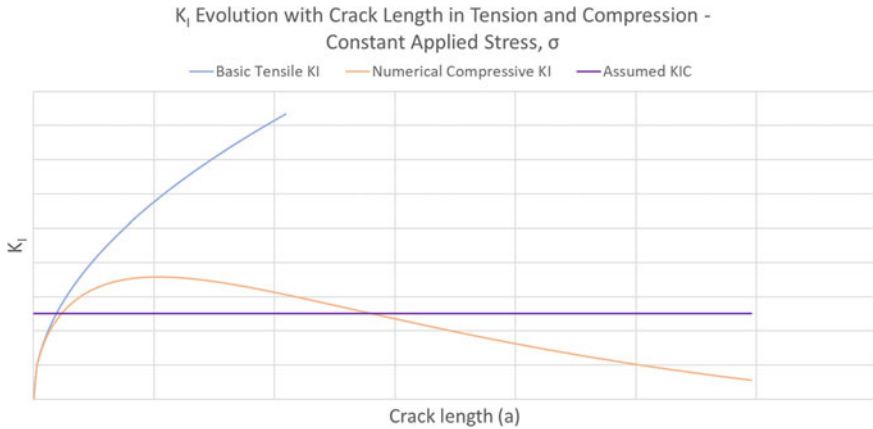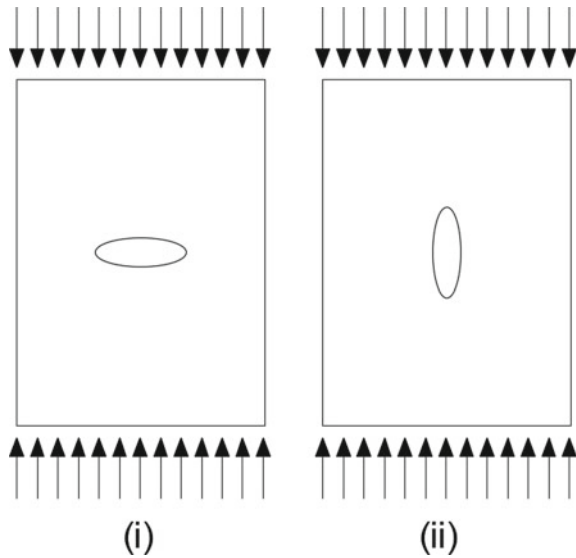
**Fig. 7** $K_I$ as a function of crack length in the tension and compression. The difference in these curves explains the observation of stable crack propagation in compression

**Fig. 8** Two ellipses analysed by Iskander and Shrive in their parametric study of shape influence on compressive $K_I$ values—ellipse (i) produced a higher $K_I$, contrary to Griffith-based intuition



parametric study—circles of 5 mm and 20 mm diameter, as well as the two ellipses shown in Fig. 8. $K_I$ values were calculated entirely by post-processing the stresses along the line of expected crack propagation (a vertical line from the top of the void). Crack length (a) was defined as shown in Fig. 6 (ii), and $K_I$ for a crack of a given length originating from the void was simply computed as $K_I = \sigma(a)\sqrt{\pi a}$, where $\sigma(a)$ was defined as the tensile stress at the position of the crack tip. Conceptually, $K_I$ along the notch crack propagating from the void was considered to evolve identically to $K_I$

as in the case of a notch in a field of uniaxial tension, but the "distant applied tension" in the equation was simply taken to be the stress along the line of propagation.

As shown in Fig. 9, the $K_I$ vs. crack length curve took an identical form via both approaches. Joint consideration of the terms whose product comprised the post-processed $K_I$ value ($\sigma(a)$ and $\sqrt{a}$), as shown in the right-hand side of Fig. 9, explains the shape of the obtained curve. The rate of change of the $\sqrt{a}$ term is high at short crack lengths and low at larger values. Contrarily, in a uniaxial compressive stress field, $\sigma(a)$ begins as a tensile value at the crack surface and immediately begins decreasing, approaching the distant compressive stress the further one travels from the void surface. If this rate of decrease is sharp (i.e. the stress changes from tensile to compressive across a short distance), the $\sigma(a)$ term in the product will decrease faster than the $\sqrt{a}$ term increases, and a low peak $K_I$ value will be obtained at a short crack length. However, if the rate of decrease of $\sigma(a)$ is slow (i.e. the decrease happens over a large length), the product of $\sigma(a)$ and $\sqrt{a}$ will produce large values over a bigger range of crack lengths. This will yield a larger peak $K_I$ value at a comparatively long crack length. It is important to note that the $\sqrt{a}$ term in the product will not vary with void geometry. Regardless of the geometry of the void, $a$ will be defined the same way and $\sqrt{a}$ will be computed identically. Conversely, the stress distribution, $\sigma(a)$, will vary depending on void characteristics (shape and size). The behaviour and trends of $K_I$ should be completely characterized by $\sigma(a)$.

This approach explains the unintuitive results obtained regarding shape influence on $K_I$. Firstly, while the maximum tensile stress is identical for two identically shaped voids regardless of absolute size, the radius of influence of the void increases with void size. The resulting effect is that the stress plot provided on the right in Fig. 9 is stretched—higher tensile stress values are maintained over a larger range of crack lengths, allowing for higher overall $K_I$ values to be obtained at later crack lengths. This logic exactly matches the results Iskander and Shrive [12] obtained—for a constant shape, as absolute void size was increased, larger $K_I$ values were obtained, and the peak was observed at increasingly large crack lengths.

Explanations considering the variation of $\sigma(a)$ also straightforwardly address the dilemma presented in Fig. 8. The same stress analysis was conducted on two
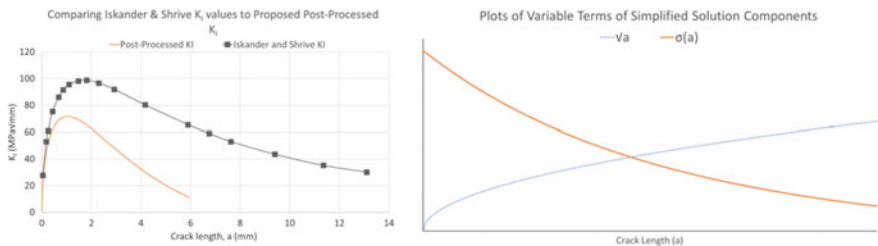


**Fig. 9** Left—$K_I$ vs. crack length for a notch crack propagating from a circular void 20 mm in diameter, via Iskander and Shrive's approach and the proposed approach. Both approaches produce curves of the same family. Right—relative values of extracted tensile stress and crack tip terms in the product used to post-process $K_I$
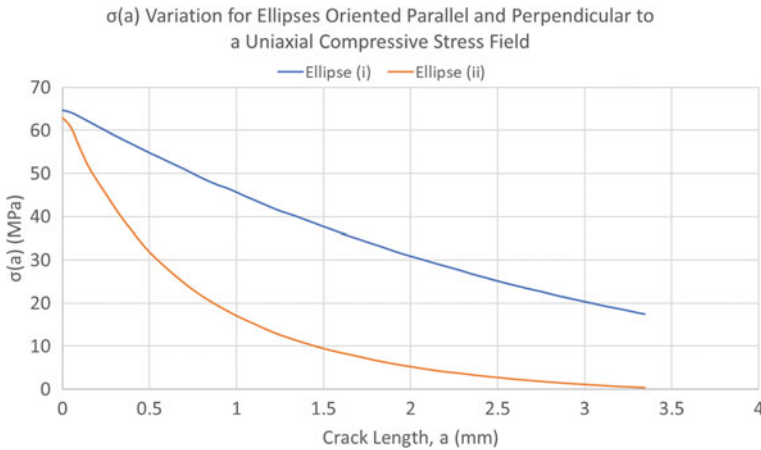
**Fig. 10** $\sigma(a)$ curves for ellipse (i) and (ii) from Fig. 8. Each ellipse had minor and major diameters of 10 mm and 20 mm, respectively. The low rate of change and consequent high values obtained from the curve for ellipse (i) explains the higher $K_I$ values produced by this shape

ellipses, each 10 mm $\times$ 20 mm in diameter, but with one oriented parallel to the field of compression and one perpendicular to it. The tensile stresses along the line of expected crack propagation (a vertical line originating at the top of the void) were determined and plotted. A far lower rate of change in $\sigma(a)$ was observed in ellipse (i) compared to ellipse (ii), as shown in Fig. 10. Since $\sigma(a)$ for ellipse (i) maintains high values over a large range of crack lengths, a high peak $K_I$ value is obtained at a longer corresponding crack length. Conversely, the $\sigma(a)$ term in ellipse (ii) rapidly decays, and high $K_I$ values are difficult to obtain.

## 5 Conclusions and Areas of Future Work

The use of fracture mechanics to explain the failure of brittle materials in compression as well as tension matches empirical observations of the underlying cause of brittle failure, regardless of the stress state—the development and propagation of cracks. Despite the associated difficulties, this approach presents an opportunity for a rational consideration of material behaviour in compression. To proceed with this approach, it was first necessary to determine relevant sources of tensile stress in a compressive stress field. It was determined that 2D or 3D voids (depending on desired solution dimension) are a universal and overwhelmingly dominant source of tensile stresses in compressed brittle materials.

Having determined that tensile stresses originated from voids, it was found that the most sensible way to idealize crack propagation was to assume notches to be distributed along the perimeter of a given void. Crack propagation was considered as the extension of a notch crack located at the location of maximum tension at

the void. It was then proposed that $K_I$ could be calculated by treating the propagation of perimeter notch cracks as depending primarily on the distribution of tensile stresses along the line of expected crack propagation. Not only was this concept verified against Iskander and Shrive's simulation, the new perspective readily explained unintuitive results obtained from the parametric study.

These encouraging results open up several areas of future work. Firstly, the factors resulting in the discrepancy of the far simplified post-processed $K_I$ values and the numerically obtained ones require further investigation—rational determination of the source of this discrepancy can provide a simple, theoretical means of determining $K_I$ vs. crack length curves in compression for any void size and shape. This would be a significant contribution to the literature. The investigation of energy release requirements in the context of the proposed framework is also a significant gap requiring further work. Investigation of the tenability of this approach in multi-axial stress conditions is also outstanding. The authors aim to develop these concepts more rigorously and hope to contribute to the development of a rational understanding of fracture in compressive stress states.

# References

1. Hilsdorf H (1969) Investigation into the failure mechanism of brick masonry loaded in axial compression. In: Proceedings of the International Conference on Masonry Structural Systems, Houston
2. Khoo C (1972) Failure criterion for brickwork in axial compression. University of Edinburgh, Edinburgh
3. Mann W, Muller H (1982) Failure of shear-stressed masonry - an enlarged theory, tests and application to shear walls. In: Proceedings of the British Ceramic Society, No. 30, Load-bearing Brickwork, Stoke-on-Trent
4. Baker L (1982) A principal stress failure criterion for brickwork in biaxial bending. In: Proceedings of the 6th International Brick and Block Masonry Conference, Rome
5. Shrive N, El-Rahman M (1985) Understanding the cause of cracking in concrete: a diagnostic aid. Concrete Int, 39–44
6. Cormeau A, Shrive N (1995) Fracture mechanics and the future strength design of masonry. In: Proceedings of the Seventh Canadian Masonry Symposium, Hamilton
7. Iskander M, Shrive N (2018) Fracture of brittle materials under uniaxial compression. Proced Struct Integrity 13:976–981
8. Griffith A (1921) The phenomena of rupture and flow in solids. Phil Trans Royal Soc London. Series A, Containing Papers of a Mathematical or Physical Character 221:163–198
9. Wang E, Shrive N (1993) On the Griffith criteria for brittle fracture in compression. Eng Fract Mech, 15–26
10. Goodier J (1933) Concentration of stress around spherical cylindrical inclusions and flaws. J Appl Mech 55(7):39–44

11. Sadowsky M, Sternberg E (1949) Stress concentration around a triaxial ellipsoidal cavity. J Appl Mech, 149–57
12. Iskander M, Shrive N (2020) The effect of the shape and size of initial flaws on crack propagation in uniaxially compressed linear brittle materials. Theo Appl Fracture Mech 109
13. Hsu T, Slate FO, Sturman GM, Winter G (1963) Microcracking of plain concrete and the shape of the stress-strain curve. ACI Mater J 60(14):209–224
14. Mura T (1987) Micromechanics of defects in solids. Martinus Nijhoff Publishers, Hingham
15. Shrive N (1983) Compression testing and cracking of plain concrete. Mag Concr Res 35(122):27–39
16. Concrete Masonry Association of Australia (2014) CM04 concrete masonry—manufacture. Concrete Masonry Association of Australia, Artarmon
17. Shrive N, Jessop E (1980) Anisotropy in extruded clay units and its effect on masonry behaviour. In: Proceedings of Second Canadian Masonry Symposium, Ottawa
18. Shrive N (1983) A fundamental approach to the fracture of masonry. In: Proceedings of the 3rd Canadian Masonry Symposium, Edmonton
19. Shrive N (1985) Compressive strength and strength testing of masonry. In: Proceedings of the 7th International Brick Masonry Conference, Melbourne
20. Irwin G (1957) Analysis of stresses and strains near the end of a crack traversing a plate. J Appl Mech 24:361–364
21. Yuan Y, Lajtai E, Ayari M (1993) Fracture nucleation form a compression-parallel, finite-width elliptical flaw. Int J Rock Mech Min Sci 30(7):873–876
22. Iskander M, Shrive N (2021) On the fracture of brittle and quasi-brittle materials subject to uniaxial compression and the interaction of voids on cracking. Const Build Mat 290

# Correction to: Bike Share's Impact on COVID-19 Transmission and Bike Share's Responses to COVID-19: A Case Study of Washington DC

**Pedram Beigi, Mohaiminul Haque, Mohammad Sadra Rajabi, and Samer Hamdar**

**Correction to:**
**Chapter 48 in: R. Gupta et al. (eds.),** *Proceedings*
*of the Canadian Society of Civil Engineering Annual*
*Conference 2022*, **Lecture Notes in Civil Engineering 359,**
https://doi.org/10.1007/978-3-031-34027-7_48

The original version of the book was published with incorrect Reference 20 in Chapter 48, which has now been corrected. The book and the chapter have been updated with the changes.

---

The updated version of this chapter can be found at
https://doi.org/10.1007/978-3-031-34027-7_48